Geophysical Monograph Series

Including

IUGG Volumes
Maurice Ewing Volumes
Mineral Physics Volumes

94 **Double-Diffusive Convection** *Alan Brandt and H. J. S. Fernando (Eds.)*

95 **Earth Processes: Reading the Isotopic Code** *Asish Basu and Stan Hart (Eds.)*

96 **Subduction Top to Bottom** *Gray E. Bebout, David Scholl, Stephen Kirby, and John Platt (Eds.)*

97 **Radiation Belts: Models and Standards** *J. F. Lemaire, D. Heynderickx, and D. N. Baker (Eds.)*

98 **Magnetic Storms** Bruce *T. Tsurutani, Walter D. Gonzalez, Yohsuke Kamide, and John K. Arballo (Eds.)*

99 **Coronal Mass Ejections** *Nancy Crooker, Jo Ann Joselyn, and Joan Feynman (Eds.)*

100 **Large Igneous Provinces** *John J. Mahoney and Millard F. Coffin (Eds.)*

101 **Properties of Earth and Planetary Materials at High Pressure and Temperature** *Murli Manghnani and Takehiki Yagi (Eds.)*

102 **Measurement Techniques in Space Plasmas: Particles** *Robert F. Pfaff, Joseph E. Borovsky, and David T. Young (Eds.)*

103 **Measurement Techniques in Space Plasmas: Fields** *Robert F. Pfaff, Joseph E. Borovsky, and David T. Young (Eds.)*

104 **Geospace Mass and Energy Flow: Results From the International Solar-Terrestrial Physics Program** *James L. Horwitz, Dennis L. Gallagher, and William K. Peterson (Eds.)*

105 **New Perspectives on the Earth's Magnetotail** *A. Nishida, D. N. Baker, and S. W. H. Cowley (Eds.)*

106 **Faulting and Magmatism at Mid-Ocean Ridges** *W. Roger Buck, Paul T. Delaney, Jeffrey A. Karson, and Yves Lagabrielle (Eds.)*

107 **Rivers Over Rock: Fluvial Processes in Bedrock Channels** *Keith J. Tinkler and Ellen E. Wohl (Eds.)*

108 **Assessment of Non-Point Source Pollution in the Vadose Zone** *Dennis L. Corwin, Keith Loague, and Timothy R. Ellsworth (Eds.)*

109 **Sun-Earth Plasma Interactions** *J. L. Burch, R. L. Carovillano, and S. K. Antiochos (Eds.)*

110 **The Controlled Flood in Grand Canyon** *Robert H. Webb, John C. Schmidt, G. Richard Marzolf, and Richard A. Valdez (Eds.)*

111 **Magnetic Helicity in Space and Laboratory Plasmas** *Michael R. Brown, Richard C. Canfield, and Alexei A. Pevtsov (Eds.)*

112 **Mechanisms of Global Climate Change at Millennial Time Scales** *Peter U. Clark, Robert S. Webb, and Lloyd D. Keigwin (Eds.)*

113 **Faults and Subsurface Fluid Flow in the Shallow Crust** *William C. Haneberg, Peter S. Mozley, J. Casey Moore, and Laurel B. Goodwin (Eds.)*

114 **Inverse Methods in Global Biogeochemical Cycles** *Prasad Kasibhatla, Martin Heimann, Peter Rayner, Natalie Mahowald, Ronald G. Prinn, and Dana E. Hartley (Eds.)*

115 **Atlantic Rifts and Continental Margins** *Webster Mohriak and Manik Talwani (Eds.)*

116 **Remote Sensing of Active Volcanism** *Peter J. Mouginis-Mark, Joy A. Crisp, and Jonathan H. Fink (Eds.)*

117 **Earth's Deep Interior: Mineral Physics and Tomography From the Atomic to the Global Scale** *Shun-ichiro Karato, Alessandro Forte, Robert Liebermann, Guy Masters, Lars Stixrude (Eds.)*

118 **Magnetospheric Current Systems** *Shin-ichi Ohtani, Ryoichi Fujii, Michael Hesse, and Robert L. Lysak (Eds.)*

119 **Radio Astronomy at Long Wavelengths** *Robert G. Stone, Kurt W. Weiler, Melvyn L. Goldstein, and Jean-Louis Bougeret (Eds.)*

120 **GeoComplexity and the Physics of Earthquakes** *John B. Rundle, Donald L. Turcotte, and William Klein (Eds.)*

121 **The History and Dynamics of Global Plate Motions** *Mark A. Richards, Richard G. Gordon, Rob D. van der Hilst (Eds.)*

122 **Dynamics of Fluids in Fractured Rock** *Boris Faybishenko, Paul A. Witherspoon, and Sally M. Benson (Eds.)*

123 **Atmospheric Science Across the Stratopause** *David E. Siskind, Stephen D. Eckerman, and Michael E. Summers (Eds.)*

124 **Natural Gas Hydrates: Occurrence, Distribution, and Detection** *Charles K. Paull and Willam P. Dillon (Eds.)*

125 **Space Weather** *Paul Song, Howard J. Singer, George L. Siscoe (Eds.)*

126 **The Oceans and Rapid Climate Change: Past, Present, and Future** *Dan Seidov, Bernd J. Haupt, and Mark Maslin (Eds.)*

127 **Gas Transfer at Water Surfaces** *M. A. Donelan, W. M. Drennan, E. S. Saltzman, and R. Wanninkhof (Eds.)*

128 **Hawaiian Volcanoes: Deep Underwater Perspectives** *Eiichi Takahashi, Peter W. Lipman, Michael O. Garcia, Jiro Naka, and Shigeo Aramaki (Eds.)*

129 **Environmental Mechanics: Water, Mass and Energy Transfer in the Biosphere** *Peter A.C. Raats, David Smiles, and Arthur W. Warrick (Eds.)*

Geophysical Monograph 130

Atmospheres in the Solar System
Comparative Aeronomy

Michael Mendillo
Andrew Nagy
J. H. Waite
Editors

American Geophysical Union
Washington, DC

Published under the aegis of the AGU Books Board

John E. Costa, Chair; Gray E. Bebout, David Bercovici, Carl T. Friedrichs, James L. Horwitz, Lisa A. Levin, W. Berry Lyons, Kenneth R. Minschwaner, Darrell Strobel, and William R. Young, members.

Library of Congress Cataloging-in-Publication Data

Atmospheres in the solar system : comparative aeronomy / Michael Mendillo, Andrew Nagy, J. H. Waite, editors.
p. cm. -- (Geophysical monograph ; 130)
Includes bibliographical references.
ISBN 0-97590-989-2
1. Planets--Atmospheres. 2. Satellites--Atmospheres. I Mendillo, M. (Michael) II. Nagy, Andrew. III. Waite, J. H. (John H.) IV. Series.

QB603.A85 A76 2002
551.5'0999--dc21

2002025426

ISSN 0065-8448

Cover images. The auroral emissions from a planet offer the most spectacular examples of energetics, dynamics, and coupling in upper atmospheric science. The ultraviolet aurora captured by the Dynamics Explorer-1 satellite two decades ago revolutionized our understanding of magnetospheric-ionospheric interactions in the terrestrial system. Illustrated on the back cover (courtesy of L. A. Frank and J. D. Craven) is an active substorm event. The Hubble Space Telescope image of UV aurora on Saturn (front cover courtesy of J. T. Trauger) extends auroral science to the outer planets in preparation for the Cassini mission en route to the Saturnian system.

Printed in the United States of America.

CONTENTS

CONTENTS

Overleaf: Portrayed in these elegant mid-17th century copper engravings are (top) the System of Copernicus (*Systematis Copernicani*) showing the heliocentric cosmology in a context of Solar-Terrestrial emphasis, and (bottom) the *Planisphaerium Copernicanum* depicting the Sun, planets and moons as a true planetary system. In the top image, the blend of diurnal and annual solar illumination of the Earth is shown with careful attention to terrestrial geography, giving a reality to our planet, but little attention to the Moon. Mars appears as a red star with Jupiter and Saturn green, with no attempt to portray any physical difference; indeed they were still points of light and not yet real places. Venus and Mercury are ornaments to the Sun, itself with many outgoing rays and streamers filling the space out to the zodiac and beyond.

The lower figure chronicles the onset of astronomical discoveries with a depiction of the four moons of Jupiter discovered in 1610. Galileo's *Medicean Stars* encircling Jupiter are today called the Galilean satellites, Io, Europa, Ganymede and Callisto - fascinating worlds here shown with only slightly smaller symbols than used for Jupiter itself. Collectively, they have a cloud-like region to define their space. The Earth, Moon and other planets also have atmospheric-like regions surrounding them.

(From the *Atlas Coelestis seu Harmonia Macrocosmica* of Andreas Cellarius, 1660-1661 edition, Amsterdam; 25 x 28 5/8" engravings.)

PREFACE

Atmospheres are crucial components of our universe. They are the only observable regions of stars and giant planets, both within and beyond our solar system. Some terrestrial-size bodies (Venus, Earth, Mars, Titan and Triton) have permanent atmospheres while others (e.g., Mercury, Moon, Io, and Europa) have tenuous gaseous envelopes that change daily. Comets are tiny bodies by planetary yardsticks, but their atmospheres can be the largest visible objects in the night sky. Atmospheric science strives to understand how such a diverse set of atmospheres form, evolve, and disappear.

Our current understanding of the mystery of life links atmospheres to biology via such terms as "biosphere" and "astrobiology." But even aside from the question of life beyond Earth, the study of solar system atmospheres is, in its own right, an exciting and exploration-rich field of modern space science. The origin of this monograph is based on that fact. While the laws of physics are the same for each member of the solar system, the chemical constituents are not, nor are their magnetic fields, or amount of energy received from the Sun.

Within this context of diversity in solar system membership, the comparative-studies approach has emerged as the framework best suited to understanding the coupling, energetics, and dynamics of multiple atmospheric systems. To avoid a mere survey of intrinsic characteristics, to move beyond classification nomenclature being a stand-in for progress, and to probe the depth and breadth of our understanding requires a timely and comprehensive approach to a rapidly changing field. We have addressed this need with an eye towards tutorial overviews and state-of-the-art descriptions for graduate students and young professionals drawn to aeronomy. We couple this to an agenda of synthesis for veterans in the field. Thus, the six sections of this monograph (each with multiple chapters) are so structured, and all contain an excellent set of references to enrich and guide additional research.

The specific origin of this book derives from a series of workshops at the annual meeting on Coupling, Energetics and Dynamics of Atmospheric Regions (CEDAR) held each summer in Boulder, Colorado. Comparative mesospheres, gravity wave signatures, aurora and airglow, and exospheres were the principle topics discussed over a several year period. From these workshops, a clear need emerged: a comprehensive meeting devoted exclusively to Comparative Aeronomy in the Solar System. With support from NASA and NSF and organizational expertise from the Southwest Research Institute (SwRI), a Yosemite Conference was held on 8-11 February 2000 on that topic. The current work incorporates the basic topics treated at Yosemite with additional invited contributions. In brief, we engaged the best possible set of authors to treat the core topics needed for the research fields of major current activity. Cross references by section and chapter designations bring a unity to the material presented.

In addition to the authors' expertise and the development and careful preparation of their manuscripts, we acknowledge the valuable contributions of Ms. Cynthia Farmer and Dr. William Lewis of SwRI for organizing the Yosemite Meeting and Dr. Marina Galand (Boston University) and Dr. Steven Bougher (University of Arizona) for their co-convening of pre-cursor CEDAR workshops. Ms. Maria Stefanis O'Connell (Boston University) served as Editorial Assistant with care, devotion and competence, factors of crucial importance in assembling a monograph from author-produced copy. Similarly, we thank our AGU acquisitions editor, Allan Graubard, and production editor, Bethany Matsko, for their expertise on a host of development and production details and schedules. Most importantly, we thank the referees for the chapters contained in this volume. With their generous contributions of time and thoughtful suggestions on content, the colleagues listed below truly share in the success of the chapters that follow.

Several colleagues provided illustrations and images used on the cover and on the section heading pages, including J. Forbes (Section I), J. Spencer (Section II), I. Müller-Wodarg (Section IV), J. Clarke (Section V), and M. Mendillo (Frontispiece, Section III, Section VI).

Finally, in recognition of her fundamental contributions to the field of comparative aeronomy, and in acknowledgement of her enthusiastic participation in the CEDAR Workshops and Yosemite meeting dedicated to these topics, we dedicate this volume to Dr. Jane Fox with best wishes for a continuing career of active research and professional service.

Michael Mendillo
Center for Space Physics
Boston University

Andrew Nagy and J. H. Waite
Space Physics Research Laboratory
University of Michigan

REFEREES

Syun-Ichi Akasofu
David Anderson
Fran Bagenal
Jeff Baumgardner
Steven W. Bougher
Supriya Chakrabarti
John Clarke
Thomas Cravens
Alexander Dalgarno
Thomas Donahue
Rainer A. Dressler
Timothy Fuller-Rowell
Marina Galand
Randy Gladstone
Joseph Grebowsky
Caitlin Ann Griffith
Michael P. Hickey
W. Jeffrey Hughes
Donald M. Hunten
Donald E. Hunton
Bruce Jakosky
Robert E. Johnson
John Kelly
Timothy Killeen
Rosemary M. Killen
Judith L. Lean
Richard Link
Janet G. Luhmann
John Meriwether
Ingo Müller-Wodarg
Edmond J. Murad
Tobias Owen
Xiaoqing Pi
Renee Prange
Henry Rishbeth
Robert Schunk
Steve Smith
Stan Solomon
Ann L. Sprague
Darrell F. Strobel
W. Kent Tobiska
Raymond Walker
Jody Wilson
Roger Yelle
Leslie A. Young

Introduction

Michael Mendillo

Center for Space Physics, Boston University

Andrew Nagy and J. H. Waite

Space Physics Research Laboratory, University of Michigan

When asked about the age of the solar system, the standard response is to say that the Sun and planets formed about 4.6 billion years ago. What this response fails to convey is a sense of continuity or, perhaps better stated, of evolution from then to now. We have in the membership of the solar system nine wonderful experiments in planet formation, dozens of cases for moons, and countless asteroid and comet scenarios. While we can say rather comfortably that our Sun is a "typical" main sequence star, we cannot point to a "typical" planet. There is a lesson in that statement and a research challenge of considerable complexity. This monograph deals with a central component of this challenge, namely, to describe the basic structure and dynamics of the upper atmospheres and ionospheres in our solar system and, moreover, to understand their differences.

Atmospheric scientists tend to divide the gaseous regions above a planet into two broad categories called simply *lower* and *upper* atmosphere. For Earth, the study of the lower regions (*troposphere* and *stratosphere*) form the discipline of meteorology. The study of the upper regions (*mesosphere*, *thermosphere*, *exosphere*) and their ionized components (the *ionosphere*) form the discipline of *aeronomy*. The negative aspect of such a two-fold division is that it encourages thinking of the various atmospheric-spheres as isolated regions of self-contained physics, chemistry, and (in the case of Earth) biology. In reality, there is considerable coupling from lower to upper regions, an aspect of aeronomy fully appreciated only in the last decade. Complimenting this external influence from below, an upper atmosphere has long been known to experience forcing and coupling to and from regions far above it. Aeronomy thus deals with one of the most highly coupled systems in space science --- with neutrals, plasmas, and electromagnetic processes that link the planets, moon, and comets from their surfaces to the solar wind and ultimately to the Sun itself.

The key questions posed in solar system aeronomy are:

(1) What are the constituents of each atmosphere encountered?
(2) How do they absorb solar radiation?
(3) What are the thermal structures resulting from heating versus cooling processes?
(4) What types of ionospheres are formed?
(5) What are the roles of atmospheric dynamics at each site?
(6) Does a planetary magnetic field shield the ionosphere from solar wind impact?
(7) How do trapped energetic particles and electrodynamics affect the atmospheric system?

If all planets were the same, the answers to these questions would depend primarily on distance from the Sun. Such "seen-one, seen-them-all" space science would indeed render the solar system a boring cosmic neighborhood. Happily, space exploration has led to precisely the opposite situation. Distance from the Sun matters, but so do local conditions. Consider Figure 1 where the temperatures of each planet's upper atmosphere are plotted versus distance from the Sun. The temperatures at Venus, Mars, and Saturn fall well below the values that might be

Atmospheres in the Solar System: Comparative Aeronomy
Geophysical Monograph 130

10.1029/130GM01

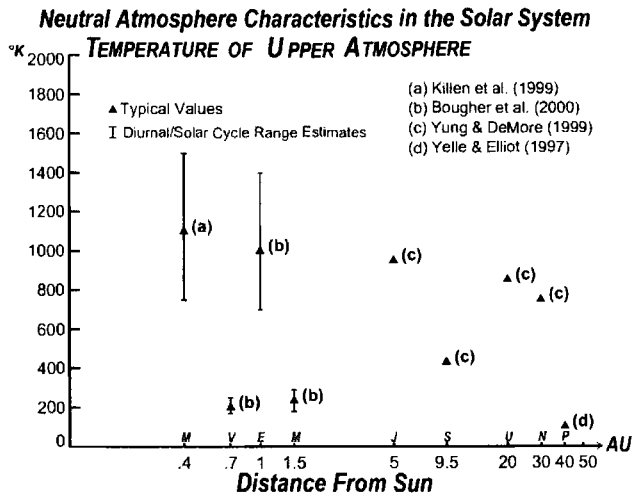

Figure 1. A comparison of the neutral (exospheric) temperature of the upper atmospheres of the planets.

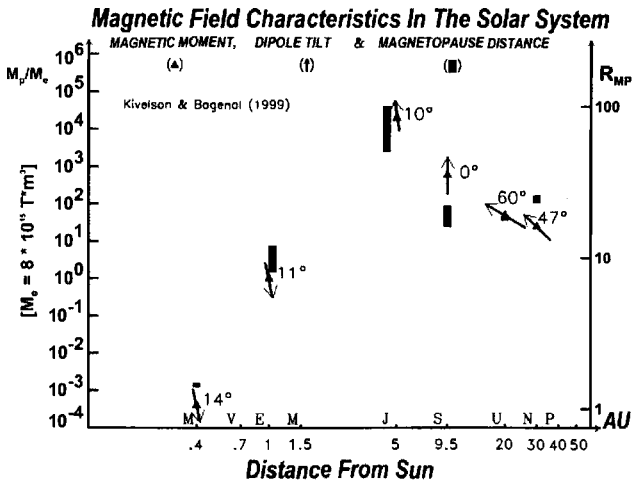

Figure 3. A comparison of the magnetic field dipole strength (normalized to Earth, left axis), dipole tilt (shown with respect to rotation axis), and magnetopause distance (in planetary radii, right axis) for the planets with known global magnetic fields.

estimated via a simple interpolation between neighbors. Composition and local energetics matter!

Using the same format, Figure 2 gives the peak electron density and its altitude for the ionosphere on each planet. Excluding Mercury's weakly ionized component of a thin transient atmosphere, it is the Earth that breaks the pattern. Again, composition (atomic vs. molecular ions) matters! Finally, in Figure 3, the magnetic field strength, orientation, and solar wind stand-off distance are given for the six planets with intrinsic dipoles. The patterns of magnetic pressure balancing solar wind kinetic energy density scale appropriately with dipole strength and distance from the Sun, with the result of all six ionospheres being well inside their planet's magnetopause. Magnetosphere–ionosphere-atmosphere coupling is thus of fundamental importance for these cases. Does the absence of auroral heating at Venus or Mars lead in any way to their low neutral temperatures in Figure 1?

In the chapters that follow, experts in aeronomy and in the fields that couple to it present up-to-date summaries of the major accomplishments and outstanding issues in the field. Tutorial reviews appear in Part I, with an emphasis on the basic principles underlying key systems. That each ionosphere/atmosphere encountered has important interactions with a surrounding plasma medium (solar wind or magnetospheric) is treated in Part II. The chemistry, energetics, and dynamics of atmospheric systems are treated in Part III, and a description of modeling capabilities appears in Part IV. The roles of new observing techniques are described in Part V. Looking beyond our heliospheric members to the emerging field of extra-solar-system planets, Part VI concludes with views of worlds unseen.

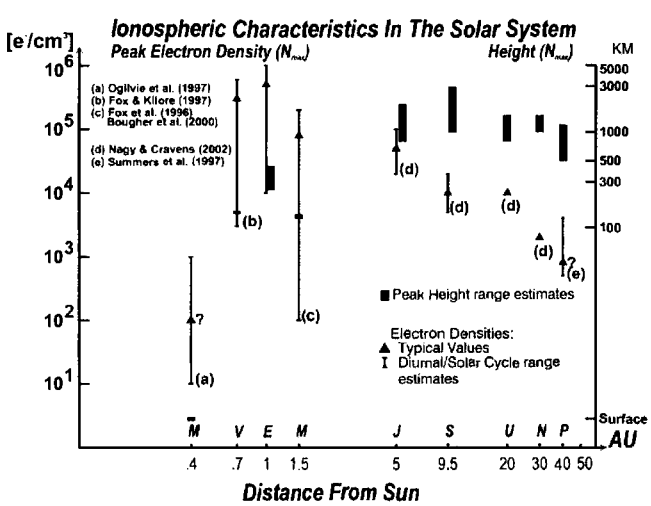

Figure 2. A comparison of the peak electron density (left axis) and its height of occurrence (right axis) of the planets.

REFERENCES

Bougher, S. W., S. Engel, R. G. Roble, and B. Foster, Comparative terrestrial planet thermospheres: 2. Solar cycle variation of global structure and winds at solstices, *J. Geophys., Res., 105*, 18669-17692, 2000.

Fox, J. L., P. Zhou, and S. W. Bougher, The Martian thermosphere/ionosphere at high and low solar activities, *Adv. Space Res.*, 17, 11, 203-218, 1996.

Fox, J. L. and A. J. Kliore, Ionosphere: Solar cycle variations, in *Venus II*, edited by S. W. Bougher, D. M. Hunten and R. J. Phillips, The University of Arizona Press, Tucson, 1997.

Killen, R. M., A. Potter, A. Fitzsimmons, and T. H. Morgan, Sodium D2 line profiles: clues to the temperature structure of Mercury's exosphere, *Planet. Space Sci., 47,* 1449-1458, 1999.

Kivelson, M. G., and F. Bagenal, Planetary magnetospheres, in *Encyclopedia of the Solar System*, edited by Weissman, Academic Press 477-498, 1997.

Nagy A. F. and T. E. Cravens, Solar System Ionospheres, this volume, 2002.

Ogilvie, K. W., J. D. Scudder, V. M. Vasyliunas, R. E. Hartle, and G. L. Siscoe, Observations at the planet Mercury by the plasma electron experiment – Mariner 10, *J. Geophys. Res.*, 82, 1807-1824, 1977.

Summers, M. E., D. F. Strobel and R. G. Gladstone, Chemical models of Pluto's atmosphere, in *Pluto and Charon*, Univ. Arizona Press (S. A. Stern and D. J. Tholen, editors), 391-434, 1997.

Yelle, R. V., and J. Elliot, Atmospheric structure and composition: Pluto and Charon, in *Pluto and Charon*, Univ. Arizona Press (S. A. Stern and D. J. Tholen, editors), 347-390, 1997.

Yung, Y. L., and W. B. De More, *Photochemistry of Planetary Atmospheres*, Oxford University Press, 1999.

Michael Mendillo, Center for Space Physics, Boston University, 725 Commonwealth Avenue, Boston, MA 02215.

Andrew Nagy and J. H. Waite, Space Physics Research Laboratory, University of Michigan, 2455 Hayward Street, Ann Arbor, MI 48109-2143.

PART I. OVERVIEWS

The upper atmospheres in our solar system share a common source of solar energy and, of course, they are subject to the universal laws of physics and chemistry. In these chapters, experts in atmospheric science provide a series of tutorial overviews that both define the basic approach to aeronomic research and provide the context for the more specific chapters that follow. Throughout these reviews is a common theme, namely, the universality of coupled systems in a multitude of diverse settings. Theory, groundbased observations, spacebased measurements, in-situ samplings, and computer simulations comprise the framework for modern aeronomy and these are all discussed in these reviews. Moreover, a robust set of references is provided to guide graduate students and researchers new to the field.

Remote sensing is the cornerstone of space science, and the messages carried by photons from atmospheric systems provide the observational basis for the descriptive components of Part I. The full breadth of the electromagnetic spectrum is used: Radio occultation techniques reveal ionospheric structure; infrared measurements portray the thermal patterns and dynamics of neutral atmospheres; visible, ultraviolet and x-ray observations characterize the beautiful aurora and airglow signatures that portray coupling and variability vividly and dramatically. That all these processes are blended in different ways at different sites forms the intellectual cornerstone for comparative aeronomy. *(Image courtesy J. Forbes.)*

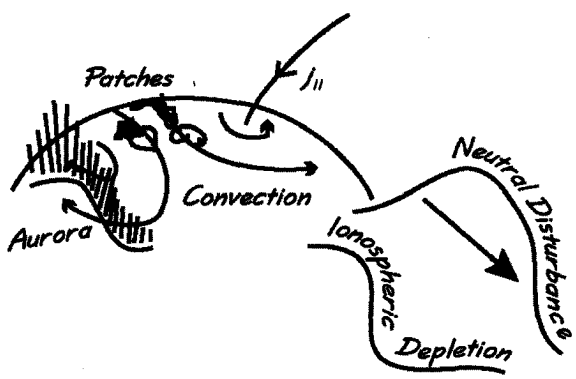

Aeronomic Systems on Planets, Moons, and Comets

Darrell F. Strobel

Departments of Earth and Planetary Sciences and Physics and Astronomy, The Johns Hopkins University

This chapter provides a basic introduction to the science of aeronomy and a comparison of aeronomic systems for planets, satellites, and comets in our solar system. The fundamental length scales of scale height, mean-free-path, and depletion length are introduced, along with the non-dimensional parameters, Mach number, the Jeans' λ ratio of gravitational potential energy to random kinetic energy, and the ratio of mean-free-path to scale height. These quantities are used to define exobase and the validity of the fluid approximation for a gas and to classify atmospheres, exospheres and comas. Planetary and satellite atmospheres are also classified by their chemical composition and photochemistry is addressed within these categories. The thermal structure of thermospheres is reviewed and the role of molecular heat conduction is emphasized. It is noted that solar heating is an insignificant thermospheric heat source on the giant planets. The general importance of wave heating is scrutinized, specifically the question is posed: why don't all planetary atmospheres have hot coronas?

1. INTRODUCTION

When a gas is bound gravitationally to a planetary or satellite solid "nucleus", it is defined to be an atmosphere. If the gas is not restricted by gravity, it is called a coma. In the case of the giant planets the "nuclei" are rocky cores on the order of 0.1 radii and the gas constitutes most of the planet. Most planets and many satellites in our solar system are surrounded by gravitationally bound atmospheres. The presence or absence of an atmosphere is an important characteristic of a planet or satellite. Why does Ganymede, the largest satellite, have an atmosphere of 10^{-12} bar, whereas slightly smaller Titan has a denser atmosphere than the Earth of 1.4 bar? Comets cannot retain gases by gravity and thus have comas. The coma is due to evaporation of nuclear ice, principally water ice for solar distances less than 3 AU, and its abundance is directly related to the evaporation rate driven by the solar radiation field. In the evaporation process considerable dust can be ejected from the nucleus.

Atmospheres in the Solar System: Comparative Aeronomy
Geophysical Monograph 130

10.1029/130GM02

2. NOMENCLATURE

While there is no universally accepted definition of the word, aeronomy, the *American Heritage Dictionary* defines it as "The study of the upper atmosphere, especially of regions of ionized gases". *Sydney Chapman* [1960] defined aeronomy as "the science of the upper region of the atmosphere, where dissocation and ionization are important". Aeronomy, from a historical perspective, is the science of atmospheric regions where dissociation and ionization are important factors in understanding composition and structure. In the Earth's

atmosphere the photochemistry of molecular oxygen leads to the formation of ozone. Ozone photochemistry results in the atmospheric heating and formation of the stratosphere. Traditionally the word, aeronomy, is synonymous with upper atmosphere, whereas a strict application of its definition could include the entire atmosphere as dissociation is also an important factor in the chemistry of the Earth's lower atmosphere known as the troposphere (see Figure 1).

The troposphere is characterized by a relatively constant negative temperature gradient, $\sim$ - 6.5 K km^{-1}. The boundary between the stratosphere, which has a positive temperature gradient $\sim$ 2 K km^{-1}, and the troposphere is the tropopause. Continuing atmospheric nomenclature based on temperature profile, we have a mesosphere above the stratosphere with a boundary known as the stratopause. The mesosphere is characterized by a negative temperature gradient of $\sim$ - 3 K km^{-1}, which is produced by ozone heating and CO_2 infrared cooling and a direct consequence of the observed O_3/CO_2 density ratio decreasing with height. Above the mesosphere, with its upper boundary known as the mesopause, is the thermosphere which is characterized by a very rapid temperature increase of $\sim$ 10-20 K km^{-1}, at low altitudes and asymptotically approaches a constant (isothermal) temperature at high altitudes. The basic physics of the thermosphere is intense heating by absorption of short wavelength solar ultraviolet radiation (< 170 nm) in the dissociation and/or ionization of molecules and atoms and the downward transport of thermal energy by heat conduction to infrared active molecules, such as CO_2, capable of radiating thermal energy away. Although this nomenclature is based on the Earth's temperature profile, it is adopted for other atmospheres, even if the physics generating their temperature profiles, illustrated in Fig. 1, may be dominated by different processes. The asymptotic isothermal thermospheric temperatures are given in Table 1.

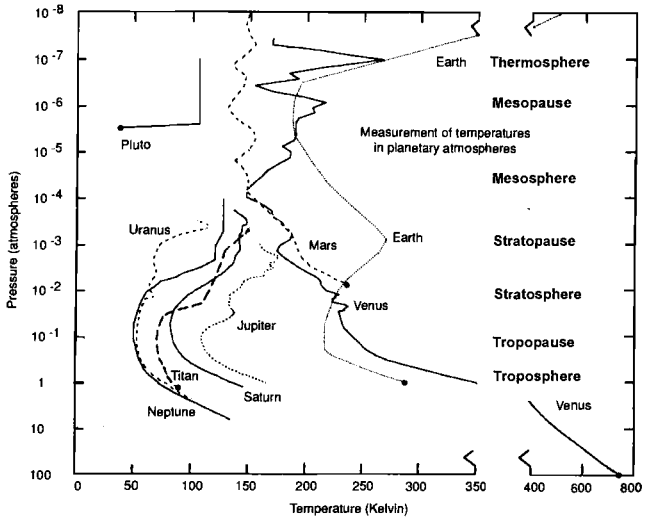

Figure 1. Nomenclature based on the U. S. Standard Atmosphere for the Earth. Temperature profiles as a function of pressure for other planetary atmospheres are based on in situ descent probes (Venus and Mars) and ground-based and spacecraft occultation data for the other planets and satellites. Small scale wave-induced temperature oscillations have been retained. Surface values are indicated by solid circles. Note temperature scale discontinuity between 350 and 400 K. This figure is based on Figure 4.4 from An Integrated Strategy For The Planetary Sciences 1995-2010, National Academy Press, Washington, DC, and used with permission.

3. FUNDAMENTAL LENGTH SCALES AND DEFINITIONS

The atmosphere can be treated as a fluid in part because the mean free path, the distance a molecule or atom travels before making a collision, is much shorter than the smallest macroscopic length scale, which is the pressure scale height, H, that characterizes the exponential decay of pressure with altitude (for the Earth, H = 8 km at the surface, where the mean free path is $\sim 10^{-5}$ cm). Individual atoms and molecules undergo many collisions in macroscopic time scales and in a volume H^3 there are a huge number of atoms and molecules that, for all macroscopic purposes, the atmosphere can be viewed as a continuum fluid.

The mean free path varies inversely as the number density and there will be some altitude ($\sim$ 450 km for the Earth's atmosphere) where the mean free path is approximately equal to the atmospheric scale height . This level, defined rigorously below, is known as the exobase and the region above the exobase is known as the exosphere. Because the exosphere has a larger mean free path than scale height, it is regarded as a quasi-collisionless region and discussed in Chapters III.2 and III.3.

To understand the physical significance of the exobase on escaping atoms and molecules and the distinction between an atmosphere and an exosphere, let us focus on the atmosphere at the exobase. The collision cross section for an atom/molecule may be defined as $\sigma = \pi d^2$, where d is the atomic/molecular diameter, because a collision occurs if the atoms or molecules touch in the rigid sphere limit. A typical value for σ is $\sim$ (3 - 4)

Table 1. General Properties of Atmospheres/Exospheres/Comas Around Solar System Objects

Atmospheric Type	Object	Main Composition	P, T at surface or 1 bar	$T_{\equiv}$	$\lambda_{1\ \mu bar}$	$\lambda_{exobase}$	Exobase Height (km), $r_{exobase}/r_p$	Escaping Constituents	Solar EUV, Particle/Joule Heating (10^9 W)
H_2-He atmospheres of the giant planets	Jupiter	H_2, He, CH_4, NH_3	1 bar, 165 K	900 K	2300	480	1600, 1		800,10^5
	Saturn	H_2, He, CH_4, NH_3	1 bar, 160 K	420 K	1300	420	2500, 1		200, 200
	Uranus	H_2, He, CH_4, NH_3	1 bar, 80 K	870 K	200	50	4700, 1.2		8, 100
	Neptune	H_2, He, CH_4, NH_3	1 bar, 80 K	600 K	450	120	2200, 1.1		3, 1
Terrestrial CO_2 atmospheres	Venus	CO_2, N_2, SO_2, Ar	90 bar, 730 K	200 K	1600	35	140, 1	H	300, -
	Mars	CO_2, N_2, Ar, O_2	7 mbar, 220 K	300 K	490	200	160, 1.1	H, H_2, O, N	25, -
N_2 atmospheres	Earth	N_2, O_2, Ar, H_2O	1 bar, 280 K	1000 K	1100	130	450, 1.1	H	500, 80
	Titan	N_2, CH_4, H_2	1.4 bar, 94 K	160 K	68	45	1500, 1.6	H, H_2, N	3, < 0.2
	Triton	N_2, CO, CH_4, H_2	14 μbar, 38 K	100 K	84	23	930, 1.7	H, H_2, N	0.05,0.1
	Pluto	N_2, CO, CH_4, H_2	3-90 μbar, 35-45 K	?	21	?	> 3000, > 3	N_2, CH_4, H, H_2	0.05, ?
Volcanic atmospheres	Io	SO_2, S_2, SO, O	0.3 nbar, 120 K	2000 K	NA	9	500, 1.3	O, S, Na	< 2, 400
Sputter generated atmospheres	Europa	O_2, O, H_2O	0.7 pbar, 100 K	1000 K?	NA	8	30, 1	O_2, O, H, H_2	0.1, 30
	Ganymede	O_2, O, H_2O	0.7 pbar, 120 K	1000 K?	NA	?	30, 1	O_2, O, H, H_2	0.3, ?
	Callisto?	CO_2, O_2, O, H_2O	0.7 pbar, 150 K	?	NA	?	30, 1		0.2, ?
	Moon	Ar, Na, K			NA		0, 1		
	Mercury	Na, K, Ca			NA		0, 1		
Comas	Comets	H_2O, CH_4, CO, CO_2, CH_3OH			NA		NA	H_2O, H, OH, O	
	Chiron	CO?			NA		NA	CO	

x 10^{-15} cm^2. Thus the exobase of a planet/satellite with radius, r_p, is rigorously defined as the height, $z_{exobase} = r_{exobase} - r_p$, where the probability for an atom or molecule traveling upward with speed in excess of the escape velocity is e^{-1} for escape without suffering a collision and given by

$$\text{Probability} = exp\left(-\int_{z_{exobase}}^{\infty} \sigma n(z)dz\right) \quad (1)$$
$$= exp(-\zeta(z_{exobase})^{-1}) = e^{-1}$$

where $\zeta(z) = (\sigma n(z)H(z))^{-1}$. Here $n(z)$ is the total number density. Note that the quantity $\zeta(z)$ in Eq. (1) is a parameter that describes the validity of treating the atmosphere as a fluid and collision-dominated gas. It is rigorously a fluid when $\zeta \ll 1$. At the exobase $\zeta = 1$ and the mean free path, $l(z)$ equals

$$l(z) = \frac{H}{\sqrt{2}} \quad (2)$$

where

$$\text{mean free path} = l(z) = \frac{\zeta(z)H(z)}{\sqrt{2}},$$
$$\text{and scale height} = H(z) = \frac{kT(z)}{mg(z)}.$$

Here $T(z)$ is the temperature, m is the mean mass of atoms and molecules, g is the gravitational acceleration $= GM_p/r^2$, where the total mass of the planet/satellite is M_p, and G = Newton's gravitational constant. Note that in this chapter height z and radius r will be used interchangeably for the independent radial variable. Exobase heights are given in Table 1.

4. FIVE BASIC PARAMETERS FOR A CLASSIFICATION SCHEME OF ATMOSPHERES, COMAS, AND EXOSPHERES

The most idealized, gravitationally bound atmosphere would be one in which the thermal escape rate is precisely zero. Although this limit is unattainable, it is instructive to examine the factors that govern thermal escape to understand what constitutes an atmosphere. In the classic model for atmospheric escape one assumes that the atmosphere at and below the exobase is fully collisional and atoms and molecules have a Maxwellian distribution of velocities with a sharp transition to a collisionless exosphere just above the exobase. The escape flux due to thermal evaporation from an atmosphere with exobase density, n, is given by the classic Jeans formula (see discussions in Chapters III.2 and III.3)

$$F_{esc}(r_{exobase}) = \frac{n(r_{exobase})U}{2\sqrt{\pi}}(\lambda + 1)exp(-\lambda) \quad (3)$$

in terms of a non-dimensional quantity evaluated at the exobase $\lambda = v_{esc}^2/U^2$, where U is the most probable velocity of a Maxwellian distribution given by

$$U = \left(\frac{2kT}{m}\right)^{\frac{1}{2}} \quad (4)$$

and the escape velocity at the exobase from the planet/satellite's gravitational potential well, v_{esc}, is defined as

$$v_{esc}(r_{exobase}) = \left(\frac{2GM_p}{r_{exobase}}\right)^{\frac{1}{2}} \quad (5)$$

The physical significance of λ can be appreciated by rewriting it as follows:

$$\lambda(r_{exobase}) = \frac{v_{esc}^2}{U^2} = \frac{\frac{GM_p m}{r_{exobase}}}{kT} \quad (6)$$
$$= \frac{\text{gravitational potential energy}}{\text{random kinetic energy}} = \frac{r_{exobase}}{H}$$

Thus in the limit $\lambda \to 0$ the atmosphere is no longer gravitationally bound and blows away due to immense random kinetic energy, whereas in the limit of large λ the atmosphere is gravitationally retained and thermal escape is negligible ($\lambda \to \infty$ being the idealized limit of no escape). The coma of a comet represents the former case, while Jupiter is an excellent example of the latter. Table 1 gives representative values of λ at the exobase for the dominant atmospheric constituent at this height for many solar system objects. Note that atmospheres with small values of λ at the exobase also have the most extended atmospheres, "large" values of $r_{exobase}/r_p$. For example in the category of the giant planets, Uranus has 1.2 for this ratio and only 50 for λ at the exobase in comparison to $\sim$ 1 and 480 for Jupiter. Titan and Triton also have more extended atmospheres of 1.6 and 1.7, respectively, with exobase λs' of 45 and 23. In addition, λ is also evaluated at the 1 μbar level, typically the mesopause region, to give a further indication of how strongly various atmospheres are gravitationally bound at higher pressures. Note that Pluto has the least gravitationally bound atmosphere of any object that possesses a surface pressure of at least 1 μbar. It is highly probable that $r_{exobase}/r_p > 3$ for Pluto, if its 1 μbar temperature of 100 K extends isothermally up to the exobase.

The limit $\lambda \to 0$, is known as the Jeans limit and is the maximum thermal escape rate

$$\lim_{\lambda \to 0} F_{esc}(r_{exobase}) = \frac{n(r_{exobase})U}{2\sqrt{\pi}} = \frac{1}{4} n(r_{exobase}) v_{thermal} \quad (7)$$

where $v_{thermal} = \left(\frac{8kT}{\pi m}\right)^{\frac{1}{2}} = 1.13U$
which is simply the upward directed thermal flux at the exobase that one could calculate from simple kinetic theory. Note that the λ parameter in Eq. (3) is linearly proportional to the particle mass and thus light constituents will have much higher escape rates and larger scale heights than heavy constituents. In Table 1 constituents that have significant escape rates from solar system objects are listed.

In order to further clarify the classification and distinction among atmosphere, exosphere, and coma, we explore analytic solutions to the equations of continuity and motion or momentum in the radial direction [*Summers et al.,* 1989]. From standard textbooks on fluid dynamics (e. g. *Landau and Lifshitz,* 1959), the momentum equation in the radial direction, r, can be written as

$$\frac{\partial}{\partial r}\left(\frac{1}{2}w^2\right) + \frac{1}{\rho}\frac{\partial p}{\partial r} + \frac{GM_p}{r^2} = 0 \quad (8)$$

where p = pressure, ρ = nm = mass density, w = radial velocity, r = radial distance from the center of the object. For an isothermal atmosphere this equation may be rewritten as

$$\frac{\partial}{\partial r}\left(\frac{w}{U}\right)^2 + \frac{1}{n}\frac{\partial n}{\partial r} - \frac{\partial \lambda}{\partial r} = 0 \quad (9)$$

and integrated to give

$$n(r) = n(r_0) exp[(\lambda(r) - \lambda_0(r_0)) - (M(r) - M_0(r_0))] \quad (10)$$

where $M(r) = \left(\frac{w(r)}{U}\right)^2$
with boundary conditions specified at some appropriate level r_0 and the density $n(r)$ and radial velocity $w(r)$ are subject to the constraint imposed by the continuity equation, e.g., in the absence of chemistry, $4\pi r^2 n(r) w(r)$ is a constant. Equation (10) illustrates a number of interesting properties. In the limit of no radial flow ($M(r) = M_0(r_0) = 0$), one obtains hydrostatic equilibrium for a gravitationally bound gas where the downward gravitational force is precisely balanced by an upward pressure gradient force

$$n(r) = n(r_0) exp(\lambda(r) - \lambda_0(r_0)) = \lim_{H/r_p \to 0} n(r_0) exp\left(-\frac{r - r_0}{H}\right) \quad (11)$$

where the right hand limit holds for atmospheres with small scale heights in comparison to the radius of the planet or satellite, r_p. The scale height H is just the radial, e-folding, macroscopic length scale of pressure. In the limit of rapidly increasing radial flow at large r, Eq. (10) implies the density profile will decrease more rapidly with r than the "no flow" limit. This additional decrease is modest for subsonic flows ($M(r) \ll 1$). To achieve dramatic decreases in density, high Mach number ($M(r) \gg 1$) flows are required, as characteristic of the sun's solar wind and the Earth's polar wind.

With radial outflow, the importance of net loss/ production processes must be evaluated. Loss processes that are far more consequential include thermal ion sputtering of the neutral atmosphere, electron impact ionization, and electron impact dissociation into fast escaping atoms, and charge exchange, all of which are especially relevant for satellites embedded in magnetospheric plasma. Specifically for the Galilean satellites Io and Europa, the loss or residence times for their atmospheres are only 2-3 days [*Strobel and Wolven,* 2001].

In steady-state with a net loss rate, L, the continuity equation for spherically symmetric radial outflow is

$$\frac{\partial}{\partial r}(r^2 n_2 w) = -Ln \quad (12)$$

If L and w are constant (L_0, w_0), then the solution to Eq. (12) is

$$n(r) = n_0(r_0)\left(\frac{r_p}{r}\right)^2 exp\left[-\left(\frac{L_0}{w_0}\right)(r - r_0)\right] \quad (13)$$

where $r - r_0 = z$ is the height above the surface. One can define a depletion length scale or scale height associated with this coronal loss model [*Summers et al.,* 1989] as

$$H_d = \left(\frac{-1}{n}\right)\left(\frac{dn}{dr}\right) \approx \frac{w_0}{L_0} \quad (14)$$

where expression (13) has the following desirable properties. For very large H_d due to either large w_0 and/or very small L, the radial density profile yields the radial outflow solution for a cometary coma in which $4\pi r^2 n w_0$ is a constant. In the other limit of negligible w_0 and/or large L such that $H_d/r_p \ll 1$, the radial density profile is dominated by the exponential term and corresponds to an isothermal atmosphere with constant gravitational acceleration.

Thus we have five basic parameters ($\zeta, \lambda, M, H, H_d$) to classify gaseous envelopes around solar system objects into atmospheres, exospheres, and comas. To be classified as an atmosphere, $0 < \zeta(r) < 1$ and λ must be large ($\gg 1$), whereas when $\zeta(r) > 1$ with large λ, it

is an exosphere. The importance of exospheric loss processes is indicated by the ratio of H_d/H being ≤ 1. For a cometary coma near the surface $\lambda \ll 1, M \sim 1, H \to \infty$, and H_d is the relevant macroscopic length scale ($\sim 10^6$ km) with L_0 essentially equal to the H_2O photodissociation rate and $w_0 \sim 1$ km s^{-1}. For subliming gases vaporization theory predicts mean efflux velocity bounded by $0.565U \leq v_e \leq 0.75U$ [*Delsemme and Miller,* 1971]. Adiabatic expansion into a vacuum with conversion of accessible enthalpy into radial kinetic energy yields for water a terminal gas velocity of 2U, which is 2.5 times the sonic velocity for water, for a ratio of specific heats, $\gamma = 1.33$. For bright comets at 1 AU, a typical water gas production rate is $Q \sim 10^{30}$ molecules s^{-1}, with radial velocity, $v_r = 2U \sim 1$ km s^{-1}, $\lambda \sim 4$ x 10^{-6}, and approximate radial density distribution for a spherically symmetric nucleus, R_c, given by

$$n(r) = \left(\frac{Q}{4\pi R_c^2}\right)\frac{R_c^2}{v_r r^2} \tag{15}$$

with mean free path from Eq. (2) of

$$l(r) = \frac{2\sqrt{2}\pi r^2}{\sigma Q}.$$

With $R_c \sim 2$ km, $l \sim 10$ cm at the surface and ~ 5 x 10^4 km at a radial distance of 5 x 10^4 km. The collision zone of a coma extends to a distance where $l(r) \sim r$. This defines the outer boundary of the inner coma (the coma's equivalent to an exobase).

While the classifications of atmospheres and comas is straightforward for very small and very large values of λ, the most difficult λ domain is for $\lambda \sim 1$, where the atmosphere is in hydrodynamic escape or blowoff. Unfortunately, an analytic description of a hydrodynamically escaping atmosphere has so far been elusive. Although no solar system atmosphere has been proven to be hydrodynamically escaping, Pluto's atmosphere is widely believed to exhibit the requisite conditions. For an isothermal atmosphere, Eq. (9) can be combined with the continuity equation for lossless radial outflow, $4\pi r^2 n(r) w(r) = 4\pi r^2 n(r) M(r) U =$ constant to obtain

$$(2M^2 - 1)\frac{\partial}{\partial r}(lnM) - \frac{2}{r} - \frac{\partial \lambda}{\partial r} = 0 \tag{16}$$

with a sonic point at $M = 1/\sqrt{2}$. If the sonic point were at the exobase with $\lambda = 1/2$, then the radial outflow velocity, w, equals $U/\sqrt{2}$ and the escape velocity. This result may be compared with the Jeans escape flux per unit density from a hydrostatic (no radial flow) atmosphere with $\lambda = 1/2$ in Eq. (3) which yields

$$\frac{F_{esc}(r_{exobase})}{n(r_{exobase})} = \frac{0.91U}{2\sqrt{\pi}} = \frac{0.91}{4} v_{thermal} = 0.36 v_{esc} \tag{17}$$

which is 91% of the Jeans limit ($\lambda \to 0$).

An alternate and more conservative threshold for onset of hydrodynamic escape is based on energy considerations and can be inferred from the continuity equation for radial flow in the absence of chemistry, $4\pi r^2 \rho(r) w(r)$ = constant, and the steady state equation for conservation of total energy for an ideal gas

$$\nabla \cdot \left[\rho \vec{v}\left(\tfrac{1}{2}\vec{v}\cdot\vec{v} + h\right) - \vec{v}\cdot\acute{\sigma}_{ik} - \kappa\nabla T\right] = Q + \rho\vec{v}\cdot\vec{F} \tag{18}$$

where h is the enthalpy of gas $= c_p T$, Q is the internal heating, κ is the thermal conductivity, $\acute{\sigma}_{ik}$ is the viscous stress tenor, and $\vec{F}$ is the external force(s) on the fluid, assumed here to be written as the gradient of potential field(s), with $-\nabla\Phi_g$ for gravity. In a conservative, dissipationless atmosphere, $\acute{\sigma}_{ik} = \kappa = Q = 0$, and the conservation of total energy reduces to, with the aid of the continuity equation $\nabla \cdot (\rho\vec{v}) = 0$,

$$\nabla \cdot \left[\rho\vec{v}\left(\frac{1}{2}\vec{v}\cdot\vec{v} + h + \Phi_g\right)\right] = 0 \tag{19}$$

and becomes for radial flow

$$r^2 \rho w = \text{constant}, \left(\frac{1}{2}\vec{v}\cdot\vec{v} + h + \Phi_g\right) = \text{constant} \tag{20}$$

which is Bernoulli's equation for potential flow of a compressible gas. At some very low altitude, $z = z_0$, $\frac{1}{2}\vec{v}\cdot\vec{v} \ll h$ and the constant in the last equation is effectively $= h_0 + \Phi_{g0}$. If $w(\infty) > 0$, then the atmosphere is escaping. The threshold conditions for atmospheric blowoff are $w(\infty) = 0$ at z or $r \to \infty$ and $h_0 = -\Phi_{g0}$, where the enthalpy of the atmosphere is converted into directed radial outflow kinetic energy which in turn is converted into gravitational potential energy. The condition $h_0 = -\Phi_{g0}$ can be rewritten as

$$\frac{\frac{GM_p}{r_0}}{c_p T_0} = \frac{R\lambda_0}{c_p} = 1 \tag{21}$$

where it is assumed that as the atmosphere expands into a vacuum its internal energy is accessible and convertible into translational energy with escape velocity $w_{esc} = (c_p/R)^{1/2} U$. For atmospheric atoms $c_p = 5/2R, w_{esc} = 1.6U, \lambda_0 = 5/2$, and for molecules N_2, O_2, $c_p = 7/2R, w_{esc} = 1.8U, \lambda_0 = 7/2$, where the gas constant $R = k/m$. The atmospheric molecules H_2

(giant planets) and CO_2 (Venus and Mars) have temperature dependent specific heats as not all rotational energy levels are populated in H_2 and some vibrational levels are populated in CO_2 at relevant atmospheric temperatures.

In a real atmosphere with internal heating and dissipation, hydrodynamic escape requires a continual source of power to replenish the enthalpy of the atmosphere and maintain atmospheric blowoff. For the terrestrial planets, the most probable power source would be solar EUV and UV heating. On the giant planets atmospheric blowoff was probably never important. Pluto is one planet where conditions may currently be favorable for hydrodynamic escape and certainly Triton, Titan, and the Galilean satellites with their weak gravity and extended atmospheres have potential for rapid escape. Current estimates for the residence times of the atmospheres of Io and Europa are only 2-3 day [*Strobel and Wolven*, 2001] based on the canonical escape rate for Io of 1.6 x 10^{28} SO_2 molecules s^{-1} and the calculated removal rate of $\sim$ 1 x 10^{27} O_2 molecules s^{-1} from Europa's atmosphere [*Saur et al.*, 1998]. At their exobases, their radial outflow speeds are $\sim$ 0.05U and 0.001U, respectively.

5. VERTICAL STRUCTURE: DIFFUSION AND MIXING

In the lower region of a planetary atmosphere known as the homosphere, chemical tracers are observed to have quasi-constant volume mixing ratios, μ_i (ratio of individual number density, n_i, to total number density, N). This property is due to the action of mean winds and atmospheric waves in the presence of some form of "dissipation", i.e. external solar heating, mechanical friction, IR radiative cooling and damping, finite chemical lifetime, which renders the atmosphere nonconservative. For example, a linear, conservative wave just oscillates a parcel of air back and forth without any net displacement or transport. The presence of active chemistry can generate net transport. Mathematically this tendency may be expressed by the globally averaged, vertical continuity equation as

$$\frac{\partial \mu_i}{\partial t} = \frac{1}{N}\frac{\partial}{\partial z}\left(NK_{zz}\frac{\partial \mu_i}{\partial z}\right)$$

where K_{zz} is the vertical eddy diffusion coefficient [*Colegrove et al.*, 1966].

In the upper atmosphere the tendency for chemical tracers in the limit of negligible chemical loss is towards a balance between a downward gravitational force and an upward partial pressure gradient force. The resulting height distribution is an exponential decrease in density with height based on tracer's scale height which is inversely proportional to its mass. This force balance is known as gravitational diffusive equilibrium. The homopause is the transition region from the well-mixed homosphere below, where chemically inert tracers tend to have constant mixing ratios, to the heterosphere above where tracers asymptotically approach gravitational diffusive equilibrium density profiles. Transport in the heterosphere is dominated by molecular diffusion, represented by coefficients D_i and D_{ij}. This tendency toward gravitational diffusive equilibrium in the heterosphere may be similarly expressed in the globally averaged, vertical continuity equation for minor constituents as

$$\frac{\partial \mu_i}{\partial t} = \frac{1}{N}\frac{\partial}{\partial z}\left\{D_i N\left[\frac{\partial \mu_i}{\partial z} + \left(\frac{1}{H_i} - \frac{1}{H}\right)\mu_i\right]\right\} + \frac{1}{N}\frac{\partial}{\partial z}\left\{K_{zz}N\frac{\partial \mu_i}{\partial z}\right\}$$

where

$$D_i^{-1} = \sum_{j \neq i}\frac{n_j}{ND_{ij}}, \text{and } D_{ij} = \frac{b_{ij}}{N}$$

Low in the atmosphere $D_i/K_{zz} \ll 1$, and molecular diffusion may be neglected. High in the atmosphere $D_i/K_{zz} \gg 1$ since $D_i \propto N^{-1}$. The transition level where $D_i = K_{zz}$ is the formal definition of the homopause. The application of the kinetic theory of molecular diffusion coupled with eddy diffusion to atmospheric transport was discussed by *Colegrove et al.* [1966].

For a minor constituent in an isothermal atmosphere with no chemistry and no net flux, the two tendency equations can be combined and integrated to yield the following steady-state, static solution [*Chamberlain and Hunten*, 1987].

$$\mu_i = (1 + e^{h/\bar{H}})^{1-\frac{\bar{H}}{H_i}}\mu_{0i}$$

where the homopause location, $h = 0$ is given by $D_i = K_{zz}$ with homopause density $N_0 = b_i/K_{zz}$. The solution has the following respective limits:

$$\mu_i \rightarrow \mu_{0i}, h \rightarrow -\infty$$
$$\mu_i = 2^{1-\frac{\bar{H}}{H_i}}\mu_{0i}, h = 0$$
$$\mu_i \rightarrow \mu_{0i} exp\left[-h\left(\frac{1}{H_i} - \frac{1}{H}\right)\right], h \rightarrow +\infty$$

Deep in the atmosphere the mixing ratio is μ_{0i}. At the homopause the mixing ratio can be considerably smaller than its deep atmosphere value, if the specie i is much heavier than the mean molecular mass of the background atmosphere, as is true for hydrocarbons in the atmospheres of the giant planets. High in the heterosphere, light species relative to major atmospheric constituents have increasing mixing ratios, whereas heavy species have decreasing mixing ratios.

6. COMPOSITION AND CHEMISTRY

Planetary and satellite atmospheres may also be classified by their chemical composition. The major types are the H_2-He atmospheres of the giant planets, the terrestrial CO_2 atmospheres, and the N_2 atmospheres of Earth, Pluto, Titan, and Triton. In addition to these categories there are the volcanic generated SO_2 atmosphere of Io, tenuous sputter-generated O_2 atmospheres on Europa and Ganymede, a CO_2 atmosphere on Callisto, and exospheres on Mercury and the Moon.

6.1. H_2-He Atmospheres

The atmospheres of the giant planets are predominantly molecular hydrogen ($\sim$ 85-95% by number) with the remainder mostly helium. Trace amounts of the saturated hydrides (CH_4, NH_3, H_2O, H_2S) of reactive atoms of cosmically abundant elements C, N, O, S are present in the deep atmospheres of the giant planets, as predicted by thermochemistry to be the dominant form of these elements. These hydrides are also the condensible substances for cloud formation. The working hypothesis for the formation of the solar system is the nebular hypothesis which first gained prominence in the writings of Kant and Laplace. The giant planets got a head start in the cooler nebular regions of the outer solar system. Solids condensed first there and subsequently collided, aggregated, and eventually became self-gravitating protoplanets sweeping up neighboring solids gravitationally and capturing H_2 and He gases in roughly solar proportions. The enhanced abundances of saturated hydrides over expectations based on solar elemental ratios (factors of 3 for Jupiter and Saturn and factors of 30 for CH_4 on Uranus and Neptune) have been measured in situ by the Galileo probe in Jupiter's atmosphere and by remote sensing on all the giant planets. These enhanced abundances are attributed to condensation of solids (the saturated hydrides) as the seed nuclei that initiated the formation process of the giant planets. Some enrichment would be predicted as 100% capture of surrounding H_2 and He gases would be improbable.

Some trace species in the upper atmospheres of the giant planets (e. g. C_2H_6, C_2H_2, C_2H_4, C_4H_2,) are too abundant to have a thermochemical origin, even if they were convected from the deep, hot interior. These species are best understood as the products of CH_4 photochemistry. The photochemistry of inorganic compounds, NH_3 and PH_3, and the formation of condensible N_2H_4 and P_2H_4 may contribute along with polyacetylenes and other hydrocarbons to the ubiquitous haze in the tropopause regions of the Jupiter and Saturn. The external (to the planet/satellite) introduction of matter by infall of meteoroids and material from rings and satellites containing oxygen leads to the photochemical formation of CO and CO_2.

The photochemistry of H_2 and He leads to the formation of ionospheres on the giant planets

$$H_2 + h\nu \rightarrow H_2^+ + e \text{ or } H + H^+ + e;$$
$$\text{I} = 5.4 \text{ x } 10^{-8}, 9.5 \text{ x } 10^{-9} \text{ s}^{-1} \text{ at 1 AU}$$
$$H + h\nu \rightarrow H^+ + e \text{ ; I} = 7.3 \text{ x } 10^{-8} \text{ s}^{-1} \text{ at 1 AU}$$
$$He + h\nu \rightarrow He^+ + e \text{ ; I} = 5.2 \text{ x } 10^{-8} \text{ s}^{-1} \text{ at 1 AU}$$
$$H_2^+ + H_2 \rightarrow H_3^+ + H \text{ ; k} = 2 \text{ x } 10^{-9} \text{ cm}^3 \text{ s}^{-1}$$
$$He^+ + H_2 \rightarrow HeH^+ + H \text{ ; k} = 4.2 \text{ x } 10^{-13} \text{ cm}^3 \text{ s}^{-1}$$

and when the plasma recombines the production of H atoms

$$H_3^+ + e^- \rightarrow H_2 + H; \alpha = 4.6 \text{ x } 10^{-6} T_e^{-0.65} \text{ cm}^3 \text{ s}^{-1}$$
$$H^+ + e^- \rightarrow H + h\nu; \alpha = 1.9 \text{ x } 10^{-10} T_e^{-0.7} \text{ cm}^3 \text{ s}^{-1}$$

and at high pressures in these atmospheres, H atoms recombine quickly to recycle H_2, either directly,

$$H + H + M \rightarrow H_2 + M \text{ ; k} = 2.7 \text{ x } 10^{-31} T^{-0.6} \text{ cm}^6 \text{ s}^{-1}$$

or catalytically through reactions involving hydrocarbons. Chapters I.2 and I.3 explore more fully the neutral and ion chemistry in the upper atmospheres of the giant planets.

6.2. Terrestrial CO_2 Atmospheres

The inner, terrestrial planets got a late start in formation because most hydrogen-bearing ices never condensed to solids in the hot, inner regions of the solar nebula. Consequently the terrestrial planets did not have as large a reservoir of solid material and could not grow as large as the giant outer planets and accrete gas and dust. Powerful solar winds after the formation of the protosun may have swept the inner solar system clean of gas and dust, leaving the late starting terrestrial

planets with far less raw material for formation. Given the absence of substantial amounts of hydrogen, the terrestrial atmospheres emerged as strongly oxidizing in contrast to the strongly reducing atmospheres of the giant planets. On Venus the high surface pressure and temperature establish a chemical region in the lowest 10 km, where thermochemical processes predominate over photochemistry and carbonate rock can liberate CO_2. The inventory ratio of atmospheric N_2/CO_2 is comparable on the twin sister planets Venus and Earth. With the inclusion of CO_2 in Earth limestones, their absolute CO_2 abundances are also comparable. Although the present Earth does not have a CO_2 atmosphere, it would have one if either life never existed and/or its surface temperature were elevated to surface conditions comparable to Venus through the liberation of CO_2 from carbonate rock and evaporation of the oceans. On Mars the permanent CO_2 southern polar cap buffers its CO_2 atmosphere. The northern polar cap is mostly water ice. Venus is almost devoid of water, whereas Earth and Mars have large and moderate surface reservoirs, respectively.

Solar photolysis generates fast destruction rates of these CO_2 atmospheres:

$$CO_2 + h\nu(\lambda < 2000\mathring{A}) \rightarrow CO + O;$$
$$\text{J} = 1.2 \text{ x } 10^{-6} \text{ s}^{-1} \text{ at 1 AU}$$

which if followed only by

$$CO + O + M \rightarrow CO_2 + M;$$
$$\text{k} = 6 \text{ x } 10^{-36} \text{ cm}^6 \text{ s}^{-1}$$

$$\text{and } O + O + M \rightarrow O_2 + M \text{ ;}$$
$$\text{k} = 5 \text{ x } 10^{-35} \exp(900/\text{T}) \text{ cm}^6 \text{ s}^{-1},$$

where the former reaction is spin-forbidden and slow, and the latter is fast, the result would be an irreversible conversion of CO_2 into CO and O_2 in only 4 million years in the massive Venusian atmosphere and only 4000 years in the Martian atmosphere. The stability of these atmospheres has been hypothesized, but not conclusively demonstrated, to be due to fast catalytic cycles involving the odd hydrogen compounds (H, OH, HO_2, HO_x) as discussed in Chapters I.2 and I.3. On Venus the HO_x is derived from H_2, which in turn is dissociated catalytically by Cl atoms liberated in HCl photolysis, whereas on Mars either photolysis of H_2O (wet phase) or H_2 oxidation by $O(^1D)$ from O_3 photolysis (dry phase) supplies HO_x.

The other topic of considerable interest on the terrestrial planets is the inventory, evolution, and escape of water and its photolysis products. The Earth, of course, has a liquid water ocean of approximate depth $\sim$ 3 km. Mars has a permanent northern, mostly water ice, cap and perhaps as much as a few hundreds of meters of water buried beneath the surface. In contrast Venus is essentially bone dry with only about 0.01 bar in its atmosphere and with a surface temperature of 730 K incapable of storing water in liquid or solid phase. Venus, the Earth's twin planet, is widely regarded to have undergone a runaway greenhouse based on the large enhancement ($\sim$ 100) of the D/H ratio derived from measurements of the $[HDO]/[H_2O]$ ratio. Evaporation of a water ocean of depth comparable to our own ocean due to a runaway greenhouse coupled with water vapor photolysis and mass dependent escape rates of H and D could in principle account for the isotopic enhancement of deuterium as discussed in Chapters I.2 and III.2. The O atoms generated from photolysis subsequently oxidized surface rocks. Alternatively, the observed water vapor abundance is maintained in steady-state balance by cometary infall and photolysis of H_2O followed by nonthermal escape of hydrogen. Over the age of solar system there is no requirement of excess primordial water to explain the observed $[HDO]/[H_2O]$ ratio[*Grinspoon and Lewis*, 1988].

In the CO_2 atmospheres of Venus and Mars, photoionization of CO_2 is the dominant source of ions

$$CO_2 + h\nu \rightarrow CO_2^+ + e \text{ ; I} = 6.6 \text{ x } 10^{-7} \text{ s}^{-1} \text{ at 1 AU}$$

The CO_2^+ reacts rapidly with atomic oxygen, which is abundant in the upper atmosphere, to form oxygen ions

$$CO_2^+ + O \rightarrow O^+ + CO_2 \text{ ; k} = 1.6 \text{ x } 10^{-10} \text{ cm}^3 \text{ s}^{-1}$$
$$CO_2^+ + O \rightarrow {O_2}^+ + CO \text{ ; k} = 9.6 \text{ x } 10^{-11} \text{ cm}^3 \text{ s}^{-1}$$

with O^+ converted rapidly to O_2^+ by

$$O^+ + CO_2 \rightarrow O_2^+ + CO \text{ ; k} = 1.1 \text{ x } 10^{-9} \text{ cm}^3 \text{ s}^{-1}$$

and ensuring that O_2^+ is the dominant, terminal ion in the ionospheres of Mars and Venus, as discussed in Chapter I.3.

6.3. N_2 Atmospheres

The last broad category is N_2 atmospheres. The emergence of life on the Earth led to the removal of CO_2 as the dominant gas and the ascent of N_2 as its prime atmospheric constituent with living organisms controlling the 21% O_2 content far from thermodynamic equilib-

rium by the processes of photosynthesis and respiration. The ocean supplies the dominant greenhouse gas, H_2O, and the most important oxidizing agent in atmospheric chemistry, the OH radical. Photochemistry of O_2 generates O_3, which sustains life by filtering out harmful solar UV before its reaches the surface. The cycle of O_3 absorbing solar radiation, dissociating to form O atoms, and the regeneration of O_3 by the reaction of O + O_2 with liberation of heat creates the thermal inversion region known as the stratosphere. In the thermosphere atomic oxygen emerges as the dominant constituent because, while photolytic destruction of O_2 is fast, no fast bimolecular reactions exist in the thermosphere to recycle O_2. Atomic oxygen recombination occurs only by downward diffusion to the mesopause region where catalytic reactions involving odd hydrogen supplemented by direct recombination O + O + M $\rightarrow$ O_2 + M lead to reformation of O_2. In contrast, molecular nitrogen is difficult to dissociate directly. Due to the absence of allowed transitions from its ground term into dissociating upper electronic terms, dissociation proceeds primarily by ionization first and then subsequent ion molecule reactions that break the N_2 bond. Atomic nitrogen does not emerge as an abundant component of the thermosphere, principally because N_2 is efficiently regenerated locally by the fast bimolecular reaction N + NO $\rightarrow$ N_2 + O, k = 3.1 x 10^{-11} cm^3 s^{-1}.

The earliest atmosphere on the Earth is speculated to have been mildly reducing with a composition similar to the present day atmosphere on Titan, the largest satellite of Saturn. Titan has the most massive N_2 atmosphere in the solar system at 1.4 bar and a surface temperature of 94 K. The next most abundant constituent is CH_4 with a volume mixing ratio of a few percent in the troposphere and $\sim$ 2% above the tropopause. The combined photochemistry of N_2 and CH_4 leads to the formation of a large suite of hydrocarbons, organic molecules, and nitriles that condense to yield an optically thick haze that envelopes Titan and elevates its optical limb about 250 km above the surface. This photochemical smog is Titan's analog to the Earth's ozone, in that it absorbs solar radiation and heats Titan's stratosphere approximately 100 K above the tropopause temperature. The H and H_2 produced in CH_4 photolysis rapidly escape Titan's extended atmosphere and weak gravitational field, ensuring the irreversible destruction of CH_4 to heavier hydrocarbons and necessitating CH_4 resupply from the interior. In Titan's ionosphere the primary ions produced are N_2^+ and N^+, which react with CH_4 to initiate a chain of reactions that yield complex organic ions as the terminal ions in an atmosphere that contains a large assortment of organic molecules as discussed in Chapter I.3.

In the distant outer solar system, the planet Pluto and the largest Neptunian satellite Triton are widely regarded as the largest end-members of Kuiper-Belt objects that occupy the region from $\sim$ 30 to 100s of AU, and serve as the source of short period comets. These "twin" objects have thin buffered N_2 atmospheres controlled by interactions with surface ice, primarily N_2 frost. Additional expected (CO) and detected (CH_4) atmospheric constituents are also controlled intimately by interaction with their surface frosts which may be well-mixed with the N_2 frost. Triton's surface pressure is $\sim$ 14$\pm$1 μbar and surface temperature is $\sim$ 38 K based on Voyager 2 data [*Yelle et al.*, 1995]. In the case of Pluto we know from the Infrared Space Observatory (ISO) that its surface is not isothermal [*Lellouch et al.*, 2000] and the surface pressure can be anywhere from at least $\sim$ 3 μbar based on the *Elliot et al.* [1989] KAO stellar occultation data to possibly as large as 100 μbar if obscuring clouds and/or haze mask the surface location in the stellar occultation data. In fact our knowledge of Pluto's atmospheric composition is very limited with only a measurement of the CH_4 column density, $\sim$ 3 x 10^{19} cm^{-2}, with large error bars from a near-IR solar reflection spectrum in the 1 μm region [*Young et al.*, 1997a]. Other species, in particular N_2 and CO, must be estimated from surface ice abundances and temperatures and the assumption of vapor pressure equilibrium. There are substantial differences in the atmospheres Pluto and Triton at the microbar level where stellar occultation measurements probe. Pluto's scale height and temperature are twice Triton's values [*Elliot et al.*, 2000].

The photochemistry of CH_4 in these atmospheres yields C_2H_4 and C_2H_2 which condense to form thin hazes, as observed by Voyager 2 on Triton, and eventually are deposited as frosts on the surface, but so far undetected on either object. Atomic and molecular hydrogen, products of methane photolysis, rapidly escape. The photochemistry of N_2 and CO lead to the formation of an ionosphere and nitriles and the production of C and N atoms, which can escape thermally. The dominant source of mass for Neptune's magnetosphere is escape of H, N, and H_2 from Triton and precipitation of energetic magnetospheric electrons may contribute two-thirds of the power input to Triton's upper atmosphere (cf. Table 1). Further discussion of these topics may be found in Chapters I.2, III.2, and IV.4.

6.4. *Volcanic Atmospheres*

The volcanic generated atmosphere of Io is in a class by itself. The innermost Galilean satellite is the site of the most active volcanism in the solar system. The volcanos are powered by tidal heating as a result of the Laplace resonance involving the orbital periods of Io, Europa, and Ganymede. The associated forces generate an eccentric motion for Io in the presence of Jupiter's enormous gravitational field with tidaling heating a natural consequence. The driving gases are SO_2, S_2, and maybe O_2 [*Zolotov and Fegley*, 1998]. SO_2, S_2, and SO are the principal components of its atmosphere [*Lellouch*, 1996; *Spencer et al.*, 2000]. SO_2 frosts are prevalent at mid and high latitudes and on the nightside where the surface temperature drops to $\sim$ 95 K. At this temperature the vapor pressure of SO_2 is only 0.0004 nbar. A typical dayside surface pressure would be $\sim$ 0.3 nbar. The fundamental question is whether the SO_2 atmosphere, which is preferentially confined to the equatorial regions, is a buffered atmosphere in equilibrium with a variable temperature surface frost or primarily an atmosphere formed by multiple volcanic plumes. Mass loss from Io's atmosphere by thermal escape, by heavy torus ion bombardment/sputtering of Io's atmosphere, exosphere, and surface [*McGrath and Johnson*, 1989] and by plasma pickup supplies copious amounts of oxygen, sodium, and sulfur to the Jupiter's inner magnetosphere. Also the torus plasma can be energized by charge exchange reactions involving neutrals in Io's atmosphere and exosphere. Torus electrons precipitate into the atmosphere and create a highly conducting ionosphere. Joule heating by Io's electrodynamic interaction with the Io torus plasma is the principal heating mechanism (cf. Table 1). Chapters II.1, II.2, and III.2 discusses these topics in much more detail.

6.5. *Sputter-Generated Atmospheres*

The next Galilean satellites Europa and Ganymede orbit also in the harsh environment of the inner Jovian magnetosphere. Their partial water ice surfaces are subjected to severe ion bombardment and ion induced ejection of substantial numbers of H_2O, H_2, and O_2 molecules off the surface (see Chapter III.3). Whereas H_2O sputtering rates are about 10 times the H_2 and O_2 rates, water is a condensible and hence has a large sticking coefficient, $\sim$ 1. Neither H_2 nor O_2 are condensible and have much smaller surface sticking coefficients ($\sim$ 0.001). Thus H_2O emerges as a minor component of their atmospheres, in spite of its much larger sputtering rate which does not compensate for its unity sticking coefficient. The H_2 molecules escape readily from these satellites leaving behind the much heavier O_2 as the dominant atmospheric species. In the case of Europa there is an adequate first order description of the mass balance of the O_2 atmosphere [*Saur et al.*, 1998]. Europa's suprathermal torus ions, with a contribution from thermal ions, sputter O_2 from the water ice surface and thermal torus ions remove the O_2 atmosphere by sputtering with a net molecular flux of $\sim 10^{27}$ O_2 s^{-1}. The resulting surface and column density just barely qualifies the gravitationally bound O_2 as an atmosphere with surface pressure of $\sim$ 0.0007 nbar. Joule heating associated with $\sim$ 1 x 10^6 Amps of ionospheric current is the dominant source of atmospheric heating (cf. Table 1). For Ganymede with its own internal magnetic field the inference of the O_2 column density and surface pressure is more complicated, but best estimates suggest comparable values to those appropriate for Europa [*Hall et al.*, 1998].

While Mercury and the Moon do not possess a conventional atmosphere, they do have tenuous alkali metal exospheres, principally Na, K, and Ca. These atoms execute ballistic orbits above the surface. These exospheres are discussed in depth in Chapter III.3.

6.6. *Comas*

In the vicinity of 1 AU, comas are predominantly water vapor. The photodissociation of H_2O is of fundamental importance.

$$H_2O + h\nu \rightarrow OH + H \ ; \ \mathrm{J} = 1 \times 10^{-5} \ \mathrm{s^{-1}} \ \text{at 1 AU}$$
$$H_2O + h\nu \rightarrow H_2 + O(^1D) \ ; \ \mathrm{J} = 1.4 \times 10^{-6} \ \mathrm{s^{-1}} \ \text{at 1 AU}$$

where in the first channel the H atom acquires the bulk of the excess energy and is ejected with a velocity of $\sim$ 25 km s^{-1} in comparison to the OH speed $\sim$ 1.5 km s^{-1} and the radial H_2O bulk speed of $\sim$ 1 km s^{-1}. The fast moving H atoms lead to the generation of a large Lyman α halo by resonance scattering of solar Lyman α radiation with characteristic dimension $\sim$ 10^7 km. Channel 2 proceeds at $\sim$ 15% of the rate of channel 1 and produces an electronically excited, highly reactive O atom. Ionization of H_2O is the predominant source of ions

$$H_2O + h\nu \rightarrow H_2O^+ + e \ ; \ \mathrm{I} = 3.3 \times 10^{-7} \ \mathrm{s^{-1}} \ \text{at 1 AU}$$
$$H_2O^+ + H_2O \rightarrow H_3O^+ + OH \ ; \ \mathrm{k} = 2 \times 10^{-9} \ \mathrm{cm^3 \ s^{-1}}$$

with conversion by the second reaction to H_3O^+ in the inner coma. Given the large suite of volatile minor constituents in the nucleus, the photochemistry of comas

involves an exceedingly large number of reaction paths and species as discussed in Chapter II.4.

7. THE THERMAL STRUCTURE OF THERMOSPHERES: THE ROLE OF MOLECULAR HEAT CONDUCTION

A survey of the atmospheres in our solar system, where we have some idea of their vertical temperature profiles, indicates upper atmospheres invariably have thermospheres with the fundamental properties of isothermal conditions near the exobase and a base region with steep temperature gradients. The latter implies substantial downward transport of heat by molecular conduction. The dominant molecules in most atmospheres are homonuclear (e. g. H_2, N_2, O_2) and thus have no permanent dipole moment and are infrared inactive with no rotational or vibrational absorptions/emissions. The terrestrial atmospheres of Venus and Mars do have the infrared active molecule CO_2 as their dominant constituent, yet still have thermospheres. (Venus has a dayside thermosphere, but not on the nightside, where the temperature decreases with increasing height, due to its slow rotation rate and long duration of a solar day - time between sunrises $\sim$ 117 Earth days.) In the presence of intense solar UV radiation CO_2 molecules are subjected to large photolysis rates and conversion to O and CO at high altitudes, with CO less susceptible to dissociation due to it large dissociation energy.

The exobase is located at column density depth, $1/\sigma \sim 3 \times 10^{14}$ cm^{-2}, whereas a typical atomic or molecular cross section for absorption of solar UV radiation is $\sim 10^{-17}$ cm^2 and hence typical penetration depth $\sim 10^{17}$ cm^{-2}, approximately 6 scale heights below the exobase. With no appreciable local radiative energy loss at the heights of maximum solar UV radiation deposition, the atmospheres must thermally conduct heat downward to the mesopause region where significant abundances of infrared active molecules are available and capable of radiating away the solar UV power deposited in the thermosphere.

The heat equation for low Mach number conditions, which ensures that c_p is the appropriate specific heat, is

$$\rho c_p \frac{\partial T}{\partial t} = -\frac{\partial}{\partial z}\left(-\kappa \frac{\partial T}{\partial z}\right) + Q_{UV} - C_{IR} \qquad (22)$$

where Q_{UV} = absorbed solar energy that is converted locally to heat, C_{IR} = infrared radiative cooling, and t = time. Now $\kappa = f\mu c_v$ from the kinetic theory of gases, where μ = coefficient of viscosity, c_v = specific heat at constant pressure, and f = Eucken's number = 2.5 for monotonic gases and ≤ 2 for diatomic gases.

In steady state $\partial T/\partial t = 0$, which also holds when Eq. (22) is averaged over a day. In averaging over a day, the flux must be reduced by 1/2 and the solar zenith angle set to $\bar{\mu}_0 = 1/2$. The global average is thus 1/4, as expected from intercepted solar flux of πr^2 and radiative cooling over $4\pi r^2$ area. Integrating (22) over time and altitude

$$\kappa \frac{\partial T}{\partial z} = \frac{1}{4}\int_z^\infty Q_{UV} dz - \int_z^\infty C_{IR} dz \qquad (23)$$

where the upper boundary condition is no net heat conducted into or out of the atmosphere $\frac{\partial T}{\partial z}|_\infty = 0$. Now $\kappa \partial T/\partial z$ is the downward heat conduction flux which is equal to the integrated heating rate above level z minus the integrated cooling rate. At high altitudes the UV optical depth is negligibly small and the atmospheric heating rate is proportional to the number density and thus decreases exponentially with increasing height. Likewise, C_{IR} is proportional to the number density of IR active molecules which are also exponentially decreasing with altitude. Equation (23) indicates $\kappa(\partial T/\partial z) \to 0$ and thus $T \to T_\infty$, the thermospheric temperature, which must be a constant temperature in the absence of additional heat sources or sinks. At lower heights, z, the temperature gradient must be sufficiently large to sustain a downward heat flow equivalent to the total UV energy absorbed above z less the IR radiative loss.

At the mesopause, $\partial T/\partial z = 0$ by definition and from (23), then

$$\frac{1}{4}\int_z^\infty Q_{UV} dz = \int_z^\infty C_{IR} dz \qquad (24)$$

i.e., the integrated UV heating above the mesopause is precisely balanced by the IR cooling. The location of the mesopause occurs at an altitude where the entire downward heat conduction flux is radiated away in the IR.

A simple illustrative model can be constructed, if all the thermospheric heating occurs at a single height, z_q, or pressure level, p_q, with a delta function source $Q_0\delta(p - p_q)$ in pressure coordinates. Similarly, assume all the IR cooling occurs at single height/pressure z_c, p_c, with delta function sink $C_0\delta(p - p_c)$. By definition of the mesopause, Eq. (24) is satisfied when the lower limit of integration is slightly below the height, z_c, where $p = p_c$, i. e., to z_c^-. Substitution of these ap-

proximations into Eq. (22) for steady state conditions and integration over the following regions give

$$\begin{aligned} &\text{if } 0 < p < p_q \quad T = T_\infty = T(p_q) \\ &\text{if } p_q < p < p_c \quad T(p)^{s+1} = T_c^{s+1}(p_c) \\ &\qquad -\frac{(s+1)F_{HC}H}{A} ln\left(\frac{p}{p_c}\right) \end{aligned} \tag{25}$$

where T_∞ is the isothermal temperature in the upper thermosphere, T_c is the "cooling" temperature at the mesopause, the thermal conductivity κ is accurately approximated by AT^s, F_{HC} is the downward heat conduction flux $| - AT^s dT/dz|$ and equal to Q_0, H is the pressure scale height which is assumed constant for integration purposes. One can rewrite (25) in height coordinates by noting that -H $ln(p/p_c)$ is just $z - z_c$. The quantities F_{HC} and Q_0 are equal to the integrated thermospheric absorption rate of solar UV and EUV radiation times the efficiency factor for conversion into heat. CO_2 absorbs solar UV radiation out to 2000 Å, whereas O_2, N_2, O, and H_2 absorb below 1750, 1000, 911, and 1100 Å, respectively. Although there are some planetary variations in fractions of the solar UV spectrum absorbed and heating efficiencies, the largest variation is the solar flux decrease with inverse distance squared. Whereas the integrated globally average heating rate in the Earth's thermosphere is a few erg cm^{-2} s^{-1}, it is only $\sim$ 0.01 erg cm^{-2} s^{-1} on Jupiter and a miniscule 0.0004 erg cm^{-2} s^{-1} at Neptune in their H_2 dominated atmospheres, as may be inferred from Table 1. Thus the thermal structure of the terrestrial planets can be understood in terms of solar UV heating, whereas in the giant planets' thermospheres it is a negligible heat source, as outlined below and treated in much greater depth in Chapters IV.1 and IV.2.

The depth of solar EUV and UV penetration for the purposes of heating calculations can be obtained by a suitable wavelength average of the absorption cross section weighted with photon energy, $< \sigma_\lambda >$. Its inverse is the penetration column density corresponding to pressure level $p_q = mg/ < \sigma_\lambda >$. For the H_2 dominated atmospheres of the giant planets, $< \sigma_\lambda > \sim 10^{-18}$ cm^2 and the mesopause is approximately at the 1 μbar level. With the integrated globally averaged heating rates given above, Eq. (25) yields for the temperature contrasts $[T(p_q) - T_c(p_c)] \sim$ 60, 30, 20, and 4 K for Jupiter, Saturn, Uranus, and Neptune, respectively. These temperature differences between the high altitude isothermal region and the mesopause region are substantially smaller than the values inferred from Voyager UV solar occultation measurements, rotational structure of H_3^+ near-IR emission, and in the case of Jupiter from Galileo probe deceleration data. Table 1 gives T_∞ for solar system objects and Fig. 1 conveys the approximate temperatures at their mesopauses.

Given the inadequacy of solar heating to account for thermal thermospheric structure on the giant planets, a number of suggestions have been made over the years with specific application to Jupiter: soft electron precipitation, energetic electrons, joule heating, gravity wave dissipation, and heavy ion precipitation (for references, see *Matcheva and Strobel*, 1999). Power input to thermospheres of the giant planets by particle precipitation and Joule heating can be substantial as indicated in Table 1. Most recently, the gravity wave heating suggestion has received the most attention, due in large part to the inference of large scale gravity waves in the Galileo probe deceleration data [*Young et al.*, 1997b; *Matcheva and Strobel*, 1999; and *Hickey et al.*, 2000]. The latter two papers concluded that gravity waves at the observed amplitudes in the probe data cannot account for Jupiter's thermospheric temperature profile.

8. WAVE HEATING: WHY DON'T ALL ATMOSPHERES HAVE CORONAS?

Wave heating of the solar corona has been a popular explanation for its very elevated temperatures ($> 10^6$ K), but has never gained universal acceptance. *Hines* [1965] was a strong advocate of gravity wave heating playing an essential role in the energetics of the Earth's upper atmosphere. But as discussed in Chapters I.2 and IV.1, solar EUV and UV heating plus approximately a 15% contribution from auroral power dissipation adequately accounts for the power input to the Earth's thermosphere. Wave and tidal coupling on Venus and Mars are discussed in Chapter III.1. Because gravity waves are ubiquitous in planetary atmospheres and can transport significant energy fluxes by vertical propagation from excitation sources in the lower atmosphere, why is it not inevitable that all planetary atmospheres have hot coronas?

Gravity waves have angular frequencies, $\omega = k_h c$, bounded on the low end by the coriolis frequency, $f = 2\Omega sin(\theta)$ and on the high frequency side by the buoyancy frequency [*Andrews et al.*, 1987; *Gill*, 1982]. Here Ω is the planet's rotation rate, k_h is the horizontal wave number, c is the horizontal wave phase speed, and θ is the latitude. For a dry atmosphere with low Mach number flow, the buoyancy frequency is $N = [(g/T)(dT/dz + g/c_p)]^{1/2}$. From observations in the Earth's atmosphere most of the gravity wave power re-

sides in hydrostatic gravity waves [*Fritts*, 1984] which obey the condition $(Hk_h^2(\bar{u}-c)^2/g \ll 1$ which is equivalent to $\omega^2 \ll N^2)$, where $\bar{u}$ is the mean zonal wind [*Andrews et al.*, 1987; *Gill*, 1982]. In addition, these hydrostatic gravity waves satisfy in many instances the further restriction in the dispersion relation known as the "Boussinesq" approximation $k_z^2 \gg 1/4H^2$ [*Andrews et al.*, 1987], where k_z is the vertical wave number. The physical meaning is the atmospheric density variation may be assumed approximately constant over one vertical wavelength, but not many scale heights. Radio and stellar occultation measurements of gravity wave spectra in other atmospheres confirm this conclusion.

The vertical transfer of energy and momentum by gravity waves requires that the ratio of group velocities $c_{gz}/c_{gh} \approx (\omega^2 - f^2)^{1/2}/N \approx k_h/k_z$ [e. g. *Andrews et al.*, 1987], should not be too small or otherwise most of the gravity wave excitation energy will be dispersed in the horizontal direction, h, rather than the vertical direction, z. This requires that $\omega^2 \gg f^2$, i. e., the wave period should not be too close to the inertial period.

Gravity wave amplitudes grow approximately exponentially with upward propagation because the Eliassen-Palm flux ($F = c_{gz}A$) is conserved in the absence of dissipation according to the generalized Eliassen-Palm theorem [*Andrews et al.*, 1987], where

$$c_{gz} = \frac{Nk_h}{k_z^2}, A = -k_h\left(\frac{E}{\hat{\omega}}\right); \qquad (26)$$
$$E = \frac{1}{2}\rho_0\left[\overline{u'^2} + \overline{v'^2} + \overline{w'^2} + \frac{N^2\overline{w'^2}}{k_h^2(\bar{u}-c)^2}\right]$$

Here $\hat{\omega} = \omega - k_h\bar{u}$ is the intrinsic or Doppler-shifted frequency, A is wave action, E is the total wave energy (or energy density), and $E/\hat{\omega}$ is the wave action density [*Andrews et al.*, 1987]. Wave energy is only strictly conserved in the absence of dissipation when $\bar{u}$ is constant. For slowly varying $\bar{u}$ with height, the monochromatic gravity wave amplitude increases with height approximately as $(\rho_0)^{-0.5}$. There is a limit to this exponential growth known as gravity wave saturation and also referred to as wave breaking. Saturation occurs when the wave drives the local temperature lapse rate (i. e., the sum of the wave and mean state temperature lapse rates, denoted by prime and subscript zero, respectively) adiabatic [*Lindzen*, 1981]. When this criterion is met the local buoyancy frequency goes to zero and locally the wave can no longer propagate because the buoyancy restoring force vanishes. For monochromatic hydrostatic gravity waves there are two other equivalent definitions that yield the same maximum amplitude: 1) the wave becomes nonlinear in the reference frame moving with the fluid velocity $\bar{u}$, and 2) the rate of vertical parcel displacement equals the vertical group velocity [*Fritts*, 1984; *Leovy*, 1982]. Mathematically the wave saturation criteria are:

$$\left|\frac{dT_0}{dz}\right| + \left|\frac{dT'}{dz}\right|_{sat} \geq \frac{g}{c_p}, T'_{sat} = \frac{N^2T_0}{gk_z} \qquad (27)$$
$$|u'|_{sat} \geq |\bar{u}-c|, |w'|_{sat} \geq c_{gz} = \frac{k_h|\bar{u}-c|}{k_z}$$

To obtain the largest gravity wave heating in the thermosphere, gravity waves need to propagate through the stratosphere and mesosphere without reaching saturation amplitudes. If a wave breaks it dissipates wave energy and deposits momentum in the saturation zones and does not carry energy and momentum to much higher altitudes. Forcing a gravity wave with too large an amplitude in the lower atmosphere is counterproductive in heating the thermosphere as the wave saturates and dissipates in the middle atmosphere. If the wave reaches the thermosphere and is still at sub-saturation amplitude, then molecular viscosity acts to dissipate the wave energy with the wave reaching a maximum amplitude at the level where wave dissipation cancels exponential $(\rho_0)^{-0.5}$ amplitude growth

$$k_{zi} \approx \frac{1}{2H}, \text{where } k_{zi} \approx k_{zr}\left(\frac{\omega_i}{\omega_r}\right) \approx \frac{\mu}{\rho_o}\omega k_z^3 \qquad (28)$$

when the WKBJ approximation is valid [*Matcheva and Strobel*, 1999]. Here subscripts r, i denote real and imaginary parts. Now the dispersion relation for "Boussinesq" hydrostatic gravity waves is $\omega \approx NK_h/k_z$ and (28) yields the mass density of the atmosphere, ρ_q, where the gravity wave reaches peak amplitude

$$\rho_q \approx 2H\mu\frac{k_z^4}{Nk_h} \qquad (29)$$

The vertical gravity wave energy flux, F_{Ez}, is

$$F_{Ez} = Ec_{gz} \approx \frac{1}{2}\rho_q\frac{g^2}{N^2}\left|\frac{\omega}{k_z}\right|\frac{\overline{T'^2}}{T_0^2} \qquad (30)$$

and reaches its maximum value at the saturation amplitude

$$F_{Ez} \approx \frac{1}{2}\rho_q\frac{N^3k_h}{k_z^4} \approx \mu HN^2 \rightarrow \frac{\mu gR}{c_p}, \qquad (31)$$
$$\text{if T = constant}$$

Note that these expressions depend only on the background properties of the atmosphere and not explicitly on any wave properties which are embedded in expression (29) for ρ_q. The wave amplitude squared grows as ρ_0^{-1} until the wave amplitude saturates or viscous dissipation retards further wave growth. The maximum

gravity wave energy flux is proportional to the background atmospheric mass density and its value will decrease exponentially with height when the wave reaches saturation amplitude.

With appropriate values for the input parameters, μ, g, and c_p/R, the maximum gravity wave energy fluxes in isothermal thermospheric regions for the terrestrial planets Venus, Earth, and Mars are 0.02, 0.1, and 0.01, respectively; for the giant planets Jupiter, Saturn, Uranus, and Neptune 0.13, 0.04, 0.04, and 0.04, respectively, and 0.0004 for Pluto in units of erg cm^{-2} s^{-1}. For the terrestrial planets these values are small in comparison to solar EUV and UV heating rates, whereas for the giant planets these values exceed substantially the solar heating rates. From the Galileo probe data the inferred downward heat flux by thermal conduction was ~ 0.5 erg cm^{-2} s^{-1}, or four times the maximum heating rate.

Larger gravity wave energy fluxes are possible in the lower thermosphere where the temperature gradients are large and positive (and also if viscous dissipation is not severe at the wave's vertical wavenumber, k_z, as noted above). In Eq. (31), H is now the density scale height given by $H[1 + (H/T)(dT/dz)]^{-1}$. For Jupiter's lower thermosphere this increases the maximum gravity energy flux to ~ 0.2 erg cm^{-2} s^{-1}. But for gravity wave heating to contribute substantially to high thermospheric temperatures the maximum wave dissipation must occur high in the thermosphere where the transition from significant temperature gradient to isothermal conditions takes place. This is imperative in order to achieve a large separation between heat input and radiative cooling and maintain a considerable temperature gradient over an extended altitude range, as is evident from Eq. (25). To attain maximum energy dissipation at high altitudes, Eq. (29) demands large vertical wavelengths/very small vertical wavenumbers because $\rho_q \propto k_z^3$. Physically, waves with large vertical wavelengths suffer smaller dissipation per unit distance and hence propagate to higher altitudes. However the WKBJ approximation breaks down for these waves and is suggestive that wave reflection may be important as *Hickey et al.* [2000] discuss. In addition, gravity waves induce a downward eddy heat flux, $c_p\overline{w'T'}$, that has the net result of lowering the effective altitude of wave dissipation [*Matcheva and Strobel*, 1999].

Finally, one might think that multiple gravity waves could supply the required thermospheric heating. However, finite amplitude waves can destructively interfere with one another and cause a wave to saturate much lower in the atmosphere. In a region where one wave has large negative dT'/dz, the local static stability is reduced substantially and may cause another wave to saturate at a much smaller amplitude and lower in the atmosphere than would occur in the absence of other waves. Thus the above values should be considered upper limits to gravity wave heating with viable values being somewhat less in magnitude.

The other important class of vertically propagating internal waves are Rossby waves whose restoring force is the meridional variation of the coriolis force and whose dynamics are based on linearized equations for conservation of potential vorticity, q [*Andrews et al.*, 1987]. Generally the potential vorticity of the atmosphere is dominated by planetary vorticity (the coriolis parameter defined above), f, with a minor contribution from relative vorticity of the velocity field, $\nabla \times \vec{v}$. As Rossby waves propagate vertically they must extract potential vorticity from the mean flow, q_0, in order for their wave potential vorticity, q', to grow exponentially in amplitude as $\rho_0^{-1/2}$, in the absence of dissipation. As *Schoeberl and Lindzen* [1982] demonstrated, the wave potential vorticity cannot exceed the basic state potential vorticity, i. e., $q' < f$ and this restricts wave amplitudes to two orders of magnitude lower than estimated by $\rho_0^{-1/2}$ amplitude growth. Because Jupiter's f is only ~ 2.5 times the terrestrial value, it is improbable that Rossby waves can produce either a hot terrestrial or a hot Jovian corona.

Acknowledgments.

Table 1 and Figure 1 are based on Table 4.2 and Figure 4.4 from AN INTEGRATED STRATEGY FOR THE PLANETARY SCIENCES 1995-2010, National Academy Press, Washington, DC. In addition the author's discussion on Composition and Chemistry is based on his contribution on pp. 113-117 from this report and used with permission. Partial support by NASA Grant NAG-5-4168 is acknowledged.

REFERENCES

Andrews, D. G., J. R. Holton, and C. B. Leovy, Middle Atmosphere Dynamics, Academic Press, Orlando, Chapter 4, 1987.

Chamberlain, J. W. and D. M. Hunten, Theory of Planetary Atmospheres, Academic Press, Orlando, Chapter 2, 1987.

Chapman, S., The Thermosphere - The Earth's Outermost Atmosphere in Physics of the Upper Atmosphere, ed. J. A. Ratcliffe, Academic Press, New York, p. 4, 1960.

Colegrove, F. D., F. S. Johnson, and W. B. Hanson, Atmospheric Composition in the lower thermosphere, *J. Geophys. Res.*, *71*, 2227-2236, 1966.

Delsemme, A. H. and D. C. Miller, Physico-chemical phenomena in comets, III. The continuum of Comet Burnham., *Planet Space Sci.*, *19*, 1229-1258, 1971.

Elliot, J. L., E. W. Dunham, A. S. Bosh, M. Slivan, L. A. Young, L. H. Wasserman, and R. L. Millis, Pluto's atmosphere, *Icarus*, *77*, 148-170, 1989.

Elliot, J. L., D. F. Strobel, X. Zhu, J. A. Stansberry, L. H. Wasserman, and O. G. Franz, The Thermal Structure of Triton's Middle Atmosphere, *Icarus*, *143*, 425-428, 2000.

Fritts, D. C., Gravity wave saturation in the middle atmosphere: A review of theory and observations, *Rev. Geophys. Space Phys.*, *22*, 275-308, 1984.

Gill, A. E., Atmosphere-Ocean Dynamics, Academic Press, New York, Sec. 8.4, 1982.

Grinspoon, D. H., and J. S. Lewis, Cometary water on Venus: implicatons of stochastic impacts, *Icarus*, *74*, 21-35, 1988.

Hall, D. T., P. D. Feldman, M. A. McGrath, and D. F. Strobel, The far-ultraviolet oxygen airglow of Europa and Ganymede, *Astrophys. J.*, *499*, 475, 1998.

Hickey, M. P., R. L. Walterscheid, and G. Schubert, Gravity wave heating and cooling in Jupiter's thermosphere, *Icarus*, *148*, 266-281, 2000.

Hines, C. O., Dynamical heating in the upper atmosphere, *J. Geophys. Res.*, *70*, 177, 1965.

Landau, L. D., and E. M. Lifshitz, Fluid Mechanics, Pergamon Press, New York, 1959.

Lellouch, E., Io's atmosphere: Not yet understood, *Icarus*, *124*, 1-21, 1996.

Lellouch, E., R. Laureijs, B. Schmitt, E. Quirico, C. de Bergh, J. Crovisier, and A. Coustenis, Pluto's Non- Isothermal Surface, *Icarus*, *147*, 220-250, 2000.

Leovy, C. B., Control of the homopause, *Icarus*, *50*, 311-321, 1982.

Lindzen, R. S., Turbulence and stress owing to gravity wave and tidal breakdown, *J. Geophys. Res.*, *86*, 9707-9714, 1981.

Matcheva, K. I., and D. F. Strobel, Heating of Jupiter's thermosphere by dissipation of gravity waves due to molecular viscosity and heat conduction, *Icarus*, *140*, 328-340, 1999.

McGrath, M. A., and R. E. Johnson, Magnetospheric plasma sputtering of Io's atmosphere, *Icarus*, *69*, 519-531, 1989.

Saur, J., D. F. Strobel, and F. M. Neubauer, Interaction of the Jovian Magnetosphere with Europa: Constraints on the Neutral Atmosphere, *J. Geophys. Res.*, *103*, 19,947-19,962, 1998.

Schoeberl, M. R., and R. S. Lindzen, A note on the limits of Rossby wave amplitudes, *J. Atmos. Sci.*, *39*, 1171-1174, 1982.

Spencer, J. R, K. L. Jessup, M. A. McGrath, G. E. Ballester, and R. V. Yelle, Discovery of Gaseous S2 in Io's Pele Plume, *Science*, *288*, 1208-1210, 2000.

Strobel, D. F. and B. C. Wolven, The Atmosphere of Io: Abundances and Sources of Sulfur Dioxide and Atomic Hydrogen, *Astrophys. Space Sci.*, *277*, 271-287, 2001.

Summers, M. E., D. F. Strobel, Y. L. Yung, J. T. Trauger, and F. Mills, The Structure of Io's Atomic Corona and Implications for Atmospheric Escape, *Astrophys. J.*, *343*, 468-480, 1989.

Yelle, R. V., J. I. Lunine, J. B. Pollack, and R. H. Brown, Lower Atmospheric Structure and Surface-Atmosphere Interaction on Triton, in Neptune and Triton, ed. D. P. Cruikshank, University of Arizona Press, Tucson, pp. 1031-1106, 1995.

Young, L. A., J. L. Elliot, A. Tokunaga, C. de Bergh, and T. Owen, Detection of Gaseous Methane on Pluto, *Icarus*, *127*, 258, 1997a.

Young, L. A., R. V. Yelle, R. E. Young, A. Seiff, and D. B. Kirk, Gravity waves in Jupiter's thermosphere, *Science*, *276*, 108-111, 1997b.

Zolotov, M. Y., and B. Fegley, Jr., Volcanic production of sulfur monoxide (SO) on Io, *Icarus*, *132*, 431-434, 1998.

D. Strobel, Departments of Earth and Planetary Sciences and Physics and Astronomy, The Johns Hopkins University, Baltimore, MD 21218-2687. (email: strobel@jhu.edu)

Solar System Upper Atmospheres: Photochemistry, Energetics, and Dynamics

G. Randall Gladstone

Southwest Research Institute, San Antonio, Texas

Roger V. Yelle

Northern Arizona University, Flagstaff, Arizona

T. Majeed

University of Michigan, Ann Arbor, Michigan

The physical modeling of most upper atmospheric processes begins with the approximation and solution of one or more of the three primary equations of conservation—mass (i.e., continuity), energy, and momentum. Here we outline the main components of these equations as they relate to the upper atmospheres of the solar system, reviewing the salient results for photochemistry, energetics, and dynamics on key terrestrial planets, jovian planets, and satellites.

1. INTRODUCTION

The most basic considerations of any study of planetary atmospheres must involve the three questions of chemistry, energetics, and dynamics. While these subjects are intimately related, it is very common to treat them separately, as far as is possible, since each is covered by one of the three great conservation equations, i.e., those of mass, energy, and momentum. Useful versions of these equations as they relate to upper atmospheres may be found in, e.g., *Banks and Kockarts* [1973] or *Rees* [1989].

Table 1 of Chapter I.1 presents the general characteristics of the various atmospheres of the solar system. In this chapter we outline the background and recent results for the photochemistry, energetics, and winds in selected planetary and satellite upper atmospheres. While we do not go into great detail here, we hopefully provide enough references for the interested reader to become more informed about each topic, as well as an introduction for some of the more focussed chapters that follow.

Atmospheres in the Solar System: Comparative Aeronomy
Geophysical Monograph 130

10.1029/130GM03

2. PHOTOCHEMISTRY

2.1. General Principles

Photochemistry begins with the dissociation, ionization, or excitation of molecules in the upper atmospheres of the planets by ultraviolet sunlight. The basic principles of the photochemistry of the atmospheres of Earth and the other planets are well discussed in such recent textbooks as *Yung and DeMore* [1999] and *Wayne* [2000].

Table 1. Bond/Ionization Energies, Photoabsorption Limits, Major Channels, and Excess Energies for Common Atmospheric Species[a]

Species	Dissociation Energy, eV (nm)	Absorption Limit, eV (nm)	Major Channel	ΔE, eV
O_3	1.05 (1180.8)	1.4 (900)	$O_3 + h\nu_{2537} \rightarrow O_2(a\,^1\Delta) + O(^1D)$	0.8
H_2O_2	2.15 (576.7)	3.5 (350)	$H_2O_2 + h\nu_{2537} \rightarrow 2\,OH$	3.2
H_2S	3.91 (317.1)	5.0 (250)	$H_2S + h\nu_{1216} \rightarrow SH + H$	2.3
C_2H_6	4.36 (284.4)	7.7 (162)	$C_2H_6 + h\nu_{1216} \rightarrow C_2H_4 + H_2$	9.0
NH_3	4.40 (281.8)	5.4 (230)	$NH_3 + h\nu_{1216} \rightarrow NH_2 + H$	1.9
CH_4	4.48 (276.7)	8.3 (149)	$CH_4 + h\nu_{1216} \rightarrow CH_3 + H$	6.5
H_2	4.52 (274.4)	11.2 (111)	$H_2 + h\nu_{977} \rightarrow 2\,H$	8.2
H_2O	5.12 (242.2)	6.4 (195)	$H_2O + h\nu_{1216} \rightarrow OH + H$	3.7
Na	5.14 (241.3)	5.1 (241)	$Na + h\nu_{1216} \rightarrow Na^+ + e$	1.0
O_2	5.17 (240.0)	6.4 (195)	$O_2 + h\nu_{1216} \rightarrow O(^1D) + O$	1.4
HCN	5.20 (238.4)	6.4 (195)	$HCN + h\nu_{1216} \rightarrow CN(A\,^2\Pi) + H$	3.8
C_2H_2	5.38 (230.4)	5.6 (220)	$C_2H_2 + h\nu_{1216} \rightarrow C_2H + H$	3.4
CO_2	5.45 (227.5)	6.2 (200)	$CO_2 + h\nu_{1216} \rightarrow CO + O(^1D)$	4.5
SO_2	5.65 (219.4)	3.2 (390)	$SO_2 + h\nu_{1216} \rightarrow SO + O$	0.5
NO	6.54 (189.7)	5.4 (230)	$NO + h\nu_{1216} \rightarrow N + O$	2.3
N_2	9.80 (126.5)	12.4 (100)	$N_2 + h\nu_{977} \rightarrow 2\,N$	3.4
S	10.36 (119.7)	10.4 (120)	$S + h\nu_{304} \rightarrow S^+ + e$	6.7
CO	11.16 (111.1)	5.8 (215)	$CO + h\nu_{977} \rightarrow C + O$	2.6
C	11.26 (110.1)	11.3 (110)	$C + h\nu_{977} \rightarrow C^+ + e$	6.6
H	13.60 (91.2)	13.6 (91)	$H + h\nu_{911} \rightarrow H^+ + e$	3.8
O	13.62 (91.0)	13.6 (91)	$O + h\nu_{304} \rightarrow O^+ + e$	23.8
N	14.53 (85.3)	14.5 (85)	$N + h\nu_{304} \rightarrow N^+ + e$	16.7
Ar	15.76 (78.7)	15.8 (79)	$Ar + h\nu_{304} \rightarrow Ar^+ + e$	11.5
He	24.59 (50.4)	24.6 (50)	$He + h\nu_{304} \rightarrow He^+ + e$	16.7

[a]Values taken from *Okabe* [1978], *Yung and DeMore* [1999], *Novotny* [1973], and *Huebner et al.* [1992].

Many of the important results of photochemical modeling may be understood as an interplay between the steep rise of the solar UV flux with increasing wavelength and the larger variety of product states and reaction likelihood as wavelength decreases. Table 1 lists the bond strengths of several important species, which may be compared with the energy of a Lyα photon of $h\nu = 10.2$ eV.

While it contains only a few of the major species found in the atmospheres of the solar system, Table 1 provides a useful reference for understanding the composition and photochemistry of the terrestrial, giant, and satellite atmospheres, which we now outline in more detail.

2.2. Terrestrial Planets

The atmospheres of Earth, Venus, and Mars are likely the result of outgassing of volatiles from similar mineral inventories, and it is not surprising that the same basic components appear in each (see Table 1 of Chapter I.1). The evolution of the large differences in the current climates on the three planets—from the hot, dry, and thick venusian super greenhouse, to the (currently) comfortable, biosphere-dominated Earth atmosphere, to the cold, dry, and thin polar-cap buffered martian atmosphere—may be largely attributed to their different distances from the Sun and their different masses. The ordering of Earth's major species abundances differs from those of Venus and Mars due to the presence of both oceans (accounting for the low CO_2 abundance through dissolution and precipitation as carbonates) and life (accounting for the high abundance of O_2 through photosynthesis and the burial of organic carbon). Regarding the upper atmospheres of the terrestrial planets, on each there are species that saturate and condense out below the tropopause, and only the most volatile are considered here. In addition, in the photochemistry of each planet there exist catalytic cycles which allow minor species to control the abundances of the major species.

The photochemistry of Mars is currently quite well understood, and has been investigated recently by *Kras-*

nopolsky [1993], *Nair et al.* [1994], *Atreya and Gu* [1994], *Krasnopolsky* [1995], *Clancy et al.* [1996], and *Krasitskii* [1998]. The major constituent, carbon dioxide, is photolyzed at altitudes of 80-100 km to yield a net result of carbon monoxide and molecular oxygen, viz.,

$$\begin{aligned} 2(CO_2 + h\nu \rightarrow CO + O) \quad & 1.2 \times 10^{-6} \\ 2O + M \rightarrow O_2 + M \quad & 1.1 \times 10^{-27} T^{-2.0} \\ net: 2CO_2 \rightarrow 2CO + O_2 & \end{aligned}$$

where M represents any third body (most likely a CO_2 molecule). Unless otherwise stated, photolysis rates in s^{-1} at 1 AU are from *Huebner et al.* [1992], and 2-body and 3-body rate coefficients (in $cm^3\ s^{-1}$ and $cm^6\ s^{-1}$, respectively) are from *Yung and DeMore* [1999]. If the atmosphere of Mars were entirely CO_2, then relatively large abundances of CO and O_2 would naturally arise in a 2:1 proportion, respectively, since the recombination reaction $CO + O \rightarrow CO_2$ is spin forbidden and so is very slow. Observations indicate that the mixing ratios of CO and O_2 are much smaller than the 8% and 4% predicted from pure CO_2, and the reason is that HO_x species (a shorthand for the group of molecules made up of the odd hydrogen species H, OH, HO_2, and H_2O_2) act to catalytically recombine CO and O, e.g., as in the cycle

$$\begin{aligned} CO + OH \rightarrow CO_2 + H \quad & 1.5 \times 10^{-13}(1 + 0.6P_{atm}) \\ H + O_2 + M \rightarrow HO_2 + M \quad & 1.3 \times 10^{-27} T^{-1.6} \\ O + HO_2 \rightarrow O_2 + OH \quad & 3.0 \times 10^{-11} e^{200/T} \\ net: CO + O \rightarrow CO_2 & \end{aligned}$$

Several other catalytic cycles exist, some involving the odd nitrogen families known as NO_x (made up of N, NO, NO_2, NO_3, and $2N_2O_5$) and NO_y (made up of NO_x and HNO_2, HNO_3, and HO_2NO_2). These cycles are able to account for the stability of CO_2 in the martian atmosphere.

Photochemistry plays an interesting role in the escape of water from Mars. The loss of H from the upper atmosphere follows the dissociation of H_2 that has diffused upward from the lower atmosphere where it results from the photolysis of H_2O. If the atmosphere is in steady state (i.e., if the crust is as oxidized as it can get) then the oxygen produced in the water photolysis must escape from the upper atmosphere as well, at 1/2 the hydrogen rate. This is accomplished by the non-thermal escape of high-velocity O fragments produced during electron recombination of ionospheric O_2^+ or solar wind induced sputtering. The regulation of the H and O escape is maintained through photochemistry. For example, a transient decrease in the O escape rate would lead to an increased O_2 abundance, which would curtail the production of H_2 and ultimately (over $\sim 10^5$ years) lower the H escape rate.

The most recent comprehensive investigation of the photochemistry of Venus was conducted by *Yung and DeMore* [1982]. On Venus the recycling of CO_2 by the catalytic HO_x cycles is short-circuited by the presence of large amounts of Cl in the atmosphere and it is catalytic ClO_x reactions that stabilize CO_2, e.g.,

$$\begin{aligned} Cl + CO + M \rightarrow ClCO + M \quad & 1.3 \times 10^{-34} e^{1000/T} \\ ClCO + O_2 + M \rightarrow ClCO_3 + M \quad & \frac{5.7 \times 10^{-15} e^{500/T}}{10^{17} + 0.05M} \\ ClCO_3 + O \rightarrow CO_2 + O_2 + Cl \quad & 1.0 \times 10^{-11} \\ net: CO + O \rightarrow CO_2 & \end{aligned}$$

where Cl is provided by photolysis of HCl at altitudes of 60–80 km.

Thermochemical equilibrium governs the dense and hot venusian atmosphere from ground level to the sulfuric acid cloud tops at $z \sim 60$ km. Species expected under equilibrium such as CO_2, SO_2, H_2O, and COS that are transported into the upper atmosphere are converted by photochemistry into CO, H_2SO_4, and S_8. The sulfuric acid droplets that make up a large fraction of the clouds are produced by the oxidation of SO_2, e.g.,

$$\begin{aligned} SO_2 + h\nu \rightarrow SO + O \quad & 1.6 \times 10^{-4} \\ 2SO \rightarrow SO_2 + S \quad & 8.3 \times 10^{-15} \\ S + O_2 \rightarrow SO + O \quad & 2.2 \times 10^{-12} \\ 2(SO_2 + O + M \rightarrow SO_3 + M) \quad & 8.0 \times 10^{-32} e^{-1000/T} \\ 2(SO_3 + H_2O \rightarrow H_2SO_4) \quad & 9.0 \times 10^{-13} \\ net: 2SO_2 + O_2 + 2H_2O \rightarrow 2H_2SO_4 & \end{aligned}$$

This process also accounts for the extremely low abundance of O_2 in the atmosphere of Venus [cf. *Mills*, 1999]. Incidentally, the bright $\sim$ 2 MR Venus dayglow emission of the O_2 IR Atmospheric Band ($a^1\Delta_g \rightarrow X^3\Sigma_g^-$) at 1.27 μm is, as on Earth and Mars, a result of chemistry and does not provide any information with regard to bulk O_2 densities. Unlike Earth and Mars (which are even brighter, at $\sim$ 20 MR and $\sim$ 26 MR, respectively), however, the source at Venus is not from ozone photolysis (cf. Table 1) but is likely a combination of sources, the most important being O atom recombination and the reaction $ClO + O \rightarrow Cl + O_2(a^1\Delta)$. It is the remarkable resistance of the O_2 $a^1\Delta$ state to quenching by CO_2 that leads to the surprisingly large brightnesses of the 1.27 μm emissions on Venus and Mars. See Chap-

ter I.5 for more details on terrestrial planet dayglow emissions.

The photochemistry of Earth's upper atmosphere is a large subject, and cannot be adequately summarized here. Useful general sources of information on the subject are *Wayne* [2000] and *Brasseur et al.* [1999]. The Earth's atmosphere is very much removed from equilibrium due to the presence of life, such that highly oxidized (e.g., CO_2) and highly reduced species (e.g., CH_4) exist together in precarious abundance. It has been estimated that a few percent increase in the current O_2 abundance would result in the spontaneous combustion of the world's forests [*Yung and DeMore*, 1999]. While the concentrations of many species in the Earth's atmosphere are thus largely a question of biogenic and anthropogenic sources and sinks, upper atmosphere photochemistry acts to modify the composition and allow the escape of hydrogen to space, much as on Venus and Mars.

2.3. Giant Planets

The investigation of hydrocarbon photochemistry on Jupiter has a long history, going back to *Wildt* [1937], although *Strobel* [e.g., 1973] was the first to explain the stability of methane due to the pyrolysis of photochemically produced higher hydrocarbons after mixing down into the deep atmosphere. Recent models have attempted to include C_3 and C_4 compounds [e.g., *Gladstone et al.*, 1996], but work is just beginning on the more important problem (in a global sense) of auroral chemistry [e.g., *Perry et al.* 1999; *Wong et al.* 2000]. For Saturn, the most recent work is by *Ollivier et al.* [2000] and *Moses et al.* [2000a,b]. On Uranus, the most recent model is by *Summers and Strobel* [1989], while for Neptune, the latest results are by *Romani et al.* [1993], *Bishop et al.* [1998], and *Dobrijevic and Parisot* [1998].

The giant planets formed beyond the "snow line" in the primitive solar nebula, where condensation of ices along with rocks provided enough protoplanetary core mass to allow the accretion of gaseous hydrogen and helium; they are large enough to have probably evolved very little over the age of the solar system. The abundances of C-N-O and heavier elements ranges from a few times solar at Jupiter and Saturn, to a few tens of times solar at Uranus and Neptune. Because of the large hydrogen abundance, the thermochemically preferred states for all of the heavier elements on the giant planets are as hydrides, e.g., CH_4, NH_3, H_2O, H_2S, etc. While this holds true in the deeper atmosphere, in the upper troposphere the temperature drops low enough that first H_2O, then H_2S (with NH_3 as NH_4SH), and finally NH_3 condense to form clouds and hazes. On Uranus and Neptune, the temperature drops even further so that even CH_4 forms aerosols. Based on its volatility relative to the other major hydrides, methane is the primary molecule in the upper atmospheres of the giant planets to undergo photochemistry. This disequilibrium chemistry results in a suite of organic molecules of varying complexity, from ethane to soot; it is likely that the ubiquitous Axel-Danielson aerosol [cf. *Podolak and Danielson*, 1977] which is responsible for mid-UV extinction on the giant planets is organic soot derived from auroral chemistry and photochemistry. Once produced, higher hydrocarbons such as butane and diacetylene find their way into the lower stratosphere, where they may condense into hazes if the temperatures are low enough and nucleation sites are available. Eventually, long-lived species such as alkanes are transported into the troposphere where they are rapidly mixed down to high pressures and temperatures and converted back to methane.

Following photodissociation of methane, the primary method for adding more C-C bonds is through CH insertion reactions, e.g.,

$$\begin{aligned} CH + CH_4 &\rightarrow C_2H_4 + H \quad 5.0 \times 10^{-11} e^{200/T} \\ CH + C_2H_2 &\rightarrow C_3H_2 + H \quad 3.5 \times 10^{-10} e^{61/T} \\ CH + C_2H_6 &\rightarrow C_3H_6 + H \quad 1.8 \times 10^{-10} e^{132/T} \end{aligned}$$

with rate coefficients in $cm^3\ s^{-1}$ from *Moses et al.* [2000a]. Methyl reactions are also important, however, and the primary source of ethane is $2CH_3 + M \rightarrow C_2H_6 + M$. Another important source of complex hydrocarbons is through photosensitized dissociation, in which photons at wavelengths longer than can be absorbed by CH_4 directly instead dissociate other hydrocarbons, e.g., C_2H_2, which are then able to dissociate methane, i.e.,

$$\begin{aligned} C_2H_2 + h\nu &\rightarrow C_2H + H \quad 1.0 \times 10^{-5} \\ C_2H + CH_4 &\rightarrow C_2H_2 + CH_3 \quad 1.2 \times 10^{-11} e^{-491/T} \\ net &: CH_4 \rightarrow CH_3 + H \end{aligned}$$

However, the formation of higher hydrocarbons on the giant planets is strongly curtailed by the presence of large amounts of H, which is very good at cracking C-C bonds. Without even considering the ion-neutral chemistry of the auroral regions—where the most interesting molecules are produced (e.g., C_6H_6 and other aromatics), at least on Jupiter—the hydrocarbon chemistry schemes can get quite involved. Figure 1 shows a schematic of the major photochemical pathways for

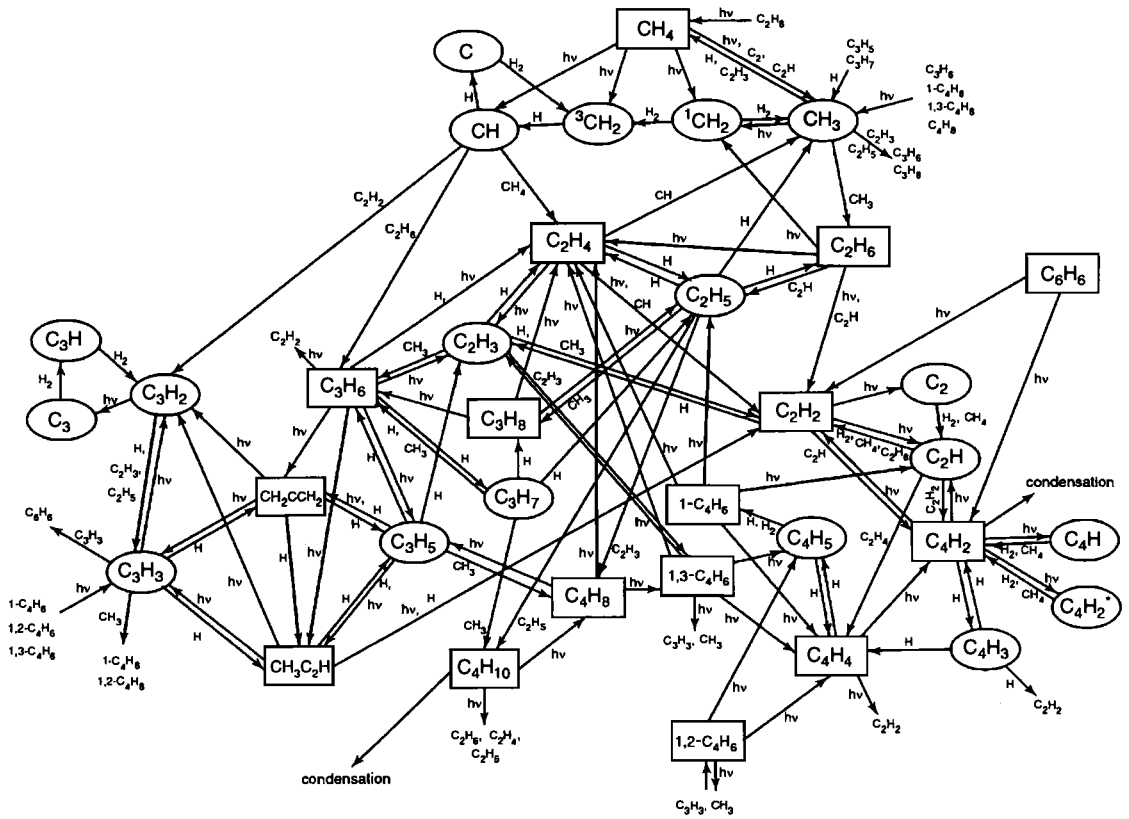

Figure 1. Schematic diagram showing the important photochemical pathways for the formation of higher hydrocarbons on the giant planets [*Moses et al.*, 2000a, Fig. 3]. Radical species are outlined by ovals and stable molecules by rectangles.

forming higher hydrocarbons on Saturn, and is representative for all the giant planets.

In addition to hydrocarbon photochemistry, the influx of meteoritic material (as described in detail in Chapter III.5) leads to other disequilibrium products, e.g., CO and CO_2. Similar products may be introduced by "injections" of material from the deeper atmospheres, where they are in thermal equilibrium.

2.4. Io, Titan, Triton, and Pluto Atmospheres

The atmosphere of Io is mainly SO_2 and has a relatively simple photochemistry, the most recent models of which are by *Summers and Strobel* [1996] and *Wong and Johnson* [1996]. The atmosphere is substantial, but fairly patchy, in keeping with the extreme range of surface temperatures associated with Io's extraordinary volcanism. Photodissociation of SO_2 results in large abundances of S and O, and lesser amounts of SO and O_2.

Titan has a rich photochemistry dominated by hydrocarbons and nitriles. In preparation for the Cassini-Huygens mission, Titan's atmospheric composition and chemistry have been subject to much attention in recent years. The classic study by *Yung et al.* [1984] has been added to in recent years by *Toublanc et al.* [1995], *Lara et al.* [1996], *Banaszkiewicz et al.* [2000], *Dire* [2000], and *Lebonnois et al.* [2001]. The ability of H and H_2 to rapidly escape from Titan's massive N_2-CH_4 atmosphere leads inexorably to the photochemical production of complex hydrocarbons which condense to form smog and are deposited on the surface. No recycling back to CH_4, as on the giant planets, is possible. Another major difference with the gas giants is that coupled CH_4-N_2 chemistry is very important on Titan, and compounds such as HCN are formed in abundance through the reaction of N atoms (produced in Titan's thermosphere by EUV and magnetospheric electron dissociation of N_2) with hydrocarbon radicals, e.g., $N + CH_2 \rightarrow HCN + H$.

Triton's cryophilic photochemistry has been investigated by *Strobel et al.* [1990b] and *Krasnopolsky and Cruikshank* [1995], while the very similar photochem-

istry of Pluto has been modeled by *Summers et al.* [1997], *Lara et al.* [1997] and *Krasnopolsky and Cruikshank* [1999]. Because of the extreme cold, the N_2, CH_4, and CO in the atmospheres of Triton and Pluto are probably in vapor equilibrium with surface ices, and any higher hydrocarbons produced photochemically are subject to rapid condensation and removal to the surface. Because of their similar compositions, the photochemistry of both Pluto and Triton is very similar to that of Titan.

3. ENERGETICS AND THERMAL STRUCTURE

3.1. General Principles

The thermosphere is the uppermost region of the atmosphere. Because of heating by solar EUV and FUV radiation, it is usually, but not always, a region of high temperature, The base of the thermosphere is at the mesopause, which can be defined as the temperature minimum created by the tendencies for a negative temperature gradient in the mesosphere, due to radiative cooling, and a positive temperature gradient in the thermosphere, due to thermal conduction. This definition has the virtue that it is based on an observable, the temperature profile, but it is also physically based because the processes that control the temperature profile change in the vicinity of the mesopause. In general, but not always, the mesopause is the boundary between the lower atmosphere, which is dominated by radiative processes, and the upper atmosphere, where thermal conduction plays a large role.

The thermal structure of the mesosphere is largely determined by absorption of solar radiation and radiative cooling in the infrared from vibrational transitions in polyatomic molecules. Most infrared radiative processes become weak in the region of the mesopause because collision rates become too slow to maintain Boltzmann populations of vibrational states. The mesopause usually occurs near a pressure of 0.1 μbar. Assuming a temperature of 200 K and a collisional de-excitation probability of 10^{-4} per collision implies a collisional de-excitation rate of 0.3 Hz. Radiative rates for vibrational transitions are typically about 1 Hz, a comparable value. Thus, radiative de-excitation rates are slower than collisional rates at pressures lower than ~ 0.1 μbar, implying a deficit of molecules in vibrationally excited states, compared with a Boltzmann distribution. As a consequence, thermal conduction tends to dominate above 0.1 μbar and radiative cooling below.

Typically, diffusive separation also sets in near a pressure of 0.1 μbar, i.e., the mesopause and the homopause are usually close to each other. This can drastically alter the composition of the thermosphere compared with the lower atmosphere. Light species become more dominant at higher altitudes. In addition, because the solar radiation absorbed in the thermosphere initiates chemistry, thermospheres are often home to photochemically-produced species, further altering the composition of the thermosphere relative to the lower atmosphere.

In addition to absorption of solar energy, absorption of magnetosphere energy in the thermosphere can be important, especially in auroral regions for planets with permanent magnetic fields. In this chapter, we are concerned primarily with the globally averaged structure of the thermosphere; thus, auroral processes will not be discussed in depth, except in those cases where they affect the global mean structure.

3.2. Terrestrial Planets

Figure 2 shows calculated heating and cooling rates for the thermospheres of Venus, Earth, and Mars. The primary balance in the upper regions of all three thermospheres is between solar EUV heating and thermal conduction. At lower altitudes, cooling by radiative emissions from the CO_2 band at 15 μm becomes important and very quickly below the mesopause the balance is primarily between IR heating and IR cooling. On Earth, radiative emissions from NO at 5.3 μm are equally as important as cooling by CO_2. In addition, in the Earth's thermosphere radiative emissions from O at 63 μm make a small contribution to the thermal balance. Both NO and O are examples of disequilibrium species that reside in the thermosphere because of chemistry initiated by absorption of solar EUV radiation. We note that the primary absorber of solar EUV radiation is CO_2 on Mars and Venus, but O_2 on Earth, and therefore the different planets could be characterized by different heating efficiencies.

The physical structure of the thermosphere is similar on all three terrestrial planets. Solar EUV energy is deposited at high altitudes and conducted downwards to the vicinity of the mesopause. Here, it is radiated away, primarily by CO_2 15 μm emissions. Conduction of energy from the upper thermosphere to the mesopause results in a positive temperature gradient and high thermospheric temperatures. Despite the similarity in basic physical processes, the resulting thermospheric temperatures on Earth are much higher than on Mars and Venus. According to *Bougher and Roble* [1991], representative exospheric temperatures are 248, 290, and 1255 K at solar maximum and 172, 180, and 737 K at solar minimum, for Venus, Mars, and Earth, respectively (see also Chapter IV.1). This is a result

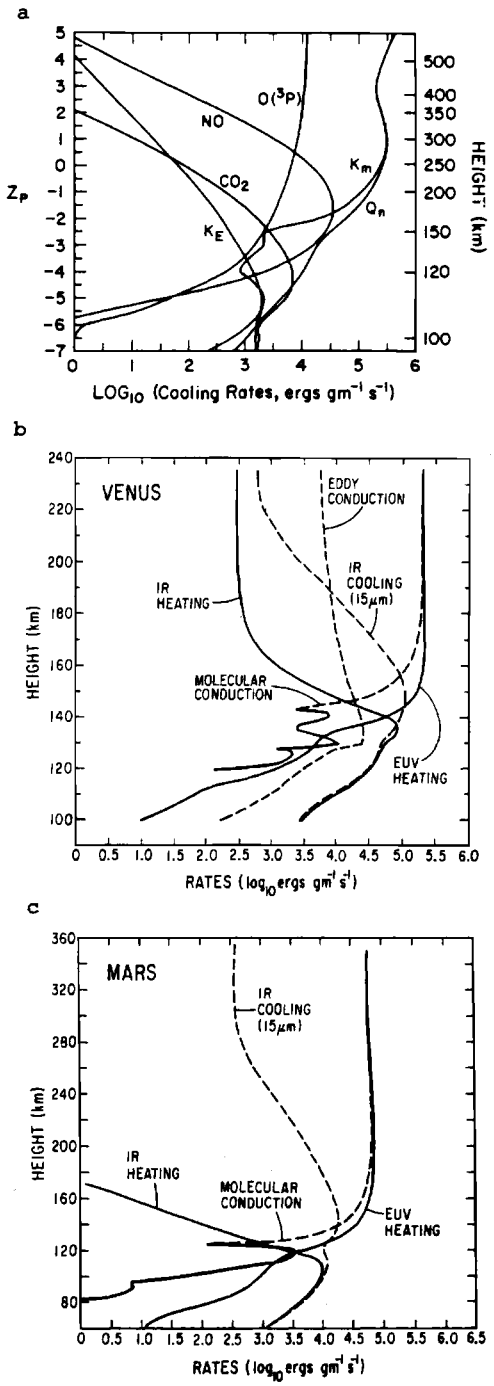

Figure 2. a) Heating and cooling rates for the Earth's upper atmosphere [*Bougher and Roble*, 1991, Fig. 3b]. b) Cooling rates in the atmosphere of Venus [*Bougher and Roble*, 1991, Fig. 3a]. K_m represents cooling by molecular conduction and K_E cooling by eddy conduction. The curves labeled by molecular formulas represent radiative cooling by the indicated species. Q_n represents the net heating rate. c) Heating and cooling rates in the upper atmosphere of Mars [*Bougher and Roble*, 1991, Fig. 3c].

of the higher CO_2 concentrations in the former atmospheres. CO_2 is the main atmospheric constituent on Mars and Venus, but a minor constituent on the Earth. As a result, CO_2 cooling is relatively weak on Earth and thermal conduction operates over a larger altitude range, producing higher temperatures. Contributing to this is the lower mean molecular mass of the Earth's thermosphere ($\sim$ 16 amu) compared with Venus and Mars ($\sim$ 44 amu), which gives the Earth a relatively large scale height, thus increasing the altitude range over which thermal conduction operates. These differences are more than sufficient to compensate for the fact that Venus absorbs 40% more solar flux than the Earth. The expected doubling in the 21st century of the preindustrial CO_2 abundance in Earth's atmosphere due to the burning of fossil fuels is predicted to cool the thermosphere by $\sim$ 10 K [*Roble and Dickinson*, 1989] (while warming the troposphere by the greenhouse effect).

3.3. Jovian Planets

Energy balance in the upper atmospheres of the jovian planets is a puzzle. Aeronomical models that are based on the balances described in the previous subsection fail to adequately describe the observed thermal structures. One might expect that solar energy deposited in the jovian thermosphere would be conducted downward to the mesopause region and radiated away by complex molecules. In this case, the temperature rise in the thermosphere would be determined by the size of the temperature gradient required to carry the conductive flux. Models based on this idea were presented by *Strobel and Smith* [1973]. Using the photochemical models of *Strobel* [1973] they concluded that the energy conducted downward from the thermosphere would be radiated away in the vicinity of the mesopause by C_2H_2 and CH_4. *Strobel and Smith* [1973] calculated the distributions of CH_4 and C_2H_2 and the thermal structure in a self-consistent manner. A cooling-to-space approximation was used to estimate radiative cooling rates; IR heating rates were ignored, so the calculations were valid down to the mesopause, but not below. The temperature rise in the jovian thermosphere was calculated to be only 15–30 K. Though they were not calculated by Strobel and Smith, we can safely assume that calculated temperatures for the other jovian planets would be even smaller because of weaker solar input.

Table 1 of Chapter I.1 includes a summary of observed thermospheric temperatures on the jovian planets. The measurements for Jupiter come from a variety of sources, but those for the other planets are based on the Voyager UVS solar occultation experiments. The agreement between the various methods

used for Jupiter provides a verification of the UVS occultation technique, so that high thermospheric temperatures on all the giant planets should be viewed as well established. The low thermospheric temperature predicted by *Strobel and Smith* [1973] is a consequence of the solar flux (because of the large distance from the Sun), the high thermal conductivity of H_2, and relatively large gravitational acceleration (which keeps the scale height small). The large disagreement between the observed and expected temperatures indicate that solar radiation is not the dominant heating source for the jovian thermospheres.

What else could heat the jovian thermospheres to such high temperatures? A number of suggestions have been made and there is insufficient space to review them all. We divide them into three groups: 1) magnetospheric input at low latitudes, 2) transport of auroral energy to low latitude, and 3) heating by gravity waves.

Usually, magnetospheric energy carried by precipitating charged particles is deposited only at high latitudes in the auroral zones. On Earth, for example, relatively little magnetospheric energy couples directly into low latitude regions. Yet, mechanisms do exist for this to happen. *Waite et al.* [1997] suggested that the diffusion of energetic charged particles across magnetospheric L shells until they were eventually absorbed by the atmosphere could explain observations of x-ray emissions from Jupiter's equatorial atmosphere. Calculations based on this hypothesis suggested that the heating rates associated with the observed x-ray brightness could explain the high thermospheric temperature on Jupiter. However, from analysis of very recent x-ray observations with Chandra, *Cravens et al.* [2001] conclude that the low-latitude emissions are more likely generated by scattering and fluorescence of solar x-rays, processes that do not generate substantial atmospheric heating.

Analysis of the temperature profile derived from Galileo Atmospheric Structure Iinvestigation (ASI) measurements find a downward conductive flux in the lower thermosphere of $\sim$ 0.6 ergs cm^{-2} s^{-1} [*Young et al.* 1997]. When integrated over the globe this yields a total power of 4×10^{13} W. The total power deposited in the jovian auroral zones has been estimated to be $\sim 10^{14}$ W [cf. *Bhardwaj and Gladstone,* 2000]. The similarity of these values suggests that transport of auroral energy to lower latitudes could be important to the energetics at low latitude. It is not clear that this necessarily happens because auroral energy is also radiated away by H_3^+ and conducted downward to the mesopause in the locality of the auroral regions while being transported horizontally; latitudinal transport also can be strongly inhibited by Coriolis forces. Attempts to account for all these processes with numerical circulation models have begun, but so far are inconclusive [*Achilleos et al.,* 1998 and Chapter IV.2]. The primary problem is that the thermal time constant in the jovian thermosphere is of order 10^7 seconds at 0.1 μbar. Thus, the numerical simulations must be run for a very long time to achieve convergence.

The existence of gravity waves in the mesopause region of Jupiter and their importance to the energetics of that region was first discussed by *French and Gierasch* [1974]. There was little subsequent work on this topic because the Voyager temperature profile appeared to be inconsistent with wave heating [*Festou et al.,* 1981; *Atreya et al.,* 1981]. *Yelle et al.* [1996] analyzed several different types of observations, including Voyager data, and derived a temperature profile very different from that presented by *Festou et al.* [1981]. *Yelle et al.* [1996] found a strong temperature gradient just above the mesopause, leading them to suggest that heating by gravity waves was an important heat source in the thermosphere. Subsequently, *Sieff et al.* [1997] analyzed Galileo ASI measurements of the temperature profile in the thermosphere. They found a mean profile similar to that derived by *Yelle et al.* [1996] upon which was superimposed periodic temperature perturbations with all the characteristics of gravity waves.

Young et al. [1997] analyzed the ASI temperature profile, separating the observed temperatures into a mean and perturbation components. They fit the periodic component to an analytic model for upwardly propagating gravity waves and found that two waves were required to fit the observations. The characteristics of the waves were derived from the analytic fits. Using the expression for the energy flux of gravity waves derived by *French and Gierasch* [1974], *Young et al.* [1997] found that the observed waves had roughly the right energy to explain the high thermospheric temperatures.

However, *Matcheva and Strobel* [1999] pointed out that the expression for gravity wave flux derived by *French and Gierasch* [1974] and used by *Young et al.* [1997] contains an error because it fails to enforce mass conservation to second order (see also Chapter I.1). This has interesting consequences for atmospheric heating. As shown in Figure 3, the correct formulation of the problem predicts a region of cooling at high altitude as well as a region of heating at lower altitude. The column-integrated rate of wave cooling is smaller than the column-integrated wave heating, but it is large enough to affect thermospheric temperatures. Using

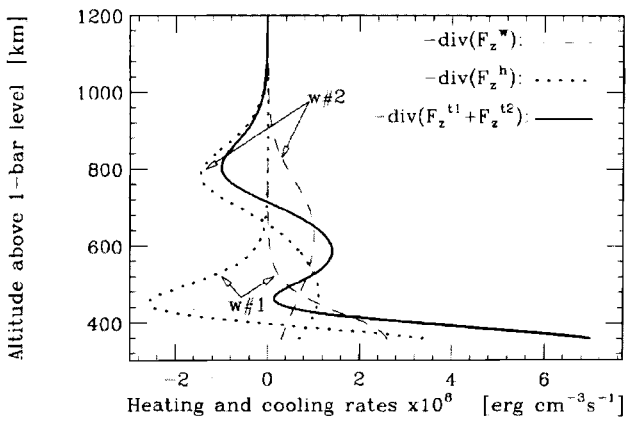

Figure 3. Wave heating rates in the jovian thermosphere [*Matcheva and Strobel*, 1999, Fig. 3]. The curves labeled w#1 and w#2 refer to Wave 1 and Wave 2 from *Young et al.* [1997]. F_z^W and F_z^h are defined by *Matcheva and Strobel* [1999]. The net wave heating is negative at high altitudes, above the location where the waves reach their maximum altitude.

their formulation, *Matcheva and Strobel* [1999] find that waves with the characteristics derived by *Young et al.* [1997] do not heat the jovian thermosphere to the observed levels, though they are still energetically important.

Both *Young et al.* [1997] and *Matcheva and Strobel* [1999] based their calculations on the WKB approximation for wave propagation. *Hickey et al.* [2000] recently carried out full numerical solutions to the wave equation. Although they did not calculate the temperature rise due to the Young et al. gravity waves, they did find that these waves would cause relatively small temperature changes to an already hot thermosphere, assuming that the temperatures and heating rates are linearly related. Presumably the relatively small effect calculated by *Hickey et al.* [2000] is due to shortcomings of the WKB approximation. However, the *Hickey et al.* [2000] analysis also assumed a linear relationship between heating rates and temperature. Since the relationship is non-linear, this assumption may also be partly responsible for differences with the earlier work.

One needs to be careful in drawing conclusions from the simple wave heating models described above because they neglect several physical effects that may be significant. These include:

- *Interaction of the wave with the mean flow.* It is well known that waves deposit momentum as well as energy. The mean flow associated with this momentum deposition may interact with the waves, altering the heating rate. For example, wind shear resulting from the momentum deposition may add to the viscous heating.
- *Radiative terms.* The models presented so far assumed a clean separation between the mesosphere and thermosphere and therefore have not included radiative cooling by hydrocarbons. In reality there is a gradual transition from the mesosphere to the thermosphere and the nature of this transition may affect the temperature profile.
- *Variability in time and location.* The Galileo data represent a snap shot of the jovian thermosphere at one time and one location. It is likely that other waves are present at different locations and times, but we know nothing about them.
- *Uncertainties in wave properties.* As noted by *Young et al.* [1997], we are unable to characterize the waves uniquely because we have only a 1-D trace of the wave amplitude. Different assumptions about the phase speed would lead to more or less energetic waves.
- *Bulk viscosity.* The models presented to date have included only shear viscosity, but it is likely that bulk viscosity is important.
- *Ion viscosity.* The models presented to date have neglected damping of the waves through their interaction with the ionosphere.

The last two points may be especially important. Although not mentioned explicitly by *Matcheva and Strobel* [1999] or *Hickey et al.* [2000], the wave cooling is due solely to the action of thermal conduction on the wave. The action of viscosity on the wave always produces a positive heating rate. Thus, the viscous terms neglected by these authors may substantially alter the relative importance of heating and cooling terms.

Finally, we note that of the three mechanisms suggested for heating Jupiter's low latitude thermosphere, perhaps only gravity wave heating is likely to apply to the other jovian planets. The magnetospheres of Saturn, Uranus, and Neptune are much less energetic than Jupiter's and any direct magnetospheric input would likely be much smaller (although on Uranus and Neptune particle deposition is much more global, due to the large large tilts of their magnetic fields). Similarly, only the jovian aurora is energetic enough to allow for altering the thermosphere of the planet on a global scale. Because the energy crisis exists on all the jovian planets, it seems plausible that there is a single explanation.

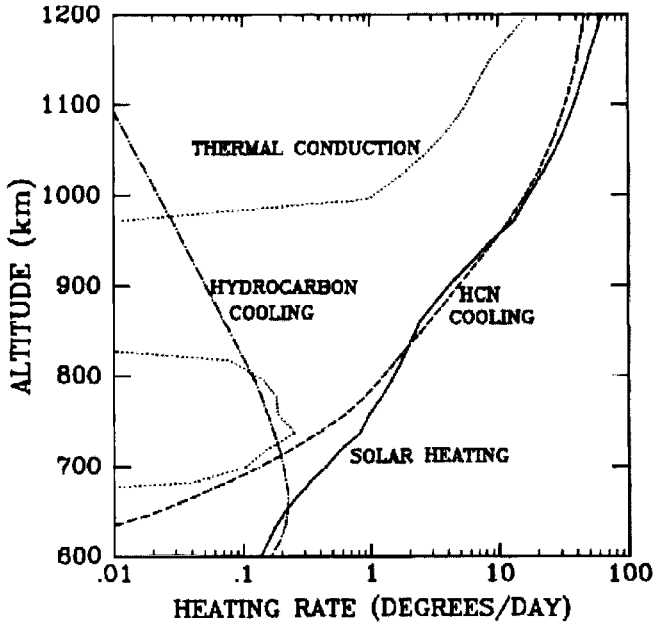

Figure 4. Heating and cooling rates in the upper atmosphere of Titan. Through much of the upper atmosphere solar EUV heating is balanced by HCN radiative cooling [*Yelle*, 1991, Fig. 15].

3.4. Titan, Triton and Pluto

The thermosphere of Titan has some unique properties. First, unlike Earth and the jovian planets, the primary radiatively active molecules (HCN, CH_4, C_2H_2, C_2H_6) are lighter or comparable in weight to the background atmosphere, which is primarily N_2. Thus, diffusive separation does not remove these more active molecules from the thermosphere, but rather enhances their abundance at high altitude. This effect is mitigated by the fact that the eddy diffusion coefficient on Titan appears to be large and diffusive separation is weak. CH_4 is the second most abundant constituent in Titan's atmosphere and the abundance in the thermosphere simply reflects that it is mixed upwards from below. C_2H_6 is a photochemically-produced species, but the bulk of the production is in the stratosphere and the thermospheric abundance is likewise determined by mixing from below. C_2H_2 and HCN are produced primarily in the thermosphere.

Yelle [1991] pointed out that the thermospheric temperature on Titan likely reflects a balance between solar heating and radiatively cooling by HCN, even at high altitudes. Thus, the thermosphere of Titan differs fundamentally from the terrestrial and jovian planets. Figure 4 shows the terms in the energy balance equation for Titan's upper atmosphere. The reason that HCN plays such a large role is that the molecule has a dipole moment and allowed rotational transitions that can cool the atmosphere. Rotational transitions are free of the non-LTE effects that drastically reduce cooling rates from vibrational transitions because rotational levels are in LTE at all atmospheric levels. The role of HCN on Titan is analogous to NO in the Earth's thermosphere, both are especially active radiative molecules created by photochemistry from the main constituents. However, as shown in Figure 4, HCN is far more important to the energy balance on Titan, than is NO on the Earth.

Titan's orbit is usually inside the magnetosphere of Saturn and it is possible that precipitation of charged particles from the magnetosphere may heat the thermosphere. To date this possibility has not been investigated in a quantitative manner.

Voyager measured a temperature of 99–105 K in Triton's upper thermosphere [*Krasnopolsky et al.*, 1993]. Calculations based solely on solar EUV heating predict a temperature of $\sim$ 70 K [*Stevens et al.*, 1992; *Krasnopolsky et al.*, 1993]. It is believed that heating from charged particles precipitating from Neptune's magnetosphere is responsible for the energy required to raise the thermospheric temperature to $\sim$ 100 K. A magnetospheric input roughly 50% larger than the solar input is needed. *Strobel et al.* [1990a], utilizing Voyger measurement of charged particle fluxes and theoretical models for the magnetospheric interaction, estimate a power input of 1.4×10^8 W, which is just about 50% larger than the solar power. Most of the energy deposited in the thermosphere is carried downward by thermal conduction, but radiation from minor species also plays an important role. Rotational line emissions from HCN and CO cool the thermosphere by about 5 and 10 K, respectively [*Stevens et al.*, 1992]. This is much smaller than the comparable effect on Titan because Triton has far less CH_4 than Titan and as a consequence has roughly 1000 times less HCN. The first application of general circulation models (GCMs) to Titan and Triton is described in Chapter IV.4.

We know very little about the thermosphere of Pluto; however, we expect it to differ in some interesting ways from the other bodies in our solar system. Because of the relatively high temperatures and low mass, Pluto's atmosphere is greatly extended compared with other atmospheres in the solar system. As a consequence, gravity becomes weak at high altitude and the scale height becomes very large. Because of this it is likely that Pluto's thermosphere is not in hydrodynamic equilibrium and that outflow rates are large. This question has been examined by several authors [e.g., *Trafton*

et al., 1997; *Hunten and Watson,* 1982; *Hubbard, Yelle, and Lunine,* 1990; *McNutt,* 1989; *Krasnopolsky,* 1999]. Rather than being conducted downward to where it is radiated away, solar energy deposited in Pluto's thermosphere is expected to flow upward, where it is used to power the outward flow. Eventually, it escapes the atmosphere.

4. DYNAMICS

The upper atmospheres of the terrestrial (Earth, Mars, Venus) and the outer planets (Jupiter, Saturn, Uranus, and Neptune) and their satellites have been observed by many spacecraft and ground-based instruments. Measurements relevant to upper atmospheric dynamics are those that establish neutral and ion densities, neutral and plasma temperatures, electric and magnetic field perturbations, absorption and emission spectra, and ion drift and neutral wind velocities [e.g., *Fesen et al.,* 2000; *Dickinson et al.,* 1984; *Niemann et al.,* 1980; *Seiff and Kirk,* 1977; *Keating et al.,* 1998; *Hinson et al.,* 1997; 2001; *Seiff et al.,* 1998; *Rego et al.,* 1999; *Broadfoot et al.,* 1981]. Although existing 1-D models for interpreting most of these observations have been useful for understanding average physical processes that take place in upper atmospheres, formulations of 3-D equations that describe and predict global behavior have provided significant insight into the relative importance of various processes. Numerical models that generate global simulations of neutral wind, temperature, and composition are called thermospheric general circulation models (TGCMs). Such models currently exist for the Earth, Mars, Venus, Jupiter and Titan, as described in Chapters IV.1, IV.2, and IV.4. Selected results for the upper atmospheric dynamics from these models, characterized by winds and ion drifts, will be described in this section.

The density of the neutral thermosphere is modified by neutral winds. These winds are generated by heat-induced pressure gradients, and are influenced by Coriolis forces (due to planetary rotation) and even more strongly by frictional forces (due to air viscosity and collisions between ions and neutral particles). The frictional force or ion-drag is generally the major factor limiting wind speeds in the thermosphere. The winds can move the ions and electrons in the direction of the magnetic field, **B**. If the field lines are inclined, the ion motion has a vertical component which can affect the ionospheric electron and ion densities [*Rishbeth,* 1979]. The neutral air is assumed to co-rotate with the modeled planet (or satellite), and in the Eulerian coordinate the neutral velocities represent the wind system. However, ion motion is influenced by co-rotation and also by the ionospheric dynamo effect (at low latitudes) and by a convection electric field, **E**, of magnetospheric origin (at high latitudes) [*Richmond et al.,* 1992; *Rishbeth and Garriott,* 1969; *Rees,* 1989]. The dynamo is most effective in the E-region; here ions and neutrals are strongly coupled via collisions while electrons are trapped on magnetic field lines, thus allowing the generation of electric fields. These electric fields map to the F-region along the highly conducting magnetic field lines and produce an $\mathbf{E} \times \mathbf{B}/B^2$ ion drift. Self-consistent coupling between the neutral wind and plasma generates an electromagnetic force, $\mathbf{J} \times \mathbf{B}$ (where **J** is current density) in the upper thermospheric region [*Roble et al.,* 1994; *Fuller-Rowell and Rees,* 1980]. Since E-region neutral winds are highly variable in time and space the resulting dynamo electric field and ion drift are likewise variable [cf. *Rishbeth and Garriott,* 1969].

The observational evidence on Earth suggests that the vertical wind is associated with atmospheric expansion and contraction due to the diurnal cycle of solar heating [*Price et al.,* 1995 and references therein]. Interpretation of wind data by global models [*Rees et al.,* 1989 and references therein] suggest a horizontal divergence (or upwelling) driven by a source other than the solar heating alone; a strong possibility is high-latitude thermospheric circulation and transport of heat to lower latitudes. The wind system on Jupiter has also been postulated to transport some of the heat deposited in the auroral region to the rest of the planet [e.g., *Waite et al.,* 1983]; and this is currently under numerical investigation [e.g., *Achilleos et al.,* 1998; *Bougher et al.,* 2001]. Although there is no evidence of high-latitude particle precipitation on Mars, Venus and Titan, it has been shown that horizontal wind divergence plays an important role in controlling the heat transport globally by solar-driven dynamics.

4.1. Fundamental Equations

The global circulation flow in the thermospheres of the Earth, Mars, Venus, Titan and Jupiter is coupled with the global energy budget, characterized by temperatures, and the global neutral and ion compositions and densities. Therefore, to calculate the global thermospheric winds, the momentum, energy, and mass conservation equations for neutral and ions are solved self-consistently as a function of time. Only the momentum equation for simulating the atmospheric wind system is described in this section. For details of other equations the readers are referred to *Dickinson et al.* [1981], *Bougher et al.* [1988a,b], *Achilleos et al.* [1998] and

Müller-Wordarg et al. [2000]. The momentum equation is described as [cf. *Rishbeth and Garriott,* 1969]:

$$d\mathbf{U}/dt + 2\boldsymbol{\Omega} \times \mathbf{U} = \mathbf{F} - \nu_{ni}(\mathbf{U} - \mathbf{V}) + (\mu/\rho)\nabla^2\mathbf{U} + g$$

where $d/dt = \partial/\partial t + (\mathbf{U} \cdot \nabla)$ shows how the horizontal wind velocity, **U**, changes with time but also through non-linear advection term. **U** has zonal (east-west) and meridional (north-south) components. Since the pressure gradient and gravity acceleration are much larger than other terms in the momentum equation, the calculation of vertical wind is typically done by using the continuity equation [cf. *Achilleos et al.,* 1998]. In the pressure coordinate, the vertical (upward-downward) wind is defined as $w = dp/dt$, where p is pressure.

For atmospheric motions in a coordinate frame fixed with respect to a rotating planet with angular velocity, $\boldsymbol{\Omega}$, the Coriolis acceleration, $2\boldsymbol{\Omega} \times \mathbf{U}$, is an important term for describing the general circulation. $\mathbf{F} = \nabla p/\rho$ is the wind-driving acceleration due to pressure gradients. The term $(\mu/\rho)\nabla^2\mathbf{U}$ represents the viscous acceleration arising from the vertical transport of horizontal momentum via intermolecular collisions; μ is the coefficient of viscosity, ρ is the mass density and g is the acceleration of gravity. The ratio μ/ρ is known as the kinematic viscosity. The ion-drag acceleration on the neutral air due to collisions with ions is defined by the term $\nu_{ni}(\mathbf{U} - \mathbf{V})$, where ν_{ni} is known as the collision frequency for momentum transfer and **V** is the ion drift velocity.

4.2. Thermospheric Global Circulation Models

The most recent TGCMs for the terrestrial planets, Jupiter, and the satellites Titan and Triton are described in Chapters IV.1, IV.2, and IV.4, respectively. However, there exists another jovian model under development, called Jupiter Thermosphere General Circulation Model (JTGCM), whose simulated results were presented recently by *Bougher et al.* [2001]. The development of the JTGCM is based on the adaptation of the National Center for Atmospheric Research (NCAR) Thermosphere General Circulation Model (TGCM8). The JTGCM retains the TGCM8 [*Roble et al.,* 1988, *Dickinson et al.,* 1981, 1984] numerical formulation for dynamics, along with the general solvers for major (H_2, H, He and H^+) and minor species (H_2^+, H_3^+) and the energy equation. However, several new subroutines have been developed to parameterize the estimated auroral and equatorial heating distribution derived from Galileo, HST, ROSAT and Voyager data. The JTGCM uses the charged particle drizzle estimated by *Waite et al.* [1997] as a source of solar heating while the particle heating calculated by *Grodent et al.* [2001] (energy spectrum was described by a three-kappa distribution with total energy, E_0 = 22 keV, and flux $\sim$ 100 ergs cm^{-2} s^{-1}) is used for the auroral region. The ion-drag scheme has been modified for the thermosphere of Jupiter. A convection electric field has been estimated and corresponding ion drifts (V_θ and V_ϕ: the meridional and zonal components of **V**) are generated using an ionospheric convection model; this model, based on Voyager measurements of ion convection in the outer magnetosphere [*Eviatar and Barbosa,* 1984], is mapped to high latitudes using the VIP4 magnetic field model [*Connerney et al.,* 1998]. Auroral morphology in the JTGCM has been represented by the polar ovals inferred from the analysis of the Jovian UV images obtained by the HST WFPC-2 from June 1996 to July 1997 [*Clarke et al.,* 1998].

The global pattern of neutral winds (weak auroral case) in the upper thermosphere (1 nbar level, which is $\sim$ 1600 km above the 1 bar level) predicted by JIM is shown in Fig. 1 of Chapter IV.2. Winds as strong as 35 m/s blow between 70° and 220° longitudes because of strong ion convection and large pressure gradients near the auroral ovals. The wind pattern in non-auroral regions is quite uniform. At low and mid-latitudes the winds reach their peak values of about 3 m/s while at the equator their speed reduces to 2 m/s. The corresponding temperature structure indicates that energy is being transported to these latitudes by strong adiabatic cooling within the auroral zone [cf. *Achilleos et al.,* 1998].

The simulated winds from the JTCGM (moderately strong auroral case) are shown in Figure 5a and 5b for the lower ($\sim$ 0.2 μb or $\sim$ 500 km) and upper ($\sim$ 5×10^{-6} μb or $\sim$ 4000 km) thermospheric regions, respectively. The wind system in the polar regions is driven by the high-latitude ion convection and large pressure gradients. In the lower thermosphere, the winds as large as 175 m/s are blowing as a result of strong ion convection and very large pressure gradients near the southern pole. A weaker ion convection near the northern pole reduces the wind speed to 40–50 m/s. At low and mid-latitudes the winds appear to be influenced by the Coriolis force (due to planetary rotation) and modified by ion-drag (which is strong due to the ionospheric peak at around 600 km). The situation is quite interesting in the exospheric region (Figure 5b), as much stronger winds are calculated in the southern hemisphere than in the northern hemisphere. This asymmetric circulation pattern is due to

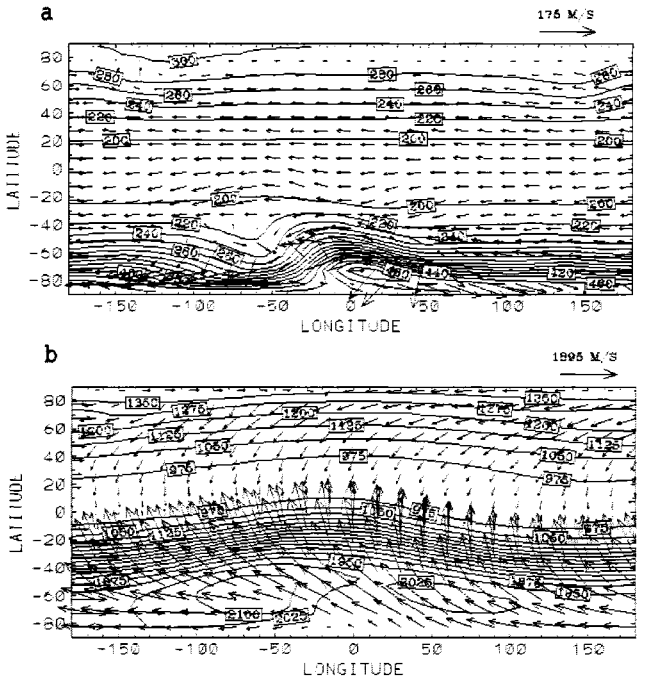

Figure 5. Contours of JTGCM neutral temperature (K) and superimposed horizontal wind vectors are shown for the inputs described in the text: a) at about 500 km and b) at about 4000 km [*Bougher et al.*, 2001].

the high-latitude ion convection which appears to be much stronger in the south than in the north. Strong upwelling or divergence of winds in the polar region (at -20° longitude in the south and at -150° longitude in the north) and subsidence or convergence at the low and mid-latitudes can be seen in Figure 6b. This increases the wind speed rapidly to a maximum value of 1.8 km/s near the jovian equator. It is also important to note that the pole-to-equator temperature difference of about 1000 K predominantly generates poleward winds of the order of km/s at the equator.

REFERENCES

Achilleos, N., S. Miller, J. Tennyson, A. D. Aylward, I. Müller-Wodarg, and D. Rees, JIM: A time-dependent, three-dimensional model of Jupiter's thermosphere and ionosphere, *J. Geophys. Res., 103,* 20,089–20,112, 1998.

Atreya, S. K., and Z. G. Gu, Stability of the Martian atmosphere: Is heterogeneous catalysis essential? *J. Geophys. Res., 99,* 13,133–13,145, 1994.

Atreya, S. K., T. M. Donahue, and M. C. Festou, Jupiter: Structure and composition of the upper atmosphere, *Astrophy. J., 247,* L43–L47, 1981.

Banaszkiewicz, M., L. M. Lara, R. Rodrigo, J. J. López-Moreno, and G. J. Molina-Cuberos, A coupled model of Titan's atmosphere and ionosphere, *Icarus, 147,* 386–404, 2000.

Banks, P. M., and G. Kockarts *Aeronomy, Part B* 355 pp., Academic Press, New York, 1973.

Bhardwaj, A. and G. R. Gladstone, Auroral emissions of the giant planets, *Rev. Geophys., 38,* 295–353, 2000.

Bishop, J., P. N. Romani, and S. K. Atreya, Voyager 2 ultraviolet spectrometer solar occultations at Neptune—Photochemical modeling of the 125–165 nm lightcurves, *Planet. Space Sci., 46,* 1–20, 1998.

Bougher, S. W. and R. G. Roble, Comparative terrestrial planet thermospheres, 1, Solar cycle variation of global mean temperatures, *J. Geophys. Res., 96,* 11,045–11,055, 1991.

Bougher, S. W., R. E. Dickinson, E. C. Ridley, and R. G. Roble, Venus mesosphere and thermosphere, 3, Three-dimensional general circulation with coupled dynamics and composition, *Icarus, 73,* 545–573, 1988a.

Bougher, S. W., R. E. Dickinson, R. G. Roble, and E. C. Ridley, Mars thermospheric general circulation model: Calculations for the arrival of Phobos at Mars, *Geophys. Res. Lett., 15,* 1511–1514, 1988b.

Bougher, S. W., J. H. Waite, Jr., T. Majeed, G. R. Gladstone, and D. Grodent, Jupiter Thermosphere General Circulation Model (JTGCM): Formulation and case studies incorporating ion-drag and Joule heating, paper presented at Jupiter, Planet, Satellites, & Magnetosphere Meeting, Boulder, Colorado, June 25 to June 30, 2001.

Brasseur, G. P., J. J. Orlando, and G. S. Tyndall (Eds.), *Atmospheric Chemistry and GLobal Change,* 654 pp., Oxford University Press, Oxford, 1999.

Broadfoot, A. L., et al., Overview of the Voyager ultraviolet spectrometry results through Jupiter encounter, *J. Geophys. Res., 86,* 8259–8284, 1981.

Clancy, R. T., and H. Nair, Annual (perihelion-aphelion) cycles in the photochemical behavior of the global Mars atmosphere, *J. Geophys. Res., 101,* 12,785–12,790, 1996.

Clarke, J. T., et al., Hubble Space Telescope imaging of Jupiter's UV aurora during the Galileo orbiter mission, *J. Geophys. Res., 103,* 20,217–20,236, 1998.

Connerney J. E. P., M. H. Acuña, N. F. Ness, and T. Satoh, New models of Jupiter's magnetic fields constrained by the Io flux tube footprint, *J. Geophys. Res., 103,* 11,929–11,940, 1998.

Cravens, T. E., A. N. Maurellis, G. R. Gladstone, and J. H. Waite, Jr., Model studies of jovian x-rays at low and high latitudes, paper presented at Jupiter, Planet, Satellites, & Magnetosphere Meeting, Boulder, Colorado, June 25 to June 30, 2001.

Dickinson, R. E., E. C. Ridley, and R. G. Roble, A three-dimensional general circulation model of the thermosphere, *J. Geophys. Res., 86,* 1499–1512, 1981.

Dickinson, R. E., E. C. Ridley, and R. G. Roble, Thermosphere general circulation with coupled dynamics and composition, *J. Atmos. Sci., 41,* 205–219, 1984.

Dire, J. R., Seasonal photochemical and meridional transport model for the stratosphere of Titan, *Icarus, 145,* 428–444, 2000.

Dobrijevic, M., and J. P. Parisot, Effect of chemical-kinetics uncertainties on hydrocarbon production in the stratosphere of Neptune, *Planet. Space Sci., 46,* 491–505, 1998.

Eviatar, A., and Barbosa, D. D., Jovian magnetospheric neutral wind and auroral precipitation flux, *J. Geophys. Res., 89,* 7393–7398, 1984.

Fesen, C. G., G. Crowley, R. G. Roble, A. D. Richmond, and B. G. Fejer, Simulation of the pre-reversal enhancement in the low latitude vertical ion drifts, *Geophys. Res. Lett., 27,* 1851–1854, 2000.

Festou, M. C., S. K. Atreya, T. M. Donahue, B. R. Sandel, D. E. Shemansky, and A. L. Broadfoot, Composition and thermal profiles of the jovian upper atmosphere determined by Voyager ultraviolet stellar occultation experiment, *J. Geophys. Res., 86,* 5715–5725, 1981.

French, R. G. and P. Gierasch, Waves in the jovian upper atmosphere, *J. Atmos. Sci., 31,* 1707–1712, 1974.

Fuller-Rowell, T. J., and D. Rees, A three-dimensional, time-dependent, global model of the thermosphere, *J. Atmos. Sci., 37,* 2545–2567, 1980.

Gladstone, G. R., M. Allen, and Y. L. Yung, Hydrocarbon photochemistry in the upper atmosphere of Jupiter, *Icarus, 82,* 1–52, 1996.

Grodent, D., J.-C. Gérard, and J. H. Waite, Jr., A self-consistent model of the jovian thermal structure, *J. Geophys. Res., 106,* 12,933–12,952, 2001.

Hinson, D. P., et al., Jupiter's ionosphere: results from the first Galileo radio occultation experiment, *Geophys. Res. Lett., 24,* 2107–2110, 1997.

Hinson, D. P., G. L. Tyler, J. L. Hollingsworth, and R. J. Wilson, Radio occultation measurements of forced atmospheric waves on Mars, *J. Geophys. Res., 106,* 1463–1480, 2001.

Hickey, M. P., R. L. Walterscheid, and G. Schubert, Gravity wave heating and cooling in Jupiter's thermosphere, *Icarus, 148,* 266–281, 2000.

Hubbard, W. B., R. V. Yelle, and J. I. Lunine, Non-isothermal Pluto atmosphere models, *Icarus, 84,* 1–11, 1990.

Huebner, W. F., J. J. Keady, and S. P. Lyon, Solar photo rates for planetary atmospheres and atmospheric pollutants, *Astrophys. Space Sci., 195,* 1–294, 1992.

Hunten, D. M., and A. J. Watson, Stability of Pluto's atmosphere, *Icarus, 51,* 665–667, 1982.

Keating, G. M., et al., The structure of the upper atmosphere of Mars: In-situ accelerometer measurements from Mars Global Surveyor, *Science, 279,* 1672–1676, 1998.

Krasnopolsky, V. A., Photochemistry of the martian atmosphere (mean conditions), *Icarus, 101,* 313–332, 1993.

Krasnopolsky, V. A., Uniqueness of a solution of a steady state photochemical problem: Applications to Mars, *J. Geophys. Res., 100,* 3263–3276, 1995.

Krasnopolsky, V. A., Hydrodynamic flow of N_2 from Pluto, *J. Geophys. Res., 104,* 5955–5962, 1999.

Krasnopolsky, V. A., and D. P. Cruikshank, Photochemistry of Triton's atmosphere and ionosphere, *J. Geophys. Res., 100,* 21,271–21,286, 1995.

Krasnopolsky, V. A., and D. P. Cruikshank, Photochemistry of Pluto's atmosphere and ionosphere near perihelion, *J. Geophys. Res., 104,* 21,979–21,996, 1999.

Krasnopolsky, V. A., B. R. Sandel, and F. Herbert, Temperature, N_2, and N density profiles of Triton's atmosphere: Observations and model, *J. Geophys. Res., 98,* 3065–3078, 1993.

Krasitskii, O. P., A photochemical model of the martian atmosphere that includes odd nitrogen

Lara, L. M., W.-H. Ip, and R. Rodrigo, Photochemical models of Pluto's atmosphere, *Icarus, 130,* 16–35, 1997.

Lara, L. M., E. Lellouch, J. J. López-Moreno, and R. Rodrigo, Vertical distribution of Titan's atmospheric neutral constituents, *J. Geophys. Res., 101,* 23,261–23,284, 1996.

Lebonnois, S., D. Toublanc, F. Hourdin, and P. Rannou, Seasonal variations of Titan's atmospheric composition, *Icarus, 152,* 384–406, 2001.

Matcheva, K. I. and D. F. Strobel, Heating of Jupiter's thermosphere by dissipation of gravity waves due to molecular viscosity and heat conduction, *Icarus, 140,* 328–340, 1999.

McNutt, R. L., Jr., Models of Pluto's upper atmosphere, *Geophys. Res. Lett., 16,* 1225–1228, 1989.

Mills, F. P., A spectroscopic search for molecular oxygen in the Venus middle atmosphere, *J. Geophys. Res., 104,* 30,757–30,767, 1999.

Moses, J. I., B. Bézard, E. Lellouch, G. R. Gladstone, H. Feuchtgruber, and M. Allen, Photochemistry of the upper atmosphere of Saturn, 1, Hydrocarbon photochemistry and comparisons with ISO observations, *Icarus, 143,* 244–298, 2000a.

Moses, J. I., B. Bézard, E. Lellouch, G. R. Gladstone, H. Feuchtgruber, and M. Allen, Photochemistry of the upper atmosphere of Saturn, 2, Effects of an influx of external oxygen, *Icarus, 145,* 166–202, 2000b.

Müller-Wodarg, I. C. F., R. V. Yelle, M. Mendillo, L. A. Young, and A. D. Aylward, *J. Geophys. Res., 105,* 20,833–20,856, 2000.

Nair, H., M. Allen, A. D. Anbar, Y. L. Yung, and R. T. Clancy, A photochemical model of the martian atmosphere, *Icarus, 111,* 124–150, 1994.

Niemann, H. B., W. T. Kasprzak, A. E. Hedi, D. M. Hunten, and N. W. Spencer, Mass spectrometric measurements of the neutral gas composition of the thermosphere and exosphere of Venus, *J. Geophys. Res., 85,* 7817–7827, 1980.

Novotny, E., *Introduction to Stellar Atmospheres and Interiors* 543 pp., Oxford University Press, New York, 1973.

Okabe, H., *Photochemistry of Small Molecules* 431 pp., John Wiley and Sons, New York, 1978.

Ollivier, J. L., M. Dobrijevic, and J. P. Parisot, New photochemical model of Saturn's atmosphere, *Planet. Space Sci., 48,* 699–716, 2000.

Perry, J. J., Y. H. Kim, J. L. Fox, and H. S. Porter, Chemistry of the jovian auroral ionosphere, *J. Geophys. Res., 104,* 16,541–16,566, 1999.

Podolak, M., and R. E. Danielson, Axel dust on Saturn and Titan, *Icarus, 30,* 479–492, 1977.

Rees, M. H. *Physics and Chemistry of the Upper Atmosphere* 289 pp., Cambridge University Press, Cambridge, 1989.

Rego, D., N. Achilleos, T. Stallard, S. Miller, R. Prange, M. Dougherty, and R. D. Joseph, Supersonic winds in Jupiter's aurorae, *Nature, 399,* 121–124, 1999.

Richmond, A. D, E. C. Ridley, and R. G. Roble, A thermosphere/ionosphere general circulation model with coupled electrodynamics, *Geophys. Res. Lett., 19,* 601–604, 1992.

Rishbeth, H., Ion-drag effects in the thermosphere, *J. Atmos. Terr. Phys., 41* 885–894, 1979.

Rishbeth, H., and O. K. Garriott, *Introduction to iono-*

spheric physics, Academic Press, New York, 1969.

Roble, R. G., and R. E. Dickinson, How will changes in carbon dioxide and methane modify the mean structure of the mesosphere and thermosphere? *Geophys. Res. Lett., 16*, 1441–1444, 1989.

Roble, R. G., E. C. Ridley, A. D. Richmond, and R. E. Dickinson, A coupled thermosphere/ionosphere general circulation model, *Geophys. Res. Lett., 15*, 1325–1328, 1988.

Romani, P. N., J. Bishop, B. Bézard, and S. Atreya, Methane photochemistry on Neptune: Ethane and acetylene mixing ratios and haze production, *Icarus, 106,* 442–463, 1993.

Seiff, A., and D. B. Kirk, Structure of the atmosphere of Mars in summer in mid-latitudes, *J. Geophys. Res., 82,* 4364–4378, 1977.

Seiff, A., et al., Thermal structure of Jupiter's atmosphere near the edge of a 5-μm hot spot in the north equatorial belt, *J. Geophys. Res., 103,* 22,857–22,890, 1998.

Stevens, M. H., D. F. Strobel, M. E. Summers, and R. V. Yelle, On the thermal structure of Triton's thermosphere, *Geophys. Res. Lett., 19,* 669–672, 1992.

Strobel, D. F., The photochemistry of hydrocarbons in the jovian atmosphere, *J. Atmos. Sci., 30,* 489–498, 1973.

Strobel, D. F., and G. R. Smith, On the temperature of the jovian thermosphere, *J. Atmos. Sci., 30,* 718–725, 1973.

Strobel, D. F., A. F. Cheng, M. E. Summers, and D. J. Strickland, Magnetospheric interaction with Triton's ionosphere, *Geophys. Res. Lett., 17,* 1661–1664, 1990a.

Strobel, D. F., M. E. Summers, F. Herbert, and B. R. Sandel, The photochemistry of methane in the atmosphere of Triton, *Geophys. Res. Lett., 17,* 1729–1732, 1990b.

Summers, M. E., and D. F. Strobel, Photochemistry of the atmosphere of Uranus, *Astrophys. J., 346,* 495–508, 1989.

Summers, M. E., and D. F. Strobel, Photochemistry and vertical transport in Io's atmosphere and ionosphere, *Icarus, 120,* 290–316, 1996.

Summers, M. E., D. F. Strobel, and G. R. Gladstone, Chemical models of Pluto's atmosphere, in *Pluto and Charon,* edited by S. A. Stern and D. J. Tholen, pp. 391–434, University of Arizona Press, Tucson, Ariz., 1997.

Toublanc, D., J. P. Parisot, J. Brillet, D. Gautier, F. Raulin, and C. P. McKay, Photochemical modeling of Titan's atmosphere, *Icarus, 113,* 2–26, 1995.

Trafton, L. M., D. M. Hunten, K. J. Zahnle, and R. L. McNutt, Jr., Escape processes at Pluto and Charon, in *Pluto and Charon,* edited by S. A. Stern and D. J. Tholen, pp. 475–522, University of Arizona Press, Tucson, Ariz., 1997.

Waite, J. H., Jr., T. E. Cravens, J. Kozyra, A. F. Nagy, S. K. Atreya, and R. H. Chen, Electron precipitation and related aeronomy of the jovian thermosphere and ionosphere, *J. Geophys. Res., 88,* 6143–6163, 1983.

Waite, J. H., Jr., G. R. Gladstone, W. S. Lewis, P. Drossart, T. E. Cravens, A. N. Maurellis, B. H. Mauk, and S. Miller, Equatorial x-ray emissions: Implications for Jupiter's high exospheric temperatures, *Science, 276,* 104–108, 1997.

Wayne, R. P., *Chemistry of Atmospheres, 3rd Edition* 775 pp., Oxford University Press, Oxford, 2000.

Wildt, R., Photochemistry of planetary atmospheres, *Astrophys. J., 86,* 321–336, 1937.

Wong, M. C., and R. E. Johnson, A three-dimensional azimuthally symmetric model atmosphere for Io, 1, Photochemistry and the accumulation of a nightside atmosphere, *J. Geophys. Res., 101,* 23,243–23,254, 1996.

Wong, A.-S., A. Y. T. Lee, Y. L. Yung, and J. M. Ajello, Jupiter: Aerosol chemistry in the polar atmosphere, *Astrophys. J., 534,* L215–L217, 2000.

Yelle, R. V., Non-LTE models of Titan's upper atmosphere, *Astrophys. J., 383,* 380–400, 1991.

Yelle, R. V., L. A. Young, R. J. Vervack, Jr., R. E. Young, L. Pfister, and B. R. Sandel, Structure of Jupiter's upper atmosphere: Predictions for Galileo, *J. Geophys. Res., 101,* 2149–2161, 1996.

Young, L. A., R. V. Yelle, R. E. Young, A. Sieff, and D. B. Kirk, Gravity waves in Jupiter's thermosphere, *Science, 276,* 108–111, 1997.

Yung, Y. L., and W. B. DeMore, Photochemistry of the stratosphere of Venus—Implications for atmospheric evolution, *Icarus, 51,* 199–247, 1982.

Yung, Y. L., M. Allen, and J. P. Pinto, Photochemistry of the atmosphere of Titan—Comparison between model and observations, *Astrophys. J. Suppl. Ser., 55,* 465–506, 1984.

Yung, Y. L., and W. B. DeMore *Photochemistry of Planetary Atmospheres* 456 pp., Oxford University Press, New York, 1999.

G. R. Gladstone, Southwest Research Institute, 6220 Culebra Road, San Antonio, TX 78238. (e-mail: randy@whistler.space.swri.edu)

R. V. Yelle, Department of Physics and Astronomy, Northern Arizona University, Flagstaff, AZ 86011. (e-mail: yelle@physics.nau.edu)

T. Majeed, University of Michigan, Space Physics Research Laboratory, 2455 Hayward Street, Ann Arbor, MI 48103. (e-mail: tariqm@engin.umich.edu)

Solar System Ionospheres

Andrew F. Nagy

Space Physics Research Laboratory, Department of Atmospheric, Oceanic and Space Sciences, University of Michigan, Ann Arbor, Michigan

Thomas E. Cravens

Department of Physics and Astronomy, University of Kansas, Lawrence, Kansas

All the planets in the solar system, except for Mercury, have ionospheres and all of these planetary ionospheres, except that of Pluto, have been observed in situ or remotely. Some planetary satellites are also known to possess reasonably dense ionospheres including Jupiter's satellites Io, Europa, Callisto and Ganymede, Saturn's satellite Titan, and Neptune's satellite Triton. Comets are also known to contain ionospheric plasma. Observations and theoretical models of the chemistry, dynamics and energetics of these ionospheres are reviewed in this paper.

1. INTRODUCTION

The ionosphere was defined in the following way by *Schunk and Nagy* [2000]:

"The ionosphere is considered to be that region of an atmosphere where significant numbers of free thermal (< 1 eV) electrons and ions are present."

If we define "significant numbers" as densities in excess of a few hundred particles per cm^{-3}, then ionospheres have been observed to be present around seven of our solar system's nine planets. No ionospheric measurements at Pluto are available, but it is estimated that an ionosphere exists around that planet, during the current epoch, with a peak density of about one thousand cm^{-3}. That means that the only planet without an atmosphere and ionosphere is Mercury [see *Johnson*, this volume]. Mercury does have a thin exosphere and thus probably also has a very tenuous ion exosphere. Ionospheres have been observed around six of the moons of the giant planets, namely Io, Callisto, Europa, Ganymede, Titan and Triton. This adds up to thirteen known ionospheres in our solar system. To this we should add the time dependent ionospheres of comets, which only exist during those relatively short time periods when the comet resides in the inner solar system. Such an ionosphere was measured by Giotto around comet P/Halley and without doubt other active comets such as Hale Bopp, whose gas production rate exceeded that of P/Halley, also have had substantial ionospheres, while they were within a few AU of the Sun. It would also be surprising if ionospheres were not present around extra-solar-system planets.

There are clearly important differences among the various ionospheres, but the basic physical and chemical processes which control all ionospheres are really very similar. Certainly the nitrogen-oxygen chemistry of the terrestrial ionosphere is different from the CO_2 based ion chemistry at Venus and Mars, and these chemistries are in turn different from the hydrogen based chemistry at the major planets, the methane-nitrogen chemistry at Titan, etc. The dynamics and energetics in an ionosphere that is created within a strong intrinsic planetary magnetic field are different from those in ionospheres of planets with weak or no magnetic fields. Differences in the gravitational force also have a strong influence. For example, at comets

Atmospheres in the Solar System: Comparative Aeronomy
Geophysical Monograph 130

10.1029/130GM04

where the gravity is basically nonexistent the atmosphere/coma extends to large distances ($\approx 10^5$ km), which in turn increases the extent of the ionosphere, whereas the ionosphere of Venus exists as a fairly narrow layer (a few hundred km), at least on the dayside. The relative importance of photoionization by solar radiation versus impact ionization by energetic charged particles also varies from ionosphere to ionosphere. Finally, the influence of the solar wind and/or planetary magnetospheres on solar system ionospheres strongly depends on whether or not a strong intrinsic magnetic field is associated with the body.

Ionospheric quantities, such as density and temperature, whether measured or calculated, are usually displayed as a function of altitude. This chapter will adhere to this tradition; however, we note that the peak photoionization rate (and for some solar system bodies the peak ionospheric electron density) is located at a neutral atmospheric pressure level of about 1 nanobar.

In this review paper we will not discuss the terrestrial ionosphere, which is covered in *Schunk* [this volume], but will concentrate on the other ionospheres in our solar system. In the next section we discuss the ionospheres of Venus and Mars. This is followed by a review of the ionospheres of the outer planets and then finally a review of our current understanding of the ionospheres of the moons and comets.

2. VENUS AND MARS

Of all the ionospheres and upper atmospheres in our solar system, except for the terrestrial one, we know the most about the atmosphere and ionosphere of Venus. Most of the information comes from a single spacecraft, the Pioneer Venus Orbiter (PVO) [*Brace et al.*, 1983; *Nagy et al.*, 1983; *Fox and Bougher*, 1991; *Brace and Kliore,* 1991; *Miller and Whitten*, 1991; *Fox and Kliore,* 1997; *Nagy and Cravens*, 1997]. In contrast, the only corresponding in situ upper atmosphere and thermal plasma measurements at Mars are those from the mass spectrometer [*Nier and McElroy*, 1977] and retarding potential analyzer [*Hanson et al.*, 1977], respectively, which were carried by the two Viking landers, and provided two vertical profiles. However, a significant number of electron density profiles from radio occultation observations are available for both planets [e.g. *Kliore and Luhmann*, 1991; *Zhang et al.*, 1990]. The upper atmospheres and ionospheres at these two planets are believed to be very similar and therefore a great deal of what we have learned about Venus applies to Mars.

The major source of daytime ionization at Venus and Mars is solar extreme ultraviolet (EUV) radiation. At Venus the photoionizaton rate peaks at an altitude of around 140 km above the surface of the planet. At this altitude the major neutral atmospheric constituent is CO_2,

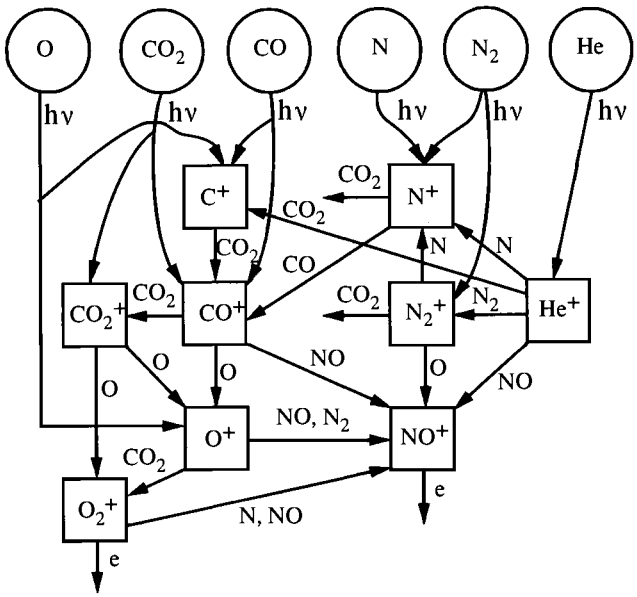

Figure 1. Block diagram of ionospheric chemistry for Venus and Mars (from Nagy et al., 1983).

but atomic oxygen is present with an abundance of about 10–20%. The predominance of CO_2 led to early predictions that the main ion in the Venus ionosphere should be CO_2^+; however it was realized [*Kumar and Hunten*, 1974], even before direct measurements could confirm it, that the presence of atomic oxygen leads to chemical reactions which quickly transform CO_2^+ to O_2^+. The main chemical reactions affecting the major ion species at these altitudes (~ 120–200 km) are:

$$CO_2 + h\nu \rightarrow CO_2^+ + e \quad (1)$$

$$CO_2^+ + O \rightarrow O_2^+ + CO \; [k = 1.64\times10^{-10} \text{ cm}^3 \text{ s}^{-1}] \quad (2)$$

$$\rightarrow O^+ + CO_2 \; [k = 9.6\times10^{-11} \text{ cm}^3 \text{ s}^{-1}] \quad (3)$$

$$O^+ + CO_2 \rightarrow O_2^+ + CO \; [k = 1.1\times10^{-9} \text{ cm}^3 \text{ s}^{-1}] \quad (4)$$

$$O_2^+ + e \rightarrow O + O \; [\alpha = 1.95\times10^{-7} (300/T_e)^{0.7} \text{ cm}^3 \text{ s}^{-1}] \quad (5)$$

where T_e denotes the electron temperature. The last of these chemical reactions indicated above, dissociative recombination of O_2^+, is the major terminal loss process for ions. Airglow produced by this chemistry is discussed in *Slanger and Wolven* [this volume]. The reaction rate coefficients, and appropriate references, which are given in this chapter, are taken from Tables 8.4 and 8.5 in *Schunk and Nagy* [2000] or *Anicich* [1993], unless otherwise

indicated. Ion production rates, such as resulting from (1), can also be found in *Schunk and Nagy* [2000].

A block diagram of the main ion chemistry of Venus and Mars is shown in Figure 1. Figures 2 and 3 show modeled and measured ion densities for the dayside ionospheres of Venus [*Nagy et al.*, 1980] and Mars [*Fox*, 1993], respectively. At Venus the peak total ion (and electron) density occurs near 140 km and the major ion is O_2^+. At Venus O^+ becomes the major ion and peaks near 200 km, while at Mars it appears that O_2^+ and O^+ become comparable near 300 km. There are many other ion species present, which are the result of a large variety of photochemical processes, some of which involve metastable species [*Fox*, 1982].

Venus has no significant intrinsic magnetic field, although at times of high solar wind dynamic pressure, a significant (~100 nT) horizontal induced magnetic field is present in the ionosphere [*Luhmann and Cravens*, 1991; *Cravens et al.*, 1997]; examples of both situations are shown in Figure 4 [*Russell and Vaisberg*, 1983]. It should be noted that narrow magnetic flux ropes are generally present even in the nonmagnetized situation [*Luhmann and Cravens*, 1991]. The global intrinsic magnetic field is also negligibly small at Mars ($<2x10^{11}$ T m^3), but there are localized patches of relatively strong remnant crustal magnetic fields present [*Acuna et al.*, 1998] as well as regions with magnetic flux ropes [*Cloutier et al.*, 1999]. Therefore, in most cases, the plasma can move relatively freely in both vertical and horizontal directions at both planets.

The chemical lifetime in the Venus ionosphere becomes long enough above about 200 km to allow transport processes, due to diffusion or bulk plasma drifts, to dominate. At Mars the transition from photochemical to transport control also takes place in the altitude region of 180 to 200 km in the dayside ionosphere. The results of the one-dimensional model calculations shown in Figures 2 and 3 do match successfully the observed daytime ion densities. However, in the case of the Mars calculations it should be remembered that no direct measurements of the neutral atomic oxygen density have been made, therefore the oxygen profile used in this model was obtained by forcing a best fit to the observed ion densities. Furthermore the best match for Mars is obtained with large upper boundary outflow conditions. The model results are relatively independent of these upper boundary conditions at the lower altitudes, but at the higher altitudes the densities depend strongly on transport, for which no data is available at this time.

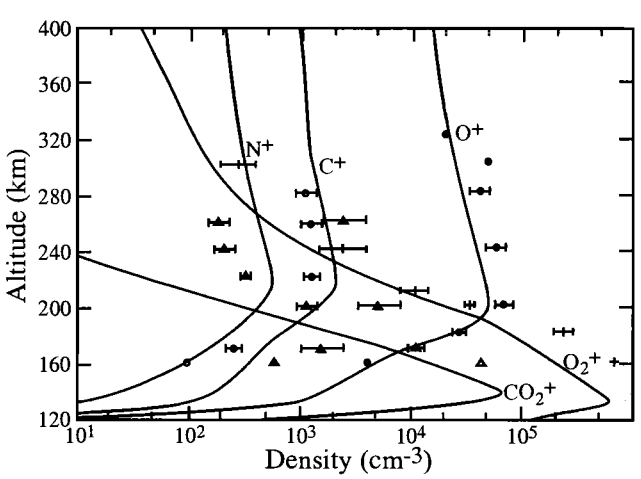

Figure 2. Ion density profiles for the dayside ionospheric of Venus (from Nagy et al., 1980).

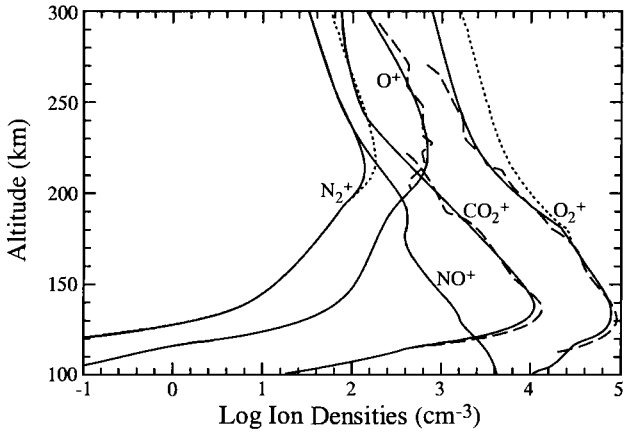

Figure 3. Ion density profiles for the dayside ionosphere of Mars (from Fox, 1993).

Measurements of ion flow velocities [*Miller and Whitten*, 1991] in the ionosphere of Venus have indicated that the horizontal velocity increases with altitude and with solar zenith angle, reaching a few km/s at the terminator, and becoming supersonic on the nightside. These velocities are, to a large degree, driven by the day to night pressure gradient. A variety of one- and multi-dimensional hydrodynamic, magnetohydrodynamic and semikinetic models have been used to study the interaction of the solar wind with these two planets [*Cravens et al.*, 1997; *Nagy et al.*, 1991; *Tanaka and Murawski*, 1997; *Liu et al.*, 1999; *Brecht*, 1990] which have provided good insights into the major processes controlling the upper ionosphere and ionopause (see next paragraph) regions. The general agreement between the model results and the observations is quite good.

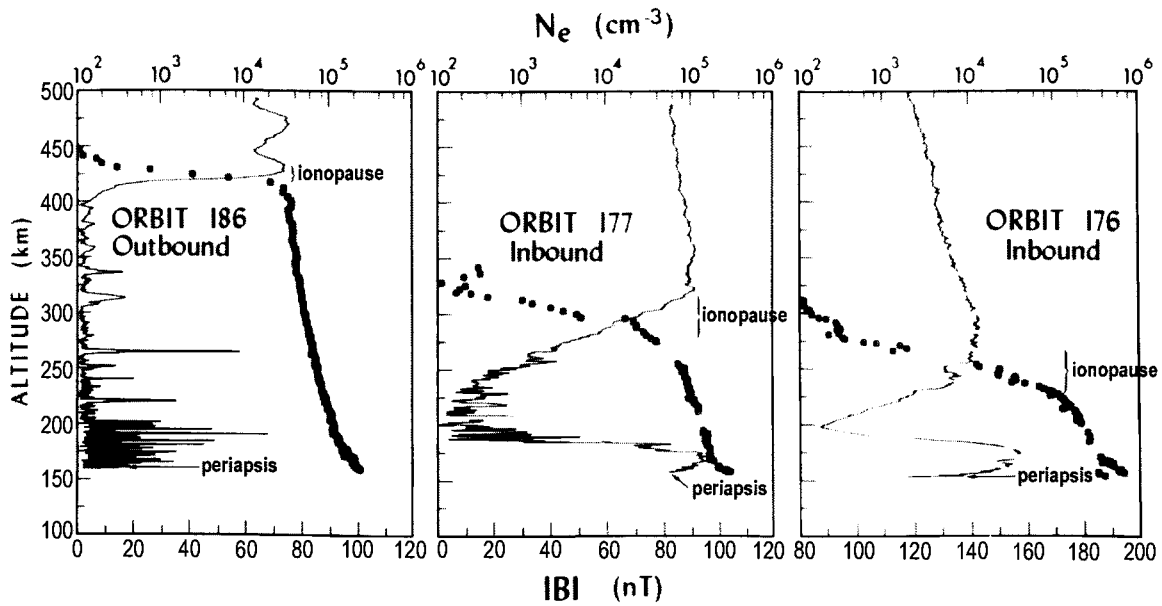

Figure 4. Magnetic field strength measured by the Pioneer Venus Orbiter versus altitude for different solar wind conditions (from Russell et al., 1983).

The ionosphere of Venus acts as an obstacle to the solar wind [*Brace et al.*, 1983; *Luhmann and Cravens*, 1991; *Cravens et al.*, 1997; see also *Brecht*, this volume], which is diverted around the planet. A bow shock is present in the flow and the interplanetary magnetic field is compressed into a magnetic barrier which lies outside the ionosphere. When the upstream solar wind dynamic pressure is significantly less than the maximum thermal pressure in the ionosphere, the ionosphere is free of large-scale magnetic fields (although magnetic flux ropes are usually present). A sharp break in the topside ionosphere is present at an altitude where the thermal plasma pressure of the ionosphere is approximately equal to the magnetic pressure in the magnetic barrier. This magnetic pressure approximately equals the solar wind dynamic pressure (Figure 4). This sharp gradient in the ionospheric thermal plasma density is called the ionopause; this pressure transition is also referred to as a tangential discontinuity in magnetohydrodynamic terminology. However, when the solar wind dynamic pressure is high, a large-scale magnetic field is known to be present in the ionosphere and the ionopause transition region is much broader (Figure 4). Given that the ionopause is at an altitude where the ionospheric thermal pressure balances the solar wind dynamic pressure, its location must change as solar wind and ionospheric conditions change [*Brace et al.*, 1983; *Luhmann and Cravens*, 1991]. For example, as the solar wind pressure increases, the ionopause height decreases. However, the height of the ionopause does not drop below about 300 km, even when the pressure exceeds about 4×10^{-8} dyne cm^{-2}. Also, the mean ionopause height rises from about 350 km at the subsolar location to about 900 km at a solar zenith angle of 90°.

Until very recently there were no observed indications, given the very limited data base, of the presence of an ionopause at Mars. However, the electron reflectometer instrument, carried by the Mars Global Surveyor (MGS) spacecraft, is now providing the first indication that an ionopause is present on the dayside with a mean altitude of about 380 km [*Mitchell et al.*, 2000]. The three dimensional, three-species, MHD model of *Liu et al.* [2002] is consistent with these observations.

The effective night on Venus lasts about 58 Earth days (solar rotation period is 117 earth days), during which time the ionosphere could be expected to disappear, because no new photoions and electrons are created to replace the ones lost by recombination. Therefore it was very surprising, at first, when Mariner 5 found a significant nightside ionosphere at Venus [*Kliore et al.*, 1967]. Subsequently, extensive measurements have confirmed the presence of a significant but highly variable nightside ionosphere. Plasma flows from the dayside [*Miller and Whitten*, 1991], along with impact ionization caused by precipitating electrons, are responsible for the observed nighttime densities; their relative importance for a given ion species depends on the solar wind pressure and solar conditions [*Cravens et al.*,

1983; *Dobe et al.,* 1995] (e.g., during solar cycle maximum conditions day to night transport is the main source of plasma for the nightside ionosphere). The nightside electron densities are extremely variable both with time and location. Order of magnitude changes have been seen by the instruments on PVO along a single path and/or between subsequent passes through the ionosphere. Terms such as disappearing ionospheres, ionospheric holes, tail rays, troughs, plasma clouds, etc. have been introduced to classify and attempt to explain the apparently different situations encountered [*Brace and Kliore,* 1991]. As an example, Figure 5 shows two ionospheric holes observed during orbit 530 of PVO [*Brace et al.,* 1982]. Strong radial magnetic fields were found to be present in these holes, thus allowing easy escape of the ionospheric thermal plasma into the tail, presumably causing the sharp drops in density.

The only information on the nightside ionosphere of Mars is that obtained by radio occultation measurements with the Mars 4 and 5 and Viking 1 and 2 spacecraft [*Savich et al.,* 1979; *Zhang et al.,* 1990]. The observed ionospheric peak densities were highly variable; at times none were detected. The mean peak density was about $5x10^3$ cm^{-3}, with a peak altitude of about 160 km. The rotation period of Mars is relatively small, close to that of the Earth, therefore the observed small densities do not seem to be especially difficult to account for. There are some indirect indications that electron impact ionization may be an important nighttime ionization source, as well as day to night transport processes, in a manner similar to the Venus conditions [*Haider et al.,* 1992].

The observed ion and electron temperatures at both Venus and Mars are significantly higher than the neutral gas temperature and cannot be explained in terms of EUV heating and classical thermal conduction [*Cravens et al.,* 1980; *Chen et al.,* 1978] as is the case for the midlatitude terrestrial ionosphere. The two suggestions which lead to model temperature values consistent with the observations are 1) an ad hoc energy input at the top of the ionosphere and/or 2) reduced thermal conductivities [*Fox and Kliore,* 1997]. The latter reduces downward heat flow and the eventual energy loss to the neutrals at the lower altitudes. There are reasons to believe that both mechanisms are present, but insufficient information to establish which is dominant, when, and why. Measurements by the plasma wave instrument carried by PVO have shown that there is significant wave activity at and above the ionopause. Different estimates of the heat input into the ionosphere, from these waves, all lead to values of the order of 10^{10} eV cm^{-2}, which is about the magnitude necessary to explain the observed plasma temperatures [*Shapiro et al.,* 1995]. There have also been suggestions that the shocked solar wind electrons from the magnetosheath and tail regions will

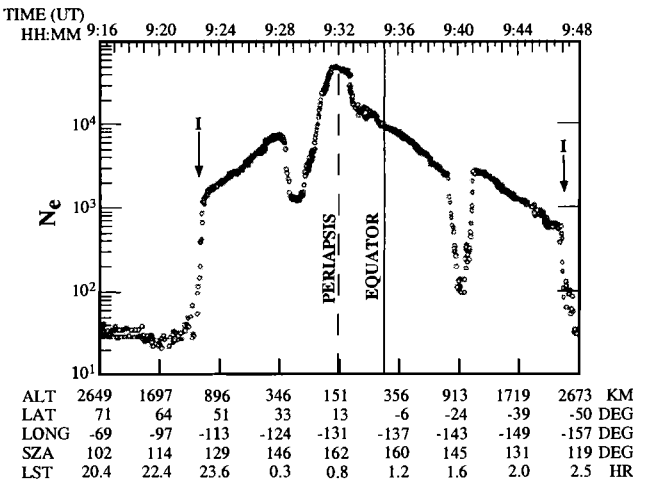

Figure 5. Ionospheric holes at Venus as observed by the Langmuir Probe on the Pioneer Venus Orbiter (from Brace et al., 1982).

move along draped field lines into the ionosphere, when it is magnetized, and provide the energy needed to explain the observed temperatures [*Gan et al.,* 1990]. A number of studies have also shown that a reduction in the thermal conductivity from its classical value can be justified, because of the presence of fluctuating small magnetic fields in the ionosphere [*Cravens et al.,* 1980].

Figure 6 shows the results of a one-dimensional model calculation for Venus, which used classical electron and ion conductivities and topside electron and ion heat flows of $3x10^{10}$ and $5x10^7$ eV cm^{-2}, respectively, and which resulted in temperatures reasonably close to the observed values. On the other hand, Figure 7 shows the results of a one-dimensional model calculation for Venus which assumes no topside heat inflow, but incorporates reduced thermal conductivities resulting from magnetic field fluctuations; this assumption also leads to calculated values consistent with the measured ones. The parameter λ, indicated in Figure 7, is the correlation length of the assumed fluctuations. It can be noted that while the electrons are strongly affected by these fluctuations the effect is small on the ions; this is the result of the significant difference in the respective gyroradii. The results of similar calculations for Mars [*Choi et al.,* 1998] are shown in Figure 8. The mechanism(s) controlling the temperatures on the nightside are even less understood. It is certainly reasonable to assume that energy is transported from the dayside to the nightside by heat flow and advection and that heat input from above or from the tail is also present. However, the detailed and/or specific roles of these different potential energy sources have not been elucidated.

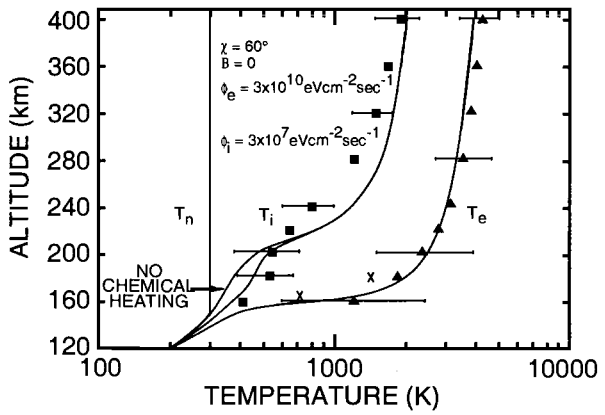

Figure 6. Electron and ion temperatures from a one-dimensional model of the ionosphere of Venus for heat flux inputs as shown and for no magnetic field effects on the thermal conductivities (from Cravens et al., 1980).

A recent detailed review [*Fox and Kliore,* 1997] concluded that there is no clear and unambiguous understanding of the mechanism(s) controlling the energetics of the ionosphere of Venus and Mars at this time, and further progress is unlikely until more direct information becomes available. It is likely that both processes mentioned above do play a role, but whether one or the other dominates at times or even whether other processes, not yet considered, are important, is not known.

3. THE OUTER PLANETS

The only direct ionospheric data available from the outer planets are electron density altitude profiles obtained from radio occultation measurements from the Pioneer 10 and 11, Voyager 1 and 2 and Galileo spacecraft. Some optical information, mainly from remote sensing observations (in the visible, infrared, ultraviolet, and x-ray parts of the electromagnetic spectrum), also provides some insight into certain ionospheric processes. In particular, infrared observations [*Drossart et al.,* 1989] have determined column densities of the important ion species H_3^+. The upper atmospheres of the major planets consist mainly of molecular hydrogen [*Atreya,* 1986; also see *Gladstone and Yelle,* this volume]; thus the major primary ion, which is formed by either photoionization or particle impact, is H_2^+. In the low and midlatitude regions electron-ion pair production is due mainly to solar EUV radiation, while at higher latitudes impact ionization by precipitating particles is believed to be dominant [see *Galand and Chakrabarti,* this volume]. The actual equilibrium concentration of H_2^+ is very small, because H_2^+ undergoes a rapid charge transfer reaction with H_2, producing H_3^+. The photoionization/photodissociation sources can be represented by:

$$H_2 + h\nu \rightarrow H + H \quad (6)$$

$$H_2^+ + e \quad (7)$$

$$H^+ + H + e \quad (8)$$

The resulting neutral atomic hydrogen can also be ionized:

$$H + h\nu \rightarrow H^+ + e \quad (9)$$

The analogous dissociation and/or ionization sources for particle impact rather than for photons exist, but for the sake of brevity are not shown here. At high altitudes where hydrogen atoms are the dominant neutral gas species, the main chemical loss process for H^+ is thought to be radiative recombination, which is a very slow ($\sim 10^{-12}$ cm^{-3} s^{-1}) process. It was suggested some time ago that H^+ could react with H_2 molecules which have been excited to a vibrational state v>4 [*McElroy,* 1973]. The vibrational distribution of H_2 has not been measured, although theoretical calculations for Jupiter [*Cravens,* 1987] indicate that the vibrational temperature is significantly elevated, particularly in the auroral regions.

H_2^+ is very rapidly transformed to H_3^+, especially at the lower altitudes where H_2 is dominant:

$$H_2^+ + H_2 \rightarrow H_3^+ + H \quad [k = 2.0x10^{-9}\ cm^3\ s^{-1}] \quad (10)$$

H_3^+ typically undergoes dissociative recombination:

$$H_3^+ + e \rightarrow H_2 + H \quad [\alpha = 4.6x10^{-6}\ T_e^{-0.65}\ cm^3\ s^{-1}] \quad (11)$$

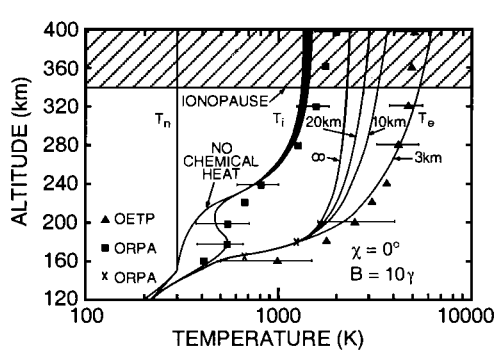

Figure 7. Electron and ion temperatures from a one-dimensional model of the ionosphere of Venus for thermal conductivities reduced by the effects of fluctuating magnetic fields (from Cravens et al., 1980).

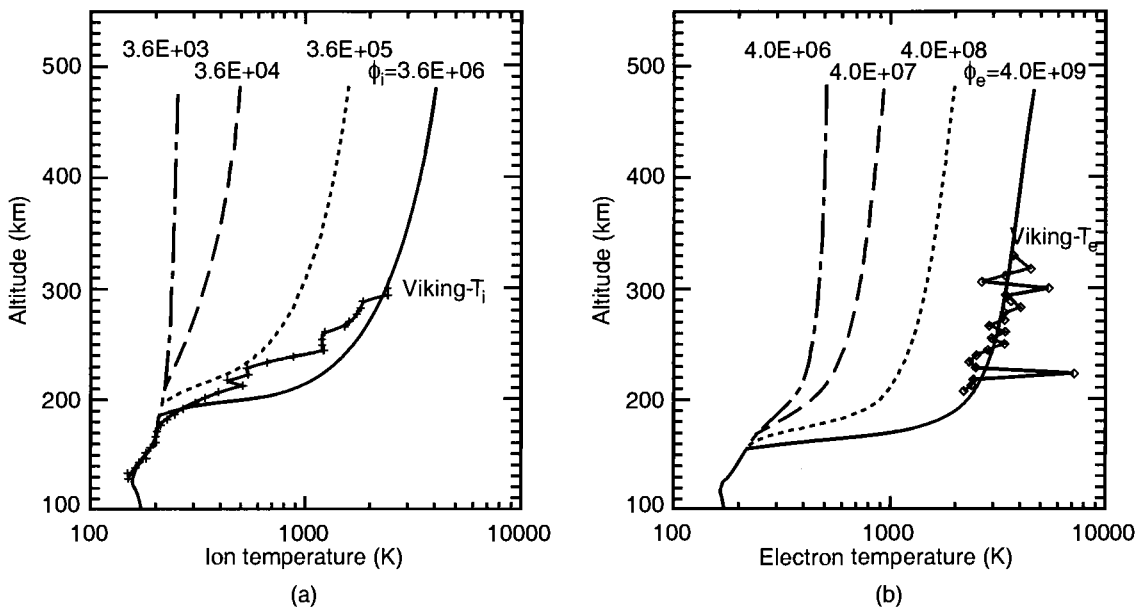

Figure 8. Measured and calculated ionospheric temperatures at Mars (from Choi et al., 1998).

Significant uncertainties have been associated with the dissociative recombination rate of H_3^+. However, recent measurements have shown that the rate is rapid even if the ion is in its lowest vibrational state [*Sundstrom et al.*, 1994; also see *Huestis and Anicich*, this volume].

Hydrocarbon ions are important in the lower ionosphere of Jupiter due to the increased abundance of methane and other neutral hydrocarbons. Recent calculations indicate that direct photoionization of hydrocarbon molecules can lead to a relatively thin, about 50 km broad, hydrocarbon ion layer at altitudes around 300 km [*Kim and Fox,* 1991]. Long-lived metallic ions are also thought to exist in the lower ionospheres of all the outer planets and might be responsible for the layered appearance in the observed electron density profiles [see *Grebowsky, Moses and Pesnell*, this volume].

We now review some specific ionospheric observations for the outer planets. The Jovian electron density profiles measured by the Voyager spacecraft, and more recently by the Galileo spacecraft, using the radio occultation technique, indicated the presence of an ionosphere with peak densities between 10^4 and 10^5 cm^{-3}, as indicated in Figure 9 [*Hinson et al.*, 1997]. These electron density profiles seem to fall in two general classes. In one, the peak electron density is located at an altitude around 2000 km, and in the other the electron density peak is near 1000 km. The two groups also exhibit different topside scale heights, with the high altitude peaks associated with the larger scale heights. There appears to be no clear latitudinal nor temporal association with these separate groups of profiles. The different peaks may be the result of a combination of different major ionizing sources (EUV versus soft x-ray versus particle impact), and/or different ion chemistries. However, the variability of the location and magnitude of the ionospheric peak cannot be modeled with purely photochemical models. Dynamical effects are believed to play a key role in controlling this ionosphere, although our understanding of the dynamics remains virtually nonexistent.

A number of different models of the ionosphere have been developed since the Voyager encounters [*Majeed and McConnell,* 1991]. The limited observational data base, combined with the large uncertainties associated with such important parameters as the relevant reaction rates, drift velocities, degree of vibrational excitation and the magnitude and nature of the precipitating particles, means that there are too many free parameters to allow a unique and definitive model of the ionosphere to be developed.

Electron density profiles of the ionosphere of Saturn were obtained by radio occultation measurements made from Pioneer 11/Saturn and Voyagers 1 and 2 spacecraft; the Voyager 2 results are shown in Figure 10 [*Waite and Cravens,* 1987]. The low frequency cut-off of the Saturn electrostatic discharges (SED), which originate in the equatorial atmosphere from lightning, indicated significant and rapid diurnal variation of the peak electron densities.

The neutral atmosphere of Saturn is very similar to that of Jupiter, therefore the ion chemistry was expected to be

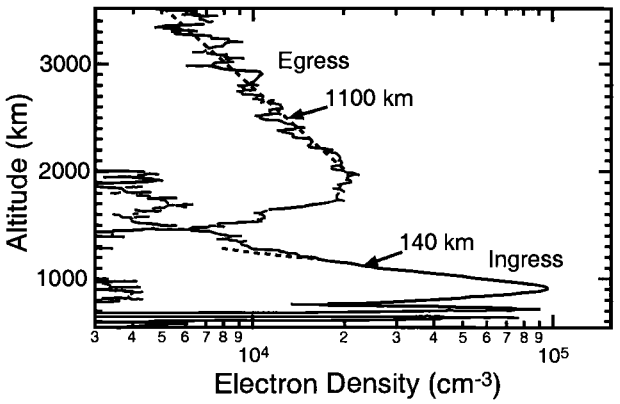

Figure 9. Electron density altitude profiles measured at Jupiter by the Galileo radio occultation experiment (from Hinson et al., 1997).

also effectively the same. The main difficulties with the "Jupiter like" ionospheric models of Saturn are that: (1) the calculated ionospheric density at the apparent main peak is about an order of magnitude larger than the observed one and (2) the rapid diurnal variations cannot be reproduced by any of the current models [*Moses and Bass,* 2000; *Waite and Cravens,* 1987; *Majeed and McConnell,* 1996].

During the last decade a number of suggestions have been put forward for how to lower the modeled electron densities to the observed values. The most reasonable and successful current models are based on the suggestion/assumption that water from the rings is being transported into Saturn's upper atmosphere, which then modifies the chemistry of the ionosphere. The presence of H_2O results in the following catalytic process:

$$H^+ + H_2O \rightarrow H_2O^+ + H \quad [k = 8.2 \times 10^{-9}\ cm^3\ s^{-1}] \qquad (12)$$

$$H_2O^+ + H_2O \rightarrow H_3O^+ + OH \quad [k = 1.85 \times 10^{-9}\ cm^3\ s^{-1}] \qquad (13)$$

$$H_3O^+ + e \rightarrow H_2O + H \qquad (14)$$

$$\rightarrow OH + H + H$$

$$\rightarrow OH + H_2$$

$$[\alpha = 1.57 \times 10^{-5}\,(300/T_e)^{0.569}\ cm^3\ s^{-1} \text{ for } T_e < 800\ K]$$

A block diagram of the chemistry scheme, involving water, is shown in Figure 11. The main ion species in models using this chemical scheme are H^+, H_3^+ and H_3O^+. It was shown [*Waite and Cravens,* 1987] that a downward flux of water from the rings into the atmosphere, of the order of a few times 10^7 cm^{-2} s^{-1} and a small (~ 0.5 ergs cm^{-2} s^{-1}) influx of low energy electrons, leads to electron density values consistent with the observed, near terminator densities, as indicated in Figure 8. Again, in the lower ionosphere of Saturn, metallic ions and hydrocarbon ions are thought to also be important [*Moses and Bass,* 2000; see also *Grebowsky, Moses and Pesnell,* this volume].

The only information concerning the ionospheres of Uranus and Neptune comes from the Voyager 2 radio occultation measurements. The ionospheric densities measured by radio occultation at the two planets are shown in Figures 12 and 13 respectively [*Lindal et al.*, 1987; *Tyler et al.,* 1989]. The observed dayside UV emissions [*Broadfoot et al.,* 1986] from Jupiter, Saturn and Uranus led to suggestions that a column integrated energy flux of about 0.1–0.3 erg cm^{-2} s^{-1}, due to soft (<15eV) electrons, may be present; this has been referred to as electroglow. However, alternate explanations of the observed emissions have also been put forward [*Yelle et al.,* 1987; *Liu and Dalgarno,* 1996]. A number of simple one-dimensional model calculations of the ionospheres of Uranus and Neptune have been published, some of which included ionization caused by postulated electroglow electrons [*Waite and Cravens,* 1987]. The calculated peak electron densities found by these models all exceeded the measured values and this has been interpreted as an indication of a significant influx of H_2O molecules, similar to the situation at Saturn.

The radio occultation data from all the giant planets (Jupiter, Saturn, Uranus and Neptune) indicate the presence of enhanced electron density layers in the lower ionosphere. The electrical conductivity associated with these lower ionosphere electron density layers is potentially

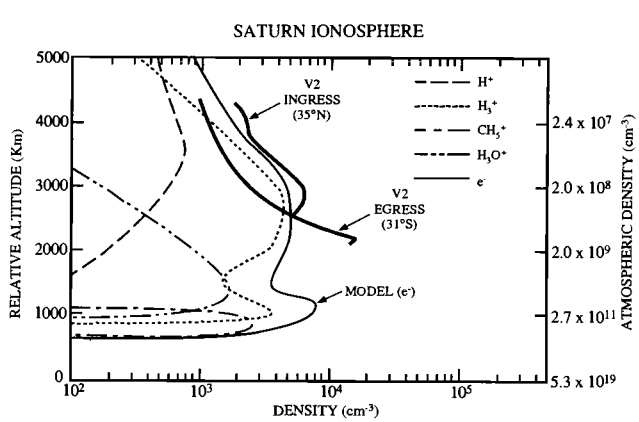

Figure 10. Electron density altitude profiles measured at Saturn by the Pioneer and Voyager radio occultation experiment (from Waite and Cravens, 1987).

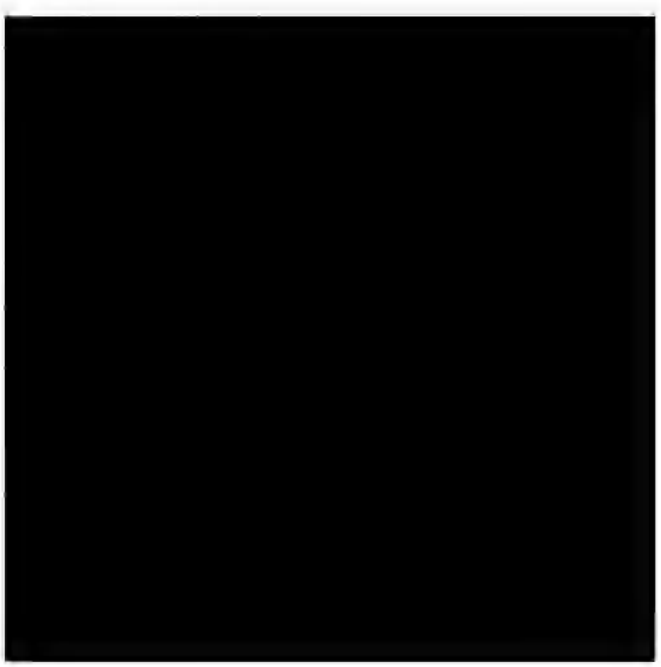

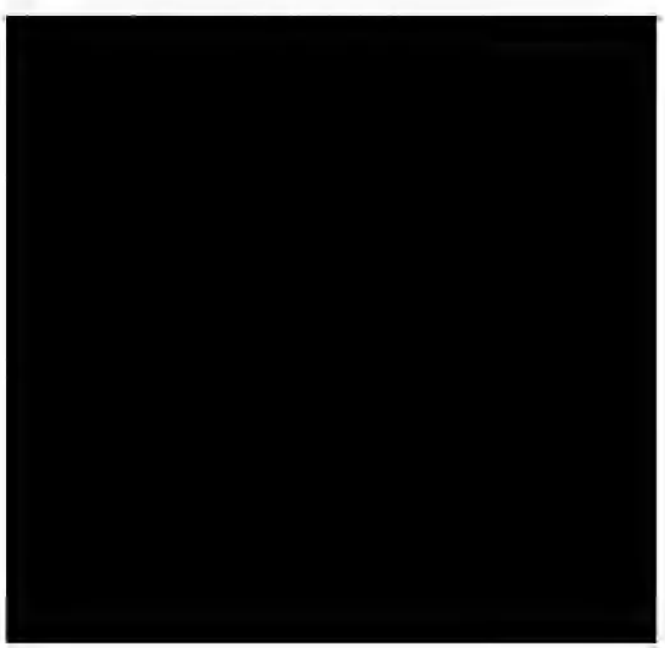

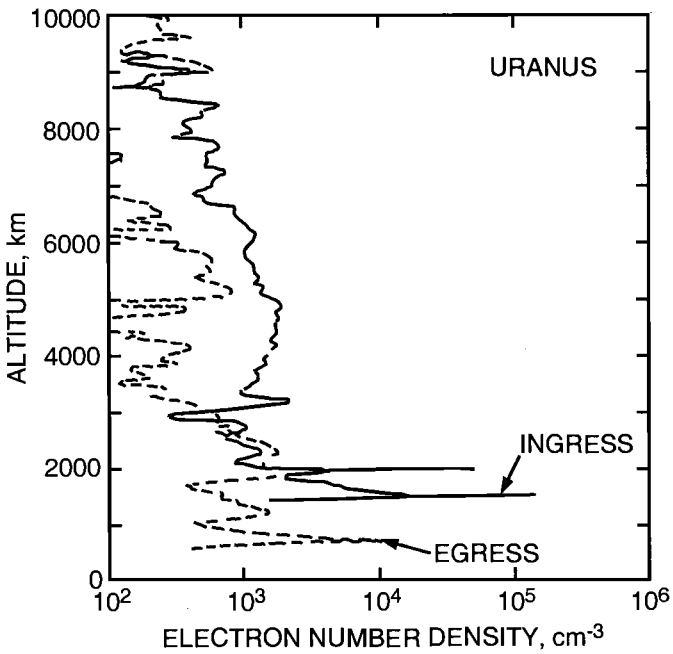

Figure 12. Electron density altitude profiles measured at Uranus by the Voyager radio occultation experiment (from Lindal et al., 1987).

atmospheric densities. This picture could be considerably modified if a significant amount of a non-condensing gas, such as O_2, is present. Another outstanding issue is the source of atmospheric Na (sodium) species, including NaO_2 and Na_2O. However, these species have lower saturation vapor pressures than SO_2, and do not sublime easily. Yet Na^+ may be a dominant ion at Io. All the Galilean satellites interact strongly with the magnetosphere of Jupiter, which certainly influences the nature and variability of the respective ionospheres. The situation is further complicated in the case of Io, where the atmosphere and ionosphere are very likely to be highly variable, both spatially and temporally, given the nature of the volcanic sources. Figure 15 shows the results of a specific model for Io's ionosphere [*Summers and Strobel*, 1996], which leads to a reasonable agreement with the Pioneer 10 "dayside" profile.

Titan, the largest satellite of Saturn, is surrounded by a substantial atmosphere and therefore one expects a correspondingly significant ionosphere. To date the only opportunity for a radio occultation measurement of this ionosphere occurred when Voyager 1 was occulted by Titan. The initial analysis of those data could only provide upper limits of $3x10^3$ cm^{-3} and $5x10^3$ cm^{-3} on the peak electron densities at the evening and morning terminators, respectively [*Lindal et al.*, 1983]. However, a careful reanalysis of the data [*Bird et al.*, 1997] indicates the presence of an electron density peak of about $2.7x10^3$ cm^{-3} at around 1190 km for a solar zenith angle of near 90°.

Titan orbits Saturn at a distance of about 20 R_S, where R_S is the radius of Saturn. The mean magnetopause location is around 24 R_S, thus Titan usually resides inside the magnetosphere, though at times it may be outside the magnetosphere. The illumination condition with respect to the ramside of Titan varies from fully sunlit to fully dark as it completes an orbit around Saturn. Thus, the various ionization sources responsible for the formation of Titan's ionosphere certainly include a mixture of solar extreme ultraviolet radiation, photoelectrons produced by this radiation and magnetospheric or shocked solar wind electrons. Calculations indicate that photoionization is the main source for the dayside ionosphere, followed by photoelectron impact and finally magnetospheric electron sources [*Gan et al.*, 1992; *Keller et al.*, 1992; *Galand et al.*, 1999]. Of course magnetospheric electrons must dominate in the nightside ionosphere.

A variety of one-dimensional calculations have been made [*Keller et al.*, 1992; *Fox and Yelle*, 1997; *Keller et al.*, 1998] and they all lead to electron density values consistent with the Voyager results. The most important initial ion is N_2^+ for altitudes up to about 1800 km and CH_4^+ is the major ion produced at the higher altitudes; N^+ and CH_3^+ are also important initial ion species. These initial ions quickly undergo a number of ion-neutral reactions leading to $HCNH^+$, which then will undergo either disssociative recombination or proton transfer, leading to more complex hydrocarbon ions [*Fox and Yelle*, 1997; *Keller et al.*, 1998]. Figure 16 shows the results of a representative set of calculations [*Fox and Yelle*, 1997] and

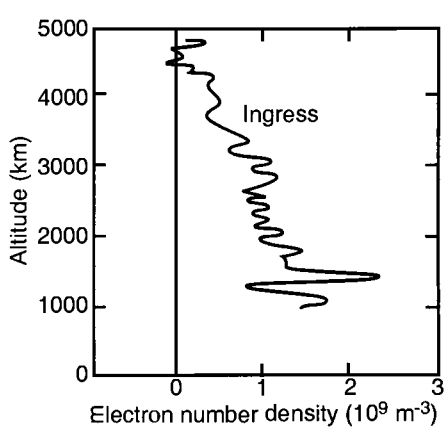

Figure 13. Electron density altitude profiles measured at Neptune by theVoyager radio occultation experiment (from Tyler et al., 1989).

Figure 17 is a chemical diagram showing the chemical complexity of this ionosphere. A recent paper looked at the galactic cosmic ray induced ionosphere of Titan; it predicts peak electron densities of about $2x10^3$ cm^{-3} at an altitude near 100 km. The predicted major ion is $C_7H_x^+$ [*Molina-Cuberos et al.*, 1999].

The transition from chemical to transport control in the ionosphere of Titan has been explored in a number of studies. Simple time constant considerations, as well as more detailed model solutions, have indicated that the transition from chemical to diffusive control takes place in the altitude region around 1500–2000 km. The plasma velocity (~120 km/s) of the external magnetospheric plasma impinging on Titan at the time of the Voyager encounter was subsonic (sound speed ~210 km/s) and superalfvenic (Alfven speed ~64 km/s), therefore no bow shock should have formed and none was observed. The plasma appeared to gradually slow as Voyager approached Titan's exosphere. Various models were able to reproduce the observed plasma behavior in the magnetosphere outside Titan's ionosphere. One important physical process was shown to be massloading. The magnetic field strength just upstream of Titan's ionosphere is enhanced in a magnetic barrier (similar to that near Venus and Mars). The magnetic field also drapes around Titan forming a magnetic tail and a plasma wake [see *Combi, Gombosi and Kabin*, this volume]. Just as at Venus and Mars, the magnetic pressure associated with the barrier is expected to be the dominant source of pressure against the ionosphere. Using reasonable magnetospheric parameters, it was shown [*Keller et al.*, 1994] that the total incident magnetospheric pressure is about $1.6x10^{-9}$ dynes cm^{-2}. This pressure corresponds to a field strength of about 20 nT, much of which is convected into the upper ram ionosphere, resulting in near horizontal magnetic fields. Using a peak electron density of $5x10^3$ cm^{-3} means that the plasma temperature needs to be greater than 700K to allow the ionosphere to hold off the external plasma (if it indeed does — in situ measurements such as those that will be made by the Cassini Orbiter will hopefully shed light on these issues). Multi-dimensional and multi-species MHD model calculations have looked at the interaction of the ionosphere with Saturn's magnetosphere. Below an altitude of about 1500–2000 km the flow appears to be slow enough that the plasma could be considered to be ionospheric in nature, whereas the plasma distribution at higher altitudes is likely to be controlled by the rapid flow associated with Saturn's magnetosphere [*Cravens et al.*, 1998; *Nagy et al.*, 2001].

The question of plasma temperatures in the ionosphere of Titan has also been studied. No observational constraints concerning these parameters exist; therefore, at best one can set some range of reasonable values through model calculations. It is expected that the temperatures on the ramside will be very different from those on the wakeside of Titan. This comes about because the draped magnetic

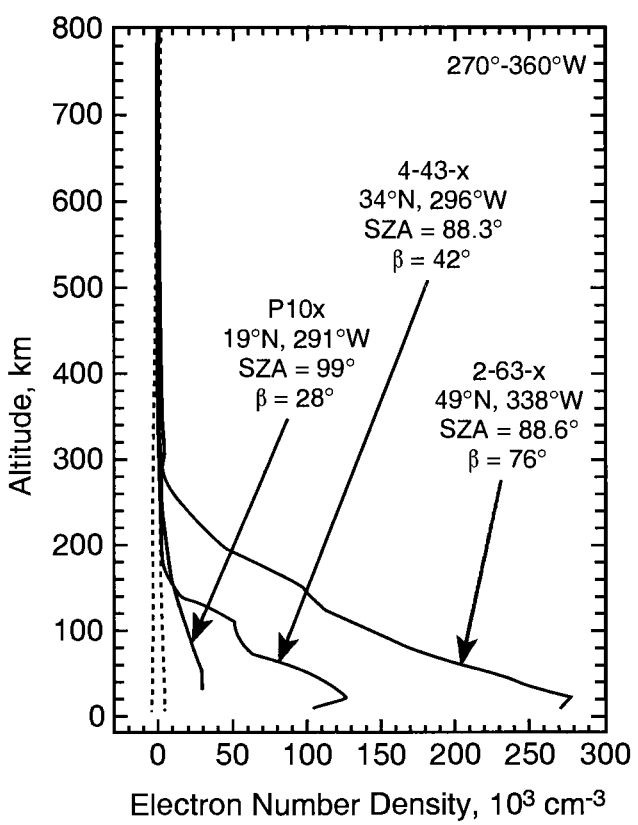

Figure 14. Electron density altitude profiles measured at Io by the Galileo radio occultation experiment (from Hinson et al., 1998).

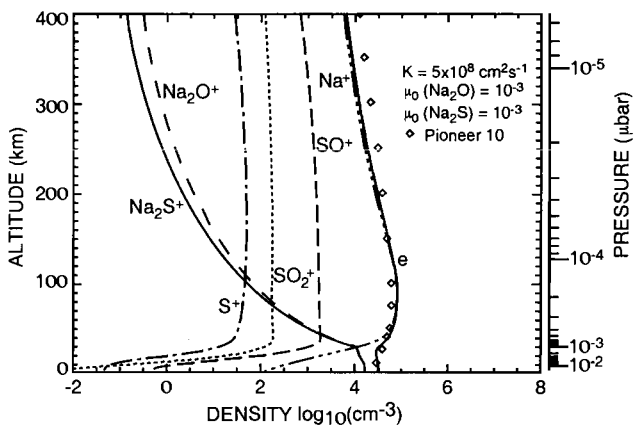

Figure 15. Density profiles from an ionospheric model of Io (from Summers and Strobel, 1996).

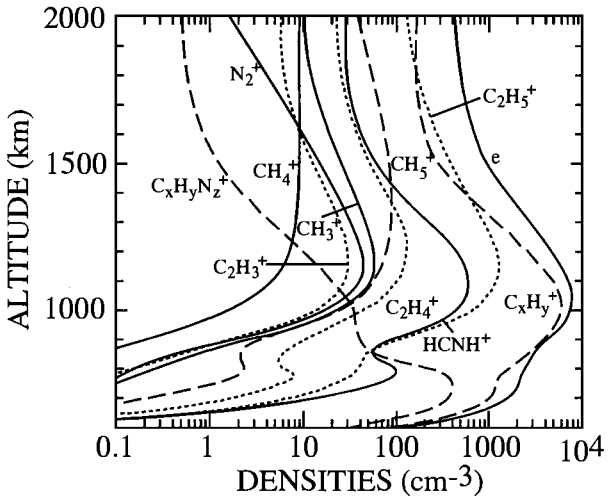

Figure 16. Ion density profiles from a model of Titan's ionosphere (from Fox and Yelle, 1997).

field on the ramside is expected to be nearly horizontal, thus reducing vertical heat flow, whereas the field on the wakeside is expected to be nearly radial. Representative results [*Roboz and Nagy*, 1994] for the ram and wakeside are shown in Figure 18.

A well established ionosphere has also been observed at Triton, the major satellite of Neptune, by the Voyager 2 radio occultation measurements [*Tyler et al.*, 1989], as shown in Figure 19. These Voyager observations prompted the development of a number of ionospheric models. All these models assumed, consistent with the airglow observations [*Broadfoot et al.*, 1989], that the main sources of ionospheric plasma are photoionization by solar EUV radiation and magnetospheric electron impact ionization. A one-dimensional model calculation [*Majeed et al.*, 1990], which solved the coupled continuity and momentum equations for the more important neutral and ion species, clearly demonstrated that Triton's ionosphere cannot be understood by considering nitrogen chemistry only; CH_4, H and H_2 must also be considered. This model led to the ionosphere shown in Figure 19, which fits the Voyager results well, given an assumed column impact ionization source of $3x10^8$ ions cm^{-2} s^{-1}. It is important to note that even though N_2 is the major neutral species, N^+ is the predicted major ion. It was pointed out that at the time of the radio occultation measurements, Triton was near the magnetic equator and magnetospheric electrons were the dominant ionization source. If this source were not present, the electron densities would decrease significantly within a few hours due to ion molecule reactions. The question of why Triton's ionosphere is so much more robust than that of Titan has also been discussed [*Strobel et al.*, 1990]. It was pointed out that in order to understand the difference one needs to compare the competing upward fluxes of CH_4 and H_2 with the column integrated ionization rates. The ion production rate for Triton is twice the sum of the neutral fluxes, whereas at Titan the ratio is only about 0.1. This implies a relatively more rapid dissociative recombination rate of the molecular ions at Titan, as compared to Triton, resulting in significantly lower equilibrium electron densities [see *Müller-Wodarg*, this volume].

The predominance of water vapor in the atmospheres of active comets, such as P/Halley, means that the following photochemical processes are believed to control their ionospheric behavior:

$$H_2O + h\nu \rightarrow H_2O^+ + e \quad (15)$$

$$\rightarrow H^+ + OH + e \quad (16)$$

$$\rightarrow OH^+ + H + e \quad (17)$$

$$H_2O^+ + H_2O \rightarrow H_3O^+ + OH \quad (18)$$

$$H_3O^+ + e \rightarrow OH + H_2$$

$$\rightarrow OH + H + H \quad (19)$$

$$\rightarrow H_2O + H$$

Note that equations (18) and (19) are the same as (13) and (14), which were introduced in the discussion of the role of inflowing water vapor to Saturn's ionosphere (see also Figure 11). The very rapid rate at which H_2O^+ is transformed into H_3O^+ means that in comets which have water dominated atmospheres, such as P/Halley, H_3O^+ is the dominant ionospheric constituent. NH_4^+ ion-neutral chemical channels also have some importance, due to the presence of ammonia among the neutral volatiles at comets; other chemical families (CO_2, CH_4, NH_3, etc.)are also present in the ionospheric chemistry.

The Giotto spacecraft carried two spectrometers which were capable of measuring the ion composition in P/Halley's ionosphere. The neutral spectrometer, operating in its ion mode, found that the H_3O^+ to H_2O^+ ratio increases with decreasing distance from the nucleus and it exceeds unity at distances less than about 20,000 km [*Krankowsky et al.*, 1986]. The variations in ion densities measured by the ion mass spectrometer carried aboard the Giotto spacecraft as it flew by comet P/Halley [*Balsiger et al.*, 1986] are shown in Figure 20. These are in qualitative agreement with model calculations of the ion composition and structure [*Korosmezey et al.*, 1987]. Except for some structure in the immediate vicinity of the boundary of the

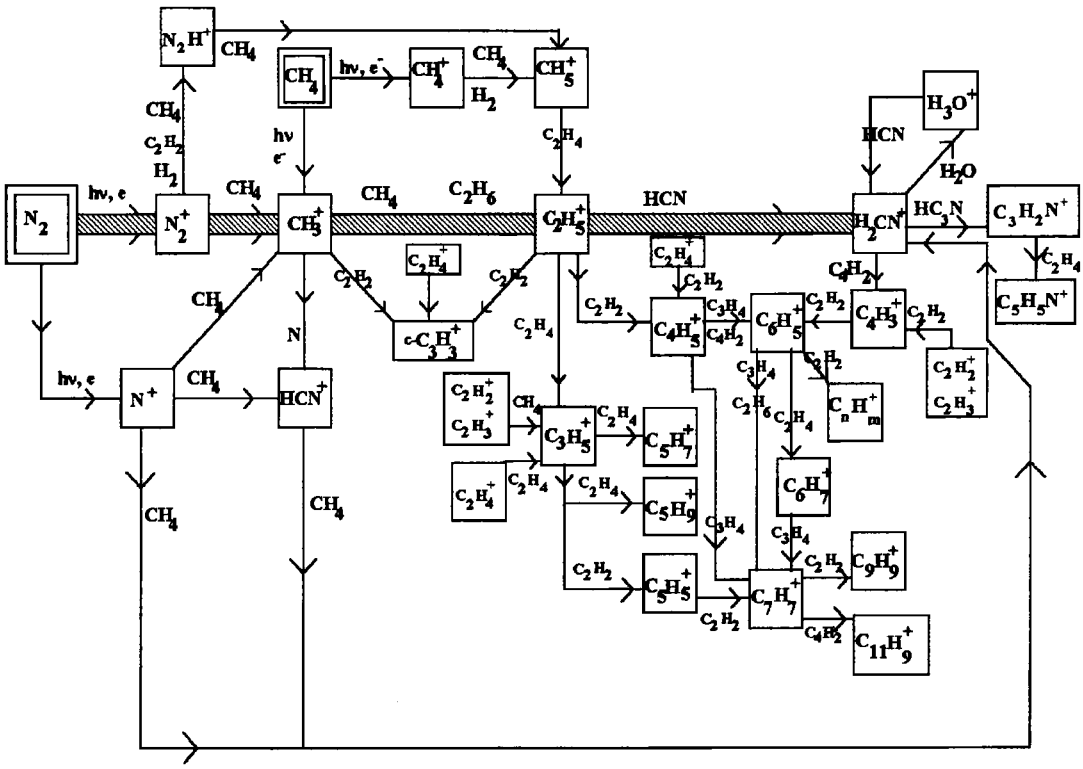

Figure 17. Block chemical scheme for the ionosphere of Titan (from Keller et al., 1998).

diamagnetic cavity, the electron density was observed to vary approximately as the inverse of the radial distance from the nucleus, out to a distance of about 10,000 km [*Balsiger et al*, 1986; *Krankowsky et al.*, 1986]. Even simple photochemical models balancing ion production and dissociative recombination are able to reproduce this simple 1/r electron density dependence [*Mendis et al.*, 1985; *Korosmezey et al.*, 1987].

The plasma measured by instruments on the Giotto and Vega spacecraft at radial distances beyond about 10^4 km and out to several times 10^4 km was clearly dense and cold enough to be called ionospheric, yet displayed characteristics indicating that it was being controlled by transport/dynamics. This dynamics is determined largely by the solar wind interaction with the comet [*Cravens*, 1991; also see *Combi, Gombosi and Kabin*, this volume]. A main feature of this interaction is the formation of a magnetic barrier and a draped magnetic tail. Giotto magnetometer data [*Neubauer et al.*, 1986] showed that this barrier is much broader than that found at Venus and Mars. The region around the nucleus, out to a radial distance of about 5000 km, was observed to be field-free [*Neubauer et al.*, 1986] and is called the diamagnetic cavity. The electron density in the immediate vicinity of the boundary of this cavity was observed [*Goldstein et al.*, 1989] to jump by a factor of 3 or so above the underlying ionospheric density, which varies as 1/r, as mentioned earlier. Plasma flows outward from the nucleus in the diamagnetic cavity and forms a layer of enhanced density when it encounters the

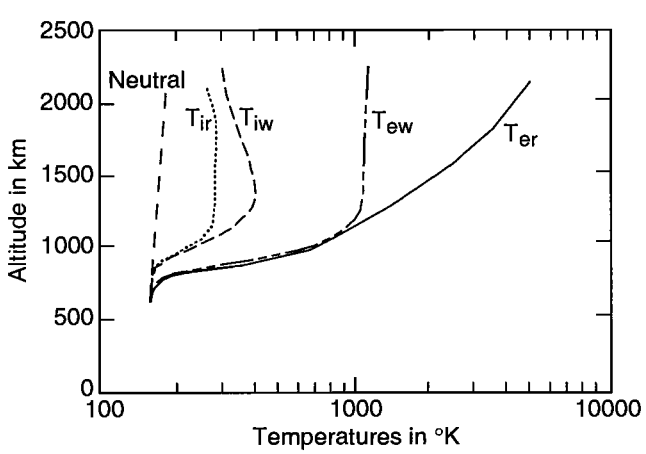

Figure 18. Electron temperatures from a model of Titan's ionosphere (from Roboz and Nagy, 1994).

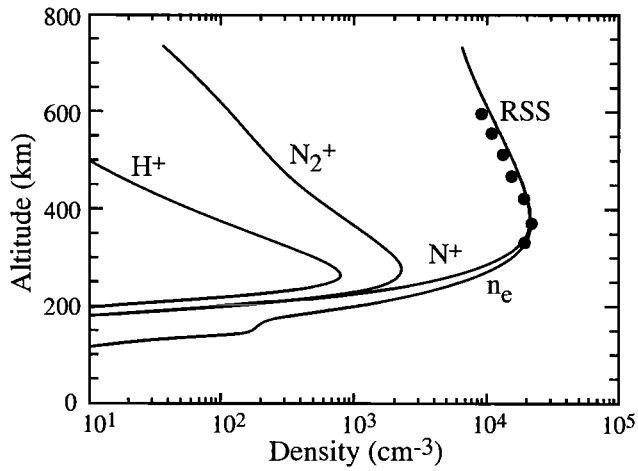

Figure 19. Electron density altitude profiles measured at Triton by the Voyager radio occultation experiment (from Tyler et al., 1989).

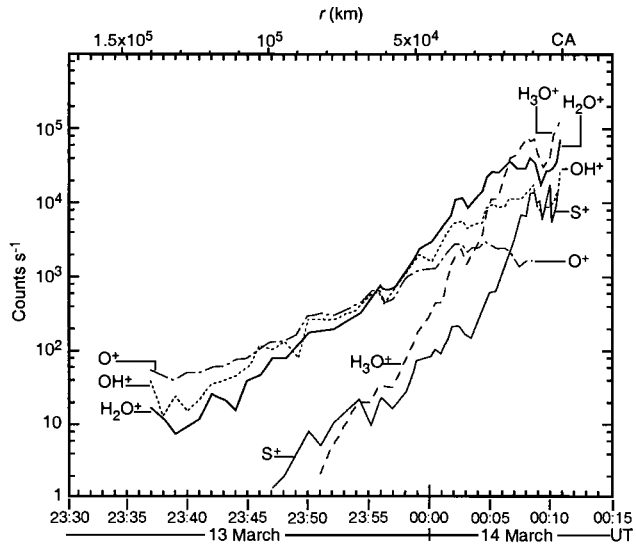

Figure 20. Ion density profiles measured by the Giotto ion mass spectrometer at comet P/Halley (from Balsiger et al., 1986).

magnetic field outside the cavity [*Cravens*, 1989; *Puhl-Quinn and Cravens*, 1995]. The excess plasma in this layer recombines dissociatively.

5. CONCLUSION

In this chapter, we have described ionospheres with very different densities, temperatures, ion species, and spatial extent. It seems appropriate to end this chapter with another quotation; this one comes from an IUGG Report [*Nagy et al.*, 1995] which states:

"The very basic processes such as ionization, chemical transformations and diffusive as well as convective transport are analogous in all ionospheres; the major differences are the result of factors such as different neutral atmospheres, intrinsic magnetic field strength, distance from the Sun, etc. Improving our understanding of any of the ionospheres in our solar system helps in elucidating the controlling physical and chemical processes in all of them."

REFERENCES

Acuna, M. H., et al., Magnetic field and plasma observations at Mars: Initial results of the Mars Global Surveyor mission, *Science, 279*, 1676, 1998.

Anicich, V. G., Evaluated bimolecular ion-molecule gas phase kinetics of positive ions for use in modeling planetary atmospheres, cometary comae, and interstellar clouds, *J. Phys. Chem. Ref. Data, 22*, 1469, 1993.

Atreya, S. K., *Atmospheres and ionospheres of the outer planets and satellites*, Springer-Verlag, Berlin, 1986.

Atreya, S. K., T. M. Donahue and M. B. McElroy, Jupiter's ionosphere: Prospects for Pioneer 10, *Science, 184*, 154, 1974.

Bagenal, F., T. E. Cravens, J. G. Luhmann, R. L. McNutt and A. F. Chang, Pluto's interaction with the Solar Wind, in *Pluto*, 523-555, edited by S. A. Stern and D. J. Tholen, U. of Arizona Press, Tucson, 1997.

Balsiger, H. et al., Ion composition and dynamics at Comet Halley, *Nature, 321*, 330, 1986.

Bird, M. K., R. Dutta-Roy, S. W. Asmar and T. A. Rebold, Detection of Titan's ionosphere from Voyager 1 radio occultation observations, *Icarus, 130*, 426, 1997.

Brace, L. H. and A. J. Kliore, The structure of the Venus ionosphere, *Space Sci. Rev., 55*, 81, 1991.

Brace, L. H., R. F. Theis, H. G. Mayr, S. A. Curtis and J. G. Luhmann, Holes in the nightside ionosphere of Venus, *J. Geophys. Res., 87*, 199, 1982.

Brace, L. H., H. A. Taylor, A. J. Kliore, W. C. Knudsen and A. F. Nagy, The ionosphere of Venus: Observations and their interpretation, in *Venus*, edited by D. M. Hunten, L. Colin, T. M. Donahue and V. I. Moroz, The University of Arizona Press, Tucson, 1983.

Brecht, S. H., Magnetic asymmetries of unmagnetized planets, *Geophys. Res. Lett., 17*, 1243, 1990.

Broadfoot, A. L., et al., Ultraviolet spectrometer observations of Uranus, *Science, 233*, 74, 1986.

Broadfoot, A. L., et al., Ultraviolet spectrometer observations of Neptune and Triton, *Science 246*, 1459, 1989.

Chen, R. H., T. E. Cravens, and A. F. Nagy, The Martian ionosphere in light of the Viking observations, *J. Geophys. Res., 83*, 3871, 1978.

Choi, Y. W. J. Kim, W. Min, A. F. Nagy and K. I. Oyama, Effect of the magnetic field on the energetics of the Mars ionosphere *Geophys. Res. Lett., 25*, 2753, 1998.

Cloutier, P. A., et al., Venus-like interaction of the solar wind with Mars, *Geophys. Res. Lett., 26*, 2685, 1999.

Cravens, T. E., Vibrationally excited molecular hydrogen in the upper atmosphere of Jupiter, *J. Geophys. Res., 92,* 11,083, 1987.

Cravens, T. E., A magnetohydrodynamical model of the inner coma of comet Halley, *J. Geophys. Res., 94,* 15025, 1989.

Cravens, T. E., Plasma processes in the inner coma, in *Comets in the Post-Halley Era*, vol. 2, p. 1211, Kluwer Acad., Norwell, Mass., 1991.

Cravens, T. E., et al., Model calculations of the dayside ionosphere of Venus: Energetics, *J. Geophys. Res., 85*, 7778, 1980.

Cravens, T. E., S. L. Crawford, A. F. Nagy, and T. I. Gombosi, A two-dimensional model of the ionosphere of Venus, *J. Geophys. Res., 88,* 5595, 1983.

Cravens, T. E., H. Shinagawa, and J. G. Luhmann, Magnetohydrodynamic processes: Magnetic fields in the ionosphere of Venus, in *Venus II: Geology, Geophysics, Atmosphere and Solar Wind Environment*, edited by S. W. Bougher, D. M. Hunten, and R. J. Phillips, pp. 61-93, Univ. of Arizona Press, Tucson, 1997.

Cravens, T. E., C. J. Lindgren and S. Ledvina, A two-dimensional multifluid MHD model of Titan's plasma environment, *Planet. Space Sci., 46*, 1193, 1998.

Dobe, Z., A. F. Nagy and J. L. Fox A theoretical study concerning the solar cycle dependence of the nightside ionosphere of Venus, *J. Geophys. Res., 100,* 14,507, 1995.

Drossart, P. et al., Detection of H_3^+ on Jupiter, *Nature, 340*, 539, 1989.

Fox, J. L., The chemistry of metastable species in the Venusian ionosphere, *Icarus, 51,* 248, 1982.

Fox, J. L., The production and escape of nitrogen atoms on Mars, *J. Geophys. Res., 98,* 3297, 1993.

Fox, J. L. and S. W. Bougher, The structure, lunimosity and dynamics of the Venus atmosphere, *Space Sci. Res.., 55*, 357, 1991.

Fox, J. L. and A. J. Kliore, Ionosphere: Solar cycle variations, in *Venus II*, edited by S. W. Bougher, D. M. Hunten and R. J. Phillips, The University of Arizona Press, Tucson, 1997.

Fox, J. L. and R. V. Yelle, A new model of the ionosphere of Titan, *Geophys. Res. Lett., 24,* 2179, 1997.

Galand, M., J. Lilensten, D. Toublanc and S. Maurice, The ionosphere of Titan: Ideal diurnal and nocturnal cases, *Icarus, 140*, 92, 1999.

Gan, L., T. E. Cravens and M. Horanyi, Electrons in the ionopause boundary layer of Venus, *J. Geophys. Res., 95,* 19023, 1990.

Gan, L., Cravens, T. E., and C. N. Keller, Electrons in the ionosphere of Venus, *J. Geophys. Res., 97*, 12137, 1992.

Goldstein, B. E., et al., Observations of a shock and a recombination layer at the contact surface of comet Halley, *J. Geophys. Res., 94,* 17251, 1989.

Haider, S. A. et al., Calculated ionization rates, ion densities and airglow emission rates due to precipitating electrons in the nightside ionosphere of Mars, *J. Geophys. Res, 97*, 10,637, 1992.

Hanson, W. B., S. Sanatani, and D. R. Zuccaro, The Martian ionosphere as observed by the Viking retarding potential analyzers, *J. Geophys. Res., 82*, 4351, 1977.

Hinson, D. P., et al., Jupiter's ionosphere: Results from the first Galileo radio occultation experiment, *Geophys. Res. Lett., 24*, 2107, 1997.

Hinson, D. P., et al., Galileo radio occultation measurements of Io's ionosphere and plasma wake, *J. Geophys. Res., 103,* 29343, 1998.

Keller, C.N., T. E. Cravens, and L. Gan, A model of the ionosphere of Titan, *J. Geophys. Res., 97,* 12,117, 1992.

Keller, C.N., T. E. Cravens, and L. Gan, One-dimensional multispecies magnetohydrodynamic models of the ramside ionosphere of Titan, *J. Geophys. Res., 99,* 6511, 1994.

Keller, C. N., V. G. Anicich, and T. E. Cravens, Model of Titan's ionosphere with detailed hydrocarbon ion chemistry, *Planet. Space Sci., 46*, 1157, 1998.

Kim, Y. H. and J. L. Fox, The Jovian ionospheric E region, *Geophys. Res. Lett., 18*, 123, 1991.

Kliore, A. J. and J. G. Luhmann, Solar cycle effects on the structure of the electron density profiles in the dayside ionosphere of Venus, *J. Geophys. Res., 96*, 21281, 1991.

Kliore, A. J. et al., Atmosphere and ionosphere of Venus from the Mariner 5 S-band radio occultation measurement, *Science, 158*, 1683, 1967.

Kliore, A. J., et al., The atmosphere of Io from Pioneer 10 radio occultation measurements, *Icarus, 24*, 407, 1975.

Korosmezey, A., et al., A new model of cometary ionospheres, *J. Geophys. Res., 92,* 7331, 1987.

Krankowsky, D. et al., In situ gas and ion measurements at Comet Halley, *Nature, 321,* 326, 1986.

Krasnopolsky, V. A. and Dale P. Cruikshank, Photochemistry of Pluto's atmosphere and ionosphere near perihelion, *J. Geophys. Res., 104*, 21979, 1999.

Kumar, S. and D. M. Hunten, Venus: An ionospheric model with an exospheric temperature of 350K, *J. Geophys. Res., 79,* 2529, 1974.

Lara, L. M., W. H. Ip and R. Rodrigo, Photochemical models of Pluto's atmosphere, *Icarus, 130*, 16, 1997.

Lindal, G. F., et al., The atmosphere of Titan: An analysis of the Voyager 1 radio occultation measurements, *Icarus, 53*, 348, 1983.

Lindal, G. F., J. R. Lyons, D. N. Sweetnam, V. R. Eshleman, D. P. Hinson and G. L. Tyler, The atmosphere of Uranus: Results of radio occultation measurements with Voyager 2, *J. Geophys. Res., 92,* 14987, 1987.

Liu, W. and A. Dalgarno, The ultraviolet spectrum of the Jovian dayglow, *Astrophys. J., 462*, 502, 1996.

Liu, Y., A. F. Nagy, D. L. DeZeeuw, T. I. Gombosi and K. G. Powell, 3D multi-fluid MHD studies of the solar wind interaction with Mars, *Geophys. Res. Lett., 26,* 2689, 1999.

Liu, Y., A. F. Nagy, T. I. Gombosi, D. L. De Zeeuw and K. G. Powell, The solar wind interaction with Mars: Results of three dimensional three species MHD studies, *Adv. Space Res.*, in press, 2002.

Luhmann, J. G. and T. E. Cravens, Magnetic fields in the ionosphere of Venus, *Space Sci. Rev., 55*, 201, 1991.

Majeed, T. and J. C. McConnell, The upper ionospheres of Jupiter and Saturn, *Planet. Space Sci., 39,* 1715, 1991.

Majeed, T., and J. C. McConnell, Voyager electron density measurements on Saturn: Analysis with a time dependent ionospheric model, *J. Geophys. Res., 101,* 7589, 1996.

Majeed, T., J. C. McConnell, D. F. Strobel and M. E. Summers, The ionosphere of Triton, *Geophys. Res. Lett., 17,* 1721, 1990.

Matchera, K. I., D. F. Strobel and F. M. Flasar, Interaction of gravity waves with ionospheric plasma: Implications for Jupiter's ionosphere, *Icarus, 152,* 347, 2001.

McElroy, M. B., The ionospheres of the major planets, *Space Sci. Rev., 14,* 460, 1973.

Mendis, D. A., H. L. F. Houpis, and M.L. Marconi, The physics of comets, in *Fundamentals of Cosmic Physics*, edited by V. M. Canuto and B. C. Elmegreen, Vol. 10, No 1-4, pp. 198-222, Gordon and Breach, NY, 1985.

Miller, K. L. and R. C. Whitten, Ion dynamics in the Venus ionosphere, *Space Sci. Rev., 55,* 165, 1991.

Mitchell, D. L., et al., Oxygen Auger electrons observed in Mars' ionosphere, *Geophys. Res. Lett., 27,* 1801, 2000.

Molina-Cuberos, G. J., J. J. Lopez-Moreno, R. Rodrigo and L. M. Lara, Chemistry of the galactic cosmic ray induced ionosphere of Titan, *J. Geophys. Res., 104,* 21997, 1999.

Moses, J. I. and S. F. Bass, The effects of external material on the chemistry and structure of Saturn's ionosphere, J. Geophys. Res., 105, 7013, 2000.

Nagy, A. F. and T. E. Cravens, Ionosphere: Energetics, in *Venus II,* edited by S. W. Bougher, D. M. Hunten and R. J. Phillips, The University of Arizona Press, Tucson, 1997.

Nagy, A. F., T. E. Cravens, S. G. Smith, H. A. Taylor and H. C. Brinton, Model calculations of the dayside ionosphere of Venus: Ionic composition, *J. Geophys. Res., 85,* 7795, 1980.

Nagy, A. F., T. E. Cravens and T. I. Gombosi, Basic theory and model calculations of the Venus ionosphere, in *Venus*, edited by D. M. Hunten, L. Colin, T. M. Donahue and V. I. Moroz, The University of Arizona Press, Tucson, 1983.

Nagy, A. F., A. Korosmezey, J. Kim and T. I. Gombosi, A two dimensional shock capturing hydrodynamic model of the Venus ionosphere, *Geophys. Res. Lett., 18,* 1801, 1991.

Nagy, A. F., T. E. Cravens and H. J. Waite, All ionospheres are not alike; Report from other planets, *Rev. Geophys. Splmnt., 525,* 1995.

Nagy, A. F., et al., The interaction between the magnetosphere of Saturn and Titan's ionosphere, *J. Geophys. Res., 106,* 6151, 2001.

Neubauer, F. M., et al., First results from the Giotto magnetometer experiment at comet Halley, *Nature, 321,* 352, 1986.

Nier, A. O. and M. B. McElroy, Composition and structure of Mars' upper atmosphere: Results from the neutral mass spectrometers on Viking 1 and 2, *J. Geophys. Res., 82,* 4341, 1977.

Puhl-Quinn, P. and T. E. Cravens, One-dimensional hybrid simulations of the diamagnetic cavity boundary region of comet Halley, *J. Geophys. Res., 100,* 21631, 1995.

Roboz, A. and A. F. Nagy, The energetics of titan's ionosphere, *J. Geophys. Res., 99,* 2087, 1994.

Russell, C. T. and O. Vaisberg, The interaction of the solar wind with Venus, in *Venus*, edited by D. M. Hunten, L. Colin, T. M. Donahue and V. I. Moroz, The University of Arizona Press, Tucson, 1983.

Savich, N. A. et al., The nighttime ionosphere of Mars from Mars 4 and Mars 5 radio occultation dual-frequency measurements, *Solar Wind Interaction with the Planets Mercury, Venus and Mars,* edited by N. F. Ness, *NASA Special Publication 397,* Washington, D.C., 1979.

Schunk, R. W., and A. F. Nagy, *Ionospheres*, Cambridge University Press, Cambridge, 2000.

Shapiro, V. D., et al., On the interaction between the shocked solar wind and the planetary ions on the dayside of Venus, *J. Geophys. Res., 100,* 21289, 1995.

Strobel, D. F., et al., Magnetospheric interaction with Triton's ionosphere, *Geophys. Res. Lett., 17,* 1661, 1990.

Summers, M. E. and D. F. Strobel, Photochemistry and vertical transport in Io's atmosphere and ionosphere, *Icarus, 120,* 290, 1996.

Sundstrom, G. et al., Destruction rate of H_3^+ by low energy electrons measured in a storage-ring experiment, *Science, 263,* 785, 1994.

Tanaka, T. and K. Murawski, Three-dimensional MHD simulation of the solar wind interaction with the ionosphere of Venus: Results of two-component reacting plasma simulation, *J. Geophys. Res., 102,* 19805, 1997.

Tyler, G. L. et al., Voyager radio science observations of Neptune and Triton, *Science, 246,* 1466, 1989.

Waite, J. H. and T. E. Cravens, Current review of the Jupiter, Saturn and Uranus ionospheres, *Adv. Space Sci., 7,* (12) 119, 1987.

Yelle, R. V., J. C. McConnell, B. R. Sandell and A. L. Broadfoot, The dependence of electroglow on the solar flux, *J. Geophys. Res., 92,* 15110, 1987.

Zhang, M. H. G., J. G. Luhmann and A. J. Kliore, An observational study of the nightside ionospheres of Mars and Venus with radio occultation methods, *J. Geophys. Res., 95,* 17095, 1990.

T. E. Cravens, Department of Physics and Astronomy, University of Kansas, Lawrence, KS 66045.

A. F. Nagy, Space Physics Research Laboratory, University of Michigan, 2455 Hayward St., Ann Arbor, MI 48109-2143.

Auroral Processes in the Solar System

Marina Galand and Supriya Chakrabarti

Center for Space Physics, Boston University, Boston, Massachusetts

Studies of the aurora constitute a fundamental component of geophysical research. The observational, theoretical, and modeling advances achieved in understanding terrestrial auroral activity mark a high point in space science and, in particular, in defining linkages between energetics, dynamics, and coupling within the solar wind-magnetospheric-atmospheric system. One of the major achievements of space age technology has been the detection of auroral emissions on other solar system bodies. While the mechanisms responsible for auroral structure on other worlds involve the same basic physics operating on Earth, the settings are of vastly different scale and with sources often unique to each site. Defining an aurora as any optical manifestation of the interaction of extra-atmospheric energetic electrons, ions, and neutrals with an atmosphere, we review the observational inventory of aurora in the solar system and discuss the different steps used for modeling auroral processes. Aurora offers us a unique and extremely valuable remote sensing of magnetic field configuration and is a tracer of plasma interactions. It is an indicator of the atmospheric composition and energy source and can be used for remote sensing of the characteristics of the incident energetic particles. The diversity of magnetic field geometries, plasma interactions, energy sources, and atmospheric constituents, all make comparative auroral studies a rich field, which should lead us to further understanding of interactions taking place at different solar system bodies.

1. INTRODUCTION

Since the dawn of human history, the aurora has stirred human imagination, curiosity, and fear, creating a mixture of conflicting emotions. Seen as huge green curtains of light beating under a ghostwind, or red veils firing the nightsky, auroral displays have always fascinated human minds [e.g., *Eather*, 1980]. Eskimos in Alaska described the aurora borealis as the dancing souls of their favorite animals; for the Inuits in southern Canada the aurora had the power to decapitate people.

Auroral emissions are not restricted to the Earth. With improved observation capabilities over the last decades we have discovered aurorae on other bodies of the solar system, such as on the Jovian moon Ganymede. On Earth alone auroral emissions span the entire optical wavelength band. Temporal variabilities are observed from few milliseconds to over several hours, and the spatial structures extend from a meter to hundreds of kilometers.

The definition we propose for aurora is any optical manifestation of the interaction of extra-atmospheric energetic electrons, ions, and neutrals, with an at-

Atmospheres in the Solar System: Comparative Aeronomy
Geophysical Monograph 130

10.1029/130GM05

mosphere. The spectral range includes γ-rays [about 0.001-1 pm], soft X-rays [1-10 nm], Extreme UltraViolet (EUV) [10-90 nm], Far-UltraViolet (FUV) [90-200 nm], Near-UltraViolet (NUV) [200-300 nm], visible [300-800 nm], near-InfraRed (IR) [0.8-15 μm], far-InfraRed [15-200 μm]. The shorter wavelength emissions are produced by incident particles with higher energy penetrating deeper in the atmosphere. We choose to focus on optical emissions, even though radio emissions [above 0.2 mm] have been observed in the auroral regions of the Earth and the giant planets [*Zarka*, 1998]. The interaction of the energetic particles with the atmosphere can be direct - the excitation and subsequent light emission are the result of the impact of an energetic particle with an atmospheric species. It can also be indirect, when the excitation results from a chain of reactions initiated by energetic particles. It has to be distinguished from airglow, which is the result of chemical reactions initiated by solar photons [see *Chap I.5 and IV.5*]. For emissions to be called aurora, we propose that the energetic particles have to be extra-atmospheric. Photo-electrons, electrons produced by interaction of the solar photons with an atmosphere, are excluded as energy source of an aurora. The energetic particles at the source of aurora have a large variety of origins, including the solar wind, sputtering of Saturnian rings and icy moon surfaces by magnetospheric ions, Io's volcanic plumes, or the planetary magnetosphere. The particles can be accelerated by magnetospheric convection, diffusion, wave-particle interaction, pick-up (e.g., in the Venusian upper atmosphere), or induced by rotation of the planet (e.g., at Jupiter). The energetic particles can be part of an open flow, precipitating from a magnetosphere, or of solar wind origin. They also can be part of a field-aligned current closing within the ionosphere, as in the current system that exists between the Jovian ionosphere and its moon Io. Heat flux is excluded as it is conduction, not particle transport. It is assumed that the energetic particles impact only on an atmosphere. Even though partly ionized, the dense atmospheres encountered around solar system bodies are dominated by neutral constituents.

The interaction of an energetic particle with an ambient neutral can lead to the excitation of the atmospheric species. During de-excitation, the excess energy is re-emitted as a photon whose wavelength is precisely governed by the same quantum rules which dictate the available energy levels surrounding a given nucleus [e.g., *Chamberlain*, 1995]. The auroral emissions can also be produced by the energetic particle itself. For instance, energetic protons precipitating into an atmosphere can capture an electron (charge-exchange) and become hydrogen atoms in an excited state. As a result, doppler-shifted H emissions are produced, such as Lyman α (121.6 nm) and the Balmer lines, Hα (656.3 nm) and Hβ (486.1 nm). Sometimes for heavy ions such as oxygen, K-shell lines arise as the energetic ions are nearly stripped of electrons and then are either directly excited or charge exchanged into an excited state, which subsequently emits an X-ray photon. As for electrons, bremsstrahlung continuum X-rays are produced when the suprathermal electron is scattered by Coulomb interactions with an atmospheric nuclei and electrons. Auroral IR radiations can be produced by cooling processes in an atmosphere heated by energetic particles. Hydrocarbons are efficient coolers in the giant planets, and NO, He, and CO_2 in the terrestrial thermosphere.

Auroral emissions have been extensively observed and studied. We do not pretend to provide a comprehensive review of the aurora. Detailed reviews can be found in the works by *Fox* [1986] and *Bhardwaj and Gladstone* [2000a]. We would like, rather, to give some insights on the diversity of auroral emissions encountered in our solar system, on the modeling of auroral processes, on the relevance of auroral studies, and the comparative approach.

2. OBSERVATIONS OF AURORAL EMISSIONS IN THE SOLAR SYSTEM

Auroral emissions have been observed throughout the solar system. To cover the large range of wavelengths, different instruments from ground-based to Earth orbiting observatories have been used. Visible and IR observations are usually performed from the ground. At Mauna Kea, Hawaii, the Keck telescope has been used to observe Ganymede in the red window, and the Canada-France-Hawaii Telescope (CFHT) and Infrared Telescope Facility (IRTF) have observed Jupiter in the IR. The terrestrial atmosphere has been extensively observed from ground with photometers and spectrometers at visible wavelengths. Since UV and X-rays radiation is absorbed in the Earth's atmosphere, the instruments operating in these wavelengths are all space-based. The Polar spacecraft has instruments covering a large spectral range: the UltraViolet Imager (UVI), the Visible Imaging System (VIS), and the Polar Ionospheric X-ray Imaging Experiment (PIXIE). Polar as well as Dynamics Explorer (DE) and the recent Imager for Magnetopause-to-Aurora Global Exploration (IMAGE) satellite have provided crucial global images of the Earth's auroral ovals. The International Ul-

traviolet Explorer (IUE) satellite at geo-synchronous orbit from 1978 to 1996 and the Extreme UltraViolet Explorer (EUVE) observatory operating at about 430 km from 1992 to January 2001 provided precious data about the giant planets and comets. The Goddard High Resolution Spectrograph (GHRS), onboard the Hubble Space Telescope (HST) orbiting at 600 km, operated until 1997 and was then replaced by the Space Telescope Imaging Spectrograph (STIS) for imaging from UV to near-IR. Also aboard the HST, the Faint Object Camera (FOC), operating in visible and UV wavelengths, and the Wide Field Planetary Camera (WFPC), operating from UV to near-IR, have been extensively used for observations of Saturn, Jupiter, and its Galilean moons, Ganymede, Io, and Europa. The Rossi X-ray Timing Explorer (XTE), the Röntgen satellite (ROSAT), the High Energy Astronomical Observatory 2 (Einstein), and the recent Chandra X-ray Observatory (CXO) have been crucial in the detection of X-rays at comets, Jupiter, and Saturn.

For distant bodies with faint emission or fine spatial structure, spacecraft flybys provide data that near Earth observatories cannot. The UltraViolet Spectrometer (UVS) onboard Pionner Venus Orbiter (PVO) and UVS onboard the Voyager 1 and 2 spacecrafts have recorded auroral emissions on Venus and on the giant planets, respectively. The Solid State Imaging (SSI) instrument on Galileo observing the visible nighttime Jovian aurora gave us images with unprecedented spatial resolution. Over December 2000 - January 2001 (Jupiter Millennium Campaign), the Cassini swing-by of Jupiter along with Galileo and HST observations offered us the first comprehensive, coordinated set of data of the Jupiter's atmosphere and environment [*Clarke*, 2001].

2.1. Earth

On the Earth, the aurora has been studied scientifically for a long time (see for example, *Mairan* [1733] and other historical references listed in *Chamberlain* [1995]). Many reviews have summarized auroral studies with different emphases (see *Vallance Jones* [1974], *Gordiets* [1986], *Rees* [1989], *Meng et al.* [1991], *Stadsnes et al.* [1997], and *Chakrabarti* [1998]). Terrestrial aurorae have been observed from gamma rays associated to MeV protons [*Share and Murphy*, 2001] to radio [e.g., *Liou et al.*, 2000]. Recent advances include multi-spectral and multi-point observations of aurora, from space and ground-based platforms. In this section, we will discuss some of the results not covered in the reviews listed above.

UV observations have opened up a capability that is unavailable to visible and IR - the ability to observe sunlit aurora. Rocket and satellite borne spectroscopic observations [*Vallance Jones*, 1991, and references therein] established the spectral content which has been refined by satellite observations. These observations have shown the auroral spectrum is rich even shortward of 90 nm where it is dominated by O^+ emissions, while the spectral region between 90 and 200 nm contains a large number of emission features due to H, O, N, O^+, N^+, H_2, and N_2. There were reports of argon emissions [*Christensen et al.*, 1977] and O^{++} [*Paresce et al.*, 1983], but they have not been independently validated. Spectroscopic studies of UV aurora have used emission intensity ratios to characterize the particle energies in the sunlit cusp, polar cap, and nightside aurora [e.g., *Chakrabarti*, 1986].

More recently, global imaging in the visible (e.g., DMSP), UV (e.g., DE, Viking and Polar/UVI, IMAGE) and X-rays (e.g., Polar/PIXIE) are being used for a better understanding of auroral processes. For example, the size of the auroral oval derived from global images has been related to solar wind parameters [*Siscoe*, 1991]. Evolution of the global aurora has been examined to understand the substorm onset and poleward expansion [e.g., *Craven and Frank*, 1987].

Balloons were used to study X-ray emissions from the aurora as early as 1957 [*Winckler et al.*, 1958; *Anderson*, 1965]. X-ray spectrum of an aurora has been related to the energy spectrum of the incident electrons [*Vij et al.*, 1975] and have since been used in conjunction with visible [*Mizera et al.*, 1978; *Stadsnes et al.*, 1997], UV [*Østgaard et al.*, 2000; *Anderson et al.*, 2000] and particle measurements [*Sharber et al.*, 1993]. These studies on the role of auroral X-rays in atmospheric ionization found a peak observed hemispheric power input of 40 GW and an ionization rate that exceeds solar UV and X-ray ionization rate by 2 - 3 orders of magnitude [*Chenette et al.*, 1993]. With improved technology, we now have global X-ray imagers, which have allowed a statistical classification of X-ray flux according to Kp [*Petrinec et al.*, 1999]. Simulation studies have been used to explain the X-ray darkness observed in the postnoon sector [*Chenette et al.*, 1999] in terms of attenuation of drifting plasmasheet electrons [*Chen and Schulz*, 2001].

In low latitude region, a factor of two increase in emission ratios of selected UV lines at geomagnetically disturbed times was attributed to energetic neutral atoms (ENAs) [*Abreu et al.*, 1986]. Subsequently, *Ishimoto et al.* [1992] examined enhancement of several UV emis-

sions during the main phase of a geomagnetic substorm and concluded that they were caused by precipitating energetic oxygen neutrals of ring current origin. Similar enhancement in the low-latitude nighttime N_2^+ (1N) intensities was attributed to ENAs [*Tinsley et al.*, 1994]. Recently, this increase in UV emission intensities in low latitudes due to ENAs has been extended to dayglow [*Stephan et al.*, 2000; 2001].

In a short review it is not possible to highlight all aspects of terrestrial auroral research. So, we note some recent works, which could be used to find other relevant works. *Doe et al.* [1993] observed F region plasma depletion in red line images and were able to attribute it to downward field-aligned current. Using Polar UVI and Wind's solar wind and IMF data, *Liou et al.* [1998] conclude that solar wind parameters (density, speed, and dynamic pressure) have minimal effect on the afternoon aurora. *Kozlovsky and Kangas* [2001] found a correlation of the equatorward drifting arcs with IMF B_z. The authors noted a lag of about 30 minutes of the increase of equatorward drifting of the arcs located in the region of convection shear. *Sandholt and Farrugia* [2001] studied the substorm intensification process through observations of bursty bulk flows. They were able to relate impulsive injection of electrons at geostationary altitude and brightening of the aurora. Using high spatial and temporal resolutions, *Knudsen et al.* [2001] studied the width of auroral arcs and found them to be 18 $\pm$ 9 km, which is consistent with those of *Stenbaek-Nielsen et al.* [1998].

In spite of tremendous progress in auroral studies, there is a lamentable lack of spectral imaging studies on the Earth. The spectacular global auroral images taken by DE, Viking, Polar, and IMAGE all use narrow-band filters, thereby requiring some assumptions on the spectral content within their passband. All our knowledge of optical aurora on other planets come from spectral imaging. Until we conduct a similar observation on the Earth, our understanding of comparative auroral studies will remain incomplete.

2.2. Bodies with a significant intrinsic magnetosphere

In addition to the Earth, five solar system bodies, Jupiter, Saturn, Uranus, Neptune, and the Jovian moon Ganymede, are known to have both an atmosphere and a significant intrinsic magnetosphere, conditions conducive to aurora. Although their magnetic geometries are very different, the giant planets have upper atmospheres with common features. The major species are hydrogen atoms and molecules whose emission lines and bands are the dominant UV and visible auroral radiations. Below the homopause is a hydrocarbon layer that absorbs most of the UV and visible emissions but radiates in IR. X-rays are produced by the energetic particles themselves, mainly by the heavy ions on Jupiter and probably by the electrons on Saturn. For a comprehensive survey of auroral processes on the giant planets, see *Bhardwaj and Gladstone* [2000a, 2000b] and *Chapter II.2.* Consequently, only few major characteristics of aurora on the giant planets are presented here.

Jovian auroral emissions have been observed in the X-rays, UV, visible, and IR ranges [*Waite et al.*, 2000]. The Jovian aurora is not as strongly coupled to the solar wind as the Earth is due to Jupiter's strong magnetic field [*Dessler*, 1983] (although observations with higher spatial and temporal resolution seem to disagree with this conclusion) [see *Chap II.2*]. The main ovals are driven primarily by the rapid rotation of the jovian ionosphere. X-ray auroral emissions are observed at high latitudes [*Waite et al.*, 1994], and at low latitudes [*Waite et al.*, 1997]. If the major source seems to be heavy ions, it should be noted that recent data from the Jupiter Millennium campaign opens up the possibility that electrons may be important for some of the X-ray emissions [*Gladstone et al.*, 2001]. The visible aurora has not been seen on the dayside - the only hemisphere seen from Earth - due to the strong albedo. Voyager [*Smith et al.*, 1979] and Galileo [*Ingersoll et al.*, 1998] have observed the nightside visible aurora. IR observations revealed the presence of H_3^+ in the Jovian auroral regions [*Drossart et al.*, 1989] and the variability of the thermal IR emissions from hydrocarbons in high latitude suggests that they are driven by auroral processes [*Caldwell et al.*, 1980; *Kim et al.*, 1985]. The H_2 near-IR emissions in the auroral oval are a direct consequence of electron precipitation [*Kim and Maguire*, 1986]. The most peculiar auroral feature encountered on Jupiter is the emissions related to the magnetic flux tube footprint of Io observed in IR [*Connerney et al.*, 1993], UV [*Prangé et al.*, 1996; *Clarke et al.*, 1998], and visible [*Vasavada et al.*, 1999]. Magnetic footprints of Ganymede and Europa were also discovered in UV with HST/ STIS [*Clarke et al.*, 2001]. The detection of these emissions proves the generation of a field-aligned current system between the Jovian ionosphere and the Galilean moons [see *Chap II.2*].

Saturn's aurora has been observed in UV [*Trauger et al.*, 1998], IR [*Geballe et al.*, 1993], and X-rays [*Ness and Schmitt*, 2000]. While Saturn is similar in size and composition to Jupiter, its magnetic field is similar in surface strength to the Earth's. As a result, auroral emission brightnesses on Saturn are much more mod-

est than on Jupiter, with about 10^3 and 100 times less emitted power in UV and IR, respectively. The high latitude auroral ovals located at about 80° latitude are very stable as a result of the alignment of the rotation and magnetic dipole axis. As a consequence of its modest magnetic field (compared to Jupiter), the auroral emission features on Saturn indicate that the local time effects play an important role in the auroral morphology [*Trauger et al.*, 1998]. The detection of IR emissions in auroral regions is associated with the excitation of H_3^+ but the low brightness observed has not yet been fully explained [*Bhardwaj and Gladstone*, 2000a].

The first indication of the presence of auroral activity on Uranus was based on bright and variable H Lyman α emission observed through IUE for several years [*Clarke*, 1982; *Clarke et al.*, 1986]. These emissions were too intense to be attributed to resonant scattering of solar Ly α and no correlation was found with the solar Ly α or the solar wind conditions. Voyager 2 flyby clearly showed emissions associated with the nightside southern magnetic pole [*Broadfoot et al.*, 1986] and confirmed the presence of a strong magnetic field but with a very unusual and complex configuration [*Connerney et al.*, 1987]. The angle between the magnetic and rotation axes and the offset of the dipole are very large, 58.6° and 30°, respectively. Keeping also in mind the large inclination of the Uranian equator toward the orbit (98°), the magnetotail of Uranus rotates about an axis oriented towards the Sun. Dipole, quadrupole, and octapole models have been developed for modeling the magnetic field and explaining the origin of the UV emissions [*Gao et al.*, 1998]. The main auroral features follow a circumpolar oval, even though not complete, at magnetic latitude of 60° for the northern oval and 65° for the southern oval corresponding to very low L shell values (around 4) [*Herbert and Sandel*, 1994]. The brightest auroral emission at each magnetic pole is confined to a range of 90° of magnetic longitude region centered on the magnetotail direction. The low apparent L suggests less than 10 keV energy for the precipitating particles. Even though IR H_3^+ emission has been observed on Uranus, the lack of spatial information makes it hard to interpret or conclude that these emissions are auroral in nature [*Trafton et al.*, 1999].

The UVS instrument onboard Voyager 2 revealed, for the first time, H_2 emissions on nightside of Neptune [*Broadfoot et al.*, 1989; *Sandel et al.*, 1990]. These emissions are 2 to 3 orders of magnitude weaker than the Uranian auroral emissions, largely because Neptune's magnetosphere is emptied of plasma each rotation. Two distinct types of emissions were observed. The first one is a latitudinally broad region extending from 55° South to 50° North. The second feature, seen near the south pole, is brighter and more localized in both longitude and latitude. The orientation of Neptune's spin axis (28.8° obliquity) along with the large magnetic tilt angle of 47° induces a variable geometry for Neptune's magnetosphere, changing every half-rotation (8 hours), from an "Earth-like" magnetosphere to a "pole-on" magnetosphere with only one polar cusp [*Sandel et al.*, 1990; *Bishop et al.*, 1995]. As a result of the ill-known, complex magnetic configuration, there is some controversy about the mechanisms causing each type of emission. The diffuse emissions are attributed to precipitation of conjugate photoelectrons coming from the sunlit side of the planet [*Sandel et al.*, 1990] or to trapped electrons precipitating in the region of anomalously low surface magnetic field [*Paranicas and Cheng*, 1994]. The brightest emission region seems more clearly to be auroral, but the acceleration mechanism for the charged particles is not yet unanimously accepted [*Bhardwaj and Gladstone*, 2000a]. A suggestion is that this southern aurora extracts its power from Neptune's rotational energy through the electrodynamic coupling of the ionosphere with Triton's plasma arcs [*Broadfoot et al.*, 1989; *Sandel et al.*, 1990].

Ganymede, the only moon known to have a significant intrinsic magnetic field [*Kivelson et al.*, 1996], is by far the most striking case with its double aurora. First, UV observations of the sunlit side, recorded by HST/GHRS [*Hall et al.*, 1998] and then confirmed by HST/ STIS [*Feldman et al.*, 2000] showed oxygen line emissions concentrated at the poles of the satellite. After removing the contribution of the reflected sunlight on Ganymede and of airglow emissions from Earth, they found the brightness to be up to 300 R for OI 135.6 nm. This reveals the presence of a thin oxygen atmosphere around Ganymede, most probably produced by surface sputtering and decomposition of ice from the impact of Io plasma torus ions - a process also called radiolysis - and by photolysis of ice [see *Chap III.3*]. The ratio of OI 135.6 nm to 130.4 nm lines suggests that the main excitation mechanism is electron impact on O_2 with a possible smaller contribution from electron impact on O [*Hall et al.*, 1998]. The temporal variability over a Jovian rotation and the spatial distribution of the oxygen lines observed at geographic latitudes above 40° tend to support the auroral nature of these emissions. The Galileo magnetometer data indicate that Jovian magnetic field lines linked to Ganymede's atmosphere only at high latitudes [*Kivelson et al.*, 1997]. Low energy particles coming from the Jovian magnetospheric

plasma can reach the polar atmosphere of Ganymede. The variability of both the brightness and the relative intensity between north and south hemispheres can be explained by the changing Jovian plasma environment at Ganymede. However, this explanation remains controversial today. Local acceleration of electrons induced by the interaction of the Jovian co-rotating plasma with Ganymede's magnetosphere has also been invoked [*Eviatar et al.*, 2001]. The longitudinal nonuniformity in the emission brightness and the lack of a pronounced limb, suggesting that emissions are produced close to the surface, remain unexplained. In addition to the UV polar emission, equatorial nightside aurora in OI 630.0 and 636.3 nm was revealed on Ganymede by the Keck I telescope [*Brown and Bouchez*, 1999]. These visible emissions are concentrated over a region protected by the moon's intrinsic magnetic field from direct bombardment from the Jovian magnetosphere. The excitation is likely to be induced by low energy electrons trapped in the inner magnetosphere of Ganymede [*Eviatar et al.*, 2000]. The absence of red line emissions at poles is still not yet understood.

2.3. Bodies with an induced magnetic environment

Auroral emissions have been observed around bodies which do not generate any significant magnetosphere. These bodies are typically embedded in a magnetic environment of external origin, a source of energetic particles. The induced magnetic environment results from the interaction of the atmospheric body with the solar wind, such as in the case of Venus and comets, or with the mother-planet, as for the Galilean moons, Io and Europa.

Venus has a significant dayside ionosphere, which, as a result of its lack of planetary magnetic field and its dense atmosphere, slows down the solar wind. The interplanetary magnetic field is deflected and drapes back to form a magnetotail [*see Chap II.3*]. Consequently, energetic ions - of solar wind origin or from the sunlit Venusian atmosphere, picked up by the solar wind, and accelerated - and electrons can bombard the nightside atmosphere of Venus [*Brace et al.*, 1987]. Nevertheless, it was still a surprise when the PVO/UVS instrument showed continuous but highly variable emissions at 130.4 nm on the nightside of Venus [*Phillips et al.*, 1986; *Luhmann et al.*, 1994]. The emissions appear as patches and occasionally cover the entire disk. They have typical brightness in the 10-20 R range, but spots sometimes reached intensities exceeding 100 R. The morphology and variability of these emissions suggest an auroral origin. The analysis by *Fox and Stewart* [1991] corroborates this conclusion. The 130.4 to 135.6 nm brightness ratio precludes radiative recombination of O^+ with electrons as the dominant mechanism. The observed intensities are consistent with soft electron precipitation of few tens of eV - derived from PVO particle data - impacting the atmospheric oxygen atoms. No systematic correlations between auroral brightness and the solar wind fluid parameters have been found. However, the periods of brightest emissions seem to be associated with the passage of interplanetary shocks and its bulk of energetic solar particles [*Phillips et al.*, 1986].

Another unexpected case of aurora is the soft X-ray emissions observed from comets. The first observations were from the comet Hyakutake and was a very surprising and puzzling discovery [*Lisse et al.*, 1996]. These observations, obtained by ROSAT and XTE, showed a very broad emitting region, extending well beyond cometocentric distances of 200,000 km and elongated in the direction perpendicular to the Sun-comet line. The X-ray variability had two components, one slow and the other more impulsive with a factor of 4 of increase and a time scale of one to two hours. *Dennerl et al.* [1997] found that the luminosity varies with heliocentric distance and with cometary gas production rate. Since this discovery EUV and soft X-ray emissions have been observed around more than ten comets, including comet Hale-Bopp [e.g., *Dennerl et al.*, 1997; *Mumma et al.*, 1997; *Krasnopolsky et al.*, 1997; *Lisse et al.*, 1999, 2000]. X-ray emissions seem to be a general property of comets.

Various mechanisms have been invoked to explain the X-ray emissions from comets, including scattering and fluorescence of solar X-rays by cometary dust and gas, excitation by solar wind electrons and protons and by high-energy cometary ions, electron bremsstrahlung from gas and dust, and electron capture of the solar wind ions [*Cravens*, 1997; *Krasnopolosky*, 1997]. The lack of correlation found between the X-ray emission from comet Hyakutake and the solar X-ray flux suggest that the scattering of the solar X-rays by very small (10^{-18} g) dust particles is unlikely the dominant source for this comet [*Neugebauer et al.*, 2000]. However, this conclusion does not preclude significant contributions of this process for producing X-ray emissions from very dusty comets, like Hale-Bopp [*Owens et al.*, 1998]. Note that such contributions are of non-auroral origin. Even though the fraction of heavy ions (Z>2) in the solar wind is only of the order of 0.1 % to the total ion content, electron capture of high charge state solar wind minor ions (e.g., O^{6+}, C^{5+}, N^{5+}, and Si^{10+})

with cometary neutrals (mainly H_2O, OH, and O) is the dominant mechanism for producing X-rays at several comets, in particular at Hyakutake. The modeling of this process provides a total X-ray luminosity and a spatial morphology in relatively good agreement with observations [e.g., *Cravens*, 1997; *Wegmann et al.*, 1998; *Kharchenko and Dalgarno*, 2000]. Using Solar and Heliospheric Observatory (SOHO) particle observations, *Neugebauer et al.* [2000] demonstrated that the X-ray variability around comet Hyakutake can be explained on the basis of variability in oxygen ion flux.

A critical test for the X-ray excitation mechanism is provided by spectroscopy. Early low spectral resolution observations showed a continuous spectra, which can be reproduced by the electron capture mechanism [*Wegmann et al.*, 1998]. Recently, O^{4+}, O^{5+}, C^{4+}, and Ne^{7+} emission lines were detected by EUVE observations during a close passage of the comet Hyakutake at 0.1 AU [*Krasnopolsky and Mumma*, 2000] and from CXO observations of comet Linear [*Lisse et al.*, 2000]. These detections are the first direct evidence of the production of cometary X-rays by the interaction of solar wind heavy ions with cometary gas and, therefore, of the presence of auroral emissions at some comets. The variability of cometary X-ray emission induced by solar wind was discussed by *Kharchenko and Dalgarno* [2001].

Auroral emissions have also been discovered around the Jovian moon Io. The volcanic activity on Io provides a tenuous atmosphere rich in SO_2 gas and its dissociative products (SO, S, and O). Clorine and sodium, also detected in the atmosphere, are probably produced in the lava. Sublimation and surface sputtering by heavy ions are other sources of the atmosphere [see *Chap III.3*]. Io does not seem to have a significant intrinsic magnetic field. A plasma torus produced by pick up of the iogenic newly-born ions by the Jovian magnetic field surrounds Io's orbit and co-rotates with Jupiter's magnetosphere. Its interaction with Io's atmosphere is expected to produce aurora. It is then not surprising that oxygen, sulfur, and chlorine emissions from Io's atmosphere have been imaged in UV with HST/STIS [*Roesler et al.*, 1999; *Retherford et al.*, 2000a] and in the visible, with Io in eclipse, by Galileo SSI [*Geissler et al.*, 1999] and by HST/STIS with the OI 630.0 nm filter [*Retherford et al.*, 1999].

The most striking auroral features of Io are the bright regions close to Io's equator, called "equatorial spots". The brightness of these spots reaches values up to 2.5 kR for OI 135.6 nm. The emission is brightest at about 200 km above Io's surface and extends several hundred kilometers above that height. *Retherford et al.* [2000b] conducted a comprehensive analysis of these equatorial spots, based on UV HST/STIS images. The spot location is correlated with the orientation of the Jovian magnetic field lines near Io, attesting to the interaction of the Jovian magnetosphere and Io's atmosphere. Models suggest that the emission location near the magnetic equator - defined as the place perpendicular to the local Jovian magnetic field - is caused by the strong divergence of the corotating plasma flow in the vicinity of the Io's highly conductive ionosphere [*Saur et al.*, 2000]. The brightness is correlated with Io's magnetic longitude, decreasing when Io is further away from the plasma torus' centrifugal equator, which is the densest part of the torus. This indicates that the plasma torus must control these atomic oxygen, sulfur, and chlorine emissions. Some features remain unexplained, such as the location of the anti-Jovian equatorial spots which are, on the average, closer to Io's equator than the magnetic field line tangent points.

Finally, another Jovian moon, Europa, also demonstrates auroral display. Using the HST/GHRS instrument in Earth's shadow, *Hall et al.* [1995] detected OI UV emissions. After removing the solar reflected component on Europa's surface, the OI 130.4 nm and OI 135.6 nm brightnesses were found to be of about 40 R and 70 R, respectively, with an emission region probably within less than 200 km of Europa's solid surface. Photo-excitation processes and resonance scattering of solar OI 130.4 nm photons by oxygen atoms cannot alone explained these brightnesses. *Hall et al.* [1998] showed that the most likely excitation process is electron impact on atmospheric species. The relative intensities of the two OI spectral features favors electron impact dissociation of O_2. Since Europa orbits deep within the Jovian magnetosphere and resides in the outer regions of the plasma torus roughly centered on the orbit of Io, it is likely that magnetospheric electrons of few tens of eV, as observed by Voyager 1 Plasma Science Experiment [*Bagenal*, 1994], are reaching and interacting with Europa's atmosphere.

The existence and stability of an oxygen atmosphere around Europa has been confirmed by HST/GHRS observations [*Hall et al.*, 1998] and by HST/STIS FUV images showing limb-brightening at Europa [*McGrath et al.*, 2000]. Similar to Ganymede, the major source of the atmospheric oxygen is sputtering of the icy surface and decomposition of ice by Io plasma torus ions [see *Chap III.3*]. The particle bombardment is expected to be continuous and intense at Europa's orbit. The HST/STIS images suggest that, unlike Io and Ganymede, Europa does not exhibit obvious concentra-

tion of emissions at the equator or the poles. Temporal and spatial variations do not seem to be correlated with the orientation of the Jovian magnetic field relative to Europa. The interaction of Europa's atmosphere with the ambient plasma environment is not yet fully understood and needs to be further investigated.

3. MODELING OF AURORAL PROCESSES

The first step for modeling auroral processes is to describe how the energetic extra-atmospheric electrons, ions, and neutrals lose their energy and are redistributed in angle through collisions (sections 3.1 and 3.2). The collisional interaction can lead to an excitation of the incident energetic particle or of the ambient target species. The excited state may also be produced by, or be lost through, chemical reactions between atmospheric constituents (section 3.3). Finally, the photon emitted by de-activation of the excited state may be lost by absorption by ambient species or undergo multiple scattering before a possible escape from the atmosphere (section 3.4). The different steps for modeling auroral processes are summarized in Figure 1.

3.1. Kinetic Electron Transport Model

Throughout the solar system the major source of energetic particles is suprathermal electron population. Electrons represent 85% of the energy carried by particles precipitating over the terrestrial auroral ovals [*Hardy et al.*, 1989], and more than half of the energy precipitating over the Saturnian auroral ovals [*Barbosa*, 1990]. In these magnetized planets, energetic electrons precipitate from the planetary magnetosphere. Energetic electrons have also been observed in the vicinity of non-magnetized bodies, such as Venus. Suprathermal electrons - believed to be shocked solar wind electrons moving into the magnetized ionosphere from the tail region during high solar wind dynamic pressure - have been measured in the Venus nightside ionosphere [*Gringauz et al.*, 1979; *Spenner et al.*, 1981]. Energetic electrons have been measured in the magnetotail and plasma sheet of Mars by the Phobos 2 mission [*Verigin et al.*, 1991].

In addition to numerous collisions with the ambient neutrals (elastic scattering, excitation, ionization, and dissociation), suprathermal electrons transfer energy to the ambient thermal electron population through Coulomb collisions and wave excitation [*Rees*, 1989]. Sometimes this process is neglected [*Onda et al.*, 1999]. However, it must be taken into consideration when

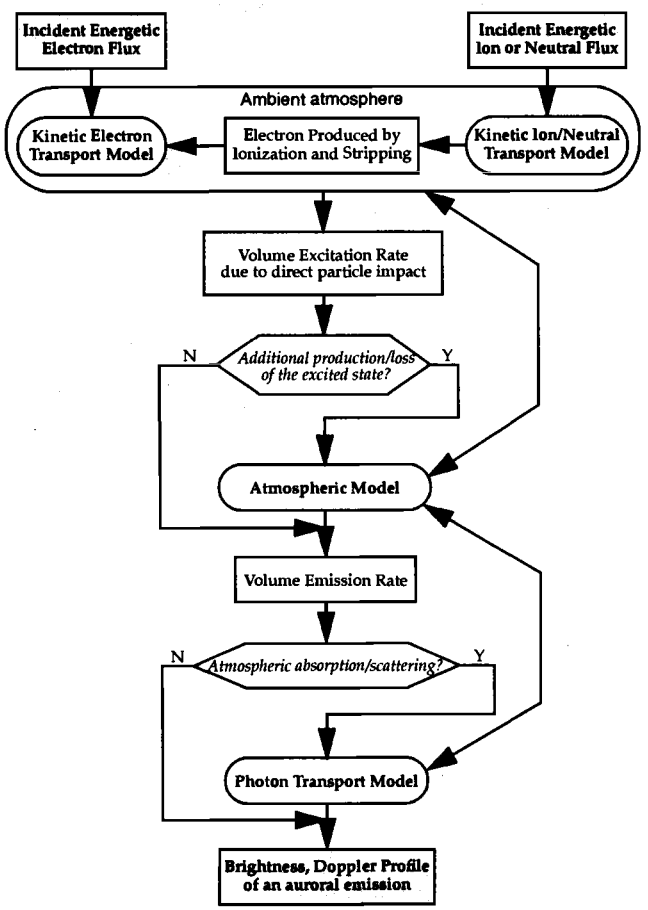

Figure 1. Diagram illustrating the modeling of auroral processes.

modeling the electron temperature of an ionosphere perturbed by electron precipitation [e.g., *Stamnes and Rees*, 1983; *Gan et al.*, 1990]. It has been shown that the wave-electron interactions could play a significant role in the electron energetics of the ionosphere of Venus [*Cravens et al.*, 1990]. Usually the electric field acceleration, magnetic field curvature, and gravity are neglected, as they have negligible effect. By neglecting all these processes, electrons are confined to spiral along the magnetic field lines with only collisional energy and angular redistributions. The electrons produced by ionization due to the precipitating energetic electrons are called secondary electrons. For many auroral emissions they are the main excitation source. It is therefore crucial to take their contributions into account [e.g., *Strickland et al.*, 1993].

To describe the transport of suprathermal electrons in an atmosphere, one of the following methods is com-

monly used: The Continuous Slowing Down Approximation (CSDA) method, the Monte-Carlo (MC) simulation, and the direct solution of the Boltzmann equation (SBE). The simulated electron population is usually considered to have energies above few eV. The upper limit of the energy range is between a few hundreds of eV to few tens of MeV. For dayside studies, the transport of the photoelectrons produced by interaction of the solar photons with the atmosphere is described by the same models. The inputs to the models are the incident energetic electron flux at the top of the atmosphere, the density profiles of the atmospheric neutrals, and the collision cross sections between the energetic electrons and the ambient neutrals. When the heating of ambient electrons is considered, electron density and temperature are used as input parameters. The electron transport models yield the electron flux at different "altitudes" along the magnetic field line, energies, and pitch angles (defined as the angle between the magnetic field line and the electron velocity). Integrated quantities, such as the altitude profiles of the electron production rate or of the excitation rates of ambient species can be derived from the electron flux, the neutral densities and the ionization or excitation cross sections.

The CSDA method is based on the equation stating that the variation in altitude of the electron energy is equal to the negative of the product of the neutral density and the energy loss [e.g., *Rees*, 1989]. This method is relatively simple to implement. Angular redistribution can be included [*Régo et al.*, 1994]. Primary and secondary electron population can be computed self-consistently using the approach of *Rees et al.* [1969]. The drawback of the CSDA method rests on its concept of continuous energy degradation. Such an assumption is not always warranted for low energy electrons and a discrete energy loss treatment is more appropriate [*Fox and Stewart*, 1991]. In addition, the equation to solve can only be integrated if the composition of the atmosphere is taken as constant over the entire atmosphere, or in several layers of different compositions, [e.g., *Singhal et al.*, 1992] or if the energy losses of the different neutral species are assumed proportional [*Régo et al.*, 1994].

The MC approach is a stochastic method based on the collision-by-collision algorithm [e.g., *Onda et al.*, 1999]. A large number of particles are considered and followed in the simulated atmosphere. The MC approach avoids the use of an energy grid. This can be of great interest for problems with electron energies ranging over five orders of magnitude, as it is the case in the high latitude terrestrial atmosphere [*Solomon*, 1993]. The drawback of the MC method is that it is computationally expensive, since it requires a large number of particles to reduce the statistical noise.

Among those presented, the most accurate method is to explicitly solve the Boltzmann equation, using two-stream or multi-stream approaches. In the former, only two pitch angles - up and down along the magnetic field lines - are considered which drastically simplifies the solution. However, for strongly anisotropic incident flux, a multi-stream approach is more suitable [*Lummerzheim et al.*, 1989]. The Boltzmann equation is applied to suprathermal electrons using the guiding center approximation [*Rees*, 1989]. The collisions between electrons and ambient neutrals are treated as discrete energy loss, whereas the energy transfer to thermal ambient electrons is considered continuous and thus introduced as a dissipative force [*Stamnes and Rees*, 1983]. Because the electron aurora on Earth is often relatively stable over several minutes and the collisional frequencies are of the order of 1-100 s^{-1}, the steady-state situation is commonly assumed. One exception is the application to flickering aurora as described by *Peticolas and Lummerzheim* [2000].

The SBE approach has been widely used in planetary studies. Examples of the two-stream approach include applications to the nightside ionosphere of Venus [*Cravens et al.*, 1983], the Venus ionopause boundary layer [*Gan et al.*, 1990], the ionosphere of Mars [*Haider et al.*, 1992], the Jovian atmosphere [*Grodent et al.*, 2001], and the atmosphere of Titan [*Gan et al.*, 1992]. The multi-stream approach has been applied to the terrestrial high-latitude [*Strickland et al.*, 1989; *Lummerzheim et al.*, 1989] and low-latitude [*Rassoul et al.*, 1993] ionosphere, the Jovian ionosphere [*Perry et al.*, 1999] and the atmosphere of Titan [*Galand et al.*, 1999].

Validation of these models can be performed by ensuring particle and energy conservation and by comparison with other models [*Lummerzheim and Lilensten*, 1994; *Solomon*, 1993]. Comparison with laboratory measurements allows one step further in the validation process, with the checking of the cross section accuracy [*Lummerzheim and Lilensten*, 1994]. Terrestrial *in situ* observations of the particle flux by rocket experiments is a further step for electron transport validation [*Lummerzheim et al.*, 1989].

The geometry of the magnetic field line needs to be taken into account in the models, as the electron trajectory is bounded to it. Magnetic field lines are usually considered vertical or slanted by the dip angle for the terrestrial auroral regions. However, on Venus, the magnetic field lines are assumed parallel to the day-

side ionopause [*Gan et al.*, 1990]. On the nightside, the magnetic field lines are considered horizontal in the magnetized ionosphere of Venus, assuming strong solar wind dynamic pressure conditions [*Cravens et al.*, 1983]. Another interesting example is Titan, whose ionosphere interacts with the corotating Saturnian plasma in which the magnetic field is frozen. Simple configurations have been adopted, like those proposed by *Gan et al.* [1992] and *Galand et al.* [1999]. The most appropriate approach for such a complicated case is to use MagnetoHydroDynamic (MHD) models [*Keller et al.*, 1994; *Ledvina and Cravens*, 1998]. Examples of such models applied to several solar system bodies are presented in *Chapters II.3 and II.4*.

The electron transport model provides the volume excitation rate associated with any excited state of the atmospheric species. If no additional atmospheric production or loss of the excited state occurs, the computation of the volume emission rate can be performed directly. That is usually the case for prompt auroral emissions, such as the 130.4 nm and 135.6 nm OI emission lines produced in the nightside ionosphere of Venus. Using an electron transport code and comparing the PVO/UVS data with the simulated brightness ratio of these lines, *Fox and Stewart* [1991] showed strong evidence for direct excitation of the OI lines by impact of low energy electrons on atomic oxygen. On the other hand, an electron transport code alone cannot model the terrestrial mid-latitude aurora where the oxygen lines are induced by precipitation of O^+ and O from the ring current [*Ishimoto et al.*, 1994; *Tinsley et al.*, 1994]. An auroral emission unique to electron precipitation is the continuum X-ray radiation produced via bremsstrahlung by the energetic electrons themselves, as illustrated by *Østgaard et al.* [1998] for the Earth and by *Singhal et al.* [1992] for Jupiter. In both cases, for the computation of the column-integrated emission rate, not only the electron transport but also the photon transport need to be described (see Section 3.4).

3.2. Kinetic Ion/Neutral Transport Model

Energetic protons, as well as heavier ions and neutrals, have been measured throughout the solar system. Their origins are as diverse as the solar wind, the planetary ionosphere, or the rings and satellites. Energetic protons and oxygen ions near Venus are most likely produced by photoionization of Venusian upper atmospheric H and O accelerated by solar wind pick-up process to few eV [*Luhmann et al.*, 1994]. Pick-up processes have also been invoked for the Martian atmosphere to explain the production of energetic protons and oxygen ions, with Phobos as a partial source of neutral water molecules. Model calculations have shown that a substantial number of the pickup ions re-impact both Venus and Mars [*Luhmann and Kozyra*, 1991]. At Mars, the re-entering flux undergoes significant neutralization, which can lead to an escape or a loss in the atmosphere. Modeling also shows that charge-exchange between solar wind protons and the Martian upper atmosphere (H, H_2, O) in the subsolar region yields suprathermal H atoms with energies less than 1 keV [*Kallio et al.*, 1997]. On the Earth, protons of both solar and ionospheric origin and oxygen ions of ionospheric origin have been measured over the auroral ovals in the keV range [*Hardy et al.*, 1989; *Rees*, 1989]. MeV protons are a major energy source over the polar cap during solar particle events [*Patterson et al.*, 2001]. At mid-latitudes energetic protons and oxygen ions precipitate from the ring current and, below 20° in latitude the precipitating population is solely hydrogen and oxygen atoms produced by neutralization of the ring current ions [*Rassoul et al.*, 1993; *Ishimoto et al.*, 1994; *Bauske et al.*, 1997]. Due to the presence of an extended corona observed on Saturn and Uranus by Voyager, similar processes yielding H atom precipitation are expected in these giant planets [*Bhardwaj*, 1997]. Heavy ions, mainly oxygen and sulfur ions, but also sodium and carbon ions, have been detected in the magnetosphere of Jupiter by Ulysses [*Lanzerotti et al.*, 1992]. These ions are thought to have escaped as neutrals from the Io plasma torus but were photoionized before they could entirely escape Jupiter's magnetosphere and gain energy as they diffuse in toward Jupiter [*Eviatar and Barbosa*, 1984]. Energetic oxygen ions are also thought to originate from the icy moons by surface sputtering induced by energetic particles precipitating from the planet's magnetosphere. In the case of Saturn, rings are suggested to be another source of oxygen ions. Finally nitrogen ions observed in the magnetospheres of Saturn and Neptune are most likely Titanogenic and Tritonogenic, respectively.

Energetic ions and neutrals interact primarily with the atmospheric neutral species through ionization, excitation, dissociation, charge-changing reactions, and scattering. In dense plasma regions, ions also interact with the ambient plasma through Coulomb collisions leading to heating [e.g., *Kozyra et al.*, 1997]. However, each type of energetic particles interact differently with the atmosphere. For example, for the terrestrial atmosphere, an incident proton beam loses more than 90% of its energy to electron and ion production, whereas about 50% and 2% of the incident energy flux goes into ionization when He^+ and O^+ are the precipitating ions,

respectively [*Ishimoto and Torr*, 1987]. Similar models are used to describe their transport in an atmosphere. The three types of approaches, CSDA, SBE, and MC, introduced for electron transport in section 3.1 are also found in the literature on ion/neutral transport modeling [*Decker et al.*, 1996].

The major difference between electron and ion/ neutral transport models come from the many ways ions/ neutrals experiences charge-changing reactions. These include capture (also called charge exchange or charge transfer) and stripping of an electron, which are not components of electron transport codes. For the CSDA models, the composition of the beam needs to be fixed and it is usually assumed that the beam is at charge equilibrium, as illustrated by *Singh* [1991] for hydrogen transport in the Jovian and Saturnian atmospheres or by *Cravens et al.* [1995] for oxygen transport in the Jovian atmosphere. The validity of the assumption of charge equilibrium is discussed by *Régo et al.* [1994; 1999] and by *Kharchenko et al.* [1998]. For hydrogen transport, when the incident particles have energies less than few keV, the equilibrium fraction favors the neutral state and a pure H atom beam can be assumed. That is the case for the ring current H atom precipitation on Saturn and Uranus [*Bhardwaj*, 1997]. For the solution of the Bolztmann equations, two coupled equations need to be solved, one for the charge state and the other for the neutral state [e.g., *Galand et al.*, 1997]. Due to the complexity of this system, only one charge state can be taken into account. The CSDA and MC methods are more appropriate to X-ray emission simulations where one must consider all charge states from heavy neutral atom up to fully stripped particle [*Cravens et al.*, 1995; *Kharchenko et al.*, 1998].

For SBE and CSDA methods, the spreading of the beam - due to the neutral paths independent of the magnetic field lines - is neglected or considered via an attenuation coefficient applied to the center of the beam [*Jasperse and Basu*, 1982]. The space variables are reduced to one coordinate taken along the magnetic field line. Such an approach is justified if the incident beam is assumed to be sufficiently broad. It is definitily not appropriate for transport of incident neutral atoms as their mean free path can be very large, or for ions with very large gyro-radii like those around Titan [*Galand et al.*, 1999] or Mars [*Brecht*, 1997]. In these cases a two or three spatial dimensional approach is needed. MC simulations can easily accomodate this as was illustrated by *Kallio and Barabash* [2001] for the Martian atmosphere bombarded by energetic H atoms. Note that for ring current particles, the time dependence needs to be included due to the ring current decay [*Bauske et al.*, 1997]. Finally, the effect of the magnetic field on the pitch angles of the energetic ions and neutrals is discussed for the case of proton aurora on Earth by *Galand and Richmond* [1999].

The magnetic field configuration is a concern for ion transport and needs to be properly accounted [e.g., *Luhmann and Kozyra*, 1991]. However, for low energy H atoms, like those precipitating into the Martian atmosphere [*Kallio and Barabash*, 2001], one need not consider the magnetic field geometry. Finally, the validation of the ion/neutral transport models [*Decker et al.*, 1996; *Galand et al.*, 1997] is performed in the same way as for electron transport codes (section 3.1).

Inside an energetic ion/neutral beam, the particles themselves can be excited by the interaction with the atmosphere. An example of such emissions is the Doppler-shifted H emissions produced by the energetic H atoms through electron capture of protons and through direct excitation. H Lyman α, H_α, and H_β Doppler-shifted emissions in the terrestrial auroral atmosphere are unique signatures of proton precipitation [e.g., *Lummerzheim and Galand*, 2001; *Burch et al.*, 2001]. Such a signature is more difficult to observe for the giant planets as their atmosphere is mainly composed of H_2 and H. Another emission produced directly by the energetic particles is the X-ray emission coming from the excitation of the energetic heavy ions (K-shell lines). Using a CSDA transport model applied to the Jovian atmosphere, *Cravens et al.* [1995] estimated the X-ray emissions induced by highly charged excited MeV oxygen and sulfur ions. Comparisons of their simulations with ROSAT data support the assertion that the Jovian X-ray emissions are produced primarily by heavy ion precipitation.

The ion/neutral transport models are not sufficient to study other auroral emissions induced by an incident ion or neutral beam. Under proton precipitation, the H_2 Lyman and Werner bands in the Jovian atmosphere are primarily induced by the secondary electrons produced through ionization and electron stripping [*Régo et al.*, 1994]. Secondaries are also responsible for the $O(^1D)$ excited state yielding the red line in proton aurora in the terrestrial atmosphere [*Lummerzheim et al.*, 2001].

3.3. Atmospheric Model

Excitation of atmospheric species is produced by impact of energetic particles with ambient neutrals. The excited state can also be produced by reactions between atmospheric species, such as dissociative recombination and, at dayside, by the solar photons and induced pho-

toelectrons. Photons are emitted when there is radiative decay to lower excited states. If the lifetime of the excited state is large, various other loss processes, such as collisional deactivation (quenching), can become dominant. Cascading from one excited state to a lower one, energy transfer between atmospheric constituents, radiative recombination, reaction with ambient thermal electrons, and atom-atom or ion-atom interchange reaction are sources of production or loss of the excited state. These processes involve atmospheric species, which can undergo diffusion and transport by neutral winds, or minor neutral or ionospheric species, whose density is perturbed by the particle precipitation. The atmosphere is also heated by interaction with the energetic particles yielding thermal IR emissions, like in the hydrocarbon layer of Jupiter [*Kim*, 1988]. For these cases, one needs a comprehensive atmospheric model, which solves the conservation equations or the first moments of the Boltzmann equations to infer the emission rate of the auroral emissions. The first 5 moments solve the density, momentum, and energy equations. Fluid models including chemical, hydrodynamic, and MHD models, are described in detail in *Chap I.3* for the ionospheric species. Global three-dimensional models, such as the General Circulation Model (GCM), have been developed for terrestrial planets [see *Chap IV.1*], for Jupiter [see *Chap IV.2*], and for moons with significant atmosphere [see *Chap IV.4*], A coupling of these models with a kinetic transport code is usually too time consuming and fast computational schemes must be developed to account for precipitating particles as source of excitation, ionization, or heating [e.g., *Roble and Ridley*, 1987].

Often chemical equilibrium is assumed for the excited state when computing the excited state density, n^*. The emission rate η is derived from: $\eta = A\ n^*$, with A being the Einstein coefficient for spontaneous radiative transition in s^{-1} [e.g., *Rees*, 1989]. Note that the computation of the total emission rate may require one to consider the contribution of additional emission sources, such as chemiluminescent reactions, which occur when fragments or ions produced by dissociation or ionization recombine and emit, as illustrated for the Venusian nightglow by *Fox* [1992].

An example of the computation of the nightside aurora requiring the use of a chemical atmospheric model is proposed by *Haider et al.* [1992] for the red line OI (630.0 nm) in the Martian atmosphere. A kinetic electron transport code is used to compute the $O(^1D)$ production rate induced by the precipitating electrons as well as the ion production rates. The incident electron flux was derived from the Phobos 2 data for the magnetotail and for the plasma sheet. Assuming chemical equilibrium, the ion densities, especially O_2^+, CO_2^+, and O^+, were determined and the excitation rate of the red line associated with the dissociative recombination of O_2^+ was derived. The authors reproduced the red line emission including quenching of the excited state $O(^1D)$ by O and CO_2. A brightness of 35 R and 20 R were obtained for the magnetotail and the plasma sheet, respectively. As a result of lower incident electron flux, these values are very small compared with the brightness of the red line in the terrestrial auroral oval, whose value reaches several kR for active magnetic conditions [*Rees and Roble*, 1986]. *Haider et al.* [1992] also showed that in the Martian nighttime atmosphere the red line is dominantely airglow [see *Chap I.5*]. The $O(^1D)$ is mainly produced by recombination of O_2^+, whereas in the terrestrial auroral regions the impact by energetic electrons is the dominant source of excitation [*Solomon et al.*, 1988].

Another example of auroral emissions is the IR radiation produced by vibrationally excited H_3^+ in the Jovian atmosphere. Analysis of the 2 μm and 4 μm IR region emissions can provide some insight into this species (abundance, temperature). In order to simulate the IR radiations produced by H_3^+ in the dayside auroral Jovian ionosphere, *Kim et al.* [1992] used an electron transport code and an ionospheric model solving the continuity equation for H^+, H_2^+, several vibrational levels of H_3^+ and H. Hydrogen atom and electron densities were self-consistently computed through several iterations between the kinetic code and the atmospheric model. A significant source of H_3^+ is the charge transfer from H^+ to vibrationally excited H_2 producing H_2^+, which quickly reacts with H_2. Molecular diffusion is important at high altitudes and the momentum equation for several vibrational levels of H_2 was also solved. The theoretical ionospheric calculations were coupled with the vibrationally excited H_2 calculations in a self-consistent manner. *Kim et al.* [1992] showed that precipitation of 10 keV electrons with a flux of 1 erg cm^{-2} s^{-1} produced vibrational distribution of H_2 and H_3^+ that are consistent with the IR emissions observed in Jovian auroral regions.

3.4. Photon transport model

Photons produced in aurora can undergo multiple scatterings before being absorbed in the atmosphere or escaping through its lower or upper boundary. If the kinetic atmospheric temperature is sufficiently high, the spectral line is Doppler broadened. If the neutral winds

are significant, the line is Doppler shifted. For emissions by energetic particles, the line is both Doppler shifted and broadened. The last step for deriving the spectral profile and the brightness of an emergent auroral emission, that is, its column integrated volume emission rate, is the description of the transport of photons in the atmosphere, also called radiative transfer.

At first, we consider the case of atmospheric absorption with negligible scattering (true absorption). The absorption by atmospheric constituents of a photon of wavelength λ, emitted at an altitude z_0 is evaluated through the optical thickness τ_λ of the atmosphere, also called absorption optical depth. For observations along the nadir, τ_λ is defined as the product of the absorption cross section and the density of the absorbing gas integrated between z_0 and the altitude of the observer. The medium is said to be optically thin to radiation of wavelength λ if $\tau_\lambda \ll 1$; Otherwise it is optically thick and the atmospheric absorption is significant and needs to be taken into account. The transport of photons emitted at a given altitude z_0 is described by the Beer-Lambert absorption law:

$$\frac{dI_\lambda^{z_0}}{d\tau_\lambda} = - I_\lambda^{z_0} \qquad (1)$$

where $I_\lambda^{z_0}$ is the brightness associated with the emission at λ and z_0 and is a function of τ_λ, which, in turn, is a function of z. The total auroral brightness, I_λ, of the emergent emission at the top of the atmosphere ($z=z_\infty$) is expressed as:

$$I_\lambda = \frac{1}{\cos\alpha} \int_0^{z_\infty} exp(-\tau_\lambda(z_0, z_\infty))\, \eta_\lambda(z_0)\, dz_0 \qquad (2)$$

where α is the viewing angle from the vertical, η_λ is the emission rate at λ, and z_∞ is the altitude of the top of the atmosphere. Because of inherent field-aligned structure the observations are usually field-aligned and α is the angle between the magnetic field and the vertical.

In the Jovian atmosphere the absorption of the auroral emissions by the hydrocarbon layer can be exploited to derive the characteristics of the precipitating particles [*Yung et al.*, 1982]. The H_2 Lyman and Werner bands (90-170 nm) induced by electrons and protons with energies of several tens of keV are produced at or below the hydrocarbon layer and thus undergo atmospheric absorption before escaping the atmosphere. As the absorption by hydrocarbon takes place mainly at wavelengths shorter than 145 nm, the brightness ratio in two different wavelength bands on either sides of 145 nm, also called the color ratio, is an indicator of the CH_4 abundance above the auroral source. This also infers the penetration depth of the particles and thus the energy of the incident particles at the origin of the aurora [*Régo et al.*, 1999]. Similarly, in the Earth's auroral atmosphere, the absorption by Schumann-Runge bands of O_2 is used to derive the mean energy of incident precipitating electrons [see *Chap II.2*].

In addition to true absorption by atmospheric constituents, the emitted photons can be temporarily absorbed by an atmospheric atom or molecule and immediately re-emitted (scattering). Resonance scattering consists of the absorption of a photon causing a transition to a higher electronic state of the absorber, followed by the emission of a photon as the state decays back to the original lower state. The wavelength of the emitted radiation is nearly the same as the wavelength of the radiation absorbed, but the directional behavior is changed. An example is the OI(130.4 nm) in the Venusian, Martian, and Earth's atmospheres. Another example is the H Lyman α emission in the outer planets. In fluorescent scattering, photons of a given wavelength are absorbed by the atoms of a medium followed by the emission of photons at a wavelength longer than the one of the absorbed photons. Upon each scattering, the upper states can decay to any of a number of lower states other than the ground state, which is called radiative cascade. Both resonance and fluorescence scatterings are limited to transitions that are dipole allowed, whereas energetic particle impact processes can produce excited states that are connected to the ground state by dipole forbidden transitions. Unlike resonance and fluorescence scatterings, Rayleigh scattering is a non-selective scattering process. In the Earth's atmosphere, it occurs over the whole visible range with a $1/\lambda^4$ dependence. The well known consequence of this scattering is the blue color of the sky and the red color of the rising or setting Sun.

In presence of multiple scattering, modeling the emergent auroral emissions at the top of the atmosphere requires one to solve the radiative transfer equation [*Meier*, 1991]:

$$\mu \frac{dI}{d\tau_\lambda} = - I + S \qquad (3)$$

where I is the intensity of the photons, in photons cm^{-2} s^{-1} sr^{-1}, in the direction $\arccos\mu$ defined from the vertical axis. I is a function of the position, propagation direction, wavelength and, in case of multiplet resonance scattering, of line component. In a scattering event, a photon may be emitted in any of the lines of the multiplet sharing a common upper state following the branching ratio. τ_λ is the vertical extinction opti-

cal depth, composed of the extinction due to scattering and true absorption. The source function, S, has several components. The photons are produced within the atmosphere by particle impact excitation, chemical excitation, and multiple scattering, and, at dayside, by the solar radiation incident at the top of the atmosphere. Through multiple scattering, S depends on the intensity I at different location or wavelength. Several approaches can be adopted to solve the radiative transfer equation (3). The general one considers the angle-dependent partial redistribution function (PFR). It is required when scattering occurs outside the Doppler core of the line. The photons retain a memory of their pre-scattered frequency. On the other hand, when incident photons with frequencies in the Doppler core of the line are mostly scattered by atoms with velocities near the thermal speed, one can assume that there is complete incoherence of frequency in the scattering process. This is known as complete frequency redistribution (CFR). It can be applied when the opacity of the scattering atmosphere (usually defined as the vertical optical depth from the top of the atmosphere down to an altitude where scattering is no longer important or where extinction dominates) is less than a few hundred [*Meier*, 1991]. When the scale height is of the order of the planet or satellite's radius, a spherical geometry needs to be considered [*Bush and Chakrabarti*, 1995].

Gladstone [1992] used a radiative transfer model to simulate the resonance scattering of OI (130.4 nm) triplet emission in the terrestrial atmosphere. Because the width of an aurora can be much smaller than the scale height for atomic oxygen in the auroral region, typically in the 25-50 km range, the radiative transfer of OI resonance emissions are distinctly non-plane-parallel in most aurorae. *Gladstone* [1992] for the first time used a two-dimensional radiative transfer code in a realistic way to simulate auroral resonance lines. A plane-parallel approximation in such a case yields a significant over-estimation of the line brightness. On the Earth, a two-dimensional simulations approach the plane-parallel brightness only when the auroral widths are several hundred to several thousand kilometers. Such an analysis can provide new insights about both the structure of the auroral atmosphere and the nature of the aurora itself.

Another example of multiple scattering deals with the H Lyman α line produced in the Jovian aurora, as proposed by *Régo et al.* [1999]. The Ly α photons produced by excitation of the atmospheric H and H_2 by precipitating electrons and protons are emitted at the rest wavelength and thus are strongly resonantly scattered due to the large abundance of atomic hydrogen in the upper atmosphere of Jupiter. The use of a radiative transfer model, along with an electron and a proton transport models (here CSDA), is required to compute the Ly α profile in the Jovian aurora produced by the atmospheric species. The simulation shows a strong reversal of the line, resulting from the absorption of the H Ly α photons by atomic hydrogen becoming resonant near the rest (or center) wavelength. After getting absorbed, the photons are partly reemitted according to the frequency redistribution function at a different wavelength in the wings of the line, where the atmosphere is optically thin. Such a conclusion corroborates earlier finding inferred from HST observations with the GHRS [*Prangé et al.*, 1997]. The width and depth of the reversal are reliable measures of the H column density along the line of sight to the emission source altitude, which is a function of the mean energy of precipitating particles. As the energy of the incident particles increases, the H column density above the emitting layer increases, the emission becomes fainter, and the line profile broadens. For a given penetration depth, the emergent line profile is comparable for proton and electron excitations. However, the analysis can be used for diagnostic of the incident energy, especially in the low energy range where traditional methods using the hydrocarbon absorption signatures in the H_2 spectra [*Régo et al.*, 1999] become inefficient.

4. CONCLUSION AND DISCUSSION

In Section 2 we offered a survey of the auroral emissions which have been observed in the solar system. The origin of these emissions is, in general, common, which allows us to develop similar models presented in Section 3. As a result, models developed for a relatively well-known atmosphere where validation is possible (e.g., the Earth) are often exported to other solar system bodies. On the other hand, the diversity of the plasma sources and atmospheres, and, therefore, of the auroral emissions, illustrated in Table 1, makes it ideal for comparative auroral studies. As discussed in Section 2, the magnetic environment can be intrinsic or induced and a large diversity of magnetospheric geometries is encountered. Auroral emissions give us unique remote sensing of magnetic field configurations and are a tracer of plasma interactions. The aurora at Io's footprint in the Jovian atmosphere further constraints the source region of the Jovian main oval within the current sheet and thereby Jupiter's magnetic field configuration [*Connerney et al.*, 1998]. X-ray emissions from certain

Table 1. Characteristics of solar system bodies around which auroral emissions have been observed.

Body	DM/DT(°)[a]	Excitation source[b]	CD (cm^{-2})[c]	Atmosph. species[d]	Auroral emissions
Venus	<0.0004 /?	e^-,H^+,He^{++}(sw); H^+, O^+, He^+, C^+ (atm)	$2\ 10^{27}$	CO_2, N_2, O, CO	UV (OI)
Earth	1/10.8°	e^-, H^+, He^+(sw); H^+/H, O^+/O (atm)	$2\ 10^{25}$	N_2, O_2, O	γ, X, UV, visible, IR
Jupiter	20,000 /9.6°	e^-,H^+ (sw, atm); O ions (icy moons) S/O/Na ions (Io, Europa	-	H_2, H, hydrocarbons	X(ions), UV(H_2,HI), visible (H), IR (H_3^+,H_2, hydrocarbons)
Io	?	From Io torus and Jovian magnetosph.	Variable	SO_2(volcano), SO, S, O, Na, Cl	UV (OI,CII, SO, SO_2), visible
Ganymede	?/10°	From magnetosph. of Ganym. & Jupit.	$\sim 5\ 10^{14}$ for O_2	O_2, O_3, O	UV at poles (OI), visible at equat.(OI)
Europa	-	From Io plasma torus and Jovian magnetosphere	$\sim 10^{15}$ for O_2	O_2, O_3, O, Na	UV (OI)
Saturn	600/<1°	e^-, H^+ (sw, atm); O^+(icy moons, rings); N^+, N_2^+, H^+(Titan)	-	H_2, H, hydrocarbons	X (e^-), UV (H_2, H) IR (H_3^+)
Uranus	50/58.6°	sw, atm	-	H_2, H, CH_4	X(?), UV (H_2,H)
Neptune	25/47°	N^+, H^+ (Triton)	-	H_2, H, CH_4	X(?), UV (H_2)
Comets	-	heavy ions (sw)	Variable	H_2O, CO, CO_2	Soft X-rays

[a]Dipole moment (Earth = 1) / Dipole tilt.
[b]The list is not exhaustive. "sw" and "atm" stand for solar wind and atmospheric origin, respectively.
[c]Column density from surface.
[d] The atmospheric species given here are the major constituents in the region of energy deposition.

comets attest to the interaction of the solar wind heavy ions with the cometary gas [*Lisse et al.*, 2000].

Auroral emissions are an indicator of the source of energetic particles and can be used for remote sensing of the characteristics of the incident particles (type, energy, flux). The OI 135.6 nm auroral emission observed around Io is prompt and is not resonantly scattered. It can be used as a valuable probe of the Jovian plasma conditions at Io, where the auroral brightness increases with the density of plasma torus at Io's location [*Retherford et al.*, 2000b]. The analysis of O and CO emissions on the nightside of Venus has shown evidence of precipitation of soft electrons [*Fox and Stewart*, 1991]. On the Earth, auroral emissions observed from ground are used to investigate proton and electron dynamics during magnetospheric substorms [e.g., *Deehr and Lummerzheim*, 2001]. From space, the entire auroral oval has been imaged by Polar in UV and X-rays for estimating the characteristics of the incident soft and hard electron populations, a crucial information for space weather applications [see *Chap II.2*].

The aurora is also a fingerprint of the atmospheric composition. Analysis of UV spectroscopic observations revealed the presence of an O_2 atmosphere on Europa [*Hall et al.*, 1995]. Recently, chlorine was detected in the auroral equatorial spots at Io [*Retherford et al.*, 2000a]. The detection of H_3^+ in the Jovian atmosphere through IR observations in the auroral regions was the

first astronomical spectroscopic identification of these spectral bands in the universe [*Drossart et al.*, 1989]. From spectroscopic analysis of the IR lines produced in the Jovian atmosphere, not only the abundance of emitting constituents was derived, but also the temperature of the ionosphere from H_3^+ emissions [*Drossart et al.*, 1993a] and of the stratosphere from the hydrocarbons emissions [*Drossart et al.*, 1993b].

Diverse magnetic configurations and origins, energetic particle sources and their energy ranges, and differing atmospheric constituents, all contribute to make comparative auroral study a rich field. If we consider X-ray emissions for instance, they are produced by electron capture of heavy solar wind ions with ambient neutrals at some comets [*Lisse et al.*, 2000]; by magnetospheric heavy oxygen and sulfur ions precipitating from the $L = 8 - 12$ region of Jupiter to high latitude ionosphere [*Bhardwaj and Gladstone*, 2000a]; by heavy ions precipitating from the inner Jovian magnetosphere (with a significant non-auroral contribution from reflected or fluoresced solar X rays) [*Gladstone et al.*, 1998]; by energetic electrons through bremsstrahlung emissions in the high latitude regions of Earth [*Østgaard et al.*, 2000] and probably at Saturn [*Ness and Schmitt*, 2000]. The known processes producing X-rays at certain comets are also expected to occur at Venus and Mars, offering a remote sensing of the interaction of the solar wind with these non-(or at least low) magnetized planets [*Cravens*, 2000; *Holmström et al.*, 2001]. It is interesting to note that the emitted X-ray power within the 0.1-2. keV band for the comet Hyakutake (4×10^8 W) [*Lisse et al.*, 1996] and the one for Jupiter (10^9 W) [*Waite et al.*, 1994] are similar. The brightness near Hyakutake is weak, of the order of 0.01 R [*Mumma et al.*, 1997], whereas in the auroral region of Jupiter it is larger than 0.1 R [*Waite et al.*, 1997]. However, the emission area around the comet is very wide, extending well beyond cometocentric distances of 200,000 km [*Lisse et al.*, 1996]. The incident energy of the particles is also very different, of the order of 1 keV/amu (atomic mass unit) for the solar wind high-charged state, heavy ions interacting with the cometary neutrals [*Cravens*, 1997], while it is about 1 MeV nucleon^{-1} or more for the oxygen and sulfur ions precipitating into the auroral region of Jupiter [*Waite et al.*, 1994]. As a result, the spectra emitted around a comet are quite different from those emitted in Jupiter's atmosphere. So, despite a similar mechanism of production of X-rays by interaction of heavy ions with a neutral gas, different characteristics are found between auroral emissions on comet Hyakutake and on Jupiter.

Another interesting emission for comparative auroral study is the OI 135.6 nm line observed around several bodies of the solar system. In the terrestrial high latitude regions, the oxygen line is produced over the auroral ovals by keV particles and its brightness is on the order of kR. On the nightside of Venus, the oxygen emissions appear as patches, with a typical brightness of 1 R above the background [*Fox and Stewart*, 1991]. On the Galilean moons the OI 135.6 nm brightness varies from up to several kR on Io [*Roesler et al.*, 1999] down to 250 R on Ganymede [*Feldman et al.*, 2000] and to less than 100 R on Europa [*Hall et al.*, 1995]. On Europa the OI UV aurora is diffuse, whereas it is seen at the equator of Io and at the poles of Ganymede. This provides a clear example of the different interactions of the planetary magnetospheric plasma with moons. The intrinsic magnetic field of Ganymede prevents the Jovian plasma to reach low latitude regions, whereas a complex current system occurs at the highly conductive Io and less strong interaction takes place at Europa.

If aurora offers us a unique and extremely valuable probe of our solar system, its analysis and modeling can encounter challenges. To estimate the auroral brightness from observations is not always easy. In addition to auroral origin, the observed signal can be terrestrial airglow or solar scattering occurring in the dayside atmosphere or on cometary dust. The signal could be due to solar reflection on a surface like at Europa, or emissions photo-chemically produced or associated with the volcanic plumes of Io. A careful estimation of these other sources is a critical step in the auroral analysis. As for modeling, although the basic equations are similar, the uncertainties on many parameters can prevent retrival of information, such as on the energetic particle source, from the analysis of auroral emissions. Some knowledge of, or assumptions regarding, the atmospheric densities and the incident energetic particles is required. Uncertainties in cross sections or in reaction rates are limiting factors for the analysis. If the emissions undergo resonance scattering it is difficult to track the location of the source. In the presence of energetic neutral particles or for limb observations, the analysis is complicated by the likely contribution of multiple sources of different characteristics. For incident energetic electrons or ions, the configuration of the magnetic field lines needs to be known. MHD and hybrid particle models of the plasma environment are crucial tools for answering this concern [see *Chapters II.3 and II.4*].

Finally, the definition we propose for aurora can be debated. Some would consider it to be too inclusive, others too exclusive. Having taken the task of inves-

tigating aurora in our solar system, which offers such diverse emissions and having concern for clarity and consistency, we propose this definition, with its limitations, and try to follow it as closely as possible throughout the paper. Choosing to focus on optical emissions, we have excluded radio emissions, which are observed in the auroral regions of Earth and of the giant planets. Even though energetically negligible, they are the only means to determine the rotation rate of the giant planet interiors [*Zarka*, 1998]. In our definition we assume the energetic particles interact with an atmosphere. We could extend it to the surface of planets and moons. Soft X-ray observations with ROSAT have revealed an unexpected emission at the dark side of the moon [*Schmitt et al.*, 1991]. This emission probably results from energetic solar-wind electrons striking the moon's surface. Another body deprived of a significant atmosphere is Mercury, where time variable high-latitude enhancements of visible sodium radiations from the exosphere have been seen [*Killen et al.*, 1990; *Killen and Ip*, 1999]. One proposed explanation is that, during magnetic substorms, sputtering of surface minerals by precipitating ions releases sodium vapor in the polar regions [*Potter and Morgan*, 1990]. The observed emission is sunlight scattered at the sodium resonance lines. With the absence of limb brightnening, the polar aurora at Ganymede could be the result of a similar interaction of energetic particles with its surface. On the Earth, Stable Auroral Red (SAR) arcs seen in mid-latitude night sky are sub-visual emissions from oxygen at 630.0 nm. They reflect the slow energy loss from the ring current ions, but the exact sequence of physical processes occurring between the energy source and the emission region is a matter of continuing debate [*Kozyra et al.*, 1997]. Heat flux can be one possible energy transfer process down to the ionosphere. If this process is found to be the dominant mechanism, will it be a reason to rename SAR arcs? Our main concern is not how to name the emissions observed at Mercury and in the Earth's mid-latitude. It is their analysis that offers us a unique probe of the solar wind interaction with Mercury's magnetosphere or of the energy loss in the ring current of the Earth.

With improving observational techniques, with new space missions and with more comprehensive modeling tools, investigation of electromagnetic radiations, in particular multispectral observations of aurora, along with complementary measurements (plasma, neutral atmosphere), is expected to provide a wealth of precious information on our solar system and to lead us to further understanding of interactions taking place at solar system bodies, such as planets, moons, and comets.

Acknowledgments We are very grateful to M. Mendillo for enthusiastic and constructive discussions on the subject. We also thank J. Clarke, T. Cravens, and T. Cook for their helpful and valuable comments. Support for this work was provided by TERRIERS - Univ. Space Res. Assoc. Contract 1500-05 and by National Science Foundation (NSF) Grant ATM-0003175.

REFERENCES

Abreu, V.J., R.W. Eastes, J.H. Yee, S.C. Solomon, and S. Chakrabarti, UV nightglow production near the magnetic equator by neutral particle precipitation, *J. Geophys. Res.*, *91*, 11,365-11,368, 1986.

Anderson, K., Balloon measurements of X-rays in the auroral zone, in *Auroral phenomena*, M. Walt ed., 46, Stanford University Press, 1965.

Anderson, P.C., D.L. McKenzie, M. Brittnacher, M. Chen, M. Hairston and M.F. Thomsen, Global storm time auroral X-ray morphology and timing and comparison with UV measurements, *J. Geophys. Res.*, *105*, 15,757, 2000.

Bagenal, F., Empirical model of the Io plasma torus: Voyager measurements, *J. Geophys. Res.*, *99*, 11,043, 1994.

Barbosa, D.D., Auroral precipitation flux of ions and electrons in Saturn's outer magnetosphere, *Planet. Space Sci.*, *38*, 1295-1304, 1990.

Bauske, R., S. Noël, and G.W. Prölss, Ionospheric storm effects in the nighttime E region caused by neutralized ring current particles, *Ann. Geophys.*, *15*, 300-305, 1997.

Bhardwaj, A., Ring current H atom precipitation on the outer planets, *Adv. Space Res.*, *20*, 233-237, 1997.

Bhardwaj, A., and G.R. Gladstone, Auroral emissions of the giant planets, *Rev. Geophys.*, *38*, 295-353, 2000a.

Bhardwaj, A., and G.R. Gladstone, Auroras on Saturn, Uranus, and Neptune, *Adv. Space Res.*, *26*, 1551, 2000b.

Bishop, J., S.K. Atreya, P.N. Romani, G.S. Orton, B.R. Sandel, and R.V. Yelle, The middle and upper atmosphere of Neptune, in *Neptune and Triton*, edited by D. P. Cruikshank, pp. 427-487, Univ. of Ariz. Press, Tucson, 1995.

Brace, L.H., et al., The ionotail of Venus - Its configuration and evidence for ion escape, *J. Geophys. Res.*, *92*, 15, 1987.

Brecht, S.H., Solar wind proton deposition into the Martian atmosphere, *J. Geophys. Res.*, *102*, 11,287-11,294, 1997.

Broadfoot, A.L., et al., UV spectrometer observations of Uranus, *Science*, *233*, 74-79, 1986.

Broadfoot, A.L., et al., UV spectrometer observations of Neptune and Triton, *Science*, *246*, 1459, 1989.

Brown, M.E., and A. Bouchez, Observations of Ganymede's visible aurorae, *Bull. Am. Astron. Soc./ Div. Planet. Sci. Meet.*, *31*, #70.08, 1999. Note: The emissions appear to the concentrated at the equator, not poles, of the satellite.

Burch, J.L., et al., Views of Earth's magnetosphere with the IMAGE satellite, *Science*, *291*, 619-624, 2001.

Bush, B.C., and S. Chakrabati, A radiative transfer model using spherical geometry and partial frequency redistribution, *J. Geophys. Res.*, *100*, 19627-19642, 1995.

Caldwell, L., F.C. Gillett, and A.T. Tokunaga, Possible IR aurorae on Jupiter, *Icarus*, *44*, 667-675, 1980.

Chakrabarti, S., Extreme and far ultraviolet emissions from the polar cap, *J. Geophys. Res.*, *91*, 8065-8072, 1986.

Chakrabarti, S., Ground-based spectroscopic studies of sunlit airglow and aurora, *J. Atmos. Solar-Terr. Phys.*, *60*, 1403-1423, 1998.

Chamberlain, J.W., Physics of the aurora and airglow, Classics in geophysics, *AGU*, Washington, D.C., 1995.

Chen, M.W., and M. Schulz, Simulations of storm time diffuse aurora with plasmasheet electrons in strong pitch angle diffusion, *J. Geophys. Res.*, *106*, 1873-1886, 2001.

Cheng, A.F., Triton torus and Neptune aurora, *Geophys. Res. Lett.*, *17*, 1669-1672, 1990.

Chenette, D.L., D.W. Datlowe, R.M. Robinson, T.L. Schumaker, R.R. Vondrak, and J.D. Winnimgham, Atmospheric energy input and ionization by energetic electrons during the geomagnetic storm of 8 - 9 November, 1991, *Geophys. Res. Lett.*, *20*, 1323-1326, 1993.

Chenette, D.L., et al., Global energy-resolved X-ray images of northern aurora and their mappings to the equatorial magnetosphere, in *Sun-Earth Plasma Connections*, Geophys. Monog. Ser., *109*, J. Burch ed., p.65, *AGU*, Washington, D.C., 1999.

Christensen, A.B., G.J. Romick, and G.G. Sivjee, Auroral OI (989 Å) and OI (1027 Å) emissions, *J. Geophys. Res.*, *82*, 4997-5003, 1977.

Clarke, J.T., Detection of auroral hydrogen Lyman-α emission from Uranus, *Astrophys. J.*, *263*, L105-L109, 1982.

Clarke, J.T., et al., Continued observations of the H Ly α emission from Uranus, *J. Geophys. Res.*, *91*, 8771, 1986.

Clarke, J.T., et al., Hubble Space Telescope imaging of Jupiter's UV aurora during the Galileo orbiter mission, *J. Geophys. Res.*, *103*, 20,217-20,236, 1998.

Clarke, J.T., HST/Cassini Campaign of Jupiter Auroral Observations, *EOS Trans. AGU*, *82*, S252, 2001.

Connerney, J.E.P., M.H. Acnua, and N.F. Ness, The magnetic field of Uranus, *J. Geophys. Res.*, *92*, 15,329, 1987.

Connerney, J.E.P., R.L. Baron, T. Satoh, and T. Owen, Images of excited H_3^+ at the foot of the Io flux tube in Jupiter's atmosphere, *Science*, *262*, 1035-1038, 1993.

Connerney, J.E.P., M.H. Acuna, N.F. Ness, and T. Satoh, New models of Jupiter's magnetic field constrained by the Io flux tube footprint, *J. Geophys. Res.*, *103*, 11,929, 1998.

Craven, J.D., and L.A. Frank, Latitudinal motions of the aurora during substorms, *J. Geophys. Res.*, *92*, 4565, 1987.

Cravens, T.E., Comet Hyakutake X-ray source: Charge transfer of solar wind heavy ions, *Geophys. Res. Lett.*, *24*, 105-108, 1997.

Cravens, T.E., X-ray emission from comets and planets, *Adv. Space Res.*, *26*, 1443-1451, 2000.

Cravens, T.E., S.L. Crawford, A.F. Nagy, and T.I. Gombosi, A two-dimensional model of the ionosphere of Venus, *J. Geophys. Res.*, *88*, 5595-5606, 1983.

Cravens, T.E., D. Wu, and H. Shinagawa, A two-dimensional kinematic dynamo model of the ionospheric magnetic field at Venus, *Geophys. Res. Lett.*, *17*, 2261-2264, 1990.

Cravens, T.E., E. Howell, J.H. Waite Jr., and G.R. Gladstone, Auroral oxygen precipitation at Jupiter, *J. Geophys. Res.*, *100*, 17,153-17,161, 1995.

Decker, D.T., B.V. Kozelov, B. Basu, J.R. Jasperse, and V.E. Ivanov, Collisional degradation of the proton-H atom fluxes in the atmosphere: A comparison of theoretical techniques, *J. Geophys. Res.*, *101*, 26,947-26,960, 1996.

Deehr, C., and D. Lummerzheim, Ground-based optical observations of hydrogen emission in the auroral substorm, *J. Geophys. Res.*, *106*, 33-44, 2001.

Dennerl, K., J. Englhauser, and J. Trümper, X-ray emissions from comets detected in the Röntgen X-ray satellite all-sky survey, *Science*, *277*, 1625-1630, 1997.

Dessler, A.J., *Physics of the jovian magnetosphere*, Cambridge Univ. Press, New York, 1983.

Doe, R.A., M. Mendillo, J.F. Vickrey, L.J. Zanetti, and R.W. Eastes, Observations of nightside auroral cavities, *J. Geophys. Res.*, *98*, 293-310, 1993.

Drossart, P. et al., Detection of H_3^+ on Jupiter, *Nature*, *340*, 539-541, 1989.

Drossart, P., J.-P. Maillard, J. Caldwell, and J. Rosenqvist, Line-resolved spectroscopy of the Jovian H_3^+ auroral emission at 3.5 micrometers, *Astrophys. J.*, *402*, L25-28, 1993a.

Drossart, P., B. Bezard, S.K. Atreya, J. Bishop, J.H. Waite, Jr., and D. Boice, Thermal profiles in the auroral regions of Jupiter, *J. Geophys. Res.*, *98*, 18,803-18,811, 1993b.

Eather, R.H., Majestic lights, The aurora in science, history, and arts, *Amer. Geophys. Union*, Washington, D.C., 1980.

Eviatar, A., and D.D. Barbosa, Jovian magnetospheric neutral wind and auroral precipitation flux, *J. Geophys. Res.*, *89*, 7393-7398, 1984.

Eviatar, A., D.J. Williams, C. Paranicas, R.W. McEntire, B. H. Mauk, and M. G. Kivelson, Trapped energetic electrons in the magnetosphere of Ganymede, *J. Geophys. Res.*, *105*, 5547-5553, 2000.

Eviatar, A., D.F. Strobel, B.C. Wolven, P.D. Feldman, M.A. McGrath, and D.J. Williams, Excitation of the Ganymede UV aurora, *Astrophys. J.*, *555*, 1013-1019, 2001.

Feldman, P.D., M.A. McGrath, D.F. Strobel, H.W. Moos, K.D. Retherford, and B.C. Wolven, HST/STIS UV imaging of polar aurora on Ganymede, *Astrophys. J.*, *535*, 1085-1090, 2000.

Fox, J.L., Models for aurora and airglow emissions from other planetary atmospheres, *Can.J.Phys.*, *64*, 1631, 1986.

Fox, J.L., Airglow and aurora in the atmospheres of Venus and Mars, *Venus and Mars: Atmospheres, ionospheres, and solar wind interactions*, Proceedings of the Chapman Conference, Balatonfured, Hungary, June 4-8, 1990, *AGU*, Washington, D.C., 191-222, 1992.

Fox, J.L., and A.I.F. Stewart, The Venus UV aurora - a soft electron source, *J. Goephys. Res.*, *96*, 9821, 1991.

Galand, M., and A.D. Richmond, Magnetic mirroring in an incident proton beam, *J. Geophys. Res.*, *104*, 4447, 1999.

Galand, M., J. Lilensten, W. Kofman, and R.B. Sidje, Proton transport model in the ionosphere 1. Multistream approach of the transport equations, *J. Geophys. Res.*, *102*, 22261-22272, 1997.

Galand, M., J. Lilensten, D. Toublanc, and S. Maurice, The ionosphere of Titan: Ideal diurnal and nocturnal cases, *Icarus*, *140*, 92-105, 1999.

Gan, L., T.E. Cravens, and M. Horanyi, Electrons in the ionopause boundary layer of Venus, *J. Geophys. Res.*, *95*, 19,023-19,035, 1990.

Gan, L., C.N. Keller, and T.E. Cravens, Electrons in the ionosphere of Titan, *J. Geophys. Res.*, *97*, 12,137, 1992.

Gao, S., C.W. Ho, T.S. Huang, and C.J. Alexander, Uranus's magnetic field and particle drifts in its inner magnetosphere, *J. Geophys. Res.*, *103*, 20,257-20,265, 1998.

Geballe, T.R., M.-F. Jagod, and T. Oka, Detection of H_3^+ IR

emission lines in Saturn, *Astrophys. J.*, *408*, L109, 1993.
Geissler, P.E., A.S. McEwen, W. Ip, M.J.S. Belton, T.V. Johnson, W.H. Smyth, and A.P. Ingersoll, Galileo imaging of atmospheric emissions from Io, *Science*, *285*, 870, 1999.
Gladstone, G.R., Auroral resonance line radiative transfer, *J. Geophys. Res.*, *97*, 1377-1387, 1992.
Gladstone, G.R., J.H. Waite Jr., and W.S. Lewis, Secular and local time dependence of Jovian X ray emissions, *J. Geophys. Res.*, *103*, 20,083-20,088, 1998.
Gladstone, G.R., et al., X-ray Emissions from Jupiter, *EOS Trans. AGU*, *82*, S301, 2001.
Gordiets, B., Excitation of vibrational emission bands in aurora and airglow, *Can. J. Phys.*, *64*, 1673-1678, 1986.
Gringauz, K.I., M.I. Verigin, T.K. Breus, and T. Gombosi, The interaction of electrons in the optical umbra of Venus with the planetary atmosphere - The origin of the nigthttime ionosphere, *J. Geophys. Res.*, *84*, 2123-2127, 1979.
Grodent, D., J.H. Waite, Jr., and J.-C. Gerard, A self-consistent model of the Jovian auroral thermal structure, *J. Geophys. Res.*, *106*, 12,933-12,952, 2001.
Haider, S.A., et al., Calculated ionization rates, ion densities, and airglow emission rates due to precipitating electrons in the nightside ionosphere of Mars, *J. Geophys. Res.*, *97*, 10,637, 1992.
Hall, D.T., D.F. Strobel, P.D. Feldman, M.A. McGrath, and H.A. Weaver, Detection of an oxygen atmosphere on Jupiter's moon Europa, *Nature*, *373*, 677-679, 1995.
Hall, D.T., P.D. Feldman, M.A. McGrath, and D.F. Strobel, The FUV oxygen airglow of Europa and Ganymede, *Astrophys. J.*, *499*, 475-481, 1998.
Hardy, D.A., M.S. Gussenhoven, and D. Brautigam, A statistical model of auroral ion precipitation, *J. Geophys. Res.*, *94*, 370-392, 1989.
Herbert, F., and B.R. Sandel, The Uranian aurora and its relationship to the magnetosphere, *J. Geophys. Res.*, *99*, 4143-4160, 1994.
Holmström, M., S. Barabash, and E. Kallio, X-ray imaging of the solar wind - Mars interaction, *Geophys. Res. Lett.*, *28*, 1287-1290, 2001.
Ingersoll, A.P., et al., Imaging Jupiter's aurora at visible wavelengths, *Icarus*, *135*, 251-264, 1998.
Ishimoto, M., and M.R. Torr, Energetic He^+ precipitation in a mid-latitude aurora, *J. Geophys. Res.*, *92*, 3284, 1987.
Ishimoto, M., G.J. Romick, L.J. Paxton, C.-I. Meng, and R.E. Huffman, Night UV spectra (1100 - 2900 Å) at mid and low latitude during a magnetic storm, *Geophys. Res. Lett.*, *19*, 813-816, 1992.
Ishimoto, M., G.J. Romick, and C.-I. Meng, Model calculation of atmospheric emission caused by energetic O^+ precipitation, *J. Geophys. Res.*, *99*, 435-447, 1994.
Jasperse, J.R., and B. Basu, Transport theoretic solutions for auroral proton and H atom fluxes and related quantities, *J. Geophys. Res.*, *87*, 811-822, 1982.
Kallio, E., and S. Barabash, Atmospheric effects of precipitating energetic hydrogen atoms on the Martian atmosphere, *J. Geophys. Res.*, *106*, 165-177, 2001.
Kallio, E., J.G. Luhmann, and S. Barabash, Charge exchange near Mars: The solar wind absorption and energetic neutral atom production, *J. Geophys. Res.*, *102*, 22,183-22,197, 1997.
Keller, C.N., T.E. Cravens, and L. Gan, One-dimensional multispecies magnetohydrodynamic models of the ramside ionosphere of Titan, *J. Geophys. Res.*, *99*, 6511, 1994.
Kharchenko, V., W. Liu, and A. Dalgarno, X ray and EUV emission spectra of oxygen ions precipitating into the Jovian atmosphere, *J. Geophys. Res.*, *103*, 26,687, 1998.
Kharchenko, V. and A. Dalgarno, Spectra of cometary X rays induced by solar wind ions, *J. Geophys. Res.*, *105*, 18,351-18,360, 2000.
Kharchenko, V. and A. Dalgarno, Variability of cometary X-ray emission induced by solar wind ions, *Astrophys. J.*, *554*, L99-L102, 2001.
Killen, R.M., A.E. Potter, and T.H. Morgan, Spatial distribution of sodium vapor in the atmosphere of Mercury, *Icarus*, *85*, 145-167, 1990.
Killen, R.M., and W.H. Ip, The surface - bounded atmospheres of Mercury and the moon, *Rev. Geophys.*, 361-406, 1999.
Kim, S.J., Infrared processes in the Jovian auroral zone, *Icarus*, *75*, 399-408, 1988.
Kim, S.J., and W. Maguire, Two micron quadrupole line emission of H_2 from the Jovian auroral zone, in *NASA Goddard Inst. for Space Studies The Jovian atmospheres*, p.95-98 (SEE N87-17598 09-91), 1986.
Kim, S.J., J. Caldwell, A.R. Rivolo, R. Wagener, and G.S. Orton, Infrared polar brightening on Jupiter. III- Spectrometry from the Voyager 1 IRIS experiment, *Icarus*, *64*, 233-248, 1985.
Kim, Y.H., J.L. Fox, and H.S. Porter, Densities and vibrational distribution of H_3^+ in the Jovian auroral ionosphere, *J. Geophys. Res.*, *97*, 6093-6101, 1992. See Erratum, *J. Geophys. Res.*, *97*, 10,283, 1992.
Kivelson, M.G., et al., Discovery of Ganymede's magnetic field by the Galileo spacecraft, *Nature*, *384*, 537-541, 1996.
Kivelson, M.G., et al., Magnetic field and magnetosphere of Ganymede, *Geophys. Res. Lett.*, *24*, 2155, 1997.
Knudsen, D.J., E.F. Donovan, L.L. Cogger, B. Jackel, and W.D. Shaw, Width and structure of mesoscale optical auroral arcs, *Geophys. Res. Lett.*, *28*, 705-708, 2001.
Kozlovsky, A., and J. Kangas, Characteristics of the postnoon auroras inferred from EISCAT radar measurements, *J. Geophys. Res.*, *106*, 1817-1834, 2001.
Kozyra, J.U., A.F. Nagy, and D.W. Slater, High-altitude energy source(s) for stable auroral red arcs, *Rev. Geophys.*, *35*, 155-190, 1997.
Krasnopolsky, V., On the nature of soft X-ray radiation in comets, *Icarus*, *128*, 368-385, 1997.
Krasnopolsky, V.A., and M.J. Mumma, EUVE spectroscopy of comet Hyakutake: First detection of solar wind charge transfer emissions, *Bull. Am. Astron. Soc./ Div. Planet. Sci. Meet.*, *32*, #40.01, 1070, 2000.
Krasnopolsky, V.A., et al., Detection of soft X-rays and a sensitive search for noble gases in comet Hale-Bopp (C/1995 O1), *Science*, *277*, 1488-1491, 1997.
Lanzerotti, L.J., et al., The hot plasma environment at Jupiter - ULYSSES results, *Science*, *257*, 1518, 1992.
Ledvina, S.A., and T.E. Cravens, A three-dimensional MHD model of plasma flow around Titan, *Planet. Space Sci.*, *46*, 1175-1191, 1998.
Liou, K., P.T. Newell, C.-I. Meng, M. Brittnacher, and G. Parks, Characteristics of the solar wind controlled auroral emissions, *J. Geophys. Res.*, *103*, 17,543-17,557, 1998.

Liou, K., C.-I. Meng, A.T.Y. Liu, P.T. Newell, and R.R. Anderson, Auroral kilometric radiation at substorm onset, *J. Geophys. Res.*, *105*, 25,325-25,331, 2000.

Lisse, C.M., et al., Discovery of X-ray and Extreme UV emission from comet C/Hyakutake 1996 B2, *Science*, *274*, 205-209, 1996.

Lisse, C.M., et al., X-ray and extreme UV emission from comet P/Encke 1997, *Icarus*, *141*, 316-330, 1999.

Lisse, C.M., et al., Discovery of charge exchange emission from C/LINEAR 1999 S4, *Bull. Am. Astron. Soc./ Div. Planet. Sci. Meet.*, *32*, #40.02, 1070, 2000.

Luhmann, J.G., and J.U. Kozyra, Dayside pickup oxygen ion precipitation at Venus and Mars - Spatial distributions, energy deposition and consequences, *J. Geophys. Res.*, *96*, 5457-5467, 1991.

Luhmann, J.G., J.B. Pollack, and L. Colin, The Pioneer mission to Venus, *Scientific American*, *270*, 90-97, 1994.

Lummerzheim, D., and J. Lilensten, Electron transport and energy degradation in the ionosphere: Evaluation of the numerical solution, comparison with lab experiments and auroral observations, *Ann. Geophys.*, *12*, 1039-1051, 1994.

Lummerzheim, D., and M. Galand, The profile of the hydrogen Hβ emission line in proton aurora, *J. Geophys. Res.*, *106*, 23-31, 2001.

Lummerzheim, D., M.H. Rees, and H.R. Anderson, Angular dependent transport of auroral electrons in the upper atmophere, *Planet. Space Sci.*, *37*, 109-129, 1989.

Lummerzheim, D., M. Galand, J. Semeter, M.J. Mendillo, M.H. Rees, and F.J. Rich, Emission of OI(630 nm) in proton aurora, *J. Geophys. Res.*, *106*, 141-148, 2001.

Mairan, J.J.D. de, Traité physique et historique de l'aurore boréale, *Imprimerie Royale*, Paris, 1733.

McGrath, M.A., P.D. Feldmann, D.F. Strobel, K. Retherford, B. Wolven, and H.W. Moos, HST/STIS UV imaging of Europa, *Bull. Am. Astron. Soc./ Div. Planet. Sci. Meet.*, *32*, #34.09, 1056, 2000.

Meier, R.R., UV spectroscopy and remote sensing of the upper atmosphere, *Space Sci. Rev.*, *58*, 1-185, 1991.

Meng, C.-I., M.J. Rycroft, and L.A. Frank, Auroral physics, *Cambridge University Press*, Cambridge, 1991.

Mizera, P.F., J.G. Luhmann, W.A. Kolasinski, and J.B. Blake, Correlated observations of auroral arcs, electrons and X-rays from a DMSP satellite, *J. Geophys. Res.*, *83*, 5573-5578, 1978.

Mumma, M.J., V.A. Krasnopolsky, and M.J. Abbott, Soft X-rays from four comets observed with EUVE, *Astrophys. J.*, *491*, L125-L128, 1997.

Neugebauer, M., et al., The relation of temporal variations od soft X-ray emission from comet Hyakutake to variations of ion fluxes in the solar wind, *J. Geophys. Res.*, *105*, 20,949-20,955, 2000.

Ness, J.-U., and J.H.M.M. Schmitt, A serach for X-ray emission from Saturn, Uranus, and Neptune, *Astron. Astrophys.*, *355*, 394-397, 2000.

Onda, K., M. Ejiri, and Y. Itikawa, Analysis of electron auroras based on the Monte Carlo method: Application to active electron arc auroras observed by the sounding rocket at Syowa Station, *J. Geophys. Res.*, *104*, 27991, 1999.

Østgaard, N., et al., Simultaneous measurements of X-rays and electrons during a pulsating aurora, *Ann. Geophys.*, *16*, 148-160, 1998.

Østgaard, N., et al., Global X-ray emission during an isolated substorm - a case study, *J. Atmos. Solar-Terr. Phys.*, *62*, 889-900, 2000.

Owens, A., et al., Evidence for dust-related X ray emission from comet C/1995 O1 (Hale-Bopp), *Astrophys. J.*, *493*, L47-L51, 1998.

Paranicas, C., and A.F. Cheng, Drift shells and aurora computed using the O8 magnetic field model for Neptune, *J. Geophys. Res.*, *99*, 19,433-19,440, 1994.

Paresce, F., S. Chakrabarti, R. Kimble, and S. Bowyer, The 300 to 900 Åspectrum of nightside aurora, *J. Geophys. Res.*, *82*, 10,247-10,252, 1983.

Patterson, J.D., T.P. Armstrong, C.M. Laird, D.L. Detrick, and A.T. Weatherwax, Correlation of solar energetic protons and polar cap absorption, *J. Geophys. Res.*, *106*, 149-163, 2001.

Perry, J.J., Y.H. Kim, J.L. Fox, and H.S. Porter, Chemistry of the Jovian auroral atmosphere, *J. Geophys. Res.*, *104*, 16,451, 1999.

Peticolas, L., and D. Lummerzheim, Time-dependent transport of field-aligned bursts of electrons in flickering aurora, *J. Geophys. Res.*, *105*, 12,895-12,906, 2000.

Petrinec, S.M., F. Fenrich, J. Mobilia, D.L. Chenette, M.A. Rinaldi, and W.L. Imhof, The positions of the auroral energetic electron precipitation region obtained from PIXIE global X-ray observations, *Adv. Space Res.*, *23*, 1735, 1999.

Phillips, J.L., J.G. Luhmann, and A.I.F. Stewart, The Venus UV aurora - Observations at 130.4 nm, *Geophys. Res. Lett.*, *13*, 1047-1050, 1986.

Potter, A.E., and T.H. Morgan, Evidence for magnetospheric effects on the sodium atmosphere of Mercury, *Science*, *248*, 835-838, 1990.

Prangé, R., D. Régo, D. Southwood, P. Zarka, S. Miller, and W. Ip, Rapid energy dissipation and variability of the Io-Jupiter electrodynamic circuit, *Nature*, *379*, 323-325, 1996.

Prangé, R., et al., Detection of self-reversed Ly α lines from the Jovian aurorae with the Hubble Space Telescope, *Astrophys. J.*, *484*, L169-L173, 1997.

Rassoul, H.K., R.P. Rohrbaugh, B.A. Tinsley, and D.W. Slater, Spectrometric and photometric observations of low-latitude aurorae, *J. Geophys. Res.*, *98*, 7695, 1993.

Régo, D., R. Prangé, and J.-C. Gérard, Auroral Lyman α and H_2 bands from the giant planets: 1. Excitation by proton precipitation in the Jovian atmosphere, *J. Geophys. Res.*, *99*, 17,075-17,094, 1994.

Régo, D., R. Prangé and L. Ben Jaffel, Auroral Lyman α and H_2 bands from the giant planets 3. Ly α spectral profile including charge exchange and radiative transfer effects and H_2 color ratios, *J. Geophys. Res.*, *104*, 5939, 1999.

Rees, M.H., *Physics and Chemistry of the Upper Atmosphere*, *Cambridge Atmos. Space Sci. Ser.*, Cambridge Univ. Press, New York, 1989.

Rees, M.H., and R.G. Roble, Excitation of O(^{1}D) atoms in aurorae and emission of the forbidden OI 6300-Åline, *Can. J. Phys.*, *64*, 1608-1613, 1986.

Rees, M.H., A.I. Stewart, and J.C.G. Walker, Secondary electrons in aurora, *Planet. Space Sci.*, *17*, 1997, 1969.

Retherford, K.D., et al., HST-Galileo Io campaign: Images of sodium and oxygen emissions in eclipse *EOS Trans. AGU*, *80*(40), F612, 1999.

Retherford, K.D., et al., Io's UV aurora: Detection of neutral hydrogen and neutral chlorine, *Bull. Am. Astron. Soc./ Div. Planet. Sci. Meet., 32*, #34.06, 1055, 2000a.

Retherford, K.D., H.W. Moos, D.F. Strobel, and B.C. Wolven, Io's equatorial spots: Morphology of neutral UV emissions, *J. Geophys. Res., 105*, 27,157-27,165, 2000b.

Roble, R.G., and E.C. Ridley, An auroral model for the NCAR thermospheric general circulation model (TGCM), *Ann. Geophys., 5*, 369-382, 1987.

Roesler, F.L., et al., FUV imaging spectroscopy of Io's atmosphere with HST/STIS, *Science, 283*, 353, 1999.

Sandel, B.R., F. Herbert, A.J. Dessler, and T.W. Hill, Aurora and airglow on the night side of Neptune, *Geophys. Res. Lett., 17*, 1693-1696, 1990.

Sandholt, P.E., and C.J. Farrugia, Multipoint observations of substorm intensifications: The high-latitude aurora and electron injections in the inner equatorial plasma sheet, *Geophys. Res. Lett., 28*, 483-486, 2001.

Saur, J., F.M. Neubauer, D.F. Strobel, and M.E. Summers, Io's UV aurora: Remote sensing Io's interaction, *Geophys. Res. Lett., 27*, 2893-2896, 2000.

Schmitt, J. H. M. M., S. L. Snowden, B. Aschenbach, G. Hasinger, E. Pfeffermann, P. Predehl, and J. Trumper, A soft X-ray image of the moon, *Nature, 349*, 583-587, 1991.

Sharber, J.R., et al., Observations of the UARS Particle Environment Monitor and computation of ionization rates in the middle and upper atmosphere during a geomagnetic storm, *Geophys. Res. Lett., 20*, 1319-1322, 1993.

Share, G.H., and R.J. Murphy, Atmospheric gamma rays from solar energetic particles and cosmic rays penetrating the magnetosphere, *J. Geophys. Res., 106*, 77-92, 2001.

Singh, V., Proton energy deposition and EUV emission in the Jovian and the Saturnian atmospheres, *Indian J. Radio Space Phys., 20*, 140-149, 1991.

Singhal, R.P., S. Chakravarty, A. Bhardwaj, and B. Prasad, Energetic electron precipitation in Jupiter's upper atmosphere, *J. Geophys. Res., 97*, 18,245-18,256, 1992.

Siscoe, G., What determines the size of the auroral oval?, in Auroral physics, p.159, *Cambridge University Press*, Cambridge, 1991.

Smith, B.A., et al., The Galiean satellites and Jupiter - Voyager 2 imaging science results, *Science, 206*, 927-950, 1979.

Solomon, S.C., Auroral electron transport using the Monte Carlo method, *Geophys. Res. Lett., 20*, 185-188, 1993.

Solomon, S.C., P.B. Hays, and V.J. Abreu, The auroral 6300 Å emission - Observations and modeling, *J. Geophys. Res., 93*, 9867-9882, 1988.

Spenner, K., W.C. Knudsen, R.C. Whitten, P.F. Michelson, K.L. Miller, and V. Novak, On the maintenance of the Venus nightside ionosphere - Electron precipitation and plasma transport, *J. Geophys. Res., 86*, 9170-9178, 1981.

Stadsnes, J., K. Aarsnes, and J. Bjordal, X-ray imaging of the aurora, *Adv. Space Sci., 20*, 1043-1054, 1997.

Stamnes, K., and M.H. Rees, Inelastic scattering effects on photoelectron spectra and ionospheric electron temperature, *J. Geophys. Res., 88*, 6301-6309, 1983.

Stenbaek-Nielsen, H.C., et al., Aircraft observations conjugate to FAST: Auroral arc thicknesses, *Geophys. Res. Lett., 25*, 2073-2076, 1998.

Stephan, A.W., S. Chakrabarti, and D.M. Cotton, Evidence of ENA precipitation in the EUV dayglow, *Geophys. Res. Lett., 27*, 2865-2868, 2000.

Stephan, A.W., S. Chakrabarti, K. Dymond, S. Budzein, S. Thonnard, and R. McCoy, FUV equatorial aurora during geomagnetic storms as observed by LORAAS, *J. Geophys. Res.*, In Press, 2001.

Strickland, D.J., R.R. Meier, J.H. Hecht, and A.B. Christensen, Deducing composition and incident electron spectra from ground-based auroral optical measurements. I - Theory and model results. II - A study of auroral red line processes. III - Variations in oxygen density, *J. Geophys. Res., 94*, 13,527-13,563, 1989.

Strickland, D.J., R.E. Daniell, Jr., J.R. Jasperse, and B. Basu, Transport-theoretic model for the electron-proton-hydrogen atom aurora. 2: Model results, *J. Geophys. Res., 98*, 21,533-21,548, 1993.

Tinsley, B., R. Rohrbaugh, M. Ishimoto, M. Torr and D. Torr, Middle- and low-latitude emissions from energetic neutral atom precipitation seen from ATLAS1 under quiet geomagnetic conditions, *J. Geophys. Res., 99*, 19577, 1994.

Trafton, L.M., S. Miller, T.R. Geballe, J. Tennyson, and G.E. Ballester, H_2 quadrupole and H_3^+ emission from Uranus: The Uranian thermosphere, ionosphere, and aurora, *Atrophys. J., 524*, 1059-1083, 1999.

Trauger, J.T., et al., Saturn's hydrogen aurora: Wide field and planetary camera 2 imaging from the Hubble Space Telescope, *J. Geophys. Res., 103*, 20,237-20,244, 1998.

Vallance Jones, A., *Aurora, D. Reidel publising company*, Dordrecht, Holland, 1974.

Vallance Jones, A., et al., The Aries auroral modelling campaign - Characterization and modelling of an evening auroral arc observed from a rocket and a ground-based line of meridian scanners, *Planet. Space Sci., 39*, 1677, 1991.

Vasavada, A.R., A.H. Bouchez, A.P. Ingersoll, B. Little, C.D. Anger, and the Galileo SSI Team, Jupiter's visible aurora and Io footprint, *J. Geophys. Res., 104*, 27,133-27,142, 1999.

Verigin, M.I., et al., On the possible source of the ionization in the nigthttime Martian ionosphere. I - PHOBOS 2 HARP electron spectrometer measurements, *J. Geophys. Res., 96*, 19,307-19,313, 1991.

Vij, K.K., D. Venkatesan, W.R. Sheldon, J.W. Kern, J.R. Benbrook, and B.A. Whalen, Simultaneous investigation of parent electrons and bremsstrahlung X-rays by rocket-borne detectors, *J. Geophys. Res., 80*, 2869-2875, 1975.

Waite, J.H., Jr., et al., ROSAT observations of the Jupiter aurora, *J. Geophys. Res., 99*, 14,799-14,809, 1994.

Waite, J.H., et al., Equatorial X-ray emissions: Implications for Jupiter's high exospheric temperatures, *Science, 276*, 104-108, 1997.

Waite, J.H., et al., Multispectral observations of Jupiter's aurora, *Adv. Space Res., 26*, 1453-1475, 2000.

Wegmann, R., H.U. Schmidt, C.M. Lisse, K. Dennerl, and J. Englhauser, X-rays from comets generated by energetic solar wind particles, *Planet. Space Sci., 46*, 603-612, 1998.

Winckler, J.R., L. Peterson, R. Arnoldy, and R. Hoffman, X-rays from visible aurorae at Minneapolis, *Phys. Rev., 110*, 1221, 1958.

Yung, Y.L., G.R. Gladstone, K.M. Chang, J.M. Ajello, and S.K. Srivastava, H_2 fluorescence spectrum from 1200 to 1700 Å by electron impact - Lab study and application to Jovian aurora, *Astrophys. J.*, *254*, L65-L69, 1982.

Zarka, P., Auroral radio emissions at the outer planets: Observations and theories, *J. Geophys. Res.*, *103*, 20,159-20,194, 1998.

M. Galand and S. Chakrabarti, Center for Space Physics, Boston University, 725 Commonwealth Avenue, Boston, MA 02215. (email: mgaland@bu.edu; supc@bu.edu)

Airglow Processes in Planetary Atmospheres

T. G. Slanger

Molecular Physics Laboratory, SRI International, Menlo Park, California

B. C. Wolven

Johns Hopkins University, Applied Physics Laboratory, Laurel, Maryland

We summarize results of recent studies of the airglows of the terrestrial and the outer planets. Since the comprehensive review of Fox a decade ago, there are new data on the Venus nightglow, including results from Pioneer Venus in the UV and visible spectral regions. Ground-based observations of the visible nightglow have also been carried out. In the infrared, there is considerable new information from ground-based observations of the O_2 Infrared Atmospheric band system. There have been no new visible/IR airglow measurements of Mars, and there are in any case no nightglow data to compare with the terrestrial and Venusian nightglows. For the terrestrial atmosphere, there is new data originating with sky spectra from large telescopes. Lidar measurements have been used extensively to study the chemistry and dynamics of metal atoms, and improvements have been made in satellite monitoring of visible emissions, particularly the nightglow continuum. The Voyager UVS provided a wealth of observations of outer planet airglow and aurorae; in the ensuing decades, these data have been supplemented by a variety of ground-based near IR and space-based UV observations. The long-standing mystery surrounding the excess brightness of giant planet dayglow emissions appears to have been resolved in favor of a predominantly solar excitation mechanism. Uncertainties in the intensity and variability of solar ultraviolet and soft X-ray emissions present the most fundamental difficulty in interpreting the dayglow spectra of the giant planets.

INTRODUCTION

Airglow is an important signature of any planet's atmosphere. Most of the planets, and even some of their satellites, have substantial atmospheres, and comparison of their airglows is revealing as to their composition and other characteristics. From the emissions we learn about energy flow, dynamics, and photochemistry, and the similarities and differences between planets often carry surprising information. This short contribution is designed to review work carried out over the last decade, with an emphasis on the Earth and Venus for the inner planets, and on Jupiter for the outer planets.

The subject of the airglows of Venus and Mars was extensively reviewed by J. L. Fox in an AGU monograph in 1992 [*Fox*, 1992], and no attempt will be made to go over the ground covered in that publication. For work prior to that date, the reader should consult Fox's review, as well

Atmospheres in the Solar System: Comparative Aeronomy
Geophysical Monograph 130

10.1029/130GM06

Table 1. Some Airglow Processes in Terrestrial Planetary Atmospheres

Examples	Day/Night
Photodissociation	
$O_3 + h\nu \rightarrow O(^1D) + O_2(a^1\Delta_g)$	D
Energy transfer	
$O(^1D) + O_2 \rightarrow O(^3P) + O_2(b^1\Sigma_g^+)$	D,N
Resonant scattering	
N_2^+,He,Na + $h\nu \rightarrow N_2^+$*,He*,Na*	D
Atom recombination	
$O + O + M \rightarrow O_2^* + M$	D,N
Dissociative recombination	
$O_2^+ + e \rightarrow O^* + O$	D,N
Radiative recombination	
$O^+ + e \rightarrow O^*$	D,N
Chemistry	
$H + O_3 \rightarrow OH(\upsilon) + O_2$	N

as others by Solomon [1991], Meriwether [1989], and Bates [1995] on the terrestrial atmosphere. .

Over the last 10 years, there have been no missions to Mars or Venus with airglow-viewing capabilities in the spectral region above 200 nm. The last such mission to Venus was the Pioneer Venus Orbiter (PVO) [*Stewart and Barth*, 1979; *Stewart et al.*, 1980], from which many airglow observations were made in the ultraviolet spectral region, most data having been collected in the first two years of the mission, 1979-1981. Data were also obtained of unresolved visible nightglow emission from the PVO [*Bougher and Borucki*, 1994]. For Mars, the existing dayglow data were obtained on the Mariner missions of 1969 [*Barth et al.*, 1971], and with the sole exception of negative results reported from the 1974 Mars 5 mission [*Krasnopol'sky and Parshev*, 1979], there are no nightglow data at all from that planet. Although the Venus nightglow can be studied from ground-based observatories, as described below, Mars (and all of the outer planets) presents a problem in this respect because as an exterior planet, only a small dark crescent is visible from earth.

Due to space limitations, by and large the discussion of the terrestrial planets is limited to nightglow emission in the visible and near-IR spectral regions. There are extensive dayglow measurements for all three planets from satellites and space probes, and the interested reader can consult some of the original literature. Excellent reviews are available [*Meier* (1991); *Paxton and Anderson*, 1992] and recent results from the FUSE mission are described by Krasnopolsky and Feldman (2001) and by Feldman et al. (2001). HUT mission results exist for Venus and Mars [*Feldman et al.*, 2000], and details of the Galileo and Cassini flybys of Venus can be found in Hord et al. (1991).

It is useful to define terms when it comes to planetary airglows. The definition given by Chamberlain [1995] is that airglow is non-thermal atmospheric radiation, excluding aurora and cataclysmic events such as lightning and meteor trails. Typically dayglow and nightglow are considered separately, although in fact the phenomena are not fully separable. There is a tendency, particular among astronomers, to consider nightglow as weak aurorae, but this is erroneous; aurorae have specific characteristics that are not found in the nightglow. The term dayglow should be limited to radiation that requires solar action, either directly through photoabsorption or indirectly by energetic photoelectrons.

There are strong similarities between dayglow and aurorae, because fast electrons are important in both cases, but aurorae and nightglow have few points in common. Most clearly, excited states of N_2 and N_2^+ are dominant auroral features, whereas these are rarely seen in the nightglow. Where there are features in common, they often have different sources.

In Table 1 are listed different types of processes that are to be seen in airglows of the terrestrial planets, with an indication of whether these are considered as dayglow or nightglow phenomena. As may be seen, there is really only one case where the reaction should not be claimed to occur in the dayglow, and that is for the H + O_3 reaction, the source of the OH Meinel band emission. This is because the ozone lifetime to solar radiation is on the order of 100-sec, so that during the day the mesospheric ozone density is strongly depleted, reforming at sunset. The asterisks refer to unspecified excited states.

The examples in Table 1 are processes associated with the terrestrial atmosphere, but each one of them can also be significant in the atmospheres of Venus and/or Mars. As O_2 emissions are important components of the nightglows of both the earth and Venus, and presumably Mars as well, we refer the reader to the O_2 potential energy curves reproduced in Chapter III.6. Included is the $^5\Pi_g$ state, about which there have been conjectures over many years [*Bates*, 1995]. It is now established that this state is important in O-atom recombination, and communicates with the Herzberg states - $A^3\Sigma_u^+$, $A'^3\Delta_u$, and $c^1\Sigma_u^-$ - so that an overall understanding of O_2 photochemistry and photophysics requires consideration of this entity [*Huestis et al.*, 1999].

In contrast to the terrestrial planets (and satellites with dense "terrestrial" atmospheres), the airglow of the giant planets is dominated by emission from various forms of hydrogen (H_2 and H in the far ultraviolet (FUV) region of the spectrum, and H_3^+ in the infrared), with minor

contributions from helium (He I λ584) in the extreme ultraviolet, and the recently detected hydrocarbon fluorescence in the near infrared. Observation of giant planet atmospheres in the FUV region of the spectrum began in 1967 with a sounding rocket experiment [*Moos et al.*, 1969], followed by the launches of the Pioneer series of spacecraft and the Copernicus satellite in the 1970's. The end of the decade saw tremendous advances in observing capability with the launch of a spaceborne observatory, the International Ultraviolet Explorer (IUE), in January 1978, permitting the first systematic observations of ultraviolet emission from the upper atmospheres of Jupiter, Saturn, and Uranus [*Durrance et al.*, 1982; *Clarke*, 1982; *Clarke et al.*, 1986; *Clarke*, 1988; *McGrath et al.*, 1989]. The launch of IUE was followed closely by Voyager Ultraviolet Spectrometer (UVS) observations of Jupiter during the Voyager flybys in 1979 [*Broadfoot et al.*, 1979, 1981; *McConnell et al.*, 1980; *Dessler et al.*, 1981], and subsequent observations of Saturn, Uranus, and Neptune as the Voyagers journeyed outward in the solar system [*Shemansky and Ajello,* 1983; *Broadfoot et al.*, 1989; *Yelle et al.*, 1989]. Jupiter has been the most intensely scrutinized of the outer planets; the majority of the outer planets discussion will concentrate on the Jovian airglow, with comparisons and contrasts to its more distant cousins when appropriate. A comprehensive review of the upper atmosphere of Uranus, including detailed discussion of both the Uranian dayglow and dayglow processes common to all of the outer planets, may be found in Strobel et al. [1991]. A thorough analysis of all major aspects of giant planet airglow (containing many details that must of necessity be omitted here) may be found in Bhardwaj [1997].

THE VENUS NIGHTGLOW

Previous Knowledge Base

Until recently, the history of Venus nightglow studies has been limited to three areas. The first observations were made by the Venera 9/10 orbiters in 1975, which viewed the atmosphere in the visible spectral region, at 400-750 nm [*Krasnopol'sky et al.*, 1976; *Krasnopol'sky*, 1986]. A few years later Pioneer Venus was put into orbit, and made ultraviolet observations at 110-330 nm [*Stewart et al.*, 1980]. Although there was no spectral resolving capability in the visible spectral region to follow up on the Venera observations, the star tracker was used to measure and map the total visible emissions [*Bougher and Borucki*, 1994]. Finally, there have been repeated ground-based measurements of the very strong 1.27 μ $O_2(a^1\Delta_g - X^3\Sigma_g^-)$ 0-0 Infrared Atmospheric band emission [*Noxon et al.*, 1976; *Connes et al.*, 1979; *Crisp et al.*, 1991; *Crisp et al.*, 1996].

The Venera measurements showed that the predominant visible emission is the v′ = 0 sequence of the $O_2(c^1\Sigma_u^- - X^3\Sigma_g^-)$ system, the Herzberg II bands [*Lawrence et al.*, 1977]. Subsequently, it was recognized that the $v = 0$ sequence of the $O_2(A^3\Delta_u - a^1\Delta_g)$ system - the Chamberlain bands - was also present in the Venera spectrum [*Slanger and Black*, 1978], and later the very weak $O_2(A^3\Sigma_u^+ - X^3\Sigma_g^-)$ Herzberg I system (the predominant terrestrial nightglow emission in the 250-450 nm region) was added [*Krasnopol'sky and Parshev*, 1983]. Conspicuously absent was the 557.7 nm oxygen atom green line, one of the most prominent terrestrial features.

The PVO nightglow observations, below 330 nm, are dominated by NO emission, in the delta ($C^2\Pi$-$X^2\Pi$) and gamma ($A^2\Sigma^+$-$X^2\Pi$) band systems, again from only the v′ = 0 sequences [*Stewart and Barth*, 1979; *Stewart et al.*, 1980]. These two emissions are related, in that the production source is three-body N + O atom recombination, which produces only NO($C^2\Pi$) in the $v = 0$ level. This molecule emits radiation both to the $X^2\Pi$ ground state and to the v = 0 level of the $A^2\Sigma^+$ excited state. The latter then also radiates to the ground state. Similar emission can be seen in the terrestrial nightglow [*Tennyson et al.*, 1986; *Gerard*, 1975].

Although the PVO NO emission spectra are well-defined, the photon collection rate was very low, typically 1-2 photons per spectral scan; the total number collected was only 4000. In the course of the mission one particular sequence stands out, where over a 10-second period the spectral intensity increased by two orders of magnitude. Analysis of the data in both time and space indicated that the cause was probably an atmosphere-grazing meteor, which caused CO_2/N_2 dissociation followed by enhanced N + O recombination [*Huestis and Slanger*, 1993].

Visible Emissions From PVO Star Tracker

The Pioneer Venus instruments were not designed to measure the visible nightglow, but creative use of the star tracker enabled data to be obtained, and maps of undifferentiated visible emission over the 400-800 nm range were created [*Bougher and Borucki*, 1994]. It was found that the observed global intensities were very similar to what had been reported from the Venera 9/10 mission [*Krasnopol'sky and Parshev*, 1983], and in repetitive data collection periods from 1988 to 1990 the range of intensities observed was 3-6 kR, and maps of the dark side emission were constructed.

Since it is presumed that both the Herzberg II and the 1.27 μ $O_2(a$-$X)$ emissions are generated in the same way, by atom recombination, one expectation would be that their intensities fluctuate in a similar manner. This is not necessarily the case, since while the production rates of the

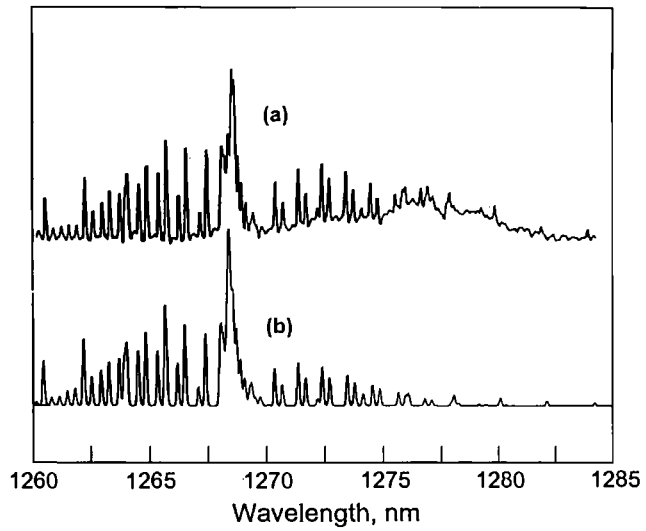

Figure 1. a) Spectrum of the $O_2(a\text{-}X)$ IR Atmospheric 0-0 band in the Venus nightglow [*Crisp et al.*, 1996]. b) DIATOM™ simulation of the band.

two emitting levels should have a fixed ratio, the loss rates will not. This is because the $O_2(a^1\Delta_g$, v = 0) level is impervious to quenching [*DeMore et al.*, 1997], whereas one expects the $O_2(c^1\Sigma_u^-$, v = 0) level to be significantly quenched. The only literature value for $O_2(c^1\Sigma_u^-)$ removal by CO_2 refers to the v = 9 level [*Copeland et al.*, 1996], for which the 300 K rate coefficient is 1.5×10^{-11} cm^3 s^{-1}; the value for the v = 0 level is likely to be substantially less.

Bougher and Borucki [1994] extensively discuss and compare the star tracker observations with the Venus thermospheric general circulation model (VTGCM) output and the $O_2(a^1\Delta_g)$ measurements on the Venus night side. They point out that the variations in emission intensities are not significantly related to the O-atom production rate on the day side, but are presumably a consequence of internal gravity waves generated at the cloud tops, which cause relatively rapid changes in the emitting layer altitudes. The only existing limb scans are from the Venera data, which indeed show marked variations in emission altitude (but not intensity) for the O_2 Herzberg II system. [*Krasnopol'sky and Parshev*, 1983] The importance of obtaining more information on the altitudes of the different emissions is evident.

The $O_2(a\text{-}X)$ Infrared Atmospheric Band Emission

Ground-based observations of $O_2(a\text{-}X)$ IR Atmospheric 0-0 band emission commenced with the work of Noxon et al. [1976] Although there is net terrestrial emission from this band as viewed from the ground, one can take advantage of the relative velocities of the two planets to get an adequate Doppler shift, thus separating the two emissions. Typical measurements are made with ~12 km/s relative velocities, corresponding to a 0.05 nm shift. Thus, if the instrumental resolution is better than this figure, good separation is achieved. Figure 1 shows an example of the 0-0 band spectrum [*Crisp et al.*, 1996] along with a 186 K simulation; the agreement is seen to be excellent.

The surprise to the $O_2(a\text{-}X)$ observations, now confirmed several times, is the magnitude of the emission intensity, considerably higher than the same emission in the terrestrial nightglow [*McDade et al.*, 1987]. It corresponds approximately to the CO_2 photodissociation rate, so that the efficiency with which CO_2 is dissociated and converted to $O_2(a)$ must be close to 100%. Moreover, on Venus the emission rate is similar on the day and the night side [*Connes*, 1979], so that atoms travel around to the night side without appreciable loss. Attempts have been made to find catalyzed reactions that could account for some of this production rate, but candidates investigated to date have proven to be inadequate [*Leu and Yung*, 1987].

In addition to the high average $O_2(a\text{-}X)$ nightglow intensity, excursions to much higher intensities are common, as well as periods and locations where the radiation is effectively extinguished [*Crisp et al.*, 1996]. Bright areas are often adjacent to dark areas, and the intensities in a particular region can change by more than 20% in an hour. The dynamic range of these changes is a factor of 50 or more, and there is little precedent in the terrestrial nightglow for variations as large.

The $O_2(a\text{-}X)$ 0-0 band emission can be very bright, both at Mars and Venus. The high intensity seen in the Mars dayglow is consistent with O_3 as detected by the Mariner 8/9 UV absorption measurements, since ozone photodissociates under UV radiation to produce almost a unity yield of $O_2(a^1\Delta_g)$. The 0-0 band has been seen in both the dayglow and the nightglow on Venus, and in this case the relatively small intensity difference has been interpreted as indicating that O_3 is not present. Nevertheless, the potential for ozone generation exists, because the $O_2(a\text{-}X)$ emission represents substantial O_2 production. From Pioneer Venus data [*Paxton*, 1985] it was reported that at 110 km the dayside O_2 mole fraction is 0.003, equivalent to a density of 3×10^{11} cm^{-3}, thus on the order of the O-atom density, and comparable to the terrestrial O_2 density at the same altitude. O_2 is lost by chemical interaction as it diffuses downwards, but it is copiously produced by atom recombination.

Keck/1999 and APO/2001

With modern astronomical instruments it is not difficult to view the nightglow of Venus, so the paucity of studies over the last twenty years is surprising. As the Venera 9/10 observations were made with a spectrometer having only 2.5 nm resolution [*Krasnopol'sky et al.*, 1976], it was important to make ground-based observations at much higher resolution. In 1999, an opportunity arose to use the 10-meter Keck I telescope on Mauna Kea to view Venus during engineering time. The HIRES echelle spectrometer was used for the measurements, with a spectral resolution of 0.02 nm. Figure 2 shows the results of this study in the region of the oxygen green line, the O(^{1}S-^{1}D) transition [*Slanger et al.*, 2001]. Because Venus was receding from earth the radiation was red-shifted, and one sees in the spectrum that the Venus green line is shifted the appropriate amount, 0.02 nm, and that the intensity as detected from earth is comparable to that of the terrestrial green line. Furthermore, limb brightening is observed, of a magnitude compatible with the fact that the footprint on the Venus atmosphere has a width of 600 km. The estimated zenith green line intensity was 150 R, with an apparently constant intensity along the measured planetary radius.

The Venera 9/10 missions reported an average $O_2(c\text{-}X)$ Herzberg II emission intensity of 2.7 kR [*Krasnopol'sky and Parshev*, 1983], and Bougher and Borucki [1994] subsequently measured 3-6 kR from the PVO. This O_2 emission was also detected in the Keck/HIRES measurements, although the individual lines are considerably weaker than the green line. The 551 nm $c\text{-}X$ 0-10 band was analyzed, leading to the determination that the total system intensity was on the order of 5 kR, and thus compatible with the earlier measurements.

The green line with an intensity of 150 R would have been easily detectable in the relatively low-resolution Venera 9/10 spectra [*Krasnopol'sky and Parshev*, 1983]. That it was not seen implies that it is highly variable, as is the case for the $O_2(a\text{-}X)$ emission. The observation has now been repeated, using the 3.5-meter APO telescope in New Mexico [*Chanover et al.*, 2001]. In this apparition the green line was found to be greatly weakened, with an intensity no more that 20% of the terrestrial line. However, the $O_2(c\text{-}X)$ 0-10 band was quite distinct, even more so than in the Keck/1999 spectrum. It therefore appears that both the constancy of the O_2 emission and the variability of the green line emission are real. This is an unexpected result, because in the terrestrial atmosphere there is a high degree of correlation between the green line and O_2 features which originate with O-atom recombination, such as the $b^1\Sigma_g^+$ - $X^3\Sigma_g^-$ Atmospheric bands and the $A^3\Sigma_u^+$ -$X^3\Sigma_g^-$ Herzberg I bands. [*Stegman and Murtagh*, 1991] It is obvious that to explain these observations it will be necessary to carry out more extensive viewings of Venus, and it will be particularly important to coordinate measurements at different wavelengths, i.e. visible and infrared.

THE TERRESTRIAL NIGHTGLOW

Keck Sky Spectra

Over the last four years, it has been demonstrated that ground-based astronomical sky spectra bring a significant new dimension to the study of the terrestrial airglow. Sky spectra are the background that astronomers collect while

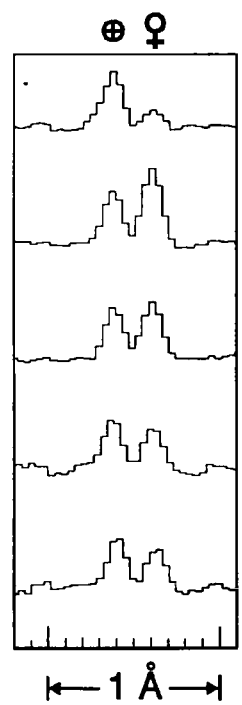

Figure 2. Spectrum of the night side of Venus, measured by Keck/HIRES on Nov. 20, 1999, showing the terrestrial and Venusian atomic oxygen green lines. The Venus line is red-shifted by 0.022 nm with respect to the terrestrial line, as Venus was receding at 12.5 km/s. The observation was made 20 minutes before dawn, and lasted eight minutes. From bottom to top, the Venus green line increases in intensity as the ~600 km region viewed moves from the disc to the limb, and then drops as the view moves off the planet. The five spectra are shifted with respect to an arbitrary zero on the planetary disc by (from bottom to top) 0, 0,95, 2.09, 3.23, and 4.37 arcsec. The terrestrial green line has a wavelength of 557.73 nm.

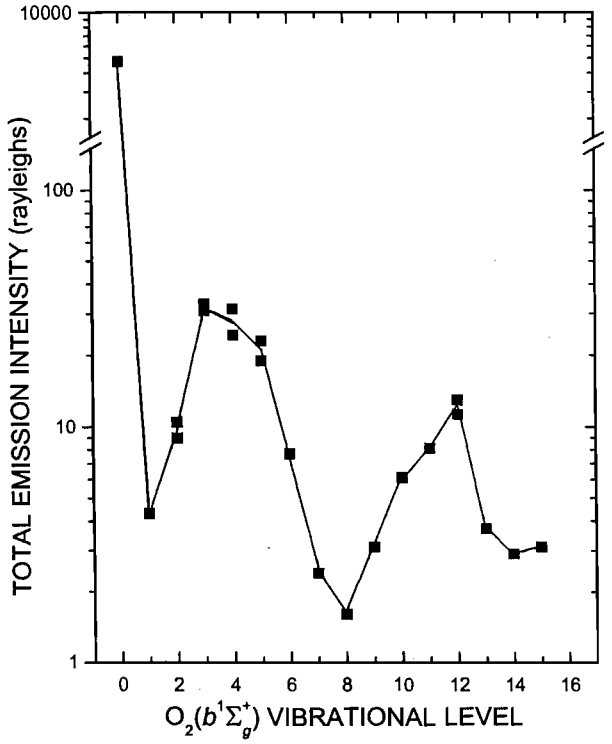

Figure 3. The vibrational distribution of the $O_2(b^1\Sigma_g^+)$ state in the terrestrial atmosphere, from Keck/HIRES. The data used in this analysis are co-added, from 100 hours of observations over a four-year period [*Slanger et al.*, 2001a].

taking spectra of their target objects, and which must ultimately be subtracted so that the target spectrum is cleansed of contaminating light. The sky spectra of course contain the terrestrial airglow, and with the large echelle spectrometers in use, these spectra have both high resolution and broad wavelength coverage. For example, the HIRES spectrometer on the Keck I telescope typically collects light over a 300 nm range with a resolution of 0.02 nm [*Vogt*, 1994].

The initial nightglow study with this instrument was published in 1996 [*Osterbrock et al.*, 1996], and was primarily devoted to cataloguing the OH lines in the 500-900 nm region. In the course of this work, new O_2 Atmospheric system bands were identified, representing the first time that rotationally-resolved $O_2(b\text{-}X)$ emission bands were seen in the atmosphere from $b^1\Sigma_g^+$ vibrational levels above $v = 0$. Further study of co-added spectra resulted in the identification of many $b\text{-}X$ bands between 600 and 900 nm, from a broad distribution of vibrational levels. Figure 3 shows the bimodal distribution observed, extending to $b^1\Sigma_g^+$ ($v = 15$) [*Slanger et al.*, 2000]. These bands are interspersed with many OH lines in the region with far greater intensities, and it is the high spectral resolution that makes identification of the O_2 lines possible.

While it is believed that the $b^1\Sigma_g^+$ ($v = 0$) emission normally measured in nightglow studies results from collisional cascading following oxygen atom recombination, the source of the distribution shown in Figure 3 is not necessarily the same. There are numerous issues yet to be addressed, such as the collisional lifetime of the vibrationally-excited levels, their emission altitude, and an explanation for the trimodal distribution.

There are a variety of other features which are seen for the first time in the atmosphere in these sky spectra. In addition, the high accuracy of the astronomers' wavelength calibration has made it possible to revise certain line positions, in particular those of the $N(^2D\text{-}^4S)$ line pair near 520 nm, and the $K(D_1)$ line at 770 nm [*Slanger and Osterbrock*, 2000b]. In Figure 4 is presented an example of a new feature, the O-atom quintet 5d-3p Rydberg transition at 533 nm, one of approximately twenty oxygen atom multiplets that are seen at 394-927 nm [*Slanger et al.*,

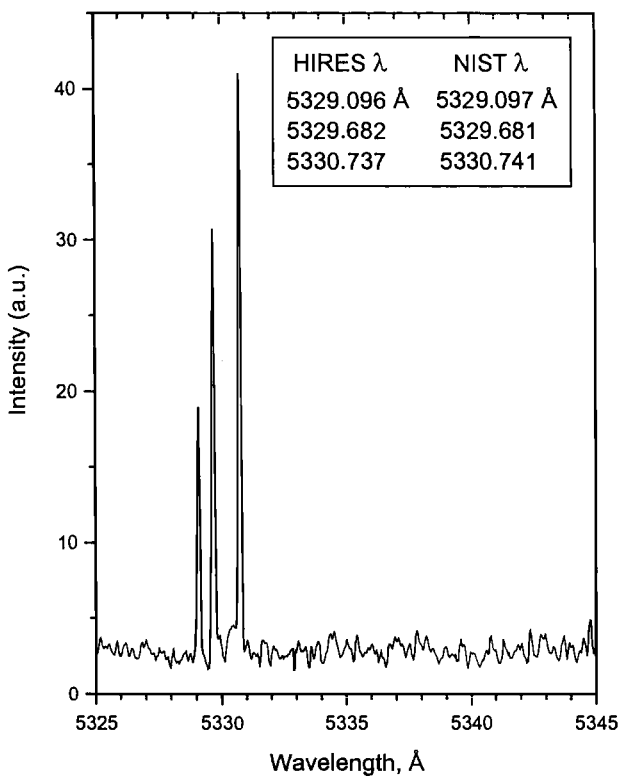

Figure 4. The quintet 5d-3p OI Rydberg lines in the terrestrial atmosphere, as measured by Keck/HIRES, Nov. 11, 1999. 50-minute data accumulation started 80 minutes after local sunset. The HIRES wavelengths are derived from Gaussian fits to the data. The only significant OH feature in this wavelength region is the 6-0 $P_1(4.5)$ line pair at 5330.39 Å.

2001b]. The measured wavelengths in comparison to the NIST line positions is shown. These OI lines are ionospheric features, whose nighttime source is believed to be radiative recombination of O^+ [*Bates*, 1995]. As such, they are equivalent to the more commonly viewed 777.4 and 844.6 nm OI multiplets, which are intrinsically more intense, but must be distinguished from nearby OH lines. The possibility of using the 844.6 nm triplet 3p-3s lines to measure O-atom densities from ground-based Fabry-Perot interferometer measurements has recently been evaluated [*Lancaster et al.*, 2000]. One conclusion is that persistent production of this radiation throughout the night is not adequately understood, and indeed, the Keck measurements bear this out.

Near-UV Comparisons

The possibility of comparison of the nightglow of the near-UV region in the Mars/Earth/Venus system is limited. There is no information on Mars, but the PVO measurements did provide data out to 330 nm. The emissions from N + O recombination are seen to trail away from the peak intensity near 200 nm, and beyond 270 nm there are no recognizable features, except for a line/band near 297 nm [*Huestis and Slanger*, 1993]. Although this is the position of the $O(^1S\text{-}^3P)$ line, the argument has been made that such an identification was inconsistent with the lack of green line in the Venera spectra, and that therefore it was more likely to be an artifact. The basis for this conclusion is now known to be invalid, and therefore it may be that $O(^1S)$ was first detected by the PVO.

In the terrestrial UV nightglow, emission in the two NO emission systems can also be detected in the nightglow [*Tennyson et al.*, 1986; *Gerard*, 1975], although the intensity is substantially weaker than at Venus. The principal near-UV emitters are the O_2 Herzberg states, giving rise to the Herzberg I system ($A^3\Sigma_u^+ \text{-}X^3\Sigma_g^-$), the Chamberlain system ($A'^3\Delta_u \text{-}a^1\Delta_g$), and the Herzberg II system ($c^1\Sigma_u^- \text{-}X^3\Sigma_g^-$), in decreasing order of intensity [*Broadfoot and Kendall*, 1968; *Chamberlain*, 1958; *Slanger and Huestis*, 1981]. The Chamberlain system lies at longer wavelength than the other two, and is strongest at 350-450 nm. It is interesting that in the Venus atmosphere, the order of intensities is just the reverse. Another difference is that these bands in the Venus atmosphere originate exclusively from $v = 0$ in the upper states, whereas in the terrestrial atmosphere the vibrational distribution peaks at much higher levels – near $v = 6$ for the $A^3\Sigma_u^+$ state, $v = 7$ for the $A'^3\Delta_u$ state, and $v = 10$ for the $c^1\Sigma_u^-$ state [*Stegman and Murtagh*, 1988, 1991]. The energies of these levels are approximately equal, 0.2-0.3 eV below the O_2 dissociation limit, which presumably represents the average energy removed by a third body in a stabilizing collision for the nascent O-O molecule.

Lidar Measurements

The upper mesosphere is a region containing relatively large amounts of meteoric material. In the visible spectral region the evidence is two-fold – spontaneous atomic emission from the alkaline metals, and the emissions seen with lidar probing. The best known atomic emission is from sodium, where the 589 nm doublet is a conspicuous nightglow feature. It is generated chemically and exhibits a marked annual cycle, being an order of magnitude more intense in winter than in summer [*Chamberlain*, 1995], also reflected in the sodium concentrations measured by lidar [*Megie et al.*, 1978]. Two of the basic reactions involve ozone and oxygen atoms, but the overall chemistry is quite complex, and the temperature dependences of some of the reactions play a significant role in the morphology of the sodium layer [*Plane*, 1998]. At twilight the emission becomes very bright, as the chemical excitation mechanism is replaced by solar pumping. Recently, the presence of the potassium D_1 line has been noted, with a substantially smaller intensity than that of sodium [*Slanger and Osterbrock*, 2000b]. In contrast to sodium, the potassium concentration does not show a seasonal variation [*Megie et al.*, 1978].

Because the observed metal transitions involve the atomic ground state, they can be artificially excited by laser (lidar) radiation. Much work has been done over the last decade in the lidar excitation of sodium, potassium, calcium, and iron, for the purpose of studying atmospheric dynamics and temperature. As the lidar systems in use have narrow bandwidths, it is possible to measure temperatures from absorption linewidths, and winds from Doppler shifts. Furthermore, altitudes are provided by the signal return times [*Taylor et al.*, 2001; *Alpers et al.*, 1993].

One of the most interesting observations made possible by lidar is the discovery of sporadic layers, where layers of metal, particularly sodium and iron, will suddenly appear with thicknesses measured in tens to hundreds of meters. These layers of enhanced concentrations are found within layers having more usual densities, and they are not necessarily associated with the passage of meteors [*Heinselmann et al.*, 1998; *Clemesha et al.*, 1996; *Swider*, 1992].

NO_2 Continuum Measurements

The observation of the continuum originating with the three-body recombination of $O(^3P)$ and NO has for many years been considered as a method of determining the [O][NO] product, which leads to the determination of either

of the reactants if one of them is known independently. A critical issue that must be addressed in this quest is the choice of viewing wavelengths, since interferences by other emissions is quite possible. This was emphasized in the ETON measurements [*McDade et al.*, 1986], where it was realized that one of the chosen wavelengths for the continuum observations was registering excess emission. This radiation was identified correctly, as subsequent studies demonstrated [*Osterbrock et al.*, 1996], as the $O_2(b^1\Sigma_g^+ - X^3\Sigma_g^-)$ 4-3 band, the strongest of the many $O_2(b\text{-}X)$ bands now known to be in the nightglow [*Slanger et al.*, 2000a].

Measurements have recently been reported from the WINDII instrument on the UARS satellite, in which the NO_2 continuum was viewed through a relatively narrow filter centered at 553.1 nm with 1.6 nm FWHM [*von Savigny et al.*, 1999]. The O-atom densities were derived from VUV measurements [*Greer et al.*, 1986], and the resultant NO densities were an order of magnitude less than had been reported earlier from measurements with much broader filters [*McDade et al.*, 1986a], and is now in much better agreement with models and earlier measurements. The ETON results had raised questions as to whether the continuum emission might not have another source entirely [*Bates*, 1993]. The only apparent structured nightglow emission in the 553 nm region is the O_2 Chamberlain 6-9 band and the weaker 4-8 band, which are faintly discernible in the Keck/HIRES data set, but should not present significant interference. On the other hand, the ETON measurements, with 11- and 12-nm filters at 532 and 540 nm, would have observed the O_2 Herzberg I 3-13, 5-14, and 7-15 bands. These can be clearly seen, though unresolved, in unpublished spectra taken by the MSX satellite (J.-H. Yee, private communication, 2000).

Satellite Spectroscopy

There have been numerous satellites that have made observations of visible/near UV/near IR nightglow emissions over the last decade. In large part, the features monitored have been the strong oxygen emissions seen from the ground – $O(^1S)$, $O_2(b^1\Sigma_g^+ - X^3\Sigma_g^-)$ 0-0, $O_2(a^1\Delta_g - X^3\Sigma_g^-)$ 0-0 – as well as the OH Meinel bands.

It is becoming increasingly clear that emissions are not necessarily confined to single layers. There are now numerous examples where double layers are formed, supporting earlier rocket observations [*Greer et al.*, 1986]. Melo et al. [2000] have shown from observation of the OH 8-3 band that it is not uncommon to see double-peaked emission layers between 80 and 95 km. The structures extend over considerable distances, from hundreds to thousands of kilometers in horizontal extent, and last as long as 1.5 hours.

Very similar observations have been made from the GLO instrument on the space shuttle with respect to $O_2(b^1\Sigma_g^+ - X^3\Sigma_g^-)$ 0-0 band emission [*Broadfoot and Bellaire*, 1999]. Patches of emission are seen with a typical horizontal extent of 3000 km, and these can often terminate quite abruptly, within a few tens of kilometers.

Table 2 represents an attempt to put in one place a list of intensities of the various emission features that have been detected on the three planets. In considering the terrestrial dayglow, it is quite difficult to assign intensities, as they are so dependent on altitude, solar cycle, and latitude, and can only be measured from space. There are dayglow features which can be seen throughout a good part of the night, and thus from the ground, e.g. $O(^1D)$, $N(^2D)$, and the OI Rydberg emissions (777.4 and 844.6 nm), but their intensities are extremely variable, with local time being another variable. We can presume that atom recombination features, e.g. the O_2 Herzberg bands, have comparable intensities day and night, since there is little O-atom diurnal variation near 95 km. On the other hand, ozone has a large diurnal variation, and thus the OH Meinel band emission should be much weaker during the day. For these reasons, we do not attempt to assign terrestrial dayglow intensities. For Venus and Mars dayglow, Fox[1] provides numerous examples of calculated and modeled intensities. It is hoped that this table will be a useful guide.

OBSERVATIONS OF OUTER PLANET AIRGLOW

The initial observations of Jovian ultraviolet emissions identified several features of interest:

- Auroral emission (produced by charged particle excitation of H_2 and H) from the north and south polar regions (Chapter III.4),
- A relatively uniform H_2 airglow across the sunlit hemisphere, spectrally similar (but not identical) to faint aurorae but of differing origin,
- Spatially nonuniform H Lyman α emission peaking near 100° magnetic longitude (the Lyman α "bulge") [*Sandel et al.*, 1980; *Clarke et al.*, 1980], a phenomenon so far unique to Jupiter.

More recently, observations made with instruments on the Hubble Space Telescope (HST) have helped to further our understanding of the morphology and temporal variations of the FUV emissions of H and H_2 on the giant planets. The Hopkins Ultraviolet Telescope (HUT), flown aboard the space shuttle during the Astro-1 (December 1990) and Astro-2 (March 1995) missions, provided a snapshot of the Jovian aurora and dayglow across a broad spectral range (82-185 nm) at higher resolution (~0.3 nm) than was previously available shortward of 115 nm. The Astro-1 and Astro-2 missions took place in periods of minimum (Astro-2) and maximum (Astro-1) solar activity,

Table 2. Estimates of Airglow Intensities for Terra/Venus/Mars

	TERRA(night)	VENUS(day)	VENUS(night)	MARS(day)
O(*558 nm*)	50-300 R[1]	80 kR[8]	<10-150 R[10,11]	20 k16
O_2(*A-X*)	100-600 R[1]		140 R[13]	
O_2(*c-X*)	25-150 R[1]		2.7-6 kR[10-12]	
O_2(*b-X*)	5 kR[2]		<200 R (11)[10]	
O_2(*a-X*)	60 kR[3]	1.5 MR[9]	<0.1-25 MR[13,14]	2-26 MR[17,18]
O_2(*A'-a*)	25-150 R[1]		450-850 R[10]	
NO(*A-X,C-X*)	55 R[4]		500-1500 R[15]	
Na(*590 nm*)	<30-200 R[5]			
K(*770 nm*)	1 R[6]			
OH	450 kR[7]			
	electron-induced			
O(*777 nm*)	0-15 R*			
O(*845 nm*)	0-10 R*			
O(*630 nm*)	0-150 R*		<15 R[10]	
N(*520 nm*)	0-10 R*			

References: 1, *Stegman and Murtagh* [1991]; 2, *McDade st al.* [1986a]; 3, *McDade et al.* [1986b]; 4, *Tennyson et al.* [1986]; 5, *Chamberlain* [1995]; 6, *Slanger and Osterbrock* [2000]; 7, *Turnbull and Lowe* [1989]; 8, *Fox* [1992]; 9, *Connes et al.* [1979]; 10, *Krasnopolsky* [1986]; 11, *Slanger et al.* [2001]; 12, *Bougher and Borucki* [1994]; 13, *Crisp et al.* [1996]; 14, *Crisp* [private communication, 2000]; 15, *Bougher et al.* [1990]; 16, *Barth et al.* [1971]; 17, *Noxon et al.* [1976]; 18, *Traub et al.* [1979].

* The intensities of the electron-induced nightglow features can vary strongly throughout the night. The upper values given here are based on the ratio to the green line intensity seen in early-evening Keck spectra taken in 2000, assuming an intensity of 100 R for the green line. On the same basis, the Na(D) intensity is 10-20% of the green line intensity in March, 2000, and 20-40% in October, 2000, but the range given by Chamberlain [1995] is quoted. The Mars 558 nm dayglow intensity is a measured value, but the Venus intensity is scaled up by Fox [1992].

providing an opportunity to study the response of the Jovian dayglow to variations in solar activity across the entire FUV spectral range. Most recently the Far Ultraviolet Spectroscopic Explorer (FUSE) observed both airglow and auroral emissions on Jupiter and Saturn [*Feldman et al.*, 2001, *Gustin et al.*, 2001].

Ground-based observations of the infrared emissions of H_3^+ [*Ballester et al.*, 1994; *Lam et al.*, 1997; *Miller et al.*, 1997; *Satoh and Connerney*, 1999] have extended our knowledge of the physical conditions, transport mechanisms, and excitation processes taking place in Jupiter's upper atmosphere. H_3^+ emission (produced by radiative relaxation of collisionally excited ions) is the primary radiative cooling mechanism at pressures less than ~ 0.1 μbar in the Jovian thermosphere, and the H_3^+ ion is an important constituent of the Jovian ionosphere. Since H_3^+ is produced by both particle precipitation and solar EUV radiation (with the relative importance of the two production mechanisms varying as a function of latitude and the energy input by precipitating particles and solar EUV photons), it cannot be classified as "purely" airglow. It nevertheless merits attention in any discussion of the thermospheres of the giant planets, as it illuminates the dynamical and chemical processes taking place in regions where the FUV emissions of molecular and atomic hydrogen are minimal (see Chapter IV.2, for further discussion.) While most Jovian H_3^+ ions appear to be produced by auroral activity, spatially resolved observations of Uranus indicate that the fundamental band H_3^+ emission is concentrated towards the subsolar point of the planet [*Trafton et al.*, 1998], suggesting that the ion is produced primarily by solar EUV (see Table 3).

The extent to which Rayleigh-Raman scattering contributes to the observed spectra of the outer planets (and complicates interpretation of dayglow emissions) is determined by the column density at which incoming solar radiation is severely attenuated by hydrocarbon absorption. The homopause, below which absorbing hydrocarbons are well mixed, thus roughly determines the lower boundary of the region where dayglow processes are important. At Lyman α, the optical depth due to methane absorption in the Jovian atmosphere typically reaches unity at a pressure of ~1 μbar, corresponding to a total vertical H_2 column of $\sim 10^{20}$ cm^{-2}. The FUV spectrum of Uranus differs substantially from that of Jupiter and Saturn at longer wavelengths owing to the severe depletion of hydrocarbons in the

Table 3. Principal dayglow processes in outer planet atmospheres

Process	Transitions	Comments
Photoionization	$H_2+h\nu(\lambda<80.4\ nm) \rightarrow H_2^+(\upsilon)+e$	
	$H+h\nu(\lambda<91.2\ nm) \rightarrow H^++e$	
	$He+h\nu(\lambda<50.4\ nm) \rightarrow He^++e$	
Photodissociation	$H_2+h\nu(\lambda<84.5\ nm) \rightarrow H+H$	
Dissociative ionization	$H_2+h\nu(\lambda<80.4\ nm) \rightarrow H^++H+e$	
Resonant scattering	$H,He+h\nu \rightarrow H^*,He^*$	H, He Lyman series
Resonant and	$H_2+h\nu^2 \rightarrow H_2(B,\upsilon) \rightarrow H_2(X,\upsilon')+h\nu$	$B^1\Sigma_u^+$-$X^1\Sigma_g^+$ (Lyman)
fluorescent scattering[1]	$H_2+h\nu^3 \rightarrow H_2(C,\upsilon) \rightarrow H_2(X,\upsilon')+h\nu$	$C^1\Pi_u$–$X^1\Sigma_g^+$ (Werner)
	$H_2+h\nu \rightarrow H_2(B',\upsilon) \rightarrow H_2(X,\upsilon')+h\nu$	$B'^1\Sigma_u^+$-$X^1\Sigma_g^+$
	$H_2+h\nu \rightarrow H_2(D,\upsilon) \rightarrow H_2(X,\upsilon')+h\nu$	$D^1\Pi_u$–$X^1\Sigma_g^+$
	$H_2+h\nu \rightarrow H_2(B'',\upsilon) \rightarrow H_2(X,\upsilon')+h\nu$	$B''^1\Sigma_u^+$-$X^1\Sigma_g^+$
	$H_2+h\nu \rightarrow H_2(D',\upsilon) \rightarrow H_2(X,\upsilon')+h\nu$	$D'^1\Pi_u$–$X^1\Sigma_g^+$
Electron impact fluorescence	$H_2+e \rightarrow H_2^* \rightarrow H_2(X,\upsilon')+h\nu$	All H_2 bands above
Electron impact fluorescence	$H_2+e \rightarrow H_2(E,F)$	Cross section peaks at
via cascade from E,F state[4]	$\rightarrow H_2(B,\upsilon) \rightarrow H_2(X,\upsilon')+h\nu$	low e energy (15.5 eV)
Electron impact excitation	$H_2+e \rightarrow H_2(a^3\Sigma_g^+)$	Produces fast H atoms and
of the a b continuum	$\rightarrow H_2(b^3\Sigma_u^+)+h\nu \rightarrow H+H$	MUV emission
Fluorescent excitation and	$H_2+e,h\nu \rightarrow H_2(B,\upsilon)$	Primarily, but not
predissociation	$\rightarrow H_2(X,\upsilon'>14) \rightarrow H+H$	exclusively Lyman bands
Chemistry	$H_2^+ + H_2 \rightarrow H_3^+(\upsilon=3,4)+H$	

[1] The initial state of the H_2 molecule is assumed to be the ground electronic state, $H_2(X,\upsilon)$

[2] $h\nu(<110.9\ nm)$

[3] $h\nu(<100.9\ nm)$

[4] The *EF* state is responsible for ~80–90% of the cascade contribution, with the remainder coming from the *GK* and *H* states [*Dziczek et al.*, 2000]

Uranian upper atmosphere. The albedos of Jupiter and Saturn are small in the 120–150 nm region; essentially all of the observed emission is a consequence of dayglow processes. The Uranian atmosphere is far more transparent in this spectral region, the result of both weak vertical mixing and more rapid condensation of hydrocarbons in the cold Uranian stratosphere. The Voyager UVS spectra of Uranus show a pronounced increase in intensity longward of 120 nm due to an increasingly large component of Rayleigh-Raman scattered sunlight. A feature at 128 nm in the Voyager UVS spectrum of Uranus has been identified as Raman-scattered ($\upsilon=0 \rightarrow 1$) Lyman α [*Yelle et al.*, 1987, 1989]. This feature is lacking in the spectra of the other giant planets, where the eddy diffusion coefficient (whose value determines the altitude where molecular diffusion becomes important) is orders of magnitude larger; Raman scattering by H_2 in the 211–232 nm region has however been detected in HST Faint Object Spectrograph (FOS) observations of Jupiter. [*Betremieux and Yelle*, 1999].

The eddy diffusion coefficient in the vicinity of the homopause (K_h) has previously been estimated by analysis of either occultation data or the planetary albedo, as observed in the emission of the H Lyman α or He I λ584 line. Lyman α airglow emissions from all of the giant planets have been observed by both earth-orbiting telescopes and spacecraft-based instruments. The Voyager 2 UVS data constitute the only comprehensive set of day and nightside observations for all four bodies; the UVS observed both the bright emissions originating primarily from resonantly scattered solar Lyman α on the daysides of the planets, and the fainter nightglow produced in part by scattering of the interplanetary medium (IPM) Lyman α radiation. Estimates of the eddy diffusion coefficient based on analyses of He I λ584 emissions have been presented for Jupiter [*McConnell et al.*, 1981; *Vervack et al.*, 1995], Saturn [*Parkinson et al.*, 1998], and Neptune [*Parkinson et al.*, 1990]. Recent observations of fluorescence of the ν_3 band of methane in the atmospheres of Jupiter and Saturn [*Drossart et al.*, 1999, *Drossart et al.*, 2001 may better

constrain the eddy diffusion coefficient near the homopause.

Characteristic Airglow Processes in H_2 Atmospheres

H_2 airglow emissions on the outer planets are produced by a combination of resonant and fluorescent scattering of sunlight and photoelectron-impact-induced emission. The principal dayglow processes, including photoionization pathways responsible for the production of photoelectrons, are listed in Table 3. At lower altitudes, near the homopause, He and hydrocarbons play a more important role in the production of photoelectrons as a consequence of their rapidly increasing abundance. Further discussion of photochemical processes may be found in Chapter I.2, and references therein.

Emissions in the Lyman and Werner bands and from the higher lying Rydberg states of H_2 ($B'^1\Sigma_u^+$, $B''^1\Sigma_u^+$, $D^1\Pi_u$, and $D'^1\Pi_u$) appear in the EUV/FUV portion of the spectrum. Excitation of the *a-b* continuum leads to MUV emissions, while the EF/GK/H → B cascade transitions produce MUV, visible, and IR emission. Only the transitions from the Rydberg states (including the cascade contribution to the Lyman bands) are readily visible in dayglow spectra, owing to the large component of reflected sunlight longward of 150 nm; emission in the *a-b* continuum has been observed in the Jovian nightside aurora [*Pryor et al.*, 1998].

During the past decade improved H_2 transition data have been generated based on new laboratory measurements and calculations that take into account the perturbations between four excited electronic states ($B^1\Sigma_u^+$, $B'^1\Sigma_u^+$, $C^1\Pi_u$, $D^1\Pi_u$) and the presence of the centrifugal potential coupling rotational and vibrational motions [*Abgrall et al.*, 1992, 1993a,b, 1994]. Transition rates and energies have been tabulated for individual electronic-vibrational-rotational ($J \leq 30$) transitions of the Lyman, Werner, *B'-X*, and *D-X* band systems of H_2, as well as the total transition rates from each upper level state and the branching ratios for transitions connecting to the vibrational continuum of the ground ($X^1\Sigma_g^+$) electronic state. New profiles of the continuum emission produced by Lyman band transitions to the vibrational continuum of the ground state have also been determined [*Abgrall et al.*, 1997]. Liu et al. [1998, 2000] have updated the measured excitation functions of the Lyman and Werner systems previously determined by Shemansky et al. [1985]. A detailed description of the Abgrall data set and a comparison to laboratory measurements of H_2 emission spectra are presented in Liu et al. [1995]; revised measurements of the EF cascade contribution to the Lyman band system are presented in Dziczek et al. [2000].

Excitation Mechanisms of the Giant Planet Dayglows

Although the species responsible for the dayglow emissions of Jupiter and the other giant planets are indisputable, the means by which the FUV emissions are excited has been difficult to ascertain, despite nearly two decades of observation. The relative contributions of solar resonant and fluorescent scattering and electron impact excitation (due to photoelectrons, perhaps energized by some type of *in situ* acceleration process ("electroglow"), or some more exotic energy source) have been the subject of a lengthy and vigorous debate [cf. *Waite et al.*, 1983, *Shemansky*, 1985, *Yelle et al.*, 1987, *Clarke et al.*, 1987; *Hudson et al.*, 1989, *McGrath et al.*, 1990, *Yelle*, 1988, *Strobel et al.*, 1991, *Feldman et al.*,1993]. The fundamental matter at the heart of this debate is whether or not the observed dayglow intensities can be produced by the solar irradiance, and if they cannot, what is the nature of the energy source responsible for their production?

Liu and Dalgarno [1996], using the HUT Astro-1 dayglow spectrum of Feldman et al. [1993], and a new model of the solar EUV spectrum [*Tobiska and Barth*, 1990; *Tobiska*, 1993], proposed that all of the observed dayglow emission was accounted for by a combination of photoelectron impact (1.0 kR) and solar scattered (1.3 kR) fluorescent excitation. In order to produce a spectrum similar to that observed by Astro-1, they required an H_2 column density of 10^{20} cm^{-2} above the homopause. The inferred atmospheric temperature of 530 K was substantially higher than the value of 200 K at 1 μbar derived by Atreya et al. [1981] from analysis of Voyager data, and was cited by Yelle et al. [1996] in their argument for the existence of a large temperature gradient near the homopause. Liu and Dalgarno also pointed out that the temporal variation of the solar flux is larger at shorter wavelengths (which leads primarily to photoionization, providing a source of photoelectrons) than at longer wavelengths (where fluorescent excitation of H_2 takes place). Given dayglow spectra with sufficiently high signal-to-noise and spectral resolution, it is possible to differentiate between H_2 emission produced by photoelectron impact and that produced directly by solar photons.

Determination of the relative changes in each component over timescales corresponding to the solar cycle provides an additional means for examining the influence of solar variations on the observed dayglow emissions. Based on analyses of the variations in H_2 band emissions in

the HUT Astro-1 and Astro-2 dayglow spectra (obtained near solar maximum and solar minimum conditions, with 2375 R and 1485 R total emission, respectively), Wolven [1999], using a methodology similar to that applied by Liu and Dalgarno, but incorporating a more realistic model atmosphere, found that the observed dayglow could be explained in both cases based on the solar radiation input alone. Although historical solar XUV/EUV fluxes remain somewhat uncertain, it is hoped that recent advances in our ability to accurately measure this region of the solar spectrum [cf. *Curdt et al., 2001]*, in conjunction with improved solar proxy models for estimation of historical fluxes, will lead to substantial improvements in this regard. New observations by the solar x-ray photometer on the Student Nitric Oxide Explorer (SNOE) experiment indicate that solar soft x-ray emissions are considerably more intense than previously believed [cf. *Solomon et al.*, 2001], further reducing the necessity to invoke additional energy sources to explain the observed dayglow intensities. The uncertainties that still remain do admit the possibility of an additional excitation source, albeit of substantially less significance than previously supposed. The contribution of precipitating ring current particles (ions and neutrals) and additional discussion on possible *in situ* atmospheric electron acceleration mechanisms may be found in Bhardwaj [1997] and references therein.

The Jovian Lyman-α Bulge

Analysis of spatial scans from the Voyager ultraviolet spectrometers led to the surprising discovery of a strong longitudinal variation in the mid-latitude Jovian H Lyman-α emission [*Sandel et al.,* 1980], a result later confirmed by analyses of sounding rocket and IUE observations obtained prior to the Voyager encounters [*Clarke et al.,* 1980]. The Lyman-α "bulge" was observed to rotate with the planet, appearing at the same magnetic longitude (~100°, with a full width half maximum (FWHM) of ~100°-130°) not only during both Voyager encounters (over a period of four months), but in long-term observations with IUE [*Skinner et al.*, 1983; *McGrath*, 1991]. The brightness contours of the emission appeared to follow the particle drift equator [*Dessler et al.,* 1981]. The Lyman-α brightness enhancement was initially ascribed to an increase in the H column in the bulge region; while persistent variations in the H distribution with both local time and latitude had been observed on other planets, the presence of such an asymmetry fixed in magnetic longitude was unique to Jupiter. More puzzling still was the lack of any apparent asymmetry in the H_2 band emission, which effectively ruled out the possibility of enhanced particle precipitation as the source of the bulge asymmetry.

The brightness of both the bulge and the non-bulge regions has been observed to vary with the solar Lyman-α flux over both the ~11 year solar cycle and the 27-day solar rotation period. A change in the morphology of the bulge was noted in the 1989-1991 time period by McGrath [1991], in the form of an increase in the FWHM to ~200°. The mechanism responsible for the observed changes is not clear. Detailed models of the H Lyman-α emission line profile in the bulge and non-bulge regions [*Clarke et al.*, 1991; *Ben-Jaffel et al.*, 1993] demonstrate that the observed line shapes and center-to-limb variations are not consistent with resonant scattering of solar Lyman-α by an H column of varying abundance. The enhancement of the Lyman-α brightness in the bulge region is due to a broadening of the core of the line, rather than an increase in the optical depth at line center. The observed Lyman-α line profiles require the presence of either a collisionally-broadened internal source or non-thermal (turbulent) broadening [*Emerich et al., 1996*]; it has been suggested that turbulent broadening may be related to thermospheric circulation patterns created by the large energy inputs in the Jovian auroral region [*Sommeria et al.,* 1995].

Temperature Dependence of H_2 Fluorescence

The electron impact excitation cross sections of the Werner and Lyman bands of H_2 show little dependence on temperature [*Liu et al.*, 1998]; while the contributions to the overall excitation rate from individual rovibrational states may vary substantially, the sum over the full H_2 population distribution does not. Resonant and fluorescent scattering of solar radiation, however, often involves a coincidence in wavelength between a strong solar line and a molecular band transition originating in a specific rovibrational level of the electronic ground state of H_2. Changes in temperature (either the thermal/kinetic, rotational, or vibrational temperature, which can differ markedly [*Cravens,* 1987; *Majeed et al.*, 1991]) may significantly alter the population of a given rovibrational level, and can thus lead to substantial variations in the solar-scattered fluorescence component of the dayglow. Both the auroral and dayglow emissions are produced almost entirely via excitation from the ground vibrational state of H_2, owing to the large excitation energies of excited vibrational levels ($v = 1$ ~6000 K, $v = 2$ ~11,000 K). It thus came as a surprise to find that non-auroral spectra from the region of the Shoemaker-Levy 9 G fragment impact site [*Noll et al.*, 1995] contained strong emissions corresponding to solar Lyman-α induced fluorescence of $H_2(v = 2)$ [*Wolven et al.*, 1997], excited via the (1,2)P(5) transition at 121.607 nm and the (1,2)R(6) transition at 121.573 nm. Previous observations of Lyman-α

fluorescence in H_2 had been confined to solar spectra taken in regions containing sunspots [*Jordan et al.,* 1978, cf.] and spectra of giant stars such as α Tau [*McMurray et al.,* 1996, cf.], where temperatures are sufficiently warm to populate the higher vibrational levels. Fluorescent transitions from vibrationally excited levels may play a more important role in the dayglow spectra of hot Jupiter-like extrasolar giant planets (Chapter VI.1).

CONCLUSIONS

Comparative studies of the nightglows of Mars and Venus are still limited by lack of data. The amount of information available on the earth's atmosphere overwhelms anything we know about our nearest planetary neighbors, and in the case of Mars, there are no nightglow data. Recent ground-based measurements of the Venus nightglow have been useful in pointing out the similarities and differences with the earth's nightglow. Much can be learned from regular viewing of Venus, and it is to be hoped that progress will be made with respect to Mars either from space telescopes or from orbiters.

The dominant atmospheric species and the principal chemical pathways by which they react with one another differ markedly as we move from the inner solar system outwards to the giant planets. Nevertheless, the essential physical processes leading to the production of planetary airglows remain the same. Resonant and fluorescent scattering, photodissociation and various forms of recombination produce their own unique signatures in the airglows. The observation and interpretation of these signatures provides us with a means to understand the energy flow, dynamics, and photochemistry of the upper atmospheres of all the planets.

New and improved measurements of the solar irradiance, particularly in and shortward of the FUV region of the spectrum, will substantially improve our ability to model and understand the airglow spectra of both terrestrial and outer planets. Coupled with airglow models incorporating improved atmospheric composition and temperature data (based on observations by the Galileo spacecraft and atmospheric probe at Jupiter, and upcoming observations by Cassini at Saturn), speculation concerning the excitation mechanisms responsible for the observed outer planet dayglow intensities may finally be put to rest.

Acknowledgements. Part of the effort in preparing this article was supported by the NASA Planetary Atmospheres program. T. G. Slanger thanks the astronomers who have contributed to the collection of sky spectra. The Keck telescopes are operated jointly by the California Institute of Technology and the University of California. B. C. Wolven acknowledges helpful discussions with Randy Gladstone, particularly in locating a copy of the work by Bhardwaj (1997), and both authors express their appreciation to the reviewers for their comments.

REFERENCES

Abgrall, H., J. Le Bourlot, G. Pineau Des Forets, E. Roueff, D. R. Flower, and L. Heck, Photodissociation of H_2 and the H/H_2 transition in interstellar clouds, *Astron. Astrophys., 253* , 525–536, 1992.

Abgrall, H., E. Roueff, F. Launay, J. Y. Roncin, and J. L. Subtil, Table of the Lyman Band system of molecular hydrogen, *A & AS, 101* , 273–321, 1993a.

Abgrall, H., E. Roueff, F. Launay, J. Y. Roncin, and J. L. Subtil, Table of the Werner Band system of molecular hydrogen, *A & AS, 101* , 323–362, 1993b.

Abgrall, H., E. Roueff, F. Launay, and J. Y. Roncin, The *B'* and *D* band systems of molecular hydrogen, *Can. J. Phys., 72* , 856–865, 1994.

Abgrall, H., E. Roueff, X. Liu, and D. E. Shemansky, The emission continuum of electron-excited molecular hydrogen, *Ap. J., 481*, 557–566, 1997.

Alpers, M., T. Blix, S. Kirkwood et al., "Measurements of neutral and ionized iron densities in the upper mesosphere," *J. Geophys. Res. 98*, 275-284, 1993.

Atreya, S. K., T. M. Donahue, and M. Festou, Jupiter Structure and composition of the upper atmosphere, *Ap. J., 247*, L43–L47, 1981.

Ballester, G. E., S. Miller, J. Tennyson, L. M. Trafton, and T. R. Geballe, Latitudinal temperature variations of Jovian H_3^+ , *Icarus, 107*, 189–194, 1994.

Barth, C. A., C. W. Hord, J. B. Pearce et al., "Mariner 6 and 7 ultraviolet spectrometer experiment: Upper atmosphere data," *J. Geophys. Res. 76*, 2213-2227, 1971.

Bates, D. R., "Nightglow emissions from oxygen in the lower thermosphere," *Planet. Space Sci. 40*, 211-221, 1992.

Bates, D. R., "Cause of terrestrial nightglow continuum," *Proc. Roy. Soc. Lond. A 443*, 227-237 (1993).

Bates, D. R. "The nightglow," in *Progress and Problems in Atmospheric Chemistry*, edited by J. R. Barker (World Scientific, New Jersey, 1995), pp. 420-471.

Ben Jaffel, L., J. T. Clarke, R. Prange, G. R. Gladstone, and A. Vidal-Madjar, The Lyman alpha bulge of Jupiter Effects of nonthermal velocity field, *Geophys. Res. Lett., 20*, 747–750, 1993.

Betremieux, Y., and R. V. Yelle, HST Detection of H_2 Raman scattering in the Jovian atmosphere, *Icarus, 142*, 324–341, 1999.

Bhardwaj, A., "Airglow on the Outer Planets," internal report, Space Physics Laboratory, Vikram Sarabhai Space Centre, Trivandrum 695022, India (email: anil_bhardwaj@indiainfo.com).

Bougher, S. W., J.-C. Gerard, A.I.F. Stewart, and C. G. Fesen, "The Venus nitric oxide night airglow: Model calculations based on the Venus thermospheric general circulation model," *J. Geophys. Res. 95*, 6271-6284, 1990.

Bougher, S. W., and W. J. Borucki, "Venus O_2 Visible and IR Nightglow: Implications for lower thermosphere dynamics and chemistry," *J. Geophys. Res. 99*, 3759-3776, 1994.

Broadfoot, A. L., and K. R. Kendall, "The airglow spectrum, 3100-10,000 A," *J. Geophys. Res. 73*, 426-428, 1968.

Broadfoot, A. L., et al., Extreme ultraviolet observations from Voyager 1 encounter with Jupiter, *Science, 204*, 979–982, 1979.

Broadfoot, A. L., et al., Overview of the Voyager ultraviolet spectrometry results through Jupiter encounter, *J. Geophys. Res., 86*, 8259–8284, 1981.

Broadfoot, A. L., S. K. Atreya, J. L. Bertaux, J. E. Blamont, A. J. Dessler, and S. Linick, Ultraviolet spectrometer observations of Neptune and Triton, *Science, 246*, 1459–1466, 1989.

Broadfoot, A. L., and P. J. Bellaire, Jr., "Bridging the gap between ground-based and space-based observations of the night airglow," *J. Geophys. Res. 104*, 17127-17138, 1999.

Chamberlain, J. W., "The blue airglow spectrum," *Ap. J. 128*, 713-717, 1958.

Chamberlain, J. W., *Physics of the Aurora and Airglow* (American Geophysical Union, Washington D. C., 1995.

Chanover, N. J., K.S.J. Anderson, T. G. Slanger, P. C. Cosby, D. L. Huestis, "New Observations of the Venus Visible Nightglow," presented at the DPS meeting, New Orleans, Dec. 2001.

Clarke, J. T., H. A. Weaver, P. D. Feldman, H. W. Moos, W. G. Fastie, and C. B. Opal, Spatial imaging of hydrogen Lyman-α Emission from Jupiter, *Ap. J., 240*, 696–701, 1980.

Clarke, J. T., Detection of auroral hydrogen Lyman alpha emission from Uranus, *Ap. J., 263*, L105–L109, 1982.

Clarke, J., et al., Continued observations of the H Ly-alpha emission from Uranus, *J. Geophys. Res., 91*, 8771–8781, 1986.

Clarke, J. T., M. K. Hudson, and Y. L. Yung, The excitation of the far ultraviolet electroglow emissions on Uranus, Saturn, and Jupiter, *J. Geophys. Res., 92*, 15,139–15,147, 1987.

Clarke, J. T., IUE observations of Neptune for H Lyman-alpha emission, *Geophys. Res. Lett., 15*, 701–704, 1988.

Clarke, J. T., G. R. Gladstone, and L. B. Jaffel, Jupiter's dayglow H Ly-α emission line profile, *Geophys. Res. Lett., 18*, 1935–1938, 1991.

Connes, P., J. F. Noxon, W. A Traub et al., "$O_2(a^1\Delta_g)$ emission in the day and night airglow of Venus," *Ap. J. 233*, L29-L32, 1979.

Copeland, R. A., K. Knutsen, M. E. Onishi et al., "Collisional removal of $O_2(c^1\Sigma_u^-, v=9)$ by O_2, N_2, and He," *J. Chem. Phys. 105*, 10349-10355, 1996.

Cravens, T. E., Vibrationally excited molecular hydrogen in the upper atmosphere of Jupiter, *J. Geophys. Res., 92*, 11,083–11,100, 1987.

Crisp, D., D. A. Allen, D. H. Grinspoon et al., "The dark side of Venus: Near-infrared images and spectra from the Anglo-Australian Observatory," *Science 253*, 1263-1266, 1991.

Crisp, D., V. S. Meadows, B. Bezard et al., "Ground-based near-infrared observations of the Venus nightside: 1.27 micron $O_2(a)$ airglow from the upper atmosphere," *J. Geophys. Res. 101*, 4577-4593, 1996.

Curdt, W., P. Brekke, U. Feldman, K. Wilhelm, B. N. Dwivedi, U. Schühle, and P. Lemaire, "The SUMER spectral atlas of solar-disk features" *Astron. Astrophys. 375*, 591-613, 2001.

DeMore, W. B., S. P. Sander, D. M. Golden et al., *JPL Publication Report* No. 97-4, 1997.

Dessler, A. J., B. R. Sandel, and S. K. Atreya, The Jovian hydrogen bulge; Evidence for co-rotating magnetospheric convection, *Planet. Space Sci., 29*, 215–224, 1981.

Drossart, P., T. Fouchet, J. Crovisier, El Lellouch, T. Encrenaz, H. Feuchtgruber, and J. P. Champion, "Fluorescence in the 3μm bands of methane on Jupiter and Saturn from ISO/SWS observations" in *The Universe as Seen by ISO*, P. Cox and M. F. Kessler, eds., ESA-SP 427, 169, 1999.

Drossart, P., T. Fouchet, E. Raynaud, B. Sicardy, T. widemann, J. H. Waite, and G. R. Gladstone, "The upper atmosphere of Jupiter from VLT/ISAAC observations, in AAS/Division of Planetary Sciences Meeting, vol. 33, #3.08, 2001.

Durrance, S. T., P. D. Feldman, and H. W. Moos, The spectrum of the Jovian aurora 1150-1700 Å, *Geophys. Res. Lett., 9*, 652–655, 1982.

Dziczek, D., J. M. Ajello, D. L. Hansen, and G. K. James, A study of the cascade contribution to the H_2 Lyman band system from electron impact, *Phys. Rev. A, 61*, 64,702, 2000.

Emerich, C., L. Ben Jaffel, J. T. Clarke, R. Prange, G. R. Gladstone, J. Sommeria, and G. Ballester, Evidence for supersonic turbulence in the upper atmosphere of Jupiter, *Science* 273, pp. 1085-1087, 1996.

Feldman, P. D., M. A. McGrath, H. W. Moos, S. T. Durrance, D. F. Strobel, and A. F. Davidsen, The spectrum of the Jovian dayglow observed at 3-Å resolution with the Hopkins Ultraviolet Telescope, *Ap. J., 406*, 279–284, 1993.

Feldman, P. D., et al., FUSE Observations of the far ultraviolet spectrum of Saturn, in American Astronomical Society Meeting, v. 198, pp. 7001+, 2001.

Fox, J. L. "Airglow and Aurora in the Atmospheres of Venus and Mars," in *Venus and Mars: Atmospheres, Ionospheres, and Solar Wind Interactions*, edited by J. G. Luhmann, M. Tatrallyay, and R. O. Pepin (American Geophysical Union, Washington D.C., 1992), 66, pps. 191-222.

Gerard, J.-C., "Satellite observations of the nitric oxide nightglow," *Geophys. Res. Lett. 2*, 179-182, 1975.

Greer, R.G.H., D. R. Murtagh, I. C. McDade et al., "ETON 1: A data base pertinent to the study of energy transfer in the oxygen nightglow," *Planet. Space Sci. 34*, 771-788, 1986.

Heinselmann, C. J., J. P. Thayer, and B. J. Watkins, "A high-

latitude observation of sporadic sodium and sporadic E-layer formation," *Geophys. Res. Lett. 25*, 3059-3062, 1998.

Hudson, M. K., J. T. Clarke, and J. A. Warren, Ionospheric dynamo theory for production of far ultraviolet emissions on Uranus, *J. Geophys. Res. 94*, 6517–6522, 1989.

Huestis, D. L., and T. G. Slanger, "New perspectives on the Venus nightglow," *J. Geophys. Res. 98*, 10839-10847, 1993.

Huestis, D. L., B.-Y. Chang, P. C. Cosby et al., "Spectroscopy of the $^5\Pi_g$ state of O_2," *Eos, Trans. Am. Geophys. Union 80*, F780, 1999.

Jordan, C., G. E. Brueckner, J. D. F. Bartoe, G. D. Sandlin, and M. E. VanHoosier, Emission lines of H_2 in the extreme ultraviolet solar spectrum, *Ap. J., 226,* 687–697, 1978.

Krasnopol'sky, V. A., A. A. Krysko, V. N. Rogachev et al., "Spectroscopy of the Venus night airglow from the Venera 9 and 10 orbiters," *Cosmic Research 14*, 789-795, 1976.

Krasnopol'sky, V. A. and V. A. Parshev, "Ozone and photochemistry of the Martian lower atmosphere," *Planet. Space Sci. 34*, 511-518, 1979.

Krasnopol'sky, V. A., and V. A. Parshev, "Photochemistry of the Venus atmosphere," in *Venus*, edited by D. M. Hunten, L. Colin, T. M. Donahue et al. (Arizona Press, 1983), pp. 431-458.

Krasnopol'sky, V. A., "Oxygen emissions in the night airglow of the Earth, Venus and Mars," *Planet. Space Sci. 34*, 511-518, 1986.

Lam, H. A., S. Miller, R. D. Joseph, T. R. Geballe, L. M. Trafton, J. Tennyson, and G. E. Ballester, Variation in the H_3^+ emission of Uranus, *Ap. J., 474*, L73–76, 1997.

Lancaster, R. S., L. S. Waldrop, R. B. Kerr et al., "Brightness measurements of the nighttime OI 8446 A airglow emission from the Millstone Hill and Arecibo observatories," *J. Geophys. Res. 105*, 5275-90, 2000.

Lawrence, G. M., C. A. Barth, and V. Argabright, "Excitation of the Venus night airglow," *Science 195*, 573, 1977.

Lean, J. L., and T. P. Repoff, A statistical analysis of solar ux variations over time scales of solar rotation 1978-1982, *J. Geophys. Res., 92*, 5555–5563, 1987.

Leu, M. T., and Y. L. Yung, "Determination of $O_2(a)$ and $O_2(b)$ yields in the reaction O + ClO → Cl + O_2: Implications for photochemistry in the atmosphere of Venus," *Geophys. Res. Lett. 14*, 949-952, 1987.

Liu, W., and A. Dalgarno, The ultraviolet spectrum of the Jovian dayglow, *Ap. J.*, 462 , 502–518, 1996.

Liu, X., S. M. Ahmed, R. A. Multari, G. K. James, and J. M. Ajello, High resolution electron impact study of the far ultraviolet emission spectrum of molecular hydrogen, *Ap. J.* (Supp.), *101*, 375–399, 1995.

Liu, X., D. E. Shemansky, S. M. Ahmed, G. K. James, and J. M. Ajello, Electron impact excitation and emission cross sections of the H_2 Lyman and Werner systems, *J. Geophys. Res., 103*, 26,739, 1998.

Liu, X., D. E. Shemansky, J. M. Ajello, D. L. Hansen, C. Jonin, and G. K. James, High resolution electron impact emission spectrum of H_2. II. 760–900 ° A, *Ap. J.* (Supp.), *119*, 267–280, 2000.

Majeed, T., R. V. Yelle, and J. C. McConnell, Vibrationally excited H_2 in the outer planets thermosphere Fluorescence in the Lyman and Werner bands, *Planet. Space Sci. 39*, 1591–1606, 1991.

McConnell, J. C., B. R. Sandel, and A. L. Broadfoot, Airglow from Jupiter's nightside and crescent ultraviolet spectrometer observations from Voyager 2, *Icarus, 43*, 128–142, 1980.

McConnell, J. C., B. R. Sandel, and A. L. Broadfoot, Voyager UV spectrometer observations of He 584 Å dayglow at Jupiter, *Planet. Space Sci., 29*, 283–292, 1981.

McDade, I. C., E. J. Llewellyn, R.G.H. Greer et al., "ETON 3: Altitude profiles of the nightglow continuum at green and near infrared wavelengths`," *Planet. Space Sci. 34*, 801-810, 1986a.

McDade, I. C., D. P. Murtagh, R. G. H. Greer et al., "ETON 2: Quenching parameters for the proposed precursors of $O_2(b^1\Sigma_g^+)$ and O(^{1}S) in the terrestrial nightglow," *Planet. Space Sci. 34*, 789-800, 1986b.

McDade, I. C., E. J. Llewellyn, R.G.H. Greer, and D. P. Murtagh, "ETON 6: A rocket measurement of the O_2 Infrared Atmospheric (0-0) band in the nightglow", *Planet. Space Sci. 35*, 1541-1552 (1987).

McGrath, M. A., P. D. Feldman, G. E. Ballester, and H. W. Moos, IUE observations of the Jovian dayglow emission, *Geophys. Res. Lett., 16*, 583–586, 1989.

McGrath, M. A., G. E. Ballester, and H. W. Moos, Jovian H_2 dayglow emission (1978-1989), *J. Geophys. Res., 95*, 10,365–1037, 1990.

McGrath, M. A., An unusual change in the Jovian Lyman alpha bulge, *Geophys. Res. Lett., 18*, 1931– 1934, 1991.

McMurray, A. D., C. Jordan, A. K. Rowe, K. G. Carpenter, and R. D. Robinson, in Proceedings of the Ninth Cambridge Workshop on Cool Stars, Stellar Systems, and the Sun, A.S.P. conference series, edited by R. Pallavicini, 1996.

Megie, G., F. Bos, J. E. Blamont et al., "Simultaneous nighttime lidar measurements of atmospheric sodium and potassium," *Planet. Space Sci. 26*, 27-35, 1978.

Melo, S.M.L., R. P. Lowe, and J. P. Russell, "Double-peaked hydroxyl airglow profiles observed from WINDII/UARS," *J. Geophys. Res. 105*, 12397-403, 2000.

Meriwether,J. W. Jr., "A review of the photochemistry of selected nightglow emissions from the mesopause," *J. Geophys. Res. 94*, 14629-14646, 1989.

Miller, S., N. Achilleos, G. E. Ballester, H. A. Lam, J. Tennyson, T. R. Geballe, and L. M. Trafton, Mid to low latitude H_3^+ emission from Jupiter, *Icarus, 130*, 57–67, 1997.

Moos, H. W., W. G. Fastie, and M. Bottema, Rocket Measurement of Ultraviolet Spectra of Venus and Jupiter Between 1200 and 1800 Å, *Ap. J.* 155, p.887, 1969.

Noll, K. S., M. A. McGrath, L. M. Trafton, S. K. Atreya, J. J.

Caldwell, H. A. Weaver, R. V. Yelle, C. Barnet, and S. Edgington, HST spectroscopic observations of Jupiter after the collision of Comet Shoemaker-Levy 9, *Science*, *267*, 1307, 1995.

Noxon, J. F., W. A. Traub, N. P. Carleton et al., "Detection of O_2 dayglow emission from Mars and the Martian ozone abundance," *Ap. J. 207*, 1025-1035, 1976.

Osterbrock, D. E., J. P. Fulbright, A. R. Martel et al., "Night-Sky high-resolution spectral atlas of OH and O_2 emission lines for echelle spectrograph wavelength calibration," *Pub. Astron. Soc. Pacific 108*, 277-308, 1996).

Parkinson, C. D., J. C. McConnell, B. R. Sandel, R. V. Yelle, and A. L. Broadfoot, He 584 Å dayglow at Neptune, *Geophys. Res. Lett., 17*, 1709–1712, 1990.

Parkinson, C. D., E. Griffioen, J. C. McConnell, G. R. Gladstone, and B. R. Sandel, He 584 Å dayglow at Saturn: A reassessment, *Icarus, 133*, 210–220, 1998.

Paxton, L. J. "Pioneer Venus Orbiter ultraviolet spectrometer limb observations: Analysis and interpretation of the 166- and 156-nm data," *J. Geophys. Res. 90*, 5089-5096, 1985.

Plane, J.M.C., R. M. Cox, J. Qian et al., "Mesospheric Na layer at extreme high latitudes in summer," *J. Geophys. Res. 103*, 6381-6389, 1998.

Pryor, W. R., et al., Galileo ultraviolet spectrometer observations of Jupiter's auroral spectrum from 1600 3200 Å, *J. Geophys. Res., 103*, 20,149–20,158, 1998.

Sandel, B. R., A. L. Broadfoot, and D. F. Strobel, Discovery of a longitudinal asymmetry in the H Lyman-α brightness of Jupiter, *Geophys. Res. Lett., 7*, 5–8, 1980.

Satoh, T., and J.E.P. Connerney, Spatial and temporal variations of Jupiter's H_3^+ emission deduced from image analysis, *Geophys. Res. Lett., 26*, 1789–1792, 1999.

Shemansky, D. E., and J. M. Ajello, The Saturn spectrum in the EUV Electron excited hydrogen, *J. Geophys. Res., 88*, 459–464, 1983.

Shemansky, D. E., An explanation for the H Lyman α longitudinal asymmetry in the equatorial spectrum of Jupiter An outcrop of paradoxical energy deposition in the exosphere, *J. Geophys. Res., 90*, 2673–2694, 1985.

Shemansky, D. E., J. M. Ajello, and D. T. Hall, Electron impact excitation of H_2: Rydberg band systems and the benchmark dissociative cross section of H Lyman alpha, *Ap. J., 296*, 765–773, 1985.

Skinner, T. E., S. T. Durrance, P. D. Feldman, and H. W. Moos, Temporal variation of the Jovian H I Lyman alpha emission 1979-1982, *Ap. J., 265*, L23–L27, 1983.

Slanger, T. G., and G. Black, "The $O_2(C^3\Delta_u - a^1\Delta_g)$ bands in the nightglow spectrum of Venus," *Geophys. Res. Lett. 5*, 947-948, 1978.

Slanger, T. G., and D. L. Huestis, "$O_2(c^1\Sigma_u^- \; X^3\Sigma_g^-)$ emission in the terrestrial nightglow," *J. Geophys. Res.* 86, 3551-3554, 1981.

Slanger, T. G., P. C. Cosby, D. L. Huestis et al., "Vibrational level distribution of $O_2(b^1\Sigma_g^+, v = 0\text{-}15)$ in the mesosphere and lower thermosphere region," *J. Geophys. Res. 105*, 20557-20564, 2000a.

Slanger, T. G., and D. E. Osterbrock, "Investigation of potassium, lithium, and sodium emissions in the nightglow, and OH cross-calibration," *J. Geophys. Res. 105*, 1425-1429, 2000b.

Slanger, T. G., D. L. Huestis, P. C. Cosby et al., "Accurate atomic line wavelengths from astronomical sky spectra," *J. Chem. Phys. 113*, 8514-8520, 2000c.

Slanger, T. G., P. C. Cosby, D. L. Huestis et al., "Discovery of the atomic oxygen green line in the Venus night airglow," *Science 291*, 463-465, 2001a.

Slanger, T. G., P. C. Cosby, and D. L. Huestis, "Oxygen atom Rydberg emissions at 394-927 nm in the nightglow, as measured near solar maximum at Mauna Kea," *Eos, Trans. Amer. Geophys. Union 82*, S285, 2001b.

Solomon, S. C. "Optical Aeronomy," *Rev. Geophys. 29*, 1089-1109, (1991).

Solomon, S. C., S. M. Bailey, and T. N. Woods, "Effect of solar soft X-rays on the lower ionosphere", *Geophys. Res. Lett. 28*, 2149, 2001.

Sommeria, J., L. Ben Jaffel, and R. Prange, "On the existence of supersonic jets in the upper atmosphere of Jupiter", *ICARUS 118*, 2-24, 1995.

Stegman, J., and D. P. Murtagh, "High resolution spectroscopy of Oxygen U.V. airglow," *Planet. Space Sci. 36*, 927-934, (1988).

Stegman, J., and D. P. Murtagh, "The molecular oxygen band systems in the UV nightglow: Measured and modeled," *Planet. Space Sci. 39*, 595-609, 1991.

Stewart, A.I.F. and C. A. Barth, "Ultraviolet night airglow of Venus," *Science 205*, 59-62, 1979.

Stewart, A.I.F. J.-C. Gerard, D. W. Rusch et al., "Morphology of the Venus ultraviolet nightglow," *J. Geophys. Res. 85*, 7861, 1980.

Strobel, D. F., R. V. Yelle, D. E. Shemansky, and S. K. Atreya, The upper atmosphere of Uranus, in *Uranus*, edited by J. T. Bergstralh et al., pp. 65–109, University of Arizona Press, Tucson, AZ, 1991.

Swider, W., "Sodium chemistry: A brief review and two new mechanisms for sudden sodium layers," *Planet. Space Sci. 40*, 247-253, 1992.

Taylor, M. J., Jr., W. R. Pendleton, H.-L. Liu et al., "Large amplitude perturbations in mesospheric OH Meinel and 87-km Na lidar temperatures around the autumnal equinox," *Geophys. Res. Lett. 28*, 1899-1902 (2001).

Tennyson, P. D., P. D. Feldman, G. F. Hartig et al., "Near-midnight observations of nitric oxide delta and gamma band chemiluminescence," *J. Geophys. Res. 91*, 10,141-10,146, 1986.

Tobiska, W. K., and C. A. Barth, A solar EUV flux model, *J. Geophys. Res., 95*, 8243–8251, 1990.

Tobiska, W. K., Recent solar extreme ultraviolet irradiance

observations and modeling: A review, *J. Geophys. Res.*, *98*, 18,879–18,893, 1993.

Trafton, L. M., S. Miller, T. R. Geballe, G. E. Ballester, and J. Tennyson, On Uranus' H_2 and H_3^+ emissions, in AAS/Division of Planetary Sciences Meeting, vol. 30, pp. 4306+, 1998.

Turnbull, D. N., and R. P. Lowe, "New hydroxyl transition probabilities and their importance in airglow studies," *Planet. Space Sci. 37*, 723-738 (1989).

Vervack, R. J., B. R. Sandel, G. R. Gladstone, J. C. McConnell, and C. D. Parkinson, Jupiter's He 584 Å dayglow: New results., *Icarus*, *114*, 163–173, 1995.

Vogt, S., "HIRES: The high resolution echelle spectrometer on the Keck ten-meter telescope," *SPIE* 2198, 362-375, 1994.

Von Savigny, C.H.A., I. C. McDade, G. G. Shepherd et al., "Lower thermospheric nitric oxide concentrations derived from WINDII observations of the green nightglow continuum at 553.1 nm," *Ann. Geophysicae 17*, 1439-1446, 1999.

Waite, J. H., T. E. Cravens, J. Kozyra, A. F. Nagy, S. K. Atreya, and R. H. Chen, Electron precipitation and related aeronomy of the Jovian thermosphere and ionosphere, *J. Geophys. Res.*, *88*, 6143–6163, 1983.

Wolven, B. C., P. D. Feldman, D. F. Strobel, and M. A. McGrath, Lyman-α–induced fluorescence of H_2 and CO in Hubble Space Telescope spectra of a Comet Shoemaker-Levy 9 impact site on Jupiter, *Ap. J.*, *475*, 835–842, 1997.

Wolven, B. C., Far ultraviolet spectroscopy of Jupiter's upper atmosphere, Ph.D. Thesis, pp. 7–193, 1999.

Yelle, R. V., L. R. Doose, M. G. Tomasko, and D. F. Strobel, Analysis of Raman-scattered Ly alpha emissions from the atmosphere of Uranus, *Geophys. Res. Lett.*, *14*, 483–486, 1987.

Yelle, R. V., H_2 emissions from the outer planets, *Geophys. Res. Lett.*, *15*, 1145–1148, 1988.

Yelle, R. V., J. C. McConnell, D. F. Strobel, and L. R. Doose, The far ultraviolet reflection spectrum of Uranus Results from the Voyager encounter, *Icarus*, *77*, 439–456, 1989.

Yelle, R. V., L. A. Young, J. Vervack, Ronald J., R. Young, L. Pfister, and B. R. Sandel, Structure of Jupiter's upper atmosphere: Predictions for Galileo, *J. Geophys. Res.*, *101*, 2149–2162, 1996.

Tom G. Slanger, SRI International, Molecular Physics Laboratory, 333 Ravenswood Avenue, PS091, Menlo Park, CA 94025, tom.slanger@sri.com

Brian Wolven, The Johns Hopkins University, Applied Physics Laboratory, 11100 Johns Hopkins Road, Laurel, MD 20723, brian.wolven@jhuapl.edu

PART II. INTERACTIONS BETWEEN PLANETARY AND SMALL BODY ATMOSPHERES WITH THE SURROUNDING PLASMA MEDIUM

The concept of ionospheric layers used by Sydney Chapman in the early, defining years of space physics emphasized the self-regulating photochemical processes in our atmosphere. Input from above was assumed to be limited to the Sun's radiative component, certainly a dominant player in atmospheric scenarios. In the following four chapters, the rigid framework of stacked layers-upon-layers is modified, even shattered, by our current levels of understanding of actual plasma behavior. The crucial element is the presence or lack of a magnetic field. When present, a planetary magnetic dipole guides energetic particles and electric fields from the magnetosphere into the ionosphere. Cold ionospheric plasma diffuses upward to re-supply the magnetosphere. The aurora and plasma flow patterns imposed from above are best known on Earth and most severe Jupiter. For Venus, Mars and comets, the solar wind provides a completely different "input from above" via direct impact upon the atmosphere. For the atmospheres of unmagnetized moons that orbit within a planet's magnetosphere, the plasma impact comes from in-situ co-rotational flow and field-aligned bombardment of trapped ions and electrons. The coupling of solar wind and magnetospheric plasmas to the atmospheric-ionospheric regions comprises one of the most active areas in current space plasma physics and aeronomic research. *(Image courtesy J. Spencer.)*

Magnetosphere-Ionosphere Coupling at Earth, Jupiter, and Beyond

B. H. Mauk and B. J. Anderson

The Johns Hopkins University, Applied Physics Laboratory, Laurel, Maryland

R. M. Thorne

Department of Atmospheric Sciences, University of California at Los Angeles

In this tutorial and selective review, we define magnetosphere-ionosphere (M-I) coupling, present its basic properties, and summarize outstanding problems in the field. We compare M-I coupling processes at Earth and Jupiter. We use that comparison to argue that M-I coupling processes that generate the northern and southern auroral lights are fundamental to how some astrophysical systems behave and evolve throughout the universe, specifically those involving partially ionized gases connected by magnetic fields. Using the example of solar system formation, we finally speculate as to the importance of what we can learn about M-I coupling at Earth and Jupiter towards understanding these distant astrophysical systems.

1. INTRODUCTION

The northern and southern lights, or aurora, have fascinated people throughout recorded history [*Eather*, 1980]. The fascination may lie with auroral structuring that occurs on human scales; often sheets, curtains, rays, and other features are observed to blink, shimmer, or twist and turn directly overhead in snake-like fashion. That structuring is also the most scientifically puzzling aspect of these lights. The aurora is generated by processes that extend over spatial scales many times larger than the size of the Earth. And yet, the spatial structuring also extends down to features that have widths no larger than the size of a football field [~100 m; *Borovsky*, 1993; *Lanchester et al.*, 1997]. We do not understand why the aurora behaves in this fashion. This mystery is one of many that surround the study of the interaction that occurs between the Earth's space environment, or magnetosphere, and the ionosphere, the ionized upper layer of the Earth's atmosphere. We call this interaction magnetosphere-ionosphere (M-I) coupling.

It is the premise of this book and this chapter that much understanding of fundamental space processes may accrue from comparisons between different planets. The study of space is mostly an observational science rather than an experimental science. With an observational science the critical process of hypothesis testing is severely curtailed. For the study of the space environments of planets, we are fortunate that nature has chosen to run several different experiments for us with different conditions and parametric states. In some critical ways nature has performed the hypothesis testing for us.

For example, the interplanetary environment, or solar wind, plays a critical role in driving the dramatic aurora at Earth. At Jupiter, the solar wind influence is limited. There the space environment or magnetosphere is powered predominantly by planetary rotation. A comparison between Earth and Jovian aurora isolates critical factors in M-I coupling that lead to aurora, and it raises the issue of the universality of the M-I coupling process. The opposite extreme can occur at Uranus. A large-scale electric field distribution within the Earth's magnetosphere helps generate the electric currents that connect the magnetosphere to the ionosphere and cause aurora. That distribution at Earth reveals the influence of both the solar

Atmospheres in the Solar System: Comparative Aeronomy
Geophysical Monograph 130

10.1029/130GM07

wind and the planetary rotation. At Uranus we can examine the electric field pattern when the rotational contribution is effectively turned off because of the unique orientation that can occur between the planetary spin axis and the solar wind direction [*Selesnick and Richardson*, 1986; *Vasyliunas*, 1986].

In this tutorial and selective review, we discuss more fully what M-I coupling is, present some basic properties, and state some outstanding problems in this field. We then use findings at Jupiter to demonstrate the universality and importance of the issues surrounding M-I coupling at Earth. We discuss some recent findings at Earth that are particularly relevant to a comparison of M-I coupling processes revealed by visits to Jupiter. Finally, we speculate as to the importance of M-I coupling processes throughout the universe using the example of solar system formation. The textbooks by Parks (1991) and Kivelson and Russell (1995) present many of the fundamental physical processes invoked in this chapter.

2. AURORA AT EARTH AND JUPITER

The most puzzling aspect of the aurora is the myriad of spatial and temporal scales involved. At the largest scales the aurora is a global phenomena of the planet Earth. In Plate 1a, an ultraviolet image of the Earth's north polar regions [*Frank and Craven*, 1988] reveals the global configuration of the Earth's aurora during modestly active conditions. The auroral "oval" that encircles the polar-regions maps out along Earth's magnetic field lines to the regions of the near-Earth space environment that power the aurora. When the width of the oval is folded into the calculation, the volume of those regions is many times the volume of Earth itself. That volume extends from equatorial distances of ~6 R_E (1 R_E = 6370 km) to distances in the direction away from the Sun that are larger than 30 R_E. These field lines are "closed" in the sense that they are connected to the Earth on both of their ends. They do not connect to the interplanetary environment (i.e., they are not "open"), contrary to popular press notions about the relationship between the aurora and the Sun. It is only the poleward edge of the auroral oval that is thought to approach the boundary between open and closed magnetic field lines. Other panels in Plate 1 show aspects of the auroral structuring highlighted in the Introduction. How this structuring comes about and why the structures move and evolve the way they do are not understood.

The Earth's aurora can be quiet or active. Plate 1b shows the nightside segment of the auroral oval during very active magnetospheric conditions when the magnetic field in the solar wind is oriented (southward) for pumping energy into the magnetosphere [*McPherron*, 1995]. The figure shows a broad and highly structured auroral region with intense emissions. During quiet periods the oval is narrow, confined to high latitudes, and is relatively unstructured with emission intensities that are greatly reduced.

Recent images of Jupiter's aurora reveal similarities between the auroras of Jupiter and Earth (Plates 2 and 3). The aurora at Jupiter is global in extent, has an oval-like configuration that encircles the polar regions, and has active and inactive states [Plate 2; *Clarke*, 2000 and 1998; and, respectively, Plate 3; *Ingersoll et al.*, 1998]. Recent images from the Hubble Space Telescope (HST) Space Telescope Imaging Spectrograph (STIS) have revealed the kind of spatial structuring (Plate 2) and the kinds of dynamics that are familiar to those who study the aurora at Earth (Waite et al., 2001). Clearly, spatial structuring and temporal dynamics are common features of the M-I coupling at Earth and Jupiter. *Is it possible or likely that such structuring is fundamental to how different regions of astrophysical plasmas interact with each other when connected with magnetic fields*?

At Earth it is tempting to attribute some of the space-time structuring in the aurora to the highly dynamic state of the interplanetary medium that provides the energy for the aurora. Because of the dynamics of the energy source, the M-I system may seldom achieve an equilibrium state. The structuring at Jupiter is highly significant in that we anticipate that the M-I interaction will be less affected by the dynamics of the interplanetary medium. While at Earth, the interplanetary environment modulates the auroral intensities by orders of magnitude; at Jupiter the modulation due to interplanetary conditions is only of order 20% [*Baron et al.*, 1996].

3. WHAT IS M-I COUPLING AND WHAT ARE THE OUTSTANDING QUESTIONS?

3.1 Background on Approaches

With the description that follows, we introduce the concept of M-I coupling using an electrical circuit approach. There are pitfalls to such an approach. With electrical circuits one tends to think about discrete wires. There are no discrete electrical wires out in space. The current carrying media in space, ionized gases or plasmas, are distributed. The paths that the currents follow are difficult to ascertain *a priori*. Unlike wires, which are mechanically supported by the strength of the materials from which they are made, the current carrying media in space are free to move. They can be redistributed by electric field ($\rho\mathbf{E}$) and Lorentz ($\mathbf{J} \times \mathbf{B}/c$) forces (here ρ is charge density, $\mathbf{E}$ is vector electric field, $\mathbf{J}$ is vector current density, and $\mathbf{B}$ is vector magnetic field). On the other hand, the immense value of the electrical circuit approach is its emphasis on the interconnectedness of the different regions of space. One of the founding pioneers of the M-I coupling discipline, Hannes Alfvén, made powerful use

[redacted]

[redacted]

[redacted]

[redacted]

[redacted]

of the circuit approach. He used it to emphasize how a very localized disturbance (a sudden increase or decrease in local electrical resistance, for example) can affect the behavior of an entire cosmical plasma system spanning vastly separated regions of space [*Alfvén*, 1977]. One can take a "continuous media" approach, with its emphasis on interactions between adjacent regions and how signals propagate from one region to another. We emphasize the electrical circuit approach here because of our interest in the interconnectedness of the different parts of the system.

One may think of M-I coupling as the consequence of a system of electric circuits that connects distant regions of the Earth's magnetosphere to the ionosphere via electric currents that flow along the magnetic field lines that connect the two regions. The most intense, and for this presentation the most interesting, of the current systems is that involved with the generation of the aurora. A schematic is shown in Plate 4. It is useful to divide the M-I coupling problem into three distinct regions of space. They are the distant magnetospheric generator, the mid-altitude coupling or controller region, and the ionospheric load region.

3.2 Magnetospheric Generator

The classic plasma generator is the so-called magnetohydrodynamic (MHD) generator [e.g., *Boyd and Sanderson*, 1969]. In the laboratory, dense plasma is forced to flow (with vector velocity **v**) across or perpendicular to a strong magnetic field (vector **B**) thus generating an electromotive force per charge ($\mathbf{v} \times \mathbf{B}/c$). This force separates charges and thus generates a reactive electric field (vector **E**) that partially opposes the electromotive force, and drives a current density (vector **J**). If the plasma is collisional (a plasma with frequent collisions between its particle constituents): $\mathbf{J} = \sigma(\mathbf{E} + \mathbf{v} \times \mathbf{B}/c)$. The electrical conductivity parameter "σ" can be a tensor such that different directions in space are coupled together. Because **E** opposes the electromagnetic force, the condition $\mathbf{E}\cdot\mathbf{J} < 0$ prevails. This condition is required for a generator that creates electrical energy from mechanical energy (rather than dissipating electrical energy). The plasma flow speed, the source of mechanical energy, is constant or decelerating depending on whether or not the flow is maintained with a flow-aligned pressure gradient. As with a generator constructed with wires and magnets, the current density **J** can be tapped to drive a load.

The MHD generator concept is a good starting point for understanding the generator characteristics of the boundary layer between the interplanetary solar wind and the interior region of closed, Earth-connected magnetic field lines (the "magnetopause" boundary; Figure 1b). This boundary generator is thought to drive the dayside aurora, visible to an ultraviolet imager (dayside portion of Plate 1a). Difficulties arise here, and with all of the magnetospheric plasma regions, because the plasmas are all collisionless (collision frequencies between particle constituents are lower than other characteristic times of the system, including the time it takes a plasma parcel to flow past an object). Thus the physics that establishes the fluid viscosity (which allows momentum directed parallel to the boundary to be transported across the boundary and cause the region of closed field lines to flow) is not well established. The physics that establishes electrical conductivity is similarly uncertain. Exchange of momentum between charged particles and various waves that propagate within, and along surfaces of, plasmas ("wave-particle interactions") are thought to play key roles in either case.

The generator properties of regions deeply interior to the magnetopause boundary are even more uncertain. Electric currents are driven within the interior of the magnetosphere on closed field lines by boundary electric fields that penetrate partially into the interior. Within the comet-like magnetic tail (Figure 1a) the currents flow predominantly at the boundary between the northern lobe of Earthward directed magnetic fields and the southern lobe of tailward directed magnetic fields. The penetrating electric fields (**E**) and the current density (**J**) are both westward at large distances so that $\mathbf{E}\cdot\mathbf{J} > 0$. Thus, energy is added to the plasma in the form of both plasma heating and accelerated flow. The $\mathbf{J} \times \mathbf{B}/c$ force density at the boundary between the lobes pushes the plasmas Earthward (Figure 1b). Momentum carries the plasmas into the stronger magnetic field regions close to Earth. Electrical energy may be extracted from the flowing, but decelerating, plasmas in the fashion of a (collisionless) MHD generator. The eastward current associated with the deceleration and the electrical power generation ($\mathbf{E}\cdot\mathbf{J} < 0$) is the inertial current: $\mathbf{J}_I = \rho_m c(\mathbf{B} \times d\mathbf{U}/dt)/B^2$, where ρ_m is mass density, **U** is vector plasma flow velocity, and d/dt is the convective derivative $\partial/\partial t + (\mathbf{U}\cdot\nabla)$.

Alternatively, heated plasmas can generate currents even in the absence of plasma flow. An example is the diamagnetic current (current density $\mathbf{J}_D$). With diamagnetic materials in the laboratory, currents flow on the surface of the material. Similarly, diamagnetic currents in space flow predominantly on the boundaries of plasma regions in the presence of pressure gradients (∇P; $\mathbf{J}_D = c\mathbf{B} \times (\nabla P)/B^2$). Energy can be extracted from such pressure differentials in the presence of electric fields (where $\mathbf{E}\cdot\mathbf{J}_D < 0$). It is not known the extent to which the magnetosphere acts as an MHD generator (extracting energy through flow dynamics) or a thermoelectric generator (extracting thermal energy from the plasmas). Indeed, as the plasmas in the magnetic tail flow earthward, a pressure-balance crisis arises. That crisis is thought by some researchers to be responsible for one of the key dynamical

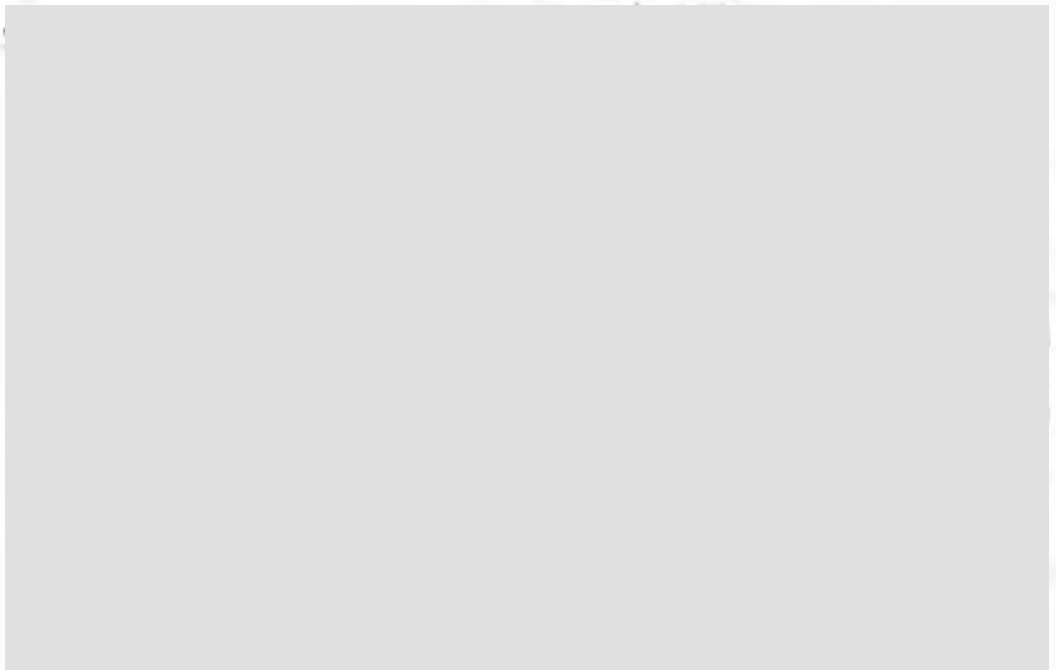

[redacted]

reconfigurations of the magnetosphere associated with the dynamics of the aurora: "magnetospheric substorms" [*Erickson and Wolf*, 1980; *Schindler and Birn*, 1982]. The pressure/thermal content of the flowing plasmas cannot be ignored. There are other sources of electric current in space plasmas that cannot be treated here due to space limitation [e.g., *Parks*, 1991]. The character of the magnetospheric generator is uncertain, in part, because of the availability of multiple mechanisms for generating current in space plasmas.

Because the near-equatorial currents created by the magnetospheric generator flow within sparse plasmas that have sharp spatial gradients, the currents strongly diverge in certain regions ($\nabla \cdot \mathbf{J}_\perp \neq 0$, where $\mathbf{J}_\perp$ is the vector component of the magnetospheric current density perpendicular to $\mathbf{B}$; e.g., *Parks*, 1991). The divergences require the flow of electric currents along the magnetic field lines either towards or away from the upper atmosphere. Such divergences occur, for example, in the presence of shear flows or density gradients for an MHD generator. They also occur where plasma pressure gradients are not aligned with magnetic field strength gradients for diamagnetic current-driven generators. Within the near-Earth magnetic tail, current divergences tend to maximize away (east and west) from the symmetry axis defined approximately by the Sun-Earth line. Such divergences are the source of the field-aligned currents in Plate 4 directed between the distant magnetosphere and the ionosphere.

It is worth noting that the field-aligned currents that arise from the divergence of the diamagnetic current (and other currents not discussed) are sometimes presented differently in the literature [e.g., *Spiro and Wolf*, 1984]. For plasma whose particle velocity distributions are isotropic (approximately uniform with respect to angular direction in the plasma's rest frame), the divergence of the diamagnetic current is identical to the divergence of the currents calculated using the guiding-center particle drift velocities. These drifts arise from the gradients and curvatures of the magnetic field configuration. Using these guiding-center drifts can be convenient even though the currents associated with them are identically canceled by contributions to the magnetization current for isotropic distributions [*Parks*, 1991]. The disadvantage of the guiding-center drift approach is that the calculated currents perpendicular to $\mathbf{B}$ are incorrect unless the magnetization currents are also included.

Among the most important questions about the nature of the magnetospheric generator are: (1) How are the currents generated in different regions? (2) What is the magnitude of the generator's impedance? and (3) What role do large-scale magnetospheric waves play in the generation of the field-aligned electric currents? Regarding the generator impedance, if it is a high value, the magnetosphere acts essentially as a current generator. As such it has a great deal of control over the magnitudes of the currents that must flow and the level of the Earth-system response (e.g., intensity of the aurora). If the generator impedance is low, it acts essentially as a voltage source. With this scenario the ionospheric response to the currents has a much greater control over the Earth-system response to the generator. The question of the impedance of the magnetospheric generator has a direct consequence for the age-old question as to whether the magnetosphere or the ionosphere controls the level of the interaction between these two systems. We do not know the impedance of the magnetospheric generator because we do not know which mechanism or mechanisms prevail in the generation of the magnetospheric currents.

In the discussion above, we have not defined the word "impedance." In electrical circuits the word "resistance" often implies a linear relationship between current and voltage. In common usage among electrical engineers, the word "impedance" is more general in several respects, and admits to nonlinear relationships between current and voltage. The relationship between current and voltage within space plasmas is generally highly nonlinear, as an example in the next subsection illustrates. However, given a specific configuration of a system component, that relationship is deterministic and can capture consequences of the physics of a specific region on the rest of the plasma system.

3.3 Mid-Altitude Controller

As the electric currents flow towards the upper atmosphere they encounter a region at mid altitudes (~0.5 to 2 R_E above the Earth's surface; Plate 4) that has difficulty carrying the higher electrical currents that the magnetosphere sends it. The difficulty arises because, given only slowly varying plasma densities along the magnetic field lines, the number of charge carriers decreases rapidly as one moves along the funnel-shaped bundle of magnetic field lines (a "flux tube") towards the Earth's upper atmosphere. One expects that as current density increases, the crisis occurs first at altitudes just above the region of gravitationally bound ionospheric plasmas (altitudes > 0.5 R_E). The crisis should extend to higher altitudes as the current densities increase.

For such high current densities the region develops effective parallel (nonlinear) impedance that resists the flow of the electric current. A consequence of that impedance is the generation of electric fields parallel to the magnetic field, required to force the flow of current that is being forced on the region by the magnetosphere. The parallel electric fields correspond to potential drops typically up to several kilovolts (kV), but sometimes as high as ~30 kV [*Arnoldy*, 1981]. These electric fields accelerate electrons and ions along the magnetic field lines. In turn, the accelerated particles cause the more intense

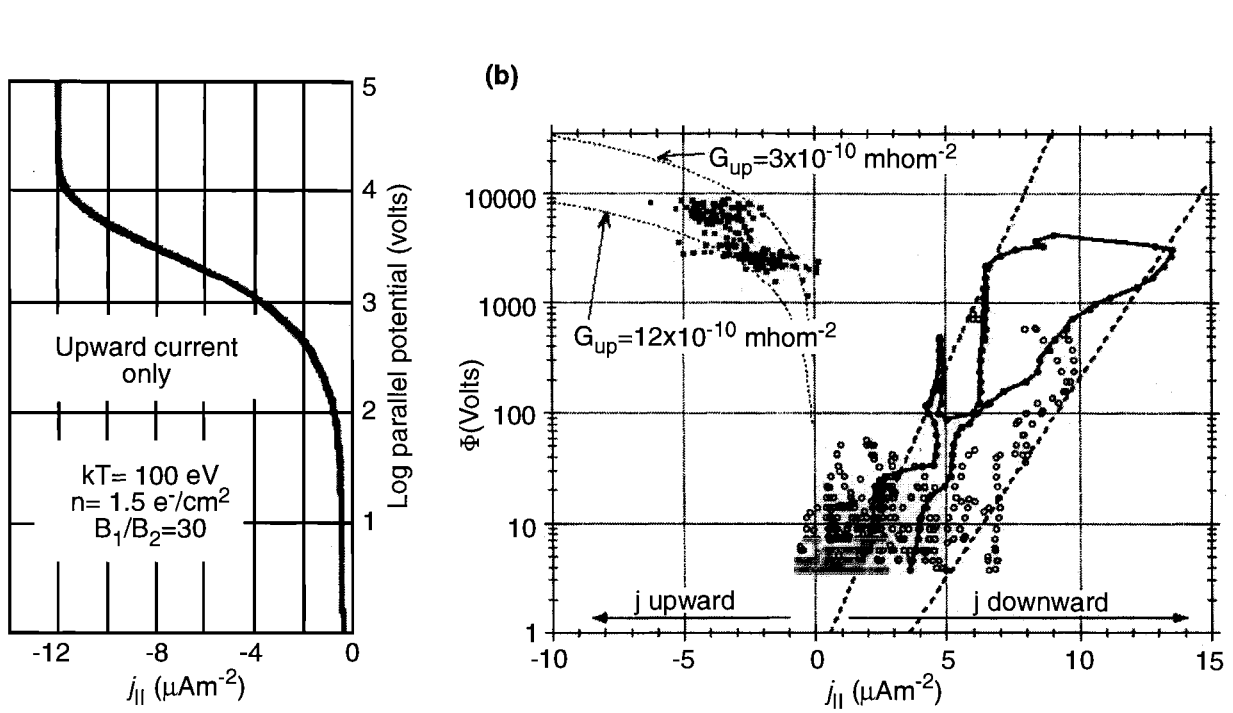

Figure 2. Magnetic field-aligned current (I) versus voltage (V) impedance curve within the mid-altitude M-I coupling controller region. (a) An ideal curve for upward currents only based solely on coherent guiding-center motion of electrons [*Knight*, 1973; *Lyons*, 1981]. (b) An attempt to obtain the true curve using FAST measurements for both upward and downward currents [*Elphic et al.*, 1998].

or "discrete" auroral lights when they impact the atmosphere. (The much less intense "diffuse" aurora results from the simple angular scattering of charged particles trapped in Earth's magnetic field so that they precipitate onto the atmosphere without additional acceleration.) In Plate 4 the parallel electric field is represented by equipotential surfaces that have a nested V-shape structure. The schematic is highly idealized since during active periods one anticipates a high degree of structuring within that pattern of potentials. Additionally, the structures may be fundamentally wave-like in nature and thus intrinsically time dependent [e.g., *Samson et al.*, 1996].

Knight (1973) developed the simplest model for the development of parallel electric fields within this "controller" region of high parallel impedance. He derived the potential drop needed to achieve a specific current value by considering the motion of fast-moving electrons along funnel-shaped magnetic flux tubes. One utilizes the guiding-center approach to solving Newton's equation ($q\,\mathbf{E} + q\,\mathbf{v} \times \mathbf{B}/c = m\,d\mathbf{v}/dt$) for which one assumes that the radius of charged particle gyration is very small and that intrinsic time variations are slow. Here one also assumes that the electric field is a **B**-aligned potential field ($\mathbf{E} = \mathbf{b}\,E \cong -\,\mathbf{b}\,d\Phi/dz$, where **b** is a unit vector along **B** and Φ is electric potential). Figure 2a shows an example of the resulting current (I) versus voltage (V) relationship (plotted using the expression of *Lyons*, 1981). Note the nonlinear character of this impedance curve.

The Knight relationship may be modified and indeed dominated by microphysical plasma processes. Specifically, plasma waves or similar collective structures such as electrostatic solitary pulses can exchange momentum with streaming electrons and ions and impede the parallel motion of these charge carriers (Plate 5b, c, d). A list of many such proposed impedance-generating processes is provided in Table 1 of *Borovsky* (1993). Examples of processes discussed in the literature are 1) "double-layers," shock-like structures that support charge-separation electric fields along **B** with the momentum changes of ions and electrons that are accelerated as they pass through the structure, 2) large-scale electric fields supported by the magnetic mirror force when the angular distributions of electrons and ions are different, and 3) parallel electric fields supported by Alfvén waves propagating at large angles to **B**.

Figure 2b shows an attempt to construct a true nonlinear impedance curve with measured parameters. Note that the abscissa is the same as that in Figure 2a. The FAST spacecraft obtained the measurements as it flew directly through the controller region [*Elphic et al.*, 1998]. The overlaying dotted lines

[redacted]

[redacted]

[redacted]

[redacted]

[redacted]

[redacted]

[redacted]

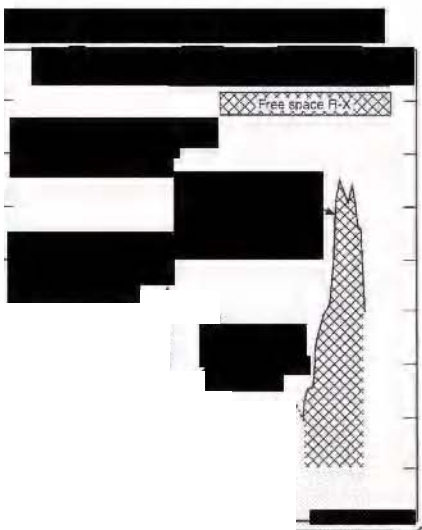

[redacted]

for negative currents (downward electrons) show what linear impedance (not the Knight expression) would look like on this semi-logarithmic display. There is no "Knight expression" for positive currents. Thus, microphysical plasma processes must provide all of the impedance relating to such currents. We do not yet have a good measurement of the true I vs. V curve for many conditions, and we do not understand much of the physics that generates those curves that we do have.

Plate 5a shows schematically that in a region where parallel electric fields prevail, field line slippage can occur; the magnetic field lines lose their identities and can no longer be mapped with impunity from one region to another. We discuss these concepts in section 5.

Critical outstanding questions for the controller region include: (1) What mechanism or mechanisms generate the parallel impedance in a collisionless plasma? and (2) Why is the controller region so highly structured in space and time? The extreme structuring of the aurora may be a consequence of the simultaneous participation of the many processes documented by *Borovsky* (1993), possibly via strong turbulent coupling between the different phenomena.

3.4 Ionospheric Load

The currents finally close across magnetic field lines within the partially collisional and resistive ionosphere, the third critical region of the M-I coupling circuit (Plate 4). With decreasing altitude, the combination of increasing cold plasma density (ionospheric plasma) and increasing neutral gas density allows the electrical conductivity "σ" to reach sufficient magnitude to allow the currents to close. The role of the neutral atmosphere is critical, specifically the thermosphere, which is the highest layer of the atmosphere that is collisional. The conductivity becomes large when collisions between neutral gas and cold ions are frequent enough to disrupt the orderly helical gyro-motions of the ions as they move in the Earth's magnetic field **B**. Following a collision, an ion can move in the direction of an applied electric field and carry current perpendicular to **B** for some fraction of a gyro-period. Because the gyro-motions are only partially disrupted, an electric field in one direction (say "x") generates current in both the "x" direction and the "y" direction (where $\mathbf{B} \equiv B\,\mathbf{z}$). The "x" and "y" currents are the Pedersen and Hall currents, respectively. Thus, the response of the ionosphere to magnetospheric forcing is complicated in the first place because the conductivity is a tensor rather than a simple scalar [*Parks*, 1991].

What makes this third region so interesting is that it is much more than just a passive load for the interaction. It responds to the electric current forcing in several additional important ways. The charged particles, particularly electrons, that are accelerated within the controller region strike the upper atmosphere, change its level of ionization, and thus modify the conductivity of the ionosphere. With this scenario there is the possibility of feedback instability that some researchers have identified as being an important aspect of M-I coupling [e.g., *Watanabe and Sato*, 1988]. An increase in current can lead to an increase in the conductivity, which in turn increases the amount of current that flows, and so on ad infinitum. *A critical question is: What is the importance of ionospheric feedback on the behavior of the M-I coupling circuit?* The answer is affected by our understanding of the impedance of the magnetospheric generator. If the magnetospheric generator impedance is high then the modifications of the ionospheric conductivity will not have a great effect on the amount of current that flows. It may still affect, however, how the current flow is distributed and thus how structured it is.

The second important, non-passive way that the ionosphere and thermosphere respond to magnetospheric forcing is to heat and accelerate ionospheric plasma out towards the controller region and into the magnetosphere [*Shelley and Collin*, 1991]. When the new plasmas come into contact with the hot magnetospheric plasmas, it is likely that microphysical plasma processes modify the current carrying properties of the controller region. Even in the absence of increases in wave or solitary structure activity, the Knight expression itself will be modified by the presence of different plasma populations. *Thus, an important question for the ionospheric response is: How are the impedance and the structuring that occur within the controller region affected by the transport of ionospheric plasmas to the mid-altitude regions*?

A third non-passive way that the ionosphere and thermosphere respond to magnetospheric forcing is to store and then redistribute magnetospheric energy. Currents applied over large spatial scales cause the ionospheric plasma to flow predominantly within planes parallel to the Earth's surface via the $\mathbf{J} \times \mathbf{B}/c$ force. Collisions between the plasma and the neutral gas cause neutral gas winds in the thermosphere [*Killeen et al.*, 1995]. When the magnetospheric source of current is shut down, momentum insures that the neutral winds continue to flow and carry the now reluctant ionospheric plasmas with them via collisions. The ionosphere-thermosphere system thus becomes a MHD generator rather than a load. It generates currents that diverge into the magnetosphere until the flow energy that resides within the neutral atmosphere is used up. The neutral thermosphere thus acts as an energy storing "flywheel" [*Lyons et al.*, 1985].

What can be lost in presentations and discussions of the M-I coupling problem is that one cannot focus on just the magnetosphere, just the controller region, or just the ionosphere. One must consider the behaviors of all three regions simultaneously. The amount of current that flows between

the magnetosphere and the ionosphere is determined by the extent and magnitude of the currents and current divergences associated with the magnetospheric generator, the impedance of the magnetospheric generator, the impedance of the controller region, and the conductivities that prevail within the ionosphere. Because they are nonlinear, the impedances themselves are a function of the amount of current that flows and on the exchanges of materials that occur between the different regions. The M-I system involves strongly coupled regions and processes and is therefore difficult to understand.

4. THE UNIVERSALITY OF M-I COUPLING: AURORAL PROCESSES AT JUPITER

M-I coupling is representative of a class of astrophysical problems involving the interaction between very different plasma regimes that are connected by magnetic fields. Jupiter, when compared to Earth, provides the strongest case for the conclusion that auroral-like processes are ubiquitous to magnetized plasmas. We have already provided evidence for such processes at Jupiter, a planet that is fundamentally distinct from Earth in many respects. Jupiter is doubly interesting in the fact that it hosts a greater variety of different kinds of auroral processes than does Earth. Here we discuss auroral processes associated with Jupiter's moon Io, Io's extended plasma environment, and Jupiter's global auroral oval.

4.1 Io's Auroral Spot

One of the most interesting of the Jovian auroral processes is that associated with the moon Io. It was discovered that auroral emissions occur in a spot-like region of Jupiter's atmosphere just where the Jovian magnetic field line that passes through this well-known volcanic moon touches down on Jupiter's upper atmosphere (at Io's magnetic footpoint; *Connerney et al.*, 1993). We now also know that there are spots associated with the moons Europa and Ganymede as well. The Io spot (with its now-recognized tail) is shown in Plate 6a [*Clarke*, 1998]. More recently, the Galileo spacecraft observed intense electron beams aligned to Jupiter's magnetic field lines directly in Io's vicinity (Plate 6b; *Williams et al.*, 1996; 1998; *Frank and Paterson*, 1999; in Plate 6b the electron enhancement along the magnetic field is periodic because of the rotation of the spacecraft.). These beams are reminiscent of similar beams observed in the Earth's equatorial magnetosphere and attributed to low-altitude auroral acceleration processes [*Klumpar et al.*, 1988; *Carlson et al.*, 1998; see *Mauk et al.*, 2001]. When the characteristics of the beams are considered in combination with both the auroral spot observations and Voyager measurement of strong magnetic field-aligned currents connecting Io and Jupiter [*Ness et al.*, 1979], a story emerges that has substantial similarities to our discussion of M-I coupling at Earth with Plate 4 (Plate 6c).

As Jupiter's magnetized plasmas flow past the partially conducting Io, it acts as an electrical generator of currents and voltages. (Plate 6c shows a highly idealized configuration that ignores the space-environment disturbances.) The currents flow away from Io along Io's magnetic flux tube to where they close across field lines in Jupiter's upper atmosphere and ionosphere. We infer from the characteristics of the electron beams [Plate 6b; *Mauk et al.*, 2001] that as the currents approach Jupiter along field lines (~0.5 to 1 R_J altitude) they encounter a region of auroral-like electrical impedance analogous to the impedance identified for the controller region of Plate 4. We conclude that the acceleration of electrons towards Jupiter within this controller region at Jupiter is the cause of the spot-like optical emissions highlighted in Plate 6a. (The electron beams observed directly in the vicinity of Io are not those that cause the auroral emissions. With respect to Jupiter they are upward accelerated electrons and are part of the return current of the electrical circuit – *Mauk et al.*, 2001.)

The similarities between the physical systems diagrammed in Plates 4 and 6c are clear even given the obvious dramatic differences between the two systems involved. Auroral-like coupling is likely a general property of magnetized space plasmas.

4.2 Io's Extended Environment

An interesting aspect of the auroral emissions at Io's magnetic footpoint on Jupiter is the presence of the long "tail." Jovian auroral emissions associated with Io have been observed to extend approximately half a Jovian rotation behind this moon's magnetic projection onto Jupiter (Plate 2). The wake region sampled immediately behind Io is essentially flow-stagnant in the reference frame of Io [*Frank et al.*, 1996]. Strong velocity shear between the stagnant wake and the adjacent, high-speed plasmas rotating with Jupiter near Io probably cause the field-aligned currents. (Recall our previous discussion of the consequence of velocity shear on MHD generators.) The extended auroral wake signature indicates that the plasmas take a considerable time to be accelerated up to the corotation speed in the region downstream of Io.

4.3 Jupiter's Auroral Oval

Jupiter's main auroral oval (Plate 7a) is thought to map along magnetic field lines to regions near the equator that are beyond about 20 R_J. Beyond 20 R_J the magnetospheric plasma flow deviates sharply from rigid corotational flow (Plate 7b). In essence, Jupiter's aurora is a distinct signature of Jupiter's


(a)


$J_{||}$
Magnetic field lines

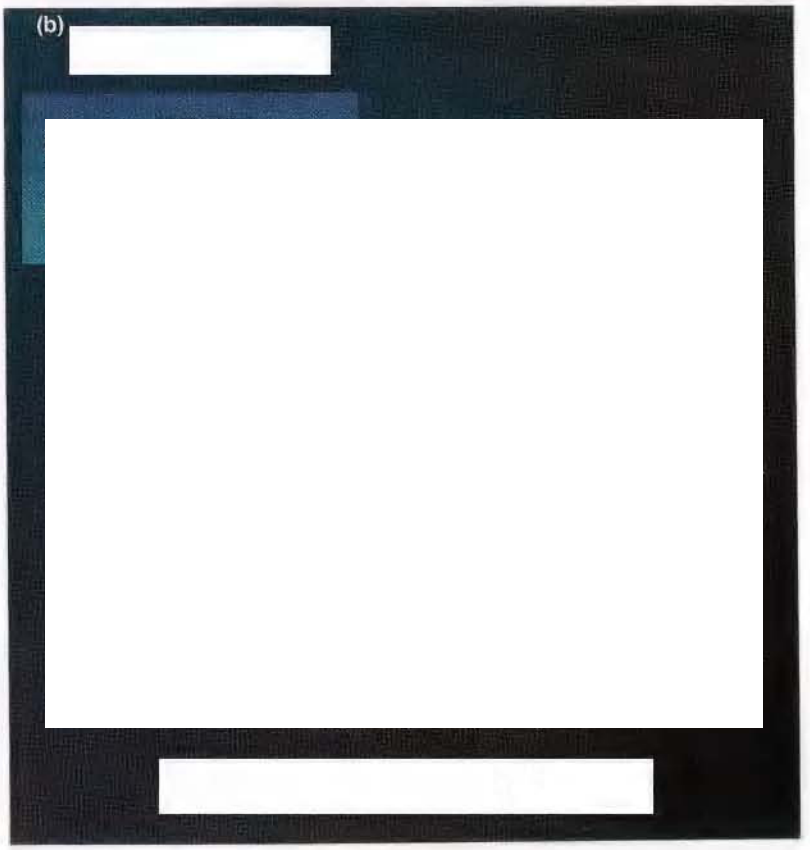
(b)

(a)

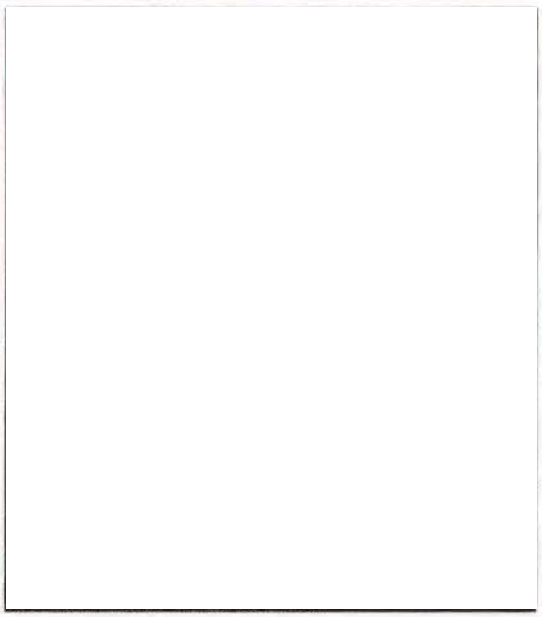

attempt to shed angular momentum by spinning up its space environment.

Jupiter sheds angular momentum using magnetic fields and electric currents. When Plate 7c [from the concepts of *Hill*, 1979, and *Vasyliunas*, 1983] is compared to Plates 4 and 6c, the story becomes increasingly familiar. When viewed in a frame of reference corotating with Jupiter (see later discussion), the distant magnetospheric region acts as a huge electromagnetic generator. Jupiter's magnetosphere must rid itself of about 1 ton of "iogenic" materials per second generated by the volcanic moon Io. The charged component of that material is transported radially outward in Jupiter's magnetic field [e.g., *Siscoe and Summers*, 1981]. The potential energy associated with those materials "falling down" the centrifugal potential well is tapped for plasma heating and for driving the electric currents that constitute the magnetospheric generator sketched in Plate 7c [*Hill*, 2001]. Specifically, as the iogenic materials move radially outward, the Coriolis force (in this rotating frame) causes azimuthal flows (counter to the nominal rotation direction) which, in the manner of a MHD generator, drive outward radial currents (**J**) in a direction against the inward radial electric field (**E**) that prevails in the rotating frame ($\mathbf{E}\cdot\mathbf{J} < 0$). (Ignored here is the thermal content of the plasmas, as discussed at the end of this section.) Just as with the case of Earth and Io, the electric currents diverge and flow along field lines towards Jupiter and close across field lines within the upper atmosphere and ionosphere. We believe that at relatively low altitudes the parallel currents encounter a region of parallel impedance that resists the flow of the currents and accelerates the electrons into Jupiter's atmosphere causing the aurora.

There have been varying ideas about the causes of the Jovian aurora [e.g., *Broadfoot et al.*, 1981; *Thorne*, 1983; *Gehrels and Stone*, 1983; *Waite et al.*, 1988]. During the Voyager epoch it was thought that the aurora was caused principally by heavy ion precipitation (S and O from Io) onto the atmosphere with a source not very far outside of the orbit of Io. At Earth there are auroral emissions, called diffuse auroral emissions, unrelated to mid-altitude impedance or controller regions. The scattering of energetic electrons (and to a lesser extent ions) that are trapped by the "magnetic bottle" of the Earth's magnetic field cause these emissions. The scattering changes the velocity vectors of a small fraction of the particles so that they point almost exactly along the magnetic field lines. This is the direction of the "loss cone" of the magnetic bottle. Particles within the loss cone escape to the atmosphere and cause optical emissions. Is Jupiter's aurora an analog to Earth's diffuse aurora? Does the simple scattering of trapped ions or electrons cause it?

The reasons we believe that the strong Jovian auroral emissions are caused by acceleration within a mid-altitude impedance region are threefold. First, since the Voyager epoch it has been shown that the aurora maps predominantly to regions beyond 15 to 20 R_J. The best evidence comes from the relationship between Io's spot and Jupiter's auroral oval, beginning with *Connerney et al.*, (1993). Second, in the regions beyond 15 to 20 R_J there is generally not enough energy intensity (I_E = ergs/cm^2·s·sr) contained within the trapped charged particles to account for the more intense auroral emissions with simple scattering (yielding a maximum precipitation flux of = πI_E ergs/cm^2·s). At ~16 R_J that intensity is ~10 ergs/cm^2·s·sr [*Mauk et al.*, 1996], and falls sharply with radial distance to values below 1 erg/cm^2·s·sr for $R > 30\ R_J$ [*Bhattacharya et al.*, 2001]. The more intense auroral emissions require > 100s of ergs/cm^2·s·sr [e.g., *Clarke et al.*, 1986]. Thus, the mid-altitude accelerator is needed to add energy to the particles to provide enough energy to the aurora. Finally *Bhattacharya et al.* (2001) observed electron angular distributions within the middle Jovian magnetosphere that are similar to the field-aligned electron beams observed in the middle magnetosphere at Earth [*Klumpar et al.*, 1988] and in the wake of Io (Plate 6b). With Earth-derived understanding, these field-aligned distributions are likely signatures of a mid-altitude impedance region.

We turn here to the issue of the "frame of reference" that we mentioned near the beginning of this section. The dominant source of energy for driving Jovian magnetospheric processes is the rotating planet. How is it, then, that we find the generator for the M-I coupling circuit to reside within the distant space environment of Jupiter and not at Jupiter itself? The answer is in our chosen frame of reference. In our very simple description of the magnetospheric generator at Jupiter, we chose to examine the system in a frame of reference rotating with Jupiter. In the nonspinning frame of reference, it is the ionosphere and upper atmosphere of Jupiter that plays the role of generator for our simple description. The $\mathbf{v} \times \mathbf{B}/c$ force resides within the ionosphere, points equatorward, and can drive currents within the ionosphere in a direction that opposes the reactive electric field ($\mathbf{E}\cdot\mathbf{J} < 0$). Our choice of a frame of reference (rotating) obviously preserves more closely the analogy between Earth and Jupiter M-I coupling. But, there is a larger issue. The generators that drive the global magnetospheric currents are likely far more complicated than the simple picture presented above. For example, the thermal energy content of the charged particles within the middle magnetosphere is substantially larger than the energy content associated with the rotational flow [*Mauk and Krimigis*, 1987; *Paranicas et al.*, 1991]. Also, the middle magnetosphere (> 15 R_J), which connects to the aurora, and the aurora itself, have structure in azimuth (both planetary longitude and local time) that is strong and maybe zero'th order in importance [e.g., Plate 2; *Satoh et al.*, 1996; *Khurana*, 2001; *Krupp et*

al., 2001]. Thermal energy can be tapped in the presence of azimuthal asymmetries, specifically when the particle pressure gradient is not aligned with the magnetic field strength gradient. We suspect that as with the Earth's magnetosphere, the degree to which the Jovian magnetosphere behaves as an MHD generator or a thermoelectric generator is not known. Thus, the role of the distant magnetospheric generator as a device for converting mechanical energy into electrical energy cannot be fully transformed away by changing coordinate systems.

5. AURORA AND ANGULAR MOMENTUM IN ASTROPHYSICAL SYSTEMS

We suggest with the previous discussions that auroral-like coupling is an ubiquitous aspect of astrophysical systems involving partially ionized plasmas and magnetic fields. Such coupling may also be important for understanding how such systems behave and evolve. The aspect of auroral-like coupling that may be important is its role in moderating the redistribution of angular momentum in astrophysical systems.

5.1 Rotation and the Global Jovian Aurora

One of the interesting questions at Jupiter is the role of the controller region impedance in moderating the rotational speeds of the Jupiter beyond 15 to 20 R_J. The observed lessening of the rotation beyond 20 R_J (Plate 7b) may occur primarily as a result of slippage that occurs within the resistive ionosphere [*Hill*, 1979; 1980]. If so, then the mid-altitude controller region may play the role that it does at Earth in modifying the ionospheric conductivities. Increasing field-aligned currents leads to increasing impedance along the field lines. Increasing impedance leads to greater field aligned electron acceleration, enhanced ionization of the upper atmosphere, and thus greater conductivity in the ionosphere. Greater conductivity in the ionosphere enhances the ability of Jupiter to accelerate its space environment up to the full corotation speed of Jupiter's atmosphere. In this way auroral-like coupling can enhance the ability of Jupiter to shed angular momentum.

Auroral-like coupling also acts to limit the effectiveness of magnetic fields as an agent of momentum redistribution. As we noted in the discussion of Plate 5, when field-aligned electric fields are present, the field lines lose their identities, and the field lines attached to the planet can "slip" with respect to the more distant field lines. Reference to "field-lines" in this context can be confusing. Field line slippage at the mid-altitude impedance region can be illustrated more concretely by the electric field drift of cold plasmas that reside just above and just below the impedance region. The field-aligned electric field yields a shearing of the perpendicular plasma flows as one moves along field lines through the mid-altitude controller region.

A possible measure of the relative importance of field-line slippage within the ionosphere and slippage within the mid-altitude controller region is the relative magnitude of the potential drop along field lines and across the field lines within the region of current flow. Magnetic field-aligned potential drops range between a few kV to several 10s of kV at Earth, and may be up to an order of magnitude greater at Jupiter. The potential drop from the equatorward to the poleward edge of the auroral oval at Jupiter may be 100s of kV to a number of MV. From this perspective, one is tempted to ignore the slippage that occurs within the mid-altitude regions. However, here is where the question of spatial structuring, highlighted in previous sections, becomes so important. If most of the field-aligned current is carried in small-scale filamentary structures, then the potential drop along the mid-altitude impedance region can be substantially greater than the potential drop across the filaments within the ionosphere. In this case the mid-altitude impedance region would be playing a substantial role in controlling the rotational dynamics of Jupiter's magnetosphere. Because quantities such as energy dissipation are nonlinear combinations of parameters (e.g., current $\times$ voltage), one may not spatially average away the effect of the structuring.

At Earth the crossover spatial scale where field-aligned and cross-field potential drops are comparable is ~100 km [*Gorney*, 1991 and references therein]. During active periods a lot of the field-aligned current is carried by structures much smaller than 100 km [*Gorney*, 1991; *Borovsky*, 1993; *Gurnett*, 1991; *Lanchester et al.*, 1997]. Thus, in the case of the active Earth auroral regions, field-line slippage at the mid-altitude controller region can provide a significant contribution to the ability of the magnetic field lines to redistribute momentum between the Earth and the space environment. The importance of spatial structuring and the mid-altitude impedance region in controlling the rotational dynamics of Jupiter's magnetosphere is not known at this time.

5.2 Momentum Redistribution in Astrophysical Systems

We have dwelled on the issue of the redistribution of angular momentum by means of electric currents because equivalent processes have been invoked for other astrophysical systems where our state of knowledge is grossly inferior to that of Earth and Jupiter. One process where magnetic field momentum management may be key is the formation of star/planetary systems. There is a general consensus in the literature on solar system formation (e.g., *Protostars and Planets III*, University of Arizona Press, 1993) that magnetic fields

play critical roles in the formation and evolution of so-called molecular cloud cores (Plate 7d, left drawing; *Shu et al.*, 1993). Molecular cloud core formation constitutes the first stage of star/planetary system formation as high-density concentrations of materials congeal out of giant molecular clouds. Recent important work on the role of magnetic fields in molecular cloud cores includes *Crutcher* (1999) and *Boss* (1999). Magnetic fields are thought to help control the collapse of the clouds, their tendency to break up into multiple star systems, their early-phase spins, and their interactions with each other and with their environments.

Much more controversial is the role of magnetic fields during later phases of the star/planet system formation. The evolution of protostars (Plate 7d, middle drawing) into stars requires the shedding of over 98% of the angular momentum of the central body. Any of a number of proposed means may accomplish momentum shedding, many of which invoke only gravitational effects. However, among those proposed are mechanisms that make use of magnetic fields (Plate 7d, right drawing; *Shu et al.*, 1993).

Our purpose here is not to stake claims about the importance of magnetic fields for any particular astrophysical system. It is rather to make the point that when one reads the literature about possible roles for magnetic fields in such systems, there is much about magnetic fields and absolutely nothing about electric current. And yet, for the several systems where some understanding about how magnetic fields do redistribute momentum has been developed (the Earth's M-I system, the rotation of Jupiter), the manner and degree to which the required parallel electric currents interact strongly with the local plasma medium may turn out to be critical. That interaction, with its associated development of magnetic field-aligned impedance, particle acceleration, and space-time structuring, may be fundamental to assessing the effectiveness of the magnetic fields in redistributing the momentum in general astrophysical systems involving partially ionized gases and magnetic fields.

For this reason the study of M-I coupling at Earth and Jupiter is more than just understanding how one or two special and peculiar space environments behave. These environments may provide key clues as to how astrophysical systems throughout the universe behave and evolve.

CONCLUSIONS

While we know much more about momentum transfer using magnetic fields for the space environments of Earth and Jupiter than we know for extrasolar environments, there remain many mysteries about M-I coupling even at Earth. We do not understand the nature of the magnetospheric generator and thus we cannot predict the degree to which M-I coupling is controlled by the magnetosphere or the ionosphere. We do not know in general how the magnetic field-aligned impedances are established nor why the controller region is so highly structured in space and time. In particular, we would like to know whether high degrees of space-time structuring, and even hierarchical structuring such as that associated with turbulence, are fundamental aspects of the coupling between different astrophysical systems by means of magnetic fields. We do not know the extent to which the response of the ionosphere (in the form of conductivity-moderated feedback or the transport of ionospheric plasmas into the controller region) changes the M-I interactions quantitatively or changes the fundamental qualitative nature of the interaction.

We must learn much more about Earth's M-I coupling system before we can predict the nature of the interactions at Jupiter, much less those at more distant systems. New classes of missions that involve the formation flying of multiple spacecraft through the auroral acceleration region will be key to addressing one of the most fundamental issues: separating spatial from temporal effects so that the fundamental nature of the impedance-generating interaction can be attacked.

We are exceedingly fortunate that Jupiter is available for intensive study in parallel with our studies of Earth. Jupiter offers an environment that is substantially different from the Earth system, but not too different, so that we can test the predictability of the theories developed for Earth. That is the power of the comparative approach when laboratory-style hypothesis testing is not viable. Jupiter is also immeasurably valuable in that it is a much closer analog to some of the extrasolar environments that we wish to understand than is the Earth system. Just as angular momentum management is a critical issue in the formation of extrasolar planetary systems, the physics of angular momentum shedding is fundamental to how Jupiter's magnetosphere-ionosphere system behaves. We find that the fundamental physical processes that control M-I coupling at Jupiter are probably shared with M-I coupling at Earth. Because of Jupiter and our ability to compare our own system with it, we know that M-I coupling processes are not only ubiquitous to astrophysical plasma systems, but they are likely important to how such systems behave and evolve.

To extrapolate our knowledge of the Earth system to extrasolar environments, we must better understand the relationship between the physics that we see at Jupiter and the physics that we see at Earth. In the area of M-I coupling, that means we must visit the high-latitude, low altitude auroral acceleration regions at Jupiter with appropriate in situ fields and particle instrumentation. Several Jupiter polar orbiter missions that are being considered by the community for flight would firmly establish the connection between the M-I coupling processes operating at both Jupiter and Earth.

Acknowledgments. B. H. Mauk acknowledges valuable discussions with Nelson C. Maynard on the organizing principles of magnetosphere-ionosphere coupling. This work was supported in part by NASA Grant NAG5-1081 on comparative magnetospheres.

REFERENCES

Alfvén, H., Electric currents in space plasmas, *Rev. Geophys. and Space Phys., 15*, 271, 1977.

Arnoldy, R. L., Review of auroral particle precipitation, *Physics of Auroral Arc Formation, Geophysical Monograph 25*, p. 56, American Geophysical Union, Washington D.C., 1981.

Baron, R. L., T. Owen, J. E. P. Connerney, T. Satoh, and J. Harrington, Solar wind control of Jupiter's H_3^+ Auroras, *Icarus, 120/2*, 437, 1996.

Bhattacharya, B., R. M. Thorne, and D. J. Williams, On the energy source for diffuse Jovian auroral emissivity, *Geophys. Res. Lett., 28*, 2751, 2001.

Borovsky, J. E., Auroral arc thickness as predicted by various theories, *J. Geophys. Res., 98*, 6101, 1993.

Boss, A. P., Collapse and fragmentation of molecular cloud cores VI. Slowly rotating magnetic clouds, *Astrophys. J., 520*, 744, 1999.

Boyd, T. J. M. and J. J. Sanderson, *Plasma Dynamics*, Barnes and Noble, Inc., New York, 1969.

Broadfoot, A. L. et al., Overview of the Voyager ultraviolet spectrometry results through the Jupiter encounter, *J. Geophys. Res., 86*, 8259, 1981.

Burch, J. L., Micro/mesoscale coupling in the auroral region: Observations, in *Cross-Scale Coupling in Space Plasmas, Geophysical Monograph 93*, p. 87, American Geophysical Union, Washington D.C., 1995.

Carlson, C. W., et al., FAST observations in the downward auroral current region, energetic upgoing electron beams, parallel potential drops, and ion heating, *Geophys. Res. Lett., 25*, 2017, 1998.

Clarke, J. T., et al., Far ultraviolet imaging of Jupiter's aurora and the Io footprint, *Science, 272*, 404, 1996.

Clarke, J. T., Satellite Footprints Seen in Jupiter Aurora, Space Telescope Science Institute Press Release STScI-PRC00-38, Baltimore, Maryland, December 14, 2000.

Clarke, J. T., et al., Hubble Space Telescope imaging of Jupiter's UV aurora during the Galileo orbiter mission, *J. Geophys. Res., 103*, 20217, 1998.

Clarke, J. T., Hubble Provides Complete View of Jupiter's Auroras, Space Telescope Science Institute Press Release STScI-PRC98-04, Baltimore, Maryland, January 7, 1998.

Connerney, J. E. P., R. Baron, T. Satoh, and T. Owen, Images of excited H_3^+ at the foot of the Io flux tube in Jupiter's atmosphere, *Science, 262*, 1035, 1993.

Crutcher, R. M., Magnetic fields in molecular clouds: observations confront theory, *Astrophys. J., 520*, 706, 1999.

Eather, R. H., *Majestic Lights : The Aurora in Science, History and the Arts*, American Geophysical Union, Washington D.C., 1980.

Elphic, R. C., et al., The auroral current circuit and field-aligned currents observed by FAST, *Geophys. Res. Lett., 25*, 2033, 1998.

Erikson, G. M., and R. A. Wolf, Is steady convection possible in the Earth's magnetotail? *Geophys. Res. Lett., 7*, 897, 1980.

Frank, L. A., and J. D. Craven, Imaging results from Dynamics Explorer I, *Reviews of Geophysics, 26*, 215, 1988.

Frank, L. A., W. R. Paterson, K. L. Ackerson, V. M. Vasyliunas, F. V. Coroniti, and S. J. Bolton, Plasma observations at Io with the Galileo spacecraft, *Science, 274*, 394, 1996.

Frank, L. A., and W. R. Paterson, Intense electron beams observed at Io with the Galileo spacecraft, *J. Geophys. Res., 104*, 28657, 1999.

Gehrels, N., and E. C. Stone, Energetic oxygen and sulfur ions in the Jovian magnetosphere and their contributions to the auroral excitation, *J. Geophys. Res., 88*, 5537, 1983.

Gorney, D. J., An overview of auroral spatial scales, in *Auroral Physics*, C. -I. Meng et al., eds., p. 325, Cambridge University Press, New York, 1991.

Gurnett, D. A., and U. S. Inan, Plasma wave observations with the Dynamics Explorer 1 Spacecraft, *Reviews of Geophysics, 26*, 285, 1988.

Heikkila, W. J., Penetration of particles into the polar cap and auroral regions, in *Critical Problems of Magnetospheric Physics*, E. R. Dyer, Jr., ed., p. 67, IUCSTP, National Acad. Sci, Washington, D. C.,1972.

Hill, T. W., Inertial limit on corotation, *J. Geophys. Res., 84*, 6554, 1979.

Hill, T. W., Corotation lag in Jupiter's magnetosphere: Comparison of observation and theory, *Science, 207*, 301, 1980.

Hill, T. W., The Jovian auroral oval, *J. Geophys. Res., 106*, 8101, 2001.

Ingersoll, A. P., et al., Imaging Jupiter's aurora at visible wavelengths, *Icarus, 135*, 251, 1998.

Khurana, K. K., Influence of solar wind on Jupiter's magnetosphere deduced from currents in the equatorial plane, *J. Geophys. Res., 106*, 25999, 2001.

Killeen, T. L., and R. G. Roble, Thermosphere dynamics: Contributions from the first 5 years of Dynamics Explorer program, *Reviews of Geophysics, 26*, 329, 1988.

Kivelson, M. G., and C. T. Russell, *Introduction to Space Physics*, Cambridge University Press, Cambridge, U.K. and New York, 1995.

Klumpar, D. M., J. M. Quinn, and E. G. Shelley, Counter-streaming electrons at the geomagnetic equator near 9 R_E, *Geophys. Res. Lett., 15*, 1295, 1988.

Knight, S., Parallel electric fields, *Planet. Space Sci., 21*, 741, 1973.

Koskinen, H. J., and A. M. Mälkki, Auroral weak double layers: A critical assessment, in *Auroral Plasma Dynamics*, Geophysical Monograph 80, p. 97, American Geophysical Union, Washington, D.C., 1993.

Krupp, N., A. Lagg, S. Livi, B. Wilken, J. Woch, E. C. Roelof, and D. J. Williams, Global flows of energetic ions in Jupiter's equatorial plane, First-order approximation, *J. Geophys. Res., 106*, 26017, 2001.

Lanchester, B. S., M. H. Ress, D. Lummerzheim, A. Otto, H. U. Frey, and K. U. Kaila, Large fluxes of auroral electrons in filaments of 100 m width, *J. Geophys. Res., 102*, 9741, 1997.

Lundin, R., L. Eliasson, and J. S. Murphree, The quiet-time aurora

and the magnetospheric configuration, in *Auroral Physics*, C. I.-Meng, M. J. Rycroft, and L. A. Frank, eds., p. 177, Cambridge University Press, New York, 1991.

Lundin, R., G. Haerendel, and S. Grahn, Introduction to special section: The Freja Mission, *J. Geophys. Res., 103*, 4119, 1998.

Lyons, L. R., The field-aligned current versus electric potential relation and auroral electrodynamics, *Physics of Auroral Arc Formation, Geophysical Monograph 25*, p. 252, American Geophysical Union, Washington, D.C., 1981.

Lyons, L. R., T. L. Killeen, and R. L. Waltescheid, The neutral wind "flywheel" as a source of quiet-time polar-cap currents, *Geophys. Res. Lett., 12*, 101, 1985.

Mauk, B. H., and S. M. Krimigis, Radial force balance within Jupiter's dayside magnetosphere, *J. Geophys. Res., 92*, 9931, 1987.

Mauk, B. H., D. J. Williams, and A. Eviatar, Understanding Io's space environment interaction: Recent energetic electron measurements from Galileo, *J. Geophys. Res., 106*, 26195, 2001.

McNutt, R. L. Jr., J. W. Belcher, and H. S. Bridge, Positive ion observations in the middle magnetosphere of Jupiter, *J. Geophys. Res., 86*, 8319, 1981.

McPherron, R. L., Magnetospheric dynamics, in *Introduction to Space Physics*, M. G. Kivelson and C. T. Russell, eds. p. 400, Cambridge University Press, New York, 1995.

Ness, N. F., M. H. Acuna, R. P. Lepping, L. F. Burlaga, K. W. Behannon, and F. M. Neubauer, Magnetic field studies at Jupiter by Voyager 1: Preliminary results, *Science, 204*, 983, 1979.

Paranicas, C. P., B. H. Mauk, and S. M. Krimigis, Pressure anisotropies in the Jovian neutral sheet, *J. Geophys. Res., 96*, 21135, 1991.

Parks, G. K., *Physics of Space Plasmas*, Addison-Wesley Publishing Co., Redwood City, California, 1991.

Samson, J. C., L. L. Cogger, and Q. Pao, Observations of field line resonances, auroral arcs, and auroral vortex structures, *J. Geophys. Res., 101*, 17373, 1996.

Satoh, T., J. E. P. Connerney, and R. L. Baron, Emission source model of Jupiter's H_3^+ aurorae: A generalized inverse analysis of images, *Icarus, 122*, 1, 1996.

Schindler, K., and J. Birn, Self-consistent theory of time-dependent convection in the Earth's magnetotail, *J. Geophys. Res.*, 87, 2263, 1982.

Selesnick, R. S., and J. D. Richardson, Plasmasphere formation in arbitrary oriented magnetosphere, *Geophys. Res. Lett., 13*, 624, 1986.

Shelley, E. G., and H. L. Collin, Auroral ion acceleration and its relationship to ion composition, in *Auroral Physics*, C.-I. Meng, M. J. Rycroft, and L. A. Frank, eds., p. 129, Cambridge University Press, New York, 1991.

Shu, F., J. Najita, D. Galli, E. Ostriker, and S. Lizano, The collapse of clouds and the formation and evolution of stars and disks, in *Protostars and Planets III*, p. 3, University of Arizona Press, Tucson, 1993.

Siscoe, G. L., and D. Summers, Centrifugally driven diffusion of iogenic plasma, *J. Geophys. Res., 86*, 8471, 1981.

Spiro, R. W., and R. A. Wolf, Electrodynamics of convection in the inner magnetosphere, in *Magnetospheric Currents, Geophysical Monograph 28*, p. 247, American Geophysical Union, Washington, D.C., 1984.

Thorne, R. M., Microscopic plasma processes in the Jovian magnetosphere, in *Physics of the Jovian Magnetosphere*, A. J. Dessler, ed., p. 454, Cambridge University Press, Cambridge, U.K., 1983.

Vasyliunas, V. M., Plasma distribution and flow, in *Physics of the Jovian Magnetosphere*, A. J. Dessler, ed., p. 395, Cambridge University Press, Cambridge, U.K. and New York, 1983.

Vasyliunas, V. M., The convection-dominated magnetosphere of Uranus, *Geophys. Res. Lett., 13*, 621, 1986.

Waite, J. H. Jr., J. T. Clarke, T. E. Cravens, and C. M. Hammond, The Jovian aurora: Electron or ion precipitation?, *J. Geophys. Res.*, **93**, 7244, 1988.

Waite, J. H., et al., Auroral "flare" observed at Jupiter, *Nature, 410*, 787, 2001.

Watanabe, K., and T. Sato, Self-excitation of auroral arcs in a three-dimensional coupled magnetosphere-ionosphere system, *Geophys. Res. Lett., 15*, 717, 1988.

Williams, D. J., B. H. Mauk, R. W. McEntire, E. C. Roelof, T. P. Armstrong, B. Wilken, J. G. Roederer, S. M. Krimigis, T. A. Fritz, and L. J. Lanzerotti, Electron beams and ion composition measured at Io and in its torus, *Science, 274*, 401, 1996.

Williams, D. J., R. M. Thorné, and B. H. Mauk, Energetic electron beams and trapped electrons at Io, *J. Geophys. Res., 104*, 14739, 1999.

Brian J. Anderson, The Johns Hopkins University Applied Physics Laboratory, 11100 Johns Hopkins Rd., Laurel, MD 20723-6099.

Barry H. Mauk, The Johns Hopkins University Applied Physics Laboratory, 11100 Johns Hopkins Rd., Laurel, MD 20723-6099.

Richard M. Thorne, University of California at Los Angeles, Department of Atmospheric Sciences, Los Angeles, CA 90095-1565

Comparison of Auroral Processes: Earth and Jupiter

J. Hunter Waite Jr.

Dept. of Atmospheric, Oceanic and Space Sciences, University of Michigan, Ann Arbor, Michigan

Dirk Lummerzheim

Geophysical Institute, The University of Alaska, Fairbanks, Alaska

Aurora at Jupiter and Earth provide both interesting contrasts and similarities in our study of comparative planetary aurora. The major contrast lies in the driving forces behind the aurora. Jupiter's magnetosphere is largely powered by the internal rotation of the planet, facilitated by the release of SO_2 from Io and its subsequent ionization and acceleration in the rapidly rotating Jovian magnetosphere. The constant angular acceleration of this plasma as it moves from Io out into the outer magnetosphere drives a global current system that results in field-aligned acceleration of electrons much like the acceleration of electrons in Earth's field-aligned current system. However, the Earth's current system is driven by the interaction of the solar wind with the Earth's magnetosphere. Thus the plasma microphysics and aeronomy of the auroral emission process are quite similar while the macroscopic driving force provides an important contrast.

INTRODUCTION

The two best observed auroras in the solar system belong to Earth and Jupiter. Earth is home. Our familiarity coupled with our observational capabilities both on the ground and in space make its aurora the best observed and the best understood within the solar system. Jupiter's aurora comes in a surprisingly close second due to its tremendous intensity driven by the most powerful magnetosphere in the solar system, the enhanced planetary astronomical capabilities of the Hubble Space Telescope and now Chandra, and the number of spacecraft that have provided in situ observations of its magnetosphere: Pioneer 10 and 11, Voyager 1 and 2, Ulysses, Galileo, and Cassini. These two auroral examples provide both interesting points of contrast and surprising similarities. The contrast between the two derives principally from the basic difference in the driving forces behind the dynamics of the planet's magnetospheres. Earth's magnetosphere is largely driven by the interaction between the solar wind and Earth's intrinsic magnetic field. This interaction dominates the dynamics of the basic ion transport pattern within the magnetosphere and is ultimately the source of energy for auroral processes. Magnetospheric transport in the Jupiter system is largely driven by the rapid rotation of the ionosphere. Magnetospheric-ionospheric coupling taps this rotational energy. The endogenous source of plasma results from ionization of volcanic material from the satellite Io. Corotational electric fields in the ionosphere and momentum transfer via field-aligned currents spin up the plasma to corotation velocities in the magnetosphere, thus driving the magnetospheric dynamics and global current system (see Chapter II.1). However, as we will see, the aurora at Jupiter also shows signs of the influence of the solar wind on the magnetosphere.

As to similarities, both the aeronomy of the energetic particle beam interaction with the upper atmosphere and the

Atmospheres in the Solar System: Comparative Aeronomy
Geophysical Monograph 130

10.1029/130GM08

plasma microphysics that lead to energetic particle precipitation into the atmosphere seem to be quite similar. At Earth and Jupiter, both energetic electrons and ions interact with the gas in the upper atmosphere at high latitudes to produce heating, ionization, and emissions that range from gamma-ray to radio wavelengths. At Earth and Jupiter the electron processes are similar but the target gases are different; at Jupiter it is H and H_2, whereas at Earth it is O, O_2, and N_2. And Jupiter's precipitating ions are largely energetic sulfur and oxygen, as opposed to predominantly protons at Earth.

While a broad overview of aurora throughout the solar system appears in Chapter I.4, a more detailed comparison between auroral processes at Earth and Jupiter is the focus of this review. The associated body of relevant research is very large, so we can only choose a few relevant points of comparison to discuss. These include: the magnetospheric origin of auroral processes, the aeronomy of the auroral emission process, and the basic morphology of the auroral emission pattern and its implications for magnetospheric dynamics.

THE MAGNETOSPHERIC ORIGIN OF AURORAL PROCESSES

The Earth's magnetospheric structure and dynamics are driven by the interaction of the solar wind with the internal magnetic field of the planet. *Axford and Hines* [1961] were the first to demonstrate how this interaction drives the convection of ions within the magnetosphere. *Dungey* [1961] demonstrated the importance that reconnection between magnetospheric magnetic field lines and interplanetary magnetic fields play in the transfer of material, momentum, and energy from the solar wind to the magnetosphere. This transfer leads to both directly-driven and "loading" processes [i.e., *Baker*, 2000] within the magnetospheric system that create the energetic particle populations in the radiation belts and lead to the redistribution of momentum that drives the global magnetospheric current system. These in turn result in the diffuse (scattered energetic particles) and discrete auroral process (accelerated electrons carrying the field-aligned current) we see in the high-latitude night sky. Diffuse aurora are created by wave-particle interactions that scatter both energetic ions and electrons into the atmospheric loss cone [*Thorne*, 1983]. Discrete aurora are the result of the field-aligned acceleration of magnetospheric electrons. *Borovsky* [1993] presents an evaluation of 22 different candidates for this acceleration process. Since then, additional processes have been suggested, in particular for generating the filamentary structure that is seen in electron aurora [*Otto and Birk*, 1993; *Temerin*, 1997; *Lotko et al.*, 1998; *McFadden et al.*, 1999; *Wygant et al.*, 2000; *Zhu et al.*, 2001]. The magnetospheric dynamics responsible for generating the conditions under which the auroral acceleration works, and the acceleration processes themselves, are the topics of much ongoing research. Yet, our purposes in this context are narrowly focused and remain simple, partially due to the breadth of the review, but largely because the corresponding information for Jupiter is much less mature due to the lack of observations, especially those at high latitudes [*Waite et al.*, 2000].

The structure and dynamics of Jupiter's magnetosphere are predominantly determined by the rapid rotation of its large intrinsic magnetic field and the resulting ionospheric-magnetospheric coupling that takes place. Another important element of the system is the volcanic outgassing of the Galilean satellite Io and the subsequent ionization of sulfur and oxygen to form a neutral/ion torus at Io [*Bagenal*, 1994]. The 9-hr-56-min rotation of Jupiter at the 5.9 R_J distance where Io orbits results in energization of ions via pickup processes (the difference between the Keplerian rotation velocity of neutral material from Io and the corotation velocity of Jupiter's ionosphere at Io's orbital distance) of 542 eV for oxygen and 271 eV for sulfur. However, this does not appear to be the major way by which the plasma in the magnetosphere is energized. Plasma from the Io torus is accelerated outwards due to centrifugal instabilities within the magnetospheric system [*Pontius and Hill*, 1989]. It is in the middle and outer magnetosphere beyond 30 R_J where this hot Io plasma disc is accelerated by an as yet poorly understood interplay between solar wind perturbations and internally-driven plasma transport as described in Chapter II.1. The resultant energetic ions have a twofold effect: 1) an inward diffusion of energetic sulfur and oxygen particles that controls the pressure balance within the magnetosphere [*Mauk et al.*, 1996] and, 2) coulomb interactions between the electrons and the hot ion population which create the Io plasma torus and control the ionization state of the neutral material outgassed from Io's volcanoes [*Smith et al.*, 1988]. Both the inward diffusing energetic particles undergoing wave-particle scattering [*Thorne*, 1983] and the large field-aligned currents that result from the redistribution of angular momentum within the system [*Hill*, 2001] lead to auroral processes.

THE AERONOMY OF THE AURORAL EMISSION PROCESS

Aurora on Earth are most commonly observed as a spectacular light show in the high-latitude winter sky. Emissions from aurora, however, extend far beyond the spectrum of visible light. Emissions range from the extremely

short wavelength of gamma rays [*Colgate*, 1955] to x-rays [*Anderson*, 1958], extreme and far ultra-violet (EUV, FUV), to visible and infrared (IR) light [*Vallance Jones*, 1974], and eventually to radio emissions with kilometer-long wavelengths. An observer on Earth is shielded from the aurora by the dense gas of the troposphere and the ionized layers of the upper atmosphere, and only observes the auroral emissions in a limited spectral range in the infrared and visible range. X-ray, UV emissions, and kilometric radiation are best observed from satellites. Observations of aurora on Earth are made from the ground, aircraft, balloons, rockets, low orbiting satellites, and satellites in high orbit. Each viewpoint has its limitations and advantages. The detailed structure of auroral filaments is best seen from the ground. Satellites and rockets can measure the auroral particle spectrum inside or just above the aurora and can obtain global views of the entire auroral oval. The major difference in observation techniques between Earth's aurora and Jupiter's aurora is that the only viewpoint we currently have of the Jovian aurora is from far away. No spacecraft has flown in a low altitude, polar orbit over the Jovian aurora, and no auroral observations from inside of the Jovian atmosphere are available. Global auroral observations of the Jovian aurora have been made with Einstein, the Rontgensatellit (ROSAT), Chandra, and the International Ultraviolet Explorer (IUE) satellites, the Hubble Space Telescope (HST), the NASA Infrared Telescope Facility [IRTF], and from the Pioneer, Voyager, Galileo and Cassini spacecrafts. HST observations are limited to UV auroral emissions. We can only see the dayside aurora from HST's viewpoint in Earth's orbit and the visible Jovian aurora is swamped by scattered light. Only a few observation from Voyager [*Cook et al.*, 1981] and Galileo [*Ingersoll et al.*, 1998; and *Vasavada et al.*, 1999] from the nightside of Jupiter show visible aurora. These limitations on observing Jupiter's aurora determine the picture that we have of it. Although most of the data we have on Earth's aurora come from visible wavelength observations, the Jovian data come mostly from ultraviolet and radio emissions.

Auroral emissions are caused by precipitating energetic particles. Both ions and electrons in the energy range from a few eV to several MeV contribute to the aurora. At Earth the precipitating particles are accelerated in the inner magnetosphere and form sheet-like structures that lead to curtain-shaped auroral displays. Electrons are confined by the magnetic field so that only minimal horizontal displacement of the precipitating electrons occurs as these electrons enter the upper atmosphere. Protons, on the other hand, can charge-exchange in collisions with the ambient neutral species. The emerging hydrogen atoms still have most of the kinetic energy of the precipitating protons, but are no longer confined by the planet's magnetic field. Proton precipitation tends to spread out horizontally leading to diffuse auroral displays. The main collision partner for charge exchange collisions in the upper atmosphere of Earth is atomic oxygen, while the upper atmosphere of Jupiter is dominated by atomic and molecular hydrogen. Ion precipitation on Earth consists mostly of protons, while aurora on Jupiter are also formed by precipitating heavy ions, especially sulphur and oxygen ions.

The energy spectra of precipitating auroral particles have only been directly measured on Earth by low orbiting satellites. Polar orbiting satellites like the Defense Meteorological Satellite Program (DMSP) and the National Oceanic and Atmospheric Administration's Advanced Television Infrared Observation Satellite (NOAA-TIROS) monitor the auroral precipitation on a regular basis. Large data bases have been built from these measurements [*Hardy et al.*, 1981, 1989; *Evans*, 1987; and *Newell et al.*, 1991]. The observations of the Upper Atmosphere Research Satellite (UARS) covered a large energy range, but due to the orbit sampled the aurora only occasionally. Data from several detectors were combined to measure the electron precipitation from 1 eV to 5 MeV and proton precipitation from 1 eV to 150 MeV [*Winningham et al.*, 1993]. Figure 1 shows an example of electron flux during a geomagnetic storm that was measured to range from more than 10^7 cm^{-2} s^{-1} sr^{-1} eV^{-1} at a few eV to 10^{-6} cm^{-2} s^{-1} sr^{-1} eV^{-1} at several MeV [*Sharber et al.*, 1993]. Observed energy flux in the precipitating particles range from a fraction of a mW m^{-2} to several hundred mW m^{-2} for small-scale auroral features,

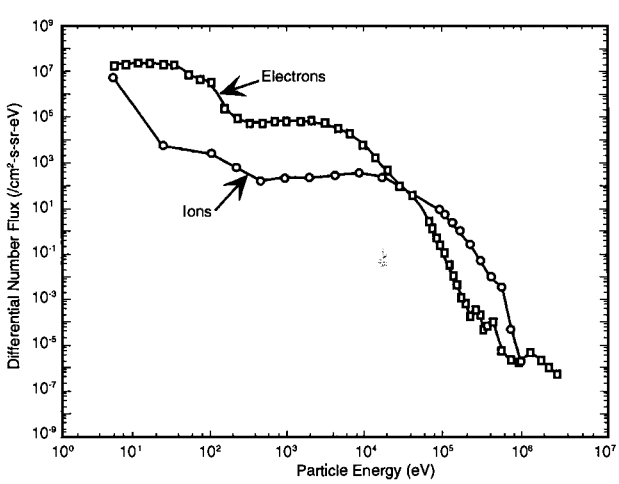

Figure 1. *Earth:* Precipitating electrons and ions measured on board the UARS satellite above a terrestrial aurora. Most aurora are caused by keV electrons, but non-Maxwellian high-energy tails are common features [from *Sharber et al.*, 1993].

with characteristic energies of 1-20 keV for electrons and several tens of keV for protons, often with high energy tails that deviate from Maxwellian distributions [*Hardy et al.*, 1981, 1989; *Newell et al.*, 1991; *Codrescu et al.*, 1997; and *Lanchester et al.*, 1997]. Jupiter, by comparison, is a giant. To generate the observed UV emission brightness of the Jovian aurora requires an electron energy flux typically in the range 0.01-1 W m^{-2} and characteristic energies of 20-50 keV. However, we have few measurements of the input energy spectrum, mostly model calculations. Integrating the energy fluxes over the entire auroral zone gives the hemispheric power, which can reach several hundred GW on Earth and 10-100 TW on Jupiter.

Models for Auroral Particle Precipitation

To model auroral emissions the first step is to calculate the particle transport into the upper atmosphere. Once the energy distribution of the incoming energetic particles is known, the emission rates can be calculated from the neutral densities and cross sections. For the transport calculation of auroral electrons and ions through the neutral atmosphere the following assumption can be made: all collisions are binary collisions, i.e., no three-body collisions need to be considered; the density of streaming particles is low compared to the ambient density; collisions only reduce the energy of the auroral particle, i.e., there are no superelastic collisions; the precipitating particles do not gain energy in the process of penetrating the atmosphere, i.e., ambient parallel electric fields are small; the time spent for an auroral particle to lose most of its energy is small compared to the time scale at which the incident particle flux changes, i.e., the transport can be considered a stationary problem. For auroral electrons one can also assume that the particles are transported only along the ambient magnetic field. A solution to the one-dimensional stationary Boltzmann equation represents a good auroral model. For ion precipitation, the transport problem is described by coupled transport equations for ions at various charge states including energetic neutrals.

Models have been developed to solve the appropriate Boltzmann equations. Some models relax the assumptions listed above, usually with a penalty of introducing other assumptions. Electron transport models for Earth's aurora have been developed by *Banks and Nagy*, [1970; see also *Nagy and Banks*, 1970] using a two-stream approach, *Banks et al.* [1974] using Monte-Carlo techniques, *Jasperse* [1976] using a theoretical method of solution, *Strickland et al.* [1976] using a multi-stream approach (i.e., with pitch angle resolution), *Stamnes* [1980, 1981] using a two-stream discrete ordinate method, *Link* [1992] applying a Feautrier solution, *Lummerzheim and Lilensten* [1994] using a discrete ordinate technique, and *Solomon* [1993] using a Monte-Carlo technique. *Min et al.* [1993] took the discrete ordinate method of *Lummerzheim and Lilensten* [1994] to include small field aligned ionospheric electric fields in order to study the influence of the ambipolar diffusion field on electron precipitation. *Peticolas and Lummerzheim* [2000] have developed a time-dependent electron transport model which can simulate flickering aurora or fast moving auroral filaments.

Similar models have been developed for application to Jupiter's aurora by substituting the appropriate neutral density profile and cross section set. *Waite et al.* [1983] applied the two-stream electron transport model of *Nagy and Banks* [1970] to Jupiter. *Perry et al.* [1999] adapted *Strickland et al.'s* [1976] multistream model to the Jovian case. Most recently, *Grodent et al.* [2001] have constrained the model of *Waite et al.* [1983] using more recent cross sections and observations and taking into account the changing auroral thermal structure from particle heating.

Proton aurora at Earth are also simulated using different methods, from Monte-Carlo simulations [*Kozelov*, 1993; *Decker et al.*, 1996; *Lorentzen et al.*, 1998; *Synnes et al.*, 1998; and *Gérard et al.*, 2000], quasi-analytical approaches [*Jasperse and Basu*, 1982; and *Basu et al.*, 1987], to explicit solutions of the coupled Boltzmann equations describing the combined proton-hydrogen-electron transport [*Basu et al.*, 1993; *Strickland et al.*, 1993; and *Galand et al.*, 1997, 1998]. Ion transport calculations of energetic oxygen ion precipitation at Jupiter have been carried out by *Horanyi et al.* [1988] using techniques similar to those for proton aurora on Earth, albeit with a somewhat decreased knowledge of the full cross section set. *Rego et al.* [1994] have produced models of proton aurora.

The majority of collisions between precipitating particles and the neutral atmosphere lead to ionization and dissociative ionization. Most excitation arises from the subsequent collision of the secondary electrons with the neutral constituents of the atmosphere. The secondary electrons are generated by precipitating electrons, ions, or x-rays from high-energy particle collisions.

The energy of the incident particles determines the altitude to which the bulk of the particles penetrate. Secondary electrons that are generated at this altitude have a much smaller mean free path than the incident energetic particles because of the energy dependence of cross sections. They tend to remain local and contribute to the excitation at the altitude where they are generated. The penetration altitude as a function of incident energy for electron aurora on Earth is shown by Figure 2. Results from several model calculations are combined to make this figure. Similar results for Jupiter are shown in Figure 3.

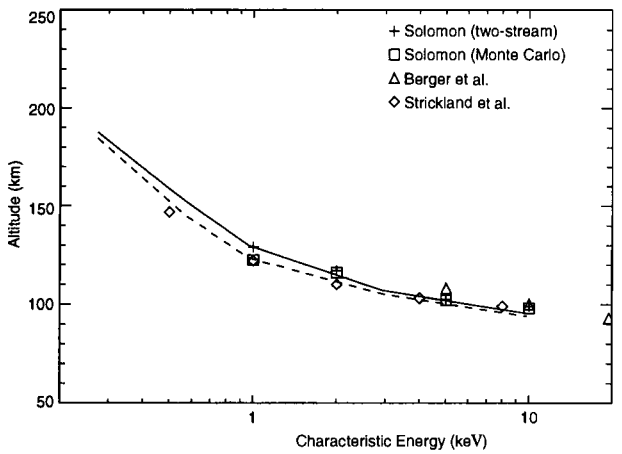

Figure 2. *Earth:* The altitude of the maximum of the N_2 ionization rate as a function of the characteristic energy of the incident electron spectra at Earth. The solid and dashed lines show the altitudes from the *Lummerzheim and Lilensten* [1994] model, using different assumptions for the energy distribution of secondary electrons. The symbols represent published values from *Solomon* [1993], *Berger et al.* [1970], and *Strickland et al.* [1989].

Multispectral Emissions at Earth and Jupiter

As energetic particles penetrate the upper atmosphere they lose energy by excitation, dissociation, and ionization of the neutral gas and by heating of the ambient plasma. The types of collisions between the energetic particles and neutral gas include ion impact on the nucleus for very high-energy protons (more than several MeV) which can lead to the emission of gamma rays. For Earth's aurora, *Colgate* [1955] estimates that the MeV gamma ray flux at about 15 km altitude in intense aurora can reach 10^2 $cm^{-2}s^{-1}$. MeV protons with access to the upper atmosphere, however, do not necessarily come from auroral sources. Energetic solar particle events produce significant gamma rays in the upper atmosphere [*Share and Murphy*, 2001]. No gamma rays have yet been detected at Jupiter.

High-energy electrons or ions impacting the nucleus of neutral atoms or molecules can lead to an emission of an x-ray photon by bremsstrahlung with an energy comparable to the energy of the incident particle. K-shell ionization is also a possible source for auroral x-rays. The scattering depth for x-ray photons is longer than for energetic electrons of the same energy. So the conversion to an x-ray photon permits a deeper penetration into the atmosphere compared to the penetration of the precipitating electrons [*Rees*, 1964; *Kamiyama*, 1966, 1970; *Berger et al.*, 1970; *Luhmann*, 1977]. The x-rays cause ionization and excitation below the altitude where the precipitating particles cause excitation and ionization, and give rise to auroral emissions deep in the atmosphere (see Figure 4).

X-ray photons from bremsstrahlung are emitted preferentially into the same direction as the incident electron's momentum. Bremsstrahlung is the dominant x-ray mechanism on Earth and the largest portion of the x-ray emission in aurora is downward. On Earth the first scientific observations of auroral x-rays were made from high-altitude balloons [*Anderson*, 1958]. A small portion of the x-ray emission is moving away from the ground and has been observed from space by x-ray imagers on the UARS [*Winningham et al.*, 1993] and POLAR [*Imhof et al.*, 1995] satellites (Plate 1). The energy spectrum of the precipitating auroral electrons can be estimated directly from the energy spectrum of the generated x-rays [*Luhmann*, 1977; *Sharber et al.*, 1993; *Østgaard et al.*, 1998, 2000]. The UARS and POLAR x-ray imagers are sensitive to x-rays of a few keV, and thus observe aurora that are generated by 2-60 keV electrons. The x-ray brightness is in agreement with UV auroral brightnesses [*Østgaard et al.*, 1999].

The x-ray emissions of Jupiter imaged with ROSAT (see Plate 2, lower right panel) [*Gladstone et al.*, 1998] are thought to be line emissions produced by the interaction of precipitating energetic sulfur and oxygen ions with Jupiter's neutral atmosphere [*Cravens*, 1995]. Although electron bremsstrahlung remains a possibility, auroral energy requirements [*Metzger et al.*, 1983] and theoretical and modeling studies [*Waite et al.*, 1994; *Cravens*, 1995] favor ion precipitation as the most plausible mechanism responsible for producing the Jovian x-ray aurora. More recent analysis of Chandra observations appear to confirm the

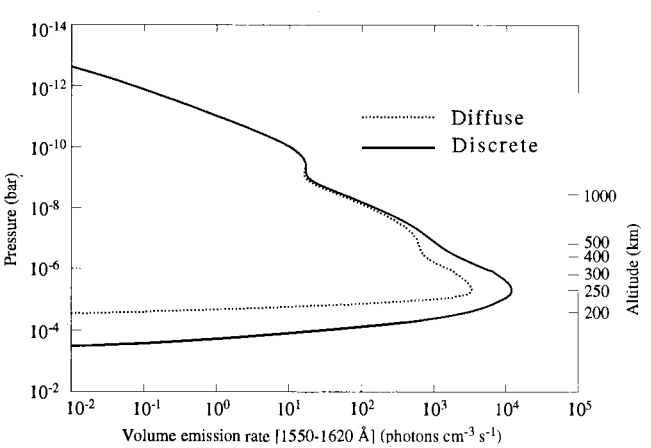

Figure 3. *Jupiter:* Vertical H_2-FUV volume emission rate profile in the 1550-1620 Å wavelength range calculated with the spectral generator [*Dols et al.*, 2000] for the discrete (solid line) and diffuse (dashed line) energy distributions at Jupiter. The altitude axis refers to the discrete auroral case [from *Grodent et al.*, 2001a].

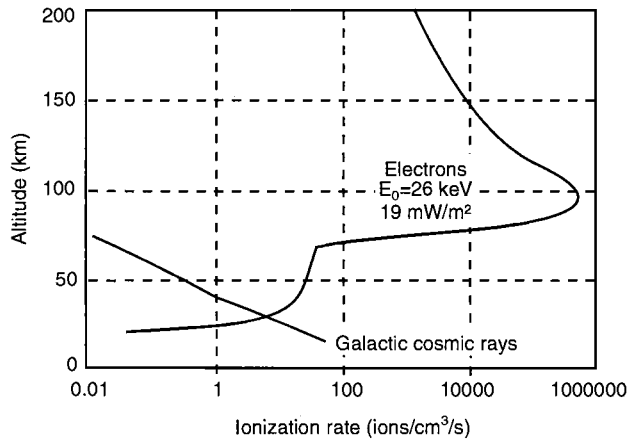

Figure 4. *Earth:* Ionization rate profile caused by auroral electrons. The main peak near 90-km altitude results from the primary electron precipitation, the ionization below about 70 km results from the secondary x-rays that are emitted in the aurora. Ionization from galactic cosmic rays is shown for comparison [from *Winningham et al.*, 1993].

identification of energetic oxygen ions as the source for the x-ray emissions. Thus, in contrast to the UV emissions which are excited by both energetic ions and electrons, the Jovian x-rays can provide an unambiguous signature of ion precipitation.

Emissions at ultraviolet, visible, and infrared wavelengths in the aurora result from particle impact on the neutral species of the upper atmosphere. The auroral particles dissociate, ionize, and excite the neutrals. These emissions come from direct excitation as well as from indirect channels involving chemical reactions of the excited and ionized atmospheric constituents. On Earth, the upper atmosphere consists mainly of atomic and molecular oxygen, and molecular nitrogen. Optical emissions are therefore lines from atomic neutral and ionized oxygen and nitrogen, and band emissions from N_2, N_2^+, O_2, and O_2^+. Hydrogen emissions occur only in proton aurora where precipitating protons undergo charge exchange collisions with atomic oxygen and subsequently radiate with the hydrogen spectral lines.

An example of global auroral images from Earth is shown in Plate 1. The top left panel shows a montage of a satellite and ground-based images to demonstrate the difference in resolution. The satellite image is from the Polar VIS instrument using a filter for the OI(557.7 nm) emission, the ground-based image is from a white light all-sky camera at Poker Flat, Alaska. Also shown is a global view of the proton aurora, imaged at the Doppler-shifted Lyman-α line, an x-ray image, and an image in the UV using a filter for the N_2 Lyman-Birge-Hopfield (LBH) band emission.

The Jovian atmosphere consists mostly of molecular hydrogen, and electron and ion precipitation both give rise to molecular and atomic hydrogen line emissions. Ultraviolet emissions (the HST STIS image in the lower left panel of Plate 2 [*Clarke et al.*, 1998a]), are a direct indicator of particle impact excitation of H_2 Lyman and Werner bands, triplet and continuum emissions from H_2, and Lyman α dissociative excitation of H_2. The spatial resolution of STIS is less than 0.1 arcseconds (350 km on the surface). As will be discussed below, complex patterns observed in the high-latitude emissions in Jupiter's aurora are important clues to the nature of the magnetospheric processes that drive the aurora.

Plate 2 presents images of Jupiter's aurora (from top left to bottom right) acquired at visible wavelengths with the Galileo imager on the nightside; with the ground-based NASA IRTF at near-infrared wavelengths; with the Hubble Space Telescope in the ultraviolet regime; and at x-ray wavelengths with ROSAT. The visible emissions (captured in this image by the Galileo Solid State Imager during the E11 orbit [*Vasavada et al.*, 1999]) result from energetic particle impact on molecular hydrogen. These produce Balmer series emissions from dissociative excitation of H_2 and additional triplet and continuum emissions from H_2 [*Pryor et al.*, 1998]. Because of scattering of sunlight in the atmosphere, these emissions are only visible on the nightside of the planet. The importance of this image lies in its unprecedented spatial resolution, which is on the order of 30 km per pixel when a sufficient star field is simultaneously imaged. The fact that the auroral arc disappears over the limb allows us to infer an altitude of 245 ±30 km [*Vasavada et al.*, 1999] above the 1 bar pressure level for the emission peak, thus clearly improving the absolute altitude scale for the auroral emissions, which had been previously determined in the UV by *Clarke et al.* [1996] (±150 km) and *Prangé et al.* [1998] (±100 km).

Hydrogen emissions in electron aurora originate from ambient hydrogen which is at rest, while hydrogen emissions in proton aurora originate in large part from precipitating protons which have recombined to hydrogen and have considerable kinetic energy. Hydrogen lines in proton aurora are therefore Doppler shifted and broadened. This Doppler broadening is observed in Earth's proton aurora [*Eather*, 1966; *Ishimoto et al.*, 1989; and Lummerzheim and Galand, 2001], but does not appear in the Jovian Lyman _ UV emissions [Clarke et al., 1989; and Rego et al., 1999] suggesting that the Jovian aurora are caused by either electron or heavy ion precipitation (see Figure 5). The Doppler-shifted profile of the hydrogen emission lines from terrestrial proton aurora can be used to find the mean energy of the proton precipitation. Since many scattering and energy degradation events occur in the aurora, the line

[redacted]

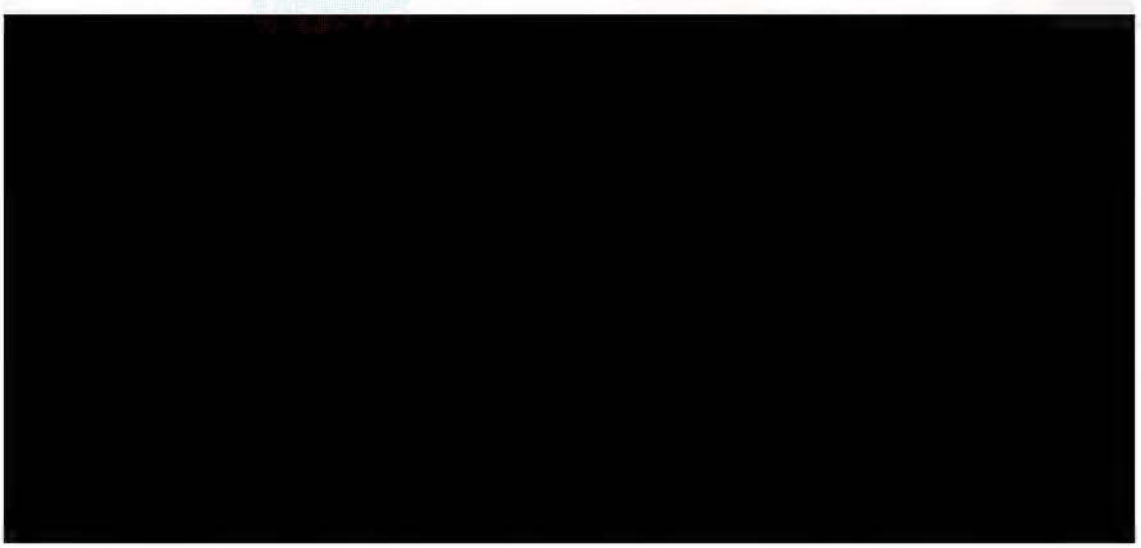

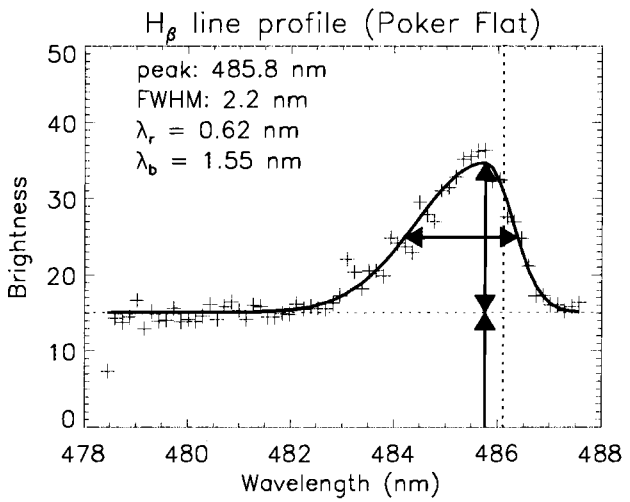

Figure 5. *Earth:* Doppler line profile of H_β in terrestrial proton aurora, observed in the magnetic zenith from Poker Flat. The dotted vertical line shows the wavelength at rest (486.1 nm), the crosses are the measurements, the solid line is a fit to the observations [from *Lummerzheim and Galand*, 2001].

shape reflects the particle distribution as it is modified by the interaction of the incident beam with the atmosphere. Galand et al. [1998] show that an increase in mean energy of the precipitating auroral protons leads to a broadening of the hydrogen emission lines rather than to a shift in the wavelength of the peak of the line. This is because the maximum of the emission comes from particles low in the atmosphere which have undergone multiple collisions and lost most of their energy. Ground-based observations of the H _ line profile in proton aurora [Lummerzheim and Galand, 2001] support this prediction. For space-based observations, in particular of the Lyman _ line in the UV, extinction has to be taken into account when interpreting the line profile. Emissions from different altitudes will experience different extinctions that distort the line profile.

The near IR in Earth's aurora is dominated by N_2^+ Meinel, N_2 1 positive, and some atomic lines (OI, OII, NI). In the mid-wavelength IR the aurora also shows emissions from vibrationally excited NO, NO^+, and CO_2 [*Espy et al.*, 1988; and *Caledonia et al.*, 1995]. These are the result of indirect excitation processes, either by chemical reactions in aurora (NO and NO^+) or energy transfer from aurorally excited N_2 vibrational states to CO_2. Spectral analysis of NO emissions show a non-thermal distribution of emission lines, indicating excess energy in some of the excitation processes.

The ground-based infrared image of the Jovian aurora [*Satoh et al.*, 1996] has a spatial resolution of about 1.0 arcsecond, which corresponds to about 3500 km on the surface. A narrow band filter was used in this observation to isolate a portion of the H_3^+ ro-vibrational band emission in a spectral region where methane absorption in the lower atmosphere provides a dark contrast. The emission intensity scales with increases in both the column density of H_3^+ and in the temperature of the thermosphere. H_3^+ column density in the auroral zone is closely correlated with the total energy deposition of energetic particle influx as a result of impact ionization of H_2. However, as discussed in Chapter IV.2, the temperature of the thermosphere is influenced by both Joule heating and dynamics as well as by particle impact. It should also be noted that the H_3^+ temperature depends on the altitude of the emission peak, which differs inside and outside of the auroral region, and depends on the energy of the primary particles or solar EUV photons [e.g., *Achilleos et al.*, 1998].

Finally, at the longest wavelengths, the terrestrial auroral emissions include intense radio emissions in the frequency range centered on 300 kHz (but extending from a few tens of kHz to several hundred kHz) now commonly called auroral kilometric radiation [*Benediktov et al.*, 1965; *Gurnett*, 1974]. These radio emissions have been shown to be closely associated with the aurora through correlations in radio and optical emissions [*Gurnett*, 1974] and through direction-finding techniques [*Kurth et al.*, 1975; *Huff et al.*, 1988; *Gurnett et al.*, 2002a]. Further, these radio emissions have also been found to provide a good proxy for various magnetic indices such as AE [*Voots et al.*, 1977; *Murata et al.*, 1997; *Kurth et al.* 1998] and show detailed correlations with the development and life cycle of magnetic substorms [*Khan et al.*, 2001]. The radio emissions are launched at large angles (60° to 90°) with respect to the magnetic field, but in aggregate, fill large cones extending generally poleward with a tilt to local midnight [*Green et al.*, 1977]. High-resolution observations show the auroral kilometric radiation spectrum is rich in narrowband tones which exhibit both organized and seemingly chaotic drifts in frequency with time [*Gurnett et al.*, 1979].

Auroral kilometric radiation is generated via the cyclotron maser instability [*Wu and Lee*, 1979] at typical altitudes of 2-4 R_E on magnetic field lines threading discrete auroral arcs. The emissions are generated at the relativistic electron cyclotron frequency, primarily in the extraordinary mode, but evidence exists both for harmonic emissions and for ordinary mode emissions. In situ studies of electron distributions in the auroral kilometric radiation source region [*Louarn and Le Queau*, 1996; *Delory et al.*, 1998; *Ergun et al.*, 2000] have shown that so-called horseshoe distributions resonate via the cyclotron maser, thereby deriving energy from the precipitating particles and parallel electric fields in the auroral acceleration region.

Jupiter possesses the most complex radio spectrum of the solar system's planets [see reviews by *Kaiser*, 1989; and *Zarka*, 1998, 2000] and the majority of the elements of this spectrum are thought to be associated with auroral processes. In general, the Jovian auroral radio emissions are generated by the cyclotron maser instability [*Wu and Lee*, 1979]. The earliest observations of Jovian radio emissions were by *Burke and Franklin* [1957] of the decametric emissions in the frequency range above 10 MHz extending to 40 MHz (the maximum electron cyclotron frequency near the planet). *Bigg* [1964] discovered that the position of Io in its orbit strongly influenced the intensity of decametric emissions observed from Earth and led to the now-familiar taxonomy of Io-related and Io-independent sources of decametric emissions [e.g. *Carr and Desch*, 1976]. While not confirmed observationally, it is almost certain that the Io-related decametric radiation is generated on magnetic field lines threading the Io footprint aurora [e.g. *Connernery et al.*, 1993; and *Clarke et al.*, 1996]. Io-independent emissions are likely associated with the more durable auroral oval such as that detailed in *Grodent et al.* [2002]. Voyager observations [*Warwick et al.*, 1979a, 1979b] showed the extension of Jovian auroral radio emissions to frequencies previously unavailable to ground-based observers (due to Earth's ionospheric cutoff) in the hectometric and kilometric wavelengths. Source locations deduced from the Voyager observations and measured by Ulysses [*Ladreiter et al.*, 1994; and *Reiner et al.*, 1993] show these emissions are generated at greater distances from the planet than the decametric emissions (lower frequencies imply smaller electron cyclotron frequencies, hence, smaller magnetic fields at the source) and at L-shells of order 15 R_J, but with large error bars and/or ranges. Recent work by *Menietti et al.* [1998, 2001] suggest that some of the hectometric emissions may be enhanced at certain phases of Ganymede and Callisto, perhaps consistent with the observation of footprint aurora from these satellites [e.g. *Clarke et al.*, 2002] although the bulk of the hectometric radiation is almost certainly a by-product of non-satellite-associated auroras. At the lowest frequencies, hence, generated at the greatest distances from Jupiter are the broadband kilometric emissions [*Warwick et al.*, 1979a; and *Kaiser and Desch*, 1980].

Somewhat surprisingly, the Jovian radio emissions often exhibit correlations with solar wind conditions not dissimilar to the situation at Earth, even though the Jovian magnetosphere derives the bulk of its plasma from Io and energy from its rapidly rotating magnetic field. Hectometric radiation shows a positive correlation with the solar wind density and pressure [*Ladreiter and Leblanc*, 1989; and *Desch and Barrow*, 1984]. Similar correlations were shown for decametric emissions [*Barrow et al.*, 1986] and broadband kilometric radiation [*Zarka and Genova*, 1983]. More recently, *Gurnett et al.* [2002b] showed the relationship between interplanetary shocks and increases in the band-integrated intensity of hectometric radiation during the joint Galileo and Cassini observations of late 2000 and early 2001.

Spectral Observations and Determination of the Incident Particle Spectrum

Methods that use UV and visible emission features to obtain the mean energy of the precipitating flux in electron aurora depend on determination of the altitude where the emissions peak. There are several processes that control the relative brightness of different spectral features as a function of the altitude of the excitation. In Earth's upper atmosphere the relative concentration of atomic oxygen and molecular species varies as a function of altitude. Relative brightness changes due to composition or quenching should therefore indicate a change in emission altitude. Emissions from forbidden transitions are also altitude dependent, and changes in the ratios of brightness between prompt and quenched emissions also indicate a change in the emission height. Finally, extinction of UV emissions by O_2 Schuman-Runge absorption is wavelength dependent, and emissions that originate from the same excited state but radiate at a different wavelength in the UV experience different extinctions. For example, changes in the brightness ratios between different vibrational bands of the N_2 LBH emission indicate changes of the altitude of the emission maximum. With auroral transport models and known atmospheric composition, one can therefore relate the ratio of the brightness of various emission features to the altitude of the emission and thus to the mean energy of the incident electron flux.

The most prominent example for this method is the red-to-blue ratio in the aurora: the red OI(630.0 nm) emission comes from high altitudes because the atomic oxygen to molecular oxygen and nitrogen density ratio increases with altitude, and because the parent state $O(^1D)$ is quenched at low altitudes. The brightness of the red line increases, therefore, when the aurora moves up in altitude. The blue N_2^+ first negative emissions at 391.4 nm or 427.8 nm are prompt emissions which result from electron impacts on neutral nitrogen molecules. The altitude where the auroral electrons deposit most of their energy depends on the total column density that the incident beam penetrates. For electrons above a few hundred eV, the column density above the maximum energy deposition altitude (see Figure 2) is mostly given by the N_2 density. As a result, the brightness of the N_2^+ first negative emissions for a given

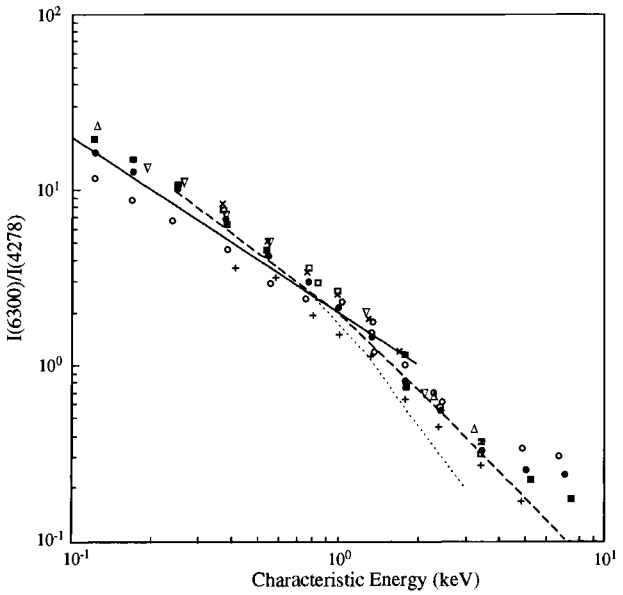

Figure 6. *Earth:* The red-to-blue brightness ratio at Earth's aurora as a function of the characteristic energy of the incident electrons. The symbols are from ground-based observations, where the characteristic energy is inferred from other emission ratios of OI(8446Å), OII(7320Å), and N_2^+ 1 neg. The different symbols are mean values representing binned averages for whole nights [from *Lummerzheim et al.*, 1990], the lines are parameterizations by *Rees and Roble* [1986] (solid), *Christensen et al.* [1987] (dashed), and *Rees and Luckey* [1974] (dotted).

energy flux is almost independent of the mean energy of the auroral electrons. The red-to-blue brightness ratio is therefore inversely related to the mean energy of the precipitation. Quantitative relationships of this ratio and the mean energy are found in *Rees and Roble* [1986] and *Lummerzheim et al.* [1990] (see Figure 6).

Prompt emissions of atomic oxygen in relation to the N_2^+ first negative emissions are also used to determine the mean energy of the precipitation. Useful oxygen emissions are OII(732.0 nm), OI(844.6 nm), and OI(777.4 nm) [*Hecht et al.*, 1985, 1989; *Lummerzheim et al.*, 1990]. OI(844.6 nm) and OI(777.4 nm) are excited by electron impacts on atomic oxygen as well as by dissociation of molecular oxygen. The dissociation products have a residual kinetic energy in excess of the thermal energy and produce broader emission lines compared to the emission from electron impacts on atomic oxygen. *Hecht et al.* [1985, 1989] make use of this and separate the two components to the emission line by high-resolution spectroscopy, while *Lummerzheim et al.* [1990] model the entire contribution from both processes to use low-resolution interference filters.

The analysis of N_2 LBH brightnesses observed from space in terms of mean energy of the auroral electrons has found application in the quantitative interpretation of POLAR UVI auroral images [*Germany et al.*, 1997, 1998a, 1998b; and *Chua et al.*, 2001]. Once the characteristic parameters of the precipitation are determined, additional modeling allows one to infer the ionospheric conductances (Figure 7) [*Rees et al.*, 1995; *Lu et al.*, 1998; and *Slinker et al.*, 1999] and field aligned currents [*Lu et al.*, 2000]. Using UVI images for this analysis allows a global analysis of the entire auroral oval. *Lu et al.* [1998] use these auroral optical observations to infer the global distribution and flow of energy in the course of a large substorm (Plate 3).

One of the uncertainties of using brightness ratios of emissions from different atmospheric constituents comes from the unknown atmospheric composition. If the mean energy and energy flux of the precipitation is known from other sources, auroral brightness ratios can be used to deduct the relative concentration of different emitting species at the altitude of the emission. *Hecht et al.* [1989, 1999] use observations of several pairs of auroral emissions to find the mean energy, energy flux, and relative composition simultaneously.

There is no in situ information about Jupiter's upper atmosphere in the auroral zone. Therefore, determination of the altitude, thermal structure, and atmospheric composition must be derived from auroral spectral observations.

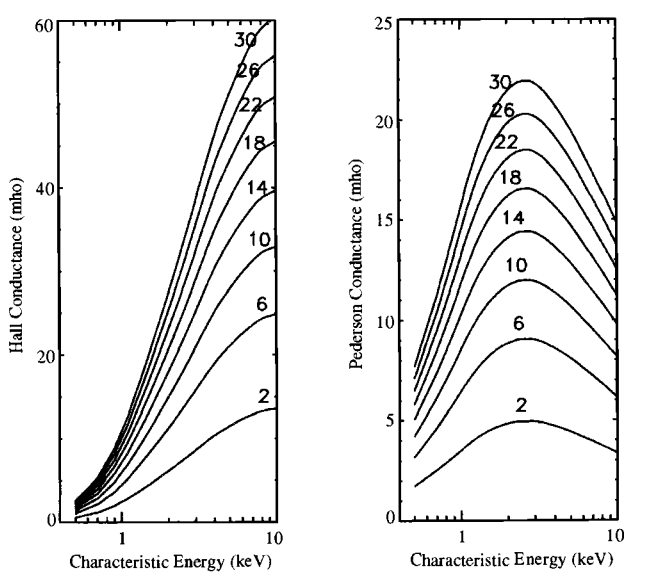

Figure 7. *Earth:* Height integrated conductivity as a function of characteristic energy and energy flux of precipitating electrons at Earth [from *Rees et al.*, 1995]. The energy flux (mW m^{-2}) is given on each line in the plot.

[redacted]

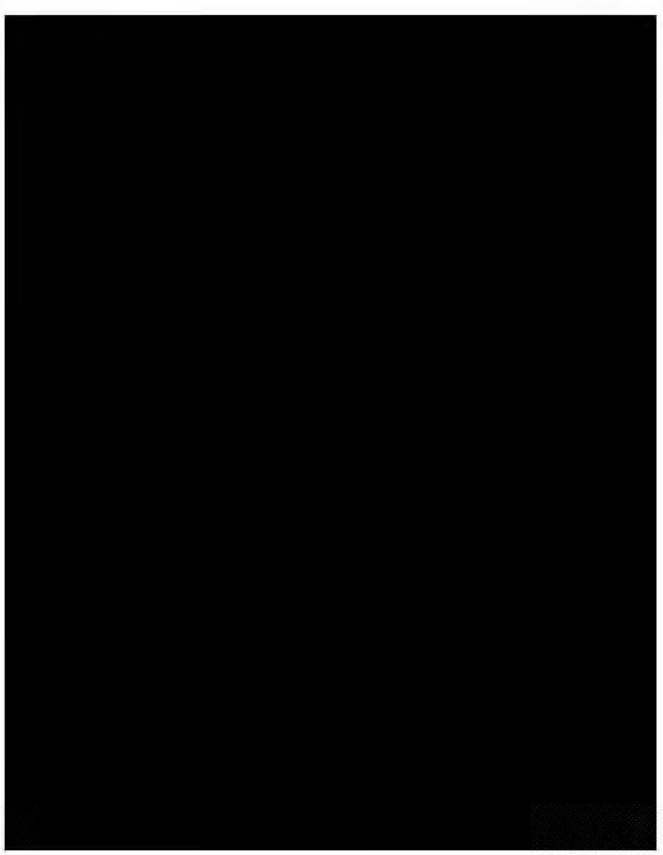

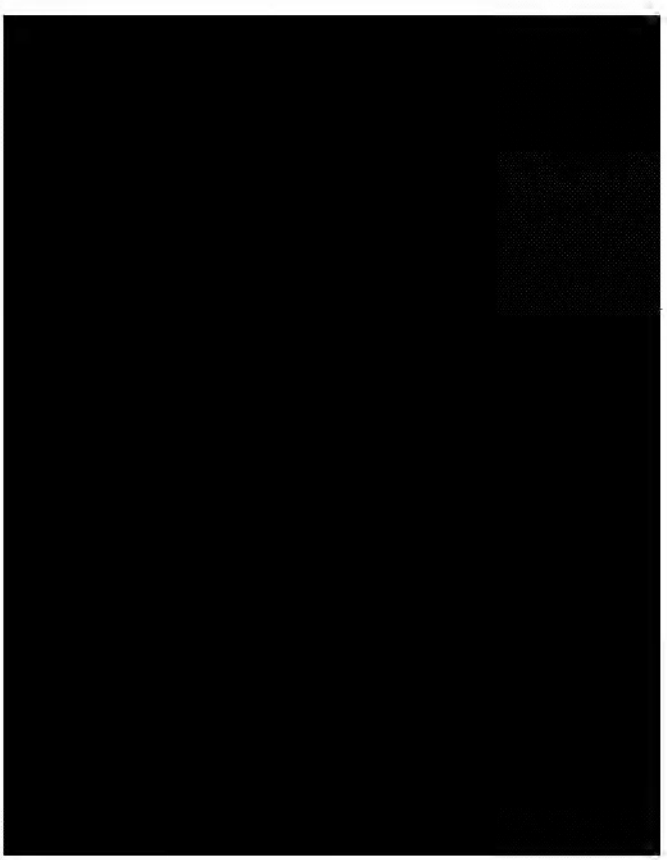

atmosphere in an attempt to achieve a more consistent fit with the constraints imposed by both the multispectral observations of Jovian auroral emissions and recent in situ data gathered by the Galileo spacecraft on energetic electron distributions in the inner Jovian magnetosphere. The principal components of the model are a neutral temperature profile derived from the Galileo ASI data used only as an initial condition [*Seiff et al.*, 1998]; a one-dimensional thermal conduction model that includes particle heating and CH_4, C_2H_2, and H_3^+ cooling; and a coupled, two-stream electron transport model used in determining the heating rates. Two auroral electron energy distributions are examined: 1) a diffuse, unstructured aurora primarily associated with the region between the main oval and the magnetic footpoint of Io's orbit, and 2) a bright, discrete arc present in the morning sector of the main oval.

In the case of the energetic scattered electrons, they can be modeled using the boundary conditions for the two-stream electron code set by the electron energy distribution derived from Galileo Energetic Particle Detector (EPD) [*Williams and McEntire*, 1992] measurements in the magnetospheric regions between 10 and 25 R_J. However, the EPD instrument is designed to measure the spectra and angular distribution of the electrons above 15 keV and is not sensitive to low-energy electrons that are known to be heating the upper atmosphere (as inferred from the EUV measurements of the upper atmosphere [*Ajello et al.*, 2001]). *Grodent et al.* [2001] have represented these electrons with a double Maxwellian, one with an energy flux of 10 m Wm^{-2} at a temperature of 3 keV and one with an energy flux of 0.5 m Wm^{-2} with a temperature of 100 eV.

Grodent et al. [2001] have also considered a discrete auroral arc that is represented by an energetic Maxwellian of 22-keV temperature and an energy flux of 100 m Wm^{-2}. Such a discrete arc is consistent with the field-aligned acceleration of electrons within the framework of the global current system that provides angular momentum coupling between the ionosphere and the magnetodisc created by Io [*Hill*, 2001; *Bunce and Cowley*, 2001a; and *Cowley and Bunce*, 2001]. Such acceleration may have similar microphysics to that of Earth's discrete aurora, but the currents in this case are driven by internal angular momentum coupling between Jupiter's magnetosphere and ionosphere rather than from the magnetospheric solar wind interaction (as in the Earth's case). This second case also includes the softer double Maxwellian that represents the high-altitude heating discussed above and that may be associated with return currents from the global current system. The auroral emission profiles for both models appear in Figure 3. Both models lead to an altitude for the emission peak of ~250 km, which is near the altitude suggested by the Galileo SSI observations. The major altitude difference of maximum emission intensity between this study and earlier studies [*Waite et al.*, 1983; and *Rego et al.*, 1994] is due to the probe derived thermal structure in the lower atmosphere and the high energy of the incoming electrons. Agreement between the models and observed values is generally good, with two exceptions: the model-generated H_2 and H_3^+ rovibrational temperatures are generally lower than observed.

THE BASIC MORPHOLOGY OF THE AURORAL EMISSION PATTERN

The energy source for Earth's aurora is the interaction of the solar wind with the magnetosphere. The processes that accelerate the particles that cause the aurora, and the morphology of the aurora and the auroral oval, are of magnetospheric origin. Since the aurora morphology represents a projection of magnetospheric processes, observation of aurora can give access to large areas of the magnetosphere. However, the mapping of auroral features into the magnetosphere is difficult and requires knowledge of magnetospheric current systems [e.g., *Lu et al.*, 2000]. The nightside aurora can be separated into the diffuse and discrete aurora. Diffuse aurora are at the low-latitude boundary of the auroral oval and are caused by trapped electrons which are pitch angle scattered into the loss cone. This belt of diffuse aurora maps to the inner magnetosphere. Discrete aurora are poleward of the diffuse aurora, but still on closed field lines. Discrete aurora on the nightside are magnetically connected to the plasma sheet. On the dayside the aurora connects to the low-latitude boundary layer, a region where the solar wind and the magnetosphere interact directly, but where reconnection can also play a role. The cusp is a region of open field lines and has auroral diffuse displays. Soft precipitation of magnetosheath origin causes high-altitude diffuse aurora that are dominated by the oxygen red line emission. Poleward-moving auroral forms (PMAF) on the dayside result from particle acceleration in areas of newly reconnected patches on the dayside magnetopause [*Milan et al.*, 2000a, 2000b; Fasel, 1995]. And finally, during quiet conditions, sun-aligned arcs may form across the polar cap [*Meng*, 1981; and *McEwen and Zhang*, 2000]. These arcs delineate the convection cells on the dawn and dusk magnetosphere-ionosphere coupled system.

Because of the variability of the solar wind, Earth's aurora shows a large range of activity levels. During large geomagnetic storms, the auroral oval can expand to 40 degrees magnetic latitude, while the quiet time aurora sits at 65-70 degrees. The total power of precipitating particles in the aurora ranges from a fraction of a GW in quiet times to several hundred GW. Pressure changes in the solar wind

can compress the entire magnetosphere by a significant fraction [*Russell et al.*, 2000]. These pressure changes cause immediate energization and precipitation of auroral particles [*Zhou and Tsurutani*, 1999; *Brittnacher et al.*, 2000; *Zesta et al.*, 2000]. The most spectacular global auroral event is the auroral substorm, an event whose global extend and significance was recognized by Akasofu in the late 1950s [*Akasofu*, 1994]. The duration of a substorm is on the order of an hour, while geomagnetic storms typically last tens of hours or days. A substorm starts out with a slow increase of the size of the auroral oval, and, for an observer on the ground, with an equatorward motion of the aurora at all local time sectors. This is followed by a sudden brightening of the first auroral arc that sits directly poleward of the diffuse aurora [*Deehr and Lummerzheim*, 2001]. This auroral breakup typically occurs near magnetic midnight [*Liou et al.*, 2001] and spreads from there along the auroral oval. The poleward boundary of the auroral oval rapidly expands after this breakup, and a westward traveling surge carries this expansion towards the afternoon sector. Substorms are the magnetospheric reaction to a strong energy transfer from the solar wind to the magnetosphere. This energy transfer is most effective when the IMF magnetic field is antiparallel to the geomagnetic field. Dayside reconnection can rapidly erode the dayside magnetosphere, and the solar wind forces transport of magnetic flux from the dayside to the nightside. This leads to a stretching of the magnetotail, thinning on the plasmasheet, expulsion of plasmoids down the magnetotail, and increased magnetospheric convection. Eventually, part of the energy is dumped into the ionosphere by dissipation of currents and by large auroral displays. In a study of a large substorm in response to the passage of an interplanetary magnetic cloud, *Lu et al.* [1998] found that about 4% of the total solar wind kinetic power incident on the magnetosphere was dissipated in the magnetosphere. Of the total dissipated power of 400 GW, 190 GW went into the ionospheric heating by currents, 120 GW was the average ring current injection, and 90 GW was dissipated by auroral precipitation. Jupiter's auroral energy dissipation is 2-3 orders of magnitude larger!

Because of the strong influence that Jupiter's intense magnetic field has on the motions of the particles within it, multispectral images of Jupiter at high latitudes offer a valuable means of relating emission regions and patterns to magnetospheric source regions and processes. Energetic ions and electrons are free to travel along field lines, but require electric fields (i.e., from planetary rotation, pickup processes, or the solar wind interaction) and/or gradient and curvature drift in the magnetic field (which becomes more important for very energetic particles) to move in a direction perpendicular to the magnetic field. Thus, given accurate knowledge of the three-dimensional magnetic field topology, the surface of the planet can be used as a "television screen" from whose images processes taking place in the magnetosphere can be deduced. However, there are two limitations to this approach: 1) the electric and magnetic fields are not perfectly known owing to the lack of measurements near the planet and of temporally varying currents in the system, such as the Io plasma torus current sheet and the field-aligned currents presumably associated with some discrete auroral features; and 2) the higher the latitude, the more tightly spaced the footpoints of the magnetic field lines become, and thus higher spatial resolution is needed to distinguish morphological features that map into the outer magnetosphere (>30 R_J). The present state of the art in magnetic field mapping is described by *Connerney et al.* [1998], who discusses the origins and limitations of the two field models (O6 and VIP4) presently in use. The VIP4 model has been improved over the O6 model by the use of HST and IRTF images of the latitude track of the Io flux tube (IFT) as a fiducial point [*Connerney et al.*, 1998]. This guarantees better agreement in the field line mapping to the region of the Io orbit, but may not improve the fits for more distant regions (i.e., near the 30 R_J limit of the field model) or at low magnetic latitudes.

The morphological features revealed in recent FOC [*Prangé et al.*, 1998], WFPC2 [*Clarke et al.*, 1998b], and STIS images [*Grodent et al.*, 2002] are generally consistent with earlier models based on analyses of the infrared [*Satoh et al.*, 1996] and earlier WFPC2 ultraviolet images (see *Waite et al.* [2000] for a discussion of these earlier morphological models). The general components of the evolving model as described by *Waite et al.* [2000] and indicated in Plate 4 are: 1) an auroral oval with a boundary that magnetically maps to 10-30 R_J in the magnetosphere [*Vasavada et al.*, 1999; *Clarke et al.*, 1998b; *Satoh et al.*, 1996; and *Grodent et al.*, 2002], 2) a local time-dependent emission enhancement in the dusk sector, a double arc extending well inside the oval [*Vasavada et al.*, 1999; *Clarke et al.*, 1998b; and *Waite et al.*, 2001], 3) a bright arc in the dawn sector [*Clarke et al.*, 1998b; and *Vasavada et al.*, 1999] that is enhanced by a series of bright storms that periodically appear in the morning sector (at a longitude of 200-260 degrees) and disappear within a Jupiter rotation (<10 hrs) [i.e., *Gérard et al.*, 1994; *Ballester et al.*, 1996; and *Clarke et al.*, 1998b], 4) Io, Europa, and Ganymede hot spots with a trailing tail [*Prangé et al.*, 1998; and *Clarke et al.*, 2002], 5) a diffuse region between the oval and the latitude that maps magnetically to Io's orbit [*Satoh et al.*,1996; *Prangé et al.*, 1998; *Clarke et al.*, 1998a; *Mauk et al.*, 2002], and 6) a bright polar cap feature [*Grodent et al.*, 2002] that corre-

[redacted]

lates with the Jupiter flare region [*Waite et al.*, 2001] with the x-ray emission region and with an enhanced infrared "hot spot" [*Gladstone et al.*, 2002].

Temporal variability occurs on time scales of seconds to weeks. *Prange et al.* [2001] have used a continuous six-week-long data set of total ultraviolet brightness of the north and south auroral zones to conclude that there is variability on three different time scales: 1) small variations of 10-20% observed on short times scales of a few hours, 2) variations by a factor of 2-4 occurring on scales of 5-10 days, and 3) a long-term trend on time scales longer than the 6 weeks of observation. The magnitude of this variability is small in comparison to the three order of magnitude intensity variation seen at Earth. However, several orders of magnitude variability on minute time scales is seen in limited regions of the polar cap of Jupiter. Recent STIS time-tagged images suggest that the diffuse emissions in the polar cap can flare in a minute or less with a power output over a small region of the polar cap that can exceed 10 TW of power [*Waite et al.*, 2001].

The large-scale dynamics of Jupiter's magnetosphere appear to be substantially dominated by planetary rotation out to distances as far as 125 R_J [*Kane et al.*, 1995]. There is general consensus that the field-aligned currents supplying the torque required to maintain this near corotation exceed current thresholds for electron acceleration near the radial distance of corotation breakdown that occurs between 20 and 30 R_J [*Hill*, 2001; and *Bunce and Cowley*, 2001a, 2001b] leading to the main auroral oval formation. However, plasma anti-corotational convective flows resulting from solar wind coupling have also been deduced from in situ measurements [*Cowley et al.*, 1993, 1996; *Hawkins et al.*, 1998; and *Dougherty et al.*, 1998]; and various phenomena have been identified that show—or may show—evidence of solar wind control. These phenomena include radio emissions at hectometer [*Desch and Barrow*, 1984] and decimeter [*Bolton et al.*, 1989] wavelengths and increases in the brightness of the H_3^+ aurora that have been correlated with increases in solar wind dynamic pressure [*Baron et al.*, 1996]. Enhancements in the intensity of ultraviolet auroral emissions, such as those reported by *Prangé et al.* [1993] and *Gérard et al.* [1994], may also be evidence of solar wind influence; however, interpretations of the UV brightenings in terms of internal magnetospheric processes are also possible [*Prangé et al.*, 1993].

The organization of auroral emissions in System III longitude and local time and their temporal variability furnish important clues as to the configuration and dynamical behavior of Jupiter's magnetosphere. However, as indicated by the uncertainty in the interpretation of the ultraviolet auroral brightening, it can be difficult to determine whether auroral features, such as those summarized above, are to be understood as signatures of internal, rotation-driven processes or as the effects of solar wind influence. Extended temporal coverage at multiple wavelengths and with high spatial and temporal resolution permits longitude dependencies indicative of rotation-controlled processes to be distinguished from local time effects and episodic phenomena that are perhaps indicative of solar wind-controlled processes. To successfully interpret the emissions as signatures of large-scale magnetospheric processes, however, it is necessary to obtain simultaneous or near-simultaneous in situ data on the solar wind upstream of Jupiter and, ideally, within the Jovian magnetosphere as well. For example, the availability of Ulysses solar wind measurements permitted correlation of brightness enhancements of the H_3^+ aurora with increased solar wind ram pressure [*Baron et al.*, 1996] and the tentative association of an intensification of the UV aurora with a CME and its associated shock [*Prangé et al.*, 1993]. *Prange et al.* [2001] have discussed the correspondence between the few-day variability of the observed auroral emissions with changes in the magnetosphere as measured by the Galileo spacecraft. Quasi-periodic variations with recurrence time of a few days have been reported for various quantities measured by Galileo, such as energetic particle intensity, energy spectra, angular distribution, and flow pattern in the magnetotail [*Krupp et al.*, 1998; *Woch et al.*, 1998], or for the intensity of auroral radio emissions and for the plasma sheet density [*Louarn et al.*, 1998]. These events have in general been interpreted as the signature of large-scale reconfiguration of the magnetotail plasma sheet, albeit a specific mechanism was not identified. They are generally described as bursty events, presumably related to explosive energy release, and compared to terrestrial substorms (although the origin of the explosive reconfiguration is not necessarily assigned to an external solar wind perturbation). *Russell et al.* [1998] have also reported impulsive signatures of reconnection in the tail." [*Prangé et al.*, 2001]. Clearly, the variability is a combination of both internal and external forcing of the magnetosphere.

The recent Cassini flyby of Jupiter in December 2000 afforded a unique opportunity for coordinated in situ solar wind measurements with the Cassini fields-and-particles instruments, Galileo in situ measurements within the Jupiter magnetosphere, and observations of auroral morphology with the HST, Chandra, IRFT, and other Earth-based telescopes. A series of papers detailing the correlations appears in a February 2002 publication of *Nature*. The most surprising result is the identification of auroral intensity increases at both radio and ultraviolet wavelengths with the passage of interplanetary shocks. Both increases in solar

Table 1. Auroral morphology comparison.

	Earth	Jupiter
Common morphological features	oval shaped auroral zone, diffuse aurora and discrete aurora, occasional polar cap aurora	
Unique morphological features	storms and substorms, strong day-night asymmetry	satellite footpoints dawn storms: long. 200°-270° lat. 60°-80° flares: long. 160°-180° lat. 60°-70°
Typical latitude	magnetic latitude in degrees: quiet: 70-75 moderate: 60-75 active: 45-75	jovigraphic latitude in degrees: diffuse <60° discrete 60-85°
Typical altitude	90-150 km	200-400 km
Time scales	storms: days substorms: hours filaments: seconds	seconds to weeks
Type of particles and typical energy	electrons: 1-20 keV protons: 1-100 keV	electrons: 20-50 keV protons: ? O^+, S^+: 20 keV to 20 MeV
Hemispheric power	1-300 GW	10-100 TW
Typical brightness of some selected emission features		
UV	H Lyman α: 15 kR OI (130.4 nm): 40 kR N_2 (LBH): 350 kR	H_2: 10-50 kR
Visible	N_2^+ 1neg: 150 kR N_2 2pos: 110 kR OI (557.7 nm): 100 kR	H_2, H (Balmer α)
IR	N_2^+ Meinel: 600 kR N_2 1pos: 880 kR O_2 (atm): 2500 kR NO (vib): 4500 kR	H_3^+ (vib): 1.5-7.5 mWm^{-2} CH_4, C_2H_2, C_2H_6 (<0.2 Wm^{-2})

wind dynamic pressure and embedded interplanetary magnetic field occur in the events discussed by *Gurnett et al.* [2002b]. However, the surprising aspect of the result is that there is a clear implication of the correlation of auroral intensity increases with the compression of the magnetosphere rather than during an expansion phase of the magnetosphere as suggested by the theoretical studies of *Southwood and Kivelson* [2001] and *Cowley and Bunce* [2001]. This is more representative of the chain of events termed "Sudden Commencements" at Earth [*Zhou and Tsurutani*, 1999] and may implicate a major readjustment of the Chapman-Ferraro magnetopause current system, which will lead to dramatic brightening near the cusp (i.e., the flare region) [*Waite et al., 2001; Pallier and Prangé*, 2001]. However, no detailed morphological images of such brightenings occurring at Jupiter have been obtained so far to verify this speculation.

Another surprising result is the determination of the location of the x-ray auroral source region at high latitudes in a region that maps to these high-latitude, cusplike regions

that are significantly affected by the realignment of the Chapman-Ferraro current system, and to the bright ultraviolet flares seen by *Waite et al.* [2001]. This result, reported by *Gladstone et al.* [2002], also shows a distinct 40-min x-ray periodicity that is similar to radio bursts observed during the time of Ulysses. Furthermore, the flux of ions needed to produce the x-ray emissions is too weak to be explained by in situ energetic oxygen and sulfur ions in Jupiter's magnetosphere and appears to require ~1 MeV accelerations that may be associated with the global return current at Jupiter.

Another auroral feature occurring at latitudes that map to the Io torus region is the diffuse emission region between the main oval and the IFT footprint and its trailing emission. Two brighter emission patches can be seen within this region (Plate 2), and the entire feature is associated with a broadening of the main oval in the afternoon-dusk sector that extends into the polar cap. It appears that the occasional brightenings observed within the diffuse emission region are related to dynamic charged particle events such as those observed with the Galileo EDP detector in Jupiter's inner magnetosphere [*Mauk et al.*, 1997, 1999]. These events are inward radial injections (1 to several R_J) of hot plasmas (>20 keV ions and electrons) over azimuthal sectors that span several degrees to >60 degrees. While the injections are observed most prominently at ~11-12 R_J, the distribution of observed events is broad, extending from <9 R_J to ~27 R_J, and encompasses at least a portion of the regions thought to map to the most intense auroral emission ring. At Earth, such injections are accompanied by enhanced precipitation of charged particles into the upper atmosphere. Thus, the injections detected with the EDP could be related to some of the dynamic variability observed in the diffuse emission region equatorward of Jupiter's main oval (thought to be caused by electron precipitation [*Mauk et al.*, 1997]). They may also be related to some variability observed within the main auroral oval itself (thought to be caused by electron precipitation). There appears to be no local time preference for the occurrence of the Jovian injection events, which are probably not coupled directly to variations in the solar wind. The ultraviolet emissions from these injections were for the first time documented during the Cassini passage and are described in detail in *Mauk et al.* [2002] (see Plate 4).

CONCLUSIONS

The plasma microphysics and aeronomy at Jupiter and Earth reveal many similarities and some differences (see Table 1). Both have field-aligned acceleration of electrons due to intense field-aligned currents, and pitch angle scattering of energetic ions and electrons play important roles as sources of auroral particle precipitation in both atmospheres. The dissipation of energy in both atmospheres is also remarkably similar except in magnitude, where Jupiter has a three-orders-of-magnitude advantage. The only marked difference is the atmospheric composition: H_2 and H at Jupiter and N_2, O_2, and O at Earth. However, the driving force behind Jupiter's magnetosphere is the internal rotation of the rapidly rotating ionosphere, facilitated by the ionization of material from Io's volcanoes that is subsequently picked up and accelerated within the magnetosphere. This drives the global current system, which is largely responsible for the auroral particle acceleration. Yet, the solar wind interaction with the magnetosphere also plays a role that is observed, but not well understood. In contrast, the solar wind interaction with the Earth's magnetosphere is the primary driver of the field-aligned current system and magnetospheric dynamics that are responsible for Earth's aurora.

Acknowledgment. D.L. was supported by NASA grant NAG5-7683. We acknowledge the contributions of Dr. William Kurth to the auroral radio emissions section. J.H.W. was supported by NASA grant NAG5-11031. We would like to thank M. Conde (UAF), H. Frey (UC Berkeley), and N. Østgaard (UC Berkeley) for providing the images in Plate 1.

REFERENCES

Achilleos, N., et al., JIM: A time-dependent, three-dimensional model of Jupiter's thermosphere and ionosphere, *J. Geophys. Res.*, *103*, 20,089, 1998.

Ajello, J. M., D. E. Shemansky, W. R. Pryor, A. I. Stewart, K. E. Simmons, T. Majeed, J. H. Waite, and G. R. Gladstone, Spectroscopic evidence for high-altitude aurora at Jupiter from Galileo Extreme Ultraviolet Spectrometer and Hopkins Ultraviolet Telescope observations, *Icarus*, *152*, 151, 2001.

Akasofu, S.-I., Past, present, and future of substorm research, in *Proc. 2nd Intl. Conf. on Substorms*, edited by J. R. Kan, J. D. Craven, and S.-I. Akasofu, p. 13, Geophys. Inst., Univ. of Alaska, 1994.

Anderson, K. A., Soft radiation events at high latitude during the magnetic storm of August 29-30, 1957, *Phys. Rev.*, *111*, 1397, 1958.

Axford, W. I., and C. O. Hines, A unifying theory of high latitude geophysical phenomena, *Can. J. Phys.*, *39*, 1433, 1961.

Bagenal, F., Empirical model of the Io plasma torus: Voyager measurements, *J. Geophys. Res.*, *99*, 11043, 1994.

Baker, D. N., Effects of the Sun on the Earth's environment, *J. Atm. Terr. Phys.*, *62*, 1669, 2000.

Ballester, G. E., et al., Time-resolved observations of Jupiter's far-ultraviolet aurora, *Science*, *274*, 409, 1996.

Banks, P. M., and A. F. Nagy, Concerning the influence of elastic scattering upon photoelectron transport and escape, *J. Geophys. Res.*, *75*, 1902, 1970.

Banks, P. M., C. R. Chappell, and A. F. Nagy, A new model for the interaction of auroral electrons with the atmosphere: spectral degradation, backscatter, optical emission, and ionization, *J. Geophys. Res.*, *79*, 1459, 1974.

Baron, R., T. Owen, J. E. P. Connerney, T. Satoh, and J. Harrington, Solar wind control of Jupiter's H_3^+ aurorae, *Icarus*, *120*, 437, 1996.

Barrow, C. H., F. Genova, and M. D. Desch, Solar wind control of Jupiter's decametric radio emission, *Astron. Astrophys.*, *165*, 244, 1986.

Basu, B., J. R. Jasperse, R. M. Robinson, R. R. Vondrak, and D. S. Evans, Linear transport theory of auroral proton precipitation: A comparison with observations, *J. Geophys. Res.*, *92*, 5920, 1987.

Basu, B., J. R. Jasperse, D. J. Strickland, and R. E. Daniell Jr., Transport-theoretic model for the electron-proton-hydrogenatom aurora, 1, Theory, *J. Geophys. Res.*, *98*, 21,517, 1993.

Benediktov, E. A., G. G. Getmantsev, Y. A. Sazonov, and A. F. Tarasov, Preliminary results of measurement of the intensity of distributed extraterrestrial radio-frequency emission at 725- and 1525-kHz frequencies by the satellite electron-2, *Kosm. Issled.*, *3*, 614, 1965.

Berger, M. J., S. M. Seltzer, and K. Maeda, Energy deposition by auroral electrons in the atmosphere, *J. Atmos. Terr. Phys.*, *32*, 1015, 1970.

Bhattacharya, B., R. M. Thorne, and D. J. Williams, On the energy source for diffuse Jovian auroral emissivity, *Geophys. Res. Lett.*, *28*, 2751, 2001.

Bigg, E. K., Influence of the satellite Io on Jupiter's decametric emission, *Nature*, *203*, 1008, 1964.

Bolton, S. J., et al., Correlation studies between solar wind parameters and the decimetric radio emission from Jupiter, *J. Geophys. Res.*, *94*, 121, 1989.

Borovsky, J. E., Auroral arc thickness as predicted by various theories, *J. Geophys. Res.*, *98*, 6101, 1993.

Brittnacher, M., M. Wilber, M. Fillingim, D. Chua, G. Parks, J. Spann, and G. Germany, Global auroral response to a solar wind pressure pulse, *Adv. Space Res.*, *25*, 2561, 2000.

Bunce, E. J., and S. W. H. Cowley, Local time asymmetry of the equatorial current sheet in Jupiter's magnetosphere, *Planet. Space Sci.*, *49*, 261, 2001a.

Bunce, E. J., and S. W. H. Cowley, Divergence of the equatorial current in the dawn sector of Jupiter's magnetosphere: Analysis of Pioneer and Voyager magnetic data, *Planet. Space Sci.*, *49*, 1089, 2001b.

Burke, B. F., and K. L. Franklin, Jupiter as a radio source, in *Radio Astronomy, Pro. 4th IAU Symp.*, edited by H. C. Van de Hulst, p. 394, Cambridge University Press, 1957.

Caledonia, G. E., R. E. Murphy, R. M. Nadile, and A. J. Ratkowski, Analysis of auroral infrared emissions observed during the ELIAS experiment, *Ann. Geophys.*, *13*, 247, 1995.

Carr, T. D, and M. D. Desch, Recent decametric and hectometric observations of Jupiter, in *Jupiter*, edited by T. Gehrels, Univ. of Arizona Press, Tucson, pp. 693-737, 1976.

Christensen, A. B., L. R. Lyons, J. H. Hecht, G. G. Sivjee, R. R. Meier, and D. G. Strickland, Magnetic field-aligned electric field acceleration and the characteristics of the optical aurora, *J. Geophys. Res.*, *92*, 6163, 1987.

Chua, D., G. Parks, M. Brittnacher, W. Peria, G. Germany, and C. Carlson, Energy characteristics of auroral electron precipitation: A comparison of substorms and pressure pulse related auroral activity, *J. Geophys. Res.*, *106*, 5945, 2001.

Clarke, J. T., J. T. Trauger, and J. H. Waite Jr., Doppler shifted H Ly α emissions from Jupiter's aurora, *Geophys. Res. Letts.*, *16*, 587, 1989.

Clarke, J. T., L. Ben Jaffel, A. Vidal-Madjar, G. R. Gladstone, J. H. Waite, Jr., R. Prangé, J.-C. Gérard, J. Ajello, and G. James, Hubble Space Telescope Goddard High-Resolution Spectrograph H_2 rotational spectra of Jupiter's aurora, *Astrophys. J.*, *430*, L73, 1994.

Clarke, J. T., et al., Far-ultraviolet imaging of Jupiter's aurora and the Io "footprint," *Science*, *274*, 404, 1996.

Clarke, J. T., et al., HST-STIS observations of Jupiter's aurora (abstract), *Bull. Am. Astron. Soc.*, *30*, 32P.21, 1998a.

Clarke, J. T., et al., Hubble Space Telescope imaging of Jupiter's UV aurora during the Galileo orbiter mission, *J. Geophys. Res.*, *103*, 20,217, 1998b.

Clarke, J. T., et al., Ultraviolet auroral emissions from the magnetic footprints of Io, Ganymede, and Europa on Jupiter, *Nature*, in press, 2002.

Codrescu, M. V., T. J. Fuller-Rowell, R. Roble, and D. S. Evans, Medium energy particle precipitation influence on the mesosphere and lower thermosphere, *J. Geophys. Res.*, *102*, 19,977, 1997.

Colgate, S. A., Prediction of auroral gamma rays, *Phys. Rev.*, *99*, 665, 1955.

Connerney, J. E. P., et al., Images of H_3^+ emission at the foot of the Io flux tube in Jupiter's atmosphere, *Science*, *262*, 1035, 1993.

Connerney, J. E. P., M. H. Acuña, N. F. Ness, and T. Satoh, New models of Jupiter's magnetic field constrained by the Io flux tube footprint, *J. Geophys. Res.*, *103*, 11,929, 1998.

Cook, A. F., A. Vallance Jones, and D. E. Shemansky, Visible aurora in Jupiter's atmosphere?, *J. Geophys. Res.*, *86*, 8793, 1981.

Cowley, S. W. H., et al., Ulysses observations of anti-sunward

flow on Jovian polar cap field lines, *Planet. Space Sci., 41*, 987, 1993.

Cowley, S. W. H., et al., Plasma flow in the Jovian magnetosphere and related magnetic effects: Ulysses observations, *J. Geophys. Res., 101*, 15,197, 1996.

Cowley, S. W. H., and E. J. Bunce, Origin of the main auroral oval in Jupiter's coupled magnetosphere-ionosphere system, *Planet. Space Sci., 49*, 1067, 2001.

Cravens, T. E., Auroral oxygen precipitation at Jupiter, *J. Geophys. Res., 100*, 17,153, 1995.

Decker, D. T., B. V. Kozelov, B. Basu, J. R. Jasperse, and V. E. Ivanov, Collisional degradation of the proton-H atom fluxes in the atmosphere: A comparison of theoretical techniques, *J. Geophys. Res., 101*, 26,947, 1996.

Deehr, C., and D. Lummerzheim, Ground-based optical observations of hydrogen emission in the auroral substorm, *J. Geophys. Res., 106*, 33, 2001.

Delory, G. T., et al., FAST observations of electron distributions within AKR source regions, *Geophys. Res. Lett., 25*, 2069, 1998.

Desch, M. D., and C. H. Barrow, Direct evidence for solar wind control of Jupiter's hectometer-wavelength radio emission, *J. Geophys. Res., 89*, 6819, 1984.

Dols, V., J.-C. Gérard, J. T. Clarke, J. Gustin, and D. Grodent, Diagnostics of the Jovian aurora deduced from ultraviolet spectroscopy: Model and GHRS observations, *Icarus, 147*,251, 2000.

Dougherty, M. K., M. Dunlop, R. Prangé, and D. Rego, Correspondence between field aligned currents observed by Ulysses and HST auroral emission, *Planet. Space Sci., 46*, 531, 1998.

Drossart, P., et al., Detection of H_3^+ on Jupiter, *Nature, 340*, 539, 1989.

Drossart, P, B. Bezard, S. K. Atreya, J. Bishop, J.H. Waite, Jr., and D. Boice, Thermal profiles in the auroral regions of Jupiter, *J. Geophys. Res., 98*, 18803, 1993.

Dungey, J. W., Interplanetary magnetic field and the auroral zones, *Phys. Rev. Lett., 6*, 47, 1961.

Eather, R. H., Red shift of auroral hydrogen profiles, *J. Geophys. Res., 71*, 5027, 1966.

Ergun, R. E., C. W. Carlson, J. P. McFadden, G. T. Delory, R. J. Strangeway, and P. L. Pritchett, Electron-cyclotron maser driven by charged-particle acceleration from magnetic field-aligned electric fields, *Astrophys. J., 538*, 456, 2000.

Espy, P. J., C. R. Harris, A. J. Steed, J. C. Ulwick, and R. H. Haycock, Rocketborne interferometer measurement of infrared auroral spectra, *Planet. Space Sci., 36*, 543, 1988.

Evans, D. S., Global Statistical Patterns of Auroral Phenomena, in *Proceedings of the Symposium on Quantitative Modeling of Magnetospheric-Ionospheric Coupling Processes*, p. 325, Kyoto, 1987 (see http://www.sel.noaa.gov/pmap/).

Fasel, G. J., Dayside poleward moving auroral forms: A statistical study, *J. Geophys. Res., 100*, 11,891, 1995.

Galand, M., J. Lilensten, W. Kofman, and R. B. Sidje, Proton transport model in the ionosphere, 1, Multistream approach of the transport equations, *J. Geophys. Res., 102*, 22,261, 1997.

Galand, M., J. Lilensten, W. Kofman, and D. Lummerzheim, Proton transport model in the ionosphere, 2, Influence of magnetic mirroring and collisions on the angular redistribution in a proton beam, *Ann. Geophys., 16*, 1308, 1998.

Gérard, J.-C., B. Hubert, D. V. Bisikalo, and V. I. Shematovich, A model of the Lyman-_ line profile in the proton aurora, *J. Geophys. Res., 105*, 15,795, 2000.

Gérard, J.-C., et al., A remarkable auroral event on Jupiter observed in the ultraviolet with the Hubble Space Telescope, *Science, 266*, 1675, 1994.

Germany, G. A., G. K. Parks, M. Brittnacher, J. Cumnock, D. Lummerzheim, J. F. Spann, L. Chen, P. G. Richards, and F. J. Rich, Remote determination of auroral energy characteristics during substorm activity, *Geophys. Res, Lett., 24*, 995, 1997.

Germany, G. A., J. F. Spann, G. K. Parks, M. J. Brittnacher, R. Elsen, L. Chen, D. Lummerzheim, and M. H. Rees, Auroral Observations from the POLAR Ultraviolet Imager (UVI), in *Encounter Between Global Observations and Models in the ISTP Era*, AGU Monograph, vol. 104, edited by J. Horwitz, D. Gallagher, and W. Peterson, p. 149, AGU, Washington, D. C., 1998a.

Germany, G. A., G. K. Parks, M. J. Brittnacher, J. F. Spann, J. Cumnock, D. Lummerzheim, F. Rich, and P. G. Richards, Energy characterization of a dynamic auroral event using GGS UVI images, in *Encounter Between Global Observations and Models in the ISTP Era*, AGU Monograph, vol. 104, edited by J. Horwitz, D. Gallagher, and W. Peterson, p. 143, AGU, Washington, D. C., 1998b.

Gladstone, G. R., et al., Secular and local time dependence of Jovian x-ray emissions, *J. Geophys. Res., 103*, 20,083, 1998.

Gladstone, G. R., et al., Chandra observations of x-rays from Jupiter during the Cassini flyby, *Nature*, in press, 2002.

Green, J. L., D. A. Gurnett, and S. D. Shawhan, The angular distribution of auroral kilometric radiation, *J. Geophys. Res., 82*, 1825, 1977.

Grodent, D., J. H. Waite, Jr., and J.-C. Gérard, A self-consistent model of the Jovian auroral thermal structure, *J. Geophys. Res., 106*, 12,933, 2001.

Grodent, D., J. T. Clarke, J. Kim, and J. H. Waite, Jr., Detailed analysis of HST-STIS Observations of Jupiter's far-ultraviolet aurora, *Icarus*, in press, 2002.

Gurnett, D. A., The Earth as a radio source: Terrestrial kilometric radiation, *J. Geophys. Res., 79*, 4227, 1974.

Gurnett, D. A., R. R. Anderson, F. L. Scarf, R. W. Fredricks, and E. J. Smith, Initial results from the ISEE-1 and -2 plasma wave investigation, *Space Sci. Rev., 23*, 103, 1979.

Gurnett, D. A., et al., First results from the Cluster wideband plasma wave investigation, *Annal. Geophysic.*, in press, 2002a.

Gurnett, D. A., et al., Control of Jupiter's radio emission and aurorae by the solar wind, *Nature*, in press, 2002b.

Hardy, D. A., W. J. Burke, M. S. Gussenhoven, N. Heinemann, and E. Holeman, DMSP/F2 electron observations of equatorward auroral boundaries and their relationship to the solar wind velocity and the north-south component of the interplanetary magnetic field, *J. Geophys. Res., 86*, 9961, 1981.

Hardy, D. A., M. S. Gussenhoven, and D. Brautigam, A statistical model of auroral ion precipitation, *J. Geophys. Res.*, *94*, 370, 1989.

Hawkins, S. E., III, A. F. Cheng, and L. J. Lanzerotti, Bulk flows of hot plasma in the Jovian magnetosphere: a model of anisotropic fluxes of energetic ions, *J. Geophys. Res.*, *103*, 20,031, 1998.

Hecht, J. H., A. B. Christensen, and J. B. Pranke, High-resolution auroral observations of the OI(7774) and OI(8446) multiplets, *Geophys. Res. Letts.*, *12*, 605, 1985.

Hecht, J. H., A. B. Christensen, D. J. Strickland, and R. R. Meier, Deducing composition and incident electron spectra from ground-based auroral optical measurements: variation in oxygen density, *J. Geophys. Res.*, *94*, 13,553, 1989.

Hecht, J. H., A. B. Christensen, D. J. Strickland, T. Majeed, R. L. Gattinger, and A. Vallance Jones, A comparison between auroral particle characteristics and atmospheric composition inferred from analyzing optical emission measurements alone and in combination with incoherent scatter radar measurements, *J. Geophys. Res.*, *104*, 33, 1999.

Hill, T. W., The Jovian auroral oval, *J. Geophys. Res.*, *106*, 8101, 2001.

Horanyi, M., T. E. Cravens, and J. H. Waite, Jr., The precipitation of energetic heavy ion into the upper atmosphere of Jupiter, *J. Geophys. Res.*, *93*, 7251, 1988.

Huff, R. L., W. Calvert, J. D. Craven, L. A. Frank, and D. A. Gurnett, Mapping of auroral kilometric radiation sources to the aurora, *J. Geophys. Res.*, *93*, 11,445, 1988.

Imhof, W. L., et al., The POLAR ionospheric x-ray imaging experiment, *Space Sci. Rev.*, *71*, 385, 1995.

Ingersoll, A. P., et al., Imaging Jupiter's aurora at visible wavelengths, *Icarus*, *135*, 251, 1998.

Ishimoto, M., C. I. Meng, G. R. Romick, R. E. Huffman, Doppler shifted auroral Lyman α observed from a satellite, *Geophys. Res. Lett.*, *16*, 143, 1989.

Jasperse, J. R., Boltzmann-Fokker-Planck model for the electron distribution function in the earth's atmosphere, *Planet. Space Sci.*, *24*, 33, 1976.

Jasperse, J. R., and B. Basu, Transport theoretic solutions for auroral proton and H atom fluxes and related quantities, *J. Geophys. Res.*, *87*, 811, 1982.

Kaiser, M. L., Observations of non-thermal radiation from planets, in *Plasma Waves and Instabilities at Comets and in Magnetospheres*, Geophysical Monograph 53, edited by B. T. Tsurutani and H. Oya, pp. 221-237, American Geophysical Union, Washington, 1989.

Kaiser, M. L., and M. D. Desch, Narrow band Jovian kilometric radiation: A new radio component, *Geophys. Res. Lett.*, *7*, 389, 1980.

Kamiyama, H., Flux of bremsstrahlung photons caused by energetic electrons precipitating into the atmosphere, *Rep. Ionos. Sp. Res. Japan*, *20*, 374, 1966.

Kamiyama, H., Ionizing effect of the bremsstrahlung associated with precipitating electrons, *Ann. Geophys.*, *26*, 625, 1970.

Kane, M. B., et al., Hot ions in Jupiter's magnetodisc: A model for Voyager 2 low-energy charged particle measurements, *J. Geophys. Res.*, *100*, 19,473, 1995.

Khan, H., S., et al., Observations of two complete substorm cycles during the Cassini Earth swing-by: Cassini magnetometer data in a global context, *J. Geophys Res.*, *106*, 30,141, 2001.

Kim, Y. H., J. L. Fox, and J. J. Caldwell, Temperatures and altitudes of Jupiter's ultraviolet aurora inferred from GHRS observations with the Hubble Space Telescope, *Icarus*, *128*, 189, 1997.

Kozelov, B. V., Influence of the dipolar magnetic field on transport of proton-H atom fluxes in the atmosphere, *Ann. Geophys.*, *11*, 697, 1993.

Krupp, N., J. Woch, A. Lagg, B. Wilken, S. Livi, D. Williams, Energetic particle bursts in the predawn Jovian magnetotail, *Geophys. Res. Lett.*, *25*, 1249, 1998.

Kurth, W. S., M. M. Baumback, and D. A. Gurnett, Direction-finding measurements of auroral kilometric radiation, *J. Geophys. Res.*, *80*, 2764, 1975.

Kurth, W. S., T. Murata, G. Lu, D. A. Gurnett, and H. Matsumoto, Auroral kilometric radiation and the auroral electrojet index for the January 1997 magnetic cloud event, *Geophys. Res. Lett.*, *25*, 3027, 1998.

Ladreiter, H. P., and Y. Leblanc, Jovian hectometric radiation - Beaming, source extension, and solar wind control, *Astron. Astrophys, 226*, 297, 1989.

Ladreiter, H. P., P. Zarka, and A. Lecacheux, Direction-finding study of Jovian hectometric and broadband kilometric radio emissions: Evidence for their auroral origin, *Planet. Space Sci.*, *42*, 919, 1994.

Lam, H. A., N. Achilleos, S. Miler, J. Tennyson, L. M. Trafton, T. R. Geballe, and G. E. Ballester, A baseline spectroscopic study of the infrared auroras of Jupiter, *Icarus*, *127*, 379, 1997.

Lanchester, B. S., M. H. Rees, D. Lummerzheim, A. Otto, H. U. Frey, and K. U. Kaila, Large fluxes of auroral electrons in filaments of 100-m width, *J. Geophys. Res.*, *102*, 9741, 1997.

Link, R., Feautrier solution of the electron transport equation, *J. Geophys. Res.*, *97*, 159, 1992.

Liou, K., P. T. Newell, D. G. Sibeck, C.-I. Meng, M. Brittnacher, and G. Parks, Observation of IMF and seasonal effects in the location of auroral substorm onset, *J. Geophys. Res.*, *106*, 5799, 2001.

Liu, W., and A. Dalgarno, The ultraviolet spectrum of the Jovian aurora, *Astrophys. J.*, *467*, 446, 1996.

Lorentzen, D. A., F. Sigernes, and C. S. Deehr, Modeling and observations of dayside auroral hydrogen emission Doppler profiles, *J. Geophys. Res.*, *103*, 17,479, 1998.

Lotko, W., A. V. Streltsov, and C. W. Carlson, Discrete auroral arc, electrostatic shock, and suprathermal electrons powered by dispersive, anomalously resistive field line resonance, *Geophys. Res. Letts.*, *25*, 4449, 1998.

Louarn, P., and D. Le Queau, Generation of the auroral kilometric radiation in plasma cavities, I. Experimental study, *Planet. Space Sci.*, *44*, 199, 1996.

Louarn, P., A. Roux, S. Perraut, W. Kurth, and D. Gurnett, A study of the large-scale dynamics of the Jovian magnetosphere

using the Galileo plasma experiment, *Geophys. Res. Lett., 25*, 2905, 1998.

Lu, G., et al., Global energy deposition during the January 1997 ISTP event, *J. Geophys. Res., 103*, 11,685, 1998.

Lu, G., M. Brittnacher, G. Parks, and D. Lummerzheim, On the magnetospheric source regions of substorm-related field-aligned currents and auroral precipitation, *J. Geophys. Res., 105*, 18,483, 2000.

Luhmann, J. G., Auroral bremsstrahlung spectra in the atmosphere, *J. Atmos. Terr. Phys., 39*, 595, 1977.

Lummerzheim, D., and J. Lilensten, Electron transport and energy degradation in the ionosphere: Evaluation of the numerical solution, comparison with laboratory experiments and auroral observations, *Ann. Geophys., 12*, 1039, 1994.

Lummerzheim, D., and M. Galand, The profile of the hydrogen Hβ emission line in proton aurora, *J. Geophys. Res., 106*, 23, 2001.

Lummerzheim, D., M. H. Rees, and G. J. Romick, The application of spectroscopic studies of the aurora to thermospheric neutral composition, *Planet. Space Sci., 38*, 67, 1990.

Maillard, J.-P., P. Drossart, J. K. G. Watson, S. J. Kim, and J. Caldwell, H_3^+ fundamental band in Jupiter's auroral zones at high resolution from 2400 to 2900 inverse centimeters, *Astrophys. J., 363*, L37, 1990.

Mauk, B. H., et al., Hot plasma parameters of Jupiter's inner magnetosphere, *J. Geophys. Res., 101*, 7685, 1996.

Mauk, B. H., D. J. Williams, and R. W. McEntire, Energy-time dispersed charged particle signatures of dynamic injections in Jupiter's inner magnetosphere, *Geophys. Res. Lett., 24* 2949, 1997.

Mauk, B. H., D. J. Williams, R. W. McEntire, K. K. Khurana, and J. G. Roederer, Storm-like dynamics of Jupiter's inner and middle magnetosphere, *J. Geophys. Res., 104*, 22,759, 1999.

Mauk, B. H., et al., Magnetospheric electron injections create transient auroral emissions at Jupiter, *Nature*, in press, 2002.

McEwen, D. J., and Y. Zhang, A continuous view of the dawn-dusk polar cap, *Geophys. Res. Lett., 27*, 477, 2000.

McFadden, J. P., C. W. Carlson, and R. E. Ergun, Microstructure of the auroral acceleration region as observed by FAST, *J. Geophys. Res., 104*, 14,453, 1999.

Meng, C. I., Polar cap arcs and the plasma sheet, *Geophys. Res. Lett., 8*, 273, 1981.

Menietti, J. D., D. A. Gurnett, W. S. Kurth, and J. B. Groene, Control of Jovian radio emission by Ganymede, *Geophys. Res. Lett., 25*, 4281, 1998.

Menietti, J. D., D. A. Gurnett, and I. Christopher, Control of Jovian radio emission by Callisto, *Geophys. Res. Lett., 28*, 3047, 2001.

Metzger, A. E., et al., The detection of X rays from Jupiter, *J. Geophys. Res., 88*, 7731, 1983.

Milan, S. E., M. Lester, S. W. H. Cowley, M. Brittnacher, Dayside convection and auroral morphology during an interval of northward interplanetary magnetic field, *Ann. Geophys., 18*, 436, 2000a.

Milan, S. E., M. Lester, S. W. H. Cowley, Convection and auroral response to a southward turning of the IMF, Polar UVI, CUTLASS, and IMAGE signatures of transient magnetic flux transfer at the magnetopause, *J. Geophys. Res., 105*, 15,741, 2000b.

Miller, S., R. D. Joseph, and J. Tennyson, Infrared emissions of H_3^+ in the atmosphere of Jupiter in the 2.1 and 4.0 micron region, *Astrophys. J., 360*, L55, 1990.

Min, Q. L., D. Lummerzheim, M. H. Rees, and K. Stamnes, The effects of a parallel electric field and the geomagnetic field in the topside ionosphere on auroral and photoelectron energy distributions, *J. Geophys. Res., 98*, 19,223, 1993.

Murata, T., H. Matsumoto, H. Kojima, and T. Iyemori, Correlations of AKR index with K_p and D_{st} indices, *Proc. NIPR Symp. Upper Atmos. Physics, 10*, 64, 1997.

Nagy, A. F., and P. M. Banks, Photoelectron fluxes in the ionosphere, *J. Geophys. Res., 75*, 6260, 1970.

Newell, P. T., S. Wing, C.-I. Meng, and V. Sigillito, The auroral oval position, structure, and intensity of precipitation from 1984 onwards: An automated online data base, *J. Geophys. Res., 96*, 5877, 1991.

Østgaard, N., J. Stadsnes, K. Aarsnes, F. Søraas, K. Måseide, M. Smith, J. Sharber, Simultaneous measurements of x-rays and electrons during a pulsating aurora, *Ann. Geophys., 16*,148, 1998.

Østgaard, N., J Stadsnes, J. Bjordal, R. R. Vondrak, S. A. Cummer, D. L. Chenette, G. K. Parks, M. J. Brittnacher, and D. L. McKenzie, Global-scale electron precipitation features seen in UV and x-rays during substorms, *J. Geophys. Res., 104*, 10,191, 1999.

Østgaard, N., J Stadsnes, J. Bjordal, R. R. Vondrak, S. A. Cummer, D. L. Chenette, M. Schultz and J. G. Pronko, Cause of the localized maximum of x-ray emission in the morning sector: A comparison with electron measurements, *J. Geophys. Res., 105*, 20869, 2000.

Otto, A., and G. T. Birk, Formation of thin auroral arcs by current striation, *Geophys. Res. Lett., 20*, 2833, 1993.

Pallier, L., and R. Prangé, More about the structure of the high latitude Jovian aurorae, *Planet. and Space Sci., 49*, 1159, 2001.

Perry, J. J., Y. H. Kim, J. L. Fox, and H. S. Porter, Chemistry of the Jovian auroral atmosphere, *J. Geophys. Res., 104*, 16,541, 1999.

Peticolas, L. M., and D. Lummerzheim, Time-dependent transport of field-aligned bursts of electrons in flickering aurora, *J. Geophys. Res., 105*, 12,895, 2000.

Pontius, D. H., Jr., and T. W. Hill, Rotation driven plasma transport: The coupling of macroscopic and microdiffusion, *J. Geophys. Res., 94*, 15,041, 1989.

Prangé, R., et al., Correlated variations of UV and radio emissions during an outstanding Jovian auroral event, *J. Geophys. Res., 98*, 18,779, 1993.

Prangé, R., et al., Detailed study of FUV Jovian auroral features with the post-COSPAR HST faint object camera, *J. Geophys. Res., 103*, 20,195, 1998.

Prangé, R., G. Chagnon, T. A. Livengood, M. G. Kivelson, W. Kurth, Temporal monitoring of Jupiter's auroral activity with IUE. Implications for magnetospheric processes, *Planet. Space Sci., 49*, 405, 2001.

Pryor, W. R., et al., Galileo ultraviolet spectrometer observations

of Jupiter's auroral spectrum from 1600-3200 R, *J. Geophys. Res., 103*, 20,149, 1998.

Rees, M. H., Ionization in the Earth's atmosphere by aurorally associated bremsstrahlung x-rays, *Planet. Space Sci., 12*, 1093, 1964.

Rees, M. H., and D. Luckey, Auroral electron energy derived from ratio of spectroscopic emissions, 1. Model computations, *J. Geophys. Res., 79*, 5181, 1974.

Rees, M. H., and R. G. Roble, Excitation of O(^{1}D) atoms in aurorae and emission of the [OI] 6300-Å line, *Can. J. Phys., 64*, 1608, 1986.

Rees, M. H., D. Lummerzheim, and R. G. Roble, Modeling of the Atmosphere-Magnetosphere-Ionosphere System MAMI, *Space Sci. Rev., 71*, 691, 1995.

Rego, D., et al., Lyman-α and H_2 bands from the giant planet, 1, Excitation by proton precipitation in the Jovian aurorae, *J. Geophys. Res., 99*, 17,075, 1994.

Rego, D., R. Prangé, and L. Ben Jaffel, Lyman α and H_2 bands from the giant planets, 3. Intensity and spectral profile of the auroral Lyman α emission, including charge exchange and radiative transfer effects, and H_2 color ratios, *J. Geophys. Res., 104*, 5939, 1999.

Reiner, M. J., J. Fainberg, and R. G. Stone, Source characteristics of Jovian hectometric radio emissions, *J. Geophys. Res., 98*, 18,767, 1993.

Russell, C. T., K. K. Khurana, D. E. Huddleston, and M. G. Kivelson, Localized reconnection in the near Jovian magnetotail, *Science, 280*, 1061, 1998.

Russell, C. T., G., P. Chi, X.-W. Zhou, J.-H. Shue, S. M. Petrinec, P. Song, F. R. Fenrich, and J. G. Luhmann, The extreme compression of the magnetosphere on May 4, 1998, as observed by the Polar spacecraft, *Adv. Space Res., 25*, 1369, 2000.

Satoh, T., J. E. P. Connerney, and R. L. Baron, Emission source model of Jupiter's H_3^+ aurorae: A generalized inverse analysis of images, *Icarus, 122*, 1, 1996.

Seiff, A., et al., Thermal structure of Jupiter's atmosphere near the edge of a 5-mm hot spot in the north equatorial belt, *J. Geophys. Res., 103*, 22,857, 1998.

Sharber, J. R., et al., Observations of the UARS particle environment monitor and computation of ionization rates in the middle and upper atmosphere during a geomagnetic storm, *Geophys. Res. Lett., 20*, 1319, 1993.

Share, G. H., and R. J. Murphy, Atmospheric gamma rays from solar energetic particles and cosmic rays penetrating the magnetosphere, *J. Geophys. Res., 106*, 77, 2001.

Slinker, S. P., J. A. Fedder, B. A. Emery, K. B. Baker, D. Lummerzheim, J. G. Lyon, and F. J. Rich, Comparison of global MHD simulations with AMIE simulations for the events of 19-20 May, 1996, *J. Geophys. Res., 104*, 28,379, 1999.

Smith, R. A., F. Bagenal, A. F. Cheng, and D. F. Strobel, On the energy crisis in the Io plasma torus, *Geophys. Res. Letts., 15*, 545, 1988.

Solomon, S. C., Auroral electron transport using the Monte Carlo method, *Geophys. Res. Lett., 20*, 185, 1993.

Southwood, D. J., and M. Kivelson, A new perspective concerning the influence of the solar wind on the Jovian magnetosphere, *J. Geophys. Res., 106*, 6123, 2001.

Stamnes, K., Analytic approach to auroral electron transport and energy degradation, *Planet. Space Sci., 28*, 427, 1980.

Stamnes, K., On the two-stream approach to electron transport and thermalization, *J. Geophys. Res., 86*, 2405, 1981.

Strickland, D. J., D. L. Book, T. P. Coffey, and J. A. Fedder, Transport equation techniques for the deposition of auroral electrons, *J. Geophys. Res., 81*, 2755, 1976.

Strickland, D. J., R. R. Meier, J. H. Hecht, and A. B. Christensen, Deducing composition and incident electron spectra from ground-based auroral optical measurements: Theory and model results, *J. Geophys. Res., 94*, 13,527, 1989.

Strickland, D. J., R. E. Daniell Jr., J. R. Jasperse, and B. Basu, Transport-theoretic model for the electron-proton-hydrogen atom aurora, 2, model results, *J. Geophys. Res., 98*, 21,533, 1993.

Synnes, S. A., F. Søraas, and J. P. Hansen, Monte-Carlo simulation of proton aurora, *J. Atmos. Sol.-Terr. Phys., 60*, 1695, 1998.

Temerin, M., What do we really know about auroral acceleration?, *Adv. in Space Res., 20*, 1025, 1997.

Thorne, R. M., Microscopic plasma processes in the Jovian magnetosphere, in *Physics of the Jovian Magnetosphere*, edited by A. J. Dessler, pp. 454-488, Cambridge University Press, Cambridge, UK, 1983.

Trafton, L. M., J. D. F. Lester, and K. L. Thompson, Unidentified emission lines in Jupiter's northern and southern 2 micron aurorae, *Astrophys. J., 343*, L73, 1989.

Trafton, L. M., J. C. Gérard, G. Munhoven, and J. H. Waite, Jr, High-resolution spectra of Jupiter's northern auroral ultraviolet emission with the Hubble Space Telescope, *Astrophys. J., 421*, 816, 1994.

Trafton, L. M., V. Dols, J.-C. Gérard, J. H. Waite, Jr., G. R. Gladstone, and G. Munhoven, HST spectra of the Jovian ultraviolet aurora: Search for heavy ion precipitation, *Astrophys. J., 507*, 955, 1998.

Vallance Jones, A., *Aurora*, 301 pp., D. Reidel Publishing Co., Dordrecht, Holland, 1974.

Vasavada, A. R., et al., Jupiter's visible aurora and Io footprint, *J. Geophys. Res., 104*, 27,133, 1999.

Voots, G. R., D. A. Gurnett, and S.-I. Akasofu, Auroral kilometric radiation as an indicator of auroral magnetic disturbances, *J. Geophys. Res., 82*, 2259, 1977.

Waite, J. H., Jr., et al., Electron precipitation and related aeronomy of the Jovian thermosphere and ionosphere, *J. Geophys. Res., 88*, 6143, 1983.

Waite, J. H., Jr., et al., ROSAT observations of the Jupiter aurora, *J. Geophys. Res., 99*, 14788, 1994.

Waite, J. H., Jr. et al., Multispectral observations of Jupiter's aurora, *Adv. Space Res. 26*, 1453, 2000.

Waite, Jr., J. H., et al., An auroral flare at Jupiter, *Nature, 410*, 2001.

Warwick, J. W., et al., Voyager 1 planetary radio astronomy observations near Jupiter, *Science, 204*, 995, 1979a.

Warwick, J. W., et al., Planetary radio astronomy observations from Voyager 2 near Jupiter, *Science, 206*, 991, 1979b.

Williams, D. J., and R. W. McEntire, The Galileo energetic particles detector, *Space Sci. Rev., 60*, 385, 1992.

Winningham, J. D., et al., The UARS Particle Environment Monitor, *J. Geophys. Res., 98*, 10,649, 1993.

Woch, J., N. Krupp, A. Lagg, B. Wilken, S. Livi, and D. Williams, Quasiperiodic modulations of the Jovian magnetotail, *Geophys. Res. Lett., 25*, 1253, 1998.

Wu, C. S., and L. C. Lee, A theory of terrestrial kilometric radiation, *Astrophys. J., 230*, 621, 1979.

Wygant, J. R. et al., Polar spacecraft based comparisons of intense electric fields and Poynting flux near and within the plasma sheet-tail lobe boundary to UVI images: An energy source for the aurora, *J. Geophys. Res., 105*, 18,675, 2000.

Yung, Y. L., G. R. Gladstone, K. M. Chang, J. M. Ajello, and S. K. Srivastava, H_2 fluorescence spectrum from 1200 to 1700 by electron impact: Laboratory study and application to Jovian aurora, *Astrophys. J., 254*, L65, 1982.

Zarka, P., Auroral radio emissions at the outer planets: Observations and theories, *J. Geophys. Res., 103*, 20,159, 1998.

Zarka, P., Radio emissions from the planets and their moons, in *Radio Astronomy at Long Wavelengths*, Geophysical Monograph 119, edited by R. G. Stone, J.-L. Bougeret, K. Weiler, and M. Goldstein, pp. 167-178, American Geophysical Union, Washington, 2000.

Zarka, P., and F. Genova, Low frequency Jovian emission and the solar wind magnetic sector structure, *Nature, 306*, 767, 1983.

Zesta, E., H. J. Singer, D. Lummerzheim, C. Russell, L. Lyons, and M. J. Brittnacher, The effect of the January 10, 1997 pressure pulse on the magnetosphere-ionosphere current system, in *Magnetospheric Current Systems, Geophys. Monogr. Ser.*, vol. 118, p. 217, 2000.

Zhou, X., and B. T. Tsurutani, Rapid intensification and propagation of the dayside aurora: Large-scale interplanetary pressure pulses (fast shocks), *Geophys. Res. Letts., 26*, 1097, 1999.

Zhu, H., A. Otto, D. Lummerzheim, M. H. Rees, and B. S. Lanchester, Ionosphere-magnetosphere simulations of small-scale structure and dynamics, *J. Geophys. Res., 106*, 1795, 2001.

Dirk Lummerzheim, Geophysical Institute, The University of Alaska, Fairbanks, Alaska 99775-7320.

J. Hunter Waite, Jr., Department of Atmospheric, Oceanic, and Space Sciences, University of Michigan, Ann Arbor, MI 48109-2143.

Numerical Techniques Associated with Simulations of the Solar Wind Interactions with Non-Magnetized Bodies

Stephen H. Brecht

Bay Area Research Corporation, Orinda, California

A brief review of the common numerical approaches used to simulate the solar wind interaction with planets having no global magnetic fields is presented. For brevity the numerical approaches are classified in this paper in the most general way as: hydrodynamic, MHD, and kinetic. Many of the basic equations and assumptions associated with these numerical methods will be discussed.

INTRODUCTION

In the past decade the global simulation of planetary magnetospheres has become very common. This is particularly true of the Earth. However, as more missions have been sent to Mars and the outer planets and their moons, the emphasis of the simulations has shifted. Originally, obtaining the magnetic field and flow field topology was the main goal. Now, the emphasis is shifting to understanding how the solar wind interacts with these bodies and more specifically how the solar wind interacts with the atmosphere/ionosphere/exosphere of these bodies.

This chapter describes the general classes of numerical approaches used in global 3-D modeling of the solar wind interaction with exospheres, ionospheres, and atmospheres. It follows previous papers of this sort [cf. *Luhmann et al.,* 1997], but the focus is to one of highlighting assumptions, utility, and applicability. It is not the purpose of this paper to espouse a particular approach to global 3-D simulations. That is left for the reader to decide. However, it is felt that no matter which scheme is chosen that the user should be aware of the limitations of each of these approaches, as well as their strengths.

In the following paragraphs, brief comparison between the planets Earth, Venus and Mars will be presented along with their respective challenges to the simulator. The various numerical schemes will be briefly discussed along with their uses. A few applications of kinetic simulations of Mars will be presented in the next section. A brief summary will conclude the paper.

Atmospheres in the Solar System: Comparative Aeronomy
Geophysical Monograph 130

10.1029/130GM09

PLANET COMPARISONS

When considering which simulation tool to use, issues of scale size become paramount. However, it isn't simply the planet size. For example, Earth and Venus are roughly the same size (> 6300 km). Yet, Venus has more in common with Mars although Mars is significantly smaller (3395 km). This rather strange scaling occurs because Earth has a strong intrinsic magnetic field. Therefore, the first planetary feature that the solar wind encounters, the bow shock, is very far from the ionosphere and exosphere. Table 1 shows a synopsis of the various planetary shock distances, as well, as approximate solar wind ion gyroradii when encountering each planet.

As mentioned, Earth's exosphere, ionosphere, and atmosphere are protected from direct solar wind interaction with the solar wind. However, Venus having no intrinsic magnetic is not so fully protected [*cf. Donahue and Russell,* 1997]. The bow shock formed by the Venus–Solar wind interaction is far enough out to protect the atmosphere from direct deposition of solar wind ions [*Brecht and Ferrante,* 1991]. The Venusian bow shock does not stop the IMF from convecting through the inner magnetosphere of Venus [*cf. Cravens et al.,* 1997]. The IMF is dragged through the outer ionosphere of Venus, providing a convection electric field to pickup oxygen ions from the ionosphere.

Although, Mars has now been found to have some crustal magnetic fields, it does not change the fact that subsolar

bow region is very close to the planet. Hence, solar wind energy is deposited directly into the ionosphere, and the exosphere of Mars is swept into the shock. Further, one expects and sees that the atmosphere/ionosphere of Mars is being eroded away at a much higher rate than at Venus. This leads to many intriguing questions concerning the former state of the atmosphere of Mars, its water content, and the source of minority species such as Helium.

Indeed, these planets (Earth, Venus, and Mars) represent complete, partial and no separation of the solar wind from the planetary atmosphere, ionosphere, and exosphere. This fact has very important implications as to what type of numerical scheme one would want to choose for doing simulations. If for example, one wants to examine energization of charged particles by the planetary bow shock then the physics of the shock must be included. If one wants to examine the motion of the atmosphere of the planet then the cell size must be small enough to resolve the scale height of the atmosphere.

realistic and matched data better. However, there is no need to address issues such as pickup ions, and energy deposition from the solar wind. More importantly the small scale sizes that a kinetic code needs to resolve make it virtually impossible with modern computers to use this tool to address reasonable sections of the Earth's magnetosphere.

In the case of Venus there is no intrinsic magnetic field. However, the shock does a relatively good job of protecting the planet from the solar wind flow. MHD is fair approximation for the overall system. However, if one is interested in pickup ions that can escape the planet and move into the tail or deposit their energy back into the atmosphere, then MHD can only be used as a source of flow fields and magnetic fields for test particle tracing. Indeed, if one is interested in the tail rays found to emanate from the night side of the planet then multiple fluids and more complex physics than the usual MHD code provides must be used. It should be noted that when examining the chemical activity of the atmosphere/ionosphere that the MHD approach offers some significant advantages over the kinetic code, unless enormous amounts of memory and computer time are available.

Table 1. Comparison between Shock Standoff Distance and Ion Gyroradius

Planet	Stand-0ff Distance	Stand-off Distance	Ion Gyroradius
Earth	10 –13 R_E	> 65,000 km	~ 365 km
Venus	1.4 R_V	~ 2400 km	~ 365 km
Mars	1.5 R_M	~ 1600 km	~ 1390 km

NUMERICAL ISSUES

The previous section illustrates the issues to be considered when simulating planets and the interaction of the solar wind with such features as the bow shock, the exosphere, the ionosphere, and the atmosphere. The first challenge to performing a valid and useful simulation is to retain as much of the physics as necessary without doing more than necessary. The simulations must be fast enough that the researcher can determine the dependencies that exist between the solar wind, the magnetosphere, and the ionosphere/atmosphere. It is essential that the models be kept as simple as possible in order for the user to be able to test and understand what is occurring in these large simulations.

All of the planets are difficult to simulate, but the difficulty depends on the questions being asked and the physics required. For example, when simulating the planet Earth the bow shock protects the atmosphere from direct interaction with the solar wind. MHD is often a very good approximation because the Earth's magnetosphere is large and many of the dynamical features are large to kinetic scales. However, more physics is needed to couple the ionosphere electrically to the rest of the magnetosphere. It has been found that by including this coupling to the "Earth boundary", the MHD simulations became more

Moving to the planet Mars the situation really becomes complex. First, Mars has no large-scale intrinsic magnetic field making it a small obstacle compared with the ion gyroradius of the incoming solar wind ions. However, one of the most surprising discoveries by the Mars Global Surveyor, MGS, mission [*Acuña et al.*, 1998] was the presence of crustal fields located near the surface with very large field strengths. The absence of a global intrinsic field and the presence of the crustal fields makes Mars a very difficult planet to simulate.

For example, the shock does not protect the ionosphere/atmosphere from the solar wind. Solar wind particles deposit directly into the ionosphere/atmosphere of Mars. The exosphere at Mars extends beyond the location of the bow shock. The bow shock is also asymmetric and with the added lumps, caused by the crustal field, the ion trajectories are very complex. As mentioned, the ion gyroradius of the ions in the solar wind can range from roughly 1300 km for protons at 425 km/s to over 3000 km for higher wind conditions measured by Phobos–2 [*Schwingenschuh et al.*, 1990; *Breus et al.*; 1991]. Further, the gyroradius of pickup ions (usually O+) is larger

than the planet radius. This all leads to the conclusion that the kinetic simulations would be best for the planet in all regions except where the atmosphere/ionosphere is collisionally coupled and chemistry is an area of prime importance.

As will become clearer in the next section, certain approaches to simulating a given planet are superior to others. However, as is often the case, many different types of simulations have been used on all of the planets. The level of success is determined by what the researcher is using the simulations for and where they are being applied. In the next section, the three major types of simulations will be discussed and their assumptions examined.

SIMULATION APPROACHES

Three general types of codes are used for global simulation of planets. These three are: gas dynamic simulations, magnetohydrodynamic (MHD) simulations, and kinetic (hybrid particle) simulations. All of these approaches conserve energy and momentum. The first two approaches make strict use of the Rankine-Hugoniot relations for the shock jump and down stream pressure and velocity. Because energy conservation and momentum is present in all of the approaches, the general location of the shock structure is reasonably good. Thus even if one of the codes is technically not appropriate for a given planet, such as Mars, all of the codes will provide to some level an "acceptable" description of the main features. This is true because with each approach the same general physics question is being asked. What are the sources of free energy in the system? Where can this energy go (i.e., what are the degrees of freedom in the system)?

Let us take the simplest situation: flow of a gas into a body. In this case the free energy is in the form of flow. When it hits the body a pressure is built up and a force is applied to the flow to move it back upstream. However, in a single fluid situation, counter streaming of flow cannot be supported plus the fluid cannot move faster than its characteristic speed (the speed of sound). So a shock is formed that takes the excess energy from the incoming flow and converts it into heat, thus changing the local sound speed so that the flow is equal to or below it. In this picture, the degrees of freedom for the flow are heat (pressure) and flow. That is all that is needed to form a shock structure in a gas dynamic simulation. If a magnetic field is added it simply goes with the flow and piles up where the flow piles up. It provides no force or additional source of free energy.

In a MHD code the magnetic field is part of the force equation and part of the pressure. One still has the same overall equations as the gas dynamic simulations, but the degrees of freedom and sources are now increased. The flow contains kinetic energy plus the magnetic field. When the flow forms a shock, the magnetic field pileup provides a force outward in addition to that provided by the gas pressure. One now has magnetic field gradients and density gradients as sources of free energy to move the plasma around. The additional degrees of freedom can be appreciated by the increase in the number of waves available to the system. In addition to the sound waves, the system now exhibits magnetosonic waves and Alfvén waves. If one goes to fully represented multi-fluid simulations with each fluid having a full set of governing equations, then even the potential for Rayleigh-Taylor instabilities and counter streaming exists. In the case of multiple fluids, but only one governing flow equation, the counters streaming flows cannot exist.

When one goes to the kinetic simulations, then the degrees of freedom increase tremendously. In the most limited of the kinetic simulations, the hybrid particle code, the degrees of freedom are still significant. The energy can now go into heating, particle acceleration, non-maxwellian distribution functions, a large number of electromagnetic modes, and the usual density gradients and magnetic field gradients. Further, the plasma can counter stream and is not forced to form a shock. The particles now gyrate around the magnetic field lines, perform a variety of drifts, and drive collective instabilities, including the gradient drift instability. Finally, features such a plasma filamentation and diamagnetic flows are present because the symmetry of the MHD equations has been broken.

The choice of simulation tool depends on the questions being asked and the number of degrees of freedom necessary to answer the question accurately. If only a bow shock, heating, and flow fields are needed, the gas dynamic approach will work well. If the role of the magnetic field is needed in addition to the previously mentioned features, the MHD method will work well. However, if more detailed questions are asked, then more degrees of freedom are necessary, and either MHD with additional physics or the kinetic approach in its many manifestations may well be the tool of choice. With these comments, the three major numerical approaches will be discussed in more detail.

Gas Dynamic Simulations

Gas dynamic simulations use the usual hydrodynamic equations. Some formulations of these equations are implicit and relax to a steady state solution and others are explicit. The flow is described by the fluid equations and the B field is simply carried by the fluid. It exerts no force on the motion of the plasma. The flow will by symmetrical around the body and have the usual stagnation point along the subsolar line. The simulations are fast and dependent on fewer parameters than the MHD or kinetic codes.

Spreiter and Stahara [1980] developed the most common model. However, other versions have been used, [*cf. Breus et al.*, 1989]. Researchers often use the Spreiter and Stahara model to obtain flow fields and a representation of the magnetic fields. These fields are often used to perform test particle trajectory calculations to see where pickup ions will go and what their velocity spectrum might be. Thus, they add more degrees of freedom to the gas dynamic model but not in a self-consistent manner. This approach has been used by a variety of researchers [*cf. Luhmann and Kozyra*, 1991; *Zhang et al.*, 1993; *Kallio et al.*, 1997] to examine such things as mass loading of the solar wind by charge exchange, impact ionization, and production of energetic neutral atoms.

MHD Simulations

MHD simulations are more complex than the gas dynamic models. They are often explicit in their time stepping and they have not only the sound waves present but the Alfven wave as well. The magnetic fields are an important component to the flow solutions. Flow around the planet will be symmetric because like the gas dynamic model, the equations are mathematically symmetric. The MHD codes are slower than a gas dynamic model, but faster than a kinetic code. They are also more complex than the gas dynamic model. In some cases the researchers using MHD simulations of Mars are using multiple fluids but only one momentum equation [*Liu et al.*, 2000 and 2001]. Others, have included Hall terms and multiple fluids but don't include ion heating [cf. *Sauer et al.*, 1994]

It is worthwhile to review the MHD equations and to examine the assumptions that are made to obtain them. The details of the equations can be found in many plasma physics books. A very good reference for the MHD equations and their assumptions *is Krall and Trivelpiece* [1986]. The governing equations for MHD are:

The continuity equation

$$\partial\rho_m/\partial t + \nabla\bullet(\rho_m \mathbf{V}) = 0 \qquad (1)$$

The momentum equation

$$\rho\, \partial\mathbf{V} / \partial t = \mathbf{J} \times \mathbf{B} / c - \nabla p \qquad (2)$$

Ohm's Law

$$\mathbf{E} + \mathbf{V} \times \mathbf{B} / c = \eta\, \mathbf{J} \qquad (3)$$

Faraday's Law

$$c\nabla \times \mathbf{E} = - \partial\mathbf{B}/\partial t \qquad (4)$$

Ampere's Law

$$\nabla \times \mathbf{B} = 4\pi\mathbf{J}/c \qquad (5)$$

Energy Equation

$$\partial e / \partial t = -p\, \nabla\bullet\mathbf{V} - \mathbf{Q}: \nabla\mathbf{V} \qquad (6)$$

Where Q is the anomalous viscosity used to create the shock, p is the pressure, e is the internal energy, **V** is the velocity vector, **E** and **B** are the electric and magnetic field vectors, **J** is the total current, and ρ is the charge mass density of the fluid.

To obtain these equations some rather significant assumptions must be made. In the following paragraphs some but not all of the assumption will be mentioned. The first assumption made is that of pressure isotropy, $\nabla\bullet\mathbf{P} = \nabla p$. This assumption has many implications but several of the strongest are the removal of several electromagnetic modes from the MHD system. These are the fire hose instability and the mirror mode instability. This truncation also means that higher order moments have been removed from the system of equations.

Another set of assumptions are often referred to as the MHD ordering are,

$$(\rho_i/L)^2 << 1 / (T\omega_{ci}) << 1, \quad (7)$$

where ρ_i is the ion gyroradius and L is the scale length of the structures to be resolved by the equations, T is the time step of solutions and ω_{ci} is the ion gyrofrequency. This relation means that to obtain the MHD equations Eq. (1 – 6) the ion gyroradius must be smaller than the scale lengths resolved in the simulations. Further, this scaling says that the time step of the simulations should be much larger than the ion gyrofrequency. These restrictions are severe when considering the physics of collisionless shocks and planetary bodies such as Mars and Saturn's moon Titan. In the case of Venus, finite larmor radius affects are present but the MHD scaling is much closer to holding, see pictures in *Brecht and Ferrante* [1991] for an example of this situation. Another assumption implicit in the MHD equations is that of the "frozen field". This assumption requires that the ratio of B/ρ_i is a constant. One final assumption worth mentioning is that charge neutrality is implicit in the MHD equations.

In the case of Mars the ion gyroradius is comparable to the distance between the bow shock of Mars and surface of the planet. It is comparable to the radius of the planet, as well. In the case of pick up ions from the ionosphere or ions created in the exosphere of the planet by impact ionization or photoionization, the gyroradius will exceed the planet's radius. Further, the gyroperiod of these heavier

ions will approach or exceed the time for the solar wind to sweep by the planet completely. In short, when simulating these aspects of Mars the MHD equations are invalid. Yet, because of energy and momentum conservation the shock and large scale flows produced by the MHD equations is not very far off from the data. Further, as one goes down in altitude toward the planet surface, the collisions increase, the magnetic fields become stronger in the pileup region and the validity of the MHD equations become much stronger. Indeed, the MHD model is more appropriate because the pressure terms become scalar due to the collisions.

Kinetic Simulations

The kinetic simulations most often used in space research are the hybrid particle simulations. Here the ions are treated as individual particles and their equation of motion is integrated in time on an individual basis. The fields are solved on a grid using the sources the particles carry (charge density, and current). The equations for the electrons are treated as a neutralizing fluid. The hybrid code can have many different ion species in a simulation, but the basic assumption that makes the code operable is that the electrons provide charge neutrality but are massless. This leads to Eq. (11), the electron momentum equation where the electrons are assumed massless and neutralizing. This equation is equivalent to the Ohms law Eq. (3), but contains more terms. These are the Hall current, $\mathbf{J_e} \times \mathbf{B}/c$, and the ∇p_e term. The Hall term breaks the symmetry of the equations and leads to among other things filamentation of plasma, and the low frequency portion of the Whistler mode. The pressure term provides for electrostatic fields along with the resistive term.

Finally, because we have a rich suite of electromagnetic modes possible in the model equations, as well as ion gyromotion, the physics of collisonless shock formation is directly simulated in this model. This includes the parallel waves and the subsequent acceleration of ions in the shock structures. One sees the classic overshoots detected in various planetary shocks. One should note that the ion pressure is not needed in any of the equations. This is a fluid dynamic concept and is not valid within the kinetic approach. However, the particle distributions and moments can be calculated to investigate the shape of the distribution functions and the ion pressure tensor.

Indeed, it is the anisotropic pressure created by the reflected ions at the shock that leads to the electromagnetic modes within the shock. These modes do two things: they lead to a very structured shock surface, and they carry away energy in the form of whistlers and Alfven ion cyclotron, AIC, modes [*Thomas and Brecht*, 1986]. The energy loss created by these waves permits the shock over shoots seen in planetary shocks. Interestingly, there is a fluid behavior similar to the overshoots seen at the planets. When a shock is formed in a highly radiative gas such as Xenon, $\gamma \geq 1$, then the jump conditions can exceed the nominal 4 found in the strong shock limit in a normal fluid. The presence of another degree of freedom, radiation, changes the results significantly.

Finally, the charge neutrality assumption and the neglect of the transverse part of the displacement current (called the Darwin approximation) truncate Maxwell's equations. The charge neutrality removes high-frequency plasma oscillations and the issues of charge separation. The Darwin approximation removes the light waves. These assumptions allow for the use of larger cell sizes and larger time steps.

With these approximations the model equations become:

Ampere's law

$$\nabla \times \mathbf{B} = (4/c)\,\mathbf{J} \tag{8}$$

Faraday's law

$$c\,\nabla \times \mathbf{E} = -\,\partial \mathbf{B}/\partial t \tag{9}$$

the ion particle equations of motion

$$m_i\, d\mathbf{v}_i / dt = q_i\,\mathbf{E} + q_i\,\mathbf{v}_i \times \mathbf{B}/c - q_i\,\eta\,\mathbf{J} \tag{10}$$

$$d\mathbf{x}_i/dt = \mathbf{v}_i \tag{11}$$

the inertialess electron momentum equation

$$0 = -e\,n_e\,\mathbf{E} + \mathbf{J_e} \times \mathbf{B}/c - \nabla p_e + e\,n_e\,\eta\,\mathbf{J} \tag{12}$$

and the requirement of quasi-neutrality

$$n_e = n_i \tag{13}$$

for scale lengths greater than the Debye length. The fields have the same definitions as the MHD equations with a several exceptions. The electric field is not calculated with a simple Ohm's law, Eq.(12), the mass is the ion mass, and the current has two components (the total current, J, and the electron current, J_e). The equations are solved with a predictor-corrector method first published by *Harned* [1982]. Full details of the hybrid formalism including the equations solved can be found in *Brecht and Thomas* [1988].

The hybrid particle code approach to global modeling is the most complete of all of the models used today. However, it has limitations and the major one is that it is very computer intensive. The time step must be small enough to resolve the fastest of the electromagnetic modes, the whistler. The cell sizes must be small enough to resolve the ion

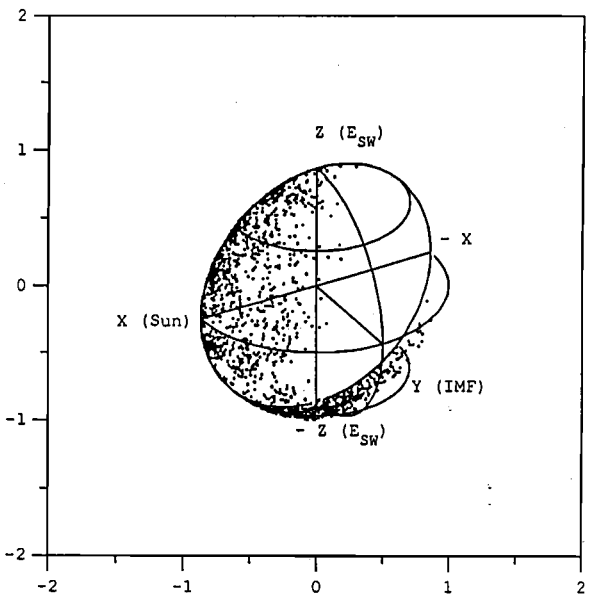

Figure 1. A typical proton deposition pattern during nominal solar wind conditions. The IMF is in the **y** direction and the convection electric field is in the polar direction [*Brecht*, 1997]

gyroradius and the Hall effects. In *Krall and Trivelpiece* [1986] it is shown that the Hall term can be neglected only when which can be written in the form

$$L\,(\omega_{pe}{}^2/\omega_{ce})\,(V_0/c^2) >> 1 \qquad (14)$$

$$L\,(\omega_{ci}/V_A)\,M_A >> 1 \qquad (15)$$

where L is the scale length of the spatial variation in the simulation, ω_{pe}, ω_{ce}, ω_{ci} are the electron plasma frequency, the electron cyclotron frequency, and the ion cyclotron frequency respectively, V_A is the Alfvén speed, and M_A is the Alfvén Mach number, V_0/V_A.

MARS SIMULATIONS

Today Mars is one of the more heavily studied planets in the solar system. It is providing many interesting new features. One of those features is the magnetic anomalies found primarily in the polar regions of the planet. However, because of Mar's lack of global magnetic field and the close proximity of the shock to the exosphere/ionosphere, many interesting questions are being raised about the evolution of the atmosphere of Mars and the rate at which the planet has lost the water that apparently existed in an earlier epoch.

A variety of questions come to mind when considering the Martian situation. How much of the atmospheric heating does the solar wind flow provide? What is the response of the ionosphere and atmosphere to this deposition? What is the impact of the magnetic anomalies on the overall magnetic topology of the planet and the solar wind interaction with the planet? Finally, what is the impact of the magnetic anomalies on the rate of the atmospheric loss of the planet? The space science community is actively studying these questions. Due to space limitations the discussion of Mars simulations and these questions will make use of some of the results obtained from the hybrid simulations with a few references to some of the MHD simulations currently being published.

One of the issues being researched is the role of the solar wind in heating and supplying energy to the ionosphere and atmosphere of Mars. *Luhmann and Kozyra* [1991] addressed this issue of pickup ion deposition into the atmosphere using test particles in a gas dynamic flow simulation. *Brecht* [1997a] addressed the issue of solar wind protons being deposited into the Martian atmosphere and found that in some of the high solar wind cases the energy deposition far exceeded the EUV flux. In normal solar wind conditions the results showed that the proton deposition was roughly 10% of the EUV flux. It was also found during these simulations that the energy deposition was not coincident with EUV. Because of the large ion gyroradii of the solar wind protons deposition occurred on the night side of the planet as well. Further, because of the convection electric field, the deposition was asymmetric in the polar regions. Figure 1 illustrates these features by plotting the deposition location of some of the particles.

Another issue is the structure of the magnetic fields around Mars. In a series of papers culminating in a paper by *Brecht* [1997b] it has been shown that the solar wind interaction with Mars is asymmetric. This is due to the diamagnetic currents set up around the planet as the solar wind interacts with it. The shock asymmetry seen in these simulations was found to be in the polar direction, an orbital orientation that was not investigated until MGS arrived on station. In addition to discovering that crustal magnetic fields existed, MGS data [*Acuña et al.*, 1998] showed that the shock was asymmetric as predicted.

This leads to the next major hurdle for the simulators to address: What is the role of the crustal fields in the solar wind interaction with Mars? *Liu et al.* [2001] started a rudimentary examination of this issue with their multi-fluid MHD code. The hybrid code was used to examine the change in the magnetic fields in the presence of such a lump. In this simulation the planet was treated as a conducting sphere, which turns out to be a good approximation. A conducting lump was added to the conducting sphere. Figure 2 illustrates this lump. Figures 3 and 4 show the change in the total magnetosphere of Mars with just this lump added. Fig. 3 shows a slice through a nominal 3-D hybrid simulation of Mars. One can see the polar asym-

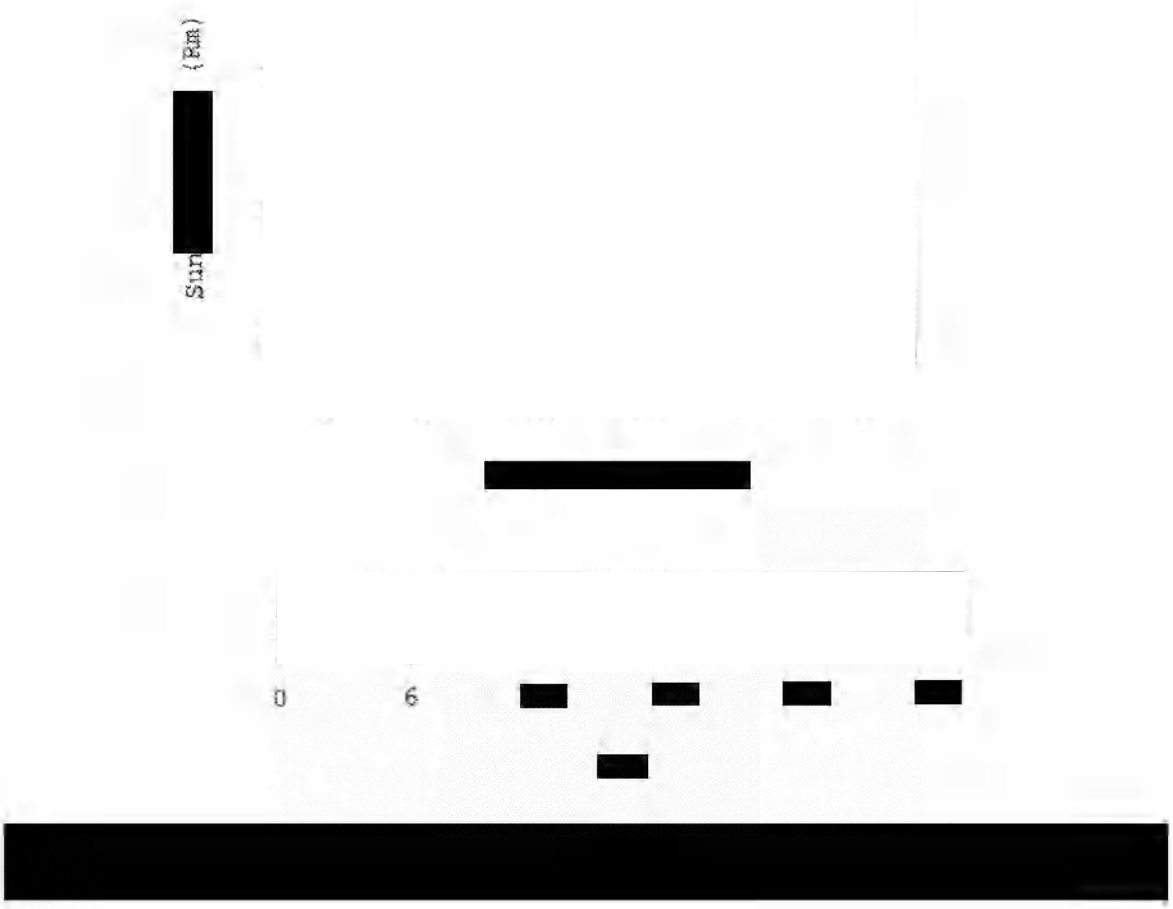
(Rm)
0
6

[redacted]

[redacted]

[redacted]

[redacted]

[redacted]

[redacted]

[redacted]

[redacted]

magnetized planets: Comparison of Venus and Mars, *J. Geophys. Res.*, *96*, 11209, 1991.

Brecht, S.H., Solar wind proton deposition into the Martian atmosphere, *J. Geophys. Res. 102*, 11287, 1997a.

Brecht, S.H., Hybrid simulations of the magnetic topology of Mars, *J. Geophys. Res., 102*, 4743, 1997b.

Brecht, S.H., Simulation of the Saturnian magnetospheric interaction with Titan, *J. Geophys. Res.*, *105*, 13119, 2000.

Breus, T.K., A.M. Krymskii, and V. Ya. Mitnitskii, Interaction of mass-loaded solar wind flow with a blunt body, *Planet. Space Sci.*, *35*, 1221, 1987.

Cravens, T.E., H. Shinigawa, and J.G. Luhmann, Magnetohydrodynamics Processes: Magnetic fields in the ionosphere of Venus, *Venus II Geology, Geophysics, Atmosphere, and Solar Wind Environment,* The Univ. of Arizona Press, p.3, 1997.

Donahue, T.M., and C.T. Russell, The Venus atmosphere and their interaction with the solar wind, *Venus II Geology, Geophysics, Atmosphere, and Solar Wind Environment,* The Univ. of Arizona Press, p.61, 1997.

Breus, T.K., A.M. Krymskii, R. Lundin, E.M. Dubinin, J.G. Luhmann, Y.G. Yeroshenko, S.V. Barabash, V.Y. Mitnitskii, N.B. Pissarenko, and V.A. Styashkin, The solar wind interaction with Mars: Consideration of Phobos 2 mission observations of an ion composition on the dayside, *J. Geophys. Res.*, *96*, 11165, 1991.

Kallio, E., J.G. Luhmann, and S. Barabash, Charge exchange near Mars: The solar wind absorption and energetic neutral atom production, *J. Geophys. Res.*, *102*, 22183, 1997.

Krall, N.A., A.W. Trivelpiece, *Principles of Plasma Physics*, San Francisco Press, Inc., San Francisco, CA. 1986.

Ledvina, S.A. and T.E. Cravens, A three-dimensional MHD model of the plasma flow around Titan, *Planet. Space Sci.*, *46*, 1175, 1998.

Liu, Y., A.F. Nagy, T.I. Gombosi, D.L. DeZeeuw, K.G. Powell, Three-dimensional multifluid MHD studies of the solar wind interaction with Mars, *Geophys. Res. Lett.*, *26*, 2689, 2000

Liu, Y., A.F. Nagy, T.I. Gombosi, D.L. DeZeeuw, K.G. Powell, The solar wind interaction with Mars: Results of three-dimensional three-species MHD studies, *Advances in Space Research*, in press, 2001.

Luhmann, J.G. and J. U. Kozyra, Dayside pickup oxygen ion precipitation at Venus and Mars: Spatial distributions, energy deposition, and consequences, *J. Geophys. Res.*, *96*, 5457, 1991.

Luhmann, J.G., S.H. Brecht, J.R. Spreiter, S.S. Stahara, R.S. Steinolfson, and A.F. Nagy, Global models of the solar wind interaction with Venus, *Venus II- Geology, Geophysics, Atmosphere, and Solar Wind Environment,* The University of Arizona Press, Ed. S.W. Bougher, D.M. Hunten, and R.J. Philips, p. 33, 1997.

Purucker, M., D. Ravat, H. Frey, C. Voorhies, T Sabaka, and M. Acuna, An altitude-normalized magnetic map of Mars and its interpolation, *Geophys. Res. Lett.*, *27*, 2449, 2000.

Sauer, K., A. Bogdanov, and K Baumgärtel, Evidence of an ion composion boundary (protonopause) in bi-ion fluid simulations of sola wind mass loading, *Geo. Res. Lett., 21*, 2255, 1994.

Schwingenschuh, K., W. Riedler, H. Lichtenegger, Ye. Yeroshenko, K. Sauer, J. Luhmann, M. Ong, and C.T. Russell, Martian bow shock: Phobos observations, *Geophys. Res. Lett., 17*, 889, 1990.

Spreiter, J. R. and S.S. Stahara, A new predictive model for determining solar wind-terrestrial planet interactions, *J. Geophys. Res.*, *85*, 7715, 1980.

Thomas, V.A. and S.H. Brecht, Two dimensional hybrid simulations of high Mach number plasma interactions, *Phys. of Fluids*, *29*, 2444, 1986.

Zhang, M.H.G., J.G. Luhmann, A.F. Nagy, J.R. Spreiter, and S.S. Stahara, Oxygen ionization rates at Mars and Venus: Relative contributions of impact ionization and charge exchange, *J. Geophys. Res.*, *98*, 3311, 1993.

Stephen H. Brecht, Bay Area Research Corp., P.O. Box 366, Orinda, CA 94563

Plasma Flow Past Cometary and Planetary Satellite Atmospheres

Michael R. Combi and Tamas I. Gombosi

The University of Michigan, Ann Arbor, Michigan

Konstantin Kabin

The University of Alberta, Edmonton, Alberta, Canada

The tenuous atmospheres and ionospheres of comets and outer planet satellites share many common properties and features. Such similarities include a strong interaction with their outer radiation, fields and particles environs. For comets the interaction is with the magnetized solar wind plasma, whereas for satellites the interaction is with the strongly magnetized and corotating planetary magnetospheric plasma. For this reason there are many common or analogous physical regimes, and many of the same modeling techniques are used to interpret remote sensing and *in situ* measurements in order to study the important underlying physical phenomena responsible for their appearances. We present here a review of various modeling approaches which are used to elucidate the basic properties and processes shaping the energetics and dynamics of these systems which are similar in may respects.

1. INTRODUCTION

Comets and several planetary satellites possess thin tenuous atmospheres which interact with their outer magnetized plasma environs and solar radiation to ultimately drive the atmospheres into escape and producing ions which mass-load the outer plasma. In the case of comets the gravity is vanishingly small (~ 10^{-4} times gravity at the Earth's surface). In the case of the planetary satellites (e.g., Jupiter's largest four moons) gravity is small, but the plasma impact processes are strong enough that only a tenuous atmosphere is maintained (see Chapter III.3) and a large neutral escape rate, comparable to a moderate comet, is maintained. For these reasons similar approaches are used for modeling various observed phenomena in order to study the underlying causes. The innermost neutral atmospheres have been treated with hydrodynamic approaches, and the outermost atmospheres have been treated with the assumption of vacuum free-flow. In between these two regions is a complicated kinetic region where collision mean free paths are large compared with relevant spatial scales, but not large enough to ignore. Interactions with cooling infrared radiation also become non-LTE because of decoupling between rotational and kinetic temperatures.

Magnetohydrodynamic (MHD) approaches have been used to study the large scale interactions of impacting magnetized plasma with the ionospheres of these bodies. For comets, it is the solar wind with its frozen-in magnetic field which impacts the cometary ionosphere. For planetary satellites, it is the corotating (or nearly corotating) plasma flow frozen into the planet's strong dipolar magnetic field which impacts the satellite ionosphere. Mass-loading via photo- and charge impact ionization and charge exchange are important for explaining the overall structure of both kinds of interactions. For comets, this interaction produces the often spectacular ion tail, which is millions of kilometers long. For planetary satellites, the Galileo spacecraft and ground-based and Earth-orbit based observing have revealed an array of auroral type emissions.

Atmospheres in the Solar System: Comparative Aeronomy
Geophysical Monograph 130

10.1029/130GM10

2. SOLAR WIND INTERACTION WITH COMET ATMOSPHERES AND IONOSPHERES

2.1. The Cometary Atmosphere

A well developed cometary atmosphere extends to distances several orders of magnitude larger than the size of the nucleus. Self-consistent models of cometary atmospheres must describe phenomena taking place at several spatial and temporal scales ranging from the initiation of the transonic dusty gas flow near the nucleus (with typical scalelength of 10^{-2}-10^{-1} km) to fast chemical reactions (typical scales are 10^{0}-10^{2} km) to the formation of the cometary ionosphere (typical scales are 10^{3}-10^{4} km), to the solar wind interaction of the cometary atmosphere (typical scales are 10^{5}-10^{7} km)..

Today little direct observational data are available on the near surface gas, dust and plasma environments of cometary nuclei. Our present understanding of this region is based on dust coma images from the Giotto spacecraft *Keller* [1986] and dusty-gasdynamic calculations having varying levels of sophistication [*Crifo et al.*, 1999a]. Verification is primarily based on comparing model predictions hundreds of nucleus radii from the nucleus with *in situ* and remote observations.

The bulk velocity of the outflowing gas is slightly subsonic at the surface (the effusion would be sonic without any gas-dust interaction: the momentum loss to the entrained dust particles results in a slightly subsonic outflow). Frequent gas-dust collisions erode and drag away grains from the surface and accelerate them to significant velocities within a few nucleus radii. Small dust particles (< 10 μm) can be fully accommodated to the gas flow and reach velocities up to several hundreds of m/s, while larger grains attain much slower velocities (the dust terminal velocity is proportional to the inverse of the grain size) [*Gombosi et al.*, 1986]. The adiabatically expanding gas converts most of its internal energy to bulk motion, while it loses some of its momentum and energy to the dust flow. This process is expected to result in a very cold (several tens of K) hypersonic gas flow in the immediate vicinity of the nucleus. The problem is also complicated by the fact that dust particles, especially the more volatile CHON particle can serve as sources for gaseous species. These particles get their name because they are composed of mostly compounds from carbon, hydrogen, oxygen and nitrogen, as opposed to the more refractory silicate dust composed of silicon and metal oxide compounds. CHON particles can thus more easily fragment and vaporize, modifying the gas and dust mass, momentum and energy densities.

Most of the species observed in cometary atmospheres are chemically unstable radicals, which clearly are photodestruction products of more stable parent molecules. Chemical reactions between evaporated parent molecules are very slow and of secondary importance, while dissociation and ionization by solar UV radiation produce highly reactive radicals and ions.

Most neutral coma modeling deals with the two limiting conditions which occur far from and near the nucleus: free-molecular and fluid-flow models. Free-molecular models describe the distributions of molecules in the outer coma where intermolecular collisions are rare. These include radial outflow models [*Haser* 1957; *Haser* 1966; *Wallace and Miller,* 1958; *Keller and Meier,* 1976], and non-radial models accounting for isotropic ejection of daughter species [*Combi and Delsemme,* 1980a; *Festou* 1981]. Fluid models describe the bulk properties of various fluids (gases, dust, and plasma) that are collisionally coupled in the inner coma. Examples of these are gas-phase chemistry models [*Giguere and Huebner,* 1978; *Mitchell et al.*, 1981; *Cochran* 1985; *Allen et al.*, 1987], combined chemical-dynamic models [*Huebner and Keady,* 1983], dusty-gasdynamic models [*Marconi and Mendis,* 1983, *Gombosi et al.* 1986], and multidimensional dusty-gasdynamic models [*Kitamura* 1986; *Kömle and Ip,* 1987; *Körösmezey and Gombosi,* 1990; *Crifo* 1995; *Crifo et al.*, 1999a; *Crifo et al.*, 1999b; *Combi et al.*, 1999].

Monte Carlo methods have bridged the gap between the fluid and free-flow regimes in the important transition region where many observations occur. After the first Monte Carlo coma model [*Combi and Delsemme,* 1980a], collisions were introduced [*Kitamura et al.*, 1985] to model the spatial distribution of the H coma and the partial collisional thermalization of H atoms. Since then this approach has been significantly generalized and extended, making a self-consistent picture of the inner and outer coma [*Combi* 1987; *Bockelée-Morvan and Crovisier,* 1987; *Combi and Smyth,* 1988a and 1988b; *Ip* 1989], added dusty-gas hydrodynamics to the inner coma [*Combi* 1989], a treatment for heavy species [*Combi et al.*, 1993], and Ly-α radiative transfer [*Combi and Feldman,* 1992]. These models have been used to analyze various observations of water dissociation products and trace species in P/Halley including spatial profiles, column abundances (production rates), and Doppler line profiles. These hybrid models have even been extended to treat the large collision region of comet Hale-Bopp (1995 O1). Figure 1 shows outflow velocities and kineitc temperatures at a function of distance from the nucleus for a number of heliocentric distances as calculated using a hybrid 1D-spherical hydrodynamics/Monte Carlo calculation [*Combi et al.*, 1999]. These predicted outflow velocities and kinetic temperatures were shown to provide a reasonable explanation for radio observations of the heliocentric distance dependence of both outflow velocity and kinetic temperature in the inner coma [*Biver et al.*, 1999] and outflow velocity in the outer coma [*Colom et al.*, 1999].

Fully kinetic iterative test particle (ITP) models developed for describing atomic species in planetary exospheres have been applied to comets [*Hodges* 1990]. *Xie and*

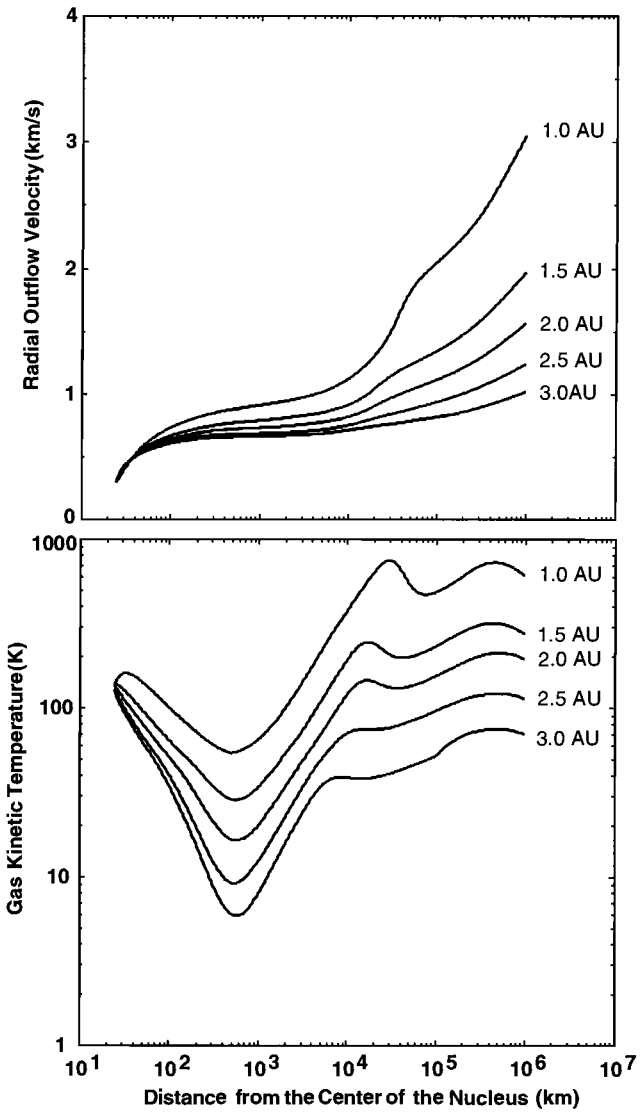

Figure 1. Radial Outflow Velocity and Kinetic Temperature in the Coma of Hale-Bopp. Shown are the results of a one-dimensional spherical hybrid kinetic/dusty-gas hydrodynamic calculations from Figure 1 in the paper by [*Combi et al.*, 1999]. Above is the variation of the radial outflow velocity with distance from the nucleus for different heliocentric distances of Comet Hale-Bopp. Below are similar curves for the gas kinetic temperature.

Mumma [1996a and 1996b] have presented improved 1D spherical and a 2D axisymmetric versions. In an ITP model the trajectories and collisions of molecules of each species are computed through a background gas of the modeled species themselves, as given by their phase space velocity distribution functions. It arrives at steady-state solutions for the species distribution functions by iteratively updating the background distributions with those accumulated from the test particle trajectories.

In recent years these test particle models have been superceded by Direct Simulation Monte Carlo calculations (DSMC) orignally pioneered by Bird for high Knudsen number gas dynamics flow problems [*Bird* 1976 and1994]. DSMC is a direct simulation of the generalized rarefied problem which is most fundamentally described by a solution to the collisional Boltzmann equation. The combination of velocity moments of the Boltzmann equation with closure arguments and the ideal gas law can be manipulated to yield the more familiar (and tractible) equations of hydrodynamics: both the Euler and Navier-Stokes versions. DSMC-type methods have been applied to ionospheric and magnetospheric plasma simulations [*Wilson et al.*, 1992; *Miller and Combi*, 1994, *Miller et al.*, 1995] and earth's corona [*Shematovich et al.*, 1994]. *Pospieszalska and Johnson*, 1992 and 1995] have presented 1D spherical particle simulations for Io's SO_2 atmosphere using a method which is philosophically between the ITP and DSMC methods, mixing elements of both. Most recent DSMC calculations for Io's tenuous atmosphere have been published by *Marconi et al.* [1996] and *Austin and Goldstein* [2000], as we will discuss in a later section. However, of particular relevance here is that DSMC has been applied to study high Knudsen number flows in neutral cometary atmospheres [*Combi* 1996; *Harris et al.*, 1997; *Skorov and Rickman* 1998].

Unlike the ion chemistry in the coma which is sparked by photochemistry (but where the detailed composition is controlled by fast ion-neutral reactions), the neutral chemistry is controlled in large measure by photochemistry. The composition of a "typical" comet is about 80% water, about 5 % each of CH_3OH, and other organics, 3% CO_2, 0.5% NH_3 and <1% HCN, CH_3CN, C_2H_2, and C_2H_6 [cf. *Crovisier* 1999]. In addition, there is significant CO and H_2CO in comets (up to 10-20 % total CO in some comets), but the fraction that comes directly as a gas from the nucleus, e.g., frozen H_2CO, as opposed to being vaporized from an extended source of grains is uncertain. The balance is also uncertain between parent molecule gases and vaporizing grains as sources for the carbon containing radicals, C_2, C_3 and CN. A fraction of the source of CN and C_2 may be associated with grains but clearly some of the CN and C_2 comes from photodissociation of HCN and C_2H_2, respectively, which are both among the parent gases emitted from the nucleus [cf. *Brooke et al.*, 1996; *Combi and Fink*, 1997; *Rauer et al.*, 1997].

2.2. The Cometary Ionosphere

The main photoionization product in the cometary coma is H_2O^+. These water ions transfer a proton to other neutral molecules, which have a higher proton affinity than the OH

[redacted]

[redacted]

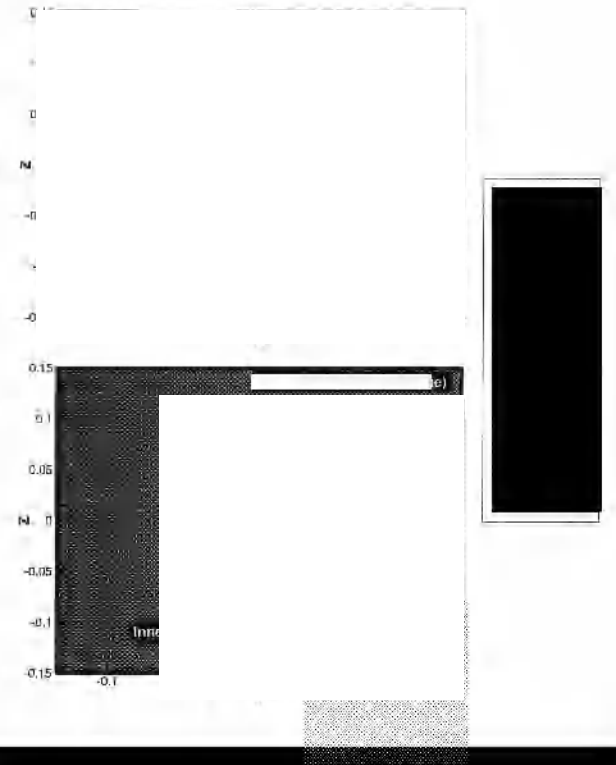

[redacted]

[redacted]

[redacted]

[redacted]

[redacted]

indicate the presence of an ionosphere [*Kliore et al.*, 1997], roughly consistent with expectations from the O detection, and a disturbed local magnetic field [*Kivelson et al.*, 1997; *Neubauer* 1998] which could be accounted for by an intrinsic field or an induced field.

Figures 3 and 4 show the main results of the simulations of Galileo's E4 Europa flyby by *Kabin et al.* [1999b]. It was found that the best agreement with observations of *Kivelson et al.* [1997] and *Gurnett et al.* [1998] can be obtained by assuming a total mass loading rate of 7 x 10^{25} O_2^+ ions per second [*Kliore et al,.* 1997]. The best agreement with observations was obtained when mass-loading was constrained to the ram side, assuming that the dominant ionization mechanism is electron impact [*Kliore et al.*, 1997]. Mass loading alone was able to account for the observed signature in B_z, while reproducing the B_x and B_y signatures required the inclusion of an intrinsic magnetic dipole of 65 nT along the y axis. This intrinsic magnetic field is consistent with the presence of a subsurface ocean [*Khurana et al.*, 1998; *Neubauer* 1999; *Zimmer et al.*, 2000] which would produce an induced intrinsic field in the (x, y) plane with B_y being the major component [*Khurana et al.*, 1998]. However, the induced magnetic field deduced by [*Khurana et al.*, 1998] is somewhat larger than this "best fit". This work required adopting a 20° rotation of the upstream torus flow toward the direction of Jupiter. A recent paper by *Paranicas et al.* [2000] suggests that this might not be a property of the actualy bulk flow of the torus ions but simply a local effect such as that which results from the electric field rotation in electrodynamic simulations [*Saur et al.*, 1998].

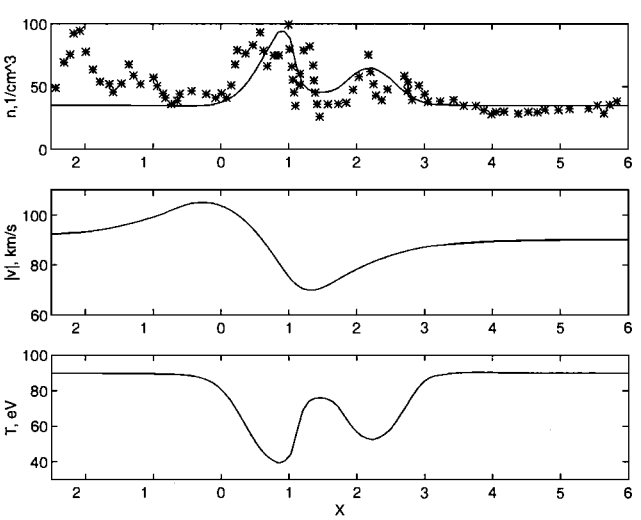

Figure 3. Comparison of measured and simulated densities, as well as simulated speed and temperature profiles along the Galileo E4 flyby trajectory.

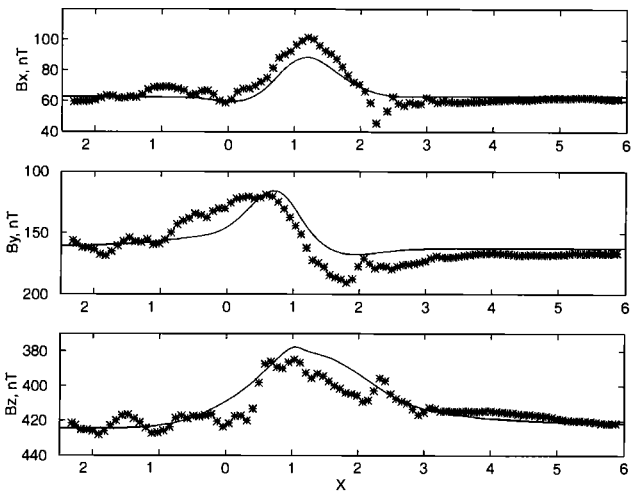

Figure 4. Comparison of measured and simulated magnetic field vectors (solid lines) along the Galileo E4 flyby trajectory.

A later two-species MHD calculation for the plasma interaction near Europa has most recently been done by *Liu et al.* [2000]. In this calculation the impacting plasma torus ions (dominated by O^{++}, S^{++}, and S^{+++}) represent one species and the local pickup ions (dominated by O_2^+) are the other. The model parameters and form were otherwise similar to those of [*Kabin et al.*, 1999b]. One difference is that with the choice of two species there was freedom to be able to better estimate electron density because of the different mean charge states of the ambient torus ions (= 2) and the local pickup ions (= 1). Furthermore, the results of the Galileo Plasma Science instrument [*Paterson et al.*, 1999] appeared in the literature in the intervening time. Figures 5 - 7 show the results of the comparison of various Galileo particles and fields instrument measurements during the E4 flyby with the two-species MHD calculations of *Liu et al.* [2000].

The agreement with the measured electron density data from the plasma wave instrument is quite good. Two density peaks in the wake region correspond to the closest approach and the center of the true corotation wake. These peaks consist mainly of O_2^+. The ambient plasma torus ions actually show a small minimum density inside the wake, consistent with calculations of flow past an obstacle when there is no mass-loading. See, for example, the first reference Io model by *Combi et al.* [1998a], who considered a perfectly conducting sphere and no mass-loading. An essentially empty wake resulted. The ion speed in Figure 6 shows approximately the correct qualitative behavior; however, the model produces more of a velocity decrease in the wake. Similarly the temperature shows the right qualitative structure; however, the model considers

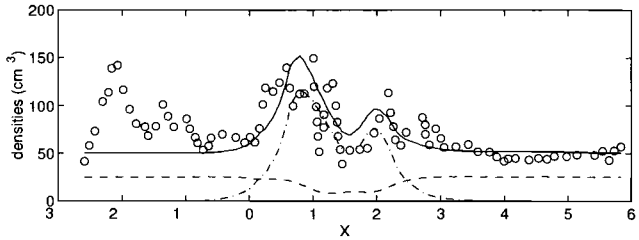

Figure 5. The calculated number densities and the observed electron density along the Galileo E4 flyby. The dashed line at the bottom gives the model density of the upstream plasma torus ions, and the dash-dot line gives the modeled density of the pickup ions. The electron density is constructed assuming the average charge state of the ambient torus ions is 2, while that for the pickup O_2^+ ions is one. The model electron density (solid line) with that inferred from the plasma wave measurements of *Gurnett et al.* [1998] (open circles).

total plasma temperature which effectively has contributions from both ion populations and electrons, whereas the observations are only of the ions. In this regime of the plasma torus the total electron temperature is uncertain, but it is believed that there is an important contribution from a population of high energy electrons which is non-negligible toward the total plasma pressure. For this reason the plot also compares twice the measured ion temperature with the MHD plasma temperature. Again the structure with three maxima is qualitatively reproduced.

Lastly, the comparison with the Galileo magnetometer measurements in Figure 7 is also quite good. The approach of *Kabin et al.* [1999b] and *Liu et al.* [2000] has been to leave the magnitude and orientation of the internal Europa magnetic field as a free parameter and use the comparison with the data to converge to the best "fit," rather than assuming from the beginning that an internal induced field from a sub-surface ocean was responsible. The magnitude and direction of the magnetic field in both of these studies, is in fact consistent with this picture of the induced internal field picture suggested by *Khurana et al.* [1998] and *Neubauer* [1999], providing an independent confirmation.

3.2. Io's Interaction with Jupiter's Magnetosphere

Our understanding of the interaction of Io with Jupiter's corotating plasma goes back to the discovery of Io-related decametric radio emission discovered by [*Bigg* 1964] and the unipole inductor model which was introduced to explain it [*Goldreich and Linden-Bell,* 1969]. The basic premise of the unipole inductor picture has recently been questioned by *Russell and Huddleson,* [2000]. There were a number of theoretical studies of this interaction during the immediate post-Voyager era (sees [*Hill* 1983] for a post-Voyager review). Early theoretical work was often done either in the context of a "thin" atmosphere (e.g., see *Cloutier* [1978]) indicative of the surface temperature (~130 K), or "thick" extended neutral atmosphere (e.g. see *Goertz* [1980]) more indicative of volcanic temperatures (~1000 K). Subsequent evidence (see the review by *Lellouch* [1996]) seems to indicate a mixed picture of the global atmosphere, which has a large extended corona like a thick atmosphere, but appears to be dominated by local major injection of hot (high speed) gas/dust plumes to high altitudes but only near active volcanic vents. Therefore, although the atmosphere is probably only locally thick, it still has a large extended neutral corona which might provide a sufficient source of impact ionization and photoionization to explain the plasma torus.

Neubauer [1980] presented an analytical model of the Alfvén standing wave current system which connects current through the ionosphere of Io. *Southwood* [1980] examined data from several Voyager instruments and examined the possible role of an intrinsic magnetic field for Io as a way to retain a robust enough ionosphere, which could provide enough conductivity for completing the Io-Jupiter current circuit. Several years after Voyager, 3D numerical studies of the plasma flow past Io were performed using electrodynamic [*Wolf-Gladrow et al.,* 1987] and magnetohydrodynamic [*Linker* 1991] approaches.

The results of the measurements by the particle and field instruments on the Galileo Orbiter during the December 1995 flyby of Io provided new and important information with which realistic simulations for the plasma interaction can be tested. The J0 flyby occurred nearly in the equator

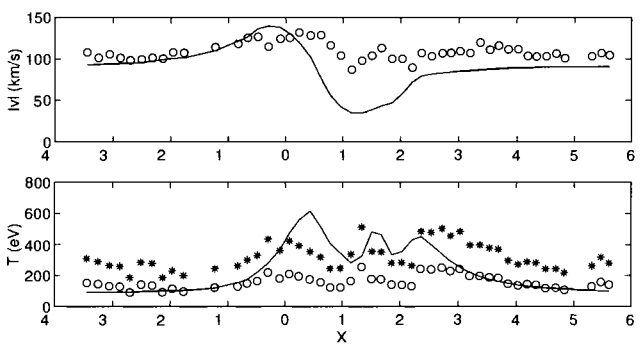

Figure 6. Speed and temperature profiles along the E4 flyby. The solid lines are the plasma speed (upper panel) and plasma temperature (lower panel) from the model results. The circles are the ion speed (upper panel and ion temperature (lower panel) data of *Paterson et al.* [1999]. Because the single-fluid plasma temperature of the MHD calculation is really the sum of the ion and electron temperature, which may be roughly comparable in this region of the torus, we show the values marked by the stars that are twice the measured ion temperature.

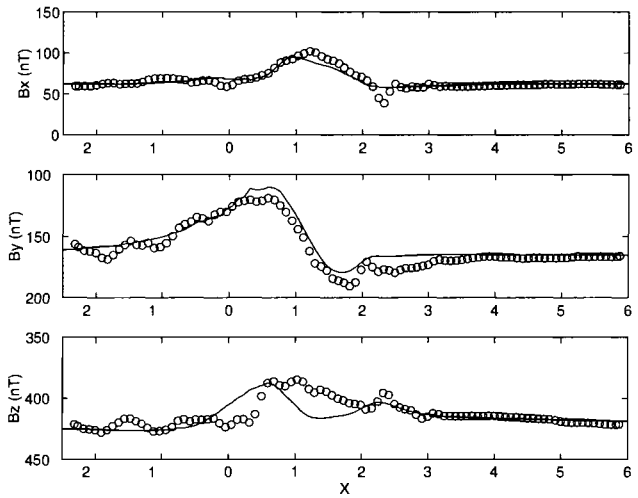

Figure 7. Magnetic field components along the E4 flyby. The solid lines are the results of the model. The circles are the data from the magnetometer measurements [*Kivelson et al.,* 1997].

plane of Io and perpendicular to a flow wake defined by the corotating plasma flow past Io. The spacecraft trajectory passed approximately 900 km down-stream of Io (in the sense of the plasma torus flow). Along that trajectory physical signatures of the wake were seen as a broad depression in the magnetic field [*Kivelson et al.,* 1996], sharp peaks in the ion [*Frank et al.,* 1996] and electron [*Gurnett et al.,* 1996] densities, a slowing of the plasma in the core of the wake, a deep ion temperature decrease in the center of the wake, and a large (factor of 3) ion temperature rise in the flanks of the wake [*Frank et al.*, 1996]. The magnetic field perturbation was broader spatially than the density peak, and showed a double-reversed structure, whereby the perturbation (as defined by the difference from the outer Jovian B-field value) was actually weaker right near the close-approach point than it was somewhat adjacent to the center of the wake.

With the goals to explain the general measured features from Galileo and to probe important properties of the interaction of the plasma torus with Io's neutral atmosphere and ionosphere, there have been recent efforts to improve and extend the pre-Galileo simulations both in terms of the MHD [*Combi et al.,* 1998a; *Linker et al.,* 1998; *Kabin et al.,* 2001] and the electrodynamic [*Saur et al.* 1999] approaches. These two approaches are distinguished by the physical assumptions which they each do and do not (or in some cases, can and cannot) include.

The single-fluid MHD approach solves a system of mass, momentum, energy, and magnetic field conservation equations treating the plasma (ions and electrons) as a single fluid. Thus it can treat the deformation (draping) of magnetic field lines around the obstacle (the near Io region) and produce reasonably realistic flow geometry in three dimensions. The imposed outside (upstream) B-field can have any value and orientation with respect to the flow direction. However, MHD cannot, at least yet, include the effects of realistic conductivities (Hall and Pederson) or charge separation effects which are likely to be important very close to Io where the neutral densities are large and electric potentials can introduce non-symmetric flow around the body. They either include constant artificial conductivity [*Linker et al.,* 1998] or assume perfect conductivity [*Combi et al.,* 1998a], however comparisons of the two sets of published results do not indicate that this choice has any important consequence. Both MHD approaches address the finite conductivity at the inner boundary, either through solutions of Laplace's equation for simple conductivity models inside of Io in the case of *Linker et al.* [1998], or by fixing the B-field inside Io to be the time-averaged imposed Jovian field by *Combi et al.* [1998a]. The latter was shown previously by Linker et al. [1998] to be the major effect of actually solving Laplace's equation inside the inner boundary. The similarity of the results of the so-called fixed-boundary model of *Combi et al.* [1998a] and the so-called conducting model of *Linker et al.* [1998] seems to bear out the validity of the simpler approach, as well as the overall consistency of the two numerical codes despite their differences in numerical algorithms and computational grids.

Both sets of MHD calculations included mass-loading and charge exchange varying spatially as the power law distribution found by *Schneider et al.* [1991] for sodium. *Linker et al.* [1998] presented results for a conducting Io with no intrinsic magnetic field as well as for a magnetized Io, similar to the vacuum superposition field originally suggested by *Kivelson et al.* [1996]. *Kabin et al.* [2001] considered a somewhat more complicated aspherical neutral atmosphere based on a lower atmosphere with an exponential scale height distribution [*Wong and Smyth,* 2000] in addition to an extended power-law distribution from the corona, which resulted in some minor improvements. Both sets of MHD results produce a cold dense plasma wake for nominal levels of mass-loading and charge exchange. The non-magnetized models produce magnetic field perturbations that are similar to the Galileo measurements, but none are quite as deep or as broad, and none have the reversal of the pertubation (the double-peaked structure) in the center of the wake. The magnetized models of *Linker et al.* [1998] produced a broad and deep perturbation, but not the self-reversal at the center of the wake (the double-peak or bite-out). Figures 8 and 9 show a comparison of the magnetized model of *Linker et al.* [1998] and the non-magnetized models of *Combi et al.* [1998a] with the measurements. They do not enable a definitive statement to be made regarding an intrinsic field. A recent review of the later Io flybys still yields similarly

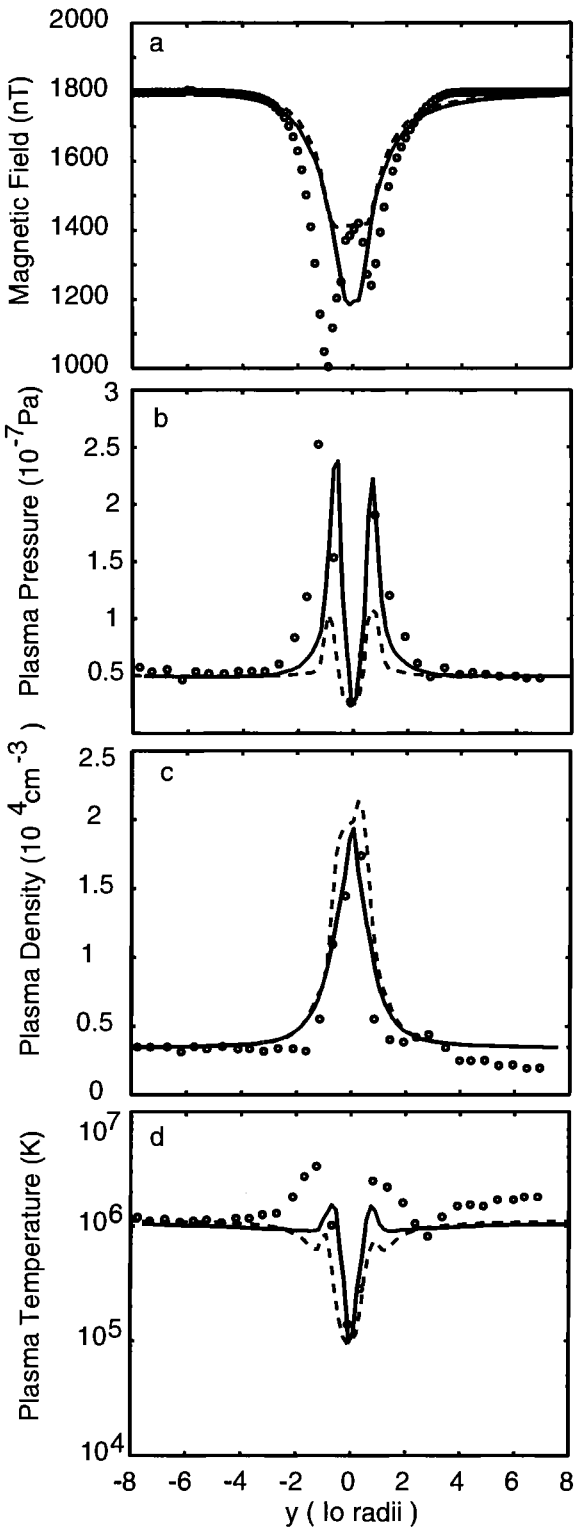

Figure 8. Comparison of the Mass-Loading Models with Galileo Particle and Field Measurements. The magnetic field measurements in (a) from *Kivelson et al.* [1996] and the plasma density (b), pressure (c), and temperature (d) from Frank et al [1996 obtained from the plasma ion instrument are shown with the *Combi et al.* [1998a] model values. The solid lines give the results for the model with mass-loading and reflective boundary conditions. The dashed lines give the results for the model with mass-loading and fixed boundary conditions.

ambiguous results [*Kivelson et al.*, 2000] in this regard, although there is some hope of a conclusive answer from a successful polar flyby during the final Galileo extended mission.

None of the standard MHD models have been able to reproduce the factor of three temperature rise in the flanks of the wake. This temperature rise is roughly coincident spatially with the broadened extent of the magnetic field perturbation. It was shown by *Khurana et al.* [1997b] that if the temperature increase were simply added in an *ad hoc* manner, it would account for all or most of the broadened extent of the magnetic field perturbation. In addition to including a more complicated neutral atmosphere distribution (as already mentioned), *Kabin et al.* [2001] also included deposition of pickup ions with their local corotation plus gyration energy in order to explain the broad magnetic field disturbance and the large temperatures in the flanks. The results generally verify the contention of *Khurana et al.*, 1997b] but do not address the source of the extra energy. It is noteworthy to point out that the simulations of *Linker et al.* [1998] all assume that the ambient (upstream) plasma temperature is 200 eV, whereas the calculations of *Combi et al.* [1998a] adopted a plasma temperature 92 eV from the measured ion results of *Frank et al.* [1996]. A careful comparison of the measured temperatures to the models of *Linker et al.* [1998] shows that they actually have the same small 10% increase of temperature in the flanks of the wake as the models of *Combi et al.* [1998a]. This increase is explained by the injection of nearly stationary pick-up ions into the supersonic plasma flow [*Szegö et al.*, 2000]. The model temperature profile of *Combi et al.* [1998a] matches the Galileo data far from the wake (92 eV) and in the center of the wake, but does not increase to 300 eV in the flanks of the wake. The model temperature profile of *Linker et al.* [1998], on the other hand, is a factor of two too large away from the wake, cuts through the increase in the flanks, and then matches the cool observed temperatures in the center of the wake.

The electrodynamic approach *Saur et al.* [1999] starts from the assumptions that the magnetic field is everywhere uniform with the local Jupiter dipole value at Io, and that the flow is initially perpendicular to this field. The electric potential equation is solved in a series of planar cuts per-

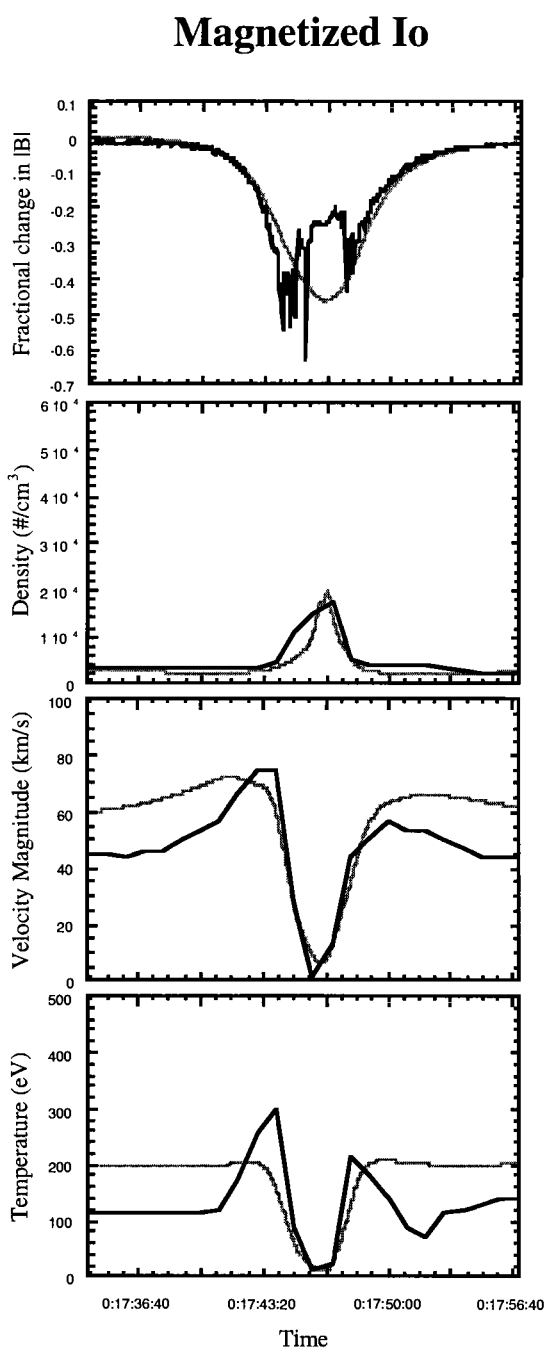

Figure 9. Comparison of simulated data traces from MHD computations of plasma flow past Io (gray curves) with the Galileo data (black curves). Results are from the magnetized model of *Linker et al.* [1998]. Data from the simulations were extracted along the Galileo trajectory for the Io flyby. (a) Fractional change in the magnitude of the magnetic field. Note the "double-valley" structure in the Galileo data. (b) Plasma density, (c) Velocity magnitude, and (d) Temperature.

pendicular to the magnetic field and through Io. The resulting flow is restricted from traveling along the magnetic field direction although it can be deflected around the obstacle within the plane from which it started. Hall and Pederson contributions to the conductivity are calculated using a neutral atmosphere having a scale height distribution similar to their previous work for Europa [*Saur et al.*, 1998]. Their conductivity, however, goes to zero at a small altitude above the surface. They also include separate descriptions for ions and electrons. From the electric field described by the conductivity and charge separation, they calculated the deflected flow and the magnitude of the perturbation to the uniform B-field. Their source terms are self-consistent, rather than fixed as in the MHD models, however, at their present level of their model sophistication the magnetic field perturbation could not be fed-back into the plasma trajectory calculations self-consistently, so that they do not account for where the magnetic field is most strongly disturbed. *Saur et al.* [1999] performed many one-dimensional path-integral calculations along trajectories defined by the electric potential solution to obtain a full three-dimensional picture of ion and electron density, velocity, and temperature.

Therefore, both the MHD and electrodynamic approaches have their strong and weak points. The high conductivity assumptions of the MHD calculations are more appropriate farther away from Io and the detailed conductivity calculations of the electrodynamic approach are better closer to Io's surface. Another important difference is that because the ion motion is restricted to the plane perpendicular to the average Jovian magnetic field, the flow in the electrodynamic approach is essentially incompressible (and inexpandable) and therefore cannot collapse in the wake behind Io as accomplished in MHD. Therefore, whereas the MHD calculations form a dense cold wake similar to the Galileo measurements, the approach of *Saur et al.* [1999] produces an empty wake.

In follow-up work published in his Ph.D. thesis, *Saur* [2000] shows that the combination of their assumed uniform B-field with their calculated perturbation field, can produce a double-peaked structure in their calculated magnetic field. However, this extra bite-out coincides with the location of the empty wake, and it is not clear that the extra bite-out would be present if their calculation produced the observed cold, dense wake as is observed and as the MHD calculations reproduce. Unfortunately, what was stated by *Linker et al.* [1998] remains true: no simulation to date has produced quantitatively and simultaneously all features of the Galileo measurements: the dense, cold plasma wake, the broad extent and the central bite-out in the B-field across the wake, and the large temperature peaks in the flanks of the wake. Clearly simulation science has a long way to go before being able to address self-consistently the physically realistic complex nature of this coupled system. In the mean time, while acknowledging

the strengths and weaknesses of both these and other approaches, much can still be gained by further studies using all of these approaches, which are complementary in many ways.

The electrodynamic approach could be generalized to include a realistic nonuniform magnetic field. This, among other things, would permit the flow to collapse behind the satellite and hopefully produce a realistic dense wake. The MHD approach could be generalized to include multiple species to account separately for newly deposited pickup ions and the background torus ions. Another possible refinement would be to include parallel and perpendicular temperatures (and pressures). It is quite clear that the newly deposited ions, either through mass-loading by new ions or by charge exchange, are introduced with a ring beam distribution. Both MHD and electrodynamic approaches need to better address the range of realistic conductivity around Io. In principle the MHD approaches treat the plasma to be perfectly conducting [*Combi et al.*, 1998a]. The equations of *Linker et al.* [1998] showed an ohmic heating term, however it was not included in most of the simulations. They did include extra viscous terms to capture sharp fronts. The electrodynamic approach, on the other hand, assumes more realistic Hall and Pederson conductivities at low altitudes. This form of the conductivity goes to zero at finite altitude, rather than asymptotically approaching large conductivities dominated by ion-electron collisions at high altitudes [*Song et al.*, 2001].

3.3. Ideal MHD for Gyration Dominated Plasma at Io

As discussed above, recent MHD models [*Combi et al.*, 1998a; *Linker et al.*, 1998] for the interaction of the Jovian plasma torus with the tenuous atmosphere of Io reproduced many aspects of the December 1995 Galileo Io fly-by measurements in the wake, such as the general flow geometry, the velocity perturbation, the density peak and the temperature trough [*Frank et al.*, 1996; *Gurnett et al.*, 1996b]. Only the intrinsic field model of *Linker et al.* [1998] produced a magnetic field signature approaching the breadth measured [*Kivelson et al.*, [1996], and neither reproduced the measured temperature peaks in the flanks on either side of the wake [*Frank et al.*, 1996], which exceeded the nearby ~ 92 eV torus values by a factor of 3. *Combi et al.* [1998a] concluded that a process which adds energy in the flanks of the wake and/or upstream of the wake was required that was not included in the published MHD calculations. This was based in part on the suggestion by *Khurana et al.* [1997b] that if a temperature increase in the flanks were somehow added, a broader magnetic field disturbance would naturally result.

There are some important issues regarding the structure of the neutral atmosphere which have been published since the previously published MHD models [*Combi et al.*, 1998a; *Linker et al.*, 1998], and so a new look is warranted. In addition, we have reconsidered one of the basic model parameters assumed before, the ratio of the specific heats, γ, which was chosen to be 5/3. It is interesting to note that often in cometary and solar-wind pickup ion simulations, investigators have noted that in situations where the pickup ions remain in pickup ring distributions, it can be argued that there are really only two translational degrees of freedom because two are effectively tied together [*Flammer et al.*, 1991; *Ellison et al.*, 1999]. In this case, the appropriate value for γ is 2 instead of 5/3. It is quite clear from the Galileo magnetometer data that the ion-cyclotron wave signatures of pickup ions in the wake of Io are present. This is caused by the fact that neither collisions nor wave-particle instabilities are efficient enough to isotropize the distribution functions of particles during the time-scale of the plasma interaction near Io. In fact, the presence of a wake footprint for Io seen in Jovian aurorae [*Clarke et al.*, 1998] more than half-way around Jupiter is an indication that particles may remain in a ring-beam distribution far downstream from Io. Although we might describe the background plasma with some thermal energy, it is clear that the nature of any magnetized plasma interaction is more gyration-like than isotropic in nature. Therefore, following the lead of other problems we explore here the effect of using a value for γ of 2 instead of 5/3.

For the first set of new model calculations presented in this paper the parameters remain the same as in the previous work of *Combi et al.* [1998a], except for taking γ to be 2, and its effect on the Mach number which now also becomes 2.0 instead of 2.2. The purpose here is not to present a substantially new step, but rather to combine a few features from published work to explore possible improvements in an up-to-date MHD calculation. For this case we use the same $r^{-3.5}$ spatial distribution for mass-loading and charge exchange as for both previous MHD models [*Combi et al.*, 1998a; *Linker et al.*, 1998], where r is the distance from the center of Io. The remaining model parameters are:

upstream plasma density	= 3500 cm^{-3}
upstream plasma temperature	= 92 eV
upstream mean molecular mass	= 22 amu
upstream magnetic field	= 1800 nT
corotation flow speed	= 56.8 km s^{-1}
Alfvén Mach number	= 0.4
Mach number	= 2.0
ratio of specific heats (γ)	= 2

We use the fixed boundary conditions at Io which correspond to setting the plasma density, velocity and magnetic field in ghost cells at the inner boundary. A physically-consistent boundary condition either at Io (or at Jupiter for that matter) relates to the magnetic field perturbation via finite ionospheric conductivity. We must set values of plasma velocity and density and magnetic field at the boundary to achieve the desired result. As mentioned above, the fixing of an internal B-field at the average Jovian field level at Io's location produces the same results as assuming a constant finite conductivity inside the inner (Io) boundary in the explicit calculations of *Linker* [1991].

We again set the lower Io boundary at an altitude of 150 km, the plasma density at 10500 cm^{-3}, and the magnetic field at the time average value from Jupiter's dipole field at Io (1800 nT). In their recent paper *Linker et al.* [1998] performed a similar calculation with a somewhat more complicated layered conductivity model inside Io. However, the similarity between their conducting model and the fixed boundary model (not including the different assumed upstream torus plasma temperatures) indicates that the conditions at the lower boundary between the two MHD groups are in fact reasonably consistent with one another. Finally, as before the simulation volume for the new calculation is 900 x 600 x 600 R_{Io}, and there are 9 levels of refinement and 92,000 cells with sizes ranging from 0.1 R_{Io} near Io to 50 R_{Io} far upstream and downstream.

The change of γ to two seems to provide a natural mechanism to explain at least some of the previous model-measurement differences, namely the temperature peaks on either side of the flanks of wake. The previous fixed-boundary model produced not only a density peak and temperature drop in the center of the wake and the general velocity field, but also a deeper magnetic field disturbance and a large increase in the temperature in the flanks of the wake, as shown by the thin solid lines in Figure 10. Also shown are the previous results [*Combi et al.*, 1998a] indicated by the dashed lines. The mass-loading and charge-exchange rates are the same as the previous result. We make no attempt to improved the fit of the density peak by lowering the mass-loading but simply show what the effect is of changing γ.

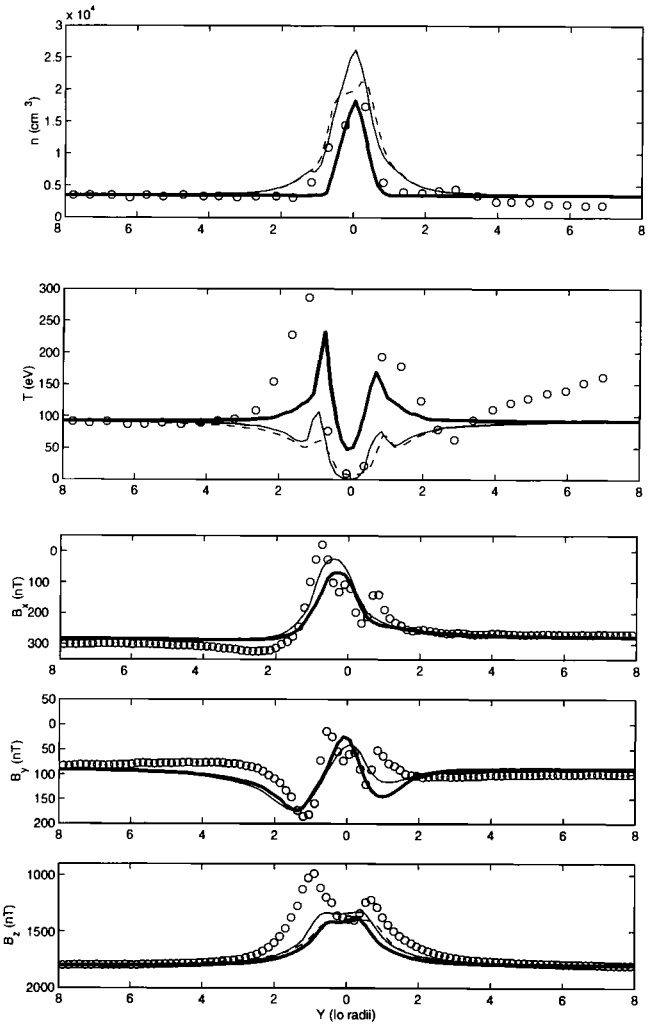

Figure 10. Comparison of Io MHD models results with Galileo measurements. Shown is a comparison of Galileo PLS [Frank et al., 1996] data and MAG [*Kivelson et al.*, 1996] (the open circles) with originally published (dashed lines) results [*Combi et al.*, 1998a], the same spatial model with $\gamma = 2$ (thin solid lines), and a two-component atmosphere model with $\gamma = 2$ (thick solid lines). The two top panels give the plasma density and temperature, and the bottom three give the magnetic field components.

3.4. Mass-Loading by a More Realistic Neutral Atmosphere

We also address here the spatial distribution of the mass loading and friction terms by incorporating a more realistic neutral atmosphere distribution. Essentially this combines the most realistic features of the extended neutral corona adopted in the MHD simulations [*Combi et al.*, 1998a, *Linker et al.*, 1998] with the scale height distribution of in lower atmosphere used in the electrodynamic simulation of [*Saur et al.*, 1999] and some recent atmosphere models.

The $r^{-3.5}$ spatial distribution for the ion mass-loading and charge exchange (friction) terms, which was adopted for the MHD simulations from the sodium eclipse measurements [*Schneider et al.*, 1991], underestimates the expected rise in neutral density near Io. Models for the neutral atmosphere consist of a dense surface atmosphere near the surface temperature (115-130K), and the corresponding scale height of only ~ 12 km [*Summers et al.*, 1996; *Wong and Johnson*, 1996, *Wong: and Smyth*, 2000]. In this region (which MHD models do not resolve anyway) there is not substan-

tial ionization. At increasing altitudes, of importance for understanding the plasma interaction, the scale height increases to eventually to values on the order of 100-200 km. At still larger distances a partially escaping corona forms with a power-law distribution like the sodium distribution as modeled by *Smyth and Combi* [1997]. To model the overall plasma interaction, a spatial profile was adopted which is consistent with these neutral atmosphere measurements and models. In particular, a scale height form for the near-surface atmosphere was chosen to be relevant for the altitudes that can be resolved by the computation grid and that merge into a power-law for higher altitudes.

In the region from 1.4 to 7 R_{Io} a power-law distribution, varying as $r^{-3.5}$ was found for the observations of the neutral sodium corona by *Schneider et al.* [1991]. However, because the bulk of the neutral corona does not consist of sodium, but rather the major SO_2 byproducts, S and O, the earlier $r^{-3.5}$ distribution may not be appropriate for the bulk constituents. The models of *Smyth and Combi* [1997], which reproduce the sodium corona measurements of *Schneider et al.* [1991], correspond to the non-thermal kinetic escape mechanism of *Sieveka and Johnson* [1984] with an most probable upward flux velocity of 0.5 km s^{-1}. Sodium has an ionization potential of only 5.1 eV, and in typical plasma torus conditions has a lifetime against electron impact ionization that is a factor of 2 to 8 shorter than for S and O, which have ionization potentials of 10.36 and 13.62 eV, respectively. Accounting for the difference in the relative loss of upwardly moving Na atoms compared with the average of S and O implies that the bulk corona density (as opposed to just the trace amounts of neutral sodium) should decrease with increasing distance as $r^{-2.5}$ rather than the steeper $r^{-3.5}$ for Na. Such a distribution is also consistent with some very recent Hubble Space Telescope measurements by *Wolven et al.* [2001, in press] of the UV emission by atomic S and O.

Therefore, we have adopted a new form for the radial dependence of the mass-loading and charge-exchange rates to be A exp(-z/H) + B $r^{-2.5}$, where A and B are constants adjusted during model-data comparison, z is the altitude, r is the distance from the center of Io, and H is an effective scale height set to 114 km for the region in question. As before, the corona is cut-off at 7 Io radii from the center of Io. We adjust only one extra free parameter compared with previous MHD models, the relative contributions from the lower atmosphere and the extended corona, with the transition being around 2600 km from the center of Io, and loosely corresponding to the atmospheric exobase. Ther inner Io boundary has been moved from 150 km above Io down to the surface, and three more levels of refinement were added making the size of the computational cells about 22 km near the surface and raising the total number of cells to about 150,000.

In Figure 10 the Galileo PLS and MAG measurements are compared with the fixed-boundary model of *Combi et al.* [1998a], that model but with $\gamma = 2$, and the two-component atmosphere model with $\gamma = 2$. The two-component model reproduces the combination of magnetic field, plasma density and temperature better than either published MHD modeling attempts. The somewhat elevated temperatures in the flanks of the wake result from a combination of the use of $\gamma = 2$ and the adjustment of the lower and upper atmosphere components. As before the velocity flow field does not change appreciably between the models, which appears essentially the same as shown by *Combi et al.* [1998a].

The total fresh ion mass-loading rate and the charge exchange rate, which contributes to the momentum and energy friction terms, is 1.2×10^{28} s^{-1}. The relative contributions from the inner atmosphere and outer corona are in the ratio of 15 to 1. The new outer corona contribution is smaller than the previous model results. The velocity of ions is again similar to previous results, the variation of which matched the measurements by *Frank et al.* [1996]. The asymptotic velocity increase to corotation down the wake is similar to the values from the radio occultation measurements [*Hinson et al.*, 1998] obtained in July 1997. These imply that the flow in the wake accelerates from near 30 km s^{-1} at around 2 R_{Io} to nearly corotational speeds by only 5 to 7 R_{Io} down the wake. On the other hand, observations of the footprint of the wake of Io by *Clarke et al.* [1998], which is weakly present even half-way around the orbit of Io (hundreds of R_{Io}), have been interpreted as indicating a persistence of subcorotational flow far down the wake.

The reversal of the magnetic field disturbance at the center of the wake [*Kivelson et al.*, 1996] is still not reproduced; the magnetic field disturbance in B_z is still not broad enough; and the temperature peaks in the flanks are not extended spatially enough. However, with the modified neutral atmosphere distribution, the new model results do provide small temperature peaks and at least an inflection point and a flat distribution in B_z at the right locations. There are a number of possible explanations, which new measurements and modeling studies might provide. The first would be an intrinsic magnetic field at Io. The I24 flyby of Io [*Linker et al.*, 1999a] is inconclusive regarding an intrinsic field, and unfortunately the failure of the I25 flyby will not yield the anticipated conclusive measurements. It is possible that the recently announced flyby in the last extended Galileo mission phase may eliminate that as a viable explanation. The spatial characteristics of the mass-loading and charge exchange source rates may just be complicated. None of the MHD calculations include a self-consistent ionization source which is based on electron impact ionization of a given neutral atmosphere. More realistic simulations could also involve latitudinal and/or longitudinal variations, or irregular (volcanic) atmospheric distributions. Finally, the inclusion of other physical processes in simulations, such as those as-

sociated with the expected pressure anisotropy, multi-species effects, electron beams, currents, other non-equilibrium or kinetic effects, or other energy sources [*Kabin et al.*, 2001; *Khurana et al.*, 1997b] might be required to substantially improve the agreement between models and data.

3.5. The Interaction of Titan with its Plasma Environs

Titan possesses a dense local atmosphere [*Kuiper*, 1944; *Lindal et al.*, 1983] which in the presence of an exterior magnetized plasma flow necessarily results in a strong and complicated interaction. Significant efforts have been invested into modeling Titan's upper atmosphere and ionosphere. These are discussed in chapters I.1., I.2 and I.3 of this monograph. Titan is also an interesting because it spends a large fraction of its orbit inside the Saturnian magnetosphere and a smaller part outside it, in the solar wind. This occurs when the solar wind flux is large and the Saturnian bow shock is pushed closer to the planet. Therefore, the plasma environment around Titan can vary considerably. During the Voyager 1 encounter, Titan was clearly inside Saturn's magnetosphere.

Voyager 1 was the only spacecraft to visit the vicinity of Titan, having a closest approach on 12 November 1980 of 2.7 Titan radii from the center of Titan. These are the only magnetic field and plasma data available to the scientific community until Cassini has its first flyby of Titan in 2004. These measurements show a strong interaction between Titan and Saturn's magnetospheric plasma [*Ness et al,*. 1982; *Hartle et al,*. 1982]. The measurements and later analysis [*Neubauer et al.*, 1984] suggest that Titan's magnetotail was produced by the draping of corotating magnetospheric field lines about Titan's ionosphere. The Saturnward aberration of the wake was ascribed to a deviation of the corotational flow by about 20° from tangential. An asymmetry in the magnetic field strength was explained by the fact that the solar direction was at a large angle from the incident plasma flow, producing an inbound/outbound difference coincident with the dayside/nightside hemispheres. *Neubauer et al.* [1984] suggested that the difference is related to two different magnetic field-line draping regimes associated with light and heavy ions.

A number of comparisons were made between Titan and the classical induced (comet-like) magnetosphere of Venus [*Kivelson and Russell*, 1983; *Veregin et al.*, 1984; *Luhmann et al.*, 1991]. While the wake structure of Titan is similar to that of Venus, it must be remembered that the flow upstream of Titan is sub-Alfvénic in Saturn's magnetosphere whereas it is always super-Alfvénic at Venus. In the last few years, encouraged by computational and numerical advances and by the interest renewed by the upcoming Cassini missions a number of numerical simulation studies have been undertaken.

Modeling Titan's interaction with the Saturn magnetosphere, or the solar wind, is complicated by the fact that the validity of a fluid approach is questionable. Fluid descriptions (like ideal MHD) are only rigorously applicable in situations where the conductivity is high, the plasma parameter (number of charged particles in a Debye sphere) is large, the ion gyroradius is small compared to the typical length scale of the problem and characteristic speeds (sonic speed and Alfvén speed) are much less than the speed of light. For Titan the only of these criteria that possibly becomes questionable is the gyroradius, which for a thermal N^+ ion is 2.25 R_{Titan}. For the much lighter H^+, the gyroradius is only 0.16 R_{Titan}. Far from Titan, this is not an issue, as long as computational cells are larger than gyroradius. However, close to Titan, both the plasma speed and temperature decrease (at ~ 1.2 R_{Titan} they are about a factor of four smaller than upstream values) while the magnetic field intensity is about a factor of two larger near the front stagnation point. This yields about an order of magntitude decrease in the gyroradius near the planet, keeping the conditions closer to the realm of ideal MHD. *Luhmann* [1996] further suggested that wave-particle interactions and plasma instabilities would also tend to decrease gyroradius.

Cravens et al. [1998] produced very useful three-species 2-D calculations of the plasma flow past Titan. The calculation successfully reproduced several main features of Titan's magnetospheric interaction, however, as in any 2-D model, it missed a number of important essentially 3-D effects. *Ledvina and Cravens* [1998] presented the first 3-D single-fluid calculations, where Titan was approximated as a region of high plasma density surrounded by an ion-producing shell. They used a nonuniform structured Cartesian grid with the small cell size of 0.1 R_{Titan} at the surface of Titan and with upstream conditions imposed at 10 R_{Titan} from the satellite. Their simulations produced a narrow wake and Alfvén wings, which are features detected by Voyager or expected from theoretical consideration. This and subsequents simulations found ion mass-loading rates on the order of 10^{25} s^{-1}. Intercomparison of variations between models, in this regard, is complicated by differences in the models' inner boundary conditions, computational cell resolution, and number and classes of species.

Kabin et al. [1999] presented results for a 3-D single-fluid calculation making use of their adaptive grid numerical scheme which simultaneously included finer resolution near Titan as well as a much larger simulation domain. Their simulations included a well resolved central body and the better numerical method and computational grid was able to reveal more detailed structures in the magnetospheric interaction. *Kabin et al.* [2000] introduced a model with an internal magnetic field, which they suggested represented the induced field created by the ionosphere and which was able to better represent asymmetric aspects of the Voyager data. They also considered the effects of asymmetric mass-loading. Subequently, *Kopp et al.* [2001] argued that nonsymmetric mass-loading similar to that of *Kabin et al.* [2000] can be used to model the effects

of the large ion gyroradius in a fluid description. The model of *Kopp et al.* [2001] provides an interesting connection between fluid and kinetic approaches. Another example of a combination of fluid and particle description is a work by *Ledvina et al.* [2000]. They have calculated the trajectories of the pickup ions in the prescribed magnetic field obtained from their earlier MHD simulation.

There have been two most recent simulations one in MHD and the other a hybrid simulation. The first is a multi-species MHD simulation by *Nagy et al.* [2001], which separately accounts for three generic species, light (e.g., H^+, H_2^+, H_3^+), medium (e.g., N^+ and CH_3^+) and heavy (N_2^+, and $HCNH^+$). This permits the effects of exospheric mass loading, chemiscal reactions and ion-neutral collisions to be treated. It reproduced the global features (magnetic barrier, magnetotail and distributions of the major ionospheric species) and implied an escape flux of major ionospheric (heavy) species to be 6.5×10^{24} s^{-1}. The other is a full hybrid simulation, like those discussed by *Brecht* [chapter II.3], which has been performed by *Brecht et al.* [2000]. The hybrid simulation accounts for particle ions and fluid electrons in addition to computing the magnetic field. It includes a similar grouping of species classes. Although this approach is better justified for Titan, it is also unfortunately more computationally expensive, so as with the case of Io above, there are always trade-offs in comparing one simulation method to another.

The hybrid simulations of *Brecht et al.* [2000] quite naturally produced an asymmetic plasma flow around Titan, something that is not possible with the ideal MHD simulations. This is produced by the inclusion of Hall terms enabled by the explicit inclusion of finite gyroradius microphysics. However, the general scale of the larger disturbance created by Titan's ionosphere and mass-loading is actually quite similar to the MHD simulations.

4. FINAL COMMENTS

The title of the paper by *Cloutier et al.* [1978], which we have cited elsewhere in this review, is "A cometary ionosphere model for Io." This clearly portends the subsequent scientific and methodological connections between planetary satellites and comets in the space science literature. In fact the reference sections of papers in both fields show clearly that each field benefits from the contributions of observers, experimentalists, and theoreticians from the other. Here we have presented a review of the many common properties, features and modeling approaches of the tenuous atmospheres, ionospheres, and outer radiation, fields and particles environs of comets and outer planet satellites. Although much progress has been made in understanding global structures and local measurements, there is much work to do in terms of fundamental theoretical modeling of the combination of global morphologies with local microphysics. As computation power continues to advance during the near future it will be more and more possible to incorporate complicated detailed physical processes in our models. The challenge will be to stay at the forefront, constantly stretching computational capabilities, in order to improve our understanding of these fascinating subjects.

Acknowledgments. This work was supported by NASA grants NAG5-4318, NAG5-8942, and HPCC CAN NCCS5-146, and the NSF-NASA-AFOSR interagency grant NSF ATM-9318181.

REFERENCES

Allen, M., M. Delitsky, W. Huntress, Y. Yung, and W.-H. Ip, Evidence for methane and ammonia in the coma of comet P/Halley, *Astron. Astrophys.*, 187, 502–512, 1987.

Austin, J. V., and D. B. Goldstein, Rarefied gas model of Io's sublimation-driven atmosphere, *Icarus*, 148, 370–383, 2000.

Bigg, E. K., Influence of the satellite Io on Jupiter's decametric emission, *Nature*, 203, 1008–1010, 1964.

Bird, G. A., *Molecular Gas Dynamics*, Clarendon Press, Oxford, 1976.

Bird, G. A., *Molecular Gas Dynamics and the Direct Simulation of Gas Flows*, Clarendon Press, Oxford, 1994.

Biver, N., et al., Long-term evolution of the outgassing of comet Hale-Bopp from radio observations, *Earth, Moon and Planets*, 78, 5–11, 1997.

Bockelée-Morvan, D., and J. Crovisier, The role of water in the thermal balance of the coma, in *Diversity and Similarity of Comets*, pp. 235–240, 1987.

Brecht, S. H, J. G. Luhmann, and D. J. Larson, Simulation of the Saturnian magnetospheric interaction with Titan, *J. Geophys. Res.*, 105, 13,119-13,130, 2000.

Brooke, T. Y., A. T. Tokunaga, H. A. Weaver, J. Crovisier, D. Bockelée-Morvan, and D. Crisp, Detection of acetylene in the infrared spectrum of comet Hyakutake, *Nature*, 383, 606–608, 1996.

Brown, M. E., and R. E. Hill, Discovery of an extended sodium atmosphere around Europa, *Nature*, 380, 229–231, 1996.

Clarke, J. T., et al., Hubble Space Telescope imaging of Jupiter's UV aurora during the Galileo orbiter mission, *J. Geophys. Res.*, 103(E9), 20,217–20,236, 1998.

Cloutier, P. A., R. E. Daniell, A. J. Dessler, and T. W. Hill, A cometary ionosphere model for Io, *Astrophys. Space Sci.*, 55, 93–112, 1978.

Coates, A. J., A. D. Johnstone, B. Wilken, and F. Neubauer, Velocity space diffusion and nongyrotropy of pickup water group ions at comet Grigg-Skjellerup, *J. Geophys. Res.*, 98, 20,995-21,002, 1993.

Cochran, A. L., Nonequilibrium chemical analysis of the coma of comet Stephan-Oterma, *Icarus*, 62, 82–96, 1985.

Colom, P., E. G′ erard, J. Crovisier, D. Bockel′ e-Morvan, N. Biver, and H. Rauer, Observations of the OH radical in comet c/1995 o1 (Hale-Bopp) with the Nancay Radio Telescope, *Earth, Moon and Planets*, 78, 37–43, 1997.

Combi, M. R., Sources of cometary radicals and their jets - gases or grains, *Icarus*, 71, 178–191, 1987.

Combi, M. R., The outflow speed of the coma of Halley's comet, *Icarus,* 81, 41–50, 1989.

Combi, M. R., Time-dependent gas kinetics in tenuous planetary atmospheres: The cometary coma, *Icarus,* 123, 207–226, 1996.

Combi, M. R., and A. H. Delsemme, Neutral cometary atmospheres. I - An average random walk model for photodissociation in comets, *Astrophys. J.,* 237, 633–640, 1980.

Combi, M. R., and P. D. Feldman, IUE observations of H Lyman-alpha in Comet P/Giacobini-Zinner, *Icarus,* 97, 260–268, 1992.

Combi, M. R., and U. Fink, A critical study of molecular photodissociation and CHON grain sources for cometary C , *Astrophys. J.,* 484, 879, 1997.

Combi, M. R., and W. H. Smyth, Monte Carlo particle-trajectory models for neutral cometary gases.I -Models and equations, *Astrophys. J.,* 327, 1026–1043, 1988a.

Combi, M. R., and W. H. Smyth, Monte Carlo particle trajectory models for neutral cometary gases. II. The spatial morphology of the Lyman-alpha coma, *Astrophys. J.,* 327, 1044–1059, 1988b.

Combi, M. R., B. J. Bos, and W. H. Smyth, The OH distribution in cometary atmospheres – A collisional Monte Carlo model for heavy species, *Astrophys. J.,* 408, 668–677, 1993.

Combi, M. R., K. Kabin, T. Gombosi, D. De Zeeuw, and K. Powell, Io's plasma environment during the Galileo flyby: Global three-dimensional MHD modeling with adaptive mesh refinement, *J. Geophys. Res.,* 103(A5), 9071–9081, 1998.

Combi, M. R., K. Kabin, T. Gombosi, D. De Zeeuw, and K. Powell, Dust-gas interrelations in comets: observations and theory, *Earth, Moon and Planets,* 79, 275–306, 1999.

Cravens, T. E., C. J. Lindgren, and S. A. Ledvina, A two-dimensional multifluid MHD model of Titan's plasma environment, *Planet. Space Sci.,* 46, 1193-1205, 1998.

Crifo, J. F., and A. V. Rodionov, Modelling the circumnuclear coma of comets: objectives, methods and current results, *Planet. Space Sci.,* 47, 797–826, 1999.

Crifo, J. F., A. L. Itkin, and A. V. Rodionov, The near-nucleus coma formed by interacting dusty gas jets effusing from a cometary nucleus: I, *Icarus,* 116, 77-112, 1995.

Crifo, J. F., A. V. Rodionov, and D. Bockelée-Morvan, The dependence of the circumnuclear coma structure on the properties of the nucleus, *Icarus,* 138, 85–106, 1999.

Crovisier, J., Infrared Observations Of Volatile Molecules In Comet Hale-Bopp, *Earth Moon and Planets,* 79, 125–143, 1999.

Ellison, D. C., F. C. Jones, and M. G. Baring, Direct acceleration of pickup ions at the solar wind termination shock: The production of anomalous cosmic rays, *Astrophys. J.,* 512, 403–416, 1999.

Festou, M. C., The density distribution of neutral compounds in cometary atmospheres. I –Models and equations, *Astron. Astrophys.,* 95, 69–79, 1981.

Flammer, K. R., D. A. Mendis, E. C. Whipple, and T. G. Northrop, A self-consistent model for the particles and fields upstream of an outgassing comet. I - Gyrotropic and isotropic ion distributions, *J. Geophys. Res., 96,* 15907–15916, 1991.

Frank, L. A., W. R. Paterson, K. L. Ackerson, V. M. Vasyliunas, F. V. Coroniti, and S. J. Bolton, Plasma observations at Io with the Galileo spececraft, *Science,* 274, 394-395, 1996.

Giguere, P. T., and W. F. Huebner, A model of comet comae. I - Gas-phase chemistry in one dimension, *Astrophys. J.,* 223, 638–654, 1978.

Goertz, C. K., Io's interaction with the plasma torus, *J. Geophys. Res.,* 85, 2949–2956, 1980.

Goldreich, P., and D. Lynden-Bell, Io, a Jovian unipolar inductor, *Astrophys. J.,* 156, 59–78, 1969.

Gombosi, T. I., A. F. Nagy, and T. E. Cravens, Dust and neutral gas modeling of the inner atmospheres of comets, *Rev. Geophys.,* 24(3), 667–700, 1986.

Gurnett, D. A., and W. S. Kurth, Radio emissions from the outer heliosphere, *Space Sci. Rev.,* 78, 53–66, 1996.

Gurnett, D. A., W. S. Kurth, A. Roux, S. J. Bolton, and C. F. Kennel, Galileo plasma wave observations near the Io plasma torus near Io, *Science,* 274, 391-392, 1996.

Gurnett, D. A., W. S. Kurth, A. Roux, S. J. Bolton, E. A. Thomsen, and J. B. Groene, Galileo plasma wave observations near Europa, *Geophys. Res. Lett.,* 25, 237–240, 1998.

Häberli, R., M. R. Combi, T. I. Gombosi, D. L. De Zeeuw, and K. G. Powell, Quantitative analysis of H_2O^+ coma images using a multiscale MHD model with detailed ion chemistry, *Icarus,* 130, 373–386, 1997.

Hall, D. T., D. F. Strobel, P. D. Feldman, M. A. McGrath, and H. A. Weaver, Detection of an oxygen atmosphere on Jupiter's moon Europa, *Nature,* 373, 677–680, 1995.

Harris, W. M., M. R. Combi, R. K. Honeycutt, and B. E. A. Mueller, Evidence for interacting gas flows and an extended volatile source distribution in the coma of comet C/1996 B2 (Hyakutake), *Science,* 277, 676–681, 1997.

Hartle, R.E., E.C. Sittler, K.W. Ogilvie, J.D. Scudder, A.J. Lazarus, and S.K. Atreya, Titan's ion exosphere oberved from Voyager 1, *J. Geophys. Res.,* 87, 1383-1394, 1982.

Haser, L., Distribution d'intensite dans la tete d'une comete, *Bull. Acad. Roy. de Belgique, Classe de Sci.,* 43(5), 740–750, 1957.

Haser, L., Calcul de distribution d'intensite relatice dans une tete cometaire, *Mem. Soc. Roy. Sci. Liege,* 12(5), 233–241, 1966.

Hill, T. W., A. J. Dessler, and C. K. Goertz, *Magnetospheric models, in Physics of the Jovian Magnetosphere,* edited by A. J. Dessler, pp. 353–395, Cambridge University Press, New York, 1983.

Hinson, D. P., A. J. Kliore, F. M. Flasar, J. D. Twicken, P. J. Schinder, and R. G. Herra, Galileo radio occultation measurements of Io's ionosphere and plasma wake, *J. Geophys. Res.,* 103(A12), 29343–29357, 1998.

Hodges, R. R., Monte Carlo simulation of nonadiabatic expansion in cometary atmospheres -Halley, *Icarus,* 83, 410–433, 1990.

Huebner, W. F., and J. J. Keady, Energy balance and photochemical processes in the inner coma, in *Cometary Exploration. I,* edited by T. I. Gombosi, pp. 165–183, Central Research Institute for Physics, Budapest, Hungary, 1983.

Ip, W., Photochemical heating of cometary comae. III - The radial variation of the expansion velocity of CN shells in comet Halley, *Astrophys. J.,* 346, 475–480, 1989.

Ip, W., Europa's oxygen exosphere and its magnetospheric

interaction, *Icarus*, 120, 317–325, 1996.
Kabin, K., M. R. Combi, T. I. Gombosi, A. F. Nagy, D. L. DeZeeuw, and K. G. Powell, On Europa's magnetospheric interaction: An MHD simulation of the E4 flyby, *J. Geophys. Res.*, 104(A9), 19,983–19,992, 1999.
Kabin, K., M. R. Combi, T. I. Gombosi, D. L. DeZeeuw, K. C. Hansen, and K. G. Powell, Io's magnetospheric interaction: an MHD model with day-night asymmetry, *Planet. Space Sci.*, 49, 337–344, 2001.
Kabin, K., T. I. Gombosi, D. L. DeZeeuw, K. G. Powell, and P.L. Israelevich, Interaction of the Saturnian magneosphere with Titan: Results of a 3D MHD simulation, *J. Geophys. Res.*, 104, 2451-2458, 1999.
Kabin, K., P. L. Israelevich, A. I. Ershkovich, F. M. Neubauer, T. I. Gombosi, D. L. de Zeeuw, K. G. Powell, Titan's magnetic wake: Atmospheric or magnetospheric interaction, *J. Geophys. Res.*, 105, 10,761-10,770, 2000.
Keller, H., et al., First Halley multicolour imaging results from Giotto, *Nature*, 321, 320–326, 1986.
Keller, H. U., and R. R. Meier, A cometary hydrogen model for arbitrary observational geometry, *Astron. Astrophys.*, 52, 273–281, 1976.
Khurana, K. K., M. G. Kivelson, and C. T. Russell, Interaction of Io with its torus: Does it have an internal magnetic field?, *Geophys. Res. Lett.*, 24, 2391–2394, 1997.
Khurana, K. K., M. G. Kivelson, D. J. Stevenson, G. Schubert, C. T. Russell, R. J. Walker, and C. Polanskey, Induced magnetic fields as evidence for subsurface oceans in Europa and Callisto, *Nature*, 395, 777–780, 1998.
Kitamura, Y., Axisymmetric dusty gas jet in the inner coma of a comet, *Icarus*, 66, 241–257, 1986.
Kitamura, Y., O. Ashihara, and T. Yamamoto, A model for the hydrogen coma of a comet, *Icarus*, 61, 278–295, 1985.
Kivelson, M. G., Ambiguities and expectations: Io's magnetic signature and magnetospheric interactions, in *AAS/Division of Planetary Sciences Meeting*, vol. 32, p. 2805, 2000.
Kivelson, M. G., K. K. Khurana, R. J. Walker, J. Warnecke, C. T. Russell, J. A. Linker, D. J. Southwood, and C. Polanskey, Io's interaction with the plasma torus: Galileo magnetometer report, *Science*, 274, 396-398, 1996.
Kivelson, M. G., K. Khurana, S. Joy, C. Russell, D. Southwood, R. J. Walker, and C. Polanskey, Europa's magnetic signature: Report from Galileo's pass on 19 December 1996, *Science*, 276, 1239–1241, 1997.
Kivelson, M.G. and C.T. Russell, The interaction of flowing plasmas with planetary atmospheres: A Titan-Venus comparison, *J. Geophys. Res.*, 88, 49-57, 1983.
Kliore, A. J., D. Hinson, F. Flasar, A. Nagy, and T. Cravens, The ionosphere of Europa from Galileo radio occultations, *Science*, 277, 355–358, 1997.
Kömle, N. I., and W. H. Ip, Anisotropic non-stationary gas flow dynamics in the coma of comet P/Halley, *Astron. Astrophys.*, 187, 405, 1987.
Kopp, A. and W.-H. Ip, Asymmetric mass loading effect at Titan's ionosphere, *J. Geophys. Res.*, 106, 8323-8332, 2001.
Körösmezey, A., and T. I. Gombosi, A time-dependent dusty gas dynamic model of axisymmetric cometary jets, *Icarus*, 84, 118–153, 1990.
Kuiper, G. P., A satellite with an atmosphere, *Astrophys. J.*, 100, 378-383, 1944.
Ledvina, S. and T.E. Cravens, A three-dimensional MHD model of plasma flow around Titan, *Planet. Space Sci.*, 46, 1175-1191, 1998.
Ledvina, S. A., T. E. Cravens, A. Salman, K. Kecskemety, Ion Trajectories in Saturn's Magnetosphere Near Titan, *Advances in Space Research*, 26, 1691-1695, 2000.
Lellouch, E., Urey Prize Lecture. Io's Atmosphere: Not yet understood, *Icarus*, 124, 1–21, 1996.
Lindal G. F., G. E. Wood, H. B. Hotz, D. N. Sweetnam, V. R. Eshleman, and G. L. Tyler, The atmosphere of Titan: An analysis of the Voyager 1 radio occultation measurements, *Icarus*, 53, 348-363, 1983.
Linker, J., M. McGrath, M. Kivelson, R. Walker, and K. Khurana, MHD modeling of Io's interaction with the plasma torus: Prediction for the upcoming Galileo flybys, in *AAS/Division of Planetary Sciences Meeting*, vol. 31, p. 7809, 1999.
Linker, J. A., M. G. Kivelson, and R. J. Walker, A three-dimensional MHD simulation of plasma flow past Io, *J. Geophys. Res.*, 96, 21,037–21,053, 1991.
Linker, J. A., K. K. Khurana, M. G. Kivelson, and R. J. Walker, MHD simulation of Io's interaction with the plasma torus, *J. Geophys. Res.*, 103(E9), 19,867-19,877, 1998.
Luhmann J. G., C.T. Russell, K. Schwinginschuh, and Y. Yeroshenko, A comparison of induced magnetotails of planetary bodies: Venus, Mars and Titan, *J. Geophys. Res.* 96, 11,199-11,208, 1991.
Luhmann, J. G., Titan's ion exosphere wake: A natural mass spectrometer?, *J. Geophys. Res.* 101, 29,387-29,393, 1996.
Liu, Y., A. F. Nagy, K. Kabin, M. R. Combi, D. L. Dezeeuw, T. I. Gombosi, and K. G. Powell, Two-species, 3D, MHD simulation of Europa's interaction with Jupiter's magnetosphere, *Geophys. Res. Lett.*, 27, 1791–1794, 2000.
Marconi, M. L., and D. A. Mendis, The atmosphere of a dirty-clathrate cometary nucleus – a two-phase, multifluid model, *Astrophys. J.*, 273, 381–396, 1983.
Marconi, M. L., L. Dagum, and W. H. Smyth, Hybrid fluid/kinetic approach to planetary atmospheres: an example of an intermediate-mass body, *Astrophys. J.*, 469, 393–401, 1996.
Miller, R. H., and M. R. Combi, A Coulomb collision algorithm for weighted particle simulations, *Geophys. Res. Lett.*, 21, 1735–1738, 1994.
Miller, R. H., C. E. Rasmussen, M. R. Combi, T. I. Gombosi, and D. Winske, Ponderomotive acceleration in the auroral region: A kinetic simulation, *J. Geophys. Res.*, 100, 23901–23916, 1995.
Mitchell, G. F., S. S. Prasad, and W. T. Huntress, Chemical model calculations of C ,C , CH, CN, OH, and NH abundances in cometary comae, *Astrophys. J.*, 244, 1087–1093, 1981.
Motschmann, U., and K. Glassmeier, Nongyrotropic distribution of pick-up ions at comet P/Grigg-Skjellerup: a possible source of wave activity, *J. Geophys. Res.*, 98, 20,977-20,983, 1993.
Nagy, A. F., Y. Liu, K. C. Hansen, K. Kabin, T. I Gombosi, M. R. Combi, and D. L. DeZeeuw, The interaction between Saturn's magnetosphere and Titan's ionosphere, *J. Geophys. Res.*, 106, 6151-6160, 2001.
Ness, N.F., M.H. Acuna, K.W. Behannon, and F.M. Neubauer, The induced magnetosphere of Titan, *J. Geophys. Res.* 87, 1269-1282, 1982.
Neubauer, F. M., Nonlinear standing Alfvén wave current

system at Io - Theory, *J. Geophys. Res.*, 85, 1171–1178, 1980.

Neubauer, F. M., The sub-Alfvénic interaction of the Galilean satellites with the Jovian magnetosphere, *J. Geophys. Res.*, 103, 19,834–19,866, 1998.

Neubauer, F. M., Alfvén wings and electronmagnetic induction in the interiors: Europa and Callisto, *J. Geophys. Res.*, 104, 28671–28684, 1999.

Neubauer, F. M., D.A. Gurnett, J.D. Scudder, and R. E. Hartle, Titan's magnetospheric interaction, in *Saturn*, edited by T. Gehrels and M.S. Matthews, pp. 760-787, Univ. of Ariz. Press, Tucson, 1984.

Neugebauer, M., R. Goldstein, B. E. Goldstein, S. A. Fuselier, H. Balsiger, and W. Ip, Densities and abundances of hot cometary ions in the coma of P/Halley, *Astrophys. J.*, 372, 291-300, 1991.

Paranicas, C., R. W. McEntire, A. F. Cheng, A. Lagg, and D. J. Williams, Energetic charged particles near Europa, *J. Geophys. Res.*, 105, 16,005–16,016, 2000.

Paterson, W. R., L. A. Frank, and K. L. Ackerson, Galileo plasma observations at Europa: Ion energy spectra and moments, *J. Geophys. Res.*, 104, 22,779–22,792, 1999.

Pospieszalska, M. K., and R. E. Johnson, Plasma heating of Io's atmosphere, *Geophys. Res. Lett.*, 19, 949–952, 1992.

Pospieszalska, M. K., and R. E. Johnson, Monte Carlo calculations of plasma ion-induced sputtering of an atmosphere: SO ejected from Io, *J. Geophys. Res.*, 101, 7565–7574, 1996.

Rauer, H., F. Roesler, F. Scherb, H. U. Schmidt, and R. Wegmann, Ion emission line profiles in cometary plasma tails., *Astron. Astrophys.*, 325, 839–846, 1997.

Russell, C. T., and D. E. Huddleston, The Unipolar Inductor Myth: Mass Addition or Motional Electric Field as the Source of Field-aligned Currents at Io, *Advances in Space Research*, 26, 1665–1670, 2000.

Saur, J., *Plasma interaction of Io and Europa with the Jovian Magnetosphere*, Ph.D. thesis, Universität zu Köln, 2000.

Saur, J., D. Strobel, and F. Neubauer, Interaction of the Jovian magnetosphere with Europa: Constraints on the neutral atmosphere, *J. Geophys. Res.*, 103, 19,947–19,962, 1998.

Saur, J., F. M. Neubauer, D. F. Strobel, and M. E. Summers, Three-dimensional plasma simulation of Io's interaction with the Io plasma torus: Asymmetric plasma flow, *J. Geophys. Res.*, 104, 25,105–25,126, 1999.

Schneider, N. M., D. M. Hunten, W. K. Wells, A. B. Schultz, and U. Fink, The structure of Io's corona, *Astrophys. J.*, 368, 298–315, 1991.

Shematovich, V. I., D. V. Bisikalo, and J. C. Gerard, A kinetic model of the formation of the hot oxygen geocorona. 1: Quiet geomagnetic conditions, *J. Geophys. Res.*, 99, 23,217–23,229, 1994.

Sieveka, E. M., and R. E. Johnson, Ejection of atoms and molecules from Io by plasma-ion impact, *Astrophys. J.*, 287, 418–426, 1984.

Skorov, Y. V. and H. Rickman, Simulation of gas flow in a cometary Knudsen layer, *Planet. Space Sci.*, 46, 975–996, 1998.

Smyth, W. H., and M. R. Combi, Io's sodium exosphere and spatially extended cloud: A consistent flux speed distribution, *Icarus*, 126, 58–77, 1997.

Song, P., T. I. Gombosi, and A. J. Ridley, Three-fluid Ohm's law, *J. Geophys. Res.*, 106, 8149–8156, 2001.

Southwood, D. J., M. G. Kivelson, R. J. Walker, and J. A. Slavin, Io and its plasma environment, *J. Geophys. Res.*, 85, 5959–5968, 1980.

Summers, M., and D. Strobel, Photochemistry and vertical transport in Io's atmosphere and ionosphere, *Icarus*, 20, 290–316, 1996.

Szegö, K., et al., Physics of mass loaded plasmas, *Space Science Reviews*, 94, 429–671, 2000.

Veregin, M. I., K. I. Gringauz, and N. F. Ness, Comparison of induced magnetospheres at Venus and Titan, *J. Geophys. Res.*, 89, 5461-5470, 1984.

Wallace, L. V., and Miller, F. D. , Isophote configurations for model comets, *Astron. J.*, 63, 213–219, 1958.

Wilson, G. R., J. L. Horwitz, and J. Lin, A semikinetic model for early stage plasmasphere refilling.I -Effects of Coulomb collisions, *J. Geophys. Res.*, 97, 1109–1119, 1992.

Wolf-Gladrow, D. A., F. M. Neubauer, and M. Lussem, Io's interaction with the plasma torus: A self-consistent model, *J. Geophys. Res.*, 92, 9949-9961, 1987.

Wong, M., and R. Johnson, A three-dimensional azimuthally symmetric model atmosphere for Io. 1. Photochemistry and the accumulation of a nightside atmosphere, *J. Geophys. Res.*, 101, 23,343–23,254, 1996.

Wong, M. C., and W. H. Smyth, Model calculations for Io's atmosphere at eastern and western elongations, *Icarus*, 146, 60–74, 2000.

Xie, X., and M. J. Mumma, Monte Carlo simulation of cometary atmospheres: Application to comet P/Halley at the time of the Giotto spacecraft encounter. I. Isotropic model, *Astrophys. J.*, 464, 442–456, 1996a.

Xie, X., and M. J. Mumma, Monte Carlo simulation of cometary atmospheres: Application to comet P/Halley at the time of the Giotto spacecraft encounter. II. Axisymmetric model, *Astrophys. J.*, 464, 457–475, 1996b.

Zimmer, C., K. K. Khurana, and M. G. Kivelson, Subsurface Oceans on Europa and Callisto: Constraints from Galileo Magnetometer Observations, *Icarus*, 147, 329–347, 2000.

Michael R. Combi and Tamas I. Gombosi: Department of Atmospheric, Ocean and Space Sciences, University of Michigan, 2455 Hayward Street, Ann Arbor, Michigan.

Konstantin Kabin: Department of Physics, University of Alberta, Edmonton, Alberta, Canada

PART III. CHEMISTRY, ENERGETICS AND DYNAMICS

Perhaps more so than in any other part of this monograph, the following chapters epitomize the remarkable breadth of sub-disciplines required to achieve a comprehensive understanding of aeronomic systems. A neutral atmosphere is a vibrant entity. If dense and long-lived, it experiences tides and waves. It absorbs not only solar energy but also tons of meteoritic input each day. Still, at high altitudes it can escape from even strong gravitational fields. For bodies without a "permanent" atmosphere, solar photons, solar wind and meteors produce one daily via a blend of surface sputtering processes.

The role of the Sun's energy—once optimistically called "the solar constant"—is clearly the primary driving force, and its variable nature remains a research focus of fundamental importance to aeronomy. Laboratory measurements of chemical reaction rates provide the complementary tool needed for quantitative modeling of atmospheric systems. Like the twins in Gemini, solar input and chemical kinetics are hand-in-hand key players in any attempt to portray the nature of aeronomic systems. *(Image courtesy M. Mendillo.)*

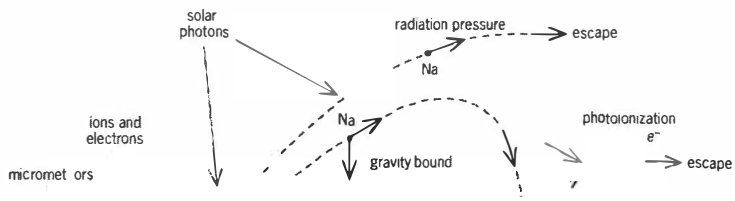

Wave Coupling in Terrestrial Planetary Atmospheres

Jeffrey M. Forbes

Department of Aerospace Engineering Sciences, University of Colorado, Boulder, Colorado, USA

The roles of gravity waves and tides in coupling lower and upper atmosphere regimes, and determining mean thermal and wind stuctures, are compared and contrasted for Earth, Mars and Venus. On Earth, gravity waves close and reverse the mean mesospheric jets and force a circulation in the meridional plane that drives the high-latitude summer mesopause (~90 km) to temperatures ~130K, much colder than radiative equilibrium values. Migrating and nonmigrating tides combine to dominate the meteorology of the 80-150 km height region. On Mars, nonmigrating tides assume even greater importance due to the extreme topography in the forcing region, and they induce longitudinal variations in density between 100 and 150 km that affect aerobraking operations. Under enhanced dust loading in the Southern Hemisphere, a thermally-direct Hadley cell (augmented by momentum flux divergences due to dissipating thermal tides) provides sufficient subsidence heating to explain the anomalously warm temperatures observed over the winter pole. The dynamical effects of gravity waves in the atmosphere of Mars have yet to be studied in earnest. On Venus, thermal tides play an key role in maintaining superrotation of the atmosphere near the cloud tops (ca. 65km), and deceleration of the circulation at higher levels. Similar to Mars' dusty atmosphere, a thermally direct Hadley cell and momentum flux divergences due to dissipating tides and other waves act in concert to determine the zonal mean wind and temperature distribution of Venus' atmosphere between 65 and 100 km. The specific contributions of gravity waves, Kelvin waves and forced Rossby waves remain to be determined, however.

1. INTRODUCTION

Planetary atmospheres are rotating stratified fluids, and thus support a variety of wave motions. Waves often represent an important mechanism for transporting energy and momentum from one point to another in an atmosphere. Some of the relevant mechanisms are illustrated in Figure 1. Gravity or buoyancy waves are excited in lower atmospheres by flow over topography, convective activity, and shear instabilities. Periodic absorption of solar radiation forces thermal tides at subharmonics of a solar day. Longer-period waves can be excited by instabilities in the mean flow, by temporal variations in convective activity (latent heating), and sometimes arise as resonant atmospheric oscillations. Many of the above waves are capable of propagating to higher altitudes where they undergo dissipation and deposit heat and momentum into the mean flow.

Several works exist which compare various types of waves in the atmospheres of Earth, Mars and Venus. *Seiff et al.* [1992] provide a comprehensive review from

Atmospheres in the Solar System: Comparative Aeronomy
Geophysical Monograph 130

10.1029/130GM11

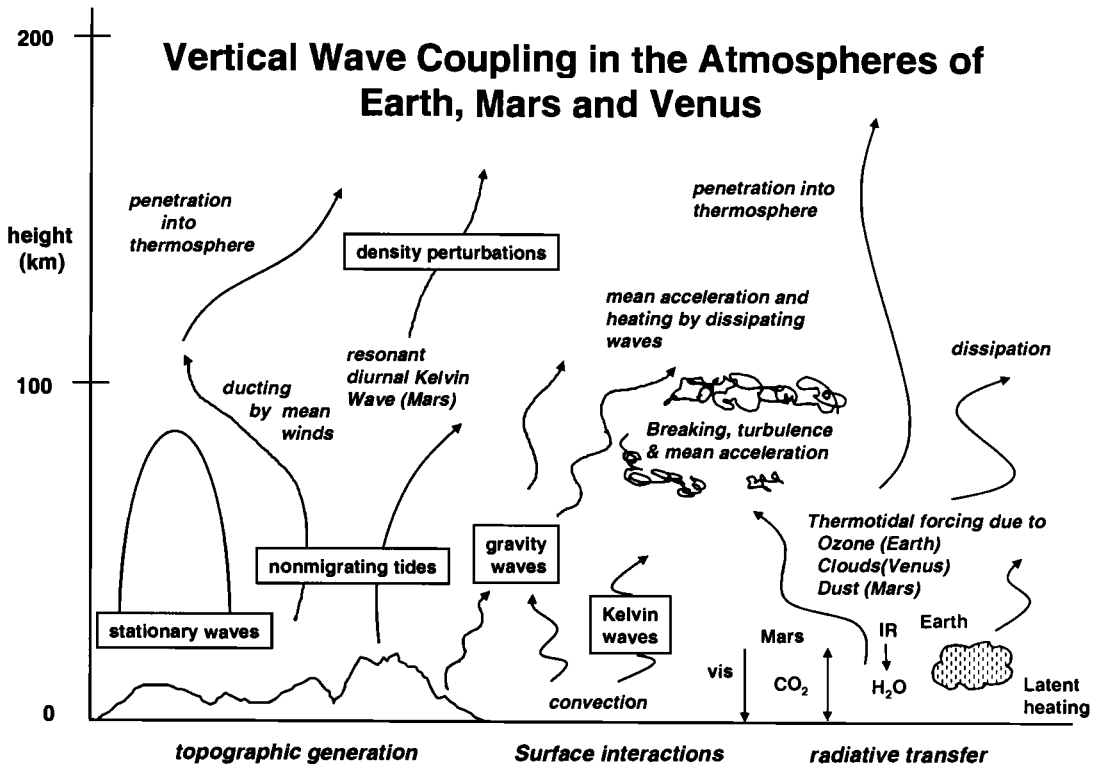

Figure 1. Schematic of various processes related to wave coupling between the lower and upper atmospheres of Earth, Mars and Venus.

an observational perspective. *Lindzen* [1970] discusses the implications of classical tidal theory for each of these planets. *Mayr et al.* [1992] compare the properties and propagation characteristics of thermospheric gravity waves due to both in-situ and lower-atmosphere sources. *Imamura and Ogawa* [1995] compare the effects of CO_2 radiative damping on the vertical propagation of internal gravity waves in the atmospheres of Earth, Mars and Venus. *Leovy* [1982] assesses the contribution of thermal tides to maintenance of homopause levels in these atmospheres. *Bougher et al.* [2000] (also references therein) comparatively examine the thermal tides excited in-situ in the thermospheres of Earth, Mars and Venus. Thus, it is recognized that there exists a degree of similarity between the types of waves that exist in the atmospheres of the so-called "terrestrial" planets. As we shall see, waves also serve to determine the mean structures of these planetary atmospheres in analogous fashions.

The primary purpose of this chapter is to form a comparative planetary perspective on the role of waves in determining the thermal and wind structures in the atmospheres of Earth, Mars and Venus. Emphasis is placed on the vertical coupling between lower and upper atmospheric regimes of these planets, and on physical mechanisms. Since vertically propagating gravity waves and thermal tides (actually, a special class of gravity waves) are so important to vertical coupling, these waves are addressed first in Sections 2 and 3, respectively. Moreover, due to the dynamic similarity between Earth and Mars, Sections 2 and 3 are mainly confined to these planets. Our knowledge of Rossby waves and normal modes for Mars and Venus is not as well developed, and these waves tend to be secondary in importance to gravity waves and tides in terms of vertical coupling. Therefore, relatively little attention is devoted to these waves. With this background in place, we then discuss in Section 4 how various wave types serve to couple atmospheric regions on Venus. Throughout, we briefly expose the reader to related information for the giant planets. The chapter concludes with a summary of outstanding problems.

2. GRAVITY WAVES ON EARTH AND MARS

2.1. General Theory and Relation to the Mean Structure of Earth's Atmosphere

In the following, the basic concepts of internal gravity wave propagation and interactions with the mean flow are developed with minimal reliance on equations. More complete and mathematical developments, all focused on Earth, may be found in *Andrews et al.* [1987], *Lindzen* [1990] and *McLandress* [1998].

Gravity waves are waves that have the buoyancy force (inherent in a stratified fluid) as the restoring force. Depending on wavelength and the background thermal and wind structure, gravity waves may be trapped or vertically propagating. The former are called external waves and the latter, which potentially couple different regions of the atmosphere, are internal gravity waves (IGWs). IGWs are often generated by vertical displacement of the atmosphere due to flow over topography or by convection, or by shear instability in the background flow. Steady flow over topography generates waves with horizontal phase speeds c = 0 with respect to the planetary surface. Time variations in excitation mechanisms produce waves that have nonzero phase speeds (generally tens of ms^{-1}) with respect to the surface. However, as we will see below, the more relevant phase speed is with respect to the mean flow ($\bar{u}$), $c\text{-}\bar{u}$, called the intrinsic phase speed. There are several "theorems" of IGW propagation [*Eliassen and Palm,* 1961] that govern the ability of waves to couple different atmospheric regimes. In the absence of dissipation and heating, the vertical flux of energy $\overline{p'w'}$ associated with an IGW (or packet of IGWs) is related to the vertical flux of net horizontal momentum ($\rho_0\overline{u'w'}$) according to:

$$\overline{p'w'} = (c - \bar{u})\rho_0\overline{u'w'} \qquad (1)$$

where p', w', u' are the perturbation pressure, vertical and eastward wind speeds, and ρ_o is the backgound density. An upward-propagating wave ($\overline{p'w'} > 0$) carries eastward(westward) momentum if the phase speed is eastward(westward) with respect to the mean flow or $c > \bar{u}$ ($c < \bar{u}$), respectively. Furthermore, the "noninteraction theorem" states that for steady-state IGWs

$$\frac{d}{dz}(\rho_0\overline{u'w'}) = 0 \; for \; \bar{u}{\neq}c \qquad (2)$$

In other words, the waves do not interact with the mean flow. However, if $\bar{u} = c$ (at a "critical level"), then the mean flow absorbs the wave and this serves as a barrier to vertical propagation. From (2), we infer that u' and w' must grow with height as $\rho_0{}^{-1/2}$ (in the absence of dissipation).

For IGWs undergoing dissipation, $\frac{d}{dz}(\rho_0\overline{u'w'}){\neq}0$ and momentum carried by the waves is deposited into the mean flow. In Earth's atmosphere, wave growth with height is such that breaking (convective instability) of the waves can occur in the mesosphere, continuing at "saturation amplitudes" to higher altitudes until acted on by other forms of dissipation (i.e., eddy and molecular diffusion) which further damp the wave. Thus, IGWs serve to transport horizontal momentum from tropospheric source regions to Earth's upper mesosphere and lower thermosphere. In order to effect change in the mean flow, however, there must be significant anisotropy in the momentum deposited into the mean flow (otherwise, for instance, deposited eastward and westward momentum would cancel each other). The anisotropy occurs as a result of critical level absorption (mentioned previously) by the mean zonal jets characteristic of the middle atmosphere. We now briefly describe how this process determines the zonal mean thermal and dynamical structure of Earth's mesopause region (ca. 80-100 km).

Consider the terrestrial zonal mean wind structure in Figure 2 for the month of June, which is reasonably representative of N. Hemisphere summer conditions. The main features include eastward and westward "jets" maximizing near 50-70 km in the S. and N. Hemispheres, respectively. Winds of opposite sign occur during N. Hemisphere winter, and weaker more symmetric eastward jets characterize the equinoctial months. Between about 70 and 100 km strong shears occur, and the winds go to zero or reverse in direction. The deceleration and possible reversal of the jets during summer(winter) reflect the removal of most westward (eastward)-propagating IGWs by critical level absorption in the main jets below, and the irreversible transfer of eastward(westward) momentum by the dissipating gravity waves above 70 km (see Figure 3).

The dissipation of IGWs in the mesopause region has two further consequences. First, it is thought that significant generation of turbulent mixing results from the convective instability process. Values of eddy diffusion coefficient of order 100-200 m^2s^{-1} are often quoted for the 80-100 km height region of Earth [i.e.,*Garcia and Solomon,* 1985], which is consistent with a turbopause level (transition from turbulent mixing to molecular diffusion-dominated transfer of momentum and heat) of order 105 km. This level of mixing is often required to bring photochemical models of minor constituents in this region of the atmosphere in accord with observational data.

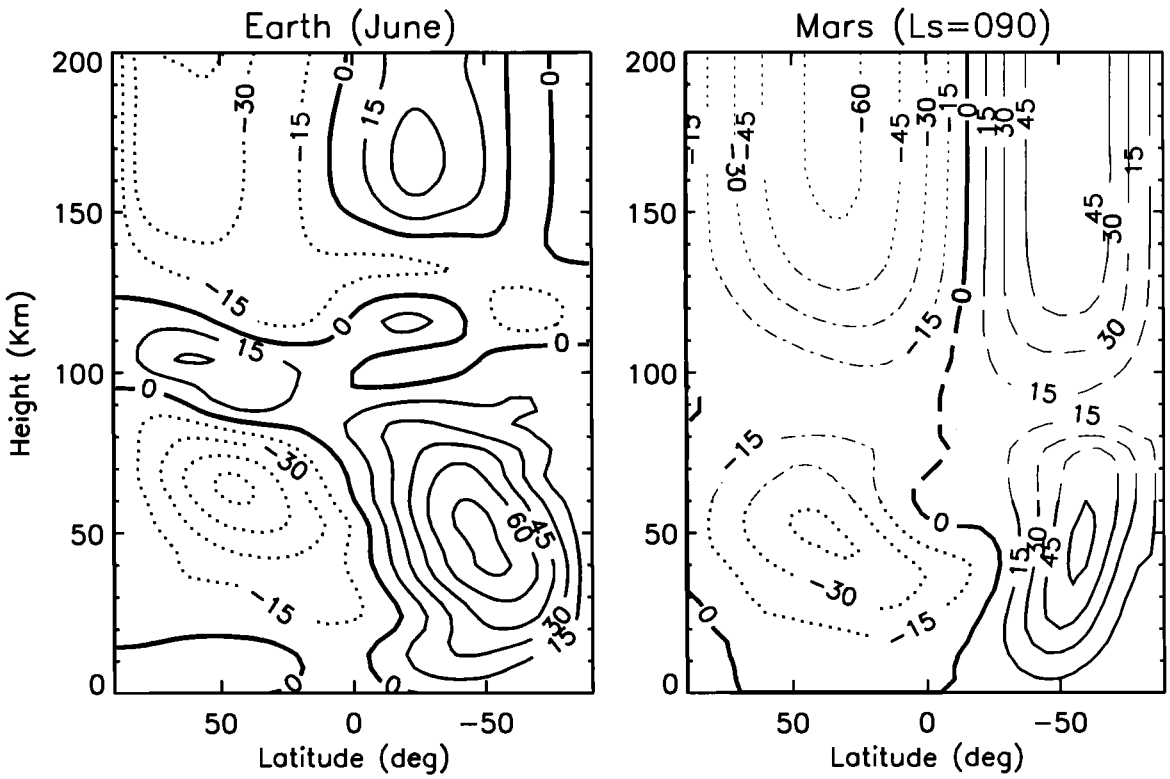

Figure 2. Comparison between mean zonal flows for Earth (left) and Mars (right) for typical N. Hemisphere summer conditions. The Earth depiction is based on the HWM93 model (Hedin, 1993) while that of Mars is based on Bougher et al. (2000) above 100 km and Haberle et al. (1993) below 70 km. The broken contour lines between 70 and 120 km in the right panel reflect our relative uncertainty concerning the wind patterns in this height regime of Mars' atmosphere. Negative (westward) wind values are indicated by the dashed contours. Contour units are ms^{-1}.

Another consequence of gravity wave dissipation is its impact on the thermal structure of the mesopause region. It is well known that mesopause temperatures (ca. 90 km) are of order 130-160 K at middle to high summer latitudes and 200-220 K in the winter hemisphere. This temperature gradient is opposite to what would exist under radiative equilibrium, and may be understood as follows (*Lindzen* [1981]; see *Forbes* [1983] for an expanded discussion). The divergence of momentum flux represents a force on the atmosphere that is balanced in the steady-state zonal momentum equation by a mean meridional flow:

$$-f\bar{v} \approx F_x \approx -\frac{1}{\rho_0}\frac{d}{dz}(\rho_0 \overline{u'w'}) \qquad (3)$$

where f is the Coriolis parameter and $\bar{v}$ is the zonal mean northward wind. This compensating meridional flow is southward ($v < 0$) in both N. Hemisphere summer ($f > 0$, $F_x > 0$) and S. Hemisphere winter ($f < 0$, $F_x < 0$); in other words, a summer-to-winter meridional circulation results. To satisfy continuity in the zonal mean meridional plane, this implies upward (downward) motions in the summer(winter) and therefore adiabatic cooling(heating), accounting for colder temperatures in summer and a meridional temperature gradient opposite to that expected on the basis of radiative equilibrium.

The gravity waves carrying much of the momentum typically have horizontal wavelengths of order 10's to 100's of km. Thus, a major part of the physics occurs at sub-grid scales in General Circulation Models of the Earth's middle and upper atmosphere, and it has been necessary to parameterize these effects. Several parameterizations currently exist. These are described in a tutorial fashion, and within the context of their performance in the Canadian Middle Atmosphere Model (CMAM), by *McLandress* [1998].

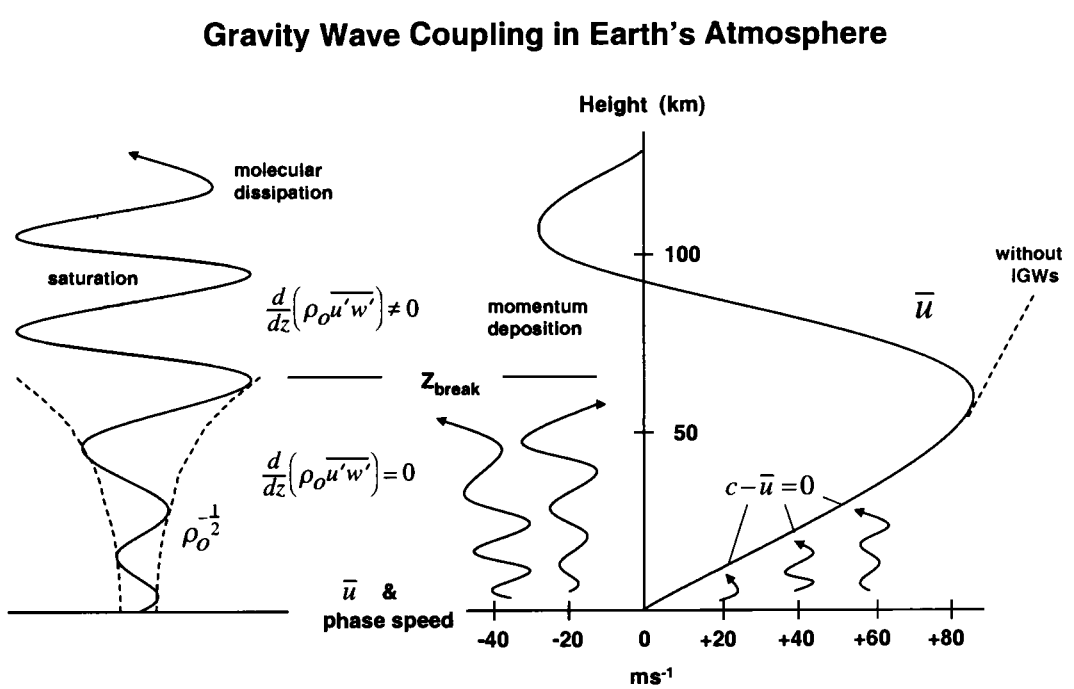

Figure 3. Schematic illustrating exponential growth, wave breaking/saturation, critical-level filtering, and deposition of anisotropic zonal momentum above the main zonal jets, leading to jet "closure" or "reversal". The IGWs with eastward phase speeds ($c > 0$) cannot propagating past critical levels ($c - \bar{u} = 0$), whereas westward propagating IGWs ($c < 0$) carry westward momentum upwards until dissipation causes westward momentum to be irreversibly transferred to the zonal-mean zonal wind field.

2.2. Gravity Waves on Mars

Gravity waves are an ubiquitous feature of planetary atmospheres. Entry probe measurements indicating the presence of gravity waves in profiles of temperature and density exist for Mars [i.e., *Seiff and Kirk,* 1977], Venus [i.e., *Seiff et al.,* 1980] and Jupiter [i.e., *Seiff et al.,* 1998]. Occultation measurements of the atmospheres of Mars [*Hinson et al.,* 1999], Venus [*Hinson and Jenkins,* 1995; i.e., see Figure 10], Jupiter [*Veverka et al.,* 1974; *French and Gierasch,* 1974] and even Neptune [*Hinson and Magalhães,* 1993; *Rouques et al.,* 1994] similarly reveal vertical structures most likely attributable to gravity waves.

On Mars the combinations of extreme topography, high surface winds and wind shears, and an intense thermal boundary layer suggest strong excitation of gravity waves and thereby influences on upper-level circulation and thermal structure similar to that on Earth. *Barnes* [1990] used a quasi-geostrophic beta-plane model of the zonal mean flow and the *Lindzen* [1981] saturation parameterization to estimate the possible effects of IGWs on the circulation of the 10-100 km atmospheric region of Mars. Numerical simulations were performed for a variety of gravity wave parameters and thermal forcings of the mean flow, with emphasis on topographically forced stationary ($c = 0$) gravity waves. For a reasonable choice of wave parameters, it is shown that intermediate-scale gravity waves (horizontal wavelengths between 100 and 1000 km) could break and induce a meridional circulation in the winter hemisphere with accompanying subsidence heating at polar latitudes. *Barnes* [1990] suggests that such heating could serve to explain measurements [*Deming et al.,* 1986] indicating that temperatures between 50 and 80 km at winter polar latitudes are far above radiative equilibrium values. However, as explained below, recent general circulation model (GCM) simulations suggest that gravity waves do not play a significant role in explaining this phenomenon, in contrast to the mesopause temperature anomaly on Earth. Further, it is important to note that stationary gravity waves can only act to decelerate the jet to $\bar{u} = 0$; vertically-propagating waves carrying westward momentum ($c - \bar{u} < 0$) would be necessary to reverse the jets.

In the summer hemisphere on Mars, zonal mean eastward winds of up to 10-20 ms^{-1} exist below ~15 km, reversing to a westward jet above about 20 km, so that only waves with large eastward phase speeds can penetrate to upper levels. Assuming that the forcing for such waves is relatively weak (as compared to stationary IGWs), *Barnes* [1990] suggests that breaking levels probably occur at much higher altitudes than in the winter hemisphere. In other words, weak IGWs must grow exponentially to much higher altitudes before they break. This suggests that wave-induced modifications of thermal structure may occur significantly above 80 km in the summer hemisphere.

GCM simulations by *Wilson* [1997] and *Forget et al.* [1999] benefit from a much higher upper boundary (> 100 km) than used in previous GCM studies. During N . Hemisphere winter, they show that enhanced dust loading in the S. Hemisphere can drive a thermally-direct Hadley cell [*Held and Hou,* 1980; *Schneider,* 1983] with sufficient subsidence heating over the winter pole to explain the temperature anomaly. Below about 50 km this circulation is momentum-conserving, but at higher altitudes momentum flux divergences associated with dissipation of the thermal tides facilitates the pole-to-pole extent of this meridional circulation. Thus, it does not appear that small-scale gravity waves are needed to explain the anomalous winter polar warming of the Martian middle atmosphere as originally suggested by *Barnes* [1990]. Further, *Forget et al.* [1999] investigate the effects of topographically steady state ($c = 0$) gravity waves on the circulation during N. Hemisphere summer hemisphere when the diabatic circulation is weaker. Zonal wind differences are of order 20-40 ms^{-1} and accelerations are of order 20-40 $ms^{-1}sol^{-1}$, i.e., a moderate effect on the overall circulation. (Note: 1 sol = 1 Mars solar day = 88775.2 s).

So what, then, do we conclude about the impacts of gravity waves on the mean thermal and density structure of Mars' atmosphere? First, as noted by *Forget et al.* [1999], the modeled impact of gravity waves is very sensitive to the chosen parameters and therefore their results and conclusions should be viewed as preliminary. Moreover, it should be reiterated that *Forget et al.* [1999] only considered stationary gravity waves, and that considerable forcing of gravity waves with phase speeds between -50 and +50 ms^{-1} might exist on Mars, as on Earth. On Earth, it appears that the shorter-scale IGWs with horizontal wavelengths of order 100 km or less carry most of the momentum. According to *Barnes* [1990], intermediate scale waves are more relevant on Mars. Thus, within the next decade, Mars GCMs may be able to resolve the most important gravity waves. It must also be considered that molecular diffusion and radiative damping above 100 km may be relatively more important than convective instability ("breaking") for dissipation of gravity waves on Mars. Thus, gravity waves may be more relevant to the heat and momentum budgets of Mars' thermosphere than mesosphere. Quantitative understanding of the role of gravity waves on the mean thermal and wind structure of the Mars upper atmosphere requires further experimental and modeling efforts wherein the sources and gravity wave characteristics are more realistically specified, improved parameterizations are implemented, and thermospheric interactions are included.

3. THERMAL TIDES ON MARS AND EARTH

3.1. Basics of Tidal Theory

Simply put, thermal tides are gravity waves with periods at some fraction of a solar day, and for which the sphericity and rotation of the planet cannot be neglected. At the beginning of the previous section, we alluded to internal (vertically-propagating) and external (vertically-trapped) gravity waves. Since the former class was more relevant to vertical coupling between atmospheric regions, our attention was therefore focused on IGWs. The effects of rotation on gravity waves can be illustrated by developing the linearized wave perturbation equations for an atmosphere over a rotating planar surface [*Lindzen,* 1971]. This simple mathematical exercise demonstrates that gravity waves can only propagate vertically if the wave frequency is greater than the rotation rate, i.e., $\sigma > f$. For the diurnal tide on a rotating spherical planet, $\sigma = \Omega$ and $f = 2\Omega \sin\theta$ where Ω = is the planetary rotation rate and θ = latitude. Hence, $\sigma < f$ poleward of 30° latitude, and $\sigma > f$ equatorward of 30°, implying "propagating-like" solutions equatorward of 30°, and "evanescent-type" solutions poleward of 30°. This is indeed confirmed by a more complete mathematical treatment [*Chapman and Lindzen,* 1970] wherein solutions to Laplace's Tidal Equation ("Hough functions") describe the horizontal structures of various wave modes for any given frequency and zonal wavenumber (i.e., solutions of the form $exp[i(\sigma t + s\lambda)]$ where σ = frequency, t = universal time, s = zonal wavenumber, and λ = longitude). The solution for the sun-synchronous diurnal tide (for which $s = 1$, see below) consists of two series of "modes", a series of evanescent (external) modes primarily confined to high latitudes, and a series of vertically-propagating (internal) modes primarily confined to low latitudes.

The degree to which any of these modes is excited in the atmosphere depends on how well the latitude distribution of heating projects onto any given mode, and moreover, on how well the vertical structure of that mode matches the vertical distribution of heating. The atmospheric response to heating which projects onto trapped modes remains confined to the levels of excitation, whereas the response to propagating modes that are excited may be felt at considerably higher levels in the atmosphere, depending on susceptibility of the propagating waves to dissipation. Semidiurnal tides are all of propagating character since $\sigma \geq f$ at all latitudes.

3.2. Thermal forcing of Atmospheric tides

Diurnal and semidiurnal atmospheric tides are thermally generated on any rotating planet absorbing radiation from the Sun. The tidal forcing and subsequent atmospheric tidal fields (velocity, density, etc.) may be represented by $A\cos(\sigma t + s\lambda - \phi)$ where A and ϕ A are latitude-dependent amplitudes and phases and the remaining variables were defined previously. Rewriting in terms of local time $t = t_{LT} - \frac{\lambda}{\Omega}$ we have for the diurnal tide:

$$A_1 \cos(\Omega t_{LT} + (s-1)\lambda - \phi_1) \tag{4}$$

and

$$A_2 \cos(2\Omega t_{LT} + (s-2)\lambda - \phi_2) \tag{5}$$

for the semidiurnal tide. The $s = 1$ ($s = 2$) component of the diurnal (semidiurnal) tide is that which possesses a zonal phase speed equal to the apparent motion of the Sun from an observer on the ground. It is these components, therefore, which are excited by the Sun's radiation being absorbed by a longitude-invariant planetary atmosphere or surface. They are the so-called migrating components. In this case we have for the migrating diurnal tide:

$$A_1 \cos(\Omega t_{LT} - \phi_1) \tag{6}$$

and

$$A_2 \cos(2\Omega t_{LT} - \phi_2) \tag{7}$$

for the migrating semidiurnal tide. The 'migrating' oscillations (6) and (7) are independent of longitude.

On Mars, the diurnal cycle of heating occurs by absorption of near-IR solar radiation by CO_2 and aerosols, and short-wave absorption by airborne dust. In addition, visible radiation absorbed by the ground drives a large surface temperature oscillation that is transmitted radiatively and convectively to the atmosphere. This latter process, which dominates the thermal forcing of tides in the dust-free Martian atmosphere, is much more efficient on Mars than Earth due to the fact that the atmosphere consists primarily of CO_2 at a relatively low pressure (6 mb as opposed to 1 bar). In Earth's atmosphere, thermal excitation of tides occurs primarily via insolation absorption by water vapor (0-20 km) in the near-IR, ozone (30-60 km) at ultraviolet wavelengths, and through latent heating associated with deep convection. On both Mars and Earth, EUV radiation absorption in the lower thermosphere (ca.100-150 km) drives in-situ tidal oscillations that extend throughout the thermosphere due to the effects of molecular diffusion. Due to the eccentricity of the Martian orbit, solar insolation is 44% smaller at aphelion than perihelion.

The interaction between radiative processes and topography, which includes consideration of topographic height and roughness, surface thermal inertia and albedo is a complicated nonlinear process. To first order, however, it is useful to consider the situation where, as the planet is rotating, the transformation of the Sun's radiation into thermal energy is modulated by a longitudinally non-uniform atmosphere/planetary surface. Figure 4 illustrates such a situation where the surface modulation is characterized by zonal wavenumber $s = 2$, which represents an important topographic zonal component over much of Mars' surface. Figure 4 illustrates how the diurnal harmonic of the westward-migrating solar radiation interacts with the $s = 2$ component of topography to excite westward and eastward propagating diurnal tides with $s = 3$ and $s = -1$. Similarly, the semidiurnal harmonic of the migrating Sun's solar radiation pattern interacts with $s = 2$ topography to generate westward-propagating ($s = 4$) and standing ($s = 0$) semidiurnal oscillations. The eastward-propagating diurnal wave with $s = -1$ is largely comprised of the so-called diurnal Kelvin wave[1], which is in near-resonance in Mars' atmosphere, and as such a significantly amplified response is anticipated. This will be discussed in more detail below.

The $s = 3$ component of topography is also large on Mars. Similar interactions would produce $s = -2$ eastward diurnal and $s = 1$ westward semidiurnal oscillations that are also thought to achieve large amplitudes in Mars' thermosphere [*Forbes et al.*, 2001a]. The other modes generated, namely the $s = 4$ westward diurnal and $s = 5$ westward semidiurnal are less likely to be important.

[1]For a given zonal wavenumber, the Kelvin wave is the gravest (most fundamental) symmetric eastward-propagating gravity-type mode.

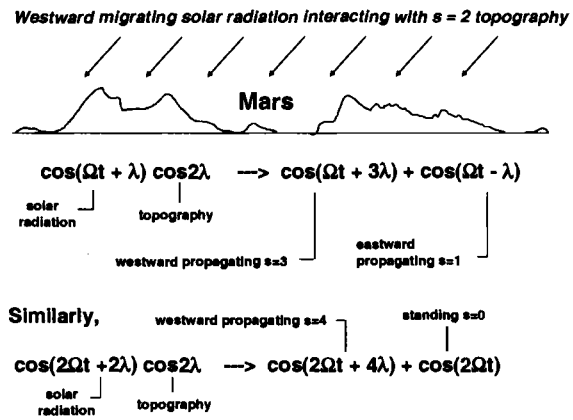

Figure 4. Schematic illustrating how solar radiation, interacting with topography dominated by zonal wavenumber $s = 2$ on a rotating planet, generates various wavenumber diurnal and semidiurnal oscillations which give rise to longitude - dependent ("nonmigrating") tidal oscillations.

3.3. Thermal Tides on Earth

On Earth, the sun-synchronous or migrating component is dominant, but nonmigrating components also make important contributions. Heat sources far from the surface and from the influences of topography (i.e., UV absorption by ozone between 35-65 km and UV and EUV absorption above 90 km) tend primarily to project onto the migrating components. The first symmetric propagating and trapped diurnal modes and the first symmetric propagating semidiurnal mode capture much of the latitude structure during the equinoxes when the heating is most symmetric about the equator. During solstices, the symmetric modes are still dominant, but added contributions from the first antisymmetric modes play a non-negligible role. The efficiency with which a mode is excited and the magnitude of atmospheric response also depend on how well the vertical structure of the mode matches that of the heating. Tropospheric sources are generally about 12-15 km deep, and consequently project efficiently onto the vertical structure of the symmetric diurnal propagating tide which has a vertical wavelength of 25-30 km, and less efficiently onto the symmetric semidiurnal tide which has a vertical wavelength in excess of 150 km. The converse is true for the deeper ozone insolation absorption that tends to excite all phases of the diurnal tide resulting in destructive interference. We will see that similar considerations apply on Mars, where near-surface migrating heat sources primarily excite the diurnal tide, but where the semidiurnal tide is preferentially excited in a much deeper layer (~0-50 km) when the atmosphere is loaded with dust.

Hagan [1996] studied the comparative effects of tropospheric and strato-mesospheric heat sources on the migrating tidal response in the region around 90-120 km where the upward-propagating tides begin to dissipate and achieve their maximum amplitudes. The prevailing opinion at the time was that the contribution due to H_2O absorption of IR was dominant, due in part (a) to the relatively greater exponential growth experienced by this component compared to that excited by UV absorption by O_3 at higher altitudes; and (b) the anticipated greater efficiency with which a tropospheric heat source would excite the first symmetric diurnal propagating mode with vertical wavelength ~25 km. However, *Hagan* [1996] found the UV-driven component to destructively interfere with the IR-driven component at the 20-40% level in the lower thermosphere depending on month. Analagous results were obtained for the semidiurnal tide, except that the tropospherically-generated component destructively interfered with the stratospherically-driven component which had theretofore been assumed to dominate.

Mean winds also affect the vertical propagation of atmospheric tides. The fundamental semidiurnal tidal mode is latitudinally very broad, with significant amplitudes where the mean zonal mesospheric jets are maximum (see Figure 2), and the zonal phase speed of the tide slows considerably. The mean winds introduce distortions into the total semidiurnal response that are accomodated by secondary excitation of higher-order modes that grow more rapidly with height than the fundamental mode (which becomes evanescent in the mesosphere). This process is called "mode coupling" [*Hong and Lindzen*, 1976]. The semidiurnal tidal response in the lower thermosphere therefore reflects the shorter vertical wavelengths (40-60 km) characteristic of these higher-order modes [*Forbes*, 1982]. The diurnal propagating tide, on the other hand, is confined to low latitudes, has a horizontal phase speed (~350-450 ms^{-1}) greater than the prevailing winds (~20-40 ms^{-1}), and is thus much less influenced by the mean wind field.

The diurnal component of tropospheric heating is much larger than that of the semidiurnal component (as would be expected from Fourier decomposition of the day-night variation in solar heating), but it is well known that the surface responses are comparable in magnitude (see Figure 5). This circumstance represented a major dilemma in early atmospheric tidal the-

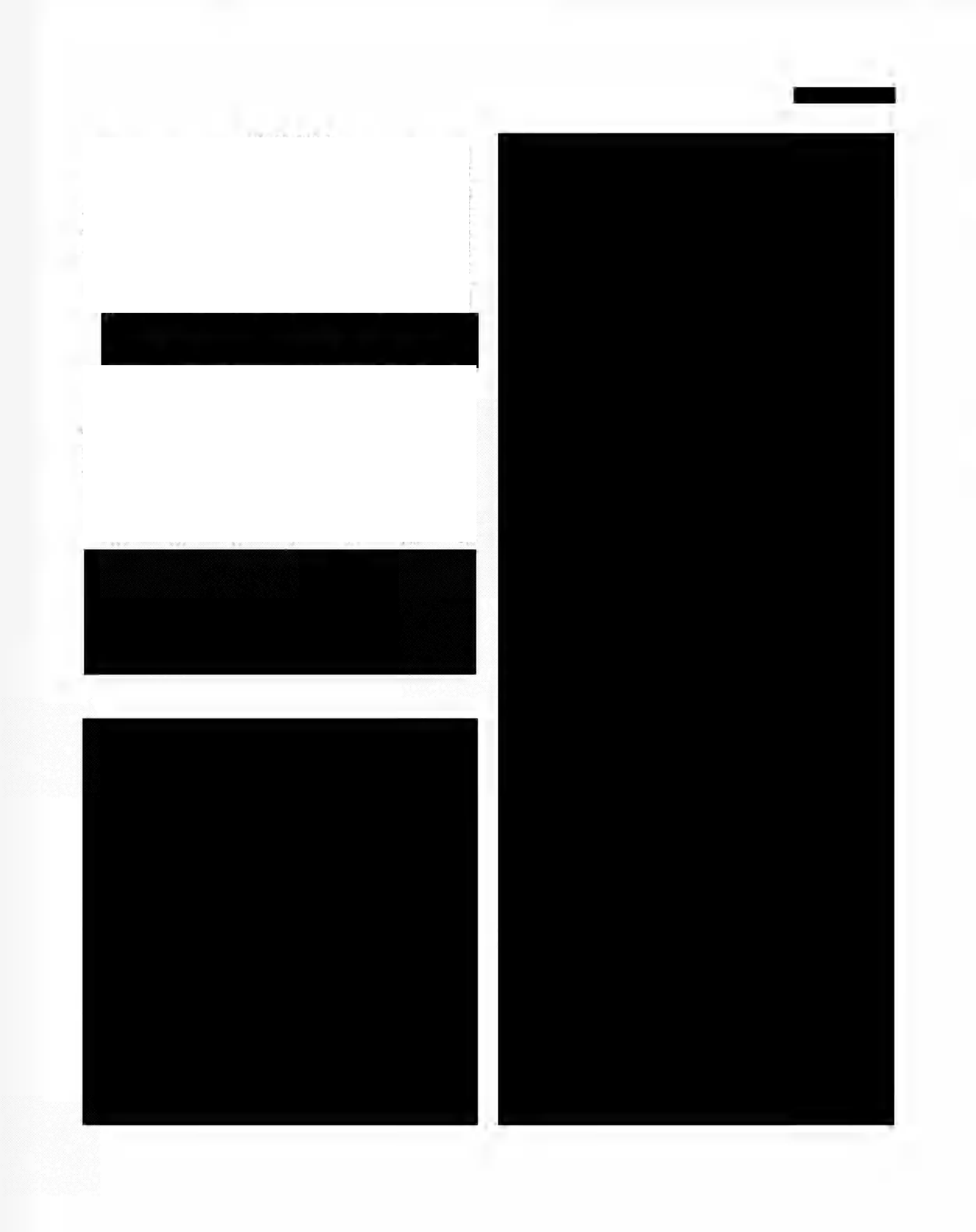

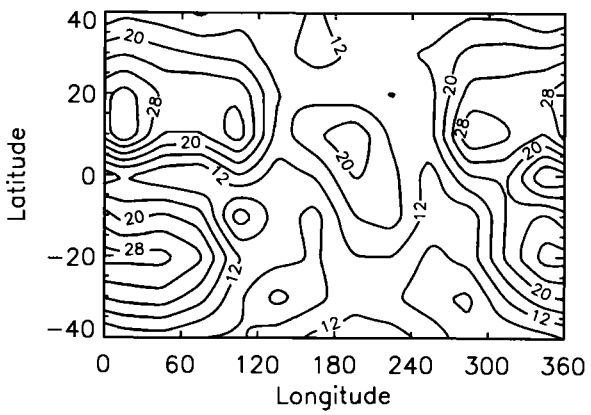

Figure 6. Contours of diurnal northward wind amplitude at 95 km determined from HRDI and WINDII wind measurements during 1992-1994 for December months (Forbes et al., 2001c). The contours (units of ms^{-1}) are reconstructed from westward propagating $s = 1$ and $s = 2$, standing $s = 0$, and eastward-propagating $s = -3$ components.

was also recognized fairly early that topography played an extremely important role in determining the diurnal tide response [*Conrath,* 1976; *Zurek,* 1976], and that dissipation of the tides could strongly influence the zonal mean circulation, at least below 60 km [*Hamilton,* 1982; *Zurek,* 1986; *Zurek and Haberle,* 1988]. General circulation models of Mars' atmosphere (NASA Ames GCM: *Haberle et al.* [1993]; CNRS/LMD: *Forget et al.* [1999]; NOAA/GFDL: *Wilson and Hamilton* [1996] and observations from Mars Global Surveyor [*Banfield et al.,* 2000; *Hinson et al.,* 2000] have significantly advanced our knowledge of global atmospheric tides on Mars. *Wilson and Hamilton* [1996] in particular provide an excellent summary of our current knowledge of Martian tides below 60 km. The NOAA/GFDL and LMD models have recently been extended up to the 100-130 km regime.

The migrating atmospheric tidal response to sun-synchronous thermal forcing on Mars may be broadly described as follows. To first order, the interplay between diurnal and semidiurnal forcing on Mars is very similar to that on Earth, except that the analog to terrestrial ozone heating is a variable heat source whose depth and intensity depend on the dust loading of the Martian atmosphere. Results from the NOAA/GFDL Mars GCM [*Wilson and Richardson,* 2000] depicted in Figure 7 illustrate well the basic concepts. The three panels illustrate height vs. local time distributions of temperature below 35 km over the equator at 180° longitude. The top panel corresponds to equinoctial conditions (L_s=355)[2] for moderate dust loading of the atmosphere (dust optical depth $\tau \sim 0.8$). The remaining two panels illustrate equatorial temperature contours for two storms during the Viking mission which occurred at $L_s = 225$ and $L_s = 290$, i.e., near S. Hemisphere solstice ($L_s = 270$). In the model these storms are characterized by values of τ near 3 and 5, respectively, distributed uniformly in latitude and up to ~35 km altitude. The simulation for moderate dust loading ($\tau \sim 0.8$), where most of the heating is confined to within 10 km of the surface, clearly reflects a dominant diurnal oscillation with downward phase progression. This is the signature of the first symmetric diurnal propagating tide, whose temperature amplitude maximizes at the equator and the eastward and northward wind amplitudes maximize in the extra-tropics. As heating becomes distributed over greater depths in the atmosphere, we see that the temperature variation becomes more semidiurnal in character, with little phase progression with height. This is due to the increased presence of the long-wavelength (first symmetric) semidiurnal tide. In progressing from $\tau = 0.8$ to $\tau = 5.0$, and as the depth of heating increases, the efficiency of exciting the short-wavelength diurnal tide decreases and the efficiency of exciting the long-wavelength semidiurnal tide increases.

By analogy with gravity wave and tidal dissipation on Earth, dissipation of thermal tides on Mars is expected to significantly affect the mean wind and thermal structure of Mars' upper atmosphere. Indeed, dissipation of migrating tides (by breaking and/or radiative damping) produces an intense (~50-100 ms^{-1}) mean westward jet in the LMD Mars GCM at altitudes ~50-90 km over the equator which is especially intense around the equinoxes [*Forget et al.,* 1999]. This is similar to the westward jet driven by eddy and molecular dissipation of the migrating diurnal tide on Earth, except that on Mars the dissipation occurs at a lower altitude. Apparently the diurnal tide does not reach sufficiently high levels to undergo molecular dissipation and thus affect the structure of Mars' thermosphere. On the other hand, the semidiurnal migrating tide has a long vertical wavelength and is much less subject to damping than the diurnal tide. Moreover, forcing of the semidiurnal tide is significantly enhanced during dust storms (cf. Figure 7). Using rough extrapolated approximations for the amplitude of the migrating semidiurnal tide

[2] L_s is the aerocentric longitude of the Sun, an angular measure of the apparent revolution of the Sun about Mars, measured from the intersection of Mars' equatorial plane with the plane of its orbit [*Kieffer et al.,* 1992]. $L_s = 0°$ corresponds to vernal equinox, $L_s = 90°$ to Northern Hemisphere summer solstice, etc.

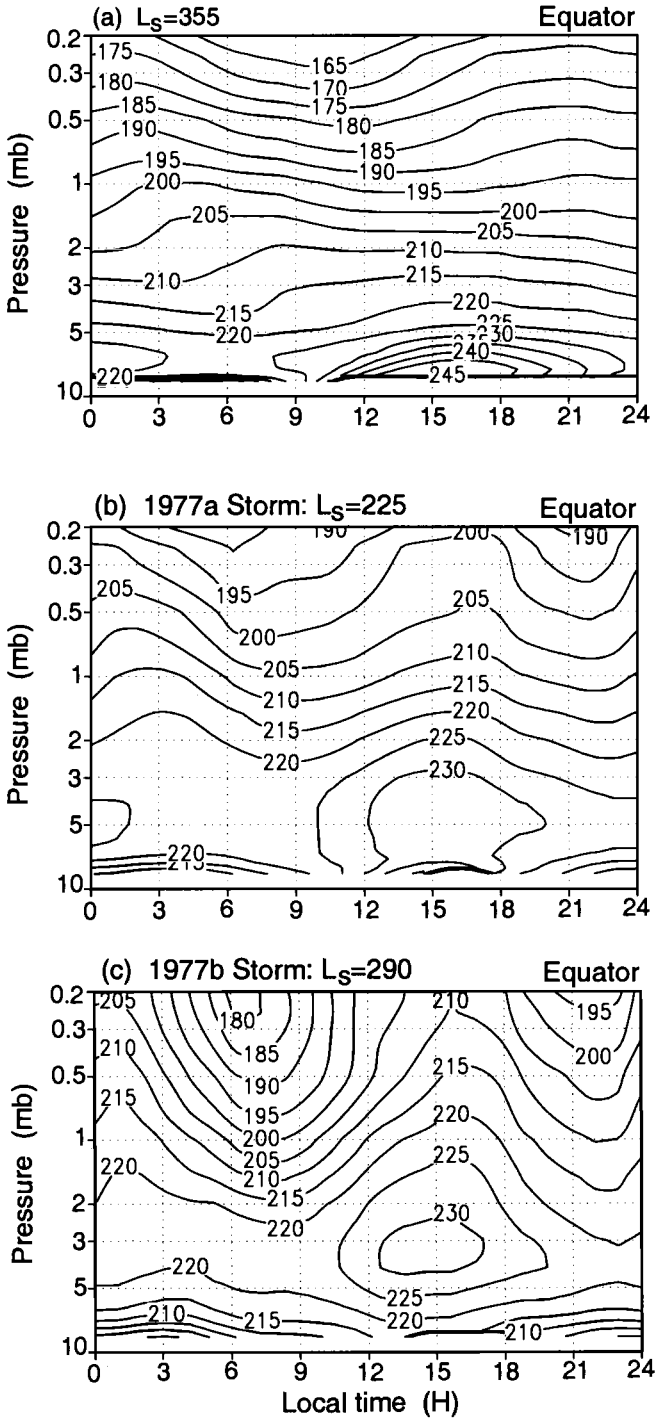

Figure 7. Simulations of Mars equatorial temperatures from the NOAA/GFDL Mars General Circulation Model (Wilson and Richardson, 2000). Top: moderate dust loading during equinox conditions. Middle: for the 1977a global dust storm. Bottom: for the 1977b global dust storm. Dust loading increases from top to bottom panel. The altitude scale extends from near the surface to about 35 km.

near the base of the thermosphere (≈100 km), *Bougher et al.* [1993] investigated the effects of the upward-propagating semidiurnal tide on the thermosphere. Effects on exospheric temperature were greatest at solar minimum and during dust-storm conditions, and typically ranged between 20-60K about diurnal mean values of order 170-250 K depending on time of day, dust loading, and level of solar activity. Significant effects were also seen in the diurnal variation of atomic oxygen concentration. These authors did not quantify effects on the zonal mean temperature and wind structure in the lower thermosphere (100-150 km) where dissipation of the tide mainly occurs.

As noted in an earlier Section, surface interactions involving westward-migrating solar radiation can lead to excitation of a spectrum of zonal wavenumbers for the diurnal and semidiurnal thermal tides. The first symmetric eastward-propagating diurnal tide with s = -1, or diurnal Kelvin wave (DKW), is particularly intriguing. This wave is close to resonance in Mars' atmosphere [*Zurek*, 1988; *Wilson and Hamilton*, 1996] so a highly amplified response is possible. Much observational evidence exists for this oscillation [*Conrath*, 1976; *Hinson et al.*, 2000; *Banfield et al.*, 2000; *Wilson*, 2000] in the lower atmosphere of Mars. *Forbes and Hagan* [2000] and *Forbes et al.* [2001a] used a linearized Global Scale Wave Model to extend into the thermosphere the DKW simulated in the lower atmosphere by the GFDL Mars GCM. Their results are illustrated in Figure 8. The perturbation winds and temperatures (not shown) are of order 10-70 ms^{-1} and 10-20 K above 120 km altitude, respectively. The eastward winds are of order 20-70 ms^{-1} above 100 km, and maximize at low latitudes as expected for a Kelvin wave. The amplitude of northward wind is of order 30-40 ms^{-1}, much larger than expected for a Kelvin wave, which according to classical theory has a much smaller meridional wind component than zonal wind component. The northward wind response depicted in Figure 8 is produced by the first antisymmetric mode that is generated via nonlinear coupling between the zonal mean winds and the Kelvin wave, and which has a meridional wind maximum at the equator. This "mode coupling" is analagous to that described for the semidiurnal tide in the terrestrial atmosphere in Section 3.3. The vertical wavelength (not shown) associated with this northward wind response is ≈60 km, consistent with that expected from classical wave theory.

The calculations of *Forbes and Hagan* [2000] were motivated by the need to explain Mars Global surveyor (MGS) accelerometer measurements near 125 km alti-

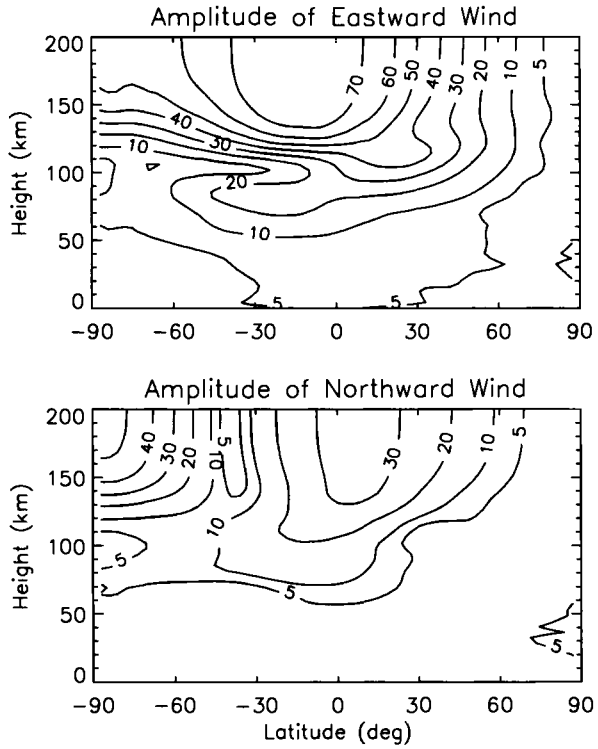

Figure 8. Mars Global Scale Wave Model (Mars GSWM) simulation of the diurnal Kelvin wave with s = -1 propagating into the thermosphere. Top: amplitude of eastward wind. Bottom: amplitude of northward wind. Asymmetries about the equator and large northward wind amplitudes reflect coupling into higher-order modes due to interactions with the zonal mean wind field. Adapted from Forbes et al. (2001).

tude [*Keating et al.*, 1998] that revealed a large ($\sim$ 22%) zonal wavenumber $s = 2$ longitudinal variation in density, and which were previously interpreted as stationary planetary waves. Forbes and Hagan offered the alternative explanation that this $s = 2$ structure was actually a manifestation of the DKW, which when viewed from sun-synchronous orbit, appeared as a stationary wave with $s = 2$. As noted earlier, the DKW (with s = -1 eastward) arises due to the interaction between westward migrating ($s = +1$) diurnal component of thermotidal forcing and the $m = 2$ component of topography. Forbes and Hagan further demonstrated that for solar forcing at any tidal frequency, the zonal wavenumber m component of topography yields nonmigrating tides that appear as $s = m$ stationary features from sun-synchronous orbit. Thus, the $s = 3$ and the s = -1 diurnal tides and the $s = 0$ and $s = 4$ semidiurnal tides generated by the $m = 2$ component of topography (see Figure 6) all appear as $s = 2$ stationary components from sun-synchronous orbit. *Forbes et al.* [2001a] went on to extend upper-level (70 km) tidal fields from the NASA Ames Mars GCM [*Haberle et al.*, 1993] into the thermosphere, showing that a number of nonmigrating tidal modes contribute significantly to the longitude structure of Mars' thermosphere. In summary, the effects of Mars' extreme topography extend throughout the atmosphere. Our understanding of this interesting aspect of Mars upper atmosphere will soon be greatly advanced when the NASA Ames Mars GCM is fully coupled with the Mars Thermosphere GCM [*Bougher et al.*, 2000; *S. Bougher*, private communication]. At present, the effects of nonmigrating tides on the mean circulation, thermal structure and compositional structure of the thermosphere remains largely unknown.

4. WAVES AND MEAN-FLOW INTERACTIONS IN VENUS' ATMOSPHERE

The atmosphere of Venus contains a cloud layer between about 45 and 70 km consisting primarily of sulfuric acid solution. Through UV images from Pioneer Venus, various planetary-scale waves have been observed to exist at the Venus cloud tops [*Del Genio and Rossow*, 1990; *Rossow et al.*, 1990]. These include diurnal and semidiurnal migrating (sun-synchronous) tides, a mid-latitude 5-day wave with zonal wavenumber s = 1, and an equatorially-trapped 4-day Kelvin wave with $s = 1$. In keeping with our treatments of wave coupling in the atmospheres of Earth and Mars, we mainly confine ourselves here to tides and IGWs and their roles in vertical coupling and maintaining the mean circulation of Venus.

4.1. Tides

As noted above, solar thermal tides have been observed in Pioneer Venus UV images of Venus' cloud tops. After sorting temperature soundings from the Pioneer Venus orbiter infrared radiometer (OIR) measurements in solar-fixed coordinates, these data are also able to provide information on the solar thermal tides from about 55 km to 110 km in Venus' atmosphere [*Schofield and Taylor*, 1983]. A sample plot for the equatorial region is provided in Figure 9. A clear semidiurnal variation is revealed with increasing amplitude from the cloud tops to about 95 km, and phase progression with height consistent with an eastward-propagating oscillation forced at the lower heights. Above 100 km the os-

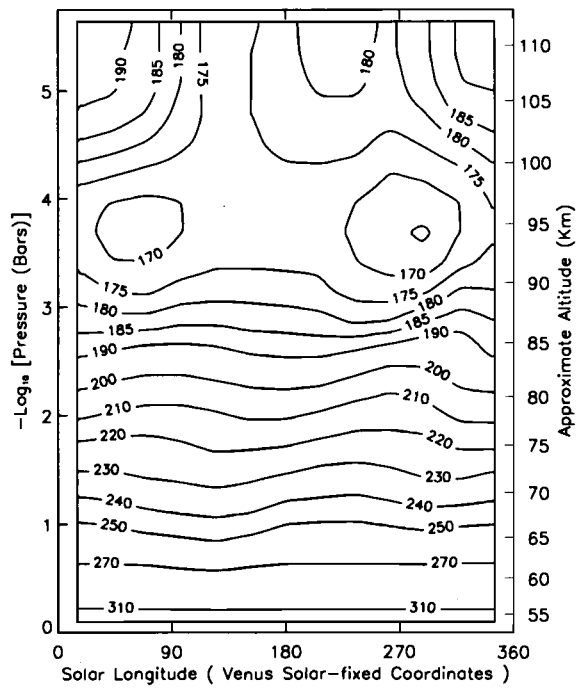

Figure 9. Temperature field for Venus' atmosphere vs. solar longitude, averaged between 0°-30°N latitude (Schofield and Taylor, 1983), based on data from the Orbiter Infrared Radiometer (OIR) on Pioneer Venus. Noon is zero longitude. Data are from Schofield and Taylor (1983).

cillation becomes more diurnal in character, consistent with the influence of increased solar radiation absorption at these levels.

Pechmann and Ingersoll [1984] simulated the Venusian tides with a linearized primitive equation model, and contributed to an improved understanding of the above measurements. First, they showed that on Venus the main propagating diurnal and semidiurnal tides were characterized by vertical wavelengths near 7 km and 30 km, respectively. The amplitude and phase structures for the semidiurnal tidal temperatures were in good agreement with the OIR measurements, indicating that the thermal forcing was reasonably specified. And, although the diurnal component of heating was much larger than the semidiurnal component, the amplitudes of the responses were similar. As we might expect from similar situations on Earth and Mars, forcing of the diurnal component is very inefficient since the depth of the heating region is much larger than the 7 km vertical wavelength of the oscillation, leading to destructive interference. Further, the weighting functions for the OIR retrievals had half-widths close to 7 km, which means that the propagating diurnal tide was washed out in the retrieval process. This is why the diurnal tide is not visible below 95 km in Figure 9. Subsequent modeling efforts relating to tides on Venus were mainly devoted to resolution of the super rotation problem. These contributions are discussed in that context in subsection 4.3.

4.2. Gravity Waves

The existence of gravity waves in the atmosphere of Venus is well established from UV images of clouds [i.e., *Rossow et al.*, 1980], temperature [i.e., *Seiff et al.*, 1980] and wind [*Counselman et al.*, 1980] profiles, and radio occultation measurements [*Hinson and Jenkins*,1995]. *Seiff et al.* [1992] provides an excellent review with a number of references. A data set representative of the general features is provided in Figure 10, which illustrates filtered temperature measurements between 35 and 90 km from one of 3 radio occultation experiments conducted at Venus from the Magellan spacecraft in October, 1991 [*Hinson and Jenkins*, 1995]. The data were obtained near (67° N, 127° E) at a local time of 22 hours. The left panel shows the temperature oscillations remaining with vertical wavelengths < 12 km after digital filtering. The larger-scale features in Figure 10 above 60 km were found to persist on consecutive orbits, suggesting thermal tides as a possible origin. However, their vertical wavelengths are too short to be associated with the first symmetric semidiurnal tide ($\lambda_z \sim$ 30 km). However, similar to the situation on Earth described previously, this oscillation, if it is a semidiurnal tide, may reflect one or more higher-order modes excited through nonlinear interaction between the gravest semidiurnal mode and the zonal mean wind structure on Venus.

The right panel in Figure 10 shows the oscillations remaining after high-pass filtering for wavelengths < 4 km; these oscillations are thought to represent the presence of gravity waves with the effects of thermal tides removed. *Hinson and Jenkins* [1995] applied gravity wave theory to this data set, and demonstrated the general consistency of the data with expectations from theory. The dashed curve in the right panel of Figure 10 represents the expected envelope based on gravity wave theory including radiative damping, which accounts for the decrease in amplitude above 65 km. The momentum flux divergence associated with this damping (cf. Figure 3) is sufficiently large to contribute to the decrease with height in the zonal wind speed that is believed to

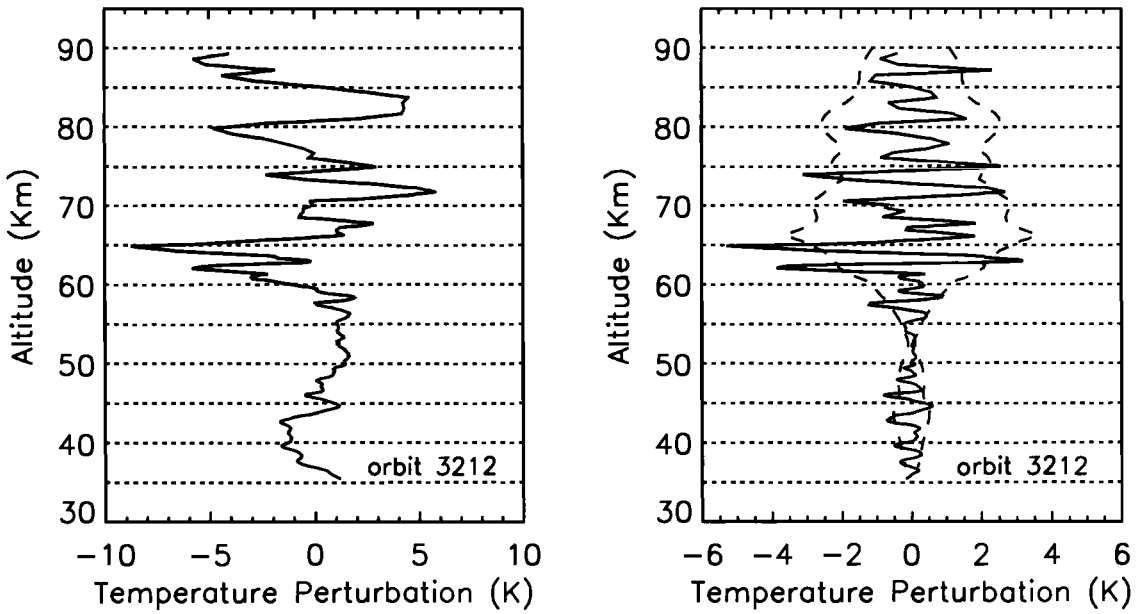

Figure 10. Filtered temperature measurements from one of 3 radio occultation experiments conducted at Venus from the Magellan spacecraft in October, 1991. These data were obtained near (67°N, 127°E) at a local time of 22 hours. The left panel shows the temperature oscillations remaining with vertical wavelengths < 12 km after digital filtering. The right panel shows the oscillations remaining after filtering for wavelengths < 4 km. The dashed curve represents the expected envelope based on gravity wave theory including radiative damping, which accounts for the decrease in amplitude above 65 km. Adapted from figures in Hinson and Jenkins (1995).

occur above the cloud tops (cf. following subsection and Figure 11).

The propagation characteristics of gravity waves in Venus' atmosphere and their potential effects on the zonal mean acceleration have been addressed in several other works [*Schubert and Walterscheid,* 1984; *Hou and Farrell,* 1987; *Leroy and Ingersoll,* 1994]. The ubiquitous appearance of gravity waves in Venus' atmosphere is not disputed; however, the absolute magnitude and relative importance of several excitation mechanisms are uncertain. Generation mechanisms often mentioned are associated with convection near the surface, the region of small static stability between 15 to 30 km, or within the cloud layer; shear instability; and topography.

4.3. The Superrotation Problem

The most prominent aspect of Venus' atmospheric circulation is its zonal retrograde superrotation. Venus rotates once every 243 days, or at a speed of 1.8 ms^{-1}. A rough depiction of the atmospheric rotational speed is provided in Figure 11 (bottom left) . The equatorial atmospheric wind speed increases from about 20 ms^{-1} at 20 km to almost 100 ms^{-1} near the cloud-top level at 65-70 km, decreasing perhaps to 20 ms^{-1} at 100 km. Thus, the atmosphere near the cloud tops is rotating about 50 times faster than the planet; this is sometimes referred to as the "4-day rotation". The latitude variation of the zonal wind speed can be inferred from temperature measurements assuming cyclostrophic balance [*Newman et al.,* 1984; *Walterscheid et al.,* 1985], or by observing cloud movements [*Rossow et al.,* 1990]. A rough depiction is provided in Figure 11 (upper left). At cloud tops, the zonal mean wind is sometimes observed to remain fairly constant from the equator to middle latitudes, and then to decrease to zero at the pole. Sometimes a "mid-latitude" jet is observed at middle to high latitudes, similar to that displayed in Figure 11.

In the altitude region between about 60-90 km, polar temperatures are warmer than in the tropics [*Schubert et al.,* 1980], whereas radiative equilibrium temperatures [*Crisp,* 1989] are up to 60K(10K) cooler(warmer) in the polar(equatorial) region. Similar to the need to

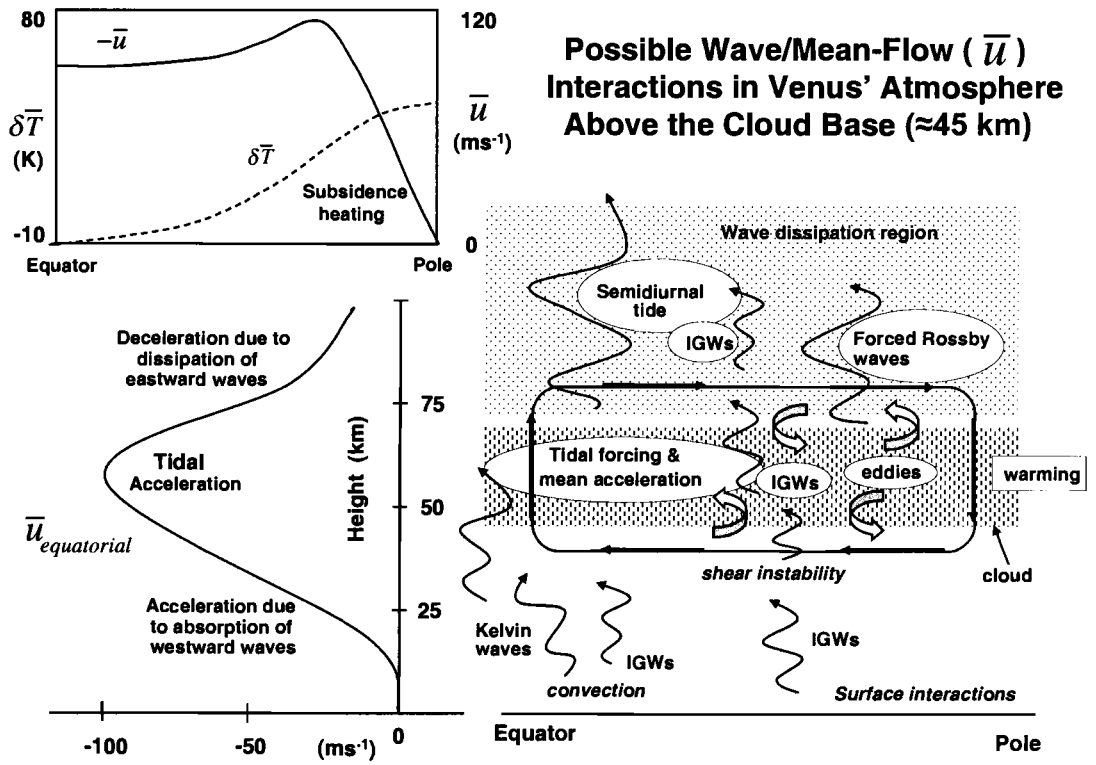

Figure 11. Schematic illustrating possible wave/mean-flow interactions in Venus' atmosphere above the cloud base. The upper left panel roughly depicts the latitude variation of the zonal mean retrograde wind near 65 km, similar to that derived from temperature measurements assuming cyclostrophic balance (Newman et al., 1984). This depiction includes a jet near 50-60° latitude which is sometimes seen in these data. Also included is the estimated temperature departure from radiative eqilibrium between 70 and 90 km (Imamura, 1997). The panel in the lower left roughly depicts the zonal mean retrograde wind profile at the equator, extrapolated from interferometric tracking of Pioneer Venus probes below 60 km (Counselman et al., 1980), and inferences based on latitudinal temperature gradients between 70 and 90 km (i.e., Schubert et al., 1980).

explain warm winter temperatures in the mesosphere of Mars and cold summer temperatures in Earth's mesosphere, it appears that a meridional circulation is necessary to provide the needed subsidence heating and adiabatic cooling implied by the above. Figure 11 (upper left) also shows a rough depiction of the departures δT from radiative equilibrium based on those illustrated in *Imamura* [1997].

The dynamics of the circulation system that maintains the superrotation of Venus' atmosphere has been the study of a number of works over the past 20 years. Much of the relevant physics occurs within the cloud layer (≈45-70 km) where most of the solar radiation is absorbed. The solar heating drives a "Hadley" circulation, i.e., rising motions near the equator, poleward motions near the top of the heating region, sinking motions at middle latitudes, and a return flow somewhere near the cloud base. Although this circulation can carry angular momentum upward into the region of equatorial superrotation maximum, it also carries it poleward leaving a deficit of angular momentum at the equator. Thus, a momentum source appears to be required in the equatorial-heating region to provide the observed high zonal winds. In addition, departures from zonal symmetry ("eddies") serve to transport momentum and heat and act in concert with the thermally-driven Hadley circulation to determine the meridional flow. The wave types thought to affect the mean zonal circulation above the cloud base are also depicted in Figure 11.

Following the laboratory experiments of *Fultz et al.* [1959] wherein a 'moving flame' heating the bottom of an annulus was shown to force a mean flow in the direction opposite to the flame movement, *Schubert and Whitehead* [1969] (see also *Schubert,* [1983]) suggested

that a similar mechanism operated on Venus. However, this theory required diffusive transport of mean momentum, which is unlikely to be very efficient > 50 km above the surface of Venus. *Fels and Lindzen* [1974] first recognized how solar thermal tides could provide the required westward acceleration at low latitudes in the region of maximum heating without the need for diffusion. They recognized, first of all, that a more generalized version of *Eliassen and Palm's* [1961] second theorem (Equation 2) is

$$\frac{d}{dz}(\rho_0 \overline{u'w'}) = -\frac{\kappa \rho_0}{(u_0 - c)} \overline{DJ} \qquad (8)$$

where $D = \frac{\zeta'}{H} + \frac{p'}{p_0}$, ζ' is a vertical displacement for small perturbations, H is the scale height, $\kappa = \frac{\gamma - 1}{\gamma}$ where γ is the ratio of specific heats $\frac{c_p}{c_v}$, J is the heating rate, and other parameters retain their previous definitions. *Eliassen and Palm* [1961] assumed J = 0. *Fels and Lindzen* [1974] further showed that the flux divergence within the heating region must accelerate the fluid within the heating region in a direction opposite to c. For the case at hand, migrating diurnal and semidiurnal tides are eastward-propagating on Venus, and thus can be expected to produce westward accelerations in the heating regions, and eastward accelerations (deceleration of the mean flow) at higher levels where propagating waves dissipate. Fels and Lindzen also showed how the joint excitation of propagating and trapped diurnal tides can lead to a horizontal redistribution of momentum within the heating region.

Following *Fels and Lindzen's* [1974] work, a series of modeling efforts followed in an attempt to obtain quantitative verification of "tidal acceleration" as the primary driver for Venus' superrotation. *Hou* [1984] and *Walterscheid et al.* [1985] performed diagnostic studies that supported regions of tidal acceleration/deceleration at the equator. The more quantitative numerical simulations that followed [i.e., *Baker and Leovy,* 1987; *Hou et al.,* 1990; *Newman and Leovy,* 1992; and references contained therein] verified these diagnostic studies. In particular, the *Newman and Leovy* [1992] study found that the interaction between trapped and diurnal tides introduced latitudinal spreading of the zonal flow as anticipated by *Fels and Lindzen* [1974]. Dissipation of the 4-day (westward-propagating) Kelvin wave has also been suggested to supply the westward momentum to maintain superrotation at low latitudes [*Leovy,* 1973], and this source may be comparable to that of the semidiurnal tide [*Del Genio and Rossow,* 1990]. However, due to lack of knowledge concerning forcing of this wave, it has not been included in wave/mean-flow interaction simulations as the semidiurnal tide.

In addition to accounting for superrotation, a number of studies focused on explaining the mid-latitude jet and polar temperatures in the 65-80 km region that were observed to be in excess of radiative equilibrium values (see Figure 11, upper left). *Walterscheid et al.* [1985] argued that poleward transport of momentum by the Hadley cell fed the midlatitude jet, and suggested its magnitude to depend on the strength of the Hadley circulation. *Hou and Goody* [i.e., 1989, and references therein] calculated what eddy momentum sources, in combination with realistic heating, would be required to maintain a prescribed zonal flow, including one that included a mid- to high-latitude jet. In addition to equatorial tidal sources similar to those anticipated by *Fels and Lindzen* [1974] to maintain superrotation, the need for midlatitude sources of momentum were implied to account for the latitudinal structure of the zonal mean wind. A diagnosis by *Imamura* [1997] indicates that the 5-day internal Rossby wave might provide the midlatitude momentum fluxes implied by the *Hou et al.* [1990] study, and to facilitate the poleward heat transport needed to raise and maintain high-latitude temperatures above radiative equilibrium between 60 and 90 km. However, the possible role of gravity waves providing this momentum flux divergence cannot be entirely ruled out. (Note the analogy here with "pumping" of the Hadley circulation by thermal tides in the upper atmosphere of Mars, thus providing subsidence heating required to account for elevated temperatures in the polar winter.) Tide/mean-flow interactions have also been shown to produce a jet ($\sim 120\ ms^{-1}$) at about 40° latitude [*Newman and Leovy,* 1992].

It is important to note that all of the above numerical studies required some "background" superrotation to exist at the cloud base. Thus, other mechanisms are required to provide superrotation from about 10 km to 45 km. As noted by *Leovy* [1973] and *Walterscheid et al.* [1985], Kelvin waves could provide some of this forcing at equatorial latitudes. It is not unreasonable to assume that convective and boundary-layer processes would produce a spectrum of Kelvin waves much in the same way as on Earth. *Hou and Farell* [1987] argue that gravity waves play an important role in maintaining superrotation below the cloud base through critical level absorption. Some of the waves with eastward phase speeds, on the other hand, are probably dissipated above the cloud tops (probably by radiative damping), and thus contribute to deceleration of Venus' superrotation between 65 and 90 km [*Schubert and Wal-*

terscheid, 1984; *Leroy and Ingersoll,* 1994; *Hinson and Jenkins,* 1995].

Most of the processes discussed above have been incorporated into the schematic of Figure 11. The reader should recognize that these processes need to be quantified and that only some of those indicated in Figure 11 may turn out to be key, while other potential wave sources may be omitted. Nevertheless, the gross general picture that is depicted is probably reasonable.

CONCLUDING REMARKS

In the present work we have concentrated mainly on the roles of gravity waves and thermal tides in coupling different atmospheric regimes together on Earth, Mars and Venus. On all of these planets, data are severely lacking in the ~60-150 km height regime where most of these waves dissipate and modify the mean circulations and thermal structures of these planets. In this regard, the situation for Earth is greatly improving with measurements from UARS and the anticipated contributions of the TIMED (Thermosphere - Ionosphere - Mesosphere Energetics and Dynamics) Mission.

The effects of waves on the middle atmosphere and thermosphere of Mars are especially profound. It is likely that nonmigrating tides introduce strong longitudinal variations in Mars' thermospheric structure, with obvious manifestations in atomic oxygen and other minor species concentrations, as well as emissions. These oxygen variations in turn modulate the CO_2 cooling rate leading to net as well as temporal modifications of temperature. The possible existence of traveling planetary waves including normal modes remains to be explored both observationally and in a modeling context. The effects and importance of gravity waves on the upper atmosphere of Mars is virtually unknown; certainly, the extreme topography and active near-surface meteorology of the planet argues for a rich spectrum of gravity waves. On Mars the greatest contributions to gravity wave dissipation may arise from radiative damping or molecular dissipation, as opposed to breaking. Even so, the intense dynamics that exists across a broad range of scales in the 50-100 km region on Mars may serve to mix constituents in manner similar to that of large-scale turbulence. Measurements that address both large-scale and small-scale dynamics over a full range of local times in the 60-150 km height region are desperately needed to understand this regime of the atmosphere, to constrain general circulation models, and to provide reliable models for aerobraking, aerocapture and descent operations in future missions to Mars.

Existing evidence indicates that the general circulation of Venus below 100 km is determined by how waves interact with the thermally driven Hadley circulation. It appears that westward-propagating gravity waves and Kelvin waves may play an important role in maintaining a retrograde circulation (superrotation) below the cloud base (≈45 km). The role of thermal tides excited within the cloud layer in maintaining superrotation in the equatorial region and deceleration of the retrograde flow above the cloud tops (65 km) is well established. The mid-latitude extent and intensity of the Hadley circulation between 45 and 80 km seems to be controlled by eddy flux divergences due to the 5-day wave and possibly gravity waves. All of these processes have important effects on the photochemistry and transport of clouds. The manner in which the mid-latitude 5-day wave and the equatorial 4-day wave remain interlocked to form "Y" features in the clouds remains to be solved. Deceleration of the jet at higher levels is probably due to dissipation of a number of eastward-propagating waves, including thermal tides, planetary waves and gravity waves. However, the impact of all of these waves on the overlying thermosphere remains unknown. In order to advance our understanding of the dynamics of Venus' atmosphere, future missions must provide measurements of temperature and winds from the surface to > 100 km, at scales ranging from 10's to 1,000's of km, with good local time coverage. Future development of a lower and middle atmosphere GCM that can eventually be coupled with the existing thermosphere GCM of *Bougher et al.* [2000] is also essential for achieving substantive progress.

Finally, while this chapter focused on vertical coupling by tides and gravity waves in terresrial planetary atmospheres, a diminished importance of these waves in other planetary atmospheres, or of the potential importance of planetary waves, should not be inferred. A brief list of gravity wave observations in the giant planetary atmospheres was provided in subsection 2.2. Other studies of gravity waves and tides for Jupiter include those of *Hickey et al.* [2000], *Matcheva et al.* [2000] and *Houben and Gierasch* [1977], for example. The potential roles of Kelvin waves and forced planetary waves in the atmosphere of Venus were noted briefly in subsection 4.3. Stationary planetary waves are known to play an important role in the dynamics of Mars' middle atmosphere [*Hollingsworth and Barnes,* 1996], as is well established for Earth. By extension of these examples, we may well expect from future data analyses and missions that forced and free planetary waves will reveal themselves as equally important components of

planetary atmosphere dynamics throughout our solar system.

Acknowledgments.

This work was supported in part by Grants NAG5-8266 and NAG5-11167 from the NASA Mars Data Analysis Program to the University of Colorado.

REFERENCES

Andrews, D.G., Holton, J.R., and C.B. Leovy, *Middle Atmosphere Dynamics,* Academic Press, New York, pp489, 1987. Apt, J., and J. Leung, Thermal periodicities in the Venus atmosphere, Icarus, 49 , 427-437, 1982.

Angelats i Coll, M., and J.M. Forbes, Nonlinear interactions in the upper atmosphere: The $s = 1$ and $s = 3$ nonmigrating tides, J. Geophys. Res., in press, 2001.

Baker, N.L., and C.B. Leovy, Zonal winds near Venus' cloud top level: a model study of the interaction between the zonal mean circulation and the semidiurnal tide, *Icarus, 69,* 202-220, 1987.

Banfield, D., Conrath, B., Pearl, J.C., Smith, M.D., and P. Christensen, Thermal tides and stationary waves on Mars as revealed by Mars global Surveyor thermal emission spectrometer, *J. Geophys. Res., 105,* 9521-9537, 2000.

Barnes, J.R., Possible effect of breaking gravity waves on the circulation of the middle atmosphere of Mars, *J. Geophys. Res., 95,* 1401-1421, 1990.

Bougher, S.W., Ridley, E.C., Fesen, C.G., and R.W. Zurek, Mars mesosphere and thermosphere coupling: Semidiurnal tides, *J. Geophys. Res., 98,* 3281-3295, 1993.

Bougher, S.W., Engel, S., Roble, R.G., and B. Foster, Comparative terrestrial planet thermospheres 3. Solar cycle variation of global structure and winds at solstices, *J. Geophys. Res., 105,* 17,669-17,692, 2000.

Chapman, S. and R. Lindzen, *Atmospheric Tides,* Gordon & Breach, New York, N.Y., 1970.

Conrath, B.J., Influence of planetary-scale topography on the diurnal thermal tide during the 1971 Martian dust storm, *J. Atmos. Sci., 33,* 2430-2439, 1976.

Counselman, C.C. III, Gourevitch, S.A., King, R.W., and G.B. Loriot, Zonal and meridional circulation of the lower atmosphere of Venus determined by radio interferometry, *J. Geophys. Res., 85,* 8026-8030, 1980.

Crisp, D., Radiative forcing of the Venus mesosphere, II, *Icarus, 7,* 391-413, 1989.

Dai, A., and J. Wang, Diurnal and semidiurnal tides in global surface pressure fields, *J. Atmos. Sci., 56,* 3874-3891, 1999.

Del Genio, A.D., and W.B. Rossow, Planetary-scale waves and the cyclic nature of cloud top dynamics on Venus, *J. Atmos. Sci., 47,* 1990.

Deming, D., Mumma, M.J., Espenal, F., Kostuik, T., and D. Zipoy, Polar warming in the middle atmosphere of Mars, *Icarus, 66,* 366-379, 1986.

Ekanayake, E.M.P., Aso, T., and S. Miyahara, Background wind effect on propagation of nonmigrating diurnal tides in the middle atmosphere,*J. Atmos. Solar-Terr. Phys., 59,* 401-429, 1997.

Eliassen, A., and E. Palm, On the transfer of energy in stationary mountain waves, *Geofys. Publikasjoner, 22,* 1-23, 1961.

Fels, S.B., and R.S. Lindzen, The interaction of thermally excited gravity waves with mean flows, *Geophys. Fluid Dyn., 6,* 149-191, 1974.

Forbes, J.M., Atmospheric Tides 2. The solar and lunar semidiurnal components, *J. Geophys. Res., 87,* 5241-5252, 1982.

Forbes, J.M., Physics of the Mesopause Region, in *Solar-Terrestrial Physics: Principles and Theoretical Foundations,* edited by R.L. Carovillano and J.M. Forbes, D. Reidel Publishing Company, 1983.

Forbes, J.M., Wave coupling between the lower and upper atmosphere: case study of an ultra-fast Kelvin wave, *J. Atmos. Solar-Terr. Phys., 62,* 1603-1621, 2000.

Forbes, J.M., and M.E. Hagan, Diurnal Kelvin wave in the atmosphere of Mars: Towards an understanding of 'stationary' density structures observed by the MGS accelerometer,*Geophys. Res. Lett., 27,* 3563-3566, 2000.

Forbes, J.M., A.C. Bridger, M.E. Hagan, J. Hollingsworth, J. Murphy and G. Keating Nonmigrating tides in the Thermosphere of Mars, paper presented at the Western Pacific Geophysics Meeting, Tokyo, Japan, June, 2000, and submitted to *J. Geophys. Res., 2001a.*

Forbes, J.M., Zhang, X., and M.E. Hagan, Simulations of diurnal tides due to tropospheric heating from the NCEP/NCAR Reanalysis Project, *Geophys. Res. Lett., in press, 2001b.*

Forbes, J.M., Zhang, X., Talat, E.R., and W. Ward, Nonmigrating diurnal tides in the thermosphere, *J. Geophys. Res., submitted, 2001c.*

Forbes, J.M., Roble, R.G., and C.G. Fesen, Acceleration, heating, and compositional mixing due to upward propagating tides,*J. Geophys. Res., 98,* 311-321, 1993.

Forget, F., Hourdin, F., Fournier, R., Hourdin, C., Talagrand, O., Collins, M., Lewis, S.R., Read, P.L., and J.-P. Huot, Improved general circulation models of the Martian atmosphere from the surface to above 80 km, *J. Geophys. Res., 104,* 24,155-24,176, 1999.

French, R.G., and P.J. Gierasch, Waves in the Jovian upper atmosphere, *J. Atmos. Sci., 31,* 1707-1712, 1974.

Fultz, D., Long, R., Owens, G., Bohan, W., Kaylor, R., and J. Weil, Studies of thermal convection in a rotating cylinder with some implications for large-scale atmospheric motions, *Meteor. Monogr., 4,* 36-39, 1959.

Garcia, R., and S. Solomon, The effect of breaking gravity waves on the dynamics and chemical composition of the mesosphere and lower thermosphere, *J. Geophys. Res., 90,* 3850-3868, 1985.

Haberle, R.M., Pollack, J.B., Barnes, J.R., Zurek, R.W., Leovy, C.B., Murphy, J. R., Lee, H., and J. Schaeffer, Mars atmospheric dynamics as simulated by the NASA-Ames general circulation model I. The zonal-mean circulation, *J. Gephys. Res., 98,* 3093-3124, 1993.

Hagan, M.E., Comparative effects of migrating solar sources on tidal signatures in the middle and upper atmosphere, *J. Geophys. Res., 101,* 21,213-21,222, 1996.

Hamilton, K., The effect of solar tides on the general circulation of the Martian atmosphere, *J. Atmos. Sci., 39,* 481-485, 1982.

Hays, P.B., Abreu, V.J., Dobbs, M.E., Gell, d.A., Grassl, H.J., and W.R. Skinner, The High Resolution Doppler Imager on the Upper Atmosphere Research Satellite, *J. Geophys. Res., 98,* 10,713-10,723, 1993.

Hedin, A.E., Fleming, E.L., Manson, A.H., Schmidlin, F.J., Avery, S.K., and S.J Franke, *Empirical wind model for the middle and lower atmosphere - Part 1: Local time average,* NASA Tech. Mem. 104581, Goddard Space Flight Center, Greenbelt, Maryland, pp. 85, 1993.

Held, I.M., and A.Y. Hou, Nonlinear axially symmetric circulations in a nearly inviscid atmosphere, *J. Atmos. Sci., 37,* 515-533, 1980.

Hickey, M.P., Walterscheid, R.L., and G. Schubert, Gravity wave heating and cooling in Jupiter's thermosphere, *Icarus, 148,* 266-281, 2000.

Hinson, D.P., and J.M. Jenkins, Magellan radio occultation measurements of atmospheric waves on Venus, *Icarus, 114,* 310-327, 1995.

Hinson, D.P., and J.A. Magalhães, Inertio-gravity waves in the atmosphere of Neptune, *Icarus, 105,* 142-161, 1993.

Hinson, D.P., Simpson, R.A., Twicken, J.D., and G.L. Tyler, Initial results from radio ocultation measurements with Mars Global Surveyor, *J. Geophys. Res., 104,* 26,997-27,012, 1999.

Hinson, D.P., Tyler, G.L., Hollingsworth, J.L., and R.J. Wilson, Radio occultation measurements of forced atmospheric waves on Mars, *J. Geophys. Res., 106,* 1463-1485, 2001.

Hong, S.-S. and R.S. Lindzen, Solar semidiurnal tide in the thermosphere, *J. Atmos. Sci., 33,* 135-153, 1976.

Hou, A.Y., Axisymmetric circulations forced by heat and momentum sources: a simple model applicable to the Venus atmosphere, *J. Atmos. Sci., 41,* 3437-3455, 1984.

Hou, A.Y., and B.F. Farrell, Superrotation induced by critical-level absorption of gravity waves on Venus: An assessment, *J. Atmos. Sci., 44,* 1049-1061, 1987.

Hou, A.Y., and R.M. Goody, Further studies of the circulation of the Venus atmosphere, *J. Atmos. Sci., 46,* 991-1001, 1989.

Hou, A.Y., Fels, S.B., and R.M. Goody, Zonal superrotation above Venus' cloud base induced by the semidiurnal tide and the mean meridional circulation, *J. Atmos. Sci., 47,* 1894-1901, 1990.

Houben, H. and P.J. Gierasch, Tides in the atmospheres of the giant planets, *Bull. Amer. Astron. Soc., 9,* 510, 1977.

Imamura, T., Momentum balance of the Venusian midlatitude mesosphere, *J. Geophys. Res., 102,* 6615-6620, 1997.

Imamura, T., and T. Ogawa, Radiative damping of gravity waves in the terrestrial planetary atmospheres, *Geophys. Res. Lett., 22,* 267-270, 1995.

Keating, G.M. et al., The structure of the upper atmosphere of Mars: in-situ accelerometer measurements from Mars Global Surveyor, *Science, 279,* 1672-1676, 1998.

Kieffer, H.H., Jakosky, B.M., and C.W. Snyder, The planet Mars: from antiquity to the present, in *Mars,* University of Arizona Press, Tucson, Arizona, 1-33, 1992.

Leovy, C.B., Rotation of the upper atmosphere of Venus, *J. Atmos. Sci., 30,* 1218-1220, 1973.

Leovy, C.B., Control of the homopause level, *Icarus, 50,* 311-321, 1982.

Leovy, C.B., and R.W. Zurek, Thermal tides and Martian dust storms: direct evidence for coupling, *J. Geophys. Res., 84,* 2956-2968, 1979.

Leroy, S.S., and A.P. Ingersoll, Convective generation of gravity waves in Venus' atmosphere: Gravity wave spectrum and momentum transport, *J. Atmos. Sci., 52,* 3717-3737, 1994.

Lindzen, R.S., The application and applicability of terrestrial atmospheric tidal theory to Venus and Mars, *J. Atmos. Sci., 27,* 536-549, 1970.

Lindzen, R.S., Atmospheric tides, Lectures in *Applied Mathematics, 14,* 293-362, 1971.

Lindzen, R.S., Turbulence and stress owing to gravity wave and tidal breakdown, *J. Geophys. Res., 86,* 9707-9714, 1981.

Lindzen, R.S., *Dynamics in Atmospheric Physics,* Cambridge University Press, New York, pp310, 1990.

Matcheva, K.I., Strobel, D.F., and F.M. Flasar, Interaction of gravity waves with ionospheric plasma: Implications for Jupiter's ionosphere, *Icarus, 152,* 347-365, 2001.

Mayr, H.G., Harris, I., and W.D. Pesnell, Properties of thermospheric gravity waves on Earth, Mars and Venus, *Venus and Mars: Atmospheres, Ionospheres, and Solar Wind Interactions,* Geophysical monograph Series, American Geophysical Union, Washington, D.C., 430pp, 91-112, 1992.

McLandress, C., On the importance of gravity waves in the middle atmosphere and their parameterization in general circulation models, *J. Atmos. Solar-Terr. Phys., 60,* 1357-1383, 1998.

Miyahara, S., Zonal mean wind induced by vertically propagating atmospheric tidal waves in the lower thermosphere, *J. Meteorol. Soc. Japan, 56,* 86-97, 1978.

Miyahara, S., and D.H. Wu, Effects of solar tides on the zonal mean circulation in the lower thermosphere: Solstice condition, *J. Atmos. Terr. Phys., 51,* 635-648, 1989.

Miyahara, S., Miyoshi, Y., and K. Yamashita, Variations of migrating and nonmigrating tides simulated by the middle atmosphere circulation model at Kyushu University, *Adv. Space Res., 24,* 1549-1558, 1999.

Newman, M., and C. Leovy, Maintenance of strong rotational winds in Venus' middle atmosphere by thermal tides,*Science, 257,* 647-650, 1992.

Newman, M., Schubert, G., Kliore, A.J., and I.R. Patel, Zonal winds in the middle atmosphere of Venus from Pioneer Venus radio occultation data, *J. Atmos. Sci., 41,* 1901-1913, 1984.

Pechmann, J.B., and A.P. Ingersoll, Thermal tides in the atmosphere of Venus: Comparison of model results with observations, *J. Atmos. Sci., 41,* 3290-3313, 1984.

Reber, C.A., Trevathan, C.E., McNeal, R.J., and M.R. Luther, The Upper Atmosphere Research Satellite (UARS) mission, *J. Geophys. Res., 98,* 10,643-10,647, 1993.

Roques, F., et al., Neptune's upper stratosphere, 1983-1990: Ground-based stellar occulatation observations III. Temperature profiles, *Astron. Astrophys., 288,* 985-1011, 1994.

Rossow, W.B., Del Genio, A.D., Limaye, S.S., Travis, L.D., and P.H. Stone, Cloud morphology and motions from Pioneer Venus images, *J. Geophys. Res., 85,* 8107-8128, 1980.

Rossow, W.B., Del Genio, A.D., and T. Eichler, Cloud-tracked winds from Pioneer Venus OCPP images, *J. At-*

mos. Sci., 47, 2053-2084, 1990.

Schneider, E.K., Martian great dust storms: Interpretive axially symmetric models, *Icarus, 55,* 302-331, 1983.

Schofield, J.T., and F.W. Taylor, Measurements of the mean, solar-fixed temperature and cloud structure in the middle atmosphere of Venus, *Quart. J. Roy. Met. Soc., 109,* 57-80, 1983.

Schubert, G.,et al., Structure and circulation of the Venus atmosphere, *J. Atmos. Sci., 85,* 8007-8025, 1980.

Schubert, G., *General circulation and the dynamical state of the Venus atmosphere,* Venus, D. M. Hunten, L. Colin, T.M. Donahue and V.I. Moroz, Eds., University of Arizona Press, 1143 pp., 1983.

Schubert, G., and R.L. Walterscheid, Propagation of small-scale acoustic-gravity waves in the Venus atmosphere, *J. Atmos. Sci., 41,* 1202-1213, 1984.

Schubert, G., and J. Whitehead, Moving flame experiment with liquid Mercury: Possible implications for the Venus atmosphere, *Science, 163,* 71-72, 1969.

Seiff, A., and D.B. Kirk, Structure of the atmosphere of Mars in summer at midlatitudes, *J. Geophys. Res., 82,* 4364-4378, 1977.

Seiff, A., Kirk, D.B., Young, R.E., Blanchard, R.C., Findlay, J.T., Kelley, G.M., and S.c. Summer, Measurements of thermal structure and thermal contrasts in the atmosphere of Venus and related dynamical observations: Results from the four Pioneer Venus probes, *J. Geophys. Res., 85,* 7903-7933, 1980.

Seiff, A., Kirk, D.B., Knight, T.C.D., Young, R.E., Mihalov, J.D., Young, L.A., Milos, F.S., Schubert, G., Blanchard, and D. Atkinson, Thermal structure of Jupiter's atmosphere in the north equatorial belt near the edge of the 5-micron hot spot, *J. Geophys. Res., 103,* 22,857-22,889, 1998.

Seiff, A., Young, R.E., Haberle, R., and H. Houben, *The evidences of waves in the atmospheres of Venus and Mars, Venus and Mars: Atmospheres, Ionospheres, and Solar Wind Interactions,* Geophysical monograph Series, American Geophysical Union, Washington, D.C., 430pp, 73-89, 1992.

Shepherd, G.G., et al., WINDII: The Wind Imaging Interferometer on the Upper Atmosphere Research Satellite, *J. Geophys. Res., 98,* 10,725-10,750, 1993.

Talaat, E.R., and R.S. Lieberman, Nonmigrating diurnal tides in mesospheric and lower thermospheric winds and temperatures, *J. Atmos. Sci., 56,* 4073-4087, 1999.

Veverka, J., Wasserman, L.H., Elliot, J., Sagan, C., and W. Liller, The occultation of beta-Scorpii by Jupiter: I. The structure of the Jovian upper atmosphere, *Astron. J., 79,* 73, 1974.

Walterscheid, R.L., Schubert, G., Newman, M., and A.J. Kliore, Zonal winds and the angular momentum balance of Venus' atmosphere within and above the clouds, *J. Atmos. Sci., 42,* 1982-1990, 1985.

Wilson, R.J., A general circulation model simulation of the Martian polar warming, *Geophys. Res. Lett., 24,* 123-127, 1997.

Wilson, R.J., Evidence for diurnal period Kelvin waves in the Martian atmosphere from Mars Global Surveyor TES data, *Geophys. Res. Lett., 27,* 3889-3892, 2000.

Wilson, R.J., and K, Hamilton, Comprehensive simulation of thermal tides in the artian atmosphere, *J. Atmos. Sci., 53,* 1290-1326, 1996.

Wilson, R.J., and M.I. Richardson, The Martian atmosphere during the viking Mission, I, Infrared measurements of atmospheric temperatures revisited, *Icarus, 145,* 555-579, 2000.

Zurek, R.W., Diurnal tide in the Martian atmosphere, *J. Atmos. Sci., 33,* 321-337,1976.

Zurek, R.W., Atmospheric tidal forcing of the zonal mean circulation: the Martian dusty atmosphere, *J. Atmos. Sci., 43,* 652-670,1986.

Zurek, R.W., Free and forced modes in the Martian atmosphere, *J. Geophys. Res.,93,* 9452-9462, 1988.

Zurek, R.W., and R.M. Haberle, Zonally symmetric response to atmospheric tidal forcing in the dusty Martian atmosphere, *J. Atmos. Sci., 45,* 2469-2485, 1988.

Zurek, R.W., and C.B. Leovy, Thermal tides in the dusty Martian atmosphere: A verification of theory, *Science, 213,* 437-439, 1981.

Jeffrey M. Forbes Department of Aerospace Engineering Sciences University of Colorado, Boulder, CO 80309 (e-mail: forbes@zeke.colorado.edu)

Exospheres and planetary escape

Donald M. Hunten

Lunar and Planetary Laboratory, The Univesity of Arizona, Tucson, Arizona

A summary is given of the theory of an exosphere, the outermost region of an atmosphere where collisions can usually be neglected, and of escape of its lighter constituents. Special cases, such as energy-limited hydrodynamic loss, are briefly discussed. Surface-bounded exospheres are treated in Chapter III.3. The exospheres and escape processes and rates of the eight planets and three satellites with exospheres are individually discussed.

1. INTRODUCTION

The exosphere is the uppermost part of an atmosphere, the region in which collisions are so infrequent that for many purposes they can be neglected. If some atoms (or molecules) have enough energy to escape, this is their source region, and those that are bound can be regarded as executing independent orbits. It is conventional and useful to define the base of the exosphere as the level where the mean free path is equal to the scale height. Its normal name is "exobase", although in the older literature the term "critical level" is used. Because of the long mean free path, vertical temperature gradients cannot exist. The classic exosphere lies above a much deeper atmosphere with which it exchanges rapidly. Its lower regions should therefore share the same energy distribution. However, at altitudes comparable to or greater than the planetary radius the velocity distribution is not isotropic and is therefore substantially non-Maxwellian, with greater and greater departures at greater and greater altitudes. The exospheres of Mercury and many satellites, including the Moon, are bounded by the surface, and their velocity distributions depend on incompletely-understood interactions of atoms and surfaces.

The theory of thermal escape was formulated in 1905 by Jeans. It was refined by Chamberlain and Smith [1971] and Brinkmann [1971] to take account of the partial depletion by escape of the more energetic atoms. A comprehensive discussion appears in the reviews by Fahr and Shizgal [1983] and Shizgal and Arkos [1996]. Measurements from planetary missions made it clear that there are a number of important nonthermal escape processes. Terrestrial examples, approximately as important as the thermal one, are charge exchange between a hot proton and a thermal H atom, in which the identities are interchanged but the kinetic energies nearly unaffected, and escape of hot protons along open polar magnetic-field lines. The energy distributions in surface-bounded exospheres are poorly-understood and controversial. Some atoms may be in thermal equilibrium with the local surface, but it is clear that most are suprathermal, at least on the Moon. An important loss process is ionization by solar photons or fast electrons, followed by sweep-up in the solar wind or corresponding magnetospheric winds for satellites of the Jovian planets. The standard reference for exospheric structure is Chamberlain [1963], most of which is included in the text by Chamberlain and Hunten [1987]. Summaries of escape include Hunten and Donahue [1967] (for the terrestrial planets); Hunten et al [1989], Hunten [1990] (with a historical emphasis) and Chamberlain and Hunten [1987].

Atmospheres in the Solar System: Comparative Aeronomy
Geophysical Monograph 130

10.1029/130GM12

2. EXOSPHERES

The definition of the exobase, as already mentioned, sets the mean free path equal to the scale height H. If the total number density is n_c and the collision cross

section Q (typically 3×10^{-15} cm^2), then n_c Q H = 1. For Earth, the number density is typically 10^8 cm^{-3} (principally O atoms), and the value for most other planets and satellites is similar; the corresponding altitude at Earth is 450-500 km. An important property of an exosphere is its temperature, which for the Earth is typically 1000 to 1300 K, depending on solar activity, and with a diurnal variation of 200 – 300 K.

The ordinary derivation of the barometric equation depends on the existence of hydrostatic equilibrium and therefore on the dominance of collisions. However, all that is really needed is the presence of a Maxwellian velocity distribution at all altitudes [Chamberlain and Hunten, 1987]. If the energy distribution is Maxwellian at the exobase, it remains so, with the same temperature, at higher altitudes because, as slower atoms are filtered out by gravity, they are replaced by those that were originally faster but have been slowed down. However, as discussed below, in the absence of any collisions the velocity distribution at higher and higher altitudes departs from Maxwellian because some directions are missing from the distribution: the speed distribution is Maxwellian but the velocity distribution is not. The total neglect of collisions in the exosphere is an approximation; it is so good for many purposes that it is easy to forget that it is not good for many others. This point is extensively discussed by Fahr and Shizgal [1983] and Shizgal and Arkos [1996] who discuss various approaches to the problem of the gradual transition from the collision-dominated region below the exobase to the exosphere where collisions are rare but still do occur.

The most widely used model of the density distribution in an exosphere is that of Chamberlain [1963], summarized in Chamberlain and Hunten [1987]. It uses the approximation of an exobase, and classifies the atoms according to their orbits as ballistic, escaping and orbiting. If there were to be a complete Maxwellian at all altitudes it would be necessary to include incoming atoms with the same flux as the escaping ones. There would also have to be a full population of satellite particles, but since their orbits do not intersect the exobase they must be absent in a fully collisionless exosphere. The density of each component is expressed as the product of a *partition function* and the barometric density.

The population of satellite atoms is a complex matter, discussed by Chamberlain [1963] and Fahr and Shizgal [1983]. Observations suggest that they are essentially absent from the Earth's exosphere. Chamberlain suggested that they might be handled by the assumption of a satellite critical level, so that any orbit that intersected this level would be populated, while any that did not would be vacant. As Fahr and Shizgal discuss, it is still very difficult to specify the level. The processes that can populate satellite orbits are slow, and the loss processes are more rapid; they include photoionization, perturbation by solar gravity, and charge exchange with solar-wind protons for orbits that extend far from the Earth. The absence of a substantial number of satellite particles is therefore reasonable.

The exobase nearly coincides with the thermopause, the upper boundary of the thermosphere, above which the atmosphere becomes isothermal. It is the level above which few solar photons are absorbed, and has an optical depth ~1 for the EUV wavelength region. The corresponding absorption cross section is smaller by a factor of ~10 than the collision cross section that enters into the definition of the exobase. Understanding and modeling of exospheric temperature therefore requires modeling of the thermosphere. The standard model of this temperature profile includes heating by production and loss of ionospheric electrons and ions, and downward conduction to the mesopause where the heat can be radiated. Part of the heat can also be radiated from the lower thermosphere. As summarized by Chamberlain and Hunten [1987], this model is fairly successful for the terrestrial planets and some satellites but fails miserably for the Jovian planets whose high temperatures require the presence of a large additional heat source. Fortunately we have good measurements: by various orbiters for the terrestrial planets, and by ultraviolet (UV) and radio occultations in the outer solar system. The UV measurements [Smith and Hunten, 1990] actually give height profiles of individual constituents in a height region that includes the exobase, from which its temperature and altitude are derived. Typical properties for the planets and some satellites are tabulated in Chapter I.1. Several suggestions for the Jovian heat source were discussed by Hunten [1976]: precipitation of soft electrons; dissipation of wave energy from below; meteor impact; and ion drag. One problem with the second and third of these is that the energy is produced at too low an altitude, close to the mesopause so that it does not have to be conducted far before it can be radiated. Ion drag is likely to spin up the neutral atmosphere to the speed of the ions, after which the energy dissipation goes away. Soft electrons do deposit their energy at a high altitude and were discussed by Hunten and Dessler [1977], but they had to postulate a source in the magnetosphere. Dissipation of gravity waves had already been suggested by French and Gierasch [1974] and was revived by Young et al [1997], but Matcheva and Strobel [2000] have pointed out that these treatments neglect the downward heat transport

that must accompany the dissipation of the mechanical energy. This paper includes a useful summary of earlier work in the area.

Objects with water ice on their surfaces are expected to have atmospheres containing oxygen, produced by charged-particle sputtering or photolysis of water vapor. Hydrogen will escape rapidly from bodies the size of the Galilean satellites or smaller, laving oxygen behind. These matters are discussed in Chapter III.3.

Lateral flow occurs in an exosphere as a consequence of lateral temperature differences at the exobase or winds in the thermosphere beneath. Before the importance of nonthermal escape processes for the Earth was realized, it was felt that the dayside abundance of H would be depleted by the more rapid escape, and a number of papers discussed the resulting lateral flow [Hanson and Patterson, 1963; McAfee, 1967; Patterson, 1970; Hodges and Johnson, 1968; Hodges, 1973]. Here we follow the abbreviated discussion in Chamberlain and Hunten [1987].

The basic nature of exospheric flow can be regarded as a random walk of individual atoms "bouncing" off the exobase. In fact, such an atom will usually penetrate this level and be replaced by a new one from beneath, but the effect is the same. In the presence of a temperature gradient the height-integrated flux is proportional to $T^{5/2}$, a result that can be understood as follows: the amount of gas in a column above the exobase is proportional to the scale height $H = kT/mg$; the range of each hop is also proportional to H; and the speed is proportional to $T^{1/2}$. It appeared that the steady state was close to zero net ballistic flux, or ZNBF, and that the number density thus varied as $T^{-5/2}$. The implication is that the ballistic transport due to the temperature differences is faster than any competing process.

Large-scale thermospheric winds can drive a concentration of light atoms in the downwind direction. The first known example of the phenomenon is the terrestrial "winter helium bulge" discussed below in the Earth section. In the winter hemisphere, gas at high altitudes flows toward the cold pole, then descends. The height-integrated flux of an element is proportional to its scale height, and the result is a concentration of helium (and atomic oxygen) over the region where the heavier gases descend. A similar phenomenon occurs with hydrogen on Venus, where the thermospheric flow runs from day to night and produces a large "hydrogen bulge" on the night sde, discussed below in section 6.

3. ESCAPE

The following summary of the various known escape processes is based on Chamberlain and Hunten [1987] and Hunten et al. [1989]. The thermal process was formulated by Jeans in 1905 and was the only one known until space-age measurements called attention to the others discussed below. It is convenient to formulate thermal escape in terms of the escape variable λ, the ratio of gravitational to thermal energies (Chapter I.1, Eq. 6). The value of λ at the exobase is λ_c, and the escape flux is BF_J where F_J, the Jeans flux, is defined in Chapter I.1 (Eq. 3) as $F_{esc}(r_{exobase})$. B is a factor of order 0.5 that allows for the partial depletion of the high-energy tail of the velocity distribution. An extensive discussion of $B = F/F_J$ may be found in Fahr and Shizgal [1983]. A typical value of λ_c for H at Earth is 10 and the corresponding flux is $\sim 10^8$ atoms cm^{-2} sec^{-1}. For O, the major constituent at the exobase, λ_c is 16 times greater and the thermal escape flux is totally negligible. If the reference level in the Jeans equation is taken elsewhere than the exobase, substitution of the barometric equation replaces the number density and λ in the exponential by their values at the new level, so the escape flux is almost unchanged. This example illustrates that, for thermal escape, the definition chosen for the exobase level makes little difference to the predicted results.

A list of suprathermal processes is given in Hunten [1982] and is reproduced in Chamberlain and Hunten [1987] and Hunten et al. [1989]. Nearly all of them involve ions in one way or another; examples important for the Earth are charge exchange between a fast proton and a slow H atom, in which the identities are exchanged but the velocities unaffected, and escape of ions along open magnetic-field lines. Other important processes include dissociative recombination of a molecular ion, yielding two fast neutral atoms, one of which is likely to be directed upwards, and creation of an ion in the solar wind or the magnetospheric wind of a Jovian planet. Sputtering by impact of fast heavy ions with the surface is certainly an important source; but a similar process acting on the atmosphere can also be a sink. Both are important for the Galilean satellites of Jupiter, and sputtering from the surface is strongly supported as an atmospheric source for the Moon and Mercury by some workers. It has not been discussed for other medium-sized satellites, but could possibly be significant. The book by Johnson [1990] is devoted to a thorough discussion of sputtering, and a summary appears in Chapter III.3.

The actual escape rate of hydrogen from the Earth and a few other bodies is diffusion-limited: it is controlled, not by the processes at the exobase, but by diffusion through the region just above the homopause. This result was embodied in a number of early mod-

els [see Hunten, 1990], but was explicitly formulated in Hunten [1973]; see also Hunten [1990] and Hunten et al. [1988]. The limiting flux is the flux that would traverse the region above the homopause if the number density of the escaping atom at the exobase were zero; it cannot be exceeded but can be closely approached even if this density is nonzero. Its value is given, to a good approximation, by

$$F_\ell = bf/H,$$

where b is the ratio of the diffusion coefficient D to the total number density n_a, f is the mixing ratio of the escaping gas, and H is the scale height, both just above the homopause. The density at the exobase adjusts itself so that the active escape processes give a flux equal to F_ℓ.

Hydrodynamic escape, or blowoff, can occur if the escaping constituent is also the major one, and if other conditions to be discussed are satisfied. It was first studied in the context of Io's atmosphere and of putative hydrogen-rich primitive atmospheres, but appears to apply also to the contemporary atmosphere of Pluto. The first attempt to apply solar-wind theory to the planetary case was the model of primitive Venus by Kasting and Pollack [1983], summarized in Chamberlain and Hunten [1987]. Simultaneous solution of the heat and dynamical equations is extremely difficult, and the most widely-quoted models of solar wind get around this problem by inserting an assumed temperature profile. This is not possible for the planetary case, and Kasting and Pollack were only able to approximate the correct solution. They found one that has a subsonic velocity at infinite distances, while it is almost certain that this velocity should be supersonic. Fortunately, it is expected that the flux of the subsonic solution should not be much smaller than the correct one, and this expectation is confirmed by Trafton's results for Pluto, discussed below.

For blowoff to occur, the temperature must be high enough to yield a small value of λ, and there must be enough solar energy to drive the flow — the flux is energy-limited. The energy that is available to drive the flow is derived from solar extreme ultraviolet, the spectral region that is most strongly absorbed. Watson et al. [1981] were the first to formulate blowoff driven by solar EUV and apply it to primitive Earth and Venus. The rapid outward flow cools the gas by adiabatic expansion, and this cooling must be offset by the absorbed solar energy. Instead of a complete solution, these authors obtain an upper bound to the flux, expressed as a pair of equations that are readily solved numerically. A simple formulation for the energy-limited flux appears in Hunten et al. [1987]. A complete solution for Pluto has been obtained by Trafton and is discussed below in the Pluto subsection. Interesting possibilities occur in the case of possible primitive atmospheres. If the hydrodynamic escape flux of hydrogen is rapid enough, it can drag away heavier gases, including noble gases [Hunten et al. 1987; Sasaki and Nakazawa, 1988]. The result can be interesting elemental and isotopic fractionation effects, that resemble those found in the terrestrial planets [Pepin, 1991].

4. EARTH

The exobase height is typically around 450 km; the principal constituent is atomic oxygen and the escape is dominated by atomic hydrogen. Deuterium and helium also escape, principally by suprathermal processes. The exospheric temperature varies strongly with solar activity and also has a diurnal variation of ~200 K. The dayside value can be as high as 1500 K, but a more typical range is 900 – 1200 K. The diurnal variation leads to a corresponding variation in the thermal escape flux. A number of early studies attempted to treat the resulting asymmetry, taking account of the lateral flow from the night to the day side. With the discovery of the nonthermal escape processes this asymmetry became much less likely, and indeed most observations seem consistent with ZNBF, the nero net ballistic flux already mentioned.

Wind-induced diffusion was discovered in the form of the Keating "winter helium bulge" discussed by Johnson [1973]. In the winter hemisphere, gas at high altitudes flows toward the cold pole, then descends. Such flow towards lower pressures does not occur at lower altitudes, because gas is forced by the Coriolis acceleration to flow at right angles to the pressure gradient. Near and within the exosphere the viscosity is large enough to permit the flow to be towards the low pressures that correspond to the low temperatures of the polar night. Because of their large scale heights, the fluxes of helium and atomic oxygen are large, and they accumulate in the polar region.

Escape of hydrogen from the Earth (as well as Venus and Mars) is discussed by Hunten and Donahue [1976], Fahr and Shizgal [1983] and Shizgal and Arkos [1996]. The principal processes are thermal, charge exchange, and ion escape along open magnetic field lines at high latitude ("polar wind"). The fast protons that participate in the charge exchange belong to the plasmasphere, a hot extension of the upper ionosphere. At high latitudes these ions can escape directly, but at lower latitudes they cannot escape because they are on closed

lines of the magnetic field; they can only escape after picking up an electron. Thus, the geographic regions where the two suprathermal processes can operate are complementary.

On average, the thermal and suprathermal processes are of approximately equal importance, but the thermal varies with exospheric temperature, which changes considerably with solar activity. Since the total flux is diffusion-limited and therefore constant, the suprathermal fluxes fall when the thermal rises. The number density of H at the exobase varies to achieve this result. This prediction was compared against two sets of observed data by Liu and Donahue [1974]. Their figure (reproduced as Fig. 4 of Hunten and Donahue [1976]) shows excellent agreement between the thermal fluxes estimated as discussed here and those obtained by use of the Jeans equation with observed temperature and H density. Table 1 of Hunten and Donahue [1976] shows the partitioning among the three escape processes for a range of exospheric temperatures.

Conditions at the exobase are such that hydrogen is in diffusion-limited flow while the deuterium flux is limited by the actual escape processes. The efficiencies of charge exchange and polar wind are essentially the same for both isotopes, but thermal escape is much less for D. The result is that the flow of D is not diffusion-limited, and the D/H ratio should be enhanced in the exosphere above its value in the lower atmosphere. Such an enhancement, by a factor of 6 near 300 km, was found by Breig et al. [1987]. Detailed modeling of these data by Breig and Hanson [1991] showed that the fluxes exceed those for thermal escape by factors of ~5 for H and in excess of 500 for D. These results are in excessent agreement with the picture outlined above. The data were obtained during 1974, a period of low solar activity and low exospheric temperature; the thermal flux was small and the suprathermal components were therefore large in comparison.

Hydrogen must flow to the exobase from the low atmosphere where its principal form is water vapor. At higher altitudes it appears in compounds such as OH, HO_2, HO_2, and H_2, and eventually as H. The H_2O abundance in the stratosphere is strongly limited by condensation and precipitation; details may be found in Hunten and Donahue [1976] and Hunten [1990]. The true situation is even more complicated, but this description suffices for the present purpose. The "cold trap" at the tropopause transmits an H_2O abundance of ~4 parts per million by volume (ppmv). It is supplemented by small amounts of methane and molecular hydrogen, so that the total mixing ratio of H atoms is f = 12 ppmv. At considerably higher altitudes the molecules of water vapor and methane are photolyzed and further reactions generate H, OH and HO_2, collectively called "odd hydrogen" because they contain an odd number of H atoms. Near the mesopause the principal form is H. There is also a significant quantity of H_2 which is converted to H atoms by reaction with atomic oxygen in the hot upper thermosphere. In the equation above for limiting flux, the diffusion parameter b is 1.46×10^{19} cm^{-1} sec^{-1} at 208 K and the scale height H is 6.2 km; the limiting flux is then $F_\ell = 2.8\times10^8$ cm^{-2} sec^{-1}, in good agreement with values deduced from observations.

Helium loss has a long, tortuous history described by Hunten [1990]. Attempts were made to deduce the exospheric temperature by use of the budgets of the two isotopes ^{3}He and ^{4}He, but as these budgets became better defined it was clear that they could not be reconciled in this way. Instead, the most significant loss process for both isotopes is the polar wind, escape of ions along open lines of the magnetic field [Axford, 1968; Johnson and Axford, 1969]. These papers give budgets for the two isotopes; ^{4}He is generated in the crust by radioactive decay and ^{3}He is mainly from auroral precipitation which in turn comes from the solar wind. Smaller contributions arise from cosmic rays, both by spallation of atmospheric atoms and precipitation of ^{3}He and tritium which decays into helium. The lifetime of helium in the atmosphere is $\sim 10^6$ years.

It was noticed by Brown [1949] and Suess [1949] that the mixing ratios of the heavier noble gases in the Earth's atmosphere are much smaller than in the primitive solar nebula. The bulk of our atmosphere can therefore not be a remnant of this nebula. It later became clear that the lighter noble gases and the lighter isotopes of each were substantially depleted relative to the heavier ones, when compared with gases in carbonaceous chondrites [see Pepin, 1989]. These effects can be quantitatively explained by the mass fractionation that occurs in hydrodynamic escape [Hunten et al., 1987; Sasaki and Nakazawa, 1988]. Pepin [1991] has generated several scenarios that account for the noble-gas compositions of Venus, Earth and Mars as well as the gases trapped in meteorites. It is necessary to assume very large initial endowments of hydrogen, either trapped from the solar nebula or in the form of H_2O that can be dissociated. The early Sun must also have radiated a much greater flux of ionizing UV radiation to provide the energy need to drive the flow. Such large fluxes have in fact been observed from many young stars of the T Tauri class; the major issue is whether the solar nebula itself would have absorbed this radiation before it could reach the planets. It cannot be said that fraction-

ation in hydrodynamic escape has been proved to have occurred, but it explains many observed facts that were previously unexplained. An alternative explanation has been proposed by Owen and Bar-Nun [2000]: that the fractionated noble gases were delivered by comets. This idea will only be testable when we have actual data on these objects.

5. VENUS

The atmosphere of Venus, like that of Mars, is dominated by the radiatively active gas CO_2 and therefore has a much lower exospheric temperature than the Earth. Because of the slow rotation, the night side is even colder, slightly more than 100 K. There is no thermosphere on this side; it has been called a "cryosphere" instead. This structure is summarized by Chamberlain and Hunten [1987] and more detail may be found in Hunten et al. [1983, 1989]. The dayside exospheric temperature of 300 – 330 K is too low for thermal escape even of hydrogen to be important [Hunten and Donahue, 1976; Donahue et al., 1997]. The dominant nonthermal processes are discussed below.

The huge temperature difference between day and night produces a huge pressure difference that drives a wind system that reaches nearly the speed of sound over the terminators. One result is a "hydrogen bulge", which is observed at a local time of ~3 a.m. The displacement from the antisolar region is thought to be the result of a rotation of the upper atmosphere with a period of ~6 days. The simplified discussion of the bulge in Chamberlain and Hunten [1987] predicts a rather small size by equating the speed of its outward diffusion with the speed of the converging winds. Perhaps the point at which the flow converges and descends varies with time.

A striking fact is a large enrichment of deuterium; the D/H ratio is 150 times its value on Earth. The original endowment of water must therefore have been at least 150 times the present value. In the likely case that D has escaped as well as H, this endowment would have been much greater. We return to ideas of atmospheric evolution below after discussing the present state.

The chapter by Donahue et al. [1997] concentrates on the evolution of H and D; the discussion of the actual escape processes occurs towards the end. The rate of the principal escape process for H is greater than that for D by just the factor required to explain the observed isotope ratio. Details may be found in Hodges [1999]. Hartle et al. [1996] showed that data from Pioneer Venus were sufficient to define the escape fluxes of H and D, averaged over the planet and over a solar cycle. In the upper part of the ionosphere there is an upward electric field that keeps electrons from escaping and supports half the weight of the dominant positive ions. For H and D ions this force is stronger than gravity; they are accelerated upwards and may escape. This process is most important in the nightside hydrogen bulge, which contains both neutrals and ions, and the loss rate, averaged over the planet and the solar cycle, is estimated to be 9×10^6 cm^{-2} sec^{-1}. Next most important is charge exchange between H atoms and hot protons, with a mean flux of 8×10^6 cm^{-2} sec^{-1}. Earlier estimates of the H flux based on remote-sensing data [Paxton et al., 1988] have been discussed by Donahue [1999]; the more recent value is consistent with the idea that the water now found in the atmosphere could have entered it as recently as half a billion years ago, consistent with the idea of a global volcanic resurfacing [Grinspoon, 1993].

The remarkable D/H ratio has encouraged many studies of atmospheric evolution, reviewed by Donahue et al. [1997]; a brief account may be found in Hunten [1993]. Several workers have sought to show that the observed hydrogen is the residue of a primitive "ocean", a quantity of water similar that that on the Earth. This scenario is certainly allowed by the observations but is not required. It is attractive because Earth and Venus have similar amounts of carbon dioxide and nitrogen and might be expected to have been endowed with similar amounts of water. The proximity to the Sun should have driven a "runaway greenhouse" in which a possible ocean would be totally evaporated: heat trapped by water vapor in a warm atmosphere would warm the ocean releasing still more vapor which would raise the temperature further. The end result could be an atmosphere containing all the water at a partial pressure ~270 bar. Photolysis could provide the hydrogen needed to drive a hydrodynamic escape. One such scenario was presented by Kumar et al. [1983]; after the hydrodynamic phase the escape would be by charge exchange on the day side, followed by a situation similar to the present where most of this charge exchange is in the region of the nightside bulge. In this rather old study direct escape of ions was not included; instead another mechanism was assumed, in which fast O atoms collided with H atoms giving them enough energy to escape.

Attractive though these ideas may be, the D/H ratio can alternatively be explained if the source of the observed water vapor is much more recent. The one that has received the most study is the impact of a modest number of large comets [Grinspoon and Lewis, 1988]. Such a source is viable because a steady state, with the observed D/H ratio, can be reached in a time considerably shorter than the age of the solar system.

6. MARS

The aeronomy of Mars is discussed by Chamberlain and Hunten [1987] and in more detail by Barth et al. [1992]. Escape is included in the review by Hunten and Donahue [1976]. Good models of the dayside exosphere were first produced on the basis of UV data from the Mariners and the in-situ entry measurements by the Viking Landers [Hanson et al., 1977]. At solar maximum the dayside exospheric temperature is 330 K and the exobase height 160 km ; the temperature at minimum is considerably less, ~220 K. A variation of ~60 K between aphelion and perihelion is predicted. The nightside temperature has not been observed, but is computed to be ~150 K [Bougher et al., 1999]. (Mars Global Surveyor has given excllent data for lower altitudes, but its measurement regime is well below the exosphere.) The H corona has been observed by UV spectrometers on Mariners 6, 7 and 9, and these results have permitted estimates of the thermal escape flux; inclusion of the Jeans ratio B = 0.5 gives 9×10^7 cm^{-2} sec^{-1}. Allowance for H_2 molecules would raise this value somewhat. The flux of both atoms and molecules is diffusion-limited and many of the molecules are converted to atoms by reaction with the ions O_2^+ and CO_2^+.

The day airglow of helium at 584 Å has been interpreted by Krasnopolsky and Gladstone [1996]. They infer a mixing ratio in the lower atmosphere of 4 ppmv and an escape rate of 7×10^{23} sec^{-1}. The principal loss process is ionization above the ionopause followed by sweeping out by the solar wind.

The gravity well of Mars is small enough to permit nonthermal escape processes that do not work on Earth and Venus, where instead they produce suprathermal coronae. An important one is dissociative recombination of a molecular ion such as N_2^+ [Brinkmann, 1971] or O_2^+ [McElroy 1972]above the exobase. A striking confirmation was obtained by the mass spectrometers on the Viking Landers, which found the ratio $^{15}N/^{14}N$ to be enhanced by a factor of 1.62 relative to the terrestrial value. The loss process itself is not appreciably isotopically selective because the atoms it produces are fast; the selectivity arises because of diffusive separation which enriches molecules containing the lighter isotope at the level where the ions recombine [Hunten, 1982]. Straightforward application of this process actually predicts too large an enhancement of the isotope ratio, and it is necessary to assume that the atmosphere was supplied with additional, unfractionated, nitrogen as the planet evolved; see for example, Fox and Hac [1997]. The D/H ratio is also enriched, by a factor of 6 [Owen et al., 1988], but no measurable enrichment has been found for carbon or oxygen. Because the suprathermal processes operate at about the same strength as for hydrogen and nitrogen, it may be concluded that the exchangeable reservoirs of carbon and oxygen are much larger.

It is easy to show that known processes can account for the enrichments of ^{15}N and D, but unique conclusions about the corresponding history do not seem to be possible. This question is reviewed by Owen [1992]. The initial endowment of nitrogen was probably about 2 mbar and could have been greater (the current partial pressure is 0.13 mbar). The enrichment of the D/H ratio can be explained if the amount of water that exchanges with the atmosphere is less than is believed to reside in the polar caps, so it may be that such exchange between various reservoirs is inefficient.

Even though there is no measurable modification of the isotopic composition of oxygen, there is another matter of interest. When McElroy [1972] first computed the escape flux, he noticed that it was almost exactly half the hydrogen flux: that is, water is escaping. He pointed out a feedback mechanism in the photochemistry near the surface that would adjust the hydrogen flux to maintain this ratio. More detailed studies by Liu and Donahue [1976] and McElroy and Yung [1976] confirmed this. However, Fox [1993a] showed that McElroy's estimate of the O escape flux is too large, because many instances of the dissociative recombination of O_2^+ lead to excited states and the kinetic energy of the fragments is too small to permit escape. Since the arguments for the O loss rate to be half that of H are still valid, one or more additional processes are required, and Fox suggested escape of ions and sputtering. O^+ ions created in the solar wind can be accelerated downstream and escape, or planetary gravity can force them to collide with other atoms in the upper atmosphere, giving them enough energy to escape. These processes had been studied for Venus, where the larger gravity makes them less important for escape, and applied to Mars by Luhmann et al. [1992]. Fox [1993b] has also studied similar processes for the escape of nitrogen.

As discussed above for the Earth, the elemental and isotopic compositions of the noble gases show strong signs that fractionation in hydrodynamic escape occurred on Mars. These compositions were measured by instruments on the Viking Landers and have been refined by laboratory analysis of gases trapped in SNC meteorites. This analysis was first used to confirm the hypothesis that these meteorites are indeed Martian. The scenarios proposed by Pepin [1991] are compatible with, though somewhat different from, those for the Earth.

Another process that is likely to have been important in the early history of Mars is erosion of the atmosphere

by large impacts. As for the suprathermal escape processes discussed above, the low escape velocity makes this process possible at Mars but not Earth or Venus. It was proposed and discussed by Melosh and Vickery [1989] and a summary appears in Hunten et al. [1989]. It seems likely that Mars may have lost all but 1% of its original atmosphere, and that there is no elemental or isotopic fractionation.

7. MERCURY, MOON

These exospheres differ from the classic ones in that their lower boundary is a surface rather than an exobase that is in a state close to thermodynamic equilibrium and rapidly exchanges with the region below. Hydrogen and helium suffer rapid thermal loss; heavier atoms are also rapidly lost by ionization followed by sweep-up in the solar wind. The principal issues are the nature of the interaction of atoms with the surface, the mechanisms by which they are released from the surface, and their energy distribution. All these matters are discussed in Chapter III.3.

8. JOVIAN PLANETS

The exospheres of Jupiter, Saturn, Uranus and Neptune are composed of H_2 and He, with much smaller amounts of H. All are subject to diffusive separation. Their structure, as observed by the Voyager UVS, is summarized in Smith and Hunten [1990]. As discussed above, the exospheric temperatures are high, 700 – 1000 K for Jupiter, 420 K for Saturn, 800K for Uranus and 750 K for Neptune. The heating mechanism is unknown, but precipitation of magnetospheric electrons and ions seems to be a likely candidate. There is little doubt that auroral precipitation at high latitudes is important, especially at Jupiter, but whether the corresponding heat can be transported to lower latitudes needs to to studied in detail.

The gravity of Uranus is small enough that there is a significant density of H atoms at the rings. It is expected that the drag on small ring particles is enough to carry them slowly into the atmosphere [Broadfoot et al, 1986; Herbert et al., 1987].

With the deep gravity wells, exospheric temperatures are not high enough for thermal escape from any of these planets to be significant. Nonthermal processes could be significant as sources of atoms to the environment, but any effects on the remaining atmospheres such as isotopic fractionation are almost impossible because of the huge amounts of gases.

A principal component of the ionospheres is expected to be H_3^+ [Atreya, 1986]. That this ion has been observed in Jupiter's magnetosphere [Hamilton et al., 1980] implies that there is some escape mechanism, but its nature is unknown.

9. IO AND ITS PLASMA TORUS

Io and its atmosphere are unique in our solar system. It seems to have lost all the normal volatiles, leaving SO_2 as the principal one. The appearance and behavior are dominated by geysers and other volcanic activity, driven by tidal heating [Nash et al., 1986]. Atmospheric atoms and molecules escape rapidly from the satellite but are still bound to Jupiter, going into orbit and forming a torus that envelops Io's orbit. Almost the same region is occupied by a plasma of ions and electrons; the plane of the plasma torus is inclined by 7 degrees to Io's orbital plane. The electrons rapidly ionize the neutral cloud and the new ions find themselves caught up in Jupiter's magnetic field, whose rotation imposes a relative velocity of 55 km/sec. As these fresh ions collide with the ambient ones, they share their energy and heat the whole torus to a temperature of around 4 eV or 50,000 K. The co-rotating ions smash into the trailing face of Io and sputter surface materials into the atmosphere and the torus. Both are rich in SO_2 which is abundant on the surface. Many of the sputtered molecules enter a suprathermal corona which is available for further sputtering. Another prominent constituent is Na, which can be observed from Earth and was the first constituent to be discovered (1974) by R.A. Brown. The outward extension of the torus to the other Galilean satellites forms an important part of their environments, discussed in Chapter III.3.

Because the neutral and plasma tori can be regarded as extensions of Io's exosphere and ionosphere, they are briefly discussed below. An excellent review is the chapter by Brown et al. [1983]; the satellite and its atmosphere are reviewed by Nash et al. [1986]and Spencer and Schneider [1996]; and a brief summary may be found in Chamberlain and Hunten [1987]. Studies of the mass budget of the torus require a source rate of 10^{28} atoms sec^{-1}, which translates into a flux from Io of 4×10^{10} atoms cm^{-2} sec^{-1}in global mean. It appears that this can be supplied by the two-stage sputtering process mentioned above, in which atoms and molecules populate an extended corona which then becomes a target for further sputtering [McGrath and Johnson, 1987]. Na atoms, which have been abundantly observed because they resonantly scatter solar photons, are unfortunately not ideal tracers because some of the ejection processes are not shared by other atoms and molecules.

The atmospheric SO_2 abundance and distribution have been studied from Earth by millimeter-wave spec-

troscopy [Lellouch et al., 1992]. The number density was found to be $10^{11} - 10^{12}$ cm^{-3}, which would put the exobase level at tens to hundreds of km. However, the gas seems to be patchy, consistent with sources in geyser plumes and sublimation of patchy snowdrifts. The temperature is 500 – 600 K. Another technique has been to deduce the vertical distribution of Na atoms by observing the shadow of Io's atmosphere on another satellite [Schneider et al., 1991]. The exobase height deduced in this way was less than 700 km but above the surface.

Because most of the SO_2 is expected to condense to the surface on the cold night side, there may be strong day-to-night winds [Ingersoll et al, 1985]. These may be moderated by the presence of O_2 produced in the photochemistry of SO_2 [Kumar, 1985]. This molecule has not been seen, because it lacks a dipole moment and is very difficult to observe remotely. The prediction is uncertain because the escape rate, as well as the production rate, are poorly understood.

Ejection of Na into the torus includes processes additional to the sputtering by torus ions mentioned above. The principal ionospheric ion is expected to be Na^+, because with the low ionization potential of the atom, other ions exchange charge with it and the recombination rate of an atomic ion is slow. Long before the discovery of the torus, Io had been found to be linked to the timing of intense decametric radio pulses, which had been discovered in the early years of radio astronomy after World War II. Goldreich and Lynden-Bell [1969] eventually proposed a model of Io as a unipolar inductor: an enormous current, generated by the relative motion of Io and Jupiter's magnetic field flows along the field lines connected to Io's sub-Jovian and anti-Jovian points. Although many details have since been added, the basic idea is still accepted. A potential drop of 411 kV exists across the satellite, and the enormous current flows through the ionosphere. Only recently [Wilson and Schneider, 1999] have these phenomena been linked to the ejection of matter. A jet of Na atoms springs from a region near the anti-Jovian point and perpendicular to Jupiter's magnetic field, just where the electric fild is vertical. Ionospheric Na^+ ions are accelerated up, and many of them exchange charge with the abundant Na atoms in Io's upper atmosphere. The resulting jet has been observed, not only from the ground, but by the camera on Galileo [Burger et al., 1999].

The plasma torus, briefly introduced above, occupies a region whose minor radius is roughly equal to that of Jupiter, and centered on Io's orbit except for the 7 degree inclination mentiond above. The following description ignores the internal structure and significant time variations. The ions are singly and multiply charged ones of S and O, with a couple of percent of Na. Ion and electron temperatures are around 4 eV or 50,000 K, a random velocity superposed on a near co-rotation with the planet. These ions bombard the backward face of Io and cause the ejection by sputtering mentioned above. The neutral atoms and molecules that escape Io go into orbits gravitationally bound to Jupiter and are rather quickly ionized by the torus electrons. Some, however, survive long enough to form a large banana-shaped cloud near Io whose Na component has been extensively studied by observations of scattered solar radiation.

A freshly-created ion finds itself subjected to Jovian magnetic-field lines sweeping past at 55 km/s. Its motion resembles a cycloid, the superposition of co-rotation and circular gyration. The latter component is damped out by collisions with other ions; the heated ions transfer energy to the electrons. Although these collisions are the principal source of energy to the system, detailed studies find a deficit. Wilson and Schneider [1999] suggest that the currents of the unipolar generator system may be another important source.

Ions are lost from the torus by diffusion, partially inwards but mainly outwards. They also can be neutralized and fly out to much greater distances in Jupiter's outer magnetosphere, where many of them are re-ionized. They can then diffuse back toward Jupiter, being energized in the process and forming a large fraction of the energetic plasma of the entire magnetosphere.

10. ICY GALILEAN SATELLITES

Europa, Ganymede and Callisto all have exposed water-ice on their surfaces and are bombarded by magnetospheric ions, especially those originating in the Io plasma torus. The atmospheres that result from these processes are discussed in Chapter III.3.

11. TITAN

Titan's atmosphere contains a large quantity of N_2 with a few percent of methane. Its exospheric temperature was measured by the Voyager UVS [see *Smith and Hunten*, 1990] and the thermal structure of its thermosphere and exosphere was modeled by Yelle [1991]. HCN, unlike the usual hydrocarbon radiators, has an electric dipole moment, with the consequence that its far-IR pure rotation band is an important radiator; the computed and observed exospheric temperatures agree well. Earlier work is reviewed by Hunten et al. [1984].

Photolysis of methane leads to the production of H_2 which is observed in the IR spectrum with a mix-

ing ratio of $\sim$ 0.1% and which escapes at a rate of 3.4×10^9 cm^{-2} sec^{-1}, accurately described by the diffusion limit. Nonthermal escape of other atoms is discussed by Hunten et al. [1984].

12. TRITON

Triton's upper atmosphere was observed by the Voyager UVS which found the major gas to be N_2, with small amounts of CH_4 and CO, and measured an exospheric temperature of 95 K [*Broadfoot* et al., 1989]. An ionosphere was also observed by radio occultaion. According to an analysis by Yelle et al. [1991] there is a thin troposphere, with the tropopause at $\sim$ 8 km surmounted by a thermosphere – there is no middle atmosphere. Heating of the thermosphere is by solar EUV and precipitation of magnetospheric particles, in a ratio of 1:2, and cooling by the rotational band of CO. The exospheric temperature is enough lower than that of Pluto to keep the escape out of the hydrodynamic regime. Studies of the upper atmosphere and ionosphere are reviewed by Strobel and Summers [1995]. The exobase height is 930 km and the escape fluxes of N and hydrogen are 9×10^9 and 9×10^{10} cm^{-2} sec^{-1} referred to the surface. As at Titan, the source of hydrogen atoms and molecules is photolysis of CH_4.

13. PLUTO

Pluto's exosphere is unlike any other in the contemporary solar system because it is undergoing energy-limited hydrodynamic escape. An early static model, based on results of a stellar occultation, estimated the radial distance of the exobase as greater than 3000 km (a height of 1820 km), but this estimate depends on the assumed temperature because the atmosphere is highly extended [Hubbard et al., 1988]. A detailed model by Trafton of the exosphere and the escape is described in Trafton et al [1997] and in the next paragraph. In such a model the exobase loses its usual significance, but the corresponding density level is at a radial distance of 4.5 Pluto radii.

The first discussion of escape from Pluto [Trafton, 1980] found a very large flux that would deplete the entire planet over geologic time. Hunten and Watson [1982] pointed out that it was not realistic to assume an isothermal exosphere because, as noted above, the large escape flux would cool it by adiabatic expansion. They adapted the treatment of Watson et al. [1981] and showed that the flux would be energy-limited to a much lower value. A detailed discussion of this and later treatments may be found in Traften et al. [1997]. Like the treatment by Hunten and Watson, those of Hubbard et al. [1990] and McNutt [1989] give upper limits to the flux, but the detailed model due to Trafton shows that these estimates are not far above the actual value. Details are shown in Table I of Trafton et al. [1997]; for a pure methane atmosphere the upper limits for the first three models are 4.7, 6.1 and 1.3 in units of 10^{10} cm^{-2} s^{-1}, while Trafton's model gives 2.1.

If the Trafton escape rate just discussed was maintained for the age of the solar system, the amount of surface material lost would amount to "a few kilometers". If the solar EUV flux declined as $10^8 t^{-5/6}$, as derived by Zahnle and Walker [1982], the amount would be greater by a factor $\sim$5. (t is time in years, with origin when the Sun reached the main sequesnce.).

14. CONCLUDING REMARKS

The solar system contains a remarkable variety of exospheres and escape processes. Although it is more than a century since the pioneering ideas of Stoney and almost a century since the publication of the Jeans equation, nearly all our knowledge was gained in the space age. Future space missions will undoubtedly lead to still further progress.

Acknowledgments. I thank Editor Michael Mendillo and the reviewers for valuable suggestions.

REFERENCES

Atreya, S.K., *Ionospheres and atmospheres of the outer planets and their satellites*, 224 pp., Springer Verlag, Berlin, 1986.

Axford, W.I., The polar wind and the terrestrial helium budget, *J. Geophys. Res., 73*, 6855 – 6859, 1968.

Barth, C.A., A.I.F. Stewart, S.W. Bougher, D.M. Hunten, S.J. Bauer and A.F. Nagy, Aeronomy of the current Martian atmosphere, in *Mars*, edited by H.H. Kieffer, B.M. Jakosky, C.W. Snyder and M.S. Matthews, pp. 1054 – 1089, University of Arizona Press, Tucson, 1992.

Bougher, S.W., S. Engel, R.G. Roble and B. Foster, Comparative terrestrial planet thermospheres 2. Solar cycle variation of global structure and winds at equinox, *J. Geophys. Res., 104*, 16,591 – 16,611, 1999.

Breig, E.L., S. Sanatani and W.B. Hanson, Deuterium in the daytime thermosphere, *J. Geophys. Res., 92*, 225 – 238, 1987.

Breig, E.L. and W.B. Hanson, Deuterium and hydrogen flows in the thermosphere, *J. Geophys. Res., 96*, 17,779 – 17,792, 1991.

Brinkmann, R.T., Mars: Has nitrogen escaped?, *Science, 174*, 944 – 945, 1971.

Broadfoot, A. L.; F. Herbert, J.B Holberg, D.M. Hunten, S. Kumar, B.R. Sandel, D.E. Shemansky, A.J. Dessler, S. Linick and R. Springer, Ultraviolet spectrometer observations of Uranus, *Science, 233*, 74 – 79.

Broadfoot, A.L. S.K. Atreya, J.L. Bertaux, J.E. Blamont, A.J. Dessler and S. Linick, Ultraviolet spectrometer observations of Neptune and Triton, *Science, 246*, 1459 – 1466, 1989.

Brown, H., Rare gases and the formation of the Earth's

atmosphere, in *The Atmospheres of the Earth and Planets*, edited by G.P. Kuiper, pp. 258 – 266, Univ. Chicago Press, 1949, 1952.

Brown, R.A., C.F. Pilcher, and D.F. Strobel, Spectrophotometric studies of the Io torus, in *Physics of the jovian magnetosphere*, edited by A.J. Dessler, pp. 197 – 225, Cambridge University Press, New York, 1983.

Burger, M.H., N.M. Schneider and J.K. Wilson, , Galileo's close-up view of the Io sodium jet, *Geophys. Res. Lett.*, *26*, 3333 – 3336, 1999.

Chamberlain, J.W., 1963, Planetary coronae and atmospheric evaporation, *Planet. Space Sci.*, *11*, 901 – 960.

Chamberlain, J.W. and D.M. Hunten, *Theory of Planetary Atmospheres*, 481 pp., Academic Press, Orlando, 1987.

Donahue, T.M., D.H. Grinspoon, R.E. Hartle and R.R Hodges, Jr., Ion/neutral escape of hydrogen and deuterium,: evolution of water, in *Venus II*, edited by S.W. Bougher, D.M. Hunten and R. J. Phillips, University of Arizona Press, Tucson, 1997.

Donahue, T.M., New analysis of hydrogen and deuterium escape from Venus, *Icarus, 141*, 226 – 235, 1999.

Fahr, H.J. and B. Shizgal, Modern exospheric theories and their observational relevance, *Rev. Geophys. Space Phys.*, *21*, 75 – 124, 1983.

Fox, J.L., On the escape of oxygen and hydrogen from Mars, *Geophys. Res. Lett.*, *20*, 47 – 50, 1993a.

Fox, J.L., The production and escape of nitrogen atoms from Mars, *J. Geophys. Res.*, *98*, 3297 – 3310, 1993b.

Fox, J.L. and Hac, A, The $^{15}N/^{14}N$ isotope fractionation in dissociative recombination of N_2^+, *J. Geophys. Res.*, *102*, 9191 – 9204, 1997.

French, R.G. and P. J Gierasch, Waves in the jovian upper atmosphere, *J. Atmos. Sci.*, *31*, 1707 – 1712, 1974.

Goldreich, P. and D. Lynden-Bell, Io, a Jovian unipolar inductor, *Astrophys. J.*, *156*, 59 – 78,1969

Grinspoon, D.H., Implications of the high D/H ratio for the sources of water in Venus' atmosphere, *Nature, 363*, 1702 – 1704, 1993.

Grinspoon, D.H. and J.S. Lewis, Cometary water on Venus: Implication of stochastic impacts, *Icarus, 74*, 21 – 35, 1988.

Hamilton, D.C., G. Gloeckler, S.M. Krimigis, C.O. Bostrom, T.P. Armstrong, W.I. Axford, C.Y. Fan, L.J. Lanzerotti. and D.M. Hunten, Detection of energetic hydrogen molecules in Jupiter's magnetosphere by Voyager 2: evidence for an ionospheric plasma source, *Geophys. Res. Lett.*, *7*, 813 – 816, 1980.

Hanson, W.B. and T.N.L. Patterson, Diurnal variation of the hydrogen concentration in the exosphere, *Planet. Space Sci.*, *11*, 1035 – 1052, 1963.

Hanson, W.B., S. Sanatani and D.R. Zuccaro, The Martian ionosphere as observed by the Viking Retarding Potential Analyzers, J. *J. Geophys. Res.*, *82*, 4351 – 4363, 1977.

Hartle, R. E., T.M. Donahue, J.M. Grebowsky and H.G. Mayr, Hydrogen and deuterium in the thermosphere of Venus: Solar cycle variations and escape, *J. Geophys. Res.*, *101*, 4525 – 4536, 1996.

Herbert, F., B.R. Sandel, R.V. Yelle, J.B. Holberg, A.L. Broadfoot, D.E. Shemansky, S.K. Atreya and P.N. Romani, The upper atmosphere of Uranus – EUV occultations observed by Voyager 2, *J. Geophys. Res.*, *92*, 15,093 – 15,109, 1987.

Hodges, R.R. Jr., Differential equation of exospheric lateral transport and its application to terrestrial hydrogen, *J. Geophys. Res.*, *78*, 7340 – 7346, 1973.

Hodges, R.R. Jr. ,An exospheric perspective of isotopic fractionation of hydrogen on Venus, *J. Geophys. Res.*, *104*, 8463 – 8471, 1999.

Hodges, R.R. Jr., J.H. Hoffman and F.S. Johnson, The lunar atmosphere, *Icarus 21*, 415 – 440, 1974.

Hodges, R.R. Jr. and F.S. Johnson, Lateral transport in planetary exospheres, *J. Geophys. Res.*, *73*, 7307 – 7317, 1968.

Hubbard, W.B., Yelle, R.V. and Lunine, J.I., Nonisothermal Pluto atmosphere models, *Icarus, 84*, 1 – 11, 1990.

Hunten, D.M., The escape of light gases from planetary atmospheres, *J. Atmos. Sci.*, *30*, 1481 – 1494, 1973.

Hunten, D.M., Atmospheres and ionospheres, in *Jupiter*, edited by T. Gehrels,, pp. 22 – 31, University of Arizona Press, Tucson, 1976.

Hunten, D.M., Thermal and nonthermal escape mechanisms for terrestrial bodies, *Planet. Space Sci.*, *30*, 773 – 783, 1982.

Hunten, D.M., Kuiper Prize Lecture: Escape of atmospheres, ancient and modern, *Icarus, 85*, 1 – 20, 1990.

Hunten, D.M., Atmospheric evolution of the terrestrial planets, *Science, 259*, 915 – 920, 1993.

Hunten, D.M. and A.J. Dessler, Soft electrons as a possible heat source for Jupiter's thermosphere, *Planet. Space Sci.*, *25*, 817 – 821, 1977.

Hunten, D.M. and T.M. Donahue, Hydrogen loss from the terrestrial planets, *Ann. Rev. Earth Planet. Sci.*, *4*, 265 – 292, 1976.

Hunten, D.M. and A.J. Watson, Stability of Pluto's atmosphere, *Icarus, 91*, 665 – 667, 1982.

Hunten, D.M., L. Colin, T.M. Donahue and V.I. Moroz (Eds), *Venus*, 1143 pp., University of Arizona Press, Tucson, 1983.

Hunten, D.M., M.G. Tomasko, F.M. Flasar, R.E. Samuelson, D.F. Strobel and D.J. Stevenson, Titan, in *Saturn*, edited by T. Gehrels and M.S. Matthews, pp. 671 – 759, University of Arizona Press, Tucson, 1984.

Hunten, D.M., R.O. Pepin and J.C.G. Walker, Mass fractionation in hydrodynamic escape, *Icarus, 69*, 532 – 549, 1987.

Hunten, D.M., R.O. Pepin, and T.C. Owen, 1988, Planetary atmospheres, in *Meteorites and the early solar system*, edited by J.F. Kerridge and M.S. Matthews, pp. 565 – 591, University of Arizona Press, Tucson, 1988.

Hunten, D.M., T.M. Donahue, J.C.G. Walker and J.F.Kasting, Escape of atmospheres and loss of water, in *Origin and evolution of planetary and satellite atmospheres*, edited by S.K. Atreya, J. B. Pollack and M.S. Matthews, pp. 386 – 422, University of Arizona Press, Tucson, 1989.

Ingersoll. A.P., M.E. Summers, and S.G. Schlipf, Supersonic meteorology of Io: Sublimation-driven flow of SO_2, *Icarus 64*. 375 – 390, 1985.

Johnson, F.S., Horizontal variations in thermospheric composition, *Rev. Geophys. Space Phys., 11*, 741 – 754, 1973.

Johnson, H.E. and W.I. Axford, Production and loss of He^3 in the Earth's atmosphere, J. Geophys. Res. 74, 2433 – 2438, 1969.

Johnson, R.E., Energetic charged-particle interactions with atmospheres and surfaces, 232 pp., Springer-Verlag, Berlin, 1990.

Kasting, J.F. and J.B. Pollack, Loss of water from Venus I.

Hydrodynamic escape of hydrogen, *Icarus, 53*, 479 – 508, 1983.

Krasnopolsky, V.A. and G.R. Gladstone, Helium on Mars: EUVE and PHOBOS data, *J. Geophys. Res., 101*, 765 – 772,1996.

Kumar, S., The SO_2 atmosphere and ionosphere of Io: ion chemistry, atmospheric escape, and models corresponding to the Pioneer 10 radio occultation measurements, *Icarus, 61*, 101 – 123, 1985.

Kumar, S., D.M. Hunten and J.B. Pollack, Nonthermal escape of hydrogen and deuterium from Venus and implications for loss of water, *Icarus, 55*, 369 – 389.

Lellouch, E., M. Belton, I. de Pater, G. Paubert, S. Gulkis, and T. Encrenaz, The structure, stability, and global distribution of SO_2 in Io's atmosphere, *Icarus, 98*, 271 – 295, 1992.

Liu, S.C. and T.M. Donahue, Realistic model of hydrogen constituents in the lower atmosphere and escape flux from the upper atmosphere, *J. Atmos. Sci., 31*, 2238 – 2242, 1974.

Liu, S.C. and T.M. Donahue, The regulation of hydrogen and oxygen escape from Mars, *Icarus, 28*, 231 – 246, 1976.

Luhmann, J. G., R.E Johnson and M.H.G. Zhang, Evolutionary impact of sputtering of the Martian atmosphere by O^+ pickup ions, *Geophys. Res. Lett., 19*, 2151 – 2154.

Matcheva ,K.I. and D.F. Strobel, Heating of Jupiter's thermosphere by dissipation of gravity waves due to molecular viscosity and heat conduction, *Icarus, 140*, 328 – 340, 2000.

McAfee, J.R., Lateral flow in the exosphere, *Planet. Space Sci., 15*, 599 – 609, 1967.

McElroy, M. B., , Mars, an evolving atmosphere, *Science, 175*, 443 – 445, 1972.

McElroy, M.B. and Y.L. Yung, Oxygen isotopes in the Martian atmosphere: Implications for the evolution of volatiles, *Planet. Space Sci., 24*, 1107 – 1113, 1976.

McGrath, M. A. and R.E. Johnson, Magnetospheric plasma sputtering of Io's atmosphere, *Icarus, 69*, 519 – 531, 1987.

McNutt, R.L., , Models of Pluto's atmosphere, *Geophys. Res. Lett., 16*, 1225 – 1228, 1989.

Melosh, H.J. and A.M. Vickery, Impact erosion of the primordial atmosphere of Mars, *Nature, 338*, 487 – 489,, 1989.

Nash, D.B., M.H. Carr, J. Gradie, D.M. Hunten, and C.F. Yoder, Io, in *Satellites*, edited by J.A. Burns and M. S. Matthews, pp. 629 – 688, University of Arizona Press, Tucson. 1986.

Owen, T.C., The composition and early history of the atmosphere of Mars, in *Mars*, edited by H.H. Kieffer, B.M. Jakosky, C.W. Snyder and M.S. Matthews, pp. 818 – 834, 1992.

Owen, T., J.-P. Maillard, C. de Bergh and B.L. Lutz, Deuterium on Mars – The abundance of HDO and the value of D/H, *Science, 240*, 1767 – 1770, 1988.

Owen, T.C. and A. Bar-Nun, Volatile contributions from icy planetesimals, in *Origin of the Earth and Moon*, edited by R.M. Canup and K. Righter, pp. 459 – 471, University of Arizona Press, Tucson, 2000.

Patterson,T.N.L., Diurnal variations in thermospheric hydrogen, *Rev. Geophys. Space Phys., 8*, 461 – 471, 1970.

Paxton, , L. J., D.E. Anderson and A.I.F. Stewart, Analysis of Pioneer Venus Orbiter ultraviolet spectrometer Lyman-α data from near the subsolar region, *J. Geophys. Res., 93*, 1766 – 1772.

Pepin, R.O., Atmospheric compositions: key similarities and differences, in *Origin and evolution of planetary and satellite atmospheres*, edited by S.K. Atreya, J. B. Pollack and M.S. Matthews, pp. 291 – 305, University of Arizona Press, Tucson, 1989.

Pepin, R.O., On the origin and evolution of terrestrial planet atmospheres and meteoritic volatiles, *Icarus, 92*, 2 – 79, 1991.

Sasaki, S. and K. Nakazawa, Origin of isotopic fractionation of terrestrial Xe: Hydrodynamic fractionation during escape of the primordial H_2 - He atmosphere, *Earth Planet. Sci. Lett., 89*, 323 – 354, 1988.

Schneider, N.M., D.M. Hunten, W.K. Wells, A.B. Schultz, and U. Fink, The structure of Io's corona, *Astrophys. J., 368*, 298 – 315, 1991.

Shizgal, B.D. and G.G. Arkos, 1996, Nonthermal escape of the atmospheres of Venus, Earth, and Mars, *Rev. Geophys., 34*, 483 – 505, 1996.

Smith, G.R. and D.M. Hunten, Study of planetary atmospheres by absorptive occultations, *Rev. Geophys., 28*, 117 – 143, 1990.

Strobel, D.F. and M.E. Summers, Triton'a upper atmosphere and ionosphere, in *Neptune and Triton*, edited by D.P. Cruikshank, pp.1107 – 1148, University of Arizona Press, Tucson, 1995.

Spencer, J.R. and N.M. Schneider, Io on the eve of the Galileo mission, *Ann. Rev. Earth Planet. Sci., 24*,125 – 190, 1996.

Suess, H.E., Die Haüfigkeit der Edelgase auf der Erde und in Kosmos, *J. Geol., 57*, 600 – 607, 1949.

Trafton, L.M. Does Pluto have a substantial atmosphere?, *Icarus 44*, 53 – 61, 1980.

Trafton, L.M., D.M. Hunten, K.J. Zahnle and R.L. McNutt. Jr. Escape processes at Pluto and Charon, in *Pluto and Charon*, edited by S.A. Stern and D.J. Tholen, pp. 475 – 522, University of Arizona Press, Tucson, 1997.

Watson, A.J., T.M. Donahue and J.C.G. Walker, The dynamics of a rapidly escaping atmosphere: Applications to the evolution of Earth and Venus, *Icarus 48*, 150 – 166, 1981.

Wilson, J.K. and N.M. Schneider, Io's sodium directional feature: Evidence for ionospheric escape, *J. Geophys. Res., 104*, 16,567 – 16,584, 1999.

Yelle, R.V, Non-LTE models of Titan's upper atmosphere, *Astrophys. J., 383*, 380 – 400, 1991.

Yelle, R.V., J.I. Lunine and D.M. Hunten, Energy balance and plume dynamics in Triton's lower atmosphere, *Icarus, 89*, 347 – 358, 1991.

Young, L.A., R.V.Yelle, R.E.Young, A.Seiff, and D.B.Kirk, Gravity waves in Jupiter's thermosphere, *Science, 276*, 108 – 111, 1997.

Zahnle, K. J and J.C. G. Walker, The evolution of solar ultraviolet luminosity, *Rev. Geophys. Space Phys., 20*, 280 – 292, 1982.

D.M. Hunten, Lunar and Planetary Laboratory, The University of Arizona, Tucson, AZ 85721. (e-mail: dhunten@lpl.arizona.edu)

Surface Boundary Layer Atmospheres

R.E. Johnson

Engineering Physics and the Department of Astronomy, University of Virginia

The solar system contains many bodies with atmospheres so thin that collisions seldom occur between the atmospheric constituents. These are called surface boundary layer atmospheres. Not only is the surface the source of the atoms and molecules, but their interactions with the surface determine the atmospheric properties. These atmospheres are interesting for two reasons. By remote sensing we can learn about the external weathering agents and we may also be able to determine the surface compositions of distant bodies. Here the physical processes that control these atmospheres are described and our knowledge of the surface boundary layer atmospheres in the solar system is reviewed.

1. INTRODUCTION

The solar system contains many small bodies with tenuous atmospheres, some so thin that the atoms and molecules leaving the surface collide only rarely if at all. In this situation the properties of the atmosphere, or ambient gas, are dominated by the interactions of the constituent atom and molecules with the surface and by loss to space. Such atmospheres are also called exospheres because atoms leaving the surface can directly escape as they do from planetary exospheres (see II.2). When collisions can be neglected, the atmosphere is a sum of independent components each characterized by a surface ejection process. Such atmospheres are referred to here as surface boundary layer atmospheres since the interactions with the surface determine the composition and density.

These atmospheres are derived from the intrinsic planetary materials, impacting materials or implanted ions. Therefore, remote sensing observations can lead to an understanding of the surface composition and the weathering processes [*Johnson and Sittler*, 1990; *Johnson and Baragiola*, 1991]. Although this is an important goal, it typically founders on our lack of understanding of those processes which lead to desorption of atoms and molecules from the surface. Desorption from a surface can occur due to thermal processes and micrometeorite impact vaporization, and it is induced by incident photons, electrons and ions. Each of these processes is not well understood for the materials composing the porous regoliths of solar systems bodies. Good observations, therefore, are often accompanied by essentially speculative models due to the lack of laboratory data or reliable models for desorption.

The Mariner and Apollo missions showed that both Mercury and the Moon had extremely rarefied atmospheres. The sources were primarily solar wind implantation of hydrogen and helium, rare gas atoms produced by radioactive decay and nuclear reactions induced by cosmic ray particles, and, possibly, some sputtered oxygen. Renewed interest in these atmospheres was generated by the observation of ambient alkali atoms, first at Mercury and then at the Moon [*Potter and Morgan*, 1985, 1986, 1988]. This led to new modeling and observational efforts with the hope that remote sensing could be used to compare the composition of the surfaces of the Moon and Mercury. However, additional species were not identified until the recent observation of Ca at Mercury [*Bida et al.*, 2000].

Atmospheres in the Solar System: Comparative Aeronomy
Geophysical Monograph 130

10.1029/130GM13

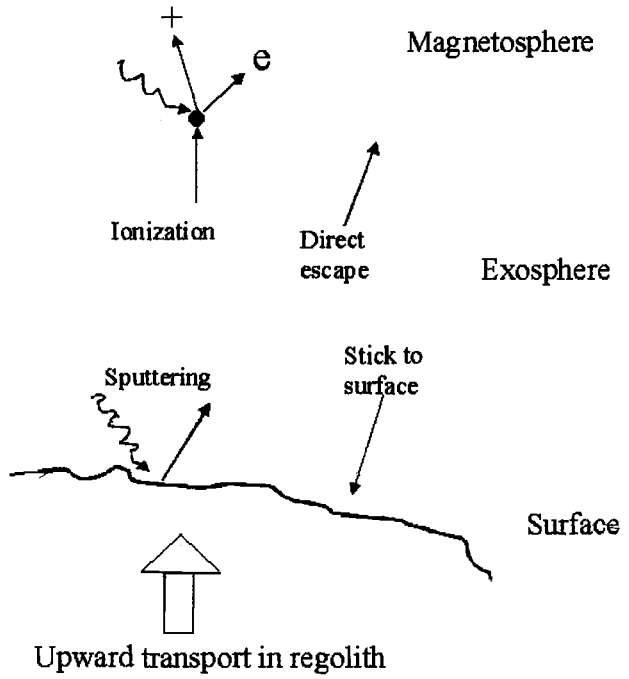

Figure 1. Source and loss processes determining the nature of the surface boundary layer atmospheres [*Cheng et al.*, 1987].

A parallel story for outer solar system bodies had been evolving for ~ 20 years. Subsequent to the first observation of sodium at Io [*Brown and Chaffee*, 1974], Voyager found that a number of the large moons of the giant planets had extremely thin, exospheric atmospheres. It also confirmed that many of these surfaces were composed primarily of frozen volatiles and were embedded in relatively intense fluxes of charged particles trapped in the giant planet magnetospheres. Based on laboratory data for sputtering of ices, these moons were predicted to have thin atmospheres [*Cheng and Lanzerotti*, 1974]. Because water ice is decomposed by energetic plasma particles [*Reimann et al.*, 1984], the icy moons were also predicted to have O_2 atmospheres [*Johnson et al.*, 1982; *Johnson*, 1990]. These predictions were both confirmed. An ambient cloud of OH was observed at Saturn by HST [*Shemansky et al.*, 1993], derived in part from H_2O escaping from the icy satellites, and O_2 was detected by 'auroral' emissions at Europa and Ganymede [*Hall et al.*, 1998]. There is now considerable excitement that atmospheric observations can give information on the evolution of Europa's surface [*Johnson et al.*, 1998] and on its ocean which has breached the surface in the past [*Pappalardo et al.*, 1999]. Alkali atoms seen in Europa's atmosphere [*Brown and Hill*, 1996] were suggested to have come from ocean material [*Johnson*, 2000; *Brown*, 2001; *Leblanc et al.*, 2001] and the search is on for other species that might suggest whether biology was initiated in Europa's ocean [*Chyba*, 2000].

In this Chapter, I first review the ejection and transport processes that determine the atmospheric properties. Because of the existence of a number of good reviews [*Hunten et al.*, 1988; *Hunten and Sprague*, 1997; *Stern*, 1999; *Killen and Ip*, 1999], I will only briefly describe our present understanding.

2. Physical Processes

An atom or molecule ejected from the surface moves in a ballistic trajectory, primarily under the influence of the body's gravitational field as seen in Figure 1. If it has sufficient energy it can escape, it can be ionized and lost, or ionized and swept into the surface by the local fields [*Manka and Michel*, 1973; *Goldstein et al.*, 1981]. Neutrals which do not escape or are not ionized return to the surface. Ejected molecules can be dissociated with their fragments following escape or bound trajectories. The contribution of these atoms and molecules to the observed density depends on the flight time, which in turn depends on its initial ejection velocity. Those particles which return to the surface ballistically or return by being ionized and swept into the surface can again be ejected. A refinement to this picture is the interaction with the radiation field. An effective pressure is produced by resonant scattering [*Smyth and Marconi*, 1995] or by collisions with the plasma particles [*Jurac et al.*, 2000]. For long flight paths, collisions with other neutrals can become relevant. An atmosphere in which collisions are important can exhibit characteristics of a surface boundary layer atmosphere if its properties are determined primarily by the interactions with the surface. Finally, each body has atmospheres at two scales: a planetary scale ambient gas above the physical surface in equilibrium with a micro-scale atmosphere in the regolith [*Hodges*, 1980].

The word source sometimes refers to the ejection process and other times to the reservoir of the observed atoms and molecules. These are the same for venting. Here I describe ejection processes and use the word source for the reservoir. Internal (endogenic) sources of atmosphere must be replenished by regolith turnover, outgassing or diffusion. External (exogenic) sources include implantation of ions from the local plasma, impacting meteoroids and comets, or ejecta from a neighboring object. The ejection and transport processes are described below.

2.1. *Thermal Processes*

Outgassing can produce a tenuous atmosphere controlled by condensation and loss to space. This can be a robust process, like volcanoes at Io or venting at Triton. The ejecta velocity distributions are determined by the temperature of the reservoir and by collisions in the expanding plume. At some distance from the source, the atmosphere becomes a thin boundary layer atmosphere. Bodies might also outgas by slow, steady thermal diffusion as suggested for the CO_2 at Callisto [*Carlson*, 1999]. Modeling requires accounting for the source rates and the velocity distributions.

Trace atoms or molecules which are bound to or adsorbed on the surface (e.g., Ar at night on the Moon) can be desorbed thermally. The rate of ejection is proportional to their surface concentrations, c_j, to their vibrational frequency on the surface, $\nu_j (\approx 10^{13}/s)$ and an exponential function of their surface binding energy, U_j: $dS/dt \approx c_j\ \nu_j\ \exp[-U_j/kT]$. Thermally desorbed species that are fully accommodated have a roughly Maxwellian velocity distribution, typically given as a normalized flux distribution, $f(E,\theta) = [2cos\theta][E/(kT)^2]\ exp(-E/kT)$.

In the subsolar region, sublimation can be important on the frozen surfaces in the outer solar system. Whereas thermal desorption refers to ejection of a trace species, like Na at Mercury, sublimation describes ejection of the principal species such as H_2O at Ganymede. The velocity distribution is typically like that above and the flux is determined from the vapor pressure at the surface, $P(T\ x)$, and the sublimation energy U: $\Phi = c[P(T)/(2\pi MkT)^{1/2}]\exp(-U/kT)$. The prefactor is related to ν_j above and the coverage, c, can account for porosity.

2.2. *Stimulated Desorption and Sputtering*

Whereas the solar photon flux heats the surface, determining the thermal desorption efficiencies, individual photons can excite a bond in the surface [*Madey et al.*, 2001]. This can lead to repulsive ejection of an atom or molecule, referred to as photon stimulated desorption or photo-sputtering. These terms have been used interchangeably but typically refer to removal of a trace or absorbed species vs. removal of the principal species. Stimulated desorption is less robust than thermal desorption but becomes important when $exp[-U_j/kT]$ is small. The dominant ejecta are neutrals. Ion ejection requires higher energy excitations (typically $>\sim$ 25eV) but as they are easy to detect the literature is predominantly on ion desorption. Because ejected ions contribute directly to the local plasma, they might at times be important, but most observed plasma ions are formed from ejected neutrals.

CO is desorbed by exciting states of internal molecular bond of CO or by exciting a state associated with the molecule / surface bond [*Madey et al.*, 2001]. These can be quenched or they can lead to repulsive ejection. Exciting a surface state can lead to ejection of a CO whereas the internal states lead to ejection of an atom, typically the O. Adsorbed or intrinsic Na is bound in an ionic form to a silicate [*Yakshinskiy and Madey*, 2000]. An incident photon can excite an electron which attaches to the sodium causing ejection [*Yakshinskiy and Madey*, 1999]. The threshold for alkali atom desorption from a silicate or an icy surface is only a few eV [*Yakshinskiy and Madey*, 1999, 2001]. The desorbed flux, Φ_j, for species j can be written as $\Phi_j = \eta_j\ \sigma_j^{des}\ \phi$, where ϕ is the incident photon flux, σ_j^{des} is the desorption cross section and η_j is the number per unit area in the surface. The quantity $(\eta_j\ \sigma_j)$ is also called the yield. The cross section σ_j^{des} is the product of an absorption cross section for the photon and the probability of ejection. Whereas gas-phase photo-absorption cross sections for outer shell electrons range from $\sim 10^{-17}$-10^{-19}cm^2, desorption cross sections can be an order of magnitude or more smaller due to the quenching of the excitations in the solid. Whereas ejected ions can have average energies $\gg$1eV, the ejected neutrals have average energies $<$1eV. Stimulated desorption is non-thermal but can have a quasi-thermal component due to the interaction of the exiting atom with other surface atoms. Since planetary surfaces are porous, a thermal distribution with an energetic tail is appropriate.

Adsorbed water can be typically dissociated by incident UV photons, [*Kimmel et al.*, 1995] If this occurs at the vacuum interface, H or H_2 is directly ejected and H_2 produced at depth diffuses out. For a vapor deposited ice, which is very rough at the molecular level, weakly attached water molecules can be directly desorbed [*Bahr et al.*, 2000]. However, removal of H_2O typically requires two photons [*Westley et al.*, 1995]. The first causes the loss of H or H_2, producing a precursor species: e.g., trapped OH or O [$H_2O{\cdot}O$]. Subsequent excitation of the precursor can lead to desorption [*Sieger et al.*, 1998]. Therefore, the yield is roughly quadratic in the radiation flux, ϕ, and is temperature dependent.

Fast ions and electrons ($>\sim 10^7 cm/s$) from the local plasma can cause desorption and sputtering by electronic excitations, a process referred to as electronic sputtering [*Johnson*, 1996]. If the density of excitations produced near the surface is low, as is the case

for incident electrons and fast protons, then electronic sputtering resembles photo-desorption [*Johnson*, 1990]. However, the fast heavy ions in the Jovian magnetospheric plasma [*Cooper et al.*, 2001] produce high excitation densities leading to large sputtering yields in ice. The yields for a number of relevant ices are often parametrized by the square of the energy deposited per unit path length in excitations and ionizations, $(dE/dx)_e$ [*Johnson*, 1990, 1998; *Shi et al.*, 1995], a tabulated quantity. The ejecta spectrum is not Maxwellian. It has an average energy <1eV, but with a slowly decaying tail, $\sim E^{-2}$ [*Johnson*, 1990], and is often parametrized using $f(E) = 2EU'/(E+U')^3$, where U' is a fitting parameter which is typically low, <0.1eV.

Incident plasma ions also transfer energy to surface atoms in 'knock-on' collisions [*Johnson*, 1990; 1998]. This is the standard sputtering process which leads to non-selective ejection. It is the dominant ejection process in most refractory solid and is most efficient at energies $\sim$ 0.1-1keV/u. It has the hardest spectrum with the parameter U' above related to the cohesive energy of the material, U. It is the most discussed sputtering process, but has not yet been shown to be dominant on any object. Although there is a large body of data and good computational tools for knock-on sputtering, details for planetary materials are sparse.

Micrometeorite impact vaporization of regolith grains and the impactor has been suggested as an atmospheric source at the Moon [*Morgan et al.*, 1989], Mercury [*Morgan et al.*, 1988; *Hunten et al.*, 1988], and Enceladus [*Haff and Eviatar*, 1986]. Micrometeorites, which produce the porous regoliths and convert lunar surface materials into glasses, also mix the surface exposing fresh material. The vapor coats lunar grains [*Hapke*, 2001] and can produce an enhancement in the sodium atmosphere during meteor showers [*Hunten et al.*, 1998; *Smith et al.*, 1998]. The ejecta exhibit a Maxwellian-like velocity distribution and the amount of material vaporized per impact is of the order of a few times the mass of the impactor. The porous regolith produced by micrometeorite bombardment can severely reduce the sputter flux by shadowing and sticking of ejecta to neighboring grains [*Hapke*, 1986; *Johnson*, 1989].

2.3. Radiolysis and Photolysis: Chemical Sputtering

The incident charged particles and photons also induce chemistry called radiolysis and photolysis [*Johnson and Quickenden*, 1997]. The surface is altered down to the depth of penetration by implantation of reactive species (e.g., H, C,O and S) and by bond breaking. That radiolysis occurs on the icy moons is indicated by the observation of peroxide [*Carlson et al.*, 1999b]. In radiolysis and photolysis new more volatile species are created which preferentially desorb, often called chemical sputtering [*Roth*, 1983]. For instance, ice is decomposed into H_2 and O_2 [*Reimann et al.*, 1984] and protons and carbon implanted into the lunar regolith can form CH_4. Volatiles produced at depth can diffuse to the surface (e.g., H_2 from CH_4 [*Lanzerotti et al.*, 1987]) and escape with a thermal energy distribution. In some materials the loss of volatiles leaves a less volatile surface, as is the case for vapor deposited SO_2 irradiated in Io's polar regions producing sulfur chains [*Johnson*, 1997]. Similarly, outer solar system surfaces containing hydrocarbons preferentially lose H (as H_2) forming carbon chains [*Strazzulla*, 1998] and many organic molecules decompose yielding CO_2 and darker material, a process possibly relevant at Callisto [*Johnson*, 2001]. The chemistry can be induced by hot atom reactions, but most measured yields vary with the surface temperature [*Johnson*, 1990, 1998]. These chemical changes compete with regolith turnover and vapor deposition in determining the surface reflectance.

2.4. Adsorption

Ejected atoms and molecules returning to the surface typically do not reflect efficiently, since their velocities are low and the surfaces are porous. If they do scatter back into the gas phase before fully accommodating to the surface temperature, their average energy is characterized by a coefficient, $\beta = [E_{out} - E_j]/[E_T - E_{in}]$, where E_{in} and E_{out} are the incident and re-ejection energies and E_T is the thermal energy [*Hunten et al.*, 1988]. Since natural surfaces are highly porous, full accommodation to the local temperature is a good assumption for all except the lightest atoms, H and He [*Hodges*, 1974; *Shemansky and Broadfoot*, 1977]. That is, the returning atoms or molecules become adsorbed weakly on the surface (physisorbed; $U_j \ll$1eV). In this state they can migrate along the surface of a grain until they find a deep adsorption or reaction (chemisorbed) site or desorb thermally. Therefore, with the exception of H and He, returning particles essentially stick ($\beta \approx 0$) with a residence time that depends on the surface temperature and the availability of deep sites [*Smith and Kay*, 1997; *Yakshinskiy and Madey*, 2000]. These are available on surfaces in a clean space environment [*Hodges*, 2001] and are produced by radiation damage [*Yakshinskiy and Madey*, 1999].

In laboratory studies a distinction can be made between direct reflection, sticking-migration-desorption, and sticking and becoming bound in a deep well [*Smith*

and Kay, 1997]. In modelling, one typically uses a net sticking coefficient, S, which combines the probability of physisorption and the probability of finding a binding site. For He there are no deep sites, but even Ar can bind at night on clean lunar grains [*Hodges*, 2001]. Water has a high apparent sticking coefficient on MgO. It chemisorbs molecularly at terrace sites and dissociatively at radiation damage sites. Interestingly, the thermal activation energy in both cases is ~63kJ/mole [*Stirniman et al.*, 1996]. *Yakshinskiy et al.* (2000) give the net sticking for Na on a silicate: S≈ 0.5 at $250K$ decreasing to 0.2 at 500K. The Na absorbed on an amorphous silicate has binding energies ranging from ~ 1.4eV to 2.7eV with a peak ~1.85eV, greater than the 1.1eV suggested earlier [*Hunten and Sprague*, 1997]. At 500K the resident time on a grain at the average binding energy is ~13 hours and at 400K it becomes ~103 yrs.

Since the grains form a regolith, desorbed molecules intersect a surface with high probability prior to contributing to the ambient gas. The atoms and molecules hopping between grain surfaces create an regolith atmosphere in equilibrium with the observed ambient gas. The net sticking coefficients in a regolith is S_{eff} ≈S/[1-(1-S)(1-P)] where P is the probability of escape. For isotropic ejection, P is ~ 0.2 [*Hodges*, 1980a; *Johnson*, 1989]. Therefore, at 250K and 500K, S_{eff} is ~0.8 and ~0.6, close to the value found when modeling observations [*Sprague*, 1992].

2.5. Interaction With the Radiation Field

The atoms and molecules in their ballistic trajectories can interact with the local radiation field. This can lead to excitation, ionization and dissociation of molecules as well as momentum transfer. The interaction of solar photons with the alkali atoms has been extensively described [*Smyth and Marconi*, 1995a]. The strong resonance scattering lines which allow trace amounts of Na and K to be studied from earth produce an average acceleration away from the sun. That is, an atom absorbs a photon receiving a momentum directed away from the sun and then re-emits in a random direction giving up some momentum. Instead of treating this stochastically, it is treated as a radiation pressure, since each event transfers a small amount of momentum and the ballistic lifetimes are generally longer than the resonant scattering time. Although a small effect, the pressure is steady, driving sodium and potassium atoms in large ballistic orbits downstream from the sun [*Wilson et al.*, 1998]. The ability to absorb is affected by the atom's radial motion relative to the sun which causes a Doppler shift. Since Mercury is both close to the sun and in an eccentric orbit, the net acceleration can vary considerably depending on Mercury's orbital position [*Smyth and Marconi*, 1995a].

Interaction with the plasma can also produce a net drag via momentum transfer to atmospheric neutrals producing, for instance, an expansion of Saturn's OH torus [*Jurac et al.*, 2000]. Since the size of the momentum transfer can be large this is typically treated stochastically. When such collisions lead to removal of a molecule from an atmosphere, it is often called atmospheric sputtering [*Johnson*, 1990].

Ionization by photons, electron impact, or charge exchange are important loss processes for a number of the surface boundary layer atmospheres. Estimating the loss requires knowledge of the plasma flux and the ionization and charge exchange cross sections. A useful quantity is the average lifetime against ionization, $\tau_i = [\phi \sigma_i]^{-1}$, where σ_i is the ionization cross section and ϕ is the radiation flux. Photoionization cross sections integrated over the solar spectrum are available for many atmospheric species [*Huebner et al.*, 1992] and plasma cross section data, though not always available, can be reasonably estimated [*Johnson*, 1990]. The biggest uncertainty is knowledge of the plasma density and temperature, especially close to the body. The interaction of the external field with the local field can be variable [*Ip*, 1986; *Kabin et al.*, 2000] and ionization followed by pick-up produces a current. This current in turn deflects the plasma flow, as modeled for Europa's O_2 atmosphere [*Ip*, 1996; *Saur et al.*, 1998]. Accurately calculating the feedback is not trivial but is important at the Jovian satellites and Mercury.

2.6. Transport and Recycling

Particles desorbed from the surface move in ballistic trajectories usually calculated in the coordinate system of the body. When no outside forces act, the radial gravitational force, $\mathbf{F_G}$, controls the motion. However, if the radiation pressure and/or the gravitational force of the sun or of a parent planet (e.g., Jupiter for Europa) is significant, then motion of the body is importnat and Coriolis and centrifugal forces must also be included (see III.4).

When considering only $\mathbf{F_G}$ and ignoring losses, the ejecta energy distribution, f(E,θ) determines atmospheric transport and escape, where E and θ are the energy and angle. The escape fraction, f_{es}, is obtained by integrating over energies greater than U^S, the satellite gravitational energy. For surface boundary layer atmospheres transport is always important since stimulated

and thermal desorption exhibit longitudinal and latitudinal dependences. For outer solar system moons phase-locked to their parent planets and moving in the magnetospheric plasma, there are differences in the bombardment flux onto the hemispheres leading and trailing the orbital motion [*Pospieszalska and Johnson*, 1989; *Paranicas et al.*, 2001]. This produces differences in the ejected flux so that trace species are moved poleward or, in the case of the Jovian satellites, to the leading hemisphere [*Sieveka and Johnson*, 1982]. When ejection depends on temperature there is a net poleward and day to night transport, so that Ar at the moon exhibits daily transients [*Hodges*, 1980a]. If the molecules are fully accommodated to the local surface temperature, then thermal desorption and adsorption events lead to a random walk across the surface and into the regolith. When hopping distances are small, the process is roughly diffusive [*Hodges*, 1974].

Ignoring loss processes, the angular excursion across the surface and the mean flight time, t_b, in a bound trajectory are easily estimated [*Johnson*, 1990]. The averages are obtained by integrating over the energy and angle distribution of the ejecta for the bound trajectories. When $t_b \ll \tau_i$ and ejection is isotropic, the column is $\Phi_j \cdot t_b$, where Φ_j is the flux discussed earlier. For sputtering of H_2O at Europa the escape fraction is $f_{es} \approx 0.3$, the mean angular excursion is $\sim 50°$, indicating relatively large ballistic trajectories, and the mean fight time is $\sim 4 \times 10^3 s$ [*Johnson*, 1990]. For O_2 at the ambient temperature on Europa's dayside hemisphere ($\sim 120K$) the escape fraction is nearly zero, the mean excursion angle is $\sim 2^o$ and the mean flight time is shorter, $\sim 200s$. Both of these times are short compared to the lifetime against ionization, $\tau_i \approx 10^6 s$. Therefore, most particles in bound trajectories return to the surface. If gas-phase ionization is the only loss process and if the residence time on the surface is short then the average number of hops across the surface is $\tilde{N} \approx \tau_i / < t_b >$. The mean excursion distance for a Maxwellian flux distribution is $\sim \pi H_j$, where H_j is the scale height, $H_j = kT/M_j g$. For the sputter energy distribution above, the mean excursion distance depends on the cut-off, E_{max}, which is typically not measured. For $E_{\max}/U_j' >> 1$, this gives $\sim \pi H_j^c \ln(E_{\max}/U_j')$. For a 2-D random walk with an average of $\tilde{N}$ hops, the mean radial distance traveled before removal is $\sim \pi H_j [\tilde{N}]^{1/2}$. This is of the order of Europa's radius for O_2 near the dayside equator.

Finally, ionized species follow the local field lines and can be re-implanted into the surface [*Manka and Michel*, 1973; *Cheng et al.*, 1987]. This produces poleward transport in the local dipole field at Ganymede or Mercury. Because of Mercury's slow rotational period, it has been suggested [*Sprague*, 1992] that this could produce a net transport process from dayside to the nightside allowing recycling of the alkalis.

2.7. *Density Calculations*

The density vs. altitude depends on the surface election rate, the ballistic flight time, t_b, and the loss processes. Atoms and molecules ejected from the surface have a residence time in every volume of space above the surface of the object. This is determined by the local velocity. Ignoring loss processes and outside forces, the densities of the bound, $n_b(r)$, and escaping, $n_{es}(r)$, components for a spherically symmetric atmosphere are readily calculated using the radial velocity, dr/dt [*Johnson*, 1990]:

$$n_b(r) = \Phi(1 - f_{es}) < 2(R_S/r)^2/(dr/dt) >_b;$$
$$n_{es}(r) = \Phi f_{es} < (R_S/r)^2 / (dr/dt) >_{es}$$

where Φ is the surface flux and R_S the satellite radius. The brackets imply averaging over the bound and escaping trajectories respectively, which can be carried out analytically for a number of characteristic energy distributions [*Johnson*, 1990]. If the flux is non-uniform and the transport distances are not large then such expressions can be used locally. If escape is negligible, then the atmosphere is locally flat. For thermal desorption this gives a density vs. altitude like the barometric law

$$n_j(z) = [N_j \ / \ H_j] \exp(-z/H_j);$$
$$N_j = \Phi_j \ [2\pi H_j/g]^{1/2}$$

with N_j the column density. Observers tend to interpret their data with such expressions even when the ejection process is not Maxwellian. Using the sputter energy distribution above for a locally flat atmosphere, then $n_j(z) = [N_j \ / 2H_j^c][1 + z/H_j^c]^{-3/2}$; $N_j = \Phi_j \pi (2U_j/M_j)^{1/2} / g$; $H_j^c = U_j/M_j g$, where H_j^c is like a 'scale' height and $\Phi_j = Y_j \phi$ with Y_j the sputter yield.

When particles hop across the surface with full accommodation, the density can very roughly as $n \propto T^{-5/2}$ exhibiting a minimum at the subsolar point [*Hodges and Johnson*, 1968]. The lunar He atmosphere roughly exhibits such a trend [*Hodges et al.*, 1974], but the lack of accommodation modifies the distribution [*Shemansky and Broadfoot*, 1977]. Lunar Ar also exhibits daily transients. Because it adsorbs at the nighttime temperatures there is a maxima near sunrise due to desorption and flow across the terminator with a smaller maximum at sunset [*Hodges*, 1980a]. Sodium is likely depleted in

the Mercury's subsolar regions, accumulating at higher latitudes where it is ejected by a stimulated desorption process. In contrast, the lunar alkali peak at the subsolar point.

Expressions can be created for non-isotropic atmospheres, but typically Monte Carlo simulations are carried out. The particles are launched from the surface using a choice of energy and angle determined from the ejecta distribution, $f(E,\theta)$. The space around the body is divided into volumes and the ejected particles are tracked in their ballistic trajectories noting the time, Δt, spent in each volume. A large number of particles are ejected and the average density is calculated from the sum of the Δt for all of the particles passing through a box times a surface flux, Φ_j, divided by the radial extent of the box and the number of simulation particles [*Bird*, 1994]. If the ionization times are comparable to the flight times, then in each box the loss probability, ΔP_L, is calculated and interaction with the solar radiation can be included. Monte Carlo models have been used to describe Ar and He at the moon [*Hodges*, 1980b] and the net transport of water molecules across the surface of Europa and Ganymede [*Sieveka and Johnson*, 1982]. More recently, they were used to describe the sodium component at Europa [*Leblanc et al.*, 2001] and at Mercury and the Moon [*Smyth and Marconi*, 1995a, b].

3. ATMOSPHERES

3.1. Mercury

Hydrogen, helium and probably oxygen were discovered by the Mariner spacecraft, but only upper limits were obtained for rare gases other than He. The H and He atmospheres are primarily due to the implantation of solar wind ions with radioisotope decay from uranium and thorium contributing He. The implantation flux is controlled by the variable interaction of the solar wind ions and fields with Mercury's magnetic field. The He distribution is roughly characterized by the surface temperature and exhibits a nighttime maximum [*Hodges et al.*, 1973]. The H atmosphere has a quasi-thermal (~400K) and a very cold (~100K) component which is not understood. Jeans escape is efficient at the dayside temperatures on Mercury. Atomic O, on the other hand, is likely a sputter product from a silicate [*Walters et al.*, 1988] and the returning O readily reacts with the surface.

The discovery of the alkali atmospheres [*Potter and Morgan*, 1985, 1986] lead to the hope that remote sensing of the ambient gas could give information on the surface composition. Although this has not been realized, considerable interest was generated in atmospheric models. Solar wind sputtering [*Potter and Morgan*, 1985] and micrometeorite vaporization [*Morgan et al.*, 1988, 1989; *Hunten and Sprague*, 1997] were initially suggested as the source of the alkalis. The solar wind ion sputtering source was found to be too small, and photon-stimulated desorption and thermal desorption were suggested to be important [*Ip*, 1986; *McGrath et al.*, 1986]. Ion sputtering can contribute an energetic tail to the ejecta and can cause enhanced diffusion of sodium to the surfaces of grains [*McGrath et al.*, 1986]. Subsequently, solar ions were shown to have had greater access to Mercury's surface than assumed. The neutrals ionized and accelerated into the surface could be sputter agents [*Cheng et al.*, 1987; *Sarantos et al.*, 2001] and could lead to alkali transport and implantation [*Sprague et al.*, 1997]. Chemical sputtering, in which the implanted hydrogen replaces alkalis, can also enhance sputtering [*Potter*, 1995] although the rates are not known. Finally, at equatorial temperatures thermal desorption is very efficient [*Hunten and Sprague*, 1997; *Madey et al.*, 1998].

The suggestion that photon-stimulated desorption was important was based on rough estimates of σ_j^{des}. *Yakshinskiy and Madey* (1999) found that σ_j^{des} had a lower than expected threshold, was relatively large, and had a non-thermal ejecta distribution. Sodium adsorbs in relatively deep wells (>1eV) [*Yakshinskiy et al.*, 2000], so that replenishment of surface Na by either radiation-enhanced diffusion, by micrometeorite mixing, or by adsorption produces similarly bound Na, simplifying the modelling of thermal and stimulated desorption.

At present there is no consensus on the importance of the various 'non-thermal' processes, but a single process cannot account for the diverse set of observations [*Sprague et al.*, 1997; *Killen et al.*, 2001]. Understanding these observations is complicated by the spatial non-uniformity and temporal variability of the atmosphere [*Sprague*, 1992; *Sprague et al.*, 1997]. These are caused by the daily surface temperature excursions, geologic features, variable solar activity and changes in Mercury's distance from the sun. However, suggestions of correlations with the solar EUV and radiation pressure were not seen in the largest single data set [*Sprague et al.*, 1997]. It is likely that thermal desorption rapidly removes Na and K in the equatorial regions and photo-desorption becomes important at high latitudes. Morning-side enhancements have been reported [*Sprague et al.*, 1997] but were not seen in other data

sets [*Killen et al.*, 1990, 2001]. Because the rotation rate is slow, observing such enhancements could be difficult. At high latitudes and on the nightside, precipitating ions can sputter the surface and pick-up alkali ions can be implanted, but the size of the region into which a significant flux of ions flows to the surface varies [*Kabin et al.*, 2000; *Sarantos et al.*, 2001]. *Sprague et al.* (1997) found little evidence for variations with solar activity, but *Killen et al.* (2001) find a 30% effect at high solar activity. They suggested that photo-desorption, ~70%, and micro-meteorite impact vaporization, ~30%, account for the observed sodium when the interaction with the solar fields is weak. Since photo-desorption is ineffective for many species but energetic ion sputtering is not, observers should look for new species at times of high solar activity such as the O observed by Mariner and the recent observation of Ca [*Bida et al.*, 2000].

Because the alkali loss rates are not negligible, replenishment is required. Energetic solar flare ions cause diffusion of sodium to the surface layers [*McGrath et al.*, 1986], meteoritic bombardment exposes fresh grains [*McGrath et al.*, 1986; *Morgan et al.*, 1989; *Sprague*, 1992; *Hunten and Sprague*, 1997] and delivers alkalis to Mercury [*Morgan et al.*, 1988; *Cintila*, 1992]. Replenishment can also be affected by the differences in the age and properties of the surface [*Sprague*, 1990; *Sprague et al.*, 1998].

3.2. The Moon

The Moon's noble gas atmosphere was studied during the Apollo program. A weak upper limit to the total atmospheric density of $2x10^7/cm^3$ and a nighttime surface density $\sim 10^2$ to $2x10^5/cm^3$ were obtained within about a factor of 2. These observations are both consistent with a surface boundary layer atmosphere. The rough upper limits, however, are larger than the maximum in the primary species observed, $\sim 5x10^4/cm^3$ each for He and Ar, suggesting other components are present. The Ar atmosphere, primarily ^{40}Ar derived from radiogenic decay of ^{40}K [*Hodges*, 1977] with ~ 10% from solar ^{36}Ar, showed a daily transient which, because it is cold-trapped at night ($\sim 100K$), exhibits maxima a large maximum at sunrise and a small maximum at sunset. For an ionization lifetime, τ_i, of ~ 25 days Ar is lost in ~ 50 days with ~80% of the time spent adsorbed [*Hodges*, 2001]. The release rate from the interior also appears to be variable, possibly due to tidal stress. Helium does not condense at night and shows an inverse correlation with surface temperature. It is primarily supplied by the solar wind with ~ 10% radiogenic component. Implanted He is removed from the regolith primarily by sputter erosion [*Hodges and Hoffman*, 1974]. Loss is due to Jeans escape with a small fraction lost by a non-thermal process. ^{222}Rn and ^{210}Po were observed through α decay. The large difference in emission rates and the much shorter half life was evidence for episodic venting of Rn near to the time of observation and their spatial distribution correlated with surface features [*Gorenstein et al.*, 1974]. Other elements are now being mapped using Lunar Prospector data [*Feldman et al.*, 1998b]. Finally, an unconfirmed, but suggestive, detection of masses 15-16, 28 and 44 was made by Apollo [*Hodges et al.*, 1974].

The initial ground-based observations of the sodium and potassium atmosphere at the Moon [*Potter and Morgan*, 1988] were followed by a large number of observation of the local [e.g., *Sprague et al.*, 1996] and distant (escaping) atmosphere [*Mendillo et al.*, 1997b, *Mendillo et al.*, 1999]. Recently, *Smith et al.* (1998) observed a pulse of sodium from the Moon seen down stream due to the solar radiation pressure and focused by the earth's gravitational field. This pulse was associated with the Leonid meteorite shower [*Hunten et al.*, 1998], confirming that meteoritic impact vaporization contributes [*Hunten et al.*, 1991]. The sodium escape increased by a factor of 2-3 during the shower [*Wilson et al.*, 1999], but the atmospheric geometry suggests that meteorite bombardment is not the dominant steady state source of sodium.

The alkali atmosphere is only $\sim 10^{-3}$ of the Ar and He atmospheres with average near surface densities of ~1-15 Na/cm^3 and maximum subsolar density ~30-70 Na/cm^3. Because the Moon does not have a global field, and because the surface temperatures are lower and the radiation pressure is smaller, the alkalis at the Moon are simpler to describe than at Mercury. Since the Moon is less massive and the excursion distances are larger, escape is more important and a large, nearly global atmosphere peaked at the subsolar point results [*Sprague et al.*, 1996; *Potter and Morgan*, 1997] as indicated in the image in Plate 1 [*Flynn and Mendillo*, 1993]. Unlike lunar Ar, thermal desorption and transport of alkalis is only possible close to the subsolar point [*Kozlowski et al.*, 1990; *Madey et al.*, 1998]. As at Mercury there has been disagreement on the dominant desorption process. Observations of the line profile indicate that the atmosphere has a non-thermal component (~1500K) [*Stern et al.*, 2000]. The scale height increases with increasing zenith angle and can be fit by a thermal and non-thermal process [*Stern and Flynn*, 1995; *Sprague et al.*, 1996]. Recent laboratory measurements for photo-

stimulated desorption and the observations during the meteor shower confirm that these processes contribute.

Mendillo et al. (1999) noted the distant atmosphere did not change by large amounts when the Moon is in the Earth's magnetotail, but *Potter et al.* (2000) saw variations when the Moon passed through the magnetotail. They concluded that solar particle bombardment affects the supply of Na and K to the surface layers of grains. This occurs by enhanced diffusion due to energetic ion bombardment [*McGrath et al.*, 1986]. Except possible near the subsolar point, the surface species are primarily ejected by photo-desorption [*Sprague et al.*, 1996] with ~15% by micrometeorites [*Mendillo et al.*, 1999]. Photo-desorption was shown to be sufficiently robust and the average ejecta speed can account for the cloud morphology [*Yakshinskiy and Madey*, 1999]. Desorption cross sections averaged over the solar spectrum are needed to convert the surface source rates into surface concentrations.

The alkali atmospheres peak more sharply than a cosine of the zenith angle [*Mendillo et al.*, 1997b; *Potter and Morgan*, 1999], due either to a contribution from thermal desorption, a temperature dependence in the photo-desorption rate or due to the product of a supply rate (sputter-enhanced diffusion) and a desorption rate both dependent on cosine of the zenith angle. *Sprague et al.* (1996) suggested a model in which stimulated desorption is followed by thermal hopping. As discussed, the recently measured adsorption energies are somewhat larger than the ones they used.

The line-of-site brightness of the sodium atmosphere over the limb decays as $\sim R^{-4}$ at half moon and $\sim R^{-2}$ at full moon [*Mendillo et al.*, 1993], where R is distance to the moon. These indicate the atmosphere has a gravitationally bound component and an extended non-thermal component as discussed. At large distances ($>4R_M$) it decays more slowly, consistent with an escaping component [*Mendillo et al.*, 1997a, b, 1999]. There is, however, unexplained variability [*Hunten et al.*, 1991] possibly due to meteorites or charging of the lunar grains, particularly near the terminator. Charging depends on the solar wind conditions and can affect alkali transport within the grains and cause levitation/exposure of grains [*Zook and McCoy*, 1991; *Manka and Michel*, 1971].

The constraints on the total atmosphere from Apollo and detection of additional masses by one Apollo instrument suggest there are additional species, but only upper limits have been obtained [*Flynn and Stern*, 1996]. Since thermal and photo-desorption appear to dominate most of the time, this places severe constraints on the ejection of other species. That is, a species must not only be more abundant than Na but also 'volatile'. However, when solar particles or micrometeorites cause ejection, additional species *should be seen.* The observed lunar pick-up ions O^+, Al^+ and Si^+ [*Mall et al.*, 1998], which have masses close to those seen by Apollo, are suggestive of an energetic ejection process. Some oxygen is always produced on sputtering of a silicate [*Walters et al.*, 1988] and oxygen is released during the formation of the iron coatings on lunar grains [*Hapke*, 2001]. Since H was not seen at levels suggested, implanted H can reduce the surface releasing oxidants which may be molecular. Since detecting even trace species is important, this might be best done by in-situ measurement of the local pick–up ions [*Manka and Michel*, 1973; *Johnson and Baragiola*, 1991].

3.3. Galilean Satellites

Although Io's atmospheric density is controlled by its interaction with the surface, it has a collisionally thick atmosphere, except, possibly, at the poles and on the nightside. It is also an atmosphere for which escape is important, hence it is discussed in II.2 and III.4. Jupiter's large icy satellites, on the other hand, appear to have global surface boundary layer atmospheres. These atmospheres are formed by radiation - induced decomposition of surface materials, sputtering and thermal desorption. To date, O_2, Na, K and possibly hydrogen have been observed at Europa and oxygen and hydrogen have been identified at Ganymede. At Callisto atmospheric CO_2 has been identified. In addition, ionospheres were observed by *Kliore et al.* (1997) on all three satellites.

These moons experience differences in tidal heating, affecting their geological evolution, and differences in the radiation flux to the surface, which increases by two to three orders of magnitude in going from Callisto to Europa [*Cooper et al.*, 2001]. Therefore, the surface age decreases from Callisto to Europa. These moons are all thought to have subsurface oceans [e.g., *Khurana et al.*, 1998]. The depth below the surface is probably the smallest at Europa, accounting for its apparent resurfacing. At Callisto primordial CO_2 may be outgassing [*Carlson*, 1999].

Impacts and radiation bombardment produce brightening of the surface in competition with thermal annealing [*Johnson*, 1997]. Micrometeorites mix the surface, primarily on the hemisphere leading the satellite's motion, and may be responsible for the accumulated dark material on Callisto. Since the principal condensed volatile is H_2O the atmospheres are assumed to have

water vapor produced by sublimation in the equatorial regions and by sputtering elsewhere. The H_2O column density is controlled by condensation on the nightside and at high latitudes. Other atmospheric species are produced by radiolysis. Whereas H_2O adsorbs when it returns to the surface, the H_2 and O_2 produced by decomposition of ice do not. The H_2 predominantly escapes but the O_2 remains and becomes the dominant gas at Europa. The loss of hydrogen produces an oxidizing surface [*Johnson and Quickenden*, 1997], which has been suggested as a potential energy source for biology [*Chyba*, 2000; *Cooper et al.*, 2001]. O_2 molecules that do not directly escape thermally desorb on each return to the surface until they are eventually dissociated or ionized. Therefore, the O_2 atmosphere will have a two component velocity distribution [*Ip*, 1996; *Shematovich and Johnson*, 2001], a large thermally accommodated component and a more energetic directly ejected component [*Johnson*, 1990]. Because the incident plasma determines both the source and loss processes, large column densities do not accumulate. Assuming electron impact ionization is the dominant loss process, a column of $\sim 3 \times 10^{15}$ O_2/cm^2 was predicted [*Johnson et al.*, 1982; *Johnson*, 1990] in equilibrium with a larger column of O_2 in the regolith.

Hall et al. (1998) detected the excited O produced by dissociation of O_2. They estimated a column density $\sim 10^{15}/cm^2$. Subsequent modeling by *Saur et al.* (1998) suggested $\sim 6 \times 10^{14}$ $/cm^2$ due to efficient loss by knock-on collisions. Recently [*Shematovich and Johnson*, 2001], ionization was found to be dominant, as initially suggested, and a larger than predicted source rate for O_2 was needed. A large source may be due to radiolysis by energetic electrons, the dominant energy source to the surface of Europa [*Paranicas eta al.*, 2001], to ionized re-impacting oxygen [*Ip*, 1996] or to over correcting for regolith structure. Photolysis of gas-phase H_2O might also contribute. A global distribution of O_2 is usually assumed in modelling even though the non-ice materials dominate the equatorial regions on Europa's trailing hemisphere. However, recent HST images suggest that the O_2 atmosphere is localized around the icy regions [*McGrath et al.*, 2000].

The Na and K observed on Europa come from decomposition and sputtering of surface materials [*Johnson*, 2001], presumably hydrated salts from the putative subsurface oceans [*Kargel*, 1991; *McCord et al.*, 1998; *Zolotov and Shock*, 2001]. Although knock-on sputtering occurs, electronic sputtering is the dominant ejection process. The Na ejected from a hydrated salt is replaced by H forming frozen hydrated sulfuric acid, which is suggested to be present by the IR spectra from the NIMS instrument on Galileo [*Carlson et al*, 1999a].

A Monte Carlo simulation of the morphology of the Na atmosphere was used to estimate a spatial and speed distribution of the ejected Na. Jupiter is the dominant perturbation as seen in the contour plot of the Na density distribution in Figure 2. Loss is due to Jeans escape and ionization but most ($\sim$70%) of the electronically sputtered Na and K return to the surface [*Johnson et al.*, 2001]. Since the average angular excursion is $\sim 60^o$, the Na is redistributed across Europa. The cloud morphology is found to be better reproduced by the measured energy distribution for electronic sputtering of Na adsorbed on ice [*Johnson et al.*, 2001] than that for Na sputtered from a salt, Na_2SO_4 [*Wiens et al.*, 1997]. This indicates that most of the ejected sodium was adsorbed in ice-rich materials [*Johnson*, 2000]. There is likely a tail corresponding to sputtering from more refractory materials, but the distant Na observations show considerable variability, probably due Europa's interaction with the jovian magnetosphere [*Leblanc et al.*, 2001]. The measured energy distributions were used to convert the observed Na/K ratio [*Brown and Hill*, 1996] into a relative surface source strength, Na/ K $\sim$20, and relative total loss rate Na / K $\sim$27 [*Johnson et al.*, 2001]. Since the desorption cross sections are similar, the surface region is rich in Na relative to K as compared to models of the putative subsurface ocean (Na/K $\sim$14-19). This is consistent with fractionation during upwelling and freezing [*Zolotov and Shock*, 2001]. The Na concentration in the optical layer is $\sim$0.01-0.005 with the atmospheric surface densities at the apex of the trailing hemisphere $\sim$300 Na/cm^3 and 15 K/cm^3.

Other species should be detectable at Europa. SO_2, seen in the irradiated dark regions, is produced radiolytically and by implantation. These regions obtain their reddened spectra due to radiolytic production of chain sulfur [*Johnson et al.*, 1988]. In Io's polar regions radiolysis of SO_2 produces sulfur [*Johnson*, 1997], but in the presence of ice radiolysis of sulfur gives the three detected forms: primarily H_2SO_4. XH_2O, with much smaller ($\sim$ 1%) amounts of SO_2 and S_x in ice and very small amounts of H_2S [*Carlson et al.*, 1999a; *Carlson et al.*, 2001]. The sulfur could be implanted by the bombarding plasma [*Lane et al.*, 1982], due to venting as at Io, or a sulfate from the subsurface ocean [*Johnson*, 2001]. The S_x, which darkens the surface, can be slowly removed by oxidation to SO_2 and sputtering. Therefore, a fresh sulfur containing surface, which is rapidly darkened radiolytically, can 'brighten' over long periods of time [*Carlson et al.*, 2001].

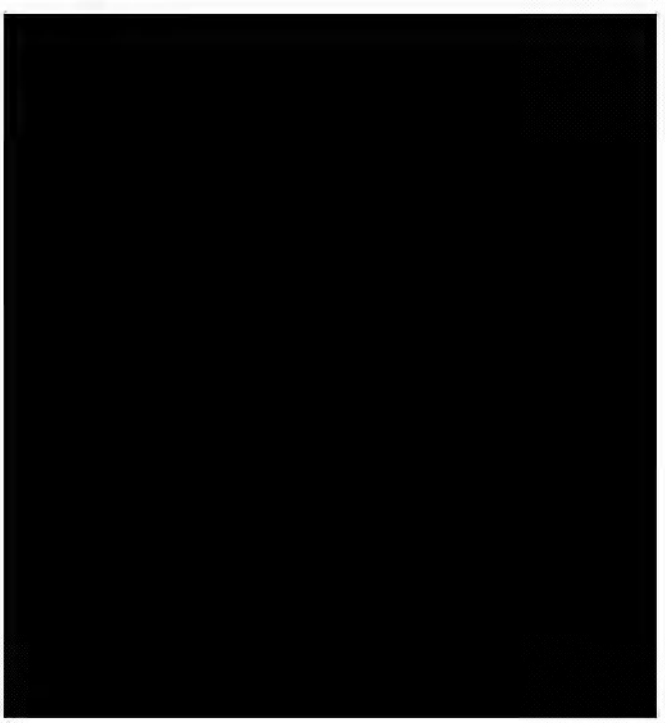

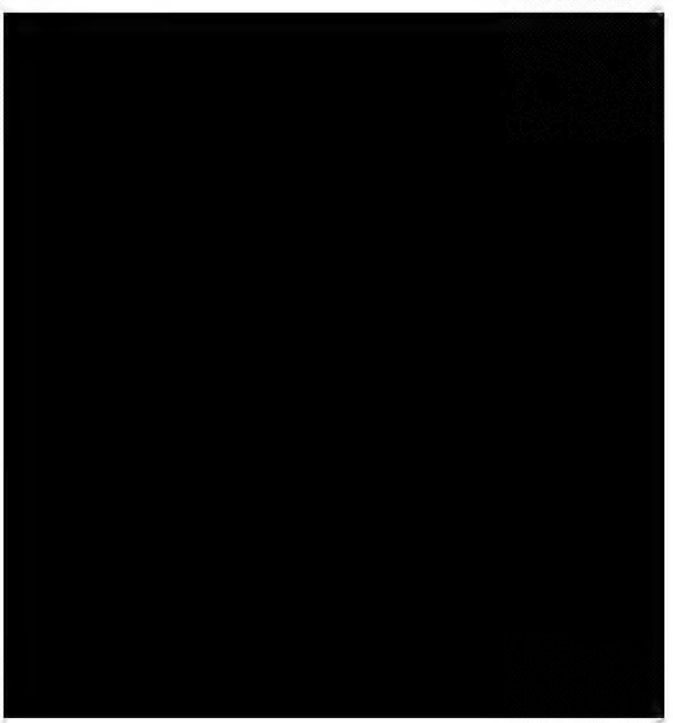

'fresh' impact features. The atmospheric CO_2 has been suggested to be due to slow outgassing, but may be a radiation-induced decomposition product of a carbonate or organic molecules in the surface [*Johnson*, 2001].

3.4. *Saturnian Satellites and Rings*

The small icy satellites of Saturn have low escape energies and very tenuous atmospheres consistent with ice at $<\sim$100K. The atmospheres are dominated by escape and the vapor pressure is low, so sputtering and particulate impacts are important sources. Consistent with radiation-induced decomposition, the reddening in the UV is suggestive of H_2O_2 and O_3 [*Noll et al.*, 1997] present in the surface. Therefore, H_2O, O_2 and H_2 are likely the dominant ejecta with smaller amounts of radicals [*Kimmel et al.*, 1995]. Based on the expected velocity distributions, the escape fractions are $\sim$0.9,0.8, 1, respectively at Dione [*Johnson*, 1990]. None of these molecules have been seen as gravitationally bound species, but their presence is inferred from the ambient OH and H [*Richardson et al.*, 1998]. That is, the escaping molecules have long ($\sim$yr.) lifetimes in orbit about Saturn. A H cloud [*Shemansky and Hall*, 1992] and a toroidal OH cloud were observed [*Shemansky et al.*, 1993]. The latter occupies the region in which the icy satellites and Saturn's E-ring particles orbit. A small fraction of H and OH is derived by sputtering of the icy satellites [*Jurac et al.*, 2001b]. Other volatiles should be seen, like the CO_2 or SO_2 seen at the Jovian satellites or nitrogen and ammonia from an ammonia hydrite.

Analysis of the OH cloud [*Jurac et al.*, 2001a] showed that a large source is missing in the vicinity of Enceladus. Therefore, more icy surface area must be present in this region, possibly produced by small colliding icy objects, or the icy surfaces contain volatiles which would make sputtering more efficient. An active Enceladus has also been suggested because of its bright surface and because the E-ring peaks near its orbit [*Stevenson*, 1982]. The surfaces of the icy satellites and objects in the main rings are bombarded by both micrometeorites [*Haff and Eviatar*, 1986; *Pospieszalska and Johnson*, 1991] and by charged E-ring grains in eccentric orbits [*Hamilton and Burns*, 1994]. These processes can produce additional water vapor, but their net effect is not well established. This is due both to the absence of data on the impacting fluxes and a lack of knowledge of the vapor production efficiency from a porous icy surface. The distant icy moons of Saturn, such as Iapetus, have surface features that also suggest weathering processes are occurring. The principal atmospheric sources are likely solar wind sputtering and photodesorption.

3.5. *Other Bodies*

The icy moons of Uranus also exist in a trapped magnetospheric plasma. However, the plasma density is small because of the unusual orientation of the magnetic field to the satellite's orbital motion. Since the plasma is primarily protons from the atmosphere of Uranus, sputtering is less robust and but radiolysis occurs. Based on their reflectance, these satellites apparently experienced radiation darkening due to a carbon containing molecule in the ice [*Lanzerotti et al.*, 1987; *Strazzulla*, 1998].

When Pluto is inside the orbit of Neptune it has a significant atmosphere which is similar to Triton's. These atmospheres are primarily N_2 with a few percent CH_4 and CO. Pluto's surface is roughly in local vapor pressure equilibrium [*Trafton*, 1990]. In its present position the atmosphere is collisional. Charon, on the other hand, has a surface which is predominantly ice with a contaminant like that seen on other icy moons, possibly an ammonia hydrite or trapped CO_2, but shows no evidence of the volatiles found on Pluto and Triton [*Buie and Grundy*, 2000]. With a disc-averaged surface temperature of $\sim$60K, solar wind sputtering and photodesorption are likely principal contributors to Charon's atmosphere. If the suggested hydrated ammonia exists on the surface, the atmosphere will contain N_2 as a decomposition product [*Johnson*, 1998]. Because of decomposition, the hydrite is removed preferentially, so the subsurface concentration is likely larger than that at surface.

Although they are not surface boundary layer atmospheres, the atmospheres of Triton and Pluto exhibit interesting interactions with their surfaces (see III.4). Nitrogen ice is in vapor pressure equilibrium with the N_2 atmosphere. Since N_2 is more strongly absorbing in the thermal IR than in the visible, sunlight is absorbed at greater depths than that depth from which thermal emission occurs producing a solid state greenhouse effect. This causes sublimation at depth into the regolith with condensation near the surface [*Grundy and Stansberry*, 2000]. Since CH_4 is much less volatile, it is seen at higher concentrations in the surface than in the atmosphere, possibly concentrated by the greenhouse effect. This effect may also seal off the surface allowing the formation of the observed geysers.

4. SUMMARY

In this chapter I have summarized our understanding of surface boundary atmospheres on a number of solar system bodies. I have also very briefly described the physical processes controlling their composition and

density. These atmospheres are interesting for two reason. By monitoring such atmospheres we can learn about the external weathering agents. But what is more exciting, because of the paucity of spacecraft missions to distant objects, remote sensing of these atmospheres can lead to information on their surface composition. Understanding of the weathering processes and composition can lead, in principal, to an understanding of the evolution of these bodies. To make this a reality, an enhanced observing effort must be accompanied by an enhanced laboratory / modeling effort to study the relevant desorption processes.

Acknowledgments. The author would like to thank the M. Combi, R. Hodges, D. Hunten, M. Mendillo and A. Sprague for comments and suggestions. This work was supported by NASA's Planetary Atmospheres Program.

REFERENCES

Bahr, D.A., M.A. Fama, R.A. Vidal, and R.A. Baragiola, Radiolysis of water ice in the outer solar system: Sputtering and trapping of radiation products, *J. Geophys. Res.* in press 2001.

Bida, T.A., R.M. Killen, T.H. Morgan, Discovery of calcium in Mercury's atmosphere, *Nature* 404, 159-161, 2000.

Bird, G.A., Molecular Gas Dynamics and Direct Simulation of Gas Flows, Clarendon, Oxford, England 1994.

Brown, M.E., R.E. Hill, Discovery of an extended sodium atmosphere around Europa, *Nature* 380, 229-231, 1996.

Brown, M.E., Potassium in Europa's atmosphere, *Icarus* 151, 190-195, 2001.

Brown, M.E., A.H. Bouchez, Observations of Ganymede's Visible Aurorae, *BAAS, DPS Meeting* #31, #70.08, 1999.

Brown, R.A., F.H. Chaffee Jr, High resolution spectra of sodium emission from Io, *Astrophys. J.* 187, L125-L126, 1974.

Buie, M.W. and W.M. Grundy, The Distribution and physical state of H_2O on Charon, *Icarus* 148, 324-339, 2000.

Calvin, W. M., R. E. Johnson, and J. A. Spencer, O_2 on Ganymede: Spectral characteristics and plasma formation mechanisms, *Geophys. Res. Lett.* 23, 673-676, 1996.

Carlson, R.W., A Tenuous carbon Dioxide Atmosphere on Jupiter's Moon Callisto, *Science* 283, 820-821, 1999.

Carlson, R.W., R.E. Johnson, and M.S. Anderson, Sulfuric acid on Europa and the radiolytic sulfur cycle, *Science* 286, 97-99, 1999a.

Carlson, R.W., +13 authors, Hydrogen peroxide on the surface of Europa, *Science* 283, 2062-2064, 1999b.

Carlson, R.W., M.S. Anderson, and R.E. Johnson, Sulfuric acid pproduction on Europa: The radiolysis of sulfur in water ice, *Icarus* submitted, 2001.

Cheng, A.F. and L.J. Lanzerotti, Ice sputtering by radiation belt protons and rings of Saturn and Uranus, *J. Geophys. Res.* 83, 2597-2602, 1978.

Cheng, A.F., R.E. Johnson, L.J. Lanzerotti, and S.M. Krimigis, Magnetosphere exosphere, and surface of mercury, *Icarus* 71, 430-440, 1987.

Chyba, F., Energy for Microbial life on Europa, *Nature* 403, 381-382, 2000.

Cintila, M.J., Impact-induced thermal effects in the lunar and Mercurian regoliths, *J. Geophys. Res.* 97, 947-973, 1992.

Cooper, J.H., R.E. Johnson, B.H. Mauk, H.B. Garrett, and N. Gehrels, Energetic ion and electron irradiation of the icy galilean satellites, *Icarus* 149, 133-159, 2001.

Eviatar, A., V. Vasyliunas, and D. Gurnett, The ionosphere of Ganymede. Planet. *Planet. Space Sci.* 49, 327-336, 2001.

Feldman, W.C., S. Maurice, A.B. Binder, B.L. Barraclough, R.C. Elphic, and D.J. Lawrence, Fluxes of fast and epithermal neutrons from Lunar Prospector: Evidence for water ice at the poles, *Science* 281, 5382, 1998a.

Feldman, W.C., B.L. Barraclough, S. Maurice, R.C. Elphic, D.J. Lawrence, D.R. Thomsen, and A.B. Binder, Major compositional units of the Moon: Lunar Prospector: data, *Science* 281, 1489-1493, 1998b.

Flynn, B. and M. Mendillo, A picture of the Moon's atmosphere, *Science* 261, 184-186, 1993.

Flynn, B. and S.A. Stern, A spectroscopic survey of metallic species abunduances in the lunar atmosphere, *Icarus* 124, 530-536, 1996.

Goldstein, B.E., S.T. Suess, and R.J. Walker, Mercury: Magnetospheric processes and the atmospheric supply and loss rates, *J. Geophys. Res.* 86, 5485-5499, 1981.

Grundy, W.M. and J.A. Stansberry, Solar gardening and the seasonal evolution of nitrogen ice on Triton and Pluto, *Icarus* 148, 340-346, 2000.

Gorenstein, P., L. Golub, and P.L. Bjorkholm, Detection of radon emission at the edges of lunar maria with the Apollo alpha-particle spectrometer, *Science* 183, 411-413, 1974.

Haff, P.K. and A. Eviatar, Micrometeoroid impact on planetary satellites as a magnetospheric mass source, *Icarus* 66, 258-269, 1986.

Hall, D.T., P.D. Feldman, M.A. McGrath, and D.F. Strobel, The far-ultraviolet oxygen airglow of Europa and Ganymede, *Astrophys. J. Lett.* 499, 475-485, 1998.

Hamilton, D. P. and J.A. Burns, Origin of Saturn's E Ring: Self-Sustained, Naturally, *Science* 264, 550-553, 1994.

Hendrix, A.R., C.A. Barth and C.W. Hord, Ganymede's ozone-like absorber: observations by the Galileo ultraviolet spectrometer, *J. Geophys. Res.* 104(E6), 14169-14178, 1999.

Hapke, B., On the sputter alteration of regoliths of the outer solar system bodies, *Icarus* 66, 270-279, 1986.

Hapke, B., Space weathering from Mercury to the asteroid belt. *J. Geophys. Res.* 106, 10039-10073, 2001.

Hibbitts, C.A., T.B. McCord, and G.B. Hansen, The distributions of CO_2 and SO_2 on the surface of Callisto, *J. Geophys. Res-Planet.* 105,E9,22541-22557, 2000.

Hodges, R.R., Differential Equation of Exospheric Lateral Transport and Its Application to Terrestrial Hydrogen, *J. Geophys. Res.* 78, 7340-7346, 1973.

Hodges, R.R., *PEPI* 14, 282-288, 1977.

Hodges, R.R., Lunar cold traps and their influence on Argon-40, *Proc. Lunar and Planet Sci. Conf.* 11, 2463-2477, 1980a.

Hodges, R.R., Methods for Monte Carlo simulation of the exospheres of the Moon and Mercury, *J. Geophys. Res.* 85, 164-170, 1980b.

Hodges, R.R., Ice in the lunar polar regions revisited, *Icarus*, in press 2001.

Hodges, R.R. and Hoffman, *Geophys. Res. Letts.* 1, 69-71, 1974.

Hogdes, R.R. and F.S. Johnson, *J. Geophys. Res.* 73, 7307-7317, 1986.

Hodges, R.R., J.H. Hoffman, and F.S. Johnson, Composition and dynamics of the lunar atmosphere, *Geochimica et Cosmo. Acta.* 3, *(Suppl. 4)* 2855-2864, 1973.

Hodges, J.H. Hoffman, and F.S. Johnson, The lunar atmosphere, *Icarus* 21, 415-440, 1974.

Huebner, W.F., J.J. Keady, and S.P. Lyon, Solar photorates for planetary atmospheres and atmospheric pollutants, *Astrophys. and Space Sci.* 195, 1-294, 1992.

Hunten,D.M., T.H. Morgan, and D.E. Shemansky, The Mercury atmosphere, in *Mercury*, edited by F. Vilas, C.R. Chapman, and M.S. Matthews, pp.562-612, Univ. of Ariz. Press, Tucson, 1988.

Hunten, D.M., The equilibrium of atmospheric sodium, *Planet. Space Sci.* 40, 1607-1614, 1991.

Hunten, D.M., R.W.H. Kozlowski, and A.L. Sprague. A possible meteor shower on the Moon, *Geophys. Res. Lett.* 18, 2101-2104, 1991.

Hunten, D.M. and A.L. Sprague, Origin and character of the Lunar and Mercurian atmospheres, *Adv. Space Res.* 19, 1551-1560, 1997.

Hunten, D.M., G. Cremonese, A.L. Sprague, R.E. Hill, S. Vernai, and R.W.H. Kozlowski, The Leonid meteor shower and the Lunar sodium atmosphere, *Icarus* 136, 298-303, 1998.

Ip, W.H., The sodium exosphere and magnetosphere of Mercury, *Geophys. Res. Lett.* 13(5), 423-426, 1986.

Ip, W. -H. Europa's oxygen exosphere and its magnetospheric interaction, *Icarus* 120, 317-325, 1996.

Johnson, R.E., Sputtering of a planetary regolith, *Icarus 78*, 206-210, 1989.

Johnson, R.E., Energetic Charged-Particle Interactions with Atmospheres and Surface, *Springer-Verlag, Berlin* 1990.

Johnson, R.E., Sputtering of ices in the outer solar system, *Rev. Mod. Phys.*, 68, 305-312, 1996.

Johnson, R.E., Polar 'caps' on Ganymede and Io revisited, *Icarus* 128, 469-471, 1997.

Johnson, R.E., Sputtering and desorption from icy surfaces, In *Solar System Ices* (B. Schmitt, C. deBergh Eds.) (Kluwer Netherlands, Dordrecht) pp.303-334, 1998.

Johnson, R.E., Sodium at Europa, *Icarus* 143,429-433, 2000.

Johnson, R.E., Surface chemistry in the Jovian magnetosphere radiation environment, *In Chemical Dynamics in Extreme Environments* (R. Dessler, Ed), *Adv. Ser. in Phys. Chem.* World Scientific, Singapore, Chapter 8, 390-419, 2001.

Johnson, R.E. and E.C. Sittler, Sputter-produced plasma as a measure of satellite surface composition: The CASSINI mission, *Geophy. Res. Letts.* 17, 1629-1632, 1990.

Johnson, R.E. and R.A. Baragiola, Lunar surface: Sputtering and secondary ion mass spectrometry, *Geophys. Res. Letts.* 18, 2169-2172, 1991.

Johnson, R.E. and W. A. Jesser, Radiation-produced microatmospheres in the surface of Ganymede, *Astrophys. J. Lett.* 480, L79-L82, 1997.

Johnson, R.E. and T.I. Quickenden, Photolysis and radiolysis of water ice on outer solar system bodies, *J. Geophys. Res.* 102, 10985-10996, 1997.

Johnson, R.E., L.J. Lanzerotti, and W.L. Brown, Planetary application of ion induced erosion of condensed-gas frosts, *Nucl. Instrum. Methods* 198, 147-158, 1982.

Johnson, R. E., M. Nelson, T.M. McCord, and J. Gradie, Voyager Images of Europa: Plasma Bombardment, *Icarus* 75, 423-436, 1988.

Johnson, R.E., R.M. Killen, J.H. Waite Jr., and W.S. Lewis, Europa's surface composition and sputter-produced ionosphere, *Geophy. Res. Letts.* 25, 3257-3260, 1998.

Johnson, R.E., F. Leblanc, B.V. Yakshinskiy, and T.E. Madey, Energy distributions for desorption of sodium and potassium from ice: the Na/K ratio at Europa, *Icarus*, in press 2001.

Jurac, S., J.D. Richardson, M.A. McGrath, and V.M. Vasyliunas, A Eviatar. OH cloud in Saturn's magnetosphere, *BAAS, DPS meeting* #32, #12.02, 2000.

Jurac, S., R.E. Johnson, and J.D. Richardson, Saturn's E-ring and production of a neutral torus, *Icarus* 149, 384-396, 2001a.

Jurac, S., R.E. Johnson, J.D. Richardson, and C. Paranicas, Satellite sputtering in Saturn's magnetosphere", *Planet Space Sci.* 49(3-4), 319-326, 2001b.

Kabin,K., T.I.Gombosi, D.L.DeZeeuw, and K.G. Powell, Interaction of Mercury with the solar wind, *Icarus* 143, 397, 2000.

Kargel, J.S., Brine volcanism and the interior structure of asteroids and icy satellites, *Icarus* 94, 368-390, 1991.

Khurana, K.K., M.G. Kivelson, D.J. Stevenson, G. Schuber, C.T. Russell, R.J. Walker, and C. Polanskey, Induced magnetic fields as evidence for subsurface oceans in Europa and Callisto *Nature* 395, 777-780, 1998.

Killen, R.M. and W.H. Ip, The surface-bounded atmospheres of Mercury and the Moon, *Rev. Geophys.* 37, 361-406, 1999.

Killen, R.M., A.E. Potter, P. Reiff, M. Sarantos, B.V. Jackson, P. Hick, and B. Giles, Evidence for space weather at Mercury, *J. Geophys. Res.* 106, 20509-20525, 2001.

Kimmel, G.A., T.M. Orlando, C. Vizina, and L. Sanche, Low energy electron-stimulated production of molecular hydrogen from amorphous water ice, *J. Chem. Phys.* 101, 3282-3286, 1994.

Kimmel, G.A. and T.A. Orlando, Low-energy (5 - 120 eV) electron stimulated dissociation of amorphous D_2O ice: $D(^2S)$, $O(^3P_{2,1,0})$, and $O(^1D)$ yields and velocity distributions, *Phys. Rev. Lett.* 75, 2606-2609, 1995.

Kivelson, M.G., K.K. Khurana, C.T. Russel, R.J. Walker, J. Warnecke, F.V. Coroniti, C. Polanskey, D.J. Southwood, and G. Schubert, Discovery of Ganymede's magnetic field by the Galileo spacecraft, *Nature* 384, 537-541, 1996.

Kliore, A., J.D.P. Hinson, F.M. Flasar, A.F. Nagis, and T.E. Crasens, The ionosphere of Europa from Galileo radio occultations, *Science* 277, 1239-1241, 1997.

Kozlowski, R.W.H., A.L. Sprague, and D.M. Hunten, Observations of potassium in the tenuous lunar atmosphere, *Geophys. Res. Letts.* 17, 2253-2256, 1990.

Kumar, S. and D.M. Hunten, The atmosphere of Io and other satellites, In *Satellites of Jupiter* (Ed.. D. Morrison) U of Arizona Press, Tucson pp782-806, 1982.

Lane, A.L., R.M. Nelson, and D. L. Matson, Evidence for sulphur implantation in Europa's UV absorption band, *Nature* 292, 38-39, 1982.

Lanzerotti, L.J., W.L. Brown, and K.J. Marcantonio, Experimental study of erosion methane ice by energetic ions and

some consideration for astrophysics, *J. Astrophys.* 313, 910-919, 1987.

Leblanc, F., R.E. Johnson, and M.E. Brown, Europa's sodium atmosphere: an ocean source? *Icarus* submitted 2001.

Madey, T.E., B.V. Yakshinskiy, V.N. Ageev, R.E. Johnson, Desorption of alkali atoms and ions from oxide surfaces: Relevance to origins of Na and K in the atmospheres of Mercury and the Moon, *J. Geophys. Res.* 103, 5873-5888, 1998.

Madey, T.E., R.E. Johnson, and T.M. Orlando, Far-out surface science: radiation-induced surface processes in the solar system, *Surface Science* in press 2001.

Mall, U., E. Kirsch, K. Cierpka, B. Wilken, A. Soding, F. Neubauer, G. Gloeckler, and A. Galvin, Direct observation of lunar pick-up ions near the Moon, *Geophys. Res. Lett.* 25, 3799-3802, 1998.

Manka, R.H. and F.C. Michel, Lunar atmosphere as a source of Argon-40 and other lunar elements, *Proc. Lunar Sci Conf. 2nd, Geochimica Cosmochim Acta Suppl.* 2, 1717-1728, 1971.

Manka, R.H. and F.C. Michel, Lunar ion flux and energy, In, Photon and Particle Interactions with surfaces in space (ed., R.J.L. Grard) (*D. Reidel, Dordrecht*) 429-442, 1973.

Matsuura, T., Hot Atom Chemistry. Kodansha, *Tokyo: Elsevier, Amsterdam* 1984.

McCord, T.B., +13 authors, Salts on Europa's surface detected by Galileo's near infrared mapping spectrometer, *Science* 280, 1242-1245, 1998.

McGrath, M.A., R.E. Johnson, and L.J. Lanzerotti, Sputtering of sodium on the planet Mercury, *Nature* 22, 694-696, 1986.

McGrath, M. A., P.D. Feldman, D.F. Strobel, K. Retherford, B. Wolven, and H.W. Moos, HST/STIS Ultraviolet imaging of Europa, *BAAS. DPS Meeting* #32, #34.09, 2000.

Mendillo, M., B. Flynn, and J. Baumgardner, Imaging experiments to detect an extended sodium atmosphere on the Moon, *Adv. Space Res.* 13(10), 313-319, 1993.

Mendillo, M., J. Wilson, J. Baumgardner, G. Cremonese, and C. Barbieri, Eclipse observations of the lunar atmosphere from the TNG site, in *The Three Galileos*, edited by J. Rahe et al. pp. 393-400, Kluwer Acad., Norwell, Mass., 1997a.

Mendillo, M., J. Emery, and B. Flynn, Modeling the Moon's extended sodium cloud as a tool for investigating sources of transient atmosphere, *Adv. Space Res.* 19(3), 1577-1586, 1997b.

Mendillo, M., J. Baumgardner, and J. Wilson, Observational Test for the Solar Wind Sputtering Origin of the Moon's Extended Sodium Atmosphere, *Icarus* 137, 13-23, 1999.

Morgan, T.H., H.A. Zook, and A.E. Potter, Impact-driven supply of sodium and potassium to the atmosphere of Mercury, *Icarus* 75, 156-170, 1988.

Morgan, T.H., H.A. Zook, and A.E. Potter, Production of sodium vapor from exposed regolith in the inner solar system, *Proc. Lunar Sci. Conf.* 19th, 297-304, 1989.

Noll, K.S., R.E. Johnson, A.L. Lane, D.L. Dominigue, and H.A. Weaver, Detection of ozone on Ganymede, *Science* 273, 341-343, 1996.

Noll, K.S., T. Roush, D. Cruikshank, R.E. Johnson, and Y.J. Pendleton, Ozone on Dione and Rhea, *Nature* 388, 45-47, 1997.

Pappalardo, R.T., J.W. Head, and R. Gredy, The hidden ocean of Europa, *Scientific American*, Oct., 34-43, 1999.

Paranicas, C., R.W. Carlson, and R.E. Johnson, Electron bombardment of Europa, *Geophys. Res. Lett.* 28, 673-676, 2001.

Pospieszalska, M. and R.E. Johnson, Plasma ion bombardment profiles: Europa and Dione, *Icarus* 78, 1-13, 1989.

Pospieszalska, M. and R.E. Johnson, Micrometeorite erosion of the main rings as a source of plasma in the inner Saturnian plasma torus, *Icarus* 93, 45-52, 1991.

Potter, A.E., Chemical sputtering could produce sodium vapor and ice on Mercury, *Geophys. Res. Lett.* 22, 3289-3292, 1995.

Potter, A.E. and T.H. Morgan, Discovery of sodium in the atmosphere of Mercury, *Science* 229, 651-653, 1985.

Potter, A.E. and T.H. Morgan, Potassium in the atmosphere of Mercury, *Icarus* 67, 336-340, 1986.

Potter, A.E. and T.H. Morgan, Discovery of sodium and potassium vapor in the atmosphere of Moon, *Science* 241, 657-680, 1988.

Potter, A.E. and T. H. Morgan, Variation of the lunar solar emission with phase angle, *J. Geophys. Res.* 21, 2263-2266, 1994.

Potter, A.E., R.M. Killen, and T.H. Morgan, Variation of lunar sodium during passage of the Moon through the Earth's magnetotail, *J. Geophys. Res.* 105, 15073-15084, 2000.

Reimann, C.T., J.W. Boring, R.E. Johnson, J.W. Garrett, K.R. Farmer, and W.L. Brown, Ion-induced molecular ejection from D_2O ice, *Surf. Sci.* 147, 227-240, 1984.

Richardson, J.D., D.A. Eviatar, M.A. McGrath, and V.M. Vasyliunas. OH in Saturn's magnetosphere: Observation and implications, *J. Geophys. Res.* 103, 20245-20255, 1998.

Roth, J., Chemical sputtering. In, Sputtering by Particle Bombardment II. Ed. R. Behrisch (*Springer Verlag, Berlin*) 91-141, 1983.

Sarantos,B., P.H. Reiff, T.W. Hill, R.M. Killen, and A.L. Urquhart. A Bx-interconnected magnetosphere model for Mercury. *Planet. Space Sci.* in press 2001.

Saur, J., D.F. Strobel, and F.M. Neubauer, Interaction of the Jovian manetosphere with Europa: Constraints on the neutral atmosphere, *J. Geophys. Res.* 103, 19947-19962, 1998.

Shemansky, D.E. and A.L. Broadfoot, Interaction of the surfaces of the Moon and Mercury with their exospheric atmospheres, *Rev. of Geophys. and Space Phys.* 15, 491-499, 1977.

Shemansky, D.E. and D.T. Hall, The distribution of atomic hydrogen in the magnetosphere of Saturn, *J. Geophys. Res.* 97, 4143-4161, 1992.

Shemansky, D.E., P. Matheson, D.T. Hall, H.-Y. Hu, and T.M. Tripp, Detection of the hydroxyl radical in the Saturn magnetosphere, *Nature* 363, 329-331, 1993.

Shematovich, V.I. and R.E. Johnson, Near-surface oxygen atmosphere at Europa, *Adv. Space Res.* 27, 1881-1888, 2001.

Shi, M., R.A. Baragiola, D.E. Grosjean, R.E. Johnson, S. Jurac, and J. Schou, Sputtering of water ice surfaces and

the production of extended neutral atmospheres, *J. Geophys. Res.* 100, 26387-26395, 1995.

Sieger, M.T., W.C. Simpson, T.M. Orlando, Production of O_2 on icy satellites by electronic excitation of low-temperature water ice, *Nature* 394, 554, 1998.

Sieveka, E.M. and R.E. Johnson, Thermal - and plasma - induced molecular redistribution on the icy satellites, *Icarus* 51, 528-548, 1982.

Smith, R.S. and B. D. Kay, Adsorption, desorption and crystallization kinetics in nanoscale water films, *Recent Res. Devel, Phys. Chem.* 1, 209-219, 1997.

Smith, S.M., J.K. Wilson, J. Baumgardner, and M. Mendillo, Discovery of the distant Lunar sodium tail and its enhancement following the Leonid meteor shower of 1998, *Geophys. Res. Lett.* 26, 1649, 1999.

Smyth, W.H. and M.L. Marconi, Theoretical overview and modeling of the sodium and potassium atmospheres of Mercury, *J. Astrophys.* 441, 839-864, 1995a.

Smyth, W.H. and M.L. Marconi, Theoretical overview and modeling of the sodium and potassium atmospheres of the Moon, *J. Astrophys.* 443, 371-392, 1995b.

Spencer, J.R. and A. Klesman, New observations of molecular oxygen on Europa and Ganymede, *Bull. AAS.*, #47.04, 1125, 2001.

Sprague, A.L., A diffusion source for sodium and potassium in the atmospheres of Mercury and the Moon, *Icarus* 84, 93-105, 1990.

Sprague, A.L., Mercury's atmospheric bright spots and potassium variations: A possible cause, *J. Geophys. Res.* 97, 18257-18264, 1992.

Sprague, A.L., R.W.H. Kozlowski, D.M. Hunten, W.K. Wells, and F.A. Grosse, The sodium and potassium atmosphere of the Moon and its interaction with the surface, *Icarus* 96, 27-42, 1996.

Sprague, A.L., R.W. Kozlowski, D.M. Hunten, N.M. Schneider, D.L. Domingue, W.K. Wells, W. Schmitt, and U. Fink, Distribution and abundance of sodium in Mercury's atmosphere, 1985-1988, *Icarus* 129, 506-527, 1997.

Sprague, A.L., W.J. Schmitt, and R.E. Hill, Mercury: Sodium atmospheric enhancements, radar-bright spots, and visible surface features, *Icarus* 136, 60-68, 1998.

Stern, S.A., The Lunar Atmosphere: History, status, current problems, and context, *Rev. Geophys.* 37, 453-491, 1999.

Stern, S.A. and B.C. Flynn, Narrow-field imaging of the lunar sodium exosphere, *J. Astron.* 109, 835-841, 1995.

Stern, S.A., A. Fitzsimmonds, R.M. Killen, and A.E. Potter, A direct measurement of the sodium temperature in the Lunar atmosphere, In *Lunar Planet. Sci. XXXI abstract 1112, Lunar Planet Inst.*, Houston TX (CD-ROM) 2000.

Stevenson, D.J., Volcanism and igneous processes in small icy satellites, *Nature* 298, 142-148, 1982.

Stirniman, M.J., C. Huang, R.S. Smith, S.A. Joyce, and B.D. Kay, The adsorption and desorption of water on single crystal MgO(100): The role of surface defects, *J. Chem. Phys.* 105, 1295-1298, 1996.

Strazzukka, G., Chemistry of ice induced by energetic charged particles, In *Solar System Ices* (ed. B. Schmitt et al., Kluwer, nethelands) p. 281-302, 1998.

Trafton, L., A two-component volatile atmosphere for Pluto, I - The bulk hydrodynamic escape regime, *Astrophys. J.* 359, 512-523, 1990.

Vidal, R.A., D.A. Bahr, R.A. Baragiola, and M. Peters, Oxygen on Ganymede: laboratory studies, *Science* 276, 1839-1842, 1997.

Walters, M., W.A. Jesser, J.W. Boring, and R.E. Johnson, Crystallization of SiO by He bombardment, *Radiat. Res.* 106, 189-201, 1988.

Westley, M.S., R.A. Baragiola, R.E. Johnson, and G.A. Baratta, Ultraviolet photodesorption from water ice, *Planet. Space Sci.* 43, 1311-1315, 1995.

Wiens, R.C., D.S. Burnett, W.F. Calaway, C.S. Hansen, K.R. Lykke, and M.L. Pellin, Sputtering products of sodium sulfate: Implications for Io's surface and for sodium bearing molecules in the Io torus, *Icarus* 128, 386-397, 1997.

Wilson, J.K., S.M. Smith, J. Baumgardner, and M. Mendillo, Modeling an enhancement of the lunar sodium tail during the Leonid meteor shower of 1998, *Geophys. Res. Lett.* 26, 1645, 1999.

Yakshinskiy, B. and T. Madey, Electronic desorption of Na from silicates, *Nature* 400, 642-644, 1999.

Yakshinskiy, B.V., T.E. Madey, and V.N. Ageev, Thermal Desorption of Sodium Atoms from Thin SiO_2 Films, *Surface Rev. and Lett.* 7, 75-87, 2000.

Yakshinskiy, B.V. and T.E. Madey, Electron and photon-simulated desorption of K from an ice surface, *J. Geophys. Res.* in press 2001.

Zolotov, M.Y. and E.L. Shock, The composition and stability of salts on the surface of Europa and their oceanic origin, *J. Geophys. Res.* in press 2001.

Zook, H.A. and J.E. McCoy, Large scale lunar horizon glow and high altitude lunar dust exosphere, *Geophys. Res. Letts.* 18, 2117-2120, 1991.

Engineering Physics and the Department of Astronomy, University of Virginia, Thornton Hall 103, Charlottesville, VA 22903

Solar Ultraviolet Variability Over Time Periods of Aeronomic Interest

Thomas N. Woods and Gary J. Rottman

Laboratory for Atmospheric and Space Physics, University of Colorado, Boulder, Colorado.

The solar ultraviolet (UV) radiation is a primary energy source for planetary atmospheres and is also a tool for remote sensing of the planets. The solar UV radiation from mostly below 300 nm dissociates molecules, ionizes the neutral atmosphere, and affects many chemical cycles in the atmospheres. In addition, solar photons scatter off the molecules and atoms in the atmospheres and provide a method of remote sensing the composition and density of the atmospheres. For such aeronomic studies, accurate values of the solar UV irradiance, primarily shortward of 200 nm, are needed over time periods of days to decades. A planet's orbital motion around the Sun and the intrinsic solar variability are the primary causes of the variation of the solar intensity at a planet. The insolation changes caused by the orbital motion are easily calculated as the inverse square of the Sun-planet distance; however, the intrinsic solar irradiance variability is more complicated and is strongly dependent on wavelength and time. The primary short-term irradiance variability over several days is caused by the solar rotation, which has a mean period of 27 days. The primary long-term variability is related to the solar dynamo that reverses the solar magnetic field and is known as the 11-year solar cycle. The variations observed during solar cycle 22 (1986-1996) are the basis for creating some reference spectra of the solar UV irradiance for use in comparative aeronomic studies. From these reference spectra, the solar cycle variability as a function of wavelength can be characterized as 15% and less at wavelengths longward of 160 nm, as 15% to 70% between 160 and 65 nm, and as a factor of 1.5 to 7 between 65 and 1 nm. The magnitude of the 27-day rotational variability is usually no more than one third of the solar cycle variability. There is not a smooth transition of variability between wavelengths, but instead the amount of intrinsic solar variability depends on the source of the radiation in the solar atmosphere. In general, the coronal emissions vary the most, then the transition region emissions vary somewhat less, chromospheric emissions vary even less, and finally the photospheric emissions vary the least, perhaps only 0.1% at the longest UV wavelengths.

INTRODUCTION

The solar ultraviolet (UV) radiation, being wavelengths less than 400 nm, is an important source of energy for aeronomic processes throughout the solar system. The solar

Atmospheres in the Solar System: Comparative Aeronomy
Geophysical Monograph 130

10.1029/130GM14

UV photons are absorbed in planetary and cometary atmospheres, as well as throughout the heliosphere, via photodissociation of molecules, photoionization of molecules and atoms, and photoexcitation including resonance scattering (e.g., see *Chamberlain* [1978]). The subdivisions of the UV spectral range for this discussion include the near ultraviolet (NUV) as the 300 to 400 nm range, the middle ultraviolet (MUV) as the 200 to 300 nm range, the far ultraviolet (FUV) as the 120 to 200 nm range, the extreme ultraviolet (EUV) as the 30 to 120 nm range, the x-ray ultraviolet (XUV) as the 1 and 30 nm range, and x-rays as wavelengths less than 1 nm. The solar EUV and XUV radiation photoionizes the neutral constituents of the atmospheres and participates in the formation of the ionosphere. The photoelectrons created in this process interact further with the neutrals, leading to excitation, dissociation, and additional ionization. The excess energy from the absorption processes goes into heating the atmosphere. As an example for Earth as shown in Plate 1, the solar MUV radiation heats the stratosphere, and the solar UV radiation shortward of 170 nm heats the thermosphere. The absorption of the solar UV radiation also initiates many chemical cycles in the atmospheres, such as the chemistry of water vapor, ozone, and nitric oxide in Earth's atmosphere (e.g., see *Brasseur and Solomon* [1986]). As depicted in Plate 1, the chemistry cycle of ozone in Earth's stratosphere is balanced largely by the creation of ozone via the photodissociation of molecular oxygen followed by the combination of the atomic oxygen with molecular oxygen and by the destruction of ozone via direct photodissociation. The longer wavelengths of the solar radiation, mainly from the NUV, visible (VIS: 400-700 nm), and near infrared (NIR: 700-10000 nm), are absorbed by aerosols, clouds, and gases in the troposphere and by land surfaces and oceans; thus, the Sun also affects those environments. All of these atmospheric processes are wavelength dependent and are expected to be as variable as the intrinsic solar variability at the appropriate wavelengths. Therefore, accurate measurements of the solar UV spectral irradiance, along with an understanding of its variability, are important for detailed studies of the aeronomic processes.

The remote sensing of the composition and density in the heliosphere, comets, and planetary atmospheres is often determined by measuring the brightness of an emission that is created by the resonant scattering of solar UV photons. In particular, the column density of a constituent is often derived by dividing the measured brightness of the emission by the g-factor, or fluorescence efficiency. The g-factor is based on well-known atomic parameters, such as the emission's oscillator strength, and the incident solar irradiance (e.g., see *Meier* [1995]). Consequently, the accuracy of the derived abundance is directly dependent on the accuracy of the emission brightness measurement and on the accuracy of the solar UV irradiance, both spectral intensity and shape. Often there are not cotemporal measurements of the solar UV irradiance, so estimates must be used in the analysis. These estimates may be calculated or derived from measurements taken at other times but projected to the desired epoch. Reference spectra of the solar UV irradiance are presented here to aid such aeronomic studies.

The solar UV irradiance can be incorporated in a variety of ways into studies of comparative aeronomy. For detailed studies of aeronomic observations, cotemporal observations of the solar UV irradiance provide the most accurate solar information. Reference spectra of the solar UV irradiance, which are normally based on actual observations, are sometimes included in aeronomic studies, for example, to determine the sensitivity of an aeronomic model to solar variability. In cases where solar observations are not available or have incomplete wavelength coverage, which is often the case for the EUV and XUV, models of the solar irradiance can provide an estimate of the solar spectrum for a given aeronomic observation. These models can be as simple as linear scaling between two reference spectra or complicated physical models of the solar irradiance. The focus here is on the general behavior of the Sun and not on any specific aeronomic study; therefore, reference solar irradiance spectra, along with a discussion of the present understanding of the solar variability, are the focus for this paper. For more detailed information about the historical background and previous results of the solar UV irradiance, one should examine reviews, for example, by *White* [1977], *Rottman* [1987], *Lean*, [1987 and 1991], *Tobiska* [1993], and *Pap et al.* [1994].

SOLAR SPECTRUM

The overall solar spectrum is fairly well characterized as a continuum similar to a blackbody with a temperature near 5800 °K. The radiation peaks near 600 nm and falls slowly and continuously toward the longer infrared wavelengths, but falls quite abruptly toward the shorter wavelengths of the ultraviolet. Moreover, for the UV wavelengths the spectrum is not smooth but is superimposed in the UV longward of 200 nm with strong absorption lines (Fraunhofer lines) and absorption edges that make the spectrum deviate from the smooth blackbody curve. Shortward of 200 nm the spectrum changes from having absorption lines to having emission lines, and by 130 nm the solar spectrum is dominated more by emission lines than by the continuum. These emission lines arise from the dominate species, H and He, and the many minor species in the higher layers of the solar atmosphere as a non-local thermodynamic equilibrium (non-LTE) effect and are strongly

sensitive to the magnetic activity on the Sun. These emissions also include the ionization continua, such as the bright H ionization continuum shortward of 91 nm. These general characteristics of the solar UV spectrum are evident in Plate 2, which includes a solar spectrum at 0.1 nm spectral resolution. This spectrum and others discussed here are the solar spectral irradiance, which is the spectral radiance (or intensity) at a single wavelength integrated over the full-disk of the Sun and observed at a distance of 1 AU. Most of the discussion here focuses on the UV shortward of 200 nm because it is the spectral range especially important for solar-aeronomic studies. This spectral range is commonly called the vacuum UV (VUV) because measurements shortward of 200 nm require a vacuum, such as from space, and the VUV is often subdivided into the XUV, EUV, and FUV ranges as shown in Plate 2.

The continuum is emitted mainly from the photosphere, and the many emissions features are emitted from the solar upper atmosphere: chromosphere, transition region, and corona. The dominant species, H and He, contribute much of the irradiance, such as the bright H I Lyman-α (121.6 nm) and He II Lyman-α (30.4 nm) emissions. The distribution of the emission features with wavelength is based on the complex atomic energy levels of the source gases. To generalize the emission spectral distribution, the higher temperature emissions arising from the more highly ionized atoms naturally have higher energy states and thus occur at shorter wavelengths. For example, the solar radiation shortward of 20 nm is dominated by coronal emissions. With the density decreasing with altitude and the temperature increasing at higher layers of the solar atmosphere, the radiation from the higher layers is, in general, more variable. In other words, the coronal emissions vary more than the transition region emissions, which in turn vary more than the chromospheric emissions.

SOURCES OF SOLAR VARIABILITY

For studies of comparative aeronomy two aspects of the solar irradiance are important: one is the absolute value of the irradiance, and the second is its variability. Both aspects are considered here, but the absolute value of the irradiance is deferred to a later discussion. The value of the solar intensity incident on a solar system body will vary for three reasons: (1) changes in the distance to the Sun, (2) changes in the radiation field directed from the Sun toward the body, and finally, (3) intrinsic variation in the output of the Sun.

Considering first the distance to the Sun, the solar intensity at a planet varies inversely as the distance squared. The resulting change in intensity is generally called insolation as it is not an intrinsic variation of the solar radiation. Table 1 lists some important orbital characteristics for the nine planets. One of the columns in Table 1 lists the "$<1/R^2>$ Effect", which is the inverse of the average Sun-planet distance squared; these values are normalized to unity for Earth, which has a mean Earth-Sun distance of 1 AU. For this discussion, the solar irradiance is considered the full-disk solar intensity at 1 AU. As an example, the intensity relative to the irradiance at Earth is a factor of 2 at Venus, 1% at Saturn, and 0.1% at Neptune. The column labeled "ε-Effect" is the orbital eccentricity effect and lists the insolation variation encountered during a planet's motion about the Sun, and the column "Orbital Period" provides the corresponding time base of this variation. For example, the Earth's orbital eccentricity ($\varepsilon = 0.017$) gives rise to a 7% insolation variation with a period of one year. In January the insolation is 7% larger while the Earth is at perihelion than in June when it is at aphelion. Likewise, Jupiter experiences about 20% insolation variation due to its orbital motion with a period of about 12 years, quite close to the 11-year solar cycle variation. Therefore, in the case of Jupiter the orbital changes in the insolation may overwhelm the intrinsic solar cycle irradiance variations at certain wavelengths, while at other wavelengths the solar cycle variations may overwhelm the orbital changes.

The second variation of solar intensity that a planet is certain to experience is due to a "search-light" effect resulting from the non-uniform distribution of bright regions on the solar disk that are modulated by the 27-day rotation period of the Sun. Regardless of whether the solar disk has many bright active regions or only a few and if the distribution of these features is non-uniform, as is usually the case, the 27-day variation of irradiance is quite apparent. If the solar irradiance is measured from Earth, then these values are only appropriate to celestial bodies in opposition (or inferior conjunction for inner planets) with the Earth. Bodies at other solar longitudes experience a time record of irradiance advanced or retarded by an appropriate phase. Fortunately, features on the Sun appear and disappear over a period of a few months, so the irradiance time series can be considered quasi-stationary, often allowing phase (time) shifts up to $\pm 180°$ with reasonable confidence.

The third type of solar variation, and the one considered in more detail in this paper, is intrinsic or inherent solar variability. The magnetic activity on the Sun is the primary cause of the intrinsic solar variability and is manifested into a variety of features on the solar disk. The plages, active network, and quiet network are a generalization of the principle features on the Sun that affect the variability of the solar UV radiation. These solar features are defined for modeling purposes and are described in more detail by *Schrijver* [1988], *Harvey and White* [1999], and *Worden et al.* [1998]. The plages are the large, bright active regions observable in the UV, as can be seen in the so-

[redacted]

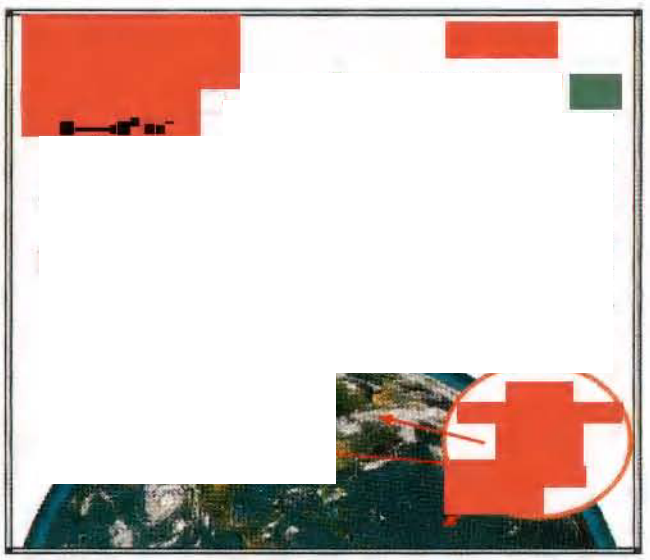

[redacted]

[redacted]

Table 1. The variations of the solar intensity due to orbital motion changes are listed for the planets where R is the distance to the Sun and ε is the orbital eccentricity.

Planet	$<1/R^2>$ Effect (1 = Earth)	ε Effect (%)	Orbit Period (yr)
Mercury	6.75	130	0.24
Venus	1.93	3.0	0.62
Earth	1	6.9	1.00
Mars	0.43	45	1.88
Jupiter	0.037	21	11.9
Saturn	0.011	25	29.5
Uranus	0.0027	21	84
Neptune	0.0011	3.7	164
Pluto	0.00064	178	248

lar image in Plate 2, and are associated with the dark sunspots and bright faculae features seen in the visible. The plages are intense, localized regions that appear primarily below 30° latitude on the Sun, and as a collective group their rotation with the solar atmosphere produces a strong 27-day rotational variability. The active network is the decay of the plages into smaller, more diffuse regions over a period of a few months. The active network is distributed almost uniformly over the solar longitudes and, consequently, has only a weak, if any, contribution to the 27-day variability. The quiet network is often assumed to have constant radiance regardless of the solar activity, although some recent results indicate that the quiet network may vary with the solar cycle [*Schühle et al.*, 2000]. During a solar cycle, the plage fractional area over the solar disk varies from 0 to 0.2, and the active network fractional area varies from 0.04 to 0.2 [*Worden et al.*, 1998 and 1999]. The quiet network fractional area is simply one minus the plage and active network fractional areas. It is important to note that the active network fractional area is not zero during solar minimum; therefore, the solar minimum irradiance is probably at slightly different levels during different solar cycles [*Worden et al.*, 1998]. *Lean et al.* [1982] and *Worden* [1996] have successfully used the area of these three components, namely plage, active network, and quiet network, to model the variability of the solar UV irradiance. Moreover, they have shown that at least these three components are needed to explain both the 27-day variability and the 11-year variability observed in the solar UV irradiance, and moreover, that emissions at different wavelengths have different sensitivities to these three components. Related to this later point, *Woods et al.* [2000b] have shown that the 11-year variability of the transition region emissions, such as the H I Lyman-α (121.6 nm) emission, has a much larger contribution from the active network regions than so for the long-term variability of the chromospheric or coronal emissions. As a summary for intrinsic solar variability, both the different layers of the solar atmosphere and the composition of features on the solar disk are needed to study the solar variability as a function of wavelength.

TIME PERIODS OF SOLAR VARIABILITY

The Sun varies over all time periods, and the amount of variability is a strong function of wavelength. The irradiance variations most important for aeronomic studies include minute-long flares, the 27-day solar rotation, and the 11-year solar cycle. Very short-term variations, lasting from minutes to hours, are related to eruptive phenomena on the Sun, short-term variations, modulated by the 27-day rotation period of the Sun, are related to the appearance and disappearance of active regions on the solar disk, and the prominent long-term solar cycle variability is related to the 22-year magnetic field cycle of the Sun caused presumably by the internal solar dynamo.

The eruptive events, such as flares, occur over time periods of a few minutes. The flare emissions are most often seen in the coronal emissions; therefore, the solar flares predominantly alter the shorter XUV wavelengths, which in turn affect more the plasma (via ionization) than the neutrals in a planetary atmosphere. There are a few large flares during a solar cycle that do have a large impact on the full-disk irradiance at many wavelengths and thus can cause detectable atmospheric changes. The GOES 1-8 Å x-ray measurements clearly show several flares per month with increases of irradiance by factors of 10 to 1000, but only two large flares have been detected in the FUV irradiance during the first 9 years of the UARS mission (1991-2000), due in large part to the UARS duty cycle and observing mode. *Brekke et al.* [1996] report increases of the transition region emissions by a factor of 12 for a very extended X3.3 class flare on February 27, 1992. A large increase, a factor of 3, of the transition region emissions was also observed for a very extended X5.7 class flare on July 14, 2000. During these large flare events the chromospheric emissions and the FUV continuum also showed increases by factors of 1.3 to 2 and 1.1 to 1.5, respectively. Because of the infrequent occurrences of large flares, it is difficult to generalize the flare irradiance as a function of wavelength.

The solar rotation of about 27-days is a strong component in the irradiance variation at essentially all wavelengths. The Sun is a differential rotator with its equator rotating with a period of about 24 days and the higher latitudes rotating more slowly with a period of about 30 days. When a single active region or a set of regions localized in

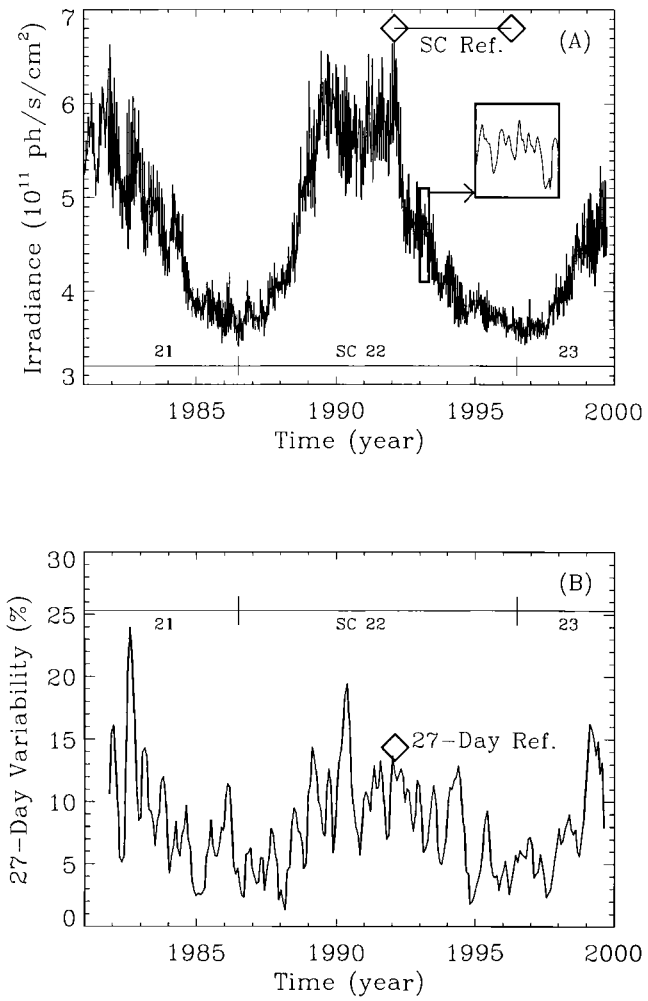

Figure 1. The irradiance time series (panel A) and the amplitudes of the 27-day variability (panel B) are shown for the H I Lyman-α (121.6 nm) irradiance during the past 20 years. The primary variations are the 27-day rotational variation and the 11-year solar cycle. The amplitude of the 27-day variability changes throughout the solar cycle. The diamond symbols in panels A and B indicate the time periods selected for the solar cycle 22 reference spectra and 27-day reference variability, respectively.

longitude dominates the Sun, the irradiance has a strong rotation variability whose period is partially dependent on the solar latitude of the primary active regions. This strong rotational variability is often maintained for a few months as active regions evolve slowly. The formation of new active regions appear somewhat random; however, there are usually 1 or 2 major outbursts each year that give rise to a strong rotation variability. This variability is referred to as the 27-day variation after the mean period found from Fourier spectral analysis of the solar irradiance time series. The period of this variability does range from 22 to 35 days due to the differential rotation of the Sun and the location of the different active regions on the Sun. The magnitude of 27-day variability for the H I Lyman-α (121.6 nm) emission is shown in Figure 1 over solar cycles 21 and 22. These short-term variations are larger during solar maximum conditions because there are more active regions during solar maximum. While many chromospheric and coronal emissions, such as F10.7, have little or no short-term variations during solar minimum conditions, the transition region emissions, such as the H I Lyman-α, usually have short-term variations throughout solar minimum.

The variations of the solar irradiance over many months and years, referred to as long-term variability, is related to the reversal of the global magnetic field on the Sun, presumably caused by the solar dynamo deep within the solar interior [e.g., *Layden et al.*, 1991, *Levy*, 1992]. This magnetic reversal has a full cycle of about 22 years, but, with the radiation intensity varying with the magnetic field amplitude and independent of polarity, the irradiance variability has a period of about 11 years, referred to as the 11-year solar cycle. The solar dynamo cycle has even longer variability periods, perhaps cyclic with periods of 88 years and longer [*Feynman and Gabriel*, 1990]. The movement of the sunspots over a solar cycle is explained by Spörer's law [*Spörer* 1894] and is illustrated by the well-known "butterfly diagram" by *Maunder* [1922] and *Babcock* [1961]. A new 11-year solar cycle is first detected by pairs of new cycle sunspots appearing at moderately high solar latitudes (~30°) with their magnetic field orientation (north-south) opposite from sunspots of the previous solar cycle. New cycle active regions usually first appear during solar minimum while old cycle active regions are still present near the solar equator. As the solar cycle progresses toward the next solar maximum, the differential rotation of the Sun effectively pulls the active regions towards the solar equator. Consequently, the new active regions are generated at lower latitudes as the 11-year cycle progresses. The latitudinal distribution of the active regions over a solar cycle has a peak near ±10°; also, the time when the active regions are centered near ±10° latitude roughly corresponds to the time of solar maximum. Approaching solar minimum the active regions are mostly near the equator.

OBSERVATIONS

Because the solar VUV radiation is absorbed entirely in Earth's atmosphere, its observations did not begin until the start of the space research era in the late 1940s. One of the first research rockets included a solar UV spectrometer [*Baum et al.*, 1946], and these early observations clearly showed that the Sun had significant UV emissions in ex-

cess of its blackbody continuum. Following these early rocket measurements, several satellite programs beginning in the 1960s included solar UV irradiance instruments. Some of the pioneering missions included the Orbiting Solar Observatory (OSO) –3 and –4, [*Hall and Hinteregger*, 1970; *Reeves and Parkinson*, 1970], a series of Solar Radiation (SOLRAD) spacecraft [*Kreplin*, 1970; *Kreplin and Horan*, 1992], and the Atmospheric Explorer (AE) –C, –D, and –E [*Hinteregger et al.*, 1973]. Most of these early missions were NASA satellites supported by the Air Force Cambridge Research Laboratories (AFCRL), the Naval Research Laboratory (NRL), and the University of Colorado (CU). With this new era of UV measurements from space, each observation was significant in showing both the magnitude of the irradiance and its possible variability. As more observations were made, it became clear that instrument pre-flight calibrations and analysis of in-flight instrument degradation needed to be improved because instrumental effects on the order of 30-100% often obscured the solar variability. The more recent solar measurements from the Upper Atmosphere Research Satellite (UARS) have addressed this issue by including two independent instruments that have accurate pre-flight calibrations traceable to the National Institute of Standards and Technology (NIST) radiometric standards and also have in-flight calibrations to precisely track instrument degradation.

Improved solar irradiance measurements are expected for solar cycle 23 from the new observations by the NASA Thermosphere Ionosphere Mesosphere Energetics and Dynamics (TIMED) and Solar Radiation and Climate Experiment (SORCE) satellites. The TIMED Solar EUV Experiment (SEE) will provide solar irradiances from 1 to 195 nm with ~10% accuracy [*Woods et al.*, 1998b]. The TIMED launch is currently planned for the Fall 2001. The SORCE satellite contains 4 solar irradiance instruments that cover the spectral range from 1 to 2000 nm, but with no EUV observations [*Woods et al.*, 2000a]. The SORCE XUV and FUV measurements will be similar to the TIMED XUV measurements and the UARS SOLSTICE FUV measurements, respectively. The goal of the SORCE measurements of the total solar irradiance (TSI) and the visible spectrum will have unprecedented accuracies of 0.01% and 0.03%, respectively. The SORCE launch is currently planned for the Summer 2002. These solar irradiance instruments on the TIMED and SORCE satellites have accurate pre-flight calibrations traceable to NIST and in-flight calibrations based on redundant channels, on-board reference detectors, or stellar observations. There are also other NASA, NOAA, and ESA missions being planned for solar cycle 24 that might include solar irradiance observations. These future missions will surely extend and improve our understanding of the solar irradiance over a longer time scale and with a higher accuracy as technology and calibration standards continue to improve.

MODELS

Because of the limited amount of actual solar data, especially for the XUV and EUV regions, models of the solar variability are sometimes necessary for aeronomic studies. Some of the more commonly used solar irradiance models are empirical models, frequently called proxy models, that are derived using linear relations between a solar proxy and existing observations of the solar UV irradiance. These models typically use a commonly available solar measurement, such as the ground-based 10.7 cm radio solar flux (F10.7), that serves as the proxy for the solar irradiance at other wavelengths. The first widely used proxy model was the *Hinteregger et al.* [1981] model, which is based on the AE-E satellite observations and several sounding rocket measurements. The original proxies for this model were the chromospheric H I Lyman-β (102.6 nm) and the coronal Fe XVI (33.5 nm) emissions. As measurements of these emissions are not generally available, they are constructed from correlations with the daily F10.7 and its 81-day average, which have been available on a daily basis since 1947. This Hinteregger model is also referred to as SERF 1 by the Solar Electromagnetic Radiation Flux (SERF) subgroup of the World Ionosphere-Thermosphere Study. *Richards et al.* [1994] developed a similar F10.7 proxy model called EUVAC but increased the solar soft X-ray irradiances by a factor of 2 to 3 as compared to the SERF 1 model. In addition, Tobiska has developed several proxy models of the solar EUV irradiance: SERF 2 by *Tobiska and Barth* [1990], EUV91 by *Tobiska* [1991], EUV97 by *Tobiska and Eparvier* [1998], and the latest version, SOLAR2000, by *Tobiska et al.* [2000]. In addition to these simple proxy models, there are physical and semi-empirical models of the solar EUV irradiance: *Fontenla et al.* [1999], *Warren et al.* [1998a and 1998b], and *Lean et al.* [1982].

For developing or improving models of the irradiance, it is recommended that the solar UV irradiance variability be split into at least three components and that the different layers of the solar atmosphere are modeled separately [*Woods et al.*, 2000b]. The three most important features on solar images to include in a solar UV irradiance model are the plages, active network, and quiet network [*Lean et al.*, 1982; *Worden*, 1996]. For the more simple proxy models, which don't use results from solar images, the three most important components to include are the solar minimum value, the short-term variability, and the long-term variability [*Woods et al.*, 2000b]. For modeling the solar UV irradiance, the chromosphere, transition region,

and corona emissions should be modeled separately as these emissions vary in different ways. A solution to include these different layers uniquely in a proxy model is to use three different proxies to represent each layer. For example, the NOAA Mg II core-to-wing ratio (available from 1978) is a good proxy for the chromospheric emissions and the photospheric continuum shortward of 200 nm, the composite H I Lyman-α (available from 1947) is a good proxy for the transition region emissions, and the F10.7 (available from 1947) is a good proxy for the coronal emissions [*Woods et al.*, 2000b]. The SOLAR2000 proxy model incorporates many of these ideas [*Tobiska et al.*, 2000].

REFERENCE SPECTRA FOR SOLAR CYCLE 22

For aeronomic studies, reference solar irradiance spectra representative of conditions during solar cycle 22 (1986-1996) are presented here. These reference spectra include spectra for solar minimum and maximum conditions and an example of 27-day rotational variability. These reference spectra are primarily established from actual observations; however, results from selected solar irradiance proxy models are used in creating and validating the reference solar spectra in the XUV and EUV range. These reference spectra are given in 1 nm intervals on 0.5 nm centers. This format is different than the commonly used 37 subdivisions for the solar EUV irradiance [e.g., *Torr and Torr*, 1985] because there are significant improvements in the accuracy of the atmospheric calculations when using the higher spectral resolution of 1 nm [*Bailey*, 1995].

The UARS solar measurements, which are limited to wavelengths longward of 115 nm, are adopted as the reference for the solar FUV irradiances presented here. The two UARS solar UV instruments are the Solar Ultraviolet Spectral Irradiance Monitor (SUSIM) [*Brueckner et al.*, 1993] and the Solar-Stellar Irradiance Comparison Experiment (SOLSTICE) [*Rottman et al.*, 1993]. While the two instruments are similar in that both are grating spectrometers with similar spectral resolution (0.1 nm) and both have pre-flight calibrations using NIST radiometric standards, they do utilize very different in-flight calibration techniques. The SUSIM uses redundant channels (optics) and on-board deuterium (D_2) lamps for its in-flight calibrations. The SOLSTICE uses about 20 early-type stars for its in-flight calibration. Both approaches have yielded similar results at the 3-10% level for the solar UV irradiance [*Woods et al.*, 1996].

The standard UARS solar product is the daily solar UV irradiance from about 115 nm to 420 nm in 1 nm intervals and on 0.5 nm centers. These UARS irradiance data are used for the FUV spectral region as the basis for the solar minimum and maximum spectra listed in Table 2. The time periods for these reference spectra are discussed later in this section. They are tabulated in 1 nm intervals up to 200 nm with an absolute accuracy (standard 1-σ uncertainty) of about 10%. For longer wavelengths, two UARS reference spectra up to 420 nm are given by *Woods et al.* [1996]. The UARS irradiances are in good agreement, to better than 10%, of the World Metrological Organization (WMO) reference spectrum [*Fröhlich and London*, 1986] above 210 nm, but the comparison between 210 nm and 200 nm, the shortest wavelength in the WMO spectrum, indicates that the UARS measurements are about 20% higher than the WMO spectrum. The validation of the UARS solar irradiances is extensive including several, nearly simultaneous measurements [*Woods et al.*, 1996], so the UARS irradiances are considered more accurate than the WMO reference spectrum.

There have been only a handful of solar EUV irradiance measurements during the past solar cycle (1986-1996). These measurements are from a few rocket measurements [*Woods et al.*, 1998a; *Ogawa et al.*, 1990; *Ogawa and Judge*, 1986] and a few observations in 1988 from the San Marco satellite [*Schmidtke et al.*, 1992; *Worden et al.*, 1996]. *Donnelly* [1987] refers to this period of sparse solar EUV measurements as the "EUV hole". Consequently, the last, more complete observation of the solar EUV irradiance by the AE-E satellite is often used for the reference EUV spectra [*Hinteregger et al.*, 1981, *Torr and Torr*, 1985]. Comparisons of the AE-E results to the more recent rocket measurements show differences by as much as a factor of 2 at some wavelengths [*Woods et al.*, 1998a]. However, it appears that the amount of variability recorded by AE-E is consistent with the limited set of recent measurements. The best characterization of the solar EUV is probably derived from combining the absolute levels of the recent, better calibrated, rocket instruments with the relative variability derived from the longer AE-E time series. Adopting this approach, the solar EUV irradiance measurement from a sounding rocket in 1994 [*Woods et al.*, 1998a] is used as the solar minimum reference spectrum, and the relative variability established by the AE-E measurements [*Hinteregger et al.*, 1981] is used to scale the solar minimum reference spectrum to a solar maximum spectrum. The SOLAR2000 model of the solar EUV irradiance [*Tobiska et al.*, 2000] incorporates both the recent rocket and past AE-E solar EUV irradiances; consequently, the SOLAR2000 model results are similar to these reference spectra. While the recent EUV measurements have uncertainties of 10-20%, the differences between these recent measurements and the AE-E and SOLAR2000 model results are 10-100%. It is difficult to assess and reconcile an absolute accuracy for the EUV reference spectra, but we

Table 2. A reference spectrum for solar cycle 22 minimum condition is listed in 1-nm intervals on 0.5 nm centers and at a solar distance of 1 AU. The values of the log (base-10) of the irradiance (log(E)) are the irradiances in units of photons s^{-1} cm^{-2}. The 27-day variability and 11-year solar cycle variability ratios are also listed on the same wavelength grid. These ratios are the maximum value divided by the minimum value for the time period chosen for the ratio. These data are contained in a text file at ftp://laspftp.colorado.edu/pub/solstice/ref_min_27day_11yr.dat. As an example, the H I Lyman-α irradiance at 121.5 nm is located under the "@ λ+1nm" column in the "120.5" λ row with a value of 11.575, which is 3.75 x 10^{11} photons s^{-1} cm^{-2}.

	@ λ+0nm			@ λ+1nm			@ λ+2nm			@ λ+3nm			@ λ+4nm		
λ (nm)	Min log(E)	27D Var	11Y Var	Min log(E)	27D Var	11Y Var	Min log(E)	27D Var	11Y Var	Min log(E)	27D Var	11Y Var	Min log(E)	27D Var	11Y Var
0.5	3.70	30.0	100.	6.00	6.0	20.0	7.00	3.0	10.0	7.455	1.66	4.70	7.834	1.56	3.29
5.5	8.282	1.42	2.26	8.288	1.44	2.37	8.409	1.37	2.11	8.247	1.41	2.12	8.395	1.31	1.80
10.5	8.000	1.27	1.68	7.902	1.22	1.64	7.739	1.22	1.61	7.755	1.22	1.63	8.218	1.40	2.05
15.5	8.206	1.54	2.98	8.542	1.28	1.72	9.192	1.36	1.86	8.827	1.49	2.45	8.782	1.57	3.11
20.5	8.422	1.61	3.77	8.285	1.65	4.28	8.645	1.46	2.46	8.392	1.42	2.26	8.778	1.48	2.49
25.5	8.986	1.51	2.71	8.381	1.64	4.10	8.723	1.57	3.27	8.590	1.72	6.21	8.393	1.49	2.47
30.5	9.873	1.24	1.57	9.045	1.48	2.41	8.799	1.74	7.28	8.807	1.74	7.23	8.849	1.48	2.41
35.5	8.750	1.53	2.77	8.892	1.53	2.79	8.381	1.10	1.17	8.025	1.10	1.17	7.980	1.17	1.43
40.5	8.215	1.17	1.43	8.003	1.73	6.50	7.976	1.10	1.17	8.268	1.30	1.60	7.957	1.10	1.17
45.5	7.923	1.22	1.64	8.471	1.33	1.75	8.099	1.22	1.64	8.337	1.21	1.59	8.628	1.59	3.65
50.5	8.532	1.19	1.51	8.061	1.21	1.59	8.093	1.56	3.19	8.192	1.21	1.59	8.048	1.16	1.38
55.5	8.700	1.17	1.42	8.172	1.19	1.52	8.156	1.22	1.64	8.903	1.24	1.71	8.286	1.16	1.41
60.5	8.734	1.49	2.49	8.403	1.16	1.38	9.024	1.21	1.51	8.410	1.22	1.64	7.823	1.16	1.38
65.5	7.691	1.21	1.58	7.682	1.16	1.38	7.688	1.17	1.44	8.224	1.20	1.48	8.077	1.25	1.61
70.5	8.541	1.16	1.39	8.174	1.18	1.47	8.012	1.24	1.72	8.133	1.24	1.72	8.229	1.24	1.72
75.5	8.443	1.21	1.58	8.865	1.19	1.50	8.735	1.40	2.10	8.964	1.25	1.61	8.663	1.18	1.48
80.5	8.641	1.24	1.72	8.702	1.24	1.72	8.876	1.24	1.72	9.150	1.19	1.51	8.981	1.24	1.72
85.5	9.032	1.24	1.72	9.063	1.24	1.72	9.144	1.24	1.72	9.207	1.24	1.72	9.296	1.24	1.72
90.5	9.375	1.24	1.71	9.269	1.23	1.68	8.821	1.23	1.70	8.777	1.22	1.65	8.632	1.23	1.67
95.5	8.438	1.17	1.44	8.460	1.17	1.44	9.699	1.20	1.54	8.775	1.18	1.45	8.968	1.18	1.45
100.5	8.582	1.17	1.44	8.649	1.17	1.44	9.568	1.24	1.71	9.589	1.23	1.69	8.802	1.17	1.44
105.5	8.734	1.17	1.44	8.718	1.17	1.43	8.748	1.17	1.43	8.975	1.17	1.44	8.807	1.17	1.44
110.5	8.839	1.17	1.44	8.856	1.10	1.17	8.837	1.19	1.50	8.793	1.10	1.17	8.628	1.10	1.17
115.5	8.847	1.10	1.17	8.904	1.10	1.17	9.473	1.19	1.51	8.963	1.10	1.17	9.447	1.17	1.39
120.5	9.875	1.27	1.73	11.575	1.22	1.64	9.499	1.17	1.33	9.346	1.24	1.37	9.231	1.21	1.37
125.5	9.220	1.16	1.32	9.361	1.21	1.50	9.124	1.17	1.29	9.047	1.16	1.25	9.098	1.18	1.38
130.5	10.020	1.15	1.29	9.255	1.12	1.19	9.132	1.14	1.25	10.057	1.22	1.57	9.088	1.12	1.25
135.5	9.453	1.12	1.23	9.262	1.14	1.26	9.297	1.12	1.24	9.300	1.11	1.21	9.700	1.22	1.60
140.5	9.652	1.17	1.43	9.464	1.10	1.22	9.505	1.10	1.20	9.572	1.10	1.21	9.563	1.09	1.20
145.5	9.599	1.09	1.20	9.695	1.11	1.20	9.799	1.07	1.16	9.809	1.09	1.17	9.766	1.08	1.17
150.5	9.817	1.08	1.16	9.853	1.08	1.16	9.946	1.10	1.21	9.998	1.10	1.20	10.228	1.16	1.31
155.5	10.162	1.12	1.24	10.182	1.08	1.16	10.141	1.06	1.16	10.128	1.07	1.15	10.134	1.06	1.13
160.5	10.185	1.06	1.15	10.258	1.05	1.14	10.320	1.06	1.14	10.359	1.06	1.16	10.406	1.10	1.17
165.5	10.613	1.09	1.12	10.467	1.04	1.07	10.531	1.07	1.12	10.592	1.04	1.06	10.710	1.05	1.07
170.5	10.772	1.04	1.08	10.769	1.05	1.11	10.808	1.05	1.09	10.815	1.05	1.08	10.907	1.05	1.07
175.5	10.999	1.05	1.08	11.037	1.04	1.07	11.118	1.04	1.08	11.168	1.05	1.08	11.159	1.05	1.08
180.5	11.245	1.07	1.12	11.325	1.08	1.15	11.311	1.05	1.09	11.345	1.05	1.09	11.283	1.04	1.08
185.5	11.343	1.04	1.08	11.403	1.05	1.09	11.469	1.04	1.09	11.496	1.04	1.09	11.548	1.04	1.10
190.5	11.567	1.04	1.08	11.608	1.04	1.09	11.638	1.04	1.09	11.521	1.03	1.08	11.744	1.04	1.08
195.5	11.735	1.04	1.08	11.791	1.04	1.08	11.799	1.04	1.07	11.805	1.03	1.06	11.843	1.03	1.06

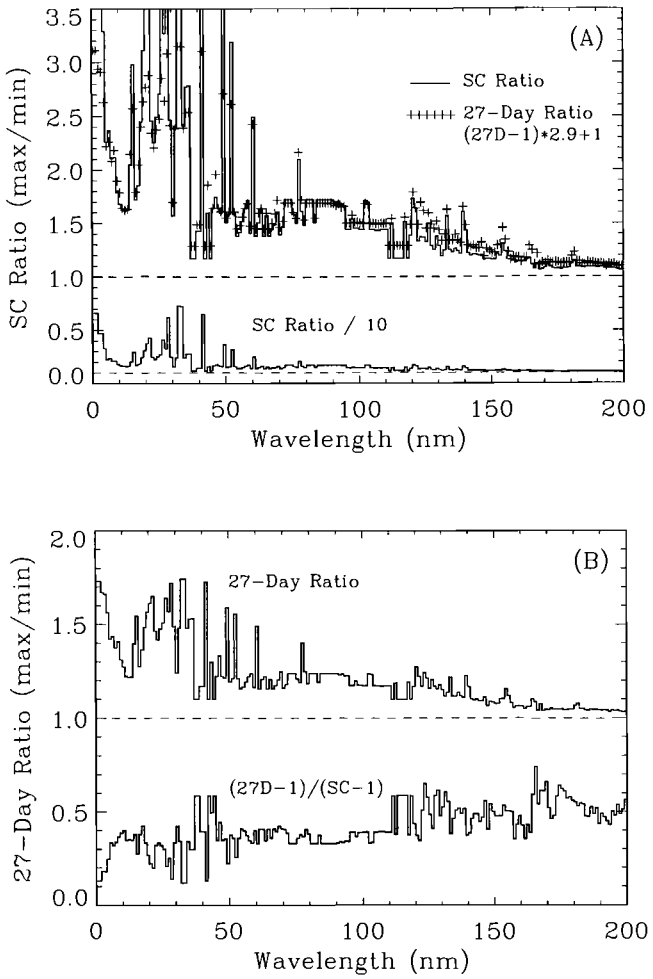

Figure 2. The variation of the solar irradiance for solar cycle 22 (SC 22) and for a 27-day period near 1992/032 are shown in panels A and B, respectively. These results used the UARS SOLSTICE measurements in 1992 and 1996 for the FUV and a combination of rocket, SNOE, and model results for the EUV and XUV. The plus symbols in panel A are the 27-day variability with a scaling factor of 2.9 so that the short-term variability is the same level as the long-term variability at 121.5 nm (H I Lyman-α). The ratio of the 27-day and SC variability, as shown in panel B, varies with wavelength due to the emissions being from different layers in the solar atmosphere.

suggest an accuracy of 30% for the EUV range (30-120 nm).

The XUV spectral region has even fewer measurements because of the technical difficulties for XUV optics and detectors. The primary knowledge of the solar XUV is from several rocket measurements [*Feng et al.*, 1989; *Bailey et al.*, 1999], the SOLRAD satellite measurements shortward of 10 nm [*Kreplin*, 1970; *Kreplin and Horan*, 1992], the GOES 1-8 Å measurements, the Yohkoh solar imaging experiment shortward of 10 nm [*Acton et al.*, 1999], the SOHO Solar EUV Monitor (SEM) daily results in the 26-34 nm bandpass [*Judge et al.* 1998; *Ogawa et al.*, 1998], and the SNOE Solar XUV Photometer (SXP) daily observations shortward of 20 nm (2-7 nm, 6-19 nm, and 17-20 nm bandpasses) [*Bailey et al.*, 2000]. The SNOE SXP and SOHO SEM measurements provide the most recent and most accurate knowledge of the solar XUV irradiance. However, these instruments have broad spectral resolution (~7 nm), so the solar XUV irradiance reference is chosen to be the SOLAR2000 model in 1 nm intervals but scaled to match the SNOE and SOHO results. *Bailey et al.* [2000] report that the SNOE XUV irradiances are a factor of 4 higher than the AE-E solar reference spectra [*Hinteregger et al.*, 1981]. In support of this increase, *Solomon et al.* [2001] show that the photoelectron flux measurements are consistent with photoelectron calculations that use a scaling factor of 4 for the solar irradiance shortward of 20 nm. This scaling factor is consistent with several other results from photoelectron and atmospheric studies [e.g., *Roble*, 1976; *Oster*, 1983; *Richards and Torr*, 1984; *Buonsanto et al.*, 1995]. The SNOE SXP and SOHO SEM irradiances have a 10-20% uncertainty. The redistribution of the low-resolution irradiances into higher spectral resolution introduces additional uncertainty, so we estimate the total uncertainty for the reference solar XUV irradiance to be about 40%.

The largest 27-day variability observed during the UARS mission occurred on 1992/032 (year / day of year), and this period is used to define a reference 27-day variability spectrum as shown in Figure 2. The solar rotational variability is strongly dependent on wavelength. The source of the emission in the solar atmosphere, which affects the active network and plage contribution to the emission, appears to be the key reason for the spectral differences. While essentially all of the emissions shortward of 200 nm appear to increase and decrease together during a solar rotation, the coronal and transition region emissions vary the most, and the chromospheric emissions and photospheric continuum vary the least. For cases when the solar observations are not available, this reference 27-day variability spectrum could be used to study aeronomic observations over a short-term period of days. As indicated by the H I Lyman-α variability in Figure 1, it may be necessary to scale this reference 27-day variability downward by as much as a factor of 6 or upward by as much as a factor of 2 when studying a specific aeronomic observation.

The solar minimum and maximum reference spectra are chosen centered on 1996/108 and 1992/032, respectively. These solar cycle spectra are obtained by averaging over 27-days to represent the mean value during a solar rotation. The solar irradiance spectra for these two periods are listed

in Table 2 for a solar distance of 1 AU. The solar 10.7 cm radio fluxes (F10.7), averaged over these two 27-day periods, are 71 and 212 for solar minimum and maximum, respectively. Because of the 27-day averaging, the 11-year variability factors are reduced from a ratio taken without any averaging. For studies needing the expected extreme values of the 11-year variability during solar cycle 22, one can multiply the 27-day variability factor and the 11-year variability factor, both given in Table 2 in 1 nm intervals. For example, the extreme 11-year variability of the H I Lyman-α emission at 121.5 nm is 2.0 (1.22 x 1.64).

The long-term variability has a spectral function similar, but not identical, to the short-term variability. The ratio of the solar maximum and minimum spectra, given in Figure 2, shows the wavelength dependence of the irradiance over the 11-year solar cycle. Our reference 27-day rotational variability is compared to the reference long-term variability, and this comparison, which is also included in Figure 2, indicates that this specific short-term variability is about a factor of 2 to 3 smaller. It is important to note that this ratio of 1/3 is appropriate for the upper chromospheric and transition region emissions, such as for H I Lyman-α, but a ratio of 1/2 and 1/4 is more appropriate for the lower chromospheric and coronal emissions, respectively. This result is expected because the different emissions have different contributions to their long-term variations from the active network features on the Sun, which causes their long-term variability relative to their short-term variability to be different [*Woods et al.*, 2000b]. Because of the different behavior of the long-term variations relative to the short-term variations as a function of wavelength, the reference 27-day variability should not be scaled to study aeronomic observations over a long-term period of several months or years. Obviously, the long-term variability derived from the solar minimum and maximum spectra is more appropriate for aeronomic studies over a long-term period.

SUMMARY

The solar UV radiation important for aeronomic studies is primarily the irradiance shortward of 200 nm. The solar variabilities important for most aeronomic studies are the 27-day solar rotation and the 11-year solar cycle. Both of these variations have a similar spectral shape, but the 11-year solar cycle variation is about a factor of 2 to 3 larger than the largest 27-day solar rotation variation. The photospheric continuum at wavelengths longward of 260 nm varies the least, by probably only 0.1% [*Fontenla et al*, 1999]. The continuum variation sharply rises shortward of 260 nm, and an even larger rise in the solar variability is observed below the Al ionization edge at 207 nm. The continuum at 200 nm has a solar cycle variation of 6%, and then the continuum variation slowly rises to 25% near 132 nm. The emissions from Ca II near 395 nm and Mg II near 280 nm are the brightest emissions from the chromosphere. There are also many other chromospheric emissions between 91 nm and 182 nm, and most of these chromospheric emissions vary by about 40% over the solar cycle. The emission from H I at 121.6 nm and He II at 30.4 nm are the brightest emissions from the transition region. There are also several transition region emissions between 23 nm and 155 nm. Most of these transition region emissions vary by about 70% over the solar cycle. The coronal emissions are primarily shortward of 63 nm, and they vary the most. The lower temperature corona emissions, like Mg X, vary by a factor of 2 over the solar cycle, and the higher temperature coronal emissions, like Fe XVI, vary by a factor of 8. In terms of the total energy variation, the chromospheric emissions contribute more than the transition region emissions, which contribute more than the coronal emissions. However, most atmospheric processes have a strong wavelength dependence, thus the solar variability at the appropriate wavelength needs to be considered for each atmospheric process. While the reference spectra included here represent the current understanding of the solar UV irradiance during solar cycle 22, there are upcoming future satellite missions that should provide even better accuracy for the solar UV irradiances and thus further refine on-going and future aeronomy research.

Acknowledgments. We thank our UARS SOLSTICE and rocket experiment teams for providing operations and data processing support in producing solar irradiance products from those experiments. We especially thank Frank Eparvier and Don Woodraska for their many useful comments about this paper. This work is supported by NASA contracts NAS5-97145 and NAS5-97045 and JHU/APL contract JH774017. The reference solar spectra can be obtained as a text data file called ref_min_ 27day_11yr.dat from the LASP FTP site (ftp://laspftp.colorado.edu/pub/solstice/), and this file can be read using the IDL code called read_dat.pro also at the LASP FTP site.

REFERENCES

Acton, L. W., D. C. Weston, and M. E. Bruner, Deriving solar x-ray irradiance from Yohkoh observations, *J. Geophys. Res., 104*, 14827, 1999.

Babcock, H. W., The topology of the Sun's magnetic field and the 22-year cycle, *Ap. J., 133*, 572, 1961.

Bailey, S. M., *Response of the Upper Atmosphere to Variations in the Solar Soft X-ray Irradiance*, dissertation, Univ. of Colo., Boulder, 1995.

Bailey, S. M., T. N. Woods, L. R. Canfield, R. Korde, C. A. Barth, S. C. Solomon, and G. J. Rottman, Sounding rocket meas-

urements of the solar soft x-ray irradiance, *Solar Phys.*, *186*, 243, 1999.

Bailey, S. M., T. N. Woods, C. A. Barth, S. C. Solomon, L. R. Canfield, and R. Korde, Measurements of the solar soft x-ray irradiance from the Student Nitric Oxide Explorer: first analysis and underflight calibrations, *J. Geophys. Res.*, *105*, 27,179, 2000.

Baum, W. A., F. S. Johnson, J. J. Oberly, E. E. Rockwood, C. V. Strain, and R. Tousey, Solar ultraviolet spectrum to 88 kilometers, *Phys. Rev.*, *70*, 781, 1946.

Brekke, P., G. J. Rottman, J. Fontenla, and P. G. Judge, The ultraviolet spectrum of a 3B class flare observed with SOLSTICE, *Astrophys. J., 468*, 418, 1996.

Brasseur, G. and S. Solomon, *Aeronomy of the Middle Atmosphere : Chemistry and Physics of the Stratosphere and Mesosphere*, Dordrecht, Boston, 1986.

Brueckner, G.E., K.L. Edlow, L.E. Floyd, J.L. Lean, and M.E. VanHoosier, The Solar Ultraviolet Spectral Irradiance Monitor (SUSIM) Experiment on board the Upper Atmospheric Research Satellite (UARS), *J. Geophys. Res.*, *98*, 10695, 1993.

Buonsanto, M. J., P. G. Richards, W. K. Tobiska, S. C. Solomon, Y.-K. Tung, and J. A. Fennelly, Ionospheric electron densities calculated using different EUV flux models and cross sections: Comparison with radar data, *J. Geophys. Res.*, *100*, 14569, 1995.

Chamberlain, J. W., *Theory of Planetary Atmospheres :An Introduction to Their Physics and Chemistry*, Academic Press, New York, 1978.

Donnelly, R. F., Gaps between solar UV & EUV radiometry and atmospheric sciences, in *Solar Radiative Output Variation*, edited by P. Foukal, pp. 139-142, Cambridge Research and Instrumentation Inc, Boulder, Colorado, 1987.

Feng, W. H. S. Ogawa, and D. L. Judge, The absolute solar soft x ray flux in the 20 - 100Å region, *J. Geophys. Res.*, *94*, 9125, 1989.

Feynman, J. and S. B. Gabriel, Period and phase of the 88-year solar cycle and the Maunder Minimum: Evidence for a chaotic Sun, *Solar Phys.*, *127*, 393, 1990.

Fontenla, J. M., O. R. White, P. A. Fox, E. H. Avrett, and R. L. Kurucz, Calculation of solar irradiances. I. Synthesis of the solar spectrum, *Astrophys. J., 518*, 480, 1999.

Fröhlich, C., and J. London, *Revised Instruction Manual on Radiation Instruments and Measurements*, WMO/TD-No. 149, World Metrological Organization, Geneva, 1986.

Hall, L. A., and H. E. Hinteregger, Solar radiation in the extreme ultraviolet and its variation with solar rotation, *J. Geophys. Res.*, *75*, 6959, 1970.

Harvey, K. L., and O. R. White, Magnetic and radiative variability of solar surface structures. 1. Image decomposition and magnetic-intensity mapping, *Astrophys. J., 515*, 812, 1999.

Hinteregger, H. E., D. E. Bedo, and J. E. Manson, The EUV spectrophotometer on Atmosphere Explorer, *Radio Science*, *8*, 349, 1973.

Hinteregger, H. E., K. Fukui, and B. R. Gilson, Observational, reference and model data on solar EUV, from measurements on AE-E, *Geophys. Res. Letters*, *8*, 1147, 1981.

Judge, D. L., D. R. McMullin, H. S. Ogawa, D. Hovestadt, B. Klecker, M. Hilchenbach, E Möbius, L. R. Canfield, R. E. Vest, R. Watts, C. Tarrio, and M. Kühne, First solar EUV irradiances obtained from SOHO by the CELIAS/SEM, *Solar Phys*, *177*, 161, 1998.

Kreplin, R. W., The solar cycle variation of soft x-ray emission, *Ann. Geophys.*, *26*, 567, 1970.

Kreplin, R. W. and D. M. Horan, Variability of x-ray and EUV solar radiation in solar cycles 20 and 21, in *Proceedings of the Workshop on the Solar Electromagnetic Radiation Study for Solar Cycle 22*, edited by R. F. Donnelly, pp. 405-425, NOAA, Boulder,1992.

Layden, A. C., P. A. Fox, J. M. Howard, A. Sarajedini, K. H. Schatten, and S. Sofia, Dynamo-based scheme for forecasting the magnitude of solar activity cycles, *Solar Phys.*, *132*, 1, 1991.

Lean, J. L., W. C. Livingston, D. F. Heath, R. F. Donnelly, A. Skumanich, and O. R. White, A three-component model of the variability of the solar ultraviolet flux 145-200 nm, *J. Geophys. Res., 87*, 10307, 1982.

Lean, J., Solar ultraviolet irradiance variations: A review, *J. Geophys. Res., 92*, 839, 1987.

Lean, J., Variations in the Sun's radiative output, *Reviews of Geophysics, 29*, 505, 1991.

Levy, E. H., The solar cycle and dynamo theory, in *The Solar Cycle*, edited by K. L. Harvey, pp. 139-149, ASP Conference Series *27*, 1992.

Maunder, E. W., The Sun and sunspots, 1820-1920, *Mon. Not. Roy. Astron. Soc., 82*, 534, 1922.

Meier, R. R., Solar Lyman series line profiles and atomic hydrogen excitation rates, *Astrophys. J., 452*, 462, 1995.

Ogawa, H. S. and D. L. Judge, Absolute solar flux measurements shortward of 575 Å, *J. Geophys. Res., 91*, 7089, 1986.

Ogawa, H. S., L. R. Canfield, D. McMullin, and D. L. Judge, Sounding rocket measurement of the absolute solar EUV flux utilizing a silicon photodiode, *J. Geophys. Res.*, *95*, 4291, 1990.

Ogawa, H. S., D. L. Judge, D. R. McMullin, and P. Gangopadhyay, First-year continuous solar EUV irradiance from SOHO by the CELIAS/SEM during 1996 solar minimum, *J. Geophys. Res., 10*, 1, 1998.

Oster, L., Solar irradiance variations, 2. Analysis of the extreme ultraviolet spectrometer measurements onboard the Atmospheric Explorer E satellite, *J. Geophys. Res*, *88*, 9037, 1983.

Pap, J. M., C. Fröhlich, H. S. Hudson, and S. K. Solanki (editors), *The Sun as a Variable Star: Solar and Stellar Irradiance Variations*, Cambridge University Press, Cambridge, 1994.

Reeves, E. M. and W. H. Parkinson, An atlas of extreme-ultraviolet spectroheliograms from OSO-IV, *Astrophys. J. Supplement, 181*, 1, 1970.

Richards, P. G. and D. G. Torr,, An investigation of the consis-

tency of the ionospheric measurements of the photoelectron flux and solar EUV flux, *J. Geophys. Res., 89*, 5625, 1984.

Richards, P. G., J. A. Fennelly, and D. G. Torr, EUVAC: A solar EUV flux model for aeronomic calculations, *J. Geophys. Res. 99*, 8981, 1994.

Roble, R. G., Solar EUV variation during a solar cycle as derived from ionospheric modeling considerations, *J. Geophys. Res, 81*, 265, 1976.

Rottman, G. J., Results from space measurements of solar UV and EUV flux, in *Solar Radiative Output Variation*, edited by P. Foukal, pp. 71-86, Cambridge Research and Instrumentation Inc, Boulder,1987.

Rottman, G. J., T. N. Woods, and T. P. Sparn, Solar Stellar Irradiance Comparison Experiment 1: 1. Instrument design and operation, *J. Geophys. Res., 98*, 10667, 1993.

Schmidtke, G., T. N. Woods, J. Worden, H. Doll, S. C. Solomon, and G. J. Rottman, Solar EUV irradiance from the San Marco ASSI: a reference spectrum, *Geophys. Res. Letters, 19*, 2175, 1992.

Schrijver, C. J., Radiative fluxes from the outer atmosphere of a star like the Sun - A construction kit, *Astron. Astrophys., 189*, 163, 1988.

Schühle, U., K. Wilhelm, J. Hollandt, P. Lemaire, and A. Pauluhn, Radiance variations of the quiet Sun at far-ultraviolet wavelengths, *Astron. Astrophys., 354*, L71, 2000.

Solomon, S. C., S. M. Bailey, and T. N. Woods, Effect of solar soft x-rays on the lower ionosphere, *Geophys. Res. Lett., 28*, 2149, 2001.

Spörer, G., Beobachtungen von Sonnenflecken in den Jahren 1885 bis 1893, *Pub. Astrophys. Obs. Potsdam, 10*, 144, 1894.

Tobiska, W. K. and C. A. Barth, A solar EUV flux model, *J. Geophys. Res., 95*, 8243, 1990.

Tobiska, W. K., Revised solar extreme ultraviolet flux model, *J. Atmos. Terr. Phys., 53*, 1005, 1991.

Tobiska, W. K., Recent solar extreme ultraviolet irradiance observations and modeling: A review, *J. Geophys. Res., 98*, 18879, 1993.

Tobiska, W. K., and F. G. Eparvier, EUV97: Improvements to EUV irradiance modeling in the soft x-rays and FUV, *Solar Phys., 177*, 147, 1998.

Tobiska, W. K., T. N. Woods, F. G. Eparvier, R. Viereck, L. Floyd, D. Bouwer, G. J. Rottman, and O. R. White, The SOLAR2000 empirical solar irradiance model and forecast tool, *J. Atmos and Sol. Terr. Phys., 62*, 1233, 2000.

Torr, M. R., and D. G. Torr, Ionization frequencies for solar cycle 21: revised, *J. Geophys. Res, 90*, 6675, 1985.

Warren, H. P., J. T. Mariska, and J. Lean, A new reference spectrum for the EUV irradiance of the quiet Sun: 1. Emission measure formulation, *J. Geophys. Res., 103*, 12077, 1998a.

Warren, H. P., J. T. Mariska, and J. Lean, A new reference spectrum for the EUV irradiance of the quiet Sun: 2. Comparisons with observations and previous models, *J. Geophys. Res., 103*, 12091, 1998b.

White, O. R. (editor), *The Solar Output and Its Variation*, Colorado Ass. Univ. Press, Boulder, 1977.

Woods, T. N., D. K. Prinz, J. London, G. J. Rottman, P. C. Crane, R. P. Cebula, E. Hilsenrath, G. E. Brueckner, M. D. Andrews, O. R. White, M. E. VanHoosier, L. E. Floyd, L. C. Herring, B. G. Knapp, C. K. Pankratz, and P. A. Reiser, Validation of the UARS solar ultraviolet irradiances: Comparison with the ATLAS 1 and 2 measurements, *J. Geophys. Res., 101*, 9541-9569, 1996.

Woods, T. N., G. J. Rottman, S. M. Bailey, S. C. Solomon, and J. Worden, Solar extreme ultraviolet irradiance measurements during solar cycle 22, *Solar Physics, 177*, 133-146, 1998a.

Woods, T. N., F. G. Eparvier, S. M. Bailey, S. C. Solomon, G. J. Rottman, G. M. Lawrence, R. G. Roble, O. R. White, J. Lean, and W. K. Tobiska, TIMED Solar EUV Experiment, *SPIE Proceedings,* **3442**, 180-191, 1998b.

Woods, T., G. Rottman, J. Harder, G. Lawrence, B. McClintock, G. Kopp, and C. Pankratz, Overview of the EOS SORCE mission, *SPIE Proceedings, 4135*, 192, 2000a.

Woods, T. N., W. K. Tobiska, G. J. Rottman, and J. R. Worden, Improved solar Lyman α irradiance modeling from 1947 through 1999 based on UARS observations, *J. Geophys. Res., 105*, 27,195 2000b.

Worden, J. R., *A Three Component Proxy Model for the Solar Far Ultraviolet Irradiance*, dissertation, Univ. of Colo., Boulder, 1996.

Worden, J., T. N. Woods, G. J. Rottman, G. Schmidtke, H. Tai, H. G. Doll, and S. C. Solomon, Calibration of the San Marco Airglow-Solar Spectrometer Instrument in the extreme ultraviolet, *Optical Eng., 35*, 554, 1996.

Worden, J. R., O. R. White, and T. N. Woods, Evolution of chromospheric structures derived from Ca II K spectroheliograms: implications for solar ultraviolet irradiance variability, *Astrophys. J., 496*, 998, 1998.

Worden, J., T. N. Woods, W. M. Neupert, and J.P. Delaboundiniere, Evolution of chromospheric structures: How chromospheric structures contribute to the solar He II 30.4 nanometer irradiance and variability, *Astrophys. J., 511*, 965, 1999.

Thomas N. Woods and Gary J. Rottman, Laboratory for Atmospheric and Space Physics, University of Colorado, 1234 Innovation Dr., Boulder, CO 80303

Meteoric Material – an Important Component of Planetary Atmospheres

Joseph M. Grebowsky

Laboratory for Extraterrestrial Physics, NASA Goddard Space Flight Center, Greenbelt, Maryland

Julianne I. Moses

Lunar and Planetary Institute, Houston, Texas

W. Dean Pesnell

Nomad Research Inc., Arnold, Maryland

Interplanetary dust particles (IDPs) interact with all planetary atmospheres and leave their imprint as perturbations of the background atmospheric chemistry and structure. They lead to layers of metal ions that can become the dominant positively charged species in lower ionospheric regions. Theoretical models and radio occultation measurements provide compelling evidence that such layers exist in all planetary atmospheres. In addition IDP ablation products can affect neutral atmospheric chemistry, particularly at the outer planets where the IDPs supply oxygen compounds like water and carbon dioxide to the upper atmospheres. Aerosol or smoke particles from incomplete ablation or recondensation of ablated IDP vapors may also have a significant impact on atmospheric properties.

1. INTRODUCTION

Atmospheric ablation of infalling meteoroids releases foreign atoms, molecules, and ions into the surrounding atmosphere. The deposited material becomes part of a planet's ionosphere and can play key roles in minor species aeronomy. In addition, the cosmic particles contain a large percentage of volatile elements like oxygen and carbon, which, when deposited at Earth, mostly blend unnoticed into the atmosphere. However, for the outer-solar-system planets they contribute to the deposition of water and/or carbon dioxide molecules that may not otherwise exist in the upper atmospheres of these planets. Each planet's interaction with the interplanetary particle population is different due to its unique atmosphere, size and position in the solar system. The biggest contrast in the effects of the ablated meteoric material is between the outer planets (Jupiter, Saturn, Uranus and Neptune) with reducing atmospheres, and the inner terrestrial planets (Venus, Earth and Mars) with oxidizing atmospheres. This paper describes some of these differences in the atmospheric and ionospheric consequences of the constant rain of interplanetary dust particles (IDPs). In this paper IDP refers to any cosmic particle with radius less than ~ 1 cm regardless of its origin.

Atmospheres in the Solar System: Comparative Aeronomy
Geophysical Monograph 130

10.1029/130GM15

2. BACKGROUND

2.1. Properties of Dust in Solar System

Accurate quantitative predictions of the effects of IDPs on an atmosphere require a knowledge of the IDP mass and velocity distributions at the planet. Extensive radar and visual meteor observations and spacecraft measurements provide information on the velocities, total impact flux and

mass (size) distribution at the Earth [*Grün et al.*, 1985; *Love and Brownlee*, 1993; *Taylor*, 1995]. Knowledge of the IDP spatial density and velocity distribution decreases the further one goes from Earth. Spacecraft-borne dust detector measurements from around the solar system combined with zodiacal light observations partially constrain the particle flux as a function of heliocentric distance [e.g., *Leinert and Grün*, 1990; *Grün*, 1994]. However, the spacecraft data contain only a small number of events and sample a range of particle sizes that may miss a sizeable portion of the population. Because of uncertainties in the mass flux and other properties of IDPs at planets other than the Earth, measurements of atmospheric and ionospheric phenomena related to IDPs provide valuable benchmarks for testing the realism of the assumed IDP distributions.

Comets and asteroids are believed to be the main source of the inner solar system IDPs. The asteroidal component is not as important in the outer solar system, where ice-rich particles should be more numerous. An IDP will impact an atmosphere with a velocity between the escape velocity of the planet and a maximum value [*Öpik*, 1958; see Table 1]. The maximum speed is that of a particle on a retrograde parabolic orbit around the Sun in a head-on collision with the planet (combined with gravitational focusing by the planet). Interstellar material with greater velocities has been observed but is not likely to be a significant contributor to the deposited mass [*Grün*, 1994]. Note from Table 1 that the range of impact speeds is much broader for the terrestrial planets. For particles encountering the planet from random directions, the most probable impact angle is 45°.

Although IDPs with a wide range of masses impact an atmosphere, most of the ~10^8 kg of yearly deposited mass at the Earth arises from small grains with radii in the size range ~0.01 to 1 mm [e.g., see the reviews in *McDonnell*, 1978]. Very small IDPs with radii less than ~10 μm radiate the frictional heat and do not evaporate for typical Earth entry velocities, while impacts of very large bodies are relatively rare on time scales relevant to the lifetime of meteoric material in the atmosphere. Free-molecular flow conditions generally apply to IDP interactions with an atmosphere. In ablation models it is commonly assumed that the particles are spheres with uniform composition, and fragmentation is ignored.

More refined measurements of the IDP distribution functions and their physical characteristics throughout the solar system are needed. At current levels of understanding, models of atmospheric consequences should be considered as order-of-magnitude estimates rather than as precise, quantitative predictions.

2.2. Ablation Process

A fast moving meteoroid heats as the kinetic energy of colliding atmospheric molecules is converted into internal energy. The same collisions can also sputter material off the surface [see chapter III.3]. This energy transfer causes melting and evaporation of surface material off the particles [*Öpik*, 1958]. The amount of material released and the altitude profile of the mass deposition depends on the particle's mass, velocity, size, physical structure, thermodynamic properties and chemical composition, and on the mass density profile of the atmosphere. Three equations describe the physics of meteoroid ablation: (1) the momentum equation, relating the reduction in speed to atmospheric drag; (2) the ablation equation, describing mass loss from the meteoroid by evaporation and sputtering; and (3) the heat equation, relating the bulk heating of the meteoroid to frictional heating, radiative energy loss and evaporative cooling. A fourth equation is used to track a particle's position as a function of time.

Using the equations and assumptions described above, models of the IDP ablation rate profiles and atmospheric effects at the Earth have been made [e.g., *Lebedinets et al.* 1973; *Hunten et al.*, 1980; *McNeil et al.* 1996; *Grebowsky and Pesnell*, 1999]. The results are consistent with available measurements. The investigations at Earth show that, with our current understanding, there are adequate modeling tools for exploring IDP effects at the other planets.

Table 1: Properties of Solar System Bodies with Significant Atmospheres

Object	Escape Speed[1] (km/s)	Maximum Speed[2] (km/s)	Important Atmospheric Constituents[3]
Venus	10.4	86	CO_2, CO, N_2, O
Earth	11.2	73	N_2, O_2, O, H_2O, O_3
Mars	5.0	59	CO_2, N_2, CO, O_2, O, O_3
Jupiter	60.0	69	H_2, He, CH_4, C_2H_6, C_2H_2, H
Saturn	36.0	44	H_2, He, CH_4, C_2H_6, C_2H_2, H
Titan	2.6	24	N_2, CH_4, H_2, H, C_2H_6
Uranus	21.0	27	H_2, He, CH_4, C_2H_6, H
Neptune	24.0	28	H_2, He, CH_4, C_2H_6, CO, H
Triton	1.5	18[4]	N_2, CO, Ar, CH_4

Notes:
[1]From *Tholen et al.* [2000].
[2]Calculated as described in text using data from *Tholen et al.* [2000].
[3]From *Yung and DeMore* [1999]. Due to changes with altitude, the actual mixing ratios are not listed.
[4]Includes orbital velocity of Triton around Neptune.

2.3. Ionospheric Processes

Ions formed by the impact of fast-moving ablated neutral atoms with atmospheric molecules are an immediate consequence of the ablation of a high-speed meteoroid (see reviews in *McDonnell* [1978]). Ion densities are initially very high in the train of a particle but are quickly reduced by diffusion. The number of ions deposited by one typical grain is not very large. For example, at Earth, for a nominal 20 km/s entrance speed an IDP with mass 10^{-6} g, (i.e., a diameter of a few 10's of microns) directly deposits 10^{12}-10^{13} ions [*Lebedinets et al.*, 1973]. However, the lifetimes of atomic ions are long. Hence the continual influx of IDPs can seed persistent meteor ion layers. The impact ionization rate of the freshly vaporized neutrals, moving at the meteoroid speed v in the Earth's atmosphere, varies as v^{α}, where α is ~3-4 for chondritic materials [*Bronshten*, 1983]. This source of ionization is particularly significant for planets with large escape velocities (see Table 1) and for high-speed meteor streams. It is not important for particles in the sporadic background entering the atmospheres of the low mass terrestrial planets.

Photoionization will also ionize the ablated neutral atoms. The wavelengths of the ionization thresholds of the metals extend from ~1500 Å for Si to ~2700 Å for K [*Swider*, 1969]. Depending upon the atmospheric composition and pressure profile, the wavelengths of the solar spectrum that can ionize specific neutral meteoric species may or may not be absorbed above the ablation region. The importance of this mechanism varies from species to species because of the differing ionization potentials, and the photoionization rate depends on the distance from the Sun. Also, because the ionization potentials of metal atoms are low compared to the ionization potentials of ambient ionospheric species (see Table 2), charge exchange with ionospheric ions is another mechanism for ionizing the neutral metal atoms [*Swider*, 1969]. The importance of this ionization source depends on the magnitude of the ambient ionospheric ion concentrations in the ablation region.

The chemical loss processes for the meteoric ions and the dynamical rearrangement of the ions will differ from planet to planet. The loss of the meteoric atomic ions at high altitudes is by radiative recombination with electrons (for Mg^+ this recombination rate is ~4×10^{-12} cm^3 s^{-1}) resulting in very long ion lifetimes (up to many weeks on Earth). With decreasing altitude, the atomic ions interact more with atmospheric neutral molecules (through two- or three-body interactions) to produce molecular metal ions. For example, Mg^+ reacting with O_3 (with a rate of ~8×10^{-10} cm^3s^{-1}) yields MgO^+, whereas the three body reactions occur at rates ~1×10^{-30} cm^6 s^{-1}, yielding molecular ions such as MgN_2^+, $Mg^+\bullet CO_2$ and MgO_2^+ [see *McNeil et al., 1996* and *Pesnell and Grebowsky,* 2000a, for a discussion of these rates]. The resulting metal ion molecules can undergo rapid dissociative recombination, providing another loss channel for atomic meteoric species. These reactions are characteristic of the inner planets. For the outer planets analogous processes can exist in which hydrogen and hydrocarbon species are the reactants for the meteoric ions. Aerosol layers (such as mesospheric cloud particles on Earth) can reduce the metal ion concentrations through clustering, as can charge capture onto dust particles.

A simple balance between these loss processes and ion production, including the effects of diffusion, would produce a single ion layer in the ablation region. Complexities are introduced by ionosphere dynamics whose importance is established for Earth; converging ion drifts due to combining neutral wind drag or electric fields with a magnetic field produce very narrow ion layers (see review by *Kelley*, [1989], and the modeling of *Carter and Forbes*, [1999]). One can assume with confidence that the terrestrial dynamic processes also apply, but to different degrees, to the other planets with magnetic fields. The very structured low altitude layers observed at Jupiter (see Figure 1a) and similar complexities observed at Saturn [*Kliore et al.*, 1980] and Neptune [*Lyons*, 1995] have been attributed to such processes.

2.4. Neutral Processes

Not all of the ablated material is ionized. Although both atoms and molecules evaporate from the IDP, subsequent atmospheric collisions will tend to break the molecules into component atoms [*Öpik*, 1958] of which only a fraction is ionized. Ablated neutral atoms have decreasing lifetimes with decreasing altitude (either because of chemical reactions transforming them into molecular species or due to condensation of the atoms about any existing aerosols.)

Table 2: Characteristic Ionization Potentials[1]

Meteoric		Atmospheric	
Species	I. P. (eV)	Species	I. P. (eV)
Si	8.15	H_2	15.43
K	4.34	He	24.59
Na	5.14	O	13.62
Fe	7.90	O_2	12.07
Mg	7.65	N_2	15.58
Li	5.39	CO_2	13.77
Ni	7.64	CH_4	13.00
Ca	6.11	Ar	15.76

Notes:
[1]Data from *Däppen* [2000].

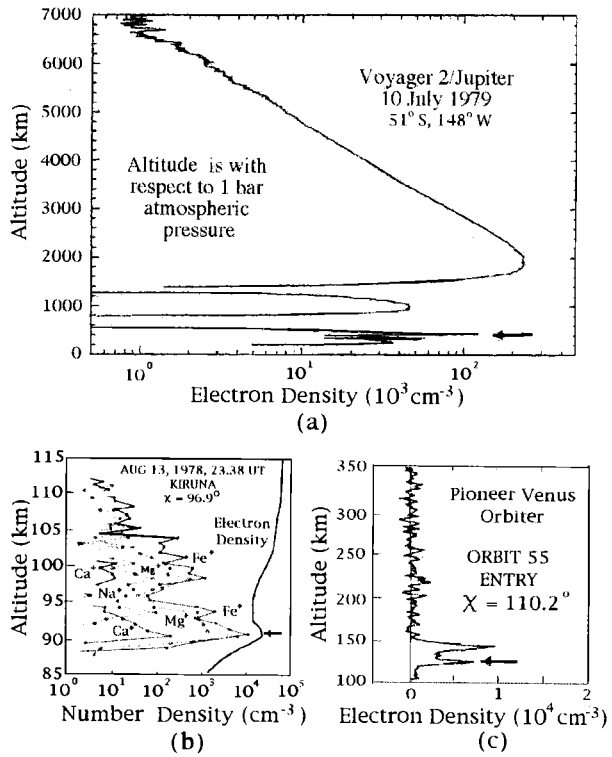

Figure 1. Planetary ionosphere measurements indicative of metal ion layers (indicated by arrows). (a) A Jupiter occultation [from *Hinson et al.*, 1998] with prominent narrow low altitude layers. (b) A sounding rocket measurement of terrestrial metal ion layers [from *Kopp*, 1997]. (c) A Venus radio occultation measurement of a low altitude layer. (Excerpted with permission from *Kliore et al., Science, 205*, page 99, 1979. Copyright 1979, American Association for the Advancement of Science.)

Layers of meteoric neutral atoms form and peak at an altitude below the corresponding metal ion layers [e.g., *McNeil et al.*, 1996]. The process of recondensation of refractive species in the dense vapor could also yield small dust (or smoke) particles [e.g., *Hunten et al.*, 1980]. Hence, in addition to the small particles that do not ablate, a broad range of particle sizes are left in the atmosphere that will slowly diffuse or fall downward to leave traces far below the ablation zone.

Unlike the metal ions, which can be dominant ionospheric species, the neutral meteoric species are always minor constituents of the neutral atmosphere. Nevertheless, by either acting as catalysts or introducing reactive species that would otherwise be absent, they can have a persistent impact on the chemistry of the major atmospheric constituents. The introduction of oxygen, carbon, nitrogen, and sulfur atoms is particularly important for the giant planets. Furthermore, the spectral lines of the metals stand out against the background and can be used as tracers for chemical and dynamical studies with lidar [*Plane et al.*, 1999] and all-sky imagers [*Taylor et al.*, 1995].

3. TERRESTRIAL PLANETS

Meteoric ion and neutral particle measurements at Earth have revealed the major chemical and dynamic processes that control the metal distributions in the lower ionosphere. Prominently observed is a persistent metal ion layer between 85 and 100 km, the region of maximum meteor activity. Most of the metal ion species have maximum concentrations at the same altitude. Fe and/or Mg are typically the dominant metal ions (Figure 1b), consistent with a chondritic meteoroid source. The altitude of the peak, the peak ion concentration, and the shape of the layer vary with atmospheric temperature and composition and are affected by atmospheric winds and electric fields (produced in the magnetosphere or by the atmosphere-generated dynamo). The dynamical processes can produce multiple, and very thin, ion layers. The metal ions at Earth are important components of the ionosphere. Metal neutral atoms charge exchange with ambient ions, thereby reducing their concentrations. Also there is a loss of ambient ions through enhanced dissociative recombination when the electron concentration increases due to the presence of the metal ions. Regions of the lower terrestrial ionosphere are often composed predominantly of metal ions, particularly at night. Specific references and discussion of all these features can be found in the reviews in *Murad and Williams* [2001].

For the other planets, there are no low altitude observations of the ion composition, but radio occultation measurements provide electron density profiles. If metal ions prevail, then, as at Earth, one would expect to see prominent electron density layers below the main ionosphere peak. Figure 1c shows evidence for such low altitude layers at the terrestrial planet Venus. *Butler and Chamberlain* [1976] were the first to note that the Venusian lower layer might be attributable to metal ions. No published radio occultation data for Mars shows the presence of such layering, but the published occultation studies do not show detailed electron density profiles at the low altitudes where IDP effects could occur.

For Mars and Venus, the ionospheric dynamics that lead to the complex, terrestrial metal ion distributions are not anticipated to play a significant role. The motions of metal ions at Earth are strongly constrained by the Earth's magnetic field. Venus has no intrinsic magnetic field, so ionospheric dynamics could be simpler. Mars is more complex in this regard because of the existence of localized remnant

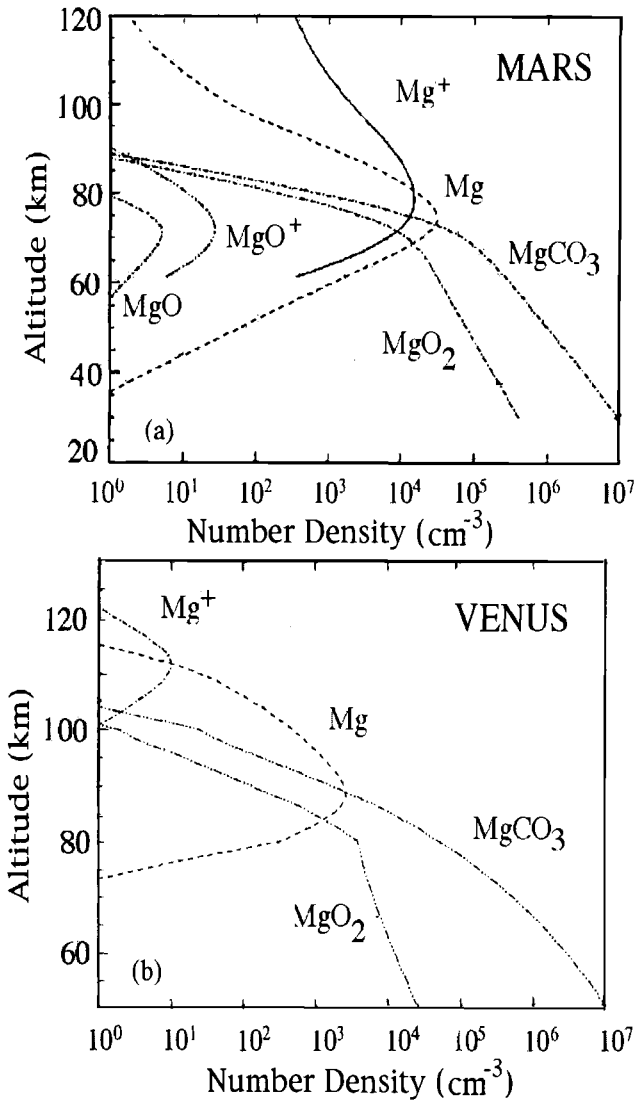

Figure 2. Model calculations of the Mg ion and neutral layers for (a) Mars and (b) Venus [*Pesnell and Grebowsky*, 2000a,b].

magnetic fields in its crust. Still, it is reasonable to assume that such processes will not affect the metal ion distributions outside of these magnetized regions.

Model studies for Mars [*Pesnell and Grebowsky*, 2000a] and Venus [*Pesnell and Grebowsky*, 2000b] have only considered the Mg profile. It is anticipated that Fe^+, the other major metal ion, would behave similarly. The calculations were steady state in one dimension. The Mars and Venus models employ the same ablation and chemical schemes used for Earth, but with background atmospheric and ionosphere models appropriate to the other planets. The assumption is made that the IDPs have the same mass distribution as at Earth. *Pesnell and Grebowsky* [2000a,b] showed that the CO_2 atmospheres of Mars and Venus do not strongly absorb the Mg-ionizing photons until well below the ambient ionosphere, so that photoionization is the main ionization process. Also, although the atmospheric composition of the three terrestrial planets differ, the chemistry pathways controlling Mg and Mg^+ involve the same reactions, albeit at different rates.

The Mars and Venus models are shown in Figure 2. Modeled Mg profiles for Earth follow similar patterns [*McNeil et al.*, 1996; *Grebowsky and Pesnell*, 1999]. The Mg^+ layers are formed by the ionization of neutral Mg atoms diffusing up from the lower-altitude, peak-ablation region. On the topside of the Mg layer, almost all of the neutrals become ionized. The Mg^+ concentration drops with decreasing altitude because it is transformed, via 3-body reactions with atmospheric neutral molecules, into molecular ions. A prominent layer with peak concentration similar to values at Earth is predicted near 80 km at Mars. However, for Venus only a very weak metal ion layer in the vicinity of 110 km is modeled. The Venus and Mars predictions appear counter to the radio occultation measurements for the two planets — i.e., no such layer has been reported for Mars while a prominent layer (due to a non-meteoric origin?) is sometimes seen at Venus (Figure 1c). More intensive investigations of the occultation measurements would help to resolve these differences.

Meteoric material can also play roles in the neutral atmospheric chemistry and aerosol distributions at the terrestrial planets. Neutral meteoric species seldom exceed part-per-billion mixing ratios in the terrestrial atmosphere. Nevertheless, meteoric metals are possible agents for the chlorine-catalyzed destruction of ozone on the Earth [*Rodriguez et al.*, 1986; *Aikin and McPeters*, 1986, *Prather and Rodriguez*, 1989]. On Venus, the only direct evidence of meteor chemistry is ultraviolet nightglow in which NO emission was seen along with what may have been an extended meteor trail [*Huestis and Slanger*, 1993].

Solid meteoritic dust in the terrestrial-planet atmospheres may affect neutral atmospheric chemistry, cloud and haze formation, radiative balance of the atmosphere, and global climate change. Tiny smoke particles formed in the mesosphere and thermosphere from the recondensation of refractory ablated vapor settle throughout the atmosphere, and larger (radius greater than ~1 μm) unablated or partially ablated micrometeorites could dominate the large-particle component of the stratospheric aerosol layer [*Hunten et al.*, 1980]. These particles could provide condensation nuclei for noctilucent clouds in the Earth's mesosphere [e.g., *Thomas*, 1991]. An increasing body of evidence also suggests that the sulfate aerosols in the

stratosphere contain meteoric debris, perhaps from heterogeneous condensation of sulfuric acid about meteoric smoke particles [*Cziczo et al.*, 2001]. The solid meteoric debris can also provide surfaces upon which heterogeneous chemical reactions occur [e.g., *Summers and Siskind*, 1999]. If meteoric dust does play an important role as condensation nuclei for stratospheric aerosols or for mesospheric noctilucent clouds, the effects on the radiative balance and global energy budget of the atmosphere could be profound. In the atmospheres of Mars and Venus, solid meteoric debris could have the same effect as on Earth. *Turco et al.* [1983] and *Michelangeli et al.* [1993] demonstrated that recondensed meteoric particles can act as nucleation sites for aerosol formation in the upper atmospheres of these planets.

4. OUTER PLANETS

Occultations of radio signals from spacecraft provide evidence for very structured and time varying ionospheres on the outer planets (see review by *Kar* [1996]). A Jovian profile is shown in Figure 1a. Neutral atmosphere measurements, in combination with IDP-atmosphere interaction models, provide independent evidence for the importance of the meteoroid inputs.

As a needed input to the models, spacecraft measurements provide a constraint on the IDP number density as a function of heliocentric distance [e.g., *Humes* 1980; *Grün*, 1994]. The window of possible IDP impact velocities into each of the outer planetary atmospheres is quite small (see Table 1). Hence ablation rate effects that are dependent upon the particle speeds are fairly well defined. However, knowledge of the velocity distribution outside of a planet's gravitational sphere is necessary to estimate the flux enhancements due to gravitational focusing. The enhancement is less than a factor of ~ 2 for the inner planets; but, for the outer planets the enhancement can range from a factor of ~6 to 200, depending on the assumed IDP orbits [*Moses et al.*, 2000]. The relative contributions from different particle sizes are unknown for the outer solar system. All ablation calculations to date have used the terrestrial mass distribution. The approach taken in the IDP-atmosphere studies has been to make reasonable estimates of the total impact flux and velocity distribution for plausible sources and orbits of the particles. Comparisons of the model results with observed electron density profiles and neutral atmospheric constituents then allow the validity of the assumptions to be checked.

In the outer solar system, the IDPs are probably comet-like mixtures of ices, silicates, and complex organic materials. During ablation, water and other volatiles will be released at higher altitudes than metal and silicate vapor because of the lower vaporization temperature of the ices. Also, since outer planetary atmospheres consist predominantly of H_2, He and hydrocarbons (Table 1), meteoric oxygen must be considered, unlike at the inner planets, where meteoric oxygen becomes a trivial component of the overall atmospheric oxygen budget. Ablated material is ionized by charge exchange and impact ionization; photoionization is not important. Detailed model studies have been made of the meteoric ionization for Jupiter [*Kim et al.*, 2001], Saturn [*Moses and Bass*, 2000], Neptune [*Lyons*, 1995], as well as for Saturn's moon Titan [*Molina-Cuberos et al.*, 2001].

The outer planet ionosphere models include hydrogen and hydrocarbon ions as well as one or more meteoric elements. Examples of the modeled ion profiles for Jupiter [*Kim et al.*, 2001] and Neptune [*Lyons*, 1995] are shown in Figure 3a and 3b. Both calculations assume a cometary composition for the ablated IDP atoms. The incident meteoroid mass flux for the Jovian calculation in Figure 3a is the terrestrial influx value of 1.5×10^{-16} g cm^{-2} s^{-1}. This flux magnitude yields a metal ion peak density comparable to the occultation measurements of a few 10^4 cm^{-3} [*Hinson et al.* 1998]. The incident flux used for the Neptunian model of Lyons was 7×10^{-16} g cm^{-2} s^{-1}, a value that lies between the *Moses* [1992] predictions for randomly inclined, highly eccentric particles and low inclination, low eccentricity particles. Saturn's ionosphere was modeled by *Moses and Bass* [2000], with Mg^+ as sole representative of the major metal ions. An IDP influx of 3×10^{-16} g cm^{-2} s^{-1} was employed, based on models of the Infrared Space Observatory (ISO) observations of H_2O and CO_2 in Saturn's upper atmosphere [*de Graauw et al.*, 1997; *Feuchtgruber et al.*, 1997; *Moses et al.*, 2000]. The altitudes and maximum densities of the metal ion layers in all three of these model studies are in agreement with the magnitude and altitude zone of the low-altitude ionospheric layers probed by radio occultation. However, these simple models do not match the complexities of the occultation-measured layers (e.g., time varying and sharp multiple layers). *Lyons* [1995] and *Moses and Bass* [2000] showed that such structures can be produced by the inclusion of ion transport associated with vertical ion drift shears, as occurs in the Earth's ionosphere. Waves in these motions will yield multiple layers. Ionospheric structures for atmosphere-bearing satellites of the outer planets may also have a meteoric origin. *Molina-Cuberos et al.* [2001] predict meteoric ion concentrations (shown in Figure 3c) on Titan comparable to those of the background ionosphere produced by photochemistry.

The 1-D average model ionospheres in Figure 3 and the model for Saturn have Mg^+ and/or Fe^+ as the major low-altitude ion. *Kim et al.* [2001] and *Moses and Bass* [2000]

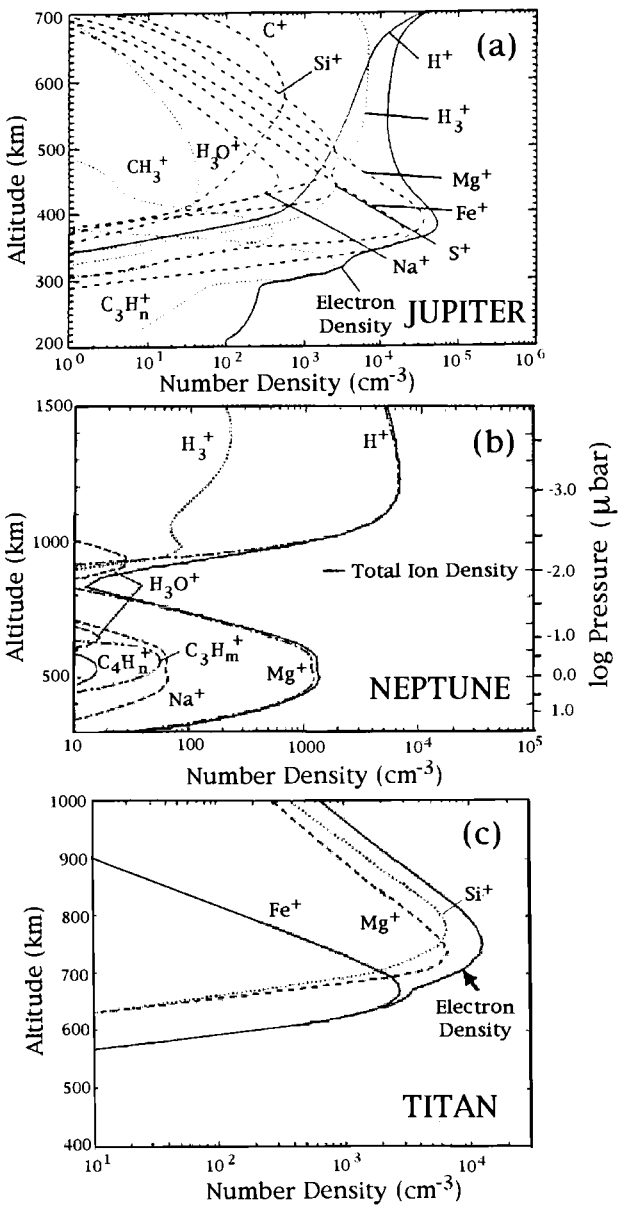

Figure 3. Meteoric ion models. (a) Model of Jovian ionosphere [from *Kim et al.* 2001] — altitude is referenced to 1 bar atmospheric pressure level. (b) Neptune model. (Reprinted with permission from *Lyons, Science, 267*, page 649, 1995. Copyright 1995, American Association for the Advancement of Science.) (c) Metal ion model for Saturn's moon Titan [*Molina-Cuberos et al.*, 2001, reprinted with permission from Elsevier Science].

also modeled local time variations for Jupiter and Saturn, respectively. They found double-layer ionosphere structures (as in Figure 3b) that were most prominent just before dawn. The upper layer was due to H^+, whereas metal ions dominated the lower layer. The molecular ion concentrations decay through the night. All the models use charge exchange as a source of metal ions, but the Jupiter calculation also includes impact ionization of the ablated neutral atoms. Because of the high incident velocity of the IDPs at Jupiter, this ion production source is dominant. For the Saturn and Neptune studies, recondensation onto dust particles is the primary low-altitude loss channel for the ablated metal atoms. For Jupiter *Kim et al.* [2001] include the loss of meteoric ions by three body reactions with H_2 and hydrocarbons. Such rates have yet to be measured for Mg^+ and Fe^+. The *Kim et al.* [2001] model depicted in Figure 3a used the laboratory-measured rates of the three body reaction of sodium with H_2 scaled for Mg^+, but considered a similar Fe^+ process unlikely. The modeled dominance of Mg^+ over Fe^+ simply reflects the relative composition of their parent neutral species in the incoming meteoroids. Laboratory studies are lacking for many of the reactions of metal atoms with hydrocarbons. The species H_3O^+ in Figure 3a is the result of the meteoric oxygen.

Because of the complex structures produced by ionospheric dynamics, it is difficult to use the occultation measurements to precisely constrain the IDP input fluxes. Neutral atmosphere measurements provide another avenue for exploring the IDP characteristics. Recognition that the oxygen-bearing vapor from extraplanetary sources could participate in stratospheric photochemistry on the outer planets first arose when CO was discovered in Jupiter's atmosphere [*Beer*, 1975]. Because carbon monoxide is a disequilibrium species in Jupiter's atmosphere, *Prather et al.* [1978] suggested meteoroid ablation as a source of water vapor in Jupiter's upper atmosphere — subsequent photochemistry would then convert the H_2O to CO. However CO could also be produced in the deep atmosphere and transported to the upper troposphere where it is observed [e.g., *Prinn and Barshay*, 1977; *Fegley and Lodders*, 1994]. The same ambiguities apply to the interpretation of the observed CO at Saturn and Neptune [e.g., *Noll et al.*, 1986; *Marten et al.*, 1993].

The definitive evidence for influxes of atmosphere-modifying material on planets other than Earth was the discovery of H_2O in the stratospheres of all the giant planets and CO_2 on Jupiter, Saturn, and Neptune [*de Graauw et al.*, 1997; *Feuchtgruber et al.*, 1997; *Bergin et al.*, 2000]. Intrinsic water vapor on the outer planets will condense deep in the tropospheres and should not observed in the stratospheres. Also although CO_2, like CO, may be transported upwards from the deeper regions in which it is thermodynamically stable, the predicted CO_2 mixing ratios in such a scenario are much smaller than what is observed [*e.g., Lellouch et al.*, 1998]. Therefore an external source is needed [e.g., *Feuchtgruber et al.*, 1997] and the most likely source is meteoroid ablation [*Moses et al.*, 2000]. Modeled

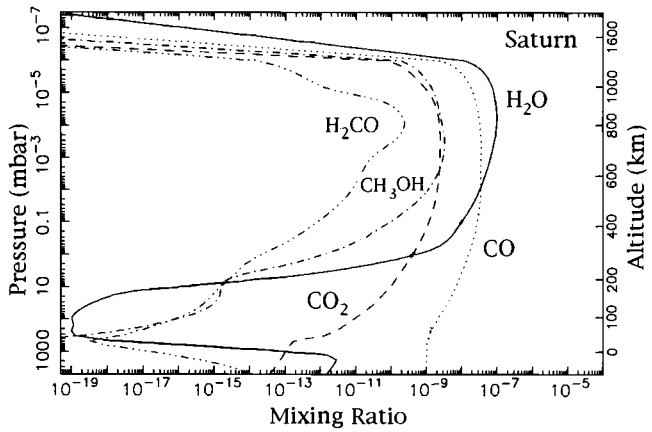

Figure 4. Modeled dominant molecular neutral species resulting from IDPs in Saturn's atmosphere [*Moses et al.*, 2000].

IDP effects in the Saturnian atmosphere from the latter study are shown in Figure 4. The oxygen species could affect the abundance of some of the less abundant atmospheric hydrocarbon molecules. IDP ablation will also introduce nitrogen- or sulfur-containing species or other volatile vapors that are not normally present in the upper atmospheres of the giant planets. Many aspects of the interaction of meteoric vapor with outer planetary atmospheres remain to be explored.

Residual micrometeorites and smoke particles formed from ablated-IDP vapors can also affect photochemistry through the attenuation of solar ultraviolet radiation. They might cause localized heating in the upper atmosphere [e.g., *Rizk and Hunten*, 1990], which could affect atmospheric dynamics. They can act as condensation nuclei to facilitate stratospheric haze formation and provide surfaces upon which heterogeneous reactions could occur.

Moons of the outer planets sample the same IDP population as their parent planet (although in different proportions). The presence of CO [*Lutz et al.*, 1983], CO_2 [*Samuelson et al.*, 1983], and H_2O [*Coustenis et al.*, 1998] in Titan's atmosphere suggests an extraplanetary supply of oxygen. *Ip* [1990] and *English et al.* [1996] show the credibility of this interpretation by modeling the meteoroid-ablation deposition of oxygen-bearing materials into the moon's atmosphere. Triton, the largest moon of Neptune, may also provide a laboratory to study the IDP population at Neptune. The surface pressure of Triton's atmosphere of roughly 10 μbar may be sufficient to ablate many IDPs [*Strobel and Summers*, 1995].

5. SUMMARY

Sufficient theoretical understanding exists to determine the ramifications that IDPs may have on all planetary atmospheres. Details of these interactions are measured at Earth, where meteoric ions often dominate the lower ionosphere and where it is suggested that IDPs could lead to the development of aerosol layers and possibly affect the stratospheric ozone population. Radio occultation measurements on the other atmosphere-bearing planets find ionospheric layers similar to the metal layers on Earth. Model studies support a metal ion interpretation. For the inner planets of Mars and Venus there is ambiguity between the modeled and measured layers. For the outer planets and Titan, IDPs can be a source for the water and carbon dioxide observed in these atmospheres. What is missing most in our understanding are measurements of ionospheric and atmospheric structures in other atmospheres and IDP properties throughout the solar system.

REFERENCES

Aikin, A. C., and R. D. McPeters, Meteoric material and the behavior of upper stratospheric polar ozone, *Geophys. Res. Lett., 13*, 1300-1303, 1986.

Beer, R., Detection of carbon monoxide on Jupiter, *Astrophys. J., 200*, L167-L170, 1975.

Bergin, E. A., et al., Submillimeter Wave Astronomy Satellite observations of Jupiter and Saturn: Detection of 557 GHz water emission from the upper atmosphere, *Astrophys. J., 539*, L147-L150, 2000.

Bronshten, V. A., *Physics of Meteoric Phenomena*, Reidel, Dordrecht, Holland, 1983.

Butler, D. M., and J. W. Chamberlain, Venus' night side ionosphere: its origin and maintenance, *J. Geophys. Res., 81*, 4757-4760, 1976.

Carter, L. N., and J. M. Forbes, Global transport and localized layering of metallic ions in the upper atmosphere, *Ann. Geophys., 17*, 190-209, 1999.

Coustenis, A., A. Salama, E. Lellouch, T. Encrenaz, G. L. Bjoraker, R. E. Samuelson, T. de Graauw, H. Feuchtgruber, and M. F. Kessler, Evidence for water vapor in Titan's atmosphere from ISO/SWS data, *Astron. Astrophys., 336*, L85-L89, 1998.

Däppen, W., Atoms and molecules, *in Allen's Astrophysical Quantities*, 4th ed., ed. A. N. Cox, Springer-Verlag, New York, pp. 27-51, 2000.

Cziczo, D. J., D. S. Thomson, and D. M. Murphy, Ablation, flux, and atmospheric implications of meteors inferred from stratospheric aerosol, *Science, 291*, 1772-1775, 2001.

de Graauw, T., et al., First results of ISO-SWS observations of Saturn: Detection of CO_2, CH_3C_2H, C_4H_2 and tropospheric H_2O, *Astron. Astrophys., 321*, L13-L16, 1997.

English, M. A., L. M. Lara, R. D. Lorenz, P. R. Ratcliff, and R. Rodrigo, Ablation and chemistry of meteoric materials in the atmosphere of Titan, *Adv. Space Res., 17* (12), 157-160, 1996.

Fegley, B., Jr., and K. Lodders, Chemical models of the deep atmospheres of Jupiter and Saturn, *Icarus, 110*, 117-154, 1994.

Feuchtgruber, H., E. Lellouch, T. de Graauw, B. Bézard, T. Encrenaz, and M. Griffin, External supply of oxygen to the atmospheres of the giant planets, *Nature, 389*, 159-162, 1997.

Grebowsky J. M., and W. D. Pesnell, Meteor showers: Modeled

and measured effects in the atmosphere, *AIAA*, paper no. 99-0503, 1999.

Grün, E., Dust measurements in the outer solar system, in *Asteroids, Comets, Meteoroids 1993*, ed. A. Milani et al., IAU, Kluwer, Dordrecht, pp. 367-380, 1994.

Grün, E., H. A. Zook, H. Fechtig, and R. H. Giese, Collisional balance of the meteoritic complex, *Icarus, 62*, 244-272, 1985.

Hinson, D. P., J. D. Twicken, and E. T. Karayel, Jupiter's ionosphere: new results from Voyager 2 radio occultation measurements. *J. Geophys. Res., 103*, 9505-9520, 1998.

Huestis. D. L. and T. G. Slanger, New perspectives on the Venus nightglow, *J. Geophys. Res., 98*, 10,839-10,847, 1993.

Humes, D. H. Results of Pioneer 10 and 11 meteoroid experiments: interplanetary and near Saturn, *J. Geophys. Res., 85*, 5841-5852, 1980.

Hunten, D. M., R. P. Turco, and O. B. Toon, Smoke and dust particles of meteoric origin in the mesosphere and stratosphere, *J. Atmos. Sci., 37*, 1342-1357, 1980.

Ip, W.-H., Meteoroid ablation processes in Titan's atmosphere, *Nature, 345*, 511-512, 1990.

Johnson, R., Surface-Boundary-Exospheres, this volume, 2002.

Kar, J., Recent advances in planetary ionospheres, *Space Science Reviews, 77*, 193-266, 1996.

Kelley, M. C., *The Earth's Ionosphere*, Academic Press, London, 1989.

Kim, Y. H., W. D. Pesnell, J. M. Grebowsky, and J. L. Fox, Meteoric ions in the ionosphere of Jupiter, *Icarus, 150*, 261-278, 2001.

Kliore, A. J., I. R. Patel, A. F. Nagy, A. F. Cravens, and T. I. Gombosi, Initial observations of the nightside of Venus from Pioneer Venus orbiter radio occultations, *Science, 205*, 99-102, 1979.

Kliore, A. J., I. R. Patel, G. F. Lindal, D. N. Sweetman, H. B. Hotz, J. H. Waite, Jr., and T. R. McDonough, Structure of the ionosphere and atmosphere of Saturn from Pioneer 11, Saturn radio occultation, *J. Geophys. Res., 85*, 5857-5870, 1980.

Kopp, E., On the abundance of metal ions in the lower ionosphere, *J. Geophys. Res., 102*, 9667-9674, 1997.

Lebedinets, V. N., A. V. Manochina, and V. B. Shuskova, Interaction of the lower thermosphere with the solid component of the interplanetary medium, *Planet. Space Sci., 21*, 1317-1332, 1973.

Leinert, C., and E. Grün, Interplanetary dust, in *Physics and Chemistry in Space – Space and Solar Physics*, Vol. 20, Physics of the Inner Heliosphere I, ed. R. Schwenn and E. Marsch, Springer-Verlag, Berlin, pp. 207-274, 1990.

Lellouch, E., H. Feuchtgruber, T. de Graauw, T. Encrenaz, B. Bézard, M. Griffin, and G. Davis, D/H ratio and oxygen source: A Jupiter-Saturn comparison, in *International Symposium: The Jovian System After Galileo, the Saturnian System Before Cassini-Huygens*, May 11-15, Nantes, France, pp. 21-22, 1998.

Love, S. G., and D. E. Brownlee, A direct measure of the terrestrial mass accretion rate of cosmic dust, *Science, 262*, 550-553, 1993.

Lutz, B. L., C. de Gergh, and T. Owen, Titan: Discovery of carbon monoxide in its atmosphere, *Science, 220*, 1374-1375, 1983.

Lyons, J. R., Metal ions in the atmosphere of Neptune, *Science, 267*, 648-651, 1995.

Marten, A., D. Gautier, T. Owen, D. B. Sanders, H. E. Matthews, S. K. Atreya, R. P. J. Tilanus, and J. R. Deane, First observations of CO and HCN on Neptune and Uranus at millimeter wavelengths and their implications for atmospheric chemistry, *Astrophys. J., 406*, 285-297, 1993.

McDonnell, J. A. M., editor, *Cosmic Dust*, Wiley-Interscience, New York, 1978.

McNeil, W. J., S. T. Lau, and E. Murad, A model for meteoric magnesium in the ionosphere, *J. Geophys. Res., 101*, 5251-5259, 1996.

Michelangeli, D. V., O. B. Toon, R. M. Haberle, and J. B. Pollack, Numerical simulations of the formation and evolution of water ice clouds in the Martian atmosphere, *Icarus, 100*, 261-285, 1993.

Molina-Cuberos, G. J., H. Lammer, W. Stumptner, K. Schwingenschuh, H. O. Rucker, J. J. Lopez-Moreno, R. Rodrigo, and T. Tokano, Ionospheric layer induced by meteoric ionization in Titan's atmosphere, *Planet. Space Sci., 49*, 143-153, 2001.

Moses, J. I., Meteoroid ablation in Neptune's atmosphere, *Icarus, 99*, 368-383, 1992.

Moses, J. I., and S. F. Bass, The effects of external material on the chemistry and structure of Saturn's ionosphere, *J. Geophys. Res., 105*, 7013-7052, 2000.

Moses, J. I., E. Lellouch, B. Bézard, G. R. Gladstone, H. Feuchtgruber, and M. Allen, Photochemistry of Saturn's atmosphere. II. Effects of an influx of external oxygen, *Icarus, 145*, 166-202, 2000.

Murad, E., and I. P. Williams, editors, *Meteors in the Earth's Atmosphere*, Cambridge Univ. Press, New York, in press, 2001.

Noll, K. S., R. F. Knacke, T. R. Geballe, and A. T. Tokunaga, The detection of carbon monoxide in Saturn, *Astrophys. J., 309*, L91-L94, 1986.

Öpik, E. J., Physics of Meteor Flight in the Atmosphere, *Interscience*, New York, 1958.

Pesnell, W. D., and J. Grebowsky, Meteoric magnesium in the Martian atmosphere, *J. Geophys. Res.*, 105, 1695-1707, 2000a.

Pesnell, W. D., and J. M. Grebowsky, Persistent meteoric ions in the atmosphere of Venus, *EOS Trans. AGU, 81*, F808, 2000b.

Plane, J. M. C., R. M. Cox, and R. J. Rollaston, Metallic ion layers in the mesopause and lower thermosphere region, *Adv. Space Res., 24(11)*, 1559-1570, 1999.

Prather, M. J., J. A. Logan, and M. B. McElroy, Carbon monoxide in Jupiter's upper atmosphere: An extraplanetary source, *Astrophys. J., 223*, 1072-1081, 1978.

Prather, M. J., and J. M. Rodriguez, Antarctic ozone: Meteoric control of HNO_3, *Geophys. Res. Lett., 15*, 1-4, 1988.

Prinn, R.G., and S. S. Barshay, Carbon monoxide on Jupiter and implications for atmospheric convection, *Science, 198*, 1031-1034, 1977.

Rizk, B., and D. M. Hunten, Solar heating of the Uranian mesopause by dust of ring origin, *Icarus, 88*, 429-447, 1990.

Rodriguez, J. M., M. K. W. Ko, and N. D. Sze, Possible impact of sodium species on ClO and O_3 in the upper stratosphere, *Geophys. Res. Lett., 13*, 499-502, 1986.

Samuelson, R. E., W. C. Maguire, R. A. Hanel, V. G. Kunde, D. E. Jennings, Y. L. Yung, and A. C. Aikin, CO_2 on Titan, *J. Geophys. Res., 88*, 8709-8715, 1983.

Summers, M. E., and D. E. Siskind, Surface recombination of O and H_2 on meteoric dust as a source of mesospheric water vapor, *Geophys. Res. Lett.*, 26, 1837-1840, 1999.

Strobel, D. F., and M. E. Summers, Triton's upper atmosphere and ionosphere, in *Neptune and Triton*, eds. D. P. Cruikshank, M. S. Matthews, and A. M. Schumann, Univ. Ariz. Press, Tucson, Az., pp. 1107-1120, 1995.

Swider, W., Jr., Processes for meteoric elements in the E-region, *Planet. Space Sci., 17*, 1233-1246, 1969.

Taylor, A. D., The Harvard Radio Meteor Project meteor velocity distribution reappraised, *Icarus, 116*, 154-158, 1995.

Taylor, M. J., M. B. Bishop, and V. Taylor, All-sky measurements of short period waves imaged in the OI(557.7 nm) and Na(589.2 nm) and near infrared OH and O2 (0.1) nightglow emissions during the ALOHA-93 campaign, *Geophys. Res. Lett.*, 22, 2833-2836, 1995.

Tholen, D. J., V. G. Teijfel, and A. N. Cox, Planets and satellites, in *Allen's Astrophysical Quantities*, 4th ed., ed. A. N. Cox, Springer-Verlag, New York, pp. 293-313. 2000.

Thomas, G. E., Mesospheric clouds and the physics of the mesopause region, *Rev. Geophys., 29*, 553-575, 1991

Turco, R. P., O. B. Toon, R. C. Whitten, and R. G. Keese, Venus: Mesospheric hazes of ice, dust, and acid aerosols, *Icarus, 53*, 18-25, 1983.

Yung, Y. L., and W. B. DeMore, *Photochemistry of Planetary Atmospheres*, Oxford Univ. Press, New York, 1999.

J. M. Grebowsky, Laboratory for Extraterrestrial Physics, Code 695, NASA/Goddard Space Flight Center, Greenbelt, MD 20771. (u5jmg@lepvax.gsfc.nasa.gov).

J. I. Moses, Lunar and Planetary Institute, 3600 Bay Area Blvd., Houston, TX 77058-1113. (moses@lpi.usra.edu).

W. D. Pesnell, Nomad Research, Inc., 795 Scarborough Court, Arnold, MD 21012. (pesnell@nomadresearch.com).

Current Laboratory Experiments For Planetary Aeronomy

David L. Huestis

Molecular Physics Laboratory, SRI International, Menlo Park, California

Guidance is provided for finding atomic and molecular reaction rate coefficients, cross sections, and other properties in the primary literature and in useful reviews. Recent laboratory and theoretical work on a few microscopic processes of importance in solar system aeronomy is summarized. Specific examples focus on, (a) the recombination of oxygen atoms—important in understanding the atmospheres of Venus, Earth, and Mars, (b) formation and electron-ion dissociative recombination of H_3^+—important for understanding the aurora on Jupiter, Saturn, and Uranus, and (c) recombination of methyl radicals—the key photochemical intermediate leading to the complex organic molecules on the giant planets and moons.

1. INTRODUCTION

Three communities of scientists collaborate in the investigation, understanding, and interpretation of planetary atmospheres. "Observers" record atmospheric "data" using direct-sampling instruments on planetary probes, remote sensing instruments on Earth-orbiting satellites and planetary orbiters, and ground-based spectrometers, radio facilities, and optical telescopes. "Modelers" attempt to explain atmospheric observations by simulations based on microscopic processes that hopefully are well known from laboratory investigations. "Laboratory investigators" use experiments and fundamental theory to quantitatively characterize the underlying microscopic processes.

Atoms, molecules, electrons and ions, their internal energy levels and translational energy content, and their collisional interactions, are clearly central to atmospheric science. Historically, observations in the atmosphere have often provided the first information about atomic and molecular structure and collisional processes. In these cases, the modeler is "free" to infer the numerical values of microscopic parameters by "fitting" or adjusting the model to match or explain the atmospheric observations. Sometimes this works beautifully in deriving values that are subsequently confirmed by laboratory measurements. In any case, the atmosphere supplies a continuing list of microscopic processes that appear to be important enough to justify devising approaches to characterize them quantitatively. What should not be done is to assume that the modeling inference alone is the final answer.

All of this presents the modeler with daunting prospects. First, the list of microscopic processes is very long. Second, it is hard to know in advance which ones will have a significant effect on the observables being modeled. Third, not all of the important microscopic processes will have been already examined in the laboratory. Fourth, it is a big job to survey the primary literature to find the rates and cross sections that have been measured. Finally, it is difficult for the modeler to assess the accuracy of laboratory measurements, whose details and vulnerabilities are outside his/her primary areas of expertise.

One purpose of this chapter is to provide general advice about how to find useful reviews and relevant primary literature. A second purpose is to summarize recent laboratory experimental and theoretical work on a few microscopic processes of importance in solar system aeronomy. A specific focus is on the recombination of oxygen atoms—important in understanding the atmospheres of Venus, Earth, and Mars, formation and electron-ion

Atmospheres in the Solar System: Comparative Aeronomy
Geophysical Monograph 130

10.1029/130GM16

dissociative recombination of H_3^+—important for understanding the aurora on Jupiter, Saturn, and Uranus, and recombination of methyl radicals—the key photochemical intermediate leading to the complex organic molecules on the giant planets and moons.

2.0 DATA RESOURCES

One of the reasons that the study of planetary atmospheres is so interesting is that the subject is very interdisciplinary. It is especially stimulating to collaborate with colleagues in neighboring fields. However, this stimulation comes at a price. We have a vast literature to find, understand, evaluate, and incorporate into our own work. Some help with the "finding" part is provided in Table 1, which lists a collection of on-line resources that may be helpful in finding laboratory and other data of interest for aeronomy of the solar system. Some additional suggestions about finding information are provided below, along with some advice about the "understanding" and "evaluating" parts.

2.1 The Importance of Primary Literature

The easiest approach to finding information about atmospheric microscopic processes is to copy the parameters used in a major modeling study or catalogued in a summary monograph. Some examples could be taken from the works of Banks and Kockarts [1973a, b], Fox [*Fox and Dalgarno*, 1979; *Fox and Sung*, 2001], Roble [1995], Yung [*Yung and DeMore*, 1999], and Moses [*Moses, et al.*, 2000]. However, this approach is not without risk. The primary emphasis, in such works, is usually on "explaining" atmospheric observations. Space limitations often prevent the authors from reviewing the history of the parameters used or their possible uncertainties. In the worst cases there is no indication of the origin of the numbers or the extent to which the values used have been selected from the literature, modified for best fit, or are just plausible guesses.

The message here is that atmospheric scientists must maintain a healthy suspicion of everything outside their own area of expertise. Importing knowledge from other areas is essential, but it is unwise to assume that just because something has been published necessarily implies that it must be accurately known. Thus the obligation is to either (1) find, understand, and evaluate the primary literature, (2) rely on authors with a documented history of careful evaluation, or (3) use the results of critical reviews of the literature, if they happen to be available.

2.2 The Importance of Critical Review

Among the best examples of critical review of the basis of understanding of atmospheric microscopic processes are the serial publications by the Defense Nuclear Agency (DNA) in the 1970s and 1980s attempting to understand the response of the atmosphere to nuclear weapons and by the NASA Panel for Data Evaluation in the 1980s and 1990s attempting to understand the response of the atmosphere to anthropogenic release of chlorofluorocarbons (CFCs). In both of these cases a principle concern was to quantify the statistical uncertainty limits of our knowledge and ability to make quantitative predictions.

The last update of the DNA Reaction Rate Handbook [*Bortner and Baurer*, 1983] has been out of print for some time, but still has value. The NASA panel issued its final printed version (Evaluation Number 12) of the report in 1997 [*DeMore, et al.*, 1997] and has posted the year-2000 version on-line at http://jpldataeval.jpl.nasa.gov/ The principal limitation for aeronomy of the NASA Panel review is that it concentrates on the middle and lower atmosphere.

In 1991, Fox published an excellent review of "Cross Sections and Reaction Rates of Relevance to Aeronomy" [*Fox*, 1991] with more than 30 subsections and about 450 references to the primary literature and previous reviews. The combustion and lower atmosphere communities have a long history of publishing critical reviews, only a few of which can be cited here [*Atkinson, et al.*, 1997; *Kerr and Drew*, 1987; *Baulch, et al.*, 1976; *Johnson*, 1968; *Schofield*, 1967; *Trotman-Dickenson and Milne*, 1967]. Rate coefficients for reactions of electronically excited states have also been reviewed [*Schofield*, 1979]. Ion molecule reactions have also been extensively reviewed [*Anicich*, 1993a, b; *Ikezoe, et al.*, 1987; *Anicich and Huntress*, 1986]. The Anicich database is available from JPL on-line at http://astrochem.jpl.nasa.gov/asch/ and has been included in the UMIST database http://www.rate99.co.uk/ For some years NBS (now NIST) published sorted bibliographies of cross sections for atomic and molecular collisions [*Gallagher, et al.*, 1981]. Electron impact cross sections were reviewed in 1983 [*Trajmar, et al.*, 1983] with more recent reviews on individual atoms and molecules [*Kanik, et al.*, 2000; *Itikawa and Ichimura*, 1990; *Itikawa, et al.*, 1989; *Itikawa, et al.*, 1986]. The classic texts on photoabsorption cross sections are by Okabe [1978] and Berkowitz [1979].

3.0 OXYGEN NIGHT AIRGLOW CHEMISTRY OF EARTH, VENUS, AND MARS

For decades it has been known that excited electronic states of molecular oxygen are leading sources of near-ultraviolet and visible emissions from the night atmospheres of Earth [*Dufay*, 1941; *Slanger and Huestis*, 1981] and Venus [*Krasnopolsky, et al.*, 1976], and possibly Mars. For

Table 1. On-line Resources for Laboratory Aeronomy of the Solar System

Web Address	Title/Content/Comments
http://www-mpl.sri.com/inserts/lab_aeronomy.html	Web version of this table
General Purpose Search Engine	
http://www.google.com	Personal favorite
Searchable Abstracts of Primary Literature	
http://adsabs.harvard.edu/index.html	NASA Astrophysics Data System (many scanned journals)
http://pubsci.osti.gov	DOE Physical Science Citation Database
http://192.102.233.24/login.asp	AGU journals (authors and titles only)
Databases of Rates, Cross Sections, and other Atomic and Molecular Data	
http://jpldataeval.jpl.nasa.gov/	NASA: Stratosphereic chemical kinetics and photochemistry
http://www.rate99.co.uk	The UMIST database for astrochemistry 1999
http://physics.nist.gov/PhysRefData/	NIST: Spectroscopy and electron impact
http://www.nist.gov/srd/kinet.htm	NIST: Chemical kinetics
http://www.nist.gov/srd/phys.htm	NIST: Atomic and molecular physics
http://webbook.nist.gov/	NIST: Chemistry Webbook
http://cfa-www.harvard.edu/amdata/ampdata/ampdb.shtml	CfA AMP: Atomic and Molecular Databases
http://plasma-gate.weizmann.ac.il/DBfAPP.html	Weizmann: Databases for atomic and plasma physics
http://allen.rad.nd.edu/	Notre Dame Radiation Chemistry Data Center
Data about the Sun and Planets	
http://mesola.obspm.fr/form_spectre.html	BASS 2000 Solar Spectrum
http://ssd.jpl.nasa.gov/horizons.html	Locate solar system objects in the sky
Mail List Servers with Archives	
http://www.jiscmail.ac.uk/lists/atomic-collisions.html	Atomic Collisions
http://www.jiscmail.ac.uk/lists/molecular-dynamics-news.html	Molecular Dynamics News
Directories of Investigators	
http://directory.aas.org	AAS membership directory
http://192.102.233.24/login.asp	AGU membership directory
http://www.aps.org/memb/enter-directory.html	APS membership directory
http://star-www.rl.ac.uk/astrolist/astrosearch.html	International astronomers/astrophysicists
Award Abstracts	
http://www.fastlane.nsf.gov/a6/A6SrchAwdf.htm	NSF awards (Org=AST,ATM,CHE,PHY)
http://spacescience.nasa.gov/codesr/results/ross2000/GEOabstracts.html	NASA Geospace SR&T, active in FY01
http://spacescience.nasa.gov/codesr/results/NRA-98-OSS-03-33.html	NASA Planetary Atmospheres FY99 awards

"quiet" or non-auroral conditions, the energy source of molecular oxygen nightglow emissions is dayside photodissociation by solar ultraviolet photons:

$$O_2 + h\nu \rightarrow O + O \qquad \text{Earth}$$

$$CO_2 + h\nu \rightarrow CO + O \qquad \text{Venus and Mars}$$

After transport to the nightside by planetary rotation or by high-altitude atmospheric winds, the chemical energy stored as oxygen atoms is converted by termolecular recombination into electronic, vibrational, and rotational energy, eventually appearing as ultraviolet, visible, and infrared nightglow emissions:

$$O + O + M \rightarrow O_2(^5\Pi_g, A^3\Sigma_u^+, A'^3\Delta_u, c^1\Sigma_u^-, b^1\Sigma_g^+, a^1\Delta_g, X^3\Sigma_g^-)$$

$$O_2(A^3\Sigma_u^+, A'^3\Delta_u, c^1\Sigma_u^-, b^1\Sigma_g^+, a^1\Delta_g) \rightarrow \text{250-1270 nm emission}$$

Sidney Chapman [1931] was the first to suggest that oxygen atom recombination provided the energy of the visible nightglow, although he was thinking of the atomic oxygen green line, whose mechanistic origin is still controversial [*Slanger and Black*, 1977; *Slanger, et al.*, 2001].

Figure 1 shows potential energy curves for several electronic states of molecular oxygen. It also illustrates the schemes for laser-preparation of individual rovibronic states as well as multi-photon-ionization detection of the initially populated levels and subsequent products of collisional relaxation. The lowest 6 electronic states, $A^3\Sigma_u^+$, $A'^3\Delta_u$, $c^1\Sigma_u^-$, $b^1\Sigma_g^+$, $a^1\Delta_g$, $X^3\Sigma_g^-$ are well known from laboratory spectroscopy [*Huber and Herzberg*, 1979; *Huestis, et al.*, 1994] and from nightglow emissions [*Chamberlain*, 1961; *Slanger and Huestis*, 1981]. The $^5\Pi_g$ state was predicted in quantum chemistry calculations [*Saxon and Liu*, 1977; *Partridge, et al.*, 1991], but only recently discovered experimentally [*Huestis, et al.*, 1998], and thus has now become accessible for characterizing its importance as a "gateway state" for oxygen atom recombination.

Below we will discuss recent progress in the supporting laboratory research that is needed to establish what can be learned from the observed atmospheric emissions of molecular oxygen. Some areas of interest are (1) the distribution of electronic states produced in O + O recombination, (2) how much population flows by collisional relaxation through each excited state, (3) the temperature-dependent quenching/relaxation rate coefficients and product branching ratios, (4) what can be learned from the contrast between the nightglows of Earth and Venus, (5) what we might expect on Mars, and (6) what inferences should be drawn from molecular oxygen emissions that might be observed in the night atmospheres of extra-solar planets.

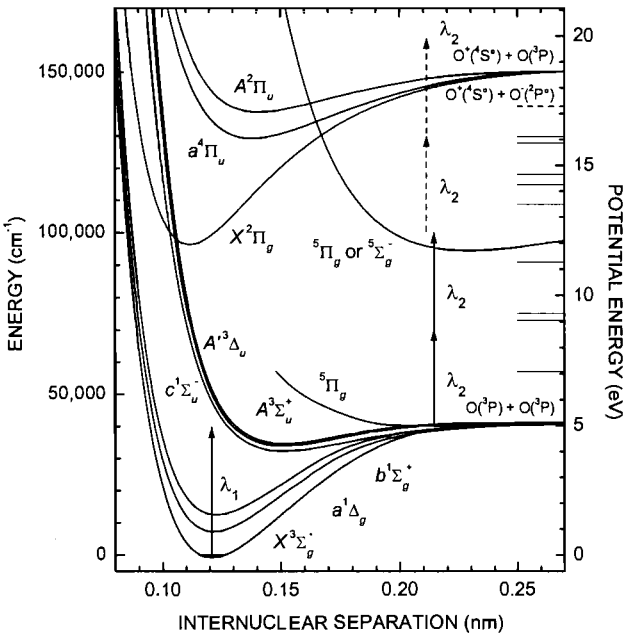

Figure 1. Selected Potential Energy Curves for Electronic States of O_2 and O_2^+. The vertical solid-line arrow at the left (λ_1) indicates the energy of the "pump" photon that prepares population in a specific rovibronic state (shown as one of the Herzberg states: $c^1\Sigma_u^-$, $A'^3\Delta_u$, $A^3\Sigma_u^+$). The double-arrows at the right (λ_2) indicate the energy of the "probe" resonance-enhanced-multiphoton-ioniziation (REMPI) excitation (solid) and ionization (dashed) photon (shown for detection of the $^5\Pi_g$ state).

3.1 Laser Preparation and Detection of O_2 Excited States

Many previous kinetics studies have used oxygen atom recombination to generate excited states of molecular oxygen [*Kenner and Ogryzlo*, 1980, a, b]. Collisional removal of the excited population is inferred by following the intensity of excited-state emission versus time or the pressure of an additive. This approach has a number of interpretative difficulties. The recombination process produces high vibrational levels of multiple excited electronic states [*Slanger*, 1978; *Slanger and Huestis*, 1981; *Slanger, et al.*, 2000]. The wavelengths of emission

of the various excited states overlap. Vibrational and electronic relaxation are also time and pressure dependent, thus can contribute to the inferred rate coefficient, and are difficult to measure independently.

A new regime in quantitative understanding of the kinetics of the Herzberg states of O_2 was entered [*Copeland*, 1994] through application of the laser-based state-specific excitation and detection technique called resonance-enhanced multiphoton ionization (REMPI). The approach is illustrated schematically in Figures 1. Briefly stated, the "excitation" or "preparation" laser (λ_1) is tuned to excite O_2 to a specific rotational, vibrational, and electronic state. The "ionization" or "probe" laser (λ_2) is tuned to a frequency matching the energy separation between the initially pumped level and a known higher excited state, which in turn is also ionized by this second laser pulse. The resulting O^+ or O_2^+ ions are collected by a negatively charged wire electrode. Alternatively, the ionization laser can be tuned to monitor the rising and falling population of a level produced by collisional relaxation of the initially pumped level. By varying the time delay between the excitation and ionization laser pulses we can use the intensity of the ion signal to monitor the time evolution of the selected level. In general, this time delay is chosen to be long enough for collisional rotational equilibration to have been achieved, implying that the derived collisional rates reflect vibrational and electronic mixing, relaxation, and quenching. In some cases we prepare the initial excited population by another means, such as photodissociation of ozone.

The approach for production of excited states is illustrated by

$$O_2 + h\nu \rightarrow O_2(A,A',c,b)$$

$$O_2(A) + M \rightarrow O_2(^5\Pi_g) + M$$

$$O_3 + h\nu \rightarrow O_2(b,a,X)_v + O$$

The REMPI scheme for detection of the time evolution of excited states resulting from collisional relaxation and chemical reaction is illustrated by

$$O_2(^5\Pi_g) + 2h\nu \rightarrow O^+O^-(^5\Pi_g) + 2h\nu \rightarrow O_2^+$$

$$O_2(A,c) + h\nu \rightarrow O_2(C^3\Pi_g) + h\nu \rightarrow O_2^+$$

$$O_2(A) + O_2 \rightarrow O_3 + O + 3h\nu \rightarrow O^+$$

$$O_2(b,a) + 2h\nu \rightarrow O_2(d^1\Pi_g;3d\pi\,^1\Sigma_g^+,{}^1\Delta_g) + h\nu \rightarrow O_2^+$$

3.2 Overview of Experimental Results

Table 2 presents a summary of laboratory determinations of rate coefficients for removal (relaxation and energy transfer) of O_2 electronically and vibrationally excited states in collisions with a variety of gases. Additional discussion of some of the details and interpretations follows below.

3.3 The $^5\Pi_g$ State of O_2 and Oxygen Atom Recombination

Experimental discovery of the $^5\Pi_g$ state of O_2 occurred incidentally during investigations of the kinetics of $O_2(A^3\Sigma_u^+)$ [*Huestis, et al.*, 1998]. Collisions with oxygen or nitrogen molecules produced a longer lived excited state, whose resonance enhanced multiphoton ionization (REMPI) spectrum that could not be assigned to any known singlet or triplet system. Subsequent spectroscopic experiments and simulations [*Huestis, et al.*, 1999] confirm the spectroscopic assignment of a two-photon transition from the $^5\Pi_g$ valence state to the $^5\Pi_g$ ion-pair state. The observed spectrum is complex, dense, and unresolved with an effective two-photon resolution of 0.1 cm^{-1}. At least 25 strong rotational branches are expected, with closely spaced lines resulting from small rotational constants, about 0.4 cm^{-1}. Separations between sharp Q-branch spikes reflect differences in spin-orbit constants. The vibrational dependence of the band shapes allows approximate determination of rotational constants, but the relative intensities of the various v'-v" bands are still not quantitatively understood. Subsequent studies [*Amaral, et al.*, 2001] of the temperature dependent yields of $O_2(^5\Pi_g,v=0,1)$ from $O_2(A^3\Sigma_u^+,v=7-10)$ confirm the spectroscopic assignment and the calculated [*Partridge, et al.*, 1991] bond strength of about 1000 cm^{-1}.

Although quite weakly bound, at large internuclear distances the $^5\Pi_g$ state is predicted [*Saxon and Liu*, 1977; *Partridge, et al.*, 1991] to be the lowest of the states dissociating to ground state atoms, and because of its high spin-orbit degeneracy should be a key intermediate state in O + O recombination, contributing more than 70% according to early estimates [*Wraight*, 1982]. On the other hand, Bates [1988, 1989, 1995] concluded that $O_2(^5\Pi_g)$ would be a relatively insignificant participant, assuming that collisional spin-changing relaxation should be orders of magnitude slower than collision-induced dissociation.

The SRI measurements, summarized in Table 2, show that the collisional removal by both oxygen and nitrogen is actually about a factor of 6 *faster* than the dissociation rate estimated by Bates [1988]. In addition, studies [*Chang, et al.*, 1999; *Copeland, et al.*, 2001; *Amaral, et al.*, 2001] of the temperature dependence of the rates of collisional

Table 2. Rate Coefficients for Collisional Removal of Excited States of O_2

State	Collider	Level	Vibrational ($cm^3 s^{-1}$)	k(300) k(T) [a]	References [b]
$O_2(^5\Pi_g)$	O_2	0	$(3.1\pm0.3) \times 10^{-11}$	yes	1, 2, 3
		1	$(3.4\pm0.4) \times 10^{-11}$	yes	1, 4
	N_2	0	$(1.7\pm0.3) \times 10^{-11}$	yes	1, 2, 3
	CO_2	0	$(3.6\pm0.7) \times 10^{-11}$	yes	1, 2, 3
$O_2(A^3\Sigma_u^+)$	O_2	0–5	$(2.9\pm2.0) \times 10^{-14}$	no	5
		6	$(2.8\pm0.3) \times 10^{-11}$	yes	6, 7
		7	$(3.5\pm0.3) \times 10^{-11}$	yes	6, 7
		8	$> 1.8 \times 10^{-11}$	no	8
		9	$(5.7\pm0.4) \times 10^{-11}$	yes	6, 9
		10	$> 7 \times 10^{-11}$	no	10
		11	$> 4 \times 10^{-10}$	no	10
	N_2	0-5	$(9.3\pm1.7) \times 10^{-15}$	no	11
		6	$(1.4\pm0.4) \times 10^{-11}$	yes	6, 7
		7	$(2.4\pm1.0) \times 10^{-11}$	yes	6, 7
		8	$> 1 \times 10^{-12}$	no	12
		9	$(4.3\pm0.3) \times 10^{-11}$	yes	6, 9
	CO_2	2	7×10^{-13}	no	13
		6	$(7.6\pm1.8) \times 10^{-11}$	yes	7
		7	$(7.2\pm1.5) \times 10^{-11}$	no	6
		9	$(1.1\pm0.2) \times 10^{-10}$	yes	6, 14
	He	9	$(2.8\pm0.2) \times 10^{-11}$	yes	6, 14
	Ar	2	7.2×10^{-16}	no	13
		7	$\sim 1 \times 10^{-11}$	no	6
		9	$(2.9\pm0.3) \times 10^{-11}$	yes	6, 14
$O_2(c^1\Sigma_u^-)$	O_2	0	3×10^{-14}	no	13
		9	$(5.2\pm0.6) \times 10^{-12}$	yes	15, 16
		10	$(3.0\pm0.3) \times 10^{-11}$	yes	16
		16	$\sim 10^{-10}$	no	16
	N_2	9	$(3.2\pm0.4) \times 10^{-12}$	yes	15, 16
	CO_2	0	$< 6 \times 10^{-14}$	no	13
		9	$(1.9\pm0.2) \times 10^{-11}$	yes	16
	He	0	6×10^{-15}	no	13
		9	$(7.5\pm0.9) \times 10^{-12}$	yes	15, 16

Table 2. Rate Coefficients for Collisional Removal of Excited States of O_2 (Continued)

State	Collider	Level	Vibrational ($cm^3 s^{-1}$)	k(300) k(T) [a]	References [b]
$O_2(b^1\Sigma_g^+)$	O_2	0	3.9×10^{-17}	no	17
		1	$(1.52\pm0.04) \times 10^{-11}$	yes	18, 19
		2	$(2.7\pm0.2) \times 10^{-12}$	yes	18, 19
		3	$(1.7\pm0.4) \times 10^{-13}$	yes	20
		14	$(4.1\pm1.0) \times 10^{-12}$	235	21
		15	$(2.5\pm0.5) \times 10^{-12}$	235	21
	N_2	0	2.1×10^{-15}	yes	17
		1	$< 7 \times 10^{-13}$	yes	18, 19
		2	$< 9 \times 10^{-13}$	yes	18, 19
		3	$< 9 \times 10^{-14}$	yes	20
		15	$(3.9\pm0.5) \times 10^{-13}$	235	21
	CO_2	0	4.2×10^{-13}	yes	17
		1	$< 1.2 \times 10^{-12}$	yes	18, 19
		2	$(1.7\pm0.5) \times 10^{-12}$	yes	18, 19
		3	$(1.9\pm0.2) \times 10^{-12}$	yes	20
		15	$> 1 \times 10^{-11}$	235	21
$O_2(a^1\Delta_g)$	O_2	0	3.6×10^{-18}	yes	17
		1	$(6.9\pm1.1) \times 10^{-11}$	no	22
		2	$(3.6\pm0.4) \times 10^{-11}$	no	22
	N_2	0	$< 10^{-20}$	no	17
		1	$< 9 \times 10^{-15}$	no	22
		2	$< 1.6 \times 10^{-14}$	no	22
	CO_2	0	$< 2 \times 10^{-20}$	no	17
		1	$< 5.4 \times 10^{-14}$	no	22
		2	$(3.9\pm0.4) \times 10^{-13}$	no	22

[a] "yes" indicates that the temperature dependence of the rate coefficient has been measured. "no" or a single temperature value indicates that it has not.

[b] References: 1, *Thom, et al.* [1998]; 2, *Chang, et al.* [1999]; 3, *Copeland, et al.* [2001]; 4, *Amaral, et al.* [2001]; 5, *Kenner and Ogryzlo* [1980]; 6, *Knutsen, et al.* [1994]; 7, *Copeland and Kalogerakis* [2000]; 8, *Slanger, et al.* [1984]; 9, *Hwang and Copeland* [1997]; 10, *Copeland, et al.* [1994]; 11, *Kenner and Ogryzlo* [1983b]; 12, *Wildt, et al.* [1991]; 13, *Kenner and Ogryzlo* [1983a]; 14, *Hwang, et al.* [1996]; 15, *Copeland, et al.* [1996]; 16, *Hwang and Copeland* [2001]; 17, *DeMore, et al.* [1997]; 18, *Bloemink, et al.* [1998]; 19, *Hwang, et al.* [1999]; 20, *Kalogerakis, et al.* [2000a]; 21, *Kalogerakis, et al.* [2000b]; 22, *Hwang, et al.* [1998].

removal shows that the rate coefficients for removal of $O_2(^5\Pi_g,v=0,1)$ in collisions with O_2, N_2, and CO_2 are nearly independent of temperature from 295 to 175 K. At 150 K collisional removal is significantly faster. These studies prove that the the mechanism of collisional removal of $O_2(^5\Pi_g)$ is downward relaxation to other electronic states. Bates' hypothesis of upward collision-induced dissociation would require that collisional removal become much slower at lower temperatures. Thus the dominance of $O_2(^5\Pi_g)$ in oxygen atom recombination is reestablished.

3.4 Yields of O_2 Electronic States in Oxygen Atom Recombination

By unifying laboratory measurements with field observations of the nightglows of Earth and Venus we have assembled a self-consistent picture of the production and relaxation of the electronic states of O_2 following oxygen atom recombination [*Huestis, et al.*, 2000a, b].

In the past it has been assumed [*Wraight*, 1982; *Smith*, 1984] that mixing of O_2 electronic states in collisions with ambient atmospheric constituents is much slower than vibrational relaxation within a single electronic state. In contrast, the state-resolved kinetics studies summarized above show that electronic mixing can be very fast and sometimes provides the mechanism for vibrational relaxation.

As discussed in Chapter I.5, another source of understanding is the intensity of oxygen molecule nightglow emission from the atmospheres of Earth and Venus. On both planets the observed O_2(a-X) 1.27μ emission intensity approximately matches the total calculated column-integrated rate of oxygen atom recombination. Emissions from the O_2(c,A',A) Herzberg states are strongly quenched in both atmospheres, but when the observed intensities are adjusted for quenching, the summed rate of production of population in the Herzberg states again approximately matches the total oxygen atom recombination. From the corrected intensity of the oxygen Atmospheric Band emission on Earth we conclude that O_2(b) is produced in approximately 10% of recombination reactions. Of course, the ground electronic state O_2(X) is eventually produced in every recombination. We would also argue that the weakly bound $O_2(^5\Pi_g)$ state is the likely precursor of population in the Herzberg states. The results of this analysis are summarized in Table 3 (the % values indicate the percentage of all O + O recombinations that pass through the indicated states). Thus, we suggest that fast collisional mixing and relaxation, rather than statistical weights, dominate the production of electronic states following oxygen atom recombination. As higher electronic states are relaxed to lower ones,

$$O + O + M \rightarrow O_2(^5\Pi_g) \rightarrow O_2(c,A',A) \rightarrow O_2(a,b) \rightarrow O_2(X),$$

the population flow can be observed more than once, leading to a total apparent yield that is well over 100% (about 400% in the above analysis).

4.0 GIANT PLANET AURORA: H_3^+ FORMATION AND DISSOCIATIVE RECOMBINATION

Infrared emissions from excited rovibrational levels of H_3^+ are known to be major components of the aurora on Jupiter [*Drossart, et al.*, 1989], Saturn [*Geballe, et al.*, 1993], and Uranus [*Trafton, et al.*, 1993]. H_3^+ is also a key player in the ion chemistry of the interstellar medium [*Dalgarno*, 1999]. H_3^+ is formed in the fast exothermic reaction of H_2^+ with H_2,

$$H_2^+ + H_2 \rightarrow H_3^+ + H$$

The principal loss mechanism for H_3^+ is dissociative recombination with electrons

$$H_3^+ + e \rightarrow H + H + H, \text{ or } H_2 + H$$

Knowledge of the temperature-dependent rate coefficient for this reaction is important in understanding planetary and interstellar ion chemistry. As discussed by many authors [*Fox*, 1991; *Larsson*, 1995; *Larsson*, 1997; *Oka*, 1999], the history of experimental and theoretical investigations of this reaction has been long, controversial, and confusing. The values in the literature range from large, $0.7\text{-}3 \times 10^{-7}$ cm^3s^{-1}, to small, $1\text{-}2 \times 10^{-8}$, to unmeasurable, $\leq 10^{-10}$, without obvious trends with respect to experimental technique or year. Most of these experiments use afterglow techniques that do require some calibration and interpretation, but have been successful for other molecular ions.

Early theoretical work [*Michaels and Hobbs*, 1984] suggested that the "direct" mechanism involving a crossing between the potential energy surface of the ion (plus zero-energy electron) with that of a repulsive surface of the neutral would result in extremely slow dissociative recombination of $H_3^+(v=0)$. Bates [1993] subsequently suggested that additional mechanisms might lead to larger rate coefficients. Recent calculations by Schneider et al., [1999] suggest that the "indirect" mechanism involving predissociation of H_3^* Rydberg intermediate states can lead to dissociative recombination cross sections that are consistent with the large experimental ones.

As noted by Fox [1991] both theoretical and experimental evidence suggests that vibrational excitation of the

Table 3. Yields of Electronic States on Earth-Venus

States	Production	Radiation	Quenching
$^5\Pi_g$	100%	0%	100%
$A^3\Sigma_u^+, A'^3\Delta_u, c^1\Sigma_u^-$	100%	1–0.3%	99%
$b^1\Sigma_g^+$	10%	5–0%	5–10%
$a^1\Delta_g$	94-99%	94-99%	0%
$X^3\Sigma_g^-$	100%	0%	0%

initial H_3^+ would lead to much faster dissociative recombination. When initially created, the H_3^+ ions contain as much as 1.4 eV of rovibrational internal energy [*Peterson, et al.*, 1992], of which about 0.23 eV is rotational energy [*Kreckel, et al.*, 2001]. The actual rovibrational distribution at the time of dissociative recombination depends on the details of the ion source and other experimental conditions. Eliminating the problem of contamination by vibrationally excited levels has been accomplished by using an ion storage ring to introduce a 10 second delay between formation in the ion source and interaction with electrons [*Larsson*, 1997], a time adequate for all the vibrationally excited ions to radiate in the infrared. This approach has been used successfully for a wide range of molecular ions. The rate coefficient obtained is 1.15×10^{-7} $cm^3 s^{-1}$ at 300 K, which should be considered the most reliable value available. The remaining potential uncertainty is residual rotational excitation in $H_3^+(v=0)$. This issue can be addressed by using a cooled high-pressure ion source, such as one used to investigate dissociative recombination of $N_2^+(v=0)$ [*Peterson, et al.*, 1998].

5.0 GIANT PLANET HYDROCARBON PHOTOCHEMISTRY: $CH_3 + CH_3$ RECOMBINATION

Observational spectroscopy of solar system objects was recently revolutionized by the ISO (Infrared Space Observatory) mission [*Encrenaz*, 1998], which provided observations from launch in November 1995 through May 1998. Planetary emissions of the methyl radical, CH_3, were observed for the first time on Saturn and Neptune [*Bezard, et al.*, 1999; *Atreya, et al.*, 1999]. CH_3 is produced by VUV photolysis of CH_4 and is the key photochemical intermediate leading to complex organic molecules on the giant planets and moons.

The CH_3 emissions from Saturn were found to be about 10 times weaker than predicted by current models [*Atreya, et al.*, 1999], which various authors say could be explained either by significantly increasing the rate of chemical removal of CH_3 or by reducing the CH_3 eddy diffusion coefficient (which accesses faster chemistry at lower altitudes). The suggested remedy is to increase the rate of the recombination reaction,

$$CH_3 + CH_3 + H_2 \rightarrow C_2H_6 + H_2$$

at 140 K to a value at least 10 times that measured experimentally at room temperature in rare gases. This flexibility in the model appears plausible because extrapolations to 140 K of the two formulas used to represent recent experimental recombination rates [*Macpherson, et al.*, 1983; *Slagle, et al.*, 1988] differ by about a factor of 300.

Decades of research on hydrocarbon combustion reactions have provided a wealth of rate data at temperatures from 300 K up to 3000 K. However, it is not reliable to extrapolate the empirical formulas used to fit high-temperature combustion data. In addition, very few of the theoretical examinations have provided guidance about using molecular parameters to extrapolate to low temperatures. For recombination reactions in particular, extrapolations of simple formulas without theoretical basis give widely differing results and produce unconstrained uncertainties. Good pressure- and temperature-dependent rate constants and interpolation expressions for methyl radical recombination exist at and above 300 K [*Macpherson, et al.*, 1983; *Slagle, et al.*, 1988; *Walter, et al.*, 1990]. However, the relevant planetary conditions are T = 140-220 K and P < 1 mbar. Only two experimental rate constants exist below 300 K, both 200 K values at the high pressure limit [*Walter, et al.*, 1990; *Stief*, 1999].

The simplest description of recombination reactions is the Lindemann model [*Smith and Huestis*, 1981; *Holbrook, et al.*, 1996] of the "activated complex," AB^*,

$$A + B \rightarrow AB^* \quad k_{-2},$$

where AB^* represents the ensemble of quasi-stable states above the energetic dissociation limit. For technical reasons, recombination is usually investigated theoretically as the equilibrium reverse of dissociation (thus the notation of k_{-x} for the stabilization or recombination direction). For reasonably large molecules (say, five atoms or more), the large number of energetically equivalent levels of AB^* (high entropy) means that the lifetime of AB^* before spontaneous dissociation,

$$AB^* \rightarrow A + B \quad k_2,$$

is longer than many vibrations, allowing time for stabilization:

$$AB^* + M \rightarrow AB + M \quad k_{-1}$$

The stabilization reaction itself is reversible, in that the stable AB molecule can be excited from below to above the dissociation limit in collisions with the background gas,

$$AB + M \rightarrow AB^* + M \quad k_1$$

We write the rate expressions for collision-induced dissociation and recombination reactions as effective pressure-dependent two-body reactions.

$$k_{diss}(M) = k_1[M]\, k_2 / (k_{-1}[M] + k_2)$$

$$\begin{aligned} k_{recomb}(M) &= k_{diss}(M)\,(k_{-1}k_{-2})/(k_1k_2) \\ &= k_{-1}[M]\, k_{-2} / (k_{-1}[M]+k_2) \end{aligned}$$

At high pressures the rate is independent of presssure,

$$k_{recomb}(M\rightarrow\infty) \sim k_{-2} = k_\infty.$$

At low pressures, the rate is linear in pressure,

$$k_{recomb}(M\rightarrow 0) \sim k_{-1}[M]\, k_{-2}/k_2 = k_0[M].$$

Intermediate pressures are called the falloff region.

For this discussion, we could substitute A = B = CH_3, AB = C_2H_6, and M = H_2. Radical-radical recombinations, such as CH_3 + CH_3 or CH_3 + H, typically have attractive potential energy surfaces, corresponding to the new chemical bond being formed. Thus, we expect [*Stewart, et al.*, 1989] that the reaction

$$CH_3 + CH_3 \rightarrow C_2H_6^* \quad k_{-2}$$

will have a weakly negative temperature dependence (slightly faster at lower temperature). Similarly, as the temperature decreases, stabilization by buffer gas collisions (k_{-1}) becomes more likely than activation (k_1). Thus we can be confident that the overall reaction,

$$CH_3 + CH_3 + M \rightarrow C_2H_6 + M \quad k_{recomb}$$

will be faster at lower temperature. The actual temperature dependence is sensitive to details discussed below.

The simplified Lindemann mechanism does not make clear that the rate constants must be considered as functions of energy, and that the collisional steps represented by reactions 1 and -1 require a theory of energy transfer to and from excited molecules. The Lindemann mechanism is too simple, however, in that it assumes that all excited molecules, AB^*, are the same, and that the product forming step, k_2, proceeds with a single rate. In fact, k_1, k_{-1}, and k_2 are all functions of the energy and rotational quantum numbers of AB^*. The RRKM and master equation approaches [*Eyring et al.*, 1980] extend this Lindemann model.

As mentioned above, a sound theoretical model is essential for temperature extrapolation. It is also important for identifying the pressure conditions over which experimental investigations can provide the most effective calibration. Preliminary calculations [*Smith and Huestis*, 2001] suggest that the low pressure recombination rate coefficient, k_0, rises with decreasing temperature much faster than does k_∞. This means that low temperature laboratory experiments need to be performed at quite low pressures, say 0.01 mbar or less, in order to extrapolate to the 0.001 mbar and below characteristic of the relevant regions of the giant planet atmospheres [*Moses, et al.*, 2000]. This is consistent with the recent work in Stief's laboratory [*Stief*, 1999; *Cody, et al.*, 2000], in which no pressure dependence was observed at 202 K for pressures from 0.8 to 2.6 mbar.

6. CONCLUSIONS

Planetary atmospheres are very complicated, involving dozens of chemical species and hundreds of different collisions and chemical reactions. The small community of atomic and molecular experimenters and theorists helps in the understanding of planetary atmospheres by accurate determination of the fundamental parameters, such as energy levels, radiative properties, reaction rate coefficients, and collision cross sections that are needed for quantitative models. This chapter reviews the recent laboratory progress in characterizing a of a few selected chemical processes of importance in planetary aeronomy. It also provides hints about modelers can find and evaluate the available fundamental data.

Acknowledgments. The research reported here was supported by the NASA Geospace Sciences (ITM) and Planetary Atmospheres programs, and by the NSF Atmospheric Chemistry, Aeronomy, and Planetary Astronomy programs. Preparation of the manuscript was supported by Grant No. NAG5-7955, from the NASA Geospace Sciences (ITM) program.

The author thanks Dr. Vincent G. Anicich for providing text and references on ion-molecule reactions, as well as Drs. Tom G. Slanger, Richard A. Copeland, James R. Peterson, Gregory P. Smith, and Philip C. Cosby and other members of SRI's Molecular Physics Laboratory for assistance in preparing this manuscript, permission to report some results in advance of publication, and fruitful discussions.

REFERENCES

Amaral, G., W. Lapcharoensap, R. A. Copeland, and D. L. Huestis, Temperature Dependent Rates and Branching Ratios for $O_2(^5\Pi_g, v=0,1)$, *2001 Fall Meeting of the Am. Geophys. Union*, San Francisco, CA, December 10-14, 2001.

Anicich, V. G., and W. T. Huntress, Jr., A Survey of Bimolecular Ion-Molecule Reactions for use in Modeling the Chemistry of Planetary Atmospheres, Cometary Comae, and Interstellar Clouds, *Astrophys. J. Suppl.* 62, 553-672, 1986.

Anicich, V. G., A Survey of Bimolecular Ion-Molecule Reactions for use in Modeling the Chemistry of Planetary Atmospheres, Cometary Comae, and Interstellar Clouds: 1992 Supplement, *Astrophys. J. Suppl.* 84, 215-315, 1993a.

Anicich, V. G., Evaluated Bimolecular Ion-Molecule Gas Phase Kinetics of Positive Ions for use in Modeling the Chemistry of Planetary Atmospheres, Cometary Comae, and Interstellar Clouds, *J. Phys. Chem. Ref. Data* 22, 1469-1569, 1993b.

Atkinson, R., D. L. Baulch, R. A. Cox, R. F. Hampton, Jr., J. A. Kerr, M. J. Rossi, and J. Troe, Evaluated Kinetic and Photochemical Data for Atmospheric Chemistry: Supplement VI. IUPAC Subcommittee on Gas Kinetic Data Evaluation for Atmospheric Chemistry, *J. Phys. Chem. Ref. Data*, 26, 1329-1499, 1997.

Atreya, S. K., S. G. Edgington, Th. Encrenaz, and H. Feuchtgruber, ISO Observations of C_2H_2 on Uranus and CH_3 on Saturn, in *The Universe as Seen by ISO*, P. Cox and M. F. Kessler, Eds. (ESA-SP 427, 1999).

Banks, P. M., and G. Kockarts, *Aeronomy, Part A* (Academic Press, New York, 1973a).

Banks, P. M., and G. Kockarts, *Aeronomy, Part B* (Academic Press, New York, 1973b).

Bates, D. R., Excitation and Quenching of the Oxygen Bands in the Nightglow, *Planet. Space Sci.* 36, 875-881, 1988.

Bates, D. R., Quenching of O_2 ($^5\Pi_g$) by N_2 and Termolecular Asociation of A Atoms, *Chem. Phys. Lett.* 162, 313-316, 1989.

Bates, D. R., The Nightglow, in *Progress and Problems in Atmospheric Chemistry*, J. R. Barker, Ed. (World Scientific Pub., Singapore, 1995).

Bates, D. R., M. F. Guest, and R. A. Kendall, Enigma of H_3^+ Dissociative Recombination, *Planet. Space Sci.* 41, 9-15, 1993.

Baulch, D. L., D. D. Drysdale, J. Duxbury, and S. J. Grant, *Evaluated Kinetic Data for High Temperature Reactions* Vol. 3 Homogeneous Gas Phase Reactions of the O_2-O_3 System, the CO-O_2-H_2 System, and of Sulphur-Containing Species, (Butterworths, London, 1976).

Berkowitz, J., *Photoabsorption, Photoionization, and Photoelectron Spectroscopy* (Academic Press, New York, 1979).

Bezard, B., Romani, P. N., Feuchtgruber, H., and T. Encrenaz, Detection of Methyl Radical in Neptune, *Astrophys. J.* 515, 868-872, 1999.

Bloemink, H. L., R. A. Copeland, and T. G. Slanger, Collisional Removal of $O_2(b^1\Sigma_g^+, v=1,2)$ by O_2, N_2, and CO_2, *J. Chem. Phys.* 109, 4237-4245, 1998.

Bortner, M. H., and T. Baurer, Eds. *Defense Nuclear Agency Reaction Rate Handbook*, 2nd Ed., Revision No. 9, (DNA-1948H-Rev 9, DASIAC, Santa Barbara, CA, 1983).

Chamberlain, J. W., *Physics of the Aurora and Airglow* (Academic Press, New York, 1961) [Am. Geophys. Union, reprint, 1995].

Chang, B.-Y., D. L. Huestis, and R. A. Copeland, Temperature Dependence of the Collisional Removal of $O_2(^5\Pi_g)$ Between 150 and 300 K, *1999 Spring Meeting of the Am. Geophys. Union*, (Boston, MA, 1-4 June 1999) [Eos, Trans. AGU, 80, S239, 1999].

Chapman, S., Some Phenomena of the Upper Atmosphere, (Bakerian Lecture) *Proc. Roy. Soc.* (London) A 132, 353-374, 1931.

Cody, R. J., W. A. Payne, R. P. Thorn, and L. J. Stief, Rate Constant for the Recombination of CH_3 Free Radicals: A Loss Process in Outer Planet Atmospheres, *32nd Meeting of the AAS Division for Planetary Science* (Pasadena, CA, 23-27 October 2000) [Bull. AAS 32, 1020, 2000].

Copeland, R. A., Laser Double Resonance Study of Collisional Removal of $O_2(A^3\Sigma_u^+, v=7)$ with O_2, J. Chem. Phys. 100, 744-745, 1994.

Copeland, R. A., K. Knutsen, and T. G. Slanger, Using Laser-Induced Fluorescence to Study Molecules of Atmospheric Importance, in *Proc. Int'l Conf. Lasers '93*, V. J. Corcoran and T. G. Goldman, Eds. (Lake Tahoe, NV, December 6-9, 1993) [STS Press, McLean, VA, pp. 318-325, 1994].

Copeland, R. A., K. Knutsen, M. E. Onishi, and T. Yalcin, Collisional Removal of $O_2(c^1\Sigma_u^-, v=9)$ by O_2, N_2, and He, *J. Chem. Phys.* 105, 10349-10355, 1996.

Copeland, R. A., and K. S. Kalogerakis, The Temperature Dependence of the Collisional Removal of $O_2(A^3\Sigma_u^+, v=6,7)$, *2000 Fall Meeting of the Am. Geophy. Union* (San Francisco, 15-19 December 2000) [Eos, Trans. AGU 81, F943, 2000].

Copeland, R. A., J. Marschall, K. S. Kalogerakis, B.-Y. Chang, and D. L. Huestis, Collisional Removal of $O_2(^5\Pi_g)$ from 295 to 150 K, 2001 Spring Meeting of the Am. Geophys. Union (Boston, MA, May 29-June 2, 2001) [Eos, Trans. AGU 82, S283, 2001].

Dalgarno, A., Dissociative Recombination in Astrophysical Environments, in *Dissociative Recombination Theory, Experiment, and Applications IV*, M. Larsson, J.B.A Mitchel, and I. F. Schneider, Eds. (World Scientific, Singapore, pp. 1-12, 1999).

DeMore, W. B., S. P. Sander, D. M. Golden, R. F. Hampson, M. J. Kurylo, C. J. Howard, A. R. Ravishankara, C. E. Kolb, and M. J. Molina, Chemical Kinetics and Photo-

chemical Data for Use in Stratospheric Modeling, Evaluation Number 12, *JPL Publication 97-4* (Jet Propulsion Laboratory, California Institute of Technology, Pasadena, CA, January 15, 1997).

Drossart, P., J.-P. Maillard, J. Caldwell, S. J. Kim, J.K.G. Watson,, W. A. Majewski, J. Tennyson, S. Miller, S. L. Atreya, J. T. Clarke, J. H. Waite, Jr., and R. Wagener, Detection of H_3^+ on Jupiter, *Nature* 340, 539-541, 1989.

Dufay, J., Une Interpretation Possible de Certaines, Radiations Intenses du ciel Nocturne dans la Region Ultraviolette, *Compt. Rend.* 213, 284-286, 1941.

Encrenaz, T., Observation of Solar System Objects with the ISO Satellite, *Bull. Am. Astron. Soc.* 30, 1059, 1998.

Eyring, H., S. H. Lin, and S. M. Lin, *Basic Chemical Kinetics* (John Wiley & Sons, New York, 1980).

Fox, J. L., and A. Dalgarno, Ionization, Luminosity, and Heating of the Upper Atmosphere of Mars, *J. Geophys. Res.* 84(A12), 7315-7333, 1979.

Fox, J. L., Cross Sections and Reaction Rates Relevant to Aeronomy, in *US National Report to International Union of Geodesy and Geophysics 1987-1990*, published in Rev. Geophys. 29 (Supplement), 1110-1131, April 1991.

Fox, J. L., and K. Y. Sung, Solar Activity Variations of the Venus Thermosphere/Ionosphere, *J. Geophys. Res.* 106 (A10), 21,305-21,335, 2001.

Gallagher, J. W., J. V. Blerkom, E. C. Beaty, and J. R. Rumble, Jr., Data Index for Energy Transfer Collisions of Atoms and Molecules, *NBS Spec. Pub. 593* (USGPO, Washington, DC, 1981).

Geballe, T. R., M.-F. Jadod, and T. Oka, Detection of H_3^+ Infrared Emission Lines in Saturn, *Astrophys. J.* 408, L109-L112, 1993.

Holbrook, K. A., M. J. Pilling, and S. H. Robertson, *Unimolecular Reactions*, 2nd ed. (J. Wiley, New York, 1996).

Huber, K. P., and G. Herzberg, Molecular Pectra and Molecular Structure. IV. Constants of Diatomic Molecules (Van Nostrand Reinhold, New York, 1979).

Huestis, D. L., R. A. Copeland, K. Knutsen, T. G. Slanger, R. T. Jongma, M.G.H. Boogaarts, and G. Meijer, Branch Intensities and Oscillator Strengths for the Herzberg Absorption Systems in Oxygen, *Can. J. Phys,* 72, 1109-1121, 1994.

Huestis, D. L., C. G. Bressler, and R. A. Copeland, $O_2(^5\Pi_g)$ and Atmospheric Oxygen Atom Recombination, *NASA Laboratory Space Science Workshop* (Cambridge, MA, 1-3 April 1998).

Huestis, D. L., B.-Y. Chang, P. C. Cosby, C. G. Bressler, and R. A. Copeland, Spectroscopy of the $^5\Pi_g$ States of O_2, *1999 Fall Meeting of the Am. Geophys. Union* (San. Francisco, CA, 13-17 December 1999) [Eos, Trans. AGU, 80, F780, 1999].

Huestis, D. L., R. A. Copeland, and T. G. Slanger, Laboratory Studies of O_2 Kinetics Relevant to the Aeronomy of Earth, Venus, and Mars, *Yosemite 2000: Comparative Aeronomy in the Solar System* (Yosemite National Park, CA, February 8-11, 2000a).

Huestis, D. L., R. A. Copeland, and T. G. Slanger, Yields of O_2 Electronic States in Oxygen Atom Recombination, *2000 Fall Meeting of the Am. Geophys. Union* (San Francisco, CA, 15-19 December 2000) [Eos, Trans. AGU 81, F930, 2000b].

Hwang, E. S., T. P. Shiau, and R. A. Copeland, Rate Constants for the Collisional Removal of O_2 in the Herzberg States from 150 to 300 K, *1996 Fall Meeting of the Am. Geophys. Union* (December 1996, San Francisco, CA) [Eos Trans. AGU 77(46), F535, 1996].

Hwang, E. S., and R. A. Copeland, Temperature Dependence of the Collisional Removal of $O_2(A^3\Sigma_u^+, v=9)$ by O_2 and N_2, *Geophys. Res. Lett.* 24, 643-646, 1997.

Hwang, E. S., R. A. Copeland, R. M. Robertson, and T. G. Slanger, Collisional Removal of $O_2(a^1\Delta_g)$ and $O_2(b^1\Sigma_g^+)$ from Photodissociation of Ozone at 310-340 nm, *1998 Fall Meeting of the Am. Geophys. Union* (San Francisco, CA, December 6-10, 1998) [Eos, Trans. AGU 79, F85, 1998].

Hwang, E. S., A. Bergman, R. A. Copeland, and T. G. Slanger, Temperature Dependence of Collisional Removal of $O_2(b^1\Sigma_g^+, v=1,2)$ at 110-260 K and Atmospheric Applications, *J. Chem. Phys.* 110, 18-24, 1999.

Hwang, E. S., and R. A. Copeland (in preparation, 2001).

Ikezoe, Y., S. Matsuoka, M. Takebe, and A. Viggiano, *Gas Phase Ion-Molecule Reaction Rate Constants Through 1986* (Maruzen, Tokyo, 1987).

Itikawa, Y., M. Hayashi, A. Ichimura, K. Onda, K. Sakimoto, K. Takayanagi, M. Nakamura, H. Nishimura, and T. Takayanagi, Cross Sections for Collisions of Electrons and Photons with Nitrogen Molecules, *J. Phys. Chem. Ref. Data* 15, 985-1010, 1986.

Itikawa, Y., A. Ichimura, K. Onda, K. Sakimoto, K. Takayanagi, Y. Hatano, M. Hayashi, H. Nishimura, and S. Tsurubuchi, Cross Sections for Collisions of Electrons and Photons with Oxygen Molecules, *J. Phys. Chem. Ref. Data* 18, 23-42, 1989.

Itikawa, Y., and A. Ichimura, Cross Sections for Collisions of Electrons and Photons with Atomic Oxygen, *J. Phys. Chem. Ref. Data* 19, 637-651, 1990.

Johnson, H. S., *Gas Phase Reaction Kinetics of Neutral Oxygen Species*, NSRDS-NBS 20 (USGPO, Washington, DC, 1968).

Kalogerakis, K. S., R. A. Copeland, and T. G. Slanger, Temperature Dependence of the Collisional Removal Rates Constants for $O_2(b^1\Sigma_g^+)$, *2000 Spring Meeting of the Am. Geophys. Union* (Washington, DC, May 30-June 3, 2000) [Eos, Trans. AGU 81, S332, 2000a].

Kalogerakis, K. S., A. Totth, P. C. Cosby, T. G. Slanger, and R. A. Copeland, Laboratory Studies of the Production of Highly Vibrationally Excited $O_2(a^1\Delta_g$ and $b^1\Sigma_g^+)$ from $O_2(A^3\Sigma_u^+)$ Relaxation, *2000 Fall Meeting of the Am. Geophy. Union* (San Francisco, 15-19 December 2000) [Eos, Trans. AGU 81, F944, 2000b].

Kanik, I., L. W. Beegle, J. M. Ajello, and S. C. Solomon, Electron-Impact Excitation/Emission and Photoabsorption

Cross Sections Important in the Terrestrial Airglow and Auroral Analysis of Rocket and Statellite Observations, *Phys. Chem. Earth* 25, 573-581, 2000.

Kenner, R. D., and E. A. Ogryzlo, Deactivation of $O_2(A^3\Sigma_u^+)$ by O_2, O, and Ar, Int. *J. Chem. Kinetics* 12, 501-508, 1980.

Kenner, R. D., and E. A. Ogryzlo, Quenching of $O_2(c^1\Sigma_u^-)_{v=0}$ by $O(^3\Pi)$, $O_2(a^1\Delta_g)$, and Other Gases, Can. *J. Chem.* 61, 921-926, 1983a.

Kenner, R. D., and E. A. Ogryzlo, Rate Constant for Deactivation of $O_2(A^3\Sigma_u^+)$ by N_2, *Chem. Phys. Lett.* 103, 209-212, 1983b.

Kerr, J. A., and R. M. Drew, Eds. *CRC Handbook of Bimolecular and Termolecular Gas Reactions, Volume III, Part A* (CRC Press, Boca Raton, FL, 1987).

Knutsen, K., M. J. Dyer, and R. A. Copeland, Laser Double Resonance Study of Collisional Removal of $O_2(A^3\Sigma_u^+$, v=6, 7, and 9) with O_2, N_2, CO_2, Ar, and He, *J. Chem. Phys.* 101, 7415-7422, 1994.

Krasnopolsky, V. A., A. A. Krysko, V. N. Rogachev, and V. A. Parshev, Spectroscopy of the Venus Night Airglow from the Venera 9 and 10 Orbiters, *Cosmic Res.* 14, 789-795, 1976.

Kreckel, H., S. Krohn, L. Lammich, J. Levin, D. Schwalm, D. Strasser, R. Wester, A. Wolf, and D. Zaifman, Storage Ring Experiments with H_3^+: How Cold can you Get? ICPEAC XXII, 342, 2001.

Larsson, M., Dissociative Recombination in Ion Storage Rings, *Int. J. Mass Spectrom. Ion Processes* 149/150 403-414, 1995.

Larsson, M., Dissociative Recombination with Ion Storage Rings, *Ann. Rev. Phys. Chem.* 48 151-179, 1997).

Macpherson, M. T., M. J. Pilling, and M.J.C. Smith, The Pressure and Temperature Dependence of the Rate Constant for Methyl Radical Recombination over the Temperature Range 296-577 K, *Chem. Phys. Lett.* 94, 430-433, 1983.

Michaels, H. H., and R. H. Hobbs, Low-Temperature Dissociative Recombination of e + H_3^+, *Astrophys. J. Lett.* 286, L27-L29, 1984.

Moses, J. I., B. Bezard, E. Lellouch, H. Feuchtgruber, and G. R. Gladstone, and M. Allen, Photochemical Models of Saturn's Atmosphere: I. Hydrocarbon Chemistry and Comparisons with ISO Observations, *Icarus* 143, 244-298, 2000.

Oka, T., H_3^+ in the Diffuse Interstellar Medium: The Enigma Related to Dissociative Recombination, in *Dissociative Recombination Theory, Experiment, and Applications IV*, M. Larsson, J.B.A Mitchel, and I. F. Schneider, Eds. (World Scientific, Singapore, pp. 13-24, 1999).

Okabe, H., *Photochemistry of Small Molecules* (John Wiley & Sons, New York, 1978).

Partridge, H., C. W. Bauschlicker, Jr., S. R. Langhoff, and P. R. Taylor, Theoretical Study of the Low-Lying Bound States of O_2, *J. Chem. Phys.* 95, 8292-8300, 1991.

Peterson, J. R., P. Devynck, Ch. Herzler, and W. G. Graham, Predissociation of H_3 n=2 Rydberg States: Product Branching and Isotope Effects, *J. Chem. Phys.* 96, 8128-8135, 1992.

Peterson, J. R., A. Le Padellec, H. Danared, G. H. Dunn, M. Larsson, A. Larson, R. Peverall, C. Strömholm, S. Rosen, M. af Ugglas, and W. J. van der Zande, Dissociative Recombination and Excitation of N_2^+: Cross Sections and Product Branching Ratios, *J. Chem. Phys.* 108, 1978-1988, 1998.

Roble, R. G., Energetics of the Mesosphere and Thermosphere, in *The Upper Mesosphere and Lower Thermosphere: A Review of Experiment and Theory*, R. M. Johnson and T. L. Killeen, Eds., Geophysical Monograph 87 (Am. Geophys. Union, New York, pp. 1-21, 1995).

Saxon, R. P., and B. Liu, *Ab Initio* Configuration Interaction Study of the Valence States of O_2, *J. Chem. Phys.* 67, 5432-5441, 1977.

Schneider, I. F., M. Larsson, A. E. Orel, and A. Suzor-Weiner, Dissociative Recombination of H_3^+ and Predissociation of H_3, in *Dissociative Recombination Theory, Experiment, and Applications IV*, M. Larsson, J.B.A Mitchel, and I. F. Schneider, Eds. (World Scientific, Singapore, pp. 131-141, 1999).

Schofield, K., An Evaluation of Kinetic Rate Data for Reactions of Neutrals of Atmospheric Interest, *Planet. Space Sci.* 15, 643-670, 1967.

Schofield, K., Critical Evaluated Rate Constants for Gaseous Reactions of Several Electronically Excited Species, *J. Phys. Chem. Ref. Data* 8, 723-798, 1979.

Slagle, I. R., D. Gutman, J. W. Davies, and M. J. Pilling, Study of the Recombination Reaction $CH_3 + CH_3 \rightarrow C_2H_6$. 1. Experiment, *J. Phys. Chem.* 92, 2455-2462, 1988.

Slanger, T. G., and G. Black, $O(^1S)$ in the Lower Thermosphere-Chapman vs Barth, Planet. Space Sci. 25, 79-88, 1977.

Slanger, T. G., Generation of $O_2(c^1\Sigma_u^-, C^3\Delta_u, A^3\Sigma_u^+)$ from Oxygen Atom Recombination, *J. Chem. Phys.* 69, 4779-4791, 1978.

Slanger, T. G., and D. L. Huestis, $O_2(c^1\Sigma_u^- \rightarrow X^3\Sigma_g^-)$ Emission in the Terrestrial Nightglow, *J. Geophys. Res.* 86, 3551-3554, 1981.

Slanger, T. G., W. K. Bischel, and M. J. Dyer, Photoexcitation of O_2 at 249.3 nm, *Chem. Phys. Lett.* 108. 472-474, 1984.

Slanger, T. G., P. C. Cosby, D. L. Huestis, and D. E. Osterbrock, Vibrational Level Distribution of $O_2(b^1\Sigma_g^+$, v=0-15) in the Mesosphere and Lower Thermosphere Region, *J. Geophys. Res.* 105(D16), 20,557-20,564, 2000.

Slanger, T. G., P. C. Cosby, D. L. Huestis, and T. A. Bida, Discovery of the Atomic Oxygen Green Line in the Venus Night Airglow, *Science* 291, 463-465, 2001.

Smith, G. P., and D. L. Huestis, Molecular Recombination in Laser Media. I. Theoretical Study of $NF_2 + F + Ne \rightarrow NF_3 + Ne$, J. Appl. Phys. 52, 6041-6045, 1981.

Smith, G. P., and D. L. Huestis (unpublished, 2001).

Smith, I.W.M., The Role of Electronically Excited States in Recombination Reactions, Int. *J. Chem. Kinetics* 16, 423-443, 1984.

Stewart, P. H., C. W. Larson, and D. M. Golden, Pressure and Temperature Dependence of Reactions Proceeding via a

Bound Complex. 2. Application to $2CH_3 \rightarrow C_2H_5 + H$, *Combust. Flame* 75, 25-32, 1989.

Stief, L. J. (private communication, 1999).

Thom, R. L., C. G. Bressler, E. S. Hwang, and R. A. Copeland, Collisional Production and Removal of $O_2(^5\Pi_g)$, an Important Intermediate in Atmospheric O-Atom Recombination, 1998 Fall Meeting of the Am. Geophys. Union (San Francisco, CA, December 1998) [Eos, Trans. AGU 79(45), F669, 1998].

Trafton, L. M., T. R. Geballe, S. Miller, J. Tennyson, and G. E. Ballister, Detection of H_3^+ from Uranus, *Astrophys. J.* 405, 761-766, 1993.

Trajmar, S., D. F. Register, and A. Chutjian, Electron Scattering by Molecules II. Experimental Methods and Data, *Physics Reports* 97, 219-356, 1983.

Trotman-Dickenson, A. F., and G. S. Milne, *Tables of Bimolecular Gas Reactions*, NSRDS-NBS 9 (USGPO, Washington, DC, 1967).

Walter, D., H.-H. Grotheer, J. W. Davies, M. J. Pilling, and A. F. Wagner, Experimental and Theoretical Study of the Recombination Reaction $CH_3 + CH_3 \rightarrow C_2H_6$, *Proc. Combust Inst.* 23, 107-114, 1990.

Wildt, J., G. Bednarek, E. H. Fink, and R. P. Wayne, Laser Excitation of the $A^3\Sigma_u^+$, $A'^3\Delta_u$, and $c^1\Sigma_u^-$ States of Molecular Oxygen, *Chem. Phys.* 156, 497-508, 1991.

Wraight, P. C., Association of Atomic Oxygen and Airglow Excitation Mechanism, *Planet. Space Sci.* 30, 251-259, 1982.

Yung, Y. L., and W. B. DeMore, *Photochemistry of Planetary Atmospheres* (Oxford Univ., New York, 1999).

D. L. Huestis, Molecular Physics Laboratory, SRI International, 333 Ravenswood Avenue, Menlo Park, CA 94025

PART IV. MODELS OF AERONOMIC SYSTEMS

A discipline reaches the plateau of maturity when models of its central function evolve from conceptual to computational. By that yardstick, models of solar system upper atmospheres range from youthful (for giant planets and their moons) to adult (for terrestrial planets). If a "reliable predictive capability" is the criterion for full maturity, then even terrestrial aeronomy (with its decades of empirical, semi-empirical, and first-principle models) has yet to reach middle age. In these chapters, state-of-the-art summaries are given by a group of experts who themselves span the range of young professionals to senior researchers in the field.

The growing use of general circulation models (GCMs) is clearly evident in what follows. With heritage from terrestrial origins, these GCMs have evolved to Mars and Venus, and then to the giant planets. The most recent application has been to the moons of giant planets. The remote sensing and modeling of the airglow signatures from these Earth-like atmospheres offer comparative studies of terrestrial-sized systems at vastly different distances from the Sun. *(Image courtesy I. Müller-Wodarg.)*

Simulations of the Upper Atmospheres of the Terrestrial Planets

Stephen W. Bougher

Lunar and Planetary Laboratory, University of Arizona, Tucson, Arizona

Raymond G. Roble

High Altitude Observatory, National Center for Atmospheric Research, Boulder, Colorado

Timothy Fuller-Rowell

NOAA Space Environment Center, and CIRES, University of Colorado, Boulder, Colorado

The comparative approach to planetary aeronomy is becoming increasingly fruitful as new information from various planet atmospheres is assimilated. In particular, Venus, Earth, and Mars thermospheric observations and modeling over the past 30-years provide a useful platform for addressing similar upper atmosphere processes in various planetary settings. Basic features of the structure and dynamics of the Venus, Earth, and Mars thermospheres can be understood by examining the implications of their fundamental planetary parameters. Different features are notably the result of unique forcings on variable timescales that drive the energetics, chemistry, and dynamics of these upper atmospheres. The present maturity of available Venus and Earth planetary databases (and the promise for Mars) as well as numerical modeling capabilities permit us to compare the thermospheres of these 3 planets using well tested and individually validated three-dimensional (3-D) thermospheric general circulation models (TGCMs). Important TGCM simulation products are examined and constrasted in this chapter. In particular, the role of O-CO_2 enchanced 15-μm cooling is investigated in the context of global dynamics and its effect on atomic-O and thermal distributions. It is found that CO_2 cooling is an effective thermostat for control of the Venus dayside temperatures, while Mars and Earth are only moderately affected. By contrast, the role of global dynamics in controlling temperature distri-

Atmospheres in the Solar System: Comparative Aeronomy
Geophysical Monograph 130

10.1029/130GM17

butions is most pronounced for Mars and the Venus nightside. Clearly, the geocentric perspective when applied to other planet atmospheres is initially helpful, but must be revised as new planetary data and model simulations combine to challenge our understanding of thermospheric processes in new planetary environments.

1. INTRODUCTION AND MOTIVATION

Recent studies have shown that substantial advances in understanding can be realized by investigating common aeronomic processes as they apply in different planetary settings. In particular, the comparison of planetary thermospheres using global databases and models is ripe for examination. Earth ground-based and spacecraft observations compiled over nearly 40-years provide a global characterization of the thermosphere-ionosphere over the solar cycle, seasons, and various auroral/ magnetospheric conditions. Venus upper atmosphere data captured by the Pioneer Venus Probes and Orbiter (1978-1992) have yielded a first-order examination of the global thermosphere-ionosphere above ~100 km. Finally, recent Mars Global Surveyor aerobraking and radio science measurements of the Mars thermosphere-ionosphere (and the promise of new campaigns over the next decade) provide the beginnings of a global database that can be used to investigate thermospheric and ionospheric features and processes (see chapters I.3, IV.3, and IV.4).

An important objective in the study of comparative planetary thermospheres is to contrast and compare the physical and chemical processes responsible for the structure and dynamics of the terrestrial-like thermospheres of Venus, Earth, and Mars. Traditionally, these upper atmospheres are grouped together for discussion of planetary mesopause and thermospheric features, since their composition, temperatures, winds, and fundamental parameters (see Table 1a) are somewhat similar [*Bougher and Roble,* 1997]. The Venus, Earth, and Mars thermospheres are also driven by similar forcing agents that subsequently change over time, both naturally and in the case of the Earth as a result of human influence. The proximity of these three planets to the sun determines that solar ultraviolet forcing is important for the maintenance of their thermospheres. However, a strong link exists between the strength of a planetary magnetic field and its thermospheric temperature distribution and global winds. For example, the Earth's upper atmosphere is subject to additional forcing due to strong auroral processes that result from its significant intrinsic magnetic field. Conversely, "non-magnetic" planets (Venus and Mars) have upper atmospheres that are primarily driven by solar EUV/UV processes, with smaller heating efficiencies, giving rise to cooler temperatures. Solar wind inputs to the ionospheres of Venus and Mars are also being investigated (see chapter II.3).

The present maturity of available planetary databases and modeling capabilities permits us to extend the comparison of terrestrial planetary thermospheres beyond the limited capability of one-dimensional models to global multi-dimensional models [e.g., *Bougher and Roble,* 1997; *Bougher et al.,* 1999b; 2000]. State-of-the-art three-dimensional (3-D) thermospheric general circulation models (TGCMs) can now address the feedbacks inherent in coupled dynamical, energetic, and chemical processes that control the thermospheric structure and wind system. Various TGCM models have been developed, exercised, and largely validated over the last few decades to study the global circulation, composition and temperature structures of each of these terrestrial planet thermospheres [e.g. *Bougher et al.,* 1999b; 2000].

In this chapter, we review the basic thermospheric features and processes common to Venus, Earth, and Mars (sections 2.1-3). Prominent thermospheric modeling groups are identified and a few important TGCM models are briefly described to survey the current modeling capabilities (section 3). A suite of TGCM simulations emphasizing solar EUV/UV forcing is presented to illustrate the relative importance of common thermal and dynamical processes for these planets over the solar cycle at equinox and solstices (section 4). TGCM simulations illustrating the impacts of a few unique processes for each of these planets are described in section 5. Overall, we demonstrate that new planetary databases and TGCM simulations are being combined to expand our understanding of thermospheric processes in new planetary environments.

2. BASIC THERMOSPHERIC FEATURES AND PROCESSES

2.1. Overview of Structure and Dynamics

The thermosphere is that rarefied portion of a planetary atmosphere which extends from the top of the middle atmosphere (mesosphere) to the beginning of outer space (exosphere). On most planets, the thermo-

Table 1a. Terrestrial Planet Parameters

Parameter	Earth	Venus	Mars
Gravity, cm/s^2	982	888	373
Heliocentric distance AU	1.0	0.72	1.38-1.67
Radius, km	6371	6050	3396
Ω, rad/s	7.3(-5)	3.0(-7)	7.1(-5)
Magnetic dipole moment (wrt Earth)	1.0	$\leq$4.0(-5)	$\leq$2.5(-5)
Obliquity, deg	23.5	1-3	25.0

sphere is characterized by temperatures which increase dramatically with altitude due to various solar and non-solar heating mechanisms. The temperature asymptotically approaches a maximum (becomes isothermal) in the exosphere. The thermosphere is also the topmost bound layer; above, in the exosphere, and atoms or molecules may escape to space. The level of minimum temperature at the base of the thermosphere is referred to as the mesopause. Thermospheres are generally subject to forcing both from below (e.g. planetary scale waves, tides, gravity waves) and above (e.g. solar output).

The terrestrial thermospheres are controlled by the highly variable components of the Sun's energy output, composed of both electromagnetic radiation (5-200 nm), and the solar wind (a flow of charged particles/plasma from the Sun). Most of the Sun's electromagnetic energy is in the visible portion of the spectrum, passing directly through the tenuous upper atmosphere. Solar radiation in the ultraviolet (UV), at wavelengths shorter than 200 nm, strongly interacts with the gases in a planetary thermosphere to establish its basic chemical, thermal, and dynamic structure. The amount of this ultraviolet radiation reaching a planet's upper atmosphere varies significantly with the Sun-planet (heliocentric) distance, the planet's obliquity (which determines the local season), and the changing solar radiation itself. The Sun is observed to undergo a cyclic variation in its electromagnetic and solar wind output that spans a period of roughly 11 Earth-years. The extreme ultraviolet (EUV) portion of the solar spectrum (5.0 - 110.0 nm) can vary by a factor of 2 to 10 over this solar cycle period (see chapter III.4).

The basic thermospheric temperature structures of Venus, Earth, and Mars are compared in Figure 1 and Figure 2. In each case, dayside temperatures increase dramatically above mesopause values (around 140-185 K). The Venus (100-125 km), Earth (90-100 km), and Mars (90-110 km) mesopause levels are quite close in altitude, yet different in pressure. EUV/UV flux activity over the solar cycle clearly drives significant changes in the thermospheric temperature profiles of these three planets. Dayside exospheric temperatures typically range over 900-1500 K (Earth), 230-310K (Venus), and 200-350K (Mars). Earth thermospheric temperatures vary most strongly as a function of changing solar fluxes plus auroral activity. Venus dayside temperatures are surprisingly cold (and vary least over the solar cycle), despite the fact that it is the closest of these three planets to the sun. It is noteworthy that Venus and Mars dayside thermospheric temperatures are comparable, owing to similar EUV heating efficiencies (see section 3.3). The biggest surprise is the nightside thermosphere of Venus which is observed to be colder than its dayside mesopause region. This Venus nightside upper atmosphere has been termed a "cryosphere" in accord with its very cold temperatures (100-130 K) [see *Fox and Bougher,* 1991]. Finally, note the absence of a stratopause for Venus and Mars, both of which lack the O_3 heating responsible in the Earth's middle atmosphere.

The thermosphere is also distinguished by a transition region called the homopause, below which atomic and molecular constituents are well mixed by winds and dissipative turbulence (eddy diffusion). For Earth, the bulk atmosphere is composed mostly of a uniform relative composition of O_2 and N_2. The Venus and Mars bulk atmospheres are composed largely of CO_2. Homopause levels (dayside) for these three planets are found at 136 km (Venus), ~100 km (Earth), and ~125 km (Mars) [*Bougher and Roble,* 1997]. Above, in the heterosphere, individual species begin to diffusively separate according to their unique masses owing to molecular diffusion. The heavier molecular species are thus the most abundant in the lower thermosphere, leaving the lighter molecular and atomic species to dominate at the base of the exosphere (primarily atomic O for all three planets). Figure 3 illustrates the basic heterospheric composition for the (a) Venus, (b) Earth, and (c) Mars thermospheres [*Bougher and Roble,* 1997]. It

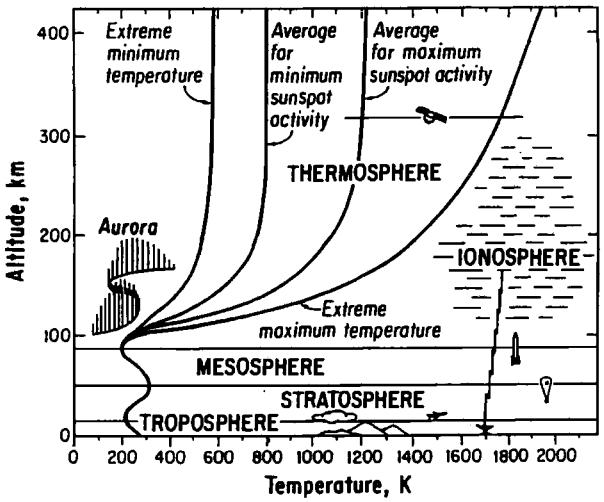

Figure 1. Temperature structure of the Earth's atmosphere. Temperatures vary more in the thermosphere than in lower regions of the atmosphere. Taken from Bougher and Roble, [1997]

is noteworthy that the atomic O abundance is nearly 5-10 times larger in the dayside thermosphere of Venus (~140 km) than for Mars (~125 km). Venus's proximity to the sun permits stronger photolysis of CO_2 [*Bougher*, 1995].

The local rate of absorption or heating depends on the product of the species absorption cross section and the total abundance of the absorbing species along the path through the atmosphere. This product is known as the optical depth; where it becomes unity, maximum absorption occurs. Figure 4 shows the altitude of unit optical depth as a function of EUV/UV wavelengths (20.0-180.0 nm) for (a) Earth, (b) Venus, and (c) Mars [*Paxton and Anderson*, 1992]. Per volume heating rates maximize near ~125 km (Mars) and 140 km (Venus), in concert with the locations of their photochemical ionospheric peaks (at low solar zenith angles) [*Zhang et al.*, 1990]. Conversely, Earth EUV/UV absorbers vary as a function of wavelength, providing peak ion-neutral and neutral-neutral chemical heating generally over 150 to 200 km. See section 4 for the details of the dayside heat balances of these three planets.

The Venus, Earth, and Mars thermospheres are also subject to large scale winds. These winds are driven by differential solar and non-solar heating which undergoes a daily, seasonal, orbital, or solar cycle variation [*Roble*, 1986]. Dayside heating causes the atmosphere to expand; the lack of heat at night causes it to contract. This heating pattern creates pressure differences that drive a global thermospheric circulation, transporting heat from the warm dayside to the cool nightside. The fluid motions are governed by the same equations as those used by meteorologists studying weather systems in the lower atmosphere. However, the thermosphere is more stable since the temperature increases with altitude [*Bougher and Roble*, 1997].

2.2. Implications of Fundamental Parameters

The basic features of the structure and dynamics of the Venus, Earth, and Mars thermospheres can be understood by examining the implications of their fundamental planetary parameters [e.g. *Bougher et al.*, 1999b; *Bougher and Roble*, 1997] (see Table 1b).

Venus is essentially a nonrotating planet with a very small intrinsic magnetic field. Its obliquity is also quite small, yielding little in the way of seasonal effects. The resulting circulation pattern is thus largely symmetric about the subsolar (SS) and antisolar (AS) points (see Figure 5, top panel). The observed large day-to-night thermospheric temperature and density variations (see Figure 6) can be understood provided that the solar-driven winds are mechanically slowed by turbulence induced friction (gravity wave drag) (see review by *Bougher et al.* [1997b]). This permits an even stronger isolation of the day and nightsides than afforded by the slow planetary rotation (see section 5.1). As a result, calculated nightside "cryosphere" temperatures are quite cold, unlike any other upper atmosphere seen in the solar system [*e.g. Fox and Bougher*, 1991]). Measured Pioneer Venus distributions of night airglow (Figure 7) and helium densities provide excellent tracers of the thermospheric circulation [*Mengel et*

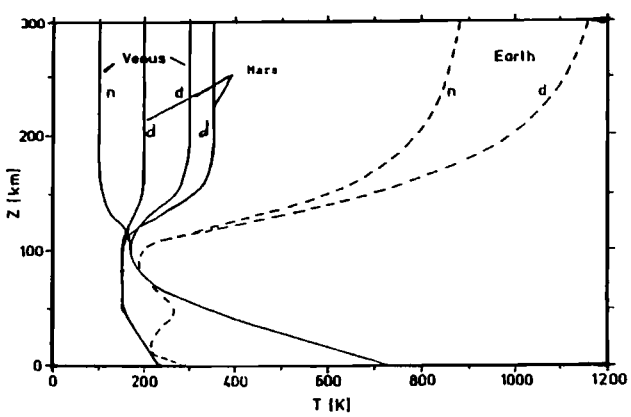

Figure 2. Temperatures of the neutral atmospheres of Earth, Venus, and Mars. Nightside temperatures of the Mars thermosphere (above 130 km) are not measured. Adapted from Fox and Bougher, [1991]

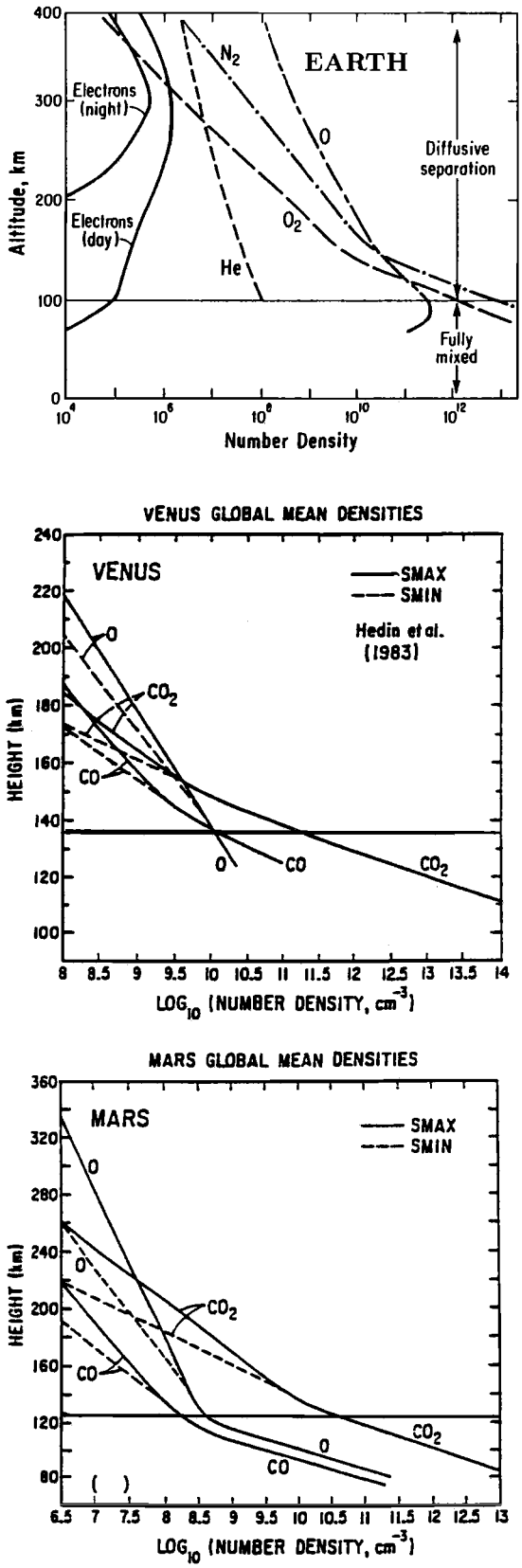

al., 1989; *Bougher et al.*, 1990a], confirming the existence of a modest asymmetric zonal flow (typically retrograde) that modifies the predominant symmetric subsolar-to-antisolar (SS-AS) circulation pattern.

Mars also has a very weak intrinsic magnetic field [*Acuna et al.*, 1998], like Venus, suggesting the absence of high-latitude, aurorally driven winds. However, unlike Venus, Mars rotates nearly as fast as the Earth and has an "Earth-like" seasonal cycle (see Table 1b). The resulting thermospheric circulation pattern for equinox or solstice conditions should display features common to the Earth at geomagnetically quiet conditions [*Bougher and Roble*, 1997]. There is no predicted nightside cryosphere for Mars, unlike Venus, since the Mars planetary rotation seems to preclude any effective isolation of its day and night sides. Table 2 summarizes the fact that Mars upper atmosphere observations are very limited in their spatial and temporal coverage. Most of what we presently know regarding the Mars thermosphere is derived from Viking 1 and 2 descent (dayside) temperature and density profiles [*Seiff and Kirk*, 1977; *Hanson et al.*, 1977], recent Mars Pathfinder (MPF) descent (nightside) temperature (Figure 8) and density (Figure 9) profiles [*Magalhaes et al.*, 1999], and a vast collection of Mars Global Surveyor (MGS) accelerometer densities and inferred temperatures (110-160 km) obtained over ~900 aeropasses during its two aerobraking phases (Ls = 184-300; 30-90) [*Keating et al.*, 1998a; 2001]. Ls is an angular measure of the Mars seasons (Ls = 0, 90, 180, 270 corresponds to the start of northern spring, summer, fall and winter, respectively). Density profiles from these various observational eras are compared in Figure 9, suggesting that Mars diurnal and seasonal variations near 130 km are significant [*Keating et al.*, 1998a]. In addition, Mars upper atmosphere data also confirm that dust storms originating in the lower atmosphere, and the concomitant aerosol heating, have a profound effect on the Martian thermospheric densities and overall structure (see section 5.3).

The intrinsic magnetic field of the Earth (see Table 1a) produces a distinctive interaction with the solar wind and its embedded magnetic field. The interaction results in precipitation of energetic electrons and protons from the magnetosphere, generating the characteristic auroral oval, and a magnetospheric convection electric field. The magnetospheric fields are mapped to

Figure 3. One dimensional global mean SMIN/SMAX density profiles for (a) Earth, (b) Venus, and (c) Mars. From Bougher and Roble, [1991]

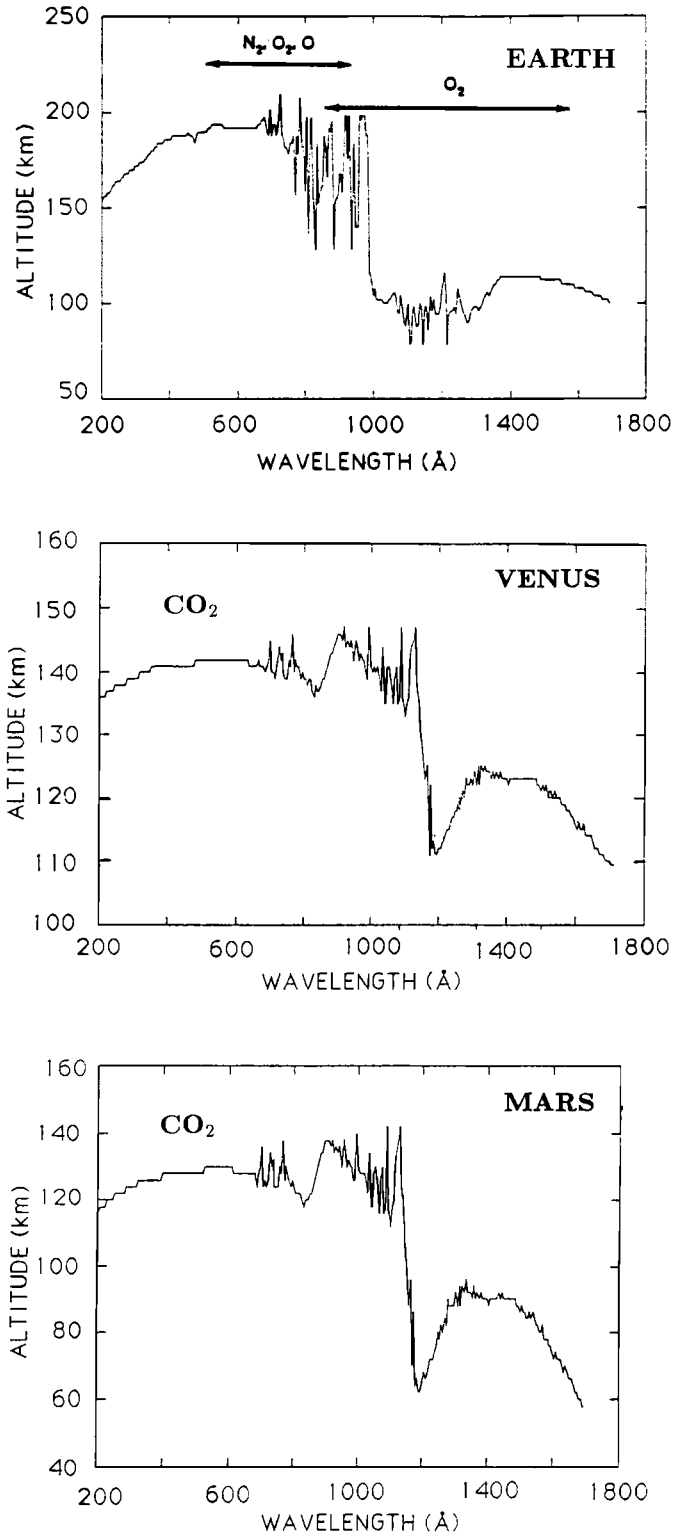

Figure 4. Solar UV radiation is absorbed by atmospheric constituents at various depths. Taken from Paxton and Anderson, [1992]

the upper atmosphere at high latitudes, driving strong ionospheric convection. The auroral particles typically provide only a modest energy source, but they do serve to enhance the conductivity of the high latitude thermosphere [*Fuller-Rowell and Evans,* 1987]. The Earth's upper atmosphere responds to this geomagnetic energy source in a number of ways (see section 5.2). Auroral heating and magnetospheric convection can reverse the "nominal" zonally averaged latitudinal temperature distribution and can dominate in driving the neutral winds (particularly during geomagnetic storms), thereby overwhelming the background solar EUV forcing [*Roble,* 1986]. The resulting thermospheric circulation pattern for Earth (see Figure 10) is much different from Venus (Equinox) and Mars (Solstice and Equinox) [*Bougher and Roble,* 1997].

2.3. Common Thermospheric Processes

The large vertical temperature gradient typical of the thermospheres of these planets results from the absorption of solar EUV/UV (Figure 4) or solar wind energy and the lack of any effective means of thermal emission in the altitude region (see section 3.3). Heat sources and sinks eventually become negligible and temperatures become isothermal within the exosphere. Molecular conduction cools the upper thermosphere by transferring the heat down-gradient toward the mesopause, where it is effectively radiated to space by an infrared (IR) active cooling agent. The height and temperature of the mesopause is controlled by the effectiveness of the IR cooling process(es). For the Earth, Venus, and Mars this IR cooling results primarily from CO_2 emission at 15-μm. The IR agent must have an emitting "window to space" at a wavelength that corresponds to the radiating temperature of that region. In this way, a thermostatic control is maintained which regulates lower thermosphere temperatures. Indeed, the relative abundance of IR active gases may be large enough to permit IR cooling to serve as a thermostat far above the mesopause (e.g. at Venus).

A thermospheric system is also subject to large scale winds, which can have a profound impact on thermospheric compositional and temperature distributions. As global scale winds diverge from the warm dayside, the corresponding upwelling winds lead to adiabatic cooling which may compete with other cooling mechanisms to regulate local temperatures. Conversely, nightside convergent winds result in downwelling flow and adiabatic heating which may also compete with other local heating processes. The relative importance of adiabatic heating and cooling processes varies strongly with the strength and variation of the planetary wind

Table 1b. Implications of Parameters

Effect	Earth	Venus	Mars
Scale heights, km	10-50	4-12	8-22
Major EUV heating, km	~200-300	~140-160	120-160
	broad	narrow	intermediate
O Abundance (ion peak)	~40%	~7-20%	~1-4%
CO_2 15-μm cooling	$\leq$130 km	$\leq$160 km	$\leq$125-130 km
Dayside thermostat	conduction	CO_2 cooling	winds/conduction
Dayside solar cycle T	900-1500 K	230-310 K	220-325 K
Rotational forces	important	negligible	important
Cryosphere	no	yes	no
Auroral/Joule heating	yes	no	no
Seasons	yes	no	yes

system, yielding a feedback between winds and temperatures. The hydrostatic expansion (contraction) of the thermosphere with heating (cooling) causes the heavy specie densities (CO_2 for Venus and Mars; N_2 for Earth) to increase (decrease) at a given pressure level. Conversely, light species (like helium and atomic oxygen) are subject to transport by the thermospheric wind system and tend to decrease in density at a given pressure level with local heating. The net effect is to increase the heavy to light specie mixing ratios with the passage of a heating event (e.g. geomagnetic storms for Earth; see section 5.2).

The Venus, Earth, and Mars thermospheres are also coupled to their lower atmospheres both hydrostatically and dynamically. The latter takes the form of upward propagating tides (migrating and non-migrating), global scale planetary waves, and gravity waves. The Earth and Mars thermospheres are clearly influenced from below by tidal forcing; however, the forcing agent is solar absorption by O_3 and water for Earth, and solar absorption by dust on Mars (see chapter III.1).

3. THREE DIMENSIONAL MODELING TOOLS

Various TGCM modeling groups have emerged over the last 20-30 years; each has contributed in a substantial way to the development of TGCM codes that are still used today. We have selected four prominent TGCMs to illustrate Venus, Earth, and Mars upper atmosphere features and to contrast common and unique physical processes. We review here the historical development and salient differences of these four models in order to set the context for simulations to follow in sections 4 and 5.

For each of these three-dimensional (3-D) finite difference codes, the continuity, momentum and energy equations encompassing relevant thermospheric processes are numerically solved to calculate TGCM global dis-

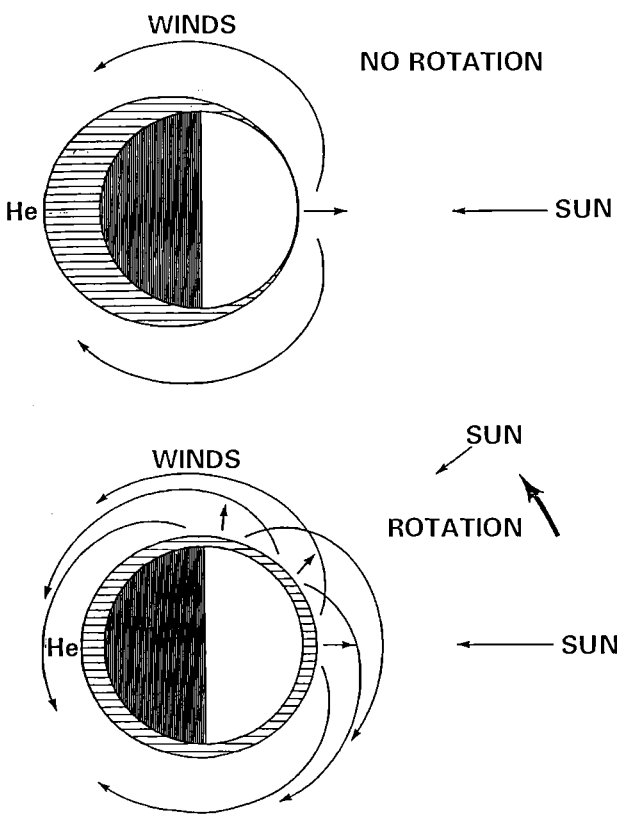

Figure 5. Cartoon of the SS-AS flow versus superrotating flow and its effects on the local time distribution of helium in the Venus thermosphere. Taken from Mengel et al., [1989]

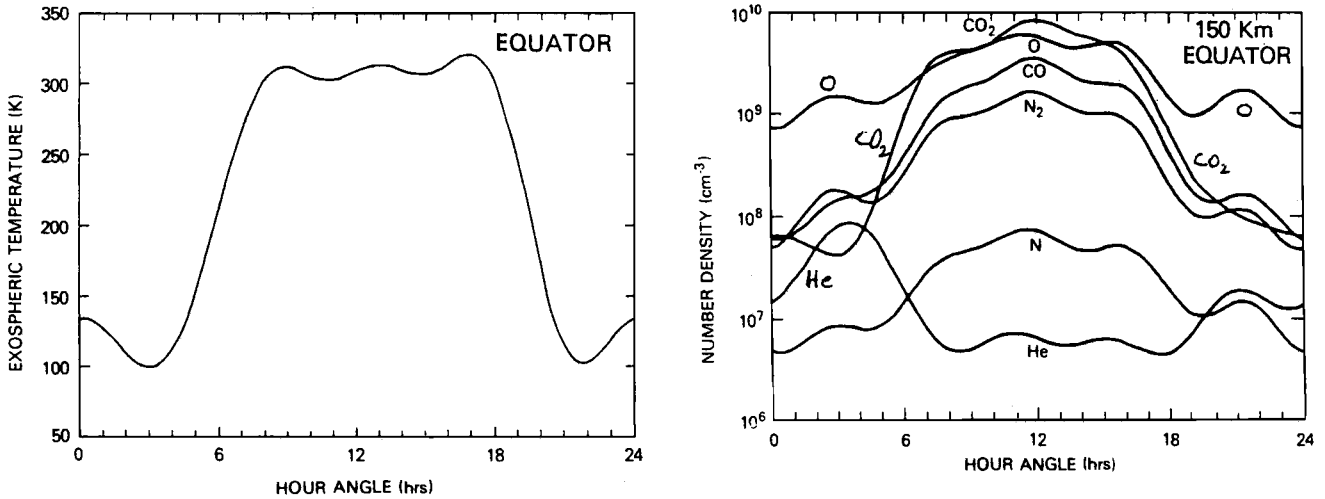

Figure 6. Hedin et al. (VTS3) empirical model (a) exospheric temperatures as a function of local time at the equator; (b) densities as a function of local time at 150 km at the equator. Taken from Hedin et al., [1983]

tribution of major and minor neutral species, ion densities (both photochemical and subject to transport), and the day-night temperature contrasts and the corresponding 3-component neutral winds. In addition, pressure is used as the vertical coordinate for each model, with vertical resolutions that vary from 0.25 to 1.0 scale height. Integration of the hydrostatic equation provides the corresponding height scales for each model. Table 3 summarizes the specific TGCM input parameters, calculated fields, and computational domains for the Venus, Earth, and Mars models discussed below.

3.1. Historical Development of Thermospheric GCMs

The development of the National Center for Atmospheric Research (NCAR) TGCM, incorporating increasing sophistication and internal self-consistency, began with pre-Pioneer Venus efforts to predict the global structure and wind system of the Venus thermosphere [e.g. *Dickinson and Ridley,* 1977]. Since that time, Earth semi-empirical models have given way to various TGCM versions (e.g. TGCM : Thermosphere General Circulation Model; TIGCM : Thermosphere Ionosphere General Circulation Model; TIE-GCM : Thermosphere Ionosphere Electrodynamics General Circulation Model) [e.g. *Dickinson et al.,* 1984; *Roble et al.,* 1988; *Richmond et al.,* 1992], culminating in the fully coupled 3-D TIME-GCM (Thermosphere Ionosphere Mesosphere Electrodynamics) code that spans 30-500 km [*Roble and Ridley,* 1994]. Venus (VTGCM) and Mars (MTGCM) adaptations of appropriate versions of the Earth TGCM have been developed, making use of the common TGCM modeling framework and post-processing software [e.g. *Bougher et al.,* 1988; *Bougher et al.,* 1990b]. Planet specific parameters, processes, and computational domains are addressed while solving the same basic energy, momentum, and coupled continuity-diffusion equations. This approach has greatly facilitated comparative thermospheres studies in recent years [*Bougher et al.,* 1999b; 2000].

CTIM, the Coupled Thermosphere Ionosphere Model for Earth, evolved from an integration of a neutral thermospheric code and a high and mid latitude ionosphere model. The neutral thermospheric model was originally developed by *Fuller-Rowell and Rees,* [1980] at University College London (UCL), and the ionospheric model originated from Sheffield University [*Quegan et al.,* 1982]. A global 3-D time-dependent model of the Martian thermosphere and ionosphere, based on the basic structure of CTIM, was developed by *Winchester and Rees,* [1995] and compared with Viking data. A new version of the CTIM code (CTIP) [*Millward et al.,* 1996] is presently being exercised which includes the Earth's mid- and low-latitude plasmasphere and ionosphere. Finally, the application of the CTIM model to Jovian planets is discussed in chapter IV.2; further application of CTIM to terrestrial-like moons is reviewed in chapter IV.4.

3.2. Brief Descriptions of Thermospheric GCMs

3.2.1. VTGCM. The Venus Thermosphere General Circulation Model (VTGCM) simulates the physics of the Venus CO_2 dominated thermosphere, and has been

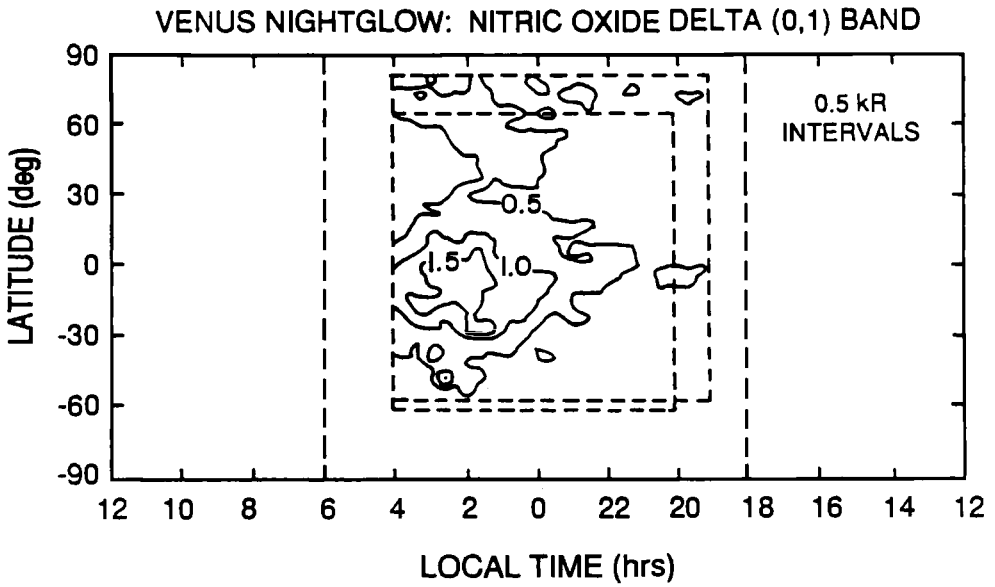

Figure 7. Pioneer Venus OUVS NO(0,1)δband 198 nm vertical intensity distribution as obtained and revised in absolute intensity according to Bougher et al. [1990]. This statistical map of the airglow is obtained over 35 orbits early in the PVO mission, and exhibits a dark-disk average intensity (120-180 ° SZA) of 460 ± 120 R. This map reflects the nightside convergence of the net thermospheric wind system. The spatial variability of the observed 198 nm individual bright airglow patches comprising this statistical map implies strong (and variable) zonal winds. Taken from Bougher et al., [1990a]

documented in detail by *Bougher et al.* [1988; 1997b] and *Zhang et al.* [1996]. Table 3 outlines the VTGCM input parameters, calculated fields, and its computational domain. In addition, O_2 visible (400-800 nm), IR (1.27 μm), and NO ultraviolet (198.0 nm) nightglow distributions can be explicitly calculated. A combination of collisionally enhanced CO_2 15-μm cooling, wave drag, and standard eddy diffusion formulations are incorporated into the VTGCM (see section 3.3). Rayleigh friction was used initially in the VTGCM to mimic wave drag on the mean flow and a superrotating zonal wind was prescribed to simulate the asymmetry of the circu-

Table 2. Mars Spacecraft Observations of the Upper Atmosphere

Mission	Dates(s)	F10.7	Ls	Dsm	SZA	T_{exo}
M4	July 15, 1965	77.0	139.0	1.553	67.0	212.0
M67	July 31, 1969	167.0	200.0	1.425	0-44.0	315-350.0
	Aug. 5, 1969	188.0				
M9N	fall 1971	103.0	306.0	1.440	50-60.0	325.0
M9E	spring 1972	100.0	38.0	1.630	70-90.0	268.0
VL1	July 20, 1976	69.0	96.0	1.647	44.0	186.0
VL2	Sept. 3, 1976	76.0	117.0	1.612	44.0	145.0
MPF	July 4, 1997	70.0	143.0	1.557	135.0	153.0
MGS1	Jan. 16, 1998	93.0	256.0	1.382	73.5	220.0
MGS2	Oct. 27, 1998	127.0	48.5	1.653	57.0	230.0

F10.7 refers to the 10.7-cm index used to select reference EUV/UV flux data sets; Ls, refers to, the angular measure of the Mars seasons (Ls = 90 is northern summer solstice, Ls = 270 is southern summer solstice, etc.); Dsm refers to the Mars heliocentric distance (AU); SZA refers to solar zenith angle; and T_{exo} refers to exospheric temperature. Spacecraft are indicated as follows; M4 (Mariner 4), M67 (Mariner 6 and 7), M9E (Mariner 9 extended), M9N (Mariner 9 nominal), VL1 (Viking Lander 1), VL2 (Viking Lander 2), MPF (Mars Pathfinder), MGS1 (Mars Global Surveyor phase 1 aerobraking sample), MGS2 (Mars Global Surveyor phase 2 aerobraking sample).

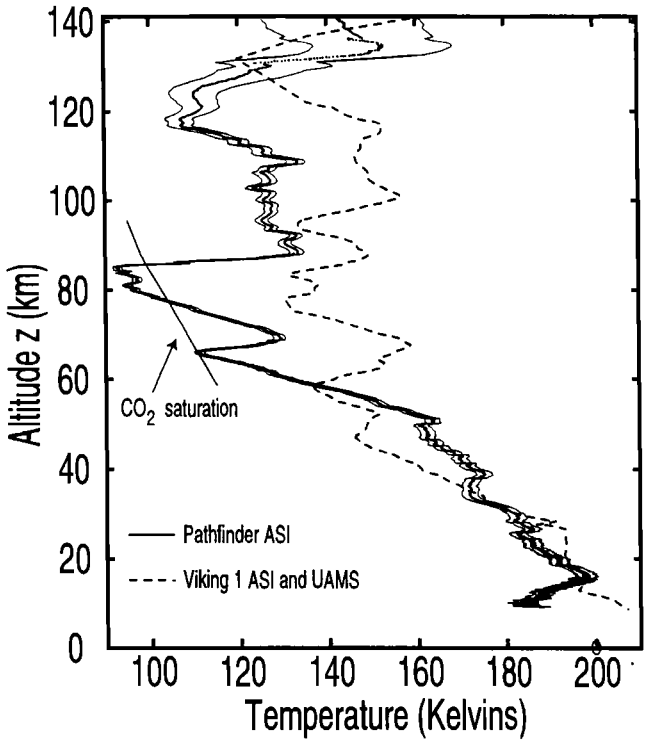

Figure 8. Mars Pathfinder (MPF) temperature profile from the entry phase. Temperatures from the Viking 1 ASI [Seiff and Kirk, 1977] and UAMS [Nier and McElroy, 1977] experiments are plotted for comparison. Taken from Magalhaes et al., [1999]

lation [*Bougher et al.*, 1988]. In recent years, a gravity wave drag parameterization has been tested in the VT-GCM that may replace Rayleigh friction and the prescribed asymmetric flow [*Zhang et al.*, 1996; *Bougher et al.*, 1997b] (see section 5.1).

Solar cycle variations of Venus thermospheric temperatures, densities, and airglow intensities have been monitored using Pioneer Venus Orbiter (PVO) and Magellan measurements taken over a fraction of two 11-year periods [*Kasprzak et al.*, 1997]. Many of the features of these observed solar cycle responses are captured in two empirical models: VIRA (Venus International Reference Atmosphere) [*Keating et al.*, 1985; 1998b] and that of *Hedin et al.* [1983] (see Figure 6).

3.2.2. TIE-GCM. The NCAR Thermosphere Ionosphere Electrodynamics GCM (TIE-GCM) is the latest in a series of general circulation models of the Earth's upper atmosphere and ionosphere that have been developed during the past two decades [*Richmond et al.*, 1992]. Table 3 summarizes the TIE-GCM input parameters, simulated fields, and computational domain. The model is driven by a time-dependent specification of solar EUV and UV spectral irradiance and magnetic conjugate auroral particle precipitation and ionospheric convection patterns at the upper boundary of the model. The TIE-GCM computes self-consistently the coupled thermosphere and ionosphere dynamics, the associated dynamo electric field and currents, and the electrodynamic feedback on the neutral and plasma motion and thermodynamics as described by *Richmond et al.*, [1992]. Mutual couplings between the thermosphere and ionosphere occur at each model time step and at each point of the geographic grid. Migrating tidal amplitudes and phases are prescribed at the TIE-GCM lower boundary (diurnal and semi-diurnal). This TIE-GCM code has been used for numerous studies of the thermosphere and ionosphere structure of the Earth's upper atmosphere and its response to solar and auroral variability. Recently, eccentricity variations have also been included in the TIE-GCM [*Bougher et al.*, 2000].

Solar cycle variations of Earth thermospheric temperatures, densities, winds, and airglow intensities have been monitored over the last 40 years. Empirical models have been constructed to capture these solar cycle responses of the terrestrial thermosphere structure and dynamics. The most recent and presently useful empirical models for the Earth's upper atmosphere are the MSIS-90 (structure) and HWM (winds) codes [*Hedin*, 1991; *Hedin et al.*, 1991].

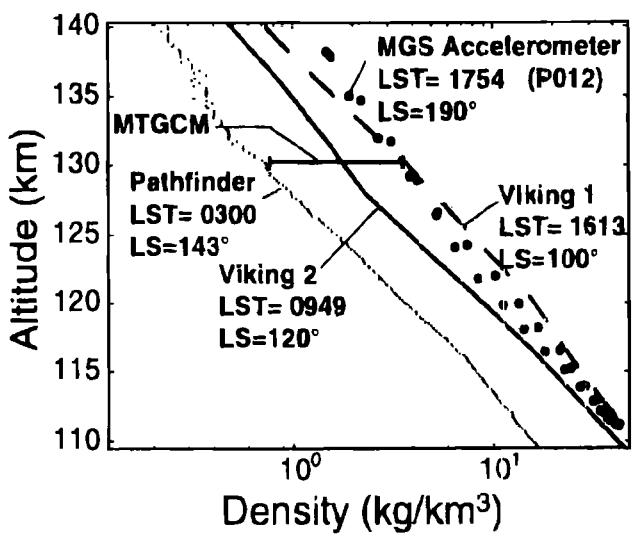

Figure 9. Mars Global Surveyor (MGS) accelerometer data between 110 and 140 km for Orbit 12 (Ls = 190; LT = 1800) compared to previous in-situ martian thermospheric density profiles. The horizontal line (at 130 km) shows the change between MPF (night) and MGS (day) values is due to both seasonal and diurnal differences based upon MTGCM simulations. Adapted from Keating et al., [1998a]

[redacted]

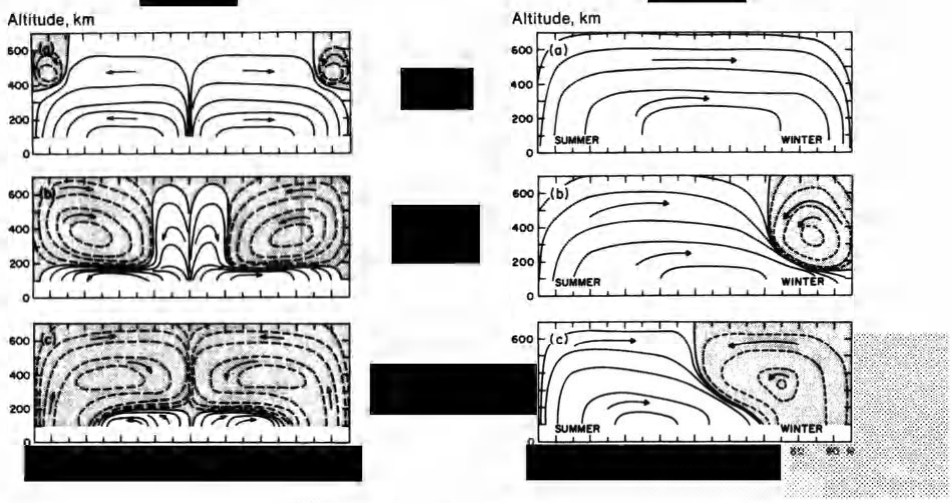

[redacted]

Table 3. TGCM Input Parameters, Fields, and Computation Domains

TGCM	Domain -Alt Range -Pres Range Resolution (LatxLon)	Major Species	Minor Species	Ions	Time-Step (secs)	Homopause Kzz (cm2/sec)	Heating Efficiencies (EUV vs. UV)
VTGCM	94-200 km 11-4.6E-7 Pa 33-levels 5x5 degrees	CO_2 CO O N_2	O_2 He NO N(4S) N(2D)	CO_2+ O_2+ O+ NO+ (PCE)	180	1.0E+7 (at 136 km)	EUV = 20% UV=22%
MTGCM	70-300 km 0.13-1.5E-8 Pa 33-levels 5x5 degrees	CO_2 CO O N_2	O_2 He Ar NO N(4S)	CO_2+ O_2+ O+ NO+ CO+ N_2+ (PCE)	150	1-2.0E+7 (at 125 km)	EUV= 22% UV=22%
TIE-GCM	95-800 km 0.06-4.6E-8 Pa 29-levels 5x5 degrees	N_2 O_2 O	He Ar NO N(4S) N(2D)	O+ (DYN) O_2+ NO+ N_2+ N+ (PCE)	300	1.6E+6 (at 100 km)	EUV=30-40% UV-30-40% Chem $\leq$60% (< 200 km)
CTIM	80-600 km 1-8.6E-7 Pa 15-levels 2x18 degrees	N_2 O_2 O	NO N(4S) N(2D)	H+ O+ (100-10000 km) O_2+ NO+ N_2+ N+ (PCE)	60	1.0.E+6 (at 100 km)	EUV = 30-65% UV=30-40%

Where PCE refers to photochemical equilibrium; DYN refers to vertical diffusion and horizontal advection; Chem signifies neutral-neutral and ion-neutral chemical heating below 200 km; EUV refers to Extreme Ultraviolet heating efficiency; UV refers to Ultraviolet heating efficiency. In addition, 1E-7 is interpreted as $1x10^{-7}$.

temperatures to constrain the MTGCM for SMIN to SMED conditions [*Magalhaes et al.*, 1999; *Keating et al.*, 1998a; 2001].

3.3. Standard Inputs and Forcings for TGCMs

A standard suite of VTGCM, TIE-GCM, and MTGCM simulations was recently conducted [*Bougher et al.*, 1999b, 2000] and is reviewed in this chapter in order to examine common processes driven solely by solar EUV/UV forcing. Both solar cycle and seasonal variations were contrasted for these models, each of which was initiated with common inputs, rate coefficients, and formulations for small scale mixing. Common TGCM inputs and forcings are outlined in detail in *Bougher et al.*, [1999b]. Here, we briefly summarize these inputs and parameters to provide the context for equinox and solstice simulations described in section 4.

The reference solar X-ray/EUV/UV fluxes (ranging from 2.0 to 200 nm) used by these three-planet TGCMs are identical to those specified in *Bougher et al.*, [1999b, 2000]. Standard parameterizations are employed, based upon the F10.7-cm index, yielding reference solar flux datasets consistent with typical solar maximum (SMAX) F10.7 = 200, solar moderate (SMED) F10.7 = 130, and solar minimum (SMIN) F10.7= 68 conditions.

These computationally time consuming TGCM models typically make use of EUV and UV heating efficiencies calculated independently (offline) by others. *Fox*

[1988] describes detailed calculations yielding reasonable Venus EUV (20-25%) and UV (22%) heating efficiencies currently employed in the VTGCM code. Similarly, *Fox and Dalgarno* [1979, 1981] presents detailed simulations producing EUV (20-25%) and UV (22%) efficiencies which are presently used in the MTGCM code. It is remarkable that these Venus and Mars heating efficiencies are so low [see details in *Bougher et al.*, 1999b]. For Earth, *Roble et al.*, [1987] and *Roble* [1995] discuss the details of EUV and UV energy partitioning and energy balance calculations (non-local) that are largely performed within the TIE-GCM code itself. Overall, UV heating (120-200 km) results in efficiencies between 30-40%; EUV heating (200-300 km) yields efficiencies between 30-40%; and neutral-neutral and ion-neutral chemical heating efficiencies below 200 km approach 60%.

Atomic oxygen collisions are known to be especially effective in exciting CO_2 (ν=2) vibrational states, resulting in enhanced 15-μm emissions and cooling at thermospheric heights where non-local thermodynamic equilibrium (NLTE) conditions prevail. The importance of this CO_2-O enhancement mechanism upon thermospheric 15-μm cooling rates depends on (1) relative O-densities, (2) relative CO_2 densities, and (3) the collisional energy transfer rate coefficient. The corresponding CO_2 relaxation rate has only recently been measured in the laboratory and estimated from atmospheric radiance studies for the first time; significant discrepancies remain [e.g. *Wintersteiner et al.*, 1992; *Bougher et al.*, 1994]. However, it is important to consistently incorporate a common CO_2-O relaxation rate in calculations of all three terrestrial planet thermospheres. For the VTGCM, TIE-GCM and MTGCM simulations of this chapter, a currently accepted (moderate) value of the CO_2-O deactivation rate coefficient of 3 x 10^{-12} cm^3/s (at 300 K) is used [*Bougher et al.*, 1999b, 2000].

The eddy diffusion coefficient profiles used in these three TGCM codes are each parameterized according to standard aeronomic formulations. A key feature to notice about Venus and Mars is that the magnitude of the eddy coefficient is a factor of 3-5 smaller less than corresponding 1-D continuity-diffusion models would suggest [c.f. *Bougher et al.*, 1999b]. For the VTGCM (MTGCM), a nominal maximum eddy coefficient of ~1-2 x 10^7 cm^2/s at 136 km (near 125 km) was employed. In both cases, the global-scale circulation appears to play a major role in the determination of vertical density profiles, thereby reducing the requirement for vertical eddy diffusion (and eddy conduction) [*Bougher et al.*, 1999b, 2000]. For the Earth, the *Roble et al.* [1987] 1-D global mean model simulations of observed densities require the maximum eddy coefficient to be ~1.6 x 10^6 cm^2/s (near 100 km), in accord with the minimal role of eddy conduction in the energy budget of the terrestrial mesopause region. A similar eddy coefficient parameterization was employed in the TIE-GCM code, with an additional variation prescribed as a function of latitude.

Tidal parameters are specified at the lower boundaries of the TIE-GCM and MTGCM codes consistent with typical values for the required seasons. These tidal parameters (diurnal and semidiurnal amplitudes and phases) are well documented according to ground-based and spacecraft observations of the Earth's mesosphere and lower thermosphere (MLT) region [e.g., *Forbes*, 1982; *McLandress et al.*, 1996]. However, no Mars MLT data presently exist that describe global tidal parameters as a function of season and latitude. Instead, the MTGCM tidal parameters (semidiurnal amplitudes and phases) are taken from the NASA Ames General Circulation Model (MGCM) of the Mars lower atmosphere [e.g. *Bridger and Murphy*, 1998], which was exercised for a Mars year for dust-free and dusty conditions. The exchange of tidal parameters from an MGCM upper level to the MTGCM lower boundary (at roughly 70 km) is described in detail by *Bougher et al.* [1993, 1997a, 1999a].

Low auroral activity parameters were chosen for implementation in the Earth TIE-GCM for all solar cycle cases conducted. The purpose here is to focus upon the model variations due to solar EUV/UV flux variability, with minimal influence from auroral processes. For the TIE-GCM simulations of this chapter, the cross-tail potential was held constant at 45 KV, while the integrated global power input was selected to be 16.0 GW. The importance of auroral forcing in the Earth's upper atmosphere is discussed further in section 5.2.

4. SIMULATIONS ILLUSTRATING COMMON THERMOSPHERIC PROCESSES

4.1. Equinox : Venus, Mars, and Earth

4.1.1. VTGCM. A composite of VTGCM temperature profiles (~100-200 km) for three solar cycle cases for dayside and nightside local times is presented in Figure 11a [*Bougher et al.*, 1999b]. VTGCM dayside exospheric temperatures are calculated to vary from 308 K to 231 K (77 K) over the solar cycle, in general accord with observations [SMAX (1978-1980) : *Kasprzak et al.*, 1997; SMED (1992) : *Keating and Hsu*, 1993; SMIN (1994) : *Keating et al.*, 1998b]. These temperatures are quite cold and this solar cycle variation is

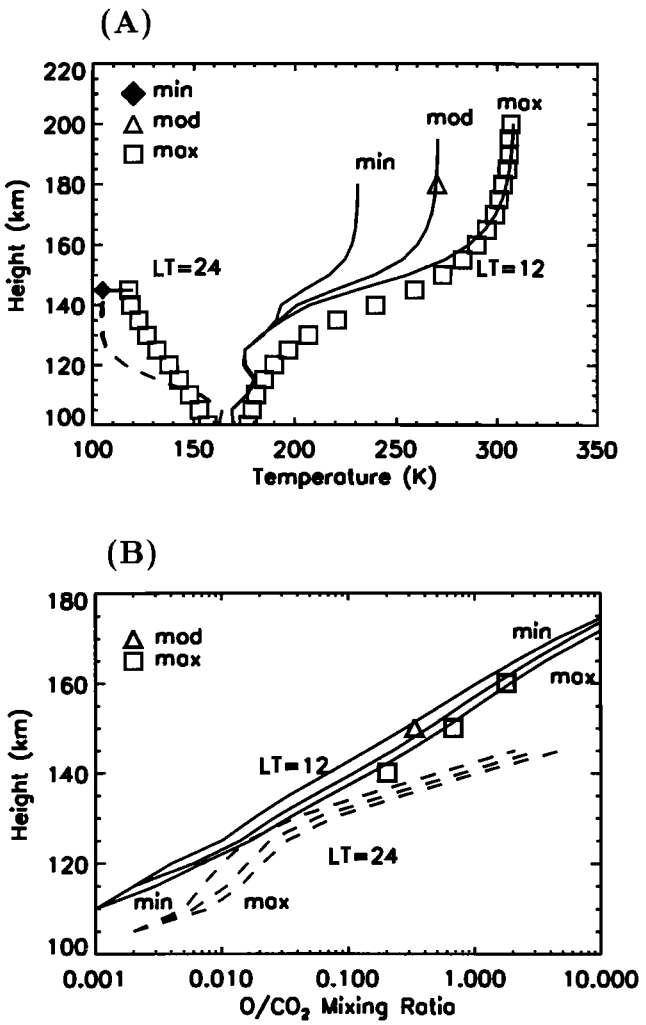

Figure 11. VTGCM equatorial fields and their variations over the solar cycle. Hedin et al. [1983] empirical model temperatures over-plotted (squares); Magellan (drag) inferred temperatures and mixing ratios (140-160 km) over-plotted (triangles). (a) Noon (LT = 1200, solid), and midnight (LT = 2400, dashed) temperature profiles over 100 to 220 km for SMIN, SMED, and SMAX cases; (b) noon (LT = 1200, solid) and midnight (LT = 2400, dashed) O/CO_2 profiles over 100 to 180 km for the same 3-EUV flux cases. Adapted from Bougher et al., [1999b]

rather small for a thermosphere that is the closest to the Sun of these three terrestrial planets. The day-to-night contrast of VTGCM simulated exospheric temperatures is as much as 200 K for solar maximum conditions, in accord with surprising PVO observations during its first diurnal cycle (1978-1980) (e.g., see reviews by *Fox and Bougher* [1991]. Furthermore, nightside temperatures are observed by Magellan and PVO to vary little over the solar cycle [e.g., *Kasprzak et al.*, 1997], consistent with current VTGCM simulations [e.g., *Bougher et al.*, 1999b].

Figure 11b illustrates a corresponding composite of VTGCM O/CO_2 mixing ratio profiles for the same local times over the solar cycle. Historically, the abundance ratio of O/CO_2 at the altitude of the Venus dayside ionospheric peak (~140 km) has been used as an indicator for the degree of net CO_2 dissociation of Venus's upper atmosphere [*von Zahn et al.*, 1983]. With the advance of the solar cycle, it is expected that CO_2 net dissociation will increase, providing enhanced O and depleted CO_2 thermospheric densities. The overall effect on the largely photochemically controlled dayside thermosphere is to increase its O/CO_2 mixing ratios from SMIN to SMAX conditions. VTGCM values of this ratio near 140 km range from 7-8% (SMIN) to 15-16% (SMAX) near noon on the equator. This factor of 2 variation over the solar cycle is consistent with available PVO observations [*von Zahn et al.*, 1983; *Hedin et al.*, 1983; *Keating and Hsu*, 1993]. VTGCM atomic oxygen surpasses CO_2 in the dayside thermosphere as the dominant species near 155 km (SMAX) and 160 km (SMIN), in accord with that observed.

The relative importance of CO_2 15-micron cooling as a thermostat regulating thermospheric temperatures is different for each terrestrial planet. In general, CO_2 15-μm cooling is highly nonlinearly temperature dependent, resulting in a potential thermostatic control pending the relative magnitude and vertical placement of the peak cooling rate in these thermospheres [e.g., *Bougher et al.*, 1994]. For Venus, CO_2 cooling makes a very strong contribution, nearly offsetting the peak EUV heating over 130-150 km (see Figure 12a). This balance determines that the simulated VTGCM dayside exospheric temperatures are not very sensitive to molecular thermal conduction. Over the solar cycle, this strong CO_2 15-micron cooling mitigates the importance of increasing EUV heating, resulting in a small variation of Venus thermospheric temperatures ($\leq$75 K), just as observed (see Figure 11a) [*Kasprzak et al.*, 1997]. This VTGCM thermostat is further regulated by changing atomic O, owing to the doubling of dayside O-mixing ratios with the advance of the solar cycle (see Figure 11b) [e.g., *Bougher et al.*, 1999b]. This highly efficient "O-regulated CO_2 thermostat" results in the very rapid ($\leq$1-day) equilibration of Venus dayside temperatures (above 160 km) due to solar EUV/UV perturbations [*Bougher et al.*, 1999b]. Thus, the Venus cold dayside temperatures and their relatively small solar cycle variation are explained by very strong 15-micron cooling which largely balances its EUV heating (see section 3.1 [*Fox and Bougher*, 1991]). Dayside upwelling winds ap-

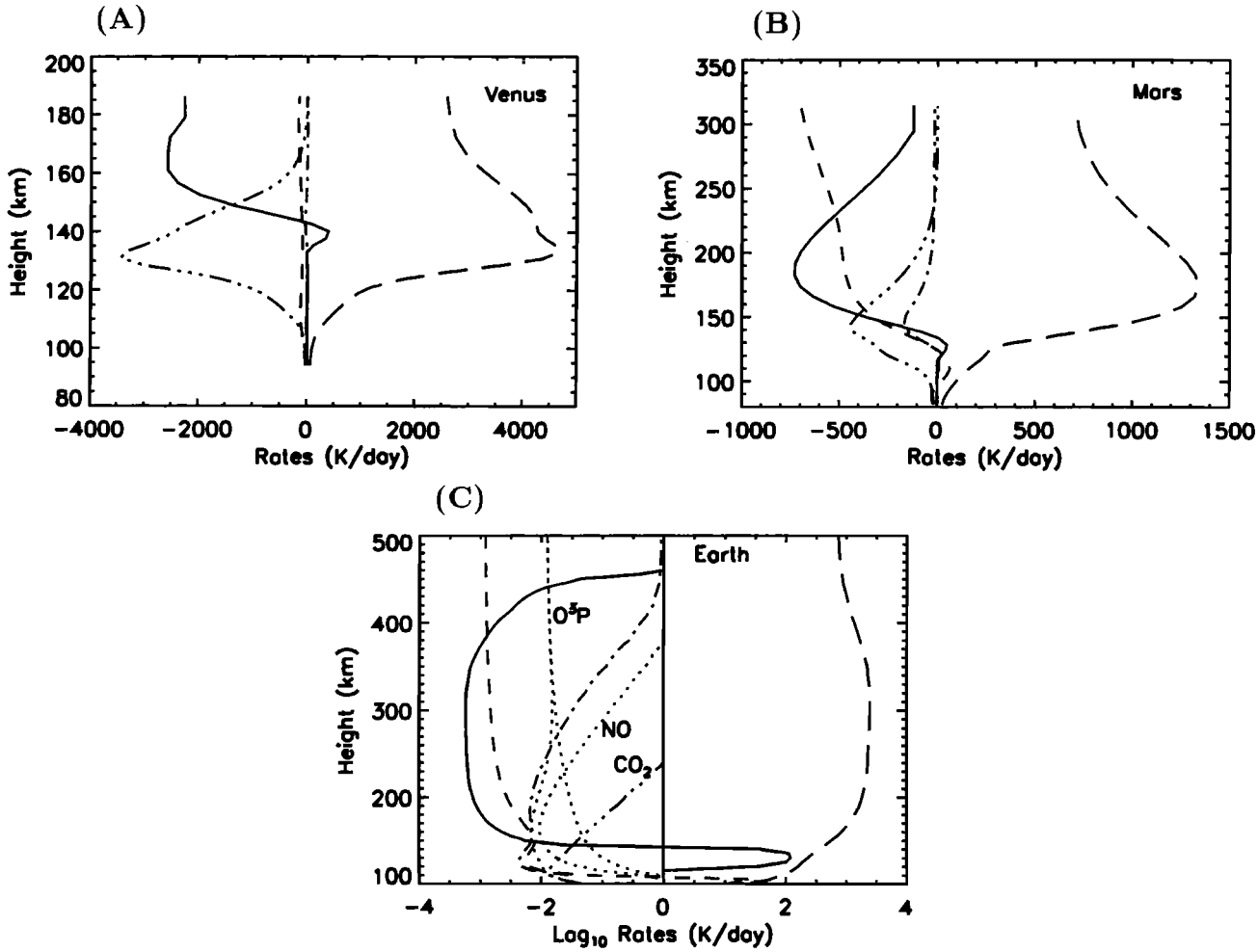

Figure 12. TGCM dayside equatorial thermal balance plots for SMED conditions (F10.7 = 130). Curves are delineated as follows: (long dash) total solar heating, (solid) molecular conduction, (short dash) adiabatic cooling, (dot-dash-dot) hydrodynamic advection (horizontal plus vertical), and (dot-dot-dot-dash) CO_2 cooling : (a) VTGCM thermal balance terms (K/day) at noon (LT= 1200); (b) MTGCM equatorial thermal balance terms (K/day) at mid-afternoon (LT= 1500); (c) TIE-GCM equatorial thermal balance terms (log10-K/day) at mid-afternoon (LT= 1600). Earth rates for CO_2 (15-μm), NO (4.3-μm), and O(^{3}P) IR cooling are labeled. Taken from Bougher et al., [1999b]

pear to have little effect on the Venus thermal structure, in stark constrast to the large impact of subsiding winds on the nightside [*Bougher et al.*, 1988]. See section 5.1 for details regarding the maintenance of this nightside "cryosphere".

Figure 13 illustrates the behavior of the VTGCM temperatures and global wind system near exobase altitudes (~200 km dayside; ~145 km nightside) for SMAX conditions. Dayside temperatures reach 308 K, in accord with PVO measurements [*Kasprzak et al.*, 1997]; nightside values drop to 105 K near 0100 LT. The collapse of the altitude scale for the nightside thermosphere is due to the very cold nightside temperatures [*Kasprzak et al.*, 1997]. The large day-to-night temperature (~200 K) and corresponding pressure contrast drives horizontal winds that reach magnitudes of 260 m/s, which are balanced by wave drag and molecular viscosity (see section 5.1). The subsolar-to-antisolar (SS-AS) symmetric component of the circulation is augmented by an asymmetric retrograde superrotating zonal (RSZ) flow [e.g., *Bougher et al.*, 1997b]. This superposition of wind components is clearly reproduced in the terminator zonal winds which are faster at the evening terminator (+263 m/s) than at dawn (-220 m/s). This asymmetry results in upwelling and divergence of horizontal winds near LT=1000 (on the equa-

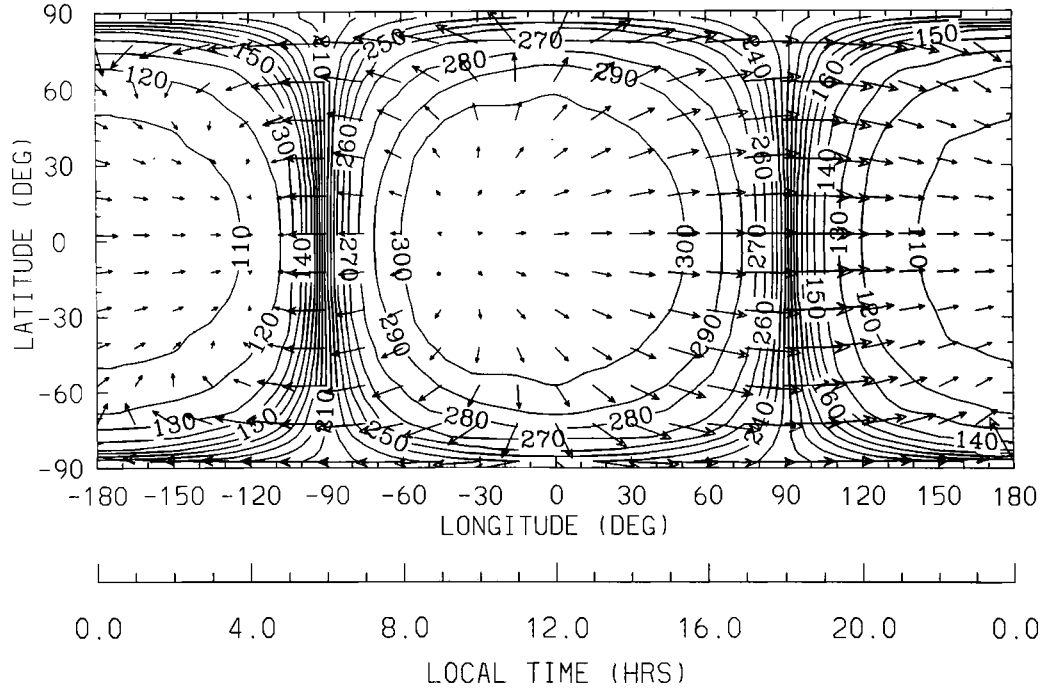

Figure 13. VTGCM SMAX simulation. Horizontal temperature and wind variations are displayed with an exobase T+(U,V) plot at z = 7.0 (~200 km dayside; ~145 km nightside), showing the horizontal wind pattern and underlying temperature structure; maximum arrow (winds) corresponds to 263 m/s. Exospheric temperatures range from a nightside minimum (104 K) to a dayside maximum (308 K), yielding a day-night contrast of 204 K. Cold (170-180 K) mesopause temperatures (not shown) appear on the dayside over 100-125 km. Taken from Bougher et al., [1999b]

tor) and subsidence and convergence near LT=0300-0400. This asymmetry is consistent with nightside airglow intensities which peak after midnight (see Figure 7) [e.g., *Bougher and Borucki*, 1994].

4.1.2. MTGCM. Figure 14a presents a composite of dust-free MTGCM temperature profiles for three solar cycle cases for dayside and nightside local times. These profiles correspond to local times of peak dayside and minimum nightside temperatures, similar to the Earth's thermosphere (with a comparable rotation rate) (see Table 1a). MTGCM dayside exospheric temperatures are calculated to vary from 325 to 220 K (105 K) over the solar cycle, in general agreement with limited Mars equinox observations (see Table 2). Recent MGS accelerometer data taken near equinox during SMIN conditions (low dust) imply exospheric temperatures of 220-230 K [*Bougher et al.*, 1999b], in accord with these MTGCM values. Few measurements exist at present to constrain Mars nightside thermospheric temperatures. Mars Pathfinder descent values of 127-153 K were obtained near 130 km at LT=0300 [*Magalhaes et al.*, 1999]. Figure 14a also illustrates that the day-to-night contrast of MTGCM simulated exospheric temperatures is predicted to be as much as 160 K for SMAX conditions, less than observed for Venus (see Figure 11a). The Mars rotation seems to preclude an effective isolation of its day and nightside thermospheres, unlike Venus (see section 2).

A composite of MTGCM O/CO_2 mixing ratio profiles for the same solar cycle cases and local times is illustrated in Figure 14b. As for Venus, it is expected that the advance of the solar cycle will provide enhanced O and depleted CO_2 dayside thermospheric densities. Since in-situ measurements of Mars thermospheric O densities are lacking, values of O mixing ratios are derived from Viking ionospheric and Mariner airglow data [*Hanson et al.*, 1977; *Stewart et al.*, 1992]. The direct solar cycle control of O/CO_2 mixing ratios is indeed evident for the largely photochemically controlled Mars lower thermosphere (below 160 km), where limited data indicate values increasing from 1.25% (SMIN) [*Hanson et al.*, 1977] to ~3.0% (SMAX) [*Stewart*, 1972]. Corresponding MTGCM values of the O mixing ratio over 125-130 km (mid-day ionospheric peak) range from

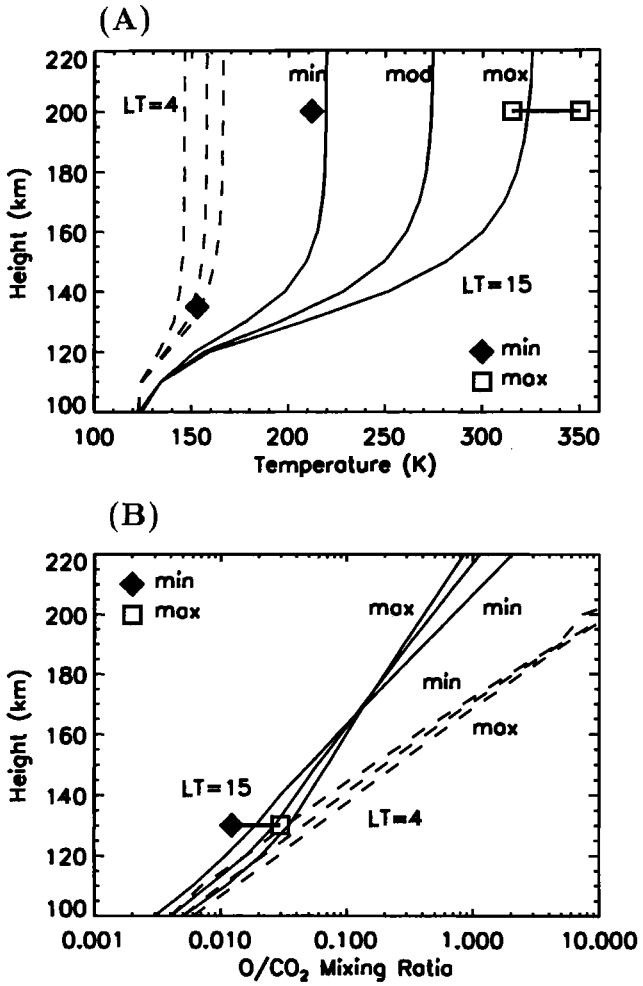

Figure 14. MTGCM equatorial fields and their variations over the solar cycle. Curves are delineated as follows : LT=1500 (solid) and LT=0400 (dashed). (a) temperature profiles over 100 to 220 km for SMIN, SMED, and SMAX cases; observed "near Equinox" exospheric temperatures are over-plotted from Table 2; (b) O/CO_2 mixing ratio profiles over 100 to 220 km for the same 3-EUV flux cases. At the F1-ionospheric peak (~130 km) at LT=1500, the observed O-mixing ratio varies from ~1.25-3% over the solar cycle. Taken from Bougher et al., [1999b]

~2% (SMIN) to ~4% (SMAX). This variation in O abundance helps to modulate the importance of CO_2 15-μm cooling in the Mars lower thermosphere over the solar cycle. However, above 170 km, we see a reversal of the variation in the predicted O abundance, with maximum values during SMIN conditions. This is due to the effect of dynamics (global wind advection and diffusion) on the densities. MTGCM winds deplete the mid-afternoon upper thermosphere of oxygen atoms more effectively during SMAX conditions (strongest horizontal winds) than SMIN conditions (weakest winds). Global thermospheric measurements of O densities over the solar cycle and throughout the Mars seasons are sorely needed (see section 6.0).

Figure 12b examines the dayside (LT=1500) heat budget for the Mars thermosphere. MTGCM molecular conduction provides the primary cooling offsetting peak EUV heating over 150-200 km. CO_2 15-μm cooling peaks at slightly lower altitudes and is thus unable to serve as an efficient thermostat for Mars temperatures. In addition, mid-afternoon upwelling winds (resulting from divergent flow) generate significant cooling that readily competes with conduction above ~225 km. This dynamical cooling mechanism increases in importance as the solar cycle advances [*Bougher et al.*, 1999b], thereby providing an alternative thermostatic control of local temperatures. Overall, these MTGCM dayside thermal balances suggest that Mars thermospheric temperatures are very sensitive to molecular conduction and global winds, while CO_2 cooling does not appear to be dominant in the dayside heat budget. These thermal balances give rise to larger simulated temperature variations over the solar cycle (~110 K) than observed for Venus (compare Figures 11a and 14a). In addition, the resulting rapid (~1-day) equilibration of Mars dayside temperatures (above 165 km) due to solar EUV/UV perturbations is similar to that of Venus [*Bougher et al.*, 1999b].

The global thermospheric wind pattern for Mars is presently unconstrained by any observations. Figure 15 illustrates the MTGCM predicted behavior of the Mars temperatures and global wind system near exobase altitudes (~230 km dayside; ~190 km nightside) for SMAX conditions. Exospheric temperatures peak at 328 K (LT=1500) and are a minimum at 140.6 K (LT=0400), both at midlatitudes. Notice that winds diverge (strong upwelling) near LT=1500-1600 on the equator, and converge (strong subsidence) after midnight near the equator. This asymmetric circulation pattern is the result of symmetric solar heating plus the Mars rotation (similar to the Earth). Upwelling gives rise to strong adiabatic cooling in the mid-afternoon, with corresponding subsidence and strong heating just after midnight. The modest day-to-night temperature contrast (170-180 K) drives horizontal winds that reach magnitudes of ~300 m/s across the terminators and near the poles. This predicted Mars diurnal temperature variation is less than observed and calculated for Venus (see Figure 11a). Global thermospheric wind measurements at Mars are needed to characterize the circulation patterns

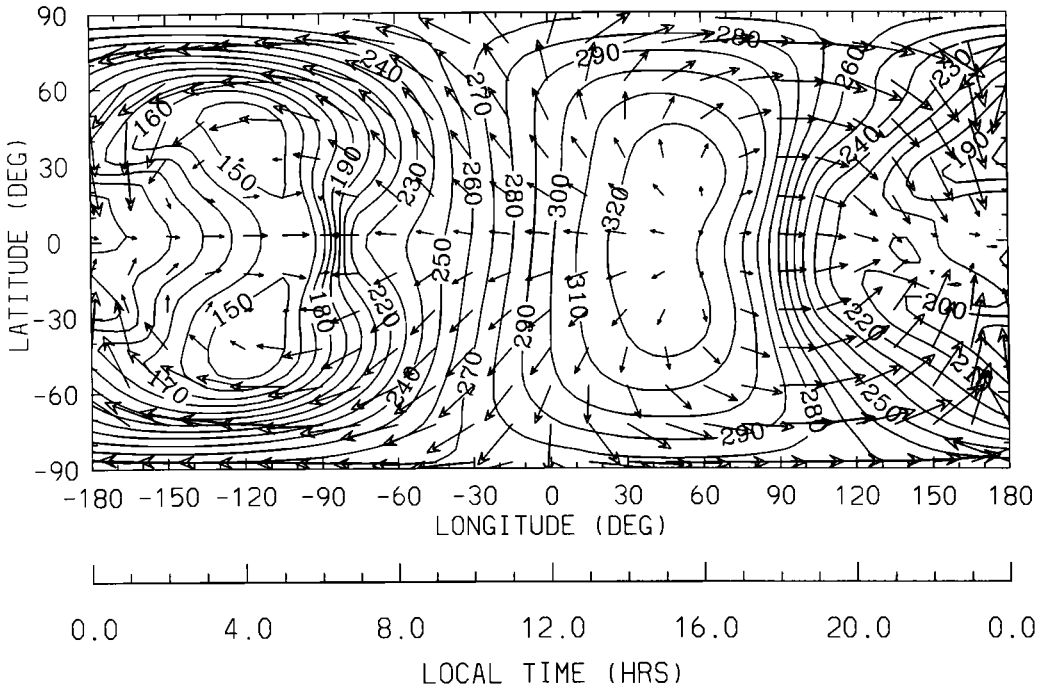

Figure 15. MTGCM SMAX simulation. Horizontal temperature and wind variations are displayed with an exobase T+(U,V) plot at z = 6.0 (230 km dayside; 190 km nightside), showing the horizontal wind pattern and underlying temperature structure; maximum arrow corresponds to 305 m/s. Exospheric temperatures range from a nightside minimum (141 K) to a dayside maximum (327 K), yielding a day-night contrast of 187 K. Cold (~113-135 K) mesopause temperatures (not shown) appear on the dayside over 90-110 km. Taken from Bougher et al., [1999b]

for comparison to Earth and Venus (see Figures 5 and 10).

4.1.3. TIE-GCM. A composite of TIE-GCM temperature profiles for all three solar cycle cases for dayside and nightside local times is presented in Figure 16a [e.g., *Bougher et al.*, 1999b]. Low auroral activity parameters were chosen for implementation in each of these TIE-GCM cases in order to focus upon the model variations due to solar EUV/UV flux variability (see section 3.3). These TIE-GCM temperature profiles are compared with MSIS-90 empirical model values [*Hedin*, 1991]. TIE-GCM dayside exospheric temperatures are calculated to vary from 900 to 1475 K (575 K) over the solar cycle. This solar cycle exospheric temperature variation is much larger than observed and calculated for Venus and Mars (see Figures 11a and 14a). SMAX (1475 K) and SMIN (900 K) values of TIE-GCM dayside exospheric temperatures are in rough agreement with comparable MSIS values (1423 and 835 K, respectively). Similarly, nightside SMAX (1100 K) and SMIN (720 K) values of TIE-GCM exospheric temperatures are in approximate agreement with MSIS values (1025 and 650 K, respectively). Recall that the Earth's EUV/UV heating efficiency is much larger than for either Venus or Mars (see section 3.3), resulting in much warmer terrestrial thermospheric temperatures [*Bougher and Roble*, 1997]. In addition, the large vertical temperature gradient from 100 to 300 km suggests that molecular thermal conduction is the dominant cooling agent throughout most of the terrestrial thermosphere during low auroral activity conditions [e.g., *Roble et al.*, 1987; *Bougher and Roble*, 1997].

Figure 16b illustrates a composite of $O/(N_2 + O_2)$ mixing ratio profiles for SMIN and SMAX TIE-GCM cases for identical dayside and nightside local times [e.g., *Bougher et al.*, 1999b]. The thermospheric densities which comprise this ratio are controlled by dynamical processes above ~150 km (global winds and diffusion). As such, the variation of EUV/UV fluxes over the solar cycle results in an elevated mixing ratio for SMIN conditions. Below 150 km, O abundances increase photochemically by only a few percent with the advance of the solar cycle. This weak variation is particularly noteworthy since this is the region where NO

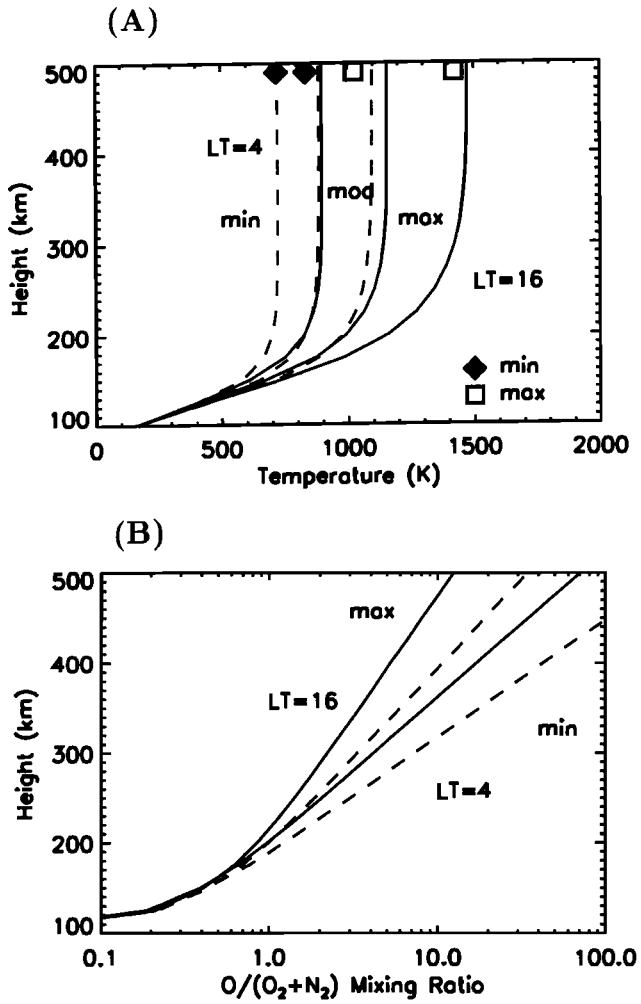

Figure 16. TIE-GCM equatorial fields and their variations over the solar cycle. Curves are delineated as follows : LT=1600 (solid) and LT=0400 (dashed), for SMIN, SMED, and SMAX cases. (a) temperature profiles over 100 to 500 km for SMIN, SMED, and SMAX cases; (b) $O/(N_2 + O_2)$ profiles over 100 to 500 km for the SMIN and SMAX cases. Taken from Bougher et al., [1999b]

(4.3-μm) and CO_2 (15-μm) cooling contribute to the thermal budget [e.g. *Bougher et al.*, 1994]. In short, Earth IR cooling agents (100-170 km) are not throttled by O abundance variations over the solar cycle, in stark contrast to the CO_2 cooling for Venus (see Figure 11b).

Dayside thermospheric temperatures for Earth are not greatly affected by either CO_2 15-μm cooling or dynamical thermostats, with molecular conduction instead providing the bulk of the cooling that offsets increasing EUV heating as the solar cycle advances (see Figure 12c). In particular, terrestrial IR (CO_2) cooling is important only below 130 km, well removed from the peak Earth heating at higher altitudes [*Roble et al.*, 1987; *Bougher et al.*, 1994]. For these quiet auroral conditions, the Earth solar cycle exospheric temperature variation on the dayside (550-600K) is the largest of the three planets (see Figure 16a), owing to the inefficient role of conduction as a thermostat. This weak thermostatic control also results in the rather sluggish (~5-day) equilibration of Earth dayside temperatures (above 300 km) due to solar perturbations [*Bougher et al.*, 1999b]. The important contribution of CO_2 15-μm cooling below 130 km implies that the Earth lower thermosphere does not require significant eddy heat conduction, consistent with independent estimates of a weak mesopause eddy diffusion coefficient.

The long-term implications of mesosphere thermosphere CO_2 15-micron cooling were addressed by *Roble and Dickinson*, [1989] and *Risbeth and Roble*, [1992]; both studies estimated the effect on the mesosphere and thermosphere of the predicted doubling of the mixing ratios of CO_2 and CH_4 over the next 100-years. These calculations revealed a cooling at 400 km of ~50K in thermospheric temperatures over the next century. A correspondingly large reduction in densities at 400 km (factor of 2) was also predicted. Clearly, the fidelity of these calculations estimating the greenhouse cooling effect on the Earth's upper atmosphere depends on the O-CO_2 relaxation rate assumed for simulating CO_2 cooling rates. The success of the TGCM simulations of Venus, Earth, and Mars for reproducing realistic heat budgets and observed thermal structures (using a common CO_2-O relaxation rate) has helped constrain the Earth's greenhouse CO_2 cooling rates as well [*Bougher et al.*, 1999b].

The global thermospheric wind pattern for Earth is well constrained by spacecraft and ground-based observations [*Hedin et al.*, 1991]. Figure 17 illustrates the behavior of the TIE-GCM temperatures and winds near the exobase for SMAX conditions [*Bougher et al.*, 1999b]. Low to midlatitude exospheric temperatures peak at 1480 K (LT=1500-1600) with a minimum at 1064 K (LT=0400). Notice that winds diverge (strong upwelling) near LT=1500-1600 on the equator, and converge (strong subsidence) after mid-night near the equator. This EUV driven asymmetric circulation pattern is similar to that of Mars and is the result of symmetric solar heating plus the Earth's rotation. Upwelling gives rise to modest adiabatic cooling in the midafternoon (molecular conduction generally dominates). However, the corresponding subsidence and heating just after midnight is substantial; i.e. a tongue of warm air is visi-

ble near the equator after midnight due to this adiabatic heating. This feature has been termed the "midnight temperature maximum (MTM)" and has been the focus of various studies that include seasonal tidal structures properly incorporated at the bottom boundary of TGCM codes [e.g., *Fesen et al.*, 1986; *Fesen*, 1996; *Colerico et al.*, 1996]. It is likely that some combination of in-situ and upward propagating tidal structures are responsible for the maintenance of the equatorial MTM above 200 km. Similar MTM features may also be present on Mars near its equator [*Bougher et al.*, 1993]. The rather large day-to-night temperature contrast at low to midlatitudes (~400 K) drives horizontal winds reaching nearly 250-300 m/s. Furthermore, these wind magnitudes do not change appreciably over the solar cycle, due to the corresponding variation in the importance of ion drag. *Hagan and Oliver* [1985] conclude that the solar cycle variation of ion drag modulates the overall adiabatic cooling efficiency of the thermosphere; the resulting impact on the thermal structure minimizes the wind variations over the solar cycle.

4.2. Solstices : Earth and Mars

TGCM simulations have also focused on extreme solstice situations for Earth and Mars to illustrate the obvious differences and similarities in global thermospheric wind and temperature distributions. It is clear that solstice conditions drive strong inter-hemispheric flow for both the Earth and Mars thermospheres (e.g. Figure 10). Seasonal-solar cycle extremes in Mars exospheric temperatures are calculated to range from 200 to 380 K, corresponding to SMIN (plus aphelion) and SMAX (plus perihelion) conditions, respectively (see Figure 18). These temperature variations drive maximum horizontal winds of nearly 215 to 400 m/s. Corresponding extremes in Earth exobase temperatures are 800 to 1600 K, yielding rather small variations in global winds. The orbital eccentricities (alone) for Earth and Mars are shown to drive substantial variations in their thermospheric temperatures. For Mars, dayside exobase temperatures vary by ~60 K (18%) from aphelion to perihelion during SMAX conditions (see Figure 18). Such large temperature variations strongly impact thermospheric densities and winds over the Mars year. The corresponding Earth dayside temperatures also vary by 60-80 K between solstices. However, the percent temperature variation (5%) over the Earth's orbit and its overall impact on the thermospheric structure and winds are much smaller [*Bougher et al.*, 2000]. Auroral activity may in fact obscure the impact of these orbital variations on the Earth's thermospheric structure and dynamics.

5. SIMULATIONS ILLUSTRATING IMPACTS OF UNIQUE FORCINGS

5.1. Venus : Maintenance of the Nightside Cryosphere

The large day-to-night temperature (and corresponding pressure) gradients in the thermosphere of Venus were expected to drive very strong SS-AS thermospheric winds, reaching nearly 400 m/s [*Dickinson and Ridley*, 1977]. However, the global circulation of the Venus upper atmosphere is much weaker than originally expected, and can be decomposed into two distinct flow patterns : (1) a stable SS-AS circulation cell driven by solar EUV/UV heating, and (2) an asymmetric retrograde superrotating zonal (RSZ) flow that seems to vary greatly over time (see Figures 5-7) [*Bougher et al.*, 1997b]. The typically retrograde sense of this asymmetric (RSZ) flow and its time variation are confirmed by various airglow observations [e.g. *Bougher et al.*, 1997b]. In addition, the initial concept of a solely pressure-driven wind system does not permit cold nightside temperatures (100-130 K) to exist, owing to the very strong nightside adiabatic heating that results. Instead, it is believed that upward propagating gravity waves launched at cloud-tops carry their momentum to Venus thermospheric altitudes where they break and provide a net drag force on the SS-AS wind pattern [*Alexander*, 1992; *Bougher et al.*, 1997b]. The SS-AS wind speeds are reduced, further isolating the nightside from the dayside and decreasing the nightside adiabatic heating (and temperatures) [*Bougher*, 1995]. A local time asymmetry in the gravity wave drag enables the net Venus thermospheric circulation to mimic superrotating flow yielding the observed helium and nightglow distributions (see Figures 5-7). A viable gravity wave drag mechanism must account for both the reduced SS-AS wind speeds as well as the asymmetry in the thermospheric global wind pattern implied by various temperature, density and airglow measurements [*Bougher et al.* 1997b].

Venus gravity wave drag research has generally followed studies of gravity wave effects in the Earth's upper atmosphere. Since *Lindzen*, [1981] developed a parameterization for gravity wave dissipation and momentum flux convergence (using saturation theory), there has been a growing acceptance of the fundamental control these processes have on the composition and circulation in the Earth's mesosphere and lower thermosphere [e.g. *Holton*, 1982]. All of the essential physics captured in the Lindzen-Holton parameterization should also apply on Venus. *Alexander*, [1992] hypothesized that the primary source region for waves that break in the Venus thermosphere is near the cloud

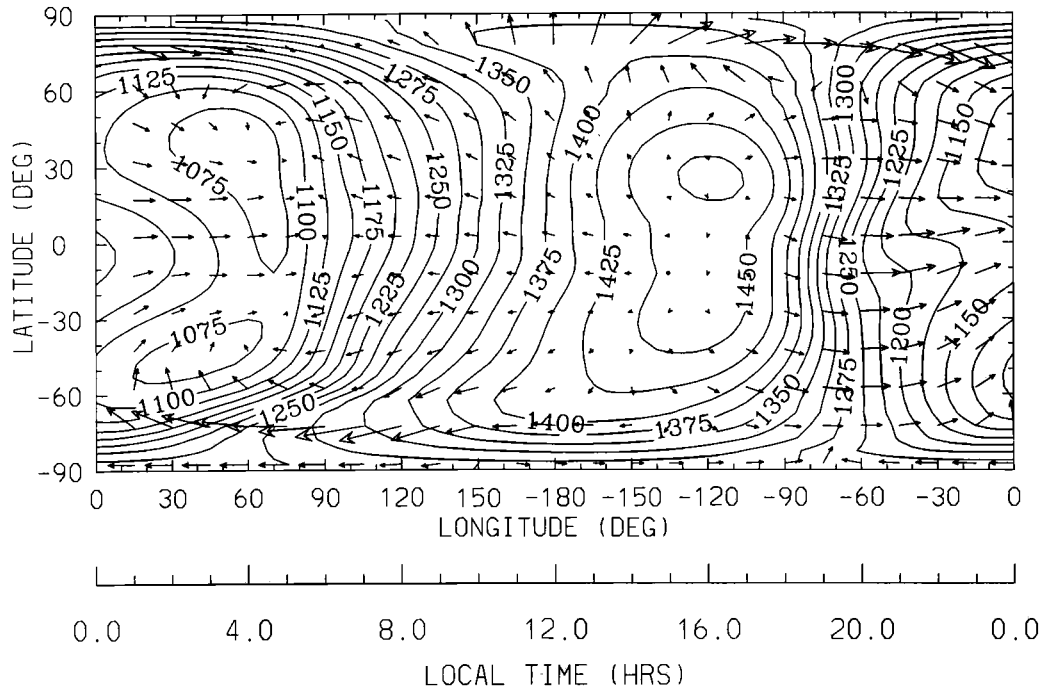

Figure 17. TIE-GCM SMAX simulation. Horizontal temperature and wind variations are displayed with an exobase T+(U,V) plot at z = 7.0, showing the horizontal wind pattern and underlying temperature structure; maximum arrow corresponds to 477 m/s. Exospheric temperatures range from a nightside minimum (1064 K) to a dayside maximum (1481 K), yielding a day-night contrast of 417 K. Cold (~160 K) mesopause temperatures (not shown) appear near 100 km. Taken from Bougher et al., [1999b]

tops. Since strong westward zonal winds with speeds $\overline{u} \sim 100$ m s $^{-1}$ prevail at these altitudes, gravity waves forced in this region will likely have large westward phase speeds also, $c \sim 100$ m s $^{-1}$. This simple hypothesis along with the Lindzen-Holton gravity wave parameterization predicts strong asymmetries in both wave drag and eddy diffusion in the thermosphere as a function of local time, arising from the interaction of the gravity waves with the local SS-AS thermospheric flow. Qualitatively, then, it is expected that for $c \sim 100$ m s^{-1}, the drag and diffusion will be much larger at morning local times than at corresponding afternoon times.

Fritts and Lu, [1993] described a spectral parameterization based on empirical observations of gravity waves in the Earth's atmosphere and saturation theory. This spectral gravity wave formulation was recently modified for application to the Venus thermosphere within the VTGCM [*Zhang et al.*, 1996]. Initial VTGCM sensitivity tests using the Fritts-Lu scheme reveal that the magnitude of the gravity wave drag peaking at the 130-140 km level (~0.0175 m/s^2) is crucial to effectively slowing down the SS-AS winds. A VTGCM asymmetric case displaying dusk (+210 m/s) and dawn (-180 m/s) wind speeds at 140 km is consistent with (a) the convergence of zonal winds near 0230 local time, and (b) the observed Venus O_2 nightglow distributions [*Zhang et*

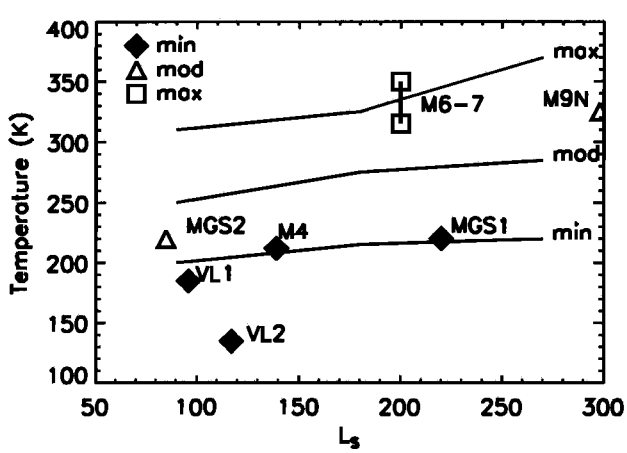

Figure 18. Mars exosphere temperatures at LT = 1500 near the equator. Exospheric temperatures over the solar cycle (symbols) and seasons (Ls) from various spacecraft measurements are compared to MTGCM simulations (solid lines). Spacecraft abbreviations are described in Table 2. Taken from Bougher et al., [2000]

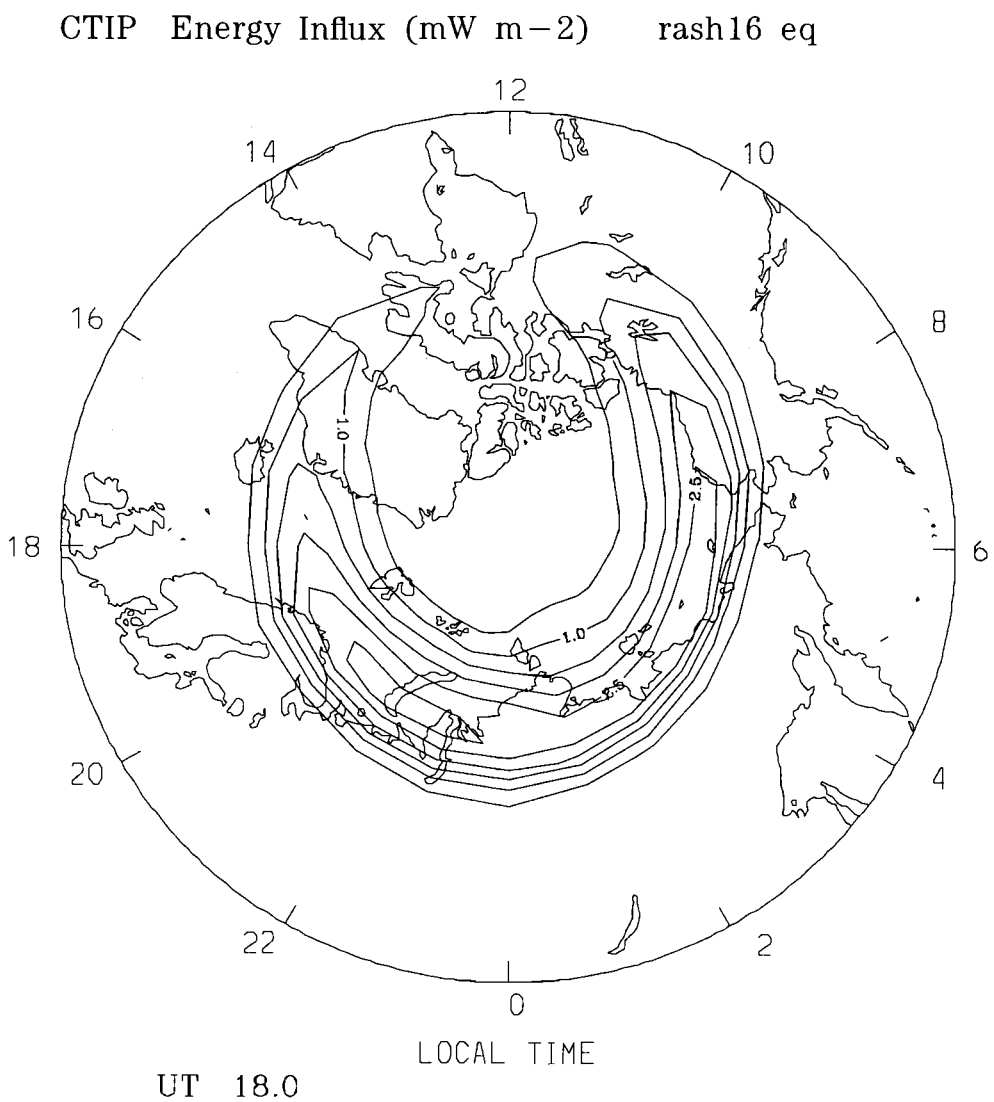

Figure 19. CTIP model fields on a polar dial with perimeter latitude = 50° : (a) Statistical pattern of auroral energy influx for average geomagnetic conditions; energy flux units of mW m^{-2} (maximum = 3 mW m^{-2}, interval = 0.5) [Fuller-Rowell and Evans, 1987]; (b) Typical pattern of ion convection velocities for average solar wind and geomagnetic conditions; maximum wind vector = 700 m s^{-1} [Weimer, 1995]

al., 1996]. Thus, gravity wave momentum flux convergence in the Venus thermosphere provides a promising in-situ mechanism for slowing SS-AS wind speeds plus producing the thermospheric superrotation [*Bougher et al.*, 1997b]. However, wave drag is poorly constrained at this time. Further investigation requires detailed sampling of Venus atmospheric winds above the cloud tops.

5.2. Earth : Auroral Forcing and Magnetospheric Convection

The geomagnetic energy source for the Earth's upper atmosphere is unique to the terrestrial planets [e.g. *Bougher and Roble*, 1997]. Figure 19a shows the statistical pattern of auroral energy influx for average geomagnetic conditions (from Tiros satellite data). The energy is deposited in an "oval" with a radius of around 20° latitude, and a peak energy influx of just a few ergs m^{-2} s^{-1} occurring on the nightside. This statistical model cannot capture narrowly distributed structure, but rather somewhat broader features. The combination of elevated Pedersen conductivity and the high ion convection produces Joule heating, which provides the bulk of the geomagnetic energy source in the Earth's thermosphere. The collisional interaction of the con-

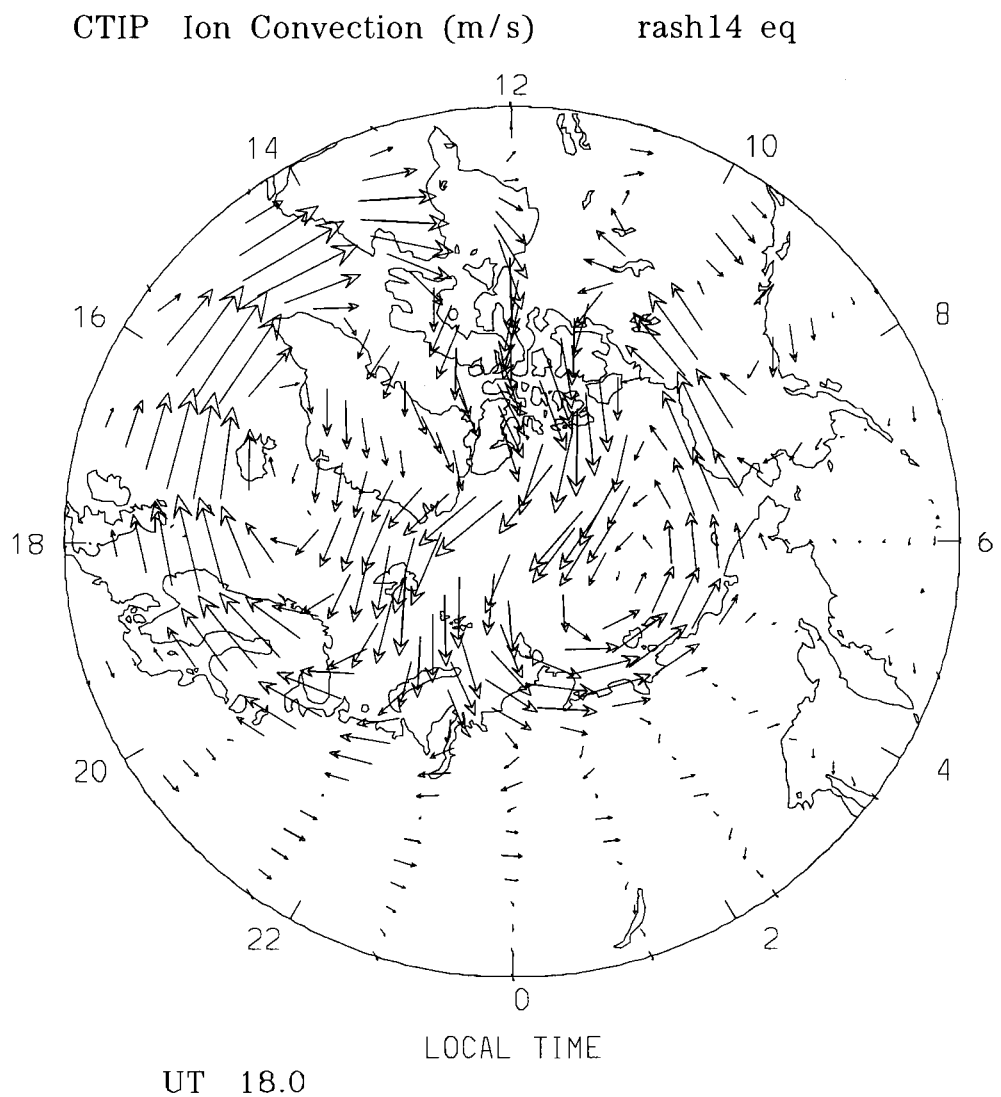

Figure 19. (Continued.)

vecting ions with the neutral gas provides a potentially significant momentum source, driving neutral winds to a level not seen anywhere else on the terrestrial planets. Figure 19b also shows the pattern of ion convection velocities expected in the upper atmosphere for average solar wind and geomagnetic conditions, from the *Weimer,* [1995] empirical model. The pattern shows the characteristic two-cell structure with anti-sunward flow over the polar cap and sunward flow in the dawn and dusk sectors of the auroral oval. Peak ion velocities are in excess of 0.7 km s^{-1}.

The Earth's upper atmosphere responds to this geomagnetic energy source in a number of ways. The response of the winds and temperatures at high latitudes in the upper thermosphere can be seen in Figure 20. The ion drag momentum source drives the neutral wind in a two-cell pattern, and accelerates the winds to several hundred meters per second. The two-cell structure is less clear in the neutral wind because of the action of the Coriolis force. The natural tendency of the gas is to move clockwise in the northern hemisphere so the winds respond resonantly to the dusk ion convection call. This inertial resonance makes a substantial contribution to the asymmetry in the neutral wind response in the dawn and dusk sectors of the auroral oval. The polar temperature structure is also shown in Figure 20. Joule heating from the geomagnetic source is four or five times larger than the direct auroral particle heating, and raises the temperature by 100 to 200 K at high latitude.

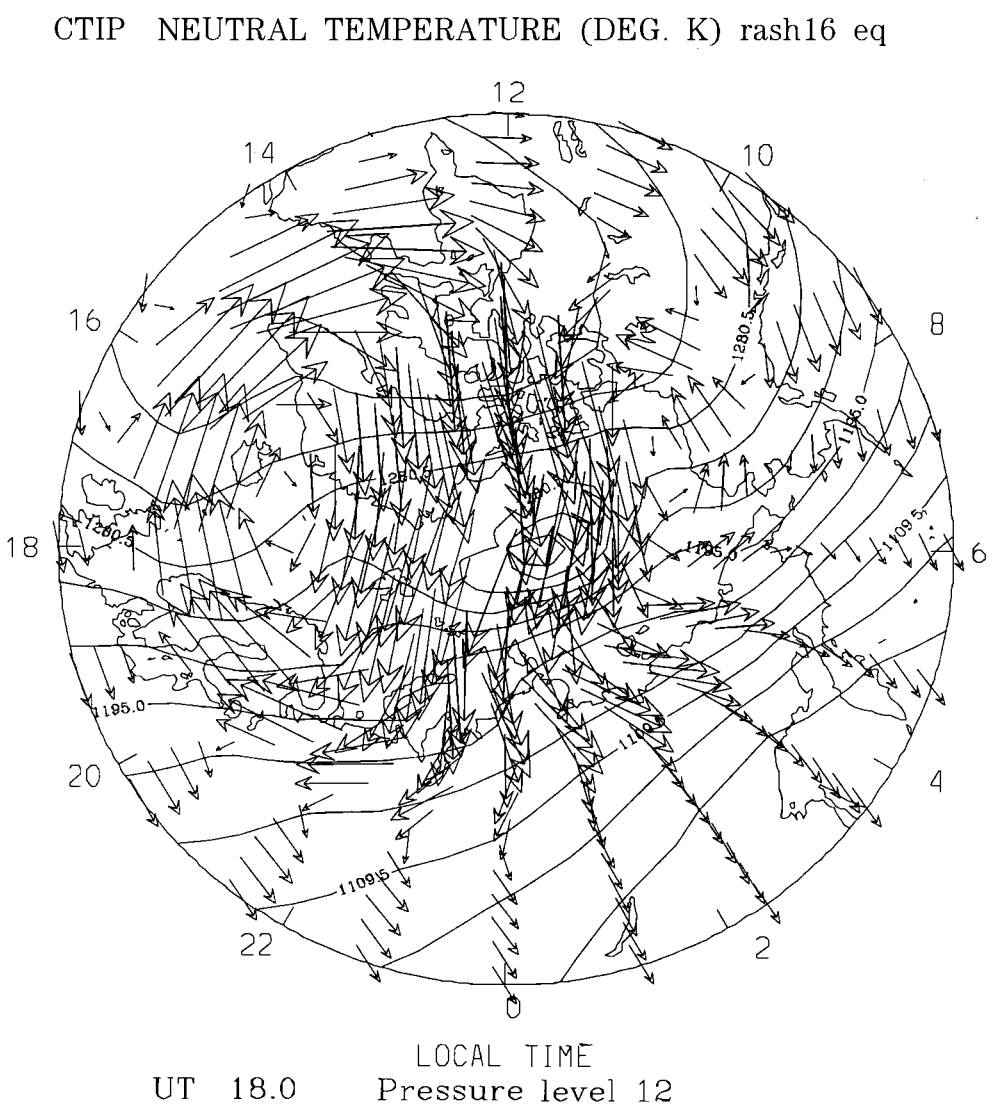

Figure 20. CTIP model fields on a polar dial with perimeter latitude = 50° : Polar wind and temperature distributions due to typical geomagnetic energy sources; temperature range = 1024 - 1366K, maximum wind vector = 450 m s^{-1}.

The geomagnetic energy source also has an impact on the global thermospheric wind and temperature distribution. The polar temperatures are raised, tending to balance or reverse the conventional equator-to-pole, zonally averaged temperature and pressure gradients. When the level of geomagnetic activity is high, the deposition of Joule heating can fundamentally change the direction of global circulation from poleward to equatorward (see Figure 10). The enhanced polar temperature elevates the mixing ratios of the molecular species N_2 and O_2 firstly due to thermal expansion of the hotter gas but also due to the change in the global circulation. A prevailing equatorward circulation cell is balanced by upwelling at high latitudes and downwelling at low latitudes. Upwelling enhances the heavy molecular species relative to the lighter atomic species, and downwelling does the reverse.

During a geomagnetic storm the energy injected from the solar wind and magnetosphere can exceed that from the total solar EUV radiation (2-6 x 10^{11} W). During geomagnetic storm periods, which are typically of the order of a day, the thermosphere and ionosphere change dramatically. When a storm occurs, auroral particle precipitation increases in magnitude and expands to

lower latitudes than normal, and the magnetospheric electric field mapped to the atmosphere intensifies and expands in concert with the aurora. Joule heating can increase from tens of gigawatts (1-10 x 10^{10} W) during quiet times, to hundreds of gigawatts (1-10 x 10^{11} W) during severe geomagnetic disturbances. The combined auroral/Joule input can dump thousands of terajoules of energy into the upper atmosphere during the course of a storm, and can raise the temperature of the gas by hundreds of degrees Kelvin. Ionospheric ions drifting in response to the electric field can drive winds in excess of 1 km/s at high latitudes. Changes in the global thermosphere winds and composition are largely responsible for the persistent storm-time ionospheric changes [*Buonsanto*, 1999; *Fuller-Rowell et al.*, 1997].

5.3. Mars : Dust Storm Impacts on the Thermosphere

Martian dust events are observed to have a significant impact on the lower atmosphere temperature structure through aerosol heating [e.g. *Zurek et al.*, 1992]. These events may include regional storms (at least one per martian year), or global encircling and planet-wide dust storms (maybe one every 3-martian years). The precise sequence of events leading to the initiation and growth of Mars dust storms is not well understood [*Zurek et al.*, 1992]. Even though dust particles do not reach thermospheric heights, the remote effects of a dusty Mars lower atmosphere are clearly experienced aloft [see *Keating et al.*, 1998a; *Bougher et al.*, 1999a,b]. The seasonal expansion and contraction of the Mars lower atmosphere due to solar IR heating results in a ~15 km variation of a reference pressure surface in the thermosphere from aphelion to perihelion (Figure 21) [*Bougher et al.*, 1999a; 2000]. The resulting expansion (contraction) of the atmosphere through the onset (decay) of a dust storm event is also communicated to thermospheric altitudes via hydrostatics, producing significant departures from this seasonal trend. The observed rise and fall of thermospheric densities (at a constant altitude) during a dust event can be dramatic [*Keating et al.*, 1998a]. The corresponding heights of constant pressure levels are seen to rise and fall during a dust event by as much as 8-20 km, in concert with the variation of the dayside (photochemical) ionospheric peak heights [*Bougher et al.*, 2001]. Finally, the Hadley circulation of the Mars deep lower atmosphere is enhanced during a dust event such that global scale winds are strengthened, upward propagating planetary wave and tidal amplitudes are enhanced, and the martian lower thermosphere is significantly perturbed [*Stewart et al.*, 1992; *Keating et al.*, 1998a].

MGS aerobreaking witnessed the onset, rise, and decay of the "Noachis" regional dust storm event (southern hemisphere), and the corresponding responses of the lower atmosphere temperatures, dust opacities, and upper atmosphere densities [*Keating et al.*, 1998a; *Bougher et al.*, 1999a]. Throughout this storm (Ls ~ 224 to 270), the thermospheric density increases (decreases) coincided with the warming (cooling) and hydrostatic expansion (contraction) of the lower atmosphere. A 3-fold increase in 130 km densities was observed by the Accelerometer at 40N latitude, approximately 2 to 3-orbits after the Noachis storm was first detected. This thermospheric response occurred in concert with a doubling of dust opacities in Northern mid-latitudes [e.g. *Christensen et al.*, 1998], and an increase of temperatures at ~30 km of at least 10-15 K [e.g. *Keating et al.*, 1998a]. An ~8 km expansion of the atmosphere was seen during the first few days of the storm. This Noachis storm event and its atmospheric impacts were rather short lived (8-10 weeks) compared to the 3-4 month abatement of the 1971-72 global dust storm [e.g. *Stewart et al.*, 1992].

The dynamical and radiative processes that drive this global connection, spanning the lower and upper atmospheres on such short time scales, are important to explain. Coupled MGCM and MTGCM simulations have thusfar been unsuccessful in capturing both the observed magnitude (factor of 3) and timescale (2-3

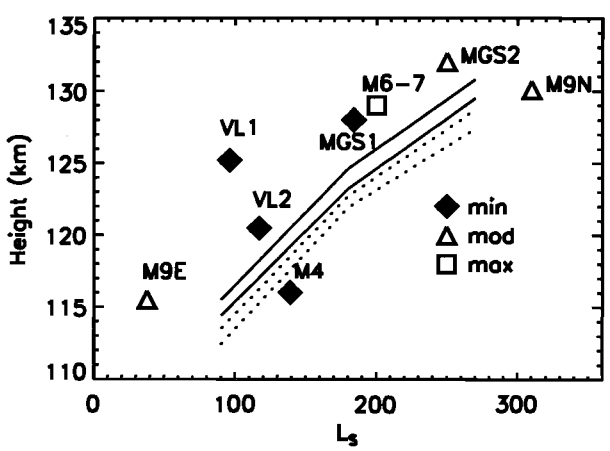

Figure 21. Reference pressure (1.26-nanobar) heights for dayside solar zenith angles (SZA) as a function of Mars season (Ls). MTGCM curves for SZA = 0° (solid) and 60° (dotted) are displayed for SMAX (top) and SMIN (bottom) conditions. Various spacecraft observations are compared to these MTGCM "dust-free" simulations. See Table 2 for a summary of Mars and solar flux parameters for each of these observing periods. Taken from Bougher et al., [2000]

day) for the responses of the Mars thermospheric densities to this Noachis storm event [*Bougher et al.*, 1999a]. These results suggest several shortcomings of the coupled MGCM and MTGCM simulations that include: (a) missing aerosol (below 30 km) and dynamical heating (above 60 km), and (b) insufficient wave coupling effects, including longitudinally fixed non-migrating tides and gravity waves. Certainly, a better scheme of coupling the MTGCM and MGCM codes is needed that permits all waves to propagate vertically into the Mars upper atmosphere.

6. CONCLUSIONS

This chapter provides a comparison of the structure, dynamics, and associated processes of the Venus, Earth, and Mars thermospheres. Clearly, the geocentric perspective when applied to other planetary thermospheres must be revised as new planetary data and TGCM simulations combine to challenge our understanding of thermospheric processes in new planetary environments. It is noteworthy that a more comprehensive comparison of these 3-planet thermospheres awaits the acquisition of Mars global composition, temperature, and wind measurements from upcoming spacecraft missions (e.g. Nozomi, Mars Express, DYNAMO). The present lack of a Mars thermospheric empirical model (like those of Venus and Earth) is a major shortcoming in our understanding of terrestrial planet thermospheres. In the future, TGCM modeling efforts must be extended to compare the planetary scale waves and tides propagating upward from the lower to the upper atmospheres of Venus, Earth, and Mars. This coupling of lower to upper atmospheric regions is best addressed using ground to exobase Whole Atmosphere Climate Models (WACMs), which should be designed to capture the physics of the entire atmosphere. Progress is underway toward the development of such codes for both Earth and Mars.

Acknowledgments. The Editor would like to thank the reviewer of this manuscript.

REFERENCES

Acuna, M. H., et al., Magnetic field and plasma observations at Mars: Initial results of the Mars Global Surveyor Mission, *Science, 279*, 1676-1680, 1998.

Alexander, M. J., A mechanism for the Venus thermospheric superrotation, *Geophys. Res. Lett., 19*, 2207-2210, 1992.

Barth, C. A., A. I. F. Stewart, S. W. Bougher, D. M. Hunten, S. A. Bauer, and A. F. Nagy, *Mars, chap. 30, Aeronomy of the Current Martian Atmosphere*, pp. 1054-1089, Univ. of Ariz. Press, Tucson, 1992.

Bougher, S. W., Comparative thermospheres: Venus and Mars, *Adv. Space Res., 15(4)*, 21-45, 1995.

Bougher, S. W., and W. J. Borucki, Venus O_2 visible and IR nightglow: Implications for lower thermosphere dynamics and chemistry, *J. Geophys. Res., 99*, 3759-3776, 1994.

Bougher, S.W., and R.G. Roble, Comparative terrestrial planet thermospheres, 1, Solar cycle variation of global mean temperatures, *J. Geophys. Res., 96*, 11045-11055, 1991.

Bougher, S. W., and R. G. Roble, Thermosphere, pp. 819-825, in *The Encyclopedia of Planetary Sciences*, edited by J. H. Shirley and R. W. Fairbridge, Chapman and Hall, New York, 1997.

Bougher, S. W., R. E. Dickinson, E. C. Ridley, R. G. Roble, Venus mesosphere and thermosphere, III, Three dimensional general circulation with coupled dynamics and composition, *Icarus, 73*, 545-573, 1988.

Bougher, S. W., J. C. Gerard, A. I. F. Stewart, and C. G. Fesen, The Venus nitric oxide night airglow: Model calculations based on the Venus Thermospheric General Circulation Model, *J. Geophys. Res., 95*, 6271-6284, 1990a.

Bougher, S. W., R. G. Roble, E. C. Ridley, and R. E. Dickinson, The Mars thermosphere, II, General circulation with coupled dynamics and composition, *J. Geophys. Res., 95*, 14811-14827, 1990b.

Bougher, S. W., E. C. Ridley, C. G. Fesen, and R. W. Zurek, Mars mesosphere and thermosphere coupling: Semidiurnal tides, *J. Geophys. Res., 98*, 3281-3295, 1993.

Bougher, S. W., D. M. Hunten, and R. G. Roble, CO_2 cooling in terrestrial planet thermospheres, *J. Geophys. Res., 99*, 14609-14622, 1994.

Bougher, S. W., J. M. Murphy, and R. M. Haberle, Dust storm impacts on the Mars upper atmosphere, *Adv. Space Research, 19(8)*, 1255-1260, 1997a.

Bougher, S. W., M. J. Alexander, and H. G. Mayr, Upper atmosphere dynamics: Global circulation and gravity waves, in *Venus II*, edited by S. W. Bougher, D. M. Hunten, and R. J. Phillips, chap. 2.4, pp. 259-292, Univ. of Ariz. Press, Tucson, 1997b.

Bougher, S. W., et al., Mars Global Surveyor aerobraking: Atmospheric trends and model interpretation, *Adv. Space Res., 23* (11), 1887-1897, 1999a.

Bougher, S. W., S. Engel, R. G. Roble, and B. Foster, Comparative terrestrial planet thermospheres, 2, Solar cycle variation of global structure and winds at equinox, *J. Geophys. Res., 104*, 16,591-16,611, 1999b.

Bougher, S. W., S. Engel, R. G. Roble, and B. Foster, Comparative terrestrial planet thermospheres, 3, Solar cycle variation of global structure and winds at solstices, *J. Geophys. Res., 105*, 17,669-17,692, 2000.

Bougher, S. W., D. P. Hinson, J. M. Forbes, and S. Engel, MGS Radio Science electron density profiles and implications for the neutral atmosphere, *Geophys. Res. Lett., 28*, 3091-3094, 2001.

Bridger, A. F. C., and J. R. Murphy, Mars' surface pressure tides and their behavior during global dust storms, *J. Geophys. Res., 103*, 8587-8601, 1998.

Buonsanto, M.J., Ionospheric storms ? A review. *Space Sci. Rev., 88*, 563, 1999.

Christensen, P. R., et al., Results from the Mars Global Surveyor Thermal Emission Spectrometer, *Science, 279*, 1692-1698, 1998.

Colerico, M., et al., Coordinated measurements of F region dynamics related to the thermospheric midnight temperature maximum, *J. Geophys. Res., 101*, 26783-26794, 1996.

Dickinson, R. E., and E. C. Ridley, Venus mesosphere and thermosphere temperature structure: II. Day-night variations, *Icarus, 30*, 163-178, 1977

Dickinson, R. E., E. C. Ridley, and R. G. Roble, A three dimensional general circulation model of the thermosphere, *J. Geophys. Res., 86*, 1499-1512, 1981.

Dickinson, R. E., E. C. Ridley, and R. G. Roble, Thermospheric general circulation with coupled dynamics and composition, *J. Atmos. Sci., 41*, 205-219, 1984.

Fesen, C. G., Simulations of the low-latitude midnight temperature maximum, *J. Geophys. Res., 101*, 26863-26874, 1996.

Fesen, C. G., R. E. Dickinson, and R. G. Roble, Simulation of thermospheric tides at equinox with the National Center for Atmospheric Research thermospheric general circulation model, *J. Geophys. Res., 91*, 4471-4489, 1986.

Forbes, J. M., Atmospheric tides, 1, Model description and results for the solar diurnal component, *J. Geophys. Res., 87*, 5222-5240, 1982.

Fox, J. L., Heating efficiencies in the thermosphere of Venus reconsidered, *Planet. Space Sci., 36*, 37, 1988.

Fox, J. L., and S. W. Bougher, Structure, luminosity, and dynamics of the Venus thermosphere, *Space Sci. Rev., 55*, 357-489, 1991.

Fox, J. L., and A. Dalgarno, Ionization, luminosity, and heating of the upper atmosphere of Mars, *J. Geophys. Res., 84*, 7315-7331, 1979.

Fox, J. L., and A. Dalgarno, Ionization, luminosity, and heating of the upper atmosphere of Venus, *J. Geophys. Res., 86*, 629-639, 1981.

Fritts, D. C. and W. Lu, Spectral estimates of gravity wave energy and momentum fluxes, Part II: Parameterization of wave forcing and variability, *J. Atmos. Sci., 50*, 3695, 1993.

Fuller-Rowell, T. J. and D. S. Evans, Height-integrated Pedersen and Hall conductivity patterns inferred from the TIROS/NOAA satellite data, *J. Geophys. Res., 92*, 7606-7618, 1987.

Fuller-Rowell, T. J. and D. Rees, A three dimensional, time-dependent, global model of the thermosphere, *J. Atmos. Sci., 37*, 2545, 1980.

Fuller-Rowell T. J., D. Rees, S. Quegan, R. J. Moffett, M. V. Codrescu, and G. H. Millward, A coupled thermosphere ionosphere model (CTIM), *Handbook of Ionospheric Models, STEP Report*, editor R. W. Schunk, 1996.

Fuller-Rowell, T. J., M. V. Codrescu, R. G. Roble, and A. D. Richmond, How does the thermosphere and ionosphere react to a geomagnetic storm, *AGU Geophysical Monograph 98 on Magnetic Storms*, 203-225, 1997.

Hagan, M. E., and W. L. Oliver, Solar cycle variability of exospheric temperature at Millstone Hill between 1970 and 1980, *J. Geophys. Res., 90*, 12265-12270, 1985.

Hanson, W. B., S. Sanatani, and D. R. Zuccaro, The Martian ionosphere as observed by the Viking retarding potential analyzers, *J. Geophys. Res., 82*, 4351-4363, 1977.

Hedin, A. E., Extension of the MSIS thermosphere model into the middle and lower atmosphere, *J. Geophys. Res., 96*, 1159-1172, 1991.

Hedin, A. E., H. B. Niemann, W. T. Kasprzak, and A. Seiff, Global empirical model of the Venus thermosphere, *J. Geophys. Res., 88*, 73-83, 1983.

Hedin, A. E., et al., Revised global model of thermosphere winds using satellite and ground-based observations, *J. Geophys. Res., 96*, 7657-7688, 1991.

Holton, J. R., The role of gravity wave induced drag and diffusion in the momentum budget of the mesosphere, *J. Atmos. Sci., 39*, 791, 1982.

Kasprzak, W. T., G. M. Keating, N. C. Hsu, A. I. F. Stewart, W. B. Coldwell, and S. W. Bougher, Solar cycle behavior of the thermosphere, in *Venus II*, edited by S. W. Bougher, D. M. Hunten, and R. J. Phillips, Chap. 2.3, pp. 225-258, Univ. of Ariz. Press, Tucson, 1997.

Keating, G. M., and N. C. Hsu, The Venus atmospheric response to solar cycle variations, *Geophys. Res. Lett., 20*, 2751-2754, 1993.

Keating, G. M., et al., Models of the Venus neutral upper atmosphere: Structure and composition, *Adv. Space Res., 5*, 117-171, 1985.

Keating, G. M., et al., The structure of the upper atmosphere of Mars: In-situ accelerometer measurements from Mars Global Surveyor, *Science, 279*, 1672-1676, 1998a.

Keating, G. M., R. H. Tolson, T. J. Schellenberg, N. C. Hsu, and S. W. Bougher, Study of Venus upper atmosphere using Magellan drag measurements, *Second Annual Progress Rep. NAG5-6081*, NASA, Washington, D. C., 1998b.

Keating, G. M. et al., MGS-M-ACCEL-5-ALTITUDE-V1.0, *NASA Planetary Data System*, 2001.

Lindzen, R. S., Turbulence and stress owing to gravity wave and tidal breakdown, *J. Geophys. Res., 86*, 9707, 1981.

Magalhaes, J. A., J. T. Schofield, and A. Seiff, Results of the Mars Pathfinder atmospheric structure investigation, *J. Geophys. Res., 104*, 8943-8955, 1999.

McLandress, C., G. G. Shepherd, and B. H. Solheim, Satellite observations of thermospheric tides: Results from the Wind Imaging Interferometer on UARS, *J. Geophys. Res., 101*, 4093-4114, 1996.

Mengel, J. G., H. G. Mayr, I. Harris, and Stevens-Rayburn, Non-linear three dimensional spectral model of the Venusian thermosphere with superrotation: II. Temperature, composition, and winds, *Planet. Sp. Sci., 37*, 707-722, 1989.

Millward, G. H., R. J. Moffett, S. Quegan, and T. J. Fuller-Rowell, A coupled thermosphere ionosphere plasmasphere model (CTIP). *Handbook of Ionospheric Models, STEP Report*, editor R. W. Schunk , 1996.

Nier, A. O., and M. B. McElroy, Composition and structure of Mars upper atmosphere: Results from the neutral mass spectrometers on Viking 1 and 2, *J. Geophys. Res., 82*, 4341-4349, 1977.

Paxton, L. J., and D. E. Anderson, Far Ultraviolet Remote Sensing of Venus and Mars, in *Venus and Mars : Atmospheres, Ionospheres, and Solar Wind Interactions, Geophys. Monogr. Ser.*, vol. 66, edited by J. G. Luhmann, M. Tatrallyay, and R. O. Pepin, pp. 113-189, AGU, Washington, D. C., 1992.

Quegan, S., G. J. Bailey, R. J. Moffett, R. A. Heelis, T. J. Fuller-Rowell, D. Rees, and R. W. Spiro, A theoretical study of the distribution of ionization in the high-latitude ionosphere and plasmasphere: First results on the mid-latitude trough and the light ion trough, *J. Atmos. Terr. Phys., 44*, 619, 1982.

Richmond, A. D., E. C. Ridley, and R. G. Roble, A thermosphere/ionosphere general circulation model with coupled electrodynamics, *Geophys. Res. Lett., 19*, 601-604, 1992.

Risbeth, H., and R. G. Roble, Cooling of the upper atmosphere by enhanced greenhouse gases - Modeling of thermospheric and ionospheric effects, *Planet. and Space Science, 40*, 1011-1026, 1992.

Roble, R. G., Chemistry in the thermosphere and ionosphere, *Chemical and Engineering News, 64, #24*, 23-38, 1986.

Roble, R. G., Energetics of the mesosphere and thermosphere, in *The Upper Mesosphere and Lower Thermosphere: A Review of Experiment and Theory, Geophys. Monogr. Ser.*, vol. 87, edited by R. M. Johnson and T. L. Killeen, pp. 1-21, AGU, Washington, D. C., 1995.

Roble, R. G., and R. E. Dickinson, How will changes in carbon dioxide and methane modify the mean structure of the mesosphere and thermosphere?, *Geophys. Res. Lett., 16*, 1441, 1989.

Roble, R. G., and E. C. Ridley, An auroral model for the NCAR thermospheric general circulation model (TGCM), *Ann. Geophys., Ser. A, 5* (6), 369-382, 1987.

Roble, R. G., and E. C. Ridley, A thermosphere, ionosphere, mesosphere, electrodynamics general circulation model (time-GCM) : Equinox solar cycle minimum simulations (30-500 km), *Geophys. Res. Lett., 21*, 417-420, 1994.

Roble, R. G., E. C. Ridley and R. E. Dickinson, Global circulation and temperature structure of the thermosphere with high-latitude convection, *J. Geophys. Res., 87*, 1599-1614, 1982.

Roble, R. G., E. C. Ridley, and R. E. Dickinson, On the global mean structure of the thermosphere, *J. Geophys. Res., 92*, 8745-8758, 1987.

Roble, R. G., E. C. Ridley, A. D. Richmond, and R. E. Dickinson, A coupled thermosphere-ionosphere general circulation model, *Geophys. Res. Lett., 15*, 1325-1328, 1988.

Seiff, A., and D. B. Kirk, Structure of the atmosphere of Mars in summer in mid-latitudes, *J. Geophys. Res., 82*, 4364-4378, 1977.

Stewart, A. I., Mariner 6 and 7 ultraviolet spectrometer experiment: Implications of the CO_2^+, CO, and O airglow, *J. Geophys. Res., 77*, 54-68, 1972.

Stewart, A. I. F., M. J. Alexander, R. R. Meier, L. J. Paxton, S. W. Bougher, and C. G. Fesen, Atomic oxygen in the Martian thermosphere, *J. Geophys. Res., 97*, 91-102, 1992.

von Zahn, U., S. Kumar, H. B. Niemann, and R. Prinn, Composition of the Venus atmosphere, in *Venus*, edited by D. M. Hunten, L. Colin, T. M. Donahue, and V. I. Moroz, pp. 299-430, Univ. of Ariz. Press, Tucson, 1983.

Weimer, D.R., Models of high latitude electric potential derived with the least error fit of spherical harmonic coefficients, *J. Geophys. Res.*, 100, 19595, 1995.

Winchester, C. and D. Rees, Numerical models of the Martian coupled thermosphere and ionosphere, *Adv. Space Res., 15*, 51, 1995.

Wintersteiner, P. P., R. H. Picard, R. D. Sharma, J. R. Winick, and R. A. Joseph, Line-by-line radiative excitation model for the non-equilibrium atmosphere: Application to CO_2 15-μm emission, *J. Geophys. Res., 97*, 18083-18117, 1992.

Zhang, M. H. G., J. G. Luhmann, A. J. Kliore, and J. Kim, A post-Pioneer Venus reassessment of the Martian dayside ionosphere as observed by radio occultation methods, *J. Geophys. Res., 95*, 14829-14839, 1990.

Zhang, S., S. W. Bougher, and M. J. Alexander, The impact of gravity waves on the Venus thermosphere and O_2 IR nightglow, *J. Geophys. Res., 101*, 23195-23205, 1996.

Zurek, R. W., et al., *Mars, chap. 26, Dynamics of the Atmosphere of Mars*, pp. 835-933, Univ. of Ariz. Press, Tucson, 1992.

S. Bougher, Lunar and Planetary Laboratory, Planetary Sciences Department, P.O.B. 210092, University of Arizona, Tucson, AZ 85721. (e-mail: sbougher@lpl.arizona.edu)

R. Roble, High Altitude Observatory, National Center for Atmospheric Research, P.O.B. 3000, Boulder, CO 80309-3000.

T. Fuller-Rowell, NOAA Space Environment Center, 325 Broadway, Boulder, CO 80303.

Thermospheric General Circulation Models for the Giant Planets: The Jupiter Case

G. H. Millward, S. Miller, A. D. Aylward, I. C. F. Müller-Wodarg, and N. Achilleos[1]

Atmospheric Physics Laboratory, University College London, United Kingdom

The upper atmosphere of Jupiter is an extremely complex region in which a unique combination of neutral and ionized gases interact chemically and dynamically. Initial attempts at modeling an "average" Jovian ionosphere as a one dimensional profile have proven successful, though inevitably such models cannot reproduce the more detailed structure. For a more complete analysis it is necessary to use a fully time-dependent global coupled ionosphere-thermosphere model. The Jovian Ionospheric Model (JIM) is the first such model to be developed and is described here. Results are shown detailing both the effects due to solar ionization, and importantly, a strong coupling with Jupiter's magnetosphere which leads to both electron precipitation and strong electric fields within the auroral region.

1. INTRODUCTION

Planets interact with the interplanetary environment through their upper atmospheres, which receive energy inputs from sunlight and high energy particles. Both sources can heat the atmosphere, and also ionize it, providing the incident photon or particle energy is sufficiently high. The result is an outer shell of atmosphere known as the thermosphere, in which the temperature increases with height up to an isothermal limit as the atmospheric density and pressure falls eventually to that of the ambient interplanetary gas. From the thermosphere, incident energy in the form of the extreme ultraviolet portion of the solar spectrum and particles with kilo- (electrons) and mega- (positive ions) electronvolt energies produce an ionosphere.

Although Jupiter is approximately five times further from the Sun than Earth, and so receives only 4% of the sunlight per unit area, it has a very well developed ionosphere as a result of high particle fluxes. These are produced both because the enormous Jovian magnetosphere intercepts a much larger area of the solar wind than does the Earth (by a factor of around 10^4) and, even more significantly, because Jupiter has a local source of particles emanating from the volcanoes of the innermost Galilean moon, Io. Jupiter's ionosphere and thermosphere both commence at the homopause, where convection no longer mixes the atmosphere, and the densities of individual atomic and molecular species are determined by their own independent scale heights. The homopause for Jupiter occurs at a pressure level of around 1 to 2 microbar, where the temperature is roughly 400K. There, for example, the scale height for H_2 is around 140 km, but less than 20 km for methane. The result is that the neutral thermosphere consists entirely of atomic and molecular hydrogen and helium, with the exception of the lowest layers. This makes the Jovian thermosphere a rather simple entity, from a chemical point of view.

Observational studies of Jupiter's upper atmosphere commenced with electron density profiles deduced from the radio science (RSS) data of the Pioneer 10 and 11, and the Voyager 1 and 2 spacecraft [*Fjeldbo* 1975, 1976; *Eshleman et al.*,

[1] Now at Space Division, Logica U.K., London, U.K.

Atmospheres in the Solar System: Comparative Aeronomy
Geophysical Monograph 130

10.1029/130GM18

1979a, 1979b]. Ultraviolet auroral and dayglow emissions were also noted by Voyager and further studied using the International Ultraviolet Explorer for well over a decade [e.g *Clarke et al.*, 1980; *Livengood et al.*, 1992]. More recently, UV studies have been made with the Hubble Space Telescope [e.g., *Ballester et al.*, 1996; *Clarke et al.*, 1998; *Gerard et al.*, 1996] and the Hopkins Ultraviolet Telescope [e.g., *Morresey et al., 1997*].

In the infrared, ground-based observations have located hot spots of hydrocarbon emission in the Jovian auroral regions [e.g., *Caldwell et al.*, 1980; *Kostiuk et al.*, 1987]. Since its first detection outside of the laboratory in Jupiter's southern aurora [*Drossart et al.* 1989], the H_3^+ molecular ion has proved an important tracer of energy inputs into the Jovian ionosphere [e.g., *Baron et al.*, 1996; *Kim et al.*, 1993, *Satoh and Connerney*, 1999] and of the energy balance of the upper atmosphere [e.g., *Miller et al.* 1990; *Miller et al.*, 2000]. Some of the latest H_3^+ studies use detailed image analysis to constrain the Jovian magnetic field parameters [e.g., *Connerney et al.* 1998] and use high resolution spectroscopy to measure auroral/polar ion wind speeds [*Rego et al.* 1999; *Stallard et al.*, 2001].

In short, there exists a wealth of data to both assist in deducing model inputs and for comparison with model outputs. Modeling studies aimed at determining Jupiter's detailed ionospheric structure [e.g., *Atreya et al.*, 1979; *Waite et al.*, 1983; *McConnell and Majeed*, 1987; *Majeed and McConnell*, 1991] have made use of the eight electron density profiles deduced from the Pioneer and Voyager spacecraft. More recently, Jovian ionospheric electron densities have been deduced from the radio science data on the Galileo satellite [e.g., *Hinson et al.*, 1997; *Majeed et al.*, 1999]. In addition, the Voyager UVS data, and measurements from the Galileo atmospheric probe, have provided Jovian thermospheric temperature profiles. Subsequent comparison with theoretical profiles has revealed the importance of various heating and cooling processes in maintaining the high temperatures in the upper thermosphere [e.g., *Atreya et al.*, 1981; *Seiff et al.*, 1997; *Waite et al.*, 1997].

Earlier modeling correctly predicted the importance of H^+ (at higher altitudes) and H_3^+ (between 0.1 and 1.0 μbar) as the main Jovian ions [e.g., *Waite et al.*, 1983; *McConnell and Majeed*, 1987]. Two important results have emerged from the comparison of these modeling studies with the available data. Firstly, the Jovian thermosphere exhibits temperatures higher than those predicted by solar EUV heating alone. Secondly, one-dimensional models, which include the effects of diffusion and chemistry, consistently over-estimate the ionospheric electron density by about an order of magnitude. In addition, the model peaks in electron density are situated at altitudes roughly 1000 km below those observed. Thermospheric winds are regarded as a likely candidate for explaining these discrepancies. It is clear that strong equatorward winds could be driven by the large energy inputs associated with the Jovian auroral regions [*Waite et al.*, 1983]. Both particle precipitation and Joule heating within the Jovian auroral regions have been estimated to be some 10 mW m^{-2}, in contrast with typical solar column heating rates of a few times 10^{-2} mW m^{-2} at the planet's equator [*Atreya*, 1986; *Prangé*, 1992 and references therein].

A thermospheric wind system could transport some of the energy deposited in the auroral zones to the rest of the planet, and so provide the extra heating required to maintain the high thermospheric temperatures. In addition, the field-aligned transport of ionospheric plasma by winds and electric fields could conceivably decrease the model electron densities, and raise the electron density peak to higher altitudes. *Sommeria et al.* [1995] have proposed that an extremely rapid auroral electrojet might be responsible for powering meridional winds from high latitudes to the equator. These winds would help disperse auroral energy across the whole planet, explaining the high Jovian exospheric temperatures. In support of this mechanism, they cite the long-established phenomenon of the "Lyman-alpha Bulge" [*Clarke et al.*, 1980; *Sandel et al.*, 1980]. This phenomenon consists of higher than average Lyman-alpha u.v. emission centred on the magnetic drift equator around longitude 100°. *Ben Jaffel et al.* [1993] showed that this could be caused if this region was one of high turbulence. The modeling by *Sommeria et al.* [1995] required the auroral electrojet to drive neutral winds of up to 20 kms^{-1}. Neutral molecules are not constrained to remain on field lines, unlike ions. Thus the asymmetry of the Jovian auroral regions (particularly in the north) would give neutral winds a strongly meridional component, rather than a purely zonal velocity. In this scheme, it was shown that winds driven by the northern and southern auroral zones would indeed meet at the equator, creating a highly turbulent region at the location of the observed Lyman-alpha Bulge. It should be noted, however, that neutral wind velocities of the magnitude envisaged by *Sommeria et al.* [1995] would be highly supersonic; the sound speed at thermospheric altitudes is roughly 2 to 3 kms^{-1}. To date, there is no direct evidence for such high auroral wind velocities. In addition, there have been studies which indicate that the upper thermospheric temperature profile may also result from the dissipation of energy by gravity waves [*Young et al.*, 1997 and see chapter I.1], although other studies suggest that this can be discounted as a serious mechanism [*Matcheva and Strobel*, 1999; *Hickey et al.*, 2000]. A further possibility is that the high thermospheric temperatures could be the result of a global precipitation of energetic ions [*Waite et al.* 1997].

In order to better assess global mechanisms of plasma and energy transport, it is necessary to extend one-dimensional thermospheric-ionospheric models and adopt a global, three-dimensional, time-dependent approach. This then enables, for example, the computation of a global velocity distribution

for thermospheric winds in a self-consistent manner. The efficiency of these winds as a means of transporting energy and charged species may then be explored.

2. THE JIM MODEL

At the present time there exist two independent three- dimensional models of the Jovian ionosphere and thermosphere. The Jovian Ionospheric Model (JIM), the first such model to be developed, has been described in full by *Achilleos et al.* [1998], and is the subject here. A second model, the Jupiter Thermosphere General Circulation Model (JTGCM), developed from an adaptation of the National Center for Atmospheric Research (NCAR) Thermosphere Ionosphere General Circulation Model (TIGCM) [*Roble et al.*, 1988], is close to completion [*Bougher et al.*, 2001].

The JIM model is a fully time-dependent, three- dimensional model of Jupiter's thermosphere and ionosphere, based on the terrestrial Coupled Thermosphere-Ionosphere Model (CTIM). The basis for CTIM was a global thermospheric model described originally by *Fuller-Rowell and Rees* [1980]. This was then enhanced by the inclusion of a fully dynamic ionospheric model at high latitudes [*Quegan et al.*, 1982; *Fuller-Rowell et al.*, 1987]. Further developments resulted in the inclusion of a model of the mid- and low-latitude ionosphere and plasmasphere [*Millward et al.*, 1996] along with coupled thermosphere-ionosphere electrodynamics [*Millward et al.*, 2001].

For the Jovian model, JIM, we use a similar numerical grid to that of the terrestrial model; a spherical, co-rotating grid which divides the model planet into 40 elements in longitude (9° resolution), 91 elements in latitude (2° resolution), and 30 elements in pressure (used instead of altitude to define the vertical dimension). The vertical grid spacing is uniform with respect to the logarithm of pressure, so that the value of pressure for the nth layer may be written:

$$P_n = P_1 \, e^{-\gamma(n-1)} \qquad (1)$$

We take $P_1 = 2$ μbar as our lower boundary and $\gamma = 0.4$ as the vertical spacing between levels in units of local pressure scale height. Our upper boundary is at pressure $P_{30} \approx 0.02$ $n$bar. The horizontal wind velocity, total energy density, neutral composition and ionospheric composition are evaluated at each grid point using explicit time stepping applied to finite-difference versions of the appropriate equations of continuity, energy transport and momentum transport. Using these solutions, the vertical wind, temperature and altitudes at each pressure level can then be re-evaluated after each timestep. We use a time step of 4s in our calculations, in order to adequately sample the minimum time scale (roughly 10s) associated with the recombination of H_3^+ ions in Jupiter's auroral ionosphere.

2.1. Equations of Continuity, Momentum, and Energy

The continuity equation used in the model, and expressed in a pressure coordinate system, is given by:

$$\nabla_P \cdot \boldsymbol{v} + \frac{\partial w}{\partial P} = \frac{1}{\rho} \Sigma_j m_j (q_j - l_j) \qquad (2)$$

where $w = dP/dt$ is the convective time derivative of pressure, and m_j, q_j and l_j are, respectively, the mass and the chemical creation and destruction rates (per unit volume) of the jth neutral species (JIM's three neutral species are H, H_2 and He). Equation 2 is integrated to obtain w at each level in the model thermosphere, assuming $w = 0$ as the upper boundary condition. In solving this equation we assume that ion and neutral populations at the upper boundary of the model are in diffusive equilibrium. In addition, the lower boundary of the model is assumed to have a constant neutral chemical composition with no charged particles present. This is consistent with organic molecules near the homopause region which act as a major sink of H^+ and H_3^+ ions.

The momentum equation, in the form solved within the JIM model, is given by:

$$\left(\frac{\partial \boldsymbol{v}}{\partial t}\right)_P = -\boldsymbol{v} \cdot \nabla_P \boldsymbol{v} - w \frac{\partial \boldsymbol{v}}{\partial P} - \nabla_P \Phi + \boldsymbol{F} \qquad (3)$$

where the left hand term represents the time derivative of the two-dimensional horizontal velocity evaluated within a pressure coordinate system. On the right hand side ∇_P is a two-dimensional operator, and Φ is the gravitational potential. Implicit within equation 3 is an assumption of hydrostatic equilibrium. The final term $\boldsymbol{F}$ represents a summation of accelerations due to the Coriolis force (arising from our choice of a rotating frame of reference), viscosity and ion-neutral collisions (see *Achilleos et al.*, [1998], for details). Forcing due to ion-neutral collisions is the most uncertain term in the momentum equation, since it requires knowledge of the planetary magnetic and electric fields. For JIM we assume a global magnetic field with an offset, tilted dipole structure [*Acuña et al.*, 1983]. Calculation of the current density requires knowledge of Jovian ionospheric conductivities and the prevailing electric fields. The former are calculated from the mobilities of electrons and ions using collision rates given by *Danby et al.* [1996], for electron-H_2 scattering, and *Geiss and Bürgi* [1986], for electron-H, ion-H, and ion-H_2 scattering. For the electric field, we assume a modified version of the Earth's electric field structure, upon which we superpose a component due to the breakdown in plasma co-rotation which occurs beyond about 20 R_J in Jupiter's equatorial plane [*Achilleos et al.*, 2001].

In solving the momentum equation we assume several boundary conditions. Firstly, both components of the horizontal wind disappear to zero at the lower boundary. This

boundary has a constant altitude, approximately 360 km above the $P = 1$ bar level. Secondly, v_x (v_y) at the upper boundary equals v_x (v_y) at the adjacent pressure level for the same latitude and longitude. Finally, $w = 0$ at the upper boundary, and is determined from the continuity equation at other pressure levels.

The energy transport equation used in our model is given by

$$\left(\frac{\partial E_i}{\partial t}\right)_P = - \boldsymbol{v} \cdot \nabla_P (E_i + \Phi) - w \frac{\partial (E_i + \Phi)}{\partial P} + \boldsymbol{v} \cdot \boldsymbol{F} + \dot{Q} \quad (4)$$

The first two terms on the right side of equation 4 represent the transport of internal energy ($E_i = c_P T + e_k$, the total specific enthalpy plus kinetic energy) through bulk motions of the thermospheric gas. The third term represents the power exerted per unit mass by the dynamic forces given in equation 3. The local heating rate per unit mass, $\dot{Q}$, is calculated by a summation of contributions from Joule heating, solar heating, and thermal conduction. In addition, the auroral regions are subject to heating due to particle precipitation (see *Achilleos et al.*, [1998], for details).

The passage of solar EUV photons into the dayside atmosphere of Jupiter deposits an energy flux of around 3.5×10^{-2} mW m^{-2}, of which approximately 50 % goes into heating of the neutral gas [*Waite et al.*, 1983]. The incident solar flux comes from the observational data of *Heroux and Hinteregger* [1978], appropriate for solar minimum, and divided by a factor of 27 to account for the dilution of flux in passing from the Earth's position to that of Jupiter. The extinction of solar flux, as it passes through the model atmosphere, arises from photoionization of H, H_2 and He, as well as photodissociation of H_2. Jupiter's thermosphere shows temperatures which increase monotonically with altitude [*Atreya et al.* 1981]. This is a defining thermal signature for this atmospheric region, and indicates that thermal conduction is an important means of transporting downwards the energy deposited in the upper thermosphere.

The energy equation is solved with an assumption that the temperature at the upper boundary of the model is equal to the temperature at the next lowest pressure level, at the same latitude and longitude. In addition, we assume a constant temperature of 400 K at the lower boundary.

The neutral species in Jupiter's dayside thermosphere are directly ionized by solar EUV radiation. They are also ionized by energetic photoelectrons produced by these photoionizations and by precipitating energetic particles in the planet's aurorae. A range of one-dimensional models have been developed to describe the ionization and heating of an atmosphere subject to the passage of photoelectrons and/or precipitating particles. These range from the approximate analytical description of ionization by photoelectron impact used by *Majeed and McConnell* [1991] to the sophisticated numerical treatment of electron transport by *Porter et al.* [1987].

We use a simplified 'downstream' model to describe the ionization and deposition of energy in the JIM thermosphere by photoelectrons and auroral electrons, based on the expressions of *Nagy and Banks* [1970]. Initial studies considered electrons with an incident energy, at the top of the thermosphere, of 10keV, and an incident energy flux component, parallel to the local magnetic field, of 8 mW m^{-2}. More recently we have studied the effects of different fluxes of auroral electrons, ranging from 0.1 mW m^{-2} to 1000 mW m^{-2}. Results for these simulations are given in section 3. The auroral oval consists of all surface points with magnetic l parameters between $l_1 = 7$ and $l_2 = 15$, chosen to correspond to the 6 R_J and 30 R_J L-shells of the O6-plus-current-sheet field model [*Connerney*, 1993].

The three neutral species in our model thermosphere are H, H_2 and He. Scale heights for these molecules in the upper Jovian thermosphere are of the order $H_o = 100$km, while diffusive coefficients are, at most, of the order $D_o = 10^6$m^2 s^{-1} [e.g., *Atreya*, 1986]. Typical diffusive time scales for these molecules are therefore, at least, approximately $H_o^2/D_o = 3$ hours, increasing to days as one descends to the homopause.

2.2. Neutral and Ion Chemistry

There are many chemical reactions affecting the concentrations of both neutral and ionic species in the Jovian thermosphere. Near and below the homopause, the presence of organic molecules introduces an enormous network of ion-molecule reactions [*Strobel and Atreya*, 1983]. For simplicity, we have mostly omitted reactions involving organic molecules from our chemical rate calculations, and concentrate mainly on modeling the regions above the homopause. This is a good approximation for the Jovian thermosphere-ionosphere, since the homopause is coincident with the thermosphere-stratosphere boundary at around the 1 to 2 μbar pressure level.

The reactions included in our model are listed in full in *Achilleos et al.* [1998] along with references for corresponding rates and cross sections. The reactions include photoionization, photodissociation, electron impact ionization/dissociation, and radiative/dissociative ion recombination. Of particular note is the rapidity of the protonation of H_2 (i.e, $H_2^+ + H_2 \rightarrow H_3^+ + H$). This reaction has a rate constant of around 10^{-9} cm^{3}s^{-1} [*Theard and Huntress*, 1974]. The corresponding destruction time scale for H_2^+ lies in the range 10^{-5} to 10 s, given the H_2 densities in our model (between 10^8 and 10^{14} cm^{-3}). This reaction therefore destroys H_2^+ on time scales too small for practical modeling. We make the assumption then that each reaction producing H_2^+ is immediately followed by the conversion of this ion to H_3^+.

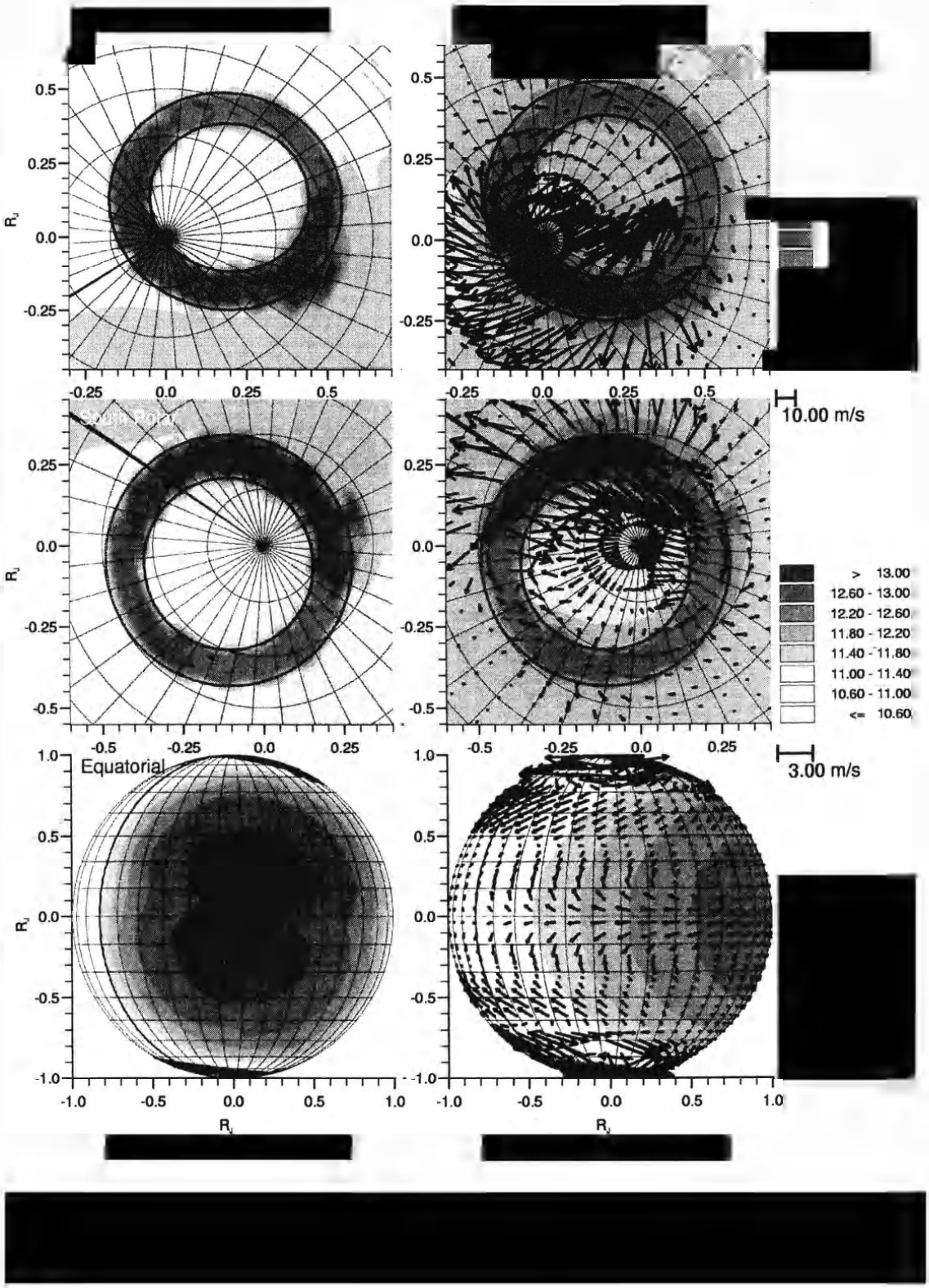
Equatorial
10.00 m/s
3.00 m/s
> 13.00
12.60 - 13.00
12.20 - 12.60
11.80 - 12.20
11.40 - 11.80
11.00 - 11.40
10.60 - 11.00
<= 10.60
R_J

Of great significance for the global ionospheric morphology are the time scales for the recombination of H_3^+ and H^+, the two principal ions in the JIM model. Firstly, H_3^+ is dominantly destroyed (above the homopause) by recombination with electrons, (i.e., $H_3^+ + e^- \rightarrow H_2 + H$ and $H_3^+ + e^- \rightarrow H + H + H$). The measurements of *Leu et al.* [1973] yielded a rate constant for this reaction of 2.3×10^{-7} cm^3 s^{-1} at 300 K. The branching ratio for the recombination was found by *Mitchell et al.* [1983] to be in the range 1:3–1:2 in favour of 3H production. The H_3^+ dissociative recombination rate has proven highly controversial, but these values are close to the presently accepted rate [*Mitchell*, 1990] and a recent determination of the branching ratio [*Datz et al.*, 1995] - see chapter III.6.

The time scale for recombination of H_3^+ is given by $\tau_r(H_3^+) = (\kappa_r[e^-])^{-1}$. The electron number density, $[e^-]$, peaks at values of the order 10^6 cm^{-3} in the auroral ionosphere and 10^4 cm^{-3} in the non-auroral ionosphere. The respective minimum values of $\tau_r(H_3^+)$, using these electron densities, are thus of the order 10 s (auroral) and 10^3 s (non-auroral).

In contrast, the H^+ recombines with electrons much more slowly than H_3^+. The rate constant for H^+ recombination by this mechanism is typically of the order $\kappa_r(H^+) \sim 10^{-12}$ cm^{3}s^{-1} (using a temperature $T = 1000$ K). The recombination time scales for H^+ will correspondingly be a factor of around 10^5 larger than those for H_3^+, and at least 10 days in magnitude.

The major sink of H^+ ions in JIM is in fact the charge transfer reaction ($H^+ + H_2(v \geq 4) \rightarrow H + H_2^+$), with rate 10^{-14} cm^{3}s^{-1} [*Majeed and McConnell*, 1991], where H^+ is neutralized by capturing an electron from vibrationally excited H_2. Although much work has been done in explicitly modeling the populations in the different vibrational levels of H_2 [*Cravens*, 1987], we follow *Majeed and McConell's* [1991] method of using a single rate constant, $\kappa_c = 10^{-14}$ cm^{3}s^{-1}, to compute the rate, assumed to be given by the expression $\kappa_c[H_2][H^+]$ ($[H_2]$ is total number density of H_2). Using this expression for the rate, we see that the time scale for neutralization of H^+ is given by $\tau_c = (\kappa_c[H_2])^{-1}$, and occupies a range of values from 1 s to 10^6 s, corresponding to the range of H_2 densities between the lower and upper boundaries of the model.

3. RESULTS

Figure 1 shows global ion column densities predicted by JIM. The upper two panels show column density distributions of H_3^+ and H^+ respectively for the northern polar region, while the middle panels show the same for the southern polar region. For this simulation, the auroral regions are subject to precipitating electrons of energy 10 keV and an energy flux of 8 mW m^{-2}. The lowest two panels show equatorial distributions of H_3^+ and H^+ respectively, similar to those seen by an Earth-based observer. The H^+ contour diagrams have arrows superposed which represent horizontal wind velocities, with arrow length indicating speed according to the scale bars shown. The central vertical meridian for all panels is at local noon. Boundaries of auroral precipitation zones are shown as dotted curves. The latitude/longitude grid has a spacing of 10°, and the bold meridian is at $\lambda_{III} = 0$.

Figure 2 shows JIM predicted altitude profiles of thermospheric parameters. All of the results are averages of separate profiles around the equatorial local noon region, with the altitude scale representing height above the 1 bar pressure level. Panel (a) gives the mass densities of the three major consitiuents; atomic hydrogen (solid line), molecular hydrogen (dotted line), and helium (dashed line). Panel (b) shows the resulting mean molecular weight. The thermospheric temperature profile is shown in panel (c), whilst panel (d) plots atmospheric pressure against altitude, for reference.

Recently, a series of simulations using the JIM model have been undertaken to investigate how ionospheric densities and conductivities respond to the intensity of electron precipitation within the auroral zones. The runs utilised electrons with an assumed initial energy of 10 keV and energy fluxes of 0.1, 0.3, 1.0, 3.0, 10.0, 30.0, 100.0, 300.0, and 1000.0 mW m^{-2}. The results can be seen in Figures 3 and 4.

Figure 3, panels (b) to (h), shows JIM model profiles of the concentrations for the ions H^+ (dashed line), H_3^+ (dotted line), and electrons (solid line), plotted against atmospheric pressure. Panels (b) and (c) show typical profiles for the equa-

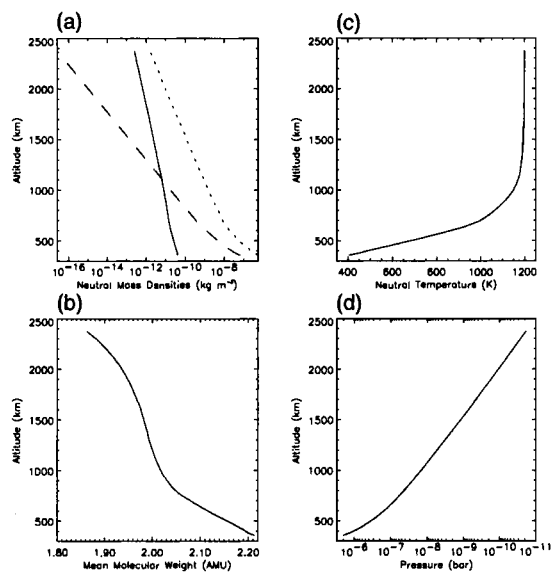

Figure 2. JIM predicted dayside equatorial profiles: (a) Mass densities of H (solid line), H_2 (dotted line), and He (dashed line); (b) mean molecular weight; (c) thermospheric temperature; (d) atmospheric pressure

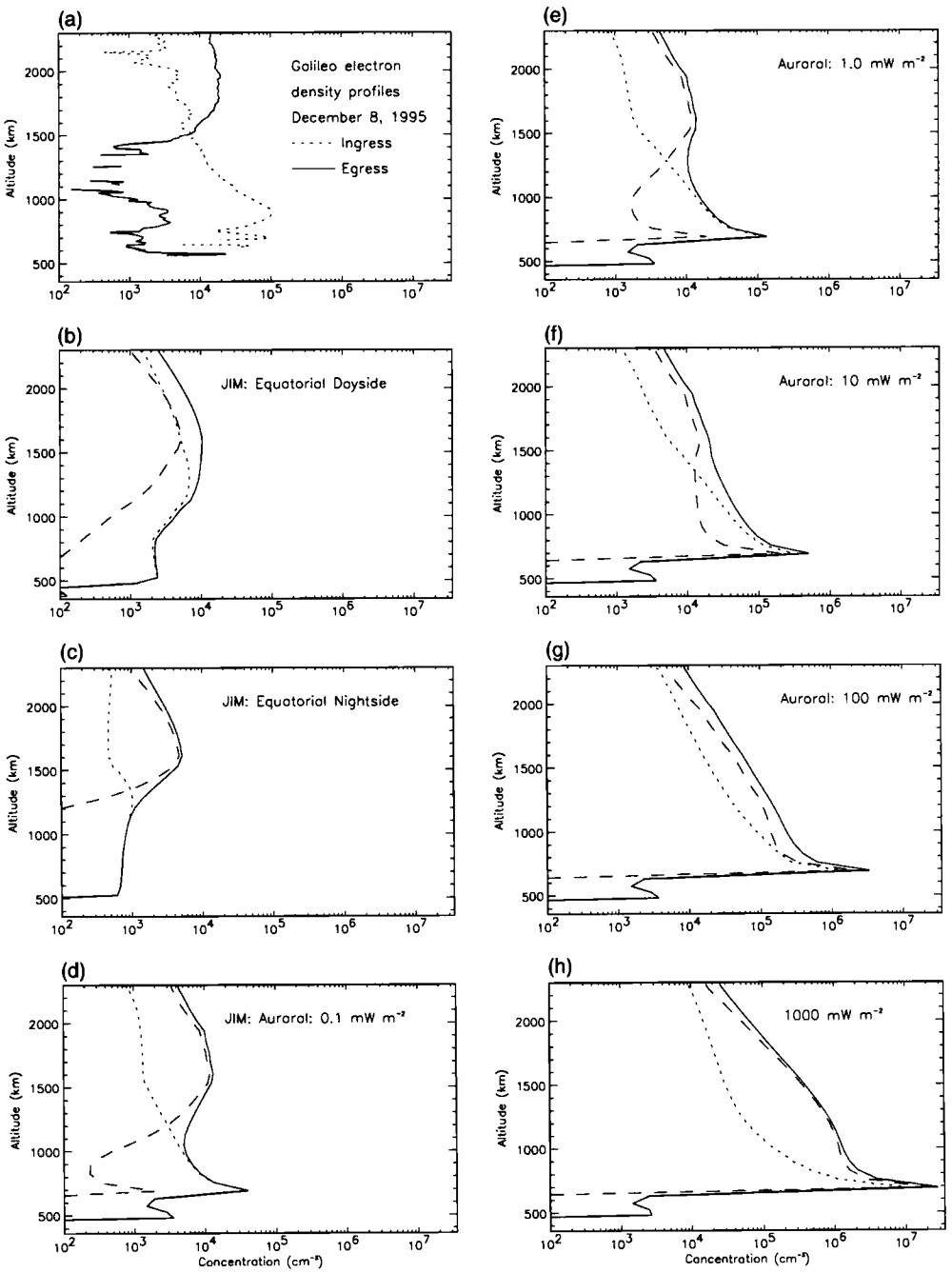

Figure 3. (a): Radio occultation measurements of electron density from Galileo, December 8, 1995; Panels (b) to (h): Predicted concentration profiles for the ions H^+ (dashed line), H_3^+ (dotted line), and electrons (solid line). Panels (b) and (c) show equatorial dayside and nightside results respectively. Panels (d) to (h) show average auroral profiles for simulations in which the auroral region is subject to electron precipitation of initial energy 10 keV and incident energy flux of 0.1, 1.0, 10.0, 100.0, and 1000.0 mW m^{-2} respectively.

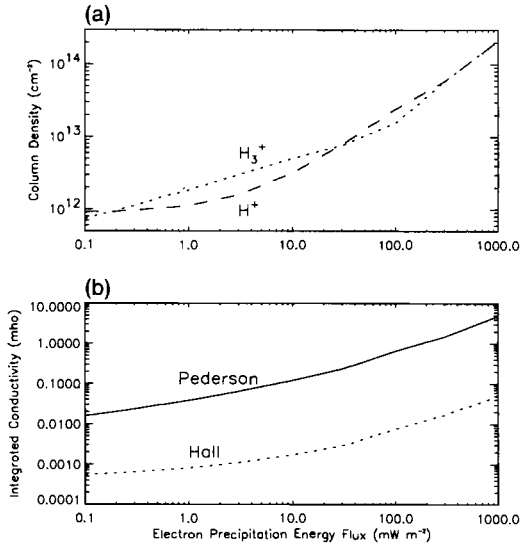

Figure 4. JIM predictions of height integrated auroral ionospheric parameters, as a function of the incident auroral electron precipitation flux. Panel (a) shows average auroral column densities for the ions H^+ (dashed line) and H_3^+ (dotted line), and (b) shows the associated integrated Pederson and Hall conductivities (solid and dotted lines respectively).

torial dayside and nightside respectively. The results show maximum ionospheric concentrations of around $10^4 cm^{-3}$. A comparison of panel (b) and panel (c) clearly demonstrates how the Jovian nightside ionosphere is maintained at higher altitudes by the longevity of the H^+ ions.

By way of comparison, Figure 3a shows radio occultation measurements of electron density made as the Galileo spacecraft passed behind Jupiter on December 8, 1995 [*Hinson et al.*, 1997], the first such results from the spacecaft. At ingress (24°S 68°W, dotted line), the principal peak of electron density is located at an altitude 900 km above the 1 bar level, with a peak density of $1 \times 10^5 cm^{-3}$. At egress (43°S 28°W, solid line), the main peak is centered near 2000 km altitude, with a peak density of $2 \times 10^4 cm^{-3}$.

The remaining panels, (d) to (h), show auroral ionospheric profiles, averaged over the latitudinal and longitudinal extent of the main auroral oval. They show how the ionosphere responds to an increasing flux of precipitating electrons, with energy fluxes of 0.1, 1.0, 10.0, 100.0, and 1000.0 mW m^{-2} respectively. As expected the incoming precipitation leads to enhanced densities of both H^+ and H_3^+ ions, with the largest increases occuring at lower altitudes, around 700 to 800 km altitude (equivalent to a pressure of 10^{-7} bar). Here, for a precipitation flux of between 10 and 100 mW m^{-2}, the ionosphere reaches maximum concentrations of $10^6 cm^{-3}$, and above. A vertical integration of these parameters yields results for auroral column densities and the associated integrated conductivities. Results are shown in Figure 4, with the column densities of H^+ and H_3^+ (panel (a)) and integrated Pederson and Hall conductivities (panel (b)) plotted against electron precipitation energy flux. It is of note that the H_3^+ column densities predicted by JIM, for both auroral and non-auroral latitudes, are consistent with spectroscopic observations by *Lam et al.* [1997] and *Miller et al.* [1997]. Also of note, the results in Figure 4b show that for large, though realistic, fluxes of precipitating electrons (say, 100 mW m^{-2}) the auroral integrated Pederson conductivity attains values of around 1 mho.

4. CONCLUSIONS

Global coupled modeling can provide us with a wealth of information about the Jovian ionosphere-thermosphere system, giving insights into the wind speeds, ionization levels, temperature and neutral composition. More importantly, the model can also help us understand how these different physical properties influence and interact with each other. The JIM model has enormous potential for modeling two-dimensional images of Jupiter and time-dependent, global events on the planet. By revealing subtle relationships between different physical aspects of the planet's atmosphere, modeling studies may also guide the types of observations we need to make, in order to obtain useful diagnostics of a particular property. Development of the model, to a spatial grid of higher resolution, will allow for a more realistic modeling of structures within the auroral zone. Future work will also be concerned with running the model for many more planetary rotations, in order to probe the long-term effects of wind transport on the atmospheric evolution.

Acknowledgments. Research using the JIM model is made possible by funding from the U.K. Particle Physics and Astronomy Research Council (PPARC). Model calculations were carried out on the High Performance Service for Physics, Astronomy, Chemistry and Earth Sciences (HiPerSPACE) Silicon Graphics Origin 2000 supercomputer, located at University College London and funded by PPARC.

REFERENCES

Achilleos, N., S. Miller, J. Tennyson, A.D. Aylward, I. Müller-Wodarg and D. Rees, JIM: a time-dependent, three-dimensional model of Jupiter's thermosphere and ionosphere, *J. Geophys. Res., 103*, 20089–20112, 1998.

Achilleos, N., S. Miller, R. Prangé, G. H. Millward and M. K. Dougherty, A dynamical model of Jupiter's auroral electrojet, *New J. Phys., 3*, 1, 2001.

Acuña, M. H., K. W. Behannon and J. E. P. Connerney, Jupiter's magnetic field and magnetosphere, in *Physics of the Jovian magnetosphere*, ed. A.J. Dessler, pp. 1–50. Cambridge University Press, Cambridge, 1983.

Atreya, S. K., *'Atmospheres and Ionospheres of the Outer Planets and their Satellites'*, Springer-Verlag, Heidelberg, 1986.

Atreya, S. K. and T. M. Donahue, Model ionospheres of Jupiter, in *Jupiter*, ed. T. Gehrels, pp. 304–318. University of Arizona Press, Tucson, 1976.

Atreya, S. K., T. M. Donahue and M. C. Festou, Jupiter: Structure and composition of upper atmosphere. *Astrophys. J., 247*, L43, 1981.

Atreya, S. K., T. M. Donahue and J. H. Waite, An interpretation of the Voyager measurements of the Jovian electron density profiles, *Nature, 280*, 795–796, 1979.

Auerbach, D., R. Casak, R. Caudano, T. D. Gaily, C. J. Keyser, J. Wm. McGowan, J. B. A. Mitchell and S. F. G. Wilk, *J. Phys. B., 10*, 3797, 1977.

Ballester, G. E., J. T. Clarke, J. T. Trauger, W. M. Harris, K. R. Stapelfeldt, D. Crisp, R. W. Evans, E. B. Burgh, C. J. Burrows, S. Casertano, J. S. Gallagher III, R. E. Griffiths, J. J. Hester, J. G. Hoessel, J. A. Holtzman, J. E. Krist, V. Meadows, J. R. Mould, R. Sahai, P. A. Scowen, A. M. Watson and J. A. Westphal, Time-resolved observations of Jupiter's far-ultraviolet aurora, *Science, 274*, 409–413, 1996.

Baron, R. L., T. Owen, J. E. P. Connerney, T. Satoh and J. Harrington, Solar wind control of Jupiter's H_3^+ auroras, *Icarus, 120*, 437–442, 1996.

Bougher, S. W., J. H. Waite, T. Majeed, G. R. Gladstone, and D. Grodent, Jupiter Thermosphere General Circulation Model (JTGCM): Formulation and Case Studies Incorporating Ion Drag and Joule Heating. Poster given at *Jupiter: Planet, Satellites and Magnetosphere* Conference, Boulder, Colorado, June 25 - 30th, 2001.

Caldwell, J., F. C. Gillett, and A. T. Tokunaga, Possible infrared aurorae on Jupiter, *Icarus, 44*, 667–675, 1980.

Clarke, J.T., H.A. Weaver, P.D. Feldman, H.W. Moos, W.G. Fastie and C.B. Opal, Spatial imaging of hydrogen Lyman-alpha emission from Jupiter, *Astrophys. J., 240*, 696–701, 1980.

Connerney, J. E. P., R. Baron, T. Satoh and T. Owen, Images of excited H_3^+ at the foot of the Io flux tube in Jupiter's atmosphere, *Science, 262*, 1035–1038, 1993.

Cravens, T. E., Vibrationally excited molecular hydrogen in the upper atmosphere of Jupiter, *J. Geophys. Res., 92*, 11083–11100, 1987.

Danby, G., B. K. Elza, M. A. Morrison and W. K. Trail, The separable representation of exchange in electron-molecule scattering: I. Elastic scattering and rotational excitation, *J. Phys. B 29*, 2265–2287, 1996.

Datz, S., G. Sundstrom, C. Biedermann, L. Brostrom, H. Danared, S. Mannervik, J. R. Mowat and M. Larsson, Branching processes in the dissociative recombination of H_3^+, *Phys. Rev. Lett., 74*, 896–899, 1995.

Drossart, P., J.-P. Maillard, J. Caldwell, S. J. Kim, J. K. G. Watson, W. A. Majewski, J. Tennyson, S. Miller, S. K. Atreya, J. Clarke, J. H. Waite, Jr. and R. Wagener, Detection of H_3^+ on Jupiter, *Nature 340*, 539–541, 1989.

Eshleman, V. R., G. L. Tyler, G. E. Wood, G. F. Lindal, J. D. Anderson, G. S. Levy, and T. A. Croft, Radio science with Voyager at Jupiter: Preliminary profiles of the atmosphere and ionosphere, *Science, 204*, 976–978, 1979a.

Eshleman, V. R., G. L. Tyler, G. E. Wood, G. F. Lindal, J. D. Anderson, G. S. Levy, and T. A. Croft, Radio science with Voyager at Jupiter: Initial Voyager 2 results and a Voyager 1 measure of the Io torus, *Science, 206*, 959–962, 1979b.

Fjeldbo, G., A. Kliore, B. Seidel, D. Sweetnam and D. Cain, The Pioneer 10 radio occultation measurements of the ionosphere of Jupiter, *Astron. Astrophys., 39*, 91–96, 1975.

Fjeldbo, G., A. Kliore, B. Seidel, D. Sweetnam, and P. Woiceshyn, The Pioneer 11 radio occultation measurements of the ionosphere of Jupiter, in *Jupiter* (edited by Gehrels, T.), University of Arizona Press, Tucson, pp. 239–246, 1976.

Fuller-Rowell, T. J. and D. Rees, A three-dimensional, time-dependent, global model of the thermosphere, *J. atmos. Sci., 37*, 2545–2567, 1980.

Fuller-Rowell, T.J., D. Rees, S. Quegan, R.J. Moffett, and G.J. Bailey, Interactions between neutral thermospheric composition and the polar ionosphere using a coupled ionosphere-thermosphere model, *J. Geophys. Res., 92*, 7744-7748, 1987.

Geiss, J. and Bürgi, A., Diffusion and thermal diffusion in partially ionized gases in the atmospheres of the Sun and planets, *Astron. Astrophys., 159*, 1–15, 1980.

Heroux, L. and H. E. Hinteregger, Aeronomical reference spectrum for solar UV below 2000 Å, *J. Geophys. Res., 83*, 5305–5308, 1978.

Hickey, M. P., R. L. Walterscheid, and G. Schubert, Gravity wave heating and cooling in Jupiter's thermosphere, *Icarus, 148*, 266-281, 2000.

Hinson, D. P., F. M. Flasar, A. J. Kliore, P. J. Schinder, J. D. Twicken, and R. G. Herrara, Jupiter's ionosphere: Results from the first Galileo radio occulation experiment, *Geophys. res. Lett., 24*, 2107-2110, 1997.

ben Jaffel, L., J. T. Clarke, R. Prangé, R. Gladstone and A. Vidal Madjar, The Lyman-alpha bulge of Jupiter: effects of non-thermal velocity field, *Geophys. Res. Lett., 20*, 747–750, 1993.

Kim, Y. H., J. L. Fox and H. S. Porter, Densities and vibrational distribution of H_3^+ in the Jovian auroral ionosphere, *J. Geophys. Res., 97*, 6093–6101, 1992.

Lam, H. A., N. Achilleos, S. Miller and J. Tennyson, A baseline spectroscopic study of the infrared auroras of Jupiter, *Icarus, 127*, 379–393, 1997.

Leu, M. T., M. A. Biondi and R. Johnsen, Measurements of recombination of electrons with H_3^+ and H_5^+, *Phys. Rev. A., 8*, 413, 1973.

Liu, W. and A. Dalgarno, The ultraviolet spectrum of the

Jovian dayglow, *Astrophys. J., 462*, 502–518, 1996.

Livengood, T. A., H. W. Moos, G. E. Ballester and R. M. Prangé, Jovian ultraviolet auroral activity 1981–1991, *Icarus, 97*, 26–45, 1992.

Majeed, T. and J. C. McConnell, The upper ionospheres of Jupiter and Saturn, *Planet. Space Sci., 39*, 1715–1732, 1991.

Majeed, T., J. C. McConnell, and G. R. Gladstone, A model analysis of Galileo electron densities on Jupiter, *Geophys. res. Lett., 26*, 2335–2339, 1999.

Matcheva, K. I., and D. F. Strobel, Heating of Jupiter's thermosphere by dissipation of gravity waves due to molecular viscosity and heat conduction, *Icarus, 140*, 328-340, 1999.

McConnell, J. C. and T. Majeed, T., H_3^+ in the Jovian ionosphere, *J. Geophys. Res., 92*, 8570–8578, 1987.

Miller, S., N. Achilleos, G. E. Ballester, H. A. Lam, J. Tennyson, T. R. Geballe and L. M. Trafton, Mid-to-low latitude H_3^+ emission from Jupiter, *Icarus, 130*, 57–67, 1997.

Millward, G. H., R. J. Moffett, S. Quegan, and T. J. Fuller-Rowell, A coupled ionosphere-thermosphere-plasmasphere model, CTIP, in STEP Handbook on Ionospheric Models, edited by R. W. Schunk, p.239, Utah State Univ., 1996.

Millward, G. H., A. D. Aylward, I. C. F. Müller-Wodarg, T. J. Fuller-Rowell, R. J. Moffett, and A. D. Richmond, An investigation into the influence of tidal forcing on *F* region equatorial vertical ion drift using a global ionosphere-thermosphere model with coupled electrodynamics, *J. Geophys. Res., 106*, 24733-24744, 2001.

Mitchell, J. B. A., The dissociative recombination of molecular ions, *Phys. Rep., 186*, 215–248, 1990.

Mitchell, J. B. A., C. T. Ng, D. P. Levac, R. E. Mitchell, P. M. Mul, W. Claeys, A. Sen and J. Wm. McGowan, *Phys. Rev. Lett., 51*, 885, 1983.

Morrissey, P.F., P. D. Feldman, J. T. Clarke, B. C. Wolven, D. F. Strobel, S. T. Durrance, and J. T. Trauger, Simultaneous Spectroscopy and Imaging of the Jovian Aurora with the Hopkins Ultraviolet Telescope and the Hubble Space Telescope, *Astrophys. J., 476*, 918, 1997.

Nagy, A. F. and P. M. Banks, Photoelectron fluxes in the ionosphere, *J. Geophys. Res., 75*, 6260–6270, 1970.

Porter, H. S., F. Varosi and H. G. Mayr, Iterative solution of the multistream electron transport equation: 1. Comparison with laboratory beam injection experiments, *J. Geophys. Res., 92*, 5933–5959, 1987.

Prangé, R., The UV and IR Jovian aurorae, *Advances in Space Research, 12*, 379–389, 1992.

Prangé, R. and M. Elkhamsi, Modeling the precipitation flux in the Jovian auroral zones 1, *J. Geophys. Res., 96*, 21371–21389, 1991.

Prangé, R., D. Rego, D. Southwood, P. Zarka, S. Miller and W. Ip, Rapid energy dissipation and variability of the Io-Jupiter electrodynamic circuit, *Nature, 379*, 323–325, 1996.

Rego, D., Prangé, R. and Gérard, J.-C., Auroral Lyman alpha and H_2 bands from the giant planets I. Excitation by proton precipitation in the Jovian atmosphere, *J. Geophys. Res., 99*, 17075–17094, 1994.

Roble, R. G., E. C. Ridley, A. D. Richmond, and R. E. Dickinson, A coupled thermosphere/ionosphere general circulation model, *Geophys. Res. Lett., 15*, 1325-1328, 1988.

Sandel B. R., A. L. Broadfoot and D. F. Strobel, Discovery of a longitudinal asymmetry in the Hy Ly-alpha brightness of Jupiter, *Geophys. Res. Lett., 7*, 5–8, 1980.

Satoh, T., J. E. P. Connerney and R. L. Baron, Emission source model of Jupiter's H_3^+ aurorae: a generalized inverse analysis of images, *Icarus, 122*, 1–23, 1996.

Seiff, A., D. B. Kirk, T. C. D. Knight, L. A. Young, F. S. Milos, E. Venkatapathy, J. D. Mihalov, R. C. Blanshard, R. E. Young and G. Schubert, Thermal structure of Jupiter's upper atmosphere derived from the Galileo Probe, *Science, 276*, 102-104, 1997.

Sommeria, J., L. Ben Jaffel and R. Prangé, On the existence of supersonic jets in the upper atmosphere of Jupiter, *Icarus, 118*, 2–24, 1995.

Strobel D. and S. Atreya, Ionosphere, in *Physics of the Jovian Magnetosphere*, ed. A.J. Dessler, pp. 51–67. Cambridge University Press, Cambridge, 1983.

Theard, L. P. and W. T. Huntress, Jr., Ion molecule reactions and vibrational deactivation of H_2^+ ions in mixtures of hydrogen and helium, *J. Chem. Phys., 60*, 2840, 1974.

Waite, J. H., Jr., T. E. Cravens, J. Kozyra, A. F. Nagy, S. K. Atreya and R. H. Chen, Electron precipitation and related aeronomy of the Jovian thermosphere and ionosphere, *J. Geophys. Res., 88*, 6143–6163, 1983.

Waite, J. H., Jr., G. R. Gladstone, W. S. Lewis, P. Drossart, T. E. Cravens, A. N. Maurellis, B. H. Maulk and S. Miller, Equatorial X-ray emissions: Implications for Jupiter's high exospheric temperatures, *Science, 276*, 104–108, 1997.

Young, L. A., R. V. Yelle, R. Young, A. Seiff and D. Kirk, Gravity waves in Jupiter's thermosphere, *Science, 276*, 108–111, 1997.

N. Achilleos, A. D. Aylward, S. Miller, G. H. Millward, and I. C. F. Müller-Wodarg, Atmospheric Physics Laboratory, Department of Physics and Astronomy, University College London, 67-73 Riding House Street, London W1P 7PP, U.K. (e-mail: george@theory.phys.ucl.ac.uk)

Ionospheric Models for Earth

R. W. Schunk

Center for Atmospheric and Space Sciences, Utah State University, Logan, Utah

The ionosphere is a highly dynamic partially-ionized plasma that exhibits a significant variation with the solar cycle, season, geomagnetic activity, and universal time. Over the years, numerous modeling approaches have been used to account for this ionospheric behavior. The modeling approaches include: (1) Empirical models based on an extensive data base of world-wide measurements; (2) Three-dimensional, time-dependent numerical models; (3) Parameterized models that are based on spherical harmonic fits to the output obtained from global numerical models; and (4) Data assimilation models. The various modeling approaches will be discussed in this brief review, with the emphasis on numerical and data assimilation models.

1. INTRODUCTION

Shortly after Marconi transmitted radio waves across the Atlantic in 1901, it was recognized that the radio waves must have been reflected by free electrical charges in the upper atmosphere [*Rishbeth*, 2001]. The first physical explanation for Marconi's experiment was given in 1902, when it was postulated that solar ultraviolet radiation was capable of ionizing the neutral particles in the upper atmosphere, thereby turning it into a conducting medium. It was at this time that ionospheric research began, although the term *ionosphere* was not introduced until 1926. In 1931, Chapman published his now famous photochemical equilibrium model of the ionosphere, and in 1946 the importance of vertical diffusion was established and a model that included production, loss, and diffusion was introduced. Currently, it is estimated that about 170 ionospheric models are in use. However, most of the models are relatively simple models that are used by practitioners to determine local ionospheric conditions for over-the-horizon (OTH) radar applications or HF communications.

Atmospheres in the Solar System: Comparative Aeronomy
Geophysical Monograph 130

10.1029/130GM19

During the last century, the ionosphere has been extensively studied with the aid of balloons, rockets, satellites, the Space Shuttle, and a wide range of ground-based instruments (radars, magnetometers, GPS receiver networks, tomography chains, and optical devices). Furthermore, there have been more than one thousand model simulations covering a wide range of geophysical conditions, including various solar cycle, seasonal, and geomagnetic activity conditions. As a result of these studies, it has been clearly established that the primary source of both ionization and energy for the ionosphere is solar EUV and x-ray radiation. The solar photons ionize the neutrals in the Earth's upper atmosphere, which leads to both thermal ions and photoelectrons. At creation, the photoelectrons have a mean energy of about 30 eV, and this excess energy is eventually transferred to the thermal electrons, ions, and neutrals via collisional processes. Although solar radiation is the main source of ionization and energy for the terrestrial ionosphere, other sources are important in certain altitude and latitude domains. At high latitudes, magnetospheric electric fields, particle precipitation, and field-aligned currents are also sources of ionization and/or energy for the ionosphere. In addition, gravity waves and tides that propagate up from the lower atmosphere can appreciably affect the lower ionosphere [*Kelley*, 1989; *Cravens*, 1997; *Schunk and Nagy*, 2000].

The various chemical, electrodynamical, radiative, and transport processes acting on and within the ionosphere act

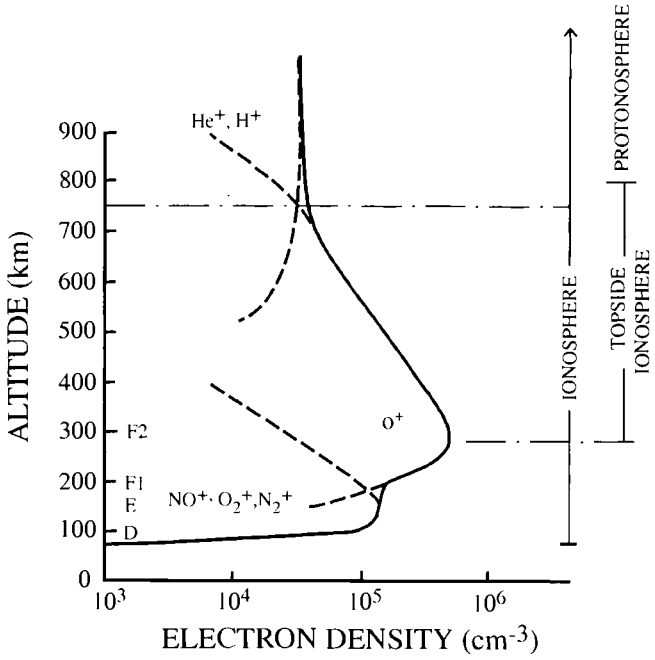

Figure 1. Typical ion density profiles for the daytime mid-latitude ionosphere showing the different regions. From *Banks et al.* [1976].

to determine the density and temperature structure of the ionosphere. However, the transport processes are affected by the Earth's strong intrinsic magnetic field, and its effect is different at high, middle, and low latitudes. The simplest situation occurs at mid-latitudes where the competition between photoproduction, chemical reactions, and diffusion along the inclined geomagnetic field acts to separate the ionosphere into distinct regions (Figure 1). The D region (60-100 km) is controlled by chemical processes and the dominant species are negative and positive molecular ions, water cluster ions, free electrons, and molecular neutrals. The E-region (100-150 km) is also controlled by chemical processes and the dominant species are molecular ions (NO^+, O_2^+, N_2^+) and neutrals (N_2, O_2). In the F_1 and F_2 regions (150-1000 km), field-aligned diffusion and wind-induced drifts become important and they compete with the chemical processes with regard to determining the plasma density profile. The dominant species are O^+ and O in the F_1 and F_2 regions. The F_2 region is where the maximum ionospheric density occurs. At higher altitudes, the light ion H^+ dominates ($\geq$ 1000 km).

The chemical processes that operate in the D and E regions are very complex, but at and above F region altitudes, only a few chemical reactions need to be taken into account (to lowest order). In the F region, O^+ is created via photoionization of atomic oxygen (O) and is lost in chemical reactions with N_2 and O_2,

$$O + h\nu \rightarrow O^+ + e;\ \alpha \approx 4\times10^{-7} \quad (1)$$

$$O^+ + N_2 \rightarrow NO^+ + N;\ k_2 = 1.2\times10^{-12} \quad (2)$$

$$O^+ + O_2 \rightarrow O_2^+ + O;\ k_3 = 2.1\times10^{-11} \quad (3)$$

The molecular ions are then lost via recombination with electrons,

$$NO^+ + e \rightarrow N + O;\ k_4 = 4.0\times10^{-7}(300/Te)^{0.5} \quad (4)$$

$$O_2^+ + e \rightarrow O + O;\ k_5 = 1.95\times10^{-7}(300/Te)^{0.7} \quad (5)$$

Where Te is the electron temperature and the reaction rates, k, are in $cm^3\ s^{-1}$. The rate α (s^{-1}) is an approximate ionization frequency. Above the F region peak, the main source and loss processes for H^+ are associated with the accidentally resonant charge exchange reaction

$$O^+ + H \underset{k_r}{\overset{k_f}{\leftrightarrow}} H^+ + O, \quad (6)$$

Where k_f and k_r are the forward and reverse reaction rates [e.g., *Schunk and Nagy*, 2000].

At altitudes above about 1000 km and at both high and low latitudes, the ionospheric description becomes more complicated because of additional electrodynamical and transport processes (Figure 2). At high latitudes, thermal ions and electrons can escape the topside ionosphere along field lines that extend deep into the geomagnetic tail (the polar wind). In addition, the dynamo electric field that is generated via the solar wind-magnetosphere interaction is mapped down to ionospheric altitudes along **B** and typically causes a 2-cell plasma flow pattern, with antisunward flow over the polar cap and return flow equatorward of the auroral oval. At mid-latitudes, the ionospheric plasma tends to corotate with the Earth. However, the plasma can readily flow along the dipolar field lines from one hemisphere to the conjugate hemisphere.

Neutral wind effects are also important at mid-latitudes. During the day, the meridional wind is poleward, which acts to drive the plasma down the **B**-field lines where the

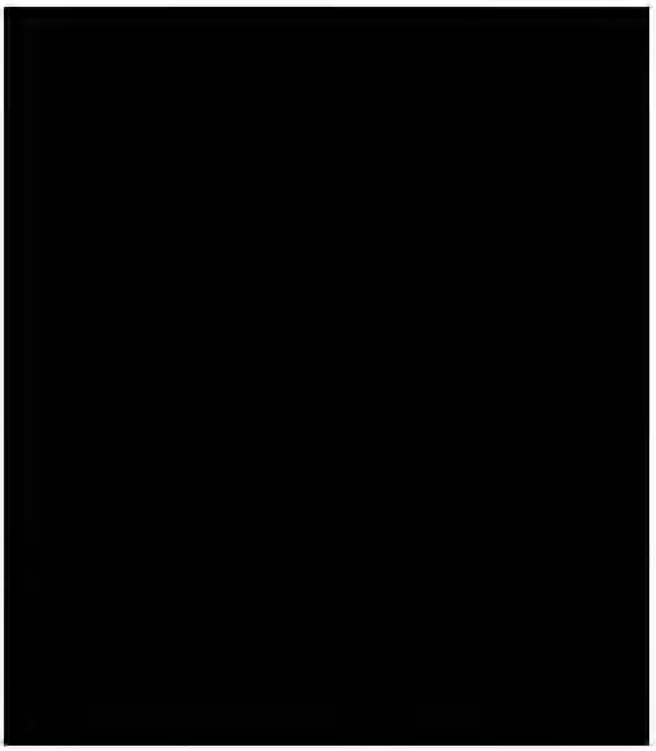

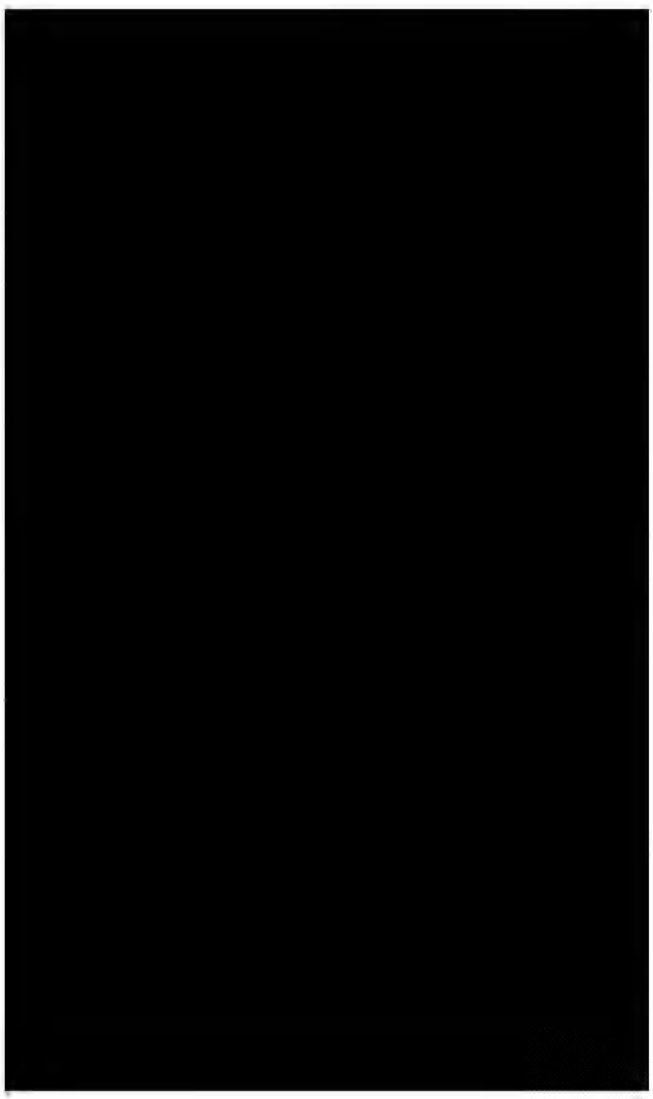

P2

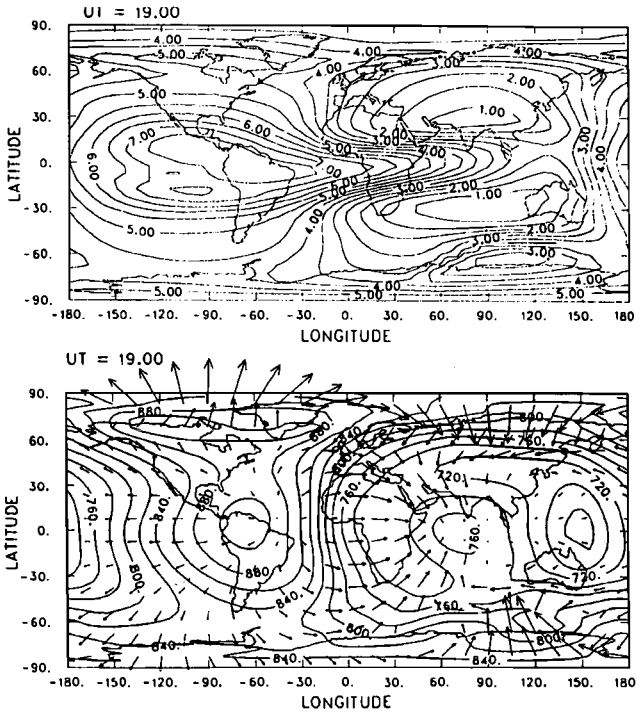

Figure 4. Contours of f_oF_2 in MHz (top panel) and contours of T_n and wind vectors (bottom panel) for solar minimum and equinox conditions at 1900 UT. From *Roble et al.* [1988].

and polar wind. Therefore, stand-alone ionospheric models require inputs, and the accuracy of the models' output depends on the quality of the inputs. The primary inputs are: (1) global distributions of neutral densities, temperatures, and winds; (2) convection electric fields and particle precipitation at high latitudes; and (3) dynamo electric fields at low latitudes. The inputs can be obtained from empirical models or via data assimilation techniques. One usually adopts empirical models for the neutral densities, temperatures, and winds if a stand-alone ionospheric model is used, because there are insufficient real-time measurements of neutral parameters for assimilation into a data-driven neutral model. However, there are sufficient measurements for assimilation into convection electric field and particle precipitation models, and the resulting time-dependent patterns can be used to drive an ionospheric model. A very successful approach for obtaining electric field and precipitation patterns is called the Assimilative Mapping of Ionospheric Electrodynamics (AMIE) procedure [*Richmond*, 1992].

One way to eliminate the need for inputs is to couple the ionospheric model to physics-based models that describe the other spatial regions. Currently, there are coupled global models of the ionosphere-thermosphere, ionosphere-plasmasphere, ionosphere-polar wind, ionosphere-thermosphere-mesosphere, and ionosphere-thermosphere-plasmasphere [cf. *Fuller-Rowell*, 1994; *Robel et al.*, 1988; *Schunk*, 1996; and reference therein]. In addition, work has begun on coupling a global ionospheric model to a global MHD magnetosphere model [*Sojka et al.*, 1997]. A significant advantage of coupled global models is that the coupling processes, time delays, and feedback mechanisms that are inherent in geospace are included in a self-consistent way. Another advantage is that it is possible to relate effects observed in one domain to causative processes in another domain. However, a disadvantage is that error propagation from model to model can lead to unreliable quantitative results. For example, if an MHD magnetospheric model produces convection electric fields that are too large, the resulting frictional heating rates in both the ionosphere and thermosphere will be too large. This, in turn, will lead to erroneous neutral winds, plasma drifts, ion and neutral composition changes, and ion and neutral temperatures.

A sample of the output from the NCAR physics-based model of the global ionosphere-thermosphere (TIGCM) system is shown in Figure 4 [*Roble et al.*, 1988]. The top panel shows contours of f_oF_2 (~300 km) over the globe at 1900 UT for solar minimum and equinox conditions. The bottom panel shows the corresponding self-consistent neutral gas temperatures and wind vectors. For this simulation, the magnetospheric inputs were characterized by a cross-polar cap potential drop of 60 kV and an auroral precipitation input of 11 GW. Note that the calculated electron density exhibits features that are in general agreement with measurements. In the auroral zones, enhanced ionization occurs in association with auroral precipitation. On the nightside at mid-latitudes, ionization troughs exist in both the northern and southern hemispheres. Also, in the equatorial region on the dayside, the Appleton anomaly is clearly visible via electron density crests that are situated on both sides of the magnetic equator. Likewise, the neutral gas parameters also display features that are in general agreement with measurements. The horizontal wind blows away from the dayside high-temperature region, flows around the globe, and then converges on the nightside low-temperature region. The antisunward winds in the polar regions are enhanced due to momentum forcing from plasma convection. The neutral and ion temperatures are also enhanced due to ion-neutral frictional heating (not shown).

During geomagnetic storms, the magnetospheric electric fields and particle precipitation are enhanced, and this leads to elevated plasma temperatures and drifts. Recently, such a situation was studied with a global physics-based model of the coupled ionosphere-polar wind

system in order to determine the feedback on the magnetosphere [*Schunk and Sojka*, 1997]. The storm-enhanced electron and ion temperatures acted to produce a large-scale upflow of O^+, as shown in Plate 1. This figure shows a snapshot of the storm-time O^+ density as a function of altitude and latitude (along the noon-midnight meridian). During the storm, the O^+ density is sufficiently elevated that O^+ becomes the dominant ion to altitudes as high as 9000 km over the bulk of the polar regions. The escaping O^+ ions can be an appreciable source of mass and momentum for the magnetosphere, and their presence can affect the recovery phase of a geomagnetic storm. The simulations also showed that during the storm the temporal variation of the plasma density at high altitudes (~9000 km) can be opposite to that at low altitudes (~300 km), which makes it difficult to elucidate storm dynamics with just one satellite.

In addition to describing large-scale ionospheric features, global models have also been successful in describing mesoscale features (horizontal dimensions of 100-1000 km). This has simply been achieved by using faster computers with enhanced memory. Global ionospheric simulations with horizontal resolutions of less than 100 km have been conducted. However, global simulations that self-consistently include the microphysics (e.g., plasma instabilities) have not yet been conducted. On the other hand, plasma instabilities have been included self-consistently in regional physics-based models. A particular area where significant progress has been made is in the equatorial region during Equatorial Spread F (ESF) bubble formation [*Ossakow et al.*, 1979; *Zalesak et al.*, 1982].

Equatorial plasma bubbles form in the following way. During the day, the neutral wind generates a dynamo electric field that is eastward and this electric field produces an upward $\mathbf{E} \times \mathbf{B}$ plasma drift, which raises the equatorial F-layer. Just before dusk, the upward plasma drift is enhanced, and as the ionosphere corotates into darkness, the bottomside of the F-layer rapidly decays. The net effect is an elevated F-layer with a steep bottomside density gradient, which is the classical configuration for the Rayleigh-Taylor (R-T) instability. Depending on the conditions, a density perturbation can trigger the R-T instability on the bottomside of the F layer, leading to spread F and plasma bubbles. Figure 5 shows the results of a typical simulation of the nonlinear evolution of equatorial spread F [*Sekar et al.*, 1994]. The simulation domain extends from 250 to 550 km in altitude and from −100 to 100 km in the east-west direction. The magnetic field direction is out of the plane of the diagram. The dotted curves in each plot show the initial electron density profile. The solid curves show the electron density contours at 700 (left panel), 900 (middle panel), and 1100 (right panel) seconds after the plasma becomes unstable. The top row corresponds to the case when only gravity is included, while for the bottom row both gravity and a downward wind are included. In both cases, a plasma bubble forms on the bottomside of the F layer and then drifts upwards. However, with allowance for a downward wind, the bubble formation is accelerated.

4. PARAMETERIZED MODELS

The physics-based numerical models provide a wealth of information about ionospheric behavior, including how the electron and ion densities, temperatures, and flow velocities vary with altitude, latitude, longitude, and universal time. In addition, simulations can be conducted for different solar cycle, seasonal, and geomagnetic activity conditions. Over the years, it has been demonstrated that the physics-based models generally display the correct trends and features, although the exact details obtained in a given simulation may not be precisely correct [*Anderson et al.*, 1997]. Some of the known ionospheric features that have been reproduced in numerical simulations include propagating plasma patches, auroral and boundary blobs, tongues of ionization, the mid-latitude trough, the polar hole, and the equatorial ionization crests. However, physics-based models are typically not user-friendly, and hence, it is unlikely that the general scientific community will ever have easy access to these models. Nevertheless, the output of the physics-based models may be useful to the general community. The output can be used by students to study ionospheric behavior, and experimentalists can compare the output to specific measurements in an effort to better understand the measurements.

Parameterized ionospheric models were constructed in an effort to disseminate the information obtained from physics-based model runs. As with empirical models, which are based on measurements, parameterized models are constructed by fitting orthogonal functions to the output obtained from a large number of numerical simulations. Then, a user-friendly interface is typically added so that the numerical data can be readily accessed. Perhaps the most well-known parameterized model is PIM, which stands for Parameterized Ionospheric Model [*Daniell et al.*, 1995]. PIM is a global model of ionospheric climatology that can be accessed by specifying a few simple inputs (date, altitude, latitude, longitude, universal time, solar activity level ($F_{10.7}$), magnetic activity level (K_p), and the direction of the IMF). The parameterized model outputs electron and ion (O^+, NO^+, O_2^+, N_2^+) densities at E and F region altitudes.

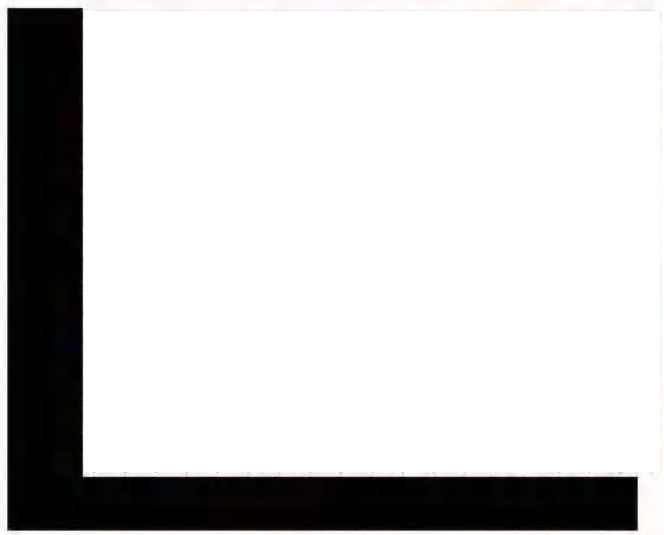

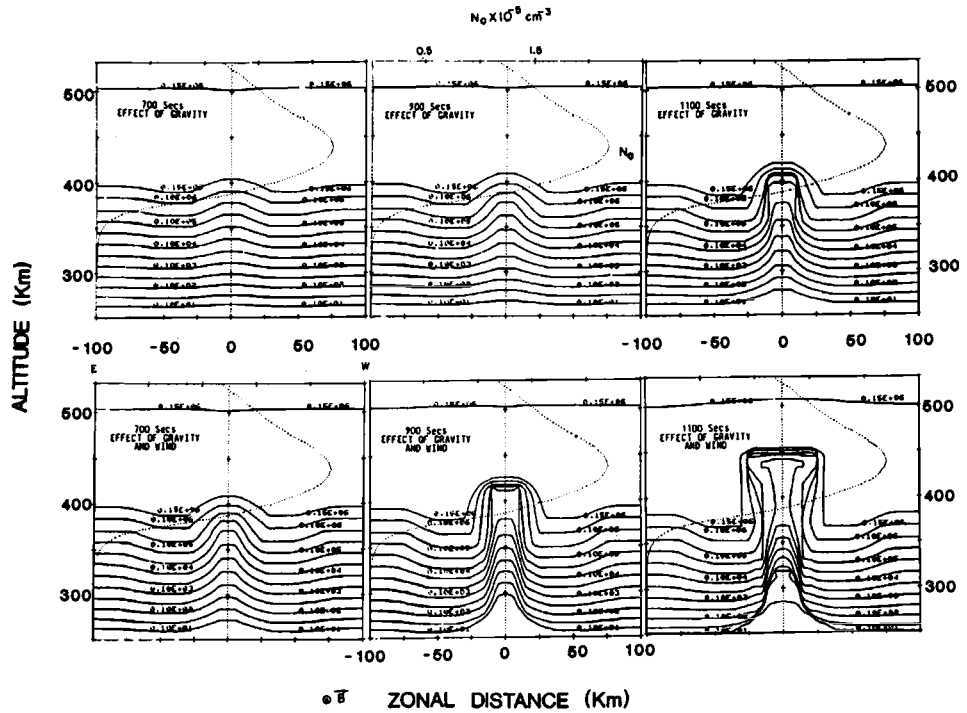

Figure 5. Numerical simulation of the nonlinear evolution of an equatorial bubble. The dotted curves in each panel correspond to the initial F layer density profile. The solid lines are electron density contours. The left, middle, and right panels correspond to snapshots at 700, 900, and 1100 s, respectively, after instability onset. The top row is the case for gravity only and the bottom row is for both gravity and a downward neutral wind of 20 m/s. From *Sekar et al.* [1994].

5. DATA ASSIMILATION MODELS

Data assimilation is becoming important for ionospheric modeling because of the large number of ionospheric measurements that are coming on line. By the end of this decade it is anticipated that there will be several hundred thousand ionospheric measurements per day from a variety of sources. Some of the data sources that are, or will be, available for assimilation into ionospheric models are shown in Plate 2. The data sources include: (1) in situ N_e measurements along DMSP satellite orbits; (2) bottomside N_e profiles from a network of digisondes; (3) line-of-sight TECs between a large network of ground stations and the GPS satellites; (4) high-quality TECs between low-altitude satellites with radio beacons and selected chains of receiving stations; (5) TECs from occultations between various low-altitude satellites and between low and high altitude satellites; and (6) line-of-sight ultraviolet emission data, which can be used to infer ionospheric parameters.

In general, data assimilation is not straightforward and the ingestion of different data types into a real-time model can lead to erroneous ionospheric reconstructions if care is not exercised. The problem is that all of the different data types have uncertainties and/or biases. Even for a given data type, different instruments can have different, and sometimes unknown, biases. Consequently, for real-time data assimilation, software must be developed to detect and eliminate bad data, to account for data gaps, and to analyze data streams for long-term problems, such as changes in biases and instrument degradation. Additional care must be exercised when dealing with line-of-sight data (slant TECs and UV emissions) so that N_e gradients are not smoothed, because a knowledge of horizontal gradients is important for some applications.

The latest approach in ionospheric data assimilation involves the use of a Kalman filter and a physics-based ionospheric model [*Howe et al.*, 1998; *Iijima et al.*, 1999; *Scherliess et al.*, 2001]. The Kalman filter combines measurements from an observing system with the physics contained in an ionospheric model, taking into account the corresponding statistical descriptions of uncertainties [*Gelb*, 1974]. The Kalman filter is a sequential least-squares procedure that finds the best estimate of the state at time t based on all of the information prior to this time. Specifically, the Kalman filter performs a recursive least-square inversion of all of the observations (e.g., slant TEC,

in situ satellite data, bottomside profiles, etc.) for the model variable (e.g., N_e) using the physics-based model as a constraint. In practice, a weighted average of the model estimate and the measurements is taken, using the relative accuracy of the two as the weights. The net result is an improved estimate (in a statistical sense) of the model variable (N_e). It has the least expected error given the measurements, model, and error statistics.

6. SUMMARY

Several different model types are currently being used by the ionospheric community, including empirical, parameterized, physics-based, tomographic, and data assimilation models. The models are being used for ionospheric specification, forecasting, and research. At present, a significant research effort is being devoted to coupling physics-based models of the near-Earth environment, including the ionosphere, thermosphere, plasmasphere, polar wind, and magnetosphere. A major challenge during the next decade is to self-consistently include the microphysics (e.g., plasma instabilities) in the global physics-based models. Another modeling approach that is rapidly becoming popular is physics-based data assimilation modeling. With the advent of hundreds of thousands of ionospheric measurements coming on line during the next decade, data assimilation modeling could provide global ionospheric reconstructions on a continuous basis throughout the day. This information, in turn, should have a major impact on the field. Finally, it should be noted that the extensive knowledge gained from the Earth's ionosphere has been invaluable for laying the foundation for studies of other ionospheres, including planets, moons, and comets. It is anticipated that this will continue to be true in the future.

Acknolwedgements. This research was supported by the NASA Sun-Earth Connection Theory Program (SEC) grant NAG5-8227 and NSF grant ATM-0000171 to Utah State University.

REFERENCES

Anderson, D. N., et al., Intercomparison of physical models and observations of the ionosphere, *J. Geophys. Res., 103*, 2179-2192, 1998.

Banks, P. M., R. W. Schunk, and W. J. Raitt, The topside ionosphere: A region of dynamic transition, *Annl. Rev. Earth Planet. Sci., 4*, 381, 1976.

Bradley, P. A., and J. R. Dudeney, A simple model of the vertical distribution of the electron concentration in the ionosphere, *J. Atmos. Terr. Phys., 35*, 2131-2146, 1973.

Burch, J. L., The magnetosphere, in *The Upper Atmosphere and Magnetosphere*, National Academy Press, 1977.

Cravens, T. E., *Physics of Solar System Plasmas*, Cambridge University Press, U.K., 1997.

Daniell, R. E., et. al., Parameterized ionospheric model: A global ionospheric parameterization based on first principles models, *Radio Sci., 30*, 1499-1510, 1995.

Fuller-Rowell, T. J., M. Codrescu, R. J. Moffett, and S. Quegan, Response to the thermosphere and ionosphere to geomagnetic storms, *J. Geophys. Res., 99*, 3893-3914, 1994.

Gelb, A., *Applied Optimal Estimation*, MIT Press, Cambridge, MA, 1974.

Kelley, M. C., *The Earth's Ionosphere*, Academic Press, New York, 1989.

Howe, B. M., K. Runciman, and J. A. Secan, Tomography of the ionosphere: Four dimensional simulations, *Radio Sci., 33*, 109-128, 1998.

Iijima, B. A., et al., Automated daily process for global ionospheric total electron content maps and satellite altimeter ionospheric calibration based on Global Positioning System data, *J. Atmos. Solar-Terr. Phys., 61*, 1205-1218, 1999.

Ossakow, S. L., et al., Dependence of altitude of F peak on bottomside background electron density gradient scale length, *J. Geophys. Res., 84*, 17, 1979.

Rawer, K., D. Bilitza, and B. W. Reinisch, International reference ionosphere, *Adv. Space Res., 27*, 2001.

Richmond, A. D., Assimilative mapping of ionospheric electrodynamics, *Adv. Space Res., 12*, 59-68, 1992.

Rishbeth, H., The centenary of solar-terrestrial physics, *J. Atmos. Solar-Terr. Phys.*, 2001.

Roble, R. G., et. al., A coupled thermosphere/ionosphere general circulation model, *Geophys. Res. Lett., 15*, 1325-1328, 1988.

Scherliess, L., et al., A physics-based Kalman filter model of the ionosphere, *J. Geophys. Res.*, 2001.

Schunk, R. W., *Handbook of Ionospheric Models*, Utah State University Press, 1996.

Schunk, R. W., and A. F. Nagy, *Ionospheres*, Cambridge University Press, New York, 2000.

Schunk, R. W., and J. J. Sojka, Global ionosphere-polar wind system during changing magnetic activity, *J. Geophys. Res., 102*, 11625-11651, 1997.

Sekar, R., R. Susasini, and R. Raghavaro, Effects of vertical winds and electric fields in the nonlinear evolution of equatorial spread F, *J. Geophys. Res., 99*, 2205-2213, 1994.

Sojka, J. J., et al., Driving a physical ionospheric model with a magnetospheric MHD model, J. *Geophys. Res., 102*, 22209-22220, 1997.

Zalesak, S. T., S. L. Ossakow, and P. K. Chaturvedi, Nonlinear equatorial spread F: The effect of neutral winds and background Pedersen conductivity, *J. Geophys. Res., 87*, 151-166, 1982.

Robert W. Schunk, Center for Atmospheric and Space Sciences, Utah State University, Logan, UT 84322-4405.

The Application of General Circulation Models to the Atmospheres of Terrestrial-Type Moons of the Giant Planets

I. C. F. Müller-Wodarg

Atmospheric Physics Laboratory, University College London, United Kingdom and Center for Space Physics, Boston University, Boston, MA

General Circulation models are for the first time applied to the upper atmospheres of Saturn's moon Titan and Neptune's moon Triton. Calculations reveal that solar driven day-night temperature differences are during solar maximum (minimum) around 20 (10) K on Titan and 1.5 (0.6) K on Triton, with day to night horizontal winds of up to 60 (30) m/sec on Titan and 3 (1) m/sec on Triton. Analysis of the heating terms reveals that solar heating is balanced primarily by vertical conduction on both moons and in addition by HCN rotational line cooling on Titan. Adiabatic processes are shown to be important in reducing the day-night temperature differences. The thermospheres of both moons extend into space by around 30% of the moons' radii, enhancing not only the vertical winds and adiabatic processes, but also high latitude nightside solar heating. This is particularly significant on Titan and implies that nighttime temperatures poleward of 60° differ little from the dayside values, with important implications on the global dynamics. Analysis of acceleration terms shows that dynamics driven by solar heating are characterized by the balance between pressure gradients and viscous drag. On Titan, curvature forces and horizontal advection play an important role as well. Geostrophic balance does not apply on either of the moons. Effects of energetic coupling to the magnetospheres of Saturn and Neptune and coupling to lower atmospheric waves and winds are predicted to be potentially important in altering temperatures and dynamics.

1. INTRODUCTION

Our solar system consists of nine planets which are orbited by at least 90 natural satellites. The moons may be divided according to their sizes into three different categories, those with radii larger than around 1000 km; those with radii ranging from around 100 to 1000 km and, thirdly, those smaller than 100 km which are mostly irregularly shaped. Given that our own moon has a radius of 1700 km, the first category are referred to as "terrestrial type moons". Apart from our own, all other of the 7 terrestrial-sized moons are located in the outer parts of our solar system, orbiting planets Jupiter, Saturn and Neptune. The Earth's moon and Jupiter's Ganymede, Io, Europa and Callisto are surrounded by thin transient gas layers, as discussed in Chapters III.2 and III.3 of this monograph. In contrast, the other two terrestrial-type moons, Saturn's Titan and Neptune's Triton possess non-transient (permanent) atmospheres.

Atmospheres in the Solar System: Comparative Aeronomy
Geophysical Monograph 130

10.1029/130GM20

Titan, located at 9.5 A.U. distance from the Sun, was discovered in 1655 by Dutch astronomer Cristiaan Huygens. It is after Ganymede the second-largest moon in our solar system, around 40% the size of Earth and larger than planet Mercury. Titan, like Venus, is permanently covered by a thick global layer of clouds, obscuring any surface features from our view. Triton is almost half the size of Titan and slightly smaller than the Earth's moon. Given its small size and large distance from the Sun of 30 A.U., Triton was discovered only in 1846 by British astronomer William Lassel and is the only moon in our solar system to orbit a planet in retrograde direction, opposite to the planet's rotation. As our own moon, Titan and Triton orbit their mother planets at the same rate as they rotate, so the same side of their surfaces always faces the planet.

This Chapter presents calculations of global wind and temperature profiles in the upper atmospheres of Titan and Triton, using general circulation models (GCM's). Similar models have proven to be very useful in understanding the behavior of the Earth's and other planetary atmospheres (see Chapters IV.1, IV.2). Section 2 gives a historical overview of milestones in the exploration of Titan's and Triton's atmospheres and lists key properties. Section 3 is a brief description of the GCM codes and Section 4 presents the results from calculations. Section 5 discusses coupling of the thermospheres to regions above and below, while Section 6 summarizes the findings.

2. ATMOSPHERIC STRUCTURE AND COMPOSITION

2.1. Titan

The atmosphere of Titan has some remarkable similarities with that of Earth, prompting the idea that Titan may resemble the Earth's atmosphere during its early pre-biotic development stages. The surface pressure on Titan is surprisingly high at around 1.6 bar, 60% larger than that on Earth, and the primary atmospheric gas is N_2, followed by hydrocarbons, mostly CH_4. Due to the smaller mass and radius of Titan, gravity is smaller than on Earth and hence the atmosphere more extended. Calculations in Section 4 will show that the extended nature of the atmosphere has important consequences for the gas behavior.

Most of our current knowledge about Titan was provided by the remote sensing experiments during the Voyager 1 and 2 flybys in November 1980 and August 1981, respectively. The atmospheric thermal structure below 200 km was measured by the radio occultation experiment (RSS), infrared interferometer spectrometer (IRIS) and ultraviolet spectrometer (UVS) of Voyager 1 in November, 1980 (*Lindal et al.*, 1983; *Lellouch et al.*, 1989; *Yelle et al.*, 1997), while the thermal structure above 500 km was derived both from the ultraviolet solar occultation experiment of UVS (*Smith et al.*, 1982) and the IRIS measurements on Voyager 2 in August, 1981 (*Letourner and Coustenis*, 1993). In their analysis of the UVS data, *Smith et al.* (1982) determined an exospheric temperature of 185±20 K, a CH_4 mole fraction of 8±3 % and a C_2H_2 mole fraction of around 1%. This pioneering investigation represented the first direct measurement of the composition of Titan's atmosphere and, along with the results from the radio occultation (*Lindal et al.*, 1983) and infrared observations (*Hanel et al.*, 1981), the first direct measurement of the temperature of Titan's atmosphere. Subsequently, *Strobel et al.*, (1992) pointed out apparent inconsistencies in the determination of CH_4 densities by *Smith et al.* and suggested a significantly lower mole fraction. A comprehensive analysis by Vervack et al. (2001) finds CH_4 and C_2H_2 mole fractions smaller than the results by *Smith et al.* and an exospheric temperature of 150±3 K, nearly 25 K cooler. Thus there remains some ambiguity about exospheric temperatures and some of the mole fractions. Further important information about Titan's atmosphere was provided by the occultation of 28 Sgr in July 1989 which allowed the derivation of temperature, pressure, haze optical depth and zonal velocities as a function of latitude and altitude in the 250 to 450 km height regime (*Hubbard et al.*, 1993). These observations suggested the presence of strong zonal jets in Titan's stratosphere and lower mesosphere with peak velocities of around 150 m/sec. These super-rotating jets may have important implications on the dynamics in the thermosphere, as discussed in Section 5. Strong jets are also found on Venus and Mars, as discussed in Chapter III.1.

Considerable advances in the exploration of Titan are expected from the forthcoming Cassini/Huygens mission, due to arrive at the Saturnian system in July 2004. The mission involves two spacecrafts, the Cassini orbiter and Huygens probe. The latter will enter Titan's atmosphere around January 2005 and, while parachuting to Titan's surface, retrieve a 1-dimensional profile of atmospheric parameters in the troposphere and stratosphere below 250 km altitude. In contrast, Titan's thermosphere will be explored by the Cassini orbiter throughout its anticipated lifetime of 4 years. On its orbit around Saturn, the Cassini spacecraft will dive into Titan's upper atmosphere, reaching down to altitudes of 950 km, and retrieve in-situ neutral and ion composition, temperatures and dynamics.

One-dimensional models for the thermal structure of Titan's upper atmosphere were presented by *Friedson and Yung* (1984), *Lellouch* (1990) and *Yelle* (1991). These models were constrained by Voyager data, primarily the solar occultation experiment observed with the ultraviolet spectrometer, and gave a comprehensive insight into the composition and energy sources and sinks. The models

suggest Titan's thermosphere to be heated primarily by absorption of solar EUV radiation through N_2 and CH_4 and cooled by radiative emissions in the rotational bands of HCN as well as downward molecular conduction. Some analyses of Voyager data inferred unusually large values for the eddy mixing coefficient of up to 10^8 cm^2/sec (*Strobel et al.*, 1992), indicating either unusually strong turbulent mixing on Titan or effective vertical transport of constituents. One-dimensional models do not calculate winds and thus cannot account explicitly for their effects on composition. Estimates of dynamics in Titan's thermosphere were presented by *Rishbeth et al.* (2000) through scale analysis of the equations of motion. First self-consistent calculations of dynamics in Titan's thermosphere were presented by *Müller-Wodarg et al.* (2000), using a global general circulation model. These calculations will form the basis for discussions in Section 4.

Titan orbits the Sun once every 29.5 years, spanning the duration of more than 2 solar cycles. As described earlier, the key observations were made in 1980/1981 and 1989, with Cassini observations due to take place between 2004 and 2008, almost one Titan year after the first observations. Figure 1 a) shows the change of Titan's sub-solar latitude with time between 1975 and 2010, with the observation dates and changes in solar activity indicated. The figure illustrates that Voyager measurements were made close to equinox conditions at solar maximum, while the Cassini mission will encounter late southern hemisphere summer to spring conditions at low to medium solar activity levels.

2.2. *Triton*

Not much was known about Neptune's largest moon Triton before the Voyager 2 flyby in summer 1989, including such fundamental parameters as mass, radius and surface albedo. Earlier ground-based observations of solar reflection spectra had already indicated the presence of surface ices on Triton, predominantly N_2 and trace amounts of CH_4 and CO (*Cruikshank and Silvaggio*, 1979), findings which were confirmed by Voyager data (*Cruikshank et al.*, 1993; *Owen et al.*, 1993). The atmosphere of Triton is considerably thinner than that of Titan, with a surface pressure of around 14 μbar (*Gurrola et al.*, 1991). Triton's atmosphere is believed to be in vapor pressure equilibrium with the surface ices, so it is maintained at a constant temperature by the surface ice through processes such as condensation and sublimation (*Trafton*, 1984; *Ingersoll*, 1990; *Yelle et al.*, 1995). This assumption constrains the one-dimensional models of vertical temperature and pressure profiles with the atmospheric measurements.

Temperature and pressure profiles were measured between the ground and 50 km altitude by the Voyager radio occultation experiment (RSS) (*Gurrola et al.*, 1991) and infrared interferometer spectrometer (IRIS) (*Conrath et al.*, 1989) and between 450 and 700 km altitude by the ultraviolet spectrometer (UVS) solar occultation experiments (*Broadfoot et al.*, 1989; *Krasnopolsky et al.*, 1993). Temperature is believed to initially decrease with altitude from its surface value by up to 1 K near 8 km height, the tropopause (*Yelle et al.*, 1991), and then increase to the exospheric value. The IRIS and UVS observations suggested temperature values of 38±3 K on the daytime surface, of 40±5 K between 0 and 50 km and exospheric values of 102±3 K between 450 and 700 km altitude. Models by *Strobel and Summers* (1995), *Krasnopolsky et al.* (1993) and *Strobel et al.* (1996) were constrained by these Voyager data and the studies by *Stevens et al.* (1992) suggested principal energy sources on Triton to be solar EUV absorption and precipitating electrons from Neptune's magnetosphere. The importance of magnetospheric heating on Triton is further discussed in Section 5. *Krasnopolsky et al.* (1993)

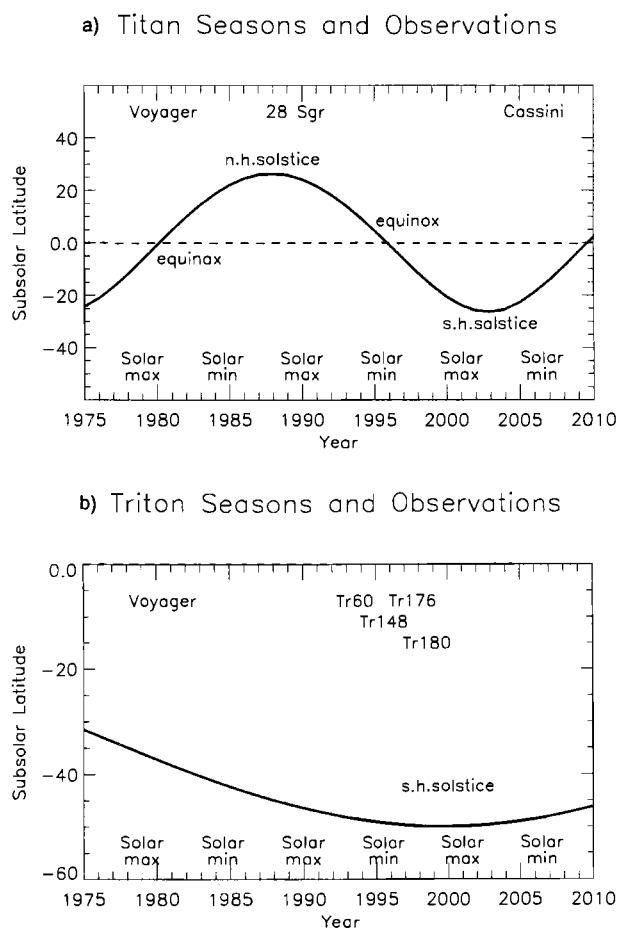

Figure 1. The change of sub-solar latitude between 1975 and 2010 for Titan (a) and Triton (b). Also shown are seasons, times of key observations and levels of solar activity.

Table 1. Fundamental parameters distinguishing the general circulation models of Titan and Triton used in this study.

Parameter	Titan	Triton
Radius	2575 km	1353 km
Sun distance	9.5 AU	30.5 AU
Pressure range	0.1 μbar - 1 *p*bar	1 μbar - 0.01 *p*bar
Height range	600 - ca. 1400 km	10 - ca. 420 km
Gravity at bottom	0.89 ms^{-2}	0.75 ms^{-2}
Rotation rate (duration of day) and orientation	4.6×10^{-6} s^{-1} (15.8 days)	-1.3×10^{-5} s^{-1} (5.6 days)
Max. subsolar latitude	$\lambda_{max} = 24°$	$\lambda_{max} = 50°$
Mixing ratios	*Yung et al.* [1984]	99.99 % N_2; 0.01 % CH_4

determined N_2 densities of 1×10^{15} cm^{-3} at the bottom of the thermosphere and *Strobel and Summers* (1995) derived CH_4 densities of 1×10^{11} cm^{-3} which become negligible at around 150 km altitude. It follows that maximum CH_4 mixing ratios on Triton are around 1×10^{-4}, considerably smaller than on Titan. Voyager UVS occultation data also suggested the presence of CH_4 haze particles in Triton's lower atmosphere (*Smith et* al., 1989; *Herbert and Sandel*, 1991) which may result from condensation of CH_4 photolysis products such as C_2H_4 (*Strobel et al.*, 1990). While N_2 and CH_4 were directly detected by the Voyager UVS solar and stellar occultations, only upper limits could be given for the CO abundance. The value has been subject of controversy, with estimates ranging from 0.01 (*Broadfoot et al.*, 1989) to 10^{-3} (*Strobel and Summers*, 1995) and 3×10^{-4} (*Stevens et al.*, 1992). Given that CO is an effective radiative coolant this value is of some importance when determining the energy loss processes in Triton's thermosphere.

First Earth-based data for the 20-100 km height regime were obtained from ground-based observations of stellar occultation in July 1993 (Tr60) and August 1995 (Tr148) (*Olkin et al.*, 1997) as well as July 1997 (Tr176) (*Elliot et al.*, 2000a) and, from the Hubble Space Telescope, in November 1997 (Tr180) (*Elliot et al.*, 1998; 2000b). These observations allowed detection of possible trends with time of the pressure and temperature values which could indicate seasonal changes. Given its long orbital period around the Sun (165 years), any seasonal changes on Triton over a few years are expected to occur slowly, and comparing Voyager observations to the stellar occultations of Tr60 and Tr148 indicated no clear trend beyond data accuracy. The Hubble Space Telescope observations of the Tr180 occultation however suggested that surface pressure had risen since the time of Voyager observations (*Elliot et al.*, 2000b), suggesting a warming of the N_2 surface frost. This trend is supported by the Tr176 occultation results (*Sicardy et al.*, 1998; *Elliot et al.*, 2000a). Triton reached southern hemisphere solstice (-49°87' sub-solar latitude) in September 2000, so a heating of the surface between 1989 and 1997 could suggest a larger concentration of N_2 ice at higher latitudes, which are illuminated strongest during solstice. Figure 1 b) illustrates the change of Triton's sub-solar latitude between 1975 and 2010 as well as the times of key observations. The figure illustrates that the occultation of Tr180 is most suitable for comparison with Voyager data since it occurred at roughly the same (high) level of solar activity, while all other occultations occurred closer to solar minimum conditions.

Several of the Voyager observations suggested the presence of strong lower atmosphere winds on Triton (*Smith et al.*, 1989; *Hansen et al.*, 1990; *Soderblom et al.*, 1990), which could be caused by N_2 maintaining vapor pressure balance with the surface ice (*Ingersoll*, 1990) or by uneven surface heating of frost and dark areas (*Elliot et al.*, 2000b). Ground-based observations of Tr60, Tr148 and Tr176 suggested a significant deviation of Triton's atmosphere from circular shape near 20 km altitude. One plausible explanation for this elliptical shape could be the presence of supersonic winds (280 m/sec, compared with a sound speed of 140 m/sec) in Triton's lower and middle atmosphere (*Elliot et al.*, 1997; *Elliot et al.*, 2000a), but since equator-to-pole variations of pressure at fixed altitude are of the same magnitude as the pressure itself, the elliptical shape is an unlikely permanent state of the atmosphere. Also, the non-spherical shapes during the Tr148 and Tr176 occultation were inconsistent with each other in terms of size and orientation (*Elliot et al.*, 2000a), so the strong jets on Triton and elliptical shape of its atmosphere are to-date still unresolved problems.

3. THE GENERAL CIRCULATION MODELS

The aim of our calculations is to compare the basic solar-driven dynamics and global temperature profiles on Titan and Triton and to understand their differences. Therefore, the types of models used here are general circulation models (GCM's). Two versions of the same GCM were used which differed only in the fundamental parameters summarized in Table 1. The calculations were carried out on a spherical co-

rotating Eulerian pressure coordinate system with fully flexible spatial and temporal resolutions which were set to 6° (latitude) by 18° (longitude) by 0.5 scale height (vertical), using a time step of 10 seconds. In essence, the two GCM's solve self-consistently the 3-dimensional time-dependent Navier-Stokes equations of energy, momentum and continuity by explicit time integration, taking into account external heating by solar EUV radiation. Solar EUV heating rates are calculated by integration of heating rates along the ray paths through the atmosphere. For Titan, the model also considers cooling in the rotational bands of HCN with full calculations of radiative transfer. Although CO and CH_4 cooling is thought to be present on Triton as well, it is in the thermosphere much less important than the HCN cooling on Titan and therefore ignored in these calculations. Other terms in the energy equation are molecular conduction, advection and adiabatic heating and cooling. The momentum equation used in both GCM's considers pressure gradients, Coriolis forces, advection, viscosity and curvature forces which arise from the gases moving along a sphere. A detailed description of the GCM for Titan, including a thorough discussion of the energy and momentum equation terms was given by *Müller-Wodarg et al.* (2000). Default boundary conditions are zero vertical gradients of temperature and winds at the top boundary and globally constant temperatures with vanishing winds at the bottom boundary. In Section 5, the implementation of winds at the lower boundary is discussed in order to account for dynamical coupling to lower heights. For Titan, the three constituents N_2, CH_4 and HCN are considered, with the former two being the main absorbers of solar EUV radiation and thus responsible for the solar heating input, while the latter, as discussed previously, is an important radiative coolant. Photochemistry and gas diffusion are not calculated here, the constituent mixing ratios are kept globally constant on pressure levels. First results from a recently developed version of the Titan GCM which calculates self-consistently the 3-component gas diffusion (*Müller-Wodarg and Yelle*, 2001) have shown that inclusion of gas diffusion has a small influence on the temperature structure and dynamics, increasing the day-night temperature gradient by 10 K at most and reducing the horizontal wind speeds by up to 10 m/sec. Ignoring photochemistry on Titan is a valid approximation for the purpose of these calculations since we are primarily interested in diurnal features and photochemical lifetimes of N_2 and CH_4 in the height regime of interest are longer than a Titan day. Gas mixing ratios in the Titan GCM are here taken from the model by *Yung et al.* (1984), while for Triton we assumed a globally constant height-independent N_2 mixing ratio of 99.99 % and CH_4 mixing ratio of 0.01 %, based on the values by *Krasnopolsky et al.* (1993) and *Strobel and Summers* (1995).

4. SOLAR DRIVEN DYNAMICS AND TEMPERATURES

4.1. Global Structures

Figure 2 shows global profiles of exospheric temperatures and horizontal winds on Titan and Triton for equinox and southern hemisphere solstice conditions, as calculated by the GCM's. Equinox simulations were carried out at solar maximum, while the solstice runs assumed solar minimum, thus mimicking seasonal and solar conditions encountered on Titan by Voyager and Cassini, respectively (see Figure 1 a). Values in Figure 2 are shown as profiles versus latitude and local time. For convenience, the days were subdivided into 24 intervals, each interval corresponding to 15.8 h on Titan (one "Titan hour") and 5.6 h on Triton (one "Triton hour"). Note that in the interest of direct comparison between the two moons Figure 2 shows temperatures and winds driven by solar heating alone. Discussions in Section 5 will show that dynamical coupling to lower altitudes and energetic coupling to the magnetospheres of Saturn and Neptune are also likely to affect the temperatures and winds. Nevertheless, it is important to be able to separate out the solar-driven component, so in the following we concentrate on that one.

The simulations shown in Figure 2 illustrate the following basic differences between the two moons: (a) Solar driven exospheric temperatures on Titan reach 178 (157) K at solar maximum (minimum), those on Triton reach 53 (44) K. Note that for Triton the measured values are 102 K (see 2.2) and the additional heating source are believed to be precipitation of magnetospheric electrons (*Stevens et al.*, 1992, see also Section 5). The solar-driven exospheric temperatures for Titan are in good agreement with measurements, suggesting that solar radiation provides the principal energy source there. On Titan, the globally averaged temperature at the base of the thermosphere for solar maximum (minimum) is around 140 (135) K. On Triton we assume a value of 40 K both at solar maximum and minimum. Exospheric values in the GCM calculations are reached near the 10 *n*bar (1200 km) level on Titan and 1 *n*bar (370 km) level on Triton. Note that values of heights associated with the pressures for Triton are lower in our simulations, compared to Triton's real atmosphere, due to the smaller temperature values calculated by the GCM. (b) Day-night temperature differences on Titan are 20 (10) K at solar maximum (minimum), corresponding to 11 (6)% of the background values. Those on Triton are 1.5 (0.6) K, or 3 (1)%. For comparison, day-night thermospheric temperature variations are on average around 25% on Earth, 40% on Mars and 80% on Venus (see Chapter IV.1 and *Bougher et al.*, 1999). The reason for the considerably smaller day-night differences on Triton is that solar heating there is considerably weaker than on Titan by a factor of 100

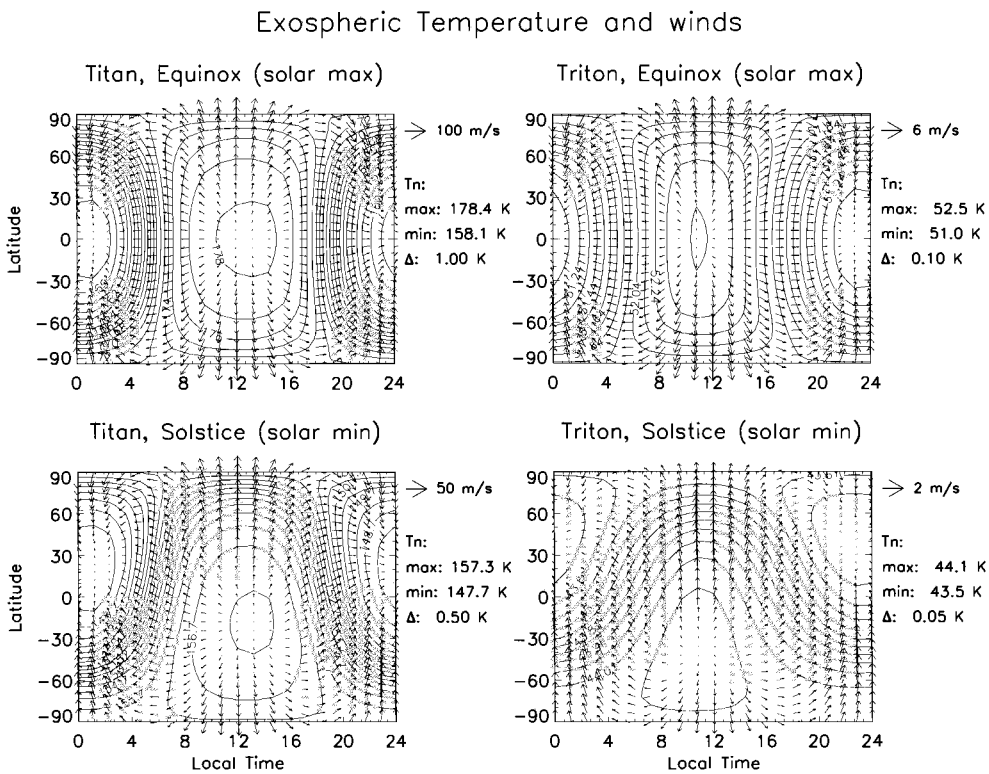

Figure 2. Exospheric solar-driven temperatures and horizontal winds on Titan (left panels) and Triton (right panels), as calculated by general circulation models for equinox conditions (upper row) and southern hemisphere solstice (lower row). The equinox simulations are for solar maximum, the solstice ones for solar minimum.

and its rotation rate around 3 times faster. Discussions of heating terms in Section 4.3 will show that adiabatic dayside cooling and nightside heating contribute towards reducing the day-night temperature differences on both moons. Adiabatic processes are important on Mars as well, due to its small radius, but less on Earth and Venus (see Chapter IV.1 and *Bougher et al.*, 1999; *Bougher et al.*, 2000). On Titan, an additional factor are the day to night winds which transport energy into the nightside. (c) Horizontal winds on Titan reach 60 (30) m/sec at solar maximum (minimum), those on Triton 3 (1) m/sec. The flow on both moons is essentially from day to night and mostly perpendicular to the isotherms (isobars), due to the balance between pressure gradients and viscosity, as discussed in 4.2. Vertical winds (not shown) reach 1.1 (0.45) m/sec on Titan during solar maximum (minimum), those on Triton 0.11 (0.03) m/sec. Vertical winds flow upward during the day and downward during night, their contours aligning well with those of the temperatures in Figure 2. These vertical winds are generated primarily by the divergence of horizontal winds and to much lesser extent by the thermal expansion and contraction of the atmosphere. (d) The daily global temperature maximum over the equator at equinox occurs roughly one "Titan hour" after local noon on Saturn's moon and one "Triton hour" before local noon on Neptune's moon. The local temperature phase depends on latitude, being largest at the latitude of the sub-solar point and decreasing with distance from it. (e) Due to the larger inclination of Triton's rotation axis and resulting larger sub-solar latitude at solstice, the summer temperature maximum on Triton occurs at higher latitude (50°) than on Titan (24°). (f) Temperatures on Titan remain fairly constant with latitude and local time on the dayside, but horizontal gradients become up to 4 times stronger at dawn, dusk and the nightside. As a result, equatorward winds on the nightside are stronger than the poleward winds on the dayside. Similarly, the day-night winds on Titan tend to accelerate when passing the terminator into the nightside.

The sharper temperature gradients on Titan's nightside are linked to a phenomenon not found as strongly on Earth and other planets, the high latitude nightside solar heating, which is illustrated in Figure 3. The diagram is a cut through Titan (round filled center) and its thermosphere (ring) from day (right) to night (left) during equinox, the poles being located at the top and bottom. The contour levels are logs of solar volume heating rates. Values are largest over the equatorial sub-solar point and decrease towards the poles due to the

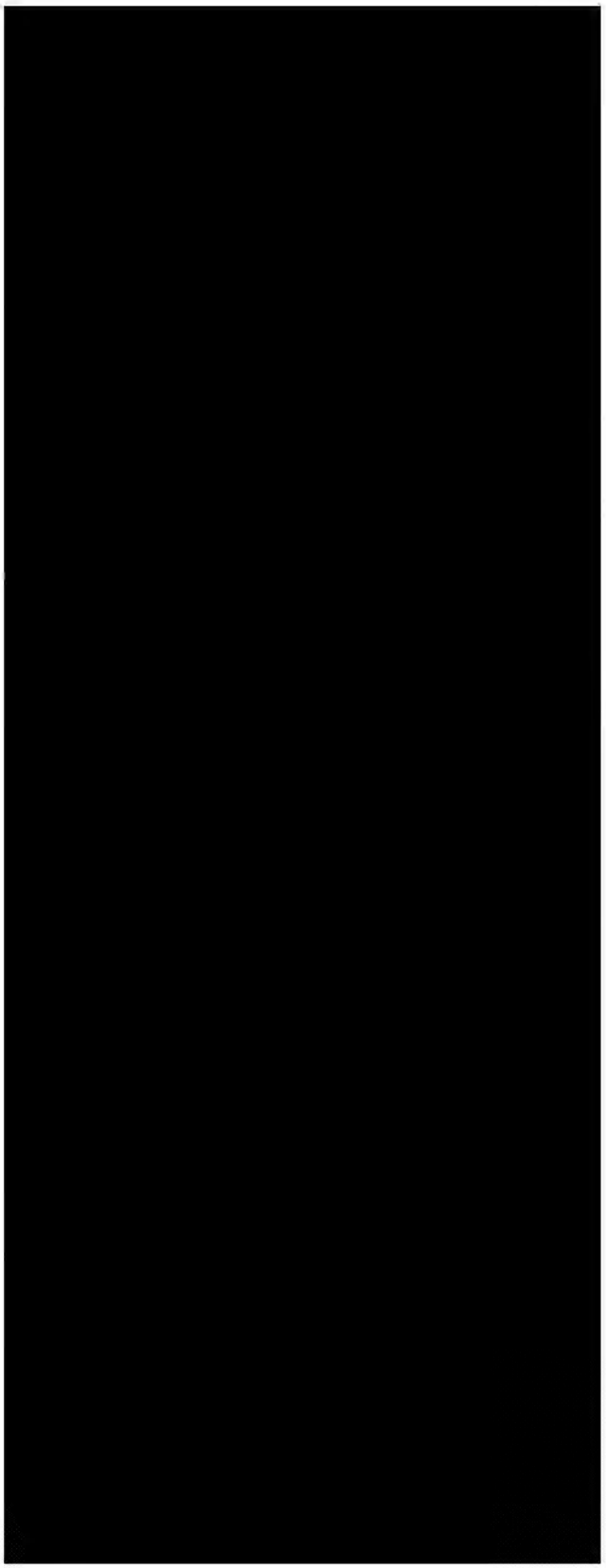

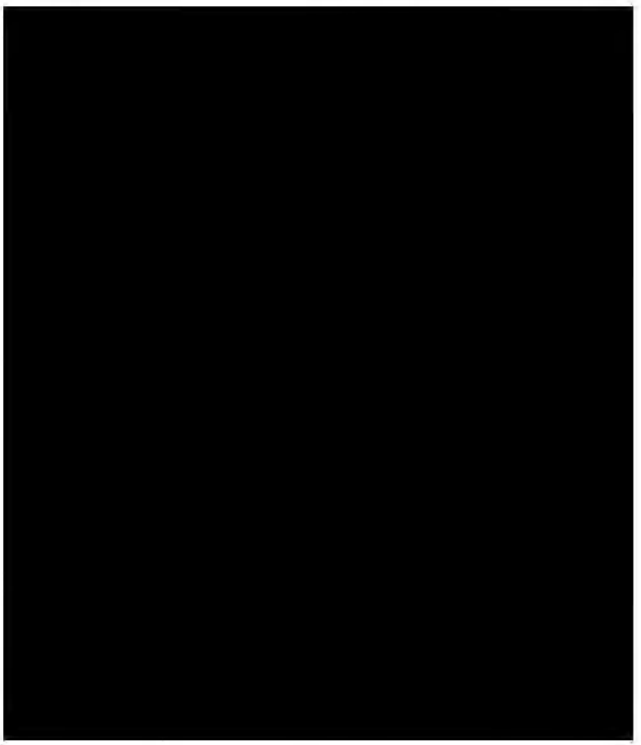

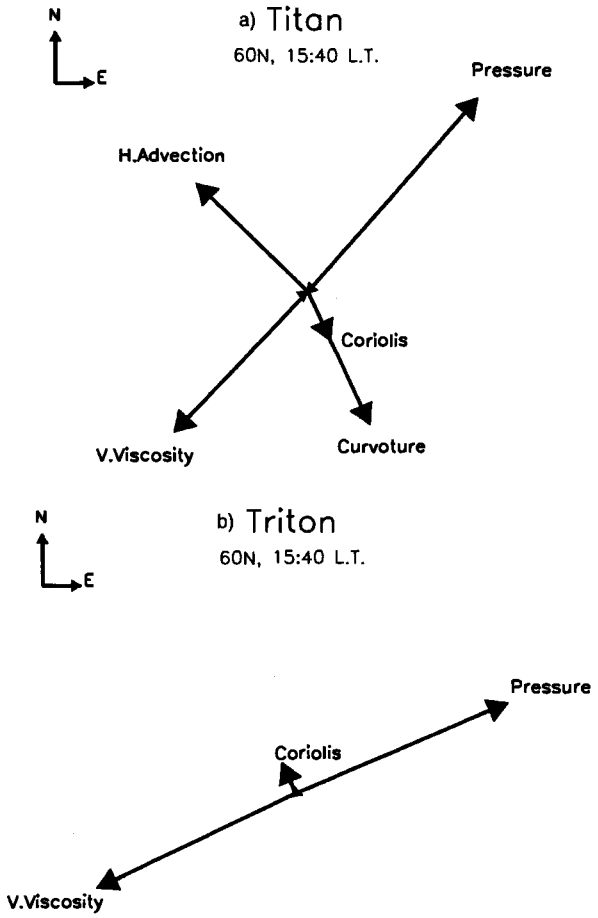

Figure 4. Horizontal acceleration terms in the exosphere at 60°N, 15:40 h local time on Titan (a) and Triton (b) during equinox conditions. North points up, east towards the right. The pressure arrow has a value of 1.6×10^{-3} m/sec^2 for Titan and 4.1×10^{-4} m/sec^2 for Triton.

4.3. Energy Sources and Sinks

The discussions of acceleration terms in the previous section can similarly be carried out for heating terms in order to explain the global structure of temperatures on Titan and Triton (contours in Figure 2). Heating terms during equinox conditions at solar maximum for latitude 60°N versus local time (LT) are shown in Figure 5 for Titan (a) and Triton (b). The main energy source on both moons in our simulations is solar heating (solid curves) which is zero between 22:00 (21:00) and 02:00 (03:00) h LT on Titan (Triton) and rises to a maximum at local noon. Note that solar heating persists for another 4 (3) hours into the evening sector on Titan (Triton) and starts earlier in the morning by the same amount of time This is a result of the nightside heating discussed in Section 4.1 and illustrated in Figure 3. Sunset occurs 1 hour later and sunrise one hour earlier on Titan than on Triton, but the solid curve in Figure 5 b) illustrates that nightside heating is also important on Triton. In terms of vertical structure (not shown), the solar heating curve on Titan peaks near the 10 and 0.1 nbar pressure levels, corresponding to around 750 and 1000 km altitude, with globally averaged solar maximum heating rates of 6×10^{-10} and 4×10^{-10} ergs/cm^3/sec, respectively. The lower of these peaks is primarily due to absorption of the Lyman α line (1216 Å) by CH_4, while the upper peak is caused by absorption in the He II line (304 Å) through N_2. This illustrates that both CH_4 and N_2 are important solar energy absorbers on Titan. Solar EUV heating on Triton in our simulations peaks near 180 km altitude at rate of around 9×10^{-11} ergs/cm^3/sec and is primarily due to the He II line absorption by N_2. Above 150 km, CH_4 disappears on Triton (*Strobel and Summers*, 1995), but Lyman α line absorption by CH_4 does occur in our simulations at the bottom of the thermosphere, near the 20 km altitude level, with a globally averaged rate of around 1×10^{-10} ergs/cm^3/sec.

Energy sinks on Titan are primarily the HCN rotational band cooling (narrow-dashed line in Fig. 5 a) and vertical molecular heat conduction (dotted line in Fig. 5 a). Simulations for solar maximum (minimum) conditions have shown the HCN radiative cooling to be the dominant cooling term below the 1 *p*bar (10 *p*bar) pressure level, corresponding to around 1450 (1200) km altitude, while at higher altitudes molecular conduction dominates. On Triton (Figure 5 b) molecular conduction is the principal cooling term at all heights throughout the thermosphere. Adiabatic heating and cooling (dashed-dotted lines), generated by the

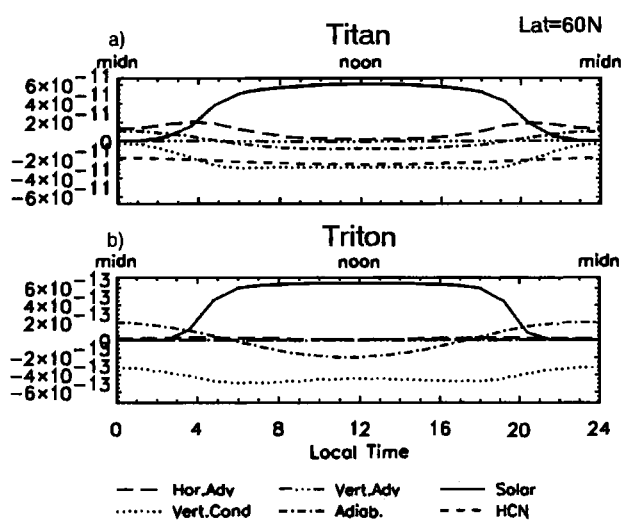

Figure 5. Heating and cooling terms in the exosphere at 60°N versus local time on Titan (a) and Triton (b). Simulations are for equinox conditions at solar maximum. Rates are given in units of ergs/cm^3/sec.

vertical motion of gases, also play an important role on both moons, cooling the dayside and heating nightside. As a result, the adiabatic processes contribute towards reducing the day-night temperature differences. The large magnitudes of adiabatic terms are partly due to the small moon radii. Another important factor is the large change of gravity acceleration with height. On Titan (Triton), gravity at the top of the thermosphere is only around 40 (60) % of the value at the bottom, while on Earth it is 86 % the bottom level value. This illustrates that changes of gravity with height are much more important on Titan and Triton than on Earth. Adiabatic processes were also found to play a role on Mars (see Chapter IV.1). Figure 5 illustrates that horizontal advection (wide-dashed lines) is important on Titan, but less so on Triton, due to the smaller winds there and faster rotation rate of the moon. Energy on Titan is transported by horizontal winds from the hotter dayside into the dawn and dusk as well as night sectors, thus also contributing towards reducing the day-night temperature difference. At dawn and dusk it amounts to roughly the same value as solar heating, while on the nightside it is as strong as adiabatic heating.

These discussions have shown that dynamical terms play an important role in determining the energy distributions on Titan and Triton. Terms such as adiabatic heating and cooling as well as horizontal advection cannot be considered in 1-D models since these do not calculate vertical and horizontal winds. The use of general circulation models have enabled us for the first time to evaluate the importance of these terms on Titan and Triton.

5. DYNAMICAL AND ENERGETIC COUPLING TO OTHER REGIONS

5.1. Coupling to the Magnetosphere

Coupling to the magnetosphere can generally occur through three different processes, particle precipitation, Joule heating and ion-neutral drag. In the first, particles originating from the magnetosphere travel along the magnetic field lines and hit the atmospheric gas molecules, causing localized ionization and heating. The second is a result of electrical currents which result from convection electric fields, generated by the moving magnetospheric field lines. Both forms of heating alter pressure gradients and thereby the direction of the neutral winds. The third form of coupling consists in momentum exchange between colliding ions and neutral particles. It only plays a role when ions are constrained in their motion by strong intrinsic magnetic fields, such as that on Earth, and the Gas Giants. Titan, Triton and other weakly magnetized bodies experience only the first two forms of coupling to the magnetosphere. For a more comprehensive discussion of magnetospheric coupling, see Chapter II.

The calculations presented in Section 4 considered solar heating as the only external source of energy on Titan and Triton. By doing so, globally averaged exospheric temperatures of around 170 (50) K were achieved on Titan (Triton) for solar maximum conditions. For Titan the value is in good agreement with Voyager observations (*Smith et al.*, 1982), but for Triton it lies far below the value of 102±3 K suggested by the Voyager UVS solar occultation experiments (*Broadfoot et al.*, 1989; *Krasnopolsky et al.*, 1993). This shows that Titan's thermal structure can be understood on the basis of solar EUV and UV heating alone, while on Triton an additional energy source is needed to maintain the 102 K thermosphere. Calculations by *Stevens et al.* (1992) showed that magnetospheric power input could provide the missing energy on Triton. The moon lies within the magnetosphere of Neptune and is exposed to energetic plasma traveling from Neptune's upper atmosphere along the magnetic field lines into the upper atmosphere of Triton. There, they cause ionization and dissociation of N_2 molecules. The generated vibrationally excited N_2 molecules collide with ionospheric electrons, thus generating translational energy, while the generated N_2^+ ions recombine and generate fast N atoms or react with H_2 to create fast H atoms. These processes generate heating at around 350 km altitude which can reach up to 20 times the solar heating rate (*Stevens et al.*, 1992). The magnetospheric heating is most effective when Triton is positioned over Neptune's magnetic equator. The 28° tilt of Neptune's rotational axis combined with the 47° tilt of its magnetic axis and Triton's 157° orbital inclination give rise to a complicated geometry of Neptune's magnetic field with respect to Triton. As Neptune rotates once every 16.1 hours and Triton once every 5.6 days, Neptune's magnetic equator crosses Triton roughly 8 times per day. Furthermore, a different side of Triton faces Neptune every time it crosses the magnetic equator, so both the intensity and global distribution of magnetospheric heating experienced on Triton will change with time. Since the heating is not distributed uniformly across the globe it will affect pressure gradients and thereby winds. Due to the complexity of the spatial distribution and time variation of these pressure gradients, the induced wind patterns will be similarly complex, with globally propagating waves. So, magnetospheric heating on Triton is likely not only to considerably affect the exospheric temperatures, but also the global winds. No calculations have so far been carried out to quantify this effect.

The impact of magnetospheric electrons from Saturn on the upper atmosphere of Titan was calculated by *Galand et al.* (1999). Their calculations suggested a magnetospheric heating rate comparable with the solar energy input. This will affect global winds as well. An interesting aspect about Titan is that it lies partly outside and partly inside Saturn's magnetosphere. When positioned between the Sun and Saturn, the solar wind pressure sufficiently pushes Saturn's

magnetosphere back for Titan to lie outside the magnetosphere and exposed to the solar wind. In this scenario, no magnetospheric heating occurs on Titan. Half an orbit later Titan lies well within the magnetosphere, shielded from the solar wind but exposed to magnetospheric particles. With the solar heating being fixed in the local time frame and the magnetospheric one in the longitude frame, the two beat against each other, sometimes heating the same hemisphere and at other times the opposite ones. So, magnetospheric heating on Titan is likely to have interesting effects on the winds as well.

5.2. Coupling to the Lower Atmosphere.

The simulations discussed in Section 4 assumed zero winds at the models' lower boundaries and thus ignored any effects of vertical coupling to lower altitudes. This coupling is important on Earth, where upwards propagating tides and planetary waves have a strong influence on the dynamics and energetics of the thermosphere (see Chapter III.1). Theoretical studies for Jupiter (*Matcheva and Strobel*, 1999; *Hickey et al.*, 2000; *Matcheva et al.*, 2001) showed that upward propagating gravity waves could explain its large exospheric temperatures. Tides are also found to affect the thermosphere of Mars (see Chapter III.1 and *Forbes and Hagan*, 2000; *Wilson*, 2000). The plausible question is thus what role this coupling to lower altitudes plays on Titan and Triton.

The presence of strong zonal jets in the stratosphere of Titan was suggested from Voyager observations by *Flasar et al.* (1981) and inferred from observations of the 28 Sgr occultation by Titan (*Hubbard et al.*, 1993). Wind speeds with peak values of up to 175 m/sec were proposed and later theoretically reproduced in calculations by *Hourdin et al.* (1995). To-date, it is unclear what happens to these jets in the 300-600 km height regime, so we do not know whether these zonal jets are still present at the base of the thermosphere. Simulations by *Müller-Wodarg et al.* (2000) have shown that the presence of such jets at the base of the thermosphere would considerably affect dynamics of the thermosphere, superimposing themselves almost linearly onto the solar-driven thermospheric winds of Figure 2. One implication of this is that wind measurements from Cassini in the thermosphere could be used to constrain dynamics at the base of the thermosphere as well, more than 350 km below the anticipated altitude of the measurements. As pointed out in Section 2.2, the presence of zonal jets was also proposed below 100 km altitude for the atmosphere of Triton (*Smith et al.*, 1989; *Hansen et al.*, 1990; *Soderblom et al.*, 1990). Since these observations provide no coherent picture no attempts were made here to simulate their effects on thermospheric dynamics. In principle, however, Triton's thermosphere should respond similarly to that of Titan.

Rishbeth et al. (2000) pointed out the possibility of gravitational semidiurnal tides on Titan. Due to the 3% eccentricity of Titan's orbit around Saturn, the gravitational pull on Titan's atmosphere varies semidiurnally. Since the same side of Titan always faces Saturn, these oscillations would be fixed in longitude. Vertical propagation of these oscillations may affect the dynamics of Titan's thermosphere. Solar tides, which are important on Earth, may also be present on Titan, but no calculations have so far been carried out to quantify them.

6. CONCLUSIONS

This chapter presented the application of general circulation models (GCM's) to the thermospheres of Titan and Triton. It showed that such models provide a deep insight into the morphology of processes, allowing to analyze the accelerations and energy balance globally. Furthermore, they allow us to put local phenomena into a global context, which is of paramount importance when carrying out localized measurements. Finally, these models allow us to study an atmosphere under various conditions of solar activity and season, more than most measurements can cover. Nevertheless, the output from such models should be met with caution. Calculations in GCM's are carried out on the basis of fundamental equations of gas dynamics and thus "physically correct". But whether the models reproduce atmospheres realistically depends critically on the physical processes considered and the accuracy of the constraints. Discussions in Section 5 provided an example for this, showing the importance of coupling to regions above and below, which hadn't been considered in the simulations presented here. Nevertheless, there is a physical justification for omitting these processes at first, in order to understand better the complex coupled systems through separation of the different contributions. The other key factor affecting results is the accuracy of constraints. Modeling magnetosphetric coupling accurately requires good knowledge of the magnetic field configuration and plasma fluxes, which in the case of Titan and Triton are yet poorly known, but Cassini measurements are anticipated to significantly improve our knowledge at least for Titan. Comparing our GCM simulations with Cassini measurements will also allow us to constrain a third contribution to thermospheric dynamics, the coupling from below. So, the use of a general circulation model for Titan's thermosphere, such as that presented here, will play an important role in the analysis of Cassini data, allowing us to potentially expand the vertical height coverage of the measurements by constraining the vertical coupling from below. Planned future extensions for the Titan GCM include self-consistent calculations of Titan's ionosphere as well.

Acknowledgments. Development of the Titan general circulation model was carried out in close collaboration with R. V. Yelle of Northern Arizona University, M. Mendillo of Boston University and A. D. Aylward of University College London (UCL). This work was funded, in part, by NSF grant AST 9816239. All calculations were carried out on the High Performance Service for Physics, Astronomy, Chemistry and Earth Sciences (HiPerSPACE) Silicon Graphics Origin 2000 supercomputer located at UCL and funded by the British Particle Physics and Astronomy Research Council (PPARC). The author wishes to thank both referees for their useful comments.

REFERENCES

Bougher, S. W., S. Engels, R. G. Roble, and B. Foster, Comparative terrestrial planet thermospheres, 2, Solar cycle variation of global structre and winds at equinox, *J. Geophys. Res.*, *104*, 16,591-16,611, 1999.

Bougher, S. W., S. Engels, R. G. Roble, and B. Foster, Comparative Terrestrial Planet Thermospheres: 3. Solar Cycle Variation of Global Structure and Winds at Solstices, *J. Geophys. Res.*, *105*, 17,669-17,689, 2000.

Broadfoot, A. L., et al., Ultraviolet spectrometer observations of Neptune and Triton, *Science*, *246*, 1459-1466, 1989.

Conrath, B., et al., Infrared observations of the Neptunian system, *Science*, *246*, 1454-1456, 1989.

Cruikshank, D. P., and P. M. Silvaggio, Triton: A satellite with an atmosphere, *Astrophys. J.*, *233*, 1016-1020, 1979.

Cruikshank, D. P., T. L. Roush, T. C. Owen, T. R. Geballe, C. de Bergh, B. Schmitt, R. H. Brown, and M. J. Bartholomew, Ices on the surface of Triton, *Science*, *261*, 742-745, 1993.

Elliot, J. L., J. A. Stansberry, C. B. Olkin, M. A. Agner, and M. E. Davies, Triton's Distorted Atmosphere, *Science*, *278*, 403-404, 1997.

Elliot, J. L., et al., Global warming on Triton, *Nature*, *393*, 765-767, 1998.

Elliot, J. L., et al., The Prediction and Observation of the 1997 July 18 Stellar Occultation by Triton: More Evidence for Distortion and Increasing Pressure in Triton's Atmosphere, *Icarus*, *148*, 347-369, 2000a.

Elliot, J. L., D. F. Strobel, X. Zhu, A. Stansberry, L. H. Waserman, and O. G. Franz, The thermal structure of Triton's middle atmosphere, *Icarus*, *143*, 425-428, 2000b.

Forbes, J. F., and M. E. Hagan, Diurnal Kelvin Wave in the Atmosphere of Mars: Towards an Understanding of 'Stationary' Density Structures Observed by the MGS Accelerometer, *Geophys. Res. Lett.*, *27*, 3563-3566, 2000.

Flasar, F. M., R. E. Samuelson, and B. J. Conrath, Titan's atmosphere: Temperature and dynamics, *Nature*, *292*, 693-698, 1981.

Friedson, A.J., and Y.L. Yung, The thermosphere of Titan, *J. Geophys. Res.*, *89*, 85-90, 1984.

Galand, M., J. Lilensten, D. Toublanc, and S. Maurice, The ionosphere of Titan: ideal diurnal and nocturnal cases, *Icarus*, *140*, 92-105, 1999.

Gurrola, E. M., E. A. Marouf, V.R. Eshleman, and G. L. Tyler, Voyager radio occultation observations of Triton's neutral atmosphere, *Bull. Am. Astron. Soc.*, *23*, 1207, 1991.

Hanel, R., et al., Infrared observations of the Saturnian system from Voyager 1, *Science*, *212*, 192-200, 1981.

Herbert, F., and B. R. Sandel, CH_4 and haze in Triton's lower atmosphere, *J. Geophys. Res.*, *96*, 19,241-19,252, 1991.

Hickey, M. P., R. L. Walterscheid, and G. Schubert, Gravity wave heating and cooling in Jupiter's thermosphere, *Icarus*, *148*, 266-281, 2000.

Hourdin, F., O. Talagrand, R. Sadourny, R. Courtin, D. Gautier, and C. P. Mc Kay, Numerical simulations of the general circulation of the atmosphere of Titan, *Icarus*, *117*, 358-374, 1995.

Hubbard, W. B., et al., The occultation of 28 Sgr by Titan, *Astron. Astrophys.*, *269*, 541-563, 1993.

Ingersoll, A. P., Dynamics of Triton's atmosphere, *Nature*, *344*, 315-317, 1990.

Krasnopolsky, V. A., B. R. Sandel, and F. Herbert, Temperature, N2, and N density profiles of Triton's atmosphere: observations and model, *J. Geophys. Res.*, *98*, 3065-3078, 1993.

Lellouch, E., A. Costenis, D. Gautier, F. Raulin, N. Dubouloz, and C. Frère, Titan's atmosphere and hypothesized ocean: A reanalysis of Voyager 1 radiooccultation and IRIS 7.7-μm data, Icarus, *79*, 328-349, 1989.

Lellouch, E., Atmospheric models of Titan and Triton, *Ann. Geophys.*, *8*, 653-660, 1990.

Letourner, B., and A. Coustenis, Titan's atmospheric structure from Voyager 2 infrared spectra, *Planet. Space Sci.*, *41*, 595-602, 1993.

Lindal, G. F., G. E. Wood, H. B. Hotz, D. N. Sweetnam, V. R. Eshleman, and G. L. Tyler, The atmosphere of Titan: An analysis of the Voyager 1 radio occultation measurements, *Icarus*, *53*, 348-363, 1983.

Matcheva, K. I., and D. F. Strobel, Heating of Jupiter s thermosphere by dissipation of gravity waves due to molecular viscosity and heat conduction. Icarus 140, 328 340, 1999.

Matcheva, K. I., D. F. Strobel, and F. M. Flasar, Interaction of Gravity Waves with Ionospheric Plasma: Implications for Jupiter's Ionosphere., *Icarus*, *152*, 347-365, 2001.

Müller-Wodarg, I. C. F., R. V. Yelle, M. Mendillo, L. A. Young, and A. D. Aylward, The thermosphere of Titan simulated by a global three-dimensional time-dependent model, *J. Geophys. Res.*, *105*, 20,833-20,856, 2000.

Müller-Wodarg, I. C. F., and R. V. Yelle, The Effect of Dynamics on the Composition of Titan's Upper Atmosphere, submitted to *Geophys. Res. Lett.*, 2001.

Olkin, C. B., et al., The thermal structure of Triton's atmosphere: Results from the 1993 and 1995 occultations, *Icarus*, *129*, 178-201, 1997.

Owen, T. C., T. L. Rousch, D. P. Cruikshank, J. L. Elliot, L. A. Young, C. de Bergh, B. Schmitt, T. R. Geballe, R. H. Brown, and M. J. Bertholomew, Surface ices and the atmospheric composition of Pluto, *Science*, *261*, 745-748, 1993.

Rishbeth, H., R. V. Yelle, and M. Mendillo, Dynamics of Titan's thermosphere, *Planet. Space Sci.*, *48*, 51-58, 2000.

Sicardy, B., et al., Structure of Triton's atmosphere from the occultation of Tr176, *Bull. Am. Astron. Soc.*, *30*, 1107, 1998.

Smith, G. R., D. F. Strobel, A. L. Broadfoot, B. R. Sandel, D. E. Shemansky, and J. B. Holberk, Titan's upper atmosphere: Composition and temperature from the EUV solar occultation results, *J. Geophys. Res.*, *87*, 1351-1359, 1982.

Smith, B. A., et al., Voyager 2 at Neptune: Imaging science results, *Science*, *246*, 1422-1449, 1989.

Soderblom, L. A., S. W. Kieffer, T. L. Becker, R. H. Brown, A. F. Cook II, C. J. Hansen, T. V. Johnson, R. L. Kirk, and E. M Shoemaker, Triton's geyser-like plumes: Discovery and basic characterization, *Science*, *250*, 410-415, 1990.

Stevens, M. H., D. F. Strobel, M. E. Summers, and R. V. Yelle, On the thermal structure of Triton's thermosphere, *Geophys. Res. Lett.*, *19*, 669-672, 1992.

Strobel, D. F., M. E. Summers, F. Herbert, and B. Sandel, the photochemistry of methane in the atmosphere of Triton, *Geophys. Res. Lett.*, *17*, 1729-1732, 1990.

Strobel, D.F, M.E. Summers, and X. Zhu, Titan's upper atmosphere: Structure and ultraviolet emmissions, *Icarus*, *100*, 512-526, 1992.

Strobel, D. F., and M. E. Summers, Triton's upper atmosphere and ionosphere, in *Neptune and Triton*, edited by D. P. Cruikshank, pp. 1107-1148, Univ. of Arizona Press, Tucson, 1995.

Strobel, D. F., X. Zhu, M. E. Summers, and M. H. Stevens, On the vertical thermal structure of Pluto's atmosphere, *Icarus*, *120*, 266-289, 1996.

Trafton, L., Large seasonal variations on Triton, *Icarus*, *58*, 312-324, 1984.

Vervack, R. J., B. R. Sandel, and D. F. Strobel, First results from a reanalysis of the Voyager 1 ultraviolet spectrometer solar occultation by Titan, submitted to *Icarus*, 2001.

Wilson, R. J., Evidence for diurnal period Kelvinwaves in the martian atmosphere from Mars Global Surveyor TES data, *Geophys. Res. Lett.*, *27*, 3563-3566, 2000.

Yelle, R.V., Non-LTE models of Titan's upper atmosphere, *Astrophys. J. 383*, 380-400, 1991.

Yelle, R. V., J. I. Lunine, and D. M. Hunten, Energy balance and plume dynamics in Triton's lower atmosphere, *Icarus 89*, 347-358, 1991.

Yelle, R. V., J. I. Lunine, J. B. Pollack, and R. H. Brown, Lower atmospheric structure and surface-atmosphere interactions on Triton, in *Neptune and Triton*, edited by D. P. Cruikshank, pp. 1031-1105, Univ. of Arizona Press, Tucson, 1995.

Yelle, R. V., E. Lellouch, D. Gautier, and D. F. Strobel, Engineering models for Titan's atmosphere, in *Huygens Science Payload and Mission, Eur. Space Agency Sci. Tech. Rep., ESA SP-1177*, 243-256, 1997.

Yung, Y. L., M. Allen, and J. P. Pinto, Photochemistry of the atmosphere of Titan: comparison between model and observations, *Astrophys. J. Suppl.*, *55*, 465-506, 1984.

I. C. F. Müller-Wodarg, Atmospheric Physics Laboratory, University College London, 67-73 Riding House Street, London W1P 7PP, U.K.

The Extreme Ultraviolet Airglow of N_2 Atmospheres

Michael H. Stevens

E.O. Hulburt Center for Space Research, Naval Research Laboratory, Washington, DC

Extreme ultraviolet (EUV) airglow observations at Titan, Triton and Earth provide a rigorous test for models of N_2 atmospheres. This is primarily because the emissions are produced in dramatically different environments. EUV spectra obtained by the Voyager Ultraviolet Spectrometer (UVS) at Titan and Triton are dominated by emission arising from electron impact on N_2 and by photodissociative ionization of N_2. Spectral analyses of the UVS data originally showed that the N_2 Carroll-Yoshino (CY) (0,0) band near 95.86 nm, the (0,1) band near 98.05 nm and the NII 108.5 nm multiplet are the brightest EUV airglow features. But the detailed processes leading to their intensity distribution are only now becoming clear. Model results have shown that the (0,0) band is optically thick and that photoelectron excitation followed by multiple scattering redistributes nearly all (0,0) band emission to the (0,1) band. Summing all emissions from other N_2 bands and NI multiplets near the (0,0) band excited by the solar EUV and X-ray irradiance indicated that the (0,0) band was misidentified. Many of these other emissions are now identified in new high-resolution terrestrial airglow spectra. The distribution of EUV airglow intensity at Triton is different than at Titan and new results are presented here from the same multiple scattering model adapted to Triton. It is found that the ratio of the (0,1) band to the blended emission near the (0,0) band is higher at Triton than at Titan and that the integrated intensity between 94.2-99.6 nm is 2.6 R at Triton, all consistent with UVS observations.

1. INTRODUCTION

Ever since Voyager 1 observations confirmed that Titan's atmosphere was almost entirely N_2, EUV airglow data obtained there by the UVS have received much scrutiny. Although the spectra appeared similar to electron impact emission spectra of N_2 obtained in the laboratory [*Broadfoot et al.*, 1981], the distribution of intensity reported among the various features was inconsistent with both laboratory observations and observations of the Earth's airglow [*Hunten et al.*, 1984].

Atmospheres in the Solar System: Comparative Aeronomy
Geophysical Monograph 130

10.1029/130GM21

Since it was clear early on that photoelectrons alone could not explain the UVS observations, some studies invoked photodissociative ionization of N_2 and others included a magnetospheric source of energetic particles to model the data. However, models could not reproduce either the absolute or the relative intensities of the brightest EUV features reported in the data [*Strobel and Shemansky*, 1982; *Hunten et al.*, 1984; *Strobel et al.*, 1991; *Strobel et al.*, 1992; *Gan et al.*, 1992; *Galand et al.*, 1999].

Interest in the problem was revived following the Voyager 2 encounter of Triton's N_2 atmosphere in 1989. Although emissions arising from electron impact on N_2 were also evident in the Triton EUV airglow spectrum, the distribution of emission was different than that of Titan [*Broadfoot et al.*, 1989; *Strobel et al.*, 1991]. This added still another piece to an already complex and unresolved puzzle.

It has been over 20 years since the Voyager 1 Titan encounter and a wealth of new results have now put the UVS observations of Titan and Triton into a clearer context than before. These include spectroscopic details of the N_2 molecule from the laboratory, results from radiative transfer models and new observations of the Earth's airglow. Together, they suggest that the distribution of EUV emission observed by the Voyager 1 UVS at Titan can be explained by solar forcing alone and that one of the brightest features had been misidentified in spectral analyses [*Stevens*, 2001]. Aeronomers now await new higher resolution Titan airglow data from the Ultraviolet Imaging Spectrograph (UVIS) on the Cassini spacecraft.

This chapter summarizes the most important new advances that contribute to this revised view of Titan's EUV airglow and their impact on models of Triton's airglow. For simplicity, this work focuses only on UVS disk observations and only on the brightest features reported in the EUV spectra heretofore. These emissions are modeled using photoelectron impact on N_2 and photodissociative ionization of N_2 exclusively. Comparisons are made with recent observations of Earth's EUV airglow at high spectral resolution where identification of spectral features in the lower resolution UVS data is ambiguous.

2. THE EUV OBSERVATIONS

The EUV is defined herein to include wavelengths between 52-110 nm where the lower bound is the limit of the UVS observations and the upper bound is set to include the relatively bright NII 108.5 nm multiplet. The UVS data from Voyagers 1 and 2 have provided the only EUV airglow data from Titan and Triton to date. But the UVS spectral resolution is ~3.3 nm so that many emissions in this complex wavelength region are blended together. Figure 1 shows a comparison of disk-averaged UVS spectra from the sunlit sides of Titan and Triton. The brightest portion of their EUV airglow is the focus of this chapter.

The UVS airglow data from Titan are brighter and of higher quality than from Triton. The three brightest EUV features at Titan are listed in Table 1 and were originally reported to be the N_2 Carroll-Yoshino (CY) $c_4'^1\Sigma_u^+ - X^1\Sigma_g^+(0,0)$ band near 95.86 nm, the CY(0,1) band near 98.05 nm, and NII 108.5 nm [*Broadfoot et al.*, 1981; *Strobel and Shemansky*, 1982; *Hall et al.*, 1992]. The CY(0,v'') bands (also called the c_4' bands or simply the c' bands) are strongly excited by photoelectron impact [*Ajello et al.*, 1989] and their identification at Titan and Triton was primarily based on the similarity of the airglow spectra to electron impact emission spectra observed in the laboratory. NII 108.5 nm is only weakly excited by photoelectron impact but strongly excited by photodissociative ionization of N_2 [*Strobel et al.*, 1991]. UVS EUV airglow uncertainties at Titan were estimated by *Strobel et al.* [1992] and are included in Table 1. Note that a wavelength range is provided in the first column, which spans the UVS spectral resolution around each feature.

This study adopts the Voyagers 1 and 2 UVS calibration revision suggested by *Holberg et al.* [1982; 1991], which is a factor of 1.6 downward for the wavelengths 91.2-105.0 nm. This UVS calibration has yielded good agreement with stellar spectra observed by the Hopkins Ultraviolet Telescope [HUT; *Kruk et al.*, 1997]. The downward revision suggested by *Holberg et al.* is extended here to include the NII 108.5 nm multiplet [*Strobel et al.*, 1991; *Strobel et al.*, 1992].

For comparison, the most relevant EUV Earth airglow data were recently obtained by the Far Ultraviolet Spectrometer Experiment (FUSE). The FUSE data have a spectral resolution that is ~0.0075 nm [*Feldman et al.*, 2001] and the nadir-viewing observations are used here to confirm proposed emission features in the UVS spectra from Titan and Triton near the CY(0,0) band.

3. MODELING APPROACH

Until recently, models of Titan's EUV airglow used the relatively large laboratory measured electron impact emission cross-section for CY(0,0) [*Ajello et al.*, 1989] which yielded CY(0,0) intensities six times brighter than CY(0,1). But perhaps the greatest challenge at Titan is that the optical depth of CY(0,0) rotational lines near peak photoelectron production is extremely high ($>10^4$). If photoelectrons excite the (0,0) band at Titan, that emission should be multiply scattered and redistributed to the more optically thin (0,1) band [*Conway*, 1983; *Ajello et al.*, 1989; *Strobel et al.*, 1991]. If CY(0,0)/CY(0,1) is near unity as reported from spectral analyses of UVS data, this photon redistribution requires another source to explain the CY(0,0) brightness. This source, moreover, would have to produce (0,0) band emission above Titan's exobase [*Shemansky et al.*, 1995].

In light of the fact that the (0,0) band is weak or absent in higher resolution airglow data from the Earth and that the spectrum is complex near 95.86 nm [*Gentieu et al.*, 1981; *Morrison et al.*, 1990; *Feldman et al.*, 2001], it seems possible that the CY(0,0) identification was not correct. A quantitative study of all known emission features in the Titan EUV airglow arising from known solar-driven processes now suggests that this is the case. The most important factors leading to this conclusion are summarized below.

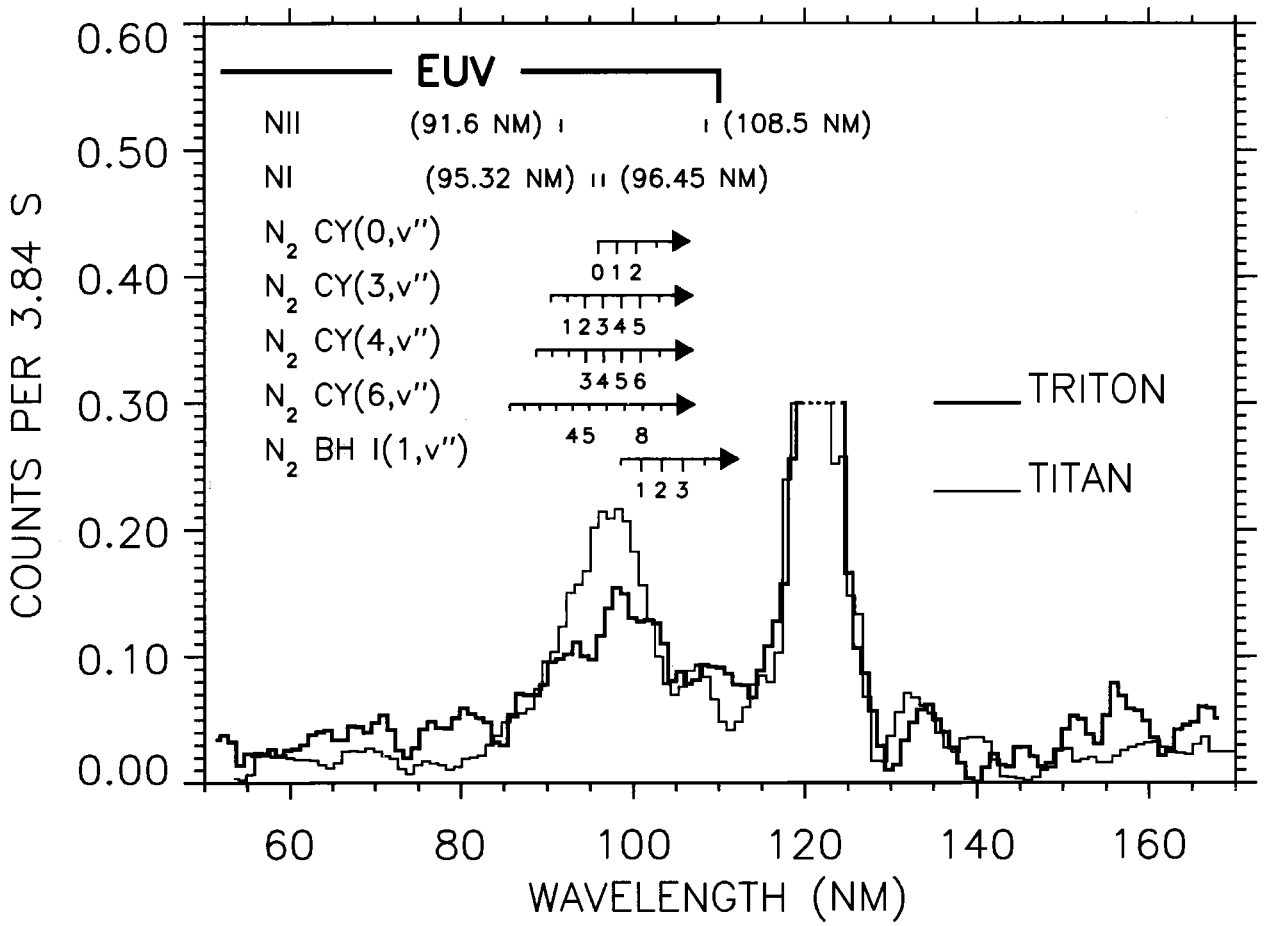

Figure 1. A comparison of uncalibrated disk-averaged UVS spectra where the Titan airglow spectrum is normalized to the Triton spectrum in the 108.5 nm region [reproduced with permission from *Broadfoot et al.*, 1989]. Note that the Lyman-α region near 121.6 nm is removed. Important NI multiplets, NII multiplets and N_2 bands between 91-110 nm that have been identified in FUSE terrestrial airglow spectra are labeled with a wavelength or numbered. Shorter N_2 band tick marks indicate emissions that are uncertain or severely blended in the FUSE data.

TABLE 1

VOYAGER UVS AIRGLOW OBSERVATIONS AND MODEL RESULTS

Wavelength (nm)	REPORTED IDENTIFICATION[a,b]	PROPOSED IDENTIFICATION[c]	TITAN		TRITON	
			Data (R)[d]	Model (R)[c]	Data (R)[e]	Model (R)[f]
95.86 ± 1.6	N_2 CY(0,0)	NI (96.45, 95.32 nm) + Others	8 ± 50%	6.7 (1.4, 1.3)	~0	0.8
98.05 ± 1.6	N_2 CY(0,1)	N_2 CY(0,1) + Others	6 ± 50%	9.4	2-3	1.8
108.5 ± 1.6	NII	NII	8 ± 50%	9.7 (7.9)	1.2-5	1.0

[a] *Broadfoot et al.* [1981]; *Strobel and Shemansky* [1982]

[b] *Broadfoot et al.* [1989]

[c] Photodissociative ionization in parentheses. Yields revised from *Stevens* [2001] (see text): $\varphi_{96.4}$=0.021, $\varphi_{95.3}$=0.019, $\varphi_{108.5}$=0.110

[d] *Strobel et al.* [1992]

[e] *Strobel et al.* [1991]

[f] This work (0% CH_4, $\tau_{CY(0,1)}$«1, 8% $c_4'(0)$ predissociation)

3.1 Titan: Progress Since Voyager 1

Recently the Titan EUV airglow spectrum was modeled by calculating the photoelectron excited CY(0,v'') emission in extremely optically thick conditions. The model included all known loss processes and explicitly included both the redistribution and loss of photons from the (0,0) band over multiple scatterings. All other N_2, NI and NII EUV emissions between 92.0-101.5 nm produced by photoelectron excitation and photodissociative ionization were treated separately for conditions of the Voyager 1 encounter at Titan [*Stevens*, 2001].

Two important inputs to the model are the predissociation yield of the $c_4'(0)$ state and the solar EUV and X-Ray irradiance. The solar irradiance below 45 nm controls both photoelectron production of $c_4'(0)$ and photodissociative ionization of N_2. Predissociation and the solar irradiance are considered separately below.

The predissociation yield of $c_4'(0)$ was measured by *Shemansky et al.* [1995] and for the temperatures in Titan's upper atmosphere it was reported to be 0.125. (Note that typesetting error in Table 2 of *Stevens* [2001] shows a predissociation yield of 0.120, which should be exchanged with the quoted (0,1) band yield of 0.125). This yield is significant because the large branching ratio to the ground state (0.73) radiatively traps (0,0) band photons. Repeated scatterings effectively increase the predissociation loss by about a factor of three above the optically thin value [*Stevens et al.*, 1994]. Photons are simultaneously redistributed to the (0,1) band where extinction by CH_4 and N_2 itself contribute to loss from the CY(0,v'') system. As a result, less than 25% of $c_4'(0)$ production appears in the (0,v'') progression and almost all of this is in the (0,1) band.

Previous EUV airglow models of Titan and Triton [*Strobel et al.*, 1991; *Strobel et al.*, 1992; *Gan et al.*, 1992] used the solar EUV and X-Ray irradiance of *Hinteregger et al.* [1981], SC21REFW. However, there is now considerable evidence that the EUV and X-Ray irradiance at these wavelengths is larger than in SC21REFW [*Richards et al.*, 1994; *Warren et al.*, 1998; *Bailey et al.*, 2000; *Bishop and Feldman*, 2002]. The quiet sun irradiance used in the airglow models presented here is from *Woods et al.* [1998] and is about a factor of two greater than SC21REFW for wavelengths below 45 nm. Scaling to active sun conditions of the Voyager 1 Titan encounter increases CY(0,1) and NII 108.5 nm nadir viewing intensities for these two features which are now consistent with reported observations. Table 1 shows model-data comparisons for CY(0,1) and the 108.5 nm multiplet where the modeled NII 108.5 intensity employs the yield of 0.11 recently inferred from data obtained by HUT [*Bishop and Feldman*, 2002]. CY(0,1) was calculated to be 81% of the 98.05 nm UVS feature at Titan.

Photodissociative ionization produces NI and NII emission at many discrete wavelengths in addition to NII 108.5 nm [*Samson et al.*, 1991; *Meier et al.*, 1991; *Bishop and Feldman*, 2002]. Two important NI multiplets near CY(0,0) at 95.86 nm are near 95.32 and 96.45 nm. These two features are each calculated to be brighter than CY(0,0) or any other photoelectron excited N_2 band at 95.86±1.6 nm. Calculated intensities of these NI multiplets and other N_2 bands nearby allowed for a Titan EUV airglow driven exclusively by the solar EUV and X-ray flux.

High-resolution nadir viewing Earth airglow spectra confirm that the NI multiplets and N_2 bands near 95.86 nm are substantially brighter than CY(0,0) [*Gentieu et al.*, 1981]. In fact, each of the eleven brightest N_2 bands and NI multiplets calculated for the Titan airglow between 92.0-101.5 nm and blended by the UVS is now identified in airglow spectra from the Earth [*cf. Stevens*, 2001; *Feldman et al.*, 2001]. Note that where there is ambiguity in assigning individual N_2 band emissions to the two blended UVS features in Table 1, the nearest feature to the emission is chosen.

A sample of the new data available from the FUSE instrument is shown in Figure 2 for a region near 95.86 nm. Figure 2 shows that CY(0,0) is weak (30 R) compared to a group of three blended features near 96.45 nm (85 R). CY(3,3) and CY(4,4) are excited by photoelectron excitation whereas NI 96.45 nm is excited primarily by photodissociative ionization.

One difficulty in establishing yields from NI and NII multiplets from the laboratory is that a synchotron continuum, from which yields are inferred, is significantly different than the solar EUV irradiance [*Meier et al.*, 1991]. Yields inferred from airglow data can therefore be more reliable. The reported FUSE NII 108.5 nm intensity of 400 R is scaled downward by 23% for the photodissociative ionization contribution to this feature [*Bishop and Feldman*, 2002]. A NI 96.45 yield is then inferred by assuming that the NI 96.45/NII 108.5 ratio inferred by *Meier et al.* [1991] is maintained. This lower yield of 0.021 is used in the results shown in Table 1 and produces 59 R in the terrestrial 96.45 feature or 69% of the blend in Figure 2. The new NI 95.32 nm yield similarly preserves the relative brightnesses of the multiplets and is not inconsistent with the FUSE data, although NI 95.32 nm not shown in Figure 2 is blended with OI emission.

3.2 Modeling CY(0,v'') on Triton

The solar driven EUV airglow is much weaker on Triton due to both its greater heliocentric distance and to the lower solar activity during the observations [*Broadfoot et al.*, 1989]. Following the procedure of *Stevens* [2001], the quiet sun spectrum [*Woods et al.*, 1998] was scaled to the

conditions of the Voyager 2 encounter on August 25, 1979 ($F_{10.7}$ ~ 180). A comparison of the solar EUV and X-Ray fluxes at 1 A.U. during the Titan and Triton UVS observations is shown in Figure 3. The photon flux integrated over the wavelengths shown is 79% of that for Titan. By also considering the greater heliocentric distance, the intensities of all calculated emission features are uniformly less by a factor of 12.6 compared to Titan.

The CH_4 mixing ratio on Triton is orders of magnitude smaller than on Titan [*Smith et al.*, 1982; *Broadfoot et al.*, 1989] so that CH_4 extinction is negligible. The extremely cold temperature (~80 K) near peak production on Triton [*Broadfoot et al.*, 1989], limits the population of the N_2 ground states to the lowest rotational levels. Therefore absorption of CY(0,1) by the accidentally resonant and predissociated N_2 Birge-Hopfield BH I $b^1\Sigma_u - X^1\Sigma_g^+(2,0)$ band [*Stevens et al.*, 1994] is also negligible. The cold temperatures at Triton also have the effect of reducing the predissociation yield from 0.125 on Titan to 0.08 [*Shemansky et al.*, 1995].

Using the Titan $c_4'(0)$ photoelectron excitation rates of *Stevens* [2001], the multiple scattering model was run for an N_2 atmosphere without CH_4, without BH I(2,0) absorption and with an optically thin predissociation yield of 0.08. CY(0,1) photons that reach the lower boundary of the model under these conditions are assumed to be lost. The resultant nadir viewing (0,v'') band intensities were scaled down to reflect the different solar forcing at Triton discussed above. All other NI and CY($v'\neq0$) emission features were calculated assuming optically thin conditions and similarly scaled to solar conditions at Triton during the Voyager 2 encounter.

4. RESULTS

4.1 Triton

The loss of $c_4'(0)$ photons at Triton is roughly divided between CY(0,1) escape from the atmosphere, predissociation and CY(0,1) loss at the surface. The CY(0,1) nadir viewing intensity is calculated to be 1.6 R (1.8 R for the feature) and the 95.86 nm blend is 0.8 R as shown in Table 1. Given the uncertainties in the UVS EUV airglow data at Titan and the low signal at Triton, the agreement in Table 1 is acceptable and far better than obtained using the optically thin (0,0) to (0,1) band electron impact emission cross sections of 6 to 1. Since the calculated 98.05 nm/95.86 nm ratio for Triton is substantially larger than for Titan and the integrated 94.2-99.6 nm intensity is also consistent with observations, the evidence mounts for the misidentification of the 95.86 nm UVS feature at Titan.

4.2 CY(0,v'') Photon Redistribution

Aside from absolute brightness, the primary difference between the Titan and Triton EUV airglow is the brightness of CY(0,1) relative to the 95.86 nm blend. The primary causes are colder temperatures and less CH_4 at Triton. The colder temperatures reduce predissociation and produce an environment where CY(0,1) is more optically thin to N_2 BH I(2,0), leading to more (0,1) band emission observed. Less CH_4 at Triton also allows preferentially more CY(0,1) to escape since the 95.86 nm blend has a significant contribution from photodissociative ionization, which is excited much higher in the atmosphere [*Strobel et al.*, 1991].

Feldman et al. [2001] reported a CY(0,1)/CY(0,0) ratio of 2.3 for the Earth's airglow using FUSE observations, much lower than the Titan and Triton model results (>30). CY(0,v'') rotational lines are Doppler broadened, so the warmer temperatures on Earth near peak photoelectron production not only populate more rotational levels but also increase the rotational line widths. For a given production rate, this reduces the amount of CY(0,0) self-absorption and the CY(0,1)/CY(0,0) ratio, consistent with observations. Warmer temperatures also enhance BH I(2,0) extinction of CY(0,1), further reducing the ratio.

Results from a multiple scattering model of the Earth's airglow by *Stevens et al.* [1994] show that for a nadir viewing geometry and an optically thin predissociation yield of 16.5%, the calculated CY(0,1)/CY(0,0) ratio is ~3. Although this ratio is in reasonable agreement with FUSE observations the CY(0,0)+CY(0,1) intensities are only 9-46 R depending on solar activity, more than a factor of two less than the 98 R reported. However, since the earlier *Stevens et al.* analysis used SC21REFW and given that recent work suggests a larger solar EUV flux than this, more detailed analysis of the FUSE data for the moderate solar activity is required and is underway.

5. SUMMARY AND FUTURE WORK

A revised view of the EUV airglow on Titan and Triton is presented that is a consequence of an elaborate multiple scattering model for calculating the redistribution of photons from the optically thick CY(0,0) band. A survey of all known features excited by the sun in this complex region of emission shows that a blend of N_2 bands and NI multiplets near 95.86 nm together constitute the UVS feature originally reported as CY(0,0). Good agreement is found with UVS data at Titan to within experimental uncertainties and new high resolution observations from Earth's airglow confirm that CY(0,0) is weak compared to neighboring emission features. New model results for

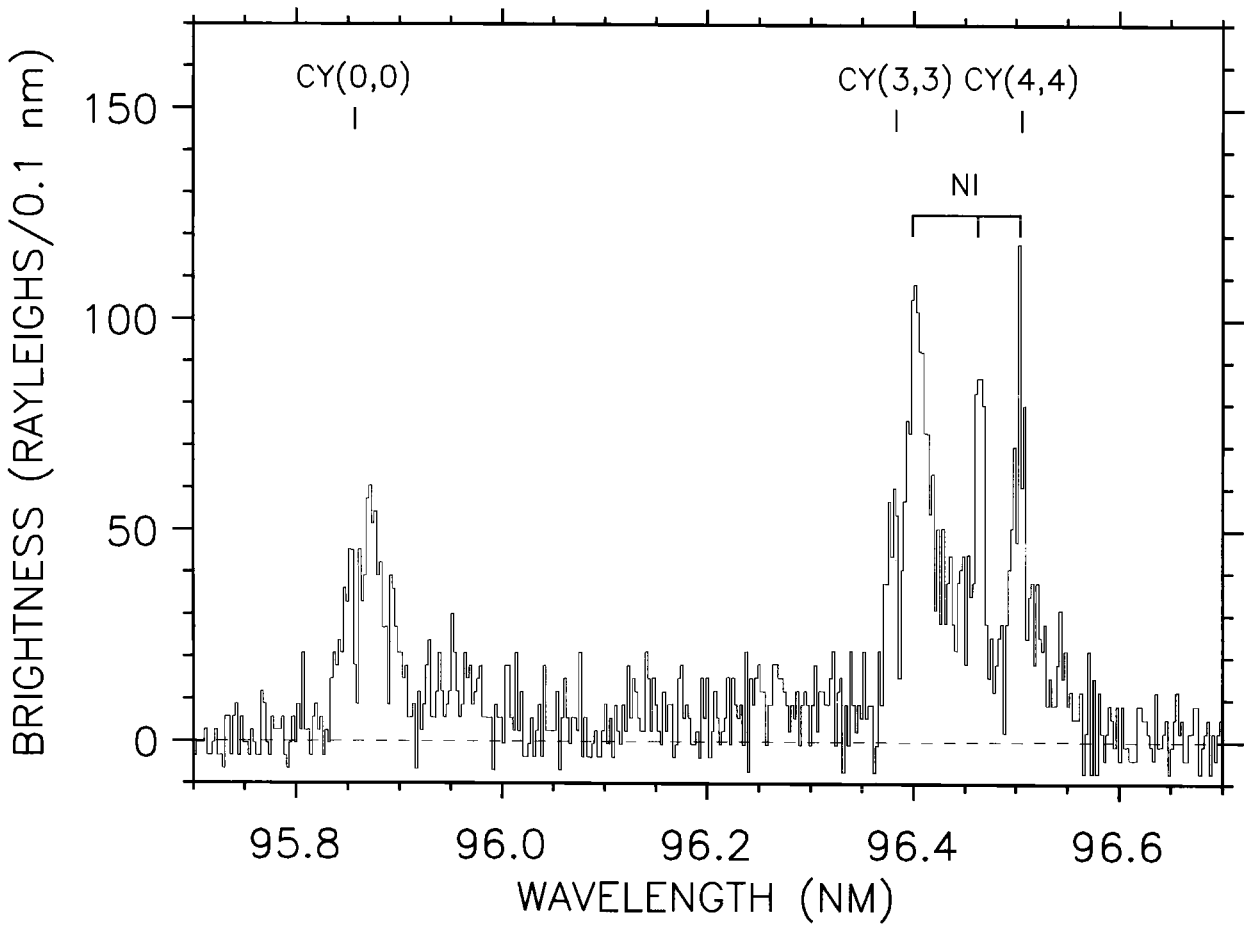

Figure 2. High-resolution terrestrial EUV airglow data of FUSE [from Figure 2 of *Feldman et al.*, 2001]. The data were taken on September 24-25, 1999 at a time of moderate solar activity ($F_{10.7} \approx 130$). Spectral analyses of the UVS airglow data at Titan and Triton argued that CY(0,0) dominates in this region. The UVS spectral resolution is over three times the wavelength region shown in this figure, so that these emissions and others were severely blended at Titan and Triton producing one feature near 95.86 nm.

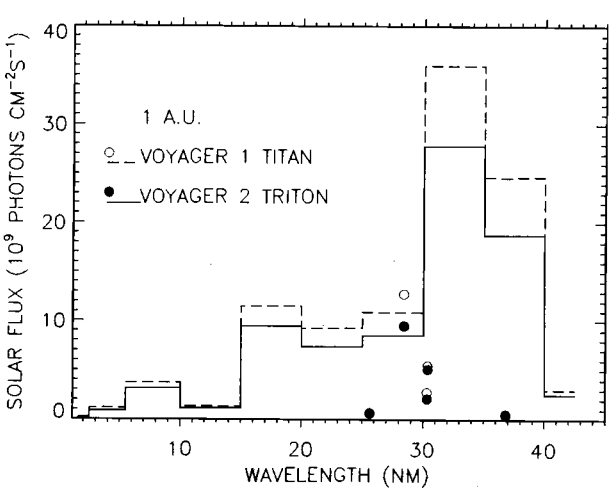

Triton's EUV airglow presented here are also in agreement with UVS data and substantiate this result.

Several advances since the Voyager encounters of Titan and Triton have contributed to this new picture. These include new evidence for a larger EUV and X-Ray solar irradiance, a quantitative determination of the $c_4'(0)$ predissociation yield, neighboring NI emissions found to be produced by photodissociative ionization, and a downward revision to the UVS EUV calibration.

Figure 3. The solar irradiances used in the calculation of the EUV airglow at Titan and Triton. Symbols indicate irradiances of discrete lines and are not included in the flux for the wavelength bins.

If a solar EUV and X-Ray irradiance is used that is about a factor of two larger than SC21REFW and the downward revision of the UVS EUV calibration is adopted, the EUV airglow intensities at Titan and Triton are much better understood. The most pressing need in this area is to isolate and identify the emissions near 95.86 nm in Titan's airglow. The UVIS on the Cassini spacecraft can help with a projected spectral resolution of better than 0.5 nm [*McClintock et al.*, 1993]. If the 95.86 nm UVS feature is primarily a blend of neighboring NI multiplets and CY N_2 bands, then the EUV airglow observed by the UVS at Titan and Triton can be placed far more clearly in the context of Earth's airglow.

Acknowledgments. The author thanks P.D. Feldman for providing the FUSE data used in this work and B.R. Sandel for the UVS spectra presented here. Helpful comments on the manuscript by R.R. Meier and D.E. Siskind are greatly appreciated. This work has benefited from productive discussions with J. Bishop. The Office of Naval Research supported this work.

REFERENCES

Ajello, J.M., G.K. James, B.O. Franklin, and D.E. Shemansky, Medium-resolution studies of extreme ultraviolet emission from N_2 by electron impact: Vibrational perturbations and cross sections of the $c_4'^1\Sigma_u$ and $b'^1\Pi_u$ states, *Phys. Rev. A Gen. Phys.*, 40, 3524-3556, 1989.

Bailey, S.M., T.N. Woods, C.A. Barth, S.C. Solomon, L.R. Canfield and R. Korde, Measurements of the solar soft X-ray irradiance by the Student Nitric Oxide Explorer: First analysis and underflight calibrations, *J. Geophys. Res.*, 105, 27179-27193, 2000.

Bishop, J. and P.D. Feldman, Analysis of the Astro-1/Hopkins Ultraviolet Telescope EUV-FUV dayside nadir spectral radiance measurements, *J. Geophys. Res.*, in Press, 2002.

Broadfoot, A.L., B.R. Sandel, D.E. Shemansky, J.B. Holberg, G.R. Smith, D.F. Strobel, J.C. McConnell, S. Kumar, D.M. Hunten, S.K. Atreya, T.M. Donahue, H.W. Moos, J.L. Bertaux, J.E. Blamont, R.B. Pomphrey, and S. Linick, Extreme ultraviolet observations from Voyager 1 encounter with Saturn, *Science*, 212,206-211, 1981.

Broadfoot, A.L., S.K. Atreya, J.L. Bertaux, J.E. Blamont, A.J. Dessler, T.M. Donahue, W.T. Forrester, D.T. Hall, F. Herbert, J.B. Holberg, D.M. Hunten, V.A. Krasnopolsky, S. Linick, J.I. Lunine, J.C. McConnell, H.W. Moos, B.R. Sandel, N.M. Schneider, D.E. Shemansky, G.R. Smith, D.F. Strobel and R.V. Yelle, Ultraviolet Spectrometer Observations of Neptune and Triton, *Science*, 246, 1459-1466, 1989.

Conway, R.R., Multiple fluorescent scattering of N_2 ultraviolet emissions in the atmospheres of the Earth and Titan, *J. Geophys. Res.*, 88, 4784-4792, 1983.

Feldman, P.D., D.J. Sahnow, J.W. Kruk, E.M. Murphy and H. Warren Moos, High-resolution FUV spectroscopy of the terrestrical day airglow with the Far Ultraviolet Explorer, *J. Geophys. Res.*, 106, 8119-8129, 2001.

Galand, M., J. Lilensten, D. Toublanc and S. Maurice, The ionosphere of Titan: Ideal diurnal and nocturnal cases, *Icarus*, 140, 92-105, 1999.

Gan, L., C.N. Keller, and T.E. Cravens, Electrons in the ionosphere of Titan, *J. Geophys. Res.*, 97, 12137-12151, 1992.

Gentieu, E.P., P.D. Feldman, R.W. Eastes, and A.B. Christensen, Spectroscopy of the extreme ultraviolet dayglow during active solar conditions, *Geophys. Res. Lett.*, 8, 1242-1245, 1981.

Hall, D.T., D.E. Shemansky, and T.M. Tripp, A reanalysis of Voyager UVS observations of Titan, Paper, Symposium on Titan, Sep. 1991, Toulouse, France, ESA SP-338, 69-74, 1992.

Hinteregger, H.E., K. Fukui, and B.R. Gilson, Observational, reference and model data on solar EUV, from measurements on AE-E, *Geophys. Res. Lett.*, 8, 1147, 1981.

Holberg, J.B., W.T. Forrester, D.E. Shemansky, and D.C. Barry, Voyager absolute far-ultraviolet spectrophotometry of hot stars, *Ap. J.*, 257, 656-671, 1982.

Holberg, J.B., B. Ali, T.E. Carone, and R.S. Polidan, Absolute far-ultraviolet spectrophotometry of hot subluminous stars from Voyager, *Ap. J.*, 375, 716-721, 1991.

Hunten, D.M., M.G. Tomasko, F.M. Flasar, R.E. Samuelson, D.F. Strobel and D.J. Stevenson, Titan, in Saturn, eds. T. Gehrels and M.S. Matthews, University of Arizona Press, Tucson, Arizona, 671, 1984.

Kruk, J.W., R.A. Kimble, R.H. Buss, Jr., A.F. Davidsen, S.T. Durrance, D.S. Finley, J.B. Holberg, and G.A. Kriss, *Astrophys. J.*, 482, 546-568, 1997.

McClintock, W.E., G.M. Lawrence, R.A. Kohnert and L.W. Esposito, Optical design of the Ultrviolet Imaging Spectrograph fo the Cassini mission to Saturn, *Opt. Eng.*, 32, 3038-3046, 1993.

Meier, R.R., J.A.R. Samson, Y. Chung, E.-M. Lee, and Z.-X. He, Production of N^{+*} from N_2 + hv: Effective EUV emission yields from laboratory and dayglow data, *Planet. Space Sci.*, 39, 1197-1207, 1991.

Morrison, M.D., C.W. Bowers, P.D. Feldman, and R.R. Meier, The EUV dayglow at high spectral resolution, *J. Geophys. Res.*, 95, 4113-4127, 1990.

Richards, P.G., J.A. Fennelly, and D.G. Torr, EUVAC: A solar EUV flux model for aeronomic calculations, *J. Geophys. Res.*, 99, 8981-8992, 1994.

Samson, J.A.R., Y. Chung, and E.-M. Lee, Excited ionic and neutral fragments produced by dissociation of the N_2^{+*} H band, *J. Chem. Phys.*, 95, 717-719, 1991.

Shemansky, D.E., I. Kanik, and J.M. Ajello, Fine-structure branching in $c_4'^1\Sigma_u$ (0), *Astrophys. J.*, 452, 480-485, 1995.

Smith, G.R., D.F. Strobel, A.L. Broadfoot, B.R. Sandel, D.E. Shemansky and J.B. Holberg, Titan's upper atmosphere: Composition and temperature from the EUV solar occultation results, *J. Geophys. Res.*, 87, 1351-1359, 1982.

Stevens, M.H., The EUV airglow of Titan: Production and loss of N_2 $c_4'(0) - X$, *J. Geophys. Res.*, 106, 3685-3689, 2001.

Stevens, M.H., R.R. Meier, R.R. Conway, and D.F. Strobel, A resolution of the N_2 Carroll-Yoshino (c_4'-X) band problem in the Earth's atmosphere, *J. Geophys. Res.*, 99, 417-433, 1994.

Strobel, D.F. and D.E. Shemansky, EUV emission from Titan's upper atmosphere: Voyager 1 encounter, *J. Geophys. Res.*, 87, 1361-1368, 1982.

Strobel, D.F., R.R. Meier, and D.J. Strickland, Nitrogen airglow sources: Comparison of Triton, Titan, and Earth, *Geophys. Res. Lett.*, 18, 689-692, 1991.

Strobel, D.F., M.E. Summers, and X. Zhu, Titan's upper atmosphere: Structure and ultraviolet emissions, *Icarus*, 100, 512-526, 1992.

Warren, H.P., J.T. Mariska, and J. Lean, A new reference spectrum for the EUV irradiance of the quiet sun 2. Comparison with observations and previous models, *J. Geophys. Res.*, 103, 12091-12102, 1998.

Woods, T.N., G.J. Rottman, S.M. Bailey, S.C. Solomon, J.R.Worden, Solar extreme ultraviolet irradiance measurements during solar cycle 22, *Solar Phys.*, 177, 133-146, 1998.

M. H. Stevens, Code 7641, Naval Research Laboratory, 4555 Overlook Ave., Washington, DC 20375

PART V. OBSERVATIONAL APPLICATIONS

Planetary science is the only area of astronomical research that includes all three components of experimental/observational methods: remote sensing, in-situ diagnostics, and sample return. Aeronomic science deals almost exclusively with the first two, with occasional analysis of "trapped gases" in Apollo lunar samples and in the martian and asteroidal meteorites found on Earth. A comprehensive review of all the state-of-the-art techniques used in solar system aeronomy is well beyond the scope of this monograph. Indeed, additional volumes would be required for its full coverage, and especially so for new radio methods and the increasing use of infrared observations.

In the chapters that follow, we focus on only three sub-topics of rather different methodologies. The terrestrial aeronomy community has developed visible light instruments and ionospheric radars for use in groundbased campaigns or multi-year monitoring projects. The CEDAR Program (for "Coupling, Energetics and Dynamics of Atmospheric Regions") of the US National Science Foundation has been particularly active in funding a new generation of optical and radio diagnostic systems. These complement long-standing Department of Defense programs such as the Defense University Research Instrumentation Program (DURIP). The new detectors developed from the programs are capable (and in some cases already used) for applications to non-terrestrial atmospheres.

Equally exciting are the developments in spacebased diagnostics. The cornerstones of planetary aeronomy have been sensors in the ultraviolet and detectors for in-situ mass spectrometry. Funded primarily by NASA, these capabilities will continue to provide cutting edge observations of planetary atmospheres. *(Image courtesy J. Clarke.)*

The Application of Terrestrial Aeronomy Groundbased Instruments to Planetary Studies

Michael Mendillo

Center for Space Physics, Boston University

Fred Roesler

Department of Physics, University of Wisconsin

Chester Gardner

Department of Electrical and Computer Engineering, University of Illinois

Michael Sulzer

Arecibo Observatory, Arecibo, Puerto Rico

In terrestrial aeronomy, remote sensing and active probing of the upper atmosphere are accomplished using both optical and radio techniques. For *passive* optical systems—imagers, spectrographs and interferometers—applications to studies of planetary atmospheres often involve the innovative use of standard methods. Here we describe three such passive methods recently applied to studies of the moon's exosphere, Mercury's surface, and the atmospheres of Jupiter's moon Io and comet Hale-Bopp. The *active* probing of a non-terrestrial atmosphere has not yet been attempted. Here we describe the challenges and potential science yield from light detection and ranging (LIDAR) probing of the lunar atmosphere and incoherent scatter radar (ISR) sounding of Venus' ionosphere.

1. INTRODUCTION

While the fundamental principles of remote sensing are the same for the atmosphere of a star, planet, comet or moon, there are practices in design and utilization of observational techniques that lead to rather specific tools for terrestrial or planetary research. For example, spectrographs with very different wavelength resolution have been used to study brightness variations of species long known to exist on Earth versus those needed to search for exotic molecules in comets and the giant planets. While Fabry-Perot interferometers (FPIs) have been the premier instrument for studying atmospheric temperatures and winds on Earth, high resolution spectrographs have often been the instrument of choice for their study on other solar system bodies. Imagers developed to observe large scale atmospheric structures

Atmospheres in the Solar System: Comparative Aeronomy
Geophysical Monograph 130

10.1029/130GM22

have, almost by definition, been wide angle cameras on Earth and narrow field telescopic systems for the planets. In this chapter, we describe an instrumentation aspect of comparative aeronomy,.namely, the extension of groundbased techniques developed initially for terrestrial research to areas of planetary atmospheres. We treat five specific cases; (1) Use of an all-sky airglow camera to study the distant exosphere of the Moon, (2) The application of a high speed auroral imager to observe the surface and atmosphere of Mercury, (3) The use of FPIs and spectrographs to observe characteristics of planetary atmospheres, (4) The development of a super-LIDAR to observe the structure and dynamics of the Moon's atmosphere, and (5) The possible use of an incoherent scatter radar (ISR) to monitor the ionosphere of Venus.

2. ALL-SKY IMAGING OF THE MOON'S DISTANT EXOSPHERE

Cameras with fisheye lenses (180° field of view) have been used for many years to monitor terrestrial phenomena such as aurora [*Akasofu*, 1968; *Eather*, 1984; *Steele and Cogger*, 1996; *Weber et al.*, 1984], mesospheric gravity waves [*Taylor et al.*, 1995; *Swenson et al.*, 1995; *Smith et al.*, 2000], and equatorial airglow depletions [*Weber et al.*, 1978; *Mendillo et al.*, 1997; *Taylor et al.*, 1997]. The data recording methods for these systems started as film-based and then evolved to image-intensified and now CCD detectors [*Baumgardner et al.*, 1993]. The low noise levels of such detectors permit the detection of extremely low-contrast structures (< 5% in brightness) in the Earth's upper atmosphere. Using such a state-of-the-art system to search for possible mesospheric effects caused by the large Leonid meteor shower expected on 17 November 1998, *Smith et al.* [1999] continued observations for the subsequent three nights using a narrow band (14 Å) sodium (Na) filter. The Moon was at new phase on 19 November, giving extremely dark sky conditions at the McDonald Observatory in Fort Davis, Texas. This allowed detection of an unusual structure that changed in shape and brightness over the 18 - 20 November 1998 period.

In Plate 1a, the top left panel gives a raw image showing the emission feature ("Na spot") taken on 19 November 1998. To the right is a magnified view of the spot, time-averaged over the night. In the all-sky view, the feature can be compared in size to the constellation Orion to the left; in the expanded panel the dimension of the box is 40° x 30° in RA and declination. The peak brightness of the Na spot was about 60 Rayleighs above background, clearly the strongest feature in the sky at sodium wavelengths on this particular night. After ruling out several possible sources, *Smith et al.* [1999] attributed it to an extended tail of neutral Na gas of lunar origin. Monte Carlo modeling conducted by *Wilson et al.* [1999], with results shown in the lower panels of Plate 1a, showed that the lunar Na tail is present continuously, but is only visible from the Earth during the 2 - 3 nights spanning new Moon. In this particular case, the spot was enhanced by the impact of Leonid meteors upon the lunar regolith, releasing high speed Na atoms that were accelerated away from the Moon by solar radiation pressure. Upon reaching the vicinity of the Earth two days later, the streaming Na atoms were focused into a narrow beam by the Earth's gravity. A careful search of archived data sets by several groups revealed that it was observed at other locations (e.g., *Shiokawa et al.*, 2000) and even on new Moon nights not following strong meteor showers. *Smith et al.* [2001] have taken several cases of its detection to examine the varying degree of high speed sodium that escapes from the Moon. Here is a clear case of one method of space science (routine all-sky imaging of sodium in the mesosphere) offering a new type of observation for the planetary community studying the origin and evolution of the transient atmosphere of the moon [*Stern*, 1999].

3. HIGH DEFINITION IMAGING OF MERCURY

State-of-the-art studies of aurora on Earth deal with the filamentary nature of intense currents impinging upon the upper atmosphere. While models once treated a steady flux of precipitating particles from the magnetosphere, simulations today address the sub-second variations of evolving auroral patterns from bursts of energetic electrons and protons [*Lanchester et al.*, 2001]. In mesospheric science, thunder storm induced "lightning" that couples to regions above gives rise to transient emissions called sprites. Central to these studies are high speed digital recording systems, such as described by *Westcott et al.* [1999] and *Stenbaek-Nielsen et al.* [1998]. With an ability to record and store bright signals at 1/60th to 1/1000th of a second, these systems offer an unprecendent opportunity to make observations at rates that are faster than atmospheric turbulence affects "seeing."

Baumgardner et al. [2000] have shown how such instrumentation can be applied to planetary work by de-

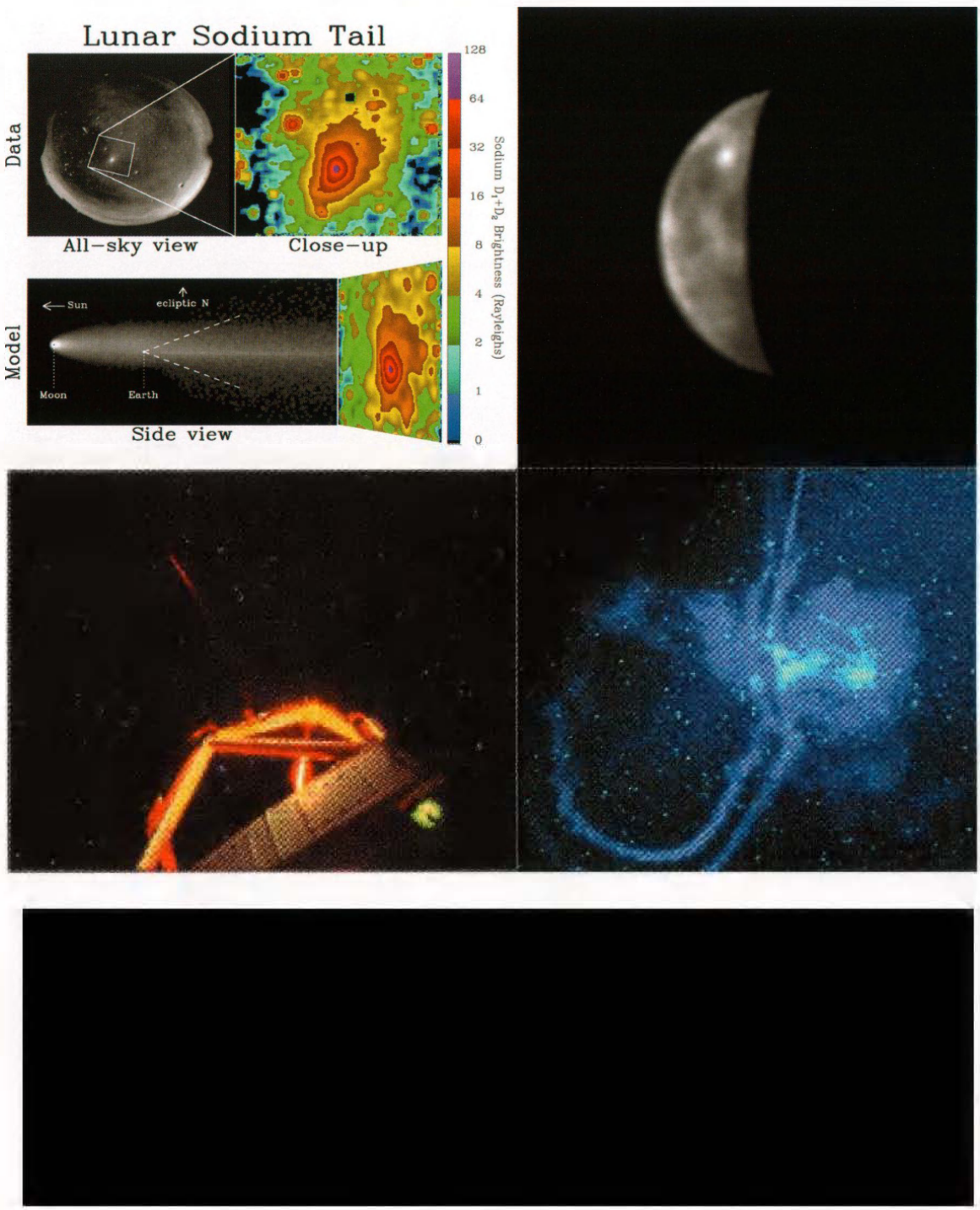
Lunar Sodium Tail
Data
All−sky view
Close−up
128
64
32
16
8
4
2
1
0
Sodium D_1+D_2 Brightness (Rayleighs)
Model
Sun
ecliptic N
Moon
Earth
Side view

scribing a system for high definition imaging (HDI) in both broadband and spectral imaging modes. Briefly, in taking pictures at video rates (1/60 sec), it is possible to find a very small subset of images when the seeing is essentially perfect, i.e., with telescope performance at nearly the diffraction limit. These images are spaced in time and appear at varying positions on the detector. By using the selective shift and add approach first suggested by *Fried* [1978], it is then possible to obtain a time exposure of non-sequential images, i.e., of only the best possible ones. The resultant image, when deconvolved with the appropriate point spread function, offers a view of the target that rivals those seen from above the atmosphere, as with the Hubble Space Telescope.

In an operational demonstration of the HDI technique, *Baumgardner et al.* [2000] used approximately 200,000 images of Mercury obtained on 29 August 1998 with the 1.5 meter telescope at the Mt. Wilson Observatory to select 60 frames taken with the best available seeing. This was done using a contrast-assessment algorithm applied to all of the stored images. The effective integration was thus one second, and the resultant image is shown in Plate 1b.

This is arguably the best groundbased image ever taken of Mercury's surface. A prior dataset taken on 22 October 1995 by *Warrell and Limaye* [2001], using the Swedish Vacuum Solar Telescope on La Palma in the Canary Islands, achieved a comparable resolution of approximate 200 km using a 0.5 meter instrument.

The portion of Mercury shown in Plate 1b represents a longitude sector ($270° - 330°$) not imaged during the Mariner 10 fly-bys in 1974 - 75. The surface contrast varies between 10 to 15% over most of the image, with one feature 30% brighter than its surroundings. While such albedo variations can be used to infer surface composition properties, the full promise of the HDI technique is in its spectral mode, as suggested by *Potter et al.* [1999] and *Baumgardner et al.* [2000] for atmospheric studies and by *Vilas et al.* [1984], *Emery et al.* [1998], *Sprague et al.* [1997] for surface reflectance studies. This is a timely development for a new technology since groundbased observations can now be used to help formulate observing strategies for the upcoming satellite missions Messenger and BepiColombo to Mercury.

4. FABRY-PEROT INTERFEROMETER APPLICATIONS IN PLANETARY SCIENCE

The Fabry-Perot interferometer (FPI) has been an important instrument for ground-based Aeronomy for many decades. A summary of the use of Fabry-Perot instruments for astronomy [*Roesler*, 1974] discusses the use of scanning FP spectrometers on astronomical telescopes. The more recent advent of low noise, high quantum efficiency imaging detectors and telescopes with adaptive optics demands a fresh look at applications, but the basic concepts remain valid.

The property of the FPI that makes it particularly advantageous for studying the faint emission lines of the night sky is that it has an internal monochromatic field of view typically hundreds of times larger than that of conventional grating spectrometers of comparable resolving power and size. At a resolving power of 50,000, for example, the FOV of the FPI is about 0.72 degrees in diameter. For a grating spectrometer (Littrow at 45 degrees) the field is 2.3×10^{-3} degrees in the dispersion direction (limited by the slit width), and typically limited to about 0.5 degrees along the slit. This yields a gain of 350 for the FPI compared to a grating spectrometer.

An important difference in the application of FPI and grating instruments arises because grating instruments are dispersive while FP instruments are filters. All the light that gets through the grating spectrometer slit ends up in the camera focal plane. For the FPI, when the one selected spectral resolution element is passed, all other elements are reflected back to the source. A grating instrument using an imaging detector records simultaneously the spectral range needed for a particular study, while the FPI must be stepped through the 10 or so required elements. The gain depends on the problem being studied, but the FPI may still have a considerable gain: 35 in this example. A newer class of grating spectrographs being developed for terrestrial aeronomy, a high throughput imaging echelle spectrometer (HiTIES), has approximately an order of magnitude more throughput at a given resolving power than a conventional grating spectrometer with a first-order plane grating [*Ckakrabarti*, 1998; *Pallamraju et al.*, 2001; *Pallamraju et al.*, 2002].

The FPI can be used in a multi-channel mode using an imager [for example, *Coakley et al.*, 1996] to achieve gains of 15 or more over the single channel mode, but each element requires additional solid angle. In contrast, the grating disperses the same solid angle element into the many spectral element channels. Even with very large telescopes, astronomical sources of interest in solar system aeronomy are unlikely to have the large solid angles (exceptions are comets, interplanetary hydrogen, and the sodium nebula associated with Jupiter) needed for this FPI mode to achieve its full power. Nevertheless, the multichannel mode may be

an advantage for astronomical studies because, with simultaneous recording, all channels are affected equally by time variations in the atmosphere and background spectrum.

Past comparative aeronomy applications of FP spectrometers on conventional ground-based telescopes have met with limited success because of the difficulty of dealing with large amounts of reflected and scattered light in their sunlit atmospheres, and because of severe dilution by "seeing" (typically around 1 arcsec) of features that might be very bright in regions a small fraction of an arc sec in extent. In this case grating instruments have a clear advantage because recording a large spectral range simultaneously is essential for the precise fitting and subtracting the solar background to find the aeronomically interesting feature, severely weakened by seeing dilution with sunlight. An important example is the recent study by *Oliversen et al.* [2001] of 630 nm [OI] emission in the sunlit atmosphere of Jupiter's moon Io using the echelle stellar spectrograph at the McMath-Pierce telescope on Kitt Peak. This emission has been connected to OI and SI far ultraviolet emission line images, obtained using the STIS instrument on HST, which show prominent features on 0.1 arc sec scales [*Roesler et al.*, 1999]. These features are far too small to be spatially resolved due to poor seeing at the McMath-Pierce solar telescope. Extremely careful fitting and removal of the solar background recorded over a 0.5 nm range was a key element in the success of this study. This would have been difficult to impossible using a scanning FPI .

However, with the advent of adaptive optics on large telescopes the balance is tilted strongly in favor of the Fabry-Perot as a high-spatial and spectral resolution imager. With AO, the advantage of the FP imager is that the entire field of view is imaged at the spatial resolution of the adaptive optics system. By contrast, with the grating instrument the slit must be narrow enough in the dispersion direction to isolate the spatial resolution element of the AO system. The result is that very many grating spectrometer exposures are likely to be needed to cover the full field. Some of the loss could be recovered using an image slicer to stack image slices along the entrance slit.

The problem of detecting small spatial features in sunlit atmospheres is greatly reduced for the FP-AO system. Using again the Io 630 nm emission example, we note that HST images yield intensities of about 10 kR in 0.1 arcsec spots. At a spectral resolving power of 100,000, such features are readily detected against the solar background with the high spectral *and* high spatial resolving power of the FP imager. Without AO the small, bright features are diluted with sunlight 25 - 100 times by seeing of 0.5-1.0 arc sec, and fall below a reliable detection limit. Analogous arguments suggest the use of the FP imaging spectrometer on AO-equipped telescopes for the study of Jovian aurora at H Balmer-alpha. With high spectral resolution, both the spatial structure and velocity profile could be studied.

An FP imaging system with resolving power of 20,000 - 100,000 for the study of sunlit atmospheres should have two Fabry-Perots in series with a narrow-band interference filter. The double etalon provides reduced parasitic light by suppression of the broad Lorentzian wing of a single FP and of the unwanted transmission peaks. Reasonably high spectral purity is required to fit and remove solar background features. The Wisconsin group has used such a system (adapted from a 150 mm aeronomy FP used in the study of geocoronal hydrogen, and moved to Kitt Peak) for studying the velocity field of H_2O^+ ions in an 8 arcmin field around the head of comet Hale-Bopp. A data cube of ten incrementally stepped images was obtained and reduced to find the centroid of the H_2O^+ feature for each pixel. AO was not needed for this large scale object, but it illustrates the technique that could be applied to small bodies with a large AO telescope.

5. A SUPER-LIDAR FOR OBSERVING THE DENSITY, TEMPERATURE AND VELOCITY OF THE MOON'S SODIUM ATMOSPHERE

Lidar (light detection and ranging) technologies, the optical counterpart to radar, have been especially important for studying the upper atmosphere from the middle stratosphere (from about 30 km altitude) to the lower thermosphere (to about 110 km altitude). Lidars typically employ high energy pulsed lasers, large optical telescopes, and range gated photon counting detectors to derive atmospheric profiles. Two primary types of lidar systems are used to probe the upper atmosphere. Rayleigh/aerosol systems monitor scattering from air molecules and ice particles to infer temperature, wind, and aerosol profiles up to about 90 km altitude. Resonance fluorescence lidars employ resonant backscattering from atomic metal layers in the mesopause region and lower thermosphere (80 - 110 km). The metal layers are formed by meteoric ablation. Lidar systems have been developed to probe mesospheric Na, Fe, K, Ca, Ca^+, and Li. Because of its relatively high abundance and large resonant backscatter cross-section, Na has been the most widely studied. Na-based systems

provide the highest resolution and most accurate wind and temperature measurements available.

To derive temperature and wind data from the backscattered Na signal, the laser is tuned over the Na D2 spectral line near 589 nm. The spectral bandwidth is related to temperature and the spectral center line is related to Doppler shift associated with the radial winds [*Papen et al.*, 1995]. Temperature, radial wind velocity, and Na density can be determine by measuring the backscattered signal at as few as three different frequencies within the Na spectrum.

While simple in concept, Na wind/temperature lidars employ sensitive ring dye lasers, pulsed dye amplifiers, and complex frequency-locking techniques to achieve the required tens of kilohertz frequency accuracy necessary for the wind and temperature observations. Because measurement accuracy and useful resolution are related to signal strength, the most accurate measurements are obtained by using large telescopes such as the 3.5 m facility operated by the Air Force Research Laboratory, Directed Energy Directorate at the Starfire Optical Range (Plate 1c).

This system has even been used to probe the winds and temperatures within several persistent meteor ablation trails left in the wake of bright fireballs as shown in Plate 1d [*Chu et al.*, 2000].

Although Na lidars are now capable of producing exquisite measurements of upper atmospheric winds and temperatures, their use is restricted to groundbased sites with environmentally controlled labs to accommodate the sensitive and complex laser systems.

The Moon has been known to have a tenuous atmosphere since in situ measurements were made on the night side during the Apollo missions [*Hodges et al.*, 1974]. As described briefly in section 2 (above) and in chapter III.3 in more detail, sodium is an extremely useful tracer of lunar exospheric processes (see also *Stern* [1999]).

Observations of a well-defined coma and tail (as shown in Plate 1a) have raised a broad host of questions about the origin and evolution of Na (and by implication other species) in the lunar atmosphere. The temperature of the gas is currently being debated over an order of magnitude ($<$ 300° K to $>$ 2000° K), and the "ejection speeds" are discussed over the full range from essentially zero to well beyond the escape velocity ($>$ 2.4 km/sec). Na densities just above the surface are estimated in the $<$ 10 cm^{-3} to $>$ 50 cm^{-3}.

The potential use of a Super-Lidar for lunar atmosphere studies offers an unprecedented opportunity for planetary research. By their very nature, remote-sensing observations in optical astronomy involve column-averaged emission features. The possibility of probing the actual line-of-sight density and temperature profile of a remote atmosphere with a terrestrial-based instrument literally brings a third dimension into research on another atmosphere in the solar system. For the lunar Na nebula, defining the density, temperature, and velocity structure above the sunlit surface would confine current models of sputtering and thermalization. Probing the tail region would characterize the physical conditions in the shadow region where sunlight cannot illuminate Na.

The Moon is located approximately 3.8 x 10^5 km from Earth and, because of the great distances involved, an observational scenario for the lunar Na nebula is considerably different from that used to profile the Earth's mesospheric Na layer. The optical round trip propagation time between the Earth and Moon is approximately 2.5 s. To avoid interference from scattering in the Earth's lower atmosphere and Na layer, it will be necessary to fire a 2.5 s burst of laser pulses toward the Moon and then wait approximately 2.5 s until the last of the nebula scattered photons are collected by the telescope. This process is repeated until sufficient signal levels have been accumulated to construct the density, temperature, and radial velocity profiles.

The laser pulse rate is limited by the line-of-sight thickness of the nebula. Again to avoid interference, the time between pulses can be no shorter than the round trip propagation time through the nebula along the line-of-sight of the lidar. For example, to probe the sunward portion of the nebula at quarter moon phase, we assume that most of the Na in the nebula is contained within a line-of-sight region 4 R_M thick. Then, the maximum permissible pulse rate is 22 pps so that each 2.5 s burst contains 55 laser pulses.

To measure Na density with an accuracy of 5-10%, temperatures with an accuracy of 5-10 K, and line of sight motion with an accuracy of 5-10 m/s, requires a signal level of approximately 1000-photons/resolution cell. The expected signal level can be calculated using the lidar equation. If we assume the overall lidar efficiency (including detector) is 10% and the atmospheric transmittance is 80%, then the total signal count rate from the lunar nebula is

$$R_s(photons/sec) = 10^{-16} C_s(m^{-2}) PA(Wm^2) \quad (1)$$

For a laser power of 10 W, telescope diameter of 10 m (PA = 785 Wm^2), and a total Na abundance in the nebula of $Cs = 1.25x10^{14}$ m $^{-2}$ [*Mendillo et al.*, 1991],

[redacted]

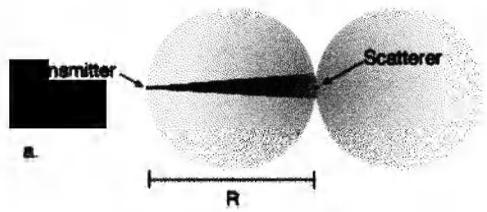

a.

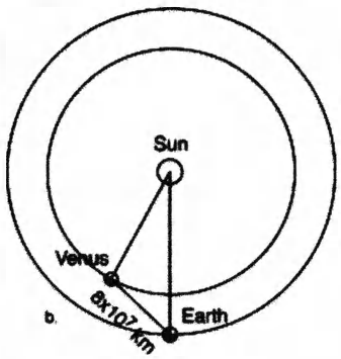

b.

[redacted]

[redacted]

$$P_s =$$ [redacted]

ometry shown in Figure 1b has an Earth-Venus separation distance of twice the closest approach (R = 8 x 10^7 km) and allows about one quarter of the dayside to be seen. The night side is about 100 times smaller so is not significant, and also a large contribution from the topside is not significant for reasons explained below. The result is $n = 2.25 \times 10^{28}$ electrons.

First consider the power and signal to noise ratio using the Arecibo radar. For Arecibo $P_t = 2 \times 10^6$ is watts, and the gain using the 96 foot long line feed with the 300 m dish is about 61 db. The effective area is $G(0)\lambda^2/4\pi$, where λ = .698m is the radar wavelength, or 48,809 m^2. The received power using the equations above is 2.13 x 10^{-29}. The noise power is given by kT_nB, where k is Boltzman's constant, T_n is the noise temperature of the system, and B is the bandwidth of the receiving system. This is 1.38 x 10^{-17} for $T_n = 100K$ and a bandwidth of 10 KHz. The bandwidth calculation assumes molecular oxygen as the dominant ion with temperature of about 2500 K. The signal to noise ratio is 8.38 x 10^{-12} which is too small for a practical measurement.

Shorter wavelengths give more gain for a given antenna size while staying within the Debye length constraints. In terrestrial incoherent scatter, there is no advantage in going to a shorter wavelength since the beam is filled with scatterers. The improvement realized here is significant but moderate, since decreasing below about .2 m would lose power from the lower density edges of the layer due to Debye length effects. Thus, .2 m loses the topside, which is the reason for ignoring it above. A noise temperature of 35 K is reasonable for this wavelength.

For constructing the large radar system necessary for this application, define a module with an area of $10^4 m^2$ and a power of 10^6 watts. Then increase the number of modules until the power is sufficient. The success of astronomical interferometers shows that, in principle, it is possible to perform the necessary phasing of the modules over distances of many kilometers, but there are some new problems to be solved in a transmitting system. With a thousand of these modules (1 Gigawatt, $10^7 m^2$, or 10 km^2) and the new parameters from above, the received power is 5.5 x 10^{-21} watts; the noise is 4.8 x 10^{-18} watts, and the signal to noise ratio is about 10^{-3}. Collecting 10^8 independent samples, which would take 10^4 seconds (about 3 hours) with a 10 KHz bandwidth and continuous wave transmission, gives a relative error of 10^{-4} for the signal plus noise, allowing detection of the signal, but nothing more. Accurate monitoring of the total electron content and the electron and ion temperatures would require several times more power.

7. SUMMARY

Passive optical systems used routinely for studies of the Earth's mesosphere and thermosphere offer new avenues of research for planetary aeronomy. Complimenting this approach is the recent initiative to use the "telluric corrections" made by astronomical telescopes for high resolution studies of the terrestrial atmosphere [*Slater et al.*, 2001]. Awaiting further study and testing are the *active* probing of nearby atmopheres using giant LIDAR and incoherent scatter radar (ISR) facilities.

Acknowledgments. Support for these studies was provided, in part, by grants from the Upper Atmosphere Research Section of the U.S. National Science Foundation.

REFERENCES

Akasofu, S.-I. *Polar and Magnetospheric Substorms,* Springer-Verlag, New York, 1968.

Baumgardner, J., B. Flynn, and M. Mendillo, Monochromatic imaging instrumentation for applications in aeronomy of the Earth and planets, *Opt. Eng., 32,* 3028-3032, 1993.

Baumgardner, J., M. Mendillo, and J. K. Wilson, A digital high-definition imaging system for spectral studies of extended planetary atmospheres. 1. Initial results in white light showing features on the hemisphere of Mercury unimaged by Mariner 10, *Astron. J., 119,* 5, 2458-2464, 2000.

Chakrabarti, S., Groundbased spectroscopic studies of sunlit airglow and aurora, *J. Geophys. Res., 60,* 1403-1424, 1998.

Chu, X., A. Liu, G. C. Papen, C. S. Gardner, M. C. Kelley, J. Drummond, and R. Fugate, Lidar observations of elevated temperatures in bright chemiluminescent meteor trails during the 1998 Leonid shower, *Geophys. Res. Letts., 27,* 13, 1815-1818, 2000.

Coakley, M. M., F. L. Roesler, R. J. Reynolds, and S. Nossal, Fabry-Perot CCD annular-summing spectroscopy: Study and implementation for aeronomy applications, *Applied Optics, 35,* 6479-6493, 1996.

Eather, R. H., Dayside auroral oval, *J. Geophys. Res., 89,* 1695-1700, 1984.

Emery, J. P., A. L. Sprague, F. C. Witteborn, J. E. Colwell, R. W. H. Kozlowski, and D. H. Wooden, Mercury: Thermal modeling and mid-infrared (5-12 mu m) observations, *Icarus, 136,*, 1, 104-123, 1998.

Evans, J. V., Theory and practice of ionosphere study by Thomson scatter radar, *Proceedings of the IEEE, 57,* 4, 1969.

Fried, D., Probability of getting a luck short-exposure image through turbulence, *J. Opt. Soc. Am., 68,* 1651-1658, 1978.

Hodges, R. R., J. H. Hoffman, and F. S. Johnson, The lunar atmospheres, *Icarus, 21,* 415-426, 1974.

Lanchester, B. S., M. H. Rees, D. Lummerzheim, A. Otton, K. J. F. Sedgemore-Schulthess, H. Zhu, and I. W. McCrea, Ohmic heating as evidence for strong field-aligned

currents in filamentary aurora, *J. Geophys. Res.*, *106*, A2, 1785-1794, 2001.

Mendillo, M., J. Baumgardner, M. Colerico, and D. Nottingham, Imaging science contributions to equatorial aeronomy: initial results from the MISETA program, *J. Atmos. Solar Terr. Phys.*, *59*,, 13, 1587-1599, 1997.

Mendillo, M., J. Baumgardner, and B. Flynn, Imaging observations of the extended sodium atmosphere of the moon, *Geophys. Res. Letts.*, *18*, 11, 2097-2100, 1991.

Oliversen, R. J., F. Scherb, W. H. Smith, M. E. Freed, R. C. Woodward, Jr., M. L. Marconi, K. D. Retherford, O. L. Lupie, and J. P. Morgenthaleret, Sunlit Io Atmospheric [O I] 6300A Emission and the Plasma Torus, *J. Geophys. Res.*, in press, 2001.

Pallamraju, D., J. Baumgardner, and S. Chakrabarti, Simultaneous ground based observations of an auroral arc in daytime/twilighttime O I 630.0 nm emission and by incoherent scatter radar, *J. Geophys. Res.*, *106*, 5543-5549, 2001.

Pallamraju, D., J. Baumgardner, and S. Chakrabarti, HIRISE: A ground-based High Resolution Imaging Spectrograph using Echelle grating for measuring daytime airglow/auroral emissions, *J. Atmosph. Sol-Terr. Phys.*, in press, 2002.

Papen, G. C., W. M. Pfenninger, and D. M. Simonich, Sensitivity analysis of sodium narrowband wind-temperature lidar systems, *Appl. Opt.*, *34*, 480-498, 1995.

Potter, A. E., R. M. Killen, and T. H. Morgan, *Planet. Space Sci.*, *47*, 1441, 1999.

Roesler, F. L., Fabry-Perot Instruments for Astronomy, in Methods of Experimental Physics, vol 12, Part A: Optical and Infrared, edited by L. Martin and N. Carleton, p.531, Academic, San Diego, CA, 1974.

Roesler, F. L., H. W. Moos, R. J. Oliversen, R. C. Woodward, K. D. Retherford, F. Scherb, M. A. McGrath, W. H. Smyth, P. D. Feldman, D. F. Strobel, Far-Ultraviolet Imaging Spectroscopy of Io's Atmosphere with HST/STIS, *Science*, *283*, 353-357, 1999.

Schunk, R. W., and A. F. Nagy, *Ionospheres: Physics, Plasma Physics, and Chemistry*, Cambridge University Press, Cambridge, UK, 2000.

Shiokawa, K. M. K. Ejiri, and T. Ogawa, Distant lunar sodium tail observed in the Japanese local-time sector during the Leonid meteor shower of 1998, *J. Geophys. Res.*, *105*, 24621-24626, 2000.

Slater, T., A Proposed Virtual Aeronomic Observatory, (private communication, 2001).

Smith, S. M., J. K. Wilson, J. Baumgardner, and M. Mendillo, Discovery of the distant lunar sodium tail and its enhancement following the Leonid meteor shower, *Geophys. Res. Letts.*, *26*, 12, pp. 1649-11652, 1999.

Smith, S. M., M. Mendillo, J. Baumgardner, and R. R. Clark, Gravity wave activity at a sub-auroral site: first results from Hillstone Hill, *J. Geophys. Res.*, 2000.

Smith, S. M., J. K. Wilson, J. Baumgardner, and M. Mendillo, Monitoring the Moon's transient atmosphere with an all-sky imager, *Adv. Space Res.*, (in press), 2001.

Sprague, A. L., D. B. Nash, F. C. Witteborn, and D. P. Cruikshank, Mercury's feldspar connection mid-IR measurements suggest plagioclase, *Adv. Space Res.*, *19*, 10, 1507-1510, 1997.

Steele, D. P., and L. L. Cogger, Polar patches and the "tongue of ionization", *Radio Sci.*, *31*, 667-677, 1996.

Stenbaek-Nielsen, H. C., T. J. Hallinan, D. L. Osborne, J. Kimball, C. Chaston, J. McFadden, G. Delory, M. Temerin, C. W. Carlson, Aircraft observations conjugate to FAST: Auroral arc thicknesses, *Geophys. Res. Let.*, *25*, 12, 2073-2076, 1998.

Stern, S. A., The lunar atmosphere: history, status, current problems and context, *Rev. Geophys.*, *37*, 453-491, 1999.

Swenson, G. R., M. J. Taylor, P. J. Espy, C. Gardner, and X. Tac, ALOHA-93 measurements of intrinsic AGW characteristics using airborne imager and groundbased Na wind/temperature LIDAR, *Geophys. Res. Lett.*, *22*, 2841-2844, 1995.

Taylor, M. J., M. B. Bishop, and V. Taylor, All-sky measurements of short period waves imaged in the OI(557.7 nm), Na(589.2 nm) and near-infrared OH and O2(0,1) nightglow emissions during the ALOHA-93 campaign, *Geophys. Res., Lett.*, *24*, 2833-2836, 1995.

Taylor, M. J., J. V. Eccles, J. LaBelle, and J.H.A. Sobral, High resolution OI(630 nm) image measurements of F-region depletion drifts during the Guara campaign, *Geophys. Res. Lett.*, *24*, 1699-1702, 1997.

Vilas, F. M. A. Leake, and W. W. Mendell, *Icarus*, *59*, 60, 1984.

Warell, J., and S. S. Limaye, Properties of the Hermean regolith: 1. global albedo variations at 200 km scale from multicolor CCD imaging, *Planet. Space Sci.*, (in press), 2001.

Weber, E., J., J. Buchau, R. Eather, and S. B. Mende, North-south aligned equatorial airglow depletions, *J. Geophys. Res.*, *83*, 712-716, 1978.

Weber, E. J., J. Buchau, J. G. Moore, J. R. Sharber, R. C. Livingston, J. D. Winningham and B. W. Reinisch, F layer ionization patches in the polar cap, *J. Geophys. Res.*, *89*, 1683-1694, 1984.

Wescott, E. M., H. Stenbaek-Nielsen, D. D. Sentman, D. R. Moudry, M. T. Heavner, and F. T. Sao Sabbas, Optical observations of Sprites and Elves during the NASA 1999 Sprites Balloon Campaign, (abstract) AGU Fall Meeting, *Trans. AGU*, *80(46)*, F217, 1999.

Wilson, J. K., S. M. Smith, J. Baumgardner, and M. Mendillo, Modeling an enhancement of the lunar atmosphere during the Leonid meteor shower of 1998, *Geophys. Res. Lett.*, *26*, 1645-1648, 1999.

M. Mendillo, Center for Space Physics, Boston University, 725 Commonwealth Avenue, Boston, MA 02215. (email: mendillo@bu.edu)

F. Roesler, Department of Physics, University of Wisconsin, 1150 University Avenue, Madison, WI 53711. (email: roesler@wisp.physics.wisc.edu)

C. Gardner, Department of Electrical and Computer Engineering, University of Illinois, 315a Coordinated Systems Laboratory, 1308 West Main, Urbana, IL 61801. (email: cgardner@uillinois.edu)

M. Sulzer, Radar Sciences Department, Arecibo Observatory, HC3 Box 53995, Arecibo, PR 00612. (email: msulzer@naic.edu)

Ultraviolet Remote Sensing Techniques for Planetary Aeronomy

John T. Clarke

Center for Space Physics, Boston University, Boston, Massachusetts

Larry Paxton

Applied Physics Laboratory, Johns Hopkins University, Laurel, Maryland

This paper presents an overview of the principles of the study of planetary atmospheres at vacuum ultraviolet wavelengths. Ultraviolet (UV) remote sensing is a powerful technique for investigating the chemistry, dynamics, energetics, and composition of planetary atmospheres. In the last fifteen years optical aeronomy has undergone a profound change. The field has begun the transformation from initial spectroscopy, in which the radiating species and their signatures are identified, to remote sensing in which the signatures are used to provide quantitative information on a global basis. This transformation has occurred as UV spectra of nearly all major planetary bodies have been obtained, either by flyby spacecraft or Earth-orbiting observatories, and the basic composition of their atmospheres is now known. We present an historical overview to show how improvements in technology have led to improved measurements. The UV is an ideal region of the spectrum for remotely sensing planetary atmospheres due to the large absorption cross sections exhibited by most of the major species and the prevalence of emission features. The flight of lightweight, compact sensors permits sensitive measurements of the upper atmospheres of the major planets and Titan, and the thin atmospheres of Mercury and Pluto as well as several planetary satellites.

1. PRINCIPLES OF ULTRAVIOLET REMOTE SENSING

For the study of planetary atmospheres, the vacuum ultraviolet spectral range will be defined as wavelengths from 50-300 nm (EUV < 100 nm, FUV < 200 nm, NUV < 300 nm). This wavelength range corresponds to energies of 4-15 eV, which encompasses the energy levels of electronic transitions in simple atoms and molecules. The most abundant species observed in the upper regions of planetary atmospheres are H, H_2, and He in the giant planets, with the addition of O, O_2, N, N_2, CO, and CO_2 in the terrestrial planets. A basic principle of optical remote sensing is that the technique is sensitive to the composition in the first few optical depths [see e.g. *Paxton and Anderson*, 1992; *Yee et al.*, 2002]. Due to the large absorption cross sections of major constituents in most planetary atmospheres, UV remote sensing works particularly well in the upper regions of thick atmospheres or a rarefied atmosphere. In addition, wavelengths $\lambda < 200$ nm are on the faint end of the solar Rayleigh-Jeans curve for typical planetary temperatures (Figure 1), providing a relatively low background from Rayleigh scattered solar continuum. Since the solar flux is relatively low, however, planetary signal levels tend to be low, and many observations are photon limited. Most ultraviolet flux from planetary atmospheres consist of re-

Atmospheres in the Solar System: Comparative Aeronomy
Geophysical Monograph 130

10.1029/130GM23

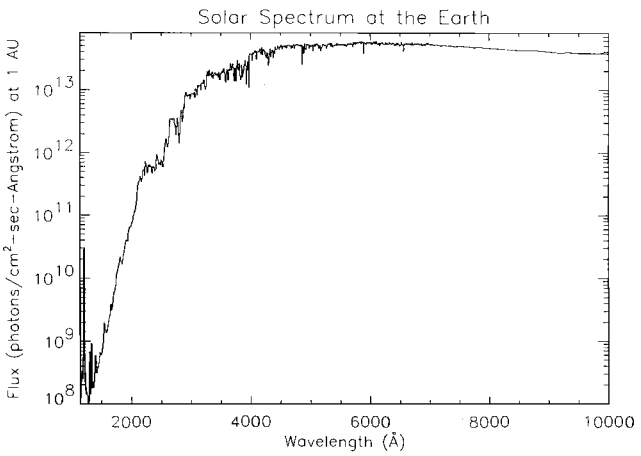

Figure 1. Flux from the Sun at the Earth over visible and UV wavelengths. The Rayleigh-Jeans tail of the blackbody distribution extends well into the near-IR, while the distribution of continuum flux drops precipitously in the UV. Below approximately 140 nm the solar emission is predominantly coronal emission lines.

flected solar emissions or charged particle collisional excitation, so that the emitted spectra depend both on the composition of the atmosphere and the solar spectrum.

2. INSTRUMENTAL METHODS OF UV REMOTE SENSING

The properties of practical optical instruments have been well known for more than one hundred years [e.g. *Samson*, 1967; *Huffman*, 1992; *Samson and Ederer*, 1998]. Recent advances in manufacturing of complex, aspheric surfaces and the use of new materials has enhanced the implementation of these basic designs. In general an optical instrument can be thought of as a means to convert photons into a signal that can be interpreted by humans. We can write the response of a generalized spectral instrument as:

$$S = (4\pi I)/(4\pi)(h/f)(m/d)\Delta\lambda A_g T(\lambda) Q_e D_e \quad (1)$$

where

S is the signal at the exit slit in counts per second

$4\pi I$ is the emergent intensity in Rayleighs (1 Rayleigh $\equiv 10^6$ photons/sec emitted isotropically from a 1 cm^2 column of atmosphere)

h is the slit height

f is the focal length of the system

m is the grating order

d is the grating spacing (in lines per unit length)

$\Delta\lambda$ is the desired spectral resolution

A_g is the filled area of the grating

$T(\lambda)$ is the optical transmission and includes the reflectivity of the grating, the blaze function of the grating, and any other reflections from mirrors as the product of those reflection efficiencies

Q_e is the quantum efficiency of the detector

D_e is the detector electronics efficiency and includes all losses due to the detection of the individual events and the conversion of those events to "counts" in the data stream.

In the normal case of photon-limited measurements with a low detector background, the goal is to maximize the above product to obtain the maximum photon counting rate. One can:

- maximize the slit length to increase the count rate for diffuse emissions (constrained by the overall instrument volume and mass, which go roughly as the square of the slit length),
- minimize the focal length to increase the angular field of view per detector pixel, to increase the count rate per pixel (shorter focal length gratings are harder to make, to focus, and to craft with good imaging properties),
- maximize the filled area of the grating (which drives the instrument size and mass)
- pick the highest spectral resolution required to do the job, while holding down the number of reflections required to produce an image of suitable quality.

The efficiency with which the detector converts light to a photoelectron is optimized for the band to be observed, with the caveat that the photocathode response to light of undesirable wavelengths (the "out of band response") is minimized. The detector electronics are designed to yield high conversion efficiencies over the range of input rates expected, while being able to function in space in a harsh radiation environment. The reader should be able to readily appreciate that two teams might come up with the different designs for the same mission or that one design might be applicable to a number of different missions. Both of these have proven to be the case. In general, instruments on spacecraft that will visit the planets have considerably tighter limits on mass, power, and data rates than Earth-orbiting instruments.

Since ultraviolet radiation is readily absorbed in air, UV instruments must be developed and tested in the laboratory in vacuum chambers, adding considerable cost and difficulty to their development. Most common optical materials show strong absorption and chromatic aberration throughout much, if not all, of the UV spectral range. Thus, all-reflection optical designs are strongly favored. As a result of the limited reflectivity, a minimum number of optics is desired at all UV wavelengths. The reflectivities of various mirror coatings are wavelength dependent, with generally high reflectivities

(~80%) for coatings such as Al + MgF_2 or LiF above 115 nm, but significantly lower (~30-50%) below 100 nm [*Content et al.* 1999]. While a simple aluminum flash coating provides high UV reflectivity, it will oxidize over a few hours to days of exposure to air and turn non-reflective in the UV. Overcoatings are needed to protect the Al surface from oxidation, while providing a high transmission to UV radiation. For wavelengths longer than 115 nm, one could consider transmissive elements (e.g. lenses), but this is usually not considered due to large variations in refractive index with wavelength of even the least opaque crystalline materials. Optical designs incorporating refractive optics are usually considered when the required wavelength range can be reduced to such a degree that chromatic aberration is not an issue. UV instrument design and fabrication faces a further challenge: contamination by water vapor and hydrocarbons must be stringently avoided. A monolayer of hydrocarbon, such as machine oil, is sufficient to reduce a mirror's UV reflectivity to 1/e of its clean value. UV optical manufacturing, assembly processes, and handling guard against contamination on the ground through long-established procedures. Before flight the instruments are purged with clean dry nitrogen and protected by closed covers. Typically, UV instruments wait three to six weeks before opening these covers to avoid contamination by material released from the spacecraft or the rocket motor used to reach space.

The type and availability of a detector suitable for responding to UV radiation has played the defining role in the design of UV instruments [see *Paxton and Anderson*, 1992 for an overview; *Paxton and Meng*, 1999]. While film could be used for sounding rockets, an electo-optical detector is required for spaceflight. In the early days of planetary missions, photomultiplier tubes (PMT's) were widely used as they were compact and robust and could be incorporated into a simple compact spectrometer. PMT's detect photons by the photoelectric effect: light falling on the photocathode at the front of the device causes an electron to be emitted from that surface, the electron is then amplified to form a cloud that can be detected by the PMT electronics as a pulse. Since UV photon fluxes are small these pulses essentially count the arrival of individual photons. Early spectrometers (a spectrometer is an instrument which records one wavelength at a time) required a scanning grating to cover the spectrum using entrance and exit slits, and obtained angular or spatial profiles by scanning the entrance aperture across the field of view with the grating set to a fixed wavelength.

Since the late 1970s, a variety of 2-dimensional imaging detectors using microchannel plates (MCP's) and position sensitive anodes have been available. These provide charge amplification as though they consisted of thousands of individual PMTs. The position sensitive anode provides the information needed to determine the spatial location of the event in the instrument field-of-view. The resolution of these detectors has increased to the point where formats of 1024 by 1024 and greater are commonly available. The achievable resolution of these detectors is driven by the design of the charge location and processing electronics, and the format and resolution of the anode [*Siegmund et al.* 1999]. Charge-coupled devices (CCDs) have been used for spaceflight most commonly with the addition of a phosphor at the end of a MCP stack. The phosphor converts the electron cloud into a visible light photon pulse that the CCD records as electrons for later processing. CCDs are somewhat sensitive to radiation effects, and are not often used for spaceflight applications. The charge-injection device or CID has also been studied for use in radiation intense environments [*Kimble et al.* 1999]. The spectral range over which these devices are sensitive is controlled by the photocathode material used to generate electrons in response to incident light. The most commonly used photocathode materials include CsI, CsTe, and KBr. The detector system can be contained in a sealed unit with a window provided wavelengths longer than 115 nm are to be imaged. If not, an openable door is used to maintain cleanliness until after launch, while removing the wavelength restriction imposed by the transmissivity of the window material. A good review of these and other UV detector technologies can be found in [*Joseph* 1995] and [*Joseph* 2000].

With the availability of robust and compact two-dimensional imaging systems, spectrographs became commonly used for planetary missions. Spectrographs (instruments recording multiple wavelengths at the same time) with one- or two-dimensional array detectors permit the detection of a range of wavelengths at the same time. Two-dimensional detector arrays allow simultaneous spectral and spatial data to be recorded, often in a format with a long narrow aperture, with spectral dispersion perpendicular to the aperture and spatial imaging along the aperture. These instruments became increasingly practical with the advent and ready availability of computer-aided design and manufacturing systems and the ability to produce gratings that were not planar. Thus, a compact spectrograph could be produced that had suitable spectral and spatial imaging properties, while minimizing the number of optical surfaces.

Photon-counting detector quantum efficiencies tend to be less than 50%, which is a continuing challenge to the field. In fact, if a semi-transparent photocathode is used, as may be the case when the photocathode is applied to the inside surface of a window on a sealed detector as-

sembly, quantum efficiencies of about 10% are not uncommon. While CCD's have higher QE values, they also have higher dark counts, read noise, and cosmic ray sensitivity, so that one must consider the overall signal/noise ratio in the choice of a detector. Increasing the quantum efficiency can be traded off against the size of the light collecting optics. MCP detectors also require high voltage (typically 2000 to 6000 volts) to provide the gain necessary to centroid the pulse at the anode. The use of high voltage necessitates the use of insulating materials (potting) with a concomitant weight penalty. Other challenges include the cleanliness of all optical surfaces, limited count rates depending on the photon counting electronics, exposure to local plasma particles for windowless detectors, and the limits to microchannel plate charge lifetimes for detectors with high gain. The lifetime of a MCP detector is defined by the total charge pulled through an area of the detector, thus enabling a tradeoff consisting of the number of events to be detected and the effective gain. The product of these thus defines the lifetime accumulated charge. None of these is insurmountable, and detectors are designed for individual missions taking into account the scientific goals and environment of that mission.

Several new detector concepts have been proposed, and initial demonstration or evaluation studies carried out. One example is the measurement of solar EUV coronal emissions by gas ionization [*Vickers et al.* 1993]. Another is the development of a single-element spectrographic instrument [*Cotton et al.* 1994]. Finally, a new detector concept based on superconducting tunnel junction (STJ) devices is under development (reviewed by [*Jacobsen* 1999]), which in principle would deliver both high quantum efficiency and wavelength resolution by measuring the energy of each photon event, obviating the need for spectral dispersing elements in the system. While the STJ detectors hold great potential, they are in an early stage of their development.

3. OBSERVATIONAL METHODS OF UV REMOTE SENSING

Several techniques have been applied to the analysis of UV spectra to extract information about planetary atmospheres. One of the first was to measure the UV spectra of the other planets, permitting the spectral identification of the constituents of their upper atmospheres. At all wavelengths, bright line and band emissions can be produced through resonant scattering and fluorescence of solar emissions. More detailed observations, including high spectral resolution, permits more detailed modeling and characterization of the atmospheric temperature, excitation rates, column abundances and their variations with altitude and location on the planet. Most of our early understanding of the composition of the upper atmospheres of the planets was accomplished through UV spectroscopy by a series of sounding rockets, deep space probes, and Earth-orbiting telescopes.

Another technique is to measure the absorption of stellar or solar radiation by the atmosphere along the line of sight (Figure 2). The Voyager Ultraviolet Spectrometer (UVS) has been particularly successful in applying this technique to the sounding of the atmospheres of the outer planets [*Broadfoot et al.* 1981]. Occultation measurements further require a relative motion of the line of sight across the limb of the planet, and therefore occur relatively infrequently for Earth-based observations. This technique is most commonly applied from a spacecraft near the planet, in which case the line of sight to the planet's limb sweeps out large angles on the sky from the motion of the spacecraft. Occultation measurements are capable of providing much higher altitude resolution, being limited by the signal to noise that can be obtained in the time that the line of sight passes through an altitude interval. Bright stars and slow relative motions provide the highest signal to noise, and thereby the highest altitude resolution. Occultation data are generally limited to the altitude range where the line of sight optical depth is near one at a particular wavelength, so that multiple bandpasses corresponding to different atomic and molecular bands are needed to sample a range of altitudes. In addition, stellar occultations are limited to wavelengths $\lambda > 91.2$ nm due to absorption of the stellar flux by interstellar hydrogen. Solar occultations can extend to much shorter wavelengths, but the line of sight will always be near the terminator, sampling either dawn or dusk conditions. Occultation measurements at all wavelengths are a very useful means of measuring thermal structure in atmospheres.

Measurement of the altitude profiles of auroral and airglow emissions is another method of studying the vertical structure and excitation of an atmosphere. Early rocket experiments studied the Earth's atmosphere and ionosphere by observing the emissions perpendicular to the zenith while flying through the atmosphere. One complication to the interpretation of both this technique and occultation data results from the spherical geometry of the atmosphere. Each line of sight covers a chord tangent to the planet, with some minimum altitude, and contributions to the signal from each parcel of the atmosphere with increasing altitude away from the tangent point. Methods of interpretation generally assume uniformity of the atmosphere along the track of the column, then divide the atmosphere into vertical layers. The

[redacted]

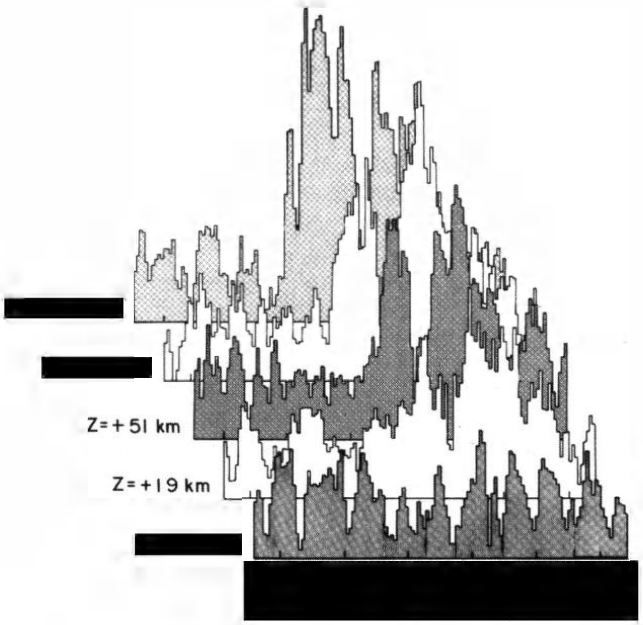

[redacted]

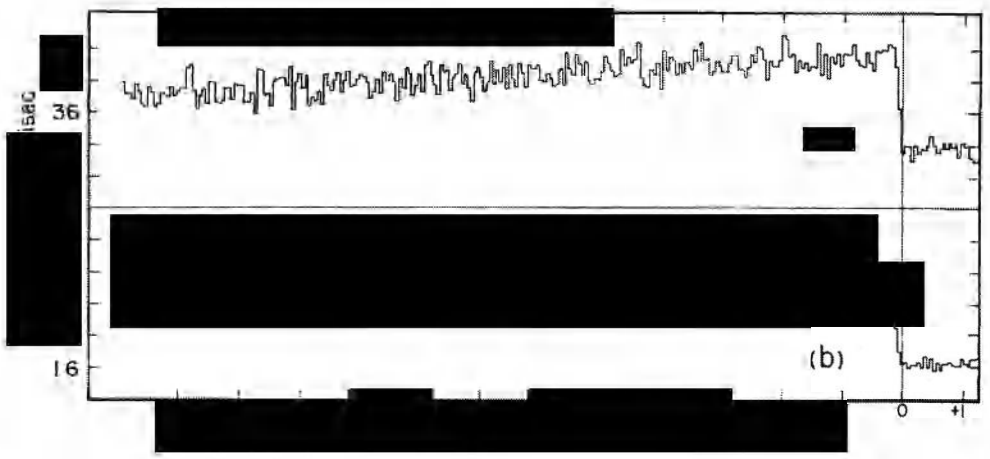

[redacted]

[redacted]

$$\tau_\lambda = \int_{s_1}^{s_2} \sum_{i=1}^{m} n_i \sigma_{i\lambda} \, ds$$

[redacted]

section has a wavelength dependence, the optical depth also has a wavelength dependence. The altitude at which τ=1 represents the maximum in the deposition rate for energy at a given wavelength (see [*Chamberlain and Hunten*, 1987]).

Since the absorption cross sections for most UV absorbers are only weakly temperature dependent, we can simplify our expression for the optical depth in an atmosphere by defining η_i as the slant column density of a constituent, *i*,

$$\eta(\chi, r_0) = \int_{r_0}^{\infty} n(r)ds \qquad (4)$$

where *ds* is the element of the slant path and $n(r)$ is the altitude dependent number density along that path. The slant column density is just the integrated number density along some angle χ from the local vertical from a point r_0 to the top of the atmosphere. The expression is transformed to a one dimensional problem by introducing the Van Rhijn function $V(\chi,r)$:

$$V(\chi, r) = \left[1 - \left(\frac{r_0}{r}\right)^2 \sin^2 \chi\right]^{-1/2} \qquad (5)$$

which is a simple geometric factor that accounts for the curvature of the atmosphere above the spherical planet (the atmosphere is assumed to be horizontally stratified):

$$\eta(\chi, r) = \int_{r_0}^{\infty} n(r)V(\chi, r)dr \qquad (6)$$

Atoms and molecules can absorb and reemit radiation. When the probability that this will occur is small (or equivalently, the line center optical depth is less than 1, see [*Paxton and Anderson* 1992] for further discussion), the emergent intensity has a particularly simple form. Let us consider then the case of an optically thin feature. Here, we only need to calculate the number of photons emitted per unit volume per unit time and integrate along the line-of-sight to calculate an observed intensity. To do this it is customary to introduce a quantity known as the *g*-factor, which is the probability that a solar photon will be scattered by an atom [in cgs units, c.f. *Chamberlain* 1961]:

$$g = \pi F \lambda^2 \frac{\pi e^2}{mc^2} f \qquad (7)$$

where

πF is the solar flux at wavelength λ,

f is the oscillator strength or effective number of electrons involved in the photon scattering,

e is the charge on an electron,

m is the mass of an electron,

c is the speed of light.

The quantity gn (photons emitted per unit volume per unit time) is referred to as the volume emission rate. The volume emission rate is not an observable quantity: only its integral along the line-of-sight is observable. The integrated volume emission rate is then

$$4\pi I(\chi, r_0) = \int_{r_0}^{\infty} g(r)n(r)ds = \int_{r_0}^{\infty} g(r)n(r)V(\chi, r)dr \qquad (8)$$

As a consequence of this expression, χ is often referred to as the "look zenith angle" in analogy with the solar zenith angle. The quantity $4\pi I$ is the observed intensity and is commonly expressed in units of Rayleighs where one Rayleigh is defined as an omnidirectional (note the 4π in the description of the emergent intensity) column emission rate of 10^6 photons cm^{-2} s^{-1}.

If we chose a limb viewing geometry (χ=90°) in an isothermal stratified atmosphere the equation takes a particularly simple form [*Hord et al.*, 1970; *Chamberlain and Hunten*, 1987] and the observed intensity or limb intensity becomes:

$$4\pi I(\chi = 90°, r_0) = g\left(\frac{2\pi r_0}{H}\right)^{\frac{1}{2}} n(r_0)H. \qquad (9)$$

For optically thick emission features the radiative transport equation must be solved. A detailed discussion of this is beyond the scope of this paper, but the most important aspects of the problem can be summarized. Under optically thick conditions, the total volume emission rate at any point in the medium has two components: a local or initial excitation rate, and the multiply-scattered component which arises from photons scattered into and out of the local volume element. The details of this problem are to be found in a number of references: *Strickland and Donahue* [1970], *Strickland and Rees* [1974], *Anderson and Hord* [1977], *Goody and Yung* [1989], or *Thomas and Stamnes* [1999].

The scattering coefficient is defined as the probability that a photon of a certain wavelength incident on a volume of atoms from a given direction will be scattered into another specific direction at a new slightly different wavelength per unit volume. For resonant scattering, a slight frequency shift arises from the velocity of the absorbing atom. The redistribution function [*Hummer*, 1962, 1969; *Mihalis*, 1978; *Meier*, 1991] describes the change in frequency during scattering and can be quite complex. In general the calculation of the scattering coefficient is complex since it must account for the variation of the input solar irradiance with wavelength, the

velocity distribution of the scatterers (which, even if it is Maxwellian, may vary due to the altitude variation of the temperature profile), and the absorption coefficient. The integral equation for a plane-parallel medium is:

$$S(\tau) = S_0(\tau) + \int H(|\tau - \tau'|, |t - t'|) S(\tau') d\tau' \quad (10)$$

where S is often referred to as the source function and is the total number of photons scattered per second per unit optical depth, S_0 is the radiation source strength, and H is the Holstein function [*Holstein*, 1947; 1951]. This equation expresses the physics of the problem. The absorption is characterized by the absorption optical depth t and the scattering by the scattering optical depth τ. The τ=1 point is usually the effective lower bound on the scattering medium. The Holstein H function gives the probability that a photon arising at a point τ' in the scattering medium (which corresponds to a point t' in the pure absorbing medium), makes it to optical depth τ, and will then be scattered. A conceptual diagram is shown in Figure 3 for the case of an external source (the Sun). The attenuation of solar photons due to absorption and scattering between a volume element in the field-of-view of the instrument and the Sun is indicated by T_{sun}. The attenuation of the contribution to the total source function from a scattering volume element located at τ' in the scattering medium is indicated as $H(|\tau-\tau'|,|t-t'|)$. These processes produce photons in a volume element labeled as the scattering element in the figure. Some of these photons are attenuated when scattered into the field-of-view of the instrument by T_{los}.

The observed quantity is the intensity and is given by the integral of the total volume emission rate along the line of sight. The contribution from each element along the line of sight is weighted by the probability that a photon arising at a point τ' in the medium will actually make it to the observer located at τ (indicated by T_{los} in Figure 3),

$$4\pi I(\tau, \chi) = \int S(\tau') T(|\tau - \tau'|) d\tau' \quad (11)$$

5. KEY TECHNOLOGY DEVELOPMENTS IN UV REMOTE SENSING

Early spectrometers were flown on sounding rockets, first to measure the Earth's upper atmosphere, and later with telescopes to observe the other planets. An important early design was the Ebert-Fastie spectrometer, which employed reflections from symmetric locations on a spherical concave mirror to collimate an incident beam of light for dispersion from a plane grating [*Fastie*, 1952; 1967]. This design is very stable to changes in alignment of the mirror and grating, a practical feature considering the vibrations of launch, and it is also compact. It permits the grating to be scanned over an angle which will pass different wavelengths across the exit aperture, thereby building up a spectrum over time using a single point detector, usually a photomultiplier tube. These simple detectors were replaced with one- then two-dimensional devices. Additionally, mirror coatings have improved as a result of development over the years. Aluminum overcoated with MgF_2 and LiF coatings today provide 80% or higher reflectivity at wavelengths $\lambda > 120.0$ nm (Figure 4), and broad bandpass filters can be made from multi-layer coatings [*Keski-Kuha et al.* 1999]. At shorter wavelengths, mirror coatings of SiC and BC_4 provide more typically 1/2 of this reflectivity. The development of higher reflectivity coatings for EUV mirrors remains an important development area for future work.

The development of diffraction gratings with higher efficiencies and lower scatter is another area where significant improvements in the technology have led to higher quality measurements. Ruled gratings, in particular echelle gratings, are now manufactured with high quality. While ruled gratings are always subject to some systematic effects due to the use of a mechanical system to create the optical surface (scattered light and grating "ghosts"), they have the potential for high efficiencies because the grooves can be shaped to efficiently scatter light of a particular wavelength in a particular direction

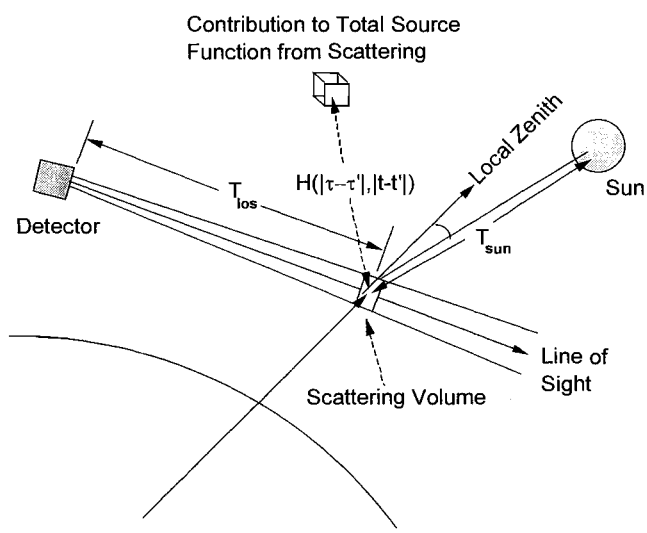

Figure 3. Diagram indicating the angles relevant to the equations in the text for scattering and absorption of radiation in a column of an atmosphere.

(the grating "blaze"). Since the late 1970s, holographic gratings have also been developed, in which the grooves are formed by chemically etching a photoresist surface prepared by an interference pattern between light sources. This technique can produce grating grooves of high uniformity, leading to much lower levels of scattered light. One challenge is to efficiently blaze holographic gratings, since the individual grooves tend to be more rounded than with ruled gratings, leading to a broader and less efficient blaze function. A number of companies now offer ion-etched blazed holographic gratings. The development of custom gratings, such as with a variable line spacing or different radii of curvature in different directions, has been made possible by holographic techniques, permitting new custom optical designs that can yield higher angular and spectral resolutions over larger ranges of angle and wavelength. Reviews of methods of grating manufacture are given by *Wilkinson* [1999] and *Duban et al.* [1999], and evaluation methods are described by *Boucarut et al.* [1999].

New instrument techniques continue to be developed. UV interferometry is an exciting, developing field. Classical approaches to interferometry which require a beam splitter or an etalon are not possible in the EUV due to the limited transmission of the materials. New approaches to high resolution spectroscopy, including all-reflecting spatial heterodyne spectroscopy, and advances in machining of optical surfaces allow the design of practical, compact high-resolution UV sensors [*Cleary et al.*, 1992; *Harlander and Roessler* 1990, *Chakrabarti et al.*, 1994; *Atkinson et al.*, 1994].

6. EXAMPLES OF AIRGLOW INSTRUMENTS

This section will list a few examples in the history of remote UV observations of planetary atmospheres. The reader is referred to the other chapters in this monograph for more details. Early observations were performed using sounding rockets beginning in the late 1940's, initially of the Earth's upper atmosphere. These early flights established the existence of solar H Ly α and other ionizing UV radiations, and identified various constituents in the UV spectrum of the Earth's airglow from zenith and limb pointing measurements of the Earth's airglow and auroral emission intensities. The emission altitude profiles are important to determine the excitation rates and thermal structure of the upper atmosphere. Later experiments employed small telescopes to observe the other planets while above the absorbing regions of the atmosphere [*Moos et al.* 1969].

Planetary missions used a variety of approaches (Figure 5). The early missions to Mars and Venus are described by *Paxton and Anderson* [1992]. The structure and composition of the Mars upper atmosphere has been examined from 110 to 400 nm by the Mariner 6, 7, and 9 probes using nearly identical instruments. Mariner 6 and 7 arrived at Mars in July and August of 1969 [*Barth et al.*, 1971]. The Mariner 6 and 7 ultraviolet spectrometers consisted of an Ebert-Fastie scanning monochromator with two photomultiplier tubes mounted at dual exit slits. The spectral range 190 to 430 nm was measured at 2 nm resolution and the 1100 to 2100 range was covered at 1 nm resolution. Unfortunately the Mariner 6 and 7 spacecraft were only able to fly by the planet and obtain limb spectra at tangent height intervals of about 21 km corresponding to the 3 seconds it took to scan the entire spectrum. The instruments were identical and used a 2160 line per mm plane replicated grating blazed at 300 nm. The most complete data set is that obtained from the Mariner 9 experiment which operated from November 1971 until October 1972 [*Barth et al.*, 1972]. This arrangement, developed and made practical by Bill Fastie [*Fastie* 1952 and *Fastie* 1967] and now known as an Ebert-Fastie spectrometer, features simple components (entrance and exit slits and a plane grating) in a mechanically stable configuration. The grating can be moved in such a way that a specific wavelength is selected for output on a PMT or scanned over the entire range of wavelengths. By placing two slits at the exit plane of this simple instrument two complementary wavelength ranges could be scanned. In the Mariner 9 instrument [*Hord et al.*, 1970] a mirror was placed behind the one exit slit to redirect the 170 to 340 nm light to a PMT with a cesium telluride photocathode and a sapphire window. This was known as the F channel be-

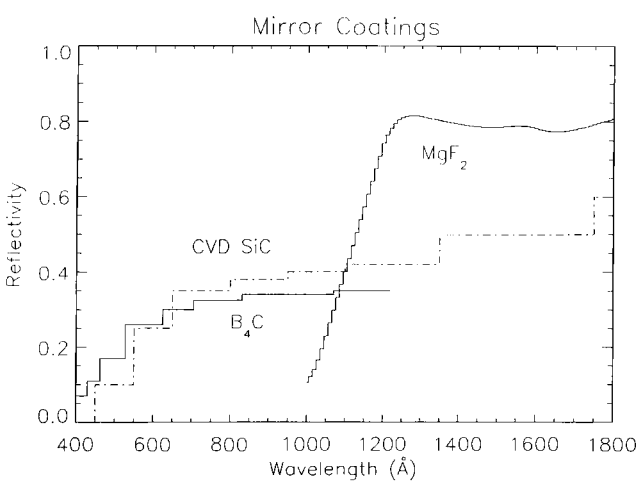

Figure 4. Measured reflective efficiencies of various mirror coatings.

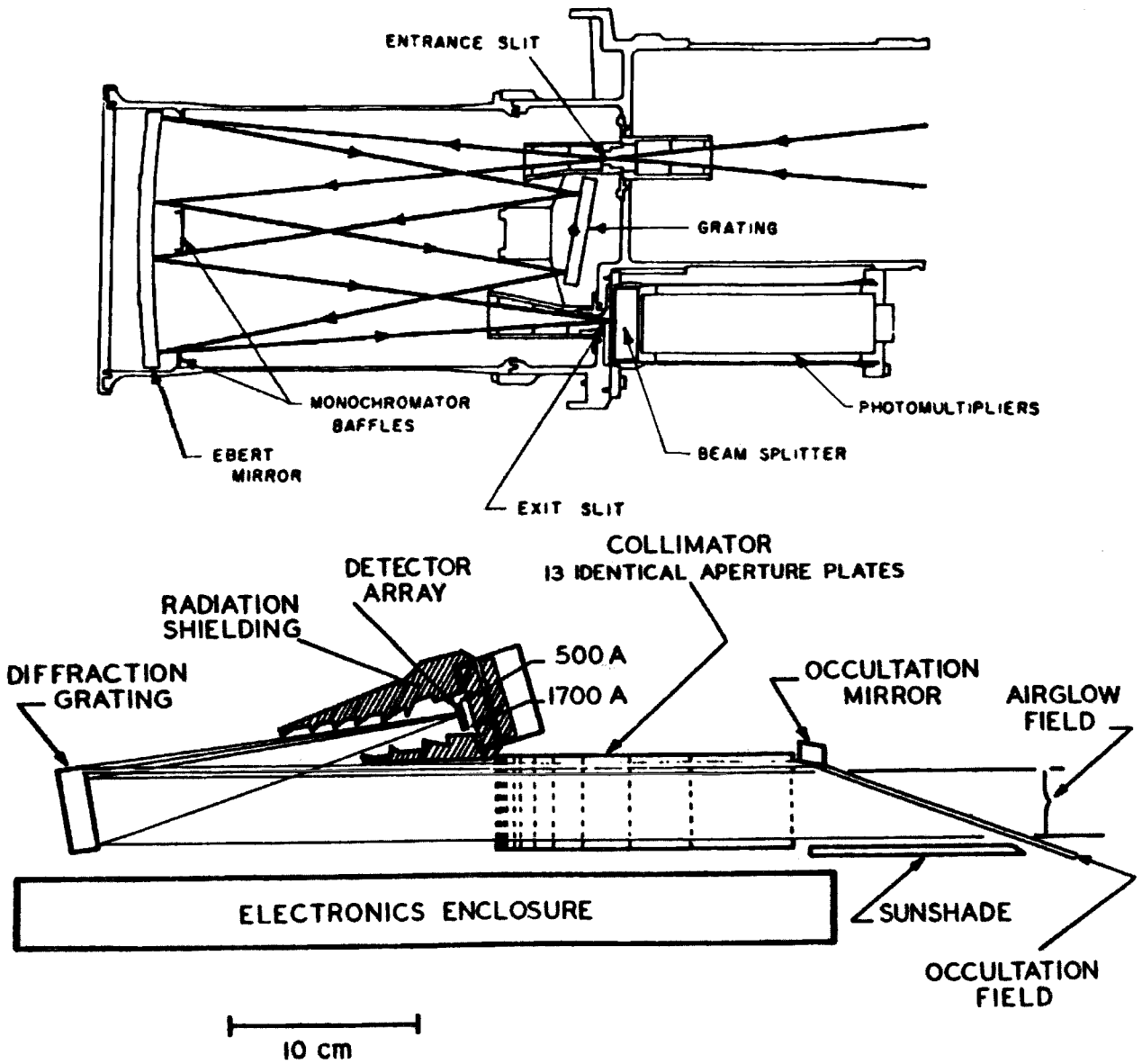

Figure 5. Opto-mechanical layouts of two early planetary airglow instruments, the OGO-IV UVS and the Voyager UVS (after *Barth and Mackey* 1969 and *Broadfoot et al.* 1977).

cause of the photomultiplier identification (EMR 541F-08) included an "F" to denote the use of a cesium telluride as the photocathode. The G channel used a PMT with a cesium iodide photocathode and a magnesium fluoride window to observe light from 110 to 170 nm. The Mariner 9 instrument took 3 seconds to scan its entire wavelength range and provided spectra with a 2 nm resolution.

The Pioneer Venus mission [*Colin* 1980] featured an orbiter and an entry probe system. The orbiter included in situ as well as remote sensing instruments. The Pioneer Venus Orbiter Ultraviolet Spectrometer (PVOUVS), described by *Stewart* [1980], was mounted on a tilted baseplate so that its line of sight was 60° from the spin axis. The Orbiter was placed in a highly eccentric orbit (e=0.843) that ranged over altitudes from as low as 150 km (during the nominal mission) to 66,000 km. This meant that the line-of-sight of the instrument swept out a cone that imaged the planet during two periods and this simple device could build up a "picture" of

the planet because the orbital motion carried the line of sight from north to south during a periapsis pass and from south to north during apoapsis. During the first view period nearly an entire hemisphere can be mapped. The second view period offered the opportunity to make observations at a local solar time 12 hours different than that of the first view period and at a higher spatial resolution. During the second view period the spatial coverage is was more limited. All local solar times were sampled over the course of one Venus year. The PVOUVS instrument was a significant departure from the Mariner instruments produced by LASP: its mass was a factor of five less (6 lbs vs. 35 lbs), very restricted data rate, and location on a spinning platform. The spectrograph was a 1/8 meter Ebert-Fastie mount fed by an *f*/5 Cassgrain telescope.

The Voyager Ultraviolet Spectrometer [*Broadfoot et al.* 1977] employed a single-reflection design to optimize the sensitivity at EUV wavelengths below 110 nm. It consisted of a concave ruled diffraction grating which imaged dispersed emissions onto a diode-array microchannel plate detector, with a mechanical collimator to limit the incoming flux of off-axis light. This design yielded a broad bandpass of 50-170 nm, but with limited spectral resolution of 3 nm to diffuse emissions. The instrument provided the first fly-by spectra of the atmospheres of all 4 giant planets and their satellites, with separate measurements from identical instruments on the Voyager 1 and 2 spacecraft, and also performed stellar and solar occultations. These instruments worked reliably for more than a decade during the Voyager tour of the outer solar system, providing a wealth of data, although some degradation of the detector response was experienced in the harsh radiation environment near Jupiter.

The Galileo Ultraviolet Spectrometer (UVS) is a direct descendent of the Mariner and Pioneer Venus instruments. The Galileo UVS is an Ebert-Fastie spectrograph that covers from 115 to 432 nm with 0.7 nm spectral resolution shortward of 190 nm and 1.3 nm resolution longward of 190 nm [*Hord et al.* 1992]. The UVS uses two photomultipliers to cover the FUV and NUV ranges. The Galileo UVS is based on the Voyager design: it is an objective grating spectrometer and covers wavelengths from 54 to 128 nm [*Hord et al.* 1992]. This instrument employed a telescope with three spectral channels, using scanning gratings and 3 photomultiplier detectors, and it had a mass of 5.2 kg. It has been successful in obtaining UV spectra of the thin atmospheres of the Galilean satellites.

An innovative design for high spectral resolution studies of planetary emission line profiles has been flown on a sounding rocket [*Harris et al.* 1993]. This UV spectrograph fed by a Cassegrain telescope is in the Ebert-Fastie configuration, but with an echelle grating. An objective prism replaces the cross-dispersion grating, permitting images of emission line Doppler profiles along a long, narrow aperture field of view. Taking advantage of the low continuum flux near bright planetary lines, like H Ly alpha, and with the small number of reflecting surfaces and relatively large field of view on the sky, this instrument achieves a higher sensitivity to emissions than even the HST along with spatial imaging along the aperture.

SPICAM Light (Spectroscopy for the Investigation of the Characteristics of the Atmosphere of Mars) [*Bertaux et al.* 2000] is a compact UV-IR instrument selected for flight on Mars Express to recover most of the science that was lost with the loss of Mars 96. A UV spectrometer is optimized for nadir viewing, limb viewing and vertical profiling by stellar occultation and weighs 3.8 kg [*Korablev et al.* 2001]. This channel covers 118 to 320 nm at about 0.5 nm resolution. An IR spectrometer observes the atmosphere during solar occultations and covers 1 to 1.7 microns [*Muller et al.* 2001].

ALICE is an instrument designed to obtain spatially resolved FUV spectra of comets and planetary atmospheres using a lightweight (2.7 kg) and low power consumption approach (4 W) [*Stern et al.* 1998]. ALICE will obtain spectra from 70 –205 nm with a resolution of about 1 nm for an extended source. ALICE has a 0.1° x 6.0° field-of-view and uses an off-axis parabaloid telescope feeding a 0.15-m normal incidence Rowland circle spectrograph with a concave holographic reflection grating. The imaging microchannel plate detector utilizes dual solar-blind opaque photocathodes (KBr and CsI) and a 2-D wedge-and-strip readout array. ALICE is a direct off-shoot of the Highly Integrated Pluto Payload System (HIPPS) [*Stern et al.* 1995].

The Cassini mission includes an Ultraviolet Imaging Spectrograph (UVIS) [*McClintock et al.*, 1992]. UVIS is part of the remote sensing payload of the Cassini Orbiter spacecraft. Its science objectives include investigation of the chemistry, clouds, and energy balance of the Titan and Saturn atmospheres; neutrals in the magnetosphere; D/H ratio for Titan and Saturn; and structure and evolution of Saturn's rings. The two short wavelength channels of UVIS provide images and spectra. A third optical path with a solar blind CsI photocathode is used for high signal to noise ratio stellar occultations by rings and atmospheres. A separate hydrogen-deuterium absorption cell (HDAC) measures the relative abundance D/H from their Lyman-alpha emission. The extreme ultraviolet channel (EUV) will be used for imaging spectroscopy

and spectroscopic measurements of the structure and composition of the atmospheres of Titan and Saturn (e.g. *Esposito et al.,* 1998). The EUV consists of a telescope with a three-position slit changer, a baffle system, and a spectrograph with a CODACON microchannel plate detector and associated electronics. The telescope consists of an off-axis parabolic section with a focal length of 100 mm, a 22 mm by 30 mm aperture, and a baffle with a field of view of 3.67 degrees by 0.34 degrees.

Earth-orbiting telescopes have also played key roles in the study of planetary atmospheres. The Copernicus mission had a limited scope for planetary work, being an echelle system at high dispersion but limited spectral coverage and sensitivity. The International Ultraviolet Explorer (IUE) was very successful in identifying many spectral emissions from planetary atmospheres, and in long term studies of the brighter emissions [*Moos and Encrenaz* 1987; *Nelson and Lane* 1987; *Festou and Feldman* 1987]. Finally, the Hubble Space Telescope (HST) has been extensively used for these studies, with its high sensitivity, very high angular resolution, and stable response over time. In the first years after launch, most aeronomical studies were performed with the High Resolution Spectrograph (GHRS) and the Faint Object Spectrograph (FOS). Somewhat later, alkali metal filters were developed for UV images of planetary atmospheres with the visible-sensitive CCD's on the Wide Field Planetary Camera 2 [*Trauger et al.* 1994; *Clarke et al.* 1999]. More recently, the highest sensitivity to planetary UV emissions has been achieved by the Space Telescope Imaging Spectrograph (STIS) [*Kimble et al.* 1998]. This instrument has many spectroscopic and imaging modes, and uses two UV-sensitive MAMA (multiple anode micro-channel array) detectors with 1024x1024 arrays with CsI and CsTe photocathodes for FUV and NUV studies, respectively. Extensive lists of papers have been published based on HST observations. While this list is beyond the scope of this paper, we refer the reader to the upcoming volume "Science and the Hubble Space Telescope", being prepared for publication by the Space Telescope Science Institute, which reviews the first 10 years of HST science.

7. AREAS FOR FUTURE IMPROVEMENT IN UV INSTRUMENTS

There are several areas where the technology for remote UV observations can be improved. Improved mirror reflectivities at normal incidence for wavelengths $\lambda <$ 110 nm is an area where there is room for much improvement. There is also room for improvement in detector quantum efficiencies at all wavelengths. However, this is a function primarily of the photoelectric efficiency of various bi-alkali materials. Current detectors employ a repelling mesh at a small potential sufficient to direct escaping photoelectrons back down into the microchannels, so that they collect most of the photoelectrons which are released from the photocathode. While present detectors can reliably achieve array formats of 1024 x 1024 pixels, more and specifically smaller pixels would assist in the optical designs and field of view of new instruments. While it is a great advantage to have a photon-counting detector, one limit is set to the overall counting rate by the speed of the electronics. Another disadvantage arises from the high multiplication of each photoelectron, requiring high voltage and a large draining of charge from the microchannel plates. The ability to have higher counting rates from faster electronics would permit brighter emissions to be viewed, and higher spatial resolution with a lower gain would allow more convenient optical designs plus a longer lifetime of the microchannel plates. Lower scatter in UV optics would improve the efficiency, spectral resolution, and angular resolution of UV measurements. Finally, the development of interferometric techniques with good efficiency in the UV could provide much higher spectral and angular resolution than now possible.

REFERENCES

Anderson, D.E., Jr., and C.W. Hord, Multidimensional radiative transfer: Application to planetary coronae, *Planet. Space Sci., 25*, 563, 1977.

Atkinson, J. Dudley and David D. Cleary, A technique for modeling interference patterns from two-beam interferometers, *Comp. Phys., 8*, 462, 1994.

Barth, C. A and E. F. Mackey, OGO-IV Ultraviolet Airglow Spectrometer, *IEEE Transactions GE-7, 2*, 114, 1969.

Barth, C.A., C.W. Hord, A.I. Stewart, and A.L. Lane, Mariner 9 ultraviolet spectrometer experiment: Initial results, *Science, 153*, 309, 1972.

Bertaux, J.-L., *et al.,* The study of the Martian atmosphere from top to bottom with SPICAM Light on Mars Express, *Planet. Space Sci.,* 1303, 2000.

Boucarut, R. et al., Ultraviolet-optical instrument development in the diffraction grating evaluation facility, in "Ultraviolet-Optical Space Astronomy Beyond HST", *Astr. Soc. of the Pacific Conference Series, 164*, 446, 1999.

Broadfoot, A.L. *et al.*, Ultraviolet spectrometer experiment for the Voyager mission, *Space Sci. Rev., 21*, 183-205, 1977.

Broadfoot, A.L., *et al.,* Overview of Voyager ultraviolet spectrometry results through Jupiter encounter, *J. Geophys. Res., 86*, 8259-8284, 1981.

Chakrabarti, S., D. M. Cotton, J. S. Vickers, and B. C. Bush, Self-compensating all reflection interferometer, *Applied Opt., 33*, 2596, 1994.

Chamberlain, J.W., Physics of the aurora and airglow, pp. 704, *Academic*, New York, 1961.

Chamberlain, J.W., and D.M. Hunten, Theory of planetary atmospheres, *Academic*, New York, 1987.

Clarke, J.T., W.R. Skinner, M.B. Vincent, T. Irgang, V. Suratkal, H. Grassl, and J.T. Trauger, "Laboratory studies of alkali metal filter deposition, ultraviolet transmission, and visible blocking", *Applied Optics, 38*, 1803, 1999.

Cleary, D. D., J. W. Nichols, and D. Scott Davis, Design of an all reflection Michelson interferometer, *Applied Opt., 31*, 433, 1992.

Colin, L., The Pioneer Venus program, *J. Geophys. Res., 85*, 7575, 1980.

Content, D., *et al.*, FUV-NIR Filter metrology in the GSFC optics branch, in "Ultraviolet-Optical Space Astronomy Beyond HST", *Astr. Soc. of the Pacific Conference Series, 164*, 453, 1999.

Cotton, DE.M., T. A. Cook, and S. Chakrabarti, A single-element imaging spectrograph, *Applied Optics,33*, 1958, 1994.

Duban, M., G.R. Lemaitre, R.F. Malina, A general method for recording high resolution holographic gratings by using a null powered multimode deformable mirror, in "Ultraviolet-Optical Space Astronomy Beyond HST", *Astr. Soc. of the Pacific Conference Series, 164*, 428, 1999.

Esposito, L.W.; Colwell, J.E.; McClintock, W.E., Cassini UVIS observations of Saturn's rings, *Planet. Space Sci., 46*, 1221, 1998.

Fastie, W.G., A plane grating monochromator, *J. Opt. Soc. Amer., 42*, 641, 1952.

Fastie, W.G., *Appl. Optics, 6*, 397, 1967.

Festou, M. C., S. K. Atreya, T. M. Donahue, D. E. Shemansky, B. R. Sandel, A. L. Broadfoot, Composition and thermal profiles of the Jovian upper atmosphere determined by the Voyager ultraviolet stellar occultation experiment, *J. Geophys. Res., 86*, 5715-5725, 1981.

Festou, M., and P.D. Feldman, Comets, in *Exploring the Universe with the IUE Satellite*, D. Reidel, p. 101, 1987.

Goody, R.M., and Y.L.Yung, *Atmospheric Radiation*, Oxford Univ. Press, New York, 1989.

Harlander, J., F. L. Roesler, and S. Chakrabarti, Spatial Heterodyne Spectroscopy: A Novel Interferometric Technique for the FUV, *Proc. SPIE, 1344*, 120-131, 1990.

Harris, W.M., J.T. Clarke, J.R. Caldwell, P.D. Feldman, B.C. Bush, D.M. Cotton, and S. Chakrabarti, High resolution ultraviolet spectrograph for sounding rocket measurements of planetary emission line profiles", *Optical Engineering, 32*, 3016, 1993.

Holstein, T., Imprisonment of resonance radiation in gases, *Phys. Rev., 72*, 1947.

Holstein, T., Imprisonment of resonance radiation in gases, II, *Phys. Rev., 83*, 1159, 1951.

Hord, C. W., C. A. Barth, and J. B. Pearce, Ultraviolet spectroscopy experiment for Mariner Mars 1971, *Icarus, 12*, 63, 1970.

Hord, C.W.; McClintock, W.E.; Stewart, A.I.F.; Barth, C.A.; Esposito, L.W.; Thomas, G.E.; Sandel, B.R.; Hunten, D.M.; Broadfoot, A.L.; Shemansky, D.E.; Ajello, J.M.; Lane, A.L.; West, R.A., Galileo ultraviolet spectrometer experiment, *Space Sci. Rev., 60*, 503, 1992.

Huffman, R. E., *Atmospheric Ultraviolet Remote Sensing*, Academic Press, Boston, 1992.

Hummer, D., *Mon. Not. Roy. Astr. Soc., 125*, 71, 1962.

Hummer, D., *Mon. Not. Roy. Astr. Soc., 425*, 95, 1969.

Jacobsen, P., Superconducting tunnel junction detectors for Optical and UV astronomy, in "Ultraviolet-Optical Space Astronomy Beyond HST", *Astr. Soc. of the Pacific Conference Series, 164*, 397, 1999.

Joseph, C.L., *Experimental Astronomy, 6*, 97, 1995.

Joseph, C.L. in "From X-rays to X band, a NASA workshop held at STScI", 2000.

Keski-Kiha, R.,A.M., J.I. Larruquert, J.S. Gum, C.M. Fleetwood, Optical coatings and materials for ultraviolet space applications, in "Ultraviolet-Optical Space Astronomy Beyond HST", *Astr. Soc. of the Pacific Conference Series, 164*, 406, 1999.

Kimble, R.A. *et al.*, The on-orbit performance of the Space Telescope Imaging Spectrograph, *Astrophys. J. Lett., 492*, 83-93, 1998.

Kimble, R.A., T.J. Norton, P.F. Morrissey, A photon-counting intensified CID detector for space astronomy, in "Ultraviolet-Optical Space Astronomy Beyond HST", *Astr. Soc. of the Pacific Conference Series, 164*, 392, 1999.

Korablev, O.I.; Bertaux, J.-L.; Dubois, J.-P., Occultation of stars in the UV: study of the atmosphere of Mars, *J. Geophys. Res., 106*, 7597, 2001.

McClintock, W. E., G. M. Lawrence, R. A. Kohnert, L. W. Esposito, Optical design of the Ultraviolet Imaging Spectrograph for the Cassini mission to Saturn, *Opt. En., 32*, 12, 3038-3046, 1992.

Meier, R.R. Ultraviolet spectroscopy and remote sensing of the upper atmosphere, *Space Sci. Rev., 58*, 1-186, 1991.

Mihalas, D., *Stellar atmospheres*, W.H. Freeman and Co., San Francisco, 1978.

Moos, H. W., W. G. Fastie, and M. Bottema, Rocket Measurement of Ultraviolet Spectra of Venus and Jupiter between 1200 Angstroms and 1800 Angstroms, *Ap. J., 155*, 887, 1969.

Moos, H.W., and T. Encrenaz, Planetary atmospheres and aurora, in *Exploring the Universe with the IUE Satellite*, D. Reidel, p. 45, 1987.

Muller, C.; Moreau, D.; Fonteyn, D.; Bertaux, J.L.; Korablev, O., SPICAM-light on Mars-Express as a monitor of surface UV radiation and atmospheric oxidants, *Planet. Space Sci., 49*, 165, 2001

Nelson, R.M., and A.L. Lane, Planetary Satellites, in *Exploring the Universe with the IUE Satellite*, D. Reidel, p. 67, 1987.

Paxton, L. J., and C.-I. Meng, Auroral imaging and space-based optical remote sensing, *APL Tech. Digest, 20*, #4, 556, 1999.

Paxton, L.J. and D.E. Anderson, Ultraviolet remote sensing of Venus and Mars, *Venus and Mars: Atmospheres, Iono-*

spheres, and Solar Wind Interactions, Geophysical Monograph 66, eds. J.G. Luhmann, M. Tatrallyay, and R.O. Pepin, pp. 113, 1992.

Samson, J. A. R., *Techniques of Vacuum Ultraviolet Spectroscopy*, Pied Publications, Lincoln, Nebraska, 1967.

Samson, J.A.R., and D.L. Ederer, *Vacuum Ultraviolet Spectroscopy 1*, Vol. 31 in *Experimental Methods in the Physical Sciences*, R. Celotta and T. Lucarorto, eds., Academic Press, New York, 1998.

Samson, J.A.R., and D.L. Ederer, *Vacuum Ultraviolet Spectroscopy 2*, Vol. 32 in *Experimental Methods in the Physical Sciences*, R. Celotta and T. Lucarorto, eds., Academic Press, New York, 1998.

Siegmund, O.H.W., Microchannel plate detector technologies for next generation UV instruments, in "Ultraviolet-Optical Space Astronomy Beyond HST", *Astr. Soc. of the Pacific Conference Series, 164*, 374, 1999.

Stern, S.A., Slater, D.C.; Gibson, W.; Scherrer, J.; A'Hearn, M.; Bertaux, J.L.; Feldman, P.D.; Festou, M.C., ALICE-an ultraviolet imaging spectrometer for the Rosetta orbiter, *COSPAR Adv. Space Res., 21*, 11, 1517, 1998.

Stern, S.A., D.C. Slater, W. Gibson, H.J. Reitsema, A. Delamere, D.E. Jennings, D.C. Reuter, J.T. Clarke, C.C. Porco, E.M. Shoemaker, and J.R. Spencer, The Highly Integrated Pluto Payload System (HIPPS): A spacecraft instrument for the Pluto mission, *Proc. SPIE EUV, X-ray, and Gamma-ray Instrumentation for Astronomy VI*, 2518, 1995.

Stewart, A. I. F., Design and operation of the Pioneer Venus Orbiter Ultraviolet Spectrometer, *IEEE Trans. Geosci. Remote Sens. GE18*, 65, 1980.

Strickland, D.J., and T.M. Donahue, Excitation and radiative transport of OI 1304 A resonance radiation - I. The dayglow, *Planet. Space Sci., 18*, 661, 1970.

Strickland, D.J., and M.H. Rees, The OI 1304 and 1356 emissions in aurorae, *Planet. Space Sci., 22*, 465, 1974.

Thomas, G.E., and K. Stamnes, Radiative Transfer in the Atmosphere and Ocean, Cambridge University Press, Cambridge, 1999.

Trauger, J.T., et al., The on-orbit performance of WFPC 2, *Astrophys. J. Lett., 435*, 1994.

Vickers, J.S., D. M. Cotton, T. A. Cook, and S. Chakrabarti, Gas ionization solar spectral monitor, *Opt. Eng., 32*, 3126, 1993.

Wilkinson, E., Maturing and developing technologies for the next generation of UV gratings, in "Ultraviolet-Optical Space Astronomy Beyond HST", *Astr. Soc. of the Pacific Conference Series, 164*, 420, 1999.

Yee, J.-H., D. F. Morrison, G. A. Murphy, M. F. Morgan III, D. C. Humm, R. Vervack, L. J. Paxton, STARS: The stellar absorption and refraction sensor, *SPIE Optical Spectroscopic Techniques & Instrumentation for Atmospheric and Space Research* IV, *4485*, in press, 2002.

J. Clarke, Center for Space Physics, Boston University, Boston, MA 02215. (email: jclarke@bu.edu)

Mass Spectrometry for Planetary Science

David T. Young

University of Michigan, Department of Atmospheric, Oceanic and Space Sciences, Ann Arbor, Michigan

Attaining a satisfactory understanding of the origin and evolution of the solar system and life within it are among the primary scientific goals of current and future planetary missions. One important clue to understanding these questions is the chemical and isotopic composition of atmospheric and surface volatile materials. Sample-return missions may one day become the method of choice for carrying out detailed laboratory studies of these materials. Until then, however, high-quality in situ measurements of volatiles will be essential to improving our current knowledge and to providing context and support for future missions. Small (~1 kg), high-performance ($M/\Delta M > 10^3$), space-qualified mass spectrometers are the only known method for quantitative analysis that is capable of delivering the isotopic, atomic, and molecular composition of trace amounts ($<10^{-13}$ moles/gram) of sample materials. Of particular interest is the identification of biomarker molecules to roughly that level on Mars. These are very difficult performance goals in their own right, but they are more so when increasingly constrained mission resources are taken into account. The current state-of-the-art in space-borne mass spectrometry is examined by defining a quality metric proportional to (performance/resources). The metric suggests that future requirements and constraints represent significant technical challenges. This paper briefly examines historical progress in planetary mass spectrometry before moving to the principles of particle optics that govern spectrometer design and implementation. Several alternative methods are examined, but only four are examined in detail: quadrupole, ion trap, magnetic, and time-of-flight spectrometry. This choice reflects both past successes and the promise of the methodology for future adaptations.

1. INTRODUCTION

Since the earliest in situ explorations of planetary (including Earth) environments, there has been broad interest in the composition of volatiles from planetary atmospheres, ionospheres, and surfaces. Recent observations of organic trace materials in samples of SNC meteorites from the Martian surface, the discovery of Europa's subsurface oceans, and the existence of pre-biotic molecules on Titan, have all spurred a renewed quest for solid analytical evidence of cosmochemical, pre-biotic or biomarker materials. The most difficult measurement objectives include accurate (errors ~1% or less) for isotopic abundances, and detection of as little as $\sim 10^{-13}$ moles/gram of large ($\sim 10^3$ Daltons) organic biomarker compounds [*Arvidson, R.*, 2001] as well as the identification of low relative abundance overlapping or isomeric compounds. Other important targets include Titan's hydrocarbon and nitrile environment [*Niemann et*

Atmospheres in the Solar System: Comparative Aeronomy
Geophysical Monograph 130

10.1029/130GM24

al., 1997] and salts and organic molecules at Europa [*Johnson et al.*, 1998]. The ideal mass spectrometer and associated gas sampling and separation components should be capable of effective mass resolution $M/\Delta M \geq 10{,}000$ and sensitivity to roughly one part per trillion (10^{-12}).

Up to now analytical measurement of planetary composition has generally been obtained using in situ mass spectrometry, sometimes coupled to gas handling and separation devices [*Biemann et al.*, 1974; and *Niemann et al.*, 1992). Optical UV and IR spectrometers are not considered in this paper. While optical methods have contributed to bulk composition measurements of surface and atmospheric constituents, their sensitivity and resolution per unit volume of sample are much smaller than that of mass spectrometers. Space-qualified mass spectrometers, compared to their laboratory counterparts, are distinguishable by rugged construction, high reliability, and high performance relative to weight and power. However, planetary missions now in planning are based on the premise that higher-performance instruments, roughly equivalent to good ground-based devices that are larger and more power hungry, will be available in the near future. Several flight spectrometers, such as the ROSINA instruments on the Rosetta mission [*Balsiger et al.*, 2001] and the GCMS and INMS instruments on Huygens [*Niemann et al.*, 1997], approach laboratory performance ideals in some areas, but they fall short of future mission ideals.

Before beginning a detailed consideration of future prospects for planetary mass spectrometry, the reader should be aware that there is much more to analytical composition measurements than just mass spectrometer optics and components. For example, the evolved gas analyzer, in which a sample is stepwise heated to drive out its volatile contents, is essential for extracting volatile samples from solid materials. In another method, secondary ion mass spectrometry (SIMS) [*Benninghoven et al.*, 1987], extraction is carried out with an inert ion beam that provides microscopic (~100 μm^2) mass spectrometric analysis of solid samples.

Once extracted, volatile samples can be concentrated by physical or chemical methods (adsorption, chemisorption) that select and concentrate desirable compounds while discriminating against less desirable ones. On Mars, for example, it is advantageous to remove the dominant molecule CO_2 from atmospheric samples and then concentrate the much less abundant water and noble gases before mass spectrometric analysis [cf. *Biemann*, 1974; and *Niemann et al.*, 1997]. The primary chemical separation method used in space-borne mass spectrometry is gas chromatography (GC). Individual compounds separated in the GC column can then be introduced one at a time into the mass spectrometer for detailed quantitative analysis. The GC process reduces the number of overlapping mass peaks that would otherwise make results from the MS ambiguous or difficult to interpret. (For a broad survey of sample extraction and separation methods see *Watson* [1997], *Settle* [1997], or *Grob* [1995]).

In most mass spectrometers gas samples are introduced into an ionization source, usually employing an electron beam operating from ~25 to ~90 eV, depending on measurement objectives. Optional ionization sources include lasers (REF), radioactive sources (REF), field emission, and so on, all of which are promising, none of which currently have flight history. Since the nature of the ionization method is irrelevant to this discussion the matter is dropped here. Ions formed in the source should mirror the makeup of the original sample. To accomplish this, any differential effects of selection or ionization must be accounted for either in design or in calibration. Ions leaving a source are formed into a well-defined beam in energy, angle, and spatial extent and then focused onto the mass spectrometer entrance. Inside the spectrometer, electric and/or magnetic fields are used to separate and focus ions in such a way that they form a sharply defined mass spectrum. If the spectrometer is properly calibrated, then identification of peak positions and amplitudes in the spectrum measures sample composition.

It is useful to have some historical perspective of previous spaceflight mass spectrometers. Table 1 gives a brief summary of space flight spectrometers categorized by their working principles: quadrupole (Q), single or double-focusing magnetic spectrometer (SF and DF), and time-of-flight mass spectrometer (TOF). An examination of Table 1 suggests that flight spectrometers could be usefully classified into three generations based on historical and future usage and technical performance. The divisions might consist of first generation instruments (typically $M/\Delta M \sim 100$ and $S \leq 10^{-6}$ (1 ppm), second generation instruments having $M/\Delta M \sim 10^3$ and $S \sim 10^{-9}$ (one part per billion, 1 ppb), and, for the future, third generation with $M/\Delta M \sim 10^4$ and $S \sim 10^{-12}$ (one part per trillion, 1 ppt). The resources used by first and second generation spectrometers, including gas separation systems if part of the spectrometer, range from a few kg up to 25 kg (Table 1). According to this classification scheme, third generation instruments are the hope for the future where detailed compositional analysis is required.

A brief summary of the basic principles of ion beam transport optics is given in Section 2. In Section 3 the principles, techniques, and limitations of mass spectrometry are discussed. Section 4 summarizes prospects for future high-performance mass spectrometry.

Table 1. Summary of Planetary Mass Spectrometers

Spectrometer Category	Mission	Date	MS Type	Spe-cies	DR	Sensitiv-ity (A/Torr)	Mass Range (Daltons)	M/Δ M	Mass (kg)	Reference
Quadropole	Atmos. Exp.-C, D, E		Q	N	10^6	10^{-5}	1-45	45	~3	*Pelz et al.*, 1973
	Pioneer Venus Orb.	1978	GC/Q	N	10^7	10^{-5}	0-46	50	3.6	*Niemann et al.*, 1980
	Dynamics Exp.-2	1981	Q	N	10^7	$4x10^{-6}$	2-50	50	~3	*Carignan et al.*, 1981
	Galileo Probe*	1989	GC/Q	N	10^8	10^{-6}	2-150	150	13	*Niemann et al.*, 1997
	Huygens Probe*	1997	GC/Q	N	10^8	$2x10^{-5}$	2-141	150	17	*Niemann et al.*, 2002
	Cassini Orbiter	1997	Q	I, N	10^8	$2x10^{-5}$	1-300	300	11	*Waite et al.*, 2002
Magnetic Sector	Atmos. Exp.-C, D, E		DF	N	10^5	10^{-5}	1-48	50	7	*Nier et al.*, 1973
	Atmos. Exp.-C, D, E		SF	I	10^6	10^{-6}	1-90	60	7.5	*Hoffman et al.*, 1973
	Viking 1, 2	1975	DF	N	10^5	$2x10^{-5}$	1-49	50	5	*Nier et al.*, 1972
	Viking 1, 2	1975	GC/Q	N	10^7	$3x10^{-6}$	12-215	~150	25	*Rushneck et al.*, 1978
	Pioneer Venus Prbs.	1978	SF	N	10^9	$5x10^{-5}$	1-208	440	11	*Hoffman et al.*, 1980
	Giotto/HERS/HIS	1985	SF	I	10^6		1-57	25	9	*Balsiger et al.*, 1987
	Giotto/NMS	1985	SF	I, N	10^{12}	0.3	1-36	240	13	*Krankowski et al.*, 1986
	Rosetta*	2003	DF	I, N	10^{10}	10^{-5}	12-100	3000	~15	*Balsiger et al.*, 2001
TOF	Rosetta*	2003	TOF	I, N	10^8	10^{-4}	1-1000	4500	~15	*Balsiger et al.*, 2001

Notes: nearly all spectrometers in Table 1 are first generation; second generation spectrometers are marked by an asterisk. DR = dynamic range; MS = mass spectrometer; Q = quadrupole MS; GC = gas chromatograph MS; DF = double focusing MS; SF = single focusing MS; TOF = time-of-flight MS; I = ion MS; N = neutral gas MS; A/Torr = amps/Torr.

2. ION OPTICS

Mass spectrometers are ion optical devices that transport, disperse, and focus ions emitted by a source of ionization. This discussion of spectrometer properties follows those of *Benninghoven et al.* [1987] and *Wollnik* [1987]. Optical descriptions are based on the properties of Gaussian optics which assume that ion trajectories travel near the principal optical axis and that axial velocities are much larger than transverse velocities. This assumption allows ion equations of motion to be written in closed form or as power series expansions from which analytical expressions can be derived for optical properties such as focal length, dispersion, and image size. (It is essential to simulate ion optics using computer ray-tracing programs before any hardware is built, but ray-tracing provides little conceptual insight in the early design phase and is not discussed here.) We further assume that particle velocities are non-relativistic, that ion beams are well below space charge limits (which may not be true for ion sources), and there are no collisions internal to the beam (collisions are discussed later). Such a beam obeys Liouville's theorem and ion phase space density is conserved. This formulation can be used to describe not only beam dispersion and resolution, but also a spectrometer's capability for current transport.

Mass spectrometer optics begin with an ion source that creates and emits ion current. Spectrometer optics must then collect and transport this current to a detector. From an optical standpoint ion source performance is defined by emittance $\varepsilon_s=\Delta A_s\ \Delta\Omega_s$ which is a geometric quantity in units of cm^2 sr. Here ΔA_s is the area of the emitted beam, $\Delta\Omega_s = \Delta\alpha_s^2$ is its angular divergence, and $\Delta\alpha_s$ is the angular half-width of a circular beam. The two-dimensional beam phase space density β_s (also called beam brightness) is a conserved quantity given by

$$\beta_s=qM(N/dx\ dy\ dp_x\ dp_y\ dt)=I_s/(\Delta A\ \Delta\Omega\ \Delta E)_s=\text{constant}. \quad (1)$$

The factor $N/dx\ dy\ dp_x\ dp_y\ dt$ is phase space density in the usual units, Mq is ion mass and charge, and the units of β_s are amps cm^{-2} sr^{-1} eV^{-1}. The second expression in (1) gives phase space density in laboratory units where ΔE_s is the ion energy spread leaving the source and I_s is the source beam current.

The ability of an ion optical system to transport a beam is given by its spatial acceptance, $(\Delta A\ \Delta\Omega)_o$ where ΔA_o is spectrometer entrance area and $\Delta\Omega_o$ the angular acceptance, multiplied by ion beam energy, qV_o. The theoretical maximum transport current in amps, I_M, is obtained by matching beam brightness to spectrometer acceptance:

$$I_M = \beta_s\ (\Delta A\ \Delta\Omega)_o\ (qV_o) = I_s\ (qV_o/\Delta E_s). \quad (2)$$

Equation 2 is obtained by requiring that $(\Delta A\ \Delta\Omega)_s=(\Delta A\ \Delta\Omega)_o$. This expresses the fact that in a perfectly matched ion optical system, transport depends only on the ratio of beam energy to the spread in ion energies. If optics are perfectly matched and corrected for image aberrations, then all ions of a chosen mass are deposited on the detector without spatial (or temporal) blurring or mixing of adjacent species—provided resolution is sufficient to do so. In this way beam transport is inextricably linked to spectrometer resolution.

Assuming perfect ion transport and detection efficiency, then the sensitivity S of a spectrometer is determined primarily by the source current emitted per unit of sample material (usually in traditional units of Amps/Torr)

$$S = I_s/N_o = I_e\ \sigma_{ie}\ x_s\ \eta_s, \quad (3)$$

where N_o is the sample density in the source, I_e is the ionizing electron current, σ_{en} is the appropriate electron-neutral cross-section, x_s is the length of the ionization region from which the beam is extracted with an efficiency η_s. Typical performance ranges from $\sim10^{-6}$ to 10^{-4} A/Torr. Since ion-neutral collisions would alter the apparent composition of the original sample, the maximum pressure at which a source can operate is limited by the ion-neutral collision mean free path, $\lambda_{in} = 1/(N_o\sigma_{in})$. Most ion sources operate around $\sim10^{-5}$ Torr (Table 1) where λ_{in} is roughly 10^3 to 10^4 times longer than source dimensions. Lower source pressures are also desirable because they reduce the amount of sample gas, and hence pumping speed, required to maintain source pressure.

3. MASS SPECTROMETRY

Mass resolution ($M/\Delta M$) is defined as the ability of a spectrometer to separate two adjacent peaks separated by ΔM when measured at 1% of the smaller of the two peak heights. A second key performance parameter is sensitivity, S, defined as the lowest abundance of a species that a spectrometer can detect relative to the size of the sample. For example, if a minor species can be identified that amounts to only one atom out of one million in the total sample then the sensitivity would be one part per million (1 ppm). Sensitivity says nothing about accuracy or precision of the measurement, which depend on calibration, total sample measurement time, and so on.

Static magnetic fields and static or dynamic electric fields can be combined to deflect and disperse ions spatially

or temporally. Dynamic magnetic fields have laboratory applications but are not practical for flight instruments). Mass spectrometers work on the principle that ions deflect and gain or lose energy/charge (E/q) in electric fields and deflect in magnetic fields by an amount proportional to their momentum per charge. Mass dispersion measures the unit deflection of an ion beam. It is produced by several methods, including path or time dispersion in radio-frequency electric fields, momentum dispersion in sector magnetic fields, or time dispersion in electric or magnetic fields. In addition to dispersion, optimum resolution and transport are obtained only if spectrometer fields form a sharp image of the "object," usually the spectrometer entrance slit or instant of ion entrance, on the detector. Then, if the energy/charge of ions entering the spectrometer is well defined, the position or time of arrival of mass-separated components at the detector will be proportional to ion mass/charge (M/q). The abundance of an ion species separated from a mixed beam is then proportional to detector current measured at the position or time when the selected ions arrive. In order to obtain measurements with minimum errors all biases introduced through sample selection, separation, ionization, transport and detection, must be eliminated or reduced. A typical goal in planetary science for measurement accuracy of minor ion species is ~1%. (Although there are no monographs covering space-borne mass spectrometry, the reader wanting more than a thumbnail sketch of mass spectrometry should consult *Blauth* [1966], *Dawson* [1976], *Duckworth et al.* [1986], *Wollnik* [1987], *Benninghoven et al.* [1987], *Cotter* [1994], or *Watson* [1997].)

3.1. Quadrupole Mass Spectrometry

Quadrupole mass spectrometers separate ions of different M/q by selecting only those ions whose trajectories are stable in quasi-static electric fields of a few MHz (i.e., Laplace's equation, $\nabla^2\phi = 0$, holds). For this reason they are classified as path stability mass spectrometers, although they are more akin to a mass filter rather than spectrometer. The quadrupole spectrometer consists of four symmetric parallel rods usually about 5-15 cm long (Figure 1). Voltages of the form $\pm(U_{DC} + V_{AC} \cos\omega t)$ are applied to adjacent sets of rods, creating a potential distribution given by $\varphi(x, y, t) = (U + V\cos\omega t)(x^2 - y^2)/r_o^2$. Ions leaving a source may be pre-selected in energy to ~0.01 $\Delta E/E$ and are then accelerated by a few tens of eV before being focused on the spectrometer entrance aperture. The quadrupole field subjects ions to a periodic force in the X-Y plane proportional to distance from the Z axis. This motion is described by

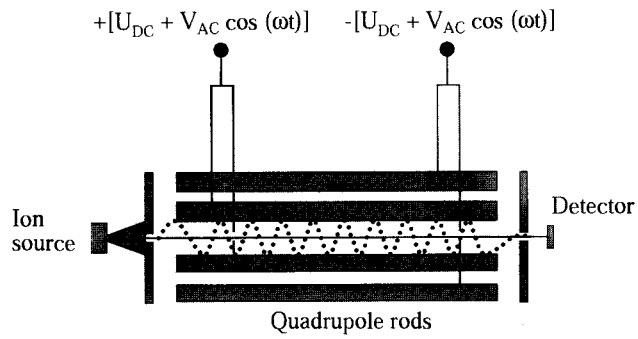

Figure 1. Schematic diagram of a quadrupole mass spectrometer viewed from the side. The dotted line through the quadrupole rods represents a single resonant ion trajectory transmitted through the exit aperture. The radius r_1 is the entrance aperture, r_o is the radius of a circle inscribed tangent to the field rods, x and y are coordinates perpendicular to the particle trajectory, and U_{AC} and V_{DC} are the voltage amplitudes.

Mathieu-type differential equations with ωt as the independent variable and $f = 2\pi\omega$ as the quadrupole field frequency [*Dawson*, 1976; and *Benninghoven et al.*, 1987]. Solutions to the Mathieu equations determine the regions of trajectory phase space that have stable trajectories. Ions that are resonant with the field oscillate close to the Z axis and are transmitted through an exit aperture located on the Z axis. Non-resonant ions undergo unstable oscillations that grow exponentially and are eventually ejected from the beam. Mass resolution is then dependent on the separation of adjacent regions of path stability corresponding to masses M and M + ΔM. Quadrupole optics, although mechanically precise, are relatively simple, lightweight, and rugged and require power and mass resources of a few kilograms and watts (see the Pioneer Venus Orbiter entry in Table 1).

Mass selection in the quadrupole is given by the equation,

$$M/q = 0.139V_{AC}/f^2r_o^2, \quad (4a)$$

where f is in MHz and r_o is the radius of rod separation in cm (Figure 1). The mass selection equation is useful in part because it expresses limitations on mass range for a given choice of spectrometer parameters. Mass spectra are obtained by scanning the amplitudes of U_{dc} and V_{dc} in such a way that 2U/V is constant chosen to maximize resolution for a given transmission. The highest mass resolution is achieved in voltage scans defined by [*Dawson*, 1976]

$$M/\Delta M = 0.506/(0.336 - 2U/V). \quad (4b)$$

[redacted]

[redacted]

[redacted]

[redacted]

[redacted]

[redacted]

[redacted]

[redacted]

[redacted]

[redacted]

[redacted]

[redacted]

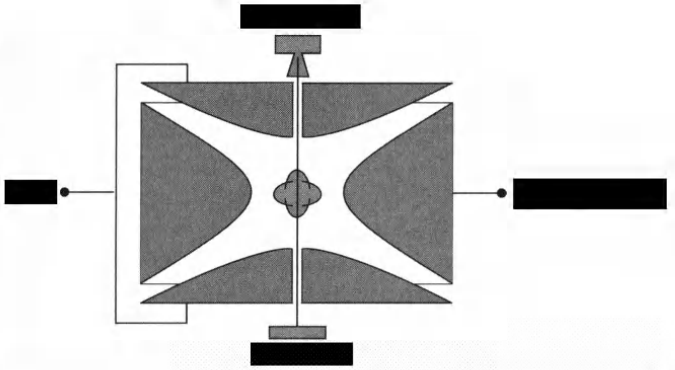

[redacted]

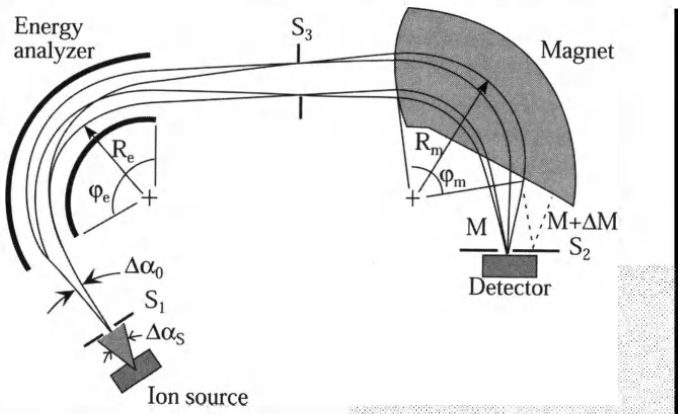
Energy
analyzer
S3
Magnet
Re
φe
Rm
φm
M
M+ΔM
S2
Detector
Δα0
S1
ΔαS
Ion source

where h is the height of the entrance slit. From (5c) the maximum transmittable current for a given geometry and acceleration voltage varies inversely with mass resolution and directly with spectrometer acceptance in energy and angle.

An obvious limitation on beam transport in (5c) is slit height. Equation (5c) applies to stigmatic (two-dimensional) focusing, which can be obtained in several ways. The first is using curvilinear magnetic field boundaries as shown in Figure 2. Other methods depend on combining toroidal-shaped electric fields with a homogenous magnetic field, or introducing a third field element consisting of a static quadrupole lens [*Matsuda*, 1990; and *Balsiger et al.*, 2001]. Two-dimensional sector fields and static quadrupoles create restoring forces that focus the beam perpendicular to the plane of Figure 3. Extra optical elements are effective [*Balsiger, et al.*, 2001], but they increase spectrometer mass, alignment requirements, and instrument complexity.

The appropriate magnetic spectrometer quality factor, obtained as for (4d), is given by

$$Q_M = qV_o R_e h \Delta\Omega_o. \quad (5d)$$

The Q-factor depends on spectrometer dispersion, expressed in the factor R_e and in the more obvious transport limitations of slit height and angular acceptance. Mass resolution does not appear explicitly, but rather indirectly through R_e. What distinguishes the magnetic spectrometer from the quadrupole, however, is the presence of the factor qV_o, which acts as a lever arm to increase transport above what can be obtained from the quadrupole. All other things being equal, the magnetic spectrometer holds two performance edges on the quadrupole: potentially much higher mass resolution or potentially higher transport capability or some combination of the two. Seen this way, the limit to transport in magnetic spectrometers arises from maximum allowable magnetic field strength and extent.

3.4. Time-of-Flight Mass Spectrometry

The fourth instrument category, time-of-flight (TOF) mass spectrometry, is relatively new to space research. Its principle of operation (Figure 4) is based on injection of a short ($\Delta T_{pulse}/T_o \leq$ few ns) ion pulse into a combination of electric fields and field-free drift regions. Ions leaving a source with an energy spread ΔE_s are accelerated to an energy $qV_o >> \Delta E_s$ before they enter the spectrometer. During travel through the spectrometer, the ions disperse in time according to M/q and, with proper optical design, are focused in time at the detector. Measurement of the ion times

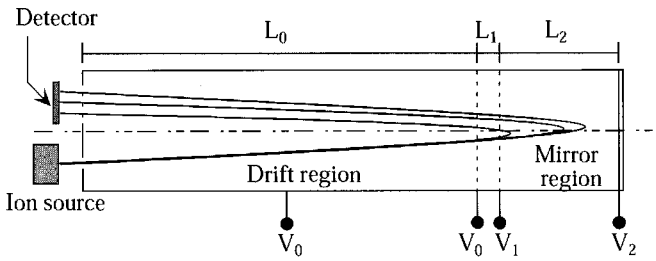

Figure 4. Schematic diagram of a time-of-flight mass spectrometer with a two-stage mirror made up of grids. The drift space is field free.

of arrival yields a spectrum from which ion M/q can be determined. The amount of dispersion, and therefore mass resolution, depends on ion path length through the optics, rather than on magnetic field strength or electric field frequency (Table 2). Mass resolution is primarily limited by the initial spread in ion energies since $T/\Delta T \sim M/\Delta M \sim qV_o/\Delta E_s$.

Mamyrin et al. [1973] made a significant breakthrough in TOF spectrometry by showing that an electrostatic mirror (Figure 4) could be used to correct aberrations caused by the initial ion energy spread. Nearly isochronous focusing occurs in a reflecting electric field ("reflectron"). The principle is that more energetic, faster ions penetrate deeper into the mirror field and spend more time there than ions with lower energy. This flight time compensation and symmetry of the ion flight path corrects the flight time aberrations to first order. It is possible to obtain second and higher order focusing by introducing one or more retarding lens elements at the front of the mirror field, thus creating two- and three-stage reflectrons and so on [*Cotter*, 1994; *Short and Todd*, 1994; and *Scheinfein and Seidman*, 1993].

Ion mirrors are most simply constructed from planar grids that create uniform mirror fields but slightly restrict transmission and, more importantly, introduce scattering. Gridless mirrors [*Schwartz et al.*, 1991; *Wollnik et al.*, 1993; and *Balsiger et al.*, 2001] with arbitrary field distributions. Only gridded spectrometer optics have analytical solutions, however, and they are discussed here. Ions created in the source are ejected in a short (~few ns) burst and are accelerated into the TOF spectrometer, acquiring an energy $E/q = V_o$. Ions travel a known path length L in the TOF, so a measurement of time-of-flight, T, determines ion M/q according to

$$M/q = 2V_oT^2L^{-2} = 1.92 \times 10^{-3} V_oT^2L^{-2}, \quad (6a)$$

where in the second expression T is measured in ns, L in cm, and V_o in kV. Logarithmic differentiation of (6a)

shows that $M/\Delta M = T/2\Delta T$. As a result, just as high-resolution magnetic spectrographs demand high spatial resolution detectors, high-resolution TOF spectrometers require good timing resolution such that the condition $\Delta T << 2L(M/\Delta M)(M/2V_o)^{1/2}$ is met. In other words, electronic timing resolution must increase with spectrometer resolution.

TOF spectrometer properties are derived by expressing the ion equation of motion in terms of expansions of mirror electric fields [*Wollnik*, 1987, 1993; and *Cotter*, 1994]. In the same way that the focusing properties of a magnetic spectrometer can be written as an expansion in field quantities, ion TOF can be written as $T = T_o + T_1 \delta + T_2 \delta^2 + \ldots$ The time T_o is that required for the principal ion ray to travel through the spectrometer. In order to find the best resolution, adjustments are made to the relative drift lengths and field distributions to minimize coefficients T_k. A relatively simple analytic solution with second order energy focusing can be obtained with a two-stage mirror field (Figure 4) [see *Mamyrin et al.*, 1973]. Mass resolution for an ion with energy $E = qV_o + \Delta E_s$ in the TOF drift tube is given by

$$M/\Delta M = 2[L_o + 2L_2(E/q - V_1)/V_2]/[(L_o)(\Delta E_s/qV_o)^{1/2}]. \quad (6b)$$

With reference to Figure 4, the drift tube of length L_o is held at the accelerating potential V_o, the retarding lens of length L_1 is set by voltage V_1, the mirror depth is L_2 and the back of the mirror is held at V_2. The distances from source and detector to the drift tube are assumed to be short relative to L_o. The purpose of the retarding lens is to slow down the ions with energies near the transport energy, permitting greater dispersion in the mirror field and also introducing a second field that can be adjusted to achieve better focusing. *Scheinfein and Seidman* [1993] and *Short and Todd* [1994], among others, discuss more optimized second and third order analytical solutions for a gridded TOF spectrometer. By ray-tracing ion paths in arbitrary field distributions, performance may be further refined to third order. Equation (6b) illustrates that mass resolution does not depend on aperture size, as it does for the quadrupole and magnetic spectrometers, but rather on the distribution of electric field strengths and length of the drift path.

Ion transport is limited by several factors, the largest being transverse spreading of ions over long flight paths. Spatial focusing transverse to the TOF axis may be obtained using a simple unipotential lens near the source [*Wollnik et al.*, 1992]. The transport of a spatially focused beam leaving the source and entering the TOF can be estimated by considering an initial divergence given by $\Delta\Omega \approx \Delta E_s/qV_o$. Then the maximum transmittable current is

$$I_M = \beta_s A_o \Delta E_s. \quad (6c)$$

Consequently, the Q-factor for a TOF spectrometer can be written as

$$Q_T = qV_o A_o \Delta\Omega (M/\Delta M). \quad (6d)$$

One feature to note is that in comparison to the quadrupole, transport in both the magnetic and TOF spectrometers is leveraged by the acceleration potential that can be several kilovolts or more.

The spread in beam energy and spatial focusing can be improved still further through the use of an orthogonal-extraction ion source that pre-focuses ions before they enter the TOF, reducing the spread in ΔE_s [*Dawson and Guilhaus*, 1989]. Other possible sources of ionization well suited to large biological molecules and TOF applications include pulsed laser ablation of sample material [*Lubman*, 1990] or collisions of heavy fission fragments with a thin layer of sample material [*Geno and Mcfarlane*, 1987]. Both methods ionize organic materials without significantly heating or cracking them, thus keeping large molecules intact. If engineering problems associated with laser power or radioactivity can be solved, then these methods seem promising for mass spectrometry applications. The other resource drivers in TOF mass spectrometry adapted to space flight are ion path length, which drives instrument volume, and high-speed electronics. Although timing and data acquisition electronics operate at much higher frequencies than do quadrupoles (~GHz vs. ~MHz) it is possible to mitigate TOF power consumption by capturing the necessary high-speed circuitry in a low-power microchip.

3.5. Spectrometry and Spectroscopy Duty Cycles

Mass peaks are measured by counting individual ions during a sampling interval, τ_s, when a peak is available at the detector. Spectra are obtained either by scanning mass range (spectrometry) or by measuring all peaks at once (spectroscopy). The number of ions detected in a single sample, C_M, at mass M is given by

$$C_M = (I_M/q)(\Psi \eta_d \tau_s), \quad (7)$$

in units of counts/ion/sample. Here I_M is given by (2), Ψ is the spectrometer transmission factor, including effects of beam loss due to grids and internal scattering, and η_d is detector efficiency. Measurement duty cycle, defined as the ratio of τ_s to the length of time it takes to measure the rest of the spectrum, is crucial to achieving good signal-to-noise ratio and measurement precision.

If a spectrum consists of N mass peaks, each sampled for a uniform interval τ_s, then the fraction of time, or duty cycle, that a single peak is sampled is $\delta_\tau = \tau_s/N(\tau_s + \tau_p) \approx 1/N$ provided that $\tau_s << \tau_p$, where τ_p is the time during which the rest of the spectrum is measured. In a true spectrograph the full range of N peaks is accommodated simultaneously on the detector so that $\tau_p \rightarrow 0$ and $\delta_\tau = N\tau_s/N(\tau_s + \tau_p) \rightarrow 1$. It is a common misconception that TOF mass "spectrometers" measure all masses "simultaneously" and therefore can be considered spectrographs. However, the TOF is spectroscopic only if ions are stored during the time required for an ion bunch to pass through the optics. If an ion source is run continuously and pulses of ions of width τ_T enter the TOF every $N\tau_T$ seconds, then the TOF duty cycle would be the same as that of a spectrometer, namely 1/N. The TOF can, however, function as a true spectrograph provided that ions that would have been lost during the time τ_p are instead stored and released later into the TOF. This has the effect of increasing duty cycle from 1/N to nearly 1 (neglecting electronic readout time).

3.6. Interferences with Measurement

Interferences within mass spectra arise from several independent sources, all of which reduce resolution, detectability of minor peaks, and peak identification. Usually the most important potential sources of interference come from elastic scattering of beam ions off residual gas molecules or inelastic scattering of ions off spectrometer surfaces. Additional sources of background are intrinsic detector noise (dark current) and penetrating energetic particle radiation from space. If a spectrometer is properly designed, then scattering off residual gas molecules, which is proportional to gas pressure along the ion trajectory, is the most important contributor. *Ioanoviciu* [1973] and others have studied this effect on DFMS with the result that the fraction of scattered current, I_{sc}, from the primary ion beam, I^+, is given by $I_{sc} = I^+/I_M = C\ \sigma_{in}\ N_o\ s\ (M/\Delta M)^{1.69}$, where C is a constant for a particular optical geometry (for example, $C_m \sim L_2/R_e + R_e/R_m \sim 20$ for the geometry in Figure 2), σ_{in} is the ion-neutral elastic scattering cross section, I_M is primary ion current, N_o is neutral gas density, and s is the width of the exit aperture. The mass resolution enters this equation because the higher the resolution the more susceptible is the spectrometer to scattering (or cross-talk) between two adjacent peaks. Since I_{sc} is proportional to gas density, the pressure in the spectrometer must be very low. Although ion flight path lengths through a spectrometer must be much smaller than the collisional mean free path, smaller instruments imply the possibility of higher operating pressures. This is important because pumps are both heavy and require electrical power.

3.7. Sample Separation and Concentration

Methods of separating and concentrating gases before they enter an ion source are important to spectrometer performance. The most widely used method in planetary science is gas chromatography in which a mixed gas sample is transported by an inert carrier gas (such as He) through a polymer-coated capillary column several to tens of meters long [*Niemann et al.*, 1992, 1997; and *Watson*, 1997]. As the mixture travels through the column, different compounds are retained to varying degrees by the polymer, so that the more mobile compounds reach the end of the capillary first followed at different times by other eluting gases. A mass spectrum can then be obtained for each compound individually thus removing interferences caused by other compounds. Sample concentrators work differently. When minor species of interest are mixed with much more abundant species (such as Martian H_2O and noble gases mixed with CO_2) then a gas concentrator, consisting of a molecular sieve or getter, can be made to selectively adsorb and trap both the major and minor gas components. Once a sample is collected, minor species can be released later in the absence of the major species and analyzed. Flight spectrometers have taken advantage of these methods to increase sensitivity [*Rushneck et al.*, 1978; and *Niemann et al.*, 1992, 1997]. Although the column itself is small, the number of valves (at 10-30 g each) and electrical power required for valves and heaters can be many tens of watts.

3.8. Miniaturization

Miniaturization of high-performance mass spectrometers will not be an easy process for several reasons. Equations that control optical performance are for the most part nonlinear which implies that optical processes such as beam formation and field generation do not scale with size in a simple way. In addition, the ultimate limit to size reduction is the ability of a spectrometer to transport sufficient current to make precise identifications and abundance measurements in a short period of time.

Scaling down the size (length, volume) of a quadrupole size at a fixed ratio of r_o/L reduces throughput as r_o^{-2} but has no effect on mass resolution as long as the frequency is increased as L^{-1}. Another factor is the volume of the transport optics needed to avoid collisions between the ion beam and spectrometer walls and other surfaces from which they might scatter. The advantages of miniaturized electrical-

mechanical systems (MEMS) in mass spectrometry are fairly obvious, but there are serious drawbacks as well. The entire subject of MEMS-based mass spectrometry is in need of detailed investigation.

If TOF miniaturization is considered, then there is a limit placed on the smallness of a TOF spectrometer by the speed of available electronics. All other parameters being equal, a miniaturized TOF spectrometer can easily reach an electronic speed limit. Current state-of-the-art in space-borne timing electronics is a few tenths of a nanosecond [*Balsiger et al.*, 2001; and *Young et al.*, 2001].

4. DISCUSSION

In the above sections we discussed mass spectrometer performance for typical but not highly developed designs. This route was taken because of the limited length of this paper and its tutorial nature. Table 2 gives a comparison of the important features of the methods considered here.

The quadrupole is relatively simple and compact but mass resolution is limited to a few hundred for reasonable sized instruments. In addition, ion transport is limited by the chosen resolution. The Q-factor suggests that balancing the operating frequency against field volume may improve overall performance, although higher frequencies require that ion energy be increased or the rods become shorter. The quadrupole ion trap discussed in Section 3.3 is mechanically simple and offers nearly unlimited resolution capabilities. It does not, however, appear to be easily adaptable to space flight. The chief drawbacks are sophisticated circuitry and operating algorithms, and a continuous He leak, needed to stabilize the trapped beam and extract it. Magnetic spectrometer resolution is determined by the size of the instrument balanced against the width of the spectrometer slits. The overall performance Q-factor takes resolution into account through R_c, but also depends strongly on the ion accelerating potential (a feature it shares with TOF spectrometry) as well as slit height and angular acceptance. The latter two factors act to limit ion transport. Thus optimal performance comes down to increasing instrument size (proportional to R_c, h, $\Delta\Omega_o$) and magnetic field strength (proportional to V_o and R_c). It is also possible to improve resolution performance by introducing other optical elements such as static quadrupole fields [*Wollnik*, 1987; *Balsiger et al.*, 2001], which again adds to instrument size and complexity. Lastly, as its Q-factor shows, the TOF spectrometer is able to transport the largest volume of phase space of all the spectrometer types without compromising mass resolution. Mass resolution of a given sized TOF instrument can be optimized by adjusting mirror voltages without having to modify any mechanical dimensions, which leaves the door open for tuning the spectrometer in flight if so desired (if the power supplies are available). Mechanical alignment requirements and overall complexity of the TOF are relatively minimal, even in comparison with the quadrupole. The electrical complexity is clearly greater because of the wide (~GHz) bandwidth required to handle events lasting ~1 ns.

In conclusion, the TOF spectrometer family would appear to hold the greatest promise for small high-performance instrumentation needed for future planetary missions. Combinations of multi-stage reflectrons with low-energy-dispersion sources such as plasma or laser desorption could potentially achieve resolutions of ~10,000 if sufficiently sophisticated timing electronics were also available. Another option, not examined here, is tandem mass spectrometry in which two magnetic or quadrupole or some combination of spectrometers are combined in series, allowing the user to obtain a mass spectrum of a mass spectrum [*Watson,* Chapt. 5, 1997]. Disadvantages of this method include greater mechanical and electrical complexity and larger optical volumes and therefore a larger instrument. A lower duty cycle also results when tandem mass scans are performed. The best choice for a tandem instrument may be the ion trap/TOF spectrometer combination [*Schwartz et al.*, 1991; and *Michael et al.*, 1992]. Finally, one should keep in mind that spectrometer optics are by no means the entire instrument. Gas handling and sampling equipment as well as vacuum pumps and ancillary equipment are all part of the complete flight instrument. However, if the spectrometer part cannot be made small, then reducing the size and mass of other components such as electronics or gas chromatography columns will not be sufficient to achieve truly low resource levels of a few kilograms and watts.

REFERENCES

Arvidson, R., Mars exploration program: Mars 2007 Smart lander mission, science definition team report, JPL Doc.

Balsiger, H., et al., The ion mass spectrometer on Giotto, *J. Phys. E: Sci. Instruments*, *20*, 7559, 1987.

Balsiger, H., et al., ROSINA: Rosetta Orbiter for Ion and Neutral Analysis, submitted to *J. Phys. E: Sci. Instrum.*, 2001.

Benninghoven, A., F. G. Rudenauer, and H. W. Werner, *Secondary Ion Mass Spectrometry: Basic Concepts, Instrumental Aspects, Applications, and Trends*, J. Wiley and Sons, N. Y., 1987.

Biemann, K., Test results from the Viking gas-chromatograph mass spectrometer experiment, *Origins of Life*, *5*, 417, 1974.

Blauth, E. W., *Dynamic Mass Spectrometers*, Elsevier, N. Y., 1966.

Carignan, G. C., et al., The neutral mass spectrometer on Dynamics Explorer B, *Space Sci. Instrumentation*, *5*, 429, 1981.

Cotter, R. J. (Ed.), *Time of Flight Mass Spectrometry*, Amer. Chem. Soc. Symposium Series 549, Amer. Chem. Soc., Washington, D. C., 1994.

Dawson, P. H. (Ed.), *Quadrupole Mass Spectrometry and Its Applications*, Elsevier, N. Y., 1976.

Dawson, J. H. J., and M. Guilhaus, Orthogonal acceleration time-of-flight mass spectrometry, *Rapid Comm. Mass Spectrometry*, *3*, 155, 1989.

Duckworth, H. E., R. C. Barber, and V. S. Venkatasubramanian, *Mass Spectroscopy*, 2nd Ed., Cambridge U. Press, N. Y., 1986.

Geno, P. W., and R. D. Mcfarlane, ^{252}Cf plasma desorption mass spectrometry using a mamyrin reflectron in a low voltage regime, *Int. J. mass Spectrometry and Ion Processes*, *77*, 75, 1987.

Grob, R. L., *Modern Practice of Gas Chromotography*, Wiley, N. Y., 1995.

Hintenberger, H., and L. A. Konig, Mass spectrometers and mass spectrographs corrected for image defects, in *Advances in Mass Spectrometry*, pp. 16-35, Pergammon Press, 1959.

Hoffman, J. H., W. B. Hanson, C. R. Lippincott, and E. E. Ferguson, The magnetic ion-mass spectrometer on Atmospheric Explorer, *Radio Sci.*, *8*, 277, 1973.

Hoffman, J. H., et al., Pioneer Venus Sounder Neutral Gas Mass Spectrometer, *IEEE Trans. Geosci. Remote Sensing*, *GE-18*, 80, 1980.

Holkeboer, D. H., et al., Miniature quadrupole residual gas analyzer for process monitoring at milli-Torr pressures, *J. Vac. Sci. Technol.*, *A 16*(3), 1157, 1998.

Ioanoviciu, D., Peak tails produced by elastic scattering in mass spectra of tandem mass spectrometers, *Int. J. of Mass Spectr. Ion Phys.*, *12*, 115, 1973.

Johnson, R. E., R. M. Killen, J. H. Waite, Jr., and W. S. Lewis, Europa's surface composition and sputter-produced ionosphere, *Geophys. Res. Lett.*, *25*, 3257, 1998.

Krankowski, D., et al., The Giotto neutral mass spectrometer, in *The Giotto Mission: Its Scientific Investigations*, ESA SP-1077, European Space Agency, pp. 109-128, Noordwijk, The Netherlands, 1986.

Lubman, D. M., *Lasers and Mass Spectrometry*, Oxford, U.K., 1990.

Mamyrin, B. A., V. I. Karataev, D. V. Shmikk, and V. A. Zagulin, The mass-reflectron, a new non-magnetic time-of-flight mass spectrometer with high resolution, *Sov. Phys., JETP*, *45*, 1973.

March, R. E., and R. J. Hughes, *Quadrupole Storage Mass Spectrometry*, Wiley Interscience, 1991.

Matsuda, T., T. Sakurai, and M. Ishihara, Recent development of ion-optical studies for mass spectrometer and mass spectrograph design, *Nucl. Instrm. Meth. Phys. Res.*, *A298*, 134, 1990.

Michael, S. M., M. Chien, and D. M. Lubman, An ion trap storage/time-of-flight mass spectrometer, *Rev. Sci. Instrum.*, *63*, 4277, 1992.

Niemann, H. B., et al., Mass spectrometric measurements of the neutral gas composition of the thermosphere and exosphere of Venus, *J. Geophys. Res.*, *85*, 7817, 1980.

Niemann, H. B., et al., Galileo Probe mass spectrometer experiment, *Space Sci. Rev.*, *60*, 111, 1992.

Niemann, H., et al., The gas chromatograph mass spectrometer aboard Huygens, in *Huygens*, ESA SP-1177, European Space Agency, pp. 85-107, Noordwijk, The Netherlands, 1997.

Nier, A. O., and J. L. Hayden, A miniature Mattauch-Hertzog mass spectrometer for the investigation of planetary atmospheres, *Int. J. Mass Spectrom. Ion Phys.*, *6*, 339, 1971.

Nier, A. O., et al., Entry science experiments for Viking 1975, *Icarus*, *16*, 74, 1972.

Nier, A. O., W. E. Potter, D. R. Hickman, and K. Mauersberger, The open-source neutral-mass spectrometer on Atmospheric Explorer-C, -D, and –E, *Radio Sci.*, *8*, 271, 1973.

Oyama, V. I., et al., Pioneer Venus sounder probe gas chromatograph, *IEEE Trans. Geosci. Remote Sensing*, *GE-18*, 85, 1980.

Pelz, D. T., C. A. Reber, A. E. Hedin, and G. R. Carrignan, A neutral-atmosphere experiment for the Atmosphere Explorer-C, -D, and -E, *Radio Sci.*, *8*, 277, 1973.

Rushneck, D. R., A. V. Diaz, D. W. Howarth, et al., Viking gas chromatograph-mass spectrometer, *Rev. Sci. Instrum.*, *49*, 817, 1978.

Scheinfein, M. R., and D. N. Seidman, Time aberrations of uniform fields: An improved reflectron mass spectrometer for an atom-probe field-ion microscope, *Rev. Sci. Instrum.*, *64*, 3126, 1993.

Schmidt, L., H. Jungclas, H.-W. Fritsch, and P. Kohl, Gridless ion acceleration systems for time-of-flight mass spectrometry, *J. Am. Soc. Mass Spectrom.*, *4*, 782, 1993.

Schwartz, J. C., J. E. P. Syka, and I. Jardine, High resolution on a quadrupole ion trap mass spectrometer, *J. Am. Soc. Mass Spectrom.*, *2*, 198, 1991.

Short, R. T., and P. J. Todd, Improved energy compensation for time-of-flight mass spectrometry, *J. Am. Soc. Mass Spectrom.*, *5*, 779, 1994.

Settle, F. A. (Ed.), *Handbook of Instrumental Techniques for Analytical Chemistry*, Prentice Hall PTR, N. J., 1977.

Waite, J. H., Jr., et al., The Cassini Ion and Neutral Mass Spectrometer (INMS) Investigation, *Space Sci. Rev.*, in press, 2002.

Watson, J. T., *Introduction to Mass Spectrometry*, 3rd Ed., Lippincott-Raven Publ., Philadelphia, PA, 1997.

Wollnik, H., *Optics of Charged Particles*, Academic Press, San Diego, 1987.

Wollnik, H., Time-of-flight mass spectrometers, *Mass Spectrom. Rev., 12*, 89, 1993.

Wollnik, H., U. Gruner, and G. Li, Time-of-flight mass spectrometers, in M. L. Gross (Ed.), *Mass Spectrometry in the Biological Sciences*, 117, Kluwer, Amsterdam, 1992.

Young, D. T., J. E., Nordholt, J. L. Burch, et al., The Plasma Experiment for Planetary Exploration (PEPE), *Space Sci. Rev.*, submitted, 2002.

David Young, University of Michigan, Department of Atmospheric Oceanic and Space Sciences, 2455 Hayward Street, Ann Arbor, MI 48109, dtyoung@umich.edu.

PART VI. ATMOSPHERES OF OTHER WORLDS

At the Division of Planetary Sciences (DPS) meeting of the American Astronomical Society in November 2001, Brother Guy Consolmagno, S. J., of the Vatican Observatory suggested that there were three landmark events in planetary science in the 1990s: (1) the discovery of extra-solar-system planets, (2) the impact of Comet Shoemaker-Levy with Jupiter, and (3) discussions of what message came with the finding of martian meteorite (AH84001) in Antarctica. Not coincidentally, all are related to issues of the origins and extinctions of life on Earth, in the solar system, and beyond. Atmospheres, and in particular their water and oxygen components, play a central role in all serious discussion of "life as we know it." In this concluding section we address the aeronomic issues of astrobiology. It is a marvelous way to conclude this monograph precisely because it offers a commencement. As occurs each spring at universities worldwide, the beginning of life beyond campus is the message of graduation. With the publication of this volume in 2002, when the latest snapshot of our stellar neighborhood reveals our nine planets to be barely 10% of all known planets, the field of comparative aeronomy is indeed in its onset years.

A depiction of planetary systems around every star in the cosmos. Called "The System According to Newton" and intended as a ridicule of non-scripture-based astronomy, this image from a publication of the Muggeltonians (a 17th Century fundamentalist sect in England) is here portrayed in Victorian times by the new "oil color printing" method of G. Baxter, from a drawing by Isaac Frost, engraved by W. P. Clubb and Son, London.

A Possible Aeronomy of Extrasolar Terrestrial Planets

W. A. Traub and K. W. Jucks

Harvard-Smithsonian Center for Astrophysics, Cambridge, Massachusetts

Terrestrial planetary systems may exist around nearby stars as the Earth-sized counterparts to the many giant planets already discovered within the solar neighborhood. In this chapter we first discuss the numerous techniques which have been suggested to search for extrasolar terrestrial planets. We then focus on the expected results from that technique in which an orbiting telescope or interferometer is used to obtain a visible or infrared spectrum of a planet, without contamination from the parent star. We show examples of such spectra for selected cases: the present Earth, the Neoproterozoic (snowball) Earth, a methane-rich Earth, and the present Mars and Venus. We conclude by discussing the implications of such spectra for the detection of life on an extrasolar terrestrial planet.

1. KNOWN EXTRASOLAR SYSTEMS

The first planet orbiting a solar-type star beyond the solar system was announced in 1995. Since then, as of October 2001, 66 planets have been found and confirmed, orbiting 58 stars with a median distance from the sun of about 28 pc. The search database contains roughly 1200 stars.

Current estimates of the frequency of massive planets range from about 3-5% to 6-7% [*J. Schneider, and G. Marcy, resp., personal communication*]. The number of detected planets is growing monthly, as observing techniques are refined, and as the time base of the record increases, allowing longer-period planet signatures to be extracted from the radial velocity sequences.

The definition of a planet can be a controversial issue, as is evidenced by the recent debate on whether Pluto should be classified as a planet, or a trans-Neptunian or Kuiper-belt object. However in the case of extrasolar planets the debate centers not on the question of the low-mass end of the scale, as for Pluto, but on the high-mass end, which is the realm of the planets discovered to date. The question is, should these objects be classified as planets, brown dwarfs, or small stars?

Here we adopt the recommendation of *Oppenheimer et al.* [2000] for objects of solar metallicity: the minimum mass for a brown dwarf is about 13 M_J (where M_J is the mass of Jupiter) or 0.013 M_{sun}, sufficient to allow deuterium burning; the minimum mass for a main sequence star is about 78 M_J or 0.075 M_{sun}, sufficient to allow hydrogen burning.

Pulsar planets, known since 1992 from variations in pulse arrival times from pulsars, are kept in a separate category from exoplanets around main-sequence stars. These bodies may have formed during the explosion that created the neutron-star pulsar.

At least two websites collect current information on exoplanets. One site is "The Search for Extrasolar Planets" [*Marcy, 2001*] originating at UC Berkeley. The other, larger, site is "The Extrasolar Planets Encyclopaedia" [*Schneider*, 2001] originating at Paris Observatory, Meudon. Both sites feature news items, discussions, tutorials, papers, bibliographies, and comprehensive lists of exoplanets, their properties, and their parent stars. Both sites are expertly edited and authoritative.

Atmospheres in the Solar System: Comparative Aeronomy
Geophysical Monograph 130

10.1029/130GM25

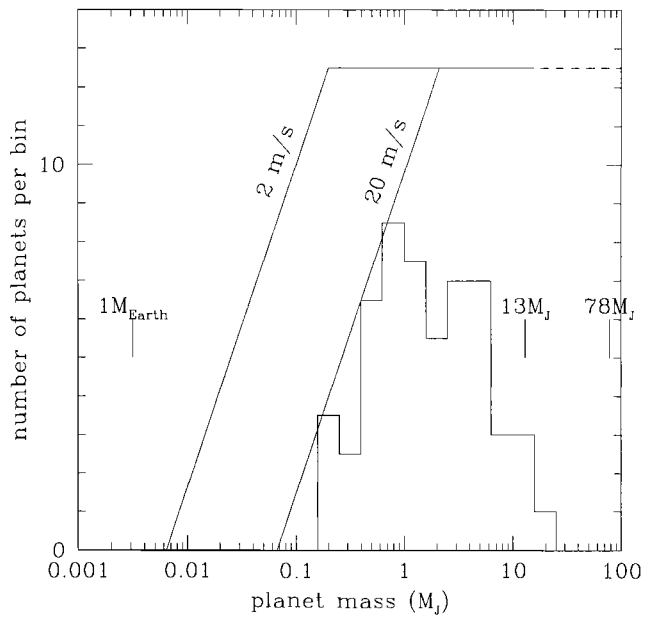

Figure 1. Histogram of discovered exoplanets, ranging from about 0.16 to 13 M_J. Theoretical curves are shown for the cases where exoplanets have a uniform density distribution in the $(\log M, \log R)$ plane, in the range $\log M = -3$ to $+1.11$, and $\log R = -2$ to $+1$, and limited by the sensitivity of radial velocity measurements to orbital velocities of 2 and 20 m/s, as indicated. The observed distribution appears to be bounded by measurement accuracy on the low-mass side, and by a lack of exoplanets on the high-mass side.

The present paper is oriented toward extrasolar terrestrial planets, i.e., those in the mass and temperature range of Venus, Earth, and Mars. However, since all known exoplanets are in the gas giant mass range, it is appropriate to ask about the prospects for finding terrestrial-mass exoplanets.

Astrometry (cf. later section) tells us the semi-major axis, eccentricity, and mass of a planet. Each of these is a clue to a part of the history of the planet, e.g., where and how it was formed, whether it has migrated since then, and whether its orbit has been perturbed by other bodies. However to learn from this data if terrestrial-sized planets might be present we must fall back on inference based on the observed frequency distribution of mass, as follows.

If we examine a plot of exoplanet mass versus semi-major axis, we see that the discoveries tend to populate the entire region between the extremes of: (a) maximum mass set by definition at about 13 M_J; (b) minimum mass set by the radial velocity detection method at about $M/M_J = 0.035vR^{1/2}$ where v (m/s) is the minimum detectable orbital velocity amplitude and R (AU) is the orbital radius; (c) maximum radius set by a total observing time of about 5 years, to get a full orbit; and (d) minimum radius set by the smallest observed orbit at about 0.01 AU. If we assume that this entire region, on a $(\log R, \log M)$ plot, might be uniformly populated, then we can calculate the expected number of planets as a function of mass.

We show in Figure 1 a histogram of the detected masses, and two "expected" distributions corresponding to velocity amplitudes of 2 and 20 m/s, the former being a nominal goal of the present radial velocity searches, and the latter being an estimate of the current level of confident detection. Although Figure 1 is undoubtedly overly simple, we may nevertheless draw two conclusions. (1) At the high-mass end, where the present searches are certainly relatively complete and unbiased, the observed distribution drops off rapidly from about 1 M_J to 13 M_J, suggesting that the exoplanet population really does exist as a separate entity from any brown dwarf population (not shown) which might fill in the 13-75 M_J range. (2) At the low-mass end, the observed population seems to be approximately fit by the 20 m/s curve, suggesting that the observations are observationally limited, and that there is no evidence for a fall-off at low masses. Thus at present we may well be sampling only the very top end of the exoplanet mass distribution curve, and it may well be that the distribution function continues all the way down to the M_{Earth} range. On this basis we optimistically look forward to someday finding terrestrial exoplanets.

2. DETECTION METHODS: GRAVITY AND AERONOMY

There is a surprising number of proposed techniques to detect or characterize exoplanets. About one-half of the techniques may be classified as being gravitational in nature, and the other half as being aeronomic (or photonic). The gravitational methods are (1) radial velocity, (2) astrometry, (3) transits, (4) pulsar timing, (5) gravitational lensing, and (6) disk shaping. The aeronomic methods are (7) visible-infrared shift, (8) reflected light, (9) transmitted light, (10) auroral emission, (11) radio emission, (12) anthropogenic transmission, (13) coronagraphic imaging, and (14) interferometric imaging.

2.1. Radial velocity

As the planet and star orbit their common center of mass, the velocity vector of the star projected along the observer's line of sight is proportional to $M \sin i$ where M is the planet mass and i is the inclination of the orbit plane to that of the sky. Doppler shifts in stellar

spectra have been measured to an accuracy of about 3 m/s; 10 m/s is common, and 1 m/s may be the ultimate limit of this technique [*Marcy and Butler*, 2000; *Santos et al.*, 2000]. By comparison, the solar velocity due to Jupiter is about 3 m/s, and that due to Earth is about 0.01 m/s.

2.2. Astrometry

The projection of stellar orbital motion onto the plane of the sky produces an astrometric shift which is measured with respect to a grid of nearby reference stars. At 10 pc, Jupiter would move the Sun by about 100 μas (1 μas = 10^{-6} arc-sec), and Earth would move the Sun by about 0.3 μas. The Hipparcos satellite had an accuracy of about 500 μas, so could not quite detect Jupiter-sized planets, but planned missions such as FAME (50 μas) [*Horner et al.*, 2001] (2004 launch planned), GAIA (2-10 μas) [*Perryman et al.*, 2001], (2012 launch planned), and SIM (1 μas) [*Danner and Unwin*, 1999] (2009 launch planned), have a good chance of detecting masses in the sub-Jupiter range, and almost down to the terrestrial limit.

2.3. Transits

If the planet's orbital plane is seen nearly edge-on, a partial eclipse of the star by the planet may occur. For the one example known to date, HD209458, [*Charbonneau et al.*, 2000], precise photometry has allowed us to infer the stellar limb darkening, the planet radius, the orbital inclination, and therefore the planet's mass. Further observation may lead to a transmitted light measurement, as discussed below. Dedicated, staring telescopic searches [*e.g., Borucki et al.*, 2001] may detect more examples of this rare transit phenomenon.

2.4. Pulsar Timing

The clock-like constancy of pulsar spin rates means that the time delay produced by line of sight displacement due to an orbital companion can be interpreted in terms of the mass and orbit of the companion [*e.g., Konacki et al.*, 2000]. Two such pulsars are known, PSR 1257+12 (3 planets, possibly 4), and PSR B1620-26 (1 planet). Interestingly the technique is sufficiently sensitive that we know that some of these pulsar planets are in the few M_{Earth} range, and one may be in the M_{Pluto} range.

2.5. Gravitational Lensing

A star in our Galaxy can cause a distant light source (a background galaxy) to apparently brighten for several days by gravitationally deflecting and lensing the distant galaxy's light as the star happens to pass in front of the galaxy. If the star hosts a planetary companion, then the planet can cause a secondary brightening [*Gaudi and Gould*, 1997]. The effect would be transient, but statistics of many events would give information on the Galactic incidence of planets.

2.6. Disk Shaping

For a star with a debris disk, the presence of a planet with non-zero eccentricity or relative orbit inclination will cause the disk to become eccentric or warped, respectively; a planet inside the dust or debris disk can also generate resonant trapping (clumps) and clearing of central holes [*Wyatt et al.*, 1999; *Liou and Zook*, 1999].

2.7. Visible-Infrared Shift

Precise astrometry of an unresolved star-planet system in the visible and infrared wavelength regions simultaneously would show a spatial shift because the star light dominates the planet's light less in the infrared. This is a detection mode planned for the Keck Interferometer and Very Large Telescope Interferometer [*Akeson et al.*, 2000; *Lopez et al.*, 2000].

2.8. Reflected Light

For a large, close-in planet, sufficient star light may be reflected from the planet that it could be directly detected as an additional component of star light, even if the system is not spatially resolved [*Charbonneau et al.*, 1999].

2.9. Transmitted Light

If a planet eclipses the parent star, then the planet's transparent upper atmosphere will transmit a portion of the starlight, with a superposed planetary absorption spectrum which could produce measurable features such as He 1.0830 μm or Na 0.589 μm [*Brown et al.*, 2001].

2.10. Auroral Emission

Auroral activity such as seen on Earth or Jupiter (e.g., O 0.5577 μm, Hα) is a non-thermal, potentially useful indicator of a planet [*e.g., Waite et al.*, 2001], but the flux rate may be so low as to not be competitive with other techniques. Detection of oxygen emission is discussed more fully in Chapter VI.2.

2.11. Radio Emission

Decametric radio wavelength radiation from electrons in the magnetic field around Jupiter and Io suggests that planets might be identified by this non-thermal

radio signature [*Bastian et al.*, 2000], but low flux might limit this method.

2.12. Anthropogenic Transmissions

(a) It has been pointed out that a directed visible laser beam from Earth could be made to outshine the sun for the duration of a pulse, and would therefore be easily visible with a modest telescope at interstellar distances [*Howard and Horowitz*, 2001]. In the hope of detecting such pulses trial experiments have been started. (b) Pulsed radio transmissions containing coded messages are likewise detectable at great distance, and have been the basis of several searches [*e.g., Horowitz and Sagan*, 1993; *Leigh and Horowitz*, 1999].

2.13. Coronagraphic Imaging

Direct visible-wavelength detection of the analog of the solar system's gas giant outer planets could be achieved using existing general-purpose telescopes, such as the Hubble Space Telescope or the planned Next Generation Space Telescope, if the residual optical imperfections in either telescope were to be corrected by adaptive optics. Dedicated coronagraphic telescopes with shaped or shaded pupils have also been proposed [*Nisenson and Papaliolios*, 2001; *Spergel*, 2001]. To detect an Earth at 10 pc and 0.5 μm wavelength requires 10^{-10} starlight rejection at 0.1 arcsec separation.

2.14. Interferometric Imaging

An infrared-wavelength imaging interferometer has been proposed as a NASA mission [*Beichman et al.*, 1999], or European Darwin mission [*Fridlund*, 2000]. To detect an Earth at 10 pc and 10 μm wavelength requires 10^{-7} starlight rejection at 0.1 arcsec separation.

3. WHY SPECTRA OF TERRESTRIAL PLANETS?

Of all the techniques mentioned to detect or characterize an extrasolar terrestrial planet, we have chosen to focus on just two: coronagraphic imaging and interferometric imaging. The reason for this is that these seem to give us the best chance to determine the atmospheric constituents of the planet, by direct observation of the reflected or emitted light from the atmosphere and surface.

The current thumbnail picture of planetary formation is as follows. A massive molecular cloud is somehow triggered to collapse; a star is formed; the star is surrounded by a remnant gas and dust cloud; rocky, metallic, and, in the outer, colder parts of the cloud, icy grains, condense and agglomerate in the surrounding cloud; and the agglomerations cascade to larger sizes to form planetary cores. Then in the outer part of the cloud, where plenty of gas is available, the gas continues to collapse around the cores, and Jupiter-like (gas giant) planets form. In the inner part of the cloud where it is hotter and less gas is available, only rocky planets form. These rocky, terrestrial-type planets can have abundant liquid water or ice, and relatively thin atmospheric envelopes, both generated by outgassing of the rocky material and possibly also by infalling comets. It is on these planets, with their solid surfaces where water can accumulate and chemical reactions occur, and their thin atmospheres where sunlight can penetrate and be used for driving chemical reactions, that we speculate that life probably has its best chance to develop. (Excellent references can be found in *Chyba et al.* [2000], *Lunine* [1999], and *Yung and DeMore* [1999]).

Once we know the abundances of key gases, we can then make informed speculations on the likelihood that life exists on the planet. However even with the restriction to terrestrial-type planets, we still have a large range of possible types of atmospheres. In the following sections, we begin to explore the range of possibilities. We start with a description of our method for calculating visible and infrared spectra for the case of the present Earth. We extend this to include Neoproterozoic icehouse and hothouse Earths, a methane-rich Earth, and the present Mars and Venus. We conclude with a brief discussion of how the presence of life might be inferred from spectra such as these.

4. PLANETARY SPECTRA: PRESENT EARTH

A graphical overview of the exoplanet detection issue is shown in Figure 2, where we plot the flux density of a model solar system as it would be seen from a distance of 10 pc, the median distance for the nearest 450 or so stars in our Galaxy.

Blackbody spectra of the Sun, Jupiter, and the 3 terrestrial planets are shown in Figure 2, for the effective temperatures of these bodies, except as follows: the spectrum of Jupiter includes its internal heat source contribution; the spectrum of Mars is an average of the day and night side spectra at different temperatures; and for Earth the average ground temperature is used, not the effective temperature. (N.B., the effective temperature of an object is the temperature of a blackbody which has the same area and total radiated power as does the object.)

The zodiacal dust cloud is modeled as a face-on, smooth, optically thin blackbody emitter with optical depth varying as $r^{-0.39}$ and temperature varying as $r^{-0.42}$ where r is distance from the central star [*Reach*, 1995].

The reflected light from Jupiter and the terrestrial planets is approximated by a scaled version of the solar spectrum, proportional to each planet's average visual albedo and area, reduced by a factor of 0.26 to approximate the brightness at quadrature, when the observer sees only one-half of the disk illuminated. The zodiacal dust reflection spectrum is modeled with the same density distribution as for the thermal emission but with an albedo selected to agree with visual observations.

The spectral line component of the Earth's spectrum in Figure 2 is calculated separately for the thermal emission and reflection cases, for a clear atmosphere, and the results combined, as described next.

4.1. Spectral Computation Method

Model Earth spectra are calculated with our SAO code originally developed to analyze balloon-borne far-infrared thermal emission spectra of the stratosphere [*e.g., Traub and Stier*, 1976; *Johnson et al.*, 1995], extended to include visible reflection spectra. The spectral line data base includes the large AFGL compilation [*Rothman et al.*, 1998] plus improvements from pre-release AFGL material and our own sources. In a few cases laboratory cross section spectra are available but spectroscopic analysis is not, so here we use an empirical pseudo-line band shape. The far wings of pressure-broadened lines can be non-Lorentzian at around 1000 times the line width and beyond, so in some cases (H_2O, CO_2, N_2) we replace the far wings of the line-by-line calculation with measured continua data in these regions. Dust and Rayleigh scattering are approximated by empirical wavelength power laws and contribute significantly only in the visible blue range. Model atmospheres from 0 to 100 km altitude are constructed from standard models discretised to appropriate layers, and additional radiative transfer methods used to ensure that line cores and optically thick layers are accurately represented.

Radiative transfer from layer to layer is explicitly calculated using the average absorption and emission properties of each layer; scattering as a source is neglected. Integration from the spherical Earth atmosphere is approximated to a few percent accuracy by a single-point calculation at a zenith angle of 60 degrees, so the effective air mass is 2 in the infrared (outgoing emission) and 4 in the visible (2 for incoming sunlight, plus 2 for outgoing reflected light).

Cloud effects are beyond the scope of this chapter, and they are not included in the calculations shown here, but they can be represented by inserting continuum absorbing/emitting layers at appropriate altitudes; broken clouds can also be represented by a weighted sum of spectra using different cloud layers. In general, the effect of clouds is to dilute the strength of line features in the visible, and to dilute, but in extreme cases cause absorption lines to appear as emission lines, in the infrared.

4.2. Thermal Emission Spectrum

The dominant features of the Earth's thermal emission spectrum are illustrated in Figure 3, where the blackbody flux and composite spectrum (Jy/sr) are shown in the top left panel, and the other panels show the relative intensities of the major infrared molecular species (H_2O, O_3, CH_4, CO_2, N_2O) as well as minor contributors (H_2S, SO_2, NH_3, SF_6, CFC-11, CFC-12). The composite spectrum is calculated for the present

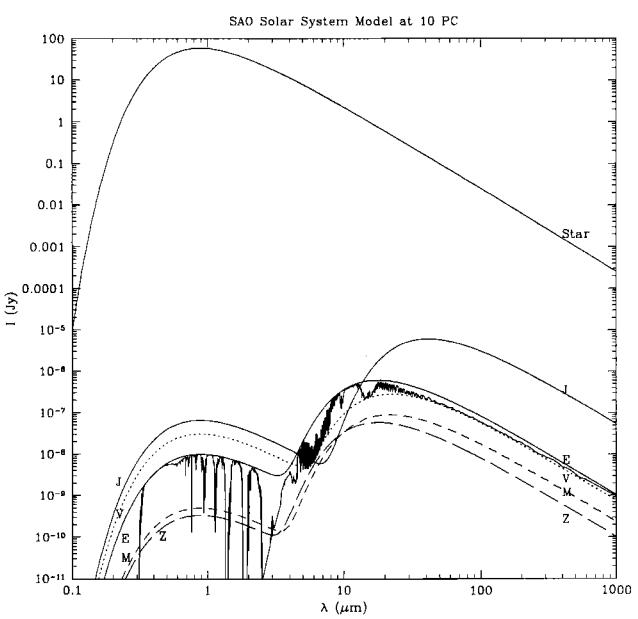

Figure 2. Solar system blackbody thermal emission spectra and reflected light spectra at 10 pc, for the Sun, Jupiter (J), Earth (E), Venus (V), Mars (M), and zodiacal dust (Z). For curve Z a telescopic field of view of 0.010 arcsec diameter centered at 0.1 arcsec from the star is assumed. For the Earth, present atmospheric abundances are used to calculate a line by line spectrum for the entire 4 decades in wavelength, for a cloud-free atmosphere. (Note 1 Jansky is 10^{-26} watt m^{-2} Hz^{-1}.)

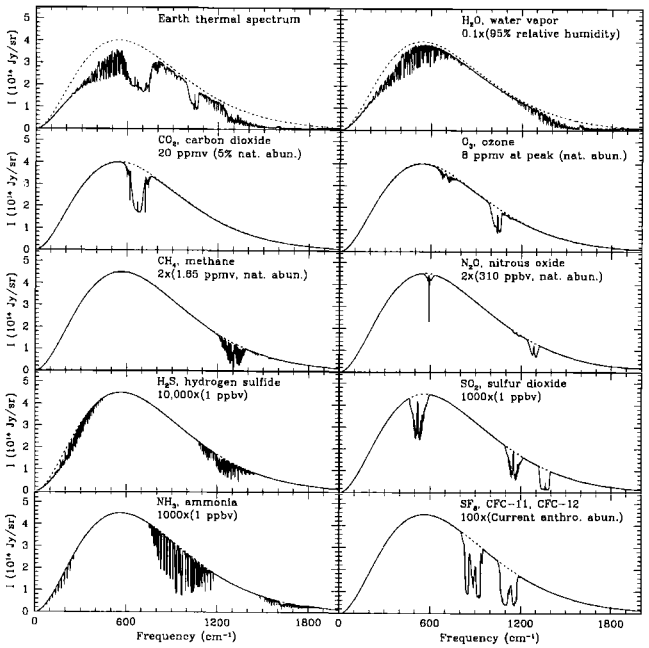

Figure 3. A calculated thermal emission spectrum of the present Earth is shown in the top left panel. The other panels show spectra of individual species, with their mixing ratio profiles scaled up or down so as to generate a maximum feature depth of roughly one-half. The calculations are performed at very high resolution and subsequently smoothed to 1 cm^{-1} for display. The panels demonstrate the concentrations needed for each species to contribute significant opacities on an Earth-like planet.

abundances of each species, but the individual species spectra are calculated for increased or decreased abundances, with the expected vertical mixing ratio profiles scaled so as to show the absorption spectrum minima at an optical depth of about unity.

The H_2O panel shows the far-infrared rotational band and the mid-infrared vibrational band, calculated for an abundance of about 0.1 times the saturated value in the lower troposphere. Even at this reduced concentration, the water lines are quite strong, but also rather diffuse, without any well-defined compact spectral features in the thermal infrared.

Carbon dioxide, on the other hand, even at 5% of present abundance, shows a very strong 15 μm (667 cm^{-1}) band in the infrared, the depth of which is limited not by abundance, but rather by the thermal structure of the Earth's atmosphere, such that the minimum brightness corresponds to the blackbody strength at the altitude at which the band core optical depth reaches values on the order of unity. Note the small spike in the center which is generated at an altitude of about 30 km by the temperature inversion in the stratosphere, causing the very strong core to appear in emission against the lower-lying cooler layers from which the near-wing emission emanates at an altitude of about 20 km.

Ozone is the third most prominent infrared feature with its strong 9 μm (1100 cm^{-1}) band, shown here at its natural abundance. The ozone feature is almost entirely due to the stratospheric O_3 layer, though there is a trace of tropospheric O_3.

Methane and nitrous oxide are both shown at twice natural abundance, and have significant features nearly overlapping in the 7 μm (1400 cm^{-1}) region, also lying in the red wing of the 6 μm (1600 cm^{-1})water band, and therefore not readily separable, but nevertheless in principle measureable. The combined effect of the current abundance of CH_4 and N_2O is seen in the composite panel, where the spectrum shows a rather sharp decrease going from about 1200 to 1300 cm^{-1}, compared to the gradual decrease in this region due to H_2O alone, as shown in the water-only panel.

The remaining species, at present Earth abundances, are not expected to be easily detectable on an exoplanet, due to the weakness of their bands. The panels show H_2S at 10,000 times natural abundance, SO_2 at 1000 times, NH_3 at 1000 times, and the anthropogenic gases SF_6, CFC-11, and CFC-12 each at 100 times current abundance.

4.3. Reflection Spectrum

Dominant features in the present Earth's reflection spectrum are shown in Figure 4, where in this case the panels give the reflected intensity normalized to the incident solar intensity, smoothed from the original high-resolution calculation to a plotted resolution of 100. The upper left panel is a composite of the 5 contributing species H_2O, O_2, O_3, CH_4, and CO_2, for present abundances. Note that the spectral range goes from the near infrared (2000 cm^{-1} = 5 μm) to the near ultraviolet (33000 cm^{-1} = 0.30 μm), with a continuum normalized everywhere to unity. We have ignored the thermal emission contribution at long wavelengths as well as the Rayleigh and dust scattering components which will show up mostly at short wavelengths.

The H_2O panel, for the present abundance of water, shows a series of absorption bands spanning the middle part of the visible spectrum and increasing in strength toward the near infrared. The strengths of these vibrational bands are essentially independent of temperature, but will increase in proportion to the abundance of water and the square root of air pressure, however since the lines are relatively saturated, the average band depth

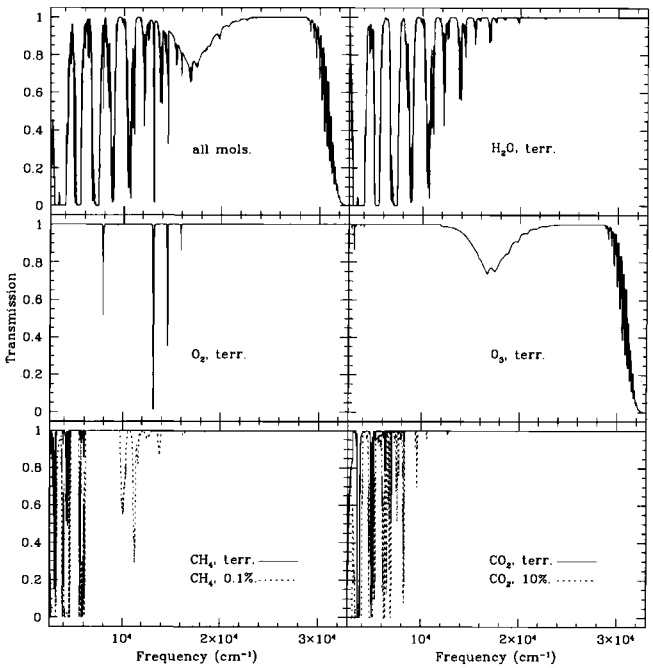

Figure 4. The reflectivity of the Earth with present atmospheric abundances is shown in the top left panel, normalized to unity. Clouds, aerosols, and Rayleigh scattering are ignored in this example. The other panels show reflection spectra for the cases where only a single species is present in terrestrial abundances. For CH_4 and CO_2 we also show spectra for greatly enhanced abundances as discussed in the text.

will only increase as the square root of band strength. The net result is that these bands should be good indicators of the presence of water over a large dynamic range of conditions, although this same property makes them less useful as quantitative indicators of water mixing ratio, unless we also have independent knowledge of temperature and pressure.

The strongest O_2 band is the Fraunhofer A-band at 0.76 μm (13000 cm^{-1}). This band too is saturated, and will still be relatively strong for significantly smaller mixing ratios than the present Earth's. It will therefore be an excellent indicator of the presence of oxygen (see Chapter VI.2).

The O_3 molecule has two broad features of note, the extremely strong Huggins band which produces the ultraviolet absorption shown here at about 0.33 μm (30000 cm^{-1}) and shorter, and the Chappuis band which shows up as a broad triangular dip in the middle of the visible spectrum from about 0.45 to 0.74 μm (22000–13000 cm^{-1}). Ozone in the stratosphere is produced from O_2 molecules, and its abundance is a nonlinear function of the O_2 abundance, such that even a small amount of O_2 can produce a relatively large amount of O_3 [*Kasting and Donahue*, 1980]; however in absolute terms the modeled column abundance of O_2 is nevertheless large compared to that of O_3 by a factor of 20,000 to 500,000.

Methane at present terrestrial abundance (1.65 ppmv) has no significant visible absorption features, but at high abundance (0.1%) it has strong visible bands at 0.9 and 1.0 μm (11000 and 10000 cm^{-1}).

Carbon dioxide has negligible visible features at present abundance, but in a high-CO_2 atmosphere (10%) it has a significant band at 1.2 μm (8000 cm^{-1}) and even stronger ones at longer wavelengths.

5. PLANETARY SPECTRA: NEOPROTEROZOIC EARTH

The present status of our secure knowledge of paleo-Earth atmospheres is easy to review, because little of our knowledge is secure, although in recent years the situation has been improving. In overview, the evolution of CO_2 has long been believed to have decreased from a high level of roughly 1 bar at about 4.5 Ga (where Ga represents 1×10^9 years ago) to 0.00035 bar at present, however recent evidence suggests that major oscillations occured around 0.5-0.8 Ga, and perhaps at other glaciations, The abundance of O_2 is believed to have been less than 0.001 bar until about 2 Ga when it rapidly began to increase toward its 0.2 bar present value, and the time of transition is roughly coincident with the beginning of abundant phytoplankton on Earth.

The equilibrium temperature of the Earth with its present albedo, present solar flux, and no greenhouse gases is about 246 K, below the freezing point of water; this corresponds to the physical temperature at a level in the stratosphere at which the Earth effectively radiates. The Earth is rescued from freezing by the greenhouse effect, which can be envisioned as being driven at temperatures below the freezing point of water by CO_2 and aided at higher temperatures by evaporated water vapor. The combination of present levels of CO_2 and H_2O is sufficient to warm the surface to 290 K, about the current average surface temperature, which is of course sufficient for liquid water.

The early Earth was illuminated by a weaker Sun, about 0.71 times the present luminosity, which without CO_2 would have resulted in an even cooler Earth, about $246(0.71)^{1/4} = 226$ K. The argument for a large amount of early CO_2 is simply that we believe that liquid water, with only intermittent glaciation, was present during most of Earth's past [*cf. e.g., Lunine* 1999, Sec. 11.10

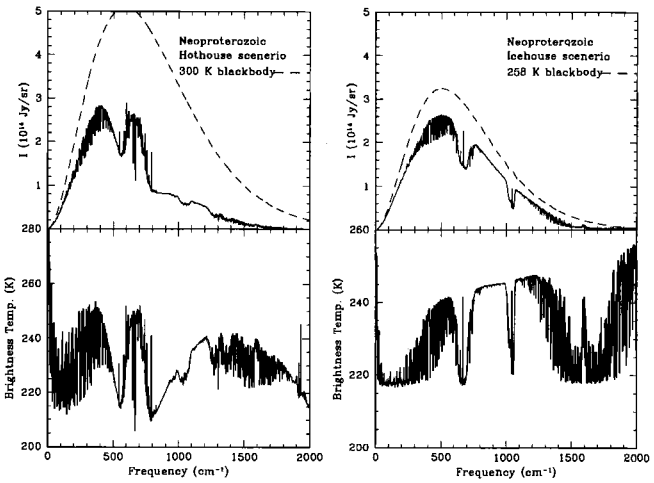

Figure 5. A calculated thermal infrared emission spectrum for a Neoproterozoic hothouse condition (left), and icehouse (right). Note the huge difference between these; for example, the 15 μm CO_2 feature is an apparent emission feature in the hothouse spectrum, but it is an apparent absorption feature in the icehouse spectrum. The apparent emission feature is a result of a warm inversion layer in the stratosphere (due to O_3 heating) combined with a CO_2 mixing ratio which gives an optical depth of about unity at the top of this layer for wavelengths in the core of the CO_2 band.

and 19.4], and this requires a large greenhouse effect, equivalent to about 0.2 bar or more CO_2. Also, since there is the equivalent of about 50 bar of CO_2 deposited in crustal rocks, the pressure may have been higher.

The level of CO_2 probably did not fall steadily since 4.5 Ga. We know that periods of major glaciation did occur, and that almost certainly these could not have begun unless the CO_2 abundance had first dropped significantly. Recently there has been a major advance in this area with the clear-cut identification of 3 major glaciation cycles alternating with warm tropical conditions at about 0.5–0.8 Ga [*Hoffman et al.*, 1998]. This period is roughly the end of the Proterozoic era (from 4.5 to 0.7 Ga), and the start of the Phanerozoic era (from 0.7 to 0.0 Ga), so the sudden glaciations are said to have produced a Neoproterozoic "snowball" Earth. The CO_2 abundances probably oscillated between roughly 0.2 bar and 0.0001 bar. The evidence for oscillation is unambiguously seen in rock layers in Namibia: repeated pairings of rounded boulders (from glaciers) topped by thick layers of carbonate rock (precipitated from seawater).

A major mystery is why these oscillations have not occurred over most of Earth's history, or more pointedly, why the oscillations started when they did and stopped after a few cycles. It is possible that the other major glaciations were accompanied by such oscillations, but this has not yet been established, or even discussed, to our knowledge.

One might expect that the icehouse state would be triggered by a sudden drop in CO_2, caused perhaps by a rapid uptake of CO_2 in the ocean, for some reason, and that the hothouse state would be triggered by the accumulation of volcanic CO_2, a direct result of plate tectonics, which at present rates would take only a geologically short interval of about 10 million years to reach greenhouse levels. However the details of the oscillations are as yet not well understood.

The implication of the Neoproterozoic oscillations for extrasolar planet searching is clear: we might encounter such a condition on an extrasolar planet, and we must be prepared to anticipate its spectral signature. We show in Figure 5 our preliminary calculation of the infrared spectra of a Neoproterozoic hothouse and icehouse Earth. To simulate the icehouse state, we use the present Arctic temperature profile, and O_2 at 1% PAL (present atmospheric level); the O_3, H_2O, N_2O, and CH_4 are modified [*Kasting*, 1980] for a 1% O_2 level, and the CO_2 is set to 100 ppm; about 1 bar of N_2 is also assumed to be present. To simulate the hothouse state, we used a present tropical temperature profile, O_2 at 10% PAL, and corresponding O_3, H_2O, N_2O, and CH_4; also CO_2 is set to 120,000 ppm.

A substantial literature is building on the snowball Earth concept, for example climate simulations [*Jenkins and Smith*, 1999; *Hyde et al.*, 2000] and realizations that life would not be totally eliminated by ice cover [*Runnegar*, 2000].

6. PLANETARY SPECTRA: METHANE

Besides CO_2, methane (CH_4) could strongly influence the surface temperature of a planet. Methane bursts may have punctuated the Earth's history. For example, carbon and oxygen isotope fractionation in marine carbonate deposits strongly imply that about 350 times the present level of CH_4 was injected into the Earth's atmosphere, during a span of less than 1000 years, about 0.055 Ga [*Bains et al.*, 1999]. The source of the CH_4 may well have been methane hydrate, which is found on the sea floor in abundance even today. That this time of injection coincided closely with a period of warming (the Late Paleocene thermal maximum) strongly suggests a cause and effect relationship between these phenomena, but it is not clear which is cause and which is effect.

Further evidence for a methane burst has been found at another epoch, 0.183 Ga [*Hesselbo et al.*, 2000]. This

event is associated with high surface temperatures and significant mass extinction. Yet other such events at 0.090 and 0.120 Ga have been similarly reported [*Kerr*, 2000]. Interestingly, each of these events, now 5 in total, occurs at about the same time that a large volume of volcanic outflow occured, and a corresponding mass extinction occured, suggesting that perhaps the volcanoes triggered the methane and this in turn triggered further warming which resulted in large-scale loss of species. Large amounts of CH_4, such as in these bursts, will produce measurable absorption features in both the infrared emission and near-infrared absorption spectra of the Earth.

7. PLANETARY SPECTRA: PRESENT VENUS AND MARS

We have calculated infrared spectra of Venus and Mars, using current models of atmospheric abundances and temperature profiles, with the added factor that the opacities of air-borne dust and aerosol droplets can be included in order to reproduce observed silicate and ice features. Clearly we have much less information on the geologic history of these planets than we do for Earth, but spectral evidence of isotopic fractionation on both planets has led to informed speculation about the past abundance of water, for example.

We show in the right panel of Figure 6 our calculated Mars spectrum using a recent model atmosphere [*Y. Yung*, 1999, private communication]. The CO_2 and H_2O features in this spectrum are a good match to many observed Mars spectra. We have repeated these calculations with the inclusion of thin ice clouds and silicate dust clouds, and these provide a reasonably good simulation of certain other observed Mars spectra. The calculations for Venus are shown in the left panel of Figure 6, based on the model atmosphere of *Bullock and Grinspoon* [2001]. This spectrum is dominated by CO_2, and does not include any aerosols, so the fact that the very bright thermal emission from the ground is not seen at the top of the atmosphere is entirely due to the opacity of the wings of the strong CO_2 bands.

8. CAN WE DETECT LIFE?

The big question, can we detect life on an extrasolar planet, was addressed in a general sense by *Lovelock*, [1965] who advocated searching for signs of chemical non-equilibrium, such as the simultaneous presence of reducing and oxidizing gases. In principle, if one knew the abundances of all species present in an atmosphere, and the boundary conditions (incident spectrum from star, surface composition, rotation rate, etc.), then one could calculate the state of photochemical and dynamical equilibrium, and its likely fluctuations, and compare this with the observed state, to see if there are significant differences which might be interpreted as signs of life, a term not included in the equilibrium calculation [*cf. Nisbet and Sleep*, 2001; *Brack*, 1998]. However our experience with the atmosphere of the present Earth tells us that the observed state is frequently not predicted by theory, so this approach may not be foolproof

From a spectroscopic point of view, it is natural to think of searching for life in terms of measuring the abundances of atmospheric constituents, and comparing these abundances with the results of calculations of thermochemical and photochemical equilibrium. In particular, the simultaneous presence of significant amounts of oxidized and reduced species, such as H_2O, CO_2, N_2O, and CH_4, or the presence of large amounts of O_2 or O_3, would both be indicators of life. Indeed both conditions are found on Earth, where there is no known means of producing anything approaching a 21% O_2 atmosphere except by photosynthesis, and the main sources of N_2O and CH_4 are biological. Earth's O_3 is produced in relatively large amounts in the stratosphere by photolysis and recombination of O_2, making it a good indicator of the presence of O_2. As signs of life in themselves, H_2O and CO_2 are secondary in importance, because although they are raw materials for life, they are not unambiguous indicators of its presence. Farther down the chain, CH_4 is a life product on

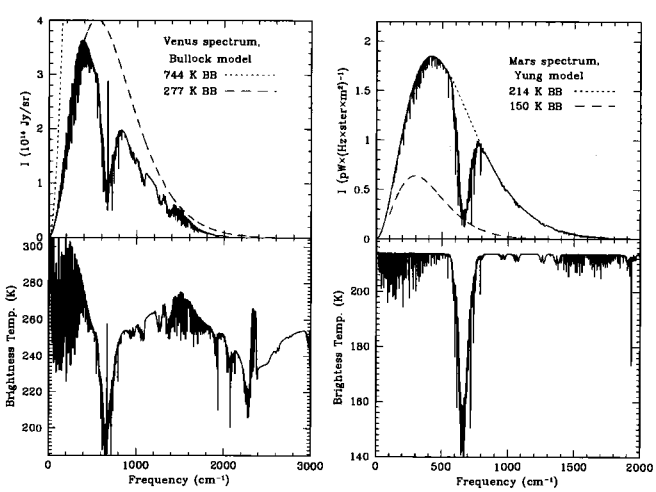

Figure 6. Calculated spectra for Venus and Mars. Both spectra are dominated by CO_2. No ice or dust features are included here, although these features are seen occasionally on Mars, and we have modeled them successfully.

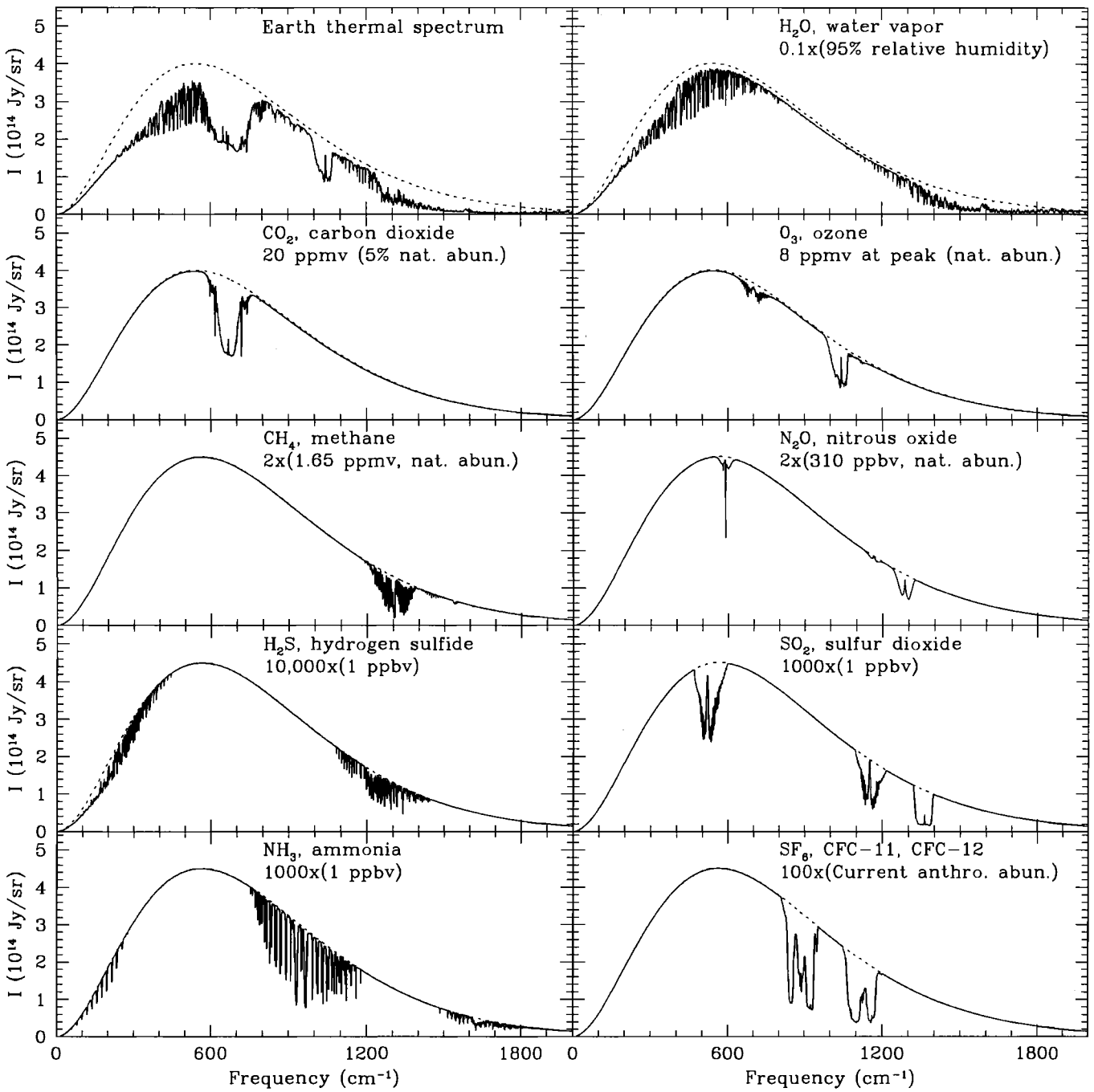

Figure 7. A calculated thermal emission spectrum of the present Earth is shown in the top left panel. The other panels show spectra of individual species, with their mixing ratio profiles scaled up or down so as to generate a maximum feature depth of roughly one-half. The calculations are performed at very high resolution and subsequently smoothed to 1 cm^{-1} for display. The panels demonstrate the concentrations needed for each species to contribute significant opacities on an Earth-like planet.

Earth, but elsewhere it is also a ubiquitous primordial species, and it is difficult to detect spectroscopically unless it is quite abundant. Likewise, N_2O is interesting because it is produced in abundance by life, and only in trace amounts by natural processes, but it can only be detected in a region which is strongly overlapped by CH_4 and H_2O, and so is an unlikely prime target.

As counterexamples, we know that small amounts of O_2 and O_3 are readily produced by non-biological means. For example, a trace amount of O_2 is seen on Venus, consistent with photochemical production from CO_2; on Mars both O_2 and O_3 are measured, but the amounts are in agreement with calculations of photochemical production from CO_2 and loss due to CO_2 and H_2O and products [*e.g., Yung and DeMore*, 1999]. In two other examples, Europa has about 10^{-11} bar of O_2 in its atmosphere (e.g., Chapter III.3), and Ganymede may have O_2 trapped in surface ice, but in both cases the observed signatures are consistent with energetic particle bombardment of a water-ice surface, and therefore they do not require a biological source.

An intriguing theory of the origin of life on Earth [*Wachtershauser*, 2000] has found experimental backing in new laboratory experiments [*Cody et al.*, 2000] which show that iron sulfide at elevated pressure and temperature can facilitate the natural generation of organometallic compounds by an autocatalytic process, in which the products of reaction catalyze the next cycle of reaction, making the process likely to be self-sustaining. This work is of interest because iron and sulfur atoms are at the center of many enzymes, and the process provides a simple explanation of their presence in living cells. The work is also of interest because it suggests that the origin of life on Earth may have been deep underground, where conditions are right for the reactions to take place, and out of the possibly less-friendly conditions on the surface of the early Earth.

The Neoproterozoic oscillations discussed above may also be critically important to the development of life on Earth, because, as the eponymic oscillations suggest, this era coincided with the explosive radiation of life forms on Earth, from simple algae types to the dramatically different types of life forms we know today. It is thought that the huge stresses, due to oscillations of temperature, nutrients, and available sunlight, imposed on simple life forms forced them to develop new adaptations in order to survive in their new environments, in what may have been the greatest Darwinian experiment ever. Thus, if we find extrasolar planets in the throes of such oscillations, we may expect that a similar life-radiation may be occuring on that planet, although we will have to wait another several tens or hundreds of million years before we can see how the experiment turns out.

Acknowledgments. This work at SAO was supported by NASA via contract JPL 1201749, and via the TPF program through a contract to Ball Aerospace & Technologies Corp.

REFERENCES

Akeson, R.L., M.R. Swain, and M.M. Colavita, Differential phase technique with the Keck Interferometer, *SPIE*, *4006*, pp. 321–327, 2000.

Bains, S., R.M. Corfield, and R.D. Norris, Mechanisms of climate warming at the end of the Paleocene, *Science*, *285*, p. 724–727, 1999.

Bastian, T.S., G.A. Dulk, Y. Leblanc, A search for radio emission from extrasolar planets, *Ap.J.*, *545*, pp. 1058–1063, 2000.

Beichman, C.A., N.J. Woolf, and C.A. Lindensmith, editors, The Terrestrial Planet Finder (TPF): A NASA Origins program to search for habitable planets, JPL Publication 99-3, 158 pp., 1999. Also see http://tpf.jpl.nasa.gov/ .

Borucki, W.J. D.A. Caldwell, D.G. Koch, L.D. Webster, J.M. Jenkens, Z. Ninkiv, and R. Showen, The Vulcan photometer: a dedicated photometer for extrasolar planet searches, *PASP*, *113*, pp. 439–451, 2001.

Brack, A., editor, The Molecular Origins of Life, 417 pp., Cambridge University Press, New York, 1998.

Brown, T.M., et al., Transmission spectra as diagnostics of extrasolar giant planet atmospheres *Ap.J.*, *553*, pp. 1006–1026, 2001.

Bullock, M.A., and D.H. Grinspoon, The recent evolution of climate on Venus, *Icarus*, *150*, pp. 19–37, 2001.

Charbonneau, D., R.W. Noyes, S.G. Korzennik, P. Nisenson, S. Jha, S.S. Vogt, and R.I. Kibrick, An upper limit on the reflected light from the planet orbiting the star tau Bootis, *Ap.J.Lett.*, *522*, pp. L145–L148, 1999.

Charbonneau, D., T.M. Brown, D.W. Latham, and M. Mayor, Detection of planetary transits across a Sun-like star, *Ap.J.Lett.*, *529*, pp. L45–L48, 2000.

Chyba, C.F., D.P. Whitmire, and R. Reynolds, Planetary habitability and the origins of life, in *Protostars and Planets IV*, edited by V. Mannings, A.P. Boss, and S.S. Russell (Univ. of Arizona Press), pp. 1365–1393, 2000.

Cody, G.D., N.Z. Boctor, T.R. Filley, R.M. Hazen, J.H. Scott, A. Sharma, and H.S. Yoder, Primordial corbonylated iron-sulfur compounds and the synthesis of pyruvate, *Science*, *289*, pp. 1337–1340, 2000.

Danner, R., and S. Unwin, editors, Space Interferometry Mission, JPL 400-811, 139 pp., 1999; also http://sim.jpl.nasa.gov.

Fridlund, M., editor, Darwin, the infrared space interferometer, concept and feasibility study report, ESA Publication ESA-SCI(2000)12, 218 pp., 2000.

Gaudi, B.S., and A. Gould, Planet parameters in microlensing events, *Ap.J.*, *486*, pp. 85–99, 1997.

Hesselbo, S.P., D.R. Grocke, H.C. Jenkyns, C.J. Bjerrum, P. Farrimond, H.S. Morgans Bell, and O.R. Green, Massive dissociation of gas hydrate during a Jurassic oceanic anoxic event, *Nature*, *406*, p. 392–395, 2000.

Hoffman, P.F., A.J. Kaufman, G.P. Halverson, and D.P.

Schrag, A Neoproterozoic snowball Earth, *Science, 281*, pp. 1342–1346, 1998.

Horner, et al., The full-sky astrometric mapping explorer - astrometry for the new millennium, in *Working on the Fringe*, edited by S.C. Unwin and R.V. Stachnik (ASP Conference Series) in press, 2001.

Horowitz, P., and C. Sagan, Five years of project META - an all-sky narrow-band radio search for extraterrestrial signals, *Ap.J., 415*, pp. 218–235, 1993.

Howard, A., and P. Horowitz, Optical SETI with NASA's Terrestrial Planet Finder, *Icarus, 150*, pp. 163–167, 2001.

Hyde, W.T., T.J. Crowley, S.K. Baum, and W.R. Peltier, Neoproterozoic 'snowball Earth' simulations with a coupled climate/ice-sheet model, *Nature, 405*, pp. 425–429, 2000.

Jenkins, G.S., and S.R. Smith, GCM simulations of snowball Earth conditions during the late Proterozoic, *GRL, 26*, p. 2263–2266, 1999.

Johnson, D.G., K.W. Jucks, W.A. Traub, and K.V. Chance, The Smithsonian stratospheric far-infrared spectrometer and data reduction system, *J. Geophys. Res., 100*, pp. 3091–3106, 1995.

Kasting, J.F., and T.M. Donahue, The evolution of atmospheric ozone, *JGR, 85*, pp. 3255–3263, 1980.

Kerr, R.A., Did volcanoes drive ancient extinctions?, *Science, 289*, pp. 1130–1131, 2000.

Konacki, M., A.J. Maciejewski, and A. Wolszczan, Improved timing formula for the PSR B1257+12 planetary system, *Ap.J., 544*, pp.921–926, 2000.

Leigh, D., and P. Horowitz, Strategies, Implementation and Results of BETA, Bioastronomy 99: a new era in bioastronomy. 6th bioastronomy meeting, Kohala Coast Hawaii, August 2-6, 1999.

Liou, J.-C., and H.A. Zook, Signatures of the giant planets imprinted on the Edgeworth-Kuiper belt dust disk, *Astron. Journ., 118*, pp. 580–590, 1999.

Lopez, B., R.G. Petrov, and M. Vannier, Direct detection of hot extrasolar planets with the VLTI using differential interferometry, *SPIE, 4006*, pp. 407–411, 2000.

Lovelock, J.E., A physical basis for life detection experiments, *Nature, 207*, pp. 568–570, 1965.

Lunine, J.I., Earth: evolution of a habitable world, 319 pp., Cambridge Univ. Press, New York, 1999.

Marcy, G., and P.R. Butler, Planets orbiting other suns, *PASP, 112*, pp. 137–140, 2000.

Marcy, G., *The search for extrasolar planets*, at the web site http://exoplanets.org , 2001.

Nisbet, E.G., and N.H. Sleep, The habitat and nature of early life, *Nature, 409*, pp. 1083–1091, 2001.

Nisenson, P., and C. Papaliolios, Detection of Earth-like planets using apodized telescopes, *Ap. J. Lett., 548*, pp. L201–L205, 2001.

Oppenheimer, B.R., S.R. Kulkarni, and J.R. Stauffer, Brown dwarfs, in *Protostars and Planets IV*, edited by V. Mannings, A.P. Boss, and S.S. Russell (Univ. of Arizona Press), pp. 1313–1338, 2000.

Perryman, M.A.C., K.S. de Boer, G. Gilmore, E. Hg, M.G. Lattanzi, L. Lindegren, X. Luri, F. Mignard, O. Pace, P.T. de Zeeuw, GAIA: composition, formation and evolution of the galaxy, *Astron. & Astrophys., 369*, pp. 339–363, 2001.

Reach, W.T., Zodiacal emission. III. Dust near the asteroid belt, *Ap. J., 392*, pp. 289–299, 1992.

Rothman, L.S., C.P. Rinsland, A. Goldman, S.T. Massie, D.P. Edwards, J.-M. Flaud, A. Perrin, C. Camy-Peyret, V. Dana, J.-Y. Mandin, J. Schroeder, A. McCann, R.R. Gamache, R.B. Wattson, K. Yoshino, K.V. Chance, K.W. Jucks, L.R. Brown, V. Nemtchinov, and P. Varanasi, The HITRAN molecular spectroscopy database and HAWKS (HITRAN atmospheric workstation): 1996 edition, *J.Q.S.R.T, 60*, pp. 665–710, 1998.

Runnegar, B., Paleoclimate: loophole for snowball Earth, *Nature, 405*, p.403, 2000.

Santos, N.C.; M. Mayor, D. Naef, F. Pepe, D. Queloz, S. Udry, A. Blecha, The CORALIE survey for southern extra-solar planets. IV. Intrinsic stellar limitations to planet searches with radial-velocity techniques, *Astron.& Astrophys., 361*, pp. 265–272, 2000.

Schneider, J., *The extrasolar planets encyclopaedia*, http://cfa-www.harvard.edu/planets/, (US mirror site for http://www.obspm.fr/encycl/encycl), 2001.

Spergel, D.N., A new pupil for detecting extrasolar planets, Appl. Optics, submitted, 2001.

Traub, W.A., and M.T. Stier, Theoretical atmospheric transmission in the mid- and far-infrared at four altitudes, *Appl. Opt., 15*, pp. 364–377, 1976.

Wachtershauser, G. Life as we don't know it, *Science, 289*, pp. 1307–1308, 2000, and references therein.

Waite, J.H., G.R. Gladstone, W.S. Lewis, R. Goldstein, D.J. McComas, P. Riley, R.J. Walker, P. Robertson, S. Desai, J.T. Clarke, and D.T. Young, An auroral flare at Jupiter, *Nature, 410*, pp. 787–789, 2001.

Wyatt, M.C. S.F. Dermott, C.M. Telesco, R.S. Fisher, K. Grogan, E.K. Holmes, R.K. Pia, How observations of circumstellar disk asymmetries can reveal hidden planets: pericenter glow and its application to the HR 4796 disk, *Ap.J., 527*, pp. 918–944, 1999.

Yung, Y.L., and W.B. DeMore, Photochemistry of planetary atmospheres, 455 pp., Oxford University Press, New York, 1999.

W. A. Traub and K. W. Jucks, Harvard-Smithsonian Center for Astrophysics, 60 Garden Street, Cambridge, MA 02138.

(email: wtraub@cfa.harvard.edu, kjucks@cfa.harvard.edu)

Can Conditions for Life be Inferred From Optical Emissions of Extra-Solar-System Planets?

Harald U. Frey

Space Sciences Laboratory, University of California, Berkeley, USA

Dirk Lummerzheim

Geophysical Institute, University of Alaska, Fairbanks, USA

The recent detection of several planets in other solar systems has revived the discussion about possibilities of extraterrestrial life and of ways of a remote detection. According to our present understanding of the development of life on Earth and the basics of a water-carbon based system, there are several environmental requirements for the development of life. These conditions, however, are necessary but not sufficient indicators for the presence of life on other planets. On Earth, early life forms had a great impact on compositional changes of the terrestrial atmosphere by the production and continued supply of free oxygen. This paper discusses spectral features of oxygen emission and absorption and the possibilities of their use for a remote characterization of the chemical composition of extraterrestrial atmospheres. Observations of planets and moons in the solar system indicate, that oxygen emissions can be produced by many processes and that only a complete characterization of an atmosphere and the detection of significant amounts of molecular oxygen can be used as an indicator for the possible existence of higher life forms.

1. INTRODUCTION

In recent years astronomers have found about 50 planets in other solar systems (see, e.g., [*Butler et al.*, 2001]). These planets were found by indirect means, measuring the change in Doppler shifted emission of the parent star, due to the gravitational interaction between the planet and the central star (see [*Traub and Jucks*, this volume]). The largest Doppler shift occurs when a high-mass planet orbits the star at close distance. Therefore, planets found so far are all high-mass giants (0.5-5 Jupiter masses). Improvement of this technique has allowed the detection of smaller planets (about the mass of Saturn) and, within coming years, further improvements for detecting slightly smaller masses can be expected. The search for such planets will certainly increase during the next decade and future space missions are planned or proposed for that purpose, such as the Terrestrial Planet Finder (TPF) [*Beichman et al.* 1999].

The discovery of extra-solar planets has re-started the discussion about extraterrestrial life, and if it would be

Atmospheres in the Solar System: Comparative Aeronomy
Geophysical Monograph 130

10.1029/130GM26

possible to detect life on these planets. The search for life so far has concentrated on the detection of signals from highly developed societies, like radio and laser signals. However, this kind of approach immediately excludes all forms of lower life and societies which, so far, have not evolved to at least human technological level. Considering that humans have used radio signals for less than 100 years, this kind of approach could only have indicated the existence of humans to other societies for the last 100 years. As the number of solar systems in less than 50 light years distance from earth is rather limited, those societies should have carefully listened and sent their reply to us shortly after they received the very first radio signals from Earth. So far, no such signal has been received.

The existence of life outside the solar system must be inferred from indirect means. This paper will first summarize the conditions for the development of life and how this life might change the environment on its planet. Then different options for detecting these conditions by optical means will be discussed.

2. CONDITIONS FOR THE DEVELOPMENT OF LIFE

The investigation of conditions for the development of life have concentrated on conditions similar to those on Earth. As we do not know of any other chemical element offering a similar vast amount of chemical combinations as the Carbon atom, we think that life should be based on a carbon-water system [*Sagan*, 1994].

Requirements for the development of higher life forms are a central star which has been stable for a sufficiently long time period, a distance between the planet and the star so that the surface temperature on the planet would be between 0° C and about 80° C, the existence of liquid water, and a stable atmosphere with considerable pressure. All these conditions limit the volume around a star with habitable conditions to a thin circular shell [*Kasting*, 1997]. Other environmental conditions like the planetary size, solid surface, tectonics, and a magnetic field helped for the development of life on Earth, but may not be necessary everywhere in the universe.

If we consider the existence of an atmosphere a basic requirement for the development of life then we can try to investigate the atmospheric composition. If a planets has an atmosphere, then it emits airglow, and if it additionally has an internal magnetic field, then we can expect aurora that can be orders of magnitude brighter than airglow or aurora from direct solar wind impact.

3. THE DEVELOPMENT OF LIFE ON EARTH

The Earth formed about 4.5 billion years ago. The release of gases from the interior formed the primitive atmosphere about 4.4 billion years ago. The composition of this primitive atmosphere was most likely dominated by carbon dioxide, with nitrogen the second most abundant gas [*Allegre and Schneider*, 1994]. Trace amounts of methane, ammonia, sulfur dioxide and hydrochloride acid were also present, but there was no oxygen. Except for the presence of abundant water, the atmosphere was similar to that of today's Venus and Mars. Carbon dioxide and/or methane played a crucial role for the development of an early greenhouse effect which permitted acceptable surface temperatures to hold liquid water and to counter act the $\approx$75 % lower solar output compared to today's radiation [*Allegre and Schneider*, 1994]. Two major processes had to change the primitive atmosphere into today's habitable composition, the reduction of CO_2 and the increase of O_2. Photolysis of H_2O and release of oxygen into such atmosphere would not drastically increase the oxygen content as the very reactive gases and surface oxidization would immediately remove it again [*Kasting*, 1997]. The huge amount of CO_2 must have been removed from the atmosphere. The most likely process is the burial of carbon into carbonate rocks, though the exact process (inorganic or biological) is still debated [*Allegre and Schneider*, 1994].

It is mostly believed that primitive algae produced oxygen. Two billion years ago, after most of the reduced minerals were oxidized, atmospheric oxygen could accumulate (Figure 1). It was either caused by, or caused the development of plants [*Kasting et al.*, 1993]. During their photosynthesis plants release oxygen into the atmosphere. The high partial pressure of oxygen can only be maintained by a continuous supply which means a stable population of living plants. If all plants on Earth would die, the atmospheric oxygen would be bound to minerals and carbon and the oxygen partial pressure would drop [*Angel and Woolf*, 1996]. A high partial pressure of oxygen in a planetary atmosphere would therefore be a good indicator for the existence of plants which could provide the opportunity for higher life forms to develop [*Allegre and Schneider*, 1994].

The presence of oxygen in the atmosphere had one more positive effect. Oxygen can easily be transformed into ozone [*Tohmatsu*, 1990]. Ozone in turn absorbs the highly dangerous solar ultra violet radiation, which would otherwise destroy larger organic molecules like DNA. This is a requirement for the development of higher life forms which could leave the oceans and populate the land.

A necessary but not sufficient indicator for the presence of life is a marked departure of the planet from thermodynamic equilibrium [*Sagan et al.*, 1993]. The simultaneous presence of large amounts of O_2 and CH_4 in the Earth atmosphere is an example of a departure from equilibrium and can only be explained with a constant supply by living organisms [*Sagan et al.*, 1993].

Because of Earth's magnetic field and its oxygen-rich atmosphere, the aurora glows brightly. To look for oxygen on other planets outside our solar system, one method could be to look for oxygen specific emissions in the aurora or the airglow from such planets.

4. GEOMETRICAL AND PHYSICAL CONSIDERATIONS

Apart from technical problems of the observation of distant planets, there are inherent physical issues too. The Sun/Earth system will be used to determine geometrical and physical parameters which observers from distant worlds would encounter.

Any signal from a planet has to be discriminated against the signal from the star. The solar spectrum can be modeled for wavelengths above 300 nm by a black body spectrum of 5777 K (Figure 2). The maximum spectral emission of such a black body is 8.3×10^7 $Wm^{-2}\mu m^{-1}$ at 502 nm wavelength (green, visible light) [see e.g. *Iqbal*, 1983]. The total spectral irradiance from such a black body at 1 AU distance is 1366 Wm^{-2}, very close to the measured solar constant of 1353 Wm^{-2}. If the thermal radiation of the Earth is modeled with a black body of 288 K, then the total spectral irradiance at 1 AU distance is 8×10^{-7} Wm^{-2}, 10^9 times smaller than from the sun. The maximum spectral emission is 31 $Wm^{-2}\mu m^{-1}$ at 9.6 μm wavelength (infrared).

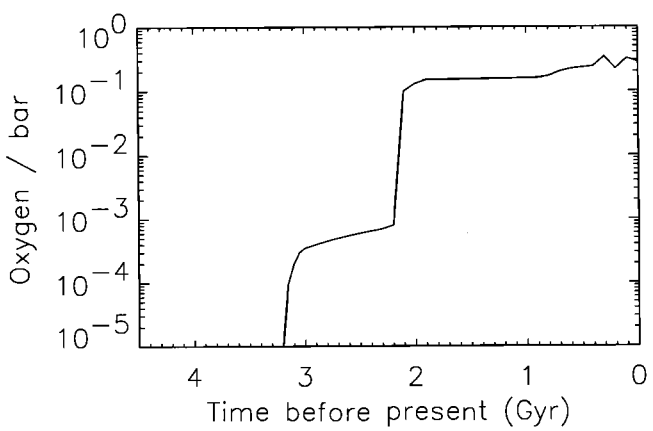

Figure 1. The composition of the Earth's atmosphere appears to have become oxygen-rich due to the presence of life, starting about two billion years ago. Redrawn and reproduced with permission from AAAS after [*Kasting et al.*, 1993].

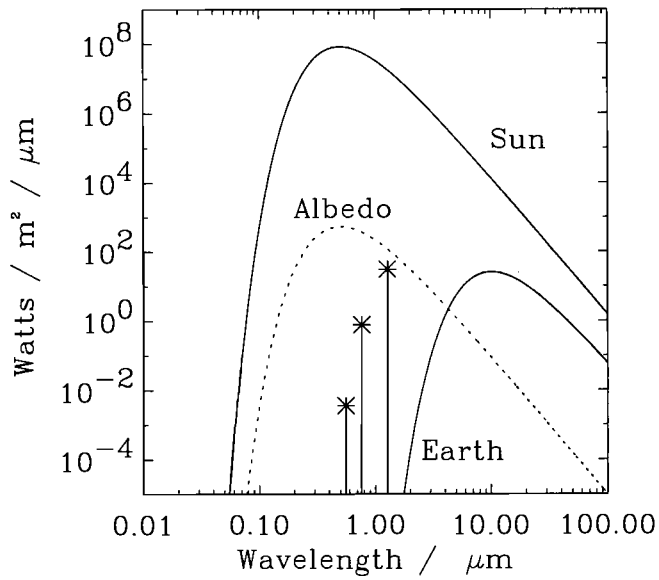

Figure 2. Spectrum of a black body with 5777 K temperature, which closely resembles that of our sun. The thermal spectrum of the Earth was calculated as a black body radiation with 288 K temperature. The albedo spectrum was calculated with an average albedo of 0.3 and the extraterrestrial solar spectrum. Some dayglow lines from Table 1 are shown and their emission was calculated for 1 nm spectral resolution.

The albedo of a planet depends on cloud cover and surface features like rocks, water or ice. On Earth an average of 30 % of the incoming solar radiation is reflected or scattered back into space [*Burroughs*, 1991]. The solar spectral irradiance at 1 AU can then be used to estimate the reflected spectrum (ignoring Rayleigh scatter, etc.). As can be seen in Figure 2, a distant observer of Earth would see a dominating effect of reflected sunlight in the spectrum below 4 μm and the thermal spectrum at longer wavelengths.

An additional difficulty of the quantitative analysis of such an observation is the unknown orientation of this planet and the planet-star line with regard to our look direction (phase). The amount of dayside, nightside, and auroral contributions would have to be determined from long term observations.

5. EMISSIONS FROM OXYGEN

There are three species of oxygen in the Earth's atmosphere: atomic oxygen at higher altitudes, molecular

Table 1. Oxygen concentrations (c in %) and typical Earth aurora, and dayglow and nightglow intensities for the terrestrial planets given in Rayleighs. Values were compiled from [*Krasnopolsky*, 1986, *Fox and Dalgarno*, 1979, 1981, *Noxon*, 1968, *Noxon et al.*, 1976, *Tohmatsu*, 1990, *Slanger et al.*, 2001 and *Vallance Jones*, 1974].

Transition	Name	Earth, c=21 %			Venus, c=0.002 %		Mars, c=0.13 %	
		Aurora	Day	Night	Day	Night	Day	Night
$O\ ^3S \rightarrow ^3P$	130.4	30000	5000	50	???	10	???	???
$O\ ^1S \rightarrow ^1D$	557.7	50000	2000	100	48000	150	12700	1
$O_2\ c^1\Sigma_u^- \rightarrow X^3\Sigma_g^-$	Herzberg	0	0	120	???	2700	???	30
$O_2\ b^1\Sigma_g^+ \rightarrow X^3\Sigma_g^-$	Atmospheric	$1.3\ 10^6$	$3.0\ 10^5$	6000	???	200	???	???
$O_2\ a^1\Delta g \rightarrow X^3\Sigma_g^-$	IR Atmospheric	$2.5\ 10^6$	$2.0\ 10^7$	10^5	$4.3\ 10^6$	$3.4\ 10^6$	$1.8\ 10^7$	???

oxygen which dominates at lower altitudes, and ozone at medium altitudes. Oxygen in an extra-solar atmosphere will interact with the light from the central star and with energetic particles from the stellar wind and the magnetospheric/auroral system. Some of the major emissions from the atmospheres of our earth-like planets are listed in Table 1.

It was suggested that one could use the green oxygen line at 557.7 nm from auroral emissions to search for extraterrestrial life [*Akasofu*, 1999]. In a reply to this suggestion *Frey* [2000] estimated that the signal from the auroral oval would generally be weaker than the signal from the dayglow of the same planet. The 557.7 nm emission arises from the spin forbidden oxygen $^1S \rightarrow ^1$D transition and can only be produced at greater heights in the atmosphere, where quenching is much reduced. Even though a stellar spectrum should not contain this line, the overall intensity in the Earth atmosphere is very weak (Figure 2) and the chances for a detection are very small. As this line is also produced in the dayglow of all terrestrial planets (Table 1), it would not even be a good indicator for the existence of a planetary magnetic field.

In the Earth dayglow the $b^1\Sigma_g^+$ state of O_2 is mostly excited by simultaneous dissociation and excitation by photons and peaks at 90 km. In the Earth nightglow the atmospheric O_2 band peaks at 94 km and is produced from the atomic oxygen O(^{3}P) state. Electronic state quenching of excited atomic oxygen is another possible source for the atmospheric band [*Rees*, 1989].

The emission of the $O_2(^1\Delta_g)$ state at 1269 nm is due to photo dissociation of ozone [*Tohmatsu*, 1990]. During daytime it is difficult to observe from the ground due to absorption in the troposphere by molecular oxygen. Weaker lines of the IR atmospheric band were used to infer the full band intensity during daylight conditions. Figure 3 shows the broad absorption in the lower atmosphere with emission cores from emission in the upper atmosphere [*Noxon et al.*, 1976]. Since the lifetime of the $a^1\Delta_g$ state is very long, this emission remains almost constant from dusk to midnight in the nightglow in spite of no new production by photo dissociation.

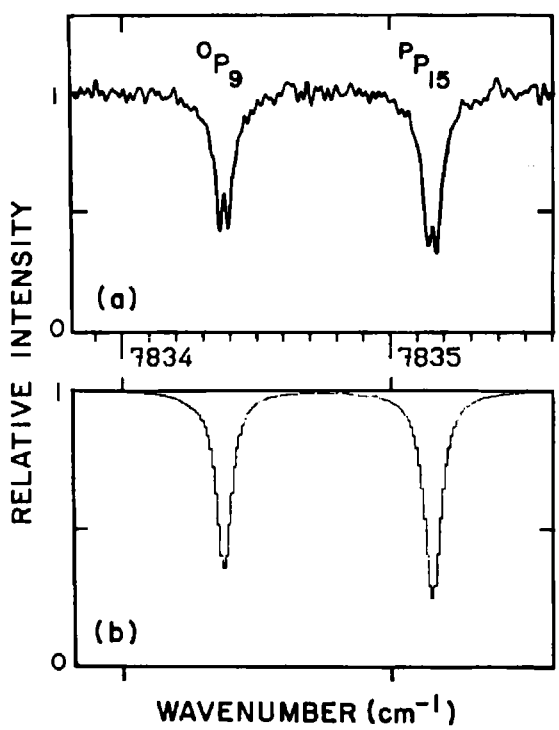

Figure 3. Two weak lines of the terrestrial O_2 IR atmospheric band dayglow which were recorded during Mars observations from the ground. The relatively broad absorption profiles were produced in the lower terrestrial atmosphere, while the emission cores were formed in the upper atmosphere. Reproduced with permission from AAS from [*Noxon et al.*, 1976].

There are advantages and disadvantages for detection of planetary emission features for various wavelength bands. Ultra-violet (UV) light is strongly absorbed by the atmosphere. The albedo is thus near zero. The black body radiation from the planet and the star is also small, so that the background near UV emission features is small compared to the brightness of the emission itself. This gives some advantage for detecting planetary UV emissions even when the planet and star can not be spatially separated. The total amount of light available from planetary UV emissions is, however, much smaller than planetary emissions in the IR.

The brightest emission in the UV is the 2^3P-3^3S^0 triplet of OI at 130.4 nm. However, there are several problems with using this emission to detect oxygen because its optical thickness complicate the quantitative evaluation and because the solar spectrum itself contains considerable emission at this line (see e.g. [*Tohmatsu*, 1990, p. 13]). It may be impossible to separate stellar and planetary emissions.

The IR and near IR emissions of a planetary atmosphere are very bright, but have to compete against the planet's black body radiation and the direct and reflected starlight. Identification of planetary IR emissions will be difficult even if spatial separation between the star and the planet can be obtained.

6. ABSORPTION BY OXYGEN

Transitions including the ground state of a molecule are the source of emission and absorption. Which process dominates is mostly determined by the partial pressure of this molecule. The atmospheric band of O_2, for instance, acts predominantly as an emitter at 50-115 km altitude and absorbs up to approximately 40 km. When stellar light reaches the surface of a planet and is partially reflected back, atmospheric oxygen will absorb some of this radiation. An external observer can try to spectroscopically search for typical absorption features.

Ozone absorbs strongly in the UV Hartley band (200-300 nm) and it weakly absorbs in the visible part between 450 nm and 850 nm (Chappuis band). Another strong ozone absorption occurs in the thermal IR at 9.6 μm, where a relatively broad band reduces the thermal emission of the Earth by about half (see [*Traub and Jucks*, this volume]). Observations of the Earth from the Nimbus satellite showed this strong absorption feature (Figure 4) [*Hanel et al.*, 1971]. They also indicate traces of CO_2, CH_4 and water. *Leger et al.* [1993] pointed out, that ozone may in some way be a better indicator for the presence of oxygen, because its abundance increases nonlinearly with the O_2 abundance.

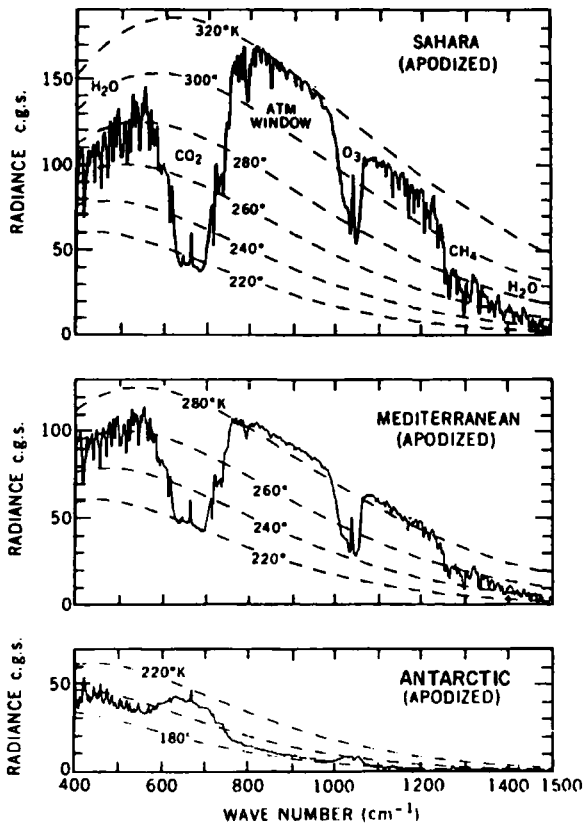

Figure 4. Spectra of the radiation emitted by the Earth-atmosphere system as measured by the Nimbus satellite above three different areas on the Earth. The radiance c.g.s. units are erg/s/cm^2/cm^{-1}. Reproduced with permission from OSA from [*Hanel et al.*, 1971].

Water vapor and molecular oxygen are the dominating absorber in the near infrared. The oxygen molecule absorbs with the (0-0) transition of the atmospheric (762 nm) and the IR atmospheric (1268.7 nm) bands, though the IR absorption is weaker [*Rees*, 1989].

The major advantage of observation in the far infrared compared to the visible is the ratio between the background radiation from the star, and the radiation from the planet itself [*Angel and Woolf*, 1996]. At the visible region this ratio is about $1/10^{10}$, and at the far infrared it is only $1/10^6$.

Until recently the specific task of identification of life on Earth by an instrumented fly-by spacecraft had never been attempted [*Sagan*, 1994]. A test of the general possibility was performed during the gravity assist encounter of the Galileo spacecraft en route to Jupiter [*Sagan et al.*, 1993]. The absorption of the O_2 atmospheric band at 762 nm and of methane at 3.31 μm

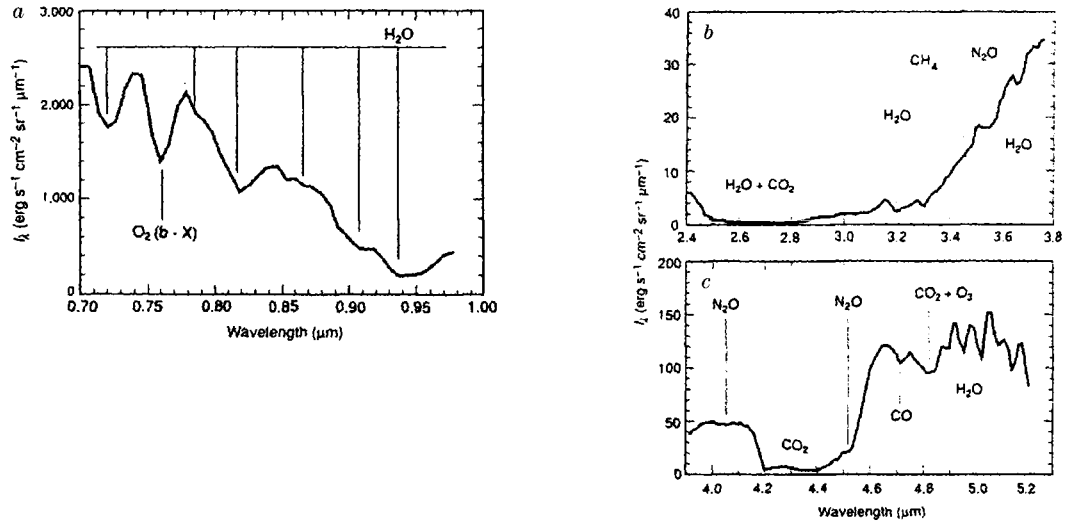

Figure 5. Spectra of the Earth in the visible and near-infrared taken by the Galileo spacecraft over relatively cloud-free region of the Pacific Ocean. The absorption of the oxygen atmospheric 0-0 band at 0.76 μm and several H_2O features together with CH_4 at 3.3 μm are evident. The concentration of methane is 140 orders of magnitude greater than the expected value from thermodynamic equilibrium and is an indicator of biological origin. Reproduced with permission from *Nature* from [*Sagan et al.*, 1993].

were evidence of a remarkable departure from thermodynamic equilibrium (Figure 5). The concentration of methane in the oxygen rich atmosphere was 140 orders of magnitude greater than its thermodynamic equilibrium value. It was concluded that only biological sources could create so large a disparity. Several other absorption features indicated large amounts of water and could lead to the conclusion of the existence of water-based biota. A similar experiment was performed by the Mars Global Surveyor spacecraft, which also detected CO_2, ozone and water absorption features in the thermal infrared [*Christensen and Pearl*, 1997].

7. WHAT CAN WE LEARN FROM OBSERVATIONS IN THE SOLAR SYSTEM?

The observation of an extra-solar planet would be very similar to that of a planet in the solar system, only the signal is very much weaker due to the much larger distance. In addition to the general feasibility of such an observation, we can also learn which results we might get from the observation of atmospheres with different composition and density.

Atomic oxygen emissions, such as the 557.7 nm, are observed on Mars and Venus [*Slanger et al.*, 2001]. However, the lack of strong absorption features in the albedo of Venus in a usual ozone range indicated that oxygen may be nearly absent [*Jenkins et al.*, 1969]. The further lack of other absorption features allowed for an estimate of the upper limit for the abundance of molecules like ammonia and sulfur dioxide. Hence we know that molecular oxygen does not exist in abundance on these planets. It is now known that the dominating process for the production of the oxygen ^1S state and the 557.7 nm emission in the Venus and Mars airglow is photo dissociation of CO_2 [*Fox and Dalgarno*, 1979, 1981]. The ^3S state and 130.4 emission arise primarily from resonance scattering on O and CO_2. The intensity of atomic oxygen emission is therefore not a direct indicator of the molecular oxygen content because it either originates from O_2 in an Earth-like atmosphere, or from CO_2 in a Mars-like atmosphere.

The spectrophotometrical investigation of the Jovian planets and Titan in the 300-1000 nm wavelength range showed many absorption features from CH_4, one of the major constituents of their atmospheres [*Karkoschka*, 1994]. Other absorption features were identified as being from Ammonia NH_3 and H_2. Another absorption feature in the Jupiter spectrum was speculated to belong to water, but no oxygen was found.

After the direct detection of ozone on Mars by the Mariner probe, measurements were performed to detect ozone with Earth-based means [*Noxon et al.*, 1976]. As in Earth's upper atmosphere, a strong dayglow arises as

a result of $O_2(^1\Delta_g)$ production from the photolysis of ozone. A search was performed to detect the IR Atmospheric band emission from Mars. The observation was carried out when the relative motion between Earth and Mars produced a sufficient Doppler shift of the Martian emission lines to move them out of the strong telluric absorption lines. The spectroscopic resolution of the instrument had to be high enough to ensure maximum contrast against the bright background of the planetary surface. The same technique was used to detect the same emission from Venus [*Connes et al.*, 1979]. The similarity of the emission rate and the production rate of fresh O atoms by photolysis on the dayside was then interpreted as an indication for strong dynamical processes in the upper atmosphere, which transport these oxygen atoms to the nightside.

Observations of the Jupiter moons Ganymede and Europa indicated that, in addition to faintly reflected sunlight, both satellites emit atomic oxygen airglow at 130.4 nm and 135.6 nm [*Hall et al.*, 1998]. The intensity of a reflected solar emission could be used to determine the albedo, and the flux ratio of the two emissions was used to estimate molecular O_2 column densities of the order of 10^{15} cm^{-2}. The spatial separation of two emission regions around the poles confirmed the occurrence of aurora and the existence of an internal magnetic field. The most likely process for the production of the molecular oxygen is direct excitation and dissociation after electron impact on water molecules [*Sieger et al.*, 1998]. There are also reports of the detection of the Hartley band of ozone on Ganymede [*Noll et al.*, 1996] and from Saturn's moons Rhea and Dione [*Noll et al.*, 1997]. The ratio of O_3/O_2 and the shift and broadening of the ozone band was used to conclude, that the ozone is not part of a gaseous atmosphere but is rather trapped in Ganymede's surface ice.

8. CONCLUSIONS

The spectroscopic investigation of extra-solar planets can certainly be considered as one of the major remaining human endeavors. The first observations will likely create more questions than final answers.

Any spectroscopic remote observation has to face two major technical challenges: the weak signal, and the huge background. The background has two contributions: the instrument background itself and the background from sources like the distant star, other astronomical objects close to the planet, and sources close to the instrument like zodiacal light from dust in our solar system [*Beichman et al.* 1999].

The observation of an extraterrestrial oxygen emission from a transition to the ground state faces the problem of the mixture with the simultaneous absorption of stellar light. As is shown in Figure 3, a mixture of absorption in the lower planetary atmosphere together with emission from the higher atmosphere and nightside would complicate the analysis. The Doppler shift which was used to separate planetary emission from terrestrial absorption [*Noxon et al.*, 1976] can not be used to separate planetary absorption and emission features as both would show the same Doppler shift.

One problem with the detection of an oxygen emission is the fact that the intensity is not necessarily a linear function of the oxygen content in an atmosphere. The intensity of the O_2 IR atmospheric band in all terrestrial planets is almost comparable, although the oxygen concentrations differ by 4 orders of magnitude, because completely different processes (photo dissociation of O_3 or CO_2) create the emission. The absorption of the planetary thermal IR spectrum by ozone also faces the problem that ozone is not a good indicator of the exact oxygen concentration [*Leger et al.*, 1993, *Beichman et al.* 1999]. On the other hand, the thermal radiation does not show such huge differences over the planetary surface as the dayglow and the nightglow, though these differences are still not negligible (Figure 4).

The advantage of operating an interferometer in the thermal IR instead of the visible spectrum is the 10^4 times larger ratio of the planet/star emission [*Kasting*, 1997]. The major technical problem is the requirement of cooling. On the other hand, the much longer wavelengths compared to the visible part of the spectrum allow for greater tolerances. Furthermore, the broad absorption bands would allow for a lower spectral resolution which could compensate for the very weak signal from the distant planet.

Observations of planets and moons in the solar system indicate, that oxygen emissions can be produced by many processes and in different environments. Just the detection of (especially atomic) oxygen can not answer the question of whether a planet harbors life. Aurora and airglow observations of distant planets can be used as a tool for the remote investigation of their atmospheres. However, only the complete characterization of the atmosphere, its content of some reduced gases like CH_4 and the presence of liquid/gaseous water, together with the knowledge of the planet's distance from the central star and its effective surface temperature, would give a good indication if the planet may be inhabited by some higher life forms [*Kasting*, 1997]. The major criterion is the partial pressure (at least several mbar, see

Figure 1) of molecular oxygen gas in the atmosphere. The first detection of oxygen will probably happen in absorption measurements due to the discussed technical reasons. The full quantitative characterization of an extra solar planetary atmosphere however, will likely be a combination of absorption measurements in the thermal IR and emission measurements in the visible/near-IR including such species as OH and N_2.

Acknowledgments. We are grateful to J. Kasting for useful discussion.

REFERENCES

Angel, J. R., and N. J. Woolf, Searching for life on other planets, *Scient. American, 274,* 60-66, 1996.

Akasofu, S., Auroral spectra as a tool for detecting extraterrestrial life, *Eos Trans. AGU, 80,* 397, 1999.

Allegre, C. J. and S. H. Schneider, The evolution of the Earth, *Scientific American, 271,* 66-75, 1994.

Beichman, C. A., N. J. Woolf, and C. A. Lindensmith (Eds.), *The Terrestrial Planet Finder (TPF): A NASA origins program to search for habitable planets,* JPL Pub., Pasadena, 1999.

Burroughs, W. J., *Watching the world's weather,* Cambridge University Press, Cambridge, 1991.

Connes, P., J. F. Noxon, W. A. Traub, and N. P. Carleton, $O_2(^1\Delta)$ emission in the day and night airglow of Venus, *Astrophys. J., 233,* L29-L32, 1979.

Butler, R. P., G. W. Marcy, D. A. Fischer, S. S. Vogt, C. G. Tinney, H. R. A. Jones, A. J. Penny, K. Apps, Statistical properties of extrasolar planets, in *Planetary Systems in the Universe: Observation, Formation and Evolution,* edited by A. Penny, P. Arlymovicz, A.-M. Lagrange, S. Russell, in press ASP Conference Series, 2001.

Christensen, P. R. and J. C. Pearl, Initial data from the Mars Global Surveyor thermal emission spectrometer experiment: observations of the Earth, *J. Geophys. Res., 102,* 10875-10880, 1997.

Fox, J. L. and A. Dalgarno, Ionization, luminosity, and heating of the upper atmosphere of Mars, *J. Geophys. Res., 84,* 7315-7333, 1979.

Fox, J. L. and A. Dalgarno, Ionization, luminosity, and heating of the upper atmosphere of Venus, *J. Geophys. Res., 86,* 629-639, 1981.

Frey, H. U., Comment on using auroral spectra to detect extraterrestrial life, *Eos Trans. AGU, 81,* 78, 2000.

Hall, D. T., P. D. Feldman, M. A. McGrath, and D. F. Strobel, The far-ultraviolet oxygen airglow of Europa and Ganymede, *Astrophys. J., 499,* 475-481, 1998.

Hanel, R. A., B. Schlachman, D. Rogers, and D. Vanous, Nimbus-4 Michelson interferometer, *Appl. Opt., 10,* 1376-1382, 1971.

Iqbal, M. *An Introduction To Solar Radiation,* 390 pp, Academic, Toronto, 1983.

Jenkins, E.B., D.C. Morton, and A.V. Sweigart, Rocket spectra of Venus and Jupiter from 2000 to 3000 A, *Astrophys. J., 157,* 913-924, 1969.

Karkoschka, E., Spectrophotometry of the Jovian planets and Titan at 300- to 1000-nm wavelength: The methane spectrum, *Icarus, 111,* 174-192, 1994.

Kasting, J. F., Earth's early atmosphere, *Science, 259* 920-925, 1993.

Kasting, J. F., Habitable zones around low mass stars and the search for extraterrestrial life, *Origins of Life and Evolution of the Biosphere, 27,* 291-307, 1997.

Krasnopolsky, V. A., Oxygen emissions in the night airglow of the Earth, Venus and Mars, *Planet. Space Sci., 34,* 511-518, 1986.

Leger, A., M. Pirre, and F. J. Marceau, Search for primitive life on a distant planet: relevance of O_2 and O_3 detections, *Astronomy and Astrophys., 277,* 309-313, 1993.

Noll, K. S., R. E. Johnson, A. L. Lane, D. L. Domingue, and H. A. Weaver, Detection of ozone on Ganymede, *Science, 273,* 341-343, 1996.

Noll, K. S., T. L. Roush, D. P. Cruikshank, and R. E. Pendleton, Detection of ozone on Saturn's satellites Rhea and Dione, *Nature, 388,* 45-47, 1997.

Noxon, J. F., Day airglow, *Space Science Rev., 8,* 92-134, 1968.

Noxon, J. F., W. A. Traub, N. P. Carleton, and P. Connes, Detection of O_2 dayglow emission from Mars and the Martian ozone abundance, *Astrophys. J., 207,* 1025-1035, 1976.

Rees, M. H., *Physics and chemistry of the upper atmosphere,* Cambridge Univ. Press, Cambridge, 1989.

Sagan, C., The search for extraterrestrial life, *Scientific American, 271,* 93-99, 1994.

Sagan, C., W. R. Thompson, R. Carlson, D. Gurnett, and C. Hord, A search for life on Earth from the Galileo spacecraft, *Nature, 365,* 715-721, 1993.

Sieger, M. T., W. C. Simpson, and T. M. Orlando, Production of O_2 on icy satellites by electronic excitation of low-temperature water ice, *Nature, 394,* 554-556, 1998.

Slanger, T. G., P. C. Cosby, D. L. Huestis, and T. A. Bida, Discovery of the Atomic Oxygen Green Line in the Venus Night Airglow, *Science, 291,* 463-465, 2001.

Tohmatsu, T., *Compendium of Aeronomy,* Kluwer, 509 pp, Dordrecht, 1990.

Vallance Jones, A., *Aurora,* Reidel Pub., Dordrecht, 1974.

H.U. Frey, Space Sciences Laboratory, University of California, Berkeley, CA 94720-7450, USA. (e-mail: hfrey@ssl.berkeley.edu)

D. Lummerzheim, Geophysical Institute, University of Alaska, Fairbanks, AK 99775. (lumm@gi.alaska.edu)